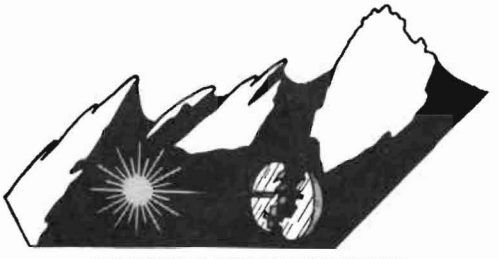
D2139U

NBS SPECIAL PUBLICATION 688

U.S. DEPARTMENT OF COMMERCE/National Bureau of Standards

Laser Induced Damage in Optical Materials: 1983



BOULDER DAMAGE SYMPOSIUM

ASTM

STP 911

HMTEC

The National Bureau of Standards[1] was established by an act of Congress on March 3, 1901. The Bureau's overall goal is to strengthen and advance the nation's science and technology and facilitate their effective application for public benefit. To this end, the Bureau conducts research and provides: (1) a basis for the nation's physical measurement system, (2) scientific and technological services for industry and government, (3) a technical basis for equity in trade, and (4) technical services to promote public safety. The Bureau's technical work is performed by the National Measurement Laboratory, the National Engineering Laboratory, the Institute for Computer Sciences and Technology, and the Institute for Materials Science and Engineering.

The National Measurement Laboratory

Provides the national system of physical and chemical measurement; coordinates the system with measurement systems of other nations and furnishes essential services leading to accurate and uniform physical and chemical measurement throughout the Nation's scientific community, industry, and commerce; provides advisory and research services to other Government agencies; conducts physical and chemical research; develops, produces, and distributes Standard Reference Materials; and provides calibration services. The Laboratory consists of the following centers:

- Basic Standards[2]
- Radiation Research
- Chemical Physics
- Analytical Chemistry

The National Engineering Laboratory

Provides technology and technical services to the public and private sectors to address national needs and to solve national problems; conducts research in engineering and applied science in support of these efforts; builds and maintains competence in the necessary disciplines required to carry out this research and technical service; develops engineering data and measurement capabilities; provides engineering measurement traceability services; develops test methods and proposes engineering standards and code changes; develops and proposes new engineering practices; and develops and improves mechanisms to transfer results of its research to the ultimate user. The Laboratory consists of the following centers:

- Applied Mathematics
- Electronics and Electrical Engineering[2]
- Manufacturing Engineering
- Building Technology
- Fire Research
- Chemical Engineering[2]

The Institute for Computer Sciences and Technology

Conducts research and provides scientific and technical services to aid Federal agencies in the selection, acquisition, application, and use of computer technology to improve effectiveness and economy in Government operations in accordance with Public Law 89-306 (40 U.S.C. 759), relevant Executive Orders, and other directives; carries out this mission by managing the Federal Information Processing Standards Program, developing Federal ADP standards guidelines, and managing Federal participation in ADP voluntary standardization activities; provides scientific and technological advisory services and assistance to Federal agencies; and provides the technical foundation for computer-related policies of the Federal Government. The Institute consists of the following centers:

- Programming Science and Technology
- Computer Systems Engineering

The Institute for Materials Science and Engineering

Conducts research and provides measurements, data, standards, reference materials, quantitative understanding and other technical information fundamental to the processing, structure, properties and performance of materials; addresses the scientific basis for new advanced materials technologies; plans research around cross-country scientific themes such as nondestructive evaluation and phase diagram development; oversees Bureau-wide technical programs in nuclear reactor radiation research and nondestructive evaluation; and broadly disseminates generic technical information resulting from its programs. The Institute consists of the following Divisions:

- Ceramics
- Fracture and Deformation [3]
- Polymers
- Metallurgy
- Reactor Radiation

[1]Headquarters and Laboratories at Gaithersburg, MD, unless otherwise noted; mailing address Gaithersburg, MD 20899.
[2]Some divisions within the center are located at Boulder, CO 80303.
[3]Located at Boulder, CO, with some elements at Gaithersburg, MD.

Laser Induced Damage In Optical Materials: 1983

Proceedings of a Symposium Sponsored by:
National Bureau of Standards
American Society for Testing and Materials
Office of Naval Research
Department of Energy
Defense Advanced Research Project Agency
Air Force Office of Scientific Research

November 14-16, 1983
NBS, Boulder, Colorado 80303

Edited by:

Harold E. Bennett
Naval Weapons Center
China Lake, California 93555

Arthur H. Guenther
Air Force Weapons Laboratory
Kirtland Air Force Base, New Mexico 87117

David Milam
Lawrence Livermore National Laboratory
Livermore, California 94550

Brian E. Newnam
Los Alamos National Laboratory
Los Alamos, New Mexico 87545



BOULDER DAMAGE SYMPOSIUM

U.S. DEPARTMENT OF COMMERCE, Malcolm Baldrige, Secretary
NATIONAL BUREAU OF STANDARDS, Ernest Ambler, Director

Issued November 1985

Library of Congress Catalog Card Number: 85:600630

National Bureau of Standards Special Publication 688
Natl. Bur. Stand. (U.S.), Spec. Publ. 688, 581 pages (Nov. 1985)
CODEN: XNBSAV

U.S. Government Printing Office
Washington:1985

For sale by the Superintendent of Documents, U.S. Government Printing Office, Washington, DC 20402

FOREWORD

The Proceedings contain the papers presented at the Fifteenth Symposium on Optical Materials for High Power Lasers held at the National Bureau of Standards (NBS) in Boulder, Colorado, on November 14-16, 1983. The Symposium was jointly sponsored by the National Bureau of Standards, the American Society for Testing and Materials, the Office of Naval Research, the Defense Advanced Research Projects Agency, the Department of Energy, and the Air Force Office of Scientific Research. The Symposium was attended by approximately 200 scientists from the United States, the United Kingdom, Israel, France, and West Germany. It was divided into sessions devoted to the following topics: Materials and Measurements, Mirrors and Surfaces, Thin Films, and finally Fundamental Mechanisms. The Symposium Co-Chairmen were Dr. Harold E. Bennett of the Naval Weapons Center, Dr. Arthur H. Guenther of the Air Force Weapons Laboratory, Dr. David Milam of the Lawrence Livermore National Laboratory, and Dr. Brian E. Newnam of the Los Alamos National Laboratory. They also served as editors of this report. Dr. Alexander J. Glass of KMS Fusion acts as Conference Treasurer with Aaron A. Sanders of the National Bureau of Standards as the Conference Coordinator.

The editors assume full responsibility for the summary, conclusions, and recommendations contained in the report, and for the summaries of discussion found at the end of each paper. The manuscripts of the papers presented at the Symposium have been prepared by the designated authors, and questions pertaining to their content should be addressed to those authors. The interested reader is referred to the bibliography at the end of the summary article for general references to the literature of laser damage studies. The Sixteenth Annual Symposium on this topic will be held in Boulder, Colorado, from October 15-17, 1984. A concerted effort will be made to ensure closer liaison between the practitioners of high-peak power and the high-average power community.

The principal topics to be considered as contributed papers in 1984 do not differ drastically from those enumerated above. We expect to hear more about improved scaling relations as a function of pulse duration, area, and wavelength, and to see a continuing transfer of information from research activities to industrial practice. New sources at shorter wavelengths continue to be developed, and a corresponding shift in emphasis to short wavelength and repetitively pulsed damage problems is anticipated. Fabrication and test procedures will continue to be developed, particularly in the diamond-turned optics and thin-film areas. Comprehensive modeling studies are, as well, anticipated.

The purpose of these symposia is to exchange information about optical materials for high power lasers. The editors will welcome comment and criticism from all interested readers relevant to this purpose, and particularly relative to our plans for the Sixteenth Annual Symposium.

H. E. Bennett, A. H. Guenther,
D. Milam, and B. E. Newnam
Co-Chairmen

DISCLAIMER

Certain papers contributed to this publication have been prepared by non NBS authors. These papers have not been reviewed or edited by NBS; therefore, the National Bureau of Standards accepts no responsibility for comments or recommendations contained therein.

Certain commercial equipment, instruments, and materials are identified in this publication in order to explain the experimental procedure adequately. Such identification in no way implies approval, recommendation, or endorsement by the National Bureau of Standards, nor does it imply that the equipment, instruments, or materials identified are necessarily the best available for the purpose.



Ann T. Glassman

1947 - 1983

How many of us will miss the smiling face, interactive personality, and professional commitment of Ann Glassman. Her untimely departure has left a void in the lives of the individuals with whom she came in contact. Nowhere will she be missed more than by those of us in the ASTM and related laser damage community.

Ann had graduated magna cum laude in physics from the University of Massachusetts, was elected Phi Beta Kappa, and received a M.S. degree in optics from the University of Rochester, to name but a few of her achievements. She had worked at the University of Dayton Research Institute and Lawrence Livermore National Laboratory before going to the Electro-optic branch of the U.S. Air Force Avionics Laboratory, Wright Patterson AFB, in 1980. But to those who read these proceedings, she will best be remembered for her tireless and often thankless efforts in developing laser standards and advancing our understanding of laser induced damage in optical materials.

We all will miss you, Ann

CONTENTS

Page

Foreword..... iii

H. E. Bennett, A. H. Guenther, D. Milam, and B. E. Newnam

Disclaimer..... iii

Memoriam..... iv

Symposium Welcome..... ix
A. H. Guenther

Welcome on Behalf of the ASTM..... xxi
J. A. Detrio

Summary of Meeting..... 1
H. E. Bennett, A. H. Guenther, D. Milam, and B. E. Newnam

1.0 Introduction..... 1

2.0 Principal Conclusions..... 2
2.1 Materials and Measurements..... 2
2.2 Surfaces and Mirrors..... 4
2.3 Thin Films..... 4
2.4 Fundamental Mechanisms..... 6

3.0 Summary of Papers..... 7
3.1 Materials and Measurements..... 8
3.2 Surfaces and Mirrors..... 12
3.3 Thin Films..... 16
3.4 Fundamental Mechanisms..... 22

4.0 Recommendations for the Future..... 26

5.0 Acknowledgments..... 27

6.0 References..... 28

Materials and Measurements

Studies of Optical and Mechanical Properties of Heavy-Metal Fluoride Glasses..... 30
B.Bendow, D. K. Burge, H. E. Bennett,
L. H. Johnston, and J. J. Mecholsky

Optical Properties of Infrared Transmitting Glasses..... 51
S. S. Mitra

Optical and Mechanical Properties of Water Clear ZnS..... 52
R. J. Harris, G. A. Graves, D. V. Dempsey, P. R. Greason,
M. E. Gangl, D. B. O'Quinn, and M. J. Lefebvre

Laser Damage in Plastics at the Frank J. Seiler Research Laboratory FJSRL)..... 59
R. M. O'Connell, T. T. Saito, T. F. Deaton, K. E. Siegenthaler,
J. J. McNally, and A. A. Shaffer

Increase in the Optical Damage Threshold of Cellulose Acetate..... 70
M. A. Acharekar

Strehl Ratio Measurements of Laser Damaged Plastics..... 80
B. W. Mullins and B. A. Richert

Damage Thresholds of Fused Silica, Plastics and KDP Crystals Measured with 0.6-ns 355-nm Pulses..... 84
M. C. Staggs and F. Rainer

Strengthening CsI Crystals for Optical Applications..... 91
W. W. Durand, B. G. Koepke, and W. W. Gerberich

Strengthening of Calcium Fluoride..... 101
C. B. Willingham, M. A. Spears, G. A. Graves,
and W. L. Knecht

Investigation of Window Materials for Repetitively Pulsed CO_2
Lasers..... 106
J. S. Goela, R. L. Taylor, M. J. Lefebvre,
P. E. Price, Jr., and M. J. Smith

Laser Induced Bulk Damage in SiO_2 at 1.064, 0.532 and 0.355 μm..... 128
L. D. Merkle, N. Koumvakalis, and M. Bass

Bulk Absorption Measurements Using Prism-Shaped Samples for Laser
Calorimetry..... 135
P. A. Temple and D. P. Arndt

Surfaces and Mirrors

Inherent Mechanical Damage in Diamond Machined Optical Surfaces..... 140
H. H. Hurt and D. L. Decker

Optical Properties of Diamond-Machined Metal Surfaces and Their Relationship to
Physical and Chemical Surface Perfection..... 147
D. L. Decker, H. H. Hurt, J. O. Porteus, and D. J. Grandjean

The Effect of Surface Finish on the Laser-Induced Damage Thresholds of Gold-Coated
Copper Mirrors..... 157
R. M. Wood, P. Waite, and S. K. Sharma

Thermally Induced Effects on the Infrared Reflectance of Metal
Mirrors..... 164
V. A. Hodgkin and D. L. Decker, and H. H. Hurt

Single-Shot, Cummulative and PRF Dependent Laser-Induced Damage
Thresholds..... 174
R. M. Wood, P. Waite, and S. K. Sharma

Damage Threshold of Fused Silica at $3\omega_o$ 179
J. F. Mengue and D. Friart

Round-Robin Testing of Low-Scatter Optics..... 183
J. M. Bennett and W. Kent Stowell

Light Scattering Characteristics of Some Metal Surfaces--A Smoothing
Effect?..... 202
J. R. McNeil, L. J. Wei, J. Casstevens, W. C. Herrmann, Jr.,
and J. C. Stover

Light Scattering from Surfaces with Microroughness and Static Density Variations
in the Bulk Dielectric Permittivity..... 211
J. M. Elson

Surface Finish Measurements on Low Scatter Laser Mirrors and Roughness
Standards..... 220
J. M. Bennett, K. H. Guenther, and P. G. Wierer

The Effects of Slope Error on the Imaging Quality of a Mirror as the Ratio of Surface
Perturbation Depth to Wavelength Approaches Zero..... 236
H. E. Bennett and D. K. Burge

Thin Films

1.06 Micron Laser Damage of Thin Film Optical Coatings - a Round Robin Experiment Involving Various Pulse Lengths and Beam Diameters..... 241
K. H. Guenther and T. W. Humpherys, J. Balmer, J. R. Bettis, E. Casparis, J. Ebert, M. Eichner, A. H. Guenther, E. Kiesel, R. Kuehnel, D. Milam, W. Ryseck, S. C. Seitel, A. Stewart, H. Weber, H. P. Weber, G. Wirtenson, and R. M. Wood

Measurements of the Dependence of Damage Thresholds on Laser Wavelength, Pulse Duration, and Film Thickness..... 268
F. Rainer, C. L. Vercimak, D. Milam, C. K. Carniglia, and T. Tuttle Hart

A Fundamental Approach Towards Improved Optical Coatings..... 277
K. L. Lewis and J. A. Savage

Development of RF-Sputtered Laser Coatings at Burleigh Northwest..... 287
D. Lunt

Comparison of Optical Coatings Deposited by Novel Physical and Chemical Techniques..... 292
F. J. Wodarczyk, D. R. Strauss, and A. B. Harker

Optical Characterization of Low-Scatter, Plasma-Deposited Thin Films..... 302
W. D. Partlow, W. J. Choyke, and J. M. Bennett, and R. M. Silva

Optical Properties of Ion-Beam Sputtered TiO_2 Films..... 311
H. Demiryont, D. B. Kerwin, and J. R. Sites

Improvement of the Damage Threshold of High Reflectivity Multidielectric Coatings at 1.06 μM..... 317
B. Geenen, A. Malherbes, J. Guerain, D. Boisgard, D. Friart, and F. Garaude

Phase Shift Variations on HEL Mirrors..... 322
T. A. Leonard and J. S. Loomis

A Review of UV Coating Material Properties..... 329
M. L. Scott

Recent Damage Results for Antireflection Coatings at 355 nm..... 340
T. Tuttle Hart, C. K. Carniglia, F. Rainer, and M. C. Staggs

Recent Damage Results on High Reflector Coatings at 355 nm..... 347
C. K. Carniglia, T. Tuttle Hart, F. Rainer, and M. C. Staggs

Alumina/Silica Multilayer Coatings for Excimer Lasers..... 354
S. R. Foltyn and L. J. Jolin

Photothermal Deflection Microscopy of HR and AR Coatings..... 360
W. C. Mundy, J. E. L. Ermshar, P. D. Hanson, and R. S. Hughes

Laser Damage in Porous-Silica Antireflection Films..... 372
W. H. Lowdermilk, J. G. Widler, N. J. Brown C. A. Gunderson, D. Milam, F. Rainer, and M. C. Staggs

Defect Damage Precursors in Visible-Wavelength Mirrors..... 378
C. D. Marrs, J. O. Porteus, and J. R. Palmer

Characterization of Micron-Sized, Optical Coating Defects by Photothermal Deflection Microscopy..... 385
J. A. Abate, A. W. Schmid, M. J. Guardalben, D. J. Smith, and S. D. Jacobs

Experimental Observation and Computer Simulation of the Microstructure of Vapor Deposited Thin Films..... 393
K. H. Guenther

A Wide Spectrum Antireflective Coating for Silica Optics and Its Damage Resistance at 350 nm..... 407
B. E. Yoldas, D. P. Partlow, and H. D. Smith

Plasma Deposited Inorganic Thin Films for Optical Applications..... 417
W. D. Partlow and J. V. R. Heberlein

Fundamental Mechanisms

Laser-Induced Emission and Laser Damage of Optical Components..... 423
D. B. Nichols, D. J. Morris, M. P. Bailey, and R. B. Hall

Charge Emission and Related Precursor Events Associated with Laser Damage..... 429
M. F. Becker, F. E. Domann, A. F. Stewart, and A. H. Guenther

Predamage Threshold Electron Emission From Insulator and Semiconductor Surfaces..... 442
W. J. Siekhaus, J. H. Kinney, and D. Milam

Laser Induced Damage of a Thin Film With an Absorbing Inclusion: Thermal Considerations of Substrates and Absorption Profiles..... 448
M. R. Lange, J. K. McIver, and A. H. Guenther

Laser Damage Threshold Predictions Based on the Effects of Thermal and Optical Properties Employing a Spherical Impurity Model..... 454
M. R. Lange, J. K. McIver, and A. H. Guenther

Analytical Model for Evaluating Transient, Steady-State, Coating Damage Threshold, Optical Distortion, and Axial Gradient for Externally Cooled Laser Mirrors..... 466
J. R. Palmer

"A Comprehensive Analytical Theory for Unifying Pulsed and Continuous Wave Laser Damage on Metal Mirrors, Encompassing the Relationship of Small Spot to Large Spot Size Damage on Metal Mirrors."..... 483
J. R. Palmer

Catastrophic versus Microscopic Damage: Applicability of Laboratory Measurements to Real Systems..... 493
S. R. Foltyn and L. J. Jolin

Toward Improved Accuracy in Limited-Scale Pulsed Laser Damage Testing via the "Onset Method"..... 502
S. C. Seitel and J. O. Porteus

The Effects of Self-Focusing on Laser Induced Breakdown..... 513
W. E. Williams, M. J. Soileau, and E. W. Van Stryland

Simple Direct Measurements of n_2..... 522
W. E. Williams, M. J. Soileau, and E. W. Van Stryland

Refractive Index of Ternary and Quaternary Compound Semiconductors Below the Fundamental Absorption Edge: Linear and Nonlinear Effects..... 532
B. Jensen and A. Torabi

APPENDIX I List of Attendees..... 551

WELCOME TO THE 15TH ANNUAL SYMPOSIUM ON OPTICAL MATERIALS FOR HIGH POWER LASERS

Dr Arthur H. Guenther
Air Force Weapons Laboratory
Kirtland Air Force Base, New Mexico

On behalf of my Co-Chairmen, Hal Bennett, Naval Weapons Center; Dave Milam, Lawrence Livermore National Laboratory; and Brian Newnam, Los Alamos National Laboratory, I would like to welcome you to the 15th Symposium on Optical Materials for High Power Lasers, our formal title. At our first meeting in 1969 it was called the Symposium on Damage in Laser Glass, the following year in 1970 it became Damage in Laser Materials and in 1972 Laser Induced Damage in Optical Materials. We had suggestions from Martin Stickley in 1974 to project a more positive image by introducing the concepts of optics reliability. In 1978 we had two suggestions, one by Harry Winsor to refer to the meeting as one on power optics while Alex Glass proposed damage avoidance. All suggestions reflect to some degree our interests, but as Hal Bennett said a few years ago, I suspect we will forever be known simply as the Boulder Damage Symposium, certainly as long as we continue to meet in Boulder, which I hope will be for a long time.

It might be of interest to pause at this 15th symposium to briefly note where we have been and speculate to some degree about where we are going. It would be impossible to do that and not recall some of the earlier stalwarts and luminaries of the meeting like Martin Stickley, already mentioned, as one of the early organizers, Johnny Myers and Haynes Lee, predecessors to John Detrio of the ASTM. And can we ever forget our frequent "words of wisdom from Winsor" (I, like more of you, feel comfortable with his already mentioned power optics to describe the general scope of this symposium). There are other individuals who have gone on to other endeavors after making their initial contributions here--Hellwarth, Marburger, Bolling, DeShazer, Guiliano, Kerr, Parks, Austin, McMahon, Bliss, Braustein, Fradin, to name but a few. There are those who are still with us from the early days--Milam, Bennett, Sparks, Bass, Edwards, and Feldman. We, of course, shouldn't overlook our frequent foreign participants who have added much in stimulating our discussions--Woods and Manenkov, to mention just two. These names and their principal interests also reflect the thrusts of our meeting over the years, e.g., let's just look at the index from the first meeting in Table I. It's refreshing to note that in the summary of that first meeting in 1969 the review started out with the following, "in a comprehensive survey of the bulk damage problem in laser glass Earlan Bliss of the Air Force Cambridge Research Laboratory stressed the importance of studying the dependence of damage thresholds on several critical parameters such as pulse duration, temperature, wavelength, and focusing configuration as a means of identifying which of several competing processes were responsible for the observed damage." There was much discussion on self-focusing with presentations from CGE (John Davit), a leader in glass laser technology at that time. While Swain talked of surface treatment by etching or repolishing, Young of American Optical talked of microinhomogenieties such as platinum and dielectric inclusions, as well as entrapped

bubbles, and their relation to the intrinsic damage level for homogeneous glasses. Some of their comments and concerns are as applicable today while in another regard we have laid to rest and passed on to other issues. In our conclusions that year we stated, "it was the goal of the symposium to review the present status of damage in laser glass. Those people most knowledgeable in the field representing government laboratories, the glass industry, laser manufacturers, and university research scientists stated their individual points of view regarding this complex and multi-faceted problem" (how many times have we used that adjective--multi-faceted). I would be remiss if I did not read the last comment by Alex Glass and myself. "In view of the number of problems remaining to be solved it is suggested that another symposium on laser damage be held in 1970. Hopefully, at that time a better understanding of the nature of damage in laser glass will be obtained. Higher threshold values will have been reproducibly achieved and some agreement can be arrived at using useful and realistic standards." Some of those desires we have achieved in an admirable manner, on others we have failed to succeed, such as in damage standards, but we are making progress as you will hear later during this meeting. The next two tables show the index from 1973, our 5th meeting. Glance at the topics and authors. As we move on to the 10th symposium shown in Tables III and IIIa you will see a continuation of the changing trends of the conference's interest as well as in its size (that was the year Jerry Bettis won our logo contest). Alex Glass, in that symposium welcome said that "it is still his annual hope that each year's symposium will be the last, not because he disliked the subject or because he found Boulder inhospitable, but that he would like to think that we could solve the problem of laser damage and move on to new challenges.

At this our 15th meeting, I appreciate Alex's earlier comments, but perhaps because of the flexibility of this meeting in moving to new problem areas as old ones are solved, I believe this meeting will die only when there is no longer a need or artereosclerosis sets in. Initially, the push was supplied by inertial confinement fusion and generally commercial applications while today we appreciate an added impetus from the defense community as evidence by President Reagan's speech calling for revolutionary defensive systems earlier this year.

It was said five years ago that the failure of optical materials either transient or permanent remains the major limit to the performance of high power laser systems. "Although there have been great advances it remains as one of the highest leverage areas for improvement" and it still is.

We must not forget that one of the purposes of these symposia and proceedings comes under the heading of consciousness raising. There is no question that this symposium series has always been willing to address new challenges and take advantage of new opportunities and certainly the proceedings have made it easy to advance the field. De Vignaud once said, "nothing holds up the progress of science so much as the right idea at the wrong time." But, I may add to that, if the work is documented properly one can go back and in many cases use those ideas when the right time does come along. After all, much of what we have recorded has been the result of a hueristic process, that is, rule of thumb which is used to guide a problem's solution, like getting the dirt out, use wide band gap materials with high melting points that are physically strong. These empirical rules are now being placed on firm quantitative footing. Furthermore, based on our improved physical understanding, sometimes we can use design tricks to get around problems. It is interesting to note that in the early days we were talking mostly about the problems associated

with easily observable catastrophic laser damage, then we concentrated on threshold conditions requiring a microscope to note the first observable pinhole and now we search for precatastrophic indicators using more sensitive approaches such as particle emission.

Over this period we have seen the growth of research groups, well regarded in the damage field such as the Naval Weapons Center, University of Southern California, Lawrence Livermore National Laboratory, Los Alamos National Laboratory, the Air Force Weapons Laboratory, and now North Texas State, together with groups outside the United States, such as G.E. Hirst, the Lebedev and the University of Hanover to name but a few. To these we could add industrial organizations, government laboratories and universities in the applied materials area as well.

The next figure attempts to show how the focus of the meeting has changed from the early emphasis on glass and the original "cry for help" which gave us the impetus to start this series of meetings. Most old issues were bulk related with self-focusing drawing the attention of experimentalists and theoreticians alike for 5 or 6 years. These interests stemmed from systems experience and much work was done in analyzing high power and high energy systems from a diffraction standpoint to avoid the failure problems. These early years were more descriptive of the interaction process addressing, among other subjects, probability and statistical issues. Then careful experimental data arrived, together with new materials, figures of merit and scaling relationships, problems principally relating to windows, and once their limits were sufficiently defined; onto surfaces and mirrors with new processing techniques such as single point diamond micromachining developed to advance their utility. The explosion of surface characterization instrumentation brought reams of revealing information to bear on our problems, too much perhaps. Finally, we could not escape thin films and recognition of them as a rat's nest of problems that must be, somehow, unwoven. Fundamental mechanisms continued at a relatively steady pace but with changes in emphasis from self-focusing to avalanches, statistics, scaling, accumulation of damage, nonlinear processes and now precatastrophic indicators and detailed thermomechanical failure analysis.

Let me now dwell a moment on thin films, the major remaining problem area when it comes to the various classes of optical materials. As many of you know, I have been concentrating my work in the thin film area for the last several years. As a result I will limit my remarks about the future to that field. I believe we are now on the verge of major improvements in the damage resistance of optical thin films. I say this for several reasons. First, I have already alluded to the improved characterization instrumentation that is available, a similar situation certainly preceded improvements in bulk and surface damage levels. Secondly, an improved and perhaps, more importantly, a great acceptance of our understanding of key issues relating to impurity initiated damage through the absorption of CW or pulsed laser radiation as a function of spot size and other parameters has evolved. And finally, through several most interesting advances in the areas of thin film deposition technology. We have as well made major improvements from a design standpoint and these tricks, if you will allow me, have worked well. The magnitude of under and over barrier layers and of nonquarterwave stacks, to name the more obvious. But we do not anticipate further major advances along those lines. The most important area, of course, is the area of deposition for its through this process that we produce useful coated optical elements. We see synergistic

relationships developing between the subjects of laser induced desorption and ion assisted deposition and what they mean in cleaning, activating, or otherwise preparing the surface for deposition. The use of the Kaufman type ion gun, a development of the National Aeronautics and Space Adminstration program in ion assisted deposition, leading to films or better microstructure, i.e., film with a structure which is on the order of 40 nanometers, random in nature, and noncolumnar and thus, less susceptible to water infiltration. Ion deposition techniques are leading to films of greater packing density, closer to bulk values with less volume for voids or impurities. Both features we feel will lead to high damage resistant films. Another emerging technique is atomic layer epitaxy (ALE) which offers films of still higher packing density and of more uniform structure. Normally the growth of films starts at random sites which then coalesces. Under these conditions it is very difficult to escape entrapped voids. ALE on the other hand deposits an atomic layer at a time, with some annealing and recrystalization of the material which apparently forms films closer to the parent materials bulk density and noncolumnar in nature. The extent to which deposition techniques such as these together with MBE, etc., will advance our ability to handle high energy and high power levels remains to be seen, but I anticipate them to be great. There is of course work underway on the laser annealing of thin films in the hopes of realizing some of the improvement noted in fused silica using a similar approach by workers at the Naval Weapons Center and Lawrence Livermore National Laboratory. Hopefully we will hear more of this work in the next few years. These impending improvements in thin film properties should also make them more stable over longer periods and more environmentally durable.

We are in good position to make use of our knowledge of the interrelationship between chemical and physical properties (structural, optical, and thermal) as regards selection of materials and predicting their performance. Laser activity in the damage area will certainly concentrate at shorter wavelengths and emphasize rep rate testing, damage accumulation, lifetime, etc., as a function of our operating parameter experience. This will come as a result of the interest in systems such as excimer and free electron lasers, etc., and will be based upon quality experimental data and computer modeling.

For several reasons we had a greater influx of papers than we expected this year, as seen in the last figure. It may be due in part to the lack of a components meeting normally held in conjunction with this symposium. We have had to do two things. Extend the meeting to 2 1/2 days. Second, we had to increase the number of poster papers from 10 to 12 each day. We are going to try something new and ask each author to give a 1 1/2 minute summary of the key aspect of his presentation. Through this we hope to accomplish many things, highlight the feature of the research, which might go unnoticed if recourse is given only to reading an abstract, written months ago, (2) let one see who the authors are (i.e., give them exposure) and (3) help them to know what some of the other poster presentations are about, which they themselves may wish to see. As usual the posters will be available in both the morning and afternoon of the first two days.

We are glad that you all have finally received your copy of the 1981 proceedings which, as you note, contained 63 papers. You will be glad to know that the 82 proceedings have gone to the printers as well and they should be in your hands shortly. The delay in the 81 proceedings in part came from accepting papers, primarily from the Soviet Union, even though they were not presented at

the meeting. They added considerably to our book's size. I guess people just want their damage related work published in these volumes. We will be looking more closely at that policy since it does add measurably to the work of the co-chairmen. The lateness of the 82 proceedings is primarily from late manuscript arrival. In this case you can help us by getting your manuscripts in on time. It has been suggested we date the manuscripts as they are received so you will all know who the good and bad guys are.

Finally, we would like to thank Bob Kamper, Aaron Sanders, Susie Rivera, Shelley Etzel, Kathy Sherlock, and Pattie Mannos. I would like to add a personal thank you to Pat Whited, my secretary, for her most welcome and professional help. We couldn't run this meeting in the style, particularly this year, without the support of our sponsors. We are thankful to the National Bureau of Standards, DARPA, ONR, DOE, AFOSR, and of course the ASTM. To all of you and especially our foreign visitors, a warm welcome to this, our 15th Boulder Damage Symposium.

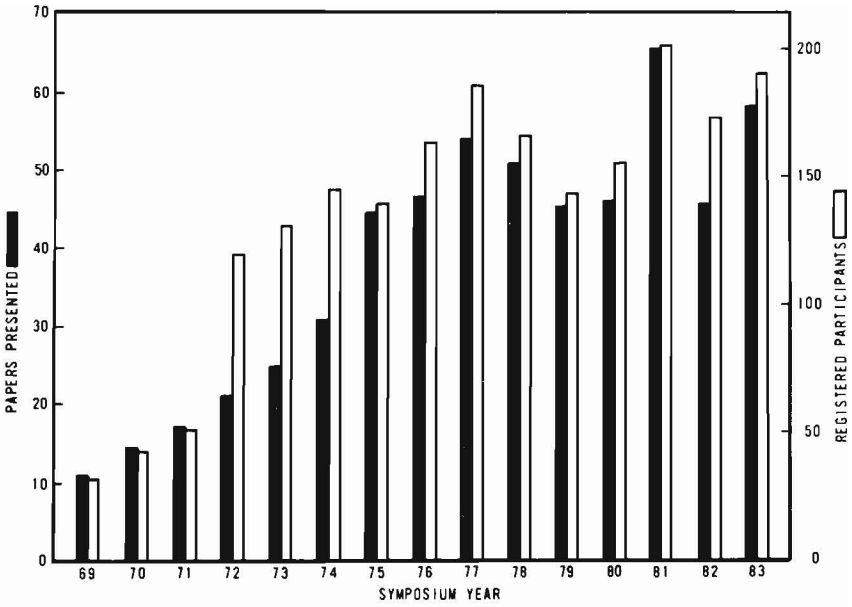

70
60
50
40
30
20
10
0
PAPERS PRESENTED
200
150
100
50
0
REGISTERED PARTICIPANTS
69
70
71
72
73
74
75
76
77
78
79
80
81
82
83
SYMPOSIUM YEAR

FIGURE 1

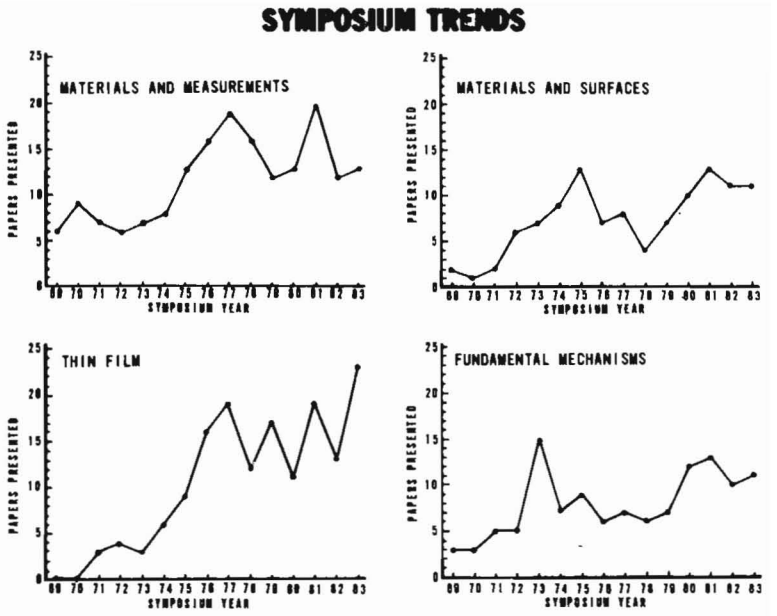

SYMPOSIUM TRENDS
MATERIALS AND MEASUREMENTS
MATERIALS AND SURFACES
THIN FILM
FUNDAMENTAL MECHANISMS
PAPERS PRESENTED
SYMPOSIUM YEAR
0
5
10
15
20
25
68 70 71 72 73 74 75 76 77 78 79 80 81 82 83

FIGURE 2

TABLE I

BOULDER DAMAGE SYMPOSIUM 1969

Laser-Damage Mechanisms in Transparent Dielectrics—E. S. BLISS . . .
Discussion . . . . . .
Laser-Beam Self-Focusing and Glass Damage Caused by Electrostrictively Driven Acoustic Waves—EDWIN L. KERR . . .
Discussion . . . . . .
Non-Destructive Damage Studies of Ruby Laser Rods—E. CHICKLIS, J. SCHWARTZ, AND CARL A. PITHA . . . . . .
Discussion . . . . . .
Applications of Electron Spin Resonance to Study of Damage in Glass Lasers—C. S. NAIMAN AND E. CHICKLIS . . . .
Surface-Damage Threshold Measurements for Several Laser Glasses —J. E. SWAIN . . . . . .
Discussion . . . . . .
Damage-Threshold Testing of Laser Glass at Owens-Illinois —H. A. LEE . . . . . .
Laser-Induced Damage in Glass—C. G. YOUNG AND R. F. WOODCOCK . . .
Discussion . . . . . .
Laser Damage in Optical Glasses—J. DAVIT . . . . . .
Discussion . . . . . .
Self-Focusing in Glass—FRED W. QUELLE . . . . . .
Glass-Laser-Materials Testing at Naval Research Laboratory —JOHN M. McMAHON . . . . . .
Discussion . . . . . .
Diagnostics and Evidence of Pre-catastrophic Damage in Transparent Solids—DAVID F. EDWARDS, Y. D. HARKER, JON D. MASSO, AND C. Y. SHE . . . . . .
Discussion . . . . . .
General Discussion . . . . . .

TABLE IIA

BOULDER DAMAGE SYMPOSIUM 1973

Opening Remarks . . . . . .
A. H. Guenther

The ARPA Program on Optical Surface and Coating Science . . . . . .
C. M. Stickley

SELF-FOCUSING

Nonlinear Refractive Index Measurements in Laser Media . . . . . .
A. Owyoung

Self-Focusing in Yittrium Aluminum Garnet and Optical Glasses . . . . . .
A. Feldman, D. Horowitz, & R. M. Waxler

A Rational Definition of Index Nonlinearity in Self-Focusing Media . . . . . .
A. J. Glass

Self-Focusing of Very Powerful Laser Beams . . . . . .
B. R. Suydam

Homogeneity Requirements for Minimizing Self-Focusing Damage . . . . . .
J. Marburger, R. Jokipii, A. Glass, & J. Trenholme

Self-Focusing and Saturation in Disk Amplifiers . . . . . .
K. A. Brueckner & J. E. Howard

Damage Control in a 100 GW High Power Laser System (Abstract only) . . . . . .
J. Tillotson, B. Guscott, & K. Moncur

SURFACE DAMAGE

Low Scatter Finishing of Optical Elements . . . . . .
W. P. Barnes

Laser Surface Damage Studies on Several Glasses . . . . . .
N. L. Boling, G. Dube', & M. D. Crisp

Some Aspects of Surface Damage That Can Be Explained With Linear Optics . . .
M. D. Crisp

Damage in Lithium Iodate With and Without Second Harmonic Generation . . . .
C. R. Giuliano & D. Y. Taeng

Laser Surface Damage Studies at Bendix . . . . . .
P. Bräunlich, J. Carrico, B. Rosenblum, & A. Schmid

Effects of Laser Flux on GaAs . . . . . .
J. L. Smith

Carrier Effects Observed In Laser-Induced Damage In A Silicon Junction Photodetector . . . . . .
J. F. Giuliani

OPTICAL COATING DAMAGE

The Role of Coating Defects in Laser-Induced Damage to Thin Films . . . . . .
L. G. DeShazer, B. E. Newnam, & K. M. Leung

The Role of Inclusions and Linear Absorption in Laser Damage to Dielectric Mirrors . . . . . .
D. Milam, R. A. Bradbury, & M. Bass

Time Resolution of Laser-Induced Damage to Thin Films . . . . . .
N. Alyassini, J. H. Parks, & L. G. DeShazer

TABLE IIB

DAMAGE TO INFRARED COMPONENTS

Investigation of Pulsed CO Laser Damage in Coated Metal Mirrors and Dielectric-Coated Windows . . . . . .
S. Holmes & P. Kraatz

Pulsed CO_2 Laser Damage Studies of Windows and Window Coatings . . . . . .
A. I. Braunstein, V. Wang, M. Braunstein, J. E. Rudisill, & J. Wada

Pulsed CO_2 Laser Damage Studies of Metal and Dielectric Coated Mirrors . . .
V. Wang, A. Braunstein, M. Braunstein, J. E. Rudisill, & J. Y. Wada

Damage Threshold in 10.6 μm Laser Materials . . . . . .
J. Davit

Radiation-Induced Damage to NaCl by 10.6 μm Fractional Joule, Nanosecond Pulses . . . . . .
W. H. Reichelt & E. E. Stark, Jr.

A Study of 10.6 μm Laser-Induced Damage in Alkali Halide Crystals . . . . . .
H. Posen, J. Bruce, J. Comer, & A. Armington

Surface and Coating Absorption Measurement With An Alphaphone . . . . . .
E. L. Kerr

THEORY AND FUNDAMENTAL PROPERTIES

Photoelastic Constants of Infrared Transmitting Materials . . . . . .
B. Bendow & P. D. Gianino

Checks of Multi-Phonon Absorption Theory . . . . . .
R. Hellwarth

Theory of Material Failure in Crystals Containing Infrared Absorbing Inclusions . . . . . .
C. J. Duthler & M. Sparks

Surface Damage by Laser-Induced Collective Electron Oscillations . . . . . .
R. A. Shatas, L. M. Narducci, J. L. Smith, H. C. Meyer, & S. S. Mitra

Studies of Intrinsic Optical Breakdown . . . . . .
D. W. Fradin & M. Bass

Laser-Induced Surface Damage in Proustite (Ag_3AsS_3) at 1.06 μm and 0.694 μm . . . . . .
C. R. Giuliano & D. Y. Tseng

Spectral Emittance Measurements on Several Crystalline Samples . . . . . .
D. L. Stierwalt

A Sensitive Interferometric Null Method for Measuring Stress-Induced Birefrengence . . . . . .
G. Birnbaum & E. Cory

TABLE III

BOULDER DAMAGE SYMPOSIUM 1978

INTRODUCTORY REMARKS

DOE Welcome--Presentation of Awards to Drs. Guenther and Glass.....
C. M. Stickley

Defense ARPA Welcome.....
H. V. Winsor

Symposium Welcome.....
A. J. Glass

MEASUREMENT OF ABSORPTION CHARACTERISTICS

Discussion of a Theory of Analysis of Rate Calorimetery which Includes Coating Absorption.....
N. C. Fernelius and G. T. Johnston

Absorption Coefficient of NaF by Attenuated Total Reflection Spectroscopy.....
D. L. Burdick

Laser Calorimetric Measurement of Two Photon Absorption.....
M. Bass, E. W. Van Stryland, and A. F. Stewart

A Comparison of Bulk and Surface Absorptions in NaCℓ and KCℓ between 9.2 and 10.8 μm.....
H. Vora, M. C. Ohmer, and T. G. Stoebe

A 1.06 μm Laser Absorption Calorimeter for Optical Coatings.....
T. H. Allen, J. H. Apfel, and C. K. Carniglia

Measured Thin Film Absorption at the Air-film Interface, the Film Bulk,
and the Film-substrate Interface.....
P. A. Temple, D. L. Decker, T. M. Donovan, and J. W. Bethke

Photoacoustic Spectroscopy Studies of Thin Film Coatings on Laser Windows.....
N. C. Fernelius and D. A. Walsh

BULK MATERIAL PROPERTIES

Piezo-optical Coefficients of Some Neodymium Doped Laser Glasses
and Single Crystals of CaF_2, BaF_2, and SrF_2.....
R. M. Waxler, A. Feldman, and D. Horowitz

Refractive Index of Strontium Fluoride.....
M. J. Dodge

The Development of Fluorides for High Power Laser Optics.....
J. F. Ready, H. Vora, R. A. Skogman, K. M. Leung, and E. Bernal G.

Optical Properties of KCℓ Forged between Optically Polished Dies.....
R. H. Anderson and J. M. Bennett

Bulk Optical Properties of Fine Grained Forged Calcium Fluoride.....
R. H. Anderson, R. A. Skogman, J. F. Ready, and J. M. Bennett

CW Laser Damage in AR Coated Alkaline Earth Flourides at 3.8 μm.....
J. A. Detrio and R. D. Petty

Lattice Absorption, Phonon Assignments, and Image Spoiling Properties of CVD ZnS
in the Infrared.....
C. Klein, B. Di Benedetto, R. Donadio, T. Kohane, and J. Pappis

Laser Induced Damage in Fluoride Glasses: A Status Report.....
S. E. Stokowski, D. Milam, and M. J. Weber

Liquids for High Repetition Rate Glass Laser Systems
J. M. Rinefierd, S. D. Jacobs, D. C. Brown, J. A. Abate,
O. Lewis, and H. Applebaum.....

TABLE IIIA

MIRRORS AND SURFACES

Physical and Optical Properties of Surfaces Generated by Diamond-Turning on an Advanced Machine
D. L. Decker and D. J. Grandjean.....

Optical and Metallurgical Characterization of Molybdenum Laser Mirrors
S. M. Wong, G. Krauss, and J. M. Bennett.....

1064 nm Laser Damage Thresholds of Polished Glass Surfaces as a Function of Pulse Duration and Surface Roughness
D. Milam.....

Large Giant and Free-running Laser Pulse Energy and Power Densities through Optical Fibers
M. J. Landry.....

THIN FILM DAMAGE

Ultraviolet Damage Resistance of Laser Coatings
B. E. Newnam and D. H. Gill.....

Multithreshold Evaluation of 100-nsec Pulsed Laser Damage to Coating Materials at 2.7 and 3.8 μm Wavelengths
J. O. Porteus, T. M. Donovan, J. L. Jernigan, and W. N. Faith.....

Multithreshold Damage Measurements on As_2S_3, As_2Se_3, and NaF at HF and DF Wavelengths
T. M. Donovan, J. O. Porteus, J. L. Jernigan, and E. J. Ashley.....

TEM Investigation of Effects of a Barrier Layer on Damage to 1.064 μm AR Coatings
C. K. Carniglia, J. H. Apfel, G. B. Carrier, and D. Milam.....

Optical Techniques for the Determination of Pulsed Laser Damage in Thin Films
T. W. Walker, A. H. Guenther, and P. E. Nielsen.....

A Statistical Analysis of Absorptive Laser Damage in Dielectric Thin Films
A. B. Budgor and K. F. Luria-Budgor.....

COATING MATERIALS AND DESIGN

New Coating Materials for IR Laser Optical Components
R. C. Pastor, J. A. Harrington, L. E. Gorre, and R. K. Chew.....

Improved PbF_2 Coatings for the Infrared
P. Baumeister, G. P. Arnold, and D. F. Edwards.....

Graded Index Coatings of Cubic Thallium Iodide (TlI) and Lead Fluoride (PbF_2)
T. J. Moravec and R. A. Skogman.....

Simple Expressions for Calculating the Effect of Volume or Interface Absorption in Thin Films on the Performance of High Reflectance or Antireflectance Multilayer Coatings
H. E. Bennett and D. K. Burge.....

Simplified Description of Dielectric Reflectors
M. Sparks and M. Flannery.....

Electric Fields near Coated Surfaces: Application to Damage Protection
H. B. Rosenstock.....

BREAKDOWN PHENOMENA

Computer Simulation of Laser Damage Morphology in the Alkali Halides
P. Kelly, D. Ritchie, P. Braunlich, and A. Schmid.....

The Relative Role of the Impact and Multiphoton Ionization Mechanisms in Laser Induced Damage of Transparent Dielectrics
B. G. Gorshkov, A. S. Epifanov, and A. A. Manenkov.....

Theory of Laser Damage in Dielectric Solids
S. Brawer and W. L. Smith.....

Laser Induced Damage in Semiconductors
Yu. K. Danileiko, A. A. Manenkov, and A. V. Sidorin.....

Frequency Dependence of Breakdown Fields in Single-Crystal NaCl and KCl
M. J. Soileau, M. Bass, and E. W. Van Stryland.....

Investigation of the Surface Breakdown Mechanism in IR-optical Materials
V. I. Kovalev and F. S. Faizullov.....

ASTM WELCOME

John A. Detrio
University of Dayton Research Institute
Chairman, ASTM Subcommittee F1.02 on Lasers

It is my pleasure to welcome you to the 1983 Boulder Damage Symposium. It is difficult to think of this as the 15th annual meeting; the field of laser damage seems as lively as ever. However, there has been a trend toward shedding more light than heat on the subject during this symposium. The early days were filled with pointed comments and controversies. Lately we have been a little more civil. Possibly another sign of maturity with the laser damage field is the convergence of experiment and theory in certain areas and greater attention to details in studying components for use in "technological" applications of laser science. Coating damage may represent the last real challenge to the systematic understanding of materials damage issues for practical components. The bulk of this year's papers concern coating damage.

I would like to share a few comments about the participation and role of the American Society for Testing and Materials. ASTM committees attempt to fulfill two purposes:

The development of standards
The dissemination of knowledge

The Boulder Damage Symposium has always been considered as addressing the secondary mission. We have hoped that at an appropriate time in the development of laser science and technology the need for standards would arise and we would be in a position to respond to the needs of the laser community.

The most significant paper with respect to justifying ASTM participation in the damage conference is the reporting of an interlaboratory comparison of 1.06 μm damage to thin films. The impetus for this round robin comes from Europe. Don't be surprised to find DIN coating damage specifications required on optics sold abroad. America's voluntary consensus standards system rarely rises to the challenge of standards development unless a clear economic threat is perceived. We in the U.S. have been invited to participate in the ISO deliberations on coating specifications but it is impractical to respond without a working organization of volunteers to support that participation. Expertise is needed to draft standards documents and to provide technical commentary on proposed standards.

If you sense the need for representing the interests of American organizations in the development of international standards, several things must be done. First, a consensus U.S. position (set of standards documents) must be developed and the U.S. must have formal representation at the Technical Group Meetings to work toward an international consensus on standards. This process can ensure that all countries receive equitable treatment but only if they invest in that participation.

I would like to thank those who provide the financial support for the Symposium including AFOSR, DARPA, DOD, ONR, and our hosts, NBS, especially Aaron Sandars and his assistants.

Once more, welcome to the Boulder Damage Symposium. Enjoy an interesting and stimulating program and an equally interesting and stimulating group of attendees.



Laser Induced Damage in Optical Materials

Fifteenth ASTM Symposium

November 14-16, 1983

The Fifteenth Annual Symposium on Optical Materials for High Power Lasers (Boulder Damage Symposium) was held at the National Bureau of Standards in Boulder, Colorado, November 14-16, 1983. The Symposium was held under the auspices of ASTM Committee F-1, Subcommittee on Laser Standards, with the joint sponsorship of NBS, the Defense Advanced Research Project Agency, the Department of Energy, The Office of Naval Research, and the Air Force Office of Scientific Research. Approximately 200 scientists attended the Symposium, including representatives of the United Kingdom, France, Israel, and West Germany. The Symposium was divided into sessions concerning Materials and Measurements, Mirrors and Surfaces, Thin Films, and finally Fundamental Mechanisms. As in previous years, the emphasis of the papers presented at the Symposium was directed toward new frontiers and new developments. Particular emphasis was given to materials for high power apparatus. The wavelength range of prime interest was from 10.6 μm to the uv region. Highlights included surface characterization, thin film-substrate boundaries, and advances in fundamental laser-matter threshold interactions and mechanisms. The scaling of damage thresholds with pulse duration, focal area, and wavelength was discussed in detail. Harold E. Bennett of the Naval Weapons Center, Arthur H. Guenther of the Air Force Weapons Laboratory, David Milam of the Lawrence Livermore National Laboratory, and Brian E. Newnam of the Los Alamos National Laboratory were co-chairmen of the Symposium. The Sixteenth Annual Symposium is scheduled for October 15-17, 1984, at the National Bureau of Standards, Boulder, Colorado.

Key words: Laser damage; laser interaction; optical components; optical fabrication; optical materials and properties; thin film coatings.

1.0 Introduction

The Fifteenth Annual Symposium on Optical Materials for High Power Lasers (Boulder Damage Symposium) was held, as in previous years, at the National Bureau of Standards in Boulder, Colorado, November 14-16, 1983. The Symposium was held under the auspices of the ASTM Committee F-1, Subcommittee on Laser Standards, with the joint sponsorship of NBS, the Defense Advanced Research Projects Agency, the Department of Energy, the Office of Naval Research, and the Air Force Office of Scientific Research. Working sessions of the Committee F-1 Subcommittee on Lasers were held on Wednesday, November 16. Approximately 200 scientists attended the Symposium, including representatives of the United Kingdon, France, Israel, and West Germany. The Symposium was divided into sessions concerning Materials and Measurements, Mirrors and Surfaces, Thin Films and finally Fundamental Mechanisms. In all, approximately 60 technical presentations were made. Harold E. Bennett of the Naval Weapons Center, Arthur H. Guenther of the Air Force Weapons Laboratory, Dave Milam of the Lawrence Livermore National Laboratory and Brian E. Newnam of the Los Alamos National Laboratory, were co-chairmen of the Symposium. Alexander J. Glass of KMS Fusion is Conference Treasurer and Aaron A. Sanders of the National Bureau of Standards acts as Conference Coordinator.

The purpose of these symposia is to exchange information about optical materials for high power lasers. The authors will welcome comments and criticism from all interested readers relevant to this purpose and particularly relative to our plans for the Sixteenth Annual Symposium, scheduled for October 15-17, 1984, at the National Bureau of Standards, Boulder, Colorado.

2.0 Principal Conclusions

One would tend to assume that after fifteen years of focused attention and hard-wrought experience on laser-induced damage to optical materials that the subject would, in general, have been laid to rest. In point of fact, we do not even have a comprehensive or coherent exposition on the subject. The best source of data and information continues to be the recorded accounts from this series of meetings, together with the attempt on the part ot the cochairman to draw conclusions, gain insight, and make recommendations as contained therein as an integral part of the proceedings. This state of affairs doesn't indicate that progress both in our understanding of the damage process and the performance of optical elements hasn't been made. They indeed have! The improvements result from a number of factors such as improved processing and manufacturing (now to "laser grade" specifications), new materials and measurements of their properties, new materials or classes of materials primarily suggested by modeling and property analysis, as well as new understanding of the basic mechanisms of damage, benchmarked by quality and sufficiently unambiguous experimental data.

The classification of the meeting into sections on Materials and Measurements, Surfaces and Mirrors, Thin Films, and Fundamental Mechanisms was appropriate for this year's symposium. But the emphasis as to operating experience, e.g., systems considerations and laser operating parameters, has changed. This especially concerns the laser wavelength and duty cycle. Emphasis has moved from the infrared through the visible to the ultraviolet. In the not too distant future we suspect that high-power laser optics for the XUV and even the x-ray regions will become of concern. The duty cycle of interest has shifted from CW through single pulse (1-on-1) to multipulse (N-on-1) to repetitive operations in the 1 to 100 pps regimes. Our expectations are that the future will demand optics for kpps to Mpps for devices like free-electron lasers. These trends will certainly place more stringent requirements on materials and their purity, growth or deposition, and fabrication to fully realize the lasers' full potential.

2.1 Materials and Measurements

This meeting continues to address the importance of careful measurements of optical and thermo-mechanical properties of optical materials. It has long been recognized that it is the absorption level and mechanical response or strength which govern failure in most instances. We have reached that stage of material quality where knowledge of the contribution of bulk and surface absorption is important. As such, new techniques are always sought which not only can measure absorption accurately but can separate the surface and bulk values. A promising technique proposed this year employs a prism-shaped sample (normal incidence at the front or entrant surface and Brewster angle at the exit surface). This sample configuration together with a polarized laser beam allows for convenient calorimetric measurement and separation of bulk and surface absorption. This adiabatic technique (uniform sample temperature with the laser off) is limited to materials with large thermal diffusivity, e.g., crystals. This year, surveys of the properties of import for infrared transmitting and heavy metal-fluoride glasses were heard together with those for water-clear ZnS. In the later material a correlation between

scattered light level and the short wavelength cutoff frequency was quite evident. The correlation between scatter and absorption level was not as evident, however.

The damage level exhibited by materials can be an indication of their intrinsic optical strength, but most assuredly it is an indication of their state of development as modified by any remaining extrinsic factors. Much data was reported this year on polymeric optical materials, both undoped and doped versions. Dye-impregnated polymers such as cellulose acetate are finding some use in range finders. Polymethylmethacrylate is currently the best condidate for plastic optics. Further efforts to remove absorbing impurities will probably increase the damage resistance of all plastics. A new technique for detecting damage was demonstrated in plexiglass G where the concurrent measurement of the Strehl ratio of a He-Ne laser beam collinear with a high-power pulsed laser was used to detect distortion of optical components within the laser beam. This technique was adequately analyzed using thermal modeling.

In another survey of damage sensitivity, it was observed that the polishing process limits the damage threshold of fused silica surfaces for 355-nm, 0.6-nsec pulses. Several types of silica all exhibited the same threshold. It was suggested that CeO_2 polishing compound was the initiating absorbing site. Subthreshold laser preirradiation of KDP was effective in raising the median damage threshold at 355 nm from 2.3 to 4.2 J/cm^2. Crystals with the lowest 1-on-1 damage threshold benefited the most from this procedure, while those with the highest threshold did not seem to improve very much. As to polymers, plastic sheets had large enough damage thresholds at 0.35, 0.53, and 1.06 μm to have potential application as shields against target debris in laser fusion experiments. In contrast, $(CH)_n$ plastic films employed as antireflection coatings on fused silica had low thresholds, discouraging further work along this avenue.

Realizing the importance of increasing the mechanical strength in transparent optics and the need to reduce fabrication costs, several approaches to these problems have been tried, from alloying (the mixing of two crustalline materials), to press forging to produce strong, low-cost polycrystalline materials primarily for use in the infrared. Heretofore, the material of choice has been CaF_2. This technique has now been extended to CsI which has been successfully press forged to obtain a 1000 psi yield strength, contrasted to 100 psi for single crystals, with no more than a 1% decrease in IR (2-40 μm) transmission.

As indicated earlier, considerable attention is being given to repetitive testing and this year two very interesting pieces of work were displayed. The first was a compilation of a variety of properties and damage test data on nineteen materials for use at 1.06 μm with 20-nsec pulses at 50 Hz. Depending on selectable operating conditions (e.g., pressure differential) and intended use, different materials were optimum. An important ancillary study addressed the wavelength (355, 532, and 1064 nm) dependence together with repetition frequency of either 1 or 10 Hz for fused silica and crystalline quartz. The damage thresholds at 355 nm were considerably lower relative to the other frequencies. It appeared that transient color centers may have been accumulating to reduce the damage thresholds. An interesting trend between

Corning 7940, Suprasil I and Sawyer crystalline quartz was observed while for multiple pulse irradiation crystalline quartz was superior.

2.2 Surfaces and Mirrors

Surface topics still reflect a preponderance of three main issues: 1) surface preparation procedures with interest both on new techniques such as float polishing and refinement of older techniques with an eye on economical, high quality and volume production such as might be achieved through single-point micro machining and forging; 2) surface properties from both a topographical and optical sense; and 3) damage testing and correlation with preparation or property differences in a generally parametric manner greatly aided by surface-analysis diagnostic instrumentation.

This year, additional insight into the surface and near-surface region of diamond machined Cu was reported through careful analysis by TEM, SEM, and STEM. As might be expected, these regions were heavily modified by the machining process resulting in correlatable optical properties. Increased IR absorption resulting from machining-induced dislocations is an example.

We are still searching for a better understanding and utilization of optical scattering. Each year we seem to make progress which, unfortunately, frequently raises more questions than it answers. One example will suffice. It was reported this year that there exists a log inverse-log relationship between minimum laser-induced damage threshold and scratch width, which was not explained. In another report on metal optics, the effects of baking on reflectivity were reported. Here, for Cu, Mo, Ag, alloys of Al, and films of various metals, reflectivity decreased typically at 0.8 μm and 9.7 μm, while surprisingly some decreased at one wavelength and were stable at another. However, for OFHC Cu and Mo reflectance generally remained stable or increased. This behavior was associated with decreased defects and improved crystallinity.

Scattering topics drew the main attention of the sessions on optical surfaces with detailed reports of round-robin testing of laser scatter optics. However, it was evident that there still is a need for inter-lab comparisons and improved diagnostics, since in many cases the roughness inferred depended on the instrument used. One might conclude that component roughness specifications require measurement procedures to be adequately stated. It is obvious that the laser has brought out the best and worst of optical surfaces from a scattering standpoint.

2.3 Thin Films

Fully forty percent of the papers presented at the conference were specific to optical thin films, a continuing indication not only of interest and attention but of hope and anticipated improvement. In fact, thin films are probably the highest leveraged area of concern to the symposium participants. Their use is pervasive and there appears to be plenty of room for advancement in performance.

As might be the case for an area of import at an ASTM meeting, several papers dealt with round-robin testing and reviews. As regards the round-robin testing of thin film damage, it was gratifying to note that in spite of gross differences in testing protocol, tested samples fit in a common rank order and differences in absolute damage threshold generally could be ascribed to testing differences, e.g., spot size, pulse length, 1-on-1, N-on-1, cleaning procedure, or damage definition based on scaling relations and data generated at this series of meetings. Other reviews evaluated damage thresholds in a parametric manner for both AR and HR film stacks particularly at shorter wavelengths.

A great preponderance of the papers on thin film related to deposition processes, either novel techniques, or improvements of older methods. Emphasis was on RF sputtering, molecular beam epitaxy, plasma deposition and ion-beam sputtered films. Many of these techniques lead to films of greater packing density at lower substrate temperature - a goal considered worthy by many. While damage results are not spectacular nor have the techniques been proven for a wide variety of coating materials, impressive strides have taken place in a short period of time. These hi-tech approaches are benefitting from greater use of in situ diagnostics and controlled atmospheres and are resulting in lower absorption levels. This is particularly true of the ZnSe films grown by MBE. Improved stability to water attack of refractory-oxide coatings of ZrO_2, SiO_2, and Al_2O_3, deposited by reactive rf sputtering, was noted. Of particular interest was the resulting stability of thin film polarizers, while studies evaluated e-beam deposition in UHV, sol-gel processes, photochemical deposition of organometallics, etc. in a comparative manner. Only e-beam deposited films yielded stoichiometic films of TiO_2. Other processes, such as dual-beam reactive-ion deposition, yielded low absorption values. Other films deposited by plasma-etched CVD techniques afforded Si_3N_4 films of almost imperceptible roughness while SiO_2 deposited in a similar manner only resulted in a value σ_{rms} = 2.8 A.

What was particularly gratifying this year was the improved correlation between deposition parameters and film structure/property. Such was the correlation of the complex refractive indices with porosity and grain size resulting from variations in background gas and ionic state.

As has been predicted for many years, the majority of thin film work is moving to shorter wavelengths. New preferred materials are surfacing such as scandia (Sc_2O_3) and magnesium fluoride (MgF_2), with which AR coatings exhibited typical thresholds of 2-3 J/cm^2 for 0.6 ns/355-nm pulses to > 5 J/cm^2 for HR coatings of the same materials tested under similar conditions. Yet thresholds as high as 9 J/cm^2 for porous-silica AR coatings have been realized, pointing to the potential of this approach where applicable. Other thin film work at 248 and 35 nm afforded 6 and 12 J/cm^2 threshold at these wavelengths for 12-15 nsec multishot irradiation, indicating a λ^2 dependence on damage sensitivity. Continued progress is noted in photo-emissive and photo thermal mapping of absorbing defects in thin films.

No section on thin films would be complete without a discussion of defects which are already the favorite initiators of thin film damage. We have heard and will hear more of the continuing search for spatially resolved defect identification. We are making improvements, although it is not easily stated whether this is due to improvements in approach, technique, instrumentation or that the films themselves are getting better. However, the occurrence of damage at identifiable defect sites has not yet been well correlated.

2.4 Fundamental Mechanisms

The subject of Fundamental Mechanisms has progressed greatly from the predominately esoteric subjects of the interaction of coherent radiation with intrinsic materials through multiphoton absorption and other non-linear behavior to avalanches, to impurity dominated thermal analysis, each step of the way becoming more complicated, more real world related in leading the way for practical application such as precatastrophic damage indication and other experimentally correlatable observables and more importantly, data analysis procedures based upon our growing understanding, a most egalitarian and utilitarian state of affairs.

As was foreseen, over the past several years precatastrophic damage indication was being sought on a broad front of diverse technical approaches. In the past it was photoacoustic or photothermal, scattering, microscopic investigation to name but a few of the dominant ones. They were all a mixed bag of success in that each technique located sites that were damage prone but unfortunately they also identified similar sites that didn't damage while other sites damaged that were undetected. This year two improvements were seen--the first related to floating a sample with IR light and immediately looking for visible wavelength emission from component surfaces. For coatings a strong correlation was evident between identified sites and damage sensitivity. One could only imagine that were the damage test wavelength used on the pretest irradiation even better correlation would have been achieved.

The other test involved precatastrophic particle emission from surfaces--ion, electrons, neutrals, etc. While this work is just beginning there appears to be information not only relating to damage sensitivity but a whole plethora of other benefits relating to conditioning, hardening, laser induced desorption as well as different behavior for different classes of materials, e.g., oxides vs fluorides which may eventually shed important insight into the physio-chemical nature of the damage process. Existing results are expected from this work in the future.

Continued progress was made this year in the modelling of impurity dominated pulsed laser induced damage to thin films. It was shown that the shape of the impurity, i.e., spherical columnar, etc., was not important as long as the volume scaled as a^3 where "a" is a linear or radial dimension, and the absorption scaled as "a" as long as irradiation is short in terms of diffusivity in cm^2/sec. Furthermore, as the impurity radius approaches zero the exponent "α" proceeds from 0.5 to 1.0 in the damage relation $E \propto (K_h t_e)^{\alpha}$ where E = damage level in J/cm^2; K_h is the thermal conductivity of the film material in J/cm·s·K and t_e is the laser pulse length in

seconds. Additional thermal analysis was presented relating to the cooling of laser components by flowing gas across the surface, a subject of considerable interest to those proposing high average power solid state crystalline or glassy laser systems. Other analytical prsentations evaluated temperature rises for metals irradiated either in the CW or pulsed mode.

Two important papers treated, from a fundamental standpoint, distinctions between microscopic and catastrophic damage and accuracy improvements resulting from the onset method vis a vis normal definitions where damage is frequently defined as midway between least fluence damage and maximum fluence no-damage values. There is no question but that we must standardize on the best damage definition and data analysis procedure. Maybe after fifteen years, the long hoped for standard damage test and agreed upon definitions are taking shape. Let's hope so!

There is often great value in returning to review results relating to a specific phenomenon to see if it all fits our understanding. From a particularly eloquent review of the effects of self focusing on laser induced breakdown, we now seem to have in hand a unified theory tying together variations between linear and circularly polarized light, wavelength, critical power and spot size. Perhaps we now can determine not only the limits imposed by selffocusing but approaches to minimize it and to understand the beam distortion resulting from it. It is not surprising that this same group identified a simple and direct method of determinig the non-linear index n_2 of paramount importance when dealing with self focusing. The rather elegant approach involves measuring the far-field pattern of a laser beam which has been focused gently through a highly transparent material, such that the deviation from a gaussian in the far field is proportional to an induced phase distortion in the medium.

Additional data indicating the level of understanding of the linear and nonlinear index of refraction was given by comparing the experimental index values to ternary and quaternary compound semiconductors below the fundamental absorption edge as calculated from first principles. Agreement to within an order of magnitude is presently obtained.

3.0 Summary of Papers

The subject matters of the Fifteenth Annual Symposium covered four, broad areas of interest to the high-power laser community: (1) Materials and Measurements, (2) Materials and Surfaces, (3) Thin Films, and finally, (4) Fundamental Mechanisms. These conference proceedings are organized accordingly. In this section, a concise summary of each paper is provided. Closely related papers are discussed together, whenever possible. The interested reader is referred to the complete manuscript of any paper for further details. Our intention here is to provide the reader with an overview of the Symposium and to identify the topics of current interest, the authors, and their organizations. To highlight this year's presented papers, each topical area is discussed with a brief statement of the underlying problems and the status of understanding within the area of interest.

3.1 Materials and Measurements

Optical material properties and the measurement thereof are continuing interests of the meeting along with the other historical topics such as bulk damage and fabrication. This year several papers dealt with both new mater ials and reviews of more classical ones.

The reporting of properties of new materials has become an important aspect of the Boulder Damage Symposium. This year was no exception. B. Bendow of the BDM Corporation, D. Burge and H. Bennett of the U. S. Naval Weapons Center, L. Johnston of the University of Idaho, and J. Mecholsky of the Sandia National Laboratory delved into the optical and mechanical properties of heavy-metal flouride (HMF) glasses for use in numerous applications, particularly those of high energy laser and electro-optic IR scenarios. The types of glasses studied included various fluoro-ziconates, rare-earth fluorides and transition-metal fluorides. Properties measured included IR absorption and emittance, total integrated scatter, fracture resistance, and thermal stress resistance, among others. Absorption co-efficients as low as 4×10^{-3} cm^{-1} at the DF wavelength were measured with fracture resistance ~1/3 that of fused silica. One disappointing disadvantage of these glasses is their susceptibility to chemical corrosion in aqueous environments.

Careful measurements of the properties of materials suitable for high power/high energy laser applications are essential in the design of high performance systems. To this end, R. Harris, G. Graves, D. Dempsey, P. Greason, M. Gangl, and D. O'Quinn of the University of Dayton Research Institute and M. Lefebvre of CVD Inc. reported on the optical and mechanical properties of ZnS including the measurement of absorption coefficients at several wavelengths, spectral transmission, thermo-optic and stress-optic coefficients, thermal expansion coefficient, as well as the density, specific heat,thermal diffusivity, and electrical resistivity. ZnS is useful over the whole spectral range from 0.4 to ~11 μm. Property variation as a function of process variation was also given. There was some evidence of a correlation between scattered light values and effective absorption coefficients and the short wavelength cutoff.

The subject of polymeric materials has been growing in interest, stimulated both by their low cost, ease of fabrication and potential high damage threshold as reported by several Soviet scientists. In, addition, they can be doped with dyes quite uniformly for a variety of applications.

Stimulated by recent Soviet achievements, a program devoted to further improvement of plastic optics was begun at the F. J. Seiler Research Laboratory at the U.S. Air Force Academy. The results of extensive single-shot and multiple-shot bulk damage studies were presented by this group which included R. O'Connell of the University of Missouri and T. Saito, T. Deaton, K. Siegenthaler, J. McNally, and A. Shaffer of the U.S. Air Force Academy. Materials studied included polymethylmethacrylate (PMMA), three grades of polycarbonate (PC), and cellulose acetate butyrate (CAB). Small-spot (46 μm 1/e diameter) single-shot damage thresholds, using 8-ns pulses from a Nd:YAG laser were 41, 15, and 15 J/cm^2 respectively. These values correlated

with the relative level of absorbing impurities in these materials. PMMA also had the largest multiple-shot threshold. Efforts to purify PMMA were rewarded by a 60 percent increase in damage resistance. Continued work to attain high-purity plastics can be expected to realize even greater improvement.

Continuing the section on polymers, M. Acharekar of International Laser Systems presented a discussion of the damage resistance of cellulose acetate which, when impregnated with a dye, is commonly used in passive Q-switches in small rangefinders. At present, commercially available cellulose acetate is too impure to use in high power applications because of a high residual impurity level, damaging at 20 mJ output energy in 20 μsec pulses under 10 Hz laser operation. As might be expected, treated or "cleared" cellulose acetate exhibited a considerable improvement in damage resistance. Unfortunately, important processing details to produce "cleared" plastic Q-switches were omitted from the paper. Review of related plastic optics papers by Manenkov and Saito at this meeting should be of considerable benefit to the interested reader.

To characterize permanent damage of plastic optical components, B. Mullins of the U.S. Air Force Academy and B. Richert of the U.S. Air Force Weapons Laboratory have devised a convenient technique to quantitatively sense the onset of damage during irradiation. Briefly, an auxiliary He-Ne beam is directed through the plastic component and focussed on a photodiode by which the Strehl ratio is determined. This method senses small wavefront distortion caused by permanent damage sites of significant diameter. Plexiglass G (polymethylmethacrylate) was evaluated with a Nd:YAG system, and damage-induced wavefront distortions as low as 0.009λ to 0.030λ were inferred to produce Strehl ratios of 0.995.

In support of the Nova glass laser fusion facility being constructed at Lawrence Livermore National Laboratory, M. Staggs and F. Rainer characterized the damage resistance at 355 nm of fused silica, KDP crystals, and a few selected plastic sheets. Measurements were conducted with a frequency-tripled Nd:YAG laser producing 0.6 ns pulses focussed to a relatively large 1-mm beam diameter (at 1/e intensity). Single-shot-per-site damage thresholds of the surfaces of three types of flame-fused silica and two types of fused natural quartz were measured. No correlation of the thresholds with the type of silica was found; however, a relationship with the surface state due to the polishing process was observed. HF etching of surfaces with low thresholds revealed significant subsurface structure, whereas etched surfaces having The authors speculted that entrapped particles of CeO_2 polishing compound, an absorber at 355 nm, were the principal sites of damage initiation.

Consistent with the results of previous tests at Livermore and Los Alamos, bulk damage in KDP took the form of isolated microfractures which generally occurred at fluence levels below the onset of surface damage. The median 1-on-1 and n-on-1 thresholds of these crystals were 2.3 and 4.2 J/cm^2, respectively. Thus, the great importance of subthreshold irradiation was again demonstrated for 355-nm irradiation as in previous tests at 1064 nm. Those crystals with the lowest one-on-one thresholds benefitted most from this procedure; negligible effect was seen for crystals with the highest thresholds.

Plastic sheets have potential application in the optical train of fusion lasers to shield expensive focussing lens from target debris. One material, FEP Teflon, was found to have substantial damage resistance: 3, 7, and 12 J/cm^2 for ~1-ns pulses at 355, 532, and 1064 nm, respectively. Even at higher laser fluences, it is possible that this material would serve as an effective shield if it would remain intact during one shot and minimally perturb the beam. Previously, Mylar films have been successfully used in the Los Alamos Helios CO_2 laser fusion test facility for a similar purpose (protection of optical components from retropulses).

Finally, $(CH)_n$ plastic films (deposited by plasma polymerization) were evaluated as antireflection coatings on fused silica. The very low damage threshold of 0.5 J/cm^2 at 355 nm, however, eliminated these from further consideration.

Strengthening of crystalline materials- particularly those that can be forged, has received considerable attention at these meetings. This year was no exception where reports on advances relating to CsI and CaF_2 were heard.

Cesium iodide, an important optical material for infrared windows because of its broad spectral transparency, suffers from its very low mechanical strength. For other alkali halide crystals with rock salt structure, e.g., KCl and NaCl, over an order of magnitude, increase in yield strength has been attained by hot press forging of single crystals to obtain a fine-grained polycrystalline structure. These crystals have a sufficient number of independent slip systems, so that above 200°C stress is relieved by plastic flow. Unfortunately, CsI has the body-centered cesium chloride structure with limited slip systems which makes forging without fracture much more difficult. However W. Durand, B. Koepke, and W. Gerberich of the Honeywell Systems and Research Center have developed a successful forging method for CsI which uses symmetric deformation geometrics to produce simultaneous flow along more than one slip system. Single crystals of pure CsI (99.999 percent) of 1.3-cm diameter and height were forged to a 50-percent reduction in height. An initial strain rate of not larger than 0.004 min^{-1} was necessary to avoid internal fracture, and the largest increase in yield strength (1014 psi compared to 100 psi for single crystal) was obtained at a low forging temperature of 30°C. No recrystallization was observed and the optical transmission between 2 and 40 μm was only 1 percent less than that for single-crystal CsI. The authors consider that scale up to 6-inch diameter windows is feasible.

Over the last ten years, the U.S. Air Force Wright Aeronautical Laboratories (AFWAL) has sponsored a number of experimental studies to determine and optimize processes which achieve mechanically strong optical window materials. Materials studied have included KCL, Al_2O_3, ZnS and CaF_2. This year C. Willingham and M. Spears of the Raytheon Company, G. Graves of the University of Dayton Research Institute (UDRI) and W. Knecht of AFWAL reported their progress in strengthening fusion-cast CaF_2, scalable to 30-cm diameters.

Elimination of surface flaws and application of a biasing surface com pressive stress were the two approaches taken. Increased grain-boundary strength was achieved at Raytheon by (1) melting CaF_2 powder in an atmosphere of CF_4 and hydrogen, which fluorinates the oxide and hydroxide contaminants, and (2) multiple remelting. A mean strength of 13.3 + 5.3 kpsi was achieved. A second process, the diffusion of strontium ions into the CaF_2 surface at high temperature (800 to 1100°C) resulted in no significant strengthening because of plastic yielding and stress relaxation. Performed at lower temperature (400 to 500°C), however, a large residual compressive stress remained. The strength was not reported for these cases.

Finally, UDRI utilized a high-fluorinating, low-oxygenating reducing gaseous atmosphere (pyrolized polytetra-fluorethylene and dry hydrogen) to achieve enhanced strength of CaF_2 castings. The average value for 24 one-inch diameter specimens was an impressive 19 ± 7 kpsi, almost a factor of two beyond the previous standard.

We continue to receive reports on damage to bulk materials. However, they now center on repetitive irradiation or shorter wavelengths. Since failure is mainly a thermal process governed by the absorption level, accurate measurements of the absorption coefficient at the surfaces and within the bulk are essential as is the identification of absorbing defects.

J. Goela of the Indian Institute of Technology, Kampur, R. Taylor, M. Lefebvre, and P. Price, Jr. of CVD, Inc. and M. Smith of Avco Everett Research Laboratory, Inc., compiled optical, thermal, and mechanical data for 19 candidate window materials and evaluated the materials for use in 10.6-μm, 20-ns lasers operating at up to 50 Hz with a two-atmosphere pressure differential across their windows. The fluence per pulse was assumed to be 14 J/cm^2 over a round aperture 30 cm in diameter. The authors considered window failure due to passive pressure loading, and/or cracking and melting in laser heated windows. They also considered beam perturbations caused either by thermal lensing or by window flexure under pressure. No one material was optimum in all aspects. The salts (NaCl, KBr and KCl) should satisfy beam distortion criteria, but are probably not strong enough to withstand thermal stresses; the materials ZnSe, GaAs, CdTe, and CdSe are tolerant of stresses, but will produce beam distortion. In initial damage testing with 15-μsec, 10.6-μm pulses from a 20-Hz laser focused to a beam with an area of 1 cm^2, samples of GaAs and ZnSe sometimes withstood single irradiations at fluences of 15-20 J/cm^2, but only CLEARTRAN ZnS withstood as many as 20 pulses at 20 to 25 J/cm^2.

The physics governing multiple-shot laser damage is more complicated than that in single-shot experiments due to the possibility of an accumulation of effects, such as color centers, microdamage, recrystallization, or surface cleaning. In an attempt to clarify this complex multiple-shot behavior, the attention of L. Merkle, N. Koumvakalis, and M. Bass of the Center for Laser Studies at the University of Southern California has been concentrated on bulk damage in SiO_2 as a function of wavelength. Last year they reported results for 1064 and 532 nm wavelengths and found that repeated irradiation made catastrophic damage more likely. However, no associated precursor phenomena, such as absorption or light scattering, could be detected

prior to a damaging pulse. This year they reported extended studies to 355 nm as well. The test parameters included 15- to 25-ns laser pulses focussed to 5- to 15-μm spotsize (e^{-2} radii), at a repetition rate of 10 Hz. Samples of fused silica (Corning 7940 and Suprasil 1) were compared with crystalline quartz (Sawyer). The general results for these tests were that multiple-pulse damage showed a much stronger dependence on material, spotsize, pulse duration, and wave length than the single-pulse damage. Among the specific findings we mention two: Whereas single-shot thresholds for all three materials were essentially identical, this was not the case for multiple-shot irradiation. Crystalline quartz withstood repeated irradiation much better than the fused silicas. For both fused and crystalline SiO_2 at 355 nm, the damage resistance for 10 Hz irradiation was significantly less. The possibility of transient color centers was advanced as an explanation. This is clearly a fertile area for continued research.

Separation of the bulk and surface contributions to the total absorption of transparent window materials is necessary for determining the effects of different polishing and window-growth techniques. Calorimetric measurements using several samples of various thickness permits this surface/bulk discrimi nation, but the approach is time consuming and subject to sample-to-sample surface variations. To avoid both of these problems, P. Temple and D. Arndt of the Michelson Laboratory described a calorimetric method which utilizes a single prism-shaped test sample. The prism angles are chosen to allow the polarized laser beam to enter the prism at nor mal incidence and exit the prism at Brewster's angle which eliminates internal reflections. Measurements made at various positions along the prism yield the desired absorption versus length with minimal surface absorption fluctuations. The calorimeter is operated in an adiabatic mode whereby the initial and final sample temperatures are measured after the laser is turned off and the entire sample is at a uniform temperature. For materials with large thermal diffusivity the data are very nearly independent of the position of the temperature detector and the position of laser irradiation. Significant systematic errors would occur for materials with low thermal diffusivity values, such as glass and fused silica. Satisfactory measurements were obtained for CaF_2 for DF laser irradiation (3.6 to 4.0 μm wavelength) providing bulk and two-surface absorption contributions of 2.1×10^{-5} cm^{-1} and 1.5×10^{-4} (unitless), respectively. (Reproducibility of repeated measurements within ±5 percent was demonstrated.) For a 1-cm thick window, this indicated that ten times more absorption occurred at the surfaces than in the bulk.

3.2 Surfaces and Mirrors

Surfaces require special attention in high-energy or high-power laser systems. As the polished boundaries of windows or mirrors (bare or coated) they can introduce undesirable losses such as scattering. In addition, they are subject to various environments and, too often, rude handling by individuals. For these reasons, they exhibit a damage sensitivity greater than the bulk interior of materials and can have relatively high absorption.

The subject of micro-machined optics has, in general, passed from reports of optical quality and damage sensitivity to one of detailed study into the mechanics and material science aspects the cutting process. H. Hurt and D. Decker of the Michelson Laboratory, long leaders in

the field, presented a discourse on the inherent mechanical damage in diamond-turned optical surfaces. In referring to works dating back to 1665 (Hooke) and 1730 (Newton), they were able to conclude, by recourse to modern-day high resolution microscopy, the not unexpected result that the near-surface region subjected to the mechanical stress during the machining process is heavily deformed, resulting in high temperature related metallurgical responses (internal recrystallization, etc.). A companion paper correlates the optical properties and laser damage thresholds with the microscopic analysis reported herein.

D. Decker, H. Hurt, J. Porteus, and D. Grandjean of the Michelson Laboratory, Naval Weapons Center, discussed alterations of diamond-turned copper surfaces due to stress at the interface between the surface and the diamond tool. Stress and surface alterations increase with increasing negative rake angle. At rake angles of -5° to -10°, local lattice dislocations are induced which harden the material and potentially increase the optical absorption at the surface. At rake angles greater than -15°, larger temperatures are reached, promoting a recovery of crystallinity and growth of a high-temperature oxide phase Cu_2O. The authors examined the effects of these surfaces alterations on hardness, optical absorption, scattering, and laser damage, and investigated the effects of various cutting lubricants. Experimental results were in general agreement with the model for surface alterations, although a number of anomalous results were obtained.

Continuing their study of the damage threshold of optical components frequently employed at 10.6 μm, R. Wood, P. Waite, and S. Sharma of the GEC Hirst Research Center presented a very descriptive paper on the correlation of substrate preparation and damage threshold for Au-coated copper mirrors. They first verified the inverse dependence of damage threshold and absorptivity between 0.5 and 1.5 percent for several uncoated diamond-turned copper mirrors. Decreases in damage thresholds at different locations were clearly associated with defects roughly 1 to 10 μm in size. All experiments were performed with a 50-mJ pulse in a 60-nsec (FWHM) initial pulse followed by a 3-μsec tail, the latter containing roughly two thirds of the pulse energy. TEM_{00} spot sizes were about 4.5 mm in diameter at the $1/e^2$ points. Surface roughness values were determined by a Talysurf-5. Three gold-coated mirrors were prepared by conventional polishing. Finishing, however, was accomplished with a different grade of diamond paste abrasive. Reflectivity and absorptivity results were very uniform and comparable to best diamond-turned mirrors. The damage thresholds, however, varied considerably and were found to orrelate with surface scratch width. An analysis of the data showed that there is a log inverse log relationship between the minimum damage threshold and the scratch width.

V. Hodgkin, D. Decker, and H. Hurt of the Michelson Laboratory measured changes in the IR reflectance of metal surfaces that had been baked in vacuum. The samples included polished and diamond-turned surfaces on substrates of Cu, Mo, Ag, and alloys of Al, and films of Cu, Ag, and Au. The samples were separated into sets containing one sample of each type. The first set was held as a control and the other two sets were baked in vacuum at either 150°C or 300°C. Reflectance was measured for each sample, at wavelengths between 0.8 μm and 9.7 μm, before and after the baking. Reflectance of diamond-turned Cu and Al samples typically decreased (-0.2 to

-1.04 percent) at 0.8 μm, but was stable or increased slightly (-0.4 to +1.3 percent) at 9.7 μm. For films of Cu on silicon baked at 300 percent, the decrease in reflectance was large, from -40 percent at 0.8 μm, to -3 percent at 9.7 μm. For both control and baked samples of Cu on silica, or of Ag on either silicon or silica, reflectance between 1.5 and 9.7 μm. Reflectance of Al films on either silicon or silica was stable to within 0.6 percent at all wavelengths. Interestingly, for polished samples of OFHC Cu and of Mo, reflectance usually remained stable or increased. The authors attributed increased reflectance to improved crystalline order, decrease of defects, and possible elimination of surface con taminants, and decreases of reflectance in Cu films to a solid-state reaction between Cu and Si.

Of course, damage testing continues, but current emphasis is on repetitive irradiation and at shorter wavelengths.

R. Wood, P. Waite, and S. Sharma of the GEC Research Laboratories have been frequent contributors to this series of meetings. This year they reported on an extension of their primarily single-pulse, infrared damage investigations by comparing that work with cumulative and repetitive (100 Hz) testings on Ge, ZnSe, ZnS, GaAs, CdTe, NaCl, KCl substrates at 10.6 μm and PMMA, fused silica, Nd:laser glass and coated components at 1.06 μm. They noted morphological changes and evaluated spot size dependencies. The presentation, being very terse and primarily descriptive in nature, made the following microscopic observations relative to cumulative or repetitive exposure: (1) enlargement of damage areas under repeated exposures, (2) damage areas which did not grow after initial failure (both large and small areas), (3) damage areas which have a subsequently higher damage threshold, and finally (4) damage growth which appears associated with a gradual buildup of temperature. None of these observations were really surprising, but they do need to be quantitized.

Fused silica is routinely used throughout the visible and near-infrared region of the spectrum as a coating material, substrate for mirrors, as well J. Mengue and D. Friart of Commisariat a' l'Energie Atomique Laboratory at Limeil reported on their evaluation of the pulsed damage threshold at 0.355 μm [(1.06/3) μm]. Samples from various suppliers and finishing houses were tested. The average threshold for 22 samples was 6.2 J/cm^2 for 3-ns pulses with the best being 8.5 J/cm^2 and the worst 5.5 J/cm^2. No indication of mode quality, important test protocol procedures was given.

As mentioned previously, scattering is an important loss mechanism. Its measurement also allows for an assessment of several surface characteristics including, for example, the effect of surface finish or image quality. Since the American Society for Testing and Materials (ASTM), is a co-sponsor of this meeting, it is not surprising to find reports of the results of round-robin tests relative to standards development.

J. Bennett of the Michelson Laboratory at the Naval Weapons Center (NWC) and K. Stowell of the Air Force Wright Patterson Aeronautical Laboratories (AFWAL) reported results of scattering and roughness measurements made at NWC, AFWAL, and the Air Force Weapons Laboratory (AFWL) on both bare and silver-coated samples of fused and crystalline quartz. The measurements made were

angular distribution of scattered light (BRDF), total integrated scatter (TIS), and talystep profiles. While the data are too numerous and complex to be properly treated in a summary, a few principal results were obtained. BRDF values measured on 10 of 14 surfaces that had been silver coated and stripped were increased 2 to 260 times over BRDF values measured prior to silver coating. On 4 of 14 surfaces, coating and stripping did not affect BRDF data. BRDF values on the silver-coated surfaces were as much as 10^4 times larger than anticipated, but these large values were well correlated with roughness values determined at AFWL and NWC by measurement of TIS. The sets of TIS data from these two laboratories were almost identical, but rms roughnesses determined by measurement of TIS on silvered samples ranged from 2.6 to 75 A, whereas roughnesses measured by NWC on 10 of the same parts by Talystep ranged from 2.6 to 6.3 A.

J. McNeil and L. Wei of the University of New Mexico, J. Casstevens and W. Herrmann, Jr. of Optics Electronic Corp., and J. Stover of Montana State University compared roughnesses measured by both scatterometers and an optical profilometer on samples of both polished and diamond-turned metal surfaces. The rms roughnesses measured by profilometry at OEC were systematically below those measured at either MSU or UNM by scatterometer, but the two measurements by scatterometer were in reasonable agreement for some samples. The authors found that rms roughness of diamond-turned Cu or Si surfaces was reduced from typical values of 40 A to values near 20 A when the metal surfaces were coated with a sputtered or evaporated layer of the same metal having thickness less than 10,000 A. This smoothing was not observed on diamond-turned Mo surfaces.

J. Elson, of the Michelson Laboratory calculated scattering amplitudes for a surface microroughness on a material with static density variations in the bulk dielectric permittivity. The calculations indicated that the polarization ratio observed in angle resolved measurements of p- and s- polarized components should be variable, depending on the autocovariance functions of, and cross-correlation between, the surface roughness and dielectric fluctuations. The author believed this effect might account for two features that have been observed in scattering measurements: (1) cross-polarized light in the scattering of a p- or s-polarized wave, and (2) variation of the ratio of scattering from p- and s-polarized waves.

J. Bennett of the Michelson Laboratory and K. Guenther and P. Wierer of Balzers AG reported roughness measurements made with four types of instruments on a set of five Zerodur substrates with graded roughnesses. The five substrates were prepared by varying their polishing time. The rms roughnesses of the surfaces were inferred from measurements of total integrated scattering made with beams of 1-mm diameter at both NWC and Balzers. They ranged from about 10 A to 150 A and an excellent agreement was found between the two sets of measurements. The rms roughnesses measured at NWC by a Talystep instrument with lateral resolution of 0.1 to 0.2 μm, using scan lengths from 15 μm to 1 mm, ranged from 6 A to 450 A. The roughness was also measured on the optical heterodyne profilometer at Lawrence Livermore Laboratory. That instrument had 2-μm lateral resolution and gave roughness values ranging from 2.3 A to 174 A rms. The final measurement at NWC with a Wyko optical profilometer with 2-μm lateral resolution gave roughnesses ranging from 1.4 A to 45 A, the latter being the instrument limit. The authors

used the data to illustrate that roughness values depend on the machine used to make the measurement, and therefore component specifications must include both a roughness limit and a measurement procedure.

H. Bennett and D. Burge of the Michelson Laboratory used both geometrical and physical optics to calculate blur circle diameters for a beam focussed by a mirror with concentric zones representing local slope errors. They concluded that blur circle diameters calculated by geometric optics were much larger than those calculated by physical optics when the zone depth was less than or equal to a wavelength, while deeper zones could be modeled by either type of calculation.

3.3 Thin Films

Thin films continued to lead the interest at the meeting with over 40 percent of the presented papers. Emphasis this year was on new processes, optical characterization, damage testing at short wavelengths, and a variety of other topics such as chemical attack, diagnostic instrumentation, and the optical effects of poor film uniformity. Two papers of considerable interest reported on (1) a world-wide round-robin test and (2) damage dependence on several film and experimental variables.

K. Guenther of Balzers AG and 17 authors from other laboratories reported the results of round-robin tests involving various pulse lengths and beam diameters on a number of commercially available optical coatings, some high reflectance and some antireflectance. A large amount of data was presented. Conclusions were that despite very different testing conditions, it is possible to deduce some common relations and parameters. However, it would be highly desirable to develop a more standardized set of test conditions in order to compare results obtained at different laboratories. Progress is currently being made in that direction.

F. Rainer, C. Vercimak, and D. Milam of Lawrence Livermore National Laboratory and C. Carniglia and T. Tuttle Hart of the Optical Coating Laboratory, Inc., presented a summary of experiments performed on a variety of high reflectance and antireflectance coatings at 351 to 355 nm and also at 527 nm and 1064 nm. Thresholds were typically in the 2 to 3 J/cm^2 range at 351 to 355 nm for 0.6 ns pulses and scaled to higher values for longer pulse lengths. Scaling was modeled as t^m where m ranged from 0.1 to 0.5 and t was the pulse length in nanoseconds. The high reflectance multilayers showed more variation in damage threshold than the antireflection films. Some high reflectors had thresholds of 5 J/cm^2 or more at a 0.6-ns pulse length at 355 nm and increased with increasing wavelength.

Because films exhibit a damage sensitivity much greater than do surfaces or the interior of optical materials, the major emphasis was on new processes and the characterization of film structures and properties in an attempt to arrive at films with more bulk-like qualities. Without question, this is the area of greatest activity in the development of optical materials for high power lasers.

Each year we hear more and more the cry to invest in high vacuum beam methods similar to those used in the semiconductor industry to fabricate quality optical thin films. This year K. Lewis and J. Savage of the Royal Signals and Radar Establishment made an eloquent case for this most fundamental approach to attaining improved optical coatings. They extolled the virtue of molecular beam epitaxy for not only producing good films but perhaps more importantly when coupled with quality diagnostics, e.g., mass spectrometry, AES, and laser calorimetry, in studying the film deposition in situ in a controlled and measurable manner. ZnSe was employed as a test case where the composition of the residual atmosphere was correlated with the rate of absorption of impurities during the coating process. Careful reduction of H_2O and CO (to the few 10^{-10} mbar range) resulted in 3 μm thick coatings with negligible absorption at 10.6 μm. We must add that physical and optical properties were of course related to deposition variables, as they should be!

The use of rf sputtering techniques to deposit high quality, complex (up to 43 layers) refractory oxide multilayers was reported by D. Lunt of Burleigh Northwest Optical Inc. Preliminary results on ZrO_2, SiO_2 and Al_2O_3 coatings have shown "useful" damage resistance, loss, and environmental behavior. Deposition was accomplished using a 3 kW, 13.56 MHz rf generator directed at 8-inch targets of Si, Zr or Al. At a sputtering gas pressure of 2.7 Pa, the reaction gas partial pressure was varied between 10 percent and 17.5 percent. Employing a deposition rate of 9.70 nm/min, the resultant refractive index of SiO_2 was very similar to bulk material measured as 1.45 at 1064 nm; 1.46 at 550 nm; 1.475 at 350 nm, and 1.50 at 249 nm. Another indication of the film's quality and bulk-like behavior was the stability in spectral behavior of thin film polarizers, there being only a measurement-limited 1 to 2 nm shift between a coating soaked in distilled water for 72 hours and the same coating subsequently baked for 24 hours in vacuum.

The laser damage threshold of coated optical components is almost always set by the damage threshold of the coating. F. Wodarczyk, D. Strauss, and A. Harker of Rockwell International Science Center have performed a systematic analysis of novel coating fabrication techniques in an attempt to identify promising approaches to raising the coating damage threshold. Processes considered included e-beam deposition in UHV, sol-gel processes, photochemical deposition of organometallics, and ion-beam deposition in a reactive atmosphere. The filming material was TiO_2. Only e-beam thermal evaporation yielded stoichiometric films in the initial tests. It is believed, however, that better results with the other techniques can be achieved in time. The dual-beam reactive-ion method yielded low absorption films, and sol-gel coatings are also promising. Work is continuing.

Generally, thin films are observed to follow the contour of the surface of the substrate on which they are deposited, but they can also add additional surface roughness. A study of the surface roughness of SiO_2 and Si_3N_4 films deposited onto silicon and silicon carbide substrates by plasma-enhanced CVD techniques was reported by W. Partlow and W. Choyke of the Westinghouse Research and Development Center, J. Bennett of the Naval Weapons Center and and R. Silva of

VTI, Inc. The films were approximately 100 A thick. The best Si_3N_4 films added almost no surface roughness, and SiO_2 films added only about 2.8 A in roughness. Particulates can be contained in the films, however, which greatly increase the above values.

It is gratifying to note an increase in the reporting of correlations between optical properties and physical structure of thin films resulting from variation in deposition processes. Along these lines, H. Demiryont, D. Kerven, and J. Sites of the Colorado State University reported on the optical properties over the spectral range from 400 to 2500 nm of ion-beam sputtered, TiO_2 films 5- to 500-nm thick deposited onto Corning 7059 and silicon substrates. For films greater in thickness than 100 nm at wavelengths greater than 1 μm, the refractive index was independent of thickness and bexhibited no measurable dispersion.

Titania is an important high-index film material, but it can exhibit widely varying optical and structural properties. This information, inter-correlating optical (complex refractive index) and structural properties (porosity and grain size) with deposition variables such as types of background gas, ion, etc., is most important. It was also gratifying to note the excellent agreement between spectrophotometric and ellipsometric measurements even for very low values of the film's extinction coefficient.

Another paper from France concerned the improvement in the damage resistance of high reflectivity coatings at 1.06 μm in support of their laser-driven inertial-confinement fusion program. To this end, B. Geenen, A. Malherbes, and J. Guerain of Societe Matra together with D. Boisgard, D. Friart, and F. Garaude of the CEA facility at Limeil reported on the doubling of the damage threshold from 3.5 J/cm^2 in 1982 to above 8 J/cm^2 in 1983. Improvement was attributed to improved deposition parameter control, including the following: a) residual oxygen pressure by means of a mass spectrometer, b) evaporation temperature and regulation of evaporation rate, and c) substrate temperature through the use of a pyrometer.

Reflectors were made of TiO_2/SiO_2. Considerable detail was given concerning evaporation parameters of importance (pressures, rates, temperatures, etc.) as well as damage threshold measurements, using a 3-ns FWHM 1.06-μm laser pulse over a diameter of ≈2 nm at the $1/e^2$ intensity points. It was concluded that the damage threshold was very sensitive to backscattering of hydrocarbons, principally from primary and secondary pumps.

The mode structure and stability of many laser cavities are quite sensitive to the degree and purity of the polarization. As such, phase shift variations on cavity mirrors are very important. T. Leonard and J. Loomis of the University of Dayton Research Institute reported on an automated infrared ellipsometer to measure the standard parameters ψ and Δ at 3.8 μm. Variations in Δ (the differential phase shift) were modeled by thickness changes, as opposed to figure errors, while ψ variations were attributable to absorption changes. These models indicated that a one percent change in film thickness should produce a -1.1° change in Δ, while

a β increase of 10 cm^{-1} which is not unreasonable in thin films, (corresponding to an extinction coefficient increase of 3 x 10^{-4}), will change ψ by -0.1°.

As with bulk materials and surfaces, thin films are now being produced and evaluated for short-wavelength applications, particularly near 350 nm. This short-wavelength interest naturally stems from the available laser sources including frequency-tripled Nd^{+3} lasers and excimers of interest for laser fusion and defense uses.

As work continues on developing ultraviolet coatings which exhibit high laser damage resistance, and a compilation of recent results is desirable periodically. M. Scott of R & D Associates, provided such a summary of research results for eleven fluorides and twelve oxides which exhibit low loss spectral transmission in the ultraviolet. Physical and thermal, as well as optical, properties were included and comments about the fabrication of these materials in thin film form were also summarized.

Antireflection coatings are a key component for transmissive optics used in ultraviolet lasers. T. Tuttle Hart and C. Carniglia of the Optical Coating Laboratory, Inc. and F. Rainer and M. Staggs of Lawrence Livermore National Laboratory reported on recent work on antireflective coatings for 355 nm wavelength. All were vacuum evaporated onto bowl-feed polished Suprasil II substrates. Both low- and high-index materials were used in these multilayer coatings. Average damage thresholds in the 2 to 3 J/cm^2 range for 0.6-ns, 355-nm laser pulses were found for coatings incorporating high-index materials and values of less than 1 to 2.8 J/cm^2 were measured for those incorporating only low-index materials. Coatings made from scandia/magnesium fluoride had the highest damage threshold.

In a companion paper on 355-nm antireflective coatings, C. Carniglia and T. Tuttle Hart of the Optical Coating Laboratories, Inc. and F. Rainer and M. Staggs of Lawrence Livermore National Laboratories reported their results on high reflective coatings for 355 nm. As before, laser damage measurements were carried out using 0.6 ns laser pulses, single-shot-per-site. Both quarterwave and nonquarterwave designs were tested. Average damage thresholds for the best coatings were 3.5 J/cm^2 for the quarterwave designs. Scandia/magnesium fluoride was the best material combination. The best nonquarterwave value achieved, again with the same material combination, was 5.1 J/cm^2. It was achieved by reducing the electric field in the outer two scandia high-index layers.

S. Foltyn and L. Jolin of Los Alamos National Laboratory reported on the laser damage threshold of alumina-silica and other multilayer coatings designed for use with excimer lasers operating at 248 and 351 nm. Thresholds as high as 6 J/cm^2 at 248 nm and 12 J/cm^2 at 351 nm for 12 to 15 ns pulses were reported for reflectors obtained from various vendors. These results suggest a λ^2 wavelength scaling relationship. Two models are suggested which fit the experimental data reasonably well. One involves avalanche breakdown, the other a defect driven

thermal process. On the basis of these models they suggested that BeO might provide even higher reflector damage thresholds than Al_2O_3 with thresholds at 248 nm in excess of 15 J/cm^2.

One nondestructive technique for detecting damage-prone coating defects is photothermal deflection microscopy (PDM) in which a probe beam (usually He-Ne), incident at a moderately large angle on a coated surface, is deflected by some surface disruption caused by a more powerful pump laser. A current hypothesis is that localized absorbing coating defects, of the order of 1 to 10 μm in diameter, are the initial sites to heat up and damage under intense laser irradiation. With sufficiently fine spatial resolution, PDM could provide a map of the relative absorption distribution of a coated test sample for comparison with the results of laser damage test. W. Mundy, J. Ermshar, P. Hanson, and R. Hughes of Pacific Union College have developed instrumentation capable of resolving absorption sites with 2-μm diameter which produces a pictorial display of small areas scanned in 4-μm steps. At present, it takes many hours to characterize an area for practical correlation with damage tests. This year they reported some interesting observations for high reflectors and antireflection coatings. For example, the absorption-site densities varied dramatically from sample to sample, from 6 sites per mm^2 for a ZrO_2/SiO_2 maximum reflector to 0 per mm^2 for a Ta_2O_5/SiO_2 AR coating. Also, absorption sites varied from 8 μm to ~100 μm in diameter.

Especially noteworthy was the increase (2X) in absorption of a TiO_2 half-wave film as it was exposed to an Argon ion laser beam for two minutes. Since the absorption returned slowly to its original value in about six hours, it is apparent that a temperature-dependent absorption was being observed. The reverse effect, i.e., a decrease in the absorption signal with pump beam exposure, was observed in a ZrO_2/SiO_2 HR coating. In this case, one possibility is that gaseous coating contaminants were desorbed. Certainly, this technique will reveal additional valuable data on thin films as it continues to be refined and applied. The degree of correlation with corresponding damage tests is awaited.

W. Lowdermilk, J. Wilder, N. Brown, C. Ganderson, D. Milam, F. Rainer, and M. Staggs of Lawrence Livermore National Laboratory used 355 nm, 0.6 ns pulses to measure the laser damage thresholds of porous-silica antireflectance coatings on fused silica substrates. Thresholds as high as 9 J/cm^2, the bare substrate level, were observed for thin coatings (f90 nm optical thickness). For thicker coatings (500 to 600 nm optical thickness) the median threshold dropped to less than 2 J/cm^2. The data suggests that carbon residues from the coating solution may be responsible for the decreased threshold observed for the thicker films.

From a basic or fundamental standpoint, work continues on coating defects, the Achilles heel that leads to low damage resistance: their production, identification, role in the damage process, and, of course, their elimination.

It is the general perception of the laser damage community that localized defects limit the damage thresholds of dielectric interference coatings to values well below the intensity required to damage defect-free material. Thus, nondestructive identification of the damage-prone defects has been a popular quest in recent years. At this symposium, C. Marrs and J. Porteus of the Michelson Laboratory and J. Palmer of Comarco, Inc., described their observations of laser-illuminated coating defects using a color video camera/telescope system. Typically, they observed a pattern of several intense localized images in the laser-irradiated areas of multilayer dielectric mirrors. They were able to correlate some, but not all, of these images with damage-initiation sites at higher laser intensities. Interestingly, these images tended to persist for some time (50 to 200 ms) on the video monitor after the background laser image had vanished. This they attributed to the peculiar lag characteristics of the video cameras used. Since the color of the defect-image changes in the visible was the same color as the wavelength of the incident dye-laser radiation (476 to 515 nm), it was concluded that scattering, not luminescence, occurred at the defect sites. Further, a significant amount of s-polarized scattered light was detected even though the laser irradiation was p-polarized -- a characteristic of depolarizing scattering sites. Finally, the relative intensity of the scattering sites varied with wavelength within the high-reflection band of the reflectors, indicating a possible correlation with the standing-wave electric fields within the individual layers.

Since some of these scattering sites damaged whereas others resisted damage for multiple shots, final conclusions relative to these interesting observations must await corroboration from complementary diagnostics. For example, the relative temperature rise of the observed scattering sites may distinguish between active and benign defects.

J. Abate, A. Schmid, M. Guardalben, D. Smith, and S. Jacobs of the Laboratory for Laser Energetics, University of Rochester, reported their work on detecting coating defects using Photothermal Deflection Microscopy. An absolute calibration for the technique was provided by introducing micron-sized absorbing copper "islands" into the film. Using these defects it was demonstrated that the photothermal technique can detect even submicron defects in the films and can generate computer-controlled defect maps of antireflective and high reflective dielectric coatings. Present limitations of this technique include the small surface area that can be mapped in a reasonable time and microcomputer memory limits.

Thin film nodule formation is frequently observed and may be linked to reduced laser damage resistance. Films also typically exhibit a columnar structure. K. Guenther of Balzers AG has summarized the available data on nodule formation and shown that it can be related to the conditions producing columnar structure in thin films. A simple model was proposed on the basis of limited surface mobility of adatoms or admolecules which predicts nodular and columnar formation and allows one to predict how to minimize these effects.

Just as in bulk materials, polymers are being investigated for their potential role as coating materials--their greatest application may be as protective coatings against adverse environments.

Thin film antireflective films have a limited spectral region in which they exhibit low reflectance. B. Yoldas and D. Partlow of Westinghouse Research and Developement Center and H. Smith of Westinghouse Hanford Laboratories reported the damage threshold of a wide spectrum antireflective coating developed for fused silica. The coating is a single-layer, graded-index film applied from a polymer oxide solution. It exhibits a damage threshold at 350 nm using a 0.6 ns pulse length as high as 9 J/cm^2, the intrinsic level of the fused silica substrate. However, values as low as 0.8 J/cm^2 have also been observed. The variation is believed to result from preparation techniques which lead to carbon formation during the heat treatment of the coating.

W. Partlow and J. Heberlein of Westinghouse Research and Development Center reviewed the plasma deposition process for thin films and reported the current status of films of refractory materials such as SiO_2, SiC and Si_3N_4 prepared by this process. The films are typically amorphous, nonporous, in compressive stress, and with low absorption. They have good adherence to many metal amorphous and crystalline substrates and introduce very little scatter when properly deposited. Thickness uniformities are typically 2 to 5 percent. Thus far, the plasma deposition process has been used mainly to produce films for non-optical applications, but more use in optical applications is anticipated.

3.4 Fundamental Mechanisms

True progress and assessment of the future rests on our understanding of the fundamental mechanisms of the interaction of light (in this case, coherent light) and matter. Substantial progress is being made along these lines in such diverse areas as precursor emission, thermal modeling of the damage process tied to basic material properties, data analysis, and nonlinear effects. The search goes on for a noncatastrophic damage indicator.

At this year's meeting there was considerable interest in all types of laser-induced emission from optical components. While most were concerned with particle emission, a few addressed visible light emission after a sub- threshold infrared illuminating pulse. One such report was by D. Nichols, D. Morris, M. Bailey, and R. Hall, all of the Boeing Aerospace Company. A correlation analysis was accomplished on a variety of optical components between microscopic surface defects visible before damage, emission (points) due to laser modulation, and damage points from high-power irradiation with a spatial resolution of $\sim$25 μm. Compared to other damage-sensitive site-identification techniques tried so far, e.g., photo-acoustic, etc., this technique exhibits the strongest correlation yet between recurrent visible emission points and low-threshold pulsed-laser damage points. The subthreshold illuminating pulses were <1 J/cm^2 in 4 μsec (FWHM) at the DF wavelength. Recording was accomplished with an S-11 photo-tube which peaks in sensitivity at 440 nm and is down in sensitivity two orders of magnitude at 310 nm and 660 nm.

M. Becker, F. Domann, A. Stewart, and A. Guenther of the Air Force Weapons Laboratory reported a study of damage precursor events such as charge emission and surface

photoconductivity observed during 5-ns, 1064-nm irradiation of diamond-turned Cu surfaces, silicon wafers, and single-layer films of ThF_4, Al_2O_3 or Ta_2O_5. In silicon wafers, single-pulse damage occurred at 1.6 J/cm^2, and damage could be induced by five pulses at 1.1 J/cm^2, but laser-induced charge emission was observed only when damage occurred. The copper damaged at 2.1 J/cm^2, and charge emission was observed at fluences as low as 0.12 J/cm^2. In the ThF_4 film tested, thresholds for charge emission and laser damage were identical, 10 J/cm^2, for one-on-one tests. Laser hardening increased thresholds in ThF_4 by as much as a factor of two. The coatings of $Al_2O_3$and Ta_2O_5 were prepared with electrode strips, but surface photoconductivity was not observed. Charge emission on these oxide coatings occurred at fluences 10 to 20 times less than the threshold for damage. The authors believed that charge emission was a useful indicator of the occurrence of damage or surface cleaning.

Evaluation of laser-induced electron emission as a predamage diagnostic for insulator and semiconductor surfaces has been pursued by a number of laboratories. To date, the results of most of these studies have been irreproducible. However, by performing experiments in a sufficiently high vacuum (10^{-7} Torr), W. Siekhaus, J. Kinney, and D. Milam of the Lawrence Livermore Laboratory have obtained remarkably consistent results. Surfaces of GeO_2, SiO_2, ZnS, CdTe, and NaCl were irradiated by 1064-nm pulses ranging from 1 to 40 ns. They found that the electron emission varied with increasing laser fluence in a manner consistent with a multiphoton excitation across the band gap. The data were inconsistent with either avalanche ionization or thermionic emission models. For a prescribed level of electron emission, the required laser fluence scaled approximately as the square root of the pulsewidth.

The advancement of modeling in this field spans short pulse to CW loading, single pulse, multipulse and repetitive loading, UV to the IR, and windows, surfaces, and thin films, with details given to linear and nonlinear behavior, and variations in experimental and material variables. This area is truly leading our development, no longer attempting to explain our observations.

For the first time, the "thin film" aspect has been included in impurity-dominated modeling (by addressing the influence of the substrate and absorption profiles) by M. Lange and J. McIver of the Institute of Modern Optics at the University of New Mexico and A. Guenther of the Air Force Weapons Laboratory. They have, as well, added the more realistic situation of a columnar rather than a spherical impurity. They concluded that "thin" films, "short" pulse ... descriptions must be addressed in terms of the scales of diffusivities (cm^2/s) of the materials involved. Expressions are given to relate the final temperature and gradient achieved to substrate conductivity, etc. Of course, for "short" single pulses the substrate may not play a role at all. It was concluded that the predictions and experimental results which show an increase in damage resistance as the film becomes thinner is almost entirely due to the reduction in impurity size allowed. In all models it is generally assumed that the impurity diameter is limited to the film thickness, and the reduction in thermal gradients. The most

important conclusion, however, is that the specific shape of the impurity is not important to the thermal diffusion aspect of the problem as long as its volume scales as the radius cubed, while the absorption cross section scales as the squared radius.

Considering their detailed modeling studies of the failure of optical thin films based on an impurity model, M. Lange and J. McIver of the Institute of Modern Optics at the University of New Mexico and A. Guenther of the Air Force Weapons Laboratory addressed the optical properties of the impurity and thin film and the wave nature of the incident laser light. The principal difference between this year's report and prior efforts concerns the utilization of Mie scattering theory as opposed to geometrical cross sections, resulting in modified scaling laws which were compared with previously published experimental data. It is shown that the damage threshold E in J/cm^2 is proportional to $(K_\eta t_\ell)^\alpha$ where K_η is the thermal conductivity of the host or film material and t_ℓ is the effective laser pulse length. The value of α goes from 0.5 to 1.0 as "α" the impurity diameter approaches 0. The use of α Mie absorption cross section allows one to treat the effects of both the linear and imaginary (absorptive) part of the refractive index. Provision is also made to consider the wavelength dependent linear and nonlinear (multiphoton absorption) processes as well.

J. Palmer of COMARCO, Inc. provided an analysis of the cooling of laser components by flowing gas across the optical surface. He provided techniques for first-order evaluation of gas velocities, film coefficients, and temperature distributions in optical elements irradiated over the full area or over an isolated spot on the surface, or irradiated by a toroidal beam. The equations provided allow general evaluation of specific problems to determine whether detailed numerical evaluation is required.

In a second paper, J. Palmer used the three-dimensional Palmer-Bennett model to calculate temperature rises for metals irradiated by either pulsed or continuous wave lasers. Both the Drude and Jakob-Kelvin models were used to relate absorptance, reflectivity, and emissivity to the conductivity of the metal. Incident laser fluences necessary to produce a surface temperature rise equal to the slip temperature were computed and compared with previously published data. Encouragingly, agreement between calculated and measured slip thresholds ranged from 99.8 percent to 82 percent.

To establish the data base required for testing of optical damage theories requires controlled experiments on adequately characterized substances. This includes proper data analysis to allow unambiguous interpretation of the numbers and for performing proper interlab correlations.

S. Foltyn and L. Jolin of Los Alamos National Laboratory reported that multiple-shot damage to coatings and surfaces tested at 351 nm usually started as microscopic craters. With continued irradiation, the size of craters in HR coatings usually increased, while microcraters in bare surfaces and AR films usually remained constant in size. The authors questioned whether

microscopic pits or larger catastrophic damage should be used as a definition of damage, and cited damage data that yielded conclusions that varied with the chosen damage definition.

S. Seitel and J. Porteus of the Naval Weapons Center described a statistical approach for using small laser-damage facilities to measure the spacing of defects responsible for threshold damage and damage thresholds usable as system design data, both of which are usually obtained only through large area testing. They measured the probability of damage as a function of intensity in experiments with 1.06-μm beams 47 μm in diameter (e^{-2} in intensity) and 2.7-μm beams 67 μm in diameter. The probability measurements were fit to a theory to allow computation the average spacing of the worst-case defects and an "onset" threshold defined to be the threshold for damage in large area beams which always contain worst case defects. The "onset" thresholds were lower by as much as a factor of 20 than their small-spot thresholds which were defined to be the intensity at which damage was obtained in 50 percent of the small-spot tests. The authors believe their metrology will allow use of small laser-damage facilities for research aimed at improving damage resistance of large components.

As is usual, we end on a subject peculiar to high-power lasers, that of nonlinear phenomena, both in manifestation as well as in the determination of salient and controlling properties. Again, both aspects must be known and taken into account in theory and experiment.

W. Williams, M. Soileau, and E. Van Stryland of North Texas State University used both linearly and circularly polarized 0.53-μm beams to measure the dependence of bulk thresholds in NaCl and fused silica on focal spot size. Because the electronic nonlinear refractive index is larger for linearly polarized beams than it is for circularly polarized beams, these experiments allowed a measurement of the influence of self focusing on bulk damage experiments. For beams with Gaussian radii ≤5 μm in silica or ≤7 μm in NaCl, the input power required to produce damage with circularly polarized beams, P_{BC}, equaled the corresponding threshold for linearly polarized beams, B_{BL}, indicating that self focusing was not a strong effect in experiments performed with these small beams. The ratio P_{BC}/P_{BL} in fused silica increased from 1 to 1.5 as the beam radius increased from 7 to 40 μm, indicating that self focusing had been an important, but not dominant, effect on measurements.

For tests with larger beams in either material, the value of P_{BC}/P_{BL} maintained saturated values of 1.5 in silica and 1.41 in NaCl, showing that selffocusing dominated those measurements. The input power at saturation corresponded to the critical power $P_2 = 3.77\ P_1$, whereas the smaller critical power P_1 has sometimes been assumed to be the power level at which self focusing becomes dominant. The authors concluded that spot-size dependencies observed in thresholds that were a small fraction of P_1 were probably due to effects other than self focusing, and suggested re-evaluation of earlier data that had been analyzed with reference to P_1.

Understanding the phenomena of self focusing and the measurement of the nonlinear refractive index n_2 of solids and liquids used in high-power laser systems were major research activities of the 1970's. However, a limited number of physics groups have continued to simplify and refine the measurement techniques to allow more accurate determination of n_2 over a range of wavelengths. An elegant technique applicable to highly transparent materials was presented this year by W. Williams, M. Soileau and E. Van Stryland North Texas State University. The technique involved measurements of beam distortions in the transmitted, time-integrated, far-field spatial intensity profile using an optical multichannel analyzer. The spatial profile was related, via a theoretical model and computer projection, to the phase distortion induced in the materail by a focused laser beam. Spatial profile measurements of 40-ps pulses at 1064 nm focused through CS_2, NaCl, and SiO_2 resulted in n_2 values (1.28, 1.37, and 0.62 x 10^{-13} esu) in reasonably close agreement with previous workers. Values obtained at 532 nm indicated very little dispersion.

B. Jensen and A. Torabi of Boston University calculated the linear and nonlinear index of refraction of the semiconductors $Hg_{1-x}Cd_xTe$, $Al_xGa_{1-x}As$ and $In_{1-x}Ga_xAs_yP_{1-y}$ as a function of mole fraction x, for frequencies below the fundamental absorption edge. In the derived result, index is given as a function of bandgap energy, electron rest mass, effective heavy-hole mass, spin-orbit splitting energy, lattice constant, and carrier concentration. For all three materials, there was good agreement between measured and calculated values of index.

4.0 Recommendations for the Future

Since this was the fifteenth annual Symposium on Optical Materials for High Power Lasers, it is probably best to keep the recommendations general in the sense of where the action is and where it needs to be.

Most all of the indications, commercial and governmental as well as academic, are driving towards shorter wavelengths mainly in the high brightness regime. The call is for high beam quality, high power, high-average power or high energy with good beam quality. Lasers have gotten better over the years and they now require better optics.

In materials and measurements most of the classical materials have been evaluated. What needs to be done is to produce them purer and more intrinsic yet stronger and less expensive, in many cases forged, alloyed or polycrystalline, with improved environmental durability. Yet, there are still searchers for new classes of materials. The chalcogenides and heavy metal-fluoride glasses are examples and maybe liquid crystals deserve emphasis now. This movement will continue to require better material property characterizations as well if we are truly to engineer materials for "systems".

It is necessary also that more attention be given to laser materials for adverse environments, such as space and high-energy radiation as well as corrosive gases present in excimer laser cavities.

As regards surfaces and mirrors the understanding and use of scatter must become more tractable to those whose careers have not been spent in the field, and more consensus is needed in better definition, instruments and procedures. Fortunately, we are seeing advances in this area. More needs to be done in surface preparation, machining, including the mechanics of cutting and polishing such as float, mechano-chemical etc. and materials processing, e.g. laser annealing of surfaces and thin films or baking. Here as well, new diagnostics will be helpful such as surface Raman scattering, particle emissions and surface potential.

It is hard to pick out any one or even a few areas in the thin film area upon which to concentrate. Both understanding and technological progress is needed. It is safe to say that accurate measurements of the properties of optical materials in thin film form are necessary for progress in theoretical and analytical work. New coating materials such as phase-separated glasses and sol-gel coatings are progressing well and are making their impact in limited applications. They even promise to extend to multilayer HR applications. But without question, we would like robust deposited films, if we knew how to make them uniformly, in large size, of requisite uniformity and expense - don't forget to add high damage threshold. Thus, deposition technology is a key area. Research on the correlation between the physical structure and optical properties is needed so that we can evaluate the importance of these characteristics on their damage resistance, durability and stability. Then, hopefully, we can move on to the more thermo-mechanical factors of stress, adhesion, abrasion resistance, etc.

Finally, we come to fundamental mechanisms. Progress is undoubtedly being made in modeling, but the final tests to confirm the models have been lacking. Thermal modeling is pointing the way for temperature dependent properties such as absorption coefficients and other thermo-optics properties. We still need a precatastrophic indicator based on sound physical understanding suitable for laboratory and shop use.

While non-linear effects seem well in hand, there may be unanticipated surprises as we delve further into the UV and even the x-ray region. We've come a long way - have a way to go - but we're sure in our approach. Thanks to these symposia and their proceedings we have a well documented history and informed practioners.

5.0 Acknowledgments

The editors would like to acknowledge the invaluable assistance of Mr. Aaron A. Sanders and the other involved staff members of the National Bureau of Standards in Boulder, Colorado, for their interest, support, and untiring efforts in the professional operation of the Symposium and particularly to Susie Rivera for her part in the preparation and publication of the Proceedings. The continued success of the Damage Symposium would not have been possible without the enthusiastic support of those named above, and Patty Mannos, Kathy Sherlock, and Shelley Etzel, all of NBS.

Again this year, the conference co-chairmen and attendees were pleased to have the assistance and presence at the Symposium of Pat Whited of the Air Force Weapons Laboratory.

A special word of thanks!

This year being the Fifteenth Annual Symposium on Optical Material for High Power Laser, a festival celebration was held with Dr. Alexander J. Glass, President KMS Fusion Industries, one of the Symposium originators as guest speaker. His talk entitled "Is There Life after the Boulder Damage Symposium" was enjoyed by all. From us to you, thanks, Alex.

6.0 References

[1] Glass, A. J.; Guenther, A. H., eds. Damage in Laser Glass. ASTM Spec. Tech. Publ. 469 ASTM, Philadelphia, PA; 1969.

[2] Glass, A. J; Guenther, A. H., eds. Damage in Laser Materials. Nat. Bur. Stand. (U.S.) Spec. Publ. 341; 1970.

[3] Bloembergen, N. Fundamentals of Damage in Laser Glass. National Materials Advisory Board Publ. NMAB-271 National Academy of Sciences; 1970.

[4] Bloembergen, N. High Power Infrared Laser Windows. National Materials Advisory Board Publ. NMAB-356 1971

[5] Glass, A. J.; Guenther, A. H., eds. Laser Induced Damage of Optical Materials: 1972. Nat. Bur. Stand. (U.S.) Spec. Publ. 372; 1972.

[6] Glass, A. J.; Guenther, A. H., eds. Laser Induced Damage in Optical Materials: 1973. Nat. Bur. Stand. (U.S.) Spec. Publ. 387; 1973.

[7] Glass, A. J.; Guenther, A. H. Laser Induced Damage in Optical Materials, 1973: A Conference Report. Appl. Opt. 13:74-88; 1974.

[8] Glass, A. J.; Guenther, A. H., eds. Laser Induced Damage in Optical Material: 1974. Nat. Bur. Stand. (U.S.) Spec. Publ. 414; 1974.

[9] Glass, A. J.; Guenther, A. H. Laser Induced Damage in Optical Materials: 6th ASTM Symposium. Appl. Opt. 14:698-715; 1975.

[10] Glass, A. J.; Guenther, A. H., eds. Laser Induced Damage in Optical Materials: 1975. Nat. Bur. Stand. (U.S.) Spec. Publ. 435; 1975.

[11] Glass, A. J.; Guenther, A. H. Laser Induced Damage in Optical Materials: 7th ASTM Symposium. Appl. Opt. 15(6):1510-1529; 1976.

[12] Glass, A. J.; Guenther, A. H., eds. Laser Induced Damage in Optical Materials: 1976. Nat. Bur. Stand. (U.S.) Spec. Publ. 462; 1976.

[13] Glass, A. J.; Guenther, A. H. Laser Induced Damage in Optical Materials: 8th ASTM Symposium. Appl. Opt. 16(5):1214-1231; 1977.

[14] Glass, A. J.; Guenther, A. H., eds. Laser Induced Damage in Optical Materials: 1977, Nat. Bur. Stand. (U.S.) Spec. Publ. 509; 1977.

[15] Glass, A. J.; Guenther, A. H. Laser Induced Damage in Optical Materials: 9th ASTM Symposium. Appl. Opt. 17(15):2386-2411; 1978.

[16] Glass, A. J.; Guenther, A. H., eds. Laser Induced Damage in Optical Materials: 1978. Nat. Bur. Stand. (U.S.) Spec. Publ. 541; 1978.

[17] Glass, A. J.; Guenther, A. H., eds. Laser Induced Damage in Optical Materials; 10th ASTM Symposium. Appl. Opt. 18(13):2212-2129; 1979.

[18] Bennett, H. E.; Glass, A. J.; Guenther, A. H.; Newnam, B. E. Laser Induced Damage in Optical Materials: 1979. Nat. Bur. Stand. (U.S.) Spec. Publ. 568; 1979.

[19] Bennett, H. E.; Glass, A. J.; Guenther, A. H.; Newnam, B. E. Laser Induced Damage in Optical Materials: 11th ASTM Symposium. Appl. Opt. 19(14):2375-2397; 1980.

[20] Bennett, H. E.; Glass, A. J.; Guenther, A. H.; Newnam, B. E. Laser Induced Damages in Optical Materials: 1980. Nat. Bur. Stand. (U.S.) Spec. Publ. 620; 1981.

[21] Bennett, H. E.; Glass, A. J.; Guenther, A. H.; Newnam, B. E. Laser Induced Damage in Optical Materials: 12th ASTM Symposium. Appl. Opt. 20(17):3003-3019; 1981.

[22] Bennett, H. E.; Guenther, A. H.; Milam, D.; Newnam, B. E. Laser Induced Damage in Optical Materials: 1981. Nat. Bur. Stand. (U.S.) Spec. Publ. 638; 1983.

[23] Bennett, H. E.; Guenther, A. H.; Milam, D.; Newnam, B. E. 13th ASTM Symposium. Appl. Opt. 22:3276-3296; 1983.

[24] Bennett, H. E.; Guenther, A. H.; Milam, D.; Newnam, B. E. Laser Induced Damage in Optical Materials: 1982. Nat. Bur. Stand. (U.S.) Spec. Publ. 669; 1984.

[25] Bennett, H. E.; Guenther, A. H.; Milam, D.; Newnam, B. E. 14th ASTM Symposium. Appl. Opt.: 3782-3795; 1984.

Studies of Optical and Mechanical Properties of Heavy-Metal Fluoride Glasses

B. Bendow*
The BDM Corporation, Albuquerque, New Mexico 87106

D. K. Burge and H. E. Bennett
Naval Weapons Center, China Lake, California 93555

L. H. Johnston
University of Idaho, Moscow, Idaho 83843

J. J. Mecholsky
Sandia National Laboratories, Albuquerque, New Mexico 87185

Heavy-metal fluoride (HMF) glasses are promising materials for many infrared (IR) components such as laser windows, missile domes, lenses, filters, and optical fibers. In this paper we report the results of studies of optical and mechanical properties of representative HMF glass samples (including fluorozirconates, rare-earth fluoride glasses, and transition metal fluoride glasses) obtained from a variety of government, academic, and commercial sources. Quantities measured include IR absorption and emission, total integrated scatter (TIS), fracture toughness, and thermal stress resistance. The glasses studied displayed smooth multiphonon edges with absorption coefficients in cm^{-1} reaching unity in the vicinity of 7 μm and becoming as low as 4×10^{-3} cm^{-1} at DF wavelengths. Thermal emittance measurements indicate that the absorption edge moves relatively little with increasing temperature. TIS values in the infrared were as low as a few parts in 10^4 and the fracture toughness was about one-third to one-half that of fused silica. Rapid heating studies performed on a representative HMF composition indicated that there was no degradation in strength even up to the melting point.

Key Words: Fluoride glasses; heavy metal fluoride glasses; IR glasses; IR absorption; optical material.

1. Introduction

There has been considerable interest recently in the use of HMF glasses for a variety of high energy laser (HEL) and electro-optic (EO) components such as windows, lenses, domes, and optical fibers [1-20]. Typical HEL applications are indicated in table 1, and some of the significant attributes of HMF glasses for optical components are listed in table 2. The purpose of this paper is to: (1) briefly review the current state of knowledge on selected optical and mechanical properties of HMF glasses and the fabrication of these glasses; and (2) report results of some recent measurements we have performed on HMF glass samples obtained from a variety of government, industrial, and academic sources.

*Research supported in part by Naval Weapons Center under U.S. Air Force Contract No. F29601-80-C-0013.

Table 1. HEL Applications for Fluoride Glass

o Laser Windows (HF/DF, Nd:YAG, I_2, FELs, Excimers)
o Beam Expanders (FELs)
o Gratings (Single or Multi-λ)
o HR/AR Coatings for Reflective/Transmissive Components
o Rugate Coatings for EO Systems Laser Hardening and for Multiwavelength Components
o Corrosion Resistant Components/Substrates for Halide Gas Lasers
o Ultralow Distortion Laser Rods

Table 2. Significant Attributes of Fluoride Glasses for HEL and EO Applications

o Multispectral Capability
- Continuous Transparency From Mid-IR to Near-UV
- Mid-IR or Visible Tracking, Shared Aperture Capabilities
o Multiwavelength Ultralow Absorption Capability
- Less than 10^{-4} cm^{-1} in Visible
- Less than 10^{-6} cm^{-1} in IR
o Low Refractive Index (less than 1.5)
o Low Dispersion in Both IR and Visible (ABBE # ~ 80)
o Low Scattering (less than fused silica)
o Low Nonlinear Coefficient
o Potentially Low Susceptibility to Nuclear Radiation
o Low Birefringence
o Low Thermal Distortion
o Resistant to Chemical Attack by Halide Gases and/or Acids
o Compositional Flexibility and Therefore Flexibility to Tailor Properties
o Flexible Size and Shape
o Fabrication is Low Cost

HMFs were discovered around 1974 by Lucas, Poulain, and their coworkers at the University of Rennes in France [21-25]. The initial systems to be discovered were fluorozirconates, where ZrF_4 is the primary constituent (greater than 50 mol %), BaF_2 is the main modifier (approximately 30 mol %), and various metal fluorides, such as ThF_4 and LaF_3, are tertiary constituents. Subsequently, many other HMFs have been synthesized and studied in laboratories throughout the world [26-40] (principally in France, in the United States, and in Japan). An important attribute of HMFs is their compositional flexibility, which allows them to be tailored to a broad range of properties. Many elements have been incorporated into HMFs to date; however, despite the virtually limitless range of compositions, only a few have been studied in depth. The main categories investigated (classified somewhat arbitrarily) are shown in table 3. So far, the most promising glasses for IR applications appear to be fluorozirconate-type and Ba/Th fluoride glasses, but it is quite likely that other promising HMF candidates will also be identified in the future.

Table 3. Selected Heavy-Metal Fluoride Glass Systems

SYSTEM	PRINCIPAL CONSTITUENTS
Fluorozirconate and Fluorohafnate Glasses	$\{ZrF_4, HfF_4\}$, BaF_2 $\{ThF_4, LaF_3, GdF_3\}$
Aluminum Fluoride and Lead Fluoride Glasses	AlF_3, PbF_2, Alkaline Earth Fluorides, Rare-Earth Fluorides
Rare-Earth/Ba/Zn Fluoride Glasses	{Rare-Earth Fluorides, YF_3} BaF_2, ZnF_2
Ba/Th Fluoride Glasses	ThF_4, BaF_2 $\{YF_3, YbF_3\}$ $\{ZnF_2, AlF_3\}$
Scandium Fluoride Glasses	ScF_3, YF_3, BaF_2
Misc. Trivalent/Divalent Fluoride Glasses	$\{GaF_3, CrF_3\}$ $\{YF_3, GdF_3\}$ $\{PbF_2, ZnF_2, SrF_2\}$ $\{LiF, NaF, AgF\}$

Although the number of compositions for HMFs is broad, the glass formation regions can be rather narrow. This is related to the strong tendency of most HMFs to crystallize [1, 11], which is due in part to the small difference between their glass formation temperature (T_g) and crystallization temperature (T_c). While BeF_2 easily forms a glass upon cooling from the melt, multicomponent fluoride glasses tend to have low viscosities at their liquidus temperature and a tendency toward crystallization. Moreover, fluoride melts are reactive with the atmosphere and with certain crucible materials, further increasing their susceptibility to crystallization and/or contamination. For these reasons, preparation of HMF glasses must be carried out under controlled conditions. In particular, nonreactive crucible materials, such as vitreous carbon or platinum, are required. Atmosphere control is necessary to prevent contamination--and possibly nucleation--associated with oxide and hydroxide impurities. Either inert atmospheres (N_2, He, Ar) or reactive atmospheres (CCl_4 , SF_6), which remove water and various other oxides from the melt, can be used [31, 41]. An example of implementing such controls is performing distillation of starting materials, and melting and casting inside a glove box. Glass melts may be obtained directly by fusing anhydrous fluorides at temperatures in the 700°C to 1,000°C range for time periods on the order of 1 hour, or by converting oxides to fluorides by heating them in the presence of ammonium bifluoride and then fusing the resulting fluorides [1, 8]. Certain glass compositions may be cast by pouring them into room-temperature or heated molds, or they may be formed directly in their crucible or in a sealed tube used for melting. More difficult compositions may require rapid quenching; for example, pouring the melt on a brass plate, then placing a second plate on top of the glass.

For the purposes of fabricating domes and other unusual shapes, it may be useful to prepare glasses by spinning melts in a container. The rotational casting process developed at NRL demonstrated that highly concentric glass objects of controlled thicknesses could be made in this way [42, 43]. These techniques, once quantified and suitably refined, should prove useful in spinning multilayer HMF structures of different sizes and shapes. Other possible approaches to preparing fluoride glasses that

have yet to be explored in detail include CVD and sol-gel. Various fabrication methods for fluoride glasses are listed in table 4, and some recently demonstrated fabrication capabilities are shown in table 5. Rome Air Development Center (RADC) has recently demonstrated an extremely promising method for obtaining high quality glass, in which melting and annealing is carried out in an evacuated and inert-gas backfilled RF induction furnace.

Table 4. Fluoride Glass Fabrication Methods

BULK COMPONENTS	COATINGS	FIBER
o Casting (D)	o CVD (UD)	o Furnace Draw From Preform (D)
o Forging (D)	o Sputtering (S)	o Single Crucible Draw (D)
o Spinning (D)	o Ion Deposition (S)	o Multicrucible Draw (S)

D = Demonstrated
UD = Under Development
S = Speculated

Table 5. Some Recently Demonstrated Fabrication Capabilities

o km-Length Fibers
o Graded Index Preforms Fabricated
o 40 x 2 cm Discs Fabricated
o High Optical Quality Samples 5x10x1 cm
o Hollow Rods and Core-Clad Rods Fabricated
o Bottles Have Been Spun
o Submicron Replication of Grating Lines
o Enamels on Selected Substrates

Various HMF glasses have been used for fiber fabrication [3]; all fibers drawn to date have been derived from compositions containing alkali fluorides, AlF_3, and/or PbF_2 additives which, generally, possess superior viscosity characteristics for fiber drawing. It should be possible, in principle, to draw fibers from virtually any HMF glass composition, but specialized techniques will be necessary due to the narrow working range and steep viscosity-temperature relations of most of these glasses.

2. Optical Properties

The desirable optical characteristics of fluoride glasses include a broad transparency range spanning the mid-IR to near-UV; low refractive index and dispersion, low Rayleigh scattering; and the potential for ultralow absorption and ultralow thermal distortion. Moreover, there are preliminary indications of very low birefringence and a high threshold for laser damage in these glasses. Some current and projected optical properties of HMF glasses are summarized in table 6 and our current state of knowledge on selected ones are shown in table 7. While some characteristics are similar to those of oxide glasses in the near-IR to near-UV, fluoride glasses provide unique capabilities for the mid-IR; and although chalcogenide glasses could also be highly transparent in this regime, they have other dis-

advantages: high refractive index, difficult to purify, softer than fluorides, and inability to transmit in the visible.

Table 6. Optical Properties of Fluoride Glasses

	CURRENT	PROJECTED
Refractive Index	1.45 - 1.60	--
Dispersion	$d^2n/d\lambda^2$ -5x10^{-3} μm^2 (IR)	--
Absorption Coefficient	~ 2x10^{-5} cm^{-1} (HF)	~ 2x10^{-8} cm^{-1} (HF/DF)
	~ 10^{-4} cm^{-1} (6348Å)	~ 10^{-5} cm^{-1} (6348Å)
Rayleigh Scattering	Similar to SiO_2	Lower than SiO_2
TIS	~ 10^{-2} to 10^{-3} (DF)	Less than 10^{-3} (mid-IR)
Birefringence	P11 - P12 ~ 0.005	--
dn/dT	(-.9) to (-1.5) x 10^{-5}/°K	--
Thermal Distortion	~ 1 x 10^{-6}/°K	~ 1 x 10^{-7}/°K
Laser Damage (Bulk)	Very Good* (DF)	Excellent
Surface Finish	Very Good	Excellent

*Classified Data

Table 7. Current Status of Optical Properties of HMF Glasses

PROPERTY	State of Knowledge GOOD	FAIR	POOR
Fundamental IR Reflectivity	X		
Raman Scattering	X		
Brillioun Scattering		X	
IR Edge Absorption	X		
UV Edge Absorption		X	
IR Impurity Absorption	X		
Refractive Index and Dispersion	X		
dn/dT			X
Photoelastic Constants		X	
Magneto-Optic Coefficients		X	
Fluorescence	X		
Rayleigh Scattering		X	

2.1 Transparency of Fluoride Glasses

As indicated above, there are many HMF glasses that possess continuous high transparency from around 0.25 μm in the near-UV out to around 7 μm in the mid-IR, depending on glass composition [1, 2]. HMF glasses are attractive for high energy IR laser transmissive optics and for ultralong-length fiber optic links because of the potentially very low intrinsic loss minima of halide glasses compared to oxides and even chalcogenides [44-80]. This minimum is determined by the intersection of the Rayleigh scattering loss and the IR absorption edge (V-curve). Moreover, since halide glasses offer potential for very low loss over a broad range of visible and IR wavelengths, they are also suitable for a variety of multispectral applications.

While most available compositions are continuously transparent, the glass can easily be colored by the addition of suitable dopants. For example, glasses containing Nd are purple, glasses with Ho are

green, and glasses with Pr are yellow. Clear glasses possessing relatively strong and narrow absorption bands in the near-IR can also be obtained with certain constituents such as Yb [20]. These properties make doped fluoride glasses interesting for passive components such as bandpass filters, and active components such as laser rods, sensors, and polarization rotating elements.

The V-curve and associated minimum intrinsic loss in the mid-IR of HMFs can be estimated once the frequency dependence of the IR edge absorption and the magnitude of Rayleigh scattering have been established. The V-curves obtained for typical fluorozirconate and Ba/Th fluoride glasses, assuming a Rayleigh scattering comparable to fused silica, indicate minimum losses in the vicinity of 10^{-8} cm^{-1}. As indicated later, it should be possible to obtain fluoride glasses whose Rayleigh scattering is lower than that of fused silica; thus, these values of minimum intrinsic loss represent fairly conservative values. For HEL windows, the scattering loss is of secondary importance compared to the absorption, which is responsible for thermal distortion and thermal fracture. Therefore, depending on the particular application, fluoride glasses may be useful as high-energy bulk optical components over a broad range of wavelengths including the visible. The lowest absorptions measured to date have been for optical fibers [3], with minimum losses of 10 dB/km near 2.7 μm, and 8.5 dB/km near 2.3 μm having been reported. The absorption features in the 1 to 2.5 μm region are attributed to transition metal impurities and the peak near 3 μm to OH [51, 52]. Measurements in bulk samples have generally yielded higher values of absorption; the lowest mid-IR value reported for bulk glass appears to be $2x10^{-3}$ cm^{-1} at DF (the deuterium fluoride wavelength 3.8 μm) for ZBT glass, with values in this study being approximately $4x10^{-3}$ cm^{-1} at DF for ZrF_4-BaF_2-LaF_3-AlF_3 glass. The results of calorimetric measurements in the visible region on alkali-fluorozirconate glasses indicate absorptions as low as 1.2×10^{-4} cm^{-1} in the vicinity of 0.65 μm [53]. The higher values obtained in the mid-IR may be due primarily to OH absorption, as is the case with fibers [51].

2.2 IR Absorption Edge

The IR edge determines the useful range of operating wavelengths for fluoride glass in the IR, and the minimum achievable loss (minimum of the V-curve). An understanding of IR edge behavior is important to guide the selection of suitable compositions for IR applications and to obtain reliable projections of the intrinsic absorption in the highly transparent regime ($\alpha < 10^{-3}$ cm^{-1}). In crystalline materials, the IR edge has been shown to stem from multiphonon processes, as established by a detailed analysis of both the frequency and temperature dependence of the edge absorption. Such analyses supply the parameters necessary to predict the absorption in regions that are not directly accessible to experiment. Similar analyses have been carried out for fluoride glasses to determine the origin and characteristics of their IR edges.

Selected measurements of absorption edge versus frequency for HMF glass samples assembled for this study yielded the results shown in figure 1. Points with arrows in the figure indicate that they are equal to, or lower than, the minimum measurement level obtainable from transmission. The absorptance for selected transition metal fluoride glasses is shown in figure 2. Both figures reveal absorption features to to OH, probably on the glass surface, in the vicinity of 3 μm. The shape and steepness of all the edges are similar to those of crystalline fluorides such as MgF_2, CaF_2, or SrF_2. The relatively smooth, exponential edge suggests dominance of ionic over covalent bonding in the glass. In contrast, chalcogenide and oxide glasses display a more pronounced structure in their edges, like crystalline semiconductors. This supports the speculation that HMF glasses are fundamentally different--from a bonding standpoint--from other commonly known glasses.

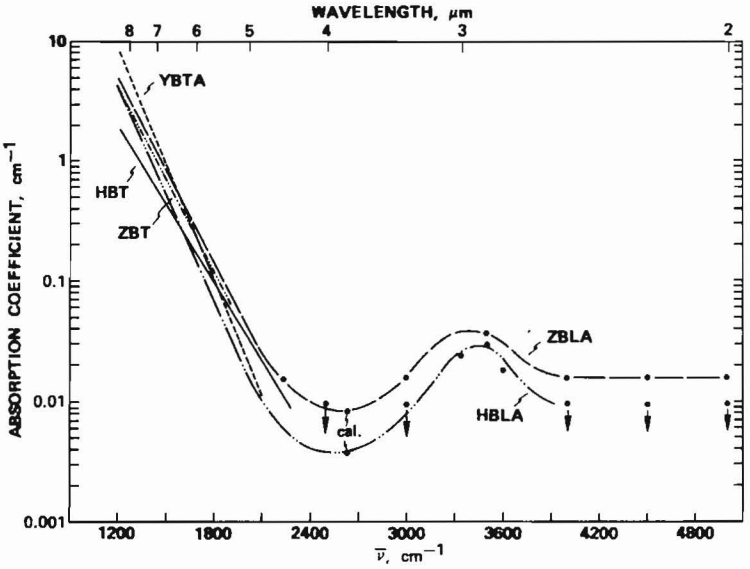


Figure 1. Absorption in Fluoride Glasses

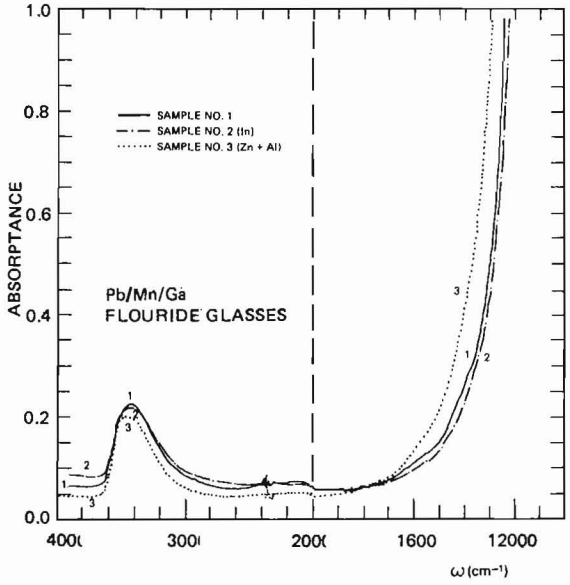


Figure 2. Absorption Versus Frequency for Transition Metal Fluoride Glasses

In order to establish the edge behavior in more detail, it is necessary to examine the frequency dependence over a range of temperatures [48]. The temperature dependence has been found to agree well with models for intrinsic multiphonon absorption applied previously to crystalline materials. Thus, certain simple models based on multiphonon absorption in ionic crystals can be used to interpret and predict the edge behavior of HMF glasses, i.e., to generate the high wavelength side of the V-curves.

The dependence of the edge properties on composition is more complicated than for crystals, where the reduced mass (through its effect on the transverse optic (TO) frequency) is the dominant factor. For example, the shift in the IR edge to longer wavelengths for glasses based on hafnium versus zirconium is much smaller than would be predicted on the basis of the difference in reduced mass. In addition, the edge in Ba/Th fluoride glasses is significantly shifted to longer wavelengths despite the

similarity in reduced masses of the constituents to those in fluorohafnate glasses [54]. These observations suggest that the local bonding and/or structure of HMF glasses--even with a given family--are very sensitive to composition. Nevertheless, general guidelines on the effect of glass constituents on the IR edge can be formulated; AlF_3 is an example of a constituent that is beneficial to glass formation but causes the IR edge to shift to shorter wavelengths [55]. Ba/Th fluoride glasses of various types possess some of the longest wavelength and steepest IR edges of HMFs investigated to date[56]. It is likely that ceratin other compositions possess even longer wavelength IR edges, but the extent of the possible shift remains uncertain at this time. For example, mixed halide glasses based on CdF_2 appear to offer extended long wavelength transparency over both fluorozirconates and rare-earth fluoride glasses [57]. Thus, appropriate mixed halides could extend transparency while retaining some of the superior physical and chemical properties of fluorides compared to heavier anion halides.

2.3 Impurity Absorption

Impurities can be introduced into the glass from a variety of sources (from the starting materials themselves, the melt container, or the atmosphere) prior to, during, and/or subsequent to glass formation. These impurities may modify edge characteristics and introduce absorption bands in various wavelength regions. The two main types of impurities impacting glass transparency are metallic ions [58, 59] with absorption bands in the visible and near-IR, and oxides and hydrides with absorptions in the mid-IR [51, 52]. Other impurities, such as Cl, can color the glass as well [60]. Another important distinction for bulk optical components is whether the impurities are surface or bulk and, in particular, if surface impurities are introduced from attack by the atmosphere [51].

Impurity absorptions due to metal ions in fluoride glasses have been investigated by various workers, and absorption losses associated with given concentrations of such ions have been determined. In one recent study, for example, the measured absorption in the near-IR in a fluoride fiber was assigned to contributions from various transition metal ions [58]. Such results provide guidelines for reducing the levels of various contaminants so that the absorption will be reduced to a specific level in a given wavelength region.

A primary impurity absorption in the mid-IR is that associated with OH, as illustrated in figures 1 and 2, which can enter the glass during batching and/or melting. Many workers have found that drastic reductions in OH absorption can be accomplished by the use of reactive atmospheres [41]. For example, the beneficial effects of a SF_6 RAP for reducing the OH peak was reported recently [43]. Oxide impurities (oxyfluorides) can contribute to IR edge absorption, and molecular water is believed to contribute to absorption in the 6 μm regime. Studies of absorption due to OH in the mid-IR using samples of varying thickness have shown typical surface absorptions of 1 percent for fluorozirconates and values up to an order of magnitude lower for selected Ba/Th glasses [8]. At the levels involved in the measurements there was no significant evidence of atmospheric attack from OH over a period of 30 days for Zr-Ba-La fluoride glass for samples stored in air. Investigations of surface absorption associated with impurities other than OH have not been reported.

Emittance measurement is a powerful tool because it allows the experimenter to sample the IR behavior of materials at elevated, as well as at room, temperatures. The IR emittance of a fluorozirconate glass at 130°C was obtained in preliminary experiments at Michelson Laboratory, Naval Weapons Center, using a liquid nitrogen-cooled emissometer [61]. A nitrogen-cooled cavity type black body was mounted behind the sample to absorb stray radiation. The sample itself was edge heated resistively. Since thermal contact in the vacuum environment was poor and no convective heat transfer could occur,

there is considerable uncertainty about the sample temperature, which was monitored by a thermocouple attached to the sample surface but near its edge. Nevertheless, the results (shown in figure 3) are in reasonable agreement--at room temperature--with those obtained by transmittance measurement and calorimetry. The multiphonon absorption edge moves to higher frequency--and hence shorter wavelength--with increasing sample temperature as predicted by theory. The absorption at shorter wavelenghts, which is presumably caused mainly by impurities or lack of stoichiometry, does not increase with increasing temperature, but instead shows a slight decrease. Theory predicts that impurity absorption should show very little temperature dependence. The qualitative behavior of the heated fluorozirconate glass is thus, as expected from theory. Quantitatively, it is surprising that the shift in wavelength with temperature is as large as it appears to be. A considerably smaller temperature dependence of the multiphonon glass edge was previously deduced for several of the fluoride glasses using transmittance data [62]. If the values found from the emittance measurements are representative of the material and not an experimental artifact, this fluorozirconate sample has an average, rather than a very low multiphonon edge, temperature dependence. The multiphonon edge at 300°C or 573°K, using a linear extrapolation of the temperature data, is shown by the dot-dash line. The predicted absorption coefficient at a wavelength of 5 μm would then be nearly 0.2 cm^{-1}, still adequately low for many applications in the 3 to 5 μm atmospheric window.

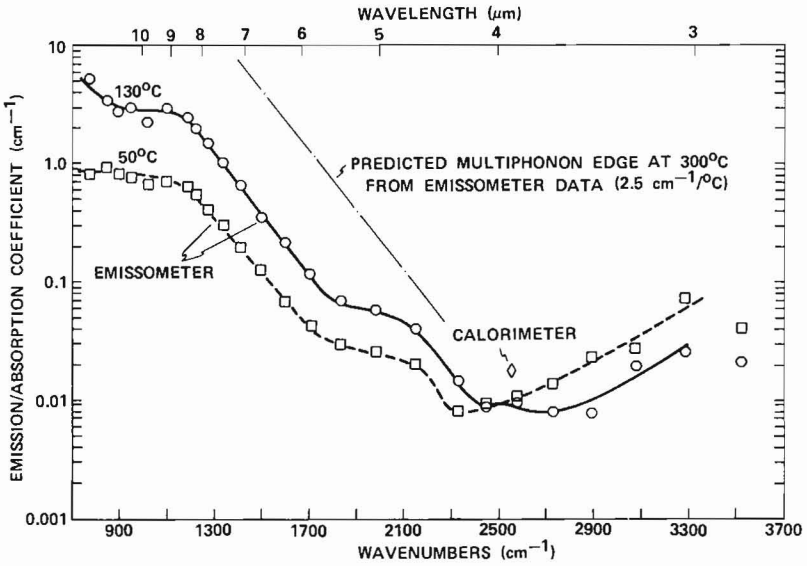


Figure 3. Emission/Absorption Coefficient of ZBLA Glass

2.4 Scattering Loss

Scattering in optical materials is important for many reasons. For example, in ultralow-loss optical fibers, Rayleigh scattering becomes a limiting loss mechanism that determines the bottom of the V-curve. The relatively low losses [63-65] (approximately 10^{-4} cm^{-1}) associated with intrinsic Rayleigh scattering throughout the IR and much of the visible spectra, are not a significant source of signal attenuation for most bulk component applications. Moreover, small scattering losses do not contribute to failure mechanisms like thermal distortion, thermal fracture, or nonlinearity-induced laser damage. On the other hand, noise from stray light generated by scattering can be detrimental when image or wavefront sensing is involved. In tactical laser systems, scattering from optical elements

may result in undesirable signatures at the aperture, which compromises concealment.

Total integrated scatter (TIS) is a useful operational measure of the scattering from all sources for an optical material. Representative values measured at IR and visible wavelengths on various samples obtained for this study are shown in table 8. The lowest values are comparable to those measured for the hardest dome materials like sapphire.

Table 8. TIS of Fluoride Glass Samples: Forward Total Integrated Scatter at λ = 0.647 and 3.39 μm

SAMPLE ID	0.6471 μm TIS	3.39 μm TIS
ZBLA-172, thin (0.058")	$(1.11 \pm 0.72) \times 10^{-3}$	$(8.39 \pm 2.12) \times 10^{-4}$
(repeat of 10/81 meas.)		
Spectran #1 (0.148")	$(7.18 \pm 5.50) \times 10^{-4}$	$(3.17 \pm 1.21) \times 10^{-4}$
Spectran #2 (0.159")	$(1.45 \pm 1.02) \times 10^{-3}$	$(7.36 \pm 5.72) \times 10^{-4}$
Spectran #11 (0.122")	$(6.89 \pm 6.07) \times 10^{-4}$	$(9.10 \pm 5.85) \times 10^{-3}$
repeat	$(7.93 \pm 6.03) \times 10^{-4}$	
Galileo GFG012 R2222 "A" (0.124")	$(5.34 \pm 1.63) \times 10^{-3}$	$(3.26 \pm 0.85) \times 10^{-3}$
Galileo GFG012 R2222 "B" (0.124")	$(3.87 \pm 0.60) \times 10^{-3}$	$(2.41 \pm 1.24) \times 10^{-3}$
Galileo GFG12N1 R2224 1 wt % NdF_3	$(5.66 \pm 3.41) \times 10^{-3}$	$(3.26 \pm 1.34) \times 10^{-3}$
Hughes ZBT (0.175") (7-16-79)	$(3.93 \pm 0.90) \times 10^{-3}$	$(3.03 \pm 1.46) \times 10^{-3}$
Hughes HBT (0.36")	Could not be measured, too much wedge	

Intrinsic Rayleigh (elastic) scattering varies as λ^{-4} and in glasses dominates other intrinsic scattering mechanisms such as Raman or Brillioun. Estimates of Rayleigh scattering show that for HMF glasses with λ (μm), $\alpha_{RS} \simeq 0.1\ \lambda^{-4}$ (dB/km). Thus, at 1 μm, for example, $\alpha_{RS} \sim 0.1$ dB/km. This estimate neglects scattering due to composition fluctuations.

Experimental measurements at NRL have shown that bulk alkali-fluorozirconate glasses display λ^{-4} scattering comparable in value to state-of-the-art fused silica, although fibers have typically displayed higher values of scattering [64]. Single wavelength (4880 Å) scattering data obtained by scanning over selected HMF glass samples indicated some values comparable to--and even lower than--fused silica, and a factor of 2 greater than predicted on the basis of theory. Since the scattering cross section is proportional to T_g, it appears that these low scattering values are due, in part, to the relatively low values of T_g for HMF glasses.

3. Physical Properties

3.1 Miscellaneous Physical and Thermal Properties

Current and projected values for selected physical properties of HMF glasses are summarized in table 9. Melting temperatures T_m are roughly related to the glass transition temperature T_g by the

two-thirds rule $T_g/T_m \sim \frac{2}{3}$; typical values of T_g are in the range of 300°C to 325°C for fluorozirconates, 350°C to 450°C for Ba/Th fluoride glasses, and less than 300°C for glasses with a high percentage of alkalis [8]. Typical densities are 4.5 to 5 (gm/cm^3) for fluorozirconates, and 5.5 to 6 for fluorohafnates and Ba/Th fluoride glasses. A significant quantity for glass formation and fiber drawing is the difference $\Delta T = T_c - T_g$, where T_c is the crystallization temperature. Generally, $\Delta T \sim 75°C$ to 100°C for the better HMF glasses [8], which are low values compared to those of most good glass formers. Selected compositions with $\Delta T \sim 100°C$ have been reported, but it is not known how large ΔT can be made while simultaneously achieving desirable optical and mechanical properties. HMF glasses possess relatively steep viscosity-temperature relations which, when combined with their low values of T_c-T_g, make both bulk glass formation and fiber drawing difficult. For ZBLA, for example, viscosities are approximately 0.4P at 670°C and 4P at 490°C. Hf-based composition have higher viscosities below the liquidus than Zr-based ones. Modification of both viscosity characteristics and T_c-T_g of HMF glasses has been pursued [66] through the addition of suitable dopants like alkali fluorides, PbF_2 and BiF_3.

Table 9. Physical/Thermal Properties

	CURRENT	PROJECTED
Fracture Strength	Approx. 10 kpsi	Approx. 300 kpsi
Stress Corrosion	N approx. 10 to 40	N greater than 100
Hardness	300 to 400 (Vickers 50 g, 15 sec)	Greater than 400
Softening Temperature	300 to 400°C	Greater than 400°C
Crystallization Temperature	400 to 500°C	Greater than 500°C
Thermal Expansion	1.4 to 1.9 x 10^{-5}/°K	Less than 1.4 x 10^5/°K
Thermal Conductivity	Similar to Silicates	--
Poisson's Ratio	.18 to .30	--
Thermal Endurance (calculated)	ΔT approx. 50-70°C	ΔT greater than 500°C

Only limited data on the elastic properties of HMF glasses have been reported [67]; typical results are shown in table 10. Moduli of HMFs are found to be less than those of high silicate glasses, but comparable to certain silicates containing lead and alkalis. The pressure and temperature dependence of elastic properties obtained for ZrF_4-BaF_2-ThF_4 glass indicate that it is "well-behaved" elastically, as opposed to vitreous BeF_2, SiO_2, or GeO_2.

The coefficient of thermal expansion α_T for HMF glasses [3] typically ranges between 14 and 20 x 10^{-6}/°C, relatively high values compared to most oxide glasses, but lower than chalcogenides. The lower range of values (about 14) is for lead and alkali-fluoride containing glasses.

Studies of heat capacity, c_p, have been conducted for various HMF glasses [8]. Below T_g, the data are fit well by the functional dependence $c_p = A+BT+C/T^2$. All the glasses measured have c_ps between 5.05 and 5.35 (cal/g-at.K). The heat capacity at constant volume was calculated to be about 3 percent lower than c_p near T_g, and correspondingly closer to c_p at lower temperatures. The low vibrational frequencies of HMFs lead to heat capacities per gram atom that are not very far--even at room temperature--from the Dulong-Petit limit of 3R = 5.97.

Table 10. Elastic Properties of Fluoride Glasses

MATERIAL	ELASTIC MODULUS MPa x 10^4	ELASTIC MODULUS (kpsi) x 10^3	BULK MODULUS MPa x 10^4	BULK MODULUS (kpsi) x 10^3	SHEAR MODULUS MPa x 10^4	SHEAR MODULUS (kpsi) x 10^3	POISSON's RATIO
Hf-Ba-La-Al Fluoride Glass	5.6	(8.1)	4.8	(6.9)	2.1	(3.1)	0.3
Zr-Ba-La-Al Fluoride Glass	5.5	(8.0)	4.8	(7.0)	2.1	(3.0)	0.3
Lead Alkali Silicate Glass (50-60% PbO)	5.7	(8.3)	3.2	(4.6)	2.3	(3.4)	0.2
Fused Silica	7.2	(10.5)	3.7	(5.3)	3.1	(4.5)	0.17

3.2 Strength and Hardness

The hardness and fracture toughness of HMF glasses is generally lower than those of high silicate content oxides, but higher than those of chalcogenides [68-70]. Measured rupture strengths of bulk specimens (values up to 35 kpsi have been quoted in the literature) are a reflection of their surface condition rather than an indicator of the ultimate strength of the material. Fracture toughness can be used to estimate intrinsic strength, and values measured to date imply strengths for HMF glasses that are somewhere between one-third and one-half of those with high silicate content [69]. Since values in excess of 800 kpsi have been reported for silicate fibers, pristine tensile strengths in the 250 kpsi to 500 kpsi range should be achievable for HMF glass fibers.

The strength of HMF fibers has been investigated recently by several groups, with British Telecom reporting [68] breaking strengths of aroung 70 kpsi, and UCLA reporting strengths of up to 100 kpsi for freshly drawn, Teflon-coated fibers of 150 μm diameter. Fractographic analysis conducted for this study at Sandia National Laboratories yielded values of fracture toughness for some HMF fibers of $K_{IC} \sim 0.5$ MPa·$m^{1/2}$. This value is lower than that of high silicate content oxide glasses but compares favorably with many other glasses; it gives projected strengths for pristine HMF fibers in the 10^6 psi range (see table 11).

Table 11. Fluoride Fibers Approach Silica in Mechanical Properties

	FLUORIDE	CHALCOGENIDE	SILICA
K_{1c} (MPa·$m^{1/2}$)	0.5	0.25	0.72
S_{avg}(MPa)	400	200	580
S_{th}(MPa)	10,000	5,000	14,000
N (Bulk Values)	8-14	17-22	15-30
	50		

Most fluorozirconates display Vickers microhardness in the range of 225 kg/mm^2 to 275 kg/mm^2. Recent measurements of Ba/Th fluoride glasses show that their hardness is higher than that of fluorozirconates [68], with typical values in the 300 kg/mm^2 to 325 kg/mm^2 range. There seems to be a relationship between hardness and composition that might eventually be exploited, as shown in tables 12 and 13. For example, selected Ba/Th/Y fluoride glasses with high percentages of BaF_2 display increased hardnesses in the vicinity of 400 kg/mm^2. Moreover, several of these compositions have displayed values of fracture toughness in the vinicity of 0.5, roughly twice that of typical fluorozirconates.

Table 12. Modest Improvements are Possible With Composition Changes

	FRACTURE TOUGHNESS (MPa·m$^{1/2}$)	HARDNESS (kg/mm^2)	ELASTIC MODULUS (MPa x 10^4)
ZBL	0.25 ± 0.05	288 ± 3	--
ZBLA	0.31 ± 0.08	267 ± 4	5.5
BZYbT	0.32 ± .01	276 ± 5	7.0
BZYT	0.33 ± .02	290 ± 2	6.7

ZBL = $62ZrF_4 \cdot 33BaF_2 \cdot 5LaF_3$
ZBLA = $57ZrF_4 \cdot 36BaF_2 \cdot 3LaF_3 \cdot 4AlF_3$
BZYbT = $15BaF_2 \cdot 28.3ZnF_2 \cdot 28.3YbF_3 \cdot 28.3ThF_4$
BZYT = $20BaF_2 \cdot 26.7ZnF_2 \cdot 26.7YF_3 \cdot 26.7ThF_4$

Table 13. Addition of BaF_2 Tends to Increase Toughness

COMPOSITION	FRACTURE TOUGHNESS (MPa·m$^{1/2}$)		
	WATER	AIR	OIL
12.5B·29Z·29Y·29T	0.26 ± .01	0.28 ± .01	0.27 ± .02
10B·30Z·30Y·30T	0.29 ± .01	0.29 ± .01	0.31 ± .01
17.5B·28Z·28Y·28T	0.26 ± .01	0.28 ± .01	0.33 ± .01
15B·28Z·28Y·28T	--	0.34 ± .01	0.32 ± .01
20B·27Z·27Y·27T	0.30 ± .01	0.33 ± .02	0.38 ± .01

B = BaF_2, Z = ZnF_2, Y = YF_3, T = ThF_4

3.3 Durability and Toughness

While the surfaces of most fluoride glasses appear to be highly stable over long periods of time in laboratory environments, their potential susceptibility to attack in aqueous environments is a concern [71-73]. For example, studies have shown that the solubility of typical fluorozirconates is many orders of magnitude greater than that of high silicates. In studies at Catholic University, normalized leach rates (g/cm^2-day) of 10^{-2} to 10^{-3} were obtained for ZBLA glass [73], compared to 10^{-7} to 10^{-8} for Pyrex, and similar results were also reported in a Norwegian study [71]. Comparative studies in water and air indicate a decrease of 10 to 20 percent in the fracture toughness of fluorozirconates in water, which suggests that they are susceptible to stress corrosion in aqueous environments [70]. Delayed failure measurements on flexure bars in air show substantial variations of the stress corrosion coefficient, n, from sample to sample; some n values lie between 8 and 14, while others are greater than 50. Moreover, measured n values did not correlate systematically with OH content in the glass. Some studies have been conducted to assess the effect of humidity and/or water on HMF fiber strength. Results indicate a rapid degradation of strength for ZrF_4-BaF_2-LaF_3-AlF_3 (ZBLA) fibers immersed in water; tests conducted at UCLA also showed that strengths of coated HMF fibers decrease significantly in wet atmospheres. In particular, water was found to permeate rapidly through FEP Teflon and lead to surface attack of the fibers. These conclusions are consistent with the susceptibility to corrosion and surface attack observed with bulk samples.

Since detailed studies to date have been limited to only a few compositions, it is not known whether others can be found with improved resistance to stress corrosion and/or lower solubility. However, in contrast to their susceptibility to aqueous corrosion, HMF glasses appear to be highly resistant to fluorinating agents such as Hf, F_2, and UF_6.

The potential susceptibility of fluoride glasses to aqueous attack, coupled with their relatively low fracture toughness and hardness, has spurred an interest in methods for toughening these glasses, some of which are indicated in table 14. Diamond-like carbon (DLC) has successfully been applied to fluoride glass substrates; preliminary hermeticity studies were conducted at Catholic University [74], which showed that the DLC coating was effective in reducing OH permeation to the surface of the glass. Once optimized, hermetic coatings such as DLC could lock in the pristine strength of the glass and protect glass surfaces indefinitely from corrosion.

Table 14. Promising Methods for Further Toughening Fluoride Glasses

o	Hermetic Coatings
	- Diamond-Like Carbon (D)
	- Metals (for optical fibers)
	- Silicon, Silicon Nitride, Boron Nitride
o	Surface Treatment
	- Thermally-Induced Recrystallization (D)
	- Ion-Exchange
	- Compressive Coatings (e.g., by CVD)

D = Demonstrated

Another approach to glass toughening involves surface treatments of various types. Thermally-induced hardening of surfaces of Ba/Mn fluoride glasses has been studied, in which up to three exothermic transitions accompanied by cumulative increases in hardness of up to 50 percent were observed [8]. Ion exchange and compressive coatings are other well known methods for toughening conventional glasses, but these have yet to be applied to HMFs. Formation of glass ceramics using heat and pressure is another approach that has not yet been systematically explored.

Appropriate choices of composition can yield glasses with improved mechanical characteristics; and, although the detailed dependence of strength, hardness, and durability on composition, processing conditions, and surface preparation has yet to be established, work to date suggests that variations in these parameters can be exploited to toughen HMF glasses.

3.4 Thermal Shock

Many complicated expressions involving geometrical and other parameters have been used in the literature to calculate thermal fracture. A highly simplified expression, useful for estimating thermal fracture is: $\Delta T_c \sim (1 - \nu)\, \sigma_F/\alpha_T E$, where ΔT_c is the critical (instantaneous) temperature rise at which fracture occurs, ν is Poisson's ratio, α_T is the linear thermal expansion coefficient, E is Young's modulus, and σ_F is the rupture strength of the specimen. For domes, the relevant ΔT is probably the temperature difference between the outer and inner sides of the dome. This approximate expression does not involve thermal conductivity or heat capacity because instantaneous heating is assumed. While ν, α_T, and E are intrinsic material properties that are relatively insensitive to preparation method and sample condition, σ_F is very sensitive to the latter. In the other extreme, it is equally inappropriate to deduce ΔT using the ultimate intrinsic strength of untoughened samples for σ_F. With these qualifications in mind and using rough numbers from the literature, one can estimate the ΔT_c's for fluoride glass compared against some typical oxides. A typical number for σ_F for ordinary unprotected samples is about 10 kpsi. Using this value, we obtain the results shown in table 15. With the excellent thermal endurance of fused silica an exception, virtually all other glasses, including fluorides, should have ΔT_c approximately 50°C to 100°C for samples with σ_F approximately 10 kpsi. With intrinsic strengths near 300 kpsi for HMF glasses, it is not unreasonable to expect attainment of σ_F's in excess of 50 kpsi for toughened versions of the glass, in which case ΔT_c would fall into the 300°C range.

Table 15. Calculated Values of ΔT_c for Several Glasses

	ν	α (10^{-6}/°C)	E (10^6 psi)	ΔT_c (°C)
Fluoride Glass (HBLA)	0.3	15	8	60
Typical Mixed Oxide Glass	0.2	12	8	80
Fused Silica	0.17	0.6	10	1,500

We performed some preliminary measurements of thermal endurance on alkali fluorozirconates obtained from Galileo E-O Corporation. Glass properties included room temperature strength σ = 4.9 kpsi, T_g approximately 225°C, and T_m approximately 325°C. A simple test was conducted by placing samples in an oven, heated to some fixed temperature, whose opening was small enough to enable rapid heating (about 20°C/sec) of a sample. After the sample reached the oven's temperature, the oven was turned off and the sample was allowed to cool to room temperature (1 to 3 hours) and the strength measured by 3-point flexure. Results of the measurements are shown in table 16; samples retained their strength at all temperatures up to melting, with samples near approaching T_m deforming, but not losing strength. Follow-on experiments with gradients in the temperature distribution in the oven need to be conducted to properly assess the thermal shock resistance of the glass.

Table 16. Fluoride Glass Retains Strength in Thermal Shock

	ANNEALED MPa	UNANNEALED MPa
R.T. (Room Temperature)	44	35
R.T. - 200°C	50	42
R.T. - 250°C	49	37
R.T. - 280°C		38*

*Approximately ±5% deformed

4. Concluding Remarks

Considerable progress has been made recently in the fabrication and characterization of HMF glasses. Many of them offer potential for low absorption and low scatter over a broad range of mid-IR to near-UV wavelengths. Although extrinsic absorption remains a problem, the principal impurities involved have been identified, as have methods for controlling or reducing them. Emittance spectroscopy is one of several promising techniques for investigating the IR absorption and its temperature dependence.

The fracture toughness of HMF glasses is relatively high, approaching that of high silicate glasses. However, HMF glass is susceptible to chemical corrosion in aqueous environments, and will probably require hermetic coatings to protect the surface of the glass. Diamond-like carbon has successfully been deposited on HMF glass surfaces, and preliminary measurements using IR spectroscopy show that it reduces the permeation of moisture into the surface. The hardness and thermal endurance of HMF glasses appear to be acceptable for most applications, although further improvements may be possible by composition variation or surface modification.

Table 17 shows that HMF glasses are believed to offer a variety of advantages for use as laser windows, IR domes, and IR optical fibers.

Table 17. Advantages of HMF Glasses for Selected Applications

IR DOMES
o Ultralow mid-IR Absorption
o Multispectral Capability (mid-IR to near-UV)
o Low Refractive Index
o Low Dispersion
o Low Scattering
o Low Stress-Induced Birefringence
o Flexible Size and Shape
o Low Cost Fabrication
LASER WINDOWS
o Ultralow Absorption at Laser Wavelengths
o Multispectral Capability
o Low Refractive Index
o Low Scattering
o Potential for Ultralow Thermal Distortion
o Potential for Fabrication of Large Sizes
o Low Cost Fabrication
IR OPTICAL FIBERS
o Ultralow Minimum Losses (less than 10^{-2} dB/km)
o Broad Transmission Window
o Low Refractive Index
o Low Dispersion
o Anticipated Reduced Susceptibility to Nuclear Radiation

We are pleased to acknowledge the technical assistance and contributions of many individuals during the course of this work. In particular, we would like to thank the following organizations and individuals: Rome Air Development Center (O. El-Bayoumi and M. G. Drexhage); Naval Weapons Center (A. Green, T. Donovan, and P. Temple); University of Rennes (J. Lucas); University of Maine (C. Jacoboni and R. DePape); Rensellaer Polytechnic Institute (C. T. Moynihan); Naval Research Lab (D. Tran and G. Sigel); University of California, Los Angeles (J. Lau and J. D. Mackenzie); SpecTran (M. Stein and R. Jaeger); Galileo E-O (J. Mansfield and T. Loretz); Hughes (M. Robinson and L. DeShazer); University of Rhode Island (P. K. Banerjee and S. S. Mitra); Air Force Weapons Lab (B. Pierce and D. Martin); University of Dayton Research Institute (R. Harris and B. Kumar); and University of Florida (K. Simmons and J. Simmons).

REFERENCES

[1.] M. G. Drexhage, C. T. Moynihan, C. T. Boulos, M. Saleh, K. P. Quinlan, "Fluoride Glasses for Visible to Mid-IR Guided Wave Optics," in Physics of Fiber Optics, B. Bendow, S. S. Mitra, eds. Amer. Ceramic Soc., Columbus, OH, 1981.

[2. M. G. Drexhage, B. Bendow, O. El-Bayoumi, T. Loretz, C. T. Moynihan, J. J. Shaffer, P. A. Temple, H. E. Bennett, "Progress in the Development of Multispectral Glasses Based on the Fluorides of Heavy Metals," 13th Boulder Damage Symposium, Boulder, CO, November 1981.

[3.] T. Miyashita and T. Manabe, "Infrared Optical Fibers," Journal of Quantum Electronics, QU-18, 1432, 1982.

[4.] B. Bendow, S. S. Mitra, "Physics of Fiber Optics," American Ceramic Society, Columbus, OH, 1981.

[5.] B. Bendow, M. G. Drexhage, "Prospective Vitreous Materials for Infrared Fiber Optics," Optical Eng. 21, 118-121, 1982.

[6.] Conference Digest, First International Symposium on Halide and Other Nonoxide Glasses, Churchill College, Cambridge, UK, 1982.

[7.] Conference Digest, Second International Symposium on Halide Glasses, RPI, Troy, NY, 1983.

[8.] C. T. Moynihan et al, "Metallic Halide Optical Glasses: Synthesis and Characterization of IR Transmitting Fluoride Glasses," Final Technical Report, RADC-TR-82-264, Catholic University of America, 1982.

[9.] L. G. DeShazer, J. A. Harrington, eds., "Advances in Infrared Fibers," SPIE Proceedings, Vol. 320, Bellingham, WA, 1982.

[10.] M. G. Drexhage, O. El-Bayoumi, C. T. Moynihan, "Progress in Heavy Metal Fluoride Glasses for Infrared Fibers," SPIE Proceedings, Vol. 320, 1982.

[11.] C. M. Baldwin, R. M. Almeida, J. D. Mackenzie, "Halide Glasses," Journal of Non-Crystalline solids 43, 309-44, 1981.

[12.] L. G. DeShazer, C. Kao, "Infrared Fibers," SPIE Proceedings, Vol. 266, Bellingham, WA, 1981.

[13.] J. R. Gannon, "Optical Fiber Materials for Operating Wavelengths Longer Than 2 μm," J. Non-Cryst. Solids 42, 239-46, 1981.

[14.] J. R. Gannon, "Materials for Mid-Infrared Waveguides," Infrared Fibers, SPIE Proceedings, 1981.

[15.] J. D. Mackenzie, "Preparation and Properties of Fluoride Glass," Final Technical Report, No. 8331705, Lawrence Livermore Laboratories, Livermore, CA, May 1978.

[16.] S. Takahashi, S. Shibata, T. Kanamori, S. Mitachi, T. Manabe, "New Fluoride Glasses for IR Transmission," in Physics of Fiber Optics, B. Bendow, S. S. Mitra, eds., Amer. Ceramic Soc., Columbus, OH, 1981.

[17.] J. Lucas, "Fluoride Glasses With Large Optical Window for IR Fibers," in Advances in IR Fibers, Technical Digest, SPIE Proceedings (paper 320-05), January 1982.

[18. B. Bendow, E. Hartouni, and J. J. Mechoslky, "Progress in the Fabrication of Mid-IR Optical Fibers," in SPIE Proceedings, Vol. 357, Lasers in Medicine and Surgery, 1982.

[19.] M. G. Drexhage, B. Bendow, C. T. Moynihan, "IR-Transmitting Fluoride Glasses," Laser Focus, October 1980.

[20.] M. G. Drexhage, O. H. El-Bayoumi, C. T. Moynihan, A. J. Bruce, K. H. Chung, D. L. Gavin, T. J. Loretz, "Preparation and Properties of Heavy Metal Fluoride Glasses Containing Ytterbium or Lutetium Fluoride," Journal of the American Ceramic Society (1982, in press).

[21.] M. Poulain, M. Chanthanasinh, J. Lucas, "New Fluoride Glasses," Materials Research Bulletin 12, 151-56, 1977.

[22. M. Poulain, J. Lucas, "A New Class of Materials: Fluoride Glasses Made With ZrF_4," Verres Refact. 32, 505-13, 1978.

[23.] M. Matecki, M. Poulain, J. Lucas, "New ZrF_4 Glasses Not Containing a Modifying Element," Materials Research Bulletin 13, 1039-46, 1978.

[24.] J. Lucas, M. Poulain, "Vitreous Rare Earth Fluorozirconates," in The Rare Earths in Modern Science and Technology, Ed. by G. J. McCarthy and J. J. Rhyne, Plenum Pub. Corp., New York, 1978.

[25.] J. Lucas, M. Chanthanasinh, M. Poulain, P. Brun, M. J. Weber, "Preparation and Optical Props of Nd Fluorozirconate Glasses," Journal of Non-Crystalline Solids 27, 273-83, 1978.

[26.] N. Aliaga, G. Fonteneau, J. Lucas, "Synthesis and Spectroscopic Study of Mixed Fluoride Glasses Based on Zr, Ba, and U," Ann. Chim. Fr. 3, 51-8, 1978.

[27.] M. Poulain, M. Poulain, J. Lucas, "Etude Comparees de Verres Fluores Dans Les Diagrammes Ternaires ZrF_4 -BaF_2-MF_n (M=Na, Ca, Ln, Th; x = 1, 2, 3, 4). Rev. Chim. Min. 16, 267-276, 1979.

[28.] J. P. Miranday, D. Jacoboni, R. DePape, "New Glasses Formed From the Fluorides of Transition Metal Elements," Rev. Chim. Min. 16, 277-82, 1979.

[29.] A. Lecoq, M. Poulain, J. Lucas, "La Fluorozirconate Glasses," Journal of Non-Crystalline Solids 34, 101-10, 1979.

[30.] S. Shibata, T. Kanamori, S. Mitachi, T. Manabe, "New Binary PbF_2-AlF_3 Glasses," Materials Research Bulletin 15, 129-37, 1980.

[31.] M. Robinson, R. C. Pastor, R. R. Turk, M. Braunstein, R. Braunstein, "IR Transparent Glasses Derived From the Fluorides of Zr, Th, and Ba," Materials Research Bulletin 15, 735-42, 1980.

[32.] A. Lecoq, M. Poulain, "Fluoride Glasses in the ZrF_4-BaF_2-YF_3-AlF_3 Quaternary System," Journal Non-Crystalline Solids 41, 209-217, 1980.

[33.] A. Lecoq, M. Poulain, "Phenomenological Study of the Stabilizing Role of Aluminum in Zirconium Tetrafluoride Glasses," Verres Refract. 34, 3, 333-42, 1980.

[34.] G. Fonteneau, F. Lahaie, J. Lucas, "A New Family of Fluoridated Glasses: Vitreous Fluorides in the System ThF_4-BaF_2-MF_2, M=Zn, Mn," Materials Research Bulletin 15, 1143-47, 1980.

[35.] G. Fonteneau, H. Slim, F. Lahaie, J. Lucas, "New Fluoride Glasses Transmitting in the Infrared in the LnF_3-BaF_2-ZnF_2 Systems," Materials Research Bulletin 15, 1425-32, 1980.

[36.] M. G. Drexhage, C. T. Moynihan, M. S. Boulos, "Infrared Transmitting Glasses Based on HfF_4," Materials Research Bulletin 15, 213-18, 1980.

[37.] M. Poulain, M. Poulain, M. Matecki, "Fluoride Glasses With a Large Optical Transmission Window and High Chemical Durability," Materials Research Bulletin 16, 555-64, 1981.

[38.] J. P. Miranday, D. Jacoboni, R. DePape, "New Transition Metal Fluoride Glasses Isolated in the PbF_2-$M_t^{II}F_2$-$M_t^{III}F_3$ Systems," Journal of Non-Crystalline Solids 43, 393-401, 1981.

[39.] M. Matecki, M. Poulain, M. Poulain, "Etude des Fluores dans les Quaternaires ZnF_2-ThF_4-AlF_3-MF_2," Materials Research Bulletin 16, 749-57, 1981.

[40.] J. Lucas, H. Slim, G. Fonteneau, "New Fluoride Glasses Based on 4f and 5f Elements," Journal of Non-Crystalline Solids 44, 31-35, 1981.

[41.] M. Robinson, R, C. Pastor, R. R. Turk, D. P. Devor, M. Braunstein, R. Braunstein, "Infrared Transparent Glasses Derived from Hafnium Fluoride," SPIE Proceedings, Vol. 266, 78-83, 1981.

[42.] D. Tran, C. Fisher, G. Sigel, "Fluoride Glass Preforms Prepared by a Rotational Casting Process," Electron. Lett. 18, 657, 1982.

[43.] D. C. Tran, R. J. Ginther, G. H. Sigel, K. H. Levin, "Preparation and Characterization of Zirconium Fluoride-Based Glass Fibers," Technical Digest of Topical Meeting on Optical Fiber Communications, Phoenix, AZ, Apr. 13-16, 1982.

[44. H. G. Lipson, B. Bendow, M. G. Drexhage, "Multiphonon Absorption in IR Glasses Based on ZrF_4 and HfF_4," in Basic Optical Properties of Materials, A. Feldman, Ed. (USGPO, Washington, DC, 1980), NBS Spec. Pub. #574.

[45.] C. T. Moynihan, M. G. Drexhage, B. Bendow, M. Saleh-Boulos, K. P. Quinlan, K. Chung, E. Gbogi, "Composition Dependence of Infrared Edge Absorption in ZrF_4 and HfF_4-Based Glasses," Materials Research Bulletin 16, 25-30, 1981.

[46.] M. G. Drexhage, B. Bendow, H. G. Lipson, C. T. Moynihan, "IR Absorption in Highly Transparent Glasses Based on HfF_4," in Proceeding of the 1980 Boulder Symposium on Optical Materials, USPGO, 1981.

[47.] M. G. Drexhage, C. T. Moynihan, B. Bendow, E. Gbogi, K. H. Chung, M. Boulos, "Influence of Processing Conditions on IR Edge Absorption in Fluorohafnate and Fluorozirconate Glasses," Materials Research Bulletin 16, 943-47, 1981.

[48.] B. Bendow, M. G. Drexhage, H. G. Lipson, "IR Absorption in Highly Transparent Fluorozirconate Glass," Journal of Applied Physics 52, 1460-61, 1981.

[49.] B. Bendow, M. G. Drexhage, H. G. Lipson, P. K. Banerjee, J. Goltman, S. S. Mitra, C. T. Moynihan, "Infrared Absorption of Fluorozirconate Glass in the 200-1800 cm^{-1} Frequency Regime," Applied Optics 20, 2875-77, 1981.

[50.] H. Poignant, "Multiphonon Absorption in Infrared Fluoride Glasses," Electron. Lett. 18(5), 199-200, 1982.

[51.] E. Gbogi, K. H. Chung, C. T. Moynihan, M. G. Drexhage, "Surface and Bulk-OH Absorption in ZrF_4 and Hf_4-Based Glasses," Journal of the American Ceramic Society 64, C51-53, 1982.

[52.] D. C. Tran, et al, "Miminization of OH Absorption and Scattering Losses in ZrF_4 Glasses," in Technical Digest, OFC'83, Optical Society of America, 1983.

[53.] H. Poignant, J. LeMellot, and J. F. Bayon, "Fluoride Glass for IR Optical Fiber," Electron. Lett., 17, pp. 295-296 (1981).

[54.] B. Bendow, P. Banerjee, M. G. Drexhage, J. Goltman, S. S. Mitra, C. T. Moynihan, "Vibrational Spectra of Fluorohafnate Glasses," Journal of the American Ceramic Society 65(1), C8-C9, 1982.

[55.] B. Bendow, P. K. Banerjee, M. G. Drexhage, O. H. El-Bayoumi, S. S. Mitra, C. T. Moynihan, D. Gavin, G. Fontaneau, J. Lucas, and M. Poulain, "Effect of Aluminum Content on IR Characteristics of BaF_2/ThF_4-Containing Glasses," Journal of the American Ceramic Society 66 (4), C-64-C-66 (1983).

[56.] M. G. Drexhage, B. Bendow, R. Brown, P, Banerjee, H. Lipson, G. Fonteneau, J. Lucas, C. T. Moynihan, "Extended IR Absorption of Multicomponent Glasses Based on the Fluorides of Thorium, Barium, and Other Metals," Applied Optics 21(6), 971-72, 1982.

[57.] M. Matecki, M. Poulain, and M. Poulain, "Progress in Cadmium Halide Glasses," paper 27, Second Int. Symposium on Halide Glases, Troy, NY (1983).

[58.] Y. Ohishi, S. Mitachi, S. Shibata, T. Manabe, "Impurity Absorption Loss due to Rare Earth Elements in a Fluoride Glass," Japan. Journal of Applied Physics 20, L191-193, 1981.

[59.] T. Ohishi, S. Mitachi, T. Kanamori, "Impurity Absorption Losses in the Infrared Region due to 3d Transition Elements in Fluoride Glass," Japan. Journal of Applied Physics 20, L787-88, 1981.

[60.] R. N. Brown, B. Bendow, M. G. Drexhage, C. T. Moynihan, "UV Absorption Edge Studies of Fluorozirconate and Fluorohafnate Glasses," Applied Optics 21, 361-63, 1982.

[61.] L. Skolnik, M. Clark, R. Koch, and W. McCann, "A Cryogenic Emittance Spectrometer for Measuring Absorption Losses in Laser Window Materials," Proceedings of the Fourth Annual Conference on Infrred Laser Window Materials, ed. by C. R. Andrews and C. L. Streaker, Air Force Materials Laboratory, Wright-Patterson AFB, OH, pp. 197-212, January 1975.

[62.] B. Bendow, "Fluoride Glass Technology Study and Assessment Final Report," The BDM Corporation report, BDM/A-83-338-TR, p. III-16, July 1983.

[63.] D. C. Tran, G. H. Sigel, Jr., K. H. Levin, and R. J. Ginther, "Rayleigh Scattering in ZrF_4-Based Glass," Electron. Lett. 18, pp. 1046-1048 (1982).

[64.] D. C. Tran, K. H. Levin, C. F. Fisher, M. J. Burk, and G. H. Sigel, Jr., "Rayleigh Scattering in Fluoride Glass Optical Fibers," Electron. Lett. 19. pp. 165-166 (1983).

[65.] J. Schroeder, "Light Scattering in Fluoride Glass," paper 45, Second Int. Symposium on Halide Glasses, Troy, NY (1983).

[66.] D. C. Tran, R. J. Ginther, G. H. Sigel, "Fluorozirconate Glasses With Improved Viscosity Characteristics for Fiber Drawing," Materials Research Bulletin 17, 9, 1982.

[67.] M. P. Brassington, T. Hailing, A. J. Miller, G. A. Saunders, "Elastic Constants of a Fluorozirconate Glass," Materials Research Bulletin 16, 613-21, 1981.

[68.] P. W. France, J. Williams, J. F. Carter, and K. J. Beales, "Mechanical Properties of IR Transmitting Fibers," Conference Digest, Second Int. Symposium on Halide Glasses, Troy, NY (1983).

[69.] J. J. Mecholsky, J. Lau, J. Mackenzie, D. Tran, B. Bendow, "Fracture Anslysis of Fluoride Glass Fibers," ibid. (1983).

[70.] J. J. Mechoslky, M. G. Drexhage, O. El-Bayoumi, C. T. Moynihan, "Effect of Composition and Environment on Fracture of Fluoride Glasses," Conf. Digest, 1st Intn'l Symposium on Halide Glasses, Cambridge, UK, 1982.

[71.] T. A. Fjeldby, "Stability of IR Fluoride Glasses Under Exposure to High Humidity and to Aqueous Solutions," ELAB Report STF44 A82222 (University of Trondheim, Norway), 1982.

[72.] C. J. Simmons, H. Sutter, J. H. Simmons, D. C. Tran, "Aqueous Corrosion Studies of a Fluorozirconate Glass," Materials Research Bulletin 17, 1203, 1982.

[73.] C. J. Simmons, S. A. Azalin, and J. H. Simmons, "Chemical Durability Studies of Heavy Metal Fluoride Glasses," paper 47, Second Int. Symposium on Halide Glasses, Troy, NY (1983).

[74.] M. Stein, A. Green, B. Bendow, O. El-Bayoumi, M. G. Drexhage, "Diamond-Like Carbon Coatings for Protection of Halide Glass Surfaces," Digest of Second Int. Halide Glass Symposium, Troy, NY (1983).

A question was raised about the mechanism that would cause the high temperature infrared absorption to be larger at long infrared wavelengths but somewhat smaller at shorter infrared wavelengths. The speaker pointed out that the long wavelength absorption is intrinsic, caused by multiphonon absorption; whereas, at shorter wavelengths it results from extrinsic effects. Also, it is very sensitive to surface effects, particularly at the shorter wavelengths. The increase in absorption with increasing temperature is qualitatively in agreement with theory, although the absolute value of the increase with temperature is uncertain.

Another question concerned what work has been done on the spectroscopy of dopants in fluoride glasses. The speaker replied that the glasses had been doped so far with erbium, holmium, dysprosium, and four or five other rare earth elements. The resulting crystals have various colors including pink, yellow, and green, and many of the dopants are infrared active. Spectroscopic analyses have been carried out in Dr. Sibley's group at Oklahoma State University and at Hebrew University in Jerusalem. However, to his knowledge, lasing action has not been observed or looked for.

A third question concerned how the glass transition temperatures of the fluoride glasses compared with each other and with silicates. The speaker responded that typical temperatures for the fluorides are 300°C to 500°C. They are thus similar to some of the mixed silicates but much lower than the pure silicates, which can go as high as 1500°C.

- Manuscript Not Received -

OPTICAL PROPERTIES OF INFRARED TRANSMITTING GLASSES*

by

S.S. Mitra
Department of Electrical Engineering
University of Rhode Island
Kingston, RI 02881

ABSTRACT

Considerable interest has recently been evidenced in infrared transmitting glasses for components such as laser windows, IR domes and IR optical fibers. In particular, multi-component heavy metal fluoride glasses based on zirconium or hafnium have displayed desirable optical characteristics, viz., low refractive index, absorption and scattering losses, and a very wide spectral transparent regime, in addition to attractive mechanical and chemical properties.

This talk will review the optical properties of this and related metal halide glasses over the entire spectral range (9 μm to 260 nm). This will include review of experimental data for the ultraviolet absorption edge, infrared edge absorption and temperature dependence, and the understanding of the latter through fundamental vibrational spectra, information regarding which is obtained from a study of infrared reflection and Raman scattering measurements. Effects of nuclear radiation on the optical properties of a number of these glasses will be presented.

Key words: infrared windows; metal-Fluoride glasses; radiation damage; Raman scattering.

*Work supported by RADC, U.S. Air Force under Contract No. F 19628-81-C-0034

RECEIVED: 12-30-83

Optical and Mechanical Properties of Water Clear ZnS*

R. J. Harris, G. A. Graves, D. V. Dempsey, P. R. Greason, M. E. Gangl, and D. B. O'Quinn

University of Dayton Research Institute
Dayton, OH 45469

and

M. J. Lefebvre

CVD, Inc.
Woburn, MA 01801

Optical and mechanical properties of water clear ZnS produced by CVD, Inc. of Woburn, MA, have been measured. These include optical absorption at several laser wavelengths, spectral transmission, thermo-optic coefficients, stress-optic coefficients, thermal expansion coefficient, density, specific heat, thermal diffusivity, and electrical resistivity. Measurements were made on production grade material and three research batches and correlations made for optical properties as a function of deposition parameters.

Key Words: ZnS, optical absorption, thermo-optic, stress-optic, transmission

1. Introduction

One of the major infrared optical materials developments in recent times has been the development of techniques in chemical vapor deposition and post-deposition processing which result in water clear ZnS. The material is colorless and highly transparent from 0.4 μm to 11 μm with no features in spectral transmission throughout this range. It has mechanical and thermal characteristics essentially the same as the older reddish brown material, but its enhanced optical performance has made it a considerably more viable candidate for multispectral applications wherein thermal imaging in the 8-12 μm band is used in conjunction with a requirement for high transparency in the visible and near infrared region.

In view of this potential application and other applications in infrared optics, CVD, Inc. of Woburn, MA, embarked on a development program under Air Force sponsorship under Contract No. F33615-81-C-5076. The process involves a post-deposition step at high temperatures and high pressures to remove defects and/or impurities which contribute to short wavelength absorption and impart the reddish brown color to the material. CVD supplied material from a standard production run and three research depositions for characterization by the University of Dayton Research Institute.

2. Experimental Procedures

Measurements performed on the samples included optical absorption at several laser wavelengths, spectral transmission in the 0.3-20 μm range, thermo-optic coefficient measurement at several laser wavelengths, stress-optic coefficient measurement at 0.6328 μm, and measurement of thermal expansion coefficient, density, specific heat, thermal diffusivity, and electrical resistivity.

2.1 Optical Absorption

The optical absorption coefficients were measured using laser rate calorimetry. This is a well established technique[1] with sensitivity approaching 10^{-5} cm^{-1}. The lasers used were a Nd:YAG operating at 1.06 μm and 1.32 μm, HF and DF lasers operating at 2.7 μm and 3.8 μm respectively, and a CO_2 laser operating at 9.27 μm and 10.6 μm.

2.2 Spectral Transmission

The spectral transmission measurements were made in the 0.3-2.5 μm range using a Beckman 5270 spectrophotometer and in the 2.5-20 μm range using a Perkin-Elmer 180 spectrophotometer. Both instruments are interfaced with a DEC LSI-11 minicomputer and the data is merged to plot the spectrum over the entire spectral range or any part of it.

* This work was done under Contract No. F33615-82-C-5137 for the Materials Laboratory, Air Force Wright Aeronautical Laboratories, Wright-Patterson Air Force Base, Ohio 45433

2.3 Thermo-Optic Coefficient

The thermo-optic coefficients were measured using a laser interferometric technique. This technique is also well established[2] and has a precision of ±1 x 10^{-6} / ^{o}C. The measurements were made at 0.6328 μm, 1.15 μm, and 3.39 μm using HeNe lasers.

2.4 Stress-Optic Coefficients

The stress-optic coefficients were measured at 0.6328 μm using the technique described by A. Feldman, et. al.[3] which monitors the change in optical path in a sample interferometrically as a function of applied uniaxial stress. The accuracy of these measurements is estimated at 3-5%.

2.5 Mechanical, Thermal, and Electrical Properties

The thermal expansion coefficient was measured in the -65°C to 200°C range using a quartz tube dilatometer. The bulk density was measured using Archimedes' water displacement technique. The specific heat was measured at 0°C, 50°C, and 100°C using a differential scanning calorimeter. The thermal diffusivity was measured using a xenon flash technique. The resistivity was measured using a 6-point Hall probe.

3. Results and Conclusions

3.1 Optical Absorption and Transmission

The spectral transmission of the water clear ZnS is considerably improved over that of the old reddish brown material. This can be seen in the transmission spectra shown in Figures 1 and 2. As can be seen in the figures, there is not only an improvement in the short wavelength transmission, but also all the absorbing impurities or defects contributing to the features seen in the 3-10 μm region have been removed.

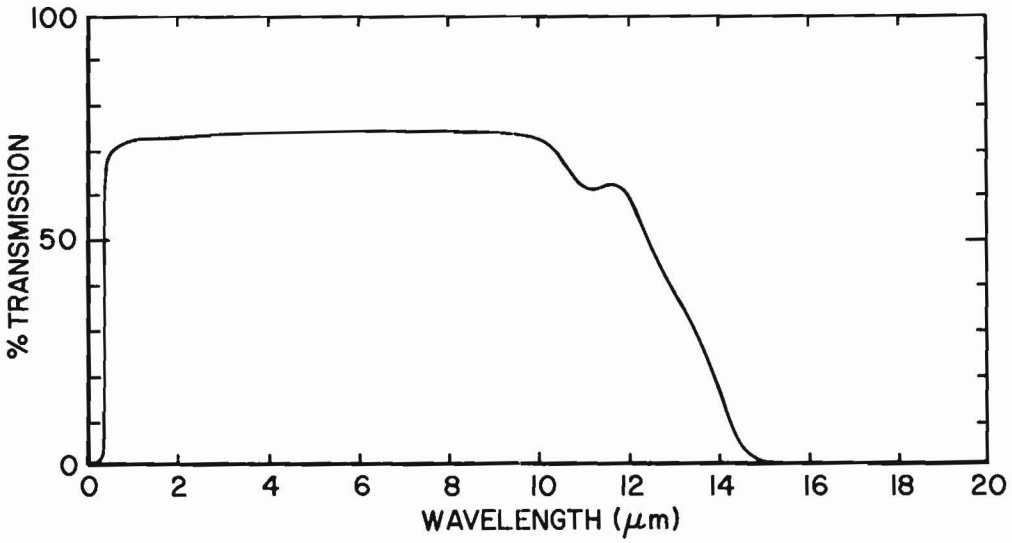


Figure 1. Spectral transmission of water clear ZnS from CVD, Inc. Sample thickness is 6.4 mm.

The optical absorption coefficients were on the order of 10^{-2} to 10^{-3} cm^{-1} at all wavelengths in the highly transparent region. There was no clear-cut difference between the production sample and the research deposition samples. The research batches were labeled AF-1, AF-4, and AF-6 by CVD. The deposition parameters for these batches are given in Table 1. The production sample was deposited under conditions similar to AF-1 and AF-4 at a temperature intermediate between the two. The results of the calorimetric absorption measurements are given in Table 2. The strongest effect on absorption was the deposition temperature, with higher temperatures producing lower absorption coefficients. Increasing the Zn injection rate and lowering the H and S flow also decreased the absorption, but not as much as the temperature variation. The samples deposited under AF-4 conditions were received in three different groups as indicated by the numbers in parentheses in the table.

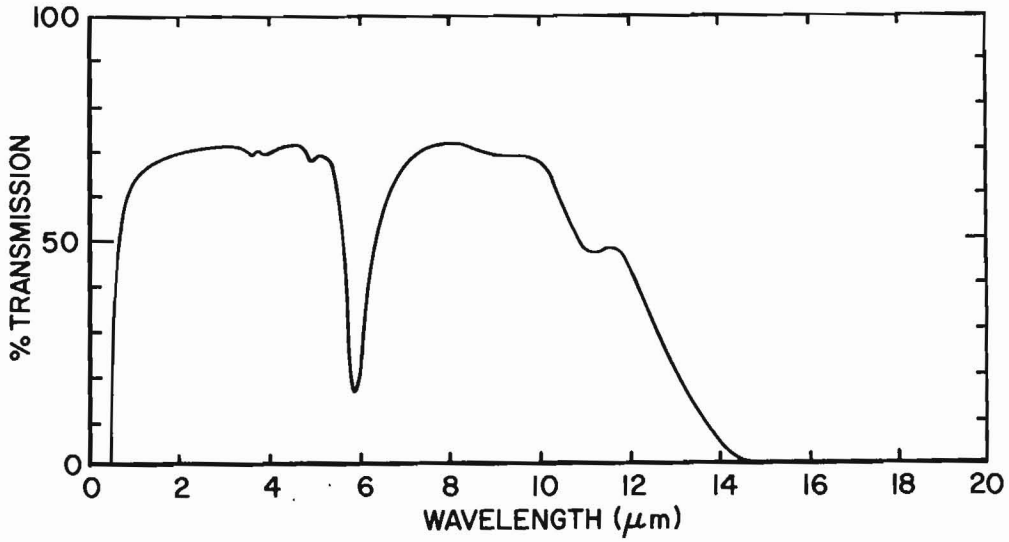


Figure 2. Spectral transmission of an old reddish brown sample of ZnS. Sample thickness is 10.8 mm.

Table 1. Deposition Conditions for CVD, Inc. Research Samples

Batch	Deposition Temperature (°C)	H & S (LPM)	Zn (g/hr)	Furnace Pressure (torr)	Deposition Time (hrs)
AF-1	670	2.7	675	38	125.5
AF-4	720	2.7	675	38	125
AF-6	670	2.1	1223	38	137

The variation in absorption at HF and 9.27 μm wavelengths for these groups indicates some differences either in deposition parameter control or post-deposition processing. The internal variation in AF-4 is smaller than the variation between the three batches; so correlations can be made with a reasonable degree of certainty.

There is a correlation between the absorption coefficients and both the total transmission away from the short wavelength cutoff in the visible and the internal scattering of the samples. Figure 3 shows the transmission of four representative research samples and sample 4110, which was included because of its low absorption at 1.32 μm, in the 0.35-5.0 μm region. The highest transmitting sample is 4110 and the lowest is from batch AF-1. Figure 4 shows a plot of the effective absorption coefficient at 1.32 μm vs. the transmission at 0.5 μm demonstrating the correlation between these two parameters. Figure 5 shows the amount of light scattered out of a 4 degree half-angle cone in the 0-2.5 μm for the same four samples, and a plot of 1.32 μm absorption vs. scattering at that wavelength is presented in Figure 6. There is also a correlation between the short wavelength cutoff and the maximum light scattered at the short wavelength limit. A plot of these values is shown in Figure 7.

3.2 Thermo-Optic and Stress-Optic Coefficients

The thermo-optic coefficients for the water clear material were consistently 15% lower than those obtained for the older reddish brown material. The values for both materials are presented in Table 3. The reasons for the difference are not known at this time.

The stress-optic coefficients for the water clear material at 0.6328 μm are 0.21×10^{-12} m^2/N for q_{11} and -0.58×10^{-12} m^2/N for q_{12} with an elastic compliance, s_{12}, equal to 0.029×10^{-12} m^2/N. We have not measured the coefficients for the older material or found literature values for comparison.

Table 2. Results of Calorimetric Absorption Measurements at Six Wavelengths

Sample No.	Batch	$\beta_{eff} \div 10^{-3} cm^{-1}$ @1.06 μm	@1.32 μm	HF	DF	@9.27 μm	@10.6 μm
4089	Prod.	2.41	1.71	10.3	6.31	15.5	182.5
4098	AF-1	15.7	13.6	17.1	16.4	19.0	259.0
4099	AF-1	23.4	16.2	21.3	20.7	22.0	245.5
4100	AF-4(1)	4.25	3.15	5.16	2.91	9.90	244.5
4101	AF-4(1)	3.44	2.98	5.33	2.29	10.0	224.0
4109	AF-4(2)	3.12	2.62	3.72	3.43	14.6	213.0
4110	AF-4(2)		0.956	2.74	2.31	12.0	207.5
4112	AF-4(3)			2.95	2.11	4.40	268.0
4113	AF-4(3)			3.07	2.52	4.47	246.0
4114	AF-4(3)			3.40	3.29	4.53	260.0
4115	AF-4(3)			3.52	2.68	4.45	237.0
4102	AF-6	5.53	5.88	15.7	7.63	13.3	228.5
4103	AF-6	10.3	10.0	21.6	9.23	13.5	237.5

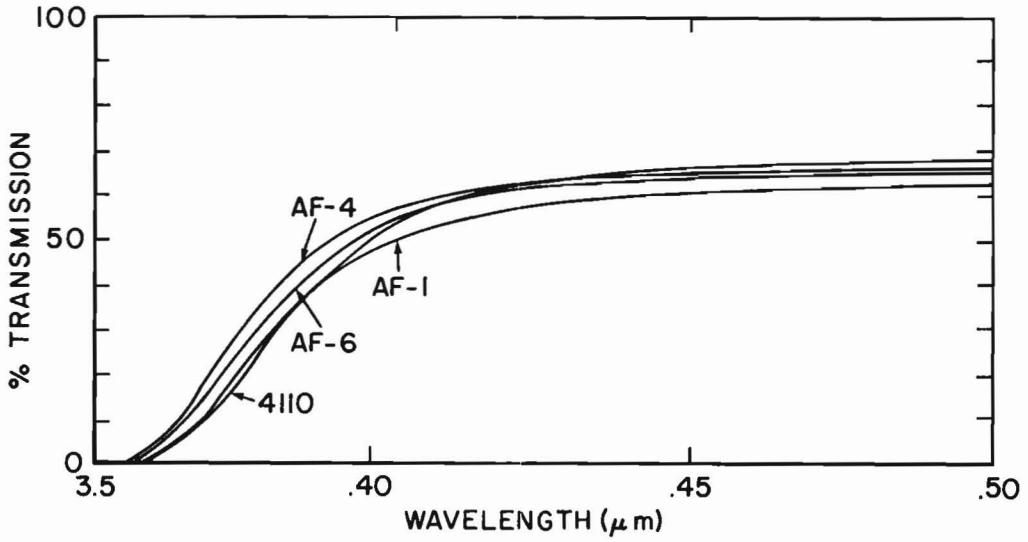


Figure 3. Short Wavelength Spectral Transmission of Four ZnS Samples. The curves labeled AF-1, AF-4, and AF-6 are representative of the three research batches, and 4110 is included because of its low absorption at 1.32 μm.

3.4 Mechanical, Thermal, and Electrical Properties

The coefficient of thermal expansion was determined from measurements made on four samples. The average coefficient over the temperature range from -65°C to 200°C was 6.5 x 10^{-6}/°C. Individual test results are presented in Table 4.

The thermal diffusivity was determined from eight measurements conducted at 25°C. The average value obtained was 0.13 cm^2/s. The specific heat values obtained were 0.123, 0.126, and 0.127 cal/g/°C for test temperatures of 0°C, 50°C, and 100°C respectively. Assuming a linear relationship with respect to temperature, the specific heat at 25°C was calculated to be 0.124 cal/g/°C. The

bulk density was determined to be 4.0 g/cm^3. From these measurements, the thermal conductivity was calculated to be 0.27 watt/cm-^{o}C.

Table 3. Thermo-Optic Coefficients for Water Clear ZnS Compared to Those for the Older Reddish Brown Material

Material	$dn/dT \div 10^{-5}/^oC$		
	@0.6328 μm	@1.15 μm	@3.39 μm
Water Clear	5.42	4.21	3.87
Reddish Brown	6.35	4.98	4.59

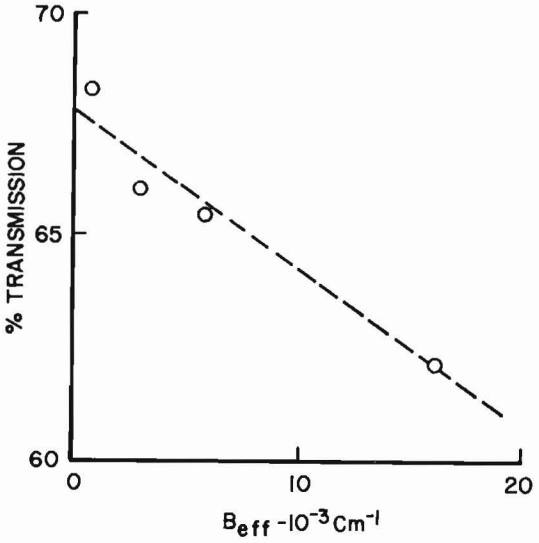


Figure 4. Plot Showing Correlation Between the Transmission of Water Clear ZnS at 0.5 μm and Effective Absorption Coefficient at 1.32 μm for CVD Material.

Table 4. Results of Thermal Expansion Measurements on Water Clear ZnS

Sample No.	Coefficient of Thermal Expansion ($X10^{-6}/^oC$)	
	-65^oC to $+25^oC$	$+25^oC$ to $+200^oC$
1	6.7	6.4 6.4
2	6.4	6.5 6.5
3	6.5	6.4 6.5
4	6.5	6.5 6.5

The electrical resistivity has been estimated to be greater than 5 x 10^{13} ohm-cm at 20°C. Due to limitations on the apparatus used to make the measurements, an exact value could not be determined; however, it was possible to estimate the lower limit reported.

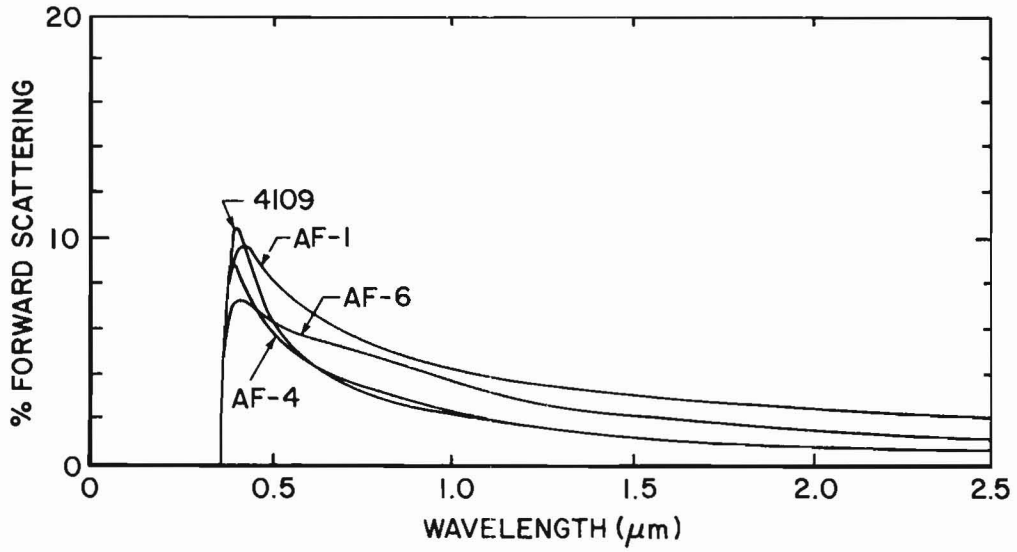


Figure 5. Percent of Light Scattered Out of a 4 Degree Half-Angle Cone by the Various Samples of Water Clear ZnS in the 0-2.5 μm Range.

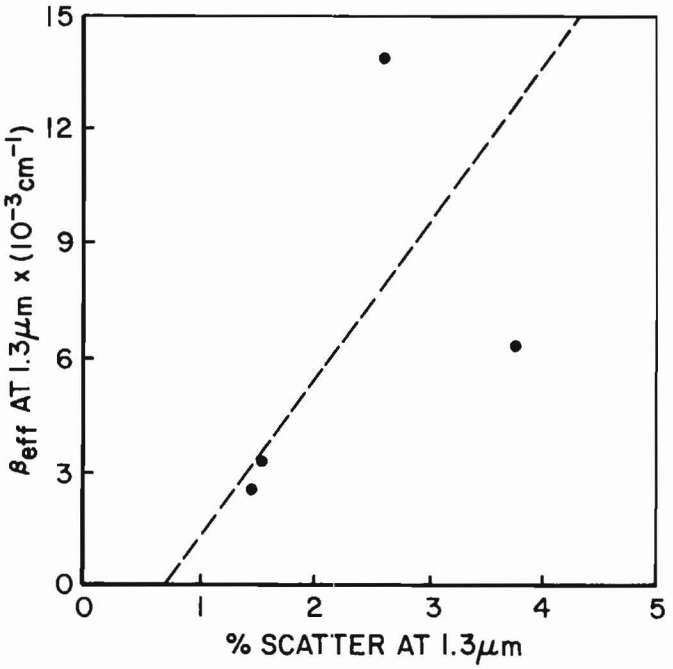


Figure 6. Plot Showing the Correlation of Scattered Light and Effective Absorption Coefficient a- 1.32 μm for Water Clear ZnS.

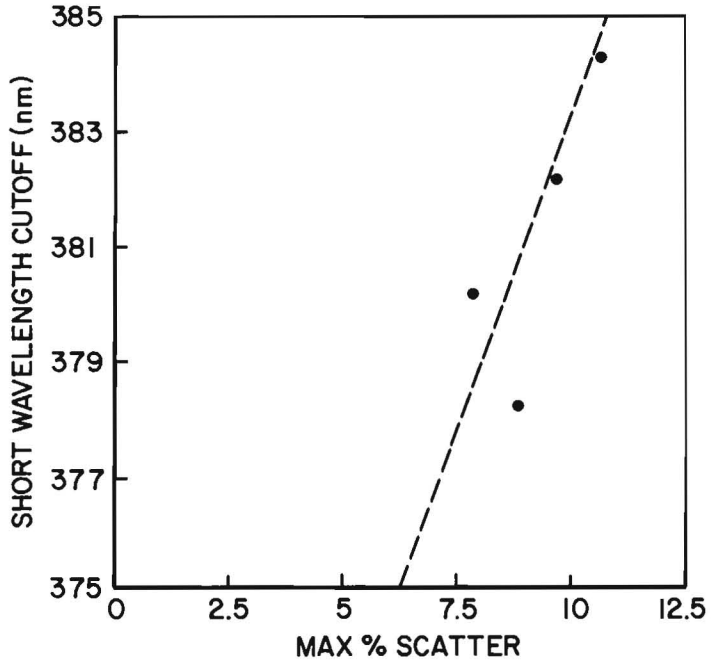


Figure 7. Plot Showing the Correlation of the Maximum Scattered Light and the Short Wavelength Cutoff for Water Clear ZnS.

3.4 Conclusions

Investigations of the optical, mechanical, thermal, and electrical properties of water clear ZnS produced by CVD, inc. have indicated that it is optically superior to the older unprocessed reddish brown material and the other properties are not significantly different. The optical absorption is correlated with the internal scattering in the material, as would be expected, and the internal scattering is a function of the deposition parameters with the deposition temperature having the greatest effect. The thermo-optic coefficients are lower for the water clear material and the transparency is considerably improved, making it a significantly more appropriate material for multi-spectral window applications than the unprocessed reddish brown ZnS.

4. Acknowledgements

The authors would like to thank Dr. George C. Miner of the University of Dayton Physics Department for his assistance in making the electrical resistivity measurements and Mr. Dale McCullum of the University of Dayton Research Institute for his assistance in making the thermal and mechanical measurements.

5. References

[1] Glass, A. J.; Guenther, A. H., eds. Laser Induced Damage in Otical Materials. Nat. Bur. Stand. (U. S.) Spec. Publ. 541; 1978. 7 p.

[2] Harris, Richard J.; Johnston, George T.; Kepple, Gary A.; Krok, Peter C.; Mukai, H. "Infrared Thermo-optic Coefficient Measurement of Polycrystalline ZnSe, ZnS, CdTe, CaF_2, and BaF_2, Single Crystal KCl, and TI-20 Glass," Appl. Opt. 16(2); 436; 1977 February 1.

[3] Feldman, A.; Horowitz, D.; Waxler, R. M.; Malitson, I.;Dodge, M. J. Optical Materials Characterization. Nat. Bur. Stand. (U. S.) NBSIR 74-525; 1974 July; 9 p.

Laser Damage in Plastics at the Frank J. Seiler Research Laboratory (FJSRL)

R.M. O'Connell*

Electrical Engineering Department
University of Missouri-Columbia
Columbia, MO 65201

T.T. Saito, T.F. Deaton, and K.E. Siegenthaler

Frank J. Seiler Research laboratory
USAF Academy
Colorado Springs, CO 80840

J.J. McNally

Physics Department
USAF Academy
Colorado Springs, CO 80840

A.A. Shaffer

Chemistry Department
USAF Academy
Colorado Springs, CO 80840

In order to study ways to improve the laser damage resistance of transparent polymers and thereby realize their advantages for high power laser system applications (e.g., they are lightweight, inexpensive, and castable), a laser damage program has been established at FJSRL. In this paper we describe the damage facility and present the results obtained during the initial year of the program.

The heart of the damage facility is a 1.06-micron wavelength Q-switched Nd:YAG laser capable of providing 300 mJ, 8 nsec FWHM pulses at repetition rates up to 10 pps. For the results reported here, the beam was focused to a 46 micron $1/e^2$ spot diameter.

Extensive single and multiple-shot bulk damage studies were made of several commercially available materials including polymethylmethacrylate (PMMA), three grades of polycarbonate (PC), and cellulose acetate butyrate (CAB). Measured single-shot damage thresholds were, respectively, 41 J/cm^2, 15 J/cm^2, and 15 J/cm^2, which correlates with the relative "dirtiness" of the materials. Of the three materials, PMMA also had the greatest multiple-shot damage resistance. However, at fluence levels ≤ 0.1 times its single-shot threshold, CAB appears to be remarkably damage resistant.

Preliminary measurements were also made on PMMA which was synthesized in-house from both unpurified and moderately purified monomers, both with and without unpurified plasticizers. The single-shot damage threshold of the material made from purified monomers (no plasticizer) was 1.6 times that of the material made from unpurified monomers. The mulitple-shot behavior of the purified material as compared to that of the unpurified material was even more remarkable.

Key words: bulk laser damage; cellulose acetate butyrate; multiple-shot; single-shot; plastics; polycarbonate; polymethymethacrylate.

* Work performed while on leave, participating in the University Resident Research Program.

1. Introduction

For several reasons, transparent organic glasses (plastics) have potential use in high power laser systems. They are lightweight and inexpensive; and they can be injection molded or cast with optical quality surface finish, eliminating the need for polishing, residues from which are a major cause of laser damage to their silicate counterparts (glasses). To date, little has been done to develop plastics for high power laser use, probably because glass is generally more rugged and because of some early results that showed the laser damage resistance of some plastics to be significantly lower than that of glass [1,2]. More recent results, however, suggest that the damage resistance of plastics can be greatly improved by monomer purification and material plasticization [3].

In light of these developments, a program has recently been established at the Frank J. Seiler Research Laboratory (FJSRL) to study laser damage in plastics, with the ultimate goal of showing that transparent plastics can be produced with laser damage resistance comparable to that of glass.

Both commercially available [4] and materials synthesized in-house are being studied. In this paper we describe the FJSRL laser damage facility and present the results of measurements of the single- and multiple-shot laser damage properties of several commercially available materials and some material that we synthesized in-house. The commercial materials studied were Plexiglas G, i.e., polymethylmethacrylate (PMMA); Lexan, Tuffack and Merlon, i.e., polycarbonate (PC); and UVEX, i.e., cellulose acetate butyrate (CAB). The results obtained with Plexiglas G constitute a baseline [5] for comparison with other commercially available plastics, with commercial grades of silicate glass, and with the products of our in-house plastics synthesis efforts.

2. FJSRL Laser Damage Facility

The heart of the FJSRL damage facility, sketched in figure 1, is a 1.06 micron wavelength Quanta-Ray DCR-2A Nd:YAG laser. It can be operated both in long pulse and Q-switched modes, and, with some external electronics [6], the pulse repetition frequency can be varied up to 10 pps. In our damage work, only 8-nsec FWHM Q-switched pulses are used. For alignment and safety purposes, red helium-neon laser light enters the system collinear with the 1.06 micron beam at mirror (2). Variable attenuation is provided by the rotatable polarizer (3). The 1° wedge (4) splits the beam into three components. The power meter (5) receives the 92% portion and monitors the energy at the sample site (8) through a previously measured calibration constant. One 4% portion of the beam is directed to the sample by a mirror (6) and through the 23 cm focal length lens (7). The other 4% portion is directed either to a Hamamatsu R1328 fast photodiode (9) for temporal characterization or to a Hamamatsu NZ14 vidicon tube which is being developed for spatial beam profiling.

The spatial profile of the focused beam is measured by the knife-edge method [7,8] as applied by Mauck [9]. We stepped a 1/16" thick steel plate across the beam in increments of 2.54 microns and measured the transmitted power with an S-1 photodiode. At each position, the average of at least 100 pulses operating at 10 Hz was read from the oscilloscope; the variation in the transmission was typically less than $\pm 5\%$. Numerical differentiation of the transmission data yielded an approximate fluence profile for the beam. A least-squares fit of a Gaussian profile [5] to this fluence profile gave a $1/e^2$ radius of 23 microns, the "spot size" of our focused beam. The beam profile generated by the numerical differentiation was used to compute the peak fluence value for a particular pulse energy. We believe the accuracy of this technique for the determination of the peak fluence of a given pulse to be only about $\pm 20\%$.

The temporal behavior of the laser pulse was more variable than either the pulse energy or spatial profile. Tracings of oscillographs of two typical pulses, as measured with the Hamamatsu R1328 photodiode and displayed on the Tektronix 7834 oscilloscope, are shown in figure 2. The structure seen is ever-present, but varies widely from pulse to pulse. We attribute this modulation to beating of longitudinal modes, and we assigned a value of 8 ± 2 nsec to the FWHM pulse duration. Because of this uncertainty in the temporal pulse behavior, the damage thresholds discussed below are generally expressed in terms of the peak fluence (J/cm^2) rather than peak intensity (W/cm^2).

The remaining components in figure 1 comprise a damage monitoring system based on Strehl ratio measurements for a collinear 2 mW helium-neon laser beam [11]. The diagnostic beam is expanded and clipped to improve its uniformity with the expanding lens (10) and aperture (11). It is then precisely aligned with the 1.06-micron damage beam via the mirrors (12), (13). Focusing lens (14) is chosen and placed such that both beams focus at the same place, i.e., the damage plane. Mirror (15) reflects a portion of the red light through the lens (16) and aperture (17) onto the UDT-20 photodiode (18) which for this work was unbiased and connected directly to a digital voltmeter yielding a typical 400 mV reading. When damage occurs to the sample, some red light is scattered

out of the main path, resulting in a drop in the Strehl ratio as determined by the photodiode output. Mirror (15) also transmits enough red light to illuminate screen (19) with a diffraction pattern produced by the damage site.

In addition to the photodiode output and the screen pattern, we watch the sample through safety glasses of KG3 Schottglass for a spark or flash during the laser pulse, and do a 100X bright-field microscope examination after illuminating several sites. Thus, the damage facility has four damage monitors. Their relative usefulness varied with experimental conditions, as will be shown in sections 3 and 4.

3. Single-Shot Damage Study in Commercial Grade PMMA

The material used was 15/16" thick plexiglas G, a readily available commercial grade of PMMA. The test sample was placed at position 8 of figure 1 such that, allowing for the refractive index of PMMA, the 1.06-micron laser focused at its thickness center (the focal depth in the material is greater than in air by the ratio of the refractive indices, i.e., 1.5/1.0). We studied bulk damage only because the surface of PMMA has been shown [12] to be twice as laser damage resistant at its bulk.

The single-shot experiment consisted of illuminating each of the 10-20 test sites in the material only once at each of a series of fluence levels. The fluence level producing damage 50% of the time (or equivalently, the average of the highest 0% and lowest 100% levels) is defined as the single-shot threshold.

To make the single-shot damage decision, we used the four above-mentioned monitors. After collecting and analyzing data from several thousand sites, we found the transmitted red diagnostic beam to be the most consistent and reliable immediate indicator. When properly aligned, the diagnostic provides a voltage drop approximately in proportion to the size of the damage site as measured with 100X magnification. We found that damage sites approximately 5-10 microns in diameter caused sufficient voltage drop, i.e., scattered light, to conclude that damage had definitely occurred. This was usually, but not always, corroborated by the appearance of a faint diffraction pattern on the screen (20 in figure 1) or by a spark. The screen pattern was often too faint, i.e., subjective to be reliable in the near-threshold cases, but it proved to be an invaluable aid in aligning the diagnostic red light with the 1.06-micron beam. Sparks were observed in the bulk in approximately 80% of the cases ultimately judged to be damaged, but were not seen in several cases of obvious damage.

For this work we formally define damage to have occurred if a measurable, permanent decrease in the transmission of the heliun-neon diagnostic through the sample is observed. The post-illumination 100X microscopic examination always corroborated an indication of damage by any of the other three monitors and occasionally revealed damage that the other techniques had not indicated. Part of the discrepancy was due to slight occasional misalignment of the red light diagnostic, which had to be periodically corrected, and part to the imprecision inherent in our definition of damage. With 100X magnification, we could see sites 1 micron or less in size that were apparently laser-induced, but which we did not judge as damaged, mainly because they caused no observable red light scatter. Sites this size are called the microscopic precursors of damage in the cumulative multiple-shot regime [13,14].

The results of the single-shot damage experiment on PMMA are compiled in figure 3 where we plot for each peak fluence level the fraction of sites damaged as determined with the data from the four monitors. The scatter in the data is due both to the pulse-to-pulse variation of the laser (temporal and spatial) and to the non-uniformity of the material (size and concentration of damage-causing impurities). The midpoint between the highest 0% peak fluence level and the lowest 100% peak fluence level is 41 J/cm^2, which is thus the single-shot threshold for our sample. The associated peak intensity, assuming a nominal pulse width of 8 nsec, is 5 GW/cm^2. The peak fluence levels in figure 3 were adjusted to account for a front surface Fresnel reflection loss and the bulk transmission to the focal plane (measured separately).

A direct comparison of our single-shot threshold results with other published values is difficult because damage thresholds in plastics measured at a given wavelength vary with pulse length [15], spotsize [16], and material purity [15,17]. As table 1 shows, the available data obtained with short (of the order of nsec) 1.06-micron wavelength pulses were obtained under widely varying conditions. Furthermore, our definition of damage might differ from that of other researchers. Despite the difficulty, a few conclusions can be drawn from table 1. First, considering the differences in pulse widths and spot sizes, our results for the peak fluence at threshold are not inconsistent with Milam's (line 2). Second, when our approximate value for the

peak intensity at threshold is compared to Felix and Machbar's result (line 3) the discrepancy is quite large although the respective pulse lengths are similar. Unfortunately, the spot size for their work [18] was not reported.

Table 1 also includes single-shot data on commercial silicate glasses. Since these data were obtained under experimental conditions very similar to ours on PMMA, they can be used to make a reasonably fair comparison of the damage thresholds of the two materials. Thus, the single-shot intensity threshold of glass is seen to be on the order of 20-50 times greater than that of PMMA. This represents one aspect of the gap to be closed if PMMA is to be competitive with glass in high-power laser systems. The other aspect concerns multiple-shot damage resistance, as will be shown in part 4.

Table 1. Short Pulse, 1.06 μm Wavelength, Single-Shot Bulk Damage Thresholds of PMMA and Various Silicate Glasses

MATERIAL DESCRIPTION	PULSE WIDTH (nsec)	FOCAL SPOT SIZE DIAMETER	PEAK FLUENCE (J/cm^2)	PEAK INTENSITY (GW/cm^2)	REFERENCE
Plexiglas G, Commercial Grade PMMA	8	46 μm	41	5	This Work
Commercial Grade PMMA [a]	0.125	2 mm	1.6	13	2
PMMA [b]	12	c	c	1550 [d]	18
PMMA [b]	20	c	1	0.05	19
Suprasil I Fused Silica	21	28 μm	2373	113	20
Corning 7940 Fused Silica	21	28 μm	2373	113	20
BSC-2 Glass	4.7	20 μm	414	88	21
Fused Quartz [b]	4.7	20 μm	414	107	21

a - Provided by Eastman Chemical Corporation
b - No other information provided
c - Not provided
d - Theoretical peak power calculated from basic optics relation $d_{min} = 2.44$

4. Mulitple-Shot Damage Study in Commercial Grade PMMA

The tendency of transparent dielectrics, especially plastics, to suffer damage when irradiated repetitively with laser pulses having fluence levels far below the single-shot threshold is, from an applications standpoint, more serious than high-power single-shot damage. We studied the sub-threshold multiple-shot behavior of Plexiglas G with the above-described laser operating at 1 pps and at the five subthreshold fluence levels F/F_{Th} = 0.69, 0.47, 0.225, 0.121, and 0.059 (expressed as fractions of the single-shot threshold fluence F_{Th}). Data were obtained using the same four damage monitors as in the single-shot study. At each fluence level we first found the critical number of pulses, N_{CR}, required to cause damage equivalent to single-shot damage. We then studied the behavior of the material when illuminated with $N < N_{CR}$ pulses.

Determining N_{CR} at the upper three subthreshold fluence levels was more easily accomplished than at the lower two levels. At F/F_{Th} = 0.69, 0.47, and 0.225, a spark always occurred which was accompanied by a significant drop in the scattered light photodiode voltage and a change in the diffraction pattern on the screen. The three indications usually occurred on the same shot, although the photodiode voltage sometimes dropped slightly, providing some warning, a few shots before the spark. The subsequent 100X microscope exam showed that the size of the damage was approximately the same as in the single-shot study.

At fluence levels F/F_{Th} = 0.121 and 0.059, sparks could not be used to indicate damage. By the time they occurred, which was rare, the material was severely damaged, as indicated by a large amount of scattered diagnostic light, a well-developed screen pattern, and the subsequent microscope exam. Instead, we used as the indicator approximately the same amount of scattered red light as at the higher fluence levels. The microscope exam verified that the size of the damage was approximately the same at both high and low fluence levels.

Figure 4 shows a plot of the N_{CR} values obtained as just described for the respective fluence levels. Each N_{CR} value is the average from several illuminated sites. The fact that the curve through the five multiple-shot points extrapolates to the single-shot point (F/F_{Th} = 1.0) would seem to indicate that that our definition of laser damage was reasonably consistent throughout the investigation. As in the single-shot study, comparison with other published results is difficult because of differing experimental conditions. Qualitatively, however, our results are in general agreement with those of Milam [2] (N_{CR} = 5 for F/F_{Th} = 0.71), Emelyanova, et al [22], Butenin and Kogan [17], and Agranat, et al [23], all of whose results were obtained with short (nsec) 1.06-micron wavelength pulses. For purposes of comparison, the multiple-shot data from Agranat, et. al. [23] are also shown in figure 4. The two sets of data agree reasonably well except for the single point at very low fluence.

As with single-shot damage, when compared to recently reported results [20] obtained with commercial grades of fused silica, the data in figure 4 show that PMMA is inferior in the multiple-shot regime, too. For example, the N_{CR} vs F/F_{Th} data in reference 20 for 1.06-micron, 21 nsec pulses suggest that a minimum F/F_{Th}, as large as 0.7, exists for the accumulation of damage to occur at all in fused silica; and at slightly larger fluence levels, several thousand pulses are needed to cause macroscopic damage. Our data in PMMA show no such minimum for fluence levels as low as 0.059, and much smaller N_{CR} values generally (see figure 4). This result is the other aspect of the above-mentioned gap in the relative damage resistance of PMMA and glass.

Having established an N_{CR} for a given peak fluence level, we fixed N at each of a series of values ranging from much smaller than N_{CR} to slightly less than N_{CR}, and illuminated several sites at the given fluence level. The behavior of the scattered light photodiode voltage during illumination and the microscope examination done afterward showed clearly that the multiple-shot damage process in PMMA is cumulative and, especially at the lower fluence levels, very subtle. For example, at all fluence levels neither the red light diagnostic nor the microscope exam gave any indication of an accumulating effect for $N < 0.6\ N_{CR}$. However, for larger N, tiny (< 1 micron in diameter) pits became evident throughout the focal volume. The 1-micron sites are too small to scatter enough red light to affect the Strehl ratio measurably. With increasing N, they grew in number and size. Within a few shots of N_{CR}, the photodiode voltage often dropped a bit, as mentioned previously. At N_{CR}, the focal volume contained 10-20 of the tiny pits, plus one to three larger ones 5-15 microns in diameter. The corresponding photodiode voltage drop was approximately as large as in the single-shot study. This observation of the growth of microdamage [13] into macrodamage together with an examination of histograms of damage probability versus the number of pulses needed to cause damage [5] provide strong evidence that the damage process is cumulative.

5. Results with other Commercial Materials

We have also studied the laser damage properties of three commercial grades of polycarbonate (PC), and one of cellulose acetate butyrate (CAB). Typical data obtained with these materials are shown in table 2, along with some commercial grade PMMA data for comparison. As can be seen, the single-shot threshold of PC and CAB, and the multiple-shot resistance of PC are all lower than the corresponding properties of PMMA. The CAB, however, has higher multiple-shot resistance at low values of F/F_{Th}. In fact, for $F/F_{Th} \leq 0.1$, damage was never observed after as many as 1000 shots in approximately 50% of the sites illuminated. In the other 50%, subtle damage of the type described above accumulated for approximately 200 shots, then stopped. This encouraging result is being investigated further.

As compared to PMMA, the relatively low damage resistance of PC generally and of CAB at higher fluence levels can be at least partly explained by the differences in their manufacturing processes. Whereas the PMMA used in this work was cell-cast, the PC and CAB were formed by extrusion, a process that introduces large amounts of micron-sized dirt. Under 100X microscopic examination, the PMMA had absolutely no observable (>1 micron) impurities, but the PC and CAB had so many in the 4-10 micron range that use of the microscope in determining the occurrence of damage was greatly restricted with these materials.

Table 2. Comparison of Laser Damage Data of Commercial Grade Polycarbonate (PC), Cellulose Acetate Butyrate (CAB), and PMMA

MATERIAL	SINGLE SHOT DAMAGE THRESHOLD F_{Th} in J/cm^2	N_{CR} for F/F_{Th} = 0.3, PRF = 1 pps	N_{CR} for F/F_{Th} = 0.1, PRF = 1 pps
PC (Lexan)	15	8	10
PC (Tuffack)	11	8	10
PC (Merlon)	12	-	--
CAB (Uvex)	15	25	$\triangleright$ 1000
PMMA (Plexiglas G)	41	22	47

6. Results with Materials Synthesized In-House

There is evidence [15,23,17,24] that the laser damage resistance of plastics can be significantly improved by purifying the monomers and/or by adding plasticizing agents to them prior to polymerization. However, the exact role of each of these processes in improving single- and multiple-shot damage resistance is still uncertain. To shed further light on the problem, the FJSRL plastics damage program includes an in-house plastics synthesis effort.

For this report, samples of PMMA were synthesized from both unpurified (research grade) and moderately purified monomers both with and without unpurified plasticizers. Monomer purification consisted of overnight drying with CaH_2 followed by fractional distillation under an N_2 atmosphere. Plasticizers used were dibutyl phthalate and n-butyl acrylate. The plastics were synthesized using bulk polymerization initiated by approximately 0.01 weight, percent azo-bis-isobutyronitrile (AIBN). Reactions were carried out at 45-55° C for 4-5 days, then at approximately 65° C for two more days. (Higher reaction temperatures usually caused voids.)

In preliminary damage tests, the materials made with plasticizers had poor damage resistance, probably because of impurities in the plasticizers. In on-going work, the plasticizers are being purified. Typical data on material made without plasticizers and from both purified and unpurified monomers are compared on the corresponding data from commercial PMMA in table 3. Note that the single-shot damage threshold of the in-house material synthesized from purified monomer was approximately 60% higher than that of the sample synthesized from unpurified monomer, a significant improvement. The multiple-shot data, however, is far more significant. Whereas the unpurified sample damaged after only 20 shots with F/F_{Th} = 0.47 at a pulse repetition frequency of 1 pps, the purified sample showed no evidence of damage after 200 shots. Although preliminary, these results tend to agree with those of Butenin and Kogan [17] concerning the benefits of monomer purification and to disagree with those of Aldoshin et al [24]. We are currently examining this more carefully.

Table 3. Comparison of Laser Damage Data of Commercial Grade and In-House-Synthesized PMMA

MATERIAL DESCRIPTION	Single-Shot Threshold F_{Th} in J/cm^2	N_{CR} for F/F_{Th} = 0.47, PRF = 1 pps	N_{CR} for F/F_{Th} = 0.47, PRF - 10 pps
Commercial Grade	41	16	--
In-House/Purified Monomers	41	> 200	47
In-House/Unpurified Monomers	26	20	--

7. Discussion and Conclusion

Using a newly established laser damage facility we have studied bulk damage in transparent plastics with 8 nsec FWHM, 1.06-micron wavelength pulses. Our criterion for damage is based on the transmission of collinear red light. We feel that this criterion is appropriate and useful, both because scattered light is directly related to the ultimate optical applications of the materials under study, and because the occurrence of damage is very subtle under low-level ($F \ll F_{Th}$) multiple-shot conditions and thus is very difficult to observe. The scattered-light method eases this difficulty.

The causes of laser damage to plastics and suggestions for improving damage resistance have been considered by several groups. We reviewed the ideas of some of these in a separate article [4] in which we concluded that monomer purification prior to polymerization and plasticization that places the material's induced elastic limit below its brittle fracture limit should improve single- and multiple-shot damage resistance, respectively. However, our preliminary results on the materials synthesized in-house suggest that monomer purification may have a greater impact on multiple-shot damage resistance than on single-shot resistance. This interesting result and its implications for damage mechanisms are currently being studied further.

Finally, because the PC and CAB used in this study were extruded and therefore quite dirty, it should be possible to greatly improve their laser damage resistance simply by fabricating cleaner material. We are currently looking into this also.

We gratefully acknowledge the support of this project by the Air Force Weapons Laboratory through Project Order No. AFWL 82-016.

8. References

[1] Ashkinadze, B.M., Vladimirov, V.I., Likhachev, V.A., Ryvkin, S.M., Salmanov, V.M., and Yaroshetskii, I.D., "Breakdown in Transparent Dielectrics Caused by Intense Laser Radiation," Sov. Phys. JETP 23(5), 788 (1966).

[2] Milam, D., "Laser-induced Damage at 1064 nm, 125 psec," Appl. Opt. 16(5), 1204 (1977).

[3] Dyumaev, K.M., Manenkov, A.A., Maslyukov, A.P., Matyushin, G.A., Nechitailo, V.S., and Prokhorov, A.M., "Transparent Polymers as a New Class of Optical Materials for Lasers," NBS Spec. Pub. 638, 31 (1981).

[4] O'Connell, R.M., and Saito, T.T., "Plastics for High-power Laser Applications: A Review," Opt. Eng. 22(4), 393 (1983).

[5] O'Connell, R.M., Deaton, T.F., and Saito, T.T., "Single and Multiple Shot Laser Damage Properties of Commercial Grade PMMA," Appl. Opt. 23(5), (1984).

[6] Pollard, J.J., and Earl, P.K., "A Counter and Controller for the Quanta-Ray Laser," FJSRL-TM-83-0009, (1983).

[7] Arnaud, J.A., Hubbard, W.M., Mandeville, G.D., de la Claviere, B., Franke, E.A., and Franke, J.M., "Technique for Fast Measurement of Gaussian Laser Beam Parameters," Appl. Opt. 10(12), 2775, (1971).

[8] Skinner, D.R., and Whitcher, R.E., "Measurement of the Radius of a High-power Laser Beam Near the Focus of a Lens," J. Phys. E 5, 237, (1972).

[9] Mauck, M., "Knife-edge Profiling of Q-Switched Nd:YAG Laser Beam and Waist," Appl. Opt. 18(5), 599, (1979).

[10] Gaskill, J.D., Linear Systems, Fourier Transforms, and Optics, (J. Wiley and Sons, New York, 1978), 339-345.

[11] Mullins, B.W., and Richert, B.A., "Strehl Ratio Measurements of Laser Damaged Plastics," These Proceedings (1983).

[12] Bebchuk, A.S., Gromov, D.A., and Nechitailo, V.S., "Measure of Surface Defectiveness and Optical Strength of Transparent Dielectrics," Sov. J. Quantum Electron. 6(8), 986, (1976).

[13] Manenkov, A.A., Nechitailo, V.S., and Tsaprilov, A.S., "Microdamage Initiation in a Transparent Polymer on Repeated Laser Irradiation," Izv. Akad. SSSR. Ser. Fiz. 46(6), 1200, (1982).

[14] Dyumaev, K.M., Manenkov, A.A., Maslyukov, A.P., Matyushin, G.A., Nechitailo, V.S., and Tsaprilov, A.S., "Influence of viscoelastic properties of the matrix and of the type of plasticizer on the optical strength of transparent polymers," Sov. J. Quantum Electron. 12(7), 838, (1982).

[15] Manenkov, A.A., and Nechitailo, V.S., "Role of Absorbing Defects in Laser Damage to Transparent Polymers," Sov. J. Quantum Electron. 10(3), 347, (1980).

[16] Aldoshin, M.I., Manenkov, A.A., Nechitailo, V.S., and Pogonin, V.I., "Frequency and Size Dependence of the Threshold for Laser Damage in Transparent Polymers," Sov. Phys. Tech. Phys. 49(11), 1412, (1979).

[17] Buenin, A.V., and Kogan, B.Y., "Mechanism of Damage of Transparent Polymer Materials Due to Multiple Exposure to Laser Radiation Pulses," Sov. J. Quantum Electron. 6(5), 611, (1976).

[18] Felix, M.P., and Nachbar, W., "A Closer Look at Laser Damage in PMMA," Appl. Phys. Lett. 25(1), 25, (1974).

[19] Agranet, M.B., Krasyuk, I.K., Novikov, N.P., Perminov, V.P., Yudin, Y.I., and Yampolskii, P.A., "Destruction of Transparent Dielectrics by Laser Radiation," Sov. Phys. JETP 33(5), 944, (1971).

[20] Merkle, L.D., Bass, M., and Swimm, R.T., "Multiple Pulse Laser Induced Bulk Damage in Crystalline and Fused Quartz at 1.064 and 0.532 um," Opt. Eng. 22(4), 405, (1983).

[21] Fradin, D.W., and Bass, M., "Comparison of Laser-induced Surface and Bulk Damage," Appl. Phys. Lett. 22(4), 157, (1973).

[22] Emelyanova, G.M., Ivanova, T.F., Votinov, M.P., Ovchinnikov, V.M., Piterkin, V.D., and Smirnova, Z.A., "Optical Strength of Copolymers of Methyl Methacrylate and Butyl Acrylate," Sov. Tech. Phys. Lett. 3(7), 280, (1977).

[23] Agranat, M.B., Novikov, N.P., Perminov, V.P., and Yampoliskii, P.A., "Some Aspects of the Initial Stage of the Development of Laser Damage in Polymethylmethacrylate," Sov. J. Quantum Electron. 6(10), 1240, (1976).

[24] Aldoshin, M.I., Gerasimov, B.G., Manenkov, A.A., and Nechitailo, V.S., "Decisive Importance of the Viscoelastic Properties of Polymers in their Laser Damage Mechanism," Sov. J. Quantum Electron. 9(9), 1102, (1979).

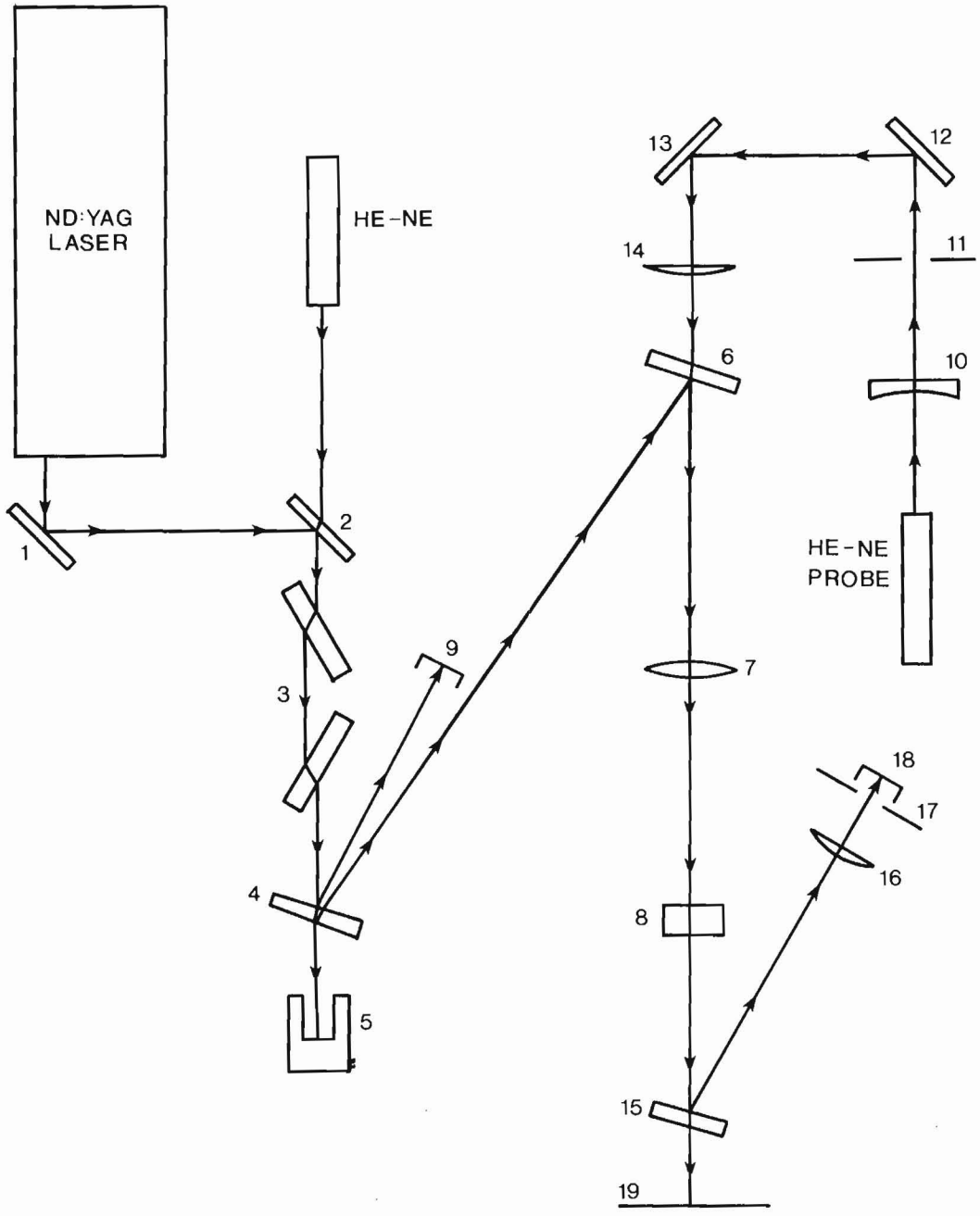


Figure 1. FJSRL Laser Damage Facility: 1,2,6,12,13,15) Turning Mirrors; 3) Rotatable Polarizer/Attenuator; 4) 1° Wedge; 5) Power Meter; 7,10,14,16) Lenses; 8) Test Sample; 9,18) Photodiodes; 11,17) Apertures; 19) Screen

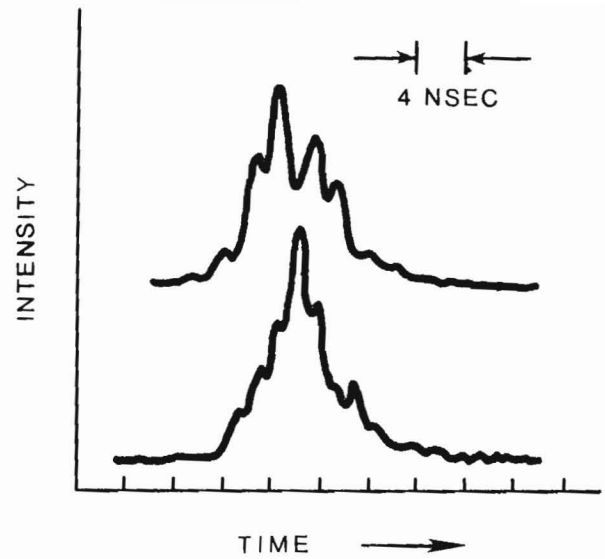


Figure 2. Temporal Shapes of Two Pulses from the 1.06 μm Laser, Showing Typical Pulse-to-Pulse Variations

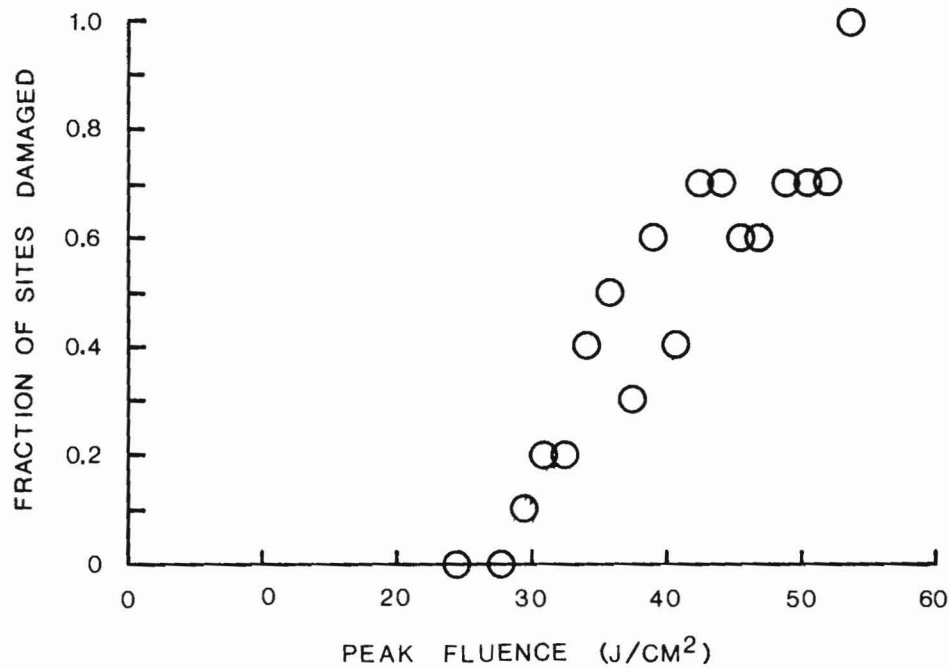


Figure 3. Results of the Single-Shot Damage Threshold Measurement on Commercial Grade PMMA

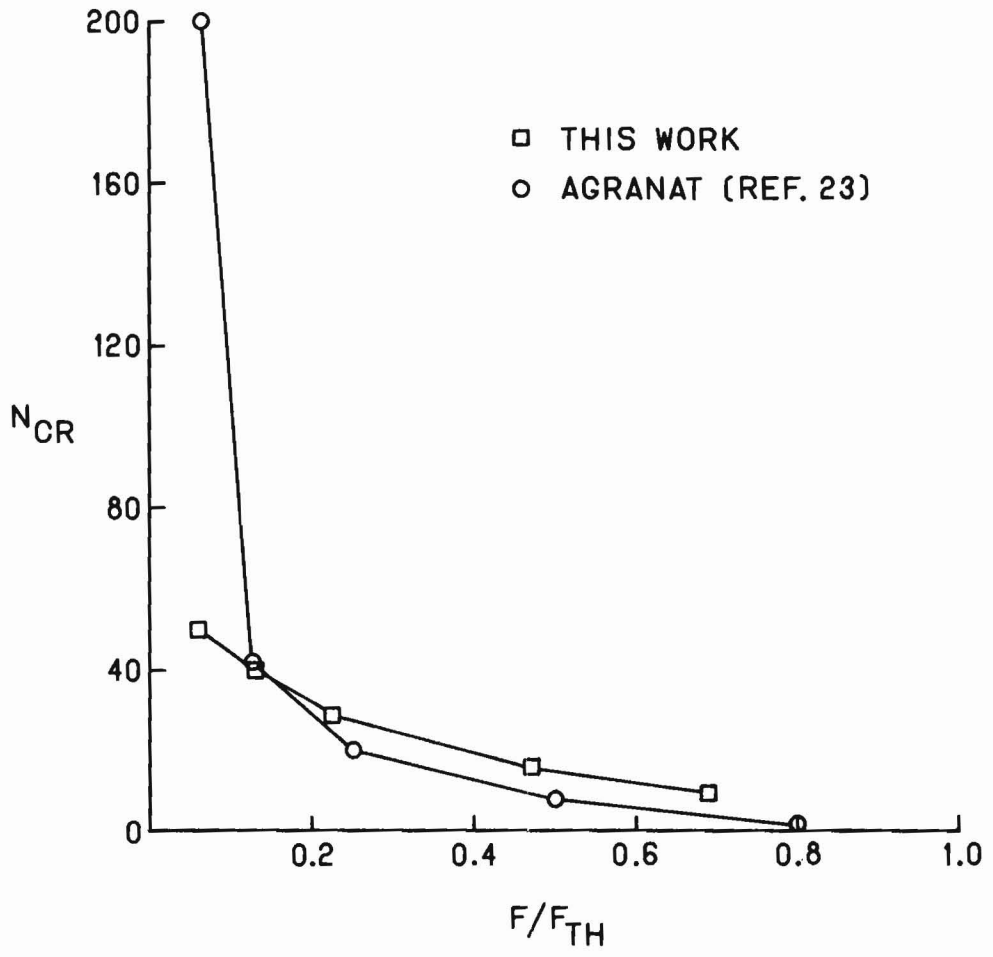


Figure 4. The Average Number of Pulses, N_{CR}, Required to Cause Damage to Commercial Grade PMMA as a Function of the Fraction of Single-Shot Threshold Fluence F/F_{Th}. The Data of Agranat, et. al. [23], also for PMMA and under Similar Experimental Conditions, are shown for Comparison

Increase In The Optical Damage Threshold Of Cellulose Acetate

Dr. M. A. Acharekar

International Laser Systems, Inc.
3404 N. Orange Blossom Trail
Orlando, FLorida 32804

Passive Q-switches manufactured with cellulose acetate are generally used in portable/handheld Nd:YAG laser rangefinders. The advantages of this type of Q-switch device are small size, economy and simplicity of operation. However, the limitation of this type of passive Q-switch is its low damage threshold.

For Nd:YAG laser, Bis (4-Dimethyaminodithiobenzil) Nickel dye is generally doped in 0.125 to 0.250 mm thick sheets of cellulose acetate material. Bis-Nickel dye in a cellulose acetate host, when inserted in a Nd:YAG laser resonator and exposed to 1.06 micron radiation, saturates and bleaches giving a giant Q-switch pulse.[1] Commercially available [2] cellulose acetate sheets of this passive Q-switch suffer permanent optical damage when operated at 20 mJ output energy in a 20 ns pulse width at 10 Hz repetition rate. To improve the damage threshold of the passive Q-switch, a process for improving transmission and optical properties (voids, inclusions, etc.) of the host cellulose acetate was developed. The details of the process will be discussed and the damage measurement data collected will be presented.

Key Words: cellulose acetate; dye Q-switch; laser damage; multiple shot laser damage; passive Q-switch.

1. Introduction

Passive Q-switches manufactured with cellulose acetate are generally used in portable/handheld Nd:YAG laser rangefinders. The advantages of this type of Q-switch device are their small size, economy and simplicity of operation. However, the limitation of this type of passive Q-switch is its low damage threshold.

For Nd:YAG lasers Bis (4-Dimethylaminodithiobenzil) Nickel dye, as shown in figure 1.0, doped in 0.125 to 0.25 mm thick sheets of cellulose acetate is used. Bis-Nickel dye in a solvent or cellulose acetate host, when inserted in Nd:YAG laser resonators and exposed to 1.06 micron radiation, as shown in figure 2.0, absorbs the radiation. When the energy level is saturated the dye does not absorb 1.06 micron radiation anymore and starts transmitting (this is called bleaching). Thus, the energy stored in the rod provides a giant pulse. The dye recovers and starts absorbing as soon as energy density on the dye is below the saturation energy density. Therefore, for a given laser rod diameter, dye concentration in cellulose acetate can be increased, thereby increasing stored energy. However, the host cellulose acetate suffers permanent optical damage when operated at 20 mJ output energy in a 20 ns pulse width at 10 Hz repetition rate in commercially available passive Q-switches.

BIS (4-Dimethylaminodithiobenzil)
Nickel Dye for Q-Switch

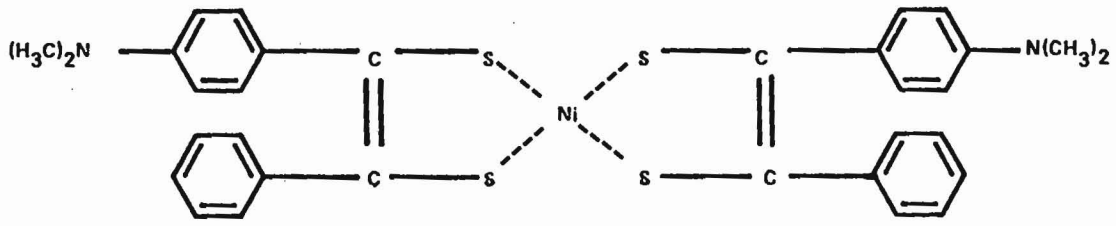


Figure 1.0

ENERGY LEVELS BIS-NICKEL

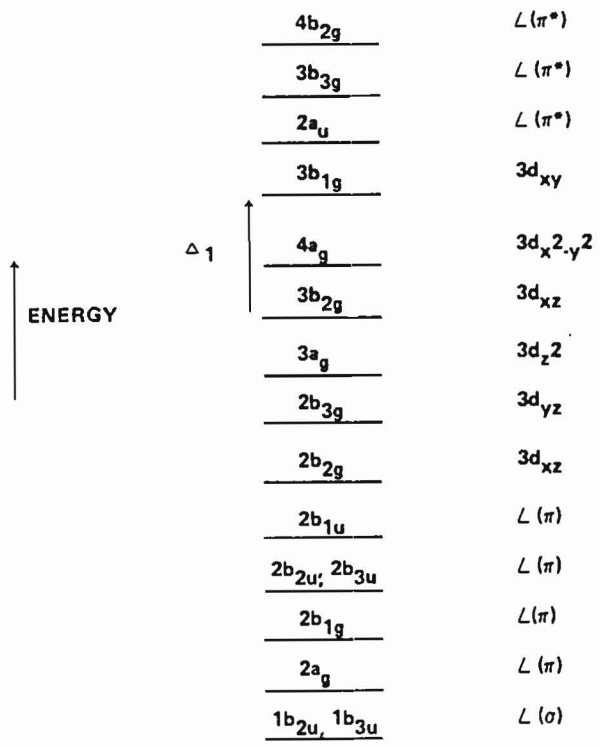


Figure 2.0

2. Clearing Cellulose Acetate

A Beckman DK-2A spectrophotometer was used for measuring the transmission of a 0.125 mm thick sheet of cellulose acetate. As seen in figure 3.0, although the wavelength of interest is 1.06 microns, the entire spectrum from 450 nm to 1200 nm was obtained to see if there were any impurities in the material. It may be noted that the basic loss is due to reflection.

Generally, the absorption loss in the cellulose acetate is due to the OH radical and the scattering loss is due to voids and inclusions in the material. Hence a process was developed to remove the OH radical and form void and inclusion free material. In figure 4.0, the transmission characteristics of the cellulose acetate treated with the new process is shown. When figure 3.0 is overlapped on figure 4.0 the improvement in transmission is noticed. It may be noted that an electrolyte KCl doped in the cellulose acetate does not affect transmission.

The improvements observed with the elimination of voids and inclusions can be seen easily under high magnification.

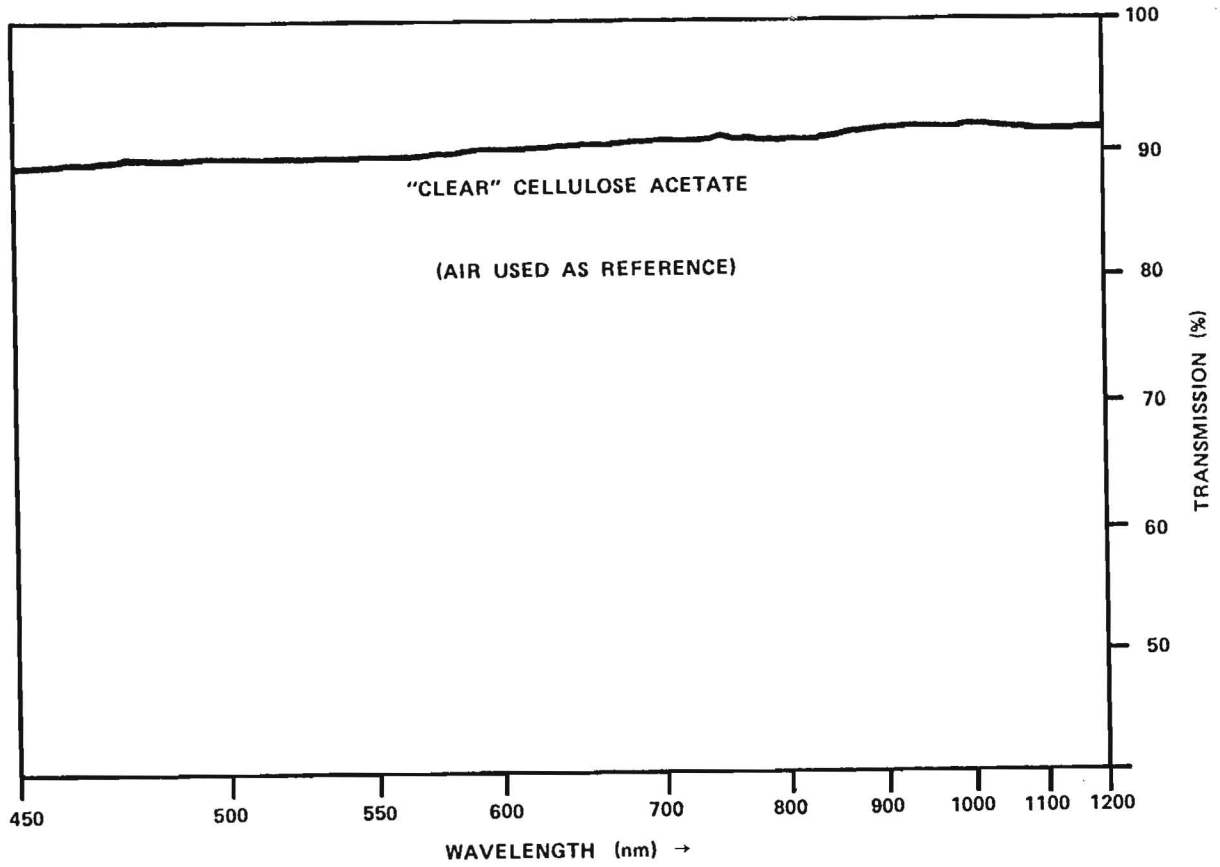


Figure 3.0

3. Damage Threshold Measurements

The damage threshold was measured using a TEM_{00}, Q-switched Nd:YAG laser. The pockel cell Q-switch used in the damage threshold test had a 17 nsec pulse width and 12 mJ output energy. The desired power density on the cellulose acetate was obtained using focusing lenses of different focal length. The spot size was calculated as well as actually measured on a photo sensitive film.

Considering the application of this material, damage due to multiple exposure to the laser radiation pulses was the only parameter measured. The laser was operated at a 1 Hz pulse rate for 300 pulses on the cellulose acetate and the surface was examined under a microscope for the damage. Several hundred samples were exposed for various power densities.

The damage data obtained for the commercial cellulose acetate and treated cellulose acetate is plotted in figure 5.0. It may be noted that the plot provides the relative power density. However, it may be noted that the increase in damage threshold appears proportional to the increase in thermal conductivity. Additional data is being collected.

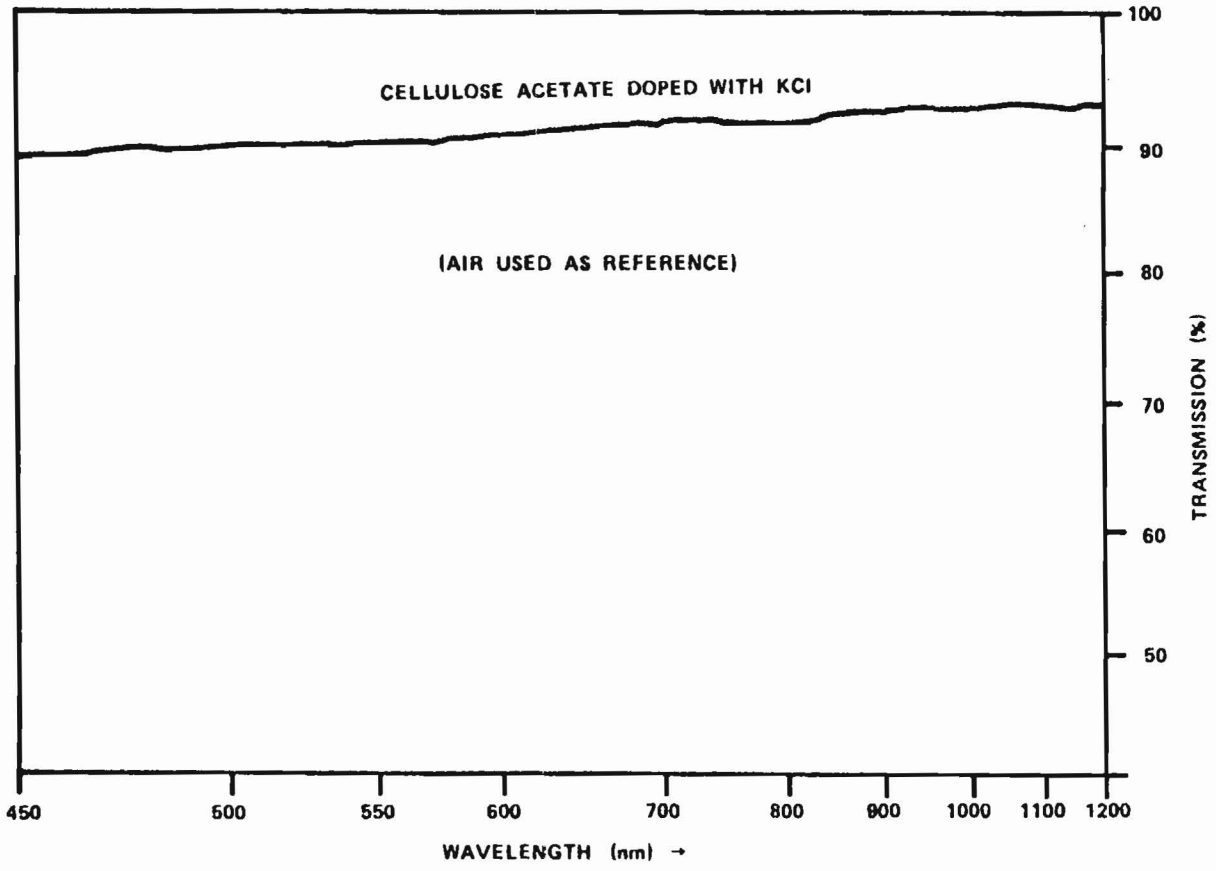


Figure 4.0

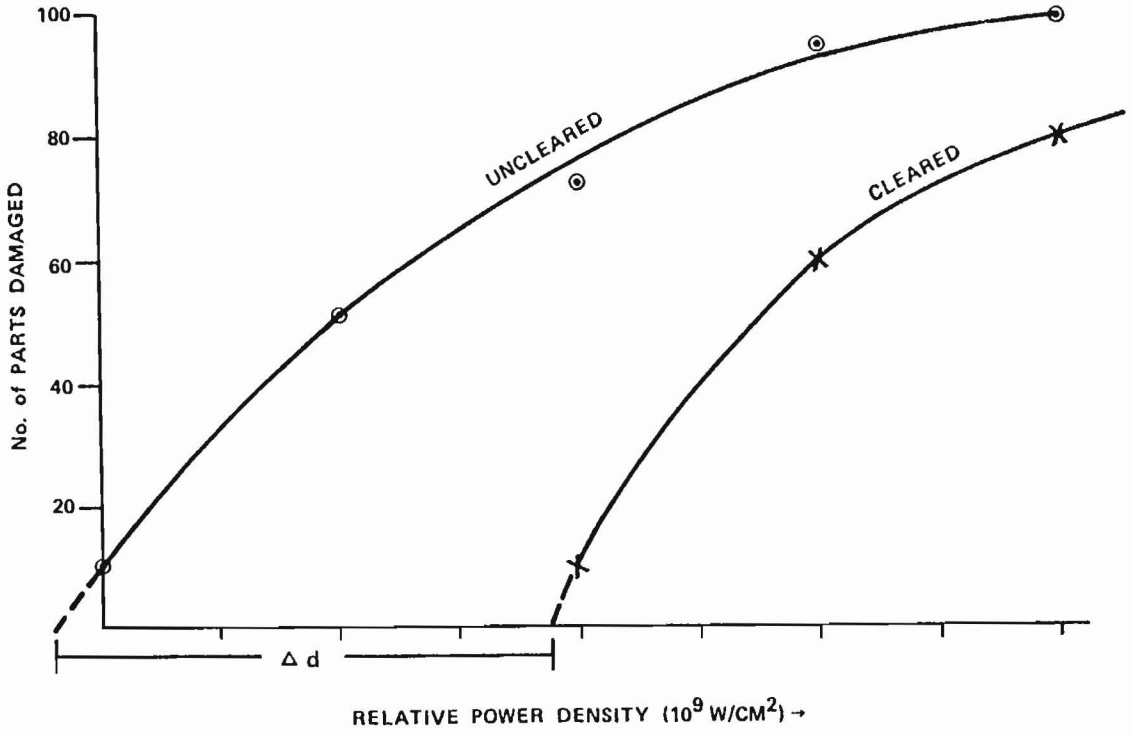


Figure 5.0

4. Cellulose Acetate Impregnated With The Dye

The treated cellulose acetate was impregnated with Bis-Nickel dye. The transmission spectrum is shown in figure 6.0. Once again, the Beckman DK-2A spectrophotometer provides this near infrared (NIR) range required for the measurements.

The transmission through the material, or the optical density of the material, can be adjusted by adjusting the dye concentration in the cellulose acetate. It may be noted that to utilize the material as a passive Q-switch, this optical density plays an important role as shown in figure 7.0. Thus, based on the laser rod diameter and input energy, the dye optical density will be selected. It is clear from figure 7.0 that the low optical density cellulose acetate will saturate with a lower total power density (lower input energy) and obviously low output energy will be obtained.

It may be noted that, unfortunately, it is difficult to obtain an optical density higher than 0.4 (less than 65% transmission) in cellulose acetate.

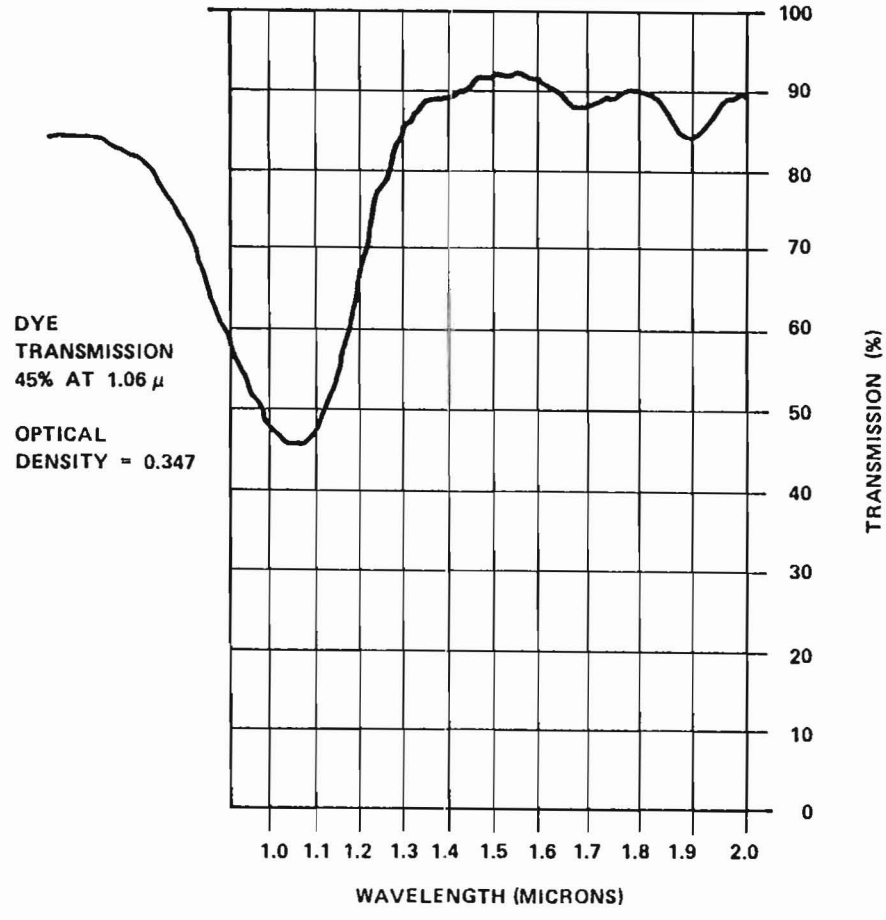


Figure 6.0

THE DYE TRANSMISSION EQUATION AS FUNCTION OF LASER IRRADIANCE:

$$T = \exp\left[\frac{-\gamma}{1 + \frac{I}{I_s}}\right]$$

WHERE γ = DYE ABSORPTION COEFFICIENT

I = TOTAL POWER DENSITY INCIDENT ON THE DYE

I_s = SATURATION INTENSITY CHARACTERISTIC OF THE DYE

Figure 7.0

5. Dye Q-Switch Cell

Since the dye impregnated cellulose acetate is inserted in the resonator, the wavefront distortion should be minimized. Secondly, to reduce the thermal load, providing a heat sink to the cellulose acetate is also important in high power applications. Hence, a cell was fabricated using sapphire windows.

Wavefront distortion observed in the cell was measured using a Zygo interferogram as shown in figure 8.0. As seen in figure 8.0 the clear aperture (rod diameter) of the cell is distortion free, although the cell as a whole appears cylindrical. In figure 9.0 details of the abberations in the cell are shown.

Cells of this type were used in a variable reflectivity cross porro resonator and achieved performance as high as 45 mJ/pulse output energy in a 20 ns pulse width at a 20 Hz repetition rate without damage to the Q-switch, as shown in figure 10.

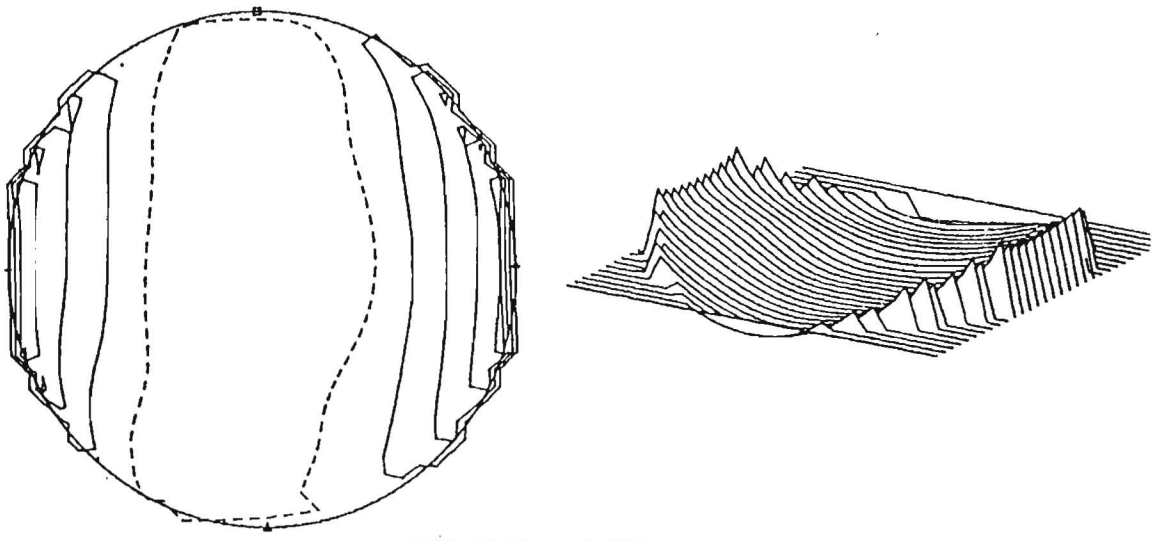


Figure 8.0

ID NUMBER 0000 * TIME 0000 * DATE 3-18-83
18-MAR-83 11:16:09 FILE: 0 SWITCH 1.DAT

WAVEFRONT DEVIATION IN UNITS OF WAVES
WAVELENGTH 0.633 MICRONS
INTERFEROGRAM HAS 11 FRINGES AND 119 DIGITIZED POINTS.

QUALITY OF FIT FOR DIFFERENT POLYNOMIAL ORDERS

	N	RMS	MAX
PLANE	2	0.068	0.185
SPHERE	3	0.049	0.114
4TH ORDER	8	0.012	0.032
6TH ORDER	15	0.010	0.028
8TH ORDER	24	0.009	0.022
COMPLETE	36	0.008	0.023

STREHL RATIO 0.908 AT BEST FOCUS

TILT	2.778	-178.9 DEG.
FOCUS	0.168	

FOURTH ORDER ABERRATIONS

MAGNITUDE WAVES	ANGLE DEG	DESIGNATION
2.776	-178.6	TILT
0.021		FOCUS
0.248	-2.8	ASTIGMATISM
0.037	74.3	COMA
0.007		SPHERICAL ABERRATION

FOLLOWING TERMS WERE SUBTRACTED FROM DATA:

TILT	
-2.7880	-0.0453

RESIDUAL WAVEFRONT VARIATIONS EVALUATED AT DATA POINTS

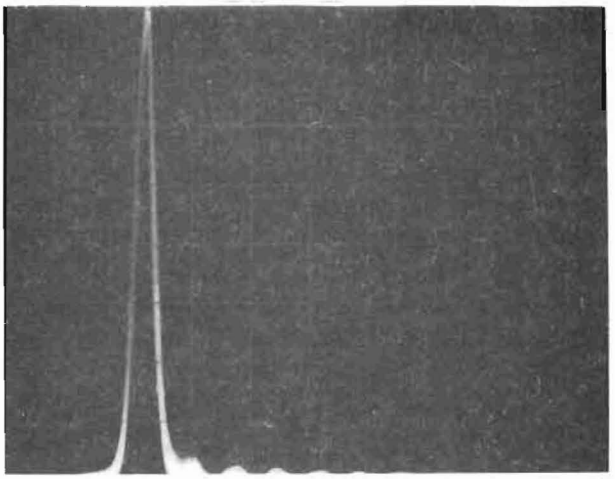
PTS	RMS	HIGH	LOW	P-V	STREHL
119	0.068	0.185	-0.084	0.268	0.831

RESIDUAL WAVEFRONT VARIATIONS OVER UNIFORM MESH

PTS	RMS	HIGH	LOW	P-V	STREHL
697	0.066	0.209	-0.074	0.283	0.841

Figure 9.0

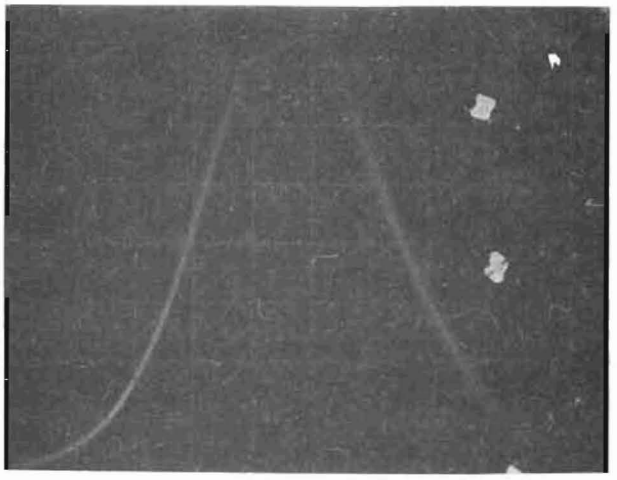
50 ns/cm 10pps 33mJ/pulse



919V Input 22 MF

Photograph Shows
Single Pulse Operation

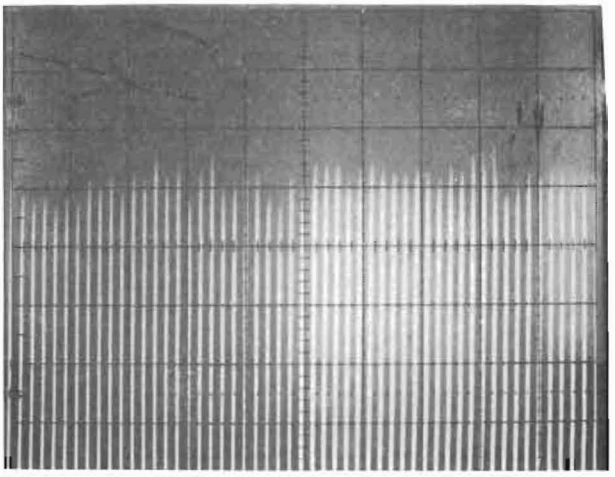
5 ns/cm 10pps



919V Input 22MF

949V Input

Photograph Shows
17 nsec Pulse Width
and the Laser Burn
Spots



Photograph Shows Pulse
to Pulse Stability
(1 div = 12.6 percent)

6. Acknowledgements

This work was a part of internal R & D supported by and conducted at International Laser Systems, Inc. The author is indebted to M. Kaplan for his assistance in chemical concept formulation.

7. References

[1] B. H. Soffer, J. Appl. Phys 35, 2551 (1964).

[2] Eastman Kodak Company, Eastman Laser Products, Publication Number JJ-169, (1979).

The question of aging of the dye was raised. The speaker reported that aging did occur. To minimize this effect, ultraviolet light was excluded. The cellulose acetate also takes up water, so a desiccator was used.

Strehl Ratio Measurements of Laser Damaged Plastics

Bill W. Mullins, Brent A. Richert*

United States Air Force Academy
Colorado Springs, Colorado 80840

Plexiglass G, manufactured by Rohm Haas, was irradiated by 10 nsec pulses from a Nd-YAG laser ranging in energy from 0.80 to 1.01 mJ/pulse. Aligned colinearly with the Nd-YAG pulse was a cw HeNe laser beam that measured changes in the transmission characteristics of the plastics. These transmission measurements enabled the Strehl Ratio, S, of the laser induced damage site to be calculated. When $S < 0.995$ there is a 92% probability of causing permanent damage. Conversely, when $S > 0.995$ there is a 94% chance of not causing permanent damage to the plastic. These probabilities were independent of laser pulse energies. Evaluation of the resulting diffraction patterns from the permanent damage sites indicates an $\sim 20\mu m$ diameter of the optical scattering center in the plastic. These damage sites cause an rms wavefront distortion ranging from 0.009λ to 0.0301λ at the HeNe wavelength.

Key words: laser damage; PMMA; Strehl ratio.

1. Introduction

The use of plastic optical components in high power laser systems has been limited due to their relatively low damage threshold when compared to glass or crystals. Little is known about the actual mechanism by which plastics damage under laser irradiation. In an effort to understand physical changes in plastics during laser irradiation, a commercial grade plastic was damaged using a single pulse Nd-YAG laser.

2. Background & Theory

A Quanta-Ray Nd-YAG laser was used to irradiate samples of Plexiglass G made by the Rohm-Haas Company. The laser damage set up was one devised by O'Connell, et al.[1] Added to his experiment was a HeNe laser probe beam (Fig 1). The HeNe beam was used to observe changes in small angle scatter by the plastic during and after the YAG pulse.

The HeNe was aligned to travel colinearly with the YAG pulse in order to have the greatest sensitivity to scatter. The divergence of the HeNe was conditioned by lenses 2 and 5 such that the HeNe and YAG focused at the same point in space by lens 8. The probe beam exiting the plastic was then split, with most of the energy going to a photodiode. The remainder of the HeNe beam fell onto a viewing screen to measure any resulting diffraction patterns produced by any damage sites. The photodiode was operated as a Strehl detector. By recording the HeNe beam's pre-shot, I_o, and immediate post-shot, I_{min}, intensities, the Strehl ratio, S, can be calculated by:

$$S = \frac{I_{min}}{I_o}$$

and can be related to the rms wavefront deviation, σ, by:

$$\sigma = \frac{1}{k}(1-S)^{\frac{1}{2}}$$

where k is the wavenumber of the HeNe beam.

*This research was done while Lt Richert was a cadet at the United States Air Force Academy. He is currently assigned to the Air Force Weapons Laboratory.

From the diffraction pattern, the diameters of the 1st and 2nd order minimums were used to calculate the diameter of the damage site. Assuming an Airy pattern, then d, the damage site diameter is equal to:

$$d = \frac{1.22\lambda R}{a_1} = \frac{2.233\lambda R}{a_2}$$

where λ = 632.8nm, R is the distance from the site to the screen and a_1 and a_2 are the diameter of the 1st and 2nd order nulls, respectively.

3. Procedure

The sample was prepared, placed in the system, and irradiated as prescribed by O'Connell.[1] The pre-shot, immediate post-shot, and final photodiode voltage levels were recorded for each shot. Also the diameter of the 1st and 2nd order nulls in any diffraction pattern were recorded. The sample was shot at seven different power levels ranging from 0.80 mJ/pulse to 1.01 mJ/pulse. Ten shots were taken at each energy level. Also, the occurrence of any flashing in the bulk plastic was noted.

4. Results

It was observed that the photodiode voltage usually dropped with irradiation of the sample by the YAG pulse. If no permanent damage occurred then the photodiode voltage returned to its original pre-shot level. If permanent damage did occur, shown by a flash inside the sample or the appearance of a diffraction pattern on the screen, then the photodiode voltage would return to a level lower than pre-shot. The recovery times of the sample was estimated to be about 1 sec for non-permanently damaged sites and about 5 sec for permanently damaged sites. A measure of an actual risetime was not made due to equipment limitations. If the pre-shot photodiode voltage is taken to represent I_o and the immediate post-shot photodiode voltage is taken to be I_{min}, then the Strehl Ratio of the HeNe beam can be calculated. Plotting S versus pulse energy (fig. 2) and noting which sites had permanent and non-permanent damage a definite break is easily seen. Of the 70 sites, only 2 had $S < 0.995$ and suffered no permanent damage. Of the 13 sites that did suffer permanent damage, only one had $S > 0.995$. From this we find for Plexiglass G that if $S > 0.995$ immediately after the YAG pulse, there is a 94% chance of no permanent damage having occurred. If $S < 0.995$, then there is a 92% chance of permanent damage having occurred in the plastic. The resulting wavefront errors, σ at λ = 632.8nm, of a beam passing through the plastic can range from 0λ to 0.014λ for non-permanently damaged sites and 0.009λ to 0.030λ for permanently damaged sites. Also, the above Strehl Ratios, corresponding wavefront errors, and the probabilities of damage do not seem to be a function of pulse energy. And the size of the damage sites from the diffraction analysis shows a rather consistant damage site size (table 1).

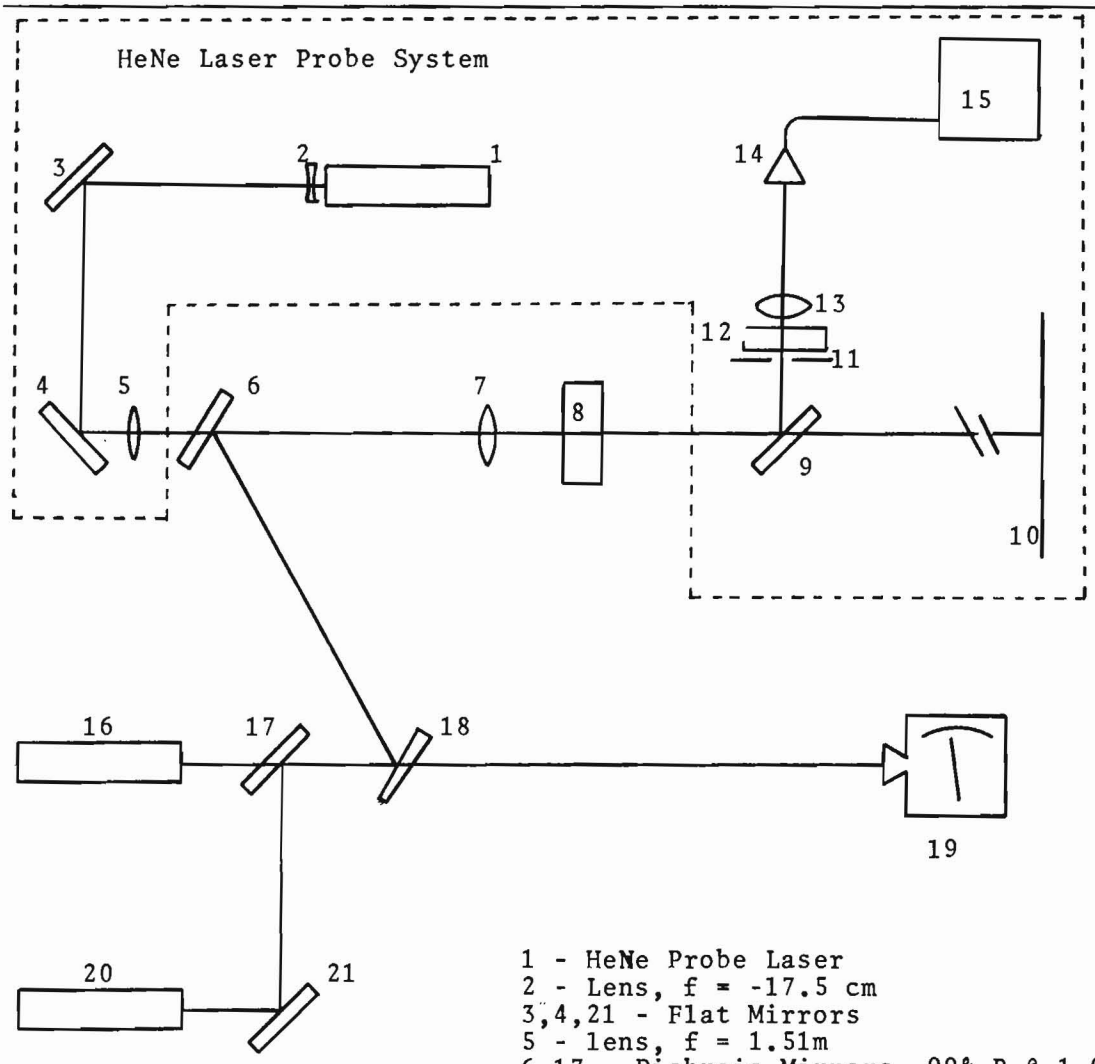
5. Conclusion

From the plastic tested a very definitive, better than 90% effective, highly sensitive test for whether the material damaged during a laser pulse was found. Also, for repetitive systems at the energy levels tested indications are that a time delay of better than one second between pulses is needed in order for the material to relax and not introduce any extraneous wavefront errors. This type of measurement, with improvements in the detector system, holds great promise for prediction of single and multi-shot damage in plastic material.

6. Reference

[1] R. O'Connell, T. T. Saito, T. F. Deaton, "Single and Multiple Shot Laser Induced Damage to PMMA", submitted to Applied Optics.

Figure 1. Laser Damage Set Up



1 - HeNe Probe Laser
2 - Lens, f = -17.5 cm
3,4,21 - Flat Mirrors
5 - lens, f = 1.51m
6,17 - Dichroic Mirrors, 99% R @ 1.06um
7 - lens, f = 24.7cm
8 - Target
9 - Dichroic mirror, 85% R @ 0.6328um
95% T @ 1.06 um
10 - Veiwing Screen
11 - Aperature
12 - KG3 cyrstal, 10^5 attenuation @ 1.06um
13 - Lens, f = 2.54cm
14 - Photodiode
15 - Digital voltmeter
16 - HeNe alignment laser
19 - Scientech Calorimeter
20 - Quanta-Ray Nd:YAG laser

Figure 2. Strehl Ratio of Plexiglass G

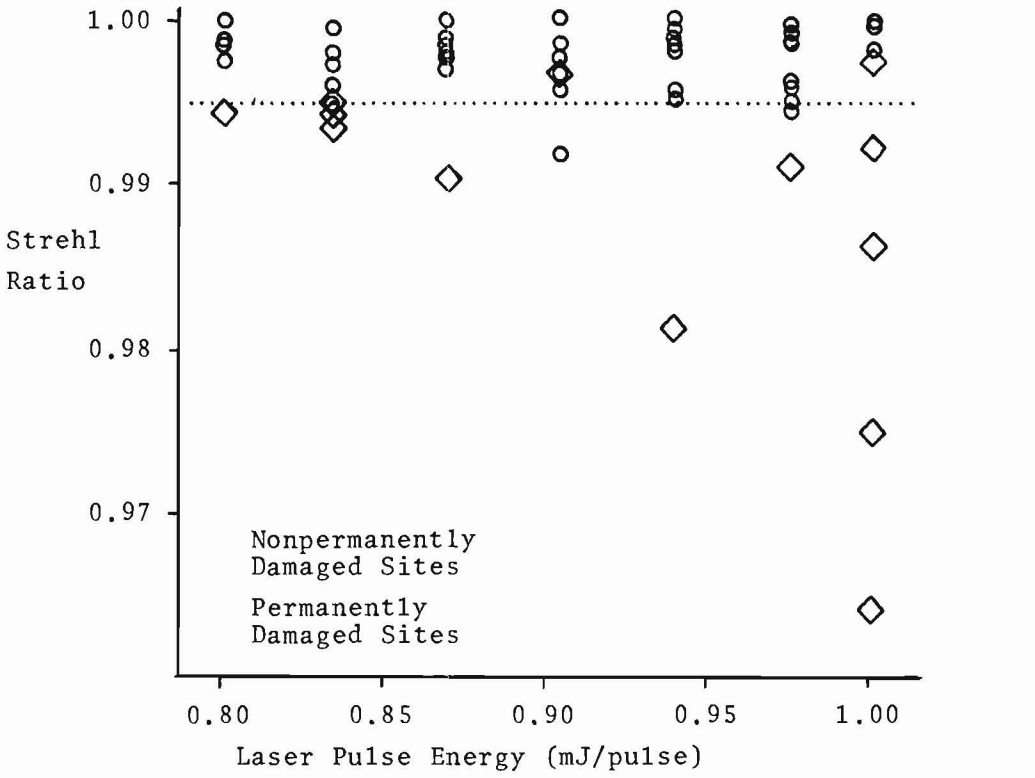


TABLE 1

Damage Site Diameter

Laser Energy (mJ/pulse)	Site Diameter 1st Order (um)	2nd Order (um)
0.097	19.3	Not Measured
0.943	17.5	18.6
0.980	20.3	17.2
0.980	24.1	18.1
1.015	24.1	Not Measured
1.015	22.7	18.6
1.015	22.7	19.1
1.015	22.1	19.1

The question was asked if the damage was permanent or only temporary until thermal relaxation occurred. The speaker said that the damage was catastrophic, but thermal relaxation at the damage site was a possibility in some cases. They could not reliably detect damage sites using an acoustic transducer mounted on the side of the sample.

Damage Thresholds of Fused Silica, Plastics and KDP Crystals Measured with 0.6-ns 355-nm Pulses*

M. C. Staggs and F. Rainer

Lawrence Livermore National Laboratory
Livermore, CA 94550

We used 355-nm, 0.6-ns pulses focused to a beam diameter of approximately 1 mm to measure the laser damage thresholds for surfaces of bare polished samples of several types of fused silica, for the bulk of crystals of potassium dihydrogen phosphate (KDP), and for a few plastics. Surface damage thresholds for fused silica ranged from 1-14 J/cm^2, and were least for surfaces with residual subsurface polishing fractures. Thresholds for inclusion damage in KDP crystals were 2-4 J/cm^2. Test volumes in these same crystals had thresholds from 2.5-7.0 J/cm^2 when they were laser hardened by repeated subthreshold irradiation. FEP teflon films had thresholds of 3 J/cm^2, which were the greatest threshold observed for a plastic.

Keywords: UV laser damage, fused silica, potassium dihydrogen phosphate, teflon, laser hardening, subsurface polishing damage.

1. Introduction

One responsibility of the laser damage group at Livermore is generation of a data base that adequately specifies safe fluence loading for existing optical components. This requires testing of enough samples to determine the distribution of thresholds likely to be encountered in a particular usage of the component. Here we present thresholds measured in two materials that will be used in the Nova laser [1], fused silica and KDP, and results of our initial 355-nm tests in plastics.

2. Measurement Procedure

Thresholds reported here were measured with 355-nm 0.6-ns pulses focused by a lens with 4-m focal length to a beam diameter of $\sim$ 1 mm (e^{-1} in intensity) at the sample. The pulses were generated by frequency tripling input 1064-nm pulses with 1-ns duration. The fluence distribution in the focused beam was circularly symmetric. The fluence profile measured along a diameter was quasi-Gaussian, but the beam shape varied with fluence as a result of the intensity dependence of harmonic conversion. The peak on-axis fluence for each shot was computed from measurements of the beam shape and pulse energy.

In tests of polished surfaces on silica samples and sheets of plastics, each test site was irradiated only once. To detect occurrence of damage in these samples, we used a Nomarski microscope to photograph the test sites both before and after irradiation. In KDP crystals we performed both 1-on-1 tests, in which each test site was irradiated once, and n-on-1 multiple irradiations of some sites. Isolated bulk damages occurred in KDP crystals at fluences below those which damaged the surfaces. The bulk damage sites were visually detected by observing scattering from a He-Ne laser beam that was colinear with the 355-nm beam.

Thresholds for all samples were defined to be the average of the greatest fluence that did not cause damage and the least fluence causing damage. In most experiments, there was little or no overlap of damaging and nondamaging fluences.

3. Damage on Polished Surfaces of Fused Silica

We tested samples made of three types of highly pure flame-fusion silica, and samples of two materials made by fusing naturally occurring quartz. These materials are listed in table 1. Each sample was 5.1 cm in diameter and about 1 cm in thickness. Fabrication of polished surfaces on these samples was performed by several vendors. Polishing was usually done with commercially available cerium oxide abrasives, but a few samples were polished with alumina.

*Work performed under the auspices of the U.S. Department of Energy by the Lawrence Livermore National Laboratory under contract W-7405-ENG-48.

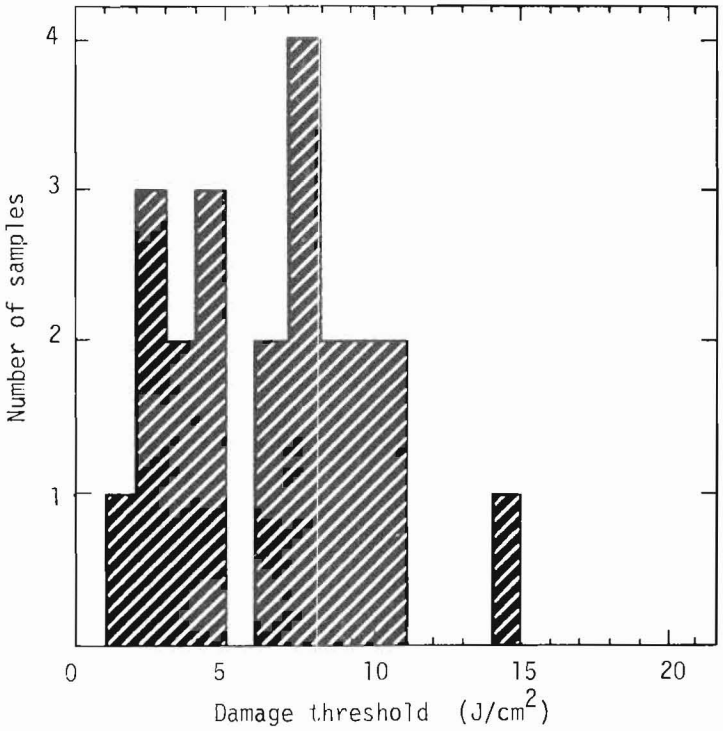


Figure 1. Surface damage thresholds (0.6-ns, 355-nm pulses) for assorted bare fused silica surfaces polished by several vendors.

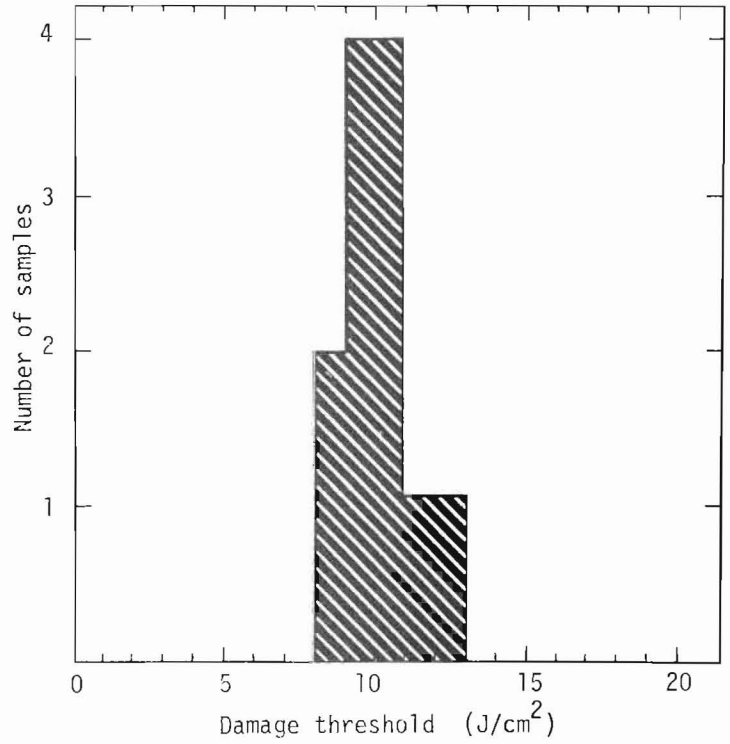


Figure 2. Surface damage thresholds (0.6-ns, 355-nm pulses) for four types of bare fused silica surfaces polished by a single vendor.

Table 1. Types of Silica Tested

Material Designation	Material Type	Vendor
7940	flame fusion	Corning Glass Works, Inc.
Optosil I	fused natural quartz	Heraeus-Amersil, Inc.
Suprasil II	flame fusion	Heraeus-Amersil, Inc.
ES	flame fusion	Nippon Silica Glass Co., Ltd.
OX	fused natural quartz	Nippon Silica Glass Co., Ltd.

Surface damage thresholds for 22 samples tested, given in figure 1, ranged from 1-14 J/cm^2, but there was no obvious relationship between thresholds and the type of silica. Instead, thresholds at 355-nm seemed to be exclusively dependent on the polishing history. To illustrate this, we show in figure 2 a histogram of thresholds measured on four types of silica for another 12 samples polished by a single vendor. The median threshold was almost 10 J/cm^2. Further, when we subjected surfaces prepared by this vendor to an HF etch, the etched surface was essentially featureless. By contrast, we show in figure 3 that etching of samples with low thresholds revealed significant subsurface structure. Therefore, we believe that low thresholds on some surfaces resulted from incorporation of polishing material into the surface.

Our results are somewhat parallel to those of previous experiments [2] that indicated that absorption in iron oxide was sufficiently large to prevent its successful use in manufacture of optical surfaces for 1064-nm lasers. Commercially available cerium oxide abrasives, though impure, [3] were found to produce satisfactory 1064-nm components. Our results suggest that absorption at 355 nm in these ceria abrasives may be unacceptably large. However, it will be difficult to make an unambiguous test of this possibility. Etching a surface may remove cerium oxide that is incorporated into the surface gel layer or trapped in polishing grooves. However, such etching usually roughens the surface. The advantages of removing ceria might be cancelled by the roughening, and interpretation of damage tests of etched surfaces has always provoked debate. It seems preferable, therefore, to simply use etching as a qualitative evaluation of polishing processes.

4. Damage in the Bulk of KDP

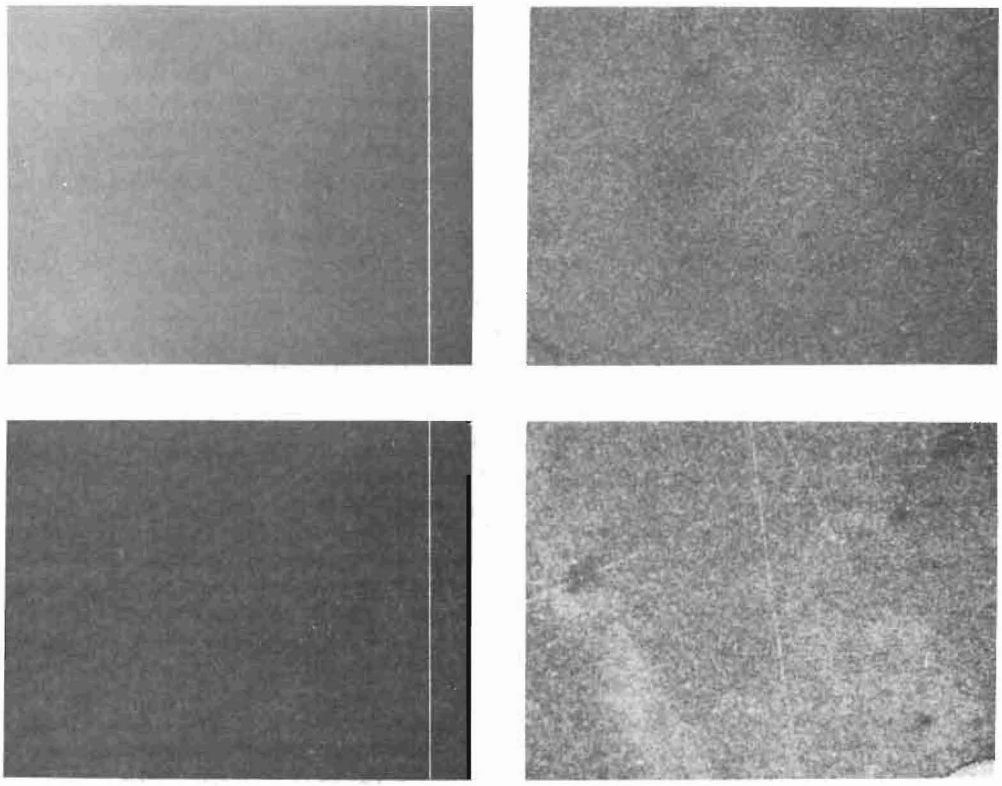
Our measurements of bulk damage thresholds in KDP crystals were made with a weakly convergent beam whose intensity did not vary significantly along the 2-cm path length through the crystal. Bulk damage can be observed in such experiments only when the threshold for bulk damage is less than the surface damage threshold, which is generally true for KDP [4]. The bulk damage produced in KDP by 355-nm beams consisted of isolated microfractures, whose volume density depended on the quality of the crystal and the fluence. In the best crystals, at fluences near threshold, only one or two microfractures were created. In some crystal with low thresholds, there were hundreds of microfractures per cubic centimeter in a trail filling the entire beam path.

Damage thresholds measured in 1-on-1 and n-on-1 tests of KDP crystals are given in figure 4. The crystals were samples taken from large boules grown to provide large aperture crystals for harmonic converters on NOVA. The median 1-on-1 and n-on-1 thresholds of these crystals were, respectively, 2.3 and 4.2 J/cm^2. Therefore, repetitive subthreshold irradiation of test volumes with 355-nm pulses produced an average increase in damage thresholds. As in similar experiments performed at 1064 nm, hardening of thresholds was not observed in every crystal [4]. Fortunately, the crystals with lowest 1-on-1 thresholds were most susceptible to hardening. This is illustrated in figures 5 and 6 which are shot records of experiments with two crystals. In the first crystal, testing of five sites indicated that the 1-on-1 threshold was 2.7 J/cm^2. The sixth site was irradiated by 9 shots at fluences up to 3.6 J/cm^2 before damage occurred on the tenth shot at 4.9 J/cm^2. Site seven survived 8 shots before damaging during the ninth shot at 5.6 J/cm^2. In this crystal, hardening occurred on both sites subjected to n-on-1 irradiations. In the second crystal, 1-on-1 tests of 5 sites and n-on-1 tests of sites 6-9 all indicated that the threshold was near 4 J/cm^2. For this crystal whose 1-on-1 threshold was among the largest observed, there was no evidence for the existence of threshold hardening.

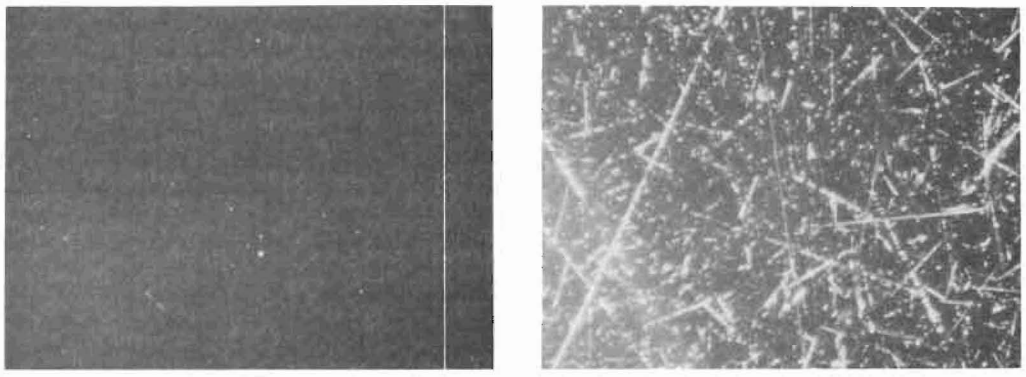
Therefore, tests of KDP at 355-nm produced results that are systematically like results of earlier studies at 1064 nm, although thresholds at 355 nm were lower. The low bulk damage thresholds of KDP will become a serious limitation to operating fluences in short pulse lasers if progress continues to be made in improving the damage resistance of other components of those lasers. Neither the defects responsible for bulk damage in KDP nor the physical mechanism for laser hardening have been determined with certainty.

As received

After etching



a. Etching of two samples which had high threshold as received.



b. Etching of a sample which had low threshold as received.

Figure 3. Nomarski photographs of silica surfaces before and after being etched overnight in dilute HF acid.

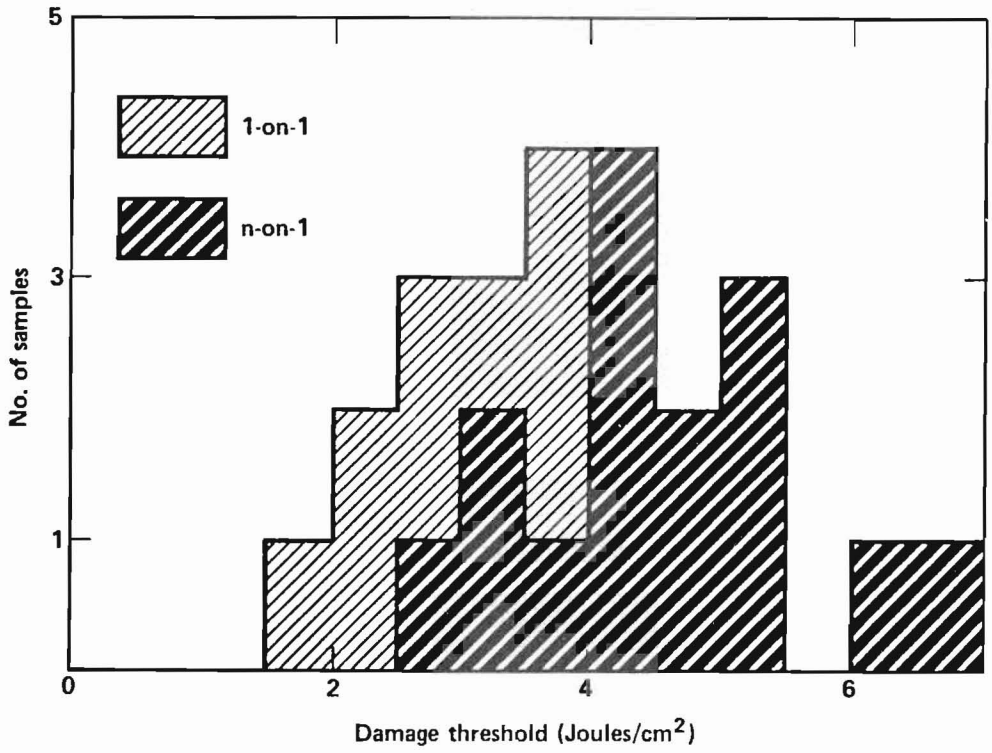


Figure 4. Bulk damage thresholds (0.6-ns, 355-nm pulses) of KDP samples from large boules. For the 1-on-1 tests samples were irradiated once at each site; for n-on-1 tests samples were irradiated at a particular site with sequentially higher fluences until damage occurred.

5. Damage in Plastics

The immediate application for plastic sheets in fusion lasers is fabrication of shields to prevent target debris from reaching the expensive focusing lenses. One material, FEP teflon [5], was found to have reasonably large damage thresholds at all three wavelengths of interest to the NOVA laser, 1053 nm, 527 nm and 351 nm. The thresholds measured at three closely similar wavelengths for a 0.025-mm thick sheet of FEP teflon are given in table 2. These thresholds are not adequate to allow the teflon to survive undamaged in a NOVA shot at full power. However, damage to an inexpensive debris shield would not be a serious problem if the plastic sheet remained intact and if damage to the sheet did not cause a major perturbation to the beam impinging on the target. Therefore, we plan to measure beam perturbation as a function of fluence in FEP teflon.

Table 2. Damage thresholds of FEP Teflon at three different harmonics

Frequency (nm)	Pulse Length (ns)	Threshold (J/cm^2)
355	0.6	3.2 $\pm$ 0.5
532	0.7	7.4 $\pm$ 1.1
1064	1.0	12.0 $\pm$ 1.3

Various plasma - polymerized plastic coatings on fused silica damaged at less than 1/2 J/cm^2.

We also evaluated the possibility of using plastic films to produce antireflection coatings on silica. Reflection loss at the air/plastic interface could be reduced by introducing microporosity to grade the refractive index of the plastic [6]. Reflection loss at the interface between the plastic and silica would be reduced below that for the bare silica by the partial index match between plastic and the substrate. We tested several films of the plastic $(CH)_n$ deposited by plasma polymerization onto silica substrates. Thresholds for all of these films were less than 0.5 J/cm^2 at 355 nm. These poor results, combined with the current success in our study of porous silica antireflection coatings, caused us to cease these films. The potential for coatings of this type remains largely unexplored.

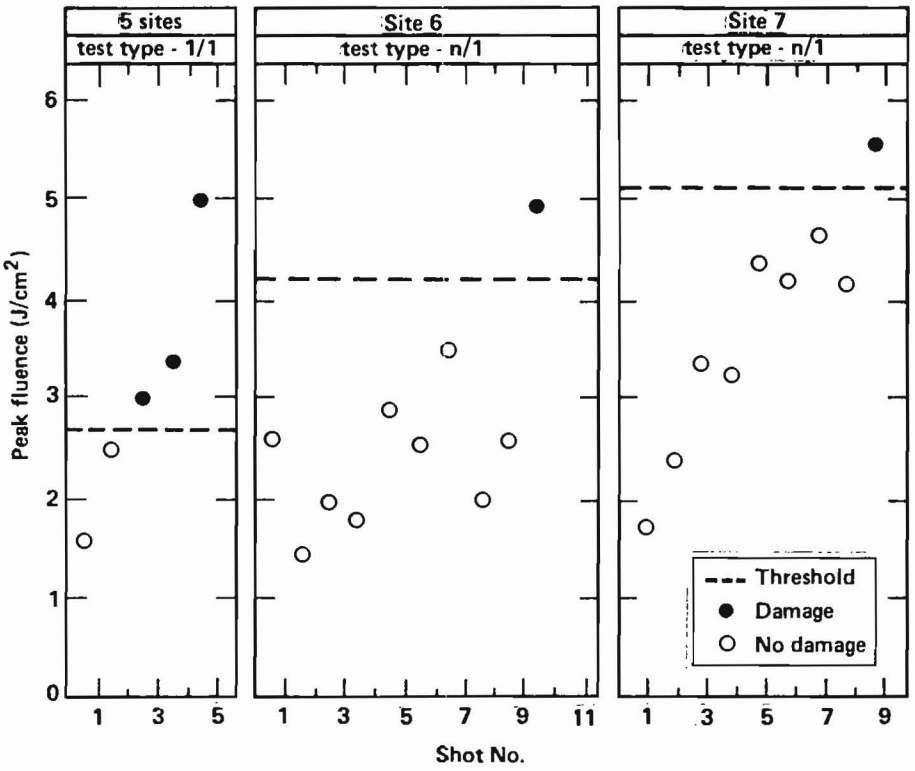


Figure 5. Record of shots used in 1-on-1 and n-on-1 testing for bulk damage of a KDP crystal which exhibited threshold hardening (0.6-ns, 355-nm pulses).

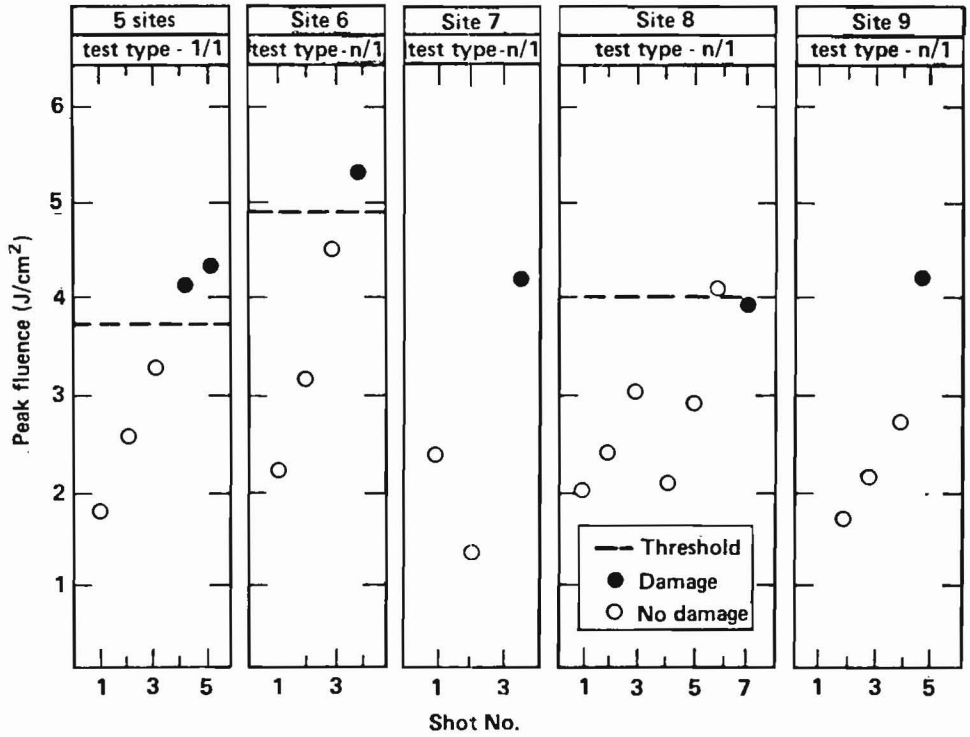


Figure 6. Record of shots used in 1-on-1 and n-on-1 testing for bulk damage of a KDP crystal which did not exhibit threshold hardening (0.6-ns, 355-nm pulses).

6. Summary

The median threshold measured with 0.6-ns 355-nm pulses on carefully polished surfaces of fused silica of five types was about 10 J/cm^2. Etching of surfaces with HF acid revealed subsurface structure on surfaces with low thresholds. Laser hardening increased the median bulk threshold of KDP crystals from 2.3 J/cm^2 measured in 1-on-1 tests to 4.2 J/cm^2 for n-on-1 tests. FEP teflon sheets withstood 3 J/cm^2 in tests at 355 nm, and are possibly useful as a debris shield in fusion lasers.

---

7. Acknowledgements

Serge Peluso assisted in troubleshooting and maintenance for the laser facility used in threshold measurements. Use of FEP teflon at 355 nm was suggested to us by R. W. Hopper. Plastic films were deposited on silica substrates by the target fabrication personnel in the laser fusion program at Livermore.

8. References

[1] Simmona, W. W.; Godwin, R. O., Nova laser fusion facility: Design and assembly overview, J. Nuclear Technology/Fusion, Vol. 4, pp. 8, 1983 July.

[2] Early studies of laser damage testing of etched optical surface are reviewed in: Boling, N. J.; Ringlien, J. A.; Dube, G., Q-switched laser induced surface damage at 1.06 microns. Nat. Bur. Stand. (U.S.) Spec. Publ. 414; 1974 December. 119 p.

[3] Lowdermilk, W. H.; Milam, D., Laser induced surface and coating damage, IEEE J. Quant. Elect., Vol. QE-17, No. 9, 1981 September.

[4] Swain, J.; Stokowski, S.; Milam, D.; Rainer, F., Improving the bulk laser damage resistance of potassium dihydrogen phosphate crystals by pulsed laser irradiation, Appl. Phys. Lett., Vol. 40, pp. 350, 1982 February.

[5] FEP teflon is a copolymer of tetrafluoroethylene and hexafluoropropylene, manufactured by E. I. Du Pont de Nemours and Co.

[6] Spiller, E.; Haller, I.; Feder, R.; Baglin, J.E.E.; Hammer, W. N., Graded index surfaces produced by ion implantation on plastic materials, Appl. Opt. Vol. 19, pp. 3022, 1980.

Strengthening CsI Crystals for Optical Applications

W.W. Durand, B.G. Koepke* and W.W. Gerberich**

Honeywell Systems and Research Center, Minneapolis, MN 55413
*Honeywell Ceramics Center, New Hope, MN 55428
**University of Minnesota, Minneapolis, MN 55455

Cesium iodide (CsI) is a very useful optical material combining a low refractive index with broad spectral transparency. Unfortunately, the mechanical weakness of CsI crystals severely limits practical applicability of the material. Nearly all uses require mechanical strengthening. The strengthening treatment cannot, of course, degrade desirable single crystal optical properties. Previous work at Honeywell has involved strengthening of alkali halides having the rocksalt structure (KCl, NaCl, etc.). Processed materials have been strengthened by as much as an order of magnitude without measurable optical degradation. Direct application of these processing methods to the dissimilar structure of CsI is impossible due to the limited number of slip systems active in the material. This investigation was, therefore, concerned with development of CsI processing methods that would effectively strengthen the material without introducing cracks or other optically degrading defects. This paper describes successful uniaxial and plane strain processing methods. Detailed process parameters and strengthened CsI material properties are included.

Key words: alkali halides; cesium iodide; deformation processing; forging; hot working; optical materials; optics; windows.

1. Introduction

Various strengthening treatments have been developed and demonstrated for alkali halide crystals. The most important treatment involves deformation processing. Single crystal potassium chloride (KCl) and KCl alloys have been processed successfully at elevated temperatures (150° to 300°C) to produce strengthened, fine grained polygonized material. Increases in yield strength as large as an order of magnitude have been obtained without optical degradation[1]. Subgrain size, dependent upon process conditions, was as small as 4 μm in the strongest material. Strength decreased as process temperature (and subgrain size) increased. Unconstrained and constrained uniaxial forging as well as rolling were used successfully to strengthen KCl and other alkali halides having the rocksalt structure. Isostatic pressure and deformable constraining rings were frequently used to inhibit edge cracking during deformation, which often involved engineering strains in excess of 60 percent.

Our approach toward strengthening cesium iodide involved application of these same techniques. Initially, there were doubts concerning the applicability of these techniques because of differences in slip characteristics between KCl and CsI. The potassium salts, and other alkali halide crystals having the rock salt structure, slip on {110} <1$\bar{1}$0> systems at room temperature[2]. There are two independent {110} <1$\bar{1}$0> slip systems. According to the Von Mises criterion, five independent slip systems are required to maintain strain continuity (i.e., prevent cracking) during large, general deformations[3,4]. Activation of the three independent {110} <001> systems (above 200°C) fulfills the strain continuity requirement and allows deformation processing of these materials. CsI, on the other hand, has the body centered cubic cesium chloride structure and slips only on the primary {110} <001> systems at all practical processing temperatures[4,5,6].

Although not straightforward, development of strengthened CsI material is clearly needed. Pure, single crystal CsI is extremely weak. Dobryak, et al.[7] deformed pure CsI crystals along the <110> direction and measured yield stresses near 1.7 MPa (250 psi) at room temperature. Berezhkova and Regal[8] tested crystals having <110> orientations and showed that yield strengths decreased continuously as temperature increased over the range from room temperature to 500°C. Johnson and Pask[9] studied the mechanical behavior of CsBr crystals (also with the CsCl structure) and showed crystals deformed along the <111> direction had slightly lower yield stresses than those deformed along the <110> direction. This was attributed to the higher resolved shear stress on the operating slip systems in this orientation. CsI crystals cannot undergo general deformation along the <100> direction because no resolved shear stress exists on any of the primary {110} <001> slip systems. Under these conditions, crystals deform inhomogeneously by kinking[5,9,10]. At large strains, kinked crystals develop microscopic fractures[11].

Since five independent slip systems do not operate in CsI under most conditions, cracks may nucleate if local stress concentrations within the material cannot be relieved by plastic flow. Stress concentrations

typically occur at the intersection of two slip bands. The intersecting bands act as mutual dislocation glide barriers and cause dislocation pile-ups yielding local stress concentrations. Nucleation of microscopic cracks in this manner has been treated in detail by Stroh and others[12-14], who found that substantial stresses could be generated. Cracks are expected to lie along slip planes based upon the nucleation geometries. Furthermore, the number of cracks is expected to increase as deformation proceeds due to the increase in slip band density. As will be shown later, this occurs in CsI under certain conditions.

There is a major difference between our work and other previously reported CsI deformation studies. In previous studies, crystals were deformed to engineering strains up to about 20 percent[8,9]. In the present study, however, crytals were typically deformed to compressive engineering strains greater than 50 percent in order to maximize substructural refinement, strength and finished billet size. Fractures induced in CsI by these large deformations have not been addressed in the previous studies. Fracture, and its prevention, is a central issue in the present work.

As a final note, we wish to reiterate that our efforts were successful. Under certain processing conditions, substantially strengthened CsI was obtained with excellent optical performance. Furthermore, the processing methods employed (particularly plane strain deformation) are compatible with efficient production of large windows. These results were obtained from pure, single crystal starting material. Additional strengthening may be possible by alloying. Several investigators have shown that even minor additions of mono or divalent cationic dopants to materials with the rocksalt structure produce appreciable strengthening[15-17]. The effects of alloying on CsI are, however, not well known. Dobryak, et al.[7] have shown considerable strengthening in CsI crystals alloyed with a number of elements but the data must be considered incomplete. We therefore elected to initially study deformation processing of only pure CsI material.

2. Approach

As previously noted, the limited number of active slip systems in CsI cast doubts on its ability to undergo large, general deformations. Symmetric deformation geometries were therefore chosen, so that the simultaneous operation of more than one slip system at the onset of deformation was favored. It was believed that this condition would minimize local stress concentrations and associated crack nucleation. Unconstrained uniaxial and plane strain forging were used as the deformation methods. In both cases, CsI crystals were loaded along the <110> and <111> directions, where either two or three slip systems were operative, respectively. Schematics of these forging methods are shown in figure 1. In the case of plane strain forging, crystals were further oriented such that the <100> slip directions were symmetric with the loading surfaces.

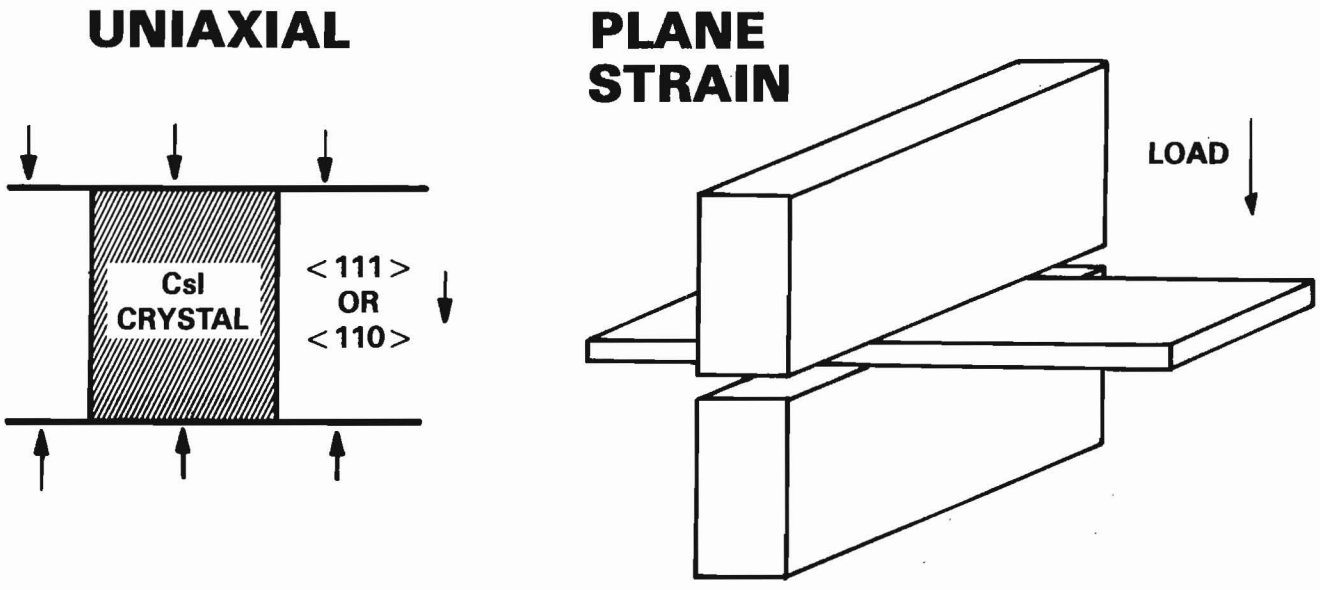


Figure 1. Diagrams showing both uniaxial and plane strain CsI forging approaches

Plane strain conditions are maintained in the deforming billet as a result of geometrical constraints[18]. These conditions are obtained when the billet thickness is less than one tenth of the billet width. Plane strain deformation confines the plastic zone to the platen contact area. This constrained plastic zone of limited size should result in more homogeneous deformation (less slip band separation) and presumably less chance of persistent slip band induced crack nucleation. Plane strain forgings were initially performed using long, narrow platens configured in the uniaxial forging apparatus. This allowed investigation of plane strain forging capabilities while simulating deformation conditions obtained during rolling. Hot rolling is a preferred method of deformation processing due to its compatibility with the production strengthening of large windows. A schematic showing the hot rolling facility in use at Honeywell is shown in figure 2. The heated rolls and tunnel furnaces situated on either side of the rolls allow the billet to maintain working temperature during the process cycle. In all cases, the billet is encased in an aluminum ring as shown. The ring provides two benefits. First, it exerts a radial constraining force on the expanding billet during a rolling pass, thereby inhibiting edge cracking. Secondly, there is a high frictional force set up between the rolls and the aluminum ring during rolling which assists in moving the billet between the rolls. Future hot rolling studies will employ deformation conditions identified in the plane strain forging experiments which will be described later.

Deformation temperatures were minimized in all cases in order to produce fine grained microstructures and billets with maximum strength. Earlier alkali halide deformation studies showed that such fine grained microstructures are produced by polygonization and not be recrystallization[1]. This was considered advantageous because low angle grain boundaries are presumably more easily penetrated by slip bands during deformation than high angle grain boundaries. Ease of slip band penetration would, of course, minimize nucleation and growth of Stroh cracks.

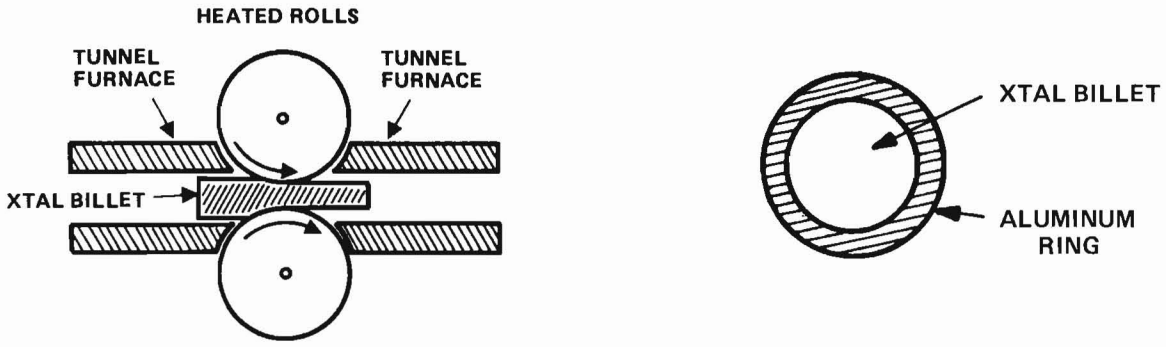


Figure 2. Continuous plane strain hot rolling apparatus used to process large window specimens. A top view of a specimen showing the aluminum constraining ring is included.

3. Experimental Procedure

3.1 Materials

Cylindrical, single crystal cesium iodide billets were obtained from the Harshaw Chemical Co., Solon, Ohio. Most crystals had a unity aspect ratio (equal diameter and height) with a 1.3 cm (0.5 inch) diameter. The crystals had a nominal purity of 99.999 percent. The axial crystal orinetations were specified as <110> and <111>. Laue x-ray measurements confirmed that these orientations were obtained within several degrees. Plane strain forging specimens were cut from the cylinders with the {111} and {110} orientations parallel to the platen surfaces. All specimens were water polished on moist felt to remove machining damage prior to forging. Mechanical properties of the as-received crystals were measured in compression using an Instron testing machine. Similarly, compression specimens were cut from forged billets with a wire saw, polished and tested at room temperature in the same machine to determine the effects of forging. CsI surfaces were routinely polished on wet felt and etched for several minutes in methanol to reveal their microstructure. Optical properties were measured using a Beckman IR-4240 scanning infrared spectrophotometer. This dual beam instrument is equipped to measure sample transmission and reflection over the

2.5 to 40.0 micron wavelength spectrum. Normalized transmission of forged specimens was measured by placing a polished single crystal specimen in the instrument reference beam with a polished forging specimen in the instrument sample beam. These normalized transmission measurements were made over the entire 2.5 to 40.0 micron wavelength spectrum.

3.2 Forging

A schematic diagram and photograph of the stainless steel forging apparatus used for this work are shown in figure 3. The upper and lower platens were heated by resistive cartridge heaters and the outer cylinder by a resistive band heater. All heaters were separately controlled and temperatures inside the chamber were controlled to within 1°C during any forging experiment. The chamber was filled with silicone oil to enhance temperature uniformity and to keep forge surfaces lubricated. During process development, thin teflon sheets were placed between the platens and billet to provide further lubrication.

Most forgings were carried out at constant crosshead speeds corresponding to initial strain rates, ranging from 10^{-3} min^{-1} to 10^{-2} min^{-1}. Forge temperatures ranged from 25°C and 250°C, but were most commonly maintained between 150°C and 250°C. Strain rate sensitivity tests were also performed during forging and loading increments corresponding to changes in crosshead speed were recorded for experimental analysis of thermally activated deformation in CsI crystals.

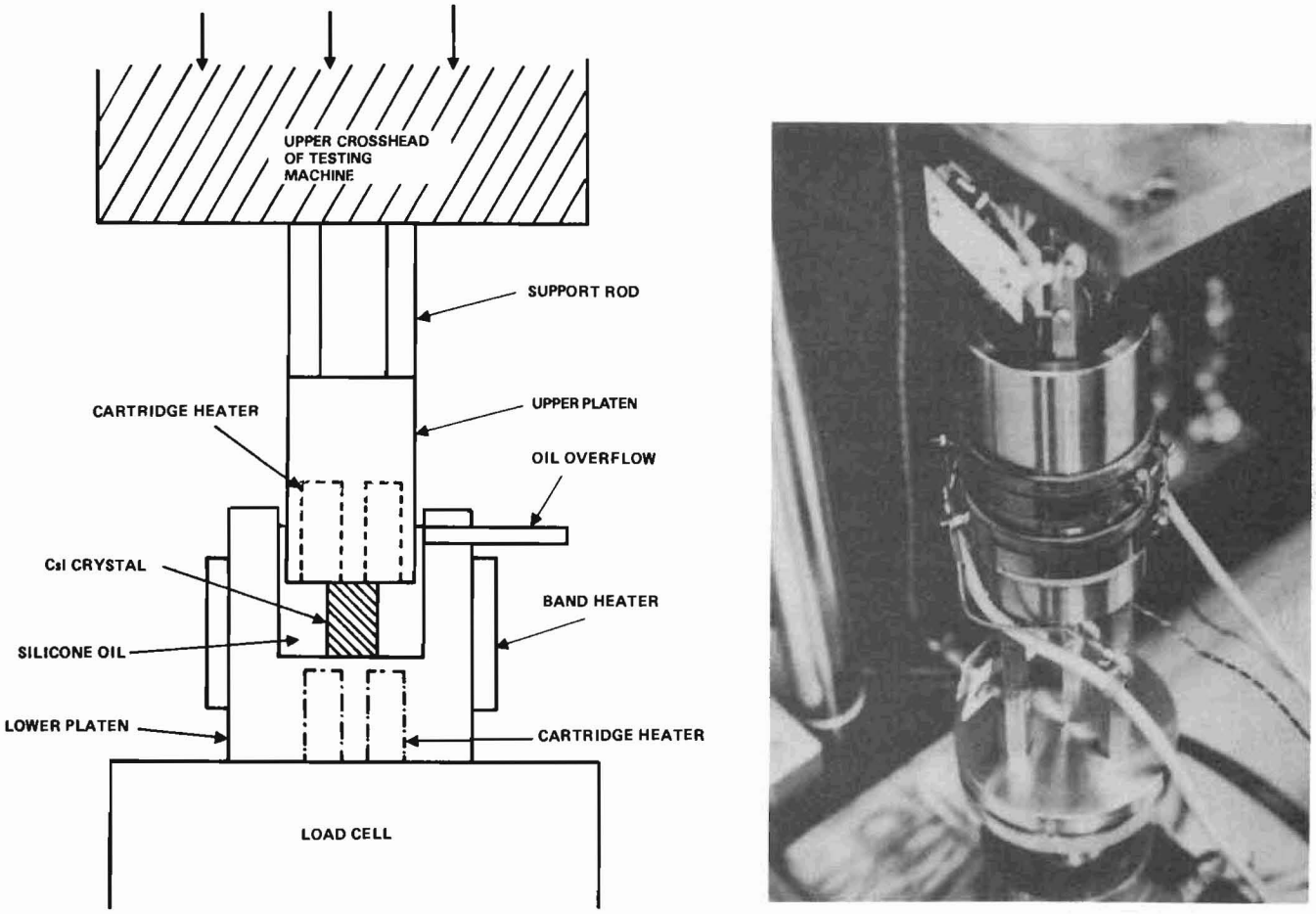


Figure 3. Schematic drawing and photograph of the CsI forging apparatus

4. Results and Discussion

4.1 Uniaxial Forging

4.1.1 Forging Stress

Stress-strain characteristics for three <111> oriented CsI crystals forged at different temperatures are shown in figure 4. These typical characteristics indicate that little apparent work hardening occurs before compressive strains greater than 20 percent are reached. Beyond 20 percent strain, forging stresses increase. We speculate that the increase in stress results from an increase in friction at the platen/billet interfaces, rather than an increase in the work hardening rate. The observed low work hardening rates at low total strains agrees with previously reported results[5]. Forging stresses decrease with increasing temperature and increase with increasing strain rate as expected. Similar results were obtained for CsI crystals forged along the <110> direction. In this case, however, forging stresses are slightly higher due to lower resolved shear stresses on the active slip systems[9].

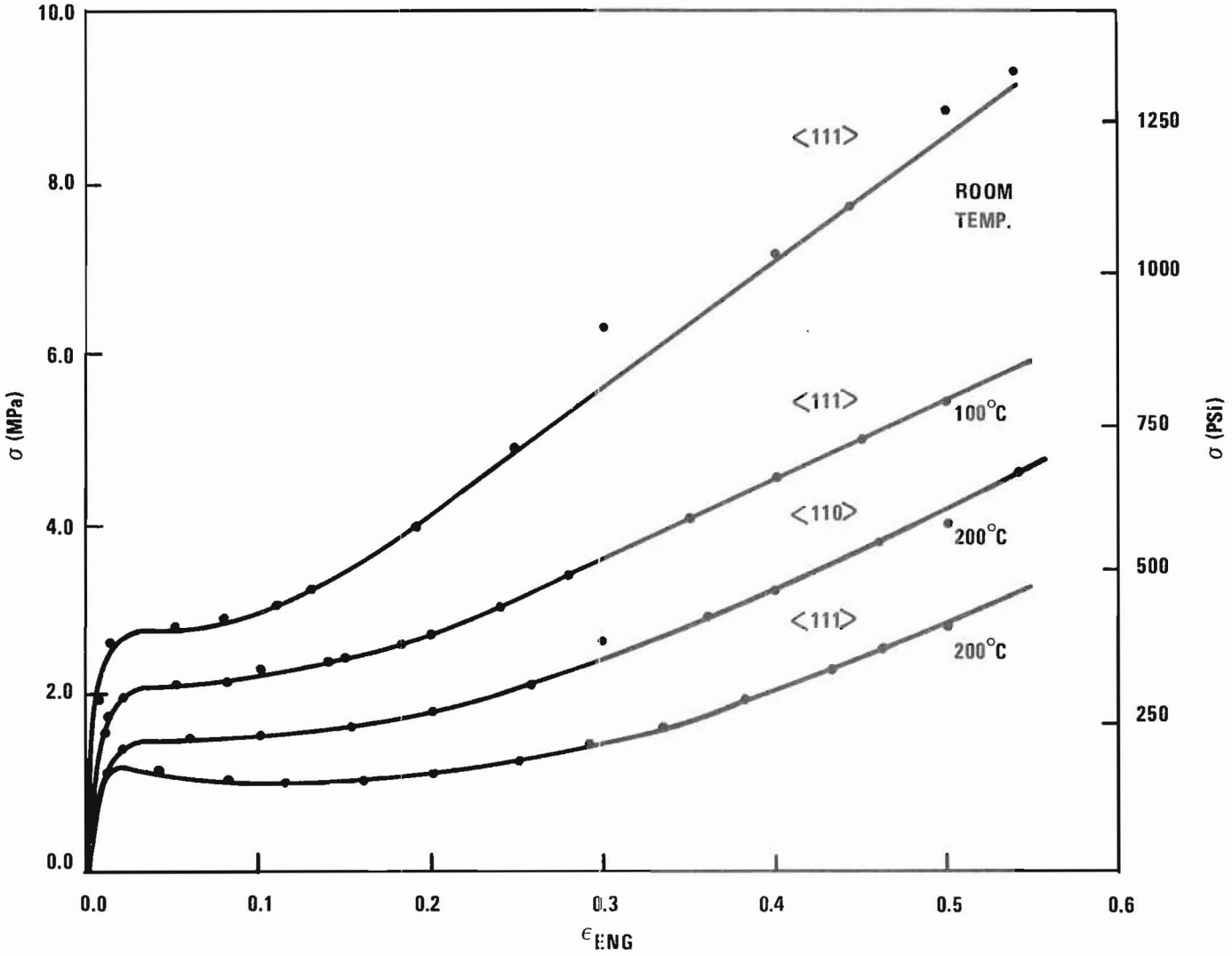


Figure 4. Stress-strain behavior during forging of CsI crystals along the <111> direction. A characteristic obtained by forging along the <110> direction is included for comparison. All forgings were made at the same constant crosshead speed ($\dot{\epsilon}_0$=0.004 min^{-1})

4.1.2 General Appearance

Clear forgings were not obtained under all conditions. Figure 5 shows that increased strain rates lead to greater internal fracturing. Although shown only for <110> oriented crystals deformed to 40 percent compressive strain, this observation applies to all forgings. As indicated in figure 5, an initial strain rate of 0.004 min^{-1} yielded a clear forging, while cloudy forgings were obtained at 0.01 and 0.2 min^{-1} initial strain rates. The forged <110> billets appear oval as a result of only two active slip systems. Crystals forged long the <111> direction under equivalent conditions are more symmetrical.

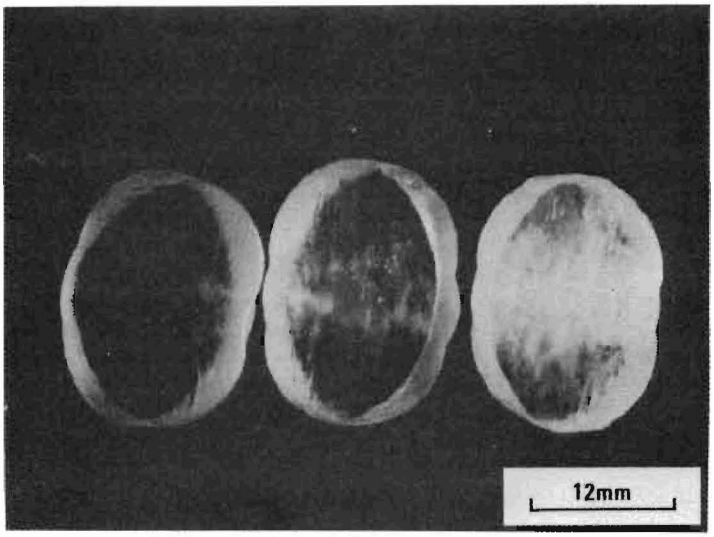


Figure 5. Effect of varying strain rate on uniaxially forged CsI crystal quality. Forgings were made at constant crosshead speed according to initial strain rates of 0.004 min^{-1} (left), 0.01 min^{-1} (center) and 0.2 min^{-1} (right). All forgings were made along the <110> direction at 250°C to 40 percent total height reductions.

4.1.3 Microstructure

All forgings introduced a fine grained microstructure into the CsI crystals. At low temperatures, microstructures have a banded appearance corresponding to relatively high strain concentrations within the slip bands. An example is shown in figure 6a. This structure, without well defined grain delineation, is typical of low temperature crystal forgings. Higher forging temperatures yield a more equiaxed microstructure as shown in figure 6b. Regardless of forging temperature, all billets forged during the study exhibited fine grained microstructures. This was of critical important in strengthening pure CsI crystals. In contrast to previous work[11], microstructures produced during the study appear stable and do not undergo grain growth or secondary recrystallization.

4.1.4 Strength and Optical Properties

After forging, samples were cut from the billets using a wire saw. These samples were then polished and tested in compression at room temperature to determine their yield strengths. Measured yield strengths are plotted as a function of forging temperature in figure 7. Yield strengths decrease linearly with forging temperature. The highest strength material obtained in the study was forged at room temperature. Strength increases as large as an order of magnitude above those for single crystals were obtained as shown. Measured strengths for crystals forged to 50 percent and 70 percent strains were approximately the same, indicating that work hardening is relatively independent of strain at large strains. This supports the contention that the flow stress increases shown in figure 4 for strains beyond about 20 percent result from frictional effects as suggested earlier.

Optical properties were measured for the forged billets according to the previously described procedure. As mentioned, all samples were polished prior to measurement in order to eliminate surface scattering effects and thereby allow accurate characterization of internal optical properties. Polished single crystals were used to perform normalized spectral transmission measurements and to establish a maximum transmission reference. Forged billets selected for optical measurement were equivalent to those characterized for yield strengths. These billets were all processed under optimized conditions and were visibly transparent. Measured infrared spectral trnamission characteristics of single crystal and forged CsI samples were virtually identical. Within the accuracy of the analog spectrophotometer output, all measurements

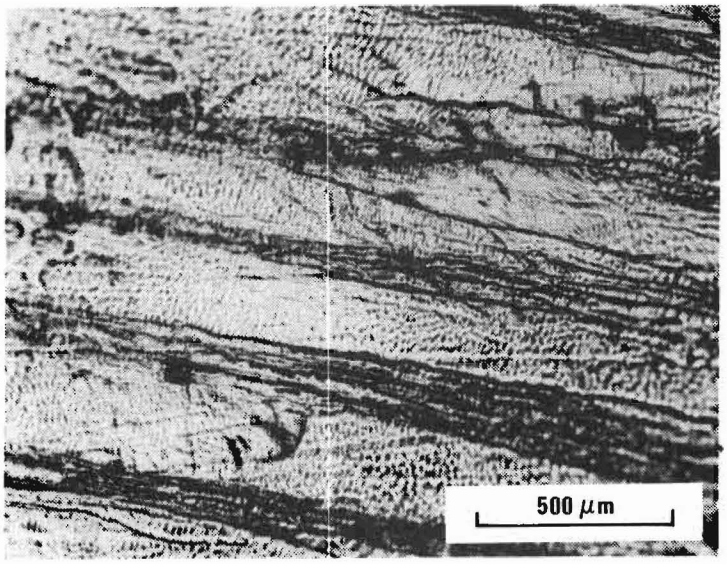


Figure 6a. Photomicrograph showing typical banded microstructures observed for low temperature (100°C) forgings. Billet was forged along the <111> direction to a 70 percent total reduction in height at a constant crosshead speed according to an initial strain rate of 0.004 min^{-1}.

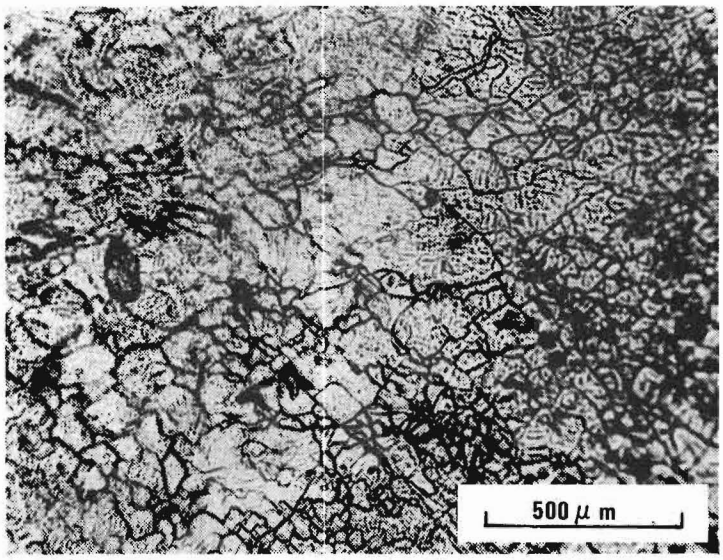


Figure 6b. Photomicrograph showing equiaxed microstructure observed for high temperature (200°C) forgings. Billet was forged along the <111> direction to a 50 percent total reduction in height at a constant crosshead speed according to an initial strain rate of 0.004 min^{-1}.

matched the maximum single crystal transmission reference value. These results are indicated in table 1. Normalized transmission values represent an average value of the entire 2.5 to 40.0 micron wavelength spectral range and include a worst case measurement inaccuracy of 1 percent. Single crystal optical properties have clearly been preserved in the forged material.

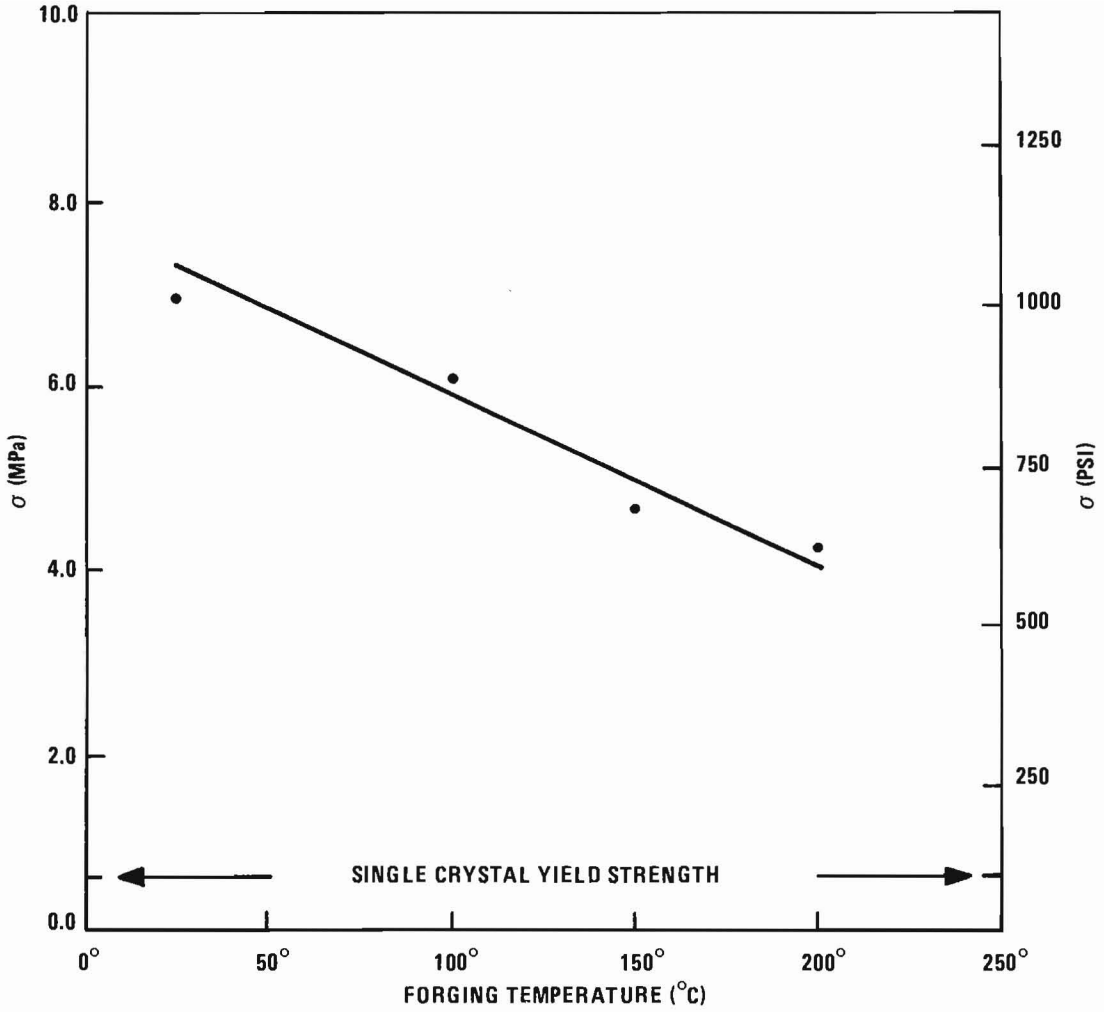


Figure 7. Room temperature yield strengths of forged CsI crystals as a function of forging temperature

4.2 Plane Strain Forging

As previously mentioned, plane strain or channel forging was investigated because it limits the size of the plastic deformation zone. This was regarded as a favorable condition in minimizing stress concentrations and associated crack nucleation. Single crystals used in the plane strain experiments were 1.3 cm (0.5 inch) diameter discs cut and polished to approximately 1.3 mm (0.05 inch) thicknesses. Channel forging platens were also 1.3 mm (0.05 inch) wide. According to Backoffen[18], these geometries will yield plane strain conditions. After forging, the crystals were reduced only along the narrow strip contacted by the platens. As such they are not useful components. As mentioned, however, channel forging adequately similates the conditions of rolling, which is a practical, production compatible processing method.

Table 1. Yield strength and infrared transmission characteristics of forged and single crystal CsI. All forgings were made at a constant crosshead speed corresponding to an initial strain rate of 0.004 min^{-1}. Billets were forged to 50 percent reduction in height at the indicated temperatures.

FORGING TEMPERATURE	ROOM TEMPERATURE YIELD STRENGTH	NORMALIZED IR TRANSMISSION
30°C	1014 PSI	0.99
100°C	889 PSI	0.98
150°C	685 PSI	0.99
200°C	633 PSI	0.99
Single Crystal	100 PSI	1.00

Photographs of crystals forged along the <100>, <110> and <111> directions under plane strain conditions are shown in figure 8. Forged channels are indicated by dotted lines. The crystal orientations are also shown. All three forgings were transparent and showed no evidence of cracking. Most interesting was the clear channel obtained in the <100> oriented crystal. Uniaxial forgings of <100> oriented crystals always yielded cloudy material as a result of kinking and fracture. As previously discussed, homogeneous deformation does not occur in crystals with this orientation because of zero resolved shear stresses on active slip systems. Apparently, the complex stress states present during plane strain forging combined with the confined plastic zones yield crack-free material. Microstructures were examined for all samples forged under plane strain conditions. They appear very similar to those observed for uniaxially forged billets. These results support the use of plane strain deformation, particularly hot rolling, as an effective processing method to produce strenthened, crack-free CsI. As previously mentioned, CsI hot rolling demonstration runs are in progress.

4.3 Thermal Activation Analysis

A thermal activation analysis was conducted using data obtained during the various crystal forgings. The purpose of the analysis was to gain some insight into the principal rate-controlling mechanism(s) operating in CsI during deformation. General analysis methodologies are described in detail elsewhere[19,20,21] and will therefore not be treated here. Material strain-rate sensitivity data was obtained during forging at different temperatures. Measurements were made by incrementally varying the crosshead displacement rate of the testing machine. Maximum crosshead speed was always kept sufficiently low to obtain clear, crack-free forgings. Well defined "steady-state" loads were always observed after an incremental change in strain-rate.

The experimental data were analyzed using relations derived from a state equation for the thermal component of the flow stress. Based on these relations, thermal activation parameters were calculated for CsI. All calculations were consistent with analysis results for other alkali halide materials[22].

Comparison of these results to theoretical models allowed a barrier profile analysis. Our calculated thermal activation parameters fit well with a dislocation jog dragging model for work hardening. Jogs in CsI are sessile. Furthermore, calculated activation volumes and enthalpies correspond well with a thermally activated cross-slip mechanism, which also explains the observed general homogeneous deformation of CsI without fracture.

5. Conclusions

This work has shown that pure CsI crystals can be strenthened by as much as an order of magnitude without optical degradation. Forged crystals exhibited yield strengths in excess of 1000 psi. Processing of alloyed material may result in even greater strengthening. The fine grained microstructures resulting from deformation processing appear extremely stable. Development of plane strain processing methods was conducted and the technique validated. Process scale-up and demonstration on a production compatible hot rolling mill is in progress. Strengthening of six inch diameter CsI windows is planned.

6. Acknowledgements

The authors wish to thank D.L. Parkin and K.M. Durbala for their dedicated assistance during the course of this research.

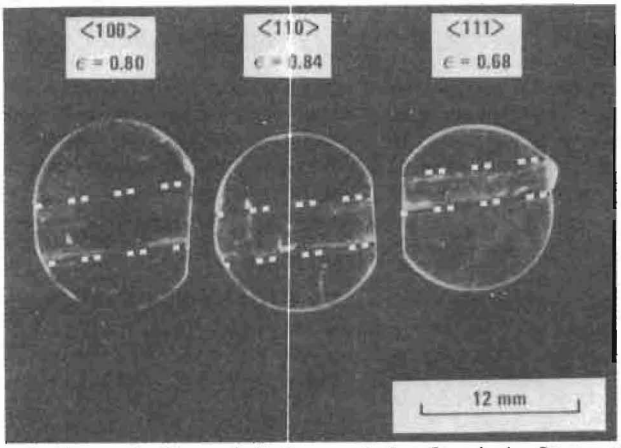


Figure 8. Photographs of channel forged CsI crystals loaded along the indicated directions. Forgings were performed with a constant crosshead speed according to an initial strain rate of 0.004 min^{-1} at 100°C. All forged channels are transparent. Observed blemishes are surface features.

7. References

[1] B.G. Koepke, R.H. Anderson and R.J. Stokes, in Deformation of Ceramic Materials, R.C. Bradt and R.E. Tressler, eds., Plenum, New York (1975) 497 p.

[2] J.J. Gilman, Acta Met. 7, 608 (1959).

[3] G.W. Groves and A. Kelly, Phil. Mag., 8, 877 (1963).

[4] M.T. Sprackling, The Plastic Deformation of Simple Ionic Crystals, Academic Press, New York (1976).

[5] V.R. Regel and G.V. Berezhkova, Soviet Phys. Crystal., 4, 718 (1959).

[6] N.L. Sizova and A.A. Urusovskaya, Kristall and Technik 12, 823 (1977).

[7] V.M. Dobryak, Ya. A. Zakharin, A.N. Panova, I.A. Rachkov and A.A. Urusovskaya, Soviet Phys. Crystal, 23, 239 (1978).

[8] G.V. Berezhkova and V.R. Regel, Soviet Phys. Crystal, 6, 115 (1961).

[9] L.D. Johnson and J.A. Pask, Journ. Amer. Ceramic Soc., 47, 437 (1964).

[10] M.V. Klassen-Neklyudova, M.A. Chernysheva and G.E. Tomilovaskii, Soviet Phys. Crystal., 5, 617 (1960).

[11] A.A. Urusovskaya and R. Thyagarajan, Phys. Stat. Sol., 10, 349 (1965).

[12] A.N. Stroh, Proc. Roy. Soc., A233, 404 (1954).

[13] A.N. Stroh, Adv. Phys., 6, 418 (1957).

[14] E. Smith and J.T. Barnby, Metal Sci. Journ., 1, 56 (1967).

[15] B.G. Koepke, R.H. Anderson, E. Bernal G and R.J. Stokes, Proc. Fourth Conf. on High Power Infrared Laser Window Materials, DARPA, Arlington, VA (1975), 621 p.

[16] W.B. Harrison, G.D. Hendrickson and J.E. Starling, Proc. Third Conf. on High Power Infrared Laser Window Materials, C.A. Pitka, A. Armington and H. Posen, eds., Air Force Cambridge Research Laboratories, AFCRL-TR-74-0085 (1974).

[17] P.F. Becher, R.W. Rice, P.H. Klein and S.W. Freiman, in Deformation of Ceramic Materials, R.C. Bradt and R.E. Tressler eds., Plenum, New York (1975), 517 p.

[18] W.A. Backofen, Deformation Processing, Addison-Wesly, Reading, MA., (1972).

[19] U.F. Kocks, A.S. Argon and M.F. Ashby, Thermodynamics and Kinetics of Slip, in Progress in Materials Science, Vol. 19, B. Chalmers, J.W. Christian and T.B. Massalski, eds., Pergamon Press, New York (1975).

[20] A.G. Evans and R.D. Rawlings, Phys. Stat. Sol., 34, 9 (1969).

[21] J.C.M. Li, Canadian Journ. Phys., 45, 493 (1967).

[22] A.G. Evans, in Deformation of Ceramic Materials, R.C. Bradt and R.E. Tressler, eds., Plenum, New York, (1975) 127 p.

The question of thermal shock properties of cesium iodide was raised. The speaker replied that they had done no thermal shock experiments. However, they pull the crystals out of hot oil and set them on a bench without thermal fracture, which suggests that the softness of the material may make it fracture resistant.

In response to another question, the author stated that the reason they could obtain a 100 crystal orientation was related to the difference between uniaxial forging and plain strain forging, i.e., channel forging or rolling. In the former case, the deformation zone deforms homogeneously and is of very limited size. They expect that the dimensional stability of the material will be improved by this process much as it is in rocksalt. A polygonized structure will result with low-angle rather than large-angle grain boundaries. They have not yet actually tested the temporal stability of the material.

STRENGTHENING OF CALCIUM FLUORIDE*

C. B. Willingham and M. A. Spears
Raytheon Company, Research Division
Lexington, MA

G. A. Graves
University of Dayton Research Institute
Dayton, OH

W. L. Knecht
Air Force Wright Aeronautical Laboratories
Wright Patterson AFB, OH

Improvements in the fracture and grain boundary strengths in fusion cast calcium fluoride are discussed. A fluorocarbon cleaning process that successfully improved the fracture strength was scaled to an apparatus capable of treating 30-centimeter diameter CaF_2 ingots. Mean fracture strengths of 132 MPa (19 ksi) were obtained. Diffusion of strontium ions into CaF_2 failed to strengthen the material because stress relaxation effects eliminated the induced stresses.

1.0 Introduction

The unpredictable fracture behavior of calcium fluoride has led to several experimental attempts to increase its strength and to decrease its variability. These programs are members of a longer series of efforts to strengthen optical materials that has been carried out, primarily under the sponsorship of the Air Force Wright Aeronautical Laboratories - Materials Laboratory, over the past ten years. In this paper, we review the current state of calcium fluoride strengthening. An Appendix summarizes earlier optical materials strengthening efforts carried out under AFWAL sponsorship.

For such brittle materials as CaF_2, fracture occurs when an applied stress, intensified by the presence of a stress-concentrating flaw, reaches the theoretical (bond breaking) strength of the material. The most familiar representation of the strength of brittle materials is given by the Griffith-Orowan equation:

$$\sigma_f = \left(\frac{E\gamma}{4c}\right)^{1/2} \qquad (1)$$

where E is the elastic modulus, γ the crack surface free energy, and c the length of the concentrating flaw. For high transparency optical materials, these flaws may be assumed to exist at the free surfaces of the materials. In principal, any of the variables in equation (1) can be varied to produce a strengthening effect. In practice, elimination of surface flaws (minimizing c) or application of a biasing surface compressive stress are the most commonly used approaches for strengthening brittle materials.

The strengthening treatments discussed below were applied to fusion cast calcium fluoride, a highly purified, directionally solidified form developed for optical applications requiring larger components than are available in single crystal form. Ingots as large as 30 centimeters diameter and three centimeters thick may be produced routinely. State of the art ingots are free of visible scatter, and have residual stress birefringences less than 20 nanometers per centimeter. Bulk absorptivities at fluoride chemical laser wavelengths are typically equal to or less than 10^{-4} cm^{-1}. Microstructurally, fusion cast CaF_2 is multicrystalline; a 30 centimeter ingot may contain fewer than twenty individual single crystals, each one of which extends through the entire thickness of the ingot. Although these experiments have treated only fusion cast CaF_2, the approaches are not specific to fusion cast material and the results should be applicable to single crystals and polycrystalline calcium fluoride as well.

*Sponsored in part by
Air Force Wright Aeronautical Laboratories
Materials Laboratory
Air Force Systems Command
United States Air Force
WPAFB, OH 45433

2.0 Experimental

Calcium fluoride strengthening studies have been in progress at the University of Dayton Research Institute[1] and at Raytheon Research Division[2]. In both cases, the program goals are to produce

1. A Strength Increase from 69 MPa (10 kpsi) to 96 MPa (14 kpsi)
2. Standard Deviation Decrease from 28 MPa (4 kpsi) to 10.3 MPa (1.5 kpsi)
3. No Optical Property Change
4. Processing Applicable to Components in Production

The UDRI effort has emphasized a fluorocarbon atmosphere treatment of polished specimens. At Raytheon, grain boundary strengths and diffusion-produced surface stresses have been investigated.

2.1 Grain Boundary Strengthening Experiments

Low grain boundary strength emerged as a major problem when the fusion casting process was scaled up to produce 30 centimeter ingots (from a 15 centimeter process). In worst cases, test specimens could not be fabricated without grain boundary failure occurring. Given the large-grained microstructure of the material, any dimunition of grain boundary strengths is a particularly serious defect. A major portion of the Raytheon program, originally intended to develop surface stressing techniques, was necessarily redirected to address the grain boundary problem.

During the fusion casting process, reagent grade calcium fluoride powder is melted in the presence of a carbon tetrafluoride atmosphere and then directionally solidified to produce the final ingot. In principal, the CF_4 atmosphere fluorinates oxide and hydroxide contaminants; cations forming volatile fluorides are removed. Thermodynamically, the fluorinating reactions are highly favored. We have found, however, that the atmosphere is significantly less effective in the furnace used to produce the large ingots than it was in the original smaller furnace used for 15 centimeter ingots. Secondary Ion Mass Spectroscopy (SIMS) of weakened grain boundaries taken from large ingots indicates the presence of chlorine, sodium, aluminum and silicon in excess of their concentrations in the bulk. In earlier ESCA experiments, oxygen has also appeared to be a grain boundary contaminant, but no excess was determined by SIMS. Additional purification was produced by improving the atmosphere exchange patterns within the large furnace, by multiple remeltings, and finally by replacing the pure CF_4 atmosphere with a mixture of CF_4 and hydrogen - in the manner of the UDRI surface strengthening experiments discussed below. Thermodynamically, CF_4/H_2 atmospheres should be slightly less fluorinating than pure CF_4. It appears, however, that the mixture improves the reaction kinetics. We have produced ingots in both the small and large furnaces using H_2/CF_4 atmospheres. SIMS analysis of grain boundaries from a small furnace ingot detected no excess impurities associated with grain boundaries.

The more extensive purification treatments appear to have overcome the grain boundary fracture problem for fusion cast CaF_2. The strength of a test beam set consisting of 14 grain boundary-containing specimens was 13.3 ± 5.3 ksi. Of the specimens, five exposed some portion of their grain boundaries during fracture. The minimum strength of these five was 9.5 ksi, and two specimens had strengths above 22 ksi. We conclude that grain boundaries need not limit the strength of fusion cast CaF_2 to unacceptably low levels. Larger ingots treated in H_2/CF_4 have not yet been tested. The improved reaction kinetics should, however, produce strong, contamination-free grain boundaries in large ingots.

2.2 Diffusional Strengthening Experiments

Surface compressional stresses may, in principal, be produced by diffusion of a large substitutional or interstitial ion into a solid surface. For the case of strontium diffused into CaF_2 surfaces, residual surface compressions on the order of 10^5 psi per percent of strontium substitution may be estimated from the relative sizes of the calcium and strontium ions. At the diffusion temperatures, the induced stresses can be diminished by plastic flow and other stress relaxation mechanisms. Final stress levels are determined by the balance of the diffusion and stress relaxation rates.

The thrust of these experiments was to attempt strengthening in disc-shaped biaxial test specimens (2.5 cm diameter x 0.25 cm thick) by means of strontium diffusions. Three types of diffusion sources were used:

[1] AFWAL-ML Contract No. 33615-82-K-5105
[2] AFWAL-ML Contract No. 33615-81-C-5151

i) Sr/CaF_2 alloy thin films deposited onto moderately (200°C) heated CaF_2 substrates.

ii) Sr/CaF_2 alloy films deposited "epitaxially" onto high temperature (400-500°C) CaF_2 substrates.

iii) Bulk Sr/CaF_2 alloy powders in which calcium fluoride test specimens were packed for diffusion.

Alloy compositions and film thicknesses were varied to produce a range of strontium "charges". Diffusions were carried out at temperatures in the range of 800-1100°C. Strengths of selected specimens were determined in biaxial flexure. Deformations produced by the diffusional processes were determined by interferometry before and after diffusion. Diffusion profiles were determined by EDAX analysis in a scanning electron microscope. Although the diffusions produced the expected deformations of the test specimens, no significant strengthening effects were produced by strontium diffusion. Residual stresses, determined by taking repeated interferograms of one surface of a typical specimen as the diffused surface was progressively removed, were shown to be less than a few hundred psi. Plastic yielding and stress relaxation effects, which occur simultaneously with the diffusion, effectively negate all compositional strengthening in the Sr/CaF_2 system.

Large residual stresses were successfully produced by depositing Sr/CaF_2 alloy films onto hot (400-500°C) calcium fluoride substrates. These stresses, produced by epitaxial-like registration of the depositing film, are not relaxed by yielding of the substrate because the temperature is too low. Strengthening based upon this effect may be a useful treatment to follow the fluorocarbon cleaning treatment discussed below.

2.3 Surface Chemical Treatments

Earlier work performed at Raytheon (unpublished) indicated that treating CaF_2 in a vacuum at 1000°C for a period of 24 hours or more increased the average flexural strength of the material significantly. However, the permanency of this effect was questionable. Later attempts to reproduce the results, though unsuccessful, prompted thoughts based on a technique available at UDRI, the fluorocarbon cleaning process (FCP). It was suggested that if strengthening could be affected by vacuum, the mechanism might be a superficial removal of dissolved oxygen (as anion substitutions) with a resultant residual surface compressive stress. Such a mechanism, although effective, would leave a high anion vacancy concentration near the surface, and the specimens would be subject to rapid recontamination upon exposure to ambient air. The FCP (invented for cleaning super-alloy metals) utilizes the pyrolysis of polytetrafluoroethylene (Teflon) and dry hydrogen to produce a low oxygenating, high fluorinating, reducing gaseous atmosphere. Thermodynamic calculations indicate that such an atmosphere, if properly controlled, would be in equilibrium with pure CaF_2 that has an oxygen content of less than 0.001 ppm. This suggested that modifications in the FCP would result in surface deoxidation and fluorine replacement in CaF_2 castings. The expected result would be an increase in strength and resistance to recontamination.

In exploratory experiments, calcium fluoride specimens heated in modified FCP atmospheres did display modest strengthening, with an average flexural strength of 17.7 ksi and a standard deviation of 2.3 ksi. These results served as a partial justification for a proposed strengthening program to determine the FCP parameters that would produce an optimal surface "purification" type strengthening for cast CaF_2.

In order to optimize the FCP processing parameters, a factorial experiment was completed. The designed experiment encompassed variations in fluoridizing strengths of the FCP atmospheres, maximum temperatures, and holding times at maximum temperature. The treatments were conducted in a retort just large enough to accommodate five rectangular flexural test specimens; of dimensions, 6.5 x 1.0 x 0.5 cm. The processing parameters considered to be optimum after completion of the study produced an average flexural strength of 130 MPa (20 ksi) with a standard deviation of 16 MPa (2.3 ksi), based on 20 specimens treated in four replications of the optimum treatment. Control specimens tested at the same time had an average strength of 73 MPa (10.6 ksi) with a standard deviation of 20 MPa (2.9 ksi).

These results led to a follow-on effort to build a furnace and retort large enough to treat 28 cm diameter fusion case CaF laser windows. The apparatus was built and is now fully operational. After early "shake down" runs, a group of 25 flexural test specimens was FCP treated in the large retort. The average flexural strength for 24 specimens (one was broken in handling) was 132 MPa (19 ksi) with a standard deviation of 47 MPa (7 ksi). No large (30 centimeter) castings were available for FCP treatment during the performance period of the program. This experiment does, however, demonstrate that the FCP process can be scaled to permit controlled treatment of large CaF_2 ingots. The process is easily controlled and could be adapted to other processes that would benefit from a "low" oxygen environment.

3.0 Summary and Conclusions

The primary results of the experimental programs are:

FCP treatments increased the mean fracture strength of CaF_2 to 132 MPa (19 ksi), well beyond the program goal of 97 MPa. Scaling of the process to an apparatus capable of treating large fluoride components was successful.

Improved purification procedures eliminate grain boundary contamination and their associated strength impairment in fusion cast ingots. A minimum grain boundary strength of 62 MPa (9 ksi) was demonstrated.

Strengthening attempts based upon strontium diffusion techniques were not successful. Surface stresses were, however, produced by thin films of Ca/Sr F_2 alloys deposited onto hot CaF_2. These may provide useful protective stresses on FCP-treated windows.

Concluding, these improved grain boundary and surface strengths should improve the position of fusion cast CaF_2 as an acceptable optical material. Additional experimental work should confirm the grain boundary strengths in large ingots and determine the long-term environmental stability of the FCP strengthening effects.

Appendix

Strengthening of Optical Materials

This Appendix summarizes efforts supported by the Air Force Wright Aeronautical Laboratories. The appropriate Final Report number is given for each entry.

A. Strengthening of KCl - AFML-TR-44-165

The work was performed by Harshaw. The approach was to add barium chloride to KCl. In this case, barium ions pin the dislocations existing in KCl. As a result, the yield strength of KCl was increased from 600 PSI to 1000 PSI. Note that since KCl fails by plastic yielding rather than brittle fracture, surface treatments were not used.

B. Strengthening of KCl - AFML-TR-79-4017

Additional work on strengthening of KCl was performed by Honeywell. In this case, both Rubdium Chloride and Europium Chloride were added to KCl. As a result, the yield strength of KCl was increased from 1050 PSI to 3200 PSI.

C. Strengthening of Sapphire - AFML-TR-79-4017

In connection with material hardening efforts for the Air Force, Raytheon developed an approach which utilizes the deposit of a SiO layer on Sapphire with succeeding high temperature firing. As a result, the tensile strength was increased from 50 KPSI to 100 KPSI. Furthermore, a considerable reduction of the standard deviation of the tensile strength was achieved.

D. Strengthening of ZnS - AFWAL-TR-82-4033

Bell Aerospace attempted to improve the mechanical properties of ZnS by:

1. Immersing in molten cadmium nitride
2. Packing in GaAs powder and fire at 850°C
3. Glazing

None of these approaches produced a statistically significant increase in mechanical strength.

E. Strengthening of CaF_2 - AFWAL-TR-81-4179

Northrop attempted three approaches:

1. Optical polishing to reduce the sizeand density of surface defects.

2. Irradiation with cobalt (60) gamma rays (5×10^6 R) to increase effective specific surface energy.

3. Optical coating to either induce a residual compressive stress in the CaF_2 or provide an outer layer which is in a compressive state of stress. Optical coatings tried were Al_2O_3 and PbF_2.

None of the techniques produced a statistically significant increase in mean flexural strength. However, the optical coatings produced significant decreases in the standard deviation of strengths and increases in Weibull Modulus.

Investigation of Window Materials for Repetitively Pulsed CO_2 Lasers

Jitendra S. Goela*
Indian Institute of Technology, Kampur, India

Raymond L. Taylor, Mark J. Lefebvre, Peter E. Price, Jr.
CVD Incorporated, Woburn, MA 01801

M. J. Smith
Avco Everett Research Laboratory, Inc., Everett, MA 02149

A need exists to develop infrared window materials for use on repetitively pulsed CO_2 lasers. Data obtained on single pulse damage criteria at 10.6 μm may not be sufficient to determine the response of materials under repetitive illumination. The optical, mechanical and physical properties of all potential transmissive optical materials at 10.6 μm were collected and compared. From this list, 19 optical materials were selected for detailed analysis using a set of baseline laser parameters. This analysis included pressure induced optical distortion, fracture criteria and thermal effects from laser energy absorption. A set of figures of merit were developed for axial and planar stress due to temperature profiles in the material and optical distortion (thermal lensing). Maps were developed to demonstrate the influence of the assumed laser parameters on these figures of merit. It was shown that no one optical material met all figures of merit. The three best materials based on this analysis are CVD ZnSe, GaAs and Polytran NaCl. Samples of these materials were fabricated and tested on a REP-pulsed CO_2 laser at fluences between 15-25 J/cm^2 with pulse trains up to 20 pulses at 20 Hz.

Key words: CO_2 laser window; laser damage; mechanical properties; optical materials; optical properties; pulsed CO_2 laser

1. Introduction

A continuing technological problem in the development of high energy lasers is the lack of transmissive materials for optical components. This is particularly true in the infrared where many materials with good transmissive characteristics, i.e., low bulk absorption, tend to be soft, brittle, or hydroscopic and, furthermore, may not be readily available in the required sizes and shapes. Because of this technical problem, many high power CO_2 lasers have been designed around an aerodynamic output window [1] to avoid the difficulty of a solid outcoupler.

It was the goal of this program to evaluate the use of infrared optical materials as output windows for generic high energy, repetitively pulsed CO_2 lasers. Although this is not a new problem, the field of infrared optical materials is continually evolving. New materials are being developed

* Work performed while employed at CVD Incorporated

and manufactured, while older materials are being improved both optically and mechanically. Therefore, a timely assessment is appropriate. In addition, a comparative assessment of all potentially useful infrared materials appears not to be readily available. Therefore, a significant portion of this study was concerned with the collection and comparison of the optical, physical and mechanical constants for a large number of potential infrared optical materials. These data were then used to select a group of "more practical" materials which were ranked for several important thermal, mechanical and optical criteria. This comparison was performed for a range of powers and fluences of interest in high power, rep-pulsed CO_2 lasers. These results should allow the laser designer to make trades in materials and/or laser operating parameters that permit the use of solid output optics.

Finally, it was also the goal of this investigation to select several of the "best" materials and subject them to rep-pulse CO_2 laser damage tests. Due to funding constraints, this portion of the effort has not been completed to date. However, the results of some initial testing are reported.

2. Properties of Potential Window Materials

The first step in this assessment was to collect and compare important optical, mechanical and physical properties of potential transmissive optical materials for use as windows on rep-pulsed CO_2 high energy lasers. To accomplish this task, a list of all those materials which transmit considerably at 10.6 μm was prepared. This list of 33 materials (shown in table 1) includes important cadmium, zinc and thallium compounds, salts, AMTIR-1 glass, gallium arsenide, germanium, and recently introduced alkaline earth-rare earth sulphides. Efforts were made to collect important properties and other engineering data for these materials from all possible sources.* A comprehensive literature search was conducted and different vendors and manufacturers were contacted for this purpose. Not all of these materials will be practical windows because they cannot be purchased in the size(s) required. Further, several of these materials cannot even be evaluated because a few of their critical properties are not available.

In the list of materials, IRTRAN 4 and 6 have been included. IRTRAN is a trade name of Eastman Kodak Company and IRTRAN-4 is ZnSe,which is included separately. IRTRAN 6 (CdTe) is no longer manufactured by the Kodak Company. Single crystal CdTe is currently manufactured, and the data used in this assessment refer to this form.

While going through the literature, one finds that different investigators have reported different values of the same property. For compilation purposes in our list, all the reported values with the corresponding references have been included.

For some materials, Poisson's ratio has not been reported but values of bulk modulus (K_B) and Young's modulus (Y) are available. For these materials, Poisson's ratio (ν) has been calculated from the following relation

$$\nu = \tfrac{1}{2}\left(1 - \frac{Y}{3\,K_B}\right) \qquad (1)$$

*This data and references for these materials are on file at CVD Inc. and limited copies may be made available to interested parties.

Table 1. List of Potential Infrared Optical Materials

AMTIR-1	Selenium (amorphous) Se
Arsenic Trisulphide, As_2S_3	Silicon, Si
Barium Fluoride, BaF_2	Silver Bromide, AgBr
Cadmium Selenide, CdSe	Silver Chloride, AgCl
Cadmium Sulphide, CdS	Sodium Chloride, NaCl
Cadmium Telluride, CdTe	Thallium Bromide, TlBr
Cesium Bromide, CsBr	Thallium Bromo-iodide, KRS-5
Cesium Iodide, CsI	Thallium Bromo-chloride, KRS-6
Cuprous Chloride, CuCl	CVD Zinc Selenide, ZnSe
Synthetic Diamond, C, Type IIb	CVD Zinc Sulphide, ZnS
Gallium Arsenide, GaAs	Water-Clear ZnS, CLEARTRAN
Gallium Arsenide (80 K)	Zinc Telluride, ZnTe
Germanium, Ge	RAP KBr
ITRAN - 4, ZnSe	RAP KCl
Potassium Bromide, KBr	Polytran NaCl
Potassium Chloride, KCl	Polytran KCl
Hot Forged KCl with RbCl	Hot forged NaCl
Potassium Iodide, KI	Calcium Lanthanum Sulfide, $CaLa_2S_4$

Of the 33 materials considered, 19 materials were selected for detailed analysis. This choice was dictated by (i) the availability of the material in large sizes and (ii) the value of important properties such as bulk absorption coefficient, etc. A list of these 19 materials and their important properties are given in table 2. For bulk absorption coefficient, those values were used which were the lowest reported in the literature. For other properties, if more than one value is found in the literature, that value is used which is quoted by the largest number of workers. For analyses purposes, a surface absorption coefficient of .001 cm^{-1} per surface was assumed for all the materials. In the case of CdS and CdSe, a few parameters were not available so appropriate values based upon the corresponding properties for CdTe were used.

Referring to table 2, we note that four different types of KCl, three different types of NaCl and two different types of KBr and GaAs are included. This has been done to compare the effect of variation in some property on the suitability of the material as a laser window. For instance, RAP KBr and KCl have the lowest bulk absorption coefficient, all other properties are the same as those for KBr and KCl respectively. Similarly, Polytran KCl is stronger in flexural strength by a factor of 5 in comparison to KCl. Finally, GaAs (80K) has a value of the thermal conductivity larger by a factor of six and an expansion coefficient smaller by a factor of 0.63 in comparison to the corresponding values for GaAs at room temperature.

Table 2. Important Properties of Materials Used for Analyses

Material	Bulk Absorption Coefficient (cm^{-1})	Density g/cc	Heat Capacity J/g °K	Thermal Conductivity w/cm °K	Expansion Coefficient x 10^{-6} K^{-1}	Poisson's Ratio	Young's Modulus PSI x 10^6	Flexural Strength PSI	Refractive Index	$\frac{dn}{dT}$ K^{-1} x 10^{-6}	Stress Optic Coefficient $(q_{\parallel} + q_{\perp})$ Pa^{-1} x 10^{-12}
CVD ZnSe	.0004	5.27	.355	.18	7.3	.28	9.75	7500	2.403	61	-1.28
CVD ZnS	.24	4.08	.463	.167	6.8	.28	10.8	15000	2.192	41.0	.804
Cleartran ZnS	.20	4.09	.463	.167	7.85	.28	10.8	12000	2.21	41.0	.804
NaCl	.00045	2.16	.857	.065	39.6	.25	5.8	350	1.49	-33	2.3
Polytran NaCl	.0014	2.16	.857	.065	39.6	.25	5.8	2140	1.49	-33	2.3
Hot Forged NaCl	.00118	2.16	.857	.065	39.6	.25	5.8	4000	1.49	-22	2.3
KCl	.00014	1.984	.68	.065	37.1	.216	4.3	330	1.45	-34.8	6.35
Hot Forged KCl	.000921	1.987	.647	.033	40	.20	3.2	3000	1.45	-31.3	6.35
Polytran KCl	.00014	1.984	.68	.065	37.1	.216	4.3	1600	1.45	-34.8	6.35
RAP KCl	$7x10^{-5}$	1.984	.68	.065	37.1	.216	4.3	330	1.45	-34.8	6.35
KBr	.00042	2.75	.43	.048	27.6	.202	3.9	160	1.525	-40	5.19
RAP KBr	$1.5x10^{-5}$	2.75	.43	.048	27.6	.202	3.9	160	1.525	-40	5.19
GaAs	.008	5.316	.267	.48	5.74	.31	12	20000	3.24	149	-1.32
GaAs (80 K)	.008	5.316	.267	2.8	3.64	.31	12	20000	3.24	149	-1.32
Ge	.012	5.327	.311	.59	5.7	.27	15	13500	4.0	277	-1.56
CdS	.01	4.82	.37	.27	4.2	.4 (assumed)	6.5	4000	2.2	107 (assumed)	-5.79 (assumed)
CdTe	.00025	5.85	.22	.063	4.5	.41	5.3	3200	2.67	107	-5.79
CdSe	.001	5.67	.26	.1 (assumed)	4.9	.4 (assumed)	6 (assumed)	3000	2.44	107 (assumed)	-5.79
AMTIR-1	.02	4.40	.3024	.00252	13	.27	3.2	2500	2.498	85	--

3. Analyses and Comparative Assessment of Materials

The next step in this assessment was to perform analyses on the 19 potential window materials emphasizing the mechanical, thermal and optical properties of importance in a high power CO_2 laser device. First, a baseline set of laser parameters, which were typical of a high power, rep-pulsed CO_2 device, were chosen and used to establish figures of merit for important thermal and optical performance criteria of a laser window. Next, selected laser parameters were varied to establish performance maps by which to rank the materials and to evaluate their sensitivity to laser power, fluence and operating time.

3.1. Baseline Laser Parameters

The laser operating parameters chosen for this investigation are shown in table 3. These values are considered typical of those of generic high power, rep-pulsed CO_2 lasers for which aerodynamic windows are usually utilized for outcoupling the power. From these parameters we can define the average laser intensity, I_{av}, and average fluence, J:

$$I_{av} = \frac{E_p s}{A_b} \tag{2}$$

$$J = \frac{E_p \tau_L s}{A_b} \tag{3}$$

where E_p is the energy of the pulse, s is the pulse repetition rate, τ_L is the laser continuous running time and A_b is the area of the beam. Using the laser parameters of table 3 and assuming that the beam area is equal to the aperture area, we see that $I_{av} = 707.4$ W/cm^2 and J = 7074 J/cm^2. To compare, we note that for a single pulse, the corresponding values are $I_{av}(SP) = 7.074 \times 10^5$ W/cm^2 and E_p = 14.15 J/cm^2. Thus, in a window failure criteria, if I_{av} is important, one should first investigate single pulse effects,while if the fluence is important, one may directly look at the multiple pulse effects.

Table 3. Baseline Laser Parameters

Fluence per Pulse (E_p):	14 J/cm^2
Pulse Width (τ_p):	20 μsec, (Triangular pulse with base, 20 μsec)
Average Power per Pulse [$I_{av}(SP)$]:	7 x 11^5 W/cm^2
Rep Rate (s):	< 50 Hz
Intensity Profile:	Flat top
Aperture:	Round, 30 cm in diameter
Δp Across Window:	2 atm.
Laser Continuous Running Time: (τ_L)	10 sec.

3.2 Window Thickness Assessment

The thickness of a window may be determined from two criteria (i) mechanical failure and (ii) pressure induced distortion. Mechanical failure of the window occurs when the pressure differential across the window produces stresses which exceed the strength of the material. For a circular window of diameter D, with the edges simply supported, the maximum stress, σ_{max}, due to a uniform pressure differential, Δp, across the window occurs in the center and is given by [2]:

$$\sigma_{max} = \frac{3}{32} \frac{D^2}{b^2} \Delta p \, (3 + \nu), \tag{4}$$

where b is the window thickness. If the window is clamped at the edges, the maximum stress occurs at the edges and is given by [2]:

$$\sigma_{max} = \frac{3 D^2 \Delta p}{16 b^2} \quad . \tag{5}$$

Since the Poisson's ratio ν is < 0.5, we can neglect it in eq (4) and combine eqs (4) and (5) to yield

$$\frac{b}{D} = \left(\frac{K_1 \Delta p}{4 \sigma_{max}} \right)^{\frac{1}{2}} , \tag{6}$$

where K_1 = 1.125, for a simply supported window,
= .75, for a clamped window.

The maximum stress in eq (6) should be equated to the material strength parameter (divided by a suitable factor of safety) under which the material is most likely to fail. For instance, if the optical properties are altered appreciably by plastic deformation, the apparent elastic limit or the yield strength is a suitable strength parameter. It is to be noted that yield strength is a conservative approximation of the apparent elastic limit. Other material strength parameters that one may use are the modulus of rupture or flexural strength. If enough information is not available, it may be safer to use the smaller of modulus of rupture, yield strength, and flexural strength. If σ_f is the appropriate material strength parameter, eq (6) may be written as

$$\frac{b}{D} = \left(\frac{K_1 \Delta p}{4 \sigma_f / SF} \right)^{\frac{1}{2}} \tag{7}$$

where SF is the factor of safety which is normally taken equal to 4.

The window thickness may also be determined from pressure induced distortion criteria. The pressure differential across the window deforms the window, causing it to become a lens with a finite focal length and aberration. According to the criteria given by Sparks and Cottis [3], the window thickness should be that thickness which is required to keep the optical distortion from halving the target intensity for a Gaussian beam. Thus the window thickness may be calculated from [3]:

$$\frac{b}{D} = K_2 \left[(\eta - 1) \left(\frac{\Delta p}{Y} \right)^2 \frac{D}{\lambda} \right]^{1/5} \tag{8}$$

where K_2 = .842, for a clamped window,
= 1.01, for a simply supported window.

Here η is the refractive index, and λ is the laser wavelength.

Window thickness for a pressure differential of 2 atmosphere was calculated from eqs (7) and (8) assuming that they are simply supported. These calculations are shown in table 4 in the first two columns. From these data it can be seen that for all the materials except GaAs and Ge, mechanical fracture criteria determine the window thickness. Chemical vapor deposited ZnS has the smallest window thickness (= 1.45 cm) and KBr has the largest thickness (= 13.64 cm).

3.3 Thermal Stresses

When a laser beam passes through a window, a part of the laser energy is absorbed by the window, and, as a result, its temperature rises. If the window is insulated and unconstrained and its absorption coefficient is uniform throughout, there will be no spatial variation of temperature in the window, and, thus, there will be no thermal stresses. However, the temperature of the window will continue to rise with the laser running time and the window ultimately may fail due to melting. In practice, the window is not insulated. It may "see" the ambient temperature at its outside surfaces and the laser cavity temperature at the inside surfaces. Further, the absorption coefficient of the window is normally not constant throughout, since there will be a different value for surface and bulk absorption. Different absorption coefficients lead to a temperature profile in the axial direction which generates thermal stresses. Similarly, if the intensity profile of the laser beam is spatially uniform, the absorption of the beam will be uniform in a plane perpendicular to the window axis, but due to the heat loss at the window edges, a temperature profile in the radial direction will develop which will generate thermal stresses with radial and azimuthal components.

In order to determine thermal stresses, first it is necessary to determine the temperature profile in the axial and radial directions. For this purpose, we model the window as a disc with two circular faces insulated (the laser beam is impinging on the inside circular face of the window), and the edges maintained at the ambient temperature as shown in figure 1. For the calculation of thermal stresses, it is the difference between the window temperature and the ambient temperature which will be required and therefore for convenience and without loss of generality, we can take the ambient temperature as 0 degree. With the above boundary conditions, the solution of the Founier heat conduction equation in three dimensionsis fairly involved. So we assume that the temperature distributions in the axial and radial directions are independent of each other. With this simplification, we can define the temperature distribution along the axis in the center of the window after a time τ_L for $0 < Z \leq b/2$ [3-5]:

$$T(r = 0, Z, \tau_L) = \frac{\left\{1 - \exp(-\beta b)\right\} I_{av}\, \tau_L}{\rho C b} + \frac{\beta_s I_{av}\, b}{4K} = \left[\left(1 - \frac{2Z}{b}\right)^2 - 1/3\right] - \frac{\beta_s I_{av}\, b}{\pi^2 K} \sum_{n=1}^{\infty} \frac{(-1)^n}{n^2} \cos\left\{n\pi \left(1 - \frac{2Z}{b}\right)\right\} \exp\left(\frac{-4\pi^2 n^2 K \tau_L}{C\rho b^2}\right) \qquad (9)$$

where ρ is the density, C is the heat capacity and K is the thermal conductivity of the material, β_s is the surface absorption coefficient and β is the overall absorption coefficient defined as

$$\beta = \frac{2\beta_s}{b} + \beta_v \qquad (10)$$

Table 4. Results of Analyses

Material	Window Thickness based on Fracture (cm)	Window Thickness based on Pressure Induced Distortion (cm)	Steady State Temperature (max.) (K)	Adiabatic Window Average Temp. after 10 sec. (K)	$(\Delta T)_{max}$ Along the Window Axis (K)	$(FOM)_a$	$(FOM)_R$	Distortion Coefficient (x) (K^{-1}) x 10^{-6}	$(FOM)_d$
CVD ZnSe	2.00	1.56	309.38	5.29	6.82	2.78	3.96	72.93	.51
CVD ZnS	1.41	1.45	4.85×10^4	762.66	4.85	7.57	.056	52.43	.006
Cleartran ZnS	1.58	1.45	4.1×10^4	644.04	5.24	4.86	.19	54.43	.0065
NaCl	9.22	1.56	406.11	2.54	15.57	.018	.042	-5.75	-3.78
Polytran NaCl	3.73	1.56	1121.54	7.37	14.34	.18	.12	-5.75	-3.24
Hot Forged NaCl	2.73	1.56	846.77	5.33	15.57	.21	.37	5.25	1.97
KCl	9.49	1.73	214.62	1.84	18.10	.022	.056	-9.16	-2.98
Hot Forged KCl + RbCl	3.15	1.94	1875.0	8.56	24.12	.19	.34	-5.42	-3.73
Polytran KCl	4.31	1.73	456.06	3.91	16.04	.12	.27	-9.16	-4.02
RAP KCl	9.49	1.73	171.35	1.47	18.11	.022	.058	-9.16	-3.72
KBr	13.64	1.85	467.58	3.39	23.00	.013	.028	-19.16	- .54
RAP KBr	13.64	1.85	133.59	.967	23.00	.013	.035	-19.16	-1.9
GaAs	1.22	1.58	762.89	45.87	4.14	12.09	1.57	160.50	.027
GaAs (80 K)	1.22	1.58	130.78	45.87	1.58	50.08	2.47	156.29	.021
Ge	1.48	1.53	890.47	56.38	3.41	8.46	.69	283.97	.013
CdS	2.73	1.77	1560.42	42.00	5.67	3.88	.85	111.15	.028
CdTe	3.05	2.06	571.43	4.98	16.38	1.21	3.27	113.32	.277
CdSe	3.15	1.90	649.13	7.85	11.79	1.30	2.24	112.61	.157
AMTIR-1	3.44	2.73	3.15×10^5	105.90	95.0	.12	0.1	109.72	.025

Here, β_v is the bulk absorption coefficient. The first term on the right hand side of eq (9) gives the average temperature. This term yields accurate results even when the absorption coefficient, β is large.

In a similar manner, we can write down the temperature distribution in the radial direction in a plane perpendicular to the window axis and with average axial temperature as [3-5]:

$$T = \frac{I_{av}\,(1 - \exp(-\beta b))\,(R^2 - r^2)}{4\,b\,K}$$

$$- \frac{2\,I_{av}\,(1 - \exp(-\beta b))}{RKb} \sum_{n=1}^{\infty} \exp\left(-\frac{K}{\rho C}\,\alpha_n^{\,2}\,\tau_L\right) \frac{J_o\,(r\alpha_n)}{\alpha_n^{\,3}\,J_1(R\,\alpha_n)} \qquad (11)$$

where R is the radius of the window and α_n are the positive roots of $J_o\,(R\alpha) = 0$.

It is of interest to calculate the average steady state temperature of the window. In reference [5], the temperature distribution as given by eq (11) is plotted as a function of the parameter, $f = \frac{Kt}{\rho C R^2}$. These curves show that the steady state temperature would be obtained after a time, t_{ss} given by

$$t_{ss} = \frac{0.7 R^2 \rho C}{K} \qquad (12)$$

The steady state temperature, T_{ss}, at r = 0 and averaged along the window axis is given by

$$T_{ss} = \frac{I_{av}\,(1 - \exp(-\beta b))R^2}{4\,K\,b} \qquad (13)$$

It is also of interest to compare the temperature at the center of the window as calculated from eq (11) with that calculated assuming that the window is completely insulated from all sides. In the latter situation, the adiabatic temperature of the window, T_a, may be determined from an energy balance as

$$T_a = \frac{I_{av}\,(1 - \exp(-\beta b))\,\tau_L}{\rho\,C\,b} \qquad (14)$$

The temperature at the center of the window was calculated for all the 19 materials listed in table 4 from eqs (11) and (14) and within 1% they were found to be the same. This shows that for a laser running time, τ_L = 10 sec, the effect of heat loss from the window edges has not penetrated to the center. We can draw the same conclusion if we look at the thermal diffusivities of the materials, which are very small.

In table 4, we list the steady state window temperature averaged over the window thickness from eq (13) and adiabatic window temperature from eq (14) for the 19 materials considered. It can be seen that windows made of CVD ZnS, CLEARTRAN ZnS, Polytran NaCl, hot forged KCl with RbCl, CdS and AMTIR-1, will all melt when subjected to rep-pulsed laser for a long time, while the other materials will survive. The lowest temperature rise is predicted for GaAs (80K), because its thermal conductivity is very large. It is to be noted that while calculating the temperatures, the material properties have been kept constant.

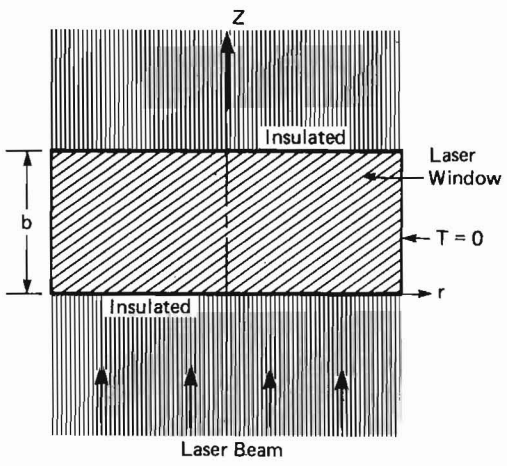


Figure 1. Window model for calculating the temperature profile

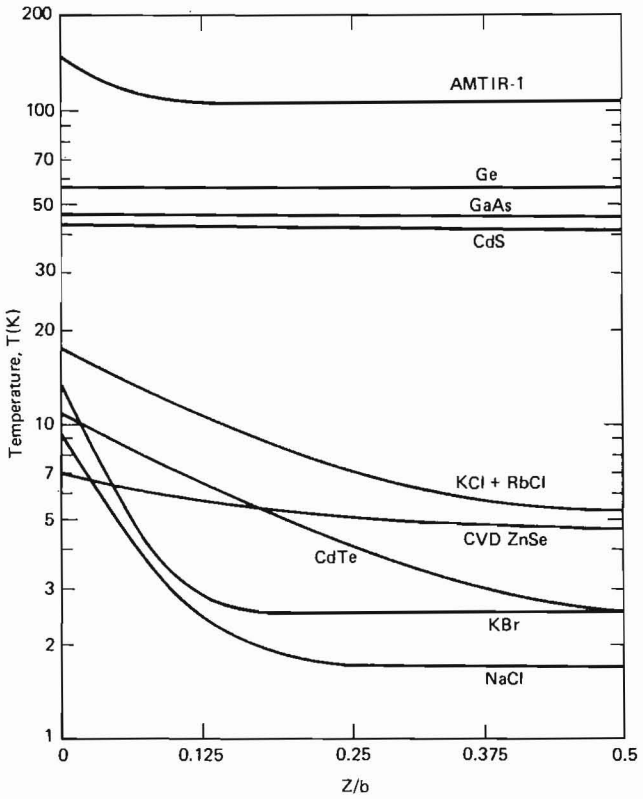


Figure 2. Axial temperature distribution in various materials.

For the adiabatic window temperature, calculated after τ_L = 10 sec, the lowest temperature rise (0.967K) is predicted for RAP KBr, while the highest temperature rise (762.66K) is predicted for CVD ZnS. The salts, ZnSe, CdTe and CdSe show a temperature rise of less than 10K.

3.4. Figure of Merit for Axial Stress

The axial temperature distribution as given by eq (9) is plotted in figure 2 for several important materials. The maximum temperature occurs at the two surfaces, while the minimum temperature is in the center (Z=b/2) of the window. From these temperature profiles, one can see that the maximum stress would occur at both surfaces, and it will be compressive. Thus, the window failure will occur when the maximum stress [4],

$$\sigma_{max} = \frac{\alpha Y}{1-\nu} \{T (r=0, z=0, \tau_L) - T_{av} (r=0, \tau_L)\} \quad , \tag{15}$$

exceeds σ_f/SF. Here α is the coefficient of thermal expansion. A figure of merit can be defined for axial stress, $(FOM)_a$, given by:

$$(FOM)_a = \frac{(\sigma_f/SF)\ (1-\nu)}{\alpha Y \{T (r=0, z=0, \tau_L) - T_a\}} \tag{16}$$

This figure of merit is defined such that if $(FOM)_a < 1$, the window fails under this criterion.

The temperature at the surface can be calculated from eq (9). However, eq (9) takes into account only the temperature rise due to an average laser intensity. To this quantity, we must add the temperature rise due to the last laser pulse. Since the last pulse is on for only 20 μsec, and since the surface absorption coefficient is rather large, the temperature rise at the surface may be appreciable.

To model the temperature rise due to the last pulse, we assume that the laser energy absorbed at the surface is distributed uniformly in a layer equal to the penetration depth of the material. The penetration depth, ℓ_p, can be approximated as

$$\ell_p \approx \left(\frac{K\ \tau_p}{\rho C}\right)^{\frac{1}{2}} \tag{17}$$

where τ_p is the pulse width. The temperature rise due to the last pulse, $T_{\ell p}$, at the surface is then given by

$$T_{\ell p} = \frac{E_p\ \beta_s}{\ell p\ \rho C\ A_b} \tag{18}$$

From Eqs (9), (16) and (18) we can obtain:

$$T\ (r=0,\ z=0,\ \tau_L) - T_a = (\Delta T)_{max}$$

$$= \frac{\beta_s\ I_{av}\ b\ \phi}{6\ K}\left[1 + \frac{6}{\phi\ b\ s}\left(\frac{K}{\rho\ C\ \tau_p}\right)^{\frac{1}{2}}\right] \tag{19}$$

where

$$\phi = 1 - \frac{6}{\pi^2}\sum_{n=1}^{\infty}\frac{(-1)^2}{n^2}\cos n\pi \exp\left(-\frac{4\pi^2 n^2 K\ \tau_L}{C\ \rho\ b^2}\right)$$

In the limit where $\dfrac{4\pi^2 K\ \tau_L}{\rho\ C\ b^2} >> 1$, $\phi = 1$. (20)

In table 4, we show $(\Delta T)_{max}$ as calculated from eq (19) and $(FOM)_a$ as calculated from eq (16). It can be seen that the salts and AMTIR-1 are not strong enough to survive this criterion. One important material property which strongly affects $(FOM)_a$ is the thermal conductivity. Since GaAs (80K) has the largest value of thermal conductivity, its $(FOM)_a$ is also the highest. The worst material under this criterion is potassium bromide. This is because it has the lowest value for flexural strength together with a very low value of thermal conductivity.

It is of interest to examine the potential improvements in materials development so that salts would not fail under this criterion. If we look at eq (16) we find that $(FOM)_a$ could be increased if flexural strength of the material is increased and Poisson's ratio, thermal expansion coefficient, Young's modulus and $(\Delta T)_{max}$ are decreased. The temperature difference, $(\Delta T)_{max}$, could be reduced by increasing thermal conductivity and reducing surface absorption. Among salts, hot forged NaCl shows the largest value for $(FOM)_a = 0.21$. Therefore one needs to increase $(FOM)_a$ by at least a factor of 5

to prevent window failure in salts. Getting a factor of 5 improvement may not be possible by improving just one material property,but efforts could be directed towards improving all the above properties so that the overall increase in $(FOM)_a$ is greater than 5.

3.5. Figure of Merit for Planar Stress

The radial temperature distribution in the window is given by eq (11). For all the materials considered, this temperature distribution is almost flat except at the edges of the window where the effect of thermal conductivity is evident. The largest value of thermal diffusivity is 1.97 cm^2/sec for GaAs (80K),while the smallest value is 1.9 x 10^{-3} cm^2/sec for AMTIR-1. For a laser running time of 10 sec, we see that the largest and smallest penetration length from the edges for these two materials are 4.44 cm and 0.14 cm respectively. These lengths are small in comparison to the window radius of 15 cm. Therefore, for the calculation of planar stresses, we can model the temperature distribution on the surface as shown in figure 3. The distance $(R-R_1)$ is taken equal to the penetration length,

$$(R - R_1) = \left(\frac{K \tau_L}{\rho C}\right)^{\frac{1}{2}} \tag{21}$$

which is different for different materials. The linear temperature distribution should be a good approximation to the actual temperature distribution as given by eq (11), because $(R-R_1)/R$ is small.

For unconstrained laser windows, the cylindrically symmetric radial and azimuthal components of the planar stresses are related to the radial temperature distribution as

$$\sigma_{rr} = \alpha Y \left[\frac{1}{R^2}\int_0^R T\, r\, dr - \frac{1}{r^2}\int_0^r T\, r\, dr\right] \tag{22}$$

and

$$\sigma_{\theta\theta} = \alpha Y \left[\frac{1}{R^2}\int_0^R T\, r\, dr + \frac{1}{r^2}\int_0^r T\, r\, dr - T\right] \tag{23}$$

T is the temperature at the window surface (figure 3) which may be written as

$$T_{oo} = T\,(\, r=0,\ z=0,\ \tau_L\,), \quad r \le R_1$$

$$= T_{oo}\left(\frac{R - r}{R - R_1}\right), \quad R_1 < r \le R. \tag{24}$$

Substituting eq (24) in eq (22) and (23), we obtain:

$$\sigma_{rr} = \alpha Y T_{oo} K_{pr}, \tag{25}$$

$$\sigma_{\theta\theta} = \alpha Y T_{oo} K_{p\theta} \tag{26}$$

where K_{pr} amd K_{pe} are the two temperature profile constants given by:

$$K_{pr} = \frac{1}{6}\left[1 + \left(\frac{R_1}{R}\right) + \left(\frac{R_1}{R}\right)^2 - 3\left(\frac{R_1}{r}\right)^2 - 3\frac{1 - \left(\frac{R_1}{r}\right)^2}{\left(1 - \frac{R_1}{R}\right)} + 2\,\frac{r}{R}\,\frac{1 - \left(\frac{R_1}{r}\right)^3}{\left(1 - \frac{R_1}{R}\right)}\right], \qquad (27)$$

and

$$K_{p\theta} = \frac{1}{6}\left[1 + \left(\frac{R_1}{R}\right) + \left(\frac{R_1}{R}\right)^2 + 3\left(\frac{R_1}{r}\right)^2 + 3\frac{1 - \left(\frac{R_1}{r}\right)^2}{\left(1 - \frac{R_1}{R}\right)} - 2\left(\frac{r}{R}\right)\frac{1 - \left(\frac{R_1}{r}\right)^3}{\left(1 - \frac{R_1}{R}\right)} - 6\left(\frac{R-r}{R-R_1}\right)\right] \qquad (28)$$

The maximum value of K_{pr} occurs at $r = R_1$ where the stress is compressive, while the maximum value of $K_{p\theta}$ occurs at $r = R$ where the stress is tensile. For all the materials considered here, $(K_{pr})_{max}$ lies in the range 0 to 0.133, while the $(K_{p\theta})_{max}$ lies in the range 1 to 0.733. An expression for the maximum value of $K_{p\theta}$ can be obtained from eq (28) by substituting $r = R$,

$$\left(K_{p\theta}\right)_{max} = \frac{1}{3}\left[1 + \left(\frac{R_1}{R}\right) + \left(\frac{R_1}{R}\right)^2\right] \qquad (29)$$

A figure of merit for planar stresses, $(FOM)_R$, can be defined as

$$(FOM)_R = \frac{\sigma_f/SF}{\alpha\, Y\, T_{oo}\, (K_{p\theta})_{max}} \qquad (30)$$

This figure of merit is defined such that if $(FOM)_R < 1$, window failure will occur. Since for all the materials considered here $(K_{p\theta})_{max} > 0.733$, we can get a conservative estimate if we put $(K_{p\theta})_{max} = 1$.

In table 4, we show $(FOM)_R$ for different materials. One can see that ZnSe has the largest value of $(FOM)_R$. The materials which do well under this criteria are ZnSe, GaAs, GaAs (80K), CdTe and CdSe, while the other materials fail. It should be noted here that $(FOM)_R$ is perhaps the least important figure of merit for window design. This is because a failure under planar stresses arises due to our assumption that there is a large heat sink at the window edge which maintains an ambient temperature. If the use of a particular material is really limited by this criterion, one can always insulate the window edges so that there is no heat loss and thus no temperature gradient in the radial direction.

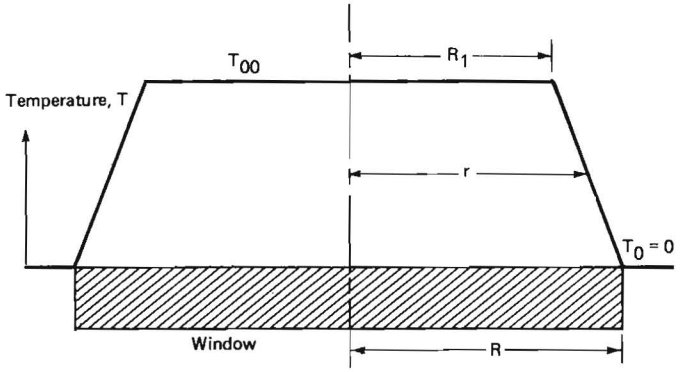


Figure 3. Radial temperature profile used for calculating the planar stresses.

3.6. Optical Distortion (Thermal Lensing)

The temperature distribution in the radial direction may also cause distortion of the optical beam in addition to producing planar stresses. This so called thermal lensing effect has been discussed by several investigators [3-5]. The degradation in the far field of axis irradiance as a consequence of thermally induced optical distortion is given by [3]:

$$\frac{I_{GF}}{I_{GF}(o)} = \exp\left\{-\left(\frac{2\pi}{\lambda}\right)^2 (bx)^2 \ \mathrm{Var}\ (T)\right\} , \tag{31}$$

where

$$\mathrm{Var}\ (T) = \frac{2}{R^2}\int_o^R T^2(r)\ r\ d\ r - \left\{\frac{2}{R^2}\int_o^R T(r)\ r\ d\ r\right\}^2 \tag{32}$$

I_{GF} is the intensity at the Gaussian focus in the presence of the window, and $I_{GF}(o)$ is the intensity without the window. The parameter, x, measures the sensitivity of the window to thermally-induced optical distortion and is given by:

$$x = \frac{dn}{dT} + (n-1)\ \alpha\ (1-\nu) + \frac{n^3\ \alpha\ Y}{4}\ (q_{\parallel} + q_{\perp}) , \tag{33}$$

where $q_{\parallel}$, $q_{\perp}$ are the stress optic coefficients.
Substituting the temperature distribution as given in eq (24) into eqs (31) and (32) and noting that for distortion, it is the average temperature of the window and not the maximum temperature which is important, we obtain:

$$\frac{I_{GF}}{I_{GF}(o)} = \exp\left[-\left(\frac{2\pi}{\lambda}\right)^2 (bx)^2\ T_a^2\ K_d^2\right] , \tag{34}$$

where K_d is a coefficient which takes into account the effect of the temperature profile.

$$K_d = \left[\frac{1}{6}\left\{\frac{1 + 3\left(\frac{R_1}{R}\right)^4 - 4\left(\frac{R_1}{R}\right)^3}{\left(1 - \frac{R_1}{R}\right)^2}\right\} - \frac{1}{9}\left\{1 + \left(\frac{R_1}{R}\right) + \left(\frac{R_1}{R}\right)^2\right\}^2\right]^{\frac{1}{2}} \tag{35}$$

In table 4, we show the coefficient, K_d, for different materials. Gallium Arsenide (80K) has the largest value for K_d (0.334), while AMTIR-1 has the smallest value (0.077). For a majority of materials, however, one can take K_d = 0.2 as a good approximation. For a Gaussian beam, K_d depends upon a truncation parameter. In reference [2], it is stated that for realistic laser beams K_d = 0.5. However, it is not clear what is meant by a realistic laser beam. Our calculations show that for a beam with a flat profile, K_d = 0.2 for a majority of materials.

If we take the left-hand side of eq (34) equal to 0.8, which corresponds to a situation in which thermal lensing reduces the focal intensity to 80% of its original value (Marechal Cirterion), we can define a figure of merit for distortion, $(FOM)_d$ as:

$$(FOM)_d = .472 \quad \frac{\lambda \rho C}{2\pi \times I_{av} \tau_L K_d (1-\exp(-\beta b))} \tag{36}$$

This figure of merit is defined such that if $(FOM)_d < 1$, the window will fail.

In table 4, we show the distortion coefficient, x, as calculated from eq (33) and $(FOM)_d$ as calculated from eq (36). We see that only the salts do well under the distortion criterion while all other materials fail. The fact that the salts pass the optical distortion figure of merit is due to their small and negative value of dn/dT as shown in the next to last column of table 2.

From eq (36) we see that $(FOM)_d$ can be increased if the absorption coefficient, window thickness, temperature profile coefficient and distortion coefficients are reduced. The window thickness could be reduced by increasing the strength of the material, while the temperature profile coefficient could be reduced by insulating the window at the edges. Since the value of $(FOM)_R$ will also increase by insulating the edges of the window, this solution appears to be the best possible under the given conditions.

3.7. Effects of Variation of Laser Parameters on Figures of Merit

From the 19 different materials, six were selected for a study of the effects of variation in laser intensity and continuous running time on the figures of merit. These six materials are ZnSe, CLEARTRAN ZnS, GaAs, CdTe, Polytran NaCl and Polytran KCl. Even though CLEARTRAN ZnS does not appear to be high on our list of potential candidate materials, this new material has been selected because it will be used in the laser damage study. Zinc selenide, GaAs, and CdTe were selected because they do well under two criteria, $(FOM)_a$ and $(FOM)_R$, while Polytran NaCl and KCl were selected because they do well under distortion criterion. Out of the above six materials, all except CdTe may be obtained in the required window size (30 cm diameter). Cadmium telluride appears to be a potential candidate for laser windows, and it may be desirable to embark on a program that can develop this material in larger sizes than currently available.

In figure 4, we show the effect of variation in average laser intensity on $(FOM)_a$ when τ_L=10 sec. For these plots, the pulse repetition rate, the pulse time and shape have been kept constant. It can be seen that if the average laser intensity is reduced (which corresponds to reducing the laser pulse energy) by an order of magnitude, both Polytran NaCl and KCl will not fail due to laser induced axial stresses. The effect of variation in laser running time is shown in figure 5. The figure of merit for axial stresses does not vary much with laser running time. These curves are valid when $\tau_L > 0.02$ sec.

In figures 6 and 7 we show the effect of I_{av} and τ_L on $(FOM)_R$. In figure 6 we see that NaCl, KCl and CLEARTRAN ZnS will not fail if the laser intensity is reduced by factors of 5, 4, 3 and 18 respectively. Alternately, as shown in figure 7, one can maintain the laser intensity at the baseline value and reduce the laser running time by factors of 14.3, 12.5 and 20 respectively. An interesting thing to note is the $(FOM)_R$ for CLEARTRAN ZnS and GaAs increases much faster with a reduction in τ_L in comparison to other materials considered here.

The figure of merit for distortion is an explicit function of the product $I_{av} \tau_L$. Therefore, in figure 8, we show the effect of variation of $I_{av} \tau_L$ on $(FOM)_d$. In these calculations the temperature profile coefficient, K_d, is assumed constant as $I_{av} \tau_L$ is varied. We see that ZnSe, CdTe, GaAs and

Cleartran ZnS can satisfy the distortion criterion if the product $I_{av}\ \tau_L$ is reduced by factors of 2, 3.7, 37 and 152 respectively.

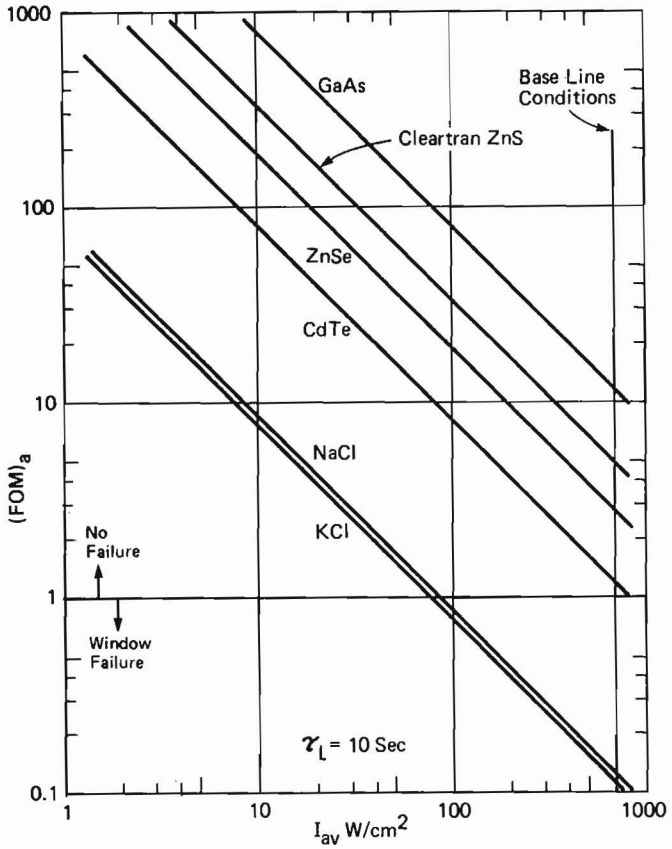


Figure 4. Effect of variation in average laser intensity on figure of merit for axial stresses. The pulse time, shape and repetition rate are kept constant.

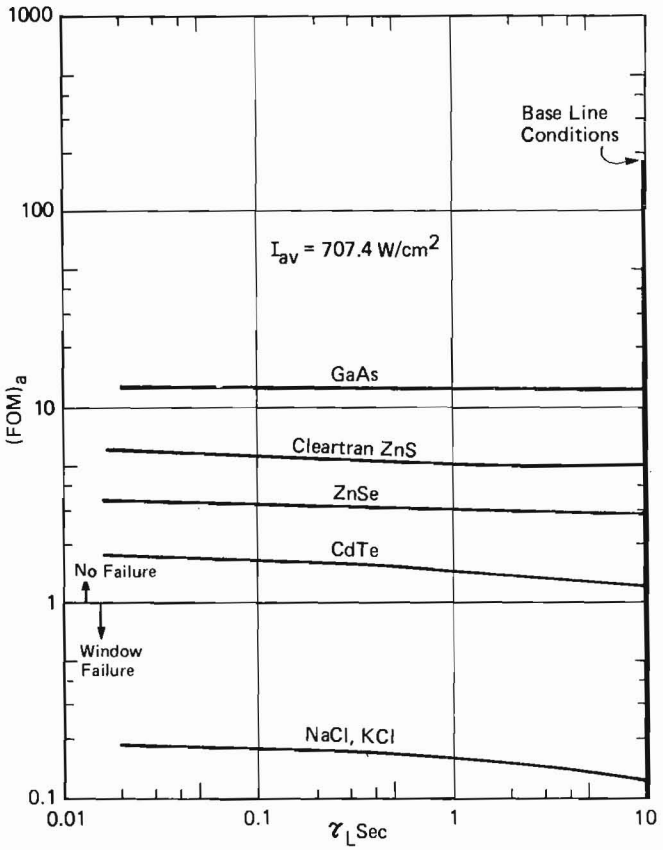


Figure 5. Effect of variation in laser continuous running time on figure of merit for axial stresses.

4. Laser Damage Experiments

At the start of this investigation, it was the intent to select the better of the materials as determined from the analyses described in the preceeding section and to subject these materials to laser damage testing with a rep-pulsed CO_2 laser. As was concluded from the analyses, no material(s) passes all criteria for a high power laser window as defined by the base line parameters. Therefore, it was decided to select materials representative of the various types studied as well as those possessing widely different mechanical and thermal properties. Due to schedule and funding limitations, the experimental work was not completed, so that the results presented herein are preliminary and incomplete.

The materials chosen for this experimental testing are CVD ZnSe, GaAs and Polytran NaCl. CVD ZnSe has a low value of bulk absorption coefficient (table 2) and is widely employed as a CO_2 laser window in more modest power devices than considered in this study. GaAs is an attractive window material because it has the second largest thermal conductivity and largest flexual strength of the materials considered (table 2). Polytran NaCl was selected as a representative of the salts, all of which have excellent absorption and dn/dT, but are mechanically weak. Polytran NaCl is one of the stronger of the salts. As is evident from figures 4-8, GaAs and NaCl are generally at the extremes of the analyses with ZnSe lying in between.

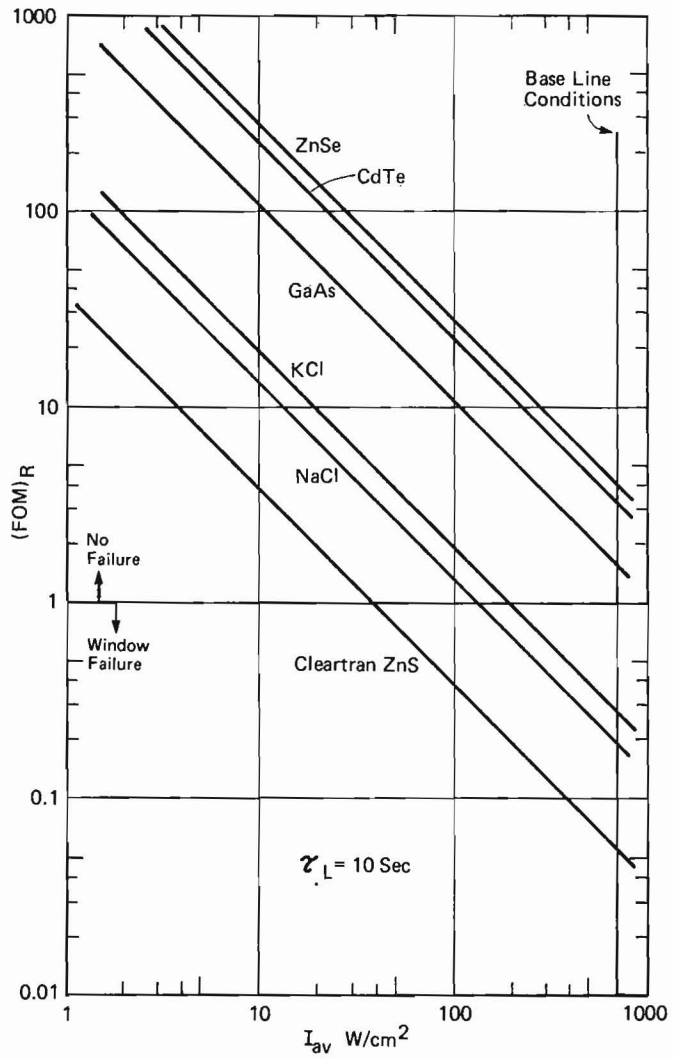


Figure 6. Figure of merit for radial stresses as a function of laser intensity.

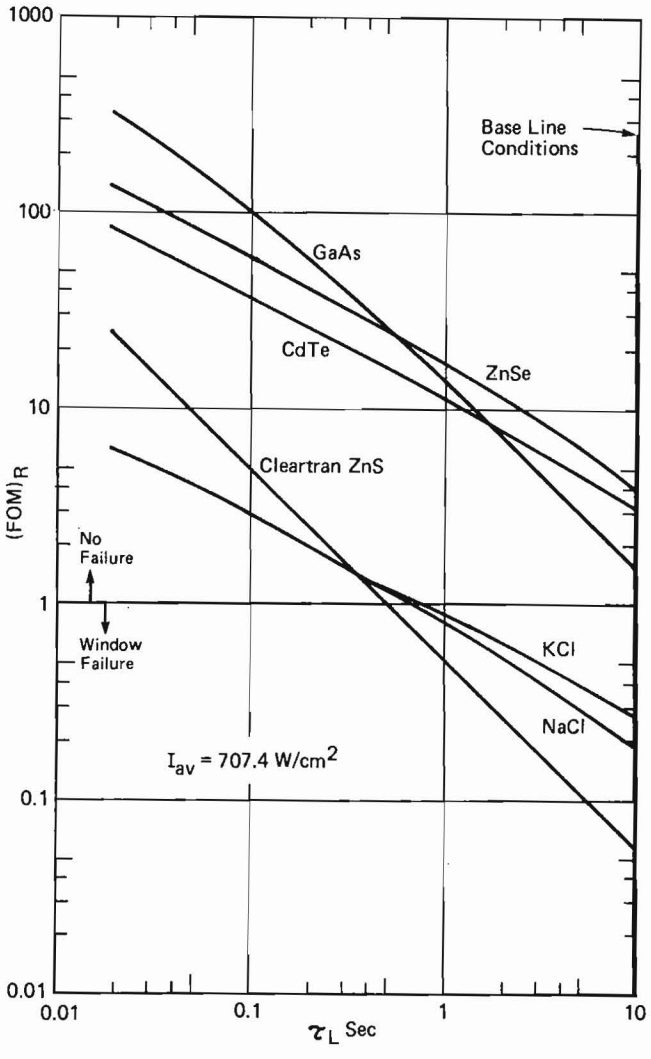


Figure 7. Figure of merit for radial stresses as a function of laser continuous running time, τ_L.

In addition to the three materials described above, water-clear ZnS (CLEARTRAN) was also included in the testing. CLEARTRAN was selected because it is a new material with potential multispectral application from the visible (0.34 μm) to the infrared (12 μm), and the sponsor thought it appropriate to obtain CO_2 laser damage data in this investigation.

Samples of these materials were obtained from appropriate suppliers and fabricated into "Bennett-size" optical blanks. An attempt was made to produce samples with optical figure and surface finish appropriate to use as a CO_2 laser window. Uncoated samples were tested first. It was planned to test various anti-reflective coatings later. The suppliers, fabricators and optical specifications are listed in tables 5 and 6.

The experimental configuration for the damage tests is shown schematically in figure 9. The repulsed CO_2 laser is pumped by an e-beam sustained discharge. The optical cavity consists of an off-

Table 5. Window Materials Selected for Laser Damage Testing

Material	Supplies	Fabricator
CVD ZnSe	CVD Inc., Woburn, MA	Janos Technology Inc. Townshend, VT
CLEARTRAN	CVD Inc., Woburn, MA	AMF Optics Arlington, MA
Polytran NaCl	Harshaw Chemical Co. Solon, OH	Janos Technology Inc. Townshend, VT
GaAs	Crystal Specialties, Inc. Monrovia, CA	Janos Technology Inc. Townshend, VT

Table 6. Optical Specifications for Window Samples

Diameter:	1.520 $^{+\ 0.000}_{-\ 0.005}$ inches
Thickness:	0.250 ± 0.010 inches
Flatness:	< λ/4 @ 0.6238 μm (both sides)
Parallelism:	< 3 arc seconds
Edges:	Beveled 0.015 inches
Clear Aperature:	1.490 inch minimum
Surface Quality:	C-B per MIL-C-48497 low scatter process 20/10 or better

axis unstable resonator with a 10 x 20 cm^2 rectangular output aperture of which about 150 cm^2 is useful. The beam train consists of various mirrors and apertures, as indicated in figure 9, which for these tests produce an approximate 1 cm^2 spot on the samples. The pulse width of the laser output is 15 μsec, and the pulse is triangular in shape.

The testing is conducted under a class 100 laminar flow clean bench. The materials are cleaned by the "tissue drag" method as developed by the Naval Weapons Center, China Lake, CA.

This procedure is as follows:

1) All work, including packaging, is conducted under a class 100 clean bench hood.
2) The optic to be cleaned is held by its edges, in a horizontal orientation.
3) A small quantity (several drops, depending on the optic size) of high purity propanol is placed on the sample.
4) A clean Kodak lens tissue is draped across the optic until it contacts the liquid and then

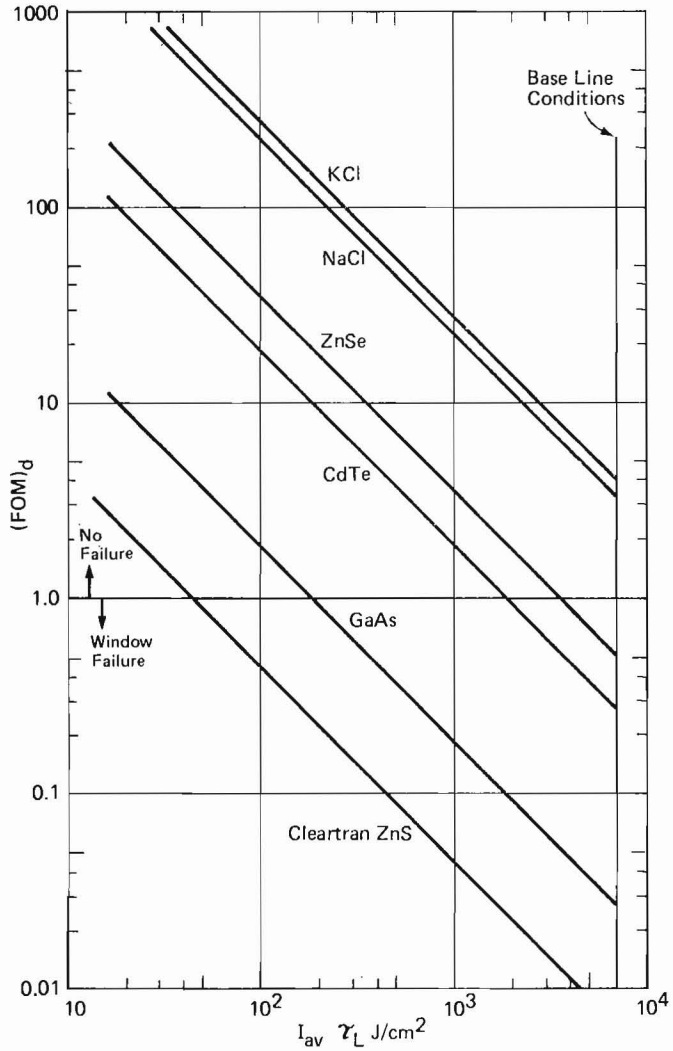


Figure 8. Figure of merit for distortion as a function of the product $I_{av}\ \tau_L$.

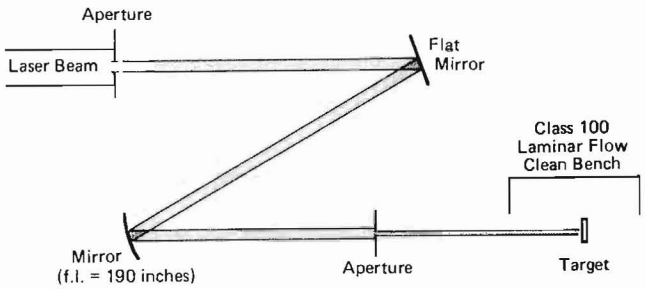


Figure 9. Schematic of laser damage experiment.

is pulled gently to one side. This wipes the liquid and trapped dust particles from the optic.

5) The optic is checked for cleanliness on a low magnification microscope (kept on the same clean bench) and the tissue drag is repeated if necessary. Any non-removable features are noted.

6) The optic is packaged in an edge-contact container that has also been similarly cleaned.

The experimental procedure was as follows: The sample under test was irradiated at the lowest fluence (15 J/cm^2) for a single laser pulse. If no damage was detected, then the fluence was increased to 20 J/cm^2 and then to 25 J/cm^2. For some samples, after a successful single pulse irradiation, the sample would be subjected to a 5, 10 or 20 pulse train at that fluence level. Samples were tested at both normal incidence and at Brewster's angle.

The onset of laser damage was defined as the occurrence of plasma formation with the observation of visible emission or by visual inspection after the irradiation. In all cases, when visible light was seen during irradiation, most inspection showed damage. However, occasionally damage was observed on the sample even when light emission was not evident.

The results of the laser damage testing are shown in table 7. First, only three of the four materials have been tested to date. Second, in all cases the damage appeared to originate at the surface. This observation is consistent with other laser damage experiments on other materials and indicates the importance of surface fabrication and/or cleaning. It should be noted that based on the analyses of Section 3, none of these samples should have failed under the fluences and powers used. Third, the irradiation at Brewster's angle did not appreciably improve the laser damage threshold. This observation is also consistent with a surface phenomenon. For some of the samples irradiated at Brewster's angle, the damage appeared on the rear surface which might suggest a focusing effect. Finally, of the three materials tested, CLEARTRAN showed the best results with one sample surviving 20 pulses at 20 J/cm^2 (see sample 3 of table 7). This sample finally failed at 25 J/cm^2 between 5 and 20 pulses. A second sample (4) gave similar results which suggests the data are reproducible.

The fact that CLEARTRAN gave better results than either ZnSe or GaAs is surprising, since its bulk absorption coefficient at 10.6 μm (0.2 cm^{-1}) is one of the largest of the materials studied. Because of this large value of bulk absorption, CLEARTRAN or CVD ZnS are not generally considered as windows for CO_2 lasers. The high laser damage threshold for CLEARTRAN compared to ZnSe or GaAs adds further support to the importance of surface fabrication and cleaning. Additional work must consider the possible differences in the fabrication steps for those materials.

Table 7. Results of Laser Damage Testing To Date

Material	Sample	Angle of Incidence	Fluence (J/cm^2)	Pulses (20 Hz)	Plasma at Failure	Comments
GaAs	2	Normal	15	1	No	Pass
GaAs	2	Normal	20	1	No	Pass
GaAs	2	Normal	25	1	Yes	Badly Damaged Surface
GaAs	3	Brewster	15	5	No	Pass
GaAs	3	Brewster	15	20	Yes	Badly Crazed
ZnSe	1	Normal	15	1	No	Pass
ZnSe	1	Normal	20	1	No	Pass
ZnSe	1	Normal	25	1	Yes	Failure
ZnSe	2	Brewster	15	1	No	Rear Surface Mark
ZnSe	3	Normal	20	1	No	Spots Front and Back Surface
ZnSe	4	Normal	15	1	No	Pass
ZnSe	4	Brewster	15	1	No	Pass
ZnSe	4	Brewster	20	1	No	Rear Surface Mark
CLEARTRAN	2	Normal	15	1	No	Failed
CLEARTRAN	3	Normal	20	1	No	Pass
CLEARTRAN	3	Brewster	20	1	No	Pass
CLEARTRAN	3	Normal	20	5	No	Pass
CLEARTRAN	3	Brewster	20	5	No	Pass
CLEARTRAN	3	Brewster	20	20	No	Pass
CLEARTRAN	3	Brewster	20	5	No	Pass
CLEARTRAN	3	Brewster	25	5	No	Pass
CLEARTRAN	3	Brewster	25	20	Yes	Surface Crazed
CLEARTRAN	4	Brewster	20	5	No	Pass
CLEARTRAN	4	Brewster	20	10	No	Pass
CLEARTRAN	4	Brewster	25	5	No	Pass
CLEARTRAN	4	Brewster	25	10	No	Failed Rear Surface

5. Conclusions

Important mechanical, optical, thermal and physical properties of 33 potential candidate materials for use as laser windows in rep-pulsed, high energy CO_2 lasers have been collected and compiled. Out of these 33 materials, 19 important materials were selected for detailed analyses based upon a given set of high power, rep-pulsed CO_2 laser parameters. The window thickness was determined from two criteria - mechanical fracture and pressure induced distortion. Temperature profiles in the radial direction and along the window axis have been obtained and steady state window temperature and the average temperature of the adiabatic window after 10 sec. have been determined. Figures of merit for laser induced thermal stresses in the radial and axial directions, and beam distortion have been computed. These analyses show that salts satisfy the distortion criteria, but they are not strong enough to withstand the thermal stresses while ZnSe, GaAs, CdTe and CdSe are strong enough to withstand laser induced thermal stresses, but they do not meet the distortion criteria. However, for a flat intensity profile, the distortion criteria becomes unimportant if the window edges are insultated. For GaAs and Ge, pressure induced distortion yields the larger value while for all other materials considered, the mechanical fracture determines the window thickness.

In addition, effects of variation in laser intensity and laser operating time have also been studied. If the laser intensity is reduced by an order of magnitude, keeping all other parameters the same, the salt windows will not fail under laser induced thermal stresses. For optical distortion, ZnSe, CdTe, GaAs and CLEARTRAN ZnS will not fail if the product $I_{av}\ \tau_L$ is reduced by factors of 2, 3.7, 37 and 152 respectively.

The material properties which the analyses show as being important in a laser window are surface absorption, bulk absorption coefficient, volumetric heat capacity, thermal conductivity, flexural strength, thermal expansion coefficient, Young's modulus, refractive index, rate of change of refractive index with temperature and stress optic coefficient. The last three properties, in fact, can be combined into a distortion coefficient. For an ideal window material, the surface and bulk absorption, thermal expansion, and distortion coefficients should be small while Young's modulus, thermal conductivity and flexural strength should be large.

Based on the analyses of window materials, GaAs and Polytran NaCl were selected as three optical materials for rep-pulsed CO_2 damage testing. The performance of CdTe and CdSe is better in comparison to that of GaAs, particularly under distortion criterion, but they were not selected because they cannot be obtained in large sizes. Germanium suffers from thermal runaway problem while the thermal conductivity of AMTIR-1 is relatively very small. Polytran NaCl wins over Polytran KCl because it is cheaper, though their performance is comparable. Water-clear ZnS was also included in the testing because it is a new material with potential multispectral applications.

The preliminary laser damage testing has been performed on only ZnSe, GaAs and water-clear ZnS (CLEARTRAN). The onset of damage occurred on the surface in all cases and supports the well-known fact that surface preparation and cleaning are very important in laser damage experiments. Of the three materials tested to date, CLEARTRAN shows the highest rep-pulsed damage threshold. This surprising fact may be due to different fabrication techniques used with this material. Additional work is required to establish the source of the high damage of CLEARTRAN.

6. References

[1] Feinberg, R. M., "A 15 kW High Energy Beam Density Apparatus", presented at the Italian Laser Conference, Vico Canavesse, Italy, 1980.

[2] Seely, F. B. and Smith, J. O., Advanced Mechanics of Materials, Wiley & Sons, pp. 227 (1955).

[3] Klein, C. A., "Methodology for Designing High Energy Laser Windows," Raytheon Company Research Paper.

[4] Boley, B. A. and Weiner, J. H., Theory of Thermal Stresses, John Wiley & Sons (1962).

[5] Klein, C, Infrared Physics 17, 343 (1977).

Laser Induced Bulk Damage in SiO_2 at 1.064, 0.532 and 0.355 μm

L. D. Merkle*, N. Koumvakalis** and M. Bass

Center for Laser Studies, University of Southern California
University Park, DRB 17, Los Angeles, CA 90089-1112

In this paper we present bulk damage measurements of crystalline quartz and fused silica under single and multiple pulse irradiation where the wavelength was extended to 0.355 μm. In previous work under irradiation at 1.06 and 0.532 μm, it was shown that whereas the single pulse damage varies little with material or wavelength, the multiple pulse damage depended strongly on both. Also, in the case of multiple pulse damage the distribution of the number of pulses needed to produce damage as a function of intensity is indicative of an accumulation process.

If the present work at 0.355 μm the multiple and single pulse damage dependence on focal spot-size, pulse duration and pulse repetition frequency is examined, it is found that the multiple pulse damage shows a much stronger dependence on material, spot-size, pulse duration and wavelength than does the single pulse damage. In addition, more pulses are needed to produce macroscopic damage at a given intensity under irradiation at a 1 Hz pulse repetition rate than at 10 Hz. Possible mechanisms of the repetition rate dependence are briefly discussed.

Key words: crystalline quartz, fused silica, single and multiple irradiation, spot-size, pulse duration and pulse repetition frequency

1. Introduction

In the 1982 Boulder Damage Sympsium we reported studies of multiple pulse laser-induced bulk damage in fused and crystalline SiO_2 irradiated at 1.064 and 0.532 μm [1]. It was shown that repeated irradiation by virtually identical pulses made catastrophic damage more likely on subsequent pulses. However, no change in absorption or scattering of the laser light could be detected prior to the pulse upon which catastrophic damage occurred. Thus, the laser-induced property changes which promote macroscopic damage appear to be more subtle in these materials than in those reported in other recent studies [2,3].

Here we report the extension of these studies to 0.355 μm and examination of the dependence of multiple pulse damage on focal spot size, pulse duration and pulse repetition frequency. The influence of the last of these is particularly significant, as it indicates the dependence of multiple pulse damage on the production of finite-lived property changes. This is a subject of active investigation in other materials as well [4-6].

In section 2, we review major aspects of the experimental apparatus and samples. Single pulse damage data will be presented in section 3 and multiple pulse data in section 4. The implications of these results and possible mechanisms will be discussed in section 5.

2. Experiment

The experimental apparatus and precedure were described in detail previously [1], and only a few points will be reviewed here. The light source was a Molectron Q-switched Nd:YAG laser providing 10 pulses per second of nearly Gaussian temporal and spatial shape, with frequency doubling and

*Present address: Physics Department, University of Arkansas, Fayetteville, AR 72701

**Present address: Litton Guidance Control Systems, 5500 Canoga Ave, Bldg. 31 MS-19, Woodland Hills, CA 91365

tripling crystals. The pulse to pulse energy variation and the waveform of the laser pulse were monitored to permit rejection of the occasional experiments in which laser instability significantly exceeded the usual ± 5%. The beam was interrupted with an electromechanical shutter to vary the pulse repetition frequency when desired. To generate bulk rather than surface damage, the beam was tightly focused into the sample.

The samples used in this work were Suprasil-1 and UV grade Corning 7940 fused silica and optical grade Sawyer single-crystal quartz. Samples of the latter were oriented such that the beam propagated along the z-axis in the 1.064 μm studies.

3. Single Pulse Data

The threshold intensities for single pulse catastrophic damage have been measured and are useful for comparison with the multiple pulse data to be discussed in the next section. In this work, the "threshold" for damage in a single pulse is defined as the average of the lowest peak intensity above which damage always occurred in one pulse and the highest peak intensity below which damage never occurred in one pulse. The width of the intensity region in which damage sometimes occurred in a single pulse was typically several percent of the threshold intensity.

The single pulse thresholds observed in this study are summarized in Table I. The focal volume and pulse duration dependence is consistent with other published results, though the thresholds reported here are somewhat lower [7,8]. Catastrophic self-focusing does not appear to control the present data [8]. A rather strong decrease of threshold with shorter wavelength is evident in Table I when similar spot size and pulse duration data are compared, generally regarded to be indicative of multiphoton processes [10]. Note also that the thresholds are practically identical for the three materials studied.

Table I. Single pulse damage thresholds
The listed parameters are the focal spot radius e^{-2} intensity, w, and the pulse duration, full width at half maximum, t

Material	$I_{threshold}$ (GW/cm^2) λ=1.064 μm	$I_{threshold}$ (GW/cm^2) λ=0.532 μm	$I_{threshold}$ (GW/cm^2) λ=0.355 μm
Crystalline Quartz (Sawyer optical grade)	130 ± 20 w = 14.5 μm t = 23 ns	100 ± 15 w = 7.0 μm t = 14 ns	45 ± 5 w = 5.9 μm t = 13 ns
Suprasil-1 fused silica	110 ± 15 w = 13.8 μm t = 24 ns	90 ± 15 w = 6.6 μm t = 15 ns	35 ± 5 w = 6.1 μm t = 13 ns
Corning 7940 fused silica	110 ± 15 w = 13.8 μm t = 24 ns 110 ± 15 w = 15.6 μm t = 19 ns 120 ± 20 w = 9.0 μm t = 27 ns 220 ± 40 w = 7.2 μm t = 18 ns	110 ± 15 w = 6.6 μm t = 16 ns	40 ± 5 w = 5.0 μm t = 14 ns

4. Multiple Pulse Data

Multiple pulse damage measurements were carried out under the same conditions as the single pulse measurements. In figure 1, the number of pulses needed to produce catastrophic damage is plotted against the intensity normalized by the single pulse threshold intensity for 1.064 μm irradiation of Corning 7940 at two combinations of spot size and pulse duration. The pulse repetition frequency is 10 Hz. The use of normalized units for the abscissa removes the spot size and pulse duration dependence of the single pulse threshold, facilitating observation of the multiple pulse behavior. Note that multiple pulse damage occurred in gradually larger numbers of pulses as the intensity was decreased in the case of large focal spot and long pulse duration. The two solid lines enclose these data to emphasize the trend. The small spot, short pulse data, however, show a nearly threshold-like behavior even for multiple pulse damage. Indeed, only one catastrophic damage event was observed at an intensity below the single pulse threshold uncertainty range indicated by the dashed lines. Data taken with intermediate parameters (small spot with long pulse and large spot with short pulse) are not conclusive. Clearly, increasing both spot size and pulse duration promotes the generation of multiple pulse damage.

Multiple pulse damage data have been taken on all three materials and at three wavelengths: 1.064, 0.532 and 0.355 μm. The data are summarized in Tables II and III by use of the "threshold" intensity for damage within 1000 pulses delivered at 10 Hz. This threshold is defined analogously to the threshold for single pulse damage. In Table II the ratio of 1000 pulse threshold to single pulse threshold is compared among the materials studied at each wavelength. Note that both types of fused silica consistently suffer damage within 1000 pulses at significantly lower fractions of single pulse threshold than crystalline quartz. This contrasts with the single pulse results noted earlier, and suggests that different mechanisms control single and multiple pulse damage.

Table II. Comparison of 10 Hz multiple pulse damage behavior among the materials studied at each wavelength

Wavelength (μm)	Material (Company)	$w^{(1/e^2)}$ (μm)	t_p (ns)	$\frac{I_{thr,\,1000}}{I_{thr,\,1}}$
1.064	Corning	13.8	24	0.77
	Suprasil	13.8	24	0.86
	Sawyer	14.5	23	0.92
0.532	Corning	6.6	16	0.58
	Suprasil	6.6	15	0.64
	Sawyer	7.0	14	0.70
0.355	Corning	5.0	14	0.56
	Sawyer	5.9	13	0.82

Table III summarizes the 10 Hz multiple pulse damage behavior of Corning 7940 with spot sizes and pulse durations similar for all the wavelengths. This comparison emphasizes the wavelength dependence. It is clear that for the focal spot size and pulse duration used multiple pulse damage occurs far more readily at 0.532 and 0.355 μm than at 1.064 μm. Since the data have been normalized by the single pulse thresholds, this dependence is even stronger than the single pulse wavelength dependence.

As noted previously, the multiple pulse damage behavior indicates that pulses prior to macroscopic damage change the sample, but the nature of those changes is uncertain (1). To determine whether the changes are permanent, experiments have been performed at two different pulse repetit frequencies: 10 Hz and 1 Hz. The results at 0.355 μm are shown in figures 2a and 2b. The curve are eye-guiding traces, solid for the 10 Hz data and dashed for the 1 Hz data. Note that for bo fused and crystalline SiO_2 more pulses are needed at a given intensity to cause damage at 1 Hz t at 10 Hz. This clearly indicates that the laser-induced material changes have a finite lifetim of order 0.1 - 1 second. A similar, though rather small, pulse reptition frequency dependence observed at 0.532 μm.

Table III. Wavelength dependence of 10 Hz multiple pulse damage behavior in Corning 7940

Wavelength (μm)	$W(1/e^2)$ (μm)	t_p (ns)	$I_{thr,\ 1000}$ / $I_{thr,\ 1}$
1.064	7.2	18	1.00
0.532	6.6	16	0.58
0.355	5.0	14	0.56

5. Discussion

It was previously concluded that multiple pulse damage in these experiments is made more likely by subtle laser-induced changes prior to the "damaging" pulse. The pulse repetition frequency dependence reported here confirms this conclusion. The fact that macroscopic damage depends on the time interval between pulses clearly shows that the earlier pulses have changed the material. The apparent pulse duration dependence is also consistent with this. A certain number of pulses is necessary to cause catastrophic damage at a given intensity, and if each pulse is longer it is reasonable to expect that fewer would be needed.

The nature of the laser-induced changes which precede the catastrophic damage is not known at present. However, the data reported here suggest possibilities. Multiple pulse damage is observed to occur at smaller fractions of single pulse threshold in fused silica than in single crystal quartz at shorter wavelength and apparently at larger focal spot sizes. One mechanism consistent with these observations is the generation of color centers which would increase absorption and provide easily-ionized electrons for subsequent pulses. Such centers would be produced by multiphoton excitation more readily as the wavelength is shortened and are believed to be more readily produced in fused than in crystalline SiO_2. Certain types of color centers may require impurities for stabilization [11] so that a larger spot size would irradiate a larger number of impurity stabilized color centers. Another mechanism may involve absorption by, and consequent growth of, randomly spaced submicron inclusions or structural imperfections. However, the lack of change of light scattering prior to damage, observed at all three wavelengths, and the nonpermanences of the laser-induced changes do not appear consistent with this model.

The transient nature of the material changes indicated by the pulse repetition frequency dependence deserves further comment. Simple thermal buildup cannot explain the accumulating by finite-lived material change. Estimates of the absorption and thermal properties predict a residual temperature rise 0.1 seconds after a pulse of less than 10^{-3}°K above ambient temperature. Similarly, electrons excited to the conduction band could not live from pulse to pulse. It is known, however, that both transient and permanent color centers can be created in SiO_2 [11-13]. Thus, color center formation remains a candidate mechanism.

The multiple pulse data, particularly in figure 2, suggest that a minimum intensity or fluence may be required to activate the observed accumulation of damage-promoting property changes. The pulse repetition frequency depndence suggests a simple interpretation. Since the laser-induced changes decay between pulses, a minimum number of such changes must be produced in a pulse to assure that an adequate number survive to the next pulse. As the interval between pulses is lengthened the number which need to be created in each pulse is increased, consistent with the data.

The authors would like to thank Floyd Williams of the Corning Glass Works for donating the ·ning 7940 material. They would also like to thank Mr. He Deng for technical assistance and cussions. This work was supported by Department of Energy project agreement number 'T03-81NE33080 and by NSF Grant No. ECS-8113428.

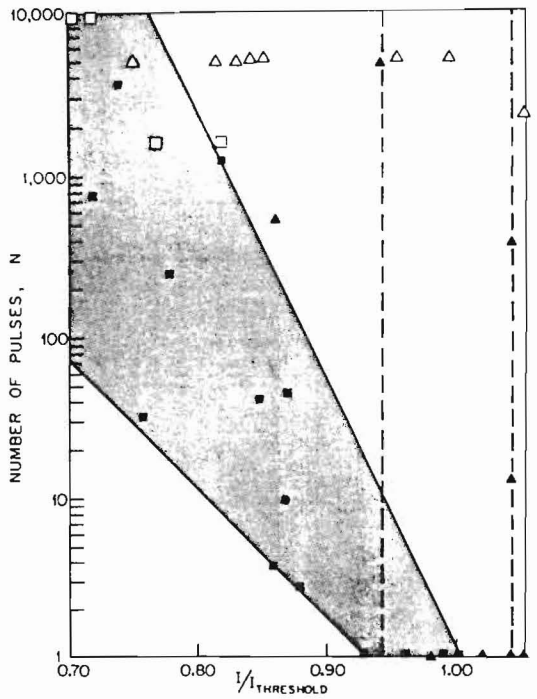


Figure 1. Multiple pulse damage data on two samples of fused silica at 1.064 μm. Full symbols indicate an experiment where damage occurred in the indicated number of pulses, while open symbols indicate no damage. The squares represent data for sample A where the laser beams characteristics were w=13.8 μm and t (FWHM)= 24ns. The triangles represent data for sample B where the laser beams characteristics were w=7.2 μm and t (FWHM)= 18 ns. The dashed as well as the shaded area are explained in the text.

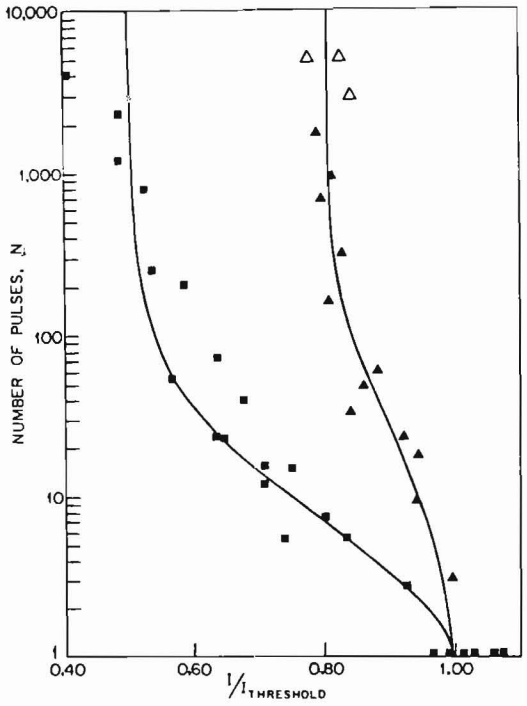


Figure 2a. Multiple pulse damage experiment on fused and crystalline SiO_2 at .355 μm.

■ : fused SiO_2, sample damaged, laser pulse repetition frequency = 10 Hz.

▲ : crystalline SiO_2, sample damaged, laser pulse repetition frequency = 10Hz.

△ : crystalline SiO_2, sample did not damage, laser pulse repetition frequency: 10 Hz.

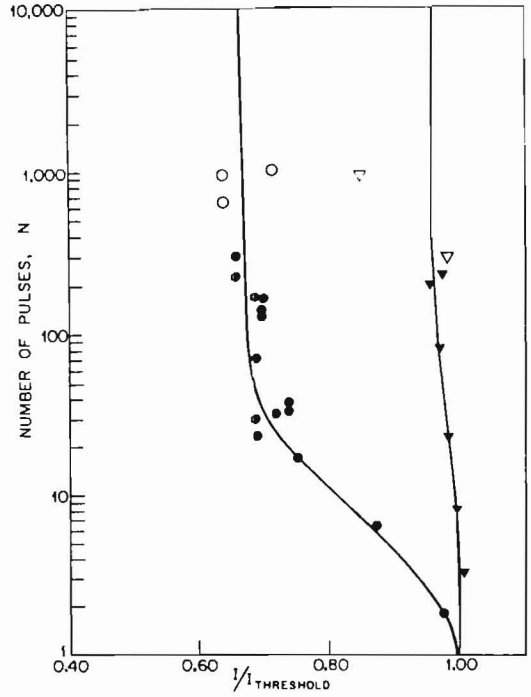


Figure 2b. Multiple pulse damage experiment on fused and crystalline Sio_2 at .355 μm.

● : fused SiO_2, sample damaged, laser pulse repetition frequency = 1Hz.

O : fused SiO_2, sample did not damage, laser pulse repetition frequency = 1Hz.

▽ : crystalline SiO_2, sample did not damage, laser pulse repetition frequency: 1Hz.

▼ : crystalline SiO_2, sample damaged, laser pulse repetition frequency: 1Hz.

7. References

[1] Merkle, L. D.; Bass, M.; and Swimm, R.T. Proc. of 1982 Symposium on Laser Induced Damage, to be published; Merkle, L. D.; Bass, M.; and Swimm, R.T. Opt. Eng.

[2] Lee, C. S.; Koumvakalis, N.; and Bass, M. Proc. of 1982 Symposium on Laser Induced Damage, to be published;

[3] Wu, S.-T.; and Bass, M. Appl. Phys. Lett. 39 (12), 948 (1981).

[4] Balitskas, S. K.; and Maldutis, E. K. Sov. J. Quant. Elect. 11 (4), 541 (1981).

[5] Wood, R. M.; Sharma, S. K.; and Waite, P. Proc. of 1982 Symposium on Laser Induced Damage, to be published.

[6] Walser, R. M.; Bordelon, M.; Jhee, Y-K.; and Becker, M. F. Proc. of 1982 Symposium on Laser Induced Damage, to be published.

[7] Van Stryland, E. W.; Soileau, M. J.; Smirl, A. L.; and Williams, W. E. Phys. Rev. B 23 (5), w144 (1981).

[8] Soileau, M. J.; and Bass, M. IEEE J. Quant. Elect. QE-16 (8), 814 (1980).

[9] Soileau, M. J. "Frequency and Focal Volume Dependence of Laser Induced Breakdown in Wide Band Gap Insulators", Ph.D. dissertation, University of Southern California, Los Angeles (1979).

[10] Smith, W. L. Opt. Eng. 17 (5), 489 (1978).

[11] Holzrichter, J. F.; and Emmett, J. L. J. Appl. Phys. 40 (1), 159 (1969).

[12] Sigel, G. H. J. Non-Crust. Sol. 13, 372 (1978/74).

[13] Tanimura, K.; Tanaka, T.; and Itoh, N. Phys. Rev. Lett. 51 (5), 423 (1983).

An observation was made that the absolute values of damage thresholds reported are apparatus dependent since long pulse widths and tiny spot sizes were used. The speaker agreed that during a single pulse the spot size would play a role but pointed out that the heat diffusion between pulses was large enough to return the sample to ambient temperature to within a few millidegrees before the next pulse arrived. Thermal buildup between pulses thus seems completely unlikely. Even the maximum temperature rise during a pulse is calculated to be only about 1°C, so it does not appear that anything thermal is going on.

It was pointed out that some evidence exists suggesting color center formation as a mechanism for damage in this experiment. Annealing studies should clarify this point but are difficult to do with these small spot sizes. Perhaps temperature dependence of damage studies would help here and could be done.

The question of surface damage was raised. The speaker said that they focused the laser beam near the center of the sample and no damage occurred near the surface.

Bulk Absorption Measurements Using Prism-Shaped Samples for Laser Calorimetry*

P. A. Temple and D. P. Arndt

Michelson Laboratory, Physics Division
Naval Weapons Center, China Lake, California 93555

A method is described where low absorption samples are cut in the shape of prisms. The prism angles are chosen to allow the (polarized) laser beam to enter the prism at normal incidence and exit the prism at Brewster's angle. This configuration eliminates internal reflections and allows for easier analysis. Measurements are then made at various positions along the prism to obtain the total absorptance for several path lengths through the sample. The method has the advantage of simplified analysis and minimal surface absorption fluctuation. The disadvantages are special sample shape and a need for a special calorimetric setup allowing sample translation. Representative data will be shown for single-crystal and fusion-cast CaF_2 at HF and DF wavelengths.

Key words: absorption; absorption coefficient; bulk absorption; CaF_2; calorimetry; laser calorimetry; optical absorption.

Introduction

Bulk absorption measurements on highly transparent materials are almost exclusively made by using laser calorimetry. In laser calorimetry, a laser beam is incident on the sample, where a small fraction of the light is absorbed, causing the temperature of the part to rise slightly. By measuring this temperature rise, it is possible to determine the fraction of the light absorbed, called the absorptance. It was realized very early that not only does the bulk of the sample absorb light, but that the surfaces also absorb. Therefore, one cannot determine the bulk absorptance properties of a material by measuring a single sample of the material. Traditionally, the bulk absorption coefficient, α, has been determined by preparing at least two samples of different thickness, measuring the absorptance of both samples and attributing the increased absorptance of the thicker sample to the absorption which takes place along the greater path length through the sample that the light must travel [1,2].[1] Besides the difficulty of having to prepare several samples, one commonly finds that the surface absorption can vary markedly from polish to polish, causing a fluctuation in absorptance data which confuses the interpretation.

In this paper we describe a method where a single sample is cut into the shape of a right prism. The prism angles are chosen to allow the polarized laser beam to enter the prism at normal incidence and exit the prism at Brewster's angle. Measurements are then made at various positions along the prism to obtain the total absorptance for several path lengths through the sample. In a sense, this emulates the multiple sample technique but allows measurements to be made for many path lengths all on the same sample. The method has the advantage of simplified analysis and minimal surface absorption fluctuation, since all regions on any one surface of the prism were prepared simultaneously. Coincidentally, it also eliminates the problem of coherent interference which may take place between the plane parallel surfaces of a slab-type sample.

Experimental setup

Figure 1 shows schematically the prism calorimetry apparatus. Figure 2 is a photograph of the apparatus with the top cover of the thermal shield removed and the cover off the beam dump optics, and figure 3 is a photograph of the apparatus as it appears when in use. In figure 1, the laser beam passes through a beam splitter which allows continuous monitoring of the incident beam power. The prism is carefully positioned with the lower face normal to the incident beam by aligning with an autocollimator attachment. The prism has been cut such that the beam exits the prism at Brewster's angle. Since the beam is polarized as shown, there is very little reflection on the exit surface. This minimizes the amount of stray light bouncing around inside the sample.

*Work supported by Navy Independent Research Funding.

[1] Numbers in brackets indicate the literature references at the end of the paper.

The calorimeter employed for these measurements is the Naval Weapons Center abiabatic instrument. This allows the sample to be translated as shown in figure 1, permitting the beam to travel through various thicknesses of sample. The instrument is designed for straight-through measurements. Therefore, the two mirrors shown above the sample must be used to realign the beam. These mirrors are large enough to allow for beam travel which occurs when the sample is translated.

The adiabatic calorimeter measures the absorptance by noting the initial and final sample temperature after the entire sample is at a uniform temperature. These data are very nearly independent of the position of the temperature detector on the sample and on the position of the beam on the sample. This is not true for an instrument where rate data are used to determine sample absorptance. The problem of detector and beam position is greater when the thermal diffusivity of the sample is small.

Data Analysis

The raw data acquired is sample absorptance as a function of sample thickness, where absorptance is the absorbed energy/incident energy. A general expression for the absorptance as a function of material properties and beam properties is

$$\text{Absorptance} = \int_0^L \frac{n(z)\langle E^2(z)\rangle}{n_o\langle E_o^2\rangle}\,\alpha(z)dz$$

where $n(z)$ is the index of the sample as a function of position, n_o is the index of the surrounding medium, $\langle E^2(z)\rangle$ is the time average of the square of the electric field within the sample, $\langle E_o^2\rangle$ is the time average of the square of the incident field far from the sample, and $\alpha(z)$ is the absorption coefficient of the sample as a function of position [3]. In this case, the sample is assumed to be uniform throughout the bulk, there are no internal reflections giving rise to fluctuations in $\langle E^2(z)\rangle$ with position, and the surface contributions can be lumped into a single term. The result is

$$A = T\alpha L + A_{surface},$$

where T is the first surface transmittance, L is the sample thickness, and $A_{surface}$ is the total surface contribution. The data are plotted as a function of sample thickness, resulting in a straight line with a slope and nonzero intercept. The bulk absorption coefficient α is then

$$\alpha = \text{SLOPE} \cdot 1/T \quad ,$$

and

$$A_{surface} = \text{INTERCEPT at } L = 0 \quad .$$

$A_{surface}$ cannot be resolved into entrance and exit surface contributions.

Data

Figure 4 shows data using a single-crystal sample of CaF_2 and a DF laser using all lines (3.6 to 4.0 μm wavelength). The solid line is a least squares fit to the data. Each data point represents a single measurement, with as many as four individual measurements being made at a single position of the prism. The calculated absorption coefficient is 2.1×10^{-5} cm^{-1}. This is about one order of magnitude lower than previously reported by Hass et al. [4] but agrees well with measurements by Willingham [5]. The surface contribution is 1.5×10^{-4}, a unitless quantity. Notice that this is

nearly an order of magnitude greater than the contribution from 1 cm of bulk material. Figure 5 shows similar data from a fusion-cast prism of CaF_2. For this prism, the bulk absorption coefficient was 2.8×10^{-5} cm^{-1} and the surface contribution was 1.7×10^{-4}.

Figure 6 shows data taken at two wavelengths in the HF laser band. The laser employed a grating within the cavity to allow single-line operation. These two lines were chosen because the 2.87 μm wavelength is more nearly into the water band at 2.9 μm while the 2.705 μm wavelength is outside this band. The sample is the same fusion-cast CaF_2 prism as used in figure 5. The data indicate that the bulk of the prism and the surfaces of the prism are absorbing more strongly in the water band, suggesting the entrapment of water on and within the sample. The greater scatter in the data for various thicknesses may be due to a nonuniform distribution of entrapped water. These absorption coefficient data -- 1.93×10^{-4} cm^{-1} at 2.87 μm and 1.41×10^{-4} cm^{-1} at 2.705 μm -- agree well with the data reported in the literature. Hass, using a multiline HF laser, reported 1.8×10^{-4} cm^{-1} as the absorption coefficient of fusion-cast CaF_2 [4].

Discussion

We have described and demonstrated a technique for making bulk absorption measurements on prism-shaped samples. The advantages are that one can obtain a large number of data points for a uniform range of sample thicknesses with a minimum of fluctuation in surface absorption. The data indicate the fluctuation from the least squares fit line. It is not easy to decide if this fluctuation, such as in figures 5 and 6, is due to experimental difficulties or in sample fluctuation. Our experience thus far with this technique is that on nearly every sample at least one or two positions give very high readings, indicating that there may have been a high absorption contaminant on the surface, etc. In the case of large deviations, these are easily recognized as anomalous. Are the smaller fluctuations seen in figure 6 similar position-to-position fluctuations? The very smooth data of figure 4 lead one to believe that the fluctuations seen in figures 5 and 6 are actual sample absorptance variations. The measurement repeatability is shown in all three figures by the multiple data points for each thickness.

One disadvantage of this technique is the need to create a sample of unusual shape. Another problem is the need for an adiabatic calorimeter to handle the problem of illumination vs temperature detector positioning. The data shown are for CaF_2, a material which is relatively insensitive to these thermal effects since it is thermally very "fast." In the case of glass, the problem is much more severe. Our experience with fused silica indicates that a period of as much as 8 min after the laser is removed may be required for the sample to reach a uniform temperature when it has been illuminated on an extreme edge. While we have not tried to make measurements on such samples in a nonadiabatic mode, we suspect the data would not be satisfactory.

References

[1] Skolnik, L. Optical properties of highly transparent solids. Mitra, S. S.; Bendow, B., ed. New York:Plenum Press; 1975. 405.

[2] Hordvik, A. Appl. Opt. 16; 2827; 1977.

[3] Temple, P. A. Handbook of optical constants of materials. Palik, E. D., ed. New York:Academic Press; Chapter 9 (in press).

[4] Hass, M.; Harrington, J. A.; Gregory, D. A.; Davisson, J. W. Appl. Phys. Lett. 28; 610; 1976.

[5] Willingham, C. B. Raytheon Co., Lexington, MA; private communication.

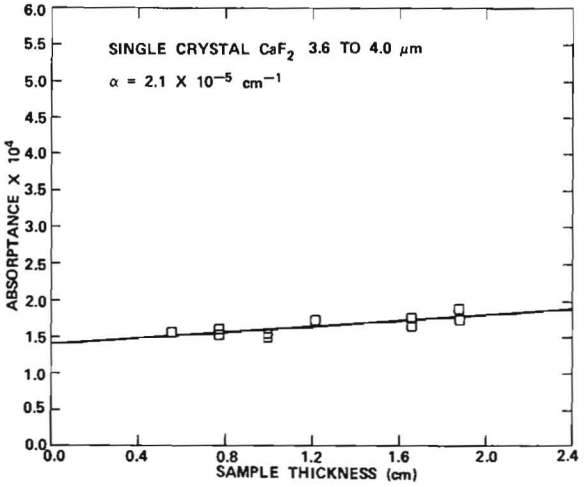


Figure 4. Absorptance data for a single-crystal CaF_2 prism using 3.6 to 4.0 μm wavelength DF radiation.

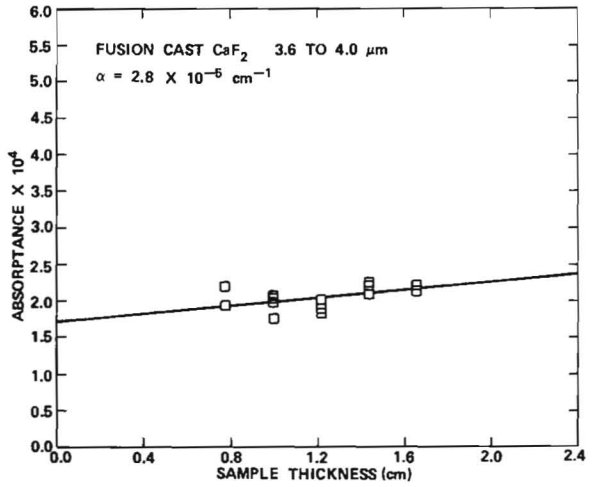


Figure 5. Absorptance data for a hot-pressed, forged CaF_2 prism using 3.6 to 4.0 μm wavelength DF radiation.

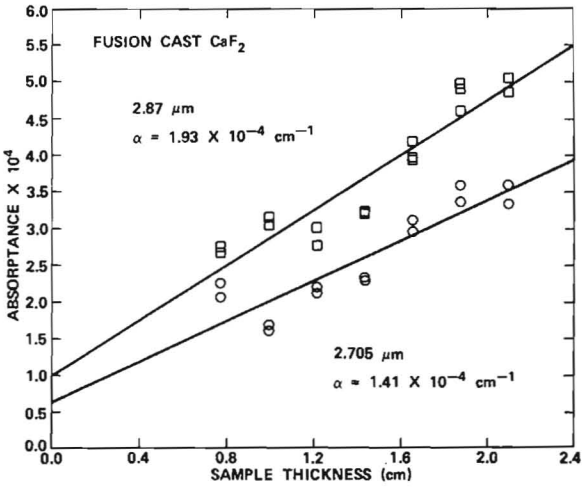


Figure 6. Absorptance data for a hot-pressed, forged CaF_2 prism using two different HF wavelengths.

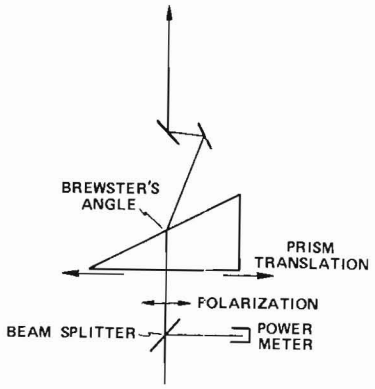


Figure 1. Schematic diagram of the prism calorimeter showing the beam path, beam polarization and sample positioning.

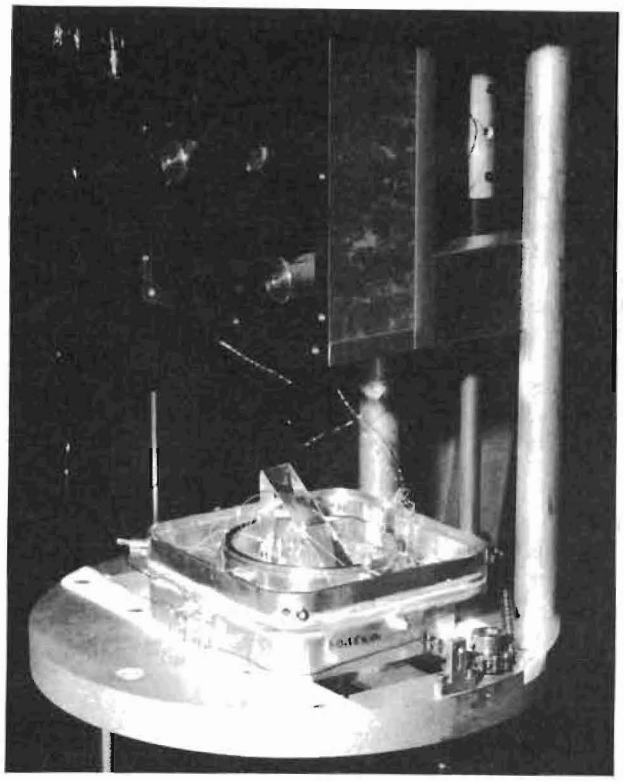


Figure 2. Photograph of the prism calorimeter with beam dump and sample chamber covers removed.

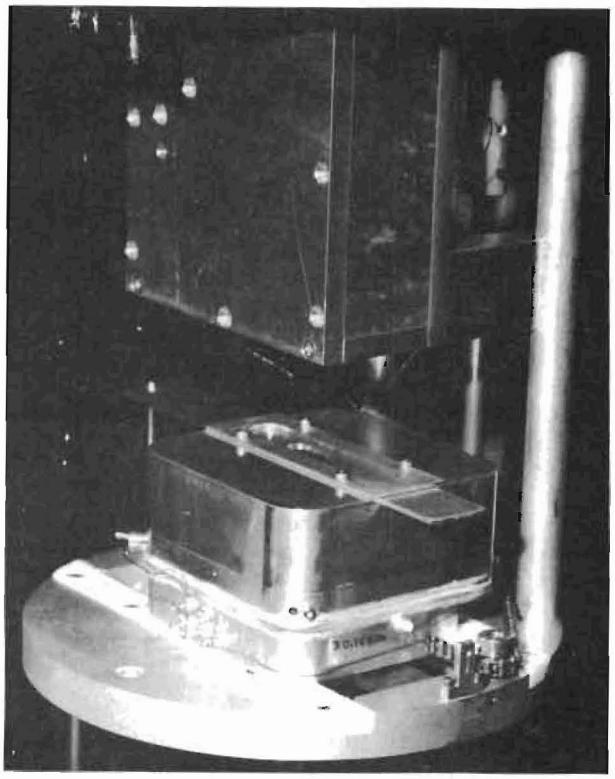


Figure 3. Photograph of the prism calorimeter with beam dump and sample chamber covers in place.

Inherent Mechanical Damage in Diamond Machined Optical Surfaces*

H. H. Hurt and D. L. Decker

Michelson Laboratory, Physics Division
Naval Weapons Center, China Lake, California 93555

The surface and near-surface regions in diamond machined Cu have been investigated by high resolution transmission electron microscopy, scanning electron microscopy, and scanning transmission electron microscopy. This study has revealed that the near-surface region produced by diamond machining is heavily deformed and that the temperature rise due to the deformation leads to interesting internal oxidation and dynamic recrystallization effects. Surface microstructure is shown to be related to the surface microtopography. A companion paper at this conference presents some correlation of this observed structure with optical properties of the surface including laser damage thresholds.

Key words: copper; deformation; machining; optical properties; oxidation; recrystallization; surface.

Introduction

The nature of the optically polished surface has been a subject of conjecture and debate for several centuries. Hooke [1][1] and Newton [2] contended that polishing was actually a cutting process where surface material was removed by the sharp abrasive particles; the finer the abrasive, the smaller the scratches on the surface until a specularly reflecting surface is obtained. The development of electron diffraction led researchers such as Bielby [3] to conclude that the mirror is produced by smearing the workpiece material across the surface, thereby filling the depressions and producing a 20 to 100 Å thick amorphous layer. Subsequent investigations on polished and abraided surfaces have failed to detect the amorphous Bielby layer [4]. Thus, current researchers have concluded that the original assumptions of Hooke and Newton were correct and that the polished surface is crystalline and is plastically deformed, the amount and depth of deformation being dependent on the polishing conditions [5].

The metal cutting process as a method of reducing a workpiece to a given shape is of great importance in the manufacture of most items used in our modern technological society. A highly specialized derivative of normal machining, the diamond machining process for the production of metal mirror surfaces has reached an advanced state of development. To date, the focus of this development effort has been directed towards improving and characterizing the microtopography of the surface produced. This is because the optical scattering is related to the statistical properties of the surface roughness [6].

The development of high fluence laser diagnostics and other methods has resulted in a wealth of data on the surface and optical properties of diamond turned mirrors. From this data, it has been determined that the diamond turned surface exhibits unique properties which are related empirically to the machining conditions [7], typically the tool rake angle. Most interesting is the variation in the optical reflectance from these mirrors that is independent of the surface microtopography and is not predicted by the simple Drude theory based on the interaction of the incident electromagnetic fields with the "free" electrons of the conductor [8]. If the electrons are perfectly free, the reflection is 100%. When the mean free path of the electrons is shortened due to collisions, damping occurs and reduces the amount reflected. At room temperature, the primary damping mechanism (and the only one considered in the theory) is phonon-electron collisions. However, electron scattering from crystalline imperfections such as dislocations, vacancies, and stacking faults also contribute. The plastic deformation of the optical surface during diamond machining results in a higher defect density, and hence the changes in the optical reflectance of diamond machined surfaces should be linked with the crystalline perfection of the near-surface region of the material. To date, the type and number of crystalline imperfections in this region due to the diamond machining process was undetermined.

*Work supported by the Office of Naval Research and conducted jointly at the Naval Weapons Center and Center for Laser Studies, University of Southern California, Los Angeles.

[1]Figures in brackets indicate the literature references at the end of the paper.

In a comprehensive study [9], the nature of the deformation introduced by the diamond machining process was investigated by several methods. This paper presents the elucidation of the structure of the surface and near-surface region by high resolution transmission electron microscopy (TEM). Sections both transverse and parallel to the deformed surface have been examined by TEM to establish the structural changes with respect to the orientation of the diamond cutting tool as it passes over the surface. Imaging of dislocation structure and density in the first few hundred angstroms of the surface that contribute to the optical reflection process is of particular importance.

TEM Examination of the Deformation Structure of the Surface

The samples were examined in a Phillips EM 420T located at the Center for Electron Microscopy and Microanalysis at the University of Southern California. The instrument utilizes a LaB_6 filament, and all examinations were done at an accelerating voltage of 120 kV. The interface on the transverse sections was aligned perpendicular to the tilting axis of the stage for maximum resolution of the interfacial region. Features of the EM 420T utilized were the high resolution scanning electron microscope (SEM) to image the surface topography in conjunction with scanning transmission electron microscopy (STEM) and standard TEM techniques including weak beam dark field methods.

Figure 1 shows schematically the sectioning views of the diamond machined surface for TEM examination. The characteristic structure of each of the rake angle surfaces will now be presented and discussed. Figures 2 and 3 show a transverse section for the -5 deg surface. The dashed line is the boundary between the machined surface and the copper plating. The demarcation line was often very hard to detect as the plating closely mirrors the structure of the surface, sometimes to the point of dislocations continuing into the plated region. The two micrographs are of the same area: figure 2 is a bright field image, and figure 3 is a weak beam dark field image to show the dislocation structure variation with depth below the surface. The weak beam condition was set up in this micrograph for high resolution of individual dislocations, and, as can be seen, the density in the very near-surface region is very high as shown by the almost continuous mass of dislocations. The dislocation density appears to taper off below the surface. Tilting the specimen revealed no discernible subgrain boundaries in the near-surface region. Further evidence of the large amount of deformation in the near-surface region is the selected area diffraction (SAD) pattern, figure 4. The SAD aperture was placed so it imaged from the interface to approximately 5 μm below, thus measuring the rotation between the surface and the underlying base material. This is shown to be 29 deg, a significant amount of rotation.

Increasing the negative rake angle to -10 deg, which is known to increase the cutting tool force and thus increase the work input into the surface, results in the interesting faceted structure shown in the surface section, figure 5. The micrograph is a simultaneous SEM-STEM image which correlates the surface structure with the underlying structure. While looking for evidence of a subgrain or other boundary, observation of one of the boundaries showed no crystallographic changes across the dark-to-light transition region (see fig. 6). The difference in contrast across the boundary is due to a step change in the foil thickness. This step is evidenced in the SEM micrograph, and, since the surface sections are back-thinned, surface topography is evidenced by thickness gradients.

In the transmission electron diffraction (TED) pattern of the -10 deg surface section are secondary spots due to the presence of Cu_2O. Imaging the oxide in dark field, figure 7 shows the particles to be around 100 Å in diameter. The Cu_2O phase is stable at 362°C and above; hence, it can be deduced that extensive heating accompanies the deformation. This leads to oxidation and possibly the faceted surface structure. The oxide could not be detected in the transverse section.

Examination of the -15 deg surface indicated that a major change in structure had taken place. Tilting the sample revealed a very low dislocation density. A high magnification view of this surface (fig. 8) reveals a nearly continuous Moire fringe pattern. The Moire pattern is evidence of Cu_2O precipitates beneath the diamond turned surface. The continuous structure of the fringes indicates epitaxial growth of the oxide film within the foil as the fringes are due to the misfit in d spacing between the (111) planes of Cu and Cu_2O. Also visible are fringes of the misfit dislocations which look like textbook examples of edge dislocations. The mechanism is double diffraction within the foil as illustrated in figure 9. The measured fringe spacing of 14 Å corresponds exactly to the model as shown. In the transverse section, the oxide was not detectable in the TEM. The transverse view shown in figure 10 indicates that the surface has recrystallized. The cross section shows three regions: (1) featureless recrystallized zone at the surface; (2) region with a complex deformation structure just below (1) (in this band can be seen a recrystallized grain); and (3) undisturbed base material just below (2).

Recrystallization of the Surface Layer During High Negative Rake Angle Machining

The -15 deg surface showed definite recrystallization of the surface layer, which probably occurred during the machining process due to the increased work input and temperature rise in the workpiece. Dynamic recrystallization, commonly termed "hot working," is a widely known phenomenon,

but this is the first report of its occurrence in machined surfaces. Correlation of the observed dynamic recrystallization with experimental studies [10,11] is difficult due to the fact that the mechanics of the surface deformation process in machining is poorly understood [12]. In addition to the TEM data, reflection electron diffraction (RED) patterns, x-ray data, and microhardness data all indicate a softer and more ordered near-surface region [9].

Internal Oxidation of the Near-Surface Region

An interesting and wholly unexpected feature of the -10 and -15 deg surfaces was oxide phase precipitates beneath the diamond turned surface. An oxide, if present, would be expected to form on the freshly machined and chemically active surface. The oxide, Cu_2O, is the equilibrium oxide phase forming at temperatures in excess of 362°C. This phenomenon should not be confused with internal oxidation, because this term generally applies to the oxidation of less noble impurities within the material by the dissolution of oxygen into the material at a pressure less than the decomposition pressure of the material [13].

Apparently, the oxide forms due to the rapid diffusion of oxygen into the workpiece at the high temperature reached during the machining process ($D = 9.5 \times 10^{-6}$ cm^2/sec at 500°C) [14]. In Cu, the high thermal conductivity aids in the transfer of heat from the primary shear zone to the subsurface region. The moving heat source in the form of the shear zone passes quickly past the point in the workpiece, and the subsequent rapid cooling leads to the nonequilibrium precipitation of Cu_2O in the subsurface region.

A most interesting phenomenon occurs at the -15 deg surface as was shown in the Moire fringe pattern in figure 8. As explained previously, the evidence from the diffraction pattern and the double-diffraction model (fig. 9) strongly supports the view that the oxide exists as a continuous epitaxial film beneath the diamond machined surface. The fringes could also be structural Moires due to a faceted cobblestone-type structure in a subsurface layer, but this is considered unlikely. Certainly a follow-on to this research would include depth profiling for oxygen by Auger electron spectroscopy or secondary ion mass spectroscopy.

The observation of the continuous epitaxial oxide film in conjunction with the recrystallization observed in the TEM cross section (fig. 10) leads to a possible explanation for this interesting phenomenon. As the recrystallization front passes from the surface to the point at which it stops beneath the surface, it leaves in the recrystallized zone a supersaturated solid solution of oxygen in the matrix. Even though the temperature has decreased to the point where the recrystallization front has stopped, there is sufficient thermal activation so that the dissolved oxygen is mobile. The oxygen can diffuse to the nearest sink, in this case the boundary between the recrystallized layer and the subsurface region. Using diffusion data for oxygen in Cu in the 300°C range, such a model is plausible and provides a possible explanation as to why the Cu_2O exists as an epitaxial layer in a surface with recrystallization and as particles when there is no recrystallization.

The source of the oxygen for the oxidation reaction is not immediately evident as the starting material is an oxygen-free grade of Cu. A continuous stream of cutting oil (Shell Diala-AX) covers the surface during machining and shields it from the atmosphere. Dissolved oxygen or water in the cutting oil is suspect, especially in recirculated oil that contains a fair amount of contaminants, chiefly the trichlorethane, used to wash the machine parts which subsequently flows into the recirculation tank. To test this hypothesis, optical Cu surfaces were placed in both pure cutting oil and contaminated oil from the machine and then heated to 80°C for 12 hrs. The surface in the contaminated oil was very severely degraded by a thick brown coating of CuO, indicating a substantial amount of water contamination. Surprisingly, the Cu surface heated in the virgin oil also showed evidence of oxidation, albeit very slight.

Conclusions

The transmission electron microscopy method used in this study indicated changes in the materials properties of the diamond machined surface as a function of the tool rake angle. From the micrographs it is concluded that as the rake angle becomes more negative, the residual damage in the machined optical surface increases and reaches a maximum at -5 deg. Past this point, the temperature rise accompanying the increased deformation at even higher negative rake angles initiates dynamic recrystallization and annealing effects. Also associated with these high negative rake angle surfaces is the presence of the high temperature oxide phase Cu_2O dispersed in the subsurface region.

A companion paper at this conference presents optical and laser damage data on identical diamond turned surfaces [7]. The Drude theory can be directly applied to explain the effect of surface damage by diamond machining on reflectance. The changes in the surface microstructure correlates well with the far-infrared reflectance data. The -5 deg surface which had the highest absorption was also the most deformed. The more defect-free high negative rake surfaces were lower in absorption. The laser

damage characteristics of the diamond machined surface also show the same effects of the microstructure on slip, melt, and selective damage thresholds.

References

[1] Hooke, I. R. Micrographia, Observation II. London; Royal Society; 1665.

[2] Newton, I. Opticks. 1730.

[3] Bielby, G. Aggregation and Flow of Solids. London; Macmillan; 1921.

[4] Samuels, L. E. J. Inst. Met. 85; 51; 1956.

[5] Turley, D. M.; Samuels, L. E. Metallography 14; 275; 1981.

[6] Bennett, H. E. Opt. Eng. 17; 480; 1978.

[7] Decker, D. L.; Hurt, H. H.; Porteus, J. O.; Grandjean, D. J. "Optical properties of diamond-machined metal surfaces and their relationship to physical and chemical surface perfection," this conference.

[8] Dekker, A. J. Solid State Physics. New Jersey; Prentice-Hall; 1957.

[9] Hurt, H. H. "A metallurgical investigation of the diamond-turned optical surface," Ph.D. thesis, University of Southern California, Los Angeles, 1984.

[10] Pachla, W.; Styczynski, L. Met. Sci. 18; 22; 1984.

[11] Jayo, R. Eighth International Conference on Electron Microscopy, Canberra, 1979.

[12] Abdelmoniem, M. Es.; Scrutton, R. F. Wear 27; 35; 1974.

[13] Peterseim, J., et al. Z. Metallk. 70; 266; 1979.

[14] Wood, G.; Stott, F. Oxidation of Metals 14; 187; 1979.

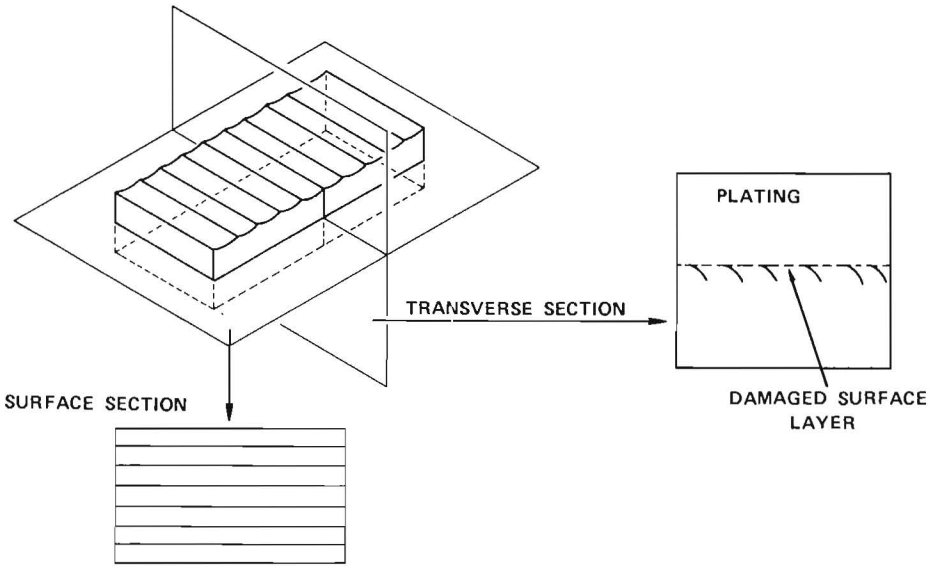


Figure 1. Sectioning views of the machined surface (indicated by the machining grooves) for transmission electron microscopy examination.

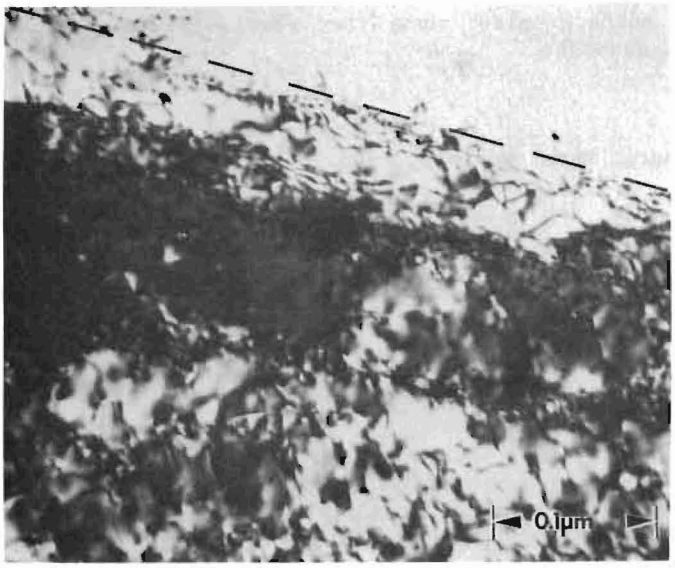


Figure 2. Bright field micrograph of the transverse section of the -5 deg rake surface. The dashed line is the boundary between the sample (lower) and the Cu electroplate (above).

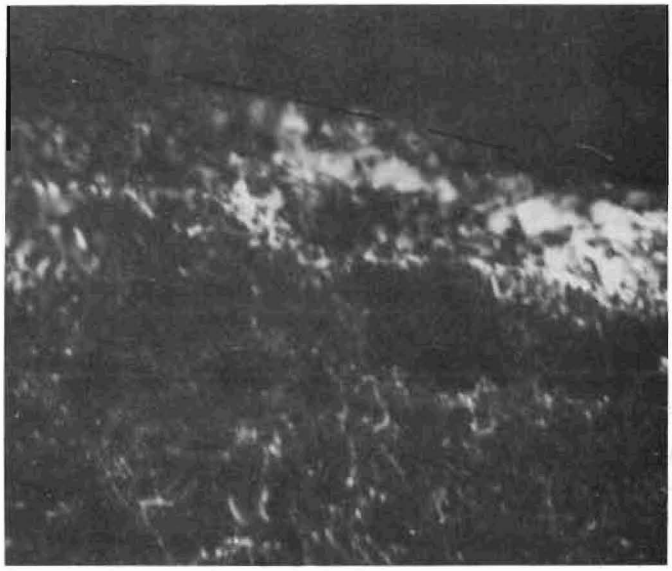


Figure 3. Weak beam dark field micrograph of figure 2.

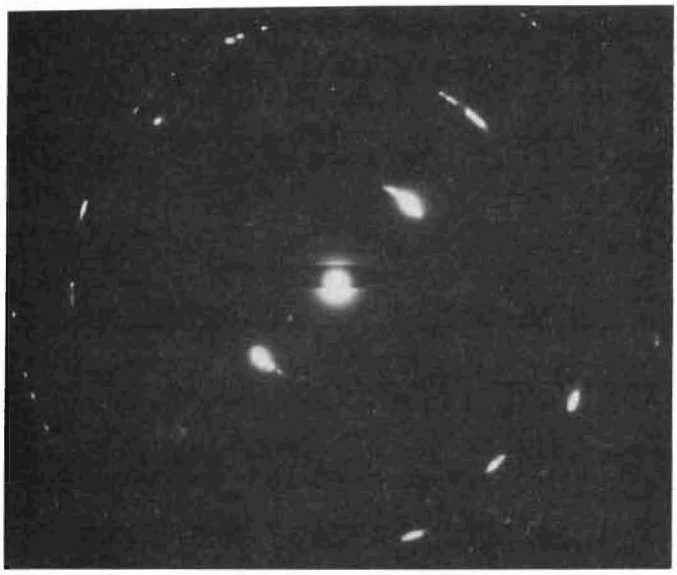


Figure 4. Selected area diffraction pattern of the subsurface deformed region of the -5 deg surface showing 29 deg of rotational misalignment.

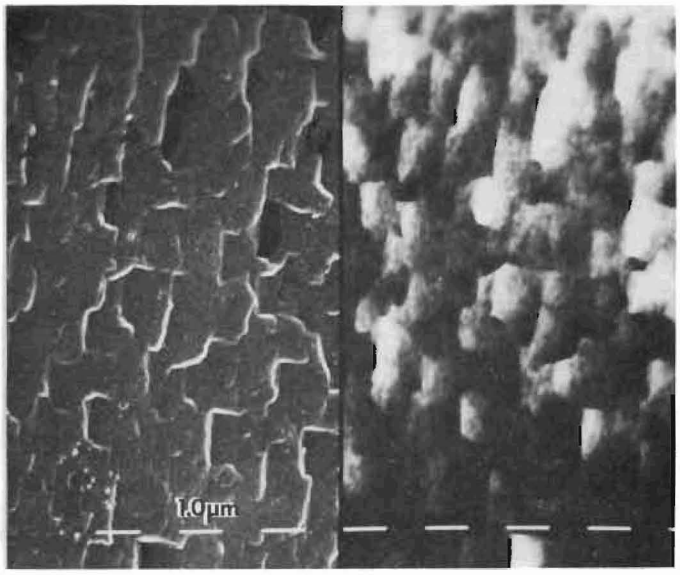


Figure 5. Simultaneous SEM and STEM micrograph of the surface of the -10 deg rake angle sample. The direction of machining is from bottom to top.

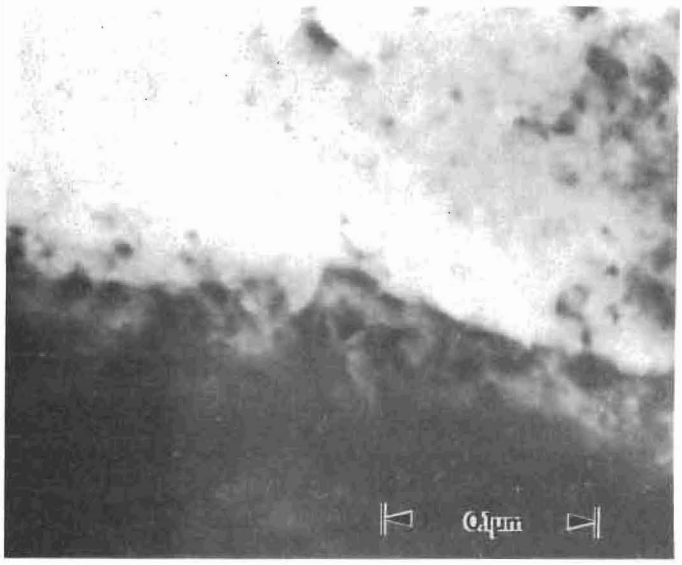


Figure 6. Bright field image of a dark-to-light boundary of the -10 deg rake angle surface.

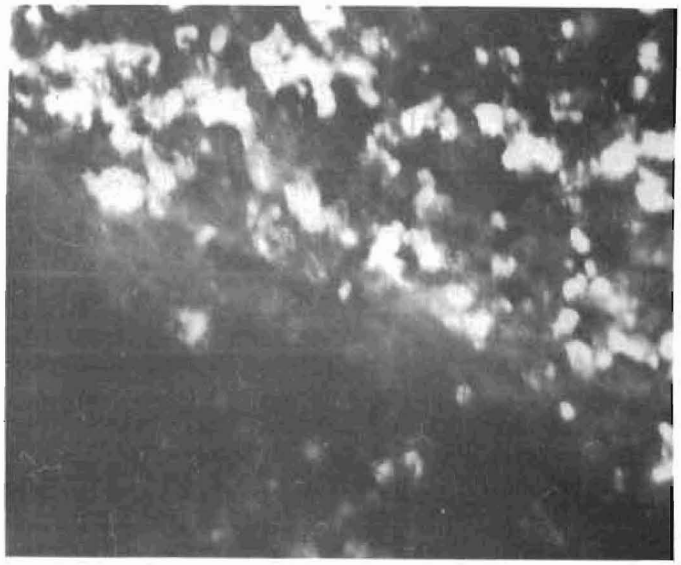


Figure 7. Dark field image of one of the Cu_2O spots in the transmission electron diffraction pattern showing the distribution of the oxide. The area is the same as figure 6.

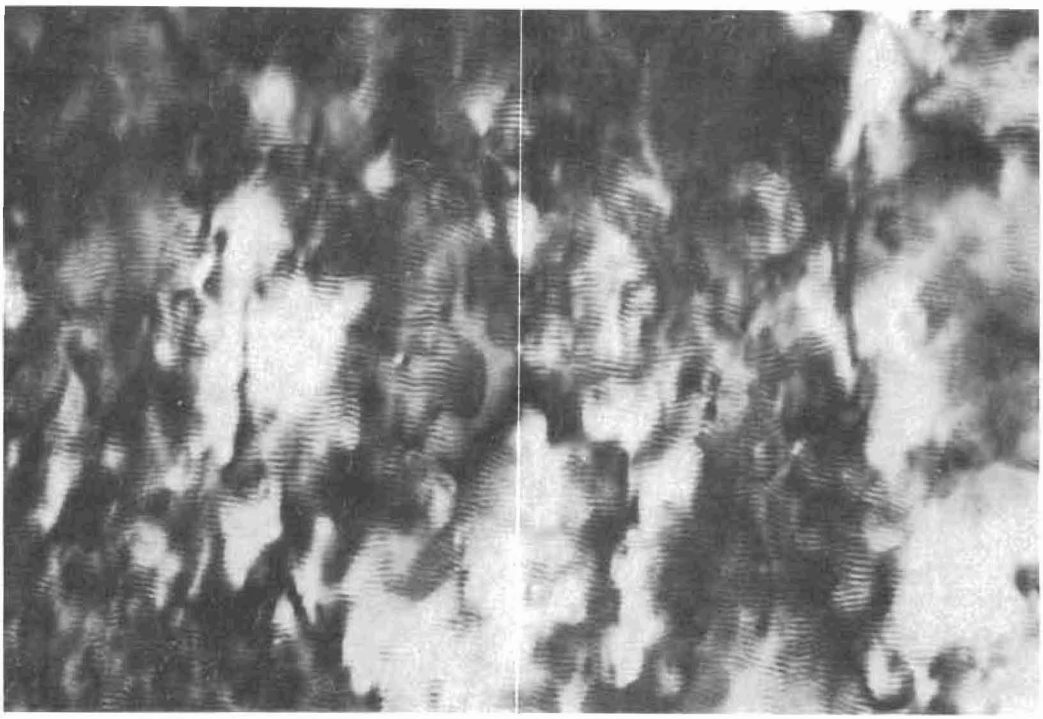


Figure 8. Moire fringe pattern on the -15 deg surface.

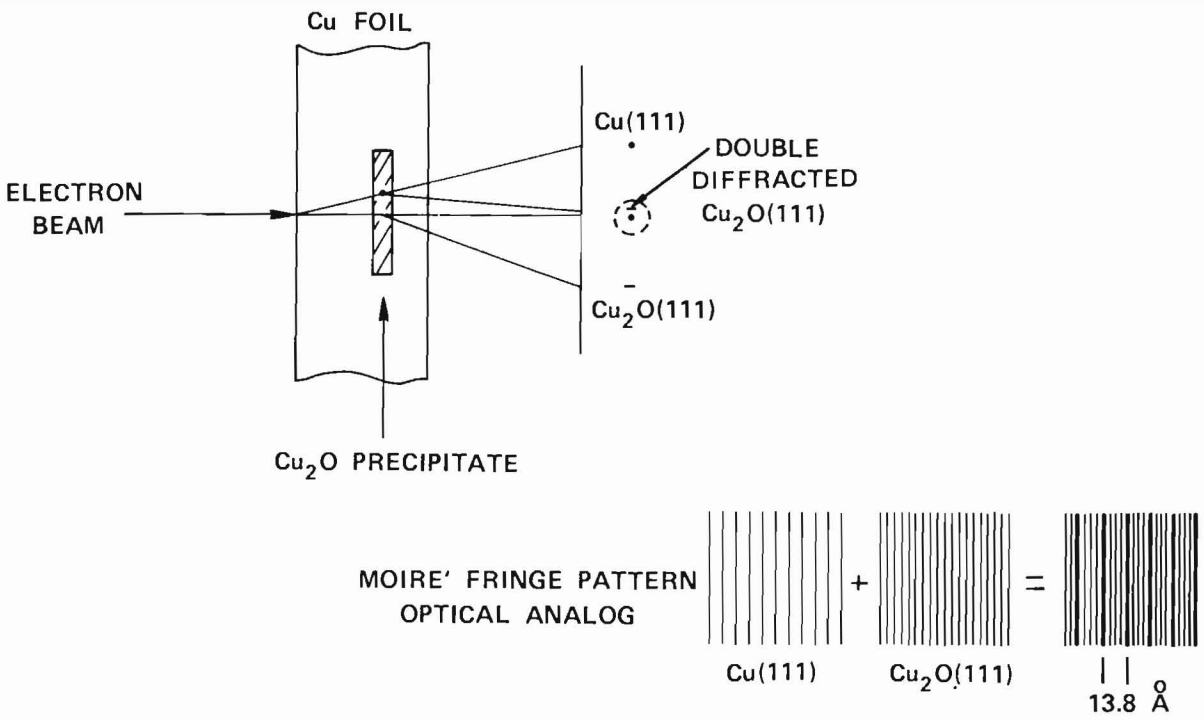


Figure 9. Double diffraction from the subsurface oxide. The machined surface faces the electron beam. The optical analog for the fringe formation is shown below.

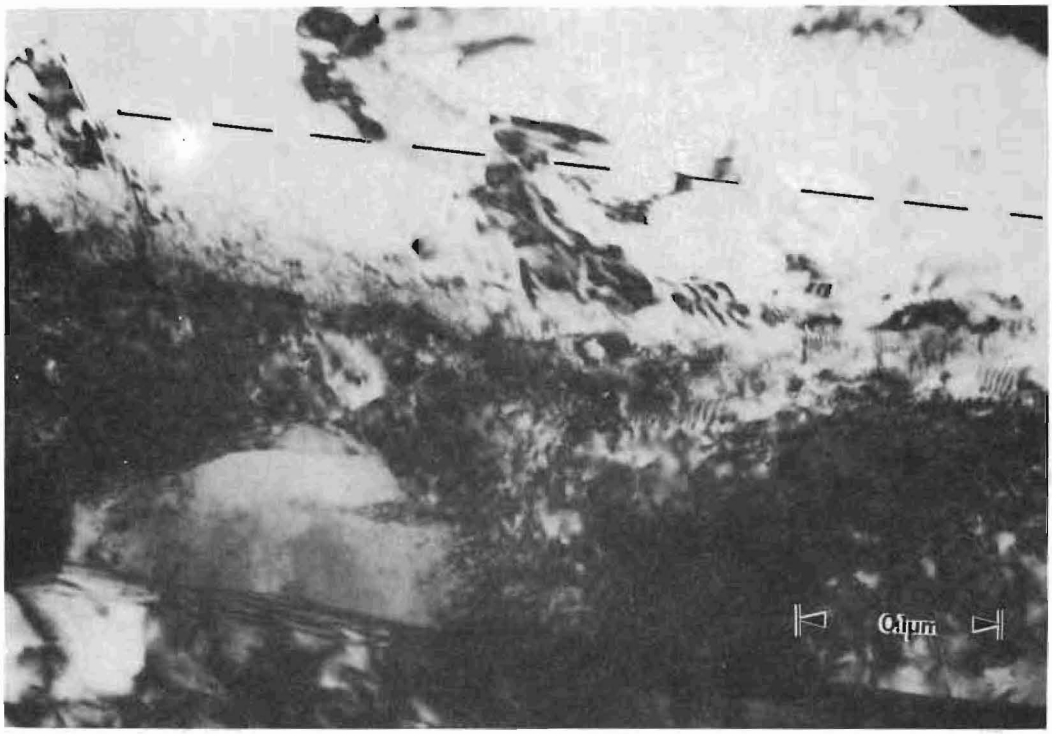


Figure 10. Transverse view of the -15 deg sample. The dashed line marks the boundary between the plating (above) and the sample.

Optical Properties of Diamond-Machined Metal Surfaces and Their Relationship to Physical and Chemical Surface Perfection

D. L. Decker, H. H. Hurt, J. O. Porteus, and D. J. Grandjean

Michelson Laboratory, Physics Division
Naval Weapons Center, China Lake, California 93555

It has been demonstrated that copper and other metal surfaces can be diamond single-point machined (DSPM) to a surface quality which will result in nearly intrinsic optical properties. Especially interesting is the observation of the interrelationship of laser-induced melt and slip thresholds for DSPM copper for different surface preparation methods. Particularly important parameters are the machining fluid and the tool geometry. Both of these factors influence the degree of cold work introduced into the surface. In a companion paper at this conference, the nature of the surface damage is correlated with machining conditions. In this paper, the same surfaces are described optically. Significant variation in optical and mechanical properties can be demonstrated. The ability to change the characteristics including laser damage properties of the machined surface can be used in some cases to advantage, to actually tailor the surface to the requirements of a specific application.

Key words: diamond-machined metals; laser damage characteristics; metallographic structure; optical properties.

Introduction

It is usually judged that a diamond single-point machined (DSPM) surface is either "good" or "bad," based upon a visual inspection. However, a more thorough optical or physical evaluation will show a large range of properties even within the boundaries of a "good" surface. The obvious effect of a single-point tool in working a surface is the formation of a chip, in the case of a ductile material like a metal (fig. 1). The idealized structure of the resulting surface, shown in profile, is illustrated in figure 2. The residual surface microstructure is readily apparent in a microscopic examination of the surface, as in the Nomarski micrograph in figure 3 [1].[1] For the purposes of this paper, it is necessary, however, to examine the structure of the machined surface and subsurface on a much smaller scale. In figure 4, a two-stage transmission electron micrograph is reproduced, showing that on a small scale, a DSPM surface can be extremely smooth. This smoothness is a consequence of the use of an exceedingly sharp tool and the well-defined shear plane in the material being worked. The corresponding subsurface structure is likewise on a fine scale. The relatively damage-free surface and subsurface is, of course, the origin for the high-quality optical characteristics which a DSPM surface can possess.

This paper discusses simple machining theory for a metal and provides a theoretical basis for optical absorption and scatter from a model of surface and subsurface structure. A discussion of the mechanical effects of surface hardness and slip is included, with reference to pulsed laser-induced damage as a tool for diagnostic or evaluation purposes. A companion paper at this conference presents thin-section transmission electron microscopy results for samples prepared in an identical fashion to those prepared for optical measurement [2].

Mechanical Effects

Much work has been expended in developing orthogonal machining theories [3]. These theories are based upon models of the mechanics of the external interaction of the tool and workpiece. These theories are somewhat useful in predicting tool forces, power requirements in machining, and other external consequences of the process [4]. However, the internal mechanics of machining, which concerns us here, has received scant attention. The problem is very difficult and is based upon

*Work supported by the Defense Advanced Research Projects Agency and by Naval Weapons Center Independent Research Funds.

[1] Numbers in brackets indicate the literature references at the end of the paper.

incomplete knowledge of the dynamic resolution of the tool force in the material. Figure 5 shows schematically the net tool force and the shear plane, which is inclined at angle θ to the work surface. The net force is, of course, compressive, with only the tangential component effective in shearing the chip from the surface. The tool rake shown in this figure is negative. Plastic deformation is not limited to a simple plane shear, but also results in a disturbed layer of some depth. Turkovich has derived an expression for the thickness of this layer and his result provides values more or less in agreement with other data [5]. If D is the layer thickness,

$$D \approx 1/3(F/K) \quad , \tag{1}$$

where F is the net tool force per unit width of cut, and K is the yield stress of the work material. For copper, $K \approx 10$ kg/mm^2, and, for a finish cut of depth 10^{-3} mm, a typical tool force, F, is ≈ 1 gm/mm, so $D \approx 10^{-4}$ mm. Contrary to the usual rule based upon common machining experience, this depth is an order of magnitude smaller than the depth of cut. The tool force is related to the yield strength of the material being worked, the depth of cut, the tool rake angle, and the friction of the chip on top of the tool. The resolution of the total tool force into normal and tangential components is shown in figure 6 as a function of tool rake angle.

As the tool rake is made increasingly negative, the total tool force is increased, with the large increase in normal force resulting in a "burnishing" action. The lattice dislocations and vacancies produced have the effect of inhibiting slip, so a harder surface is produced [6]. A very instructive set of data is shown in figure 7, where surface microhardness of DSPM OFHC copper is plotted vs tool rake angle. As the tool rake angle becomes more negative, starting at +5 deg, the hardness increases monotonically to -10 deg as expected. The 20% increase in hardness is similar to that seen in other cold-working studies [6]. The turnover at -10 deg is unexpected and is a result of a new effect. Examination of the surface microscopically reveals intergranular slip, the result of recovery [2,7]. At -20 deg, the surface is actually quite rough and is a result of actual recrystallization [2]. Data also appear in figure 7 which show the effects of machining lubricant on surface hardness. The method of application of the lubricant is also important, as is shown for the vigorous and gentle-flow mineral oil points. The hardest surface was obtained with water as a machining fluid and is not unexpected, since the lubricity of water is much poorer than the petroleum fluids examined.

Optical Effects

To understand the implications of the subsurface dislocation concentration produced by DSPM on the optical properties of the metal surface, it is necesssary to consider the consequences of the simple Drude model [8]. The infrared absorptance at normal incidence, A, is approximately given by

$$A \approx 2/\omega_p\tau \quad , \tag{2}$$

where ω_p is the plasma frequency of the free electrons in the metal, and τ is the electron relaxation time.

$$\omega_p^2 = 4\pi Ne^2/m^* \quad , \tag{3}$$

where N is the electron concentration, m^* is the effective electron mass, and e is the electronic charge.

At room temperature for a well-ordered, pure metal, the electron relaxation time is controlled by scattering from lattice phonons. For copper, $\tau \sim 3 \times 10^{-14}$ sec, so the electron mean free path is ~ 470 Å. However, for severe work hardening, scatter from dislocations can be evident also at room temperature. Hence, it should be possible to observe changes in optical absorption as the electron relaxation time is varied by introducing more or less dislocation into the surface region by changing tool rake angle or lubricant. The wavelength region where the simple theory just presented will apply is, of course, in the infrared, beyond 1 μm or so for copper. Figure 8 is a plot of absolute reflectance R vs wavelength for pure copper prepared by different methods. Neglecting scatter, $R = 1 - A$. The DSPM surface was obtained using a tool of -5 deg rake. In the infrared, no significant differences exist between these surfaces. In the near-infrared, visible, and ultraviolet, interband absorption is present and results in much more complicated effects [9]. Figure 9 is a plot of the change in reflectance normalized to the quantity 1 - R vs rake angle for OFHC copper. If scatter is neglected, which is valid except at -20 deg where the surfaces are quite rough, the quantity plotted is $\Delta A/A$. Four selected wavelengths are shown: 3200 Å, 6000 Å, 1.0 μm, and 10.6 μm.

It would be expected that the 10.6 μm and 1.0 μm data would be similar and that the 6000 Å and 3200 Å data would fall into another class. The 10.6 μm data, starting at +5 deg rake, show the expected increase in absorption with decreasing rake angle. This effect continues on to -5 deg, not to -10 deg, the rake angle at which recovery was evident in surface microhardness (see fig. 7). At the point at which recovery occurs, the absorption should show a decrease due to the greater lattice

order, as observed. The results at 1.0 μm are totally unexpected, and the steadily decreasing absorption with decreasing rake angle to −15 deg is unlike the behavior in the visible and ultraviolet as well. From table 1 it is seen that an intermediate behavior is present at 2.7 μm, in which the initial decrease in absorption with decreasing rake angle persists only to 0 deg and then shows more or less the expected trend from 0 to −20 deg. An explanation of these complicated effects is not available, but that deficiency does not reduce their practical value. At 1.0 μm, the absorptance changes by nearly 50% between +5 and −15 deg rake angle. The measured reflectance at 1.0 μm and −15 deg rake is as high or higher than values obtained by other methods known to produce excellent surfaces (see fig. 8). Kerosene was used as a lubricant for these studies. The section on Chemical Effects contains some additional conjecture on the origin of the effects observed at visible wavelengths.

Table 1. Absolute normal incidence reflectance of OFHC copper prepared by diamond single-point machining. Kerosene used as a lubricant. Accuracy ±0.001

λ	Tool rake angle in degrees					
	+5	0	−5	−10	−15	−20
3200 Å	0.3092	0.3030	0.2937	0.3038	0.3094	0.2814
4400	0.4766	0.4749	0.4631	0.4711	0.4834	0.4456
5200	0.5704	0.5682	0.5596	0.5696	0.5770	0.5401
6000	0.9049	0.9019	0.9017	0.9023	0.9083	0.8813
7600	0.9748	0.9758	0.9763	0.9765	0.9782	0.9698
1.0 μm	0.9806	0.9821	0.9831	0.9847	0.9890	0.9802
2.7	0.9939	0.9954	0.9942	0.9923	0.9942	0.9917
5.0	0.9926	0.9941	0.9909	0.9941	0.9915	0.9942
10.6	0.9912	0.9893	0.9876	0.9889	0.9888	0.9918

A limited examination of the effects of lubricant upon the reflectance was made at −5 deg rake angle. The data plotted in figure 10 are for mineral oil and water. The reference reflectance was obtained using kerosene. The ordinate is then the change in absorption with fluid (neglecting scatter) relative to the apparent absorption using kerosene. The largest effect is at 1.0 μm, where a decrease in absorptance of over 50% is seen in changing from a gentle to a vigorous flow of mineral oil. Water, like the gentle-flow oil case, also produces relatively high absorption. The obvious explanation is that both gentle mineral oil flow and water produce higher chip/tool friction, hence greater tool forces and therefore greater disturbance to the lattice and higher absorption. The results at 10.6 μm, however, are inexplicable. The results at shorter wavelengths show no significant variation with lubricant or method of application.

Optical scatter from a metal arises primarily from surface microirregularity which is a direct result of the finishing operation and to some extent the inhomogeneity of the basic material [10]. Figure 11 is a schematic illustration of the scatter produced by a rough surface. Although the angular distribution of the scattered light depends upon the detailed spatial frequency distribution of the roughness, with only simple assumptions the total integrated scattered (TIS) light can be simply related to the rms roughness δ. Figure 12 is a plot of TIS vs wavelength for DSPM OFHC copper using kerosene as a lubricant. Several different tool rake angles are shown.

In the far- and mid-infrared, all surfaces produced equivalent total scatter. However, due to recrystallization subsequent to machining, the −20 deg results are nearly an order of magnitude larger than at −10 or +5 deg at the shorter wavelengths. Consequently, surfaces machined at −20 deg rake would probably not be very useful in the visible but could be used with no qualification in the far-infrared, insofar as scattered light is considered. The angular distribution of the scattered light from a surface is a very complex subject [11]. Figure 13 is a plot of differential scattered light, normalized to the incident beam intensity vs scattering angle for a DSPM surface of OFHC copper. The angular direction of a ray of scattered light is determined by the periodicities of the surface. For a surface with a single period a, as shown in figure 14, the diffraction angle ϕ_m of the mth order is given by the simple grating equation shown [12]. It is convenient to measure the diffraction angle, θ, relative to the specular reflection direction. For the data just presented, it can be seen that the prominent structures I1 and I2 are first- and second-order peaks associated with the basic machining structure and, in fact, agree quite well with the 9.5 μm feed rate employed.

As a practical matter, not very much scattered energy is contained under the diffraction peaks associated with the basic machining structure compared to the overall distribution. However, the position of the peaks I1, ... is directly controlled by the feed rate employed, and so this scattered light can be deliberately directed to baffles or outside of the field of view when designing an optical system. The majority of the scattered light has its origin in uncontrolled tool/chip/workpiece motion and is not presently well enough understood to allow "control" in the sense discussed above.

Chemical Effects

Several previous papers have reported results of Auger analysis of diamond-machined surfaces [13,14]. For "well-cleaned" surfaces, no unambiguous evidence of residual machining oil has been obtained, either by Auger or by optical spectroscopic methods in the near-infrared. Carbon is ubiquitous on even "UHV-clean" surfaces, independent of their history, and so low-level hydrocarbon contamination is difficult or impossible to identify. However, oxygen often has been identified on fresh, machined copper surfaces as a contaminant [13,15]. Surface oxygen and carbon Auger intensities were greatly reduced by sputtering away only 10 Å of material [13]. In a companion paper at this conference, direct TEM dark-field examination of copper surfaces prepared identically to those examined in this paper, has revealed the presence of the high-temperature copper oxide phase Cu_2O. The oxide concentration becomes greater as the tool rake becomes increasingly negative [2]. Interestingly for high negative rake conditions, the cuprous oxide is growing epitaxially on the copper crystallites in a surface region on the order of 100 Å deep. The origin of the oxide growth is not known, but is highly significant since the $1/e^2$ optical penetration depth for visible and infrared wavelengths is $\sim$130 Å, and thus the optical absorption is especially sensitive to the presence of the oxide. Cuprous oxide is a direct gap semiconductor with a band edge at approximately 2 eV (0.5 μm) [16]. Hence, any optical effect of the oxide should occur at wavelengths shorter than 0.5 μm and would be negligible at larger wavelengths. Figure 15 is a plot of absorptance (1 - R) vs wavelength from 0.6 to 1 μm for various tool rake angles. As can be seen, a curious "kink" is present in the data at 0.7 μm for the -15 deg rake sample. A hint of the effect is also present for the -5 deg rake data. Actually, of course, the oxide is not present as a continuous film, and its optical effect is thus complicated by its dispersal [17]. An appropriate theoretical approach using Maxwell-Garnet theory would in fact result in the absorption shifting to longer wavelength [18]. However, using available bulk Cu_2O and Cu optical constants, several models of oxide dispersion have not yielded an absorptance curve resembling that in figure 15. It seems likely, however, that the absorptance anomaly noticeably present in the -15 deg rake data at 0.7 μm is due to the presence of dispersed Cu_2O in some way.

Laser-Induced Damage

Although laser-induced damage is usually regarded as an unwanted consequence of high intensity loading of a surface, it can be employed as a valuable diagnostic tool [19]. Figure 16 is a Nomarski micrograph of a laser-damaged site on a DSPM OFHC copper surface. Of major interest is the nonuniform, selective nature of the damage site, including evidence of localized mechanical slip and melting. A very instructive correlation has been previously discovered involving an inverse relationship between slip and melt thresholds [20]. Figure 17 is a plot of threshold data for pure copper prepared in a variety of ways. As previously discussed, as the disorder increases in the material, the yield point increases. Hence the laser-induced slip threshold is increased. At the same time, the disorder causes the absorption to increase, and hence the laser-induced melt threshold decreases. The stored energy associated with the defect population also tends to reduce the melt threshold. The samples employed to obtain the empirical "curve" identified by tool rake angle in Figure 18 were part of the reflectance and scattered light study just discussed. It would be expected that as the tool rake becomes increasingly negative, the surface would become more slip resistant. The +5 and -5 deg rake data in fact show this relationship. The -10 deg point does not continue this trend as a consequence of recovery. Since recovery or recrystallization are both time- and temperature-dependent, some inconsistency can be expected in attempting to determine a rake angle which can produce long-term, stable, hardened surfaces.

As a final example of the usefulness of high negative rake machining, consider the selective damage frequency data presented in Figure 19 [19]. The fluence used in the probe pulse was on the order of one-third of the melt threshold. If the surface was uniform in optical and thermal properties, every site on the surface would survive and the corresponding histogram bar would be at 100%. In testing the various surfaces shown in this figure, several hundred individual sites were shot. The "hard" diamond-turned sample was machined at -10 deg rake angle and produced a surface superior in uniformity to virtually all other preparation methods. This effect is apparently a result of the closing of surface microdefects, i.e., cracks or voids, and the subsequent refinement of the surface microstructure by recovery.

Conclusions

In this paper, a substantial range of optical and mechanical effects has been demonstrated, controllable by varying machining conditions. Both tool rake and machining fluid are important variables. The particular material chosen for this study was pure copper, and the specific results obviously apply only to that material. For other materials, specific investigation would be necessary. Although only an imperfect understanding of the fundamental origin of the effects observed is available at present, this is not a serious impediment to application of these results to practical problems. In a specific application, diamond single-point machined (DSPM) surfaces can be tailored empirically to provide optimum characteristics. For example, for copper, negative rake machining produces substantial improvement in surface uniformity. Such an improvement could be important in enhancing

the ability of dielectric-coated surfaces to withstand environmental attack. A film deposited on a uniform surface could have less tendency to form "pinholes." The variation in absorption has importance to the use of DSPM mirrors in industrial high power lasers. Not all "good" surfaces are identical. An understanding of their properties can be taken to practical advantage to tailor the surface properties to the specific application.

References

[1] Decker, D. L.; Bennett, J. M.; Soileau, M. J.; Porteus, J. O.; Bennett, H. E. "Surface and optical studies of diamond-turned and other metal mirrors," Proceedings of the SPIE 93; 71-80; 1976.

[2] Hurt, H. H.; Decker, D. L. "Inherent mechanical damage in diamond-machined optical surfaces," this conference.

[3] Abebe, M.; Appl, F. C. "A slip-line solution for negative rake angle cutting," Proceedings of the 9th North American Manufacturing Research Conference; 341-348; 1980.

[4] Burnham, M. W. "The mechanics of micromachining," Proceedings of the SPIE 93; 38-45; 1976.

[5] Von Turkovich, B. F. "Surface damage in metal cutting," Proceedings of the Engineering Seminar on New Industrial Technologies, Pennsylvania State University; 1965 June 27-30.

[6] Cottrell, A. H. An Introduction to Metallurgy. New York; St. Martin's Press; 1967. P. 399.

[7] Christian, J. W. The Theory of Transformation in Metals and Alloys. New York; Pergamon Press; 1965. P. 133.

[8] Stern, F. "Elementary optical properties of solids," in Solid State Physics, Vol. 15, Seitz, F.; Turnbull, D., ed. New York; Academic Press; 1963. Pp. 344-350.

[9] Johnson, P. B.; Christy, R. W. Phys. Rev. B 6; 4370; 1972.

[10] Bennett, H. E.; Porteus, J. O. J. Opt. Soc. Am. 51; 123; 1961.

[11] Elson, J. M.; Bennett, J. M. J. Opt. Soc. Am. 69; 31; 1979.

[12] Jenkins, F. A.; White, H. E. Fundamentals of Optics, 3rd Ed. New York; McGraw-Hill; 1957. P. 333.

[13] Decker, D. L.; Soileau, M. J.; Porteus, J. O.; Bennett, J. M. "Surface, optical, and laser-damage characteristics of diamond-turned metal mirrors," in Laser Induced Damage in Optical Materials: 1976, Glass, A. J.; Guenther, A. H., ed. 1976 July 13-15; Boulder, CO. Nat. Bur. Stand. (U.S.) Spec. Publ. 462; 1976 December. Pp. 158-164.

[14] Oron, M.; Svendsen, L. G.; Sorensen, G. "Laser damage resistant copper surfaces with high reflectivity after oxidation," in Laser Induced Damage in Optical Materials: 1979, Bennett, H. E.; Glass, A. J.; Guenther, A. H.; Newnam, B. E., ed. 1979 October 30-31; Boulder, CO. Nat. Bur. Stand. (U.S.) Spec. Publ. 568; 1980 July. Pp. 187-197.

[15] Unpublished Naval Weapons Center analysis results.

[16] Agekyan, V. T. Phys. Stat. Sol. a 43; 1, 11; 1977.

[17] Weichman, F. L.; Reyes, J. M. Can. J. Phys. 58; 3, 325; 1980.

[18] Maxwell Garnett, J. C. Philos. Trans. R. Soc. London 205; 237; 1906.

[19] Porteus, J. O.; Decker, D. L.; Faith, W. F.; Grandjean, D. J.; Seitel, S. C.; Soileau, M. J. IEEE J. Quantum Electron. QE-17; 2078-2085; 1981.

[20] Porteus, J. O.; Decker, D. L.; Grandjean, D. J.; Seitel, S. C.; Faith, W. N. "Defect-damage-resistant copper mirrors in laser-induced damage in optical materials," in Laser Induced Damage in Optical Materials: 1979, Bennett, H. E.; Glass, A. J.; Guenther, A. H.; Newnam, B. E., ed. 1979 October 30-31; Boulder, CO. Nat. Bur. Stand. (U.S.) Spec. Publ. 568; 1980 July. Pp. 175-186.

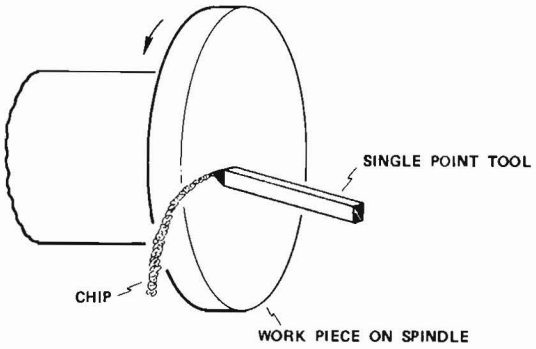
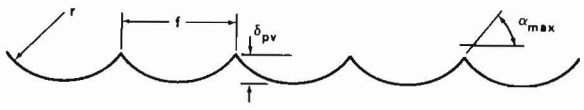


Figure 1. Schematic diagram of the basic single-point machining process showing chip formation by a single-point tool as in machining a ductile material.



$\delta_{pv} \cong f^2/8r$ ASSUMING THAT $f/r \ll 1$

$\alpha_{max} \cong f/2r$

OR RMS VALUES:

$\delta_{rms} \cong \delta_{pv}/\sqrt{5}$

$\alpha_{rms} \cong \alpha_{max}/\sqrt{3}$

Figure 2. Idealized transverse surface profile of a surface machined by a round-nosed tool of radius r and feed rate f. Shown are expressions for the peak to valley and rms finish and slope.



Figure 3. Nomarski micrograph of a diamond single-point machined (DSPM) OFHC copper surface showing the residual structure illustrated in figure 2. Notice also the grain boundaries of individual crytallites of copper which are ~250 μm across.



Figure 4. Two-stage replica transmission electron micrograph of a DSPM surface of OFHC copper. This nearly featureless surface is characteristic of a high-quality diamond-machined part.

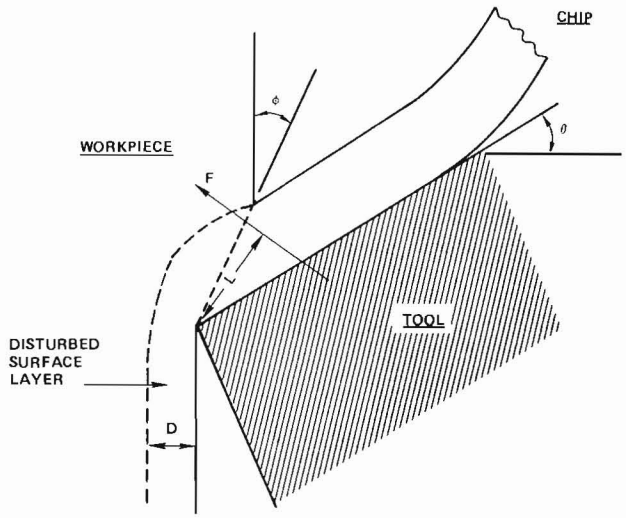


Figure 5. A simplified sectional diagram of chip formation by a single-point tool showing the direction of total tool force F which has a moment arm L about the tool tip, the idealized single shear plane shown inclined at an angle ϕ from the work surface, and a layer of depth D of disturbed surface material. Negative tool rake angle θ is shown.

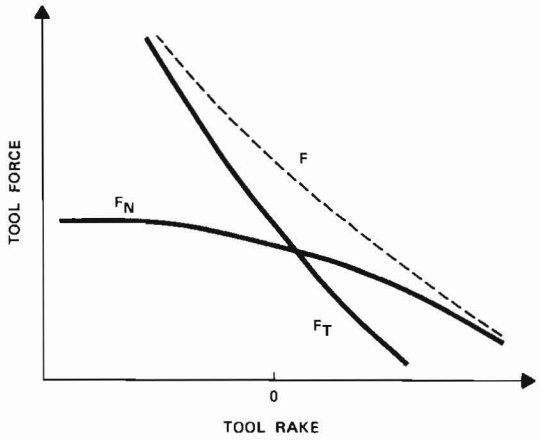


Figure 6. A schematic diagram of total tool force F and normal and tangential components F_N and F_T, respectively, vs tool rake angle. Note that the normal force tends to increase with decreasing rake angle and the tangential force tends to approach a constant value.

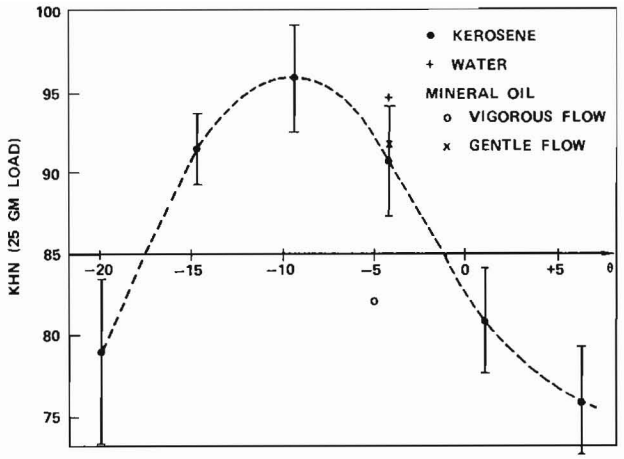


Figure 7. DSPM OFHC copper microhardness vs tool rake angle. Vicker's hardness tester loading 25 gm. Shown are points for kerosene, water, and mineral oil machining lubricant.

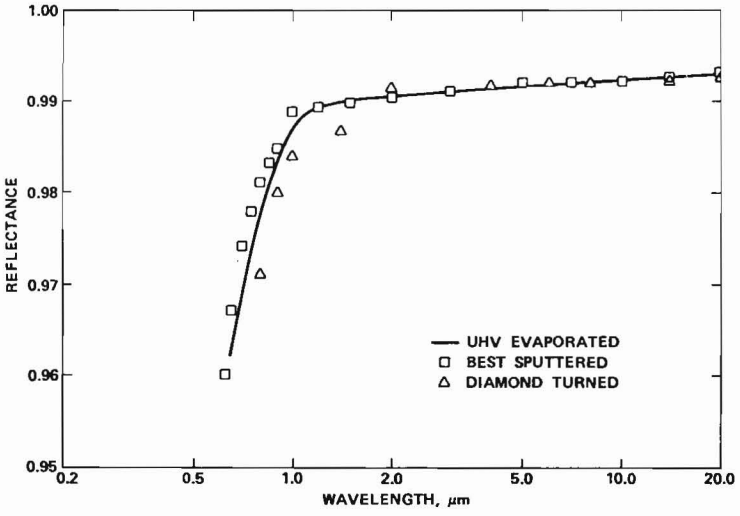


Figure 8. Absolute normal incidence reflectance vs wavelength for optical surfaces prepared by thermal evaporation and sputtering onto polished fused quartz and by DSPM at -5 deg rake angle and kerosene lubricant.

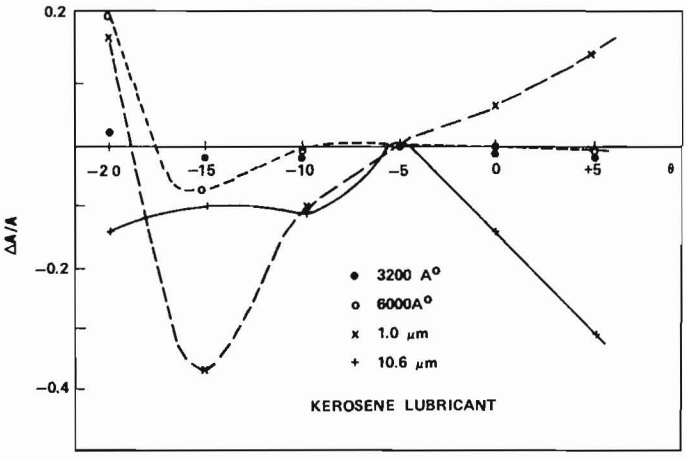


Figure 9. Normalized change in optical loss for DSPM OFHC copper at normal incidence vs rake at four wavelengths: 3200 Å, 6000 Å, 1.0 μm, and 10.6 μm. The quantity $\Delta A/A$ is derived from reflectance data and is equal to $(R_{-5}-R_\theta)/(1-R_{-5})$ (see table 1). If scatter is neglected, it is equal to the change in absorptance normalized to the absorptance. See text for details.

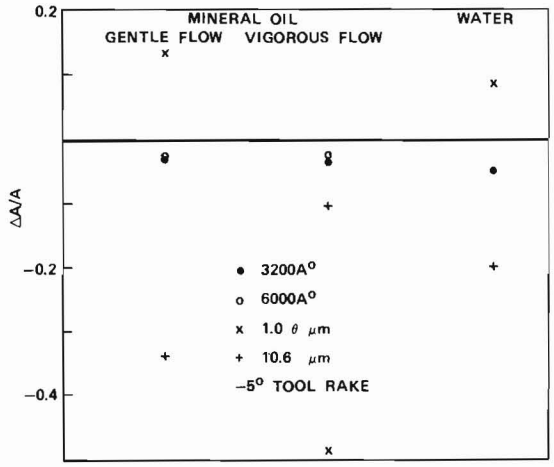


Figure 10. Normalized change in optical loss for DSPM OFHC copper at normal incidence for various lubricants at 3200 Å, 6000 Å, 1.0 μm, and 10.6 μm. See text for detailed discussion.

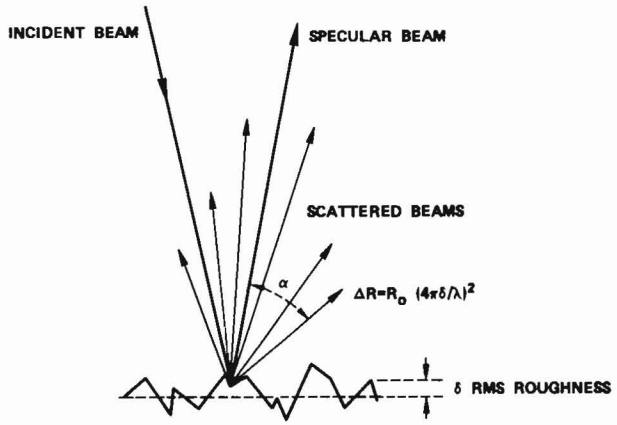


Figure 11. Schematic illustration of light scattering from a rough surface. The fraction of light scattered ΔR is related to the fraction specularly reflected R, the rms roughness δ, and the wavelength λ by the simple expression given.

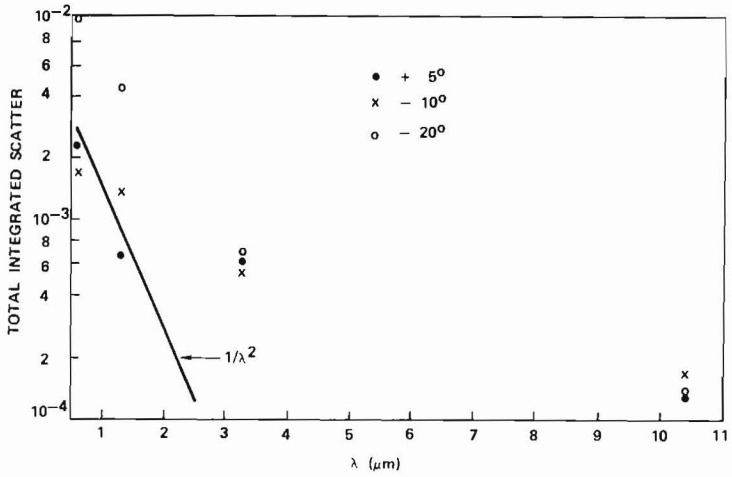


Figure 12. Plot of the total integrated scatter ΔR obtained from a Coblentz sphere scatterometer vs wavelength for DSPM OFHC copper at the rake angles +5, −10, and −20 deg. The line shown varying as $1/\lambda^2$ is the theortical wavelength dependence (see fig. 11).

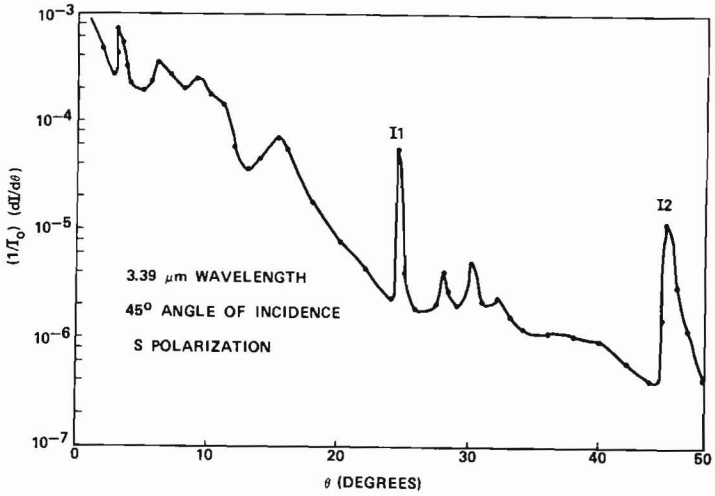
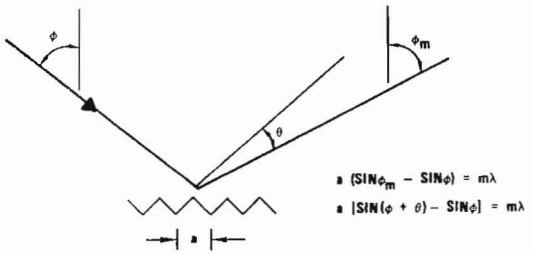


Figure 13. Angular distribution of scattered light intensity $(1/I_0)(dI/d\theta)$, where θ is measured from the specular direction. Complex structure is present. Peaks I1 and I2 are caused by first- and second-order diffraction from the residual machining structure. See text and figure 14 for details.



FOR THE DATA JUST SHOWN

m = 1
a = 3.39 μm / [SIN 45 − SIN (45 − 24.5)] = 9.50 μm
m = 2
a = 6.78 μm / [SIN 45 − SIN (45 − 45.5)] = 9.70 μm

NOMINAL SPACING FROM MACHINING PARAMETERS 9.50 μm

Figure 14. Schematic nonnormal incidence diffraction from a grating of spacing a. Data shown in figure 13 are analyzed.

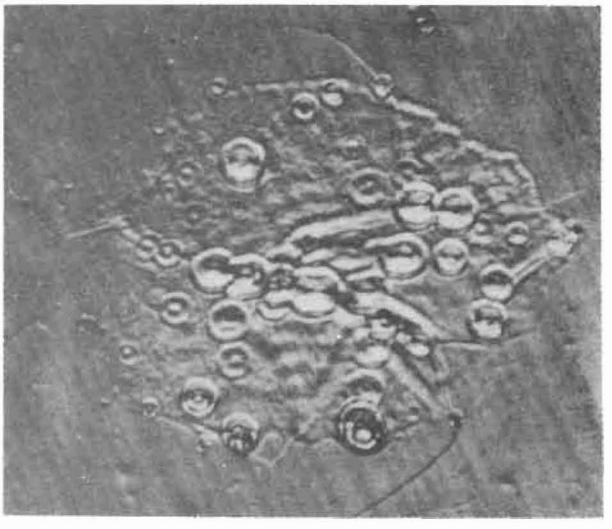


Figure 16. A laser-induced damage site on DSPM OFHC copper produced by a 2 μsec, 10.6 μm wavelength pulse. Shown are a variety of damage effects including localized (spatially selective) melt due to defects, intragranular slip (in the lower center area), and intergranular slip (at grain boundaries outside of central melt area).

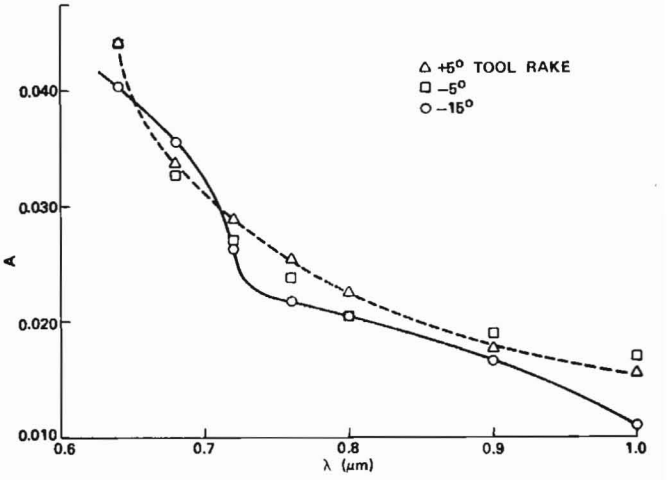


Figure 15. The apparent absorptance (1-R) for diamond-machined OFHC copper in the spectral range from 0.6 to 1.0 μm for the tool rake angles +5, -5, and -15 deg.

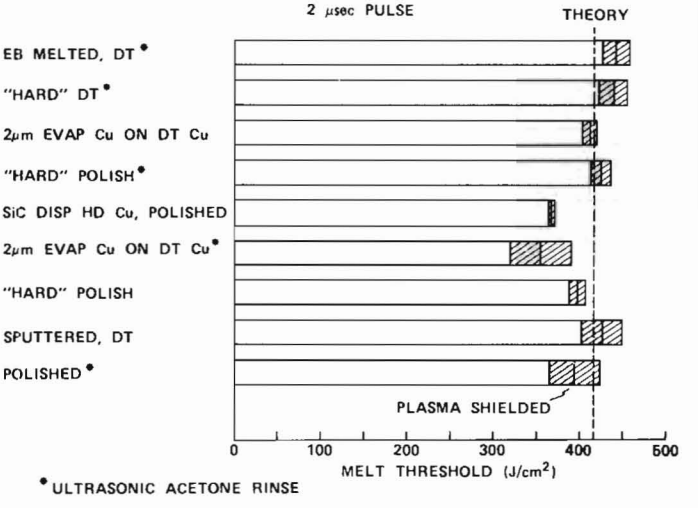


Figure 17. Melt thresholds for 2 μsec duration, single-pulse, 10.6 μm radiation for copper surfaces prepared in different ways. Most of these preparation methods yield high-quality surfaces which display a melt threshold equal to the theoretical value.

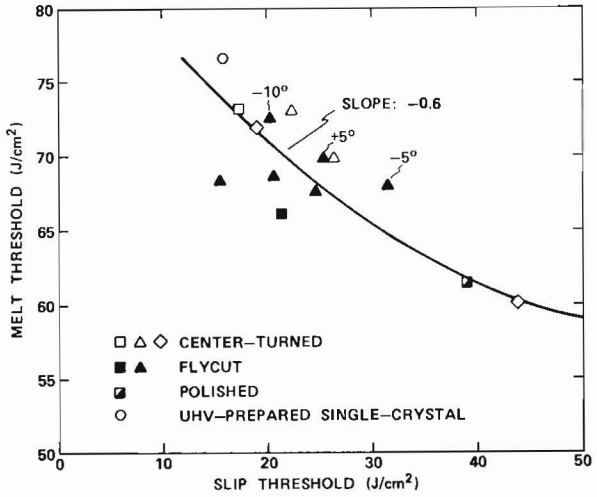


Figure 18. Plot of experimental values of laser-induced melt and slip thresholds for copper including DSPM OFHC copper. Laser pulse was 0.1 μsec in duration at 10.6 μm wavelength. Points labeled +5, -5, and -10 deg refer to tool rake angle and were obtained on samples characterized in various other ways and described earlier in this paper.

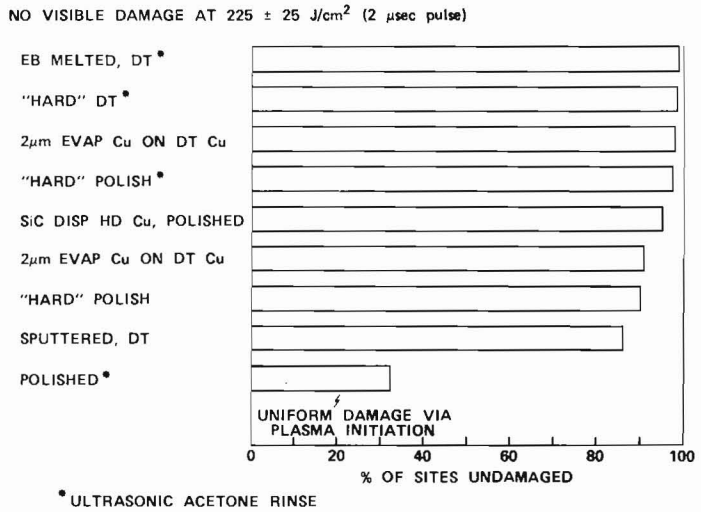


Figure 19. Fraction of sites showing selective laser-induced damage at 10.6 μm wavelength due to surface defects for copper mirror surfaces prepared by different techniques. Perfect surfaces would show no damage (100% of sites undamaged). Details of analysis given in text.

It was pointed out that the data would support more than one shape curve. The speaker agreed, pointing out that the uncertainty in the experimental points was about ±0.1%. It was also suggested that since the quality of a coating depends strongly on the quality of the substrate, the improvements in substrate surfacing might be reflected in better coatings. The speaker agreed and pointed out that the negative rake-angle, hard, diamond-turned surface is very uniform. To the extent that pinholes in dielectric substrates result from substrate defects, one would expect that dielectric films laid down on a hard diamond-turned substrate would be more environmentally durable. Tests of this hypothesis will be made; there are no data at present.

The Effect of Surface Finish on the Laser-induced Damage Thresholds of Gold-coated Copper Mirrors

R M Wood, P Waite and S K Sharma

GEC Research Laboratories, Hirst Research Centre, Wembley, Middlesex, HA9 7PP, UK.

Gold-coated copper mirrors with both diamond-turned and conventionally polished substrates have been evaluated in terms of their laser-induced damage thresholds (LIDT) at 10.6 μm. A detailed study of the surface finish on each component has revealed that a log-inverse log relationship exists between LIDT and substrate preparation.

Keywords : Laser-induced Damage Threshold, 10.6 μm, Copper Mirrors.

1 Introduction

The performance limitations of coated and uncoated copper mirrors are generally well understood. It is currently accepted that the best maximum-reflectors for 10.6 μm are made from uncoated, OFHC (oxygen-free, high conductivity) copper blanks which have been diamond-turned [1]. This combination usually produces reflectivities of about 99.5% and LIDT figures in excess of 10 MW mm^{-2}. Due to the oxidation of the copper surface [2], these mirrors degrade very quickly, causing increased absorptivity which leads to laser damage. For this reason, copper substrates are usually coated to prevent the formation of an oxide layer. Various coatings have been tried, the two most popular being thorium fluoride (ThF_4) and evaporated or electro-plated gold (Au). ThF_4 coatings, however, are very prone to contain pinholes which expose the surface to oxidation, causing component degradation as before. The best optics have so far been fabricated by plating gold onto diamond-turned copper substrates. This method typically produces mirrors which have reflectivities of 99.0% and LIDT power density figures of about 8 MW mm^{-2} (60 ns FWHM pulse). Components which are made from copper substrates which have been conventionally polished using diamond abrasives and then plated with a gold layer have generally been expected to damage at power densities of about 2 MW mm^{-2} [1]. Conventional polishing, however, is considerably lower in cost, and much easier to perform than diamond-turning. It is for these two reasons that it has been considered worthwhile to conduct an investigation into the drawbacks of the conventional method, in oder to seek an improvement in performance.

1.1 Damage at metal surfaces

When a beam of light strikes a metal surface, a small amount of radiation penetrates the metal to a distance called the skin depth. Subsequent absorption of this incident radiation by free carriers can, under certain conditions, raise the temperature of the metal surface above the melting point, causing damage to occur [3]. Correlation between damage thresholds and absorptivity, and thermal properties has been found. Figure 1 shows the relationship between LIDT and absorptivity for several uncoated, diamond-turned copper mirrors. Theory [4] shows that the LIDT energy density, E_D, is proportional to

$$\frac{(T_m-T_o)(k\rho C)^{\frac{1}{2}}}{\alpha_o} \qquad (1)$$

where T_m = melting temperature (°K)
T_o = ambient temperature (°K)
k = coefficient of thermal conductivity
ρ = density (gm cm^{-3})
C = specific heat ($J°K^{-1}$ gm^{-1})
α_o = absorptivity (at T_o, at 10.6 μm)

For a mirror with a coating (e.g. gold-coated copper) α_o is the value associated with the coating whereas k, ρ and C refer to the substrate. The melting temperature, T_m, refers to the material with the lower melting point.

Figure 2 shows that good agreement is found between the theoretically predicted LIDT given by the expression in [1] and the values measured experimentally [5,6]. All the results shown were obtained on clear areas. It can be demonstrated that variations in the LIDT values measured at different points on the surface of a sample are usually associated with defects roughly 1-10 μm in size. Under a high power microscope these features are almost invariably observed to be scratches and digs created during the preparation of the substrate. When the incident radiation hits such a site the absorptivity can become

enhanced due to diffraction, resulting in a much lower value for the LIDT.

2 Experimental

The LIDT measurements were done using a sealed-off CO_2 TEA laser [7]. The output consisted of a 50 mJ pulse in a 60 nS FWHM main peak followed by a 3 μS tail which contained two thirds of the pulse energy. The spatial intensity was a Gaussian in TEM_{00} mode with a $1/e^2$ diameter of 4.5 mm. In the LIDT experiment (fig 3), the beam is focussed on to the sample using a 2 inch AR/AR coated germanium meniscus lens to form a spot 100 μm in diameter. The beam power,which was monitored using a Rofin model 7443 germanium photon drag detector, could be varied by using selected combinations of thin polythene attenuators. Each of the pulses fired on to the sample was recorded on a Hewlett-Packard 1727A storage oscilloscope whilst, at the same time, the surface was monitored visually under a x100 magnification to check for damage.

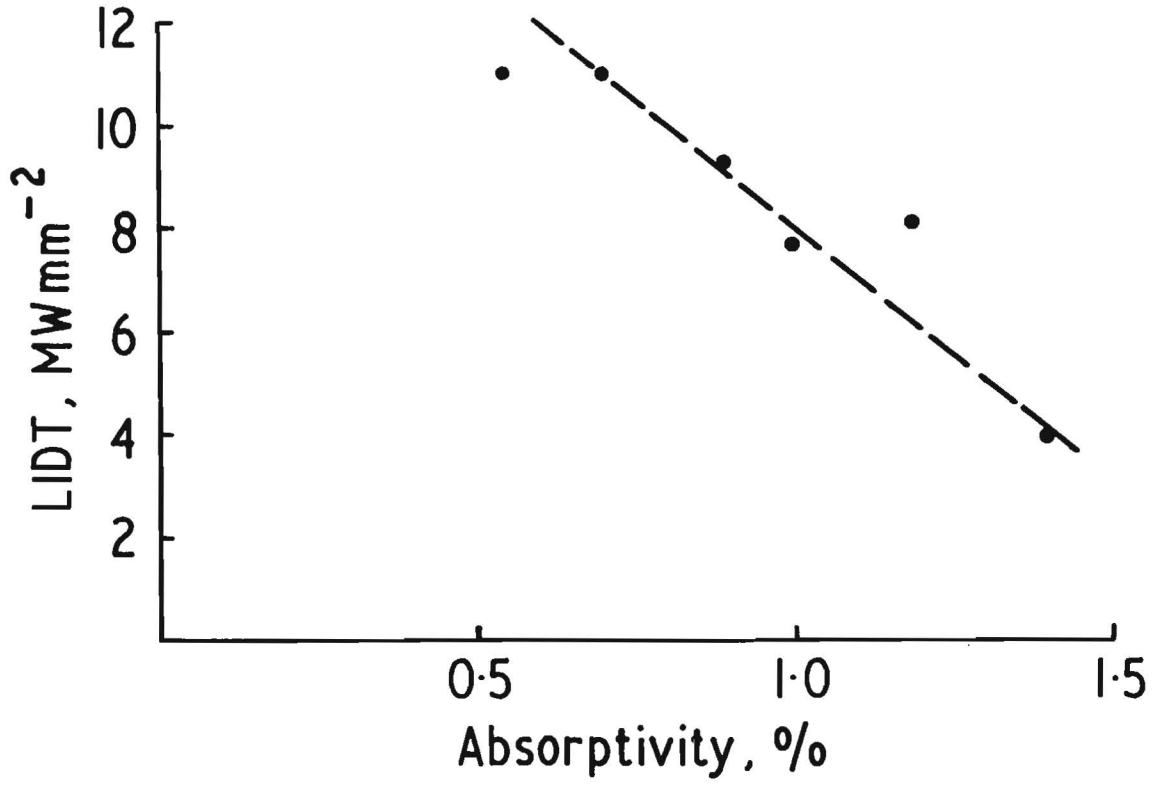


Figure 1 : The effect of absorptivity on the measured LIDT for six diamond-turned copper mirrors

Surface characterisation of the samples was carried out by using a Cambridge S600 scanning electron microscope (SEM) and a Talysurf-5 surface profile analysis system. The SEM was used to gauge scratch and defect sizes, whereas the Talysurf-5 gave an overall roughness-average (fig 7). The roughness-average (R_a) quoted in the results section is the universally recognised, and most used, international parameter of surface roughness. It is the arithmetic mean of the departures of the surface profile from its mean line, (fig 4).

The absorptivity of components at 10.6 μm was measured by a calorimetric technique [1], using an apparatus of better than 0.1% sensitivity. The irradiation source for this equipment was a 30 W CW CO_2 laser, tunable over 80 lines. The same source was chopped at 30 Hz to enable reflectivity measurements to be undertaken using pyroelectric detectors housed in integrating scatter-spheres [1]. The reflectivity measurements made on this equipment were accurate to ±0.2%.

3 Results

Three gold-coated copper mirrors were received from Mirror Techniques Ltd. These were designated M201, M202 and M203 for future reference. The copper substrate of each component had been conventionally polished by Mirror Techniques down to a different grade of diamond paste in order to ascertain the effect of surface prepartion on the absorption coefficient, the reflectivity and the LIDT at 10.6 μm. The results of this initial characterisation are shown in table 1. The reflectivity and absorption figures for all three components M201, M202 and M203 were as good as any diamond-turned copper substrate, however the LIDT values varied by a great deal. The reason for this variation was not obvious from either visual observation of the gold coating, nor from the absorptivity figures, which were all about equal.

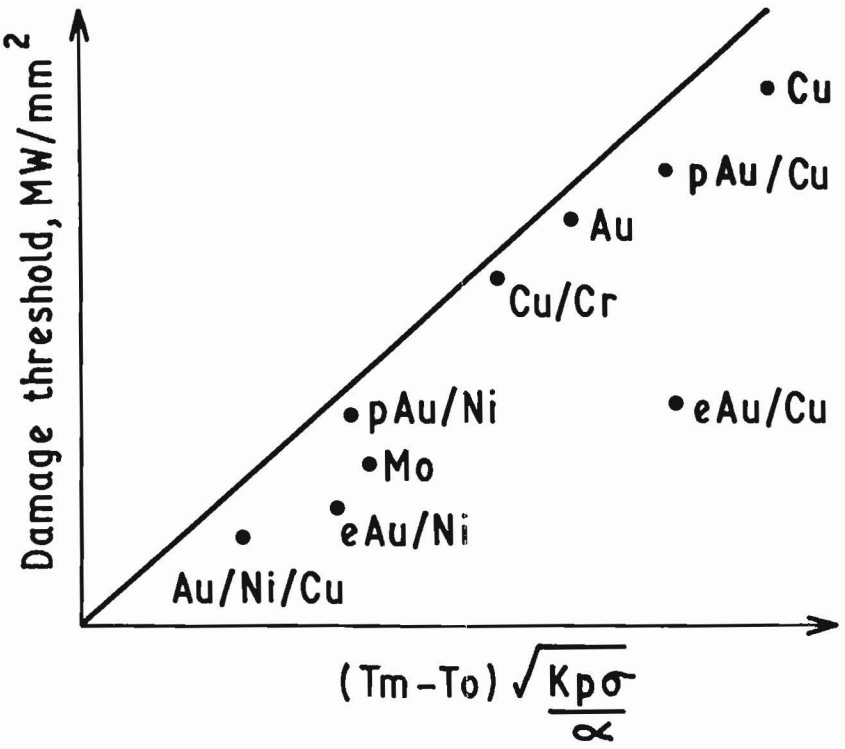


Figure 2 : Comparison of theoretical and measured laser-induced damage thresholds of metal mirrors

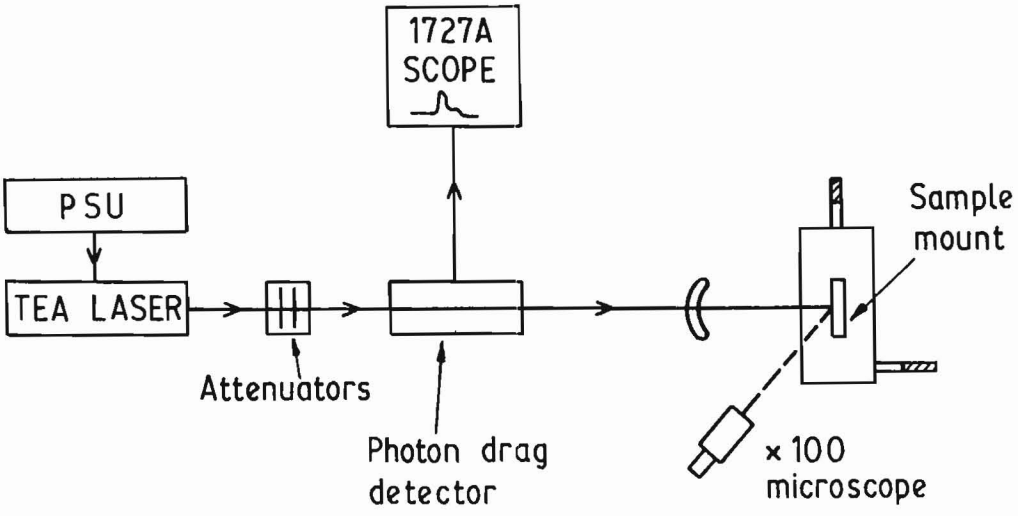
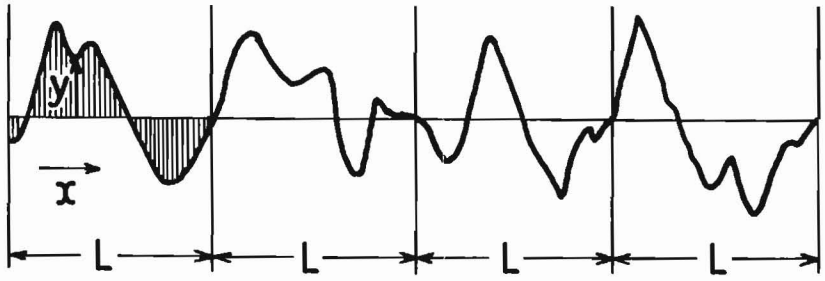


Figure 3 : Pulsed laser damage measurement apparatus



$$Ra = \frac{1}{L}\int_0^L |y(x)|\,dx$$

Figure 4 : Roughness average obtained over a surface sampling interval L

All the conventionally polished samples were photographed in the SEM to try to gauge the surface finish of each. The areas shown in Figures 5, 6 and 7 are representative of the whole surface in each

Table 1

MEASUREMENT	MIRRORS TESTED				
	M51	M53	M201	M202	M203
Absorptivity (%)	0.70	1.00	0.49	0.50	0.56
Reflectivity (%)	99.2	98.9	99.5	99.5	99.4
LIDT(MW mm^{-2})	11.0	7.8	2.0	4.5	9.8
Surface	DT Cu	DT Cu/AU	Cu/Au	Cu/Au	Cu/Au
Polish grade (μm)	Diamond-turned (DT)	Diamond-turned (DT)	0.8	0.3	0.1
Scratch width (μm)	0.1	0.3	1.0-2.5	0.5-1.0	0.25-0.5
Scratch separation (μm)	>20	>20	5	1	>20
Roughness average (μm)	0.009	0.010	0.013	0.025	0.008

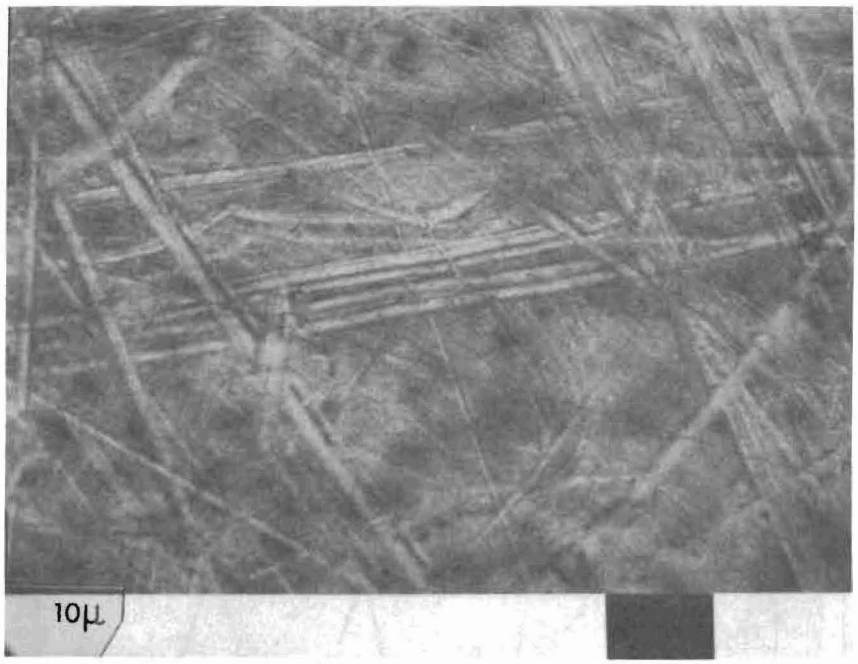


Figure 5 : Mirror M201 under 2 k magnification

case. From these pictures the scratch size and average scratch separation were estimated. The values are given in table 1 alongside the characterisation results. There is an obvious correlation between the scratch width and the LIDT. The sample finished to the finest grade of diamond paste (M203) has the highest LIDT value of 9.8 MW mm^{-2}, and samples with substrates finished with progessively coarser polishing paste have LIDT values which decrease accordingly.

The surface roughness-average was evaluated using the Talysurf-5 system. The results of the exercise are shown in table 1. It is interesting to note that the LIDT values do not correlate with the roughness-average results. This can be explained by considering the photographs in figure 5, 6 and 7. Roughness-average is directly proportional to the area under the roughness profile curve (fig 4). Consequently, sample M202 has a higher roughness-average than either M201 or M203, since the scratch

separation is much less (see table 1). Measurement of the roughness-average alone cannot, therefore, be taken as indicative of how a laser component will fare in a damage measurement. Instead, a more critical assessment of the surface damage must be undertaken, preferably with a quantitative analysis of scratch sizes.

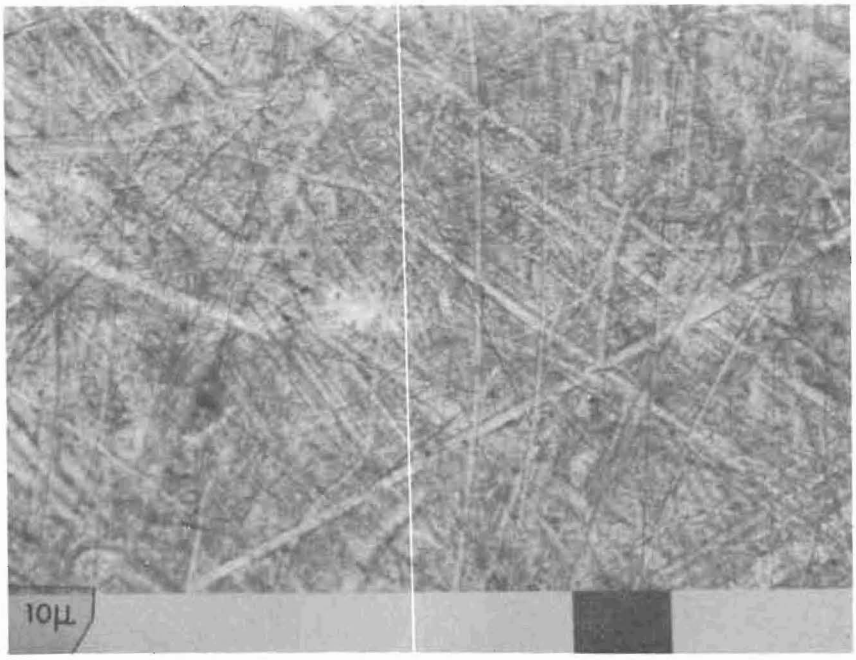


Figure 6 : Mirror M202 under 2 k magnification

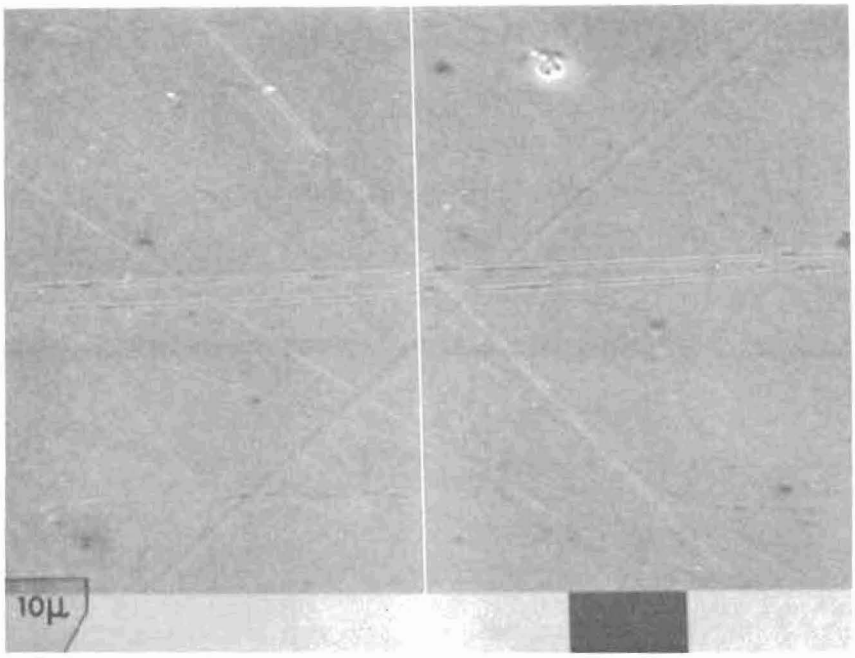


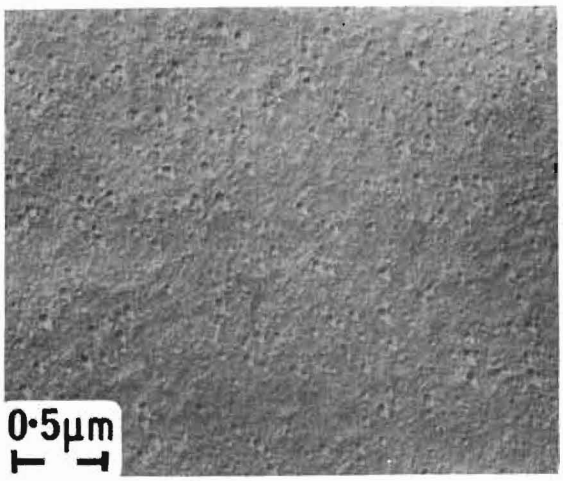
Figure 7 : Mirror M203 under 2 k magnification

Results obtained on mirrors with diamond-turned substrates (M51 and M53) are also presented to enable a comparison to be made. The uncoated mirror, M51, was found to have an absorptivity value about 0.2% higher than that of the best diamond-turned components, however the LIDT was mesured to be 11 MW mm^{-2}. Mirror M53 was a diamond-turned copper substrate, electroplated with gold. This component had a slightly higher absorptivity than M51 and a much lower LIDT (7.8 MW mm^{-2}). The photographs shown in figure 8 were taken in the SEM, and the absence of any deep scouring marks as in the case of mirror M201, for example, explains the high LIDT value. The pits in figures 8(a) and 8(b) (M51) are only about 0.1 μm in diameter,and hence do not act as low LIDT areas. The structure on the gold-coated mirror M53 is slightly larger and rougher however, which is probably the reason for the lower LIDT measured for this sample. The smoothness of diamond-turned samples is shown by the roughness average figures measured on M51 and M53.

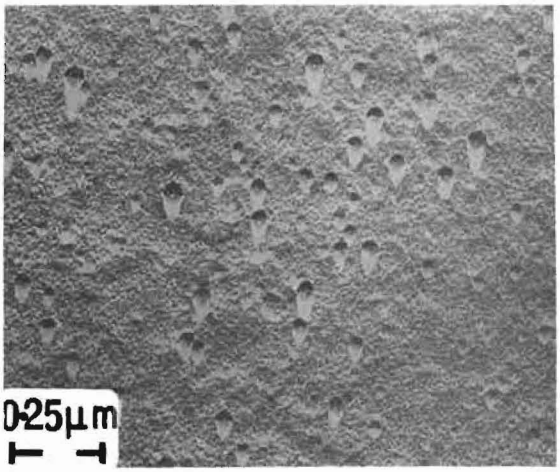
These results also show that diamond turning is no better than the best conventional polish (M203) in terms of average surface finish, although it does produce a scratch-free surface.

4 Discussion

Three gold-coated copper mirrors were characterised at 10.6 μm in terms of their absorptivity, reflectivity and LIDT. Each sample had a substrate which was prepared by conventional polishing with diamond abrasives; a different finishing grade being used in each case (see table 1). The reflectivity and absorptivity results were all very uniform, and were comparable to values obtained on the best diamond-turned copper mirrors [1]. The LIDT values, however, varied considerably and were found to correlate with surface scratch width. It was noted that the roughness-average figures produced by the Talysurf-5 system could not be taken as a reliable guide to the probable LIDT of a given component, since

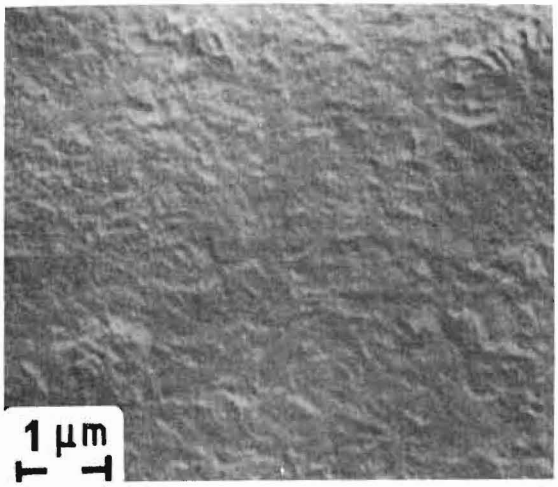


(a)

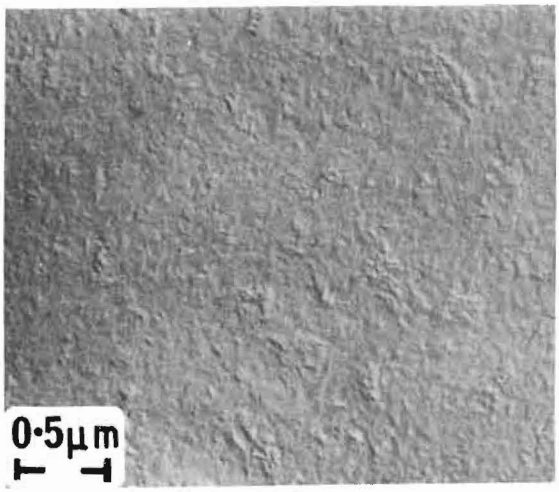


(b)

diamond-turned OFHC copper mirrors



(c)



(d)

gold-coated diamond-turned OFHC copper mirrors

Figure 8 : Scanning electron micrographs

this figure is influenced by the scratch separation. Instead, a more detailed examination of th surface is required.

The best mirror, M203, had an LIDT value of 9.8 MW mm^{-2} which is comparable to the best diamond-turned copper mirrors. The substrate of this mirror was finished with 0.1 μm grade diamond paste which yielded a very smooth surface, with few scratches (fig 7). It is possible that with a longer polishing with 0.1 μm paste the scratches present may be erradicated. This is important, since the marks shown in figure 7 might be large enough to lower the LIDT slightly.

A comparison was made with results obtained on two diamond-turned mirrors, one of which was electro-plated with gold. The average surface finish of mirror M203 was found to be slightly better than that of the best diamond-turned component. The diamond turned component was completely scratch-free although small pits were shown up by the SEM (fig 8). An analysis of the data showed that there is a log-inv.-log relationship between the MINIMUM LIDT and the scratch width. This has previously been found during measurements of LIDT at 1.06 μm on samples of fused silica [8].

5 Acknowledgement

This work was carried out with the support of the Procurement Executive, Ministry of Defence, sponsored by DCVD.

REFERENCES

1 Sharma, S.K.; Wood, R.M.; Ward, R.C. Measurement of mirror and window characteristics for use with 10.6 μm lasers. NBS Spec Publ 509 183

2 Hartman, J.S. Optical effects of energetic copper-ion irradiation on copper mirrors. Appl Opt 20 (23) 4062; 1981.

3 Ready, J.F. Change of reflectivity of metallic surfaces during irradiation by CO_2 TEA laser pulses. IEEE J Quantum Electron QE-2, 137, 1976.

4 Ready, J.F. Effects due to absorption of laser radiation. J Appl Phys 36 (2) 462, 1965.

5 Gibbs, R.; Wood, R.M. Laser induced damage of mirror and window materials at 10.6 μm. NBS Spec. Publ. 462, 181, 1976.

6 Wood, R.M.; Sharma, S.K.; Waite, P. Laser damage in optical materials at 10.6 μm. GEC Jnl. of Science and Technology 48, (3), 141, 1982.

7 Dagnall, H.; Exploring Surface Texture. Rank Taylor Hobson, 1980, p 40.

8 Wood, R.M.; Laser damage in optical materials at 1.06 μm. GEC Jnl of Science and Technology, 45 (3) 109, 1979.

Thermally Induced Effects on the Infrared Reflectance of Metal Mirrors*

V. A. Hodgkin, D. L. Decker, and H. H. Hurt

Michelson Laboratory, Physics Division
Naval Weapons Center, China Lake, California 93555

The experimentally measured infrared (IR) reflectance of metals has sometimes been known to depart significantly from that predicted by simple theory. This departure is a complex function of the bulk and surface properties, method of fabrication, age, and temperature history of the metal. This paper presents data which show the effects of the thermal history of a metal on its IR reflectance as a function of these parameters. The overall sample set consisted of copper (bulk and thin film), aluminum (thin film and bulk alloy), silver (thin film), and molybdenum (bulk) mirrors, and each metal was further categorized as to age, fabrication, and if a thin film by substrate. Reflectance measurements at wavelengths between 9.72 and 0.8 μm, inclusive, were then made for each category in air at room temperature prior to and following a thermal excursion to look for resulting effects. In addition, each category contained a control sample in order to filter out changes due entirely to age and storage, and a "standard" was periodically measured to track any instrumental drifts occurring with time. The data presented herein represent only one thermal excursion, and yet the data show that just one cycle can have complex effects upon the IR reflectance of a metal, depending upon the temperature of the excursion and how and when the mirror was made.

Key words: conventionally polished; diamond-turned; evaporated films; recrystallization; thermal cycling.

Introduction

Most simple models of infrared (IR) reflectance from metal surfaces imply that reflectance is only a function of one or more fundamental parameters. Furthermore, these parameters are determined entirely by the type of material, depend only upon current conditions, and cannot be altered by previous environments. However, experimental measurements and practical applications show that actual reflectance is rarely ever as good as predicted by theory and depends upon more than just the makeup of the mirror [1].[1] Reflectance also changes with age, temperature, and wavelength, and high-temperature-induced reflectance changes are not always reversible.

Because the experimentally measured behavior of IR reflectance of metal mirrors is more complex than that predicted by simple models, this paper documents an investigation into the effects of thermal cycling upon the resultant IR reflectance of metal mirrors as a function of (1) composition, (2) fabrication, and (3) thermal history. The basic approach consists of comparing the initial normal incidence IR reflectance of a small metal mirror to that measured after the mirror was baked.

Experimental

The investigation was designed to verify that permanent changes in IR reflectance do indeed occur and consisted of a particular sequence of events, starting with the acquisition of three identical sample sets, each composed of different metals and prepared in different ways, and measuring the reflectance of all the samples at five wavelengths, starting at 0.8 μm and ending at 9.72 μm. (The reflectance measurements were performed in an atmosphere of dry nitrogen at room temperature (25°C nominally) in the Naval Weapons Center's (NWC) relative reflectometer, which has a precision of about 0.1%.) Then one of the three sample sets was set aside to act as controls in order to separate out effects due to aging; the other two sets were designated as an intermediate temperature (T1) group and a high-temperature (T2) group, the temperatures depending upon the type of metal. (The samples of all three groups were stored together in a dust-free enclosure, but otherwise were exposed to the normal laboratory environment.)

*Work supported by Navy Independent Research Funding.
[1]Figures in brackets indicate the literature references at the end of the paper.

Those samples not acting as controls were baked for 2 hr in an ultrahigh vacuum (UHV) environment at the selected temperatures. (The 2-hr baking period commenced once the desired temperature was reached, and regulation kept it there to within a couple degrees.) At the end of the 2-hr period, the source of heat was removed and the samples were allowed to cool within the UHV environment to room temperature.

The reflectance of the baked samples and their identical controls were then measured again as soon as possible. Additionally, the reflectance of a UHV-deposited aluminum film, prepared more than a year before, was periodically measured in a manner identical to all the other samples in order to track any systematic drifts and ascertain the precision of the reflectometer system. (Since reflectance changes referenced to their initial values were the desired quantities, precision and resolution were of greater concern than the absolute accuracy of the reflectometer.)

The sample sets of copper, aluminum, silver, and molybdenum were fabricated in a variety of ways (see fig. 1). All film samples were prepared in-house on fused silica and single-crystal silicon substrates, which were baked at 250°C for 1 hr and cooled before the films (1000 Å aluminum, 1200 Å copper and silver) were deposited at room temperature. All fresh-feed, conventionally polished, and diamond-turned bulk samples were also prepared in-house. Additionally, on hand for comparison were several older diamond-turned aluminum alloys, 6061-T6 and 2024-T4, and diamond-turned OFHC copper samples. Figure 1 also depicts the baking temperatures used. These were picked somewhat arbitrarily to be below the typical metallurgical annealing temperatures to prevent gross figure and recrystallization changes. Baking time was not a variable.

Results

Copper

There does not appear to be any initial reflectance differences between films attributable to type of substrate (table 1). Baking the films on fused silica had no effect on stability greater than ±0.1% (fig. 2). In contrast, the only copper film on silicon that showed any stability, also to within ±0.1%, was the 150°C (T1) sample. Both the control (Co) and the 300°C (T2) samples deteriorated at all wavelengths. The T2 sample change was the most dramatic, losing from about 3% at 9.72 μm to nearly 40% at 0.8 μm (table 2 and figs. 3 and 4). The deterioration was very noticeable to the unaided eye, and, under Nomarski microscopy (fig. 5), it revealed a surface composed of islands of smooth, undisturbed copper surrounded by rough areas of what may be a thermally driven copper/silicon solid state reaction. Why the intermediate temperature (T1) sample appears to be unaffected is not yet known. Neither angle-resolved nor total integrated scatter (TIS) measurements were made on these samples, but presumably an increase in scatter is responsible for part of the increasing loss of reflectance at shorter and shorter wavelengths.

The old diamond-turned copper also turned out to be stable to within ±0.1% to thermally induced reflectance changes (see fig. 6). However, on close inspection, baking at 300°C does seem to have induced slip over most of the T2 sample (fig. 7). Visually, the newly made diamond-turned copper samples appeared to be of poorer quality than the older ones. However, as can be seen in table 1, such a conclusion was not supported by reflectance measurments. Overall stability to thermally induced reflectance measurements, with a few exceptions, was also just as good (see table 2 and fig. 8). One of the difficulties with the in-house diamond-turning facility at that time was a lack of uniformity even within a particular production run, and this showed up as a variation between samples at the longer wavelengths. The improvement of the 150°C (T1) sample at these wavelengths after baking may be due more to natural recovery than baking. However, whatever the cause, the improvement merely resulted in its reflectance approaching that of the other two samples. The only effect that can be certain to have been caused by baking is the accelerated recovery visible in figure 9.

The effects of thermal cycling upon conventionally polished copper were nearly as positive as those upon the copper film on silicon were negative. Baking at 300°C increased reflectance from about 0.4% at 9.72 μm to about 13.5% at 0.8 μm, and even baking at 150°C produced easily measurable reflectance increases at nearly all the wavelengths (see table 2 and fig. 10). As spectacular as these improvements may seem, particularly at the shorter wavelengths, the resulting increased reflectances were still less than those of the evaporated films or diamond-turned surfaces.

When these samples were removed from the polishing process, their surfaces showed a great deal of damage in the form of scratches and defects. Because of this and a wide variation in the measured initial reflectances, it was decided to measure TIS before and after baking. The results, made at 1.15 μm, are as follows:

$I_{hemispherical\ scatter}/I_{reflected}$ of polished copper

	Before baking	After baking
Co	.0166±.0004	.0159±.0003
T1	.0163±.0007	.0184±.0016
T2	.0152±.0004	.0194±.0002

What appears to account for both increases in scatter and reflectance is some combination of recrystallization and recovery of the disturbed surface layer (see fig. 11). An increase in grain size might be expected to provide an increased dc conductivity, which according to the Drude (free electron) model, would result in a greater IR reflectance.

The unambiguous presence of rings in reflection electron diffraction (RED) microscopy of the high-temperature (T2) sample as well as the less obvious rings in the intermediate temperature (T1) sample very clearly shows an increase in crystalline order of the surface layer with higher baking temperatures (see fig. 12).

Many of the copper samples lost on the order of 1% of their intrinsic reflectance at 0.8 μm regardless of whether they were baked or not. An accumulation of an absorbing oxide layer on the surface is suspected of being responsible. As stated earlier, the samples were only protected from dust during the period between manufacture and final reflectance measurement, which was typically four to six weeks. No data were found concerning oxidation rates nor were specific data reporting the spectral absorption characteristics of oxides of copper located in order to support or eliminate this possibility. Even though the old diamond-turned copper samples were several months old, they had been stored immediately in a small, air-tight container after manufacture, where they remained until they were measured in the reflectometer. They were remeasured 1 mo. later, which may have been long enough for oxidation to have begun after nearly a year's delay. On the other hand, the two weeks in which the new diamond-turned parts passed through the cycle may not have been long enough for many ill effects to accrue, therefore accounting for those parts not showing any significant losses at 0.8 μm.

For the most part, diamond-turned copper and copper films on fused silica seem to be very stable to thermally induced reflectance changes in the IR. Improvement can occur when the surface layer is greatly disturbed. On the other hand, drastic deterioration may result if a film is evaporated onto something with which it can interact such as silicon [2].

Aluminum

Under initial visual inspection, the evaported aluminum films on fused silica showed noticeable defects such as scratches, lines, and hazy area; whereas, the films on silicon appeared to be clean and uniform. Table 1 shows a small difference between the two substrate types at the shorter wavelengths that seems to agree with the difference in quality.

Aluminum films, like copper and silver, are also known to be sensitive to solid state interactions with silicon and thus what happened to the copper film on silicon might be expected to have been repeated. If anything did happen, it was extremely subtle and not readily measurable, except perhaps at 0.8 μm where the only decrease in reflectance (about 0.5%) occurred (see table 2 and fig. 13). These particular films on silicon appear to be immune to thermally induced effects.

The control (Co) and 100°C (T1) aluminum films on fused silica were also stable to within ±0.15%; however, baking at 150°C did result in a significant loss of reflectance between 6.24 μm and 0.8 μm on the T2 sample (see table 2 and fig. 14).

Alloys of aluminum which have lower dc conductivities than the pure metal also possess proportionally smaller IR reflectances. Table 1 clearly shows that the two diamond-turned alloys, 6061-T6 and 2024-T4, have poorer reflectances than the pure films. Of the two listed, the slightly higher reflectances belong to the alloy 6061-T6 which also has the greater dc conductivity.

Overall, the diamond-turned 6061-T6 alloy appears to be fairly stable (see fig. 15); the only significant change was a loss of reflectance on the order of 0.5% at 0.8 μm by the 150°C (T2) sample. The nearly 0.5% loss by the 6061-T6 control (Co) at 2.7 μm may have been caused by adsorbed water due to much higher than normal humidity at the time.

The diamond-turned 2024-T4 aluminum alloy turned out to be less resistant to negative thermally induced effects. Both of the baked samples incurred reflectance losses between 0.8 μm and 2.7 μm (see table 2 and fig. 16).

All of the aluminum and aluminum alloy samples suffered reflectance losses between 0.4 and 1% at 0.8 μm when baked at 150°C. Depending upon other parameters such as type of substrate or alloy, baking at 100°C or higher may also result in IR reflectance losses. On the other hand, some of the data indicate that in the case of diamond-turned 6061-T6 alloy small improvements may be realized at some points depending upon the temperature used. Most surprising perhaps was the overall stability exhibited by the aluminum films on silicon and the lack of it by an identical film on fused silica baked at 150°C.

Silver

Initial reflectance measurements of the evaporated silver films showed no difference due to type of substrate. Also, figures 17 and 18 display very similar behavior between the silver films on fused silica and those on silicon due to thermal cycling. The evidence as it is presented in table 2 indicates that whatever caused the loss of reflectance at 0.8, 1.54, and 9.72 μm, it was probably not due to baking at either 50°C (T1) or 100°C (T2). However, the losses experienced by the baked silicon samples may have been partially thermally driven. The deterioration of these samples at 0.8 and 9.72 μm is nearly identical to that suffered by the silver on fused silica at the same wavelengths, and so it is likely that the same nonthermal agent, such as a chemical reaction, was responsible. There were, however, no obvious signs of any interaction between silver and substrate, nor were there any signs of recrystallization of any of the baked samples. Of all of the metal films measured, the silver samples faired the worst overall. The conclusion from these data may be that thermal cycling hardly impacts the results-deterioration due to aging will dominate no matter what.

Molybdenum

Figure 19 indicates that baking conventionally polished molybdenum may have a positive effect on its IR reflctance just as it did on the polished copper. Several differences do exist, however. The 3% or so improvement in reflectance at 0.8 μm was probably not caused by baking at either 300°C (T1) or 600°C (T2). More than likely it resulted from the material's own natural relaxation of the disturbed surface layer, even though no change in the surface was seen as it was on the polished copper. The data do indicate, however, that baking does have some positive impact at the longer wavelengths (see table 2). Because typical annealing temperatures for molybdenum are on the order of 1000°C, baking at even high temperatures than those used here might produce even larger reflectance changes.

Conclusions

Permanent, thermally induced reflectance changes do indeed occur in metal mirrors, and, depending upon the material, type of manufacture, wavelength, and the temperature used, these changes can be either positive or negative. Most positive gains in the far-IR reflectance arise from either an increase in crystalline order or a decrease in the density of defects. In any event, the degree of improvement is limited by how much disorder exists and the theoretical reflectance inherent with the material. From this standpoint alone, if the surface layer is already well ordered, the material should be expected to be stable to thermally induced changes in the infrared (IR). Another avenue for improvement due to baking is the possibility of desorption of impurities or contaminants from the surface. On the other hand, prolonged heating can also reduce the reflectance of a metal by either initiating or accelerating chemical reactions with external media. There is evidence to suggest that in the case of silver films baking at moderate temperatures can result in an overall decrease in grain size [3], which should lead to a reduction of IR reflectance. Also, in the case of some metals, gross recrystallization produces severe surface roughening, thus increasing scattering. Finally, naturally occurring aging of the material plays a dominant role in the subsequent optical properties of a material and any effect thermal cycling might have upon them.

References

[1] Decker, D. L.; Hodgkin, V. A. "Wavelength and temperature dependence of the absolute reflectance of metals at visible and infrared wavelengths," in Laser Induced Damage in Optical Materials: 1980, Bennett, H. E.; Glass, A. J.; Guenther, A. H.; Newnam, B. E., ed. 1980 September 30-October 1; Boulder, CO. Nat. Bur. Stand. (U.S.) Spec. Publ. 620; 1981 October. Pp. 190-200.

[2] Nakamura, K.; et al. "Interaction of metal layers with polycrystalline Si," J. Appl. Phys. 47; 1278-1283; 1976.

[3] Bennett, J. M. "Optical scattering and absorption losses at interfaces and in thin films," presented at the Sixth International Conference on Thin Films; Stockholm, Sweden; 1984 August.

Table 1. Average initial reflectances

Sample type	0.8 μm	1.54 μm	2.7 μm	6.24 μm	9.72 μm
Cu film on fused silica	.979	.994	.996	.996	.996
Cu film on silicon	.980	.994	.996	.995	.994
Old diamond-turned OFHC Cu	.981	.996	.998	.999	.997
New diamond-turned OFHC Cu	.970	.995	.998	.998	.995
Polished OFHC Cu	.707	.944	.982	.989	.988
Al film on fused silica	.875	.969	.977	.985	.985
Al film on silicon	.878	.970	.977	.985	.985
Old diamond-turned 6061-T6 Al	.855	.957	.968	.979	.980
Old diamond-turned 2024-T4 Al	.851	.944	.959	.974	.976
Ag film on fused silica	.983	.993	.994	.995	.994
Ag film on silicon	.983	.993	.994	.995	.993
Polished Mo	.608	.884	.960	.980	.983

Table 2. Percent changes in reflectance due to baking

Sample type	Temp., °C	0.8 μm	1.54 μm	2.7 μm	6.24 μm	9.72 μm
Cu film on silicon	Co	-1.79±.07	-.73±.08	-.89±.09	-.17±.12	stable
	150	-1.29±.07	stable	stable	stable	stable
	300	-39.51±.07	-22.35±.05	-13.73±.08	-5.39±.14	-3.06±.14
Cu film on fused silica	Co	-1.25±.07	stable	stable	stable	stable
	150	-1.17±.07	stable	stable	stable	stable
	300	-1.09±.07	stable	stable	stable	stable
Old diamond-turned OFHC Cu	Co	-1.22±.07	stable	stable	stable	stable
	150	-1.40±.07	stable	stable	stable	stable
	300	-1.22±.07	stable	stable	stable	stable
New diamond-turned OFHC Cu	Co	stable	stable	stable	stable	no data
	150	stable	stable	stable	.21±.15	1.27±.14
	300	-.22±.07	stable	-.18±.10	stable	stable
Polished OFHC Cu	Co	-.99±.14	-1.58±.07	-.34±.07	stable	-.24±.12
	150	1.94±.08	.32±.06	.27±.08	.19±.12	stable
	300	13.53±.08	3.06±.07	.66±.08	.49±.12	.37±.12
Al film on fused silica	Co	stable	stable	stable	stable	stable
	100	stable	stable	stable	stable	stable
	150	-.57±.07	-.56±.06	-.60±.09	-.33±.12	stable
Al film on silicon	Co	-.36±.09	stable	stable	stable	stable
	100	-.15±.08	stable	stable	stable	stable
	150	-.38±.10	stable	stable	.19±.15	stable
Old diamond-turned 6061-T6 Al	Co	stable	stable	-.46±.09	stable	stable
	100	stable	.22±.06	.17±.11	stable	stable
	150	-.52±.09	stable	stable	.15±.12	.33±.12
Old diamond-turned 2024-T4 Al	Co	stable	stable	stable	stable	stable
	100	-.39±.08	-.36±.06	-.40±.10	stable	stable
	150	-.97±.08	-.30±.06	-.24±.08	stable	stable
Ag film on fused silica	Co	-1.72±.10	-.32±.09	stable	stable	-.24±.12
	50	-1.36±.08	-.17±.07	stable	stable	-.23±.14
	100	-1.61±.08	-.19±.06	stable	stable	-.18±.14
Ag film on silicon	Co	-1.28±.08	stable	stable	stable	stable
	50	-1.49±.11	-.12±.07	stable	stable	-.17±.14
	100	-1.71±.08	-.29±.06	-.21±.08	stable	-.24±.12
Polished Mo	Co	3.44±.08	stable	stable	stable	stable
	300	2.53±.10	.17±.15	.56±.18	.39±.12	stable
	600	3.24±.07	-.45±.06	.09±.07	.42±.12	.30±.12

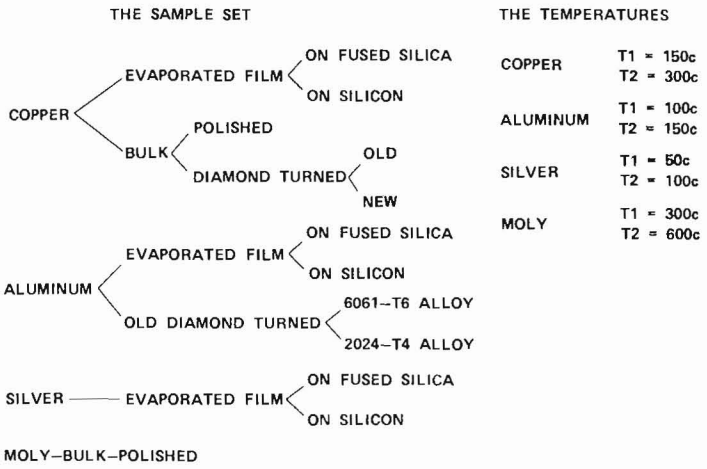


Figure 1. Sample set and baking temperatures.

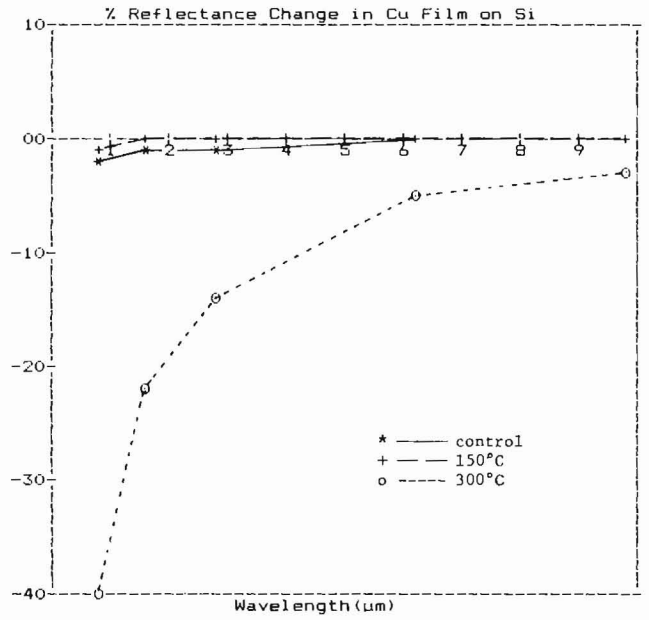


Figure 3. Percent reflectance change vs wavelength of baked evaporated Cu films on silicon.

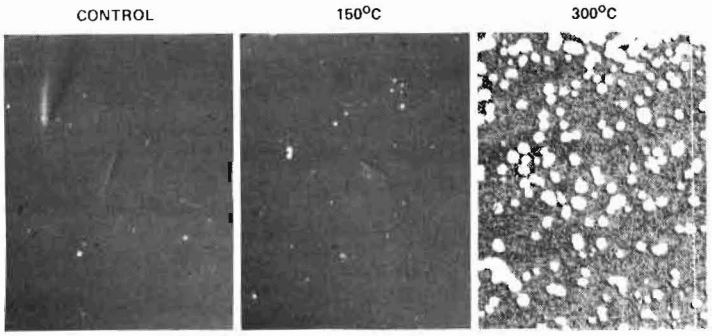


Figure 5. Nomarski photographs (180X) of the control (Co), 150°C (T1), and 300°C (T2) evaporated Cu films on silicon after baking.

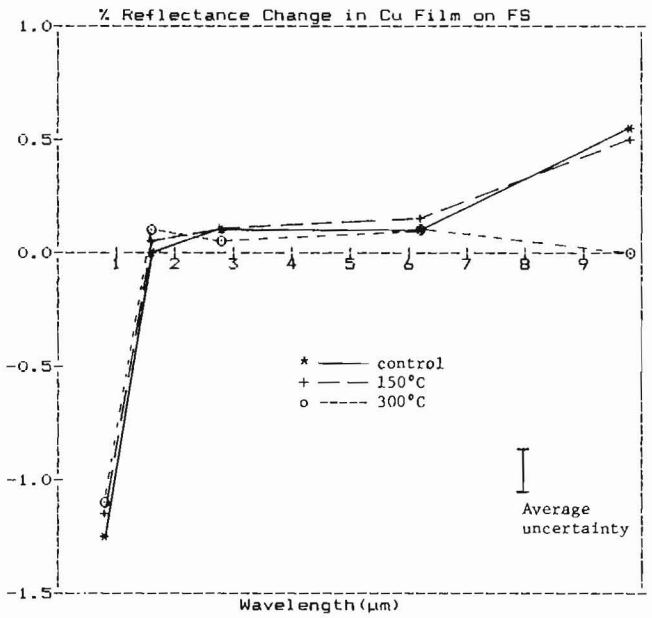


Figure 2. Percent reflectance change vs wavelength of baked evaporated Cu films on fused silica.

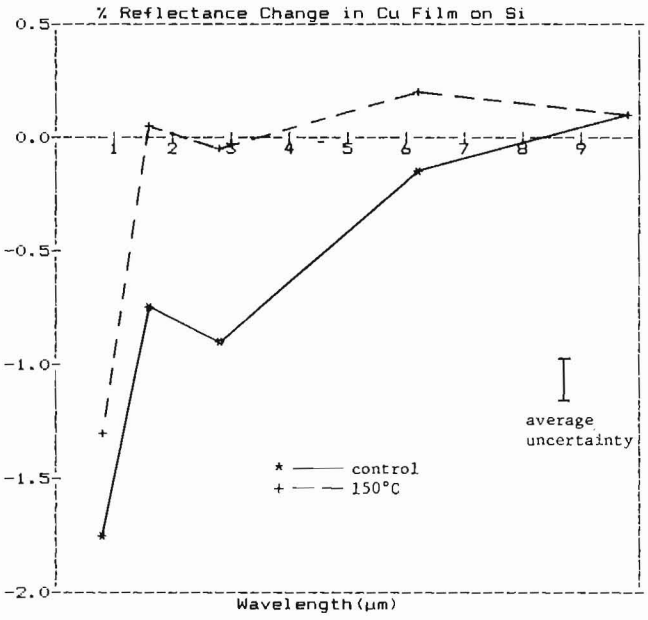


Figure 4. Percent reflectance change vs wavelength of baked evaporated Cu films on silicon.

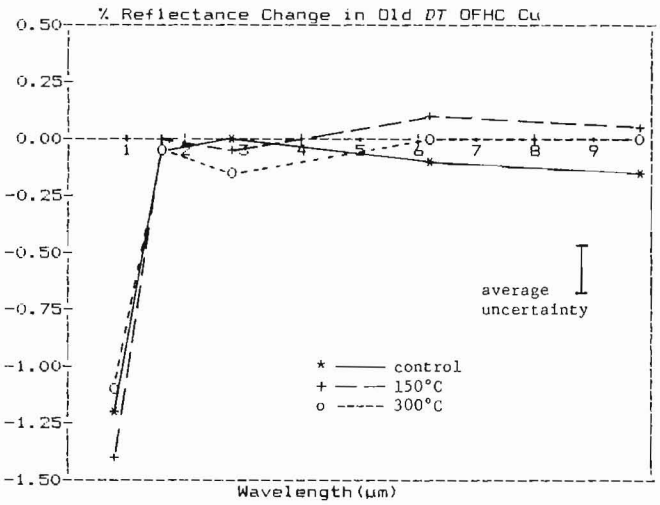


Figure 6. Percent reflectance change vs wavelength of baked old diamond-turned OFHC Cu.

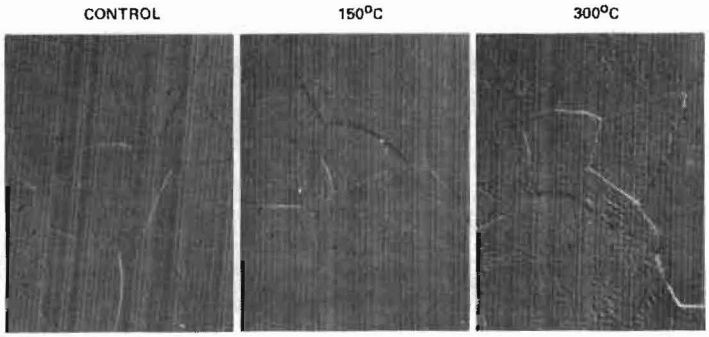


Figure 7. Nomarski photographs (180X) of the control (Co), 150°C (T1), and 300°C (T2) old diamond-turned OFHC Cu samples after baking.

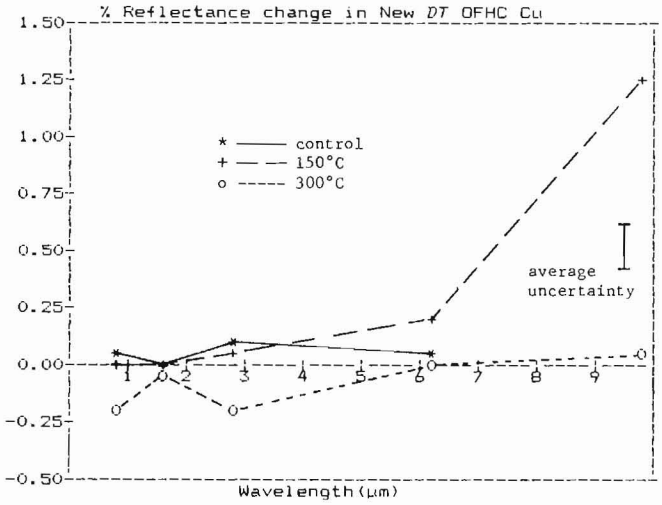


Figure 8. Percent reflectance change vs wavelength of baked new diamond-turned OFHC Cu.

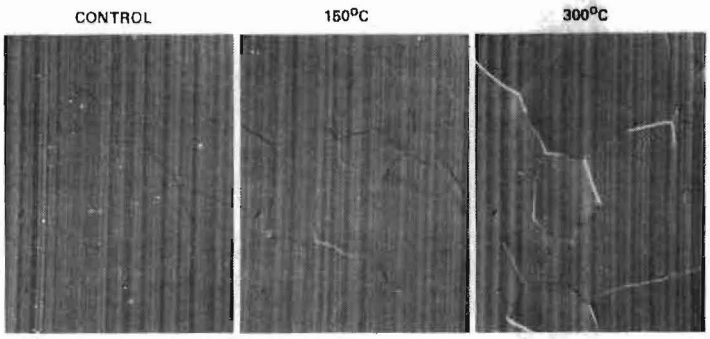


Figure 9. Nomarski photographs (180X) of the control (Co), 150°C (T1), and 300°C (T2) new diamond-turned OFHC Cu samples after baking.

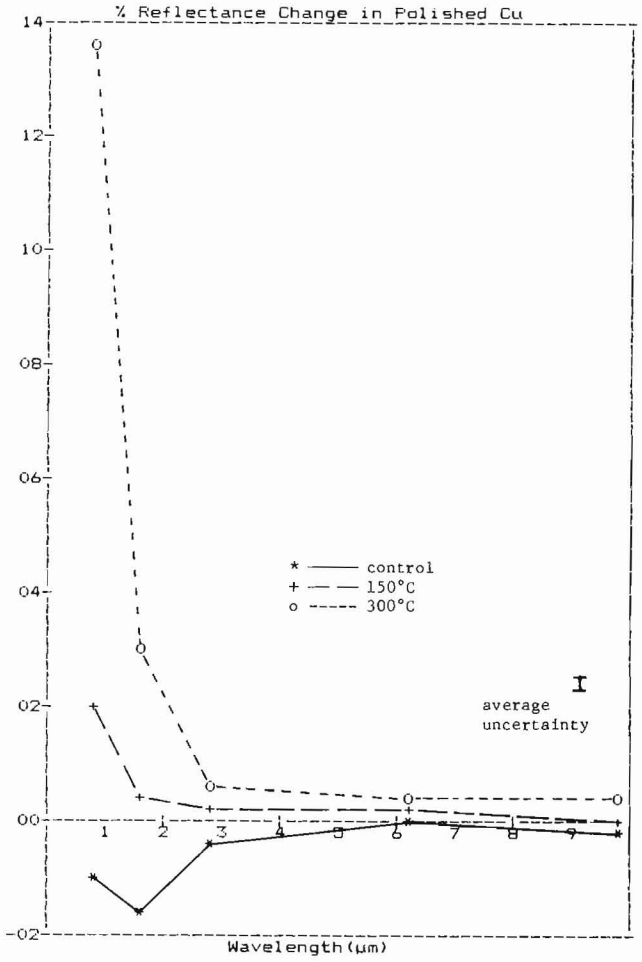


Figure 10. Percent reflectance change vs wavelength of baked conventionally polished Cu.

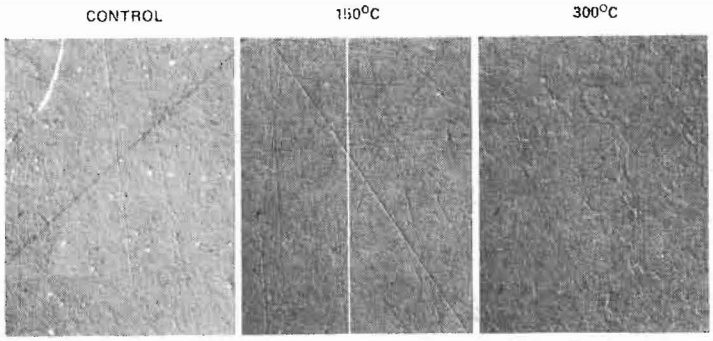


Figure 11. Nomarski photographs (180X) of the control (Co), 150°C (T1), and 300°C (T2) conventionally polished Cu samples after baking.

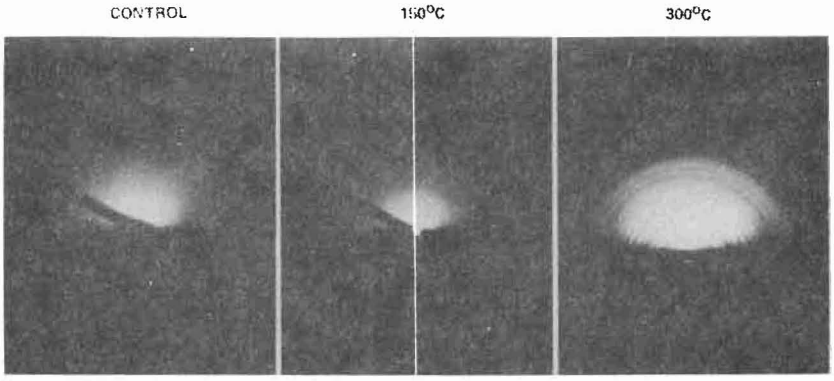


Figure 12. Reflection electron diffraction micrographs (100 kV) of the control (Co), 150°C (T1), and 300°C (T2) conventionally polished Cu samples after baking.

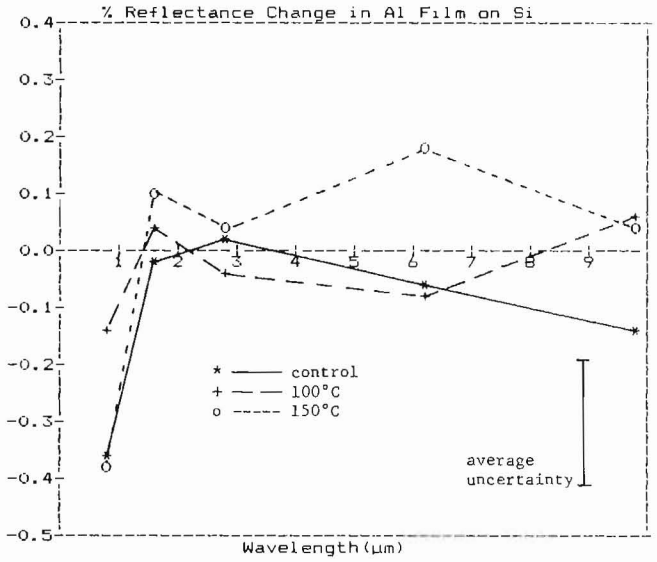


Figure 13. Percent reflectance change vs wavelength of baked evaporated Al films on silicon.

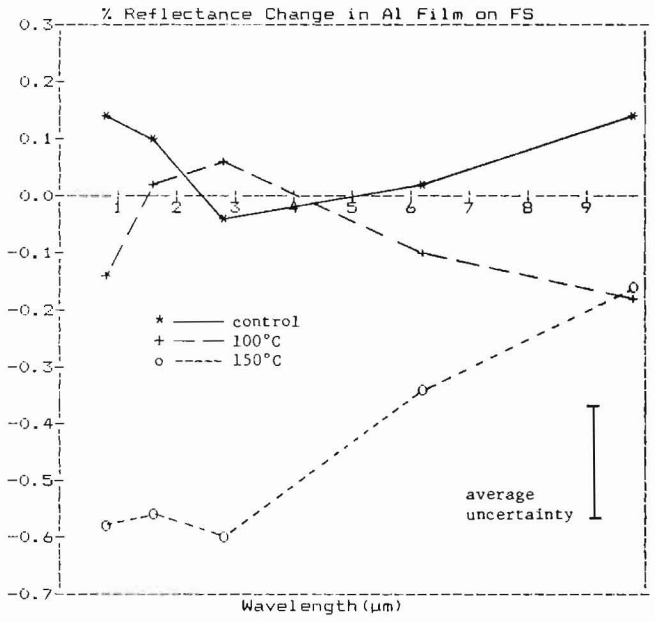


Figure 14. Percent reflectance change vs wavelength of baked evaporated Al films on fused silica.

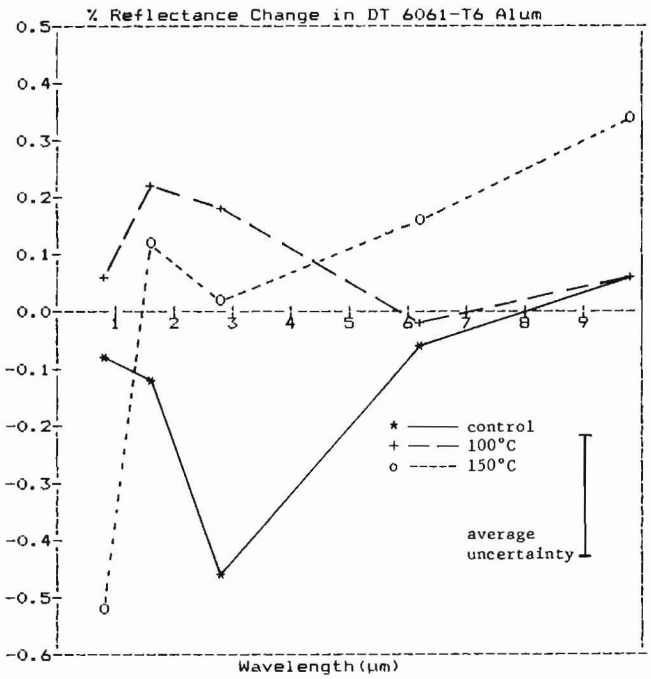


Figure 15. Percent reflectance change vs wavelength of baked old diamond-turned 6061-T6 Al.

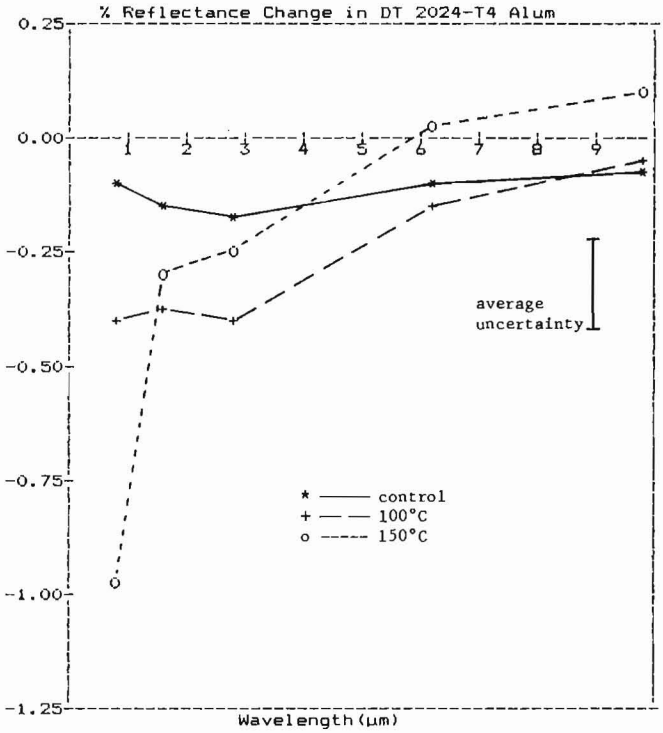


Figure 16. Percent reflectance change vs wavelength of baked old diamond-turned 2024-T4 Al.

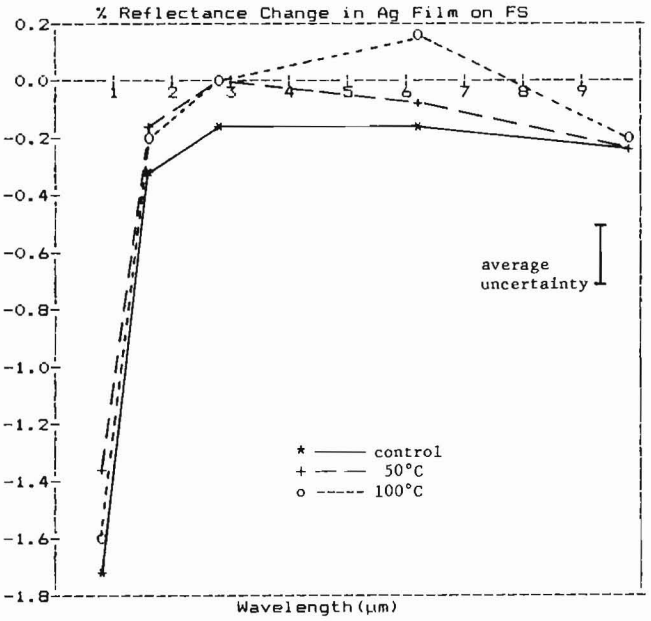


Figure 17. Percent reflectance change vs wavelength of baked evaporated Ag films on fused silica.

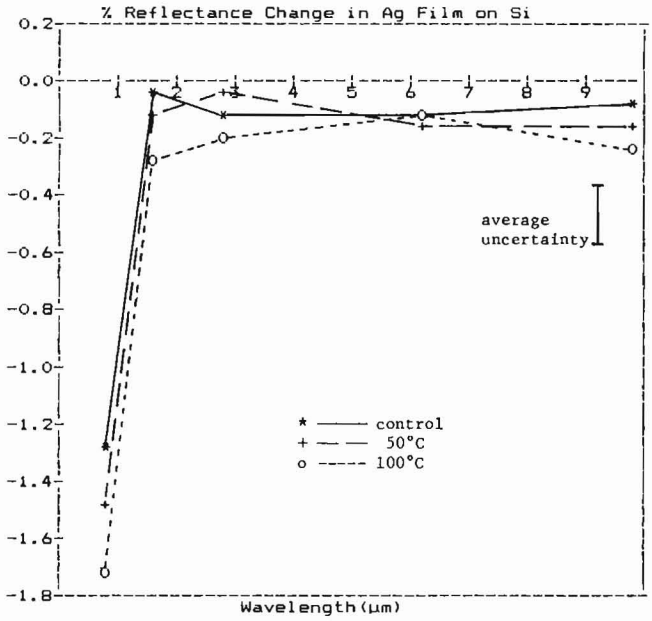


Figure 18. Percent reflectance change vs wavelength of baked evaporated Ag films on silicon.

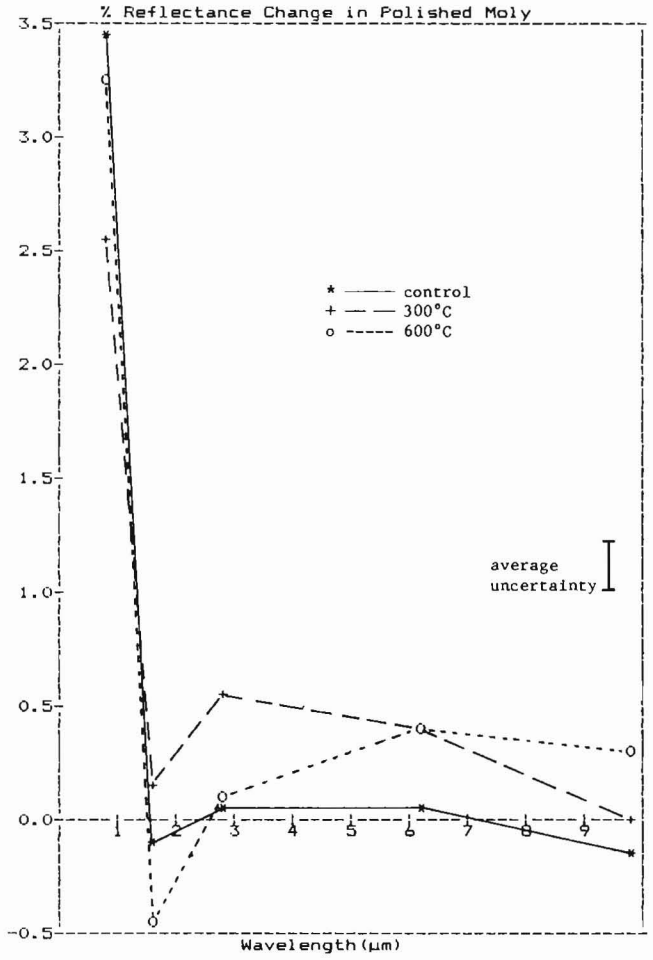


Figure 19. Percent reflectance change vs wavelength of baked conventionally polished Mo.

Single-shot, Cummulative and PRF Dependent Laser Induced Damage Thresholds

R M Wood, P Waite and S K Sharma

GEC Research Laboratories, Hirst Research Centre, Wembley, Middlesex, HA9 7PP

During the course of several laser damage programmes at HRC evidence has been accumulated on the different mechanisms and morphology of damage. This evidence has been gained at both 1.06 and 10.6 μm during single-shot, cummulative and prf testing of laser components.

This paper discusses, with both quantitative and photographic data the significance of (1) variation of the damage threshold values gained as a function of laser spot size and laser beam power and energy characteristics, and (2) the size and morphology of the damage spot gained under single shot, multiple and cummulative irradiation at prf's up to 100 Hz. Results are presented on Ge, ZnSe, ZnS, GaAs, CdTe, NaCl, KCl substrates and coated components at 10.6 μm and PMMA, fused silicon, Nd:laser glass and coated components at 1.06 μm.

Key words : Laser induced damage, 1.06 μm, 10.6 μm single shot, Cummulative, PRF dependence

1 Introduction

MOD have supported programmes which included the measurement of laser induced damage thresholds (LIDTs) at HRC since 1968. These have principally been at 1.064 μm (Nd:YAG) and 10.6 μm (CO_2) but have also included 0.53 μm (SHG of Nd:YAG), 0.69 μm (Ruby) and 2.06 μm (Ho:YLF). During the course of these programmes data has been accumulated on the different mechanisms and morphology of damage. Much of this work has never been presented before since the separate evidence was not sufficient to make a full scale paper.

This paper discusses the significance of the variations in the laser induced damage threshold values and the size and morphology of the damage gained under single-shot, multiple and cummulative irradiation of a variety of samples.

2 Variation in the single-shot laser induced damage threshold

Most experimenters have reported variations in the single-shot damage threshold levels across the surface of their damage samples. Those experiments which involve a large area irradiation spot show the least apparent variation and also always show up low LIDT's. Experiments performed on a random basis and/or with a small spot size show a wide variation and experiments performed with a small spot on a systematic basis yield both high and low values [1]. Figure 1 shows typical examples of the results gained using a small laser spot on typical damage samples.

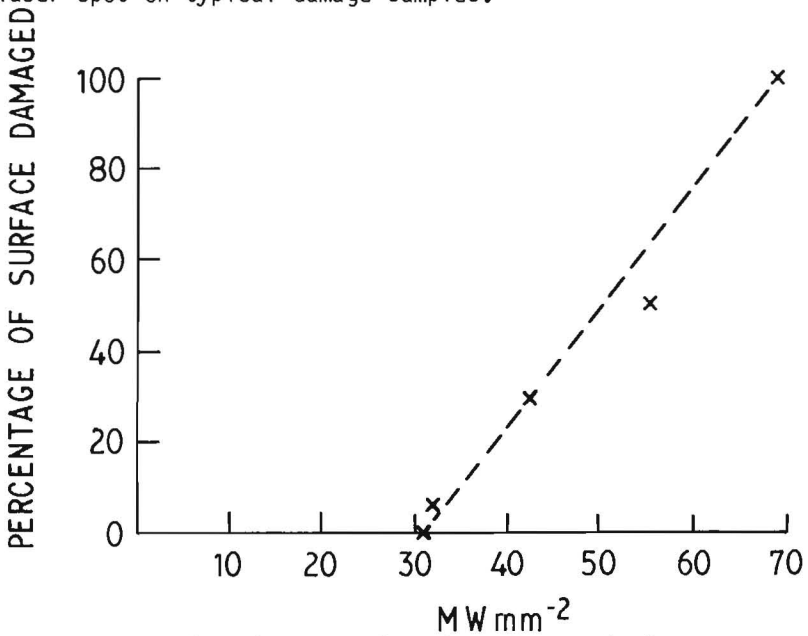


Figure 1 : Percentage of surface damaging as a function of irradiation level : fused silica : 1.064 μm

Low laser damage thresholds are recognised as being due to the presence of scratches, pits, coating defects, absorbing inclusions, and adsorbed materials. Figures 2 to 6 show photographs of such damage.

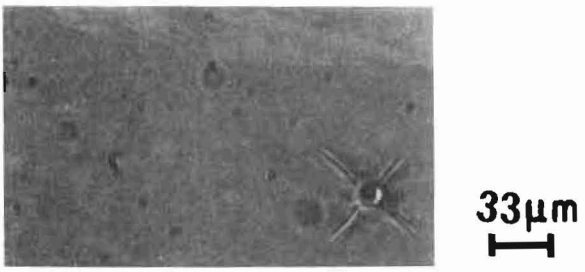


Figure 2 : Damage at a microscopic crystallite in KD*P, 1.064 µm

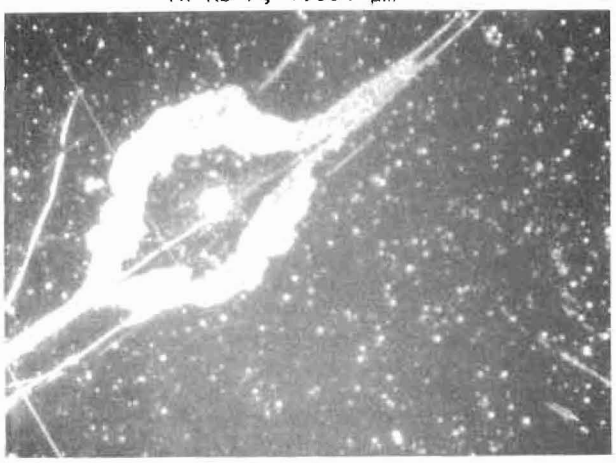


Figure 3 : Damage on a scratch in germanium 10.6 µm (x1400)

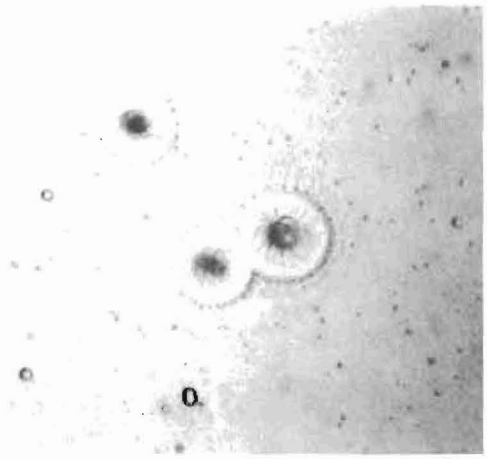


Figure 4 : Damage on polishing pits, silicon, 10.6 µm x1500

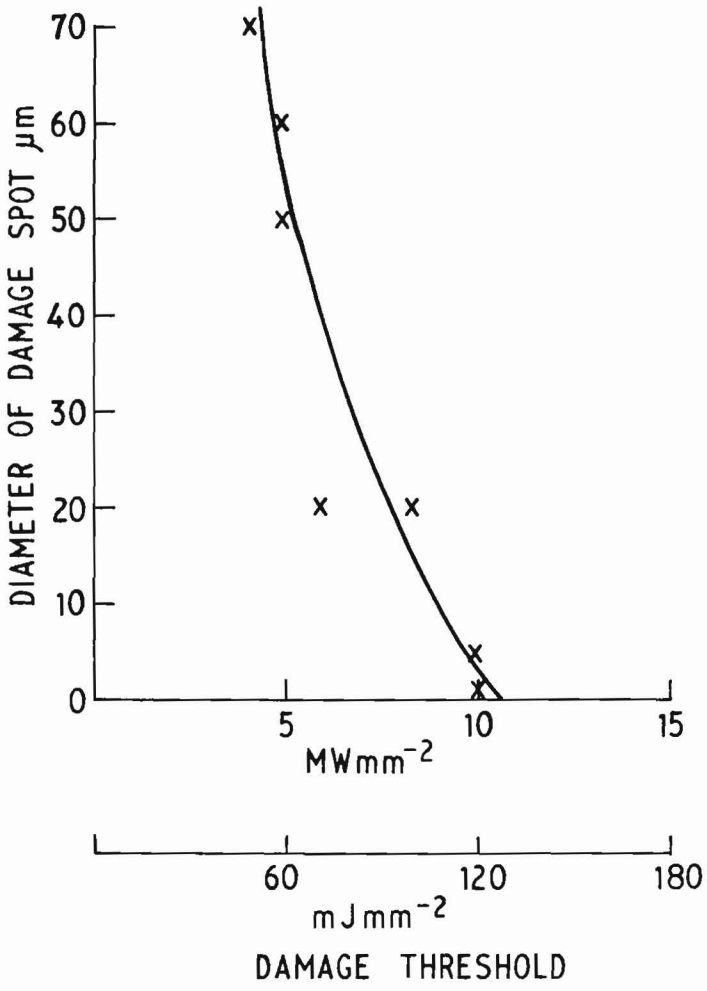


Figure 5 : Damage spot size versus LIDT, laser glass, 1.064 µm

It is now clear that what was once looked on as a spot size dependence of the LIDT is really just a probability of covering a low damage threshold region with a particular size spot. It is also clear that the lower damage thresholds correlate with defects etc and that higher LIDTs are found with near perfect surfaces and materials. The morphology of the damage spot, especially at or near the threshold for damage, therefore depends markedly on the presence and distribution of defects etc. It also depends on the peak energy density, peak power density, wavelength of irradiation and the laser beam temporal and spatial shape. These parameters determine in association with the sample parameters the relative influence of the thermal and dielectric breakdown mechanisms which lead to damage of the particular sample. Some of these differences can be seen with reference to the table (fig 8) where LIDT's on samples measured at both 1.064 and 10.6 µm are tabulated. The morphologies of the damage areas are usually distinctive but similar damage morphology can be observed from different causes, see figure 7,

where the damage is on a uniform surface irradiated by a multi-degenerate beam and (fig 4) where damage was observed on polishing pits covered by a single TEMoo laser beam. Single shot damage can therefore be observed as single spots, large spots or multiple spots - the precise sizes depend on the beam shape and laser power and energy densities relative to threshold.

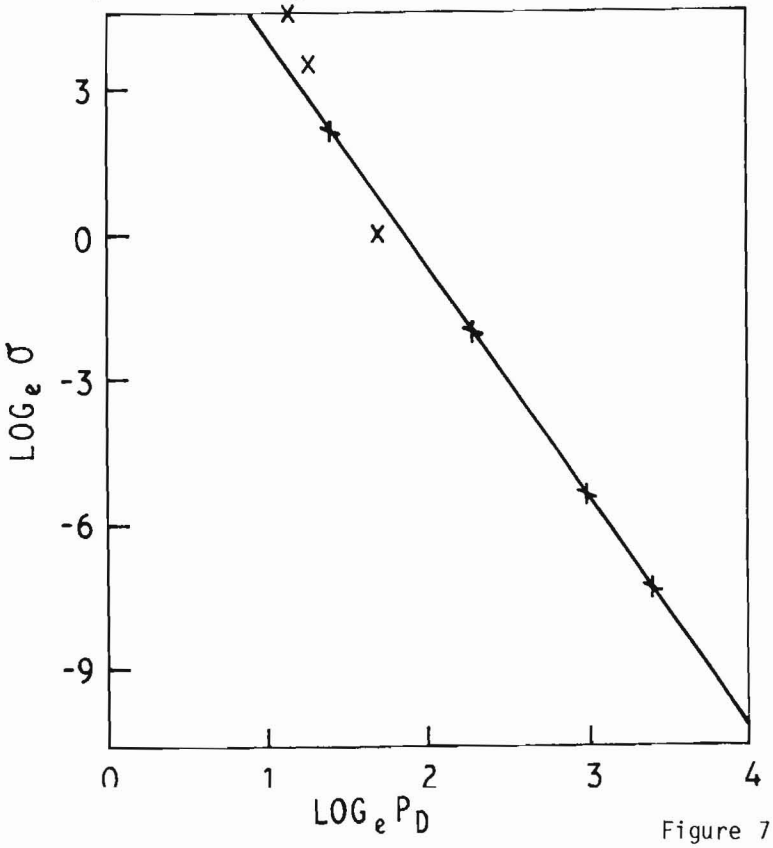


Figure 6 : LIDT versus surface finish; fused silica, 1.064 μm

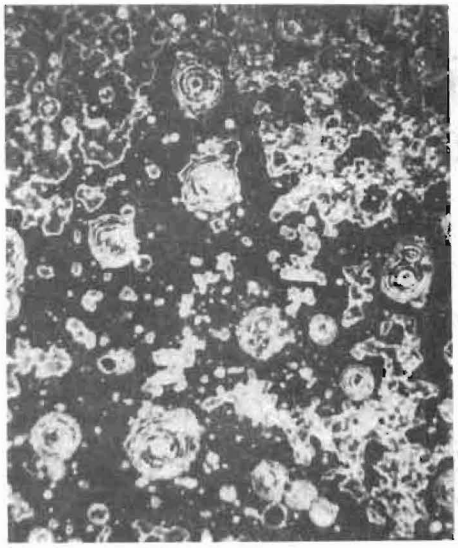
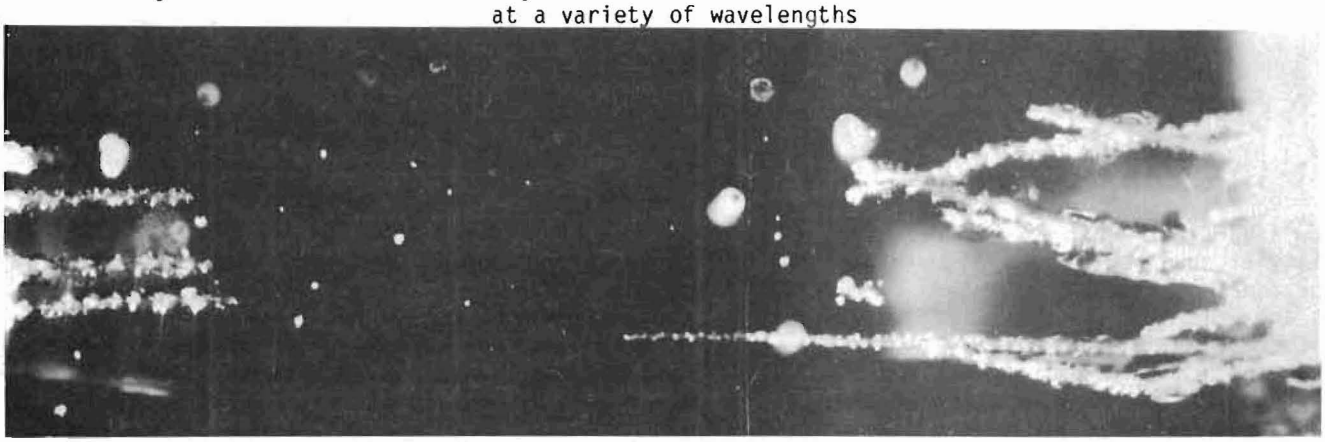


Figure 7 : Laser damage on a surface irradiated by a multi-degenerate beam, 1.064 μm (x20)

Sample	LIDT MW mm-2	
	1.064 μm	10.6 μm
Ho:YLF	13.6→15.3	3.4
Ho:YAG	11.4→12.3	11.2
Nd:YAG	8→50	1.1
Undoped YAG	8→50	1.4
Si	2.8	11.2
Diamond	36	22
KCl	50	54

Figure 8 : Laser induced damage thresholds for a selection of materials irradiated at a variety of wavelengths



Front surface

Nd:YAG laser beam direction ⟶

Rear surface

X5

Figure 9 : Damage on damage, laser glass at 1.064 μm

3 Multiple irradiation

There are several sorts of phenomenon to subsequent pulses after a sample has been damaged.

(a) Damage occurring on damage - this can be in the form of rapidly enlarging damage areas or damage cutting back through the sample towards the laser source. These both happen when small areas (sometimes defect or absorbing inclusions) damage at relatively high levels in the middle of good areas (see fig 9).

(b) Small damage spots which do not change much, e.g. absorbing inclusions in laser glass. The laser power and/or energy densities are high enough for damage but too low for subsequent damage, (fig 10).

(c) Damage spots which subsequently have a higher LIDT. This comes about after irradiating just below the catastrophic damage level. It has been observed on surfaces due to varporisation of organics on single crystal surfaces which have been laser annealed, thus erradicating scratches and pits (see fig 11) as in single crystals of KDP [2]

(d) Large damage spots which do not change in size after repeated irradiation e.g. damage to dielectric coatings on well finished substrates, figure 12

(e) Damage which grows on repeated irradiation, e.g. damage due to a chemical change. This can be seen in PMMA (see fig 13) where the incompletely polymerised perspex carbonises in small spots. These spots absorb more radiation and the black spots grow large and eventually catastrophic damage occurs. The mechanisms of this phenomena have been discussed previously [3].

(f) Damage due to a gradual build up of temperature. This can be seen by reference to thermal runaway in semiconducting samples. We showed the effect of this last year [4] in Ge. We have since shown that the same effect occurs in ZnSe and ZnS but not in KCl (fig 14) (which damages through dielectric breakdown and not a thermal effect). The interesting point about the prf dependent LIDT is that as the same mechanism is involved the percentage drop with prf is virtually independent of other material properties.

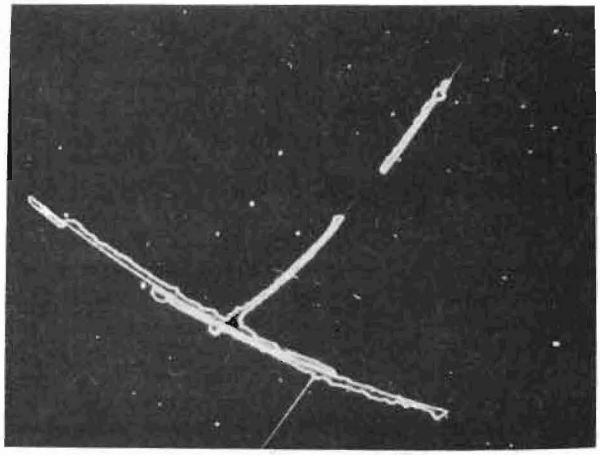
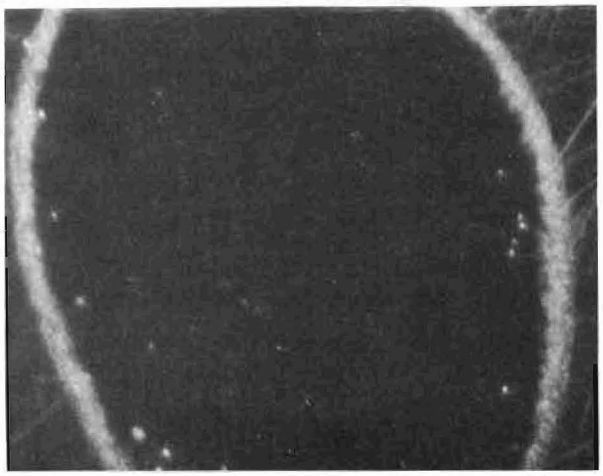


Figure 10 : Cummulative damage on a $\lambda/4$ MgF_2 A-R coating on a Nd:YAG laser rod after 2×10^6 pulses



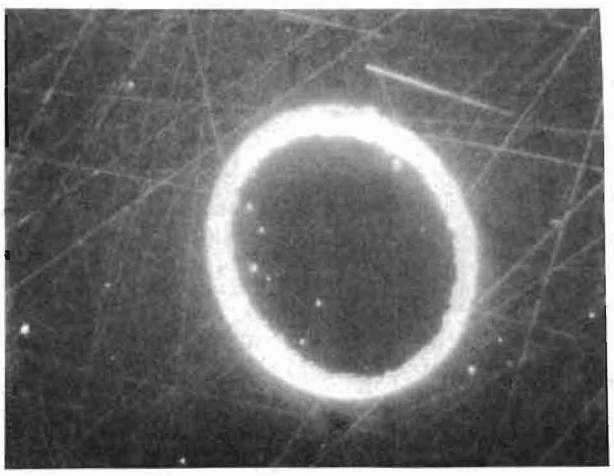
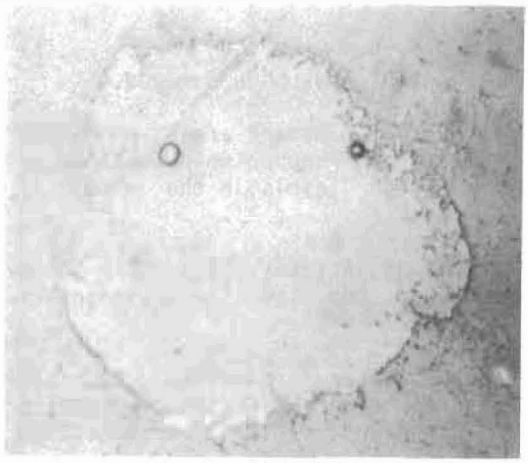


Figure 11 : 'Laser annealed' damage spots on germanium, 10.6 μm (X400)



X1000

Figure 12 : Damage to a dielectric coating, 1.064 μm



Figure 13 : Damage to PMMA, 1.064 μm X30

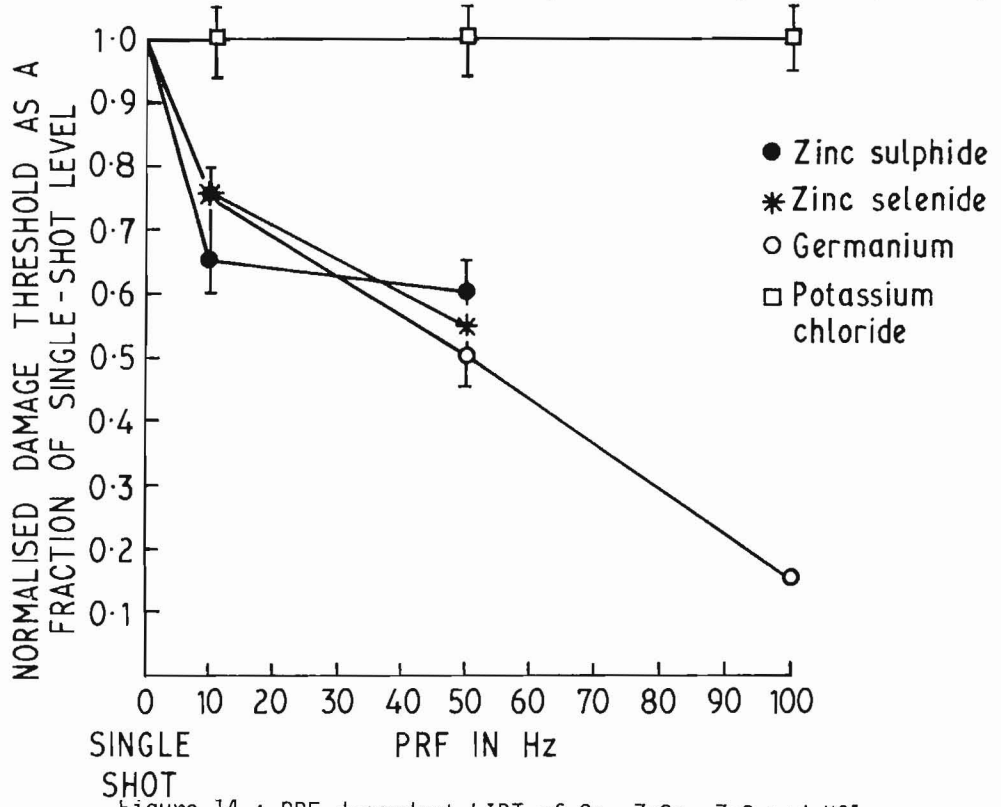


Figure 14 : PRF dependent LIDT of Ge, ZnSe, ZnS and KCl

4 Acknowledgement

This work was carried out with the support of the Procurement Executive, Ministry of Defence, sponsored by DCVD.

REFERENCES

1 Foltyn, S.E. Spotsize effects in laser damage testing. Boulder Damage Conference, November 1982

2 Swain, J.E.; Stokowski, S.E.; Milan, D.; Rainer, F. Improving the bulk laser-damage resistance of KDP by baking and pulsed laser irradiation. Boulder Damage Symposium, November 1981.

3 Manenkov, A.G.; Matyushi, G.A.; Nechitailo, B.S. The nature of accumulation effect in laser induced damage to optical materials. Boulder Damage Symposium, November 1982.

4 Wood, R.M.; Sharma, S.K.; Waite, P.; Variation of laser induced damage threshold of germanium with laser pulse repetition frequency. Boulder Damage Symposium, November 1982.

Manuscript received 1-9-84/sar

DAMAGE THRESHOLD OF FUSED SILICA AT 3ωo

J.F. MENGUE and D. FRIART

Commissariat à l'Energie Atomique
Centre d'Etudes de Limeil-Valenton
B.P. n° 27, 94190 Villeneuve-Saint-Georges, FRANCE

Our laser-matter interaction program requires the conversion of our OCTAL laser from 1.06 µm to 0.355 µm. Fused silica is used to realized the focusing lens and the last optics (KDP windows, debris-shield, etc). A damage test facility at 3ωo was build in CEA Limeil in order to compare the performance of the different French manufacturers production (polished fused silica was provided by SORO, REOSC, BERTIN ESO, STIGMA-OPTIQUE, ELECTRO-QUARTZ).

Key words : Damage threshold - 3ωo - Fused silica - Polishing

1. Damage test facility at 3ωo

It is shown on figure 1.

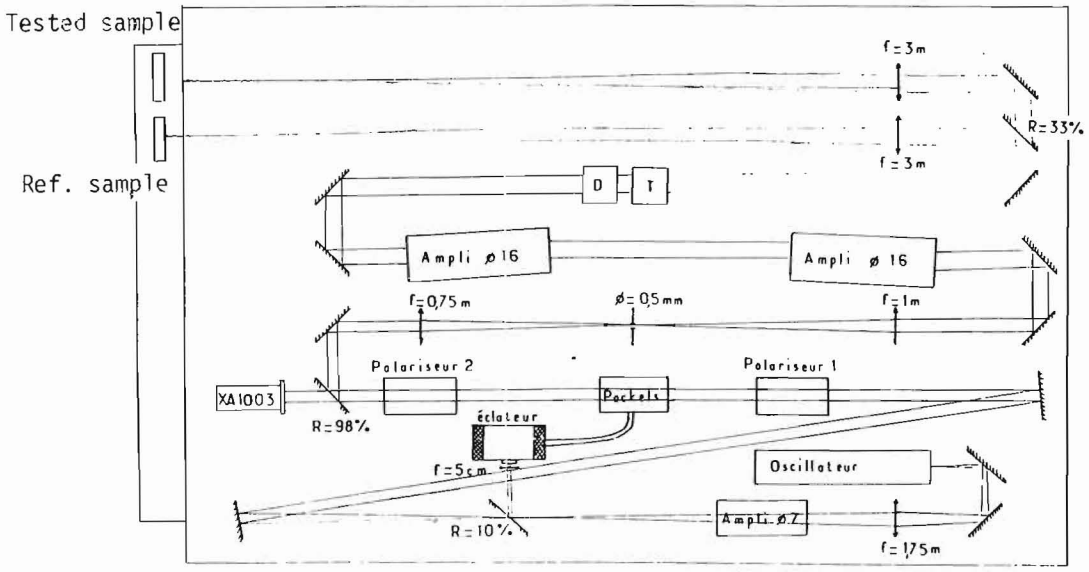
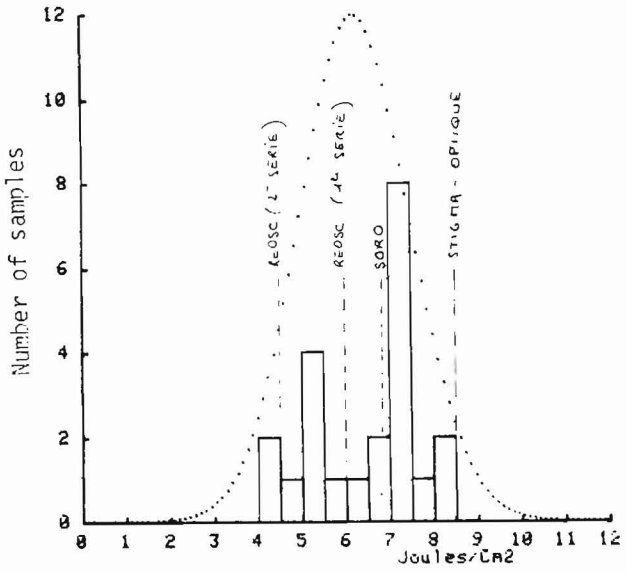
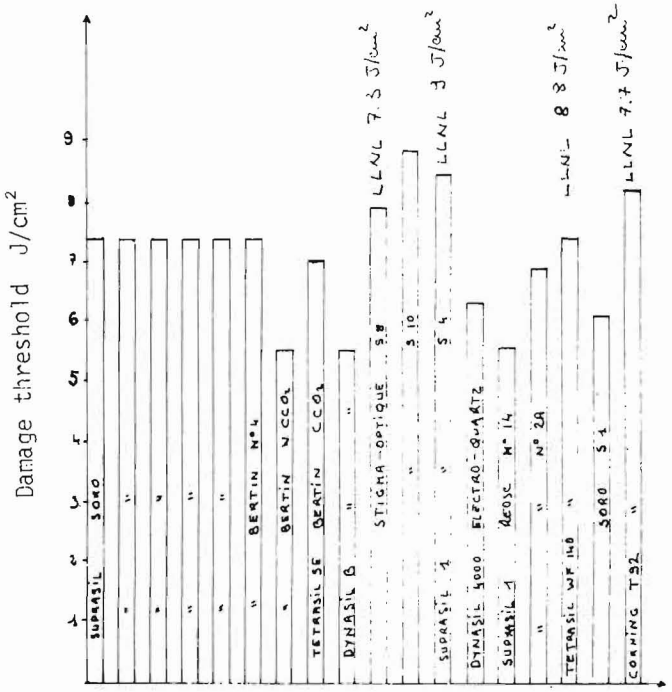


Figure 1 - Damage test facility at 3ωo



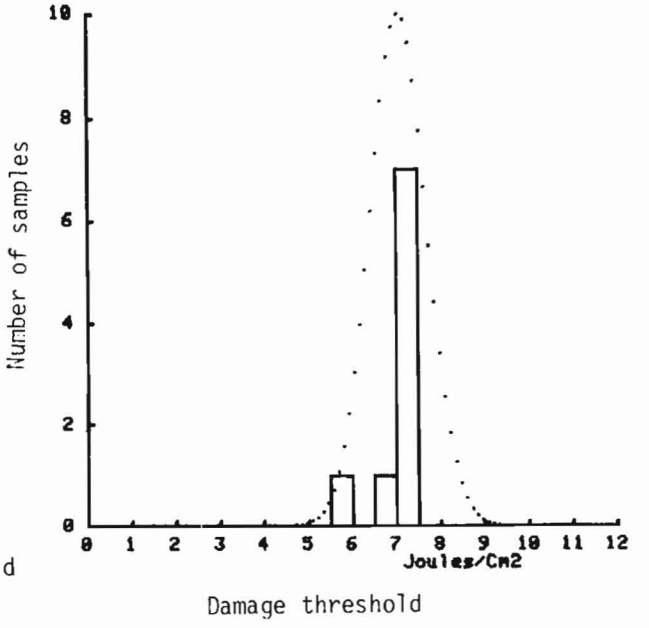
Number of sample
tested : 22
Average damage threshold
6.2 J/cm^2

. Damage threshold

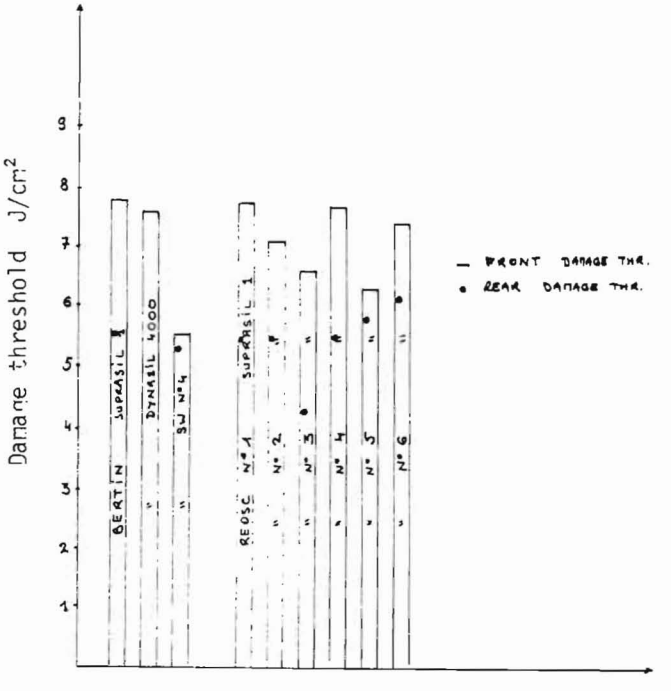


. Name of the companies
. Name of the fused silica

Figure 2 - Histograms of the first tests on fused silica



Number of sample
tested : 9
Average damage threshold
7 J/cm^2



. Name of the companies
. Name of fused silica

Figure 3 - Histograms of the second tests on fused silica

The last amplifier is a 16 mm diameter rod amplifier delivering 750 mJ in 3 ns. Frequency conversion is realized with two 3 cm length type II KDP.

Energy at $3\omega o$ is 200 mJ. Relative measurements of the fused-silica sample is made by comparison to a reference sample.

In order to realize this comparison the converted beam is divided in two arms with an energy ratio of 1/2 ωo and $2\omega o$ frequencies are eliminated by the mirrors treated at $3\omega o$.

Optical density are placed on both arms and on the main beam to compare the damage threshold of the sample and the reference.

Some samples were tested on the absolute test facility in LLNL, giving us an evaluation of the damage threshold in J/cm^2.

2. Results

Best results were obtained by STIGMA-OPTIQUE which is considered as the best optic polisher in FRANCE, with damage threshold around 8.5 J/cm^2 (figure 2).

22 samples were tested with an average value of 6.2 J/cm^2 ; the lowest results were at 5.5 J/cm^2.

In order to increase the lowest results we ordered new samples to some companies. The results were slightly better (average 7 J/cm^2) (figure 3). No indication had been given about special cleaning or polishing.

New samples will be polished and tested and we expect average results of the order of 9 to 10 J/cm^2.

Round-Robin Testing of Low-Scatter Optics*

Jean M. Bennett

Michelson Laboratory, Physics Division
Naval Weapons Center, China Lake, California 93555

and

W. Kent Stowell

Avionics Laboratory
Air Force Wright Aeronautical Laboratories
Wright-Patterson Air Force Base
Dayton, Ohio 45433

For high quality laser optics it is important to compare measurements of surface quality made in different laboratories, determine how scattering levels of silver coatings produced by different groups compare, and what effects, if any, are introduced by stripping the silver coatings and by handling and transporting samples between laboratories. A round-robin study attempted to answer these questions. Participating laboratories included the Avionics Laboratory at the Air Force Wright Aeronautical Laboratories (AFWAL), Dayton, Ohio, Michelson Laboratory at the Naval Weapons Center (NWC), China Lake, California, and the Air Force Weapons Laboratory (AFWL), Albuquerque, New Mexico. Fourteen very low-scatter, optically polished synthetic fused silica (Suprasil) and natural fused quartz (Homosil) samples were purchased from Robert M. Silva of VTI, Dayton, Ohio. Angular scattering, i.e., bidirectional reflectance distribution function (BRDF), was measured on all the uncoated samples and three silver-coated samples at AFWAL using a variable angle scatterometer. Eleven additional samples were silver coated at NWC, and total integrated scattering (TIS) was measured on all silver-coated samples. Transmission electron micrographs were made of the surfaces (silvered and also stripped) of two samples, and selected coated and uncoated samples were profiled. TIS was then measured on the instrument at AFWL. At AFWAL BRDF measurements were made on all the samples, both silver coated and then stripped, and TIS measurements were repeated on selected samples at NWC. It was found that the TIS measurements made at NWC and AFWL were in good agreement. Scattering from bare substrates increased after silver coating and stripping, and there was a large variability in the silver coatings, particularly those made at NWC. Critical factors in obtaining low-scatter silver surfaces appeared to be the cleaning and coating of the samples. The results of the round-robin measurements are discussed in detail in this paper.

Key words: fused quartz; low-scatter optics; optical characterization; scattering measurements; silver films.

Introduction

High quality, low-scatter optics such as are used, for example, in laser gyros, high energy laser systems, and x-ray and optical telescopes including the Space Telescope are difficult to make, to characterize, and to keep in their original pristine condition. Furthermore, a variety of characterization techniques are in use at different laboratories, and it is often difficult to intercompare measurements. For these reasons, a round-robin study was initiated between the Air Force Wright Aeronautical Laboratories (AFWAL), Dayton, Ohio, the Naval Weapons Center (NWC), China Lake, California, and the Air Force Weapons Laboratory, Albuquerque, New Mexico. The four major objectives of the study were to (1) correlate angle-resolved scattering measured at AFWAL with total integrated scattering (TIS) measured at NWC and AFWL, and surface profiles measured at NWC, all on the same samples, (2) determine the effect on substrate scatter and roughness of silver coating and then stripping the substrates, (3) determine the effect of handling and interlaboratory measurements on the

*Work supported by the Air Force Weapons Laboratory.

scattering levels of uncoated and silver coated-substrates, and (4) determine the correlation of laser damage thresholds (1.06 μm wavelength, 5 nsec pulse length) with scattering from uncoated substrates. The last objective was not accomplished because the laser at AFWL intended for the measurements was not operational. Possibly these measurements will be made at a later date.

Fourteen 1-in.- (25.4-mm-) diameter "quartz" substrates were used in the study. Three were Homosil, natural fused quartz, and are designated by HT; the other eleven were Suprasil, synthetic fused silica, W-1 grade (best water-free optical quality) and are designated T-22xx, where xx is the sample number. Three samples were coated at AFWAL, and eleven others at NWC with approximately 1000-Å-thick silver films. Prior to coating, the samples were cleaned by drag wiping with a nonabrasive lens tissue using methanol as a solvent. Then collodion was poured onto the surface of each sample, allowed to dry, and the collodion film stripped. (Collodion captures particulates so they are removed when the film is stripped.) The silver films were removed with a dilute solution of nitric acid. They were then rinsed in deionized water and dried using a nitrogen gas jet to chase the water off the sample.

Instrumentation

The angular distribution of scattered light or bidirectional reflectance distribution function (BRDF) [1][1] was measured on a variable angle scatterometer (VAS) [2-4] at AFWAL. Specifically, the angle of incidence of the 6328 Å He-Ne laser beam was 30°, and the scattered light was measured on the surface normal. The laser was unpolarized, but the source optics made the light incident on the sample predominantly s-polarized. In the VAS, front surface scattering can be separated from bulk and rear surface scattering [2], so that uncoated samples can be measured with as much sensitivity as coated samples. The illuminated area on the sample was a circular spot 0.5 mm in diameter, and the telescope in front of the detector had a 2 minute angular field. Figure 1 gives an example of the registration accuracy that can be obtained with the instrument. The upper three curves are three-dimensional plots of scattering from a 3 mm x 3 mm area in the center of the sample. The scattering is plotted logarithmically in the z-direction (limits of the log scale are given), while the position on the surface is given by the x-y coordinates. In the lower three polar plots, the sample remained fixed at a given location, and was then rotated about the surface normal located at that point. In each plot are superposed curves taken at five different locations: the four corners and the center of the 3 mm x 3 mm area. The two BRDF three-dimensional plots for the unsilvered surface are similar, but specific features cannot be unambiguously identified. Specifically, there are many more scattering sites in the plot on the upper right, showing that the surface was apparently damaged by the coating and stripping operation. The polar plots show that there was a surface defect that produced enhanced scattering at a particular angle; its effect was evident when the surface was silver coated, and surface defects giving unidirectional scattering were present after the film was removed.

TIS was measured at NWC using the Optical Evaluation Facility [5,6] at a wavelength λ of 6471 Å (krypton red laser line). An effective rms roughness δ can be calculated from the measured TIS using the approximate expression [5]

$$\delta = (\lambda/4\pi)\cdot\sqrt{TIS} \quad , \tag{1}$$

which holds when $\delta \ll \lambda$. The surface spatial wavelengths theoretically are in the range 0.65 μm (red laser wavelength) to ∞, but actually the angular collection limits of 2.85° to 80° for the aluminized hemisphere restrict the surface spatial wavelength range to 0.65 μm to 13 μm for normal incidence illumination on the sample. The TIS is the fraction of the reflected scattering into almost a hemisphere divided by the total sample reflectance (diffuse scattering plus specularly reflected light); for very low-scatter silver-coated surfaces, TIS is approximately equal to the scattered light divided by the specular reflectance of the sample. Thus the value of the TIS is independent of the sample reflectance and is a function only of the surface roughness. In contrast, BRDF is the ratio of light scattered into a known solid angle dΩ divided by the product of dΩ and the incident beam intensity. Thus, the BRDF value will be quite different for silver-coated and bare quartz surfaces of the same roughness, as discussed in the section on silver-coated substrates. TIS was also measured at AFWL using an instrument similar to that at NWC but with a He-Ne laser source (wavelength of 6328 Å).

Surface profiles were measured at NWC with a Talystep surface profiling instrument [7] that had a 1-μm-radius diamond stylus. A 2-mg loading was chosen so as not to mark the silver coatings. Profile lengths generally included 1.57 mm, 628 μm, 157 μm, and 15.7 μm; only the shorter two profile lengths

[1] Figures in brackets indicate the literature references at the end of the paper.

are illustrated in this paper because they give information about the surface polish and roughness of the silver films. The longer profile lengths emphasize substrate waviness which was less important in this study.

A JEOL Model 120U transmission electron microscope at NWC was used to obtain micrographs of two-stage surface replicas of uncoated and silver-coated surfaces. The replicas were made with moistened pressure-sensitive tape which was pressed onto the surface and allowed to dry. After the tape was removed, it was obliquely shadowed with a platinum/carbon film and then with a thick carbon layer deposited at normal incidence. Finally, the tape was dissolved and the carbon replica was observed in transmission to show surface details.

Results

The results of all the measurements are presented in table 1. These include initial BRDF and surface profile (rms roughness) measurements on the bare substrates, BRDF, TIS (rms roughness) and surface profile measurements on the substrates after the silver coating had been removed. These results will be discussed in detail throughout the rest of the paper.

Figures 2 and 3 show transmission electron micrographs of two-stage surface replicas of bare and silver-coated substrates made of Suprasil and Homosil. Replicas were first taken of the silver-coated surfaces. The silver was then removed with dilute nitric acid and replicas were made of the bare surfaces. Very little detail shows on either the bare or silver-coated surfaces, even though the shadowing angle was only about 10° from the plane of the surface. At this shadowing angle, a feature such as an isolated particle casts a long, well-defined shadow, as is shown in the small inset photos at the bottom of figure 2. Silver films evaporated under similar conditions onto rougher substrates, and sputtered silver films have a lumpier appearance [8]. The electron mirographs do not seem to give information as to why the silver films in this study produced proportionately more scattering than did the uncoated substrates.

Bare Substrates

In table 1 the substrates are ordered according to their initial scattering levels, and samples HT-3 and T-2217 (whose micrographs were shown in figures 3 and 2, respectively) are near the low and high ends. No obvious differences can be discerned between the bare surfaces of these samples in the electron micrographs. BRDF plots for the two samples, before coating, are shown in figure 4, where not only is the average scattering level different, but the rotational symmetry of the scattering is also much better for the lower scatter surface.

Scattering increased on most samples when they were silver coated and then stripped, as can be seen in the BRDF columns for the bare substrates and the silver-stripped substrates in table 1. Figure 5 shows BRDF plots of this effect for sample T-224. The ratios of scattering after and before coating given in the table show that 71% of the samples showed increased scattering levels after being silver coated and stripped. The scattering increase appears to be caused by an increasing number of scattering centers, and greatly increased scattering at each defect; also, there appears to be rotational asymmetry introduced into the scattering pattern after silver coating and stripping, as evidenced by the polar plot in the lower right-hand corner of figure 5. Four of the fourteen substrates (29%) showed no increase in scattering level after silver coating and stripping. Before and after BRDF plots for one, T-2216, are shown in figure 6. Even though more high scattering defect sites appear after coating and stripping, the base scattering level seems to be somewhat lower (see the polar plot at the bottom right in figure 6).

Silver-Coated Substrates

The results for the silver-coated substrates include TIS measurements at NWC and AFWL, as well as BRDF and surface profile measurements. There is excellent agreement between the TIS measurements made at the two laboratories (table 1). Thus, both instruments are measuring properties of the samples, and systematic errors within the instruments have been minimized. Figure 7 shows that there is also excellent correlation between both sets of TIS measurements and the BRDF measurements made at AFWAL. Even though both BRDF and TIS are scattering measurements, their magnitudes cannot be directly compared because the BRDF gives a value for scattering into one specific angle, while the TIS measures scattering into angles collected by the aluminized hemisphere (2.85° - 80°). However, the silvered samples that have high BRDF values also have large rms roughnesses deduced from TIS measurements, so the correlation between the two kinds of measurements is excellent.

Silver films evaporated at NWC showed a wide range of scattering levels because of cleaning and/or coating difficulties. Figures 8 and 9 show BRDF three-dimensional plots and surface profiles, respectively, of a low-scatter and a high-scatter silver-coated substrate. The BRDF values of the

uncoated substrates were essentially the same, as shown in table 1. Under Nomarski illumination the high-scatter film appeared to have bright, high-scattering point defects, and during the alignment of the sample in the Talystep instrument several large particulates and holes, ~ 50 - 60 Å in height and depth, were noted. These were avoided in the profiles shown in figure 9 because they greatly influence the rms roughness value; it is difficult to find a spot on a surface to give a true "average profile." However, the silver film between the high-scattering point defects appears to be no rougher than the low-scatter NWC silver films. The polar BRDF plots in figure 8 show that there are a few high-scatter directions for the low-scatter film, T-227, but that the scattering appears to be uniformly high in all directions for the high-scatter film, T-221, over the five 0.5-mm-diameter spots illuminated by the laser beam.

Figures 10 and 11 show BRDF plots and surface profiles, respectively, of high-scatter and low-scatter substrates silver-coated at AFWAL. The range of scattering levels for these films was only about a factor of 3 in BRDF, as compared to the factor of 300 for the NWC films shown in the preceding two figures. The polar BRDF plots in figure 10 show that the high-scatter film is rather uniform, but the lower scatter film has polar angles where its scattering level is several times the average value. Comparing the Talystep profiles in figure 11 with those in figure 9, the AFWAL high-scatter film (on T-2217) appears to be rougher and the low-scatter film (on HT-3) smoother than the two corresponding NWC-coated silver films.

It had been observed previously at AFWAL that silver films evaporated onto lower scatter substrates tended to have lower BRDF values than those deposited onto higher scatter substrates. Although this effect was not seen in the present round-robin measurements because of the anomalously high scatter of some of the films, it is of interest to compare Talystep profiles of the bare substrate and the smoothest, lowest scatter silver film (see figure 12). Although the BRDF level increased by a factor of 8 after sample HT-4 was silver coated and stripped, the Talystep profile roughness (after stripping) was still limited by instrumental noise in the Talystep. The crystallites in the silver film on HT-3 (a lower scatter substrate than HT-4) are seen to have a small but measurable effect on the surface profile. All of the bare substrates profiled either before or after silver coating and stripping were extremely smooth, and the profiles were limited by instrumental noise.

To study aging effects in silver, TIS and Talystep measurements were made 17 days apart on two silver films; both coatings had been prepared at NWC. The TIS and Talystep profiles of the higher scatter film showed no changes (table 1), but, as shown in figure 13, the profile roughness on the lower scatter film increased noticeably, and the TIS-derived roughness almost doubled. The reason for these differences is not clear.

The roughness δ_f added by the silver films as measured by the Talystep can be calculated using the approximate relation

$$\delta_f = \sqrt{\delta_{fs}^2 - \delta_s^2} \quad , \tag{2}$$

where δ_{fs} and δ_s are the measured profile roughnesses of the film-covered and bare substrates, respectively. The rms roughnesses of the silver films independent of the substrates and the instrumental noise were calculated to be about 0.1 Å lower than the measured roughnesses of the film-coated substrates.

The autocovariance function was measured for several film-covered surfaces and was found to have a nearly exponential shape, in agreement with measurements made on other film-covered substrates [7]. The correlation lengths for the silver films on T-2214 and T-224 were 0.22 μm and 0.15 μm, respectively, essentially at the 0.1 to 0.2 μm resolution limit of the Talystep instrument [7]. The longer correlation length of 7.8 μm measured on silver-coated sample HT-3 was caused by a very slight residual waviness on the polished Homosil surface (correlation lengths were determined using a 1-mm-long scan and 16,000 data points). The correlation lengths of 0.71 μm and 1.66 μm measured on silver-coated samples T-226 and T-222, respectively, were influenced by particulates profiled in the 1-mm-long scans.

In comparing the measured BRDF values for silver-coated surfaces with those for the bare surfaces before coating, remember that the scattering per unit solid angle (steradian) is measured relative to the intensity of the incident beam. Hence the BRDF of a silver-coated surface is calculated to be 23.4 times higher than that of an uncoated quartz surface of the same roughness for the scattering angles used in this experiment [9]. Thus, if the silver exactly contoured the bare surface and did not add any additional scattering, the measured silver BRDF values should vary between 0.1357 ppm/sr for sample T-229 to 1.327 ppm/sr for sample T-223. The actual silver BRDF values in table 1 are considerably higher.

Comparing the TIS equivalent roughnesses for all the silver films, there appears to be no clear correlation of roughness with the BRDF scattering level of the bare substrate. For example, two of the lowest scatter silver films are on samples T-229 and T-223, the lowest and highest bare scatter surfaces, and a third is on sample T-227 with an intermediate bare BRDF value.

Conclusions

We have shown that the BRDF of 79% of the bare substrates (11 out of 14) increased after silver coating and stripping of the silver films. The increase in scattering ranged from 2 to 260 times. For 21% of the samples (4 out of 14) the BRDF remained essentially constant. All of the substrates were so smooth that the Talystep profiles were only marginally different from the instrumental noise; no distinction could be made between the initial substrate conditions and changes which might have occurred by silver coating and stripping.

There was excellent agreement between TIS measured on silver-coated substrates at NWC and at AFWL. There was also good correlation between BRDF values measured at AFWAL and both sets of TIS values. No correlation was found between BRDF and TIS for the silver coatings and BRDF measured on the bare substrates before coating. There was a possible slight degradation in the silver coatings during the interlaboratory measurements. The BRDF values and TIS and Talystep profile roughnesses all ranked the three AFWAL silver-coated samples in the same order, but not in the order of the initial substrate scattering. There was a wide variation in BRDF and TIS for the NWC silver-coated samples. Finally, there was poor correlation between TIS and Talystep profile roughnesses for the NWC silver-coated samples, probably because of large silver crystallites on the surface which produced scattering but were not included in the Talystep profiles. More work is needed to improve the quality and reproducibility of silver coatings on ultralow-scatter substrates and to understand the physical mechanisms affecting the nucleation and growth of silver films.

The authors would like to thank Robert M. Silva of VTI, Dayton, Ohio, for providing the quartz substrates used in the study. In addition, they would like to thank Naval Weapons Center personnel P. C. Archibald for making total integrated scattering measurements and J. H. Dancy for doing the electron microscopy; Air Force Wright Aeronautical Laboratories personnel Judy Theodosakis, Keith A. Pugh, and James G. Grote for making the angle-resolved scattering measurements; and Gloria Petty at Rocketdyne Division of Rockwell International, Albuquerque, New Mexico, for making total integrated scattering measurements. Alan Stewart at the Air Force Weapons Laboratory arranged for funding to carry out the round-robin measurements.

References

[1] Nicodemus, F. E.; Richmond, J. C.; Hsia, J. J.; Ginsberg, I. W.; Limperis, T. "Geometrical considerations and nomenclature for reflectance," NBS Monograph 160; 5-6; 1977.

[2] Orazio, F. D. Jr.; Silva, R. M.; Stowell, W. K. "Instrumentation of a variable angle scatterometer," Proc. SPIE 384; 123-131; 1983.

[3] Silva, R. M.; Orazio, F. D. Jr.; Stowell, W. K. "Scatter evaluation of supersmooth surfaces," Proc. SPIE 384; 2-9; 1983.

[4] Stowell, W. K.; Orazio, F. D. Jr. "Damage effects identified by scatter evaluation," Proc. SPIE 406; 23-42; 1983.

[5] Bennett, H. E. "Scattering characteristics of optical materials," Opt. Engr. 17; 480-488; 1978.

[6] Archibald, P. C.; Bennett, H. E. "Scattering from infrared missile domes," Opt. Engr. 17; 647-651; 1978.

[7] Bennett, J. M.; Dancy, J. H. "Stylus profiling instrument for measuring statistical properties of smooth optical surfaces," Appl. Opt. 20; 1785-1802; 1981.

[8] Bennett, J. M. "Measurement and interpretation of fine form errors in optical surfaces," Symposium on Optical Surface Technology; 12-14 April 1983; Garmisch, Germany. Proceedings to be published by SPIE.

[9] Elson, J. M.; Rahn, J. P. Private communication; 1983.

Table 1. Measurements on round-robin low-scatter optics. All BRDF values are in ppm/sr and rms roughness values δ are in Å

	Bare substrate		Silver-coated substrate			Silver-stripped substrate		
		δ		δ	δ		δ	
Sample	BRDF (AFWAL)	(Taly, NWC)	BRDF (AFWAL)	(TIS, NWC)	(TIS, AFWL)	(Taly, NWC)	BRDF (AFWAL)	(Taly, NWC)	BRDF ratio
T-229	0.0058	1.6	4.68	3.6	2.7	-	0.0369	-	6.4
T-2220	0.0138	-	2420.	-	-	-	2.0331	-	147.
HT-3	0.0156	-	10.34	4.8	4.0	2.6	0.0965	-	6.2
T-2214	0.0188	-	82.08	8.7	6.8	6.3	0.0530	-	2.8
T-224	0.0207	-	33.34	3.6	2.9	3.4	0.6050	1.8	29.2
				6.5		4.6			
T-221	0.0221	-	3008.	48.0	54.2	4.1	0.5667	-	25.6
T-227	0.0248	-	9.88	3.8	3.3	3.8	0.0523	-	2.1
HT-1	0.0283	-	2036.	62.5	-	-	0.3052	1.8	10.8
T-226	0.0303	-	1163.	42.2	41.2	4.0	0.0293	-	0.97
T-2216	0.0320	-	21.53	-	-	-	0.0290	-	0.91
T-222	0.0328	-	466.5	26.0	25.5	4.0	8.752	2.1	267.
				26.7		3.9			
HT-4	0.0553	-	3035.	74.5	-	-	0.4249	1.7	7.7
T-2217	0.0555	-	34.82	5.6	3.9	5.7	0.0444	-	0.80
T-223	0.0567	1.8	10.78	3.8	2.9	-	0.0599	-	1.06

[a] Electron micrographs of silver coated and stripped surface
[b] Sample remeasured 17 days later
[c] BRDF after silver coating and stripping/BRDF before silver coating
[d] Samples silver coated at AFWAL; all others coated at NWC

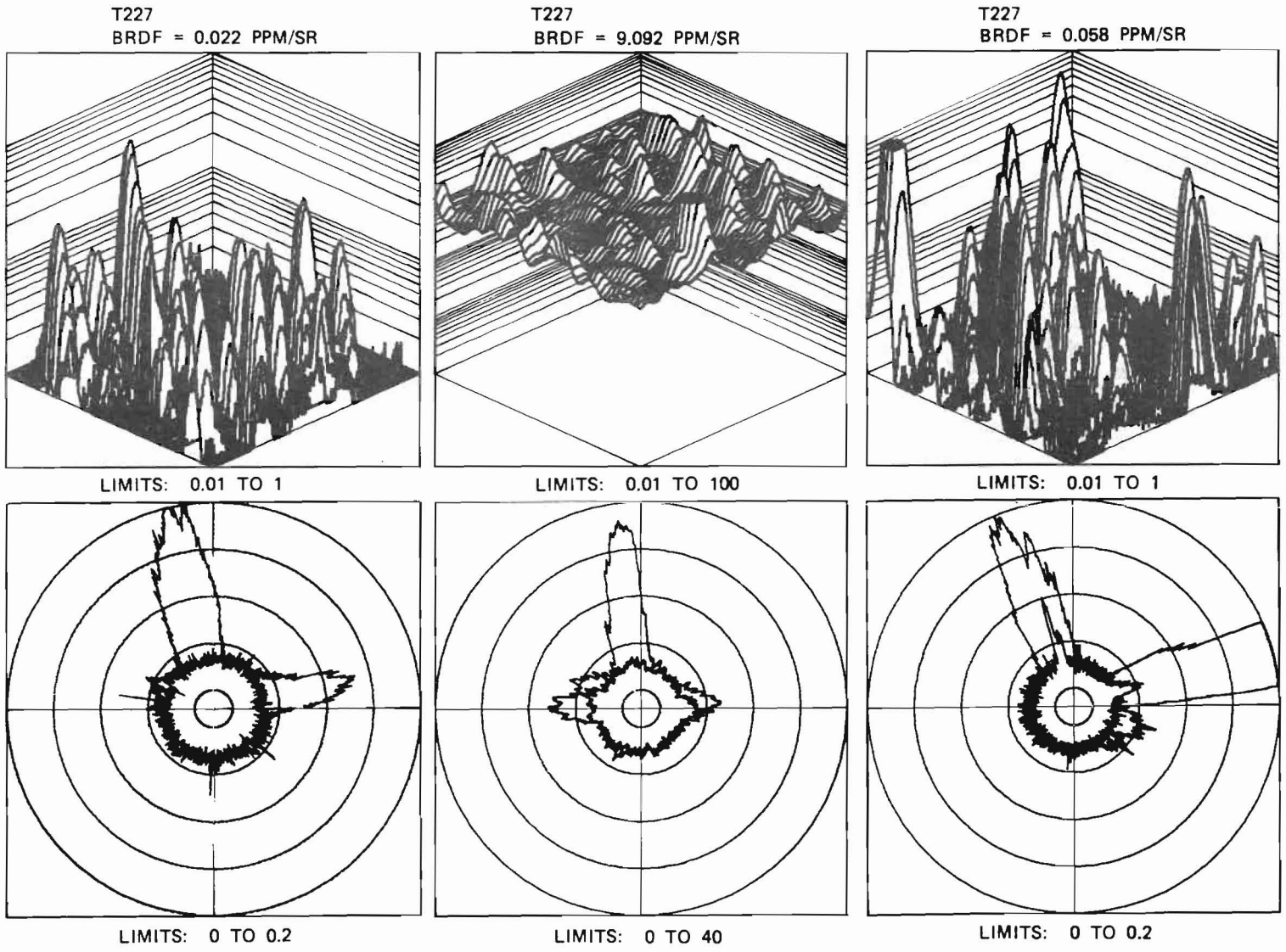


Figure 1. Registration accuracy of variable angle scatterometer.

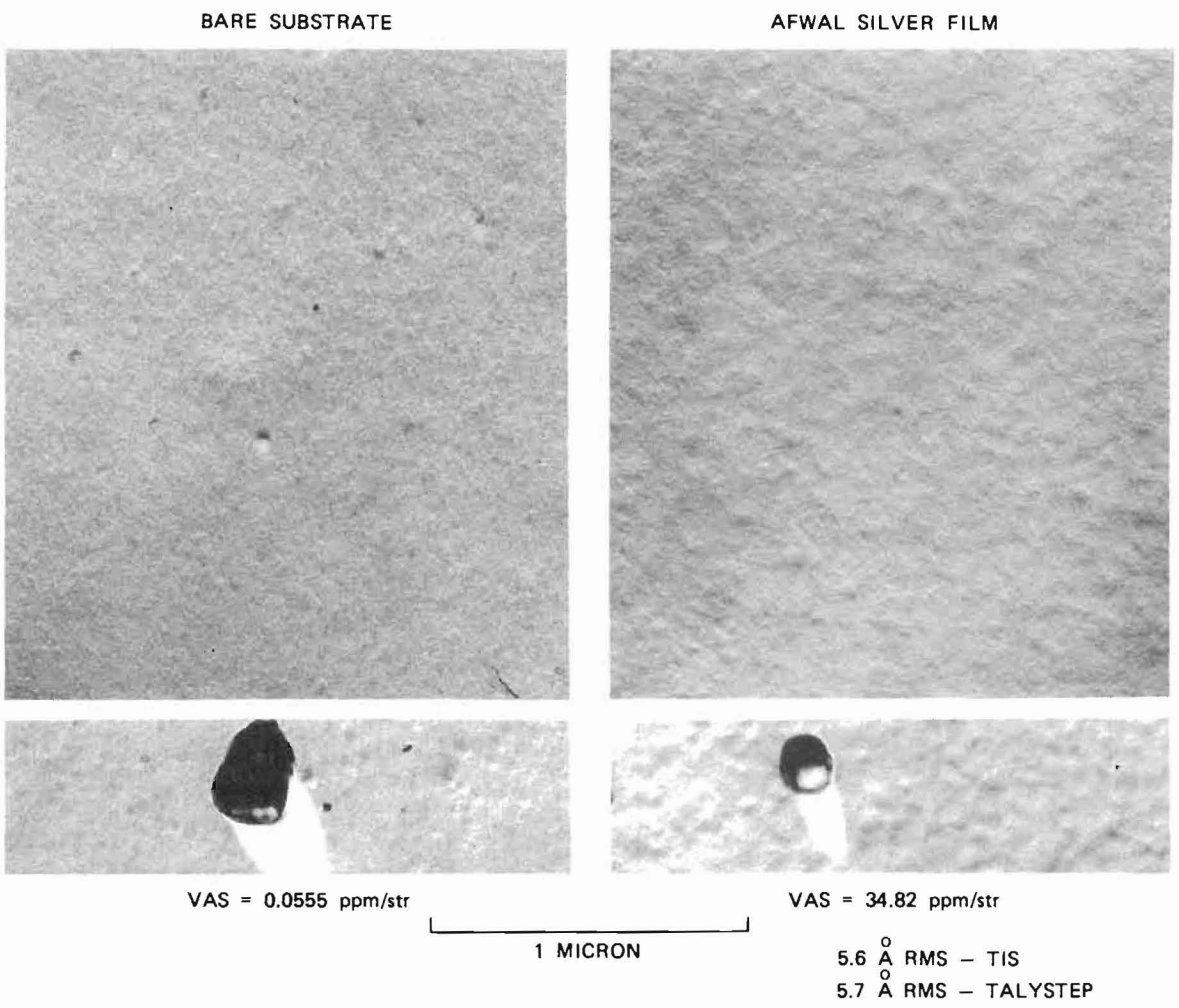


Figure 2. Transmission electron micrographs of Suprasil T-2217 bare and coated with an AFWAL silver film.

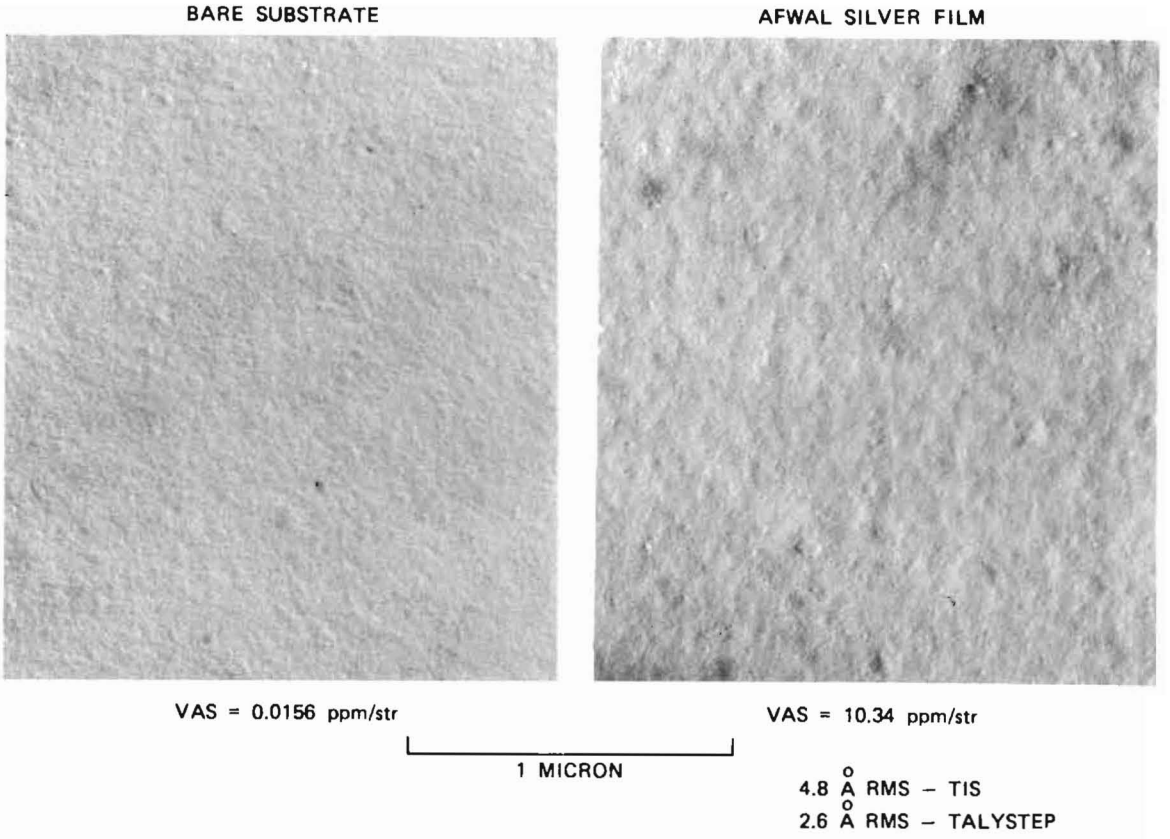


Figure 3. Transmission electron micrographs of Homosil HT-3 bare and coated with an AFWAL silver film.

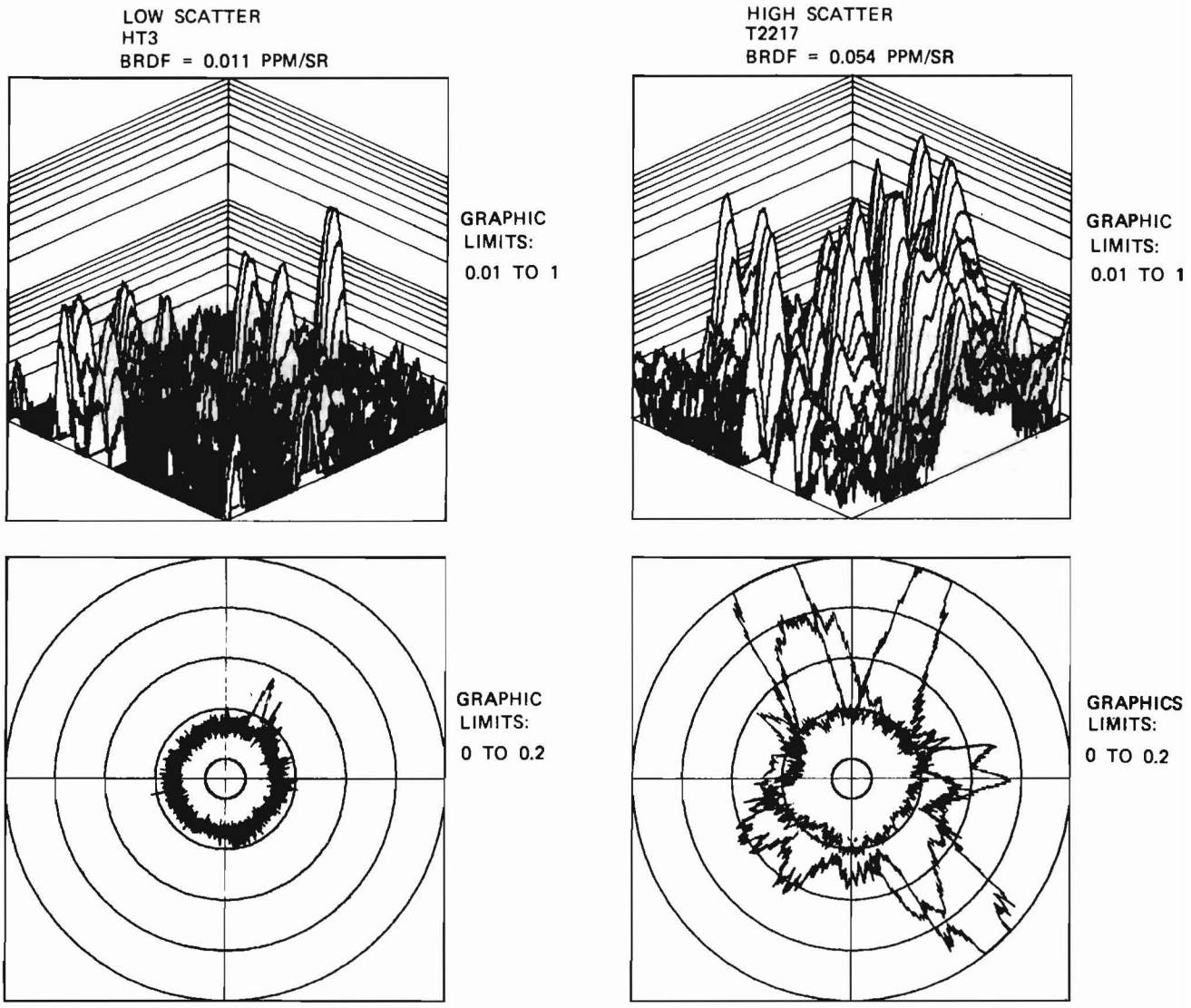


Figure 4. BRDF of low-scatter (HT-3) and high-scatter (T-2217) substrates before coating.

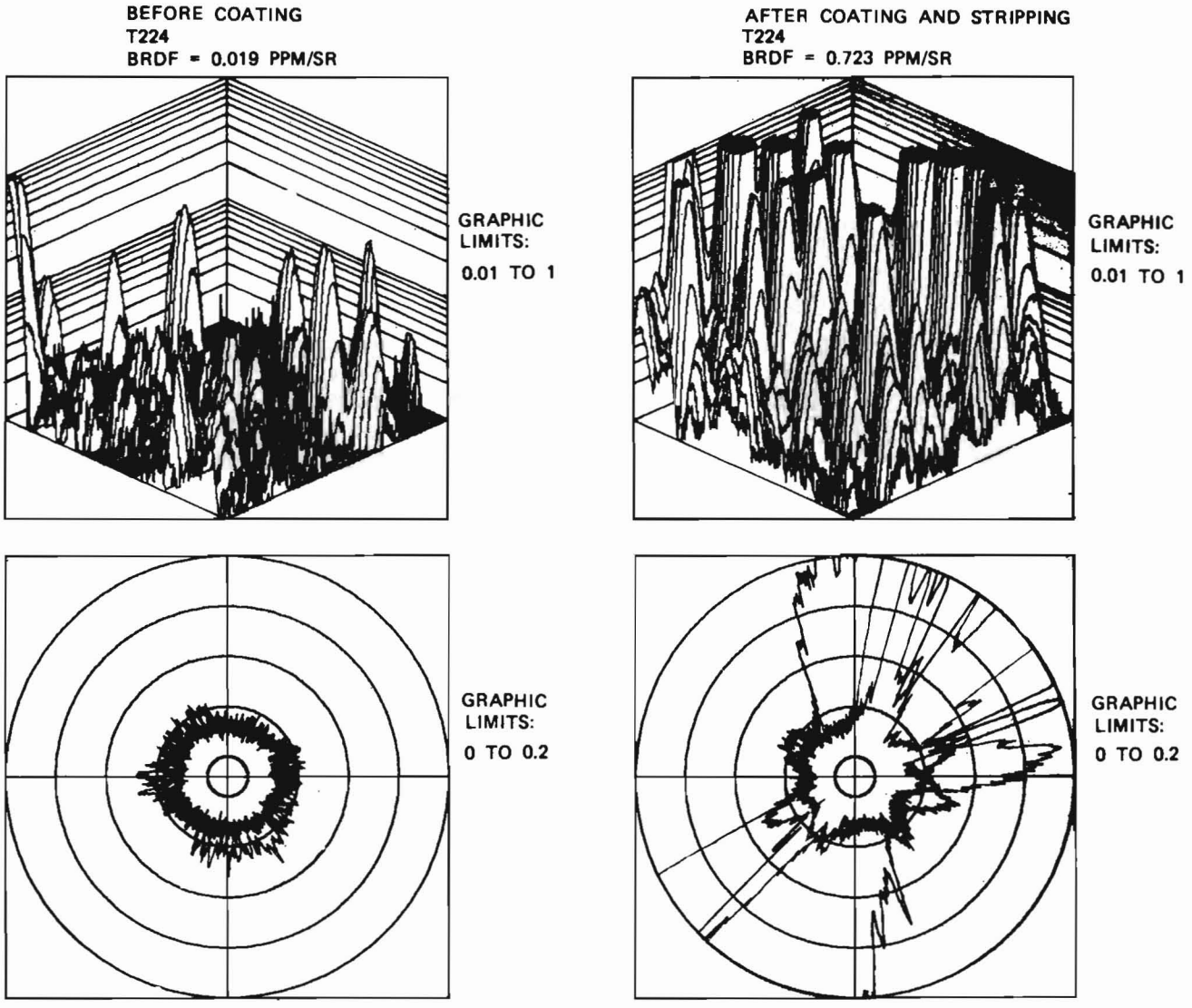


Figure 5. BRDF showing degradation of bare substrate T-224 by coating with silver and stripping.

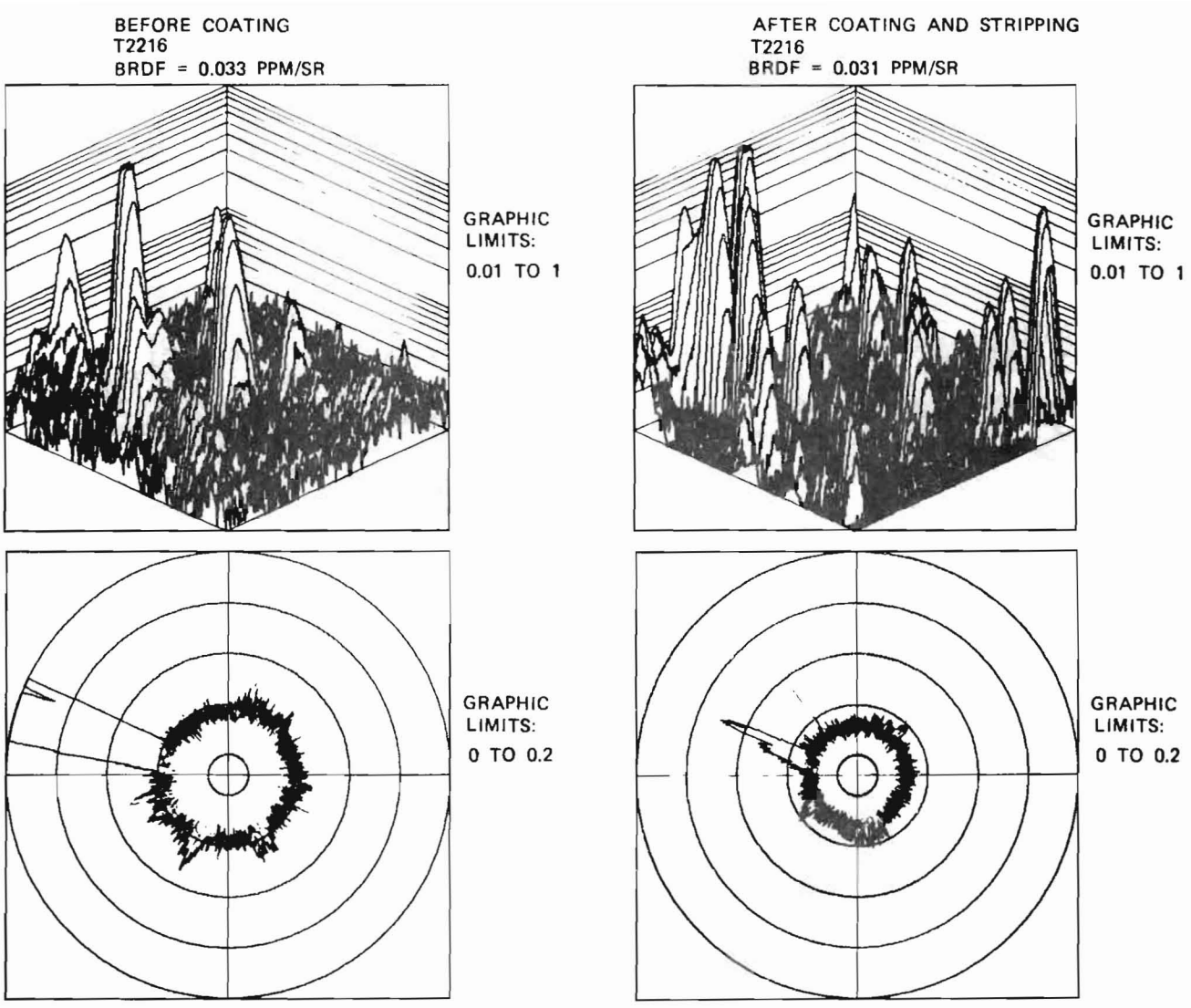


Figure 6. BRDF showing no degradation of bare substrate T-2216 by coating with silver and stripping.

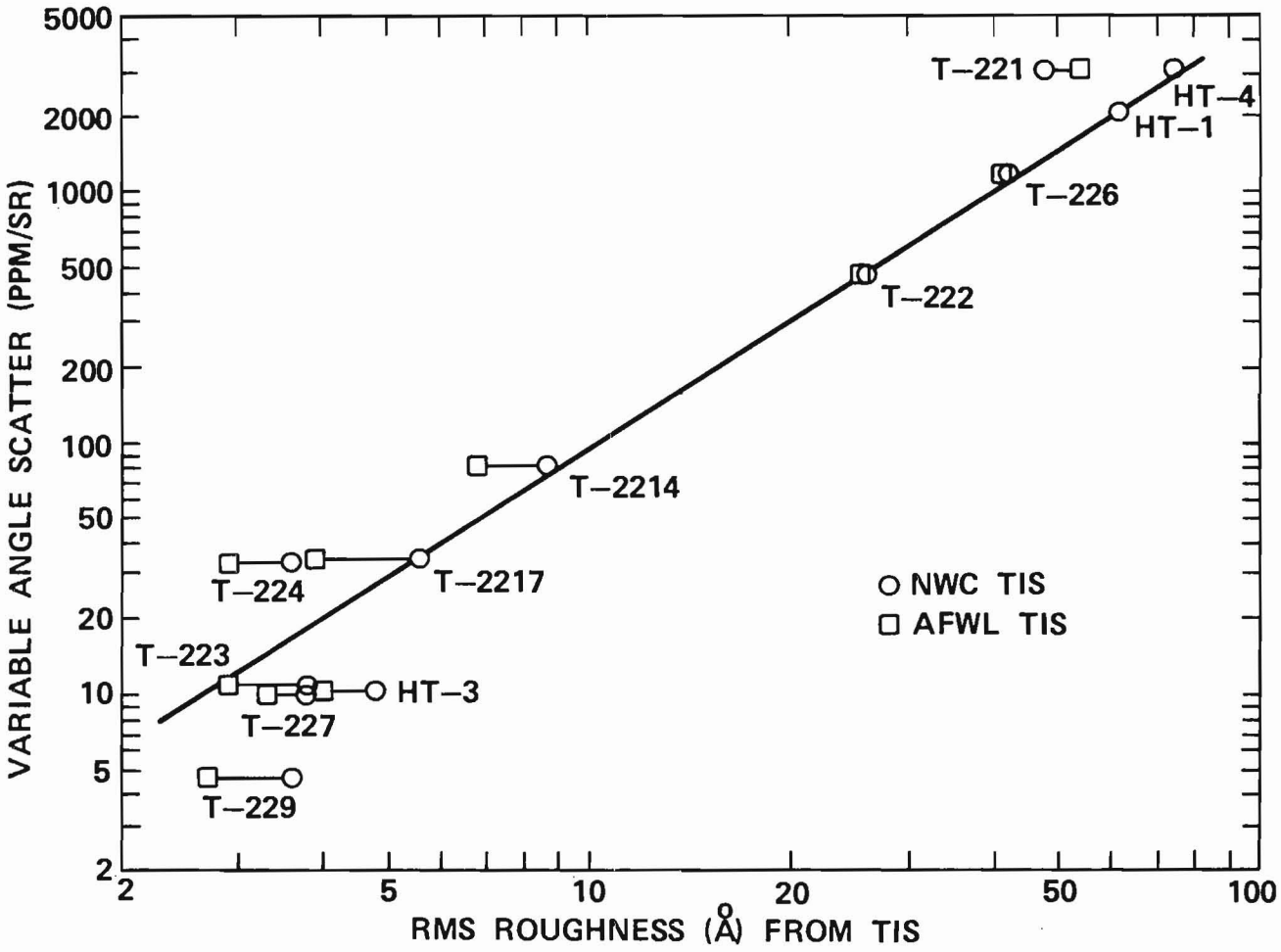


Figure 7. Correlation of variable angle scattering (BRDF) and TIS measurements on silvered surfaces.

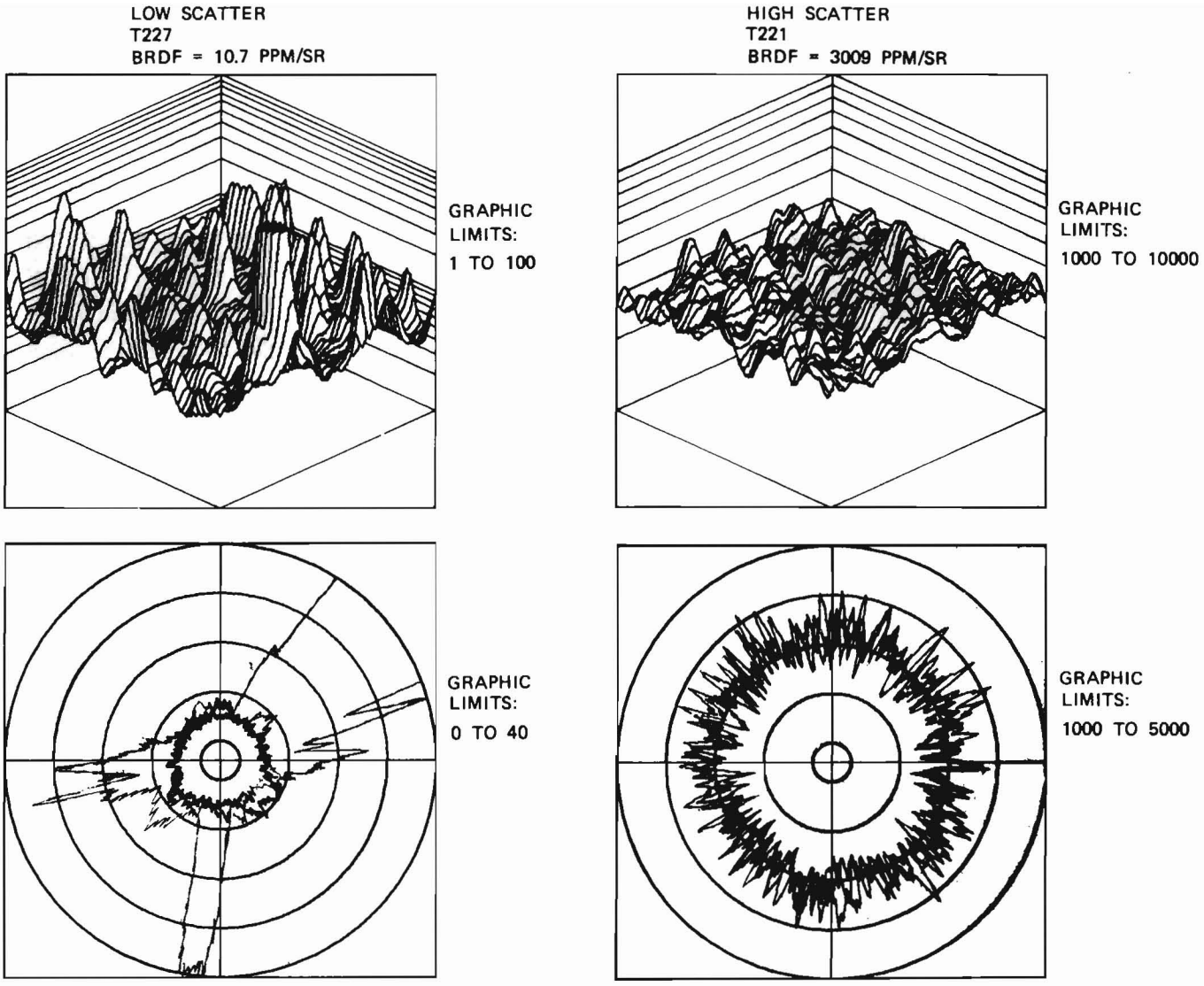


Figure 8. BRDF of low- and high-scatter NWC-coated silver films on substrates T-227 and T-221, respectively.

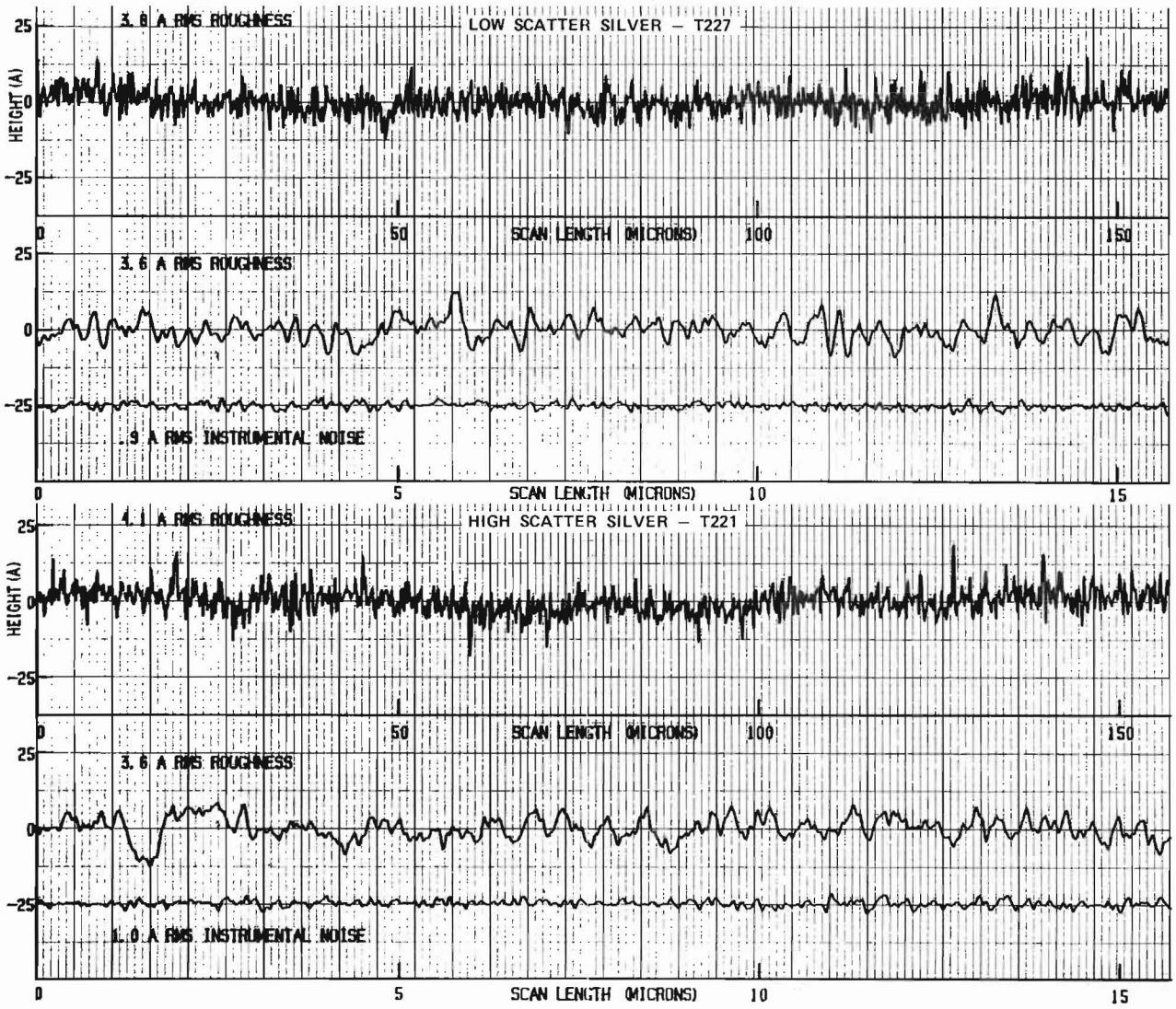


Figure 9. Surface profiles of the same low- and high-scatter silver films shown in figure 8.

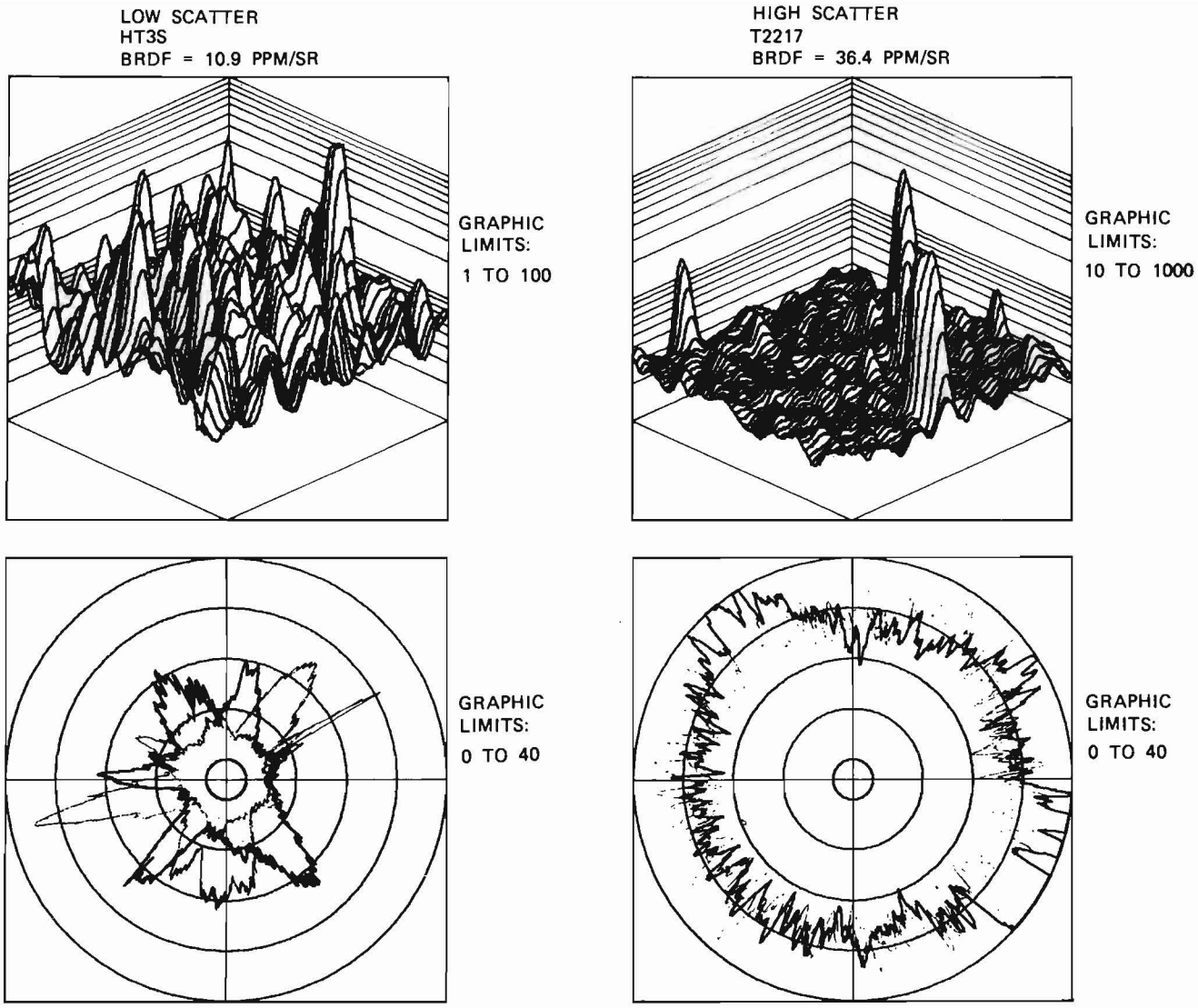


Figure 10. BRDF of low- and high-scatter AFWAL-coated silver films on substrates HT-3 and T-2217, respectively.

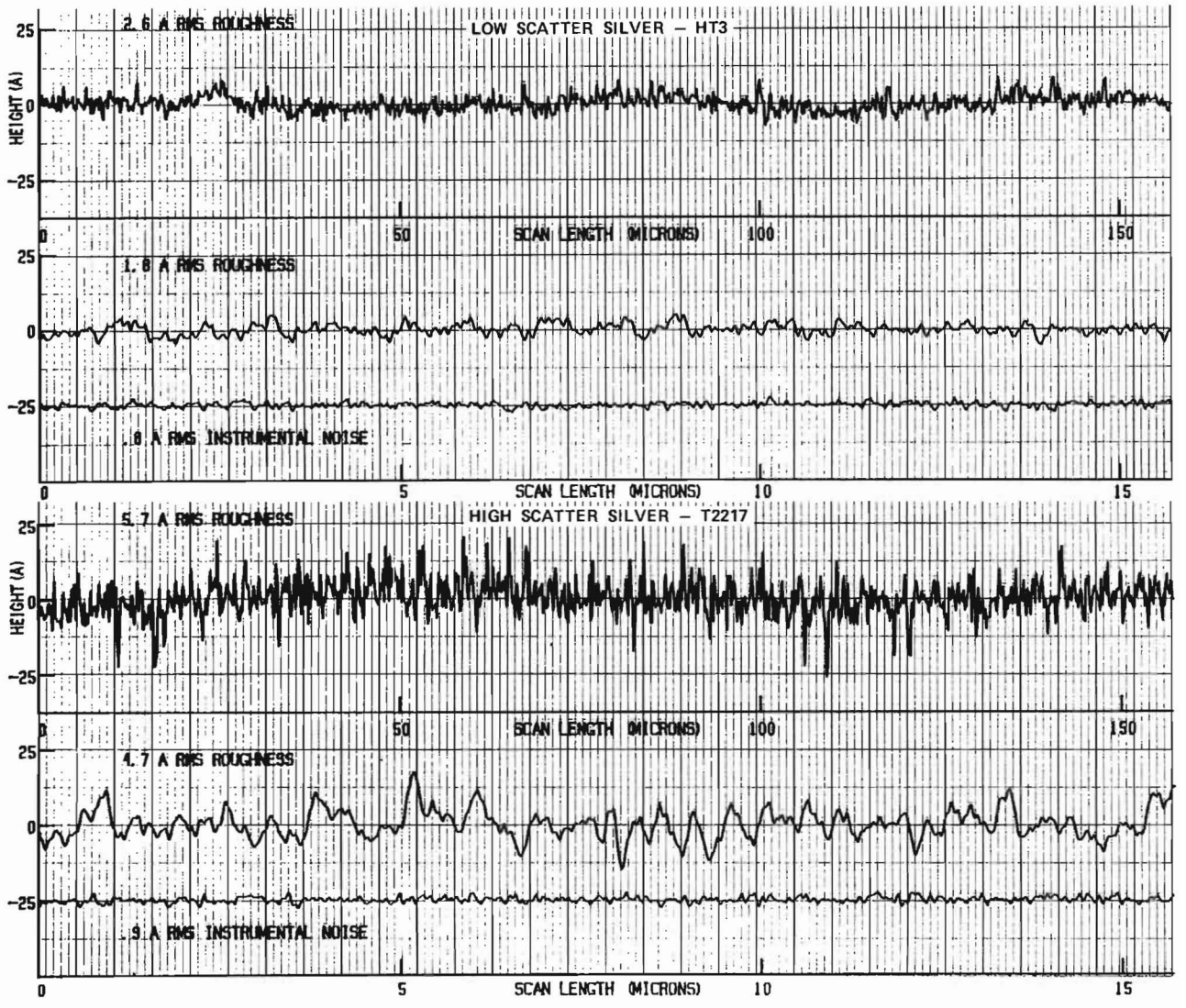


Figure 11. Surface profiles of the same low- and high-scatter silver films shown in figure 10.

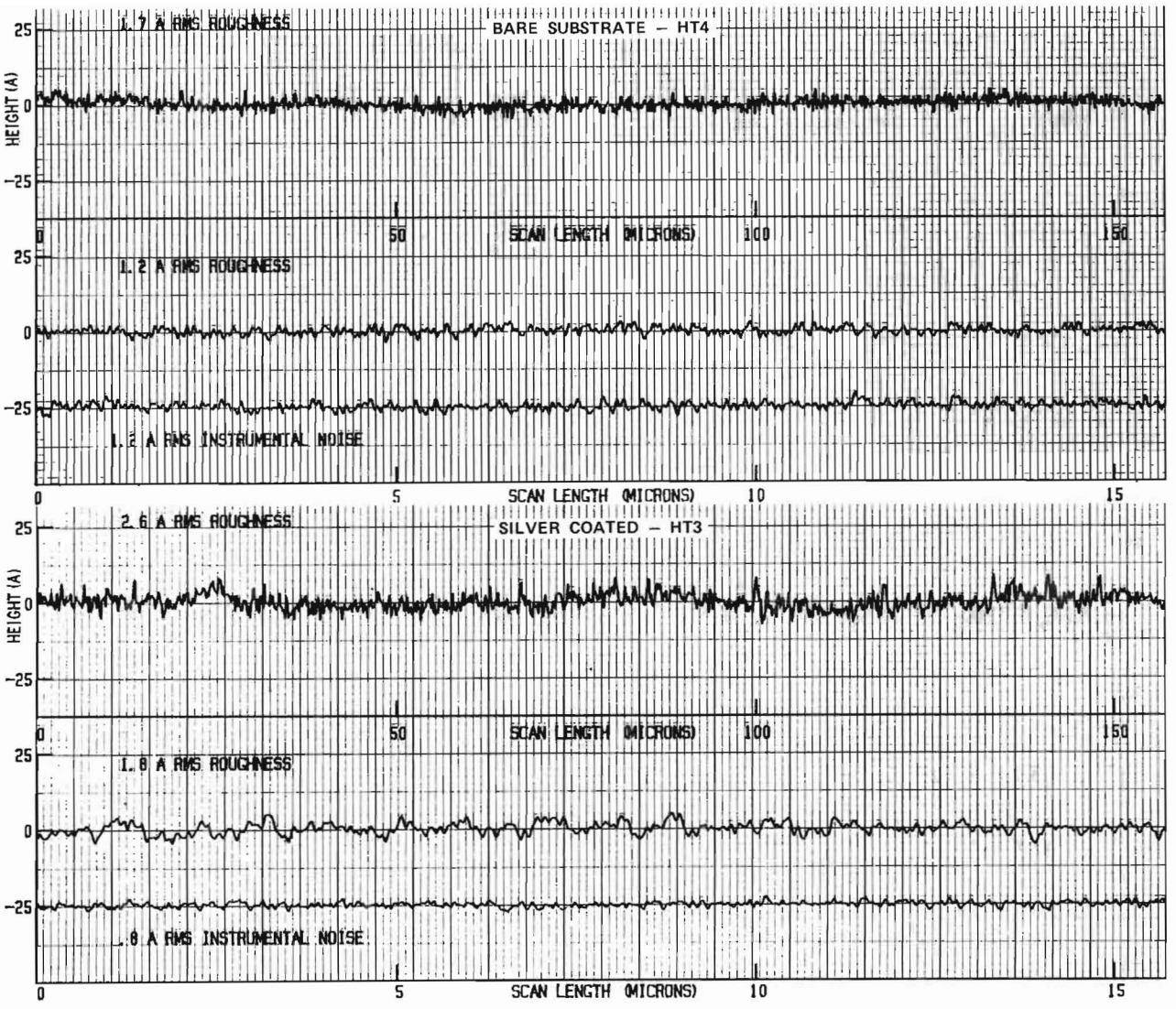


Figure 12. Surface profiles of bare substrate HT-4 and substrate HT-3 coated with a low-scatter silver film.

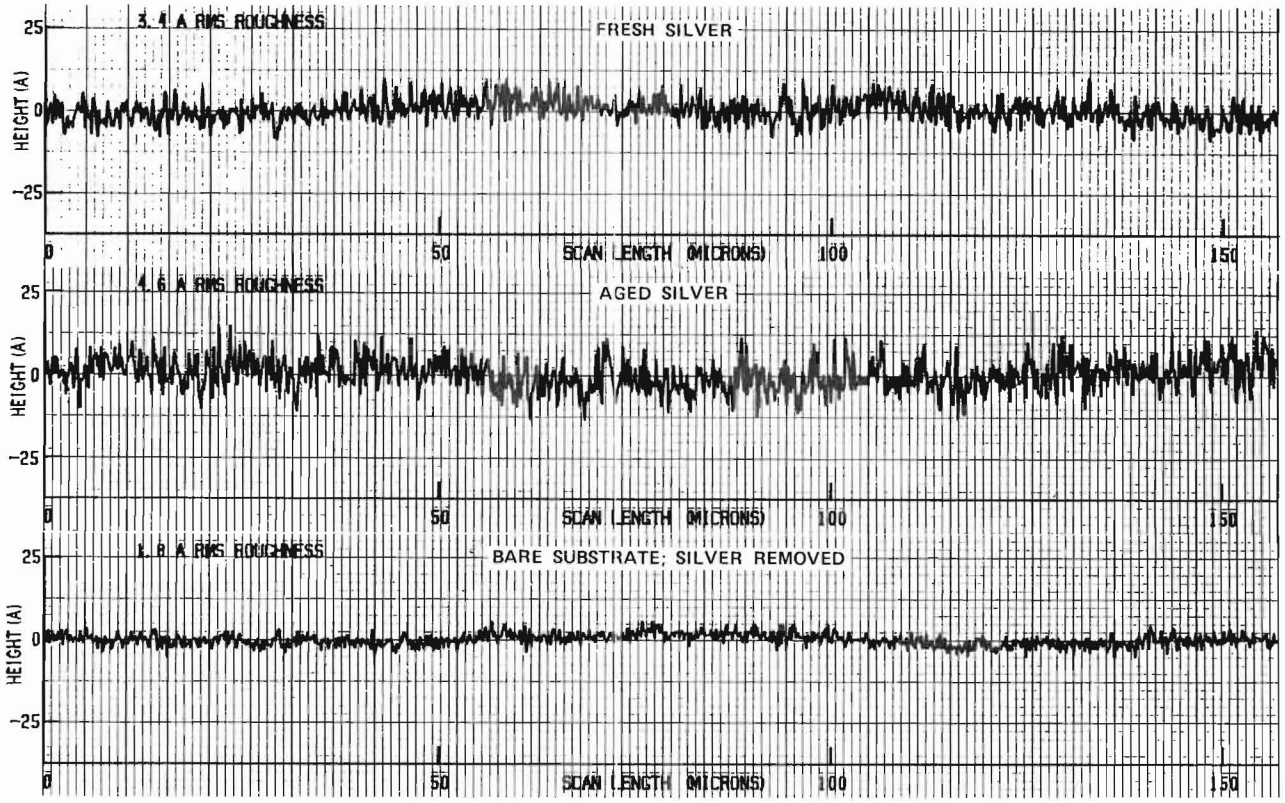


Figure 13. Surface profiles of substrate T-224 coated with fresh silver and aged silver, respectively.

It was suggested that extended polishing might move the surface below the damaged region and produce a tougher surface. The speaker agreed and reported qualitative evidence suggesting this effect. More work needs to be done. Temple from NWC reported that he had observed that CO_2-polished fused silica exhibited a similar phenomena. Lightly polished parts "looked like a dry lake bed" after CO_2 polishing, whereas parts which had been etched and polished several times did not change in appearance after CO_2 polishing.

LIGHT SCATTERING CHARACTERISTICS OF SOME METAL SURFACES --A SMOOTHING EFFECT?

J. R. McNeil and L. J. Wei
Electrical Engineering Department
University of New Mexico
Albuquerque, NM 87131

J. Casstevens and W. C. Herrmann, Jr.
Optic Electronic Corporation
Dallas, Texas 75423

J. C. Stover
Electrical Engineering Department
Montana State University
Bozeman, Montana

Angularly resolved light scattering measurements of several materials are discussed. Root mean square values of surface roughness, slope and total integrated scatter are calculated. Results are compared to measurements made using a noncontact, optical profilometer. Samples of polished and diamond turned Cu, Si, Mo and electroless Ni are examined. Some surfaces show a change in angular scatter characteristic upon deposition of films using ion beam and magnetron sputtering; scattering is changed to become more in the specular direction. In some cases, total integrated scatter is reduced up to a factor of four, and surface microroughness at high spatial frequencies is reduced by a factor of ten.

1. INTRODUCTION

There is considerable interest in characterizing surface roughness and light scattering of optical components using fast, efficient techniques. Such techniques are of obvious importance as a diagnostic for evaluation of components during fabrication. Similarly, in many optical systems, it is desirable to know or to be able to predict the angular dependence of light scatter as well as the total integrated scatter (TIS) of the system.

The problem of characterizing the light scattered from a surface and the related surface topography has been addressed by a number of investigators over the past two decades (1-6). The work reported here makes use of two measurement techniques; one involves a scatterometer that measures angularly resolved scattered light, and the other involves a noncontact optical profilometer utilizing a Mirau interferometer to examine a number of optical surfaces using both techniques are compared.

In the sections below the two measurement techniques are discussed, and the points that should be kept in mind in comparing the results of two different techniques are explained. Results from both types of measurements are then presented. Among the samples examined are surfaces that have been coated by either ion beam or magnetron sputtering a layer of metal onto an optic of the same metal.

2. SUMMARY OF SURFACE ROUGHNESS CONTRIBUTIONS

In considering the light scatter from a surface, it is useful to consider the surface roughness as being due to one or more contributions. First is the random, isotropic microroughness which is present in all surfaces. Light scatter from this type of roughness can be thought of as coming from a virtually infinite number of sinusoidal roughness components. That is, the surface can be modeled as though it resulted from a superposition of many surfaces, each with a sinusoidally varying surface of a particular spatial frequency, phase, and amplitude. Two other possible contributions to surface roughness occur in the case of machined (e.g., diamond-turned) optical surfaces and are one-dimensional (nonisotropic). One of these is periodic and is (ideally) composed of a set of parallel cusp-shaped grooves corresponding to the tool path through the material. The cusp cross-sectional shape is a function of tool radius and feed during machining. The cusp shape can be described in terms of a discrete Fourier series. The second nonisotropic contribution to roughness is random in nature but generally parallel to the set of periodic grooves just mentioned. This second contribution results usually in more light scattering than the periodic groove contribution. Sources of the random, parallel roughness include random vibration, chip scratches, and other effects that occur during machining. This contribution to roughness is approximated in terms of a continuous Fourier composition. See references 1 and 2 for additional details.

It can be seen that it is necessary to think of a surface and its roughness in terms of various spatial frequency components as well as having isotropic and nonisotropic contributions. In comparing results from different measurement systems, it is therefore important to know the spatial bandwidth limits of each system.

3. MEASUREMENT TECHNIQUES

3.1. Scatterometer System

The system illustrated in Figure 1 was used to measure the angularly resolved light scatter characteristics from a surface and follows the design discussed in references 1 and 2. The system measures and records light scattered in a plane from samples illuminated by a He-Ne laser. Normally, s-polarized illumination is used to insure that light scatter observed is due to surface topography and not from other effects (plasmons, etc.). The photomultiplier detector rotates about the scatter point on the optic in a plane and at a radius r ($\approx$ 40 cm). The incident beam converges at the detector. Thus, scatter measurements are performed in the far field. The optic can be rotated about several axes to provide observation at different angles of incidence (θ_i) and to allow examination at different points on the optic. Data is recorded on disk and includes values of intensity of specularly reflected light I_o, scattered light I_s, incident angle (θ_i), and scatter angle (θ_s) as measured from the normal to the surface. Values of θ_i are typically 0.5° to 10°; values of θ_s are θ_i + 0.5° to 80°. Data is recorded at each increment of 0.2° of θ_i. The scatter from optical components in the system (other than the optic under examination) sets a lower limit to the sensitivity of the system. Because most optics tend to have increasing amounts of scatter toward the specular direction, it is desirable to have a "quiet" measurement system and one that allows for values of θ_s that are as small as possible. In measuring scatter from smooth, low scatter optics, it is sometimes necessary to begin measurement at larger values of θ_s to avoid problems from the system scattered light. Measurements at different values of θ_s determine the scatter from surface roughness components of different spatial frequencies f^1. The grating equation relates θ_i and f as

$$\sin\theta_s = \sin\theta_i + N\lambda f, \quad N = 0, \pm 1, \pm 2, \ldots.$$

Here N represents the order of diffracted light. For smooth surfaces ($\sigma << \lambda$) only the 0 and ±1 components are significant. Thus, the system provides for measurement over the spatial frequency ranges of approximately 0.015 μ^{-1} to 1.5 μ^{-1}. Typically, the values of I_s range over four decades or more.

Analysis of the scatter data assumes only that the surface is smooth ($\sigma << \lambda$) and follows the treatment of Church [5,6]. This is based on first-order vector perturbation theory and involves calculation of the power spectral density (PSD) of the surface roughness. The rms roughness σ and rms slope m are calculated from the PSD.

When examining an isotropic surface, one measurement sweep is required to characterize the surface scatter. When examining a diamond turned sample, a measurement is made having the optic arranged with the tool grooves parallel to the measurement plane, and the isotropic contribution to the overall surface roughness is characterized. Another measurement is performed with the tool

grooves perpendicular to the detector plane to determine the nonisotropic contribution. The resulting total value for σ is found by evaluating

$$\sigma = \left[\sigma_{ID}^2 + \sigma_{ISO}^2\right]^{1/2} .$$

If the measurement system scatter is significant, it can be considered an effective noise that can be subtracted in a similar manner.

3.2. Optical Profilometer System

The second measurement technique used was a WYKO Optical NCP-1000 Digital Optical Profilometer. This system performs a noncontact surface measurement that determines the profile of the surface along one dimension. The measurement technique involves phase shifting interferometry utilizing an in-line Mirau-type interferometer. The interferometer is incorporated into a microscope with the optic under investigation magnified 20X. The interference between signals from the optic under test and an internal reference is imaged onto a one-dimensional solid state CCD detector array of 1024 elements. The profile length is 0.65 mm with each detector signal corresponding to a 0.63 μ segment of the profile. This interference pattern is analyzed to provide information concerning the test optic. The output consists of the profile of the surface, a histogram of surface height variations, and the autocovariance of the profile data. A best fit of the surface height variation to a Gaussian is also performed.

Although this measurement technique is different from the scatterometer, the spatial bandwidths of the two systems are approximately the same. The low frequency capability of the WYKO instrument is set by the length of the profile. If the surface examined includes low spatial frequency components that are to be detected, there must be sufficient number of wavelengths over the length of the profile (0.65 mm) to cause a measurable amount of scatter at the appropriate angle θ_s. If the minimum number of wavelengths is roughly 10, the maximum detectable spatial wavelength is 65 μ with a corresponding minimum frequency of 0.015 μ^{-1}. This is approximately the same as that for the scatterometer angles θ_i mentioned above. Thus it is reasonable to expect measurement results from both techniques to agree.

4. RESULTS

Scatterometer measurements were performed both at the University of New Mexico (UNM) and Montana State University (MSU); optical profilometer measurements were performed by Optic Electronic, Corp. (OEC). Some of the samples had a coating of metal on a surface of the same metal. This was deposited at UNM either by ion beam or magnetron sputtering. In these cases, the surfaces were ion beam cleaned prior to deposition.

Representative data is shown in Figures 2a and b which illustrate the results of investigating polished Cu surfaces using the scatterometer arrangements at UNM and MSU, respectively. The PSD of the surface is plotted as a function of f. Also indicated are the calculated values for σ and m. In this case the surface roughness is isotropic, and there is only one contribution to σ. The same optic was measured in eight different spots with values of σ in the range of 40 Å rms. Figure 3 represents the results of measurements using the profilometer at OEC. The surface profile is shown in 3a with the corresponding value for σ of approximately 35 Å rms; 3b illustrates the histogram of surface height variations with a Gaussian curve fit; 3c illustrates the autocovariance of the data with the first zero occurring at 40 μ.

Figure 4 illustrates the PSD of a diamond turned Ni surface. The data illustrated were taken at MSU with 4a representing the isotropic contribution to the PSD [$W_{ISO}(f)$] and 4b representing the nonisotropic contribution [$W_{ID}(f)$]. The total σ is also indicated in the figure. Similar results were obtained in examining the sample at UNM.

4.1 Comparison of Three System Results

Figures 5, 6, and 7 summarize and compare measurement results by plotting the rms roughness σ calculated from a number of measurements performed at all three locations. Note, however, that comparing results based simply on this one number is somewhat incomplete because of the other information provided by the measurements. Also this treatment assumes first that the condition of the optics does not change between the three measurements, and second that the same point can be accurately located for each of the three measurements.

Figure 5 shows results from measuring polished samples that scatter isotropically. First, note that identical measurement results from two systems would be plotted along the line of unit slope in the figure. It can be seen that results from the two scatterometer systems (MSU vs UNM) agree to within a few (<20) percent. In general the UNM scatterometer provided larger values of rms roughness. This, we believe, is due to errors in the UNM detection system. These were subsequently corrected to provide values that were slightly lower than those shown in Figure 5 upon remeasuring two of the samples. Thus it appears that the two similar scatterometer systems provide nearly the same measurement results.

Results shown in Figure 5 also compare the WYKO profilometer rms roughness values to those of the scatterometer (OEC vs UNM). It can be seen that in general the profilometer results are smaller than the scatterometer results. The reason for this trend is unclear because of lack of knowledge of the WYKO data analysis.

Figure 6 summarizes results from examining three diamond turned samples. In the case of the scatterometer measurements, the machine marks (grooves) were oriented parallel to the detection plane; similarly the profilometer observation profile (0.65 mm long) was parallel to the tool marks. In this manner the isotropic contribution to the overall surface roughness is measured. Comparison of the measurement results should be similar to those made with data shown in Figure 5. This is generally the case, with UNM scatterometer results being greater than the MSU results, and the MSU (and UNM) scatterometer results being greater than the OEC profilometer results.

The nonisotropic (1-dimensional) scatter measurement results are summarized in Figure 7. For these measurements the optic was oriented with machine grooves perpendicular to the detection plane for scatterometer measurements and also perpendicular to the observation profile of the profilometer. First note the scatterometer results (UNM vs MSU) for the Cu sample are nearly the same compared to those for the Ni and Si samples. The Cu sample was fly-cut, whereas the Ni and Si samples are both center-cut machined. This difference causes a significant difference in the one-dimensional scatter characteristic of the two types of machined surfaces. The spot size of the scattered light increases with increasing scatter angle in the case of center-cut samples; for a fly-cut sample the spot size does not change greatly. This behavior is due to the curvature of the machine tool marks which is greater for center-cut than for fly-cut samples. The UNM detection system had a fixed aperture diameter that was sometimes smaller than the spot size of the scattered light from center-cut samples. This was the case for scatter angles over approximately 45° and gave rise to incorrect (low) values of rms roughness for the Ni and Si samples. The MSU detection system had a vertical slit that could be adjusted to avoid this problem. This likely causes the difference of nearly a factor of three shown in Figure 7 for the Ni and Si samples.

The comparison of the scatterometer and profilometer results shown in Figure 7 cannot be explained. Note that for one sample (Si) the scatterometer measurement is nearly twice that of the profilometer, while the situation is opposite for the other sample (Cu). Although one sample is center-cut and one sample is fly-cut, we do not believe this would cause such an inconsistency.

4.2. Comparison of Scatterometer and Integrating Sphere TIS Techniques

Integrating sphere TIS arrangements have a spatial frequency bandwidth determined by the construction details of the sphere. Most importantly, the low frequency limit if determined by the dimensions of the aperture used to pass the laser through the sphere. Typically this low frequency limit is approximately 0.08 μ^{-1}. If an optic is examined for TIS using this type of apparatus and also examined with a scatterometer having a different spatial frequency measurement limit, the two measurement results will be different. For example, the results from examining a polished Cu sample with a scatterometer shown in Figure 2a yield a calculated rms roughness of approximately 41 Å. The low spatial frequency limit of the scatterometer is 0.014 μ^{-1}. However, when the same data is analyzed again but omitting data corresponding to spatial frequencies between 0.014 and 0.08 μ^{-1}, the calculated rms roughness is 37Å. This illustrates the importance of characterizing measurement system bandwidth capabilities, especially at low frequencies which give rise to most of the light scatter.

4.3. Measurements of Coated Samples--A Smoothing Effect?

A number of Cu optics was examined, as well as one Si and one Mo optic. Films were deposited on samples either by evaporation or by sputtering. Both magnetron and ion beam sputtering were used. Prior to film deposition the substrates were cleaned using Ar^+ bombardment from an ion beam. Ion energy was 300 eV. Substrates were unheated.

Figure 8 summarizes the results of examining two Cu optics. The left vertical scale is logarithmic and represents the power spectral density (PSD) of the surfaces, and the horizontal scale

represents frequency of surface fluctuations. The right vertical scale represents calculated rms roughness. It can be seen that the two samples have nearly identical scatter characteristics (PSD) before coating. The calculated values of rms roughness before coating these two sampels are nearly the same (41Å) when measurements are made over the spatial frequency range of 0.014 to 1.6 μ^{-1} as described above. Eight different points on each optic were examined, and the roughness characteristics were nearly the same with a point-to-point variation of less than 3 Å.

Next, half of both Cu optics was coated with 2000 Å of Cu; Optic 1 had Cu evaporated, and Optic 2 had Cu sputtered. The same eight points on the optics were then examined again. The uncoated regions had virtually the same scatter characteristics. However, the coated regions displayed a significant reduction in scatter, particularly at surface spatial frequencies above 0.3 μ^{-1}. The sputtered film caused more than a factor of ten reduction in scatter at spatial frequencies greater than 0.8 μ^{-1}. The values of rms roughness calculated from the PSD are 28.2 Å for the coated region of Optic 1 and 20.7 Å for the region of Optic 2 with 2000 Å of sputtered Cu. This is half the rms roughness of the same region before coating.

We examined additional Cu samples and observed the smoothing effect for thicker Cu films. In general, the sputtered films caused more change in scatter characteristics than evaporated films, in agreement with the information of Figure 2. Also it appears that a film thickness of less than 10,000 Å is best for displaying the smoothing effect. Although thicker films cause a change in scatter characteristics, the change is not as great as for 2,000 Å thick films.

We have confirmed that aging of the Cu surface is not an explanation for the smoothing effect. Two Cu samples were measured once and then remeasured six months later. No significant difference in roughness characteristics was observed, and the smoothing effect was still observed.

Also, we performed a series of measurements to examine the influence of ion bombardment cleaning on scatter characteristic. For the ion energy and flux levels we used for actual coating procedures, the cleaning has no influence on the scatter characteristics. Optics were examined both before and after ion cleaning; no change in scatter was observed. Also, samples were coated with one half of the sample ion cleaned and the other half unbombarded. Both halves of the optic displayed the smoothing effect and had similar scatter characteristics.

We observed the change in scatter characteristic for the Si sample coated with 2000 Å of sputtered Si. The one Mo sample examined did not demonstrate significant changes in scatter when coated with sputtered Mo. This difference in behavior we believe is related to the different topography of the substrates.

We are currently developing a simple model to explain this behavior based on enhanced surface diffusion and the microstructure of the surfaces. This will be reported at a later date (7).

5. CONCLUSIONS

From the material presented above, the following can be concluded:

1. Two scatterometer systems with similar characteristics (e.g., spatial frequency bandwidth) produce nearly equivalent measurement results.

2. The optical profilometer measurements of polished samples are smaller than scatterometer measurements of the same sample. The same is true of the isotropic contribution to surface roughness of diamond turned samples. However, the nonisotropic contribution due to the machining grooves does not produce consistent results between the two types of measurement systems. Note, though, that only a few diamond turned samples were examined and compared in this manner. It is not known if the differences mentioned above are due to different spatial frequency bandwidths of the systems or due to data analysis techniques of the profilometer.

3. For some surfaces, a change in surface microroughness can be caused by deposition of a thin film. Both material and deposition techniques determine the extent of this smoothing effect. We have observed a reduction in high spatial frequency microroughness by a factor of ten and TIS by a factor of four in some cases.

REFERENCES

1. J. C. Stover, C. H. Gillespie, Scattering in Optical Materials, SPIE Proc. V. 362, p. 172 (1982).

2. J. C. Stover, S. A. Serati, and C. H. Gillespie, Calculation of Surface Statistics from Light Scatter, SPIE Proc. V. 429, (1983).

3. J. M. Elson and J. M. Bennett, J. Opt. Soc.Am. 69, 31 (1979).

4. J. M. Eastman, Ph.D dissertation, "Surface Scattering in Optical Interference Coatings," University of Rochester, Rochester, NY (1974).

5. E. L. Church, H. A. Jenkinson, and J. M. Zavada, Opt. Eng. 18, p. 125 (1979).

6. E. L. Church and J. M. Zavada, Appl. Opt. 14, 1788 (1975).

7. J. R. McNeil, C. J. Wei, G. A. Al-Jumaily, S. Shakir, and J. K. McIver, to be published.

This work was funded in part by the U. S. Army Missile Command.

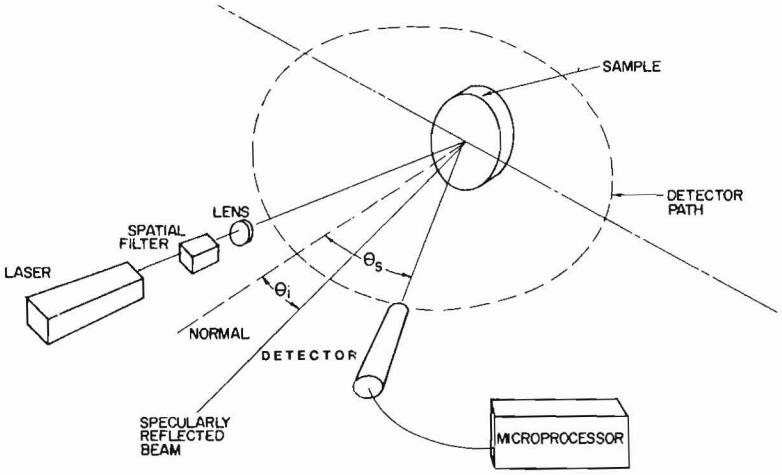


Figure 1. Experimental arrangement of the scatterometer apparatus used at UNM and MSU.

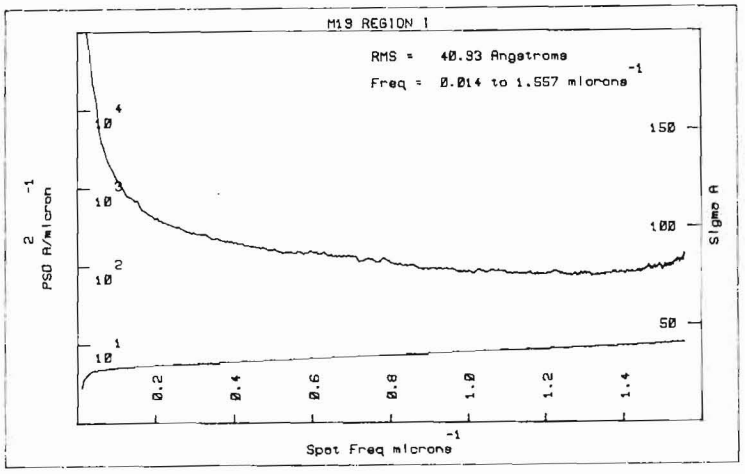


Figure 2a. Data from measurement of a polished Cu sample with rms roughness of approximately 35 Å.

a) UNM measurement

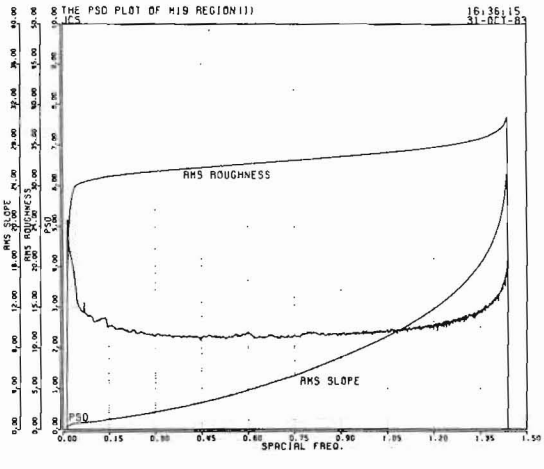


Figure 2b. Data from measurement of a polished Cu sample with rms roughness of approximately 35 Å.

b) MSU measurement

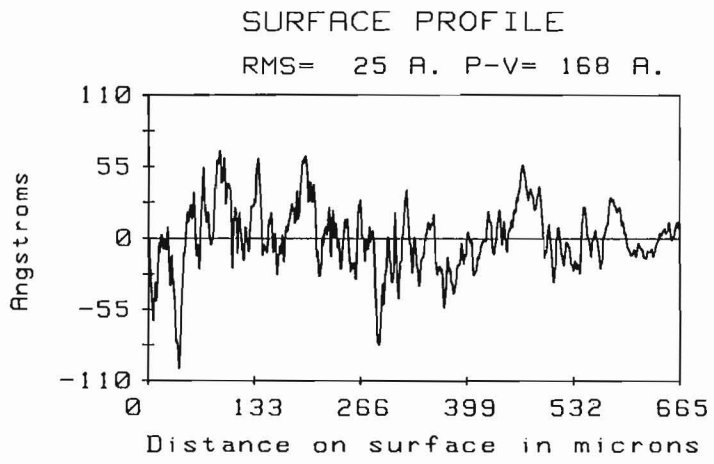


Figure 3a. Results of examining the polished Cu sample of Figure 2 with the WYKO optical profilometer showing

a) the surface profile.

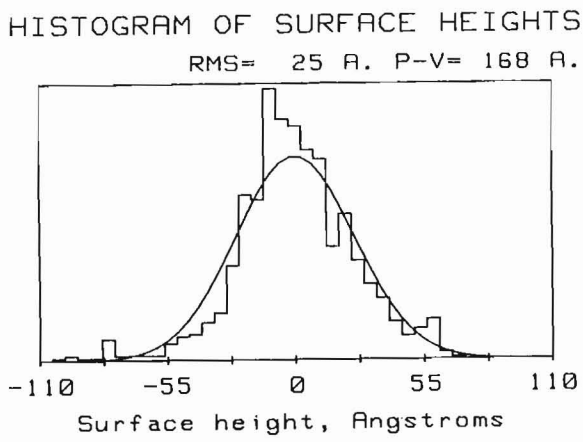


Figure 3b. Results of examining the polished Cu sample of Figure 2 with the WYKO optical profilometer showing

b) a histogram of surface height distribution.

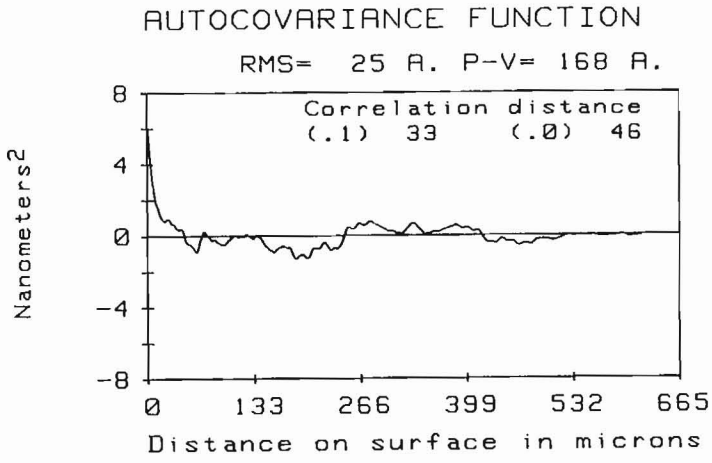


Figure 3c. Results of examining the polished Cu sample of Figure 2 with the WYKO optical profilometer showing

c) the autocovariance function of the surface profile.

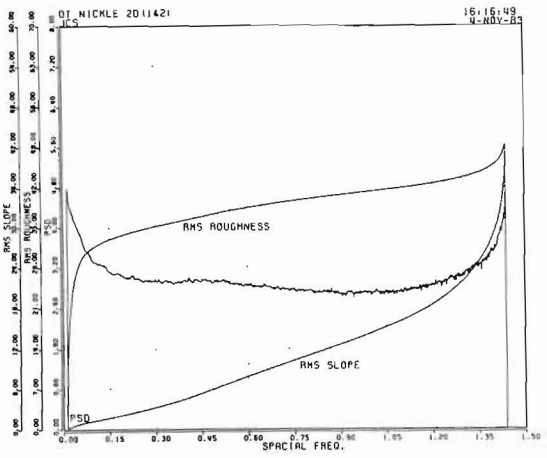


Figure 4a. Scatterometer data from examining a diamond-turned Ni sample at MSU showing

a) isotropic scatter contribution

Note that the total equivalent rms roughness is approximately 62 Å.

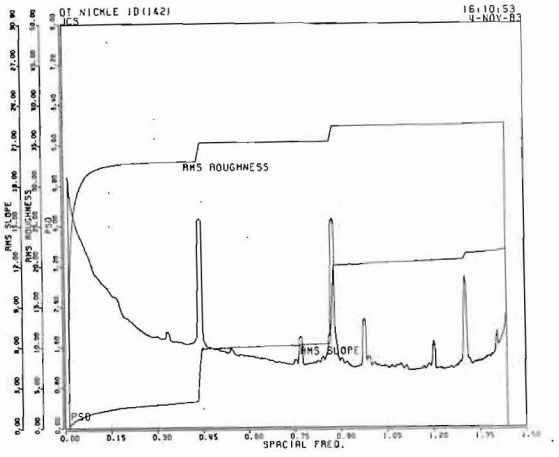


Figure 4b. Scatterometer data from examining a diamond-turned Ni sample at MSU showing

b) the nonisotropic (one-dimensional) scatter due to the machining grooves

Note that the total equivalent rms roughness is approximately 62 Å.

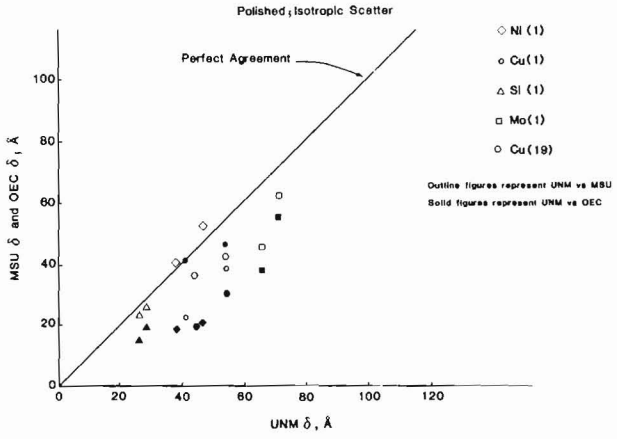


Figure 5. Comparison of isotropic scatter measurements from polished samples examined at UNM, MSU, and OEC. Values of rms roughness are plotted.

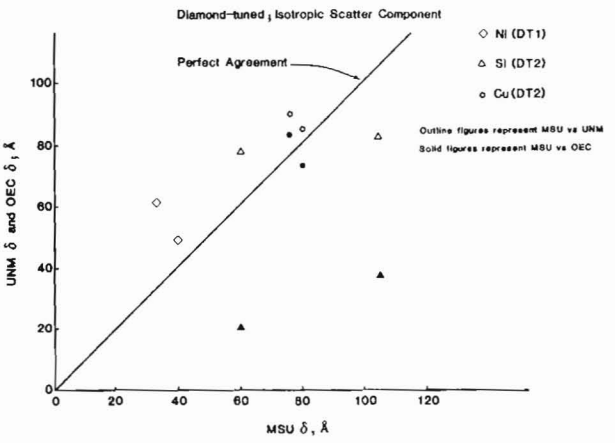


Figure 6. Comparison of measurements of isotropic scatter contribution to total scatter of diamond-turned samples examined at UNM, MSU, and OEC. Values of rms roughness are plotted.

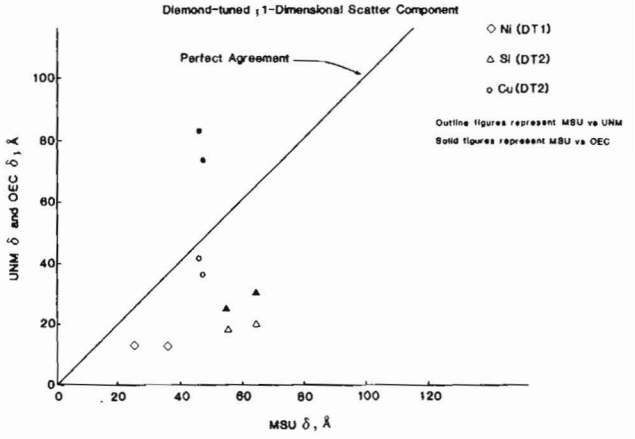


Figure 7. Comparison of measurements of non-isotropic (one-dimensional) scatter contribution of diamond-turned samples examined at UNM, MSU, and OEC. Values of rms roughness are plotted.

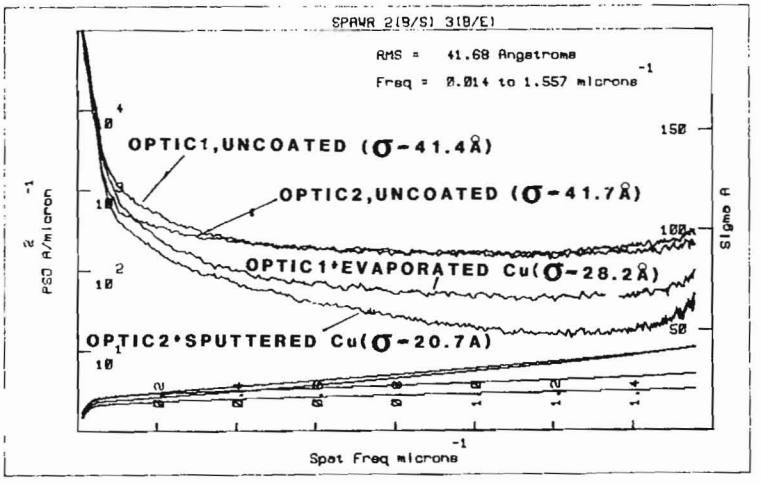


Figure 8. Effect of Cu film deposition on Cu polished optics; films were 2000 Å and were evaporated onto OPTIC 1 and sputtered onto OPTIC 2. The horizontal axis corresponds to spatial frequency of surface fluctuations and is proportional to observation angle from the normal to the optic; the vertical axis on the left is proportional to intensity of scattered light; the vertical axis on the right represents the rms surface microroughness in Å.

Light Scattering from Surfaces with Microroughness and Static Density Variations in the Bulk Dielectric Permittivity*

J. M. Elson

Michelson Laboratory, Physics Division
Naval Weapons Center, China Lake, California 93555

First-order perturbation theory is used to calculate the scattering of a plane wave from the surface of a semi-infinite medium, where the surface is slightly rough and the scattering medium is isotropic but has a dielectric permittivity which varies as a function of position. Both the roughness and dielectric permittivity perturbations, which are treated as random variables, can independently cause scattering, and there is generally interference between the two scattered fields. The scattering depends on the autocovariance functions for the surface roughness and dielectric fluctuations and their cross-correlation properties. Thus, the polarization ratio between the p and s angle resolved scattering components is found to be a variable that depends on the autocovariance functions of, and cross-correlation between, the surface roughness and dielectric fluctuations. This result is unlike predicted scattering caused by roughness or dielectric perturbations alone; in these cases, the polarization ratios do not depend on the statistical properties of the perturbation. Numerical results of the calculations of this work are consistent with some aspects of experimental measurements. In particular, measurements of the polarization ratio of light retroscattered from apparently identical silver films are seen to vary widely between samples and even from place to place on the same sample. The present work shows one physical mechanism as to how this can occur.

Key words: angle resolved scattering; BRDF; dielectric inhomogeneities; surface roughness.

Introduction

Light scattering from surfaces with microroughness has been experimentally and theoretically studied for many years [1-3].[1] Comparison of theory and experiment has frequently been successful in explaining many qualitative and quantitative features of roughness scattering. However, there are certain salient features of angle resolved scattering (ARS) measurements which are not predicted or described by a first-order theory of roughness-induced ARS. Two of these features are (1) cross-polarization in the scattered field and (2) variation in the ratio of p-polarized (electric vector parallel to plane of incidence or scattering) to s-polarized (electric vector perpendicular to plane of incidence or scattering) scattered light.

Considering (1) above (the occurrence of cross-polarization in the scattered light), a first-order roughness scattering theory [4] predicts that no cross-polarization will occur in the scattered light field observed within the plane of incidence. In other words, if the incident beam is p-polarized, then the scattered light throughout the plane of incidence is predicted to also be p-polarized. That is also true for s-polarized light where in the preceding statement, p-polarization is replaced by s-polarizaton. From the standpoint of first-order perturbation theory, this is an understandable prediction since the roughness-induced dipole currents which generate scattered light are parallel to the electric vector of the incident field. Also, multiple scattering is not considered in the context of first-order theory. However, as shown in table 1, light scattering measurements [5] from Ag films show that cross-polarization can occur. This experimental fact indicates that some other source of scattering can apparently coexist with surface roughness. Since the overall amount of scattered light is low, this additional source can be a first-order effect in analogy with scattering from microroughness.

Considering (2) above, it has been experimentally observed in light scattering measurements that for fixed experimental parameters, the ratio of p- to s-polarized scattered light measured in the

*Work supported by Navy Independent Research Funding.
[1] Numbers in brackets indicate the literature references at the end of the paper.

plane of incidence can vary between mirrors of the same material and from spot to spot on the same mirror (see reference 5 and table 1). However, first-order theory of scattering from microroughness does not predict this to occur. The theory says that for scattered light within the plane of incidence, the ratio of p- to s-polarized light will be dependent only on the wavelength, optical constants, and angles of incidence and scattering. In particular, the p/s ratio is not predicted to depend on the microroughness properties of the mirror.

It is possible that points (1) and (2) are related since the occurrence of cross-polarization can clearly affect the p/s ratio of the scattered light. However, as discussed below, it is also possible from a theoretical standpoint that the effect noted in (2) can be predicted without cross-polarization simultaneously occurring. This is in fact the primary focus of this work. In this paper, cross-polarization will not be considered. It will be assumed that isotropic static density perturbations of the dielectric permittivity are a source of scattering in addition to surface roughness. The inhomogeneity in the dielectric is considered to be a bulk effect, whereas surface roughness is a surface effect. Considering sources of scattering due to coexisting roughness and dielectric perturbations means that the p/s ratio of scattered light will now be dependent on the statistical properties of the roughness and dielectric perturbations. These statistical properties are included in the autocovariance functions of the roughness and dielectric random variables and also the cross-correlation between these variables.

The motivation for this work is further seen in figure 1, where experimental data of scattered light versus angle of scattering is given. Also given in figure 1 are predicted scattering curves for scattering due to roughness only. Note that while the p-polarization curves (upper data and theory) are resonably well matched, the s-polarization curves (lower data and theory) are not well matched. For the theoretical plots, there is no way to change the relative position of the p- and s-polarized theory curves in order to bring the experiment and theory into better agreement.

Theory

The theoretical details of this work are given elsewhere [6]. However, an outline of this work is given below. As shown in figure 2, the theory considers a first-order calculation of light scattering of a plane wave incident on a slightly rough surface (the root mean square (rms) roughness is much less than the incident wavelength), where the lower medium has spatial perturbations in the dielectric permittivity. The complex dielectric permittivity is assumed to have the form

$$\varepsilon = \varepsilon_1 + \Delta\varepsilon(x,y)\exp(\alpha z) \quad , \quad z \leq 0 \quad , \tag{1}$$

where ε_1 is a constant background value about which $\Delta\varepsilon$ fluctuates randomly. Note that the z-dependence of ε is assumed to be an exponential function, and thus the random nature of ε occurs in the x and y directions only. Since the calculation is done in the context of first-order theory, the two sources of scattering (roughness and dielectric perturbations) are linear in their contribution to the scattered field. In other words, the scattered field E_{scatt} may be written in the form

$$\vec{E}_{scatt} = \vec{E}_r + \vec{E}_d \quad , \tag{2}$$

where $\vec{E}_r$ and $\vec{E}_d$ are the first-order electric fields resulting from scattering due to roughness and dielectric perturbations, respectively. The $\vec{E}_r$ and $\vec{E}_d$ are proportional to the Fourier transform of the roughness and dielectric perturbations (both of which are random variables), respectively. Because of the random nature of the perturbations, ensemble averaging techniques are used to predict the expected distribution of scattered light. The resulting ARS formula has the form

$$\left\langle \frac{1}{P_o}\frac{dP}{d\Omega} \right\rangle = Ag_r + Bg_d + Cg_{rd} \quad , \tag{3}$$

where g_r and g_d are the power spectral density functions of the surface roughness and dielectric perturbations, respectively. The g_{rd} is the power spectral density of the correlation between the roughness and dielectric perturbations. The explicit form of the coefficients A, B, and C are given in ref. 6. The <...> denotes ensemble average. A power spectral density function may be written in terms of a covariance function as

$$g_i(\vec{k}) = \int d^2\tau \; G_i(\vec{\tau}) \exp(i\vec{k}\cdot\vec{\tau}) \quad , \tag{4}$$

where i = r, d, or rd which refer to roughness, dielectric, and roughness plus dielectric, respectively. The G_r, G_d, and G_{rd} are the autocovariance function of surface roughness, autocovariance function of dielectric perturbations, and cross-correlation function between the roughness and dielectric random variables, respectively. In this work and as discussed previously [6], the autocovariance functions are written as a sum of a Gaussian and an exponential as

$$G_r(\vec{\tau}) = \delta_{rL}^2 \exp(-|\tau|/\sigma_{rL}) + \delta_{rS}^2 \exp(-\tau^2/\sigma_{rS}^2) \tag{5a}$$

$$G_d(\vec{\tau}) = \delta_{dL}^2 \exp(-|\tau|/\sigma_{dL}) + \delta_{dS}^2 \exp(-\tau^2/\sigma_{dS}^2) \quad , \tag{5b}$$

where the d and r subscripts refer to dielectric or roughness perturbation, respectively, and the L and S subscripts refer to long- and short-range parameters, respectively. Note that we have assumed that the random variables are isotropic and that the autocovariance functions do not depend on the direction of the $\vec{\tau}$. The δ_{rL} and δ_{rS} are the rms values of the long- and short-range roughness values. The σ_{rL} and σ_{rS} are the long- and short-range correlation length values, respectively. The δ and σ parameters with d subscripts are analogous to the r subscripts except that they refer to the dielectric perturbation statistics. From eqs (4) and (5), we see that the power spectral density functions corresponding to eqs (5) are

$$g_r(\vec{k}) = 2\pi\delta_{rL}^2\sigma_{rL}^2/(1 + k^2\sigma_{rL}^2)^{3/2} + \pi\delta_{rS}^2\sigma_{rS}^2 \exp(-k^2\sigma_{rS}^2/4) \tag{6a}$$

$$g_d(\vec{k}) = 2\pi\delta_{dL}^2\sigma_{dL}^2/(1 + k^2\sigma_{dL}^2)^{3/2} + \pi\delta_{dS}^2\sigma_{dS}^2 \exp(-k^2\sigma_{dS}^2/4) \quad , \tag{6b}$$

where the power spectral density functions are also isotropic and independent of the direction of $\vec{k}$. Considering the cross-correlation nature of the statistical variables, the large number of parameters means that there are a lot of hypothetical possibilities that could be assumed. Also, the $\Delta\varepsilon$ is generally a complex quantity and therefore the cross-correlation function and cross-power spectral density function can be complex. In this work, we assume four different situations for the cross-correlation function, which will be called Cases 1, 2, 3, and 4. The cross-correlation function can be written in the form [6]

$$G_{rd}(\tau) = |G_{rd}(\tau)| e^{i\delta_{rd}} \quad , \tag{7a}$$

where the δ_{rd} is an average phase difference between the roughness and dielectric perturbation random variables. In this work, eq (7a) is assumed to have the form

$$G_{rd}(\tau) = F\left[\delta_{rdL}^2 \exp(-|\tau|/\sigma_{rdL}) + \delta_{rdS}^2 \exp(-\tau^2/\sigma_{rdS}^2)\right] \quad , \tag{7b}$$

where the statistical parameters are defined below. The F coefficient is a complex number representing the complex exponential of eq (7a). Cases 1 through 4 in this work are represented by

$$F = (0,0) \quad \text{(Case 1)} \quad , \tag{8a}$$

$$F = (0,1) \quad \text{(Case 2)} \quad , \tag{8b}$$

$$F = (-1,0) \quad \text{(Case 3)} \quad , \tag{8c}$$

$$F = (1,0) \quad \text{(Case 4)} \quad . \tag{8d}$$

Case 1 assumes that there is no statistical connection between the roughness and dielectric perturbations. In other words, the phase δ_{rd} fluctuates in such a way that G_{rd} vanishes. Case 2 assumes that on the average the phase $\delta_{rd} = \pi/2$. This implies that the roughness and the imaginary part of the dielectric perturbation are positively correlated and that either the real part of the dielectric perturbation is negligible or is statistically independent of the roughness. Cases 3 and 4 assume that the phase averages to $\delta_{rd} = \pi$ and $\delta_{rd} = 0$, respectively. For both these cases, it is assumed that the imaginary part of the dielectric perturbation is negligible or is statistically independent of the roughness. For Case 3, the roughness and real part of the dielectric perturbation are 180 deg out of phase or are anticorrelated. For Case 4, these variables are in phase or are positively correlated. The cross-power spectral density function associated with eq (7b) is

$$g_{rd}(k) = \pi F^*\left[2\delta_{rdL}^2\sigma_{rdL}^2/(1 + k^2\sigma_{rdL}^2)^{3/2} + \delta_{rdS}^2\sigma_{rdS}^2\exp(-k^2\sigma_{rdS}^2/4)\right] \quad , \tag{9a}$$

where the long- and short-range statistical parameters are defined by

$$\delta_{rdL} = [\delta_{rL}\delta_{rd}]^{1/2} \tag{9b}$$

$$\delta_{rdS} = [\delta_{rS}\delta_{dS}]^{1/2} \tag{9c}$$

$$\sigma_{rdL} = 2\sigma_{rL}\sigma_{dL}/(\sigma_{rL} + \sigma_{dL}) \tag{9d}$$

$$\sigma_{rdS} = \sigma_{rS}\sigma_{dS}/[(\sigma_{rS}^2 + \sigma_{dS}^2)/2]^{1/2} \quad . \tag{9e}$$

Note that this functional form of eq (9a) is a phenomenological blend of the long- and short-range parts of eqs (6). The long(short)-range part of eq (9a) is obtained by taking the square root of each of the long(short)-range parts of eqs (5) and multiplying them together. The F coefficient is its complex conjugate and this is discussed in detail in ref. 6.

Numerical Results and Conclusions

In order to generate numerical results, we need to assume numerical values for the rms roughness and correlation length parameters. These values are shown in table 2. The angle of incidence is 60 deg as measured from the mean surface normal. For all plots, the scattering is calculated in the plane of incidence. Both p- and s-polarization are considered. The incident wavelength is 0.6328 Å, and for Ag it is assumed that $\varepsilon_1 = (-16.4, 0.53)$.

In discussion of numerical data in the figures to follow, it will be convenient to refer to roughness-only scattering by R, to dielectric-only scattering by D, and to roughness plus dielectric scattering by RD. Figure 3 shows ARS for p-polarized incident and scattered light versus angle of incidence. It is seen that there is a concentration of scattering around the specular direction of 60 deg. This is due largely to the effect of long-range correlation length parameters which are greater than the incident wavelength. The scattering to the right of the specular direction is toward the direction of the incident beam. This scattering is in the backward direction and is due to the effect of the short-range correlation length parameters which are shorter than the incident wavelength. The scattering to the left of the specular direction is forward scattering.

Figure 3 shows $\log_{10}[\langle(1/P_o)(dP/d\Omega)\rangle]$ versus polar scattering angle for p-polarized incident light. There are six plots in all. For reference, the curves for R scattering and D scattering are shown. The remaining four curves are for RD scattering with the assumptions of Cases 1 through 4. The Case 1 and 2 curves are essentially superimposed. Thus, the imaginary part of g_{rd} has very little effect on the RD scattering. In Cases 1 and 2 the interference term between the R and D scattered fields is negligible. The difference, for Cases 1 and 2, between the R scattering and the RD scattering is due to simple addition of the two fields where constructive or destructive interference does not play a role. In the Cases 3 and 4, the situation is very much different. In these cases, the interference term plays a major role. For Cases 3 and 4, the F values are (-1,0) and (1,0), respectively, and thus the real part of g_{rd} plays an important part in the character of R plus D scattering. If the real part of g_{rd} is negative or positive, the RD scattering is increased or decreased, respectively, relative to R scattering. Note, for the Case 4 curve, the unusual behavior in the neighborhood of the specular beam. This is, in part, an artifact of the choice of cross-correlation function used in this work. At any rate, it is clear that the RD scattering can be greater or less than R scattering, and thus erroneous conclusions could be drawn from roughness-only theory if D scattering is in effect. Figure 4 is in many respects analogous to figure 3 except that the incident and scattered fields are s-polarized. Again the R scattering and D scattering curves are shown, the Case 1 and 2 curves, for RD scattering, are superimposed and the Case 3 and 4 curves are elevated and depressed, respectively, relative to R scattering. All curves have basically the same shape, and there is no unusual behavior in the specular region as in figure 3. Figure 5 shows the p/s polarization ratios for R scattering, D scattering, and RD scattering for Cases 1 through 4 which is predicted by the data in figures 3 and 4. The p/s ratio curves for R scattering and D scattering are quite different. The Case 1 and 2 curves are superimposed and are slightly different than the R curve. In the retro and forward scattering directions, the p/s ratio is slightly depressed and elevated, respectively. For Cases 3 and 4, the p/s ratios are further deviated from the R curve. For Case 3, the p/s ratio is elevated in the forward scattering region and depressed in the retroscattering region. For Case 4, this pattern is reversed. Thus, when the real part of g_{rd} is negative or positive, the p/s ratio is depressed or elevated, respectively, relative to the R curve (in the retroscattering region). This trend is consistent with experimental measurements as shown in table 1, where measured p/s values are seen to be both greater than and less than the value of 36.2 as predicted by R theory.

Figures 6 and 7 show $\log_{10}[\langle(1/P_o)(dP/d\Omega)\rangle]$ for p-polarized incident and scattered light versus polar scattering angle for three different sets of rms values for the dielectric parameters. The R curve is unchanged from figures 3 and 4. Figures 6 and 7 pertain to Case 3 and Case 4, respectively. Each figure has five plots, two of which are the R scattering and D scattering curves. The other three curves are for the values δ_{dL} = 1.00, 1.75, 2.5, and δ_{dS} = 0.2, 0.35, 0.5 for the rms dielectric parameters. In figure 6, the three R plus D curves are simply increasingly elevated from the R curve as the rms dielectric parameters increase. The correlation length parameters are the same as given in table 2.

In figure 7, the R plus D curves are generally depressed relative to the R curve. Note the sensitivity of the specular region scattering to the three different sets of rms dielectric parameters. The "trough" between the specular and retroscattering regions shifts and deepens as the rms parameters increase. Again, this trough is dependent on the type of cross-correlation function chosen.

The primary conclusion of this work is that the presence of dielectric fluctuation scattering can be significant and have bearing on the interpretation of experimental measurements when compared to theory. Of particular interest is the dependence of the theory on the cross-correlation between the roughness and dielectric parameters.

References

[1] See, e.g., Elson, J. M.; Bennett, H. E.; Bennett, J. M. 'Scattering from optical surfaces," chapter 7 in Applied Optics and Optical Engineering, Vol. VII. New York; Academic Press; 1979. Pp. 191-243, and references therein.

[2] See also Barrick, D. E. Chapter 9 in Radar Cross Section Handbook. New York; Plenum Press; 1970; Elson, J. M.; Rahn, J. P.; Bennett, J. M. "Relationship of the total integrated scattering from multilayer-coated optics to angle of incidence, polarization, correlation length, and roughness cross-correlation properties," Appl. Opt. 22; 3207; 1983; Elson, J. M.; Rahn, J. P.; Bennett, J. M. "Light scattering from multilayer optics: comparison of theory and experiment," Appl. Opt. 19; 669; 1980.

[3] See also the entire issue of Opt. Engr. 18; 1979.

[4] See, e.g., Elson, J. M. "Light scattering from semi-infinite media for non-normal incidence," Phys. Rev. B12; 2541; 1975.

[5] Bennett, J. M.; Elson, J. M.; Rahn, J. P. "Angle-resolved scattering: comparison of theory and experiment," Thin Film Technologies, SPIE 401; 234-246; 1983.

[6] Elson, J. M. "Theory of light scattering from a rough surface with an inhomogeneous dielectric permittivity," submitted to Phys. Rev. B.

Table 1. Measured polarization ratios for silver films on glass and fused quartz surfaces of various roughnesses (values given in parentheses). The notations p→p and s→s refer to the polarization of the incident and scattered light, respectively, all measured relative to the plane of incidence. The angle of incidence was 60 deg, and the 60-deg retroscattering was measured in the plane of incidence, all for an incident wavelength λ = 0.6328 μm. The theory of scattering due to roughness only predicts a p→p/s→s ratio of 36.2.

Sample (rms roughness), Å	p→p/s→s	s→p/s→s
Ag (6.5)	24.0	0.20
Ag (7.7)	14.8	0.22
Ag (12.3)	8.7	0.12
Ag (13.6)	12.2	0.14
Ag (20.2)	73.0	0.50
Ag (22.3)	80.4	1.00
Ag (48.6)	3.7	0.24
Ag (50.3)	4.9	0.34
Ag (55.6)	36.6	0.89
Ag (59.3)	18.1	0.76

Table 2. Summary of the different sets of data for the various statistical parameters used in the numerical analysis. Note that the correlation lengths are the same for the roughness and dielectric parameters. The quantities δ_r and δ_d are defined by $[\delta_{rL}^2 + \delta_{rS}^2]^{1/2}$ and $[\delta_{dL}^2 + \delta_{dS}^2]^{1/2}$, respectively. The pertinent perturbation ratios δ_r/λ and $\delta_d/|\varepsilon_1|$ are also shown. The δ and σ are rms and correlation length parameters, respectively. The r and d subscripts refer to roughness and dielectric, respectively. The L and S refer to long- and short-range parameters, respectively.

Statistical parameter	Numerical value
δ_{rL}	0.001 μm
δ_{rS}	0.003 μm
δ_r/λ	0.005
σ_{rL}	2.0 μm
σ_{rS}	0.1 μm
δ_{dL}	0.35
δ_{dS}	1.75
$\delta_d/\lvert\varepsilon_1\rvert$	0.194
σ_{dL}	2.0 μm
σ_{dS}	0.1 μm
δ_{rdL}	0.019 $\mu m^{1/2}$
δ_{rdS}	0.073 $\mu m^{1/2}$
σ_{rdL}	2.0 μm
σ_{rdS}	0.1 μm

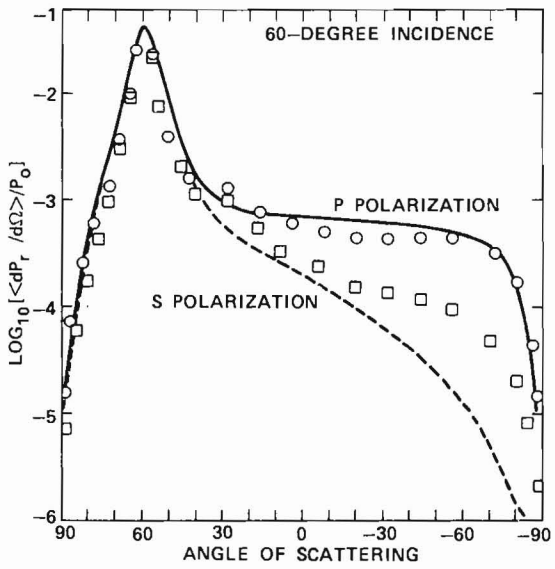


Figure 1. Experimental (circles and squares) and predicted (solid and dashed curves) angular scattering from a Ag-coated, dense flint sample for p- and s-polarized incident and scattered light, 60-deg angle of incidence, and λ = 0.6328 μm. The predicted curves are for roughness-only scattering in the plane of incidence.

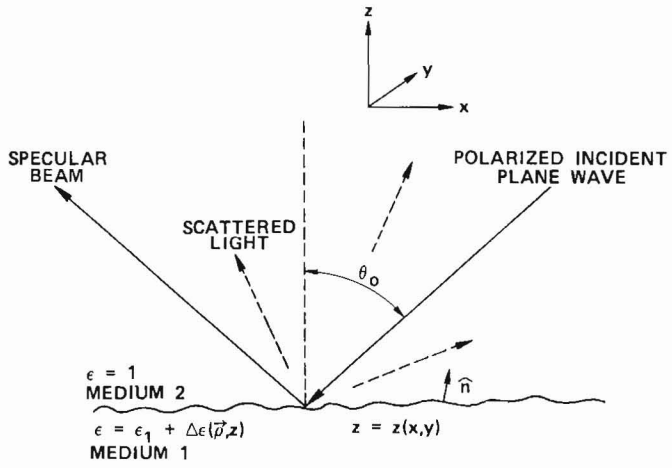


Figure 2. Schematic diagram of the problem considered here. The surface varies as z = z(x,y) and is only slightly rough where the rms roughness is much less than the wavelength. The lower medium is inhomogenous where the dielectric permittivity ε varies with position. A first-order calculation is done to predict the scattering characteristics of such a surface.

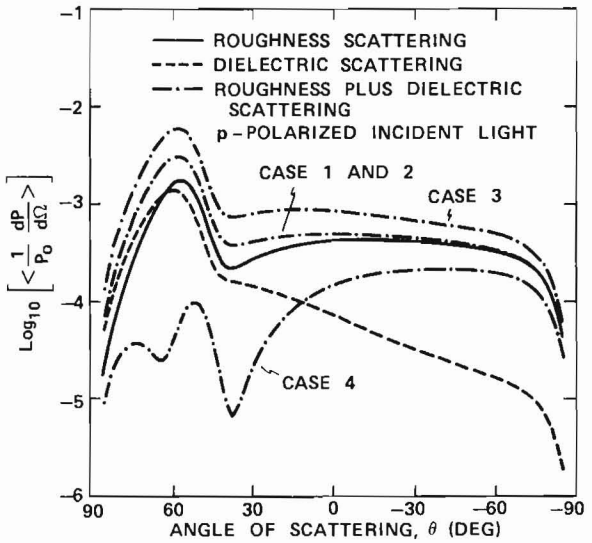


Figure 3. $\text{Log}_{10}[\langle(1/P_o)(dP/d\Omega)\rangle]$ versus polar angle of scattering. The wavelength is 0.6328 μm, and the angle of incidence is 60 deg. Cases 1 and 2 are superimposed, whereas Cases 3 and 4 are elevated and depressed relative to the roughness-only scattering, respectively. The dielectric-only scattering curve is also shown. The satistical parameters used are shown in table 2.

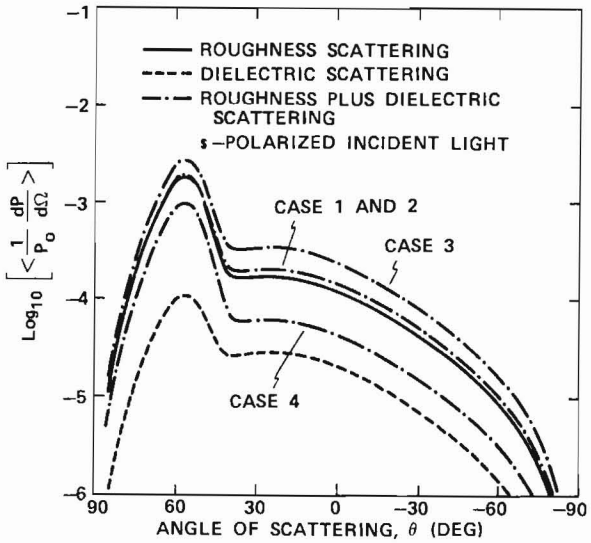


Figure 4. This figure parallels figure 3 except that the incident and scattered fields are s-polarized.

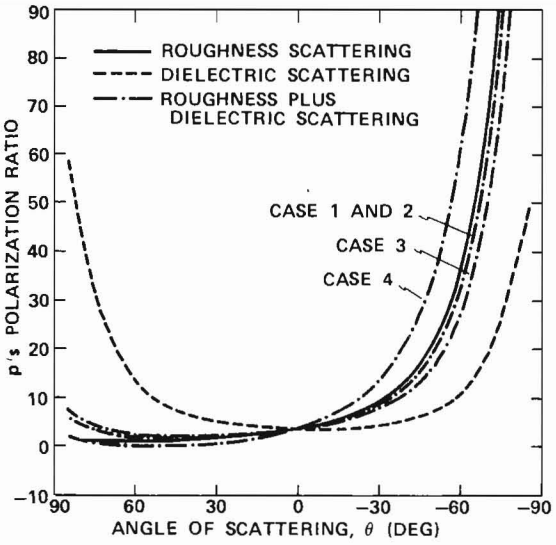


Figure 5. This figure is the p-/s- polarization ratio of the scattered light predicted in figures 3 and 4. Shown are the ratios for Cases 1 through 4. Cases 1 and 2 differ slightly from the roughness curve. Cases 3 and 4 are depressed and elevated, respectively, relative to the roughness curve.

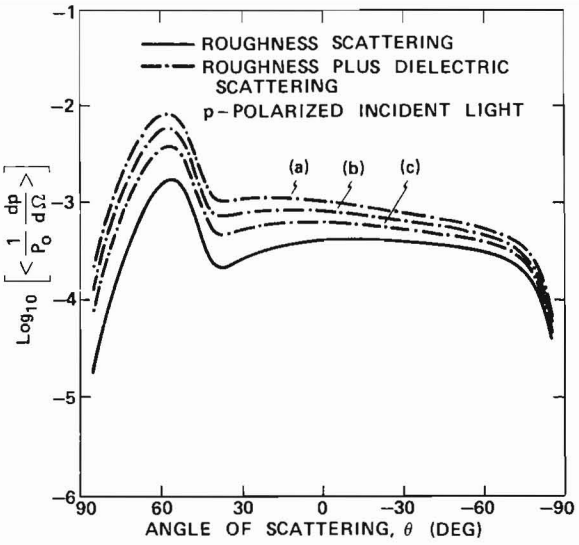


Figure 6. $\mathrm{Log}_{10}[\langle(1/P_o)(dP/d\Omega)\rangle]$ versus polar scattering angle for three different sets of rms dielectric values. The roughness-only curve (solid) is compared to roughness-plus-dielectric curves where the rms dielectric values, δ_{dL} and δ_{dS}, are (a) 2.5 and 0.5, or (b) 1.75 and 0.35, or (c) 1.0 and 0.2, respectively. The incident wavelength is 0.6328 Å and is p-polarized at 60-deg incidence angle. This figure pertains to Case 3, and the rms roughness and the correlation length values are given in table 2.

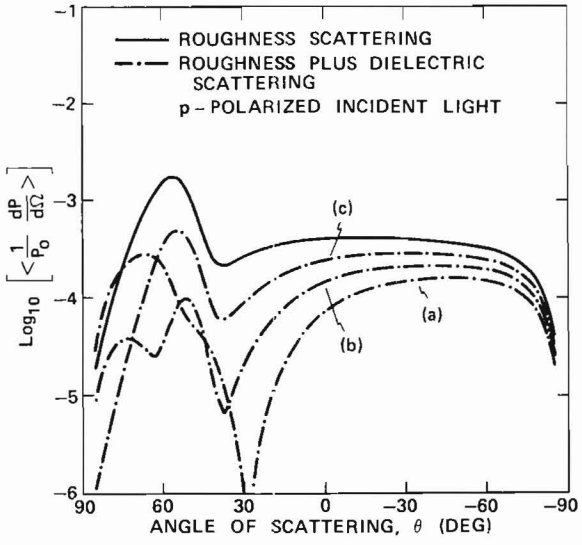


Figure 7. This figure parallels figure 6 except that Case 4 is in effect.

Surface Finish Measurements on Low-Scatter Laser Mirrors and Roughness Standards*

Jean M. Bennett
Michelson Laboratory, Physics Division
Naval Weapons Center, China Lake, California 93555

and

K. H. Guenther and P. G. Wierer
Balzers AG, FL-9496 Balzers, Liechtenstein

In assessing the surface quality of low-scatter laser mirrors, it is important to understand the advantages and limitations of various measurement methods. For example, values for the root mean square (rms) surface roughness may depend critically on the lateral resolution of the profile measuring instrument and on the surface spatial wavelength range sampled if the correlation lengths of the surface microirregularities are less than or equal to the instrumental resolution, or if appreciable long range surface waviness is present. If the surface roughness is deduced from a measurement of the total integrated scattering, the measurement wavelength, collection angles, and spatial wavelengths of the surface microroughness all have an effect. In the present study, several methods were used to measure the rms roughness of a group of samples which included low-scatter laser mirror substrates and additional samples of varying roughness, all partly coated with high reflectance dielectric multilayers and aluminum overcoatings. Measurement techniques and instruments included a diamond stylus surface profiling instrument (Talystep), Mireau heterodyne interferometer (Wyko), optical heterodyne profilometer (Lawrence Livermore National Laboratory), and total integrated scattering (Naval Weapons Center and Balzers). The roughness values thus obtained are compared and conclusions are drawn concerning the effect of the surface spatial wavelength range sampled and the instrumental lateral resolution.

Key words: laser gyro optics; multilayer films; optical scattering; roughness standards; surface roughness

Introduction

Two questions are frequently asked: "What is the roughness of this optical surface?" and "What roughness specification (or value) should I put on the drawings for the optics of the x,y,z system?" Unfortunately, there are no simple answers to these questions. As we will show in this paper, there is no single value for the root mean square (rms) roughness of an optical surface. It depends on the surface spatial wavelength range measured, the lateral resolution of the profiling instrument, and, for total integrated scattering (TIS), the surface cleanliness and illuminated area. Also, there are two basic ways the surface roughness can be determined: directly by an instrument that measures an actual profile of the surface, or indirectly by measuring the effect of the roughness, i.e., the scattered light the rough surface produces, and then calculating the roughness using a theoretical relation such as the scalar scattering theory [1][1]. In this paper we will compare rms roughness values of several low-scatter laser mirrors and a series of graded roughness standards measured by different techniques, and will explain the reasons for the differences.

Experimental Measurements and Results

Several Zerodur and a few BK-7 25.4-mm-diameter, 6-mm-thick, samples were polished to a low-scatter finish (laser gyro mirror quality) using techniques already described [2]. In addition, a series of graded roughness standards, R1 to R5, were made by fine grinding several samples and then polishing them different lengths of time to produce surfaces containing pits of varying numbers and depths. On the smoothest sample, R5, the surface finish was equivalent to that of a laser gyro mirror. Nomarski micrographs were made of the surfaces using a Zeiss Epi Microscope with Wollaston

*Work supported by Navy Independent Research Funding.
[1]Numbers in brackets indicate the literature references at the end of the paper.

prisms attached to the microscope objectives. Micrographs of the five roughness standards are shown in figure 1. (The Nomarski technique is described elsewhere [3,4].)

Part of each surface was covered with a high reflectance multilayer dielectric (MLD) stack, maximized for a 30° angle of incidence at a wavelength of 6328 Å (for laser gyro applications). Then part of each surface was overcoated with an opaque aluminum film so that scattering from the MLD coating could be compared with scattering from a surface having the same topography but covered with an opaque film. The thin (~ 1000 Å) aluminum film did not add appreciable roughness compared to the much thicker (~ 3 μm) multilayer film.

Surface Profile Measurements

The topographical structure of the smooth surfaces and the roughness standards can be understood by comparing the Nomarski micrographs with the surface profiles made with a Talystep surface profiling instrument [5]. This instrument uses a 1-μm-radius diamond stylus that has a lateral resolution 0.1 to 0.2 μm on the smoothest surfaces [5]. The Nomarski micrograph of the roughest surface, R1, shows many pits remaining from the grinding process, while the Talystep profiles of a section of this surface, figure 2, give an idea of the numbers and depths of the pits. (The profiles shown, of approximate lengths 1500, 150, and 15 μm, respectively, each contain 1,000 data points. Roughness values calculated for each scan are shown at the left of the scan.) It is of course very difficult to obtain ensemble average statistics from a single profile, or even from several profiles, so these traces should not to be considered as "ensemble averages". The roughness values for surfaces containing pits are greatly influenced by the numbers and depths of the pits. In the intermediate length scan, approximately 150 μm long, the v-shaped profiles of some of the pits indicate that they are not being completely resolved. The surface structure in between the pits is shown on the shortest (15-μm-long) scan. The 7.9 Å rms roughness value measured for this scan is typical of the roughness of a commercial polish.

Roughness standard R2 was made by doubling the polishing time that was used for making R1. As shown in the Nomarski micrograph (fig. 1) and in the Talystep scans (fig. 3), this surface has fewer pits than does R1, and those remaining are shallower. The surface between the pits is also somewhat smoother. Roughness standards R3 and R4 still contain some pits, but the number is so much smaller that the Talystep traces are essentially pit-free. The surface of standard R3 (fig. 4) is only slightly rougher than that of standard R4 (fig. 5). Roughness standard R5 (fig. 6) is of laser gyro quality. Its surface appears featureless in the Nomarski micrograph except for isolated dust particles (fig. 1); the bare surface (and also the aluminized surface) had a profile roughness of 5.0 Å rms as determined from a 1-mm-long scan containing 16,000 data points.

By comparing the 150-μm and 15-μm Talystep scans on sample R5 for the MLD-film-coated and bare Zerodur parts of the surface, it appeared that the MLD film was rougher than the uncoated substrate. However, there is some conflicting evidence from electron micrographs taken of the two areas; this subject is discussed in detail in reference [2]. For the moment, assuming that the roughness effects shown in the Talystep traces are real, we can calculate the roughness added by the MLD stack using the approximate relation:

$$\delta_f = \sqrt{\delta_{fs}^2 - \delta_s^2} \quad , \tag{1}$$

where δ_f, δ_{fs}, and δ_s are the rms roughness of the MLD film, the film-covered substrate, and the substrate, respectively. The MLD film roughness was determined to be about 5.1 Å rms, approximately equal to the roughness of the uncoated surface. No added roughness could be detected from the overcoating aluminum film.

Surface profiles were also made with two other instruments, the optical heterodyne profilometer (OHP) [6] at Lawrence Livermore National Laboratory (LLNL) and the Wyko Mireau heterodyne interferometer (HI) [7] at the Naval Weapons Center (NWC). This latter instrument is a modified optical microscope that includes a beam splitter and aluminized reference flat close to a long working distance microscope objective. Light passes through the objective to the beam splitter, where part is reflected to the reference surface and part transmitted to the test surface. After reflection the beams are recombined by the beam splitter and form interference fringes in the focal plane of the objective. Thus, one can see an image of the surface on which a series of parallel interference fringes is superposed. The orientation and spacing of the fringes can be controlled by tilting the reference surface. The surface profile is obtained by aligning the zero-order interference fringe so

that it falls on a linear diode array in the focal plane of the objective. A piezoelectric transducer oscillates the reference surface, causing the fringe to be swept sinusoidally across the diode array. The phase of the signal is detected and converted into a surface profile using an IBM Model 5150 personal computer, Hewlett-Packard Model 9836 calculator and published algorithms [8]. When measuring the very smoothest surfaces, the effect of the roughness of the reference surface can be removed. Slight curvature of the reference surface can also be eliminated from the measured profile.

Both of the heterodyne instruments have height sensitivities comparable to that of the Talystep, but their lateral resolution is only about 2 μm (1.3 μm theoretical for the Wyko instrument), or about ten times worse than that of the Talystep. Thus, features that would be resolved by the stylus instrument are only partially resolved or unresolved by the heterodyne instruments, and the measured values for the surface roughness will be smaller. Figures 7 - 10 illustrate this point with profiles of the roughness standards taken with the Livermore OHP, while figures 11 - 14 show comparable traces made with the Wyko HI. These figures are to be compared with the corresponding Talystep traces shown in figures 2 - 6. Values for the average roughnesses measured by the various instruments are summarized in table 1. Comparing the three traces made on R1 (figs. 2, 7, and 11), the pit depths measured with the Talystep are up to 4000 Å deep, but only about 200 Å deep for the Livermore OHP and about 150 Å for the Wyko HI. The average roughnesses listed in table 1: 447 Å rms, 74 Å rms, and 45 Å rms, respectively, illustrate the effect of the different lateral resolutions.

The traces for R5, the smoothest roughness standard (figs. 6, 10, and 14), have slightly different characters. The Wyko HI is essentially noise limited, so that the trace represents the instrumental noise rather than information about the surface. The Talystep data for a 1-mm-long scan give a roughness of about 5.0 Å rms (for bare Zerodur or aluminum on Zerodur) because of a long range waviness component, while the shorter 600-μm- and 60-μm-long scans show a roughness of only about 3.8 Å rms. (As mentioned previously, the MLD-coated surfaces are rougher.) The profile length of the OHP is only 628 μm and the instrument does not resolve short correlation length surface features, so the measured roughness value is smaller. Similar comments could also be made when comparing roughness values for standards R3 and R4.

Figure 15 graphically compares roughnesses measured with the Livermore and Wyko instruments on the four rougher standards, R1 to R4. In this figure, values for measurements made on the four parts of each surface (bare Zerodur, MLD on Zerodur, aluminum on MLD on Zerodur, and aluminum on Zerodur) are compared separately. It is seen that there is a good linear relationship between measurements made with the two instruments, but the relation is not what would be expected if the Wyko instrument actually had better lateral resolution than did the Livermore OHP. Since the Wyko HI is still in an experimental stage, it is expected that some of these inconsistencies will be removed later.

Light Scattering Measurements

In addition to the surface profile measurements, roughnesses were deduced from measurements of TIS made at NWC using the Optical Evaluation Facility that has an aluminized hemispherical collecting mirror [1,9] and at Balzers using an instrument with an integrating sphere and 30° angle of incidence on the sample [2]. Both instruments used red laser lines (He-Ne, wavelength of 6328 Å for Balzers and Kr wavelength of 6471 Å for NWC) and had beam diameters of about 1 mm to allow for averaging over many grinding pits and dust particles on the sample. The rms roughness δ was calculated from the TIS using the relation from scalar scattering theory [1]

$$\delta \approx (\lambda/4\pi) \cdot \sqrt{TIS} \quad . \tag{2}$$

TIS is the ratio of the light scattered into a hemisphere divided by the total reflectance of the sample (specular plus scattered light). Since the reflected scattering is being measured, the reflecting surface must be essentially opaque or else the contribution of bulk scattering plus scattering from the second surface must be able to be eliminated. The total reflectance must either be known or measured. In the NWC instrument the light is incident normally on the sample, so transparent samples cannot be measured. The Balzers instrument uses a 30° angle of incidence so scattering from the back surface of a sample can be eliminated. However, the glass ceramic Zerodur has appreciable bulk scattering, which cannot be eliminated from the measurement. Therefore, TIS could not be measured on the uncoated portions of the samples.

Figure 16 compares roughnesses derived from TIS measurements made at Balzers and at NWC on the same portions of roughness standards R1 to R5: the MLD-coated Zerodur and aluminum on MLD-coated Zerodur. The logarithmic scale is the same on both axes, and the dashed line represents equal values on each axis. There is very good agreement between the two sets of measurements, which is especially encouraging since the instruments have quite different collection geometries. The average numerical values for each sample are listed in table 1.

Comparison of Surface Profile and Light Scattering Roughness

Figure 17 graphically summarizes the roughnesses that were measured on all the roughness standards (table 1) using the previously discussed techniques. It is seen that, with the exception of the Talystep measurement on R1, the TIS measurements give the largest roughness values while the Wyko HI gives the smallest values. Other techniques give intermediate roughnesses. The TIS-derived roughnesses are approximately 2.7 times larger than the heterodyne profilometer roughnesses, but there is no constant ratio between TIS values and Talystep profile roughnesses.

Low Scatter Surfaces

In addition to the roughness standards, several other supersmooth Zerodur and BK-7 samples were prepared and measured. These measurements are described in detail in another paper [2] and will only be summarized here.

Roughness measurements on supersmooth mirrors pose special problems because contamination in the form of dust or particulates can have a large effect on the measured values. Thus, it is very encouraging to see excellent agreement between TIS-derived roughnesses measured at NWC and at Balzers using quite different instruments. Furthermore, the roughness values derived from TIS measurements made on MLD-coated Zerodur are quite similar to values obtained from aluminum films overcoating the MLD stack. (The roughness calculation for the MLD stack assumed that the entire stack could be treated as a single film.) The excellent agreement suggests that the roughnesses on the individual boundaries within the MLD stack are correlated, so that scattering from these multiple boundaries combines coherently and produces a net scattering level that is nearly identical to that from a single boundary. This point is discussed further elsewhere [2].

The Talystep profile roughnesses agree well with TIS-derived values, while the Livermore OHP roughnesses are lower by a factor of 2 to 3 because of the lower lateral resolution of surface spatial wavelengths. It was also possible to polish BK-7 samples to the same surface roughness as that of the smoothest Zerodur samples. Thus, the Balzers-polished BK-7 is among the smoothest non-quartz-type of polished glass measured to date.

The smoothest uncoated Zerodur and BK-7 samples had Talystep-measured roughnesses of about 5 Å rms, and the average added roughness of the MLD films on these substrates was about 4.6 Å rms.

Conclusions

In conclusion, figure 17 and table 1 show that there is no unique roughness value that can be assigned to an optical surface. The values depend on the surface spatial wavelength range measured, the lateral resolution of the profiling instrument, and the surface cleanliness and illuminated area for total integrated scattering (TIS) measurements. For surface profile measurements, it is difficult to obtain "ensemble average" roughnesses for samples containing pits randomly distributed on a smooth average surface from a single measurement, or even from several measurements on different places on the surface. However, a linear relation was found between the Livermore OHP-measured roughnesses and the Wyko Mireau HI values. The Talystep values were higher than those of the other profiling instruments because of the superior lateral resolution. Furthermore, the added roughness of a MLD film could be determined from Talystep measurements on the smoothest surfaces, and was found to be approximately equal to the roughness of the bare surface.

Excellent agreement has been obtained between roughnesses derived from TIS measurements made at the Naval Weapons Center and at Balzers using instruments of quite different design. The TIS-derived roughnesses were found to be approximately 2.7 times larger than roughnesses measured with heterodyne profilometer instruments. On the smoothest sample, R5, particulates and isolated surface defects probably produced more scattering than did the microroughness. Thus, surface cleanliness is extremely important when trying to measure the roughness of extremely smooth surfaces.

The answers to the questions posed in the Introduction are seen to be much more involved than one might wish. If a roughness specification is to be put on a drawing, one should state how the roughness is to be measured (TIS or profile instrument) and, if the latter, what is the profile length, lateral resolution, and number of places to be sampled. Further work is being done in this area to aid in our understanding of the problem.

The authors would like to thank P. C. Archibald at the Naval Weapons Center for making the total integrated scattering measurements, Z. Kanizsa and W. Martin at Balzers AG for polishing and coating the smooth optical samples and roughness standards, and N. J. Brown at Lawrence Livermore National Laboratory for providing the use of the optical heterodyne profilometer and assisting with the measurements. Two of the authors (K.H.G. and P.G.W.) would like to thank the management of Balzers AG for permission to publish this paper.

References

[1] Bennett, H. E. "Scattering characteristics of optical materials," Opt. Engr. 17; 480-488; 1978.

[2] Guenther, K. H.; Wierer, P. G.; Bennett, J. M. "Surface roughness measurement of low scatter mirrors and roughness standards," Appl. Opt., submitted for publication.

[3] Nomarski, G. M. "Differential microinterferometer with polarized waves," J. Phys. Radium 16; 9; 1955.

[4] Nomarski, G. M.; Weill, A. R. "Application à la métallographie des méthodes interférentielles à deux ondes polarisées," Rev. Metall. 52; 121; 1955.

[5] Bennett, J. M.; Dancy, J. H. "Stylus profiling instrument for measuring statistical properties of smooth optical surfaces," Appl. Opt. 20; 1785-1802; 1981.

[6] Sommargren, G. E. "Optical heterodyne profilometry," Appl. Opt. 20; 610-618; 1981.

[7] Manufactured by Wyko Optical, Inc., 655 North Alvernon Way, Suite 123, Tucson, Arizona 85711.

[8] Wyant, James C. "Interferometric optical metrology: basic principles and new systems," Laser Focus 18; No. 5; 65-71; May 1982.

[9] Archibald, P. C.; Bennett, H. E. "Scattering from infrared missile domes," Opt. Engr. 17; 647-651; 1978.

Table 1. Summary of roughness measurements on Balzers roughness standards (Å rms)

Sample	TIS NWC	TIS Balzers	OHP LLNL	Mireau HI, NWC	Talystep NWC
R1	140	147	74	45	447
R2	61	60	34	24	62.5
R3	22.1	19.3	6.8	7.0	11.3
R4	12.3	10.4	3.3	3.8	7.4
R5	12.7	13.5	2.3	-	6.1

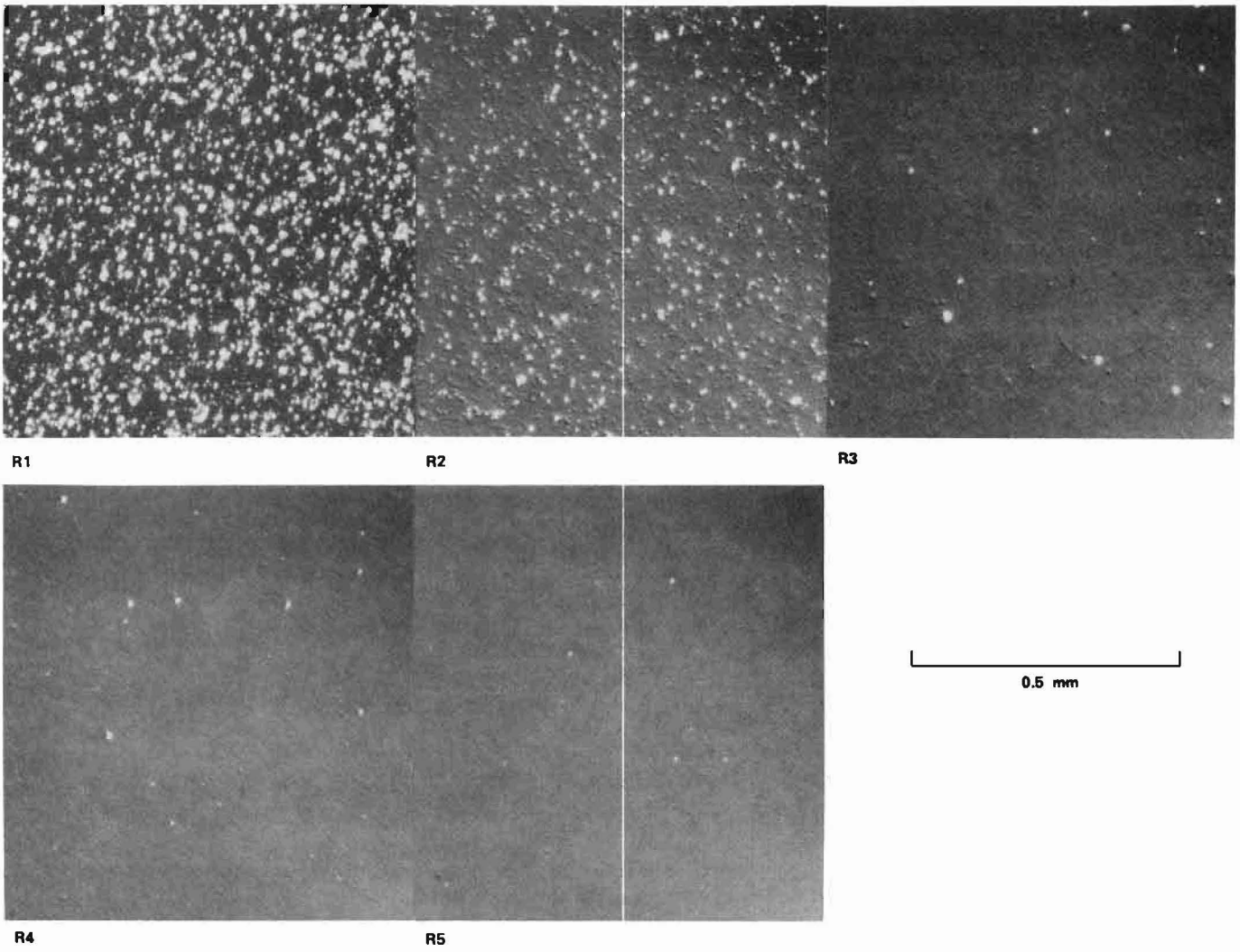


Figure 1. Nomarski micrographs of roughness standards R1 to R5.

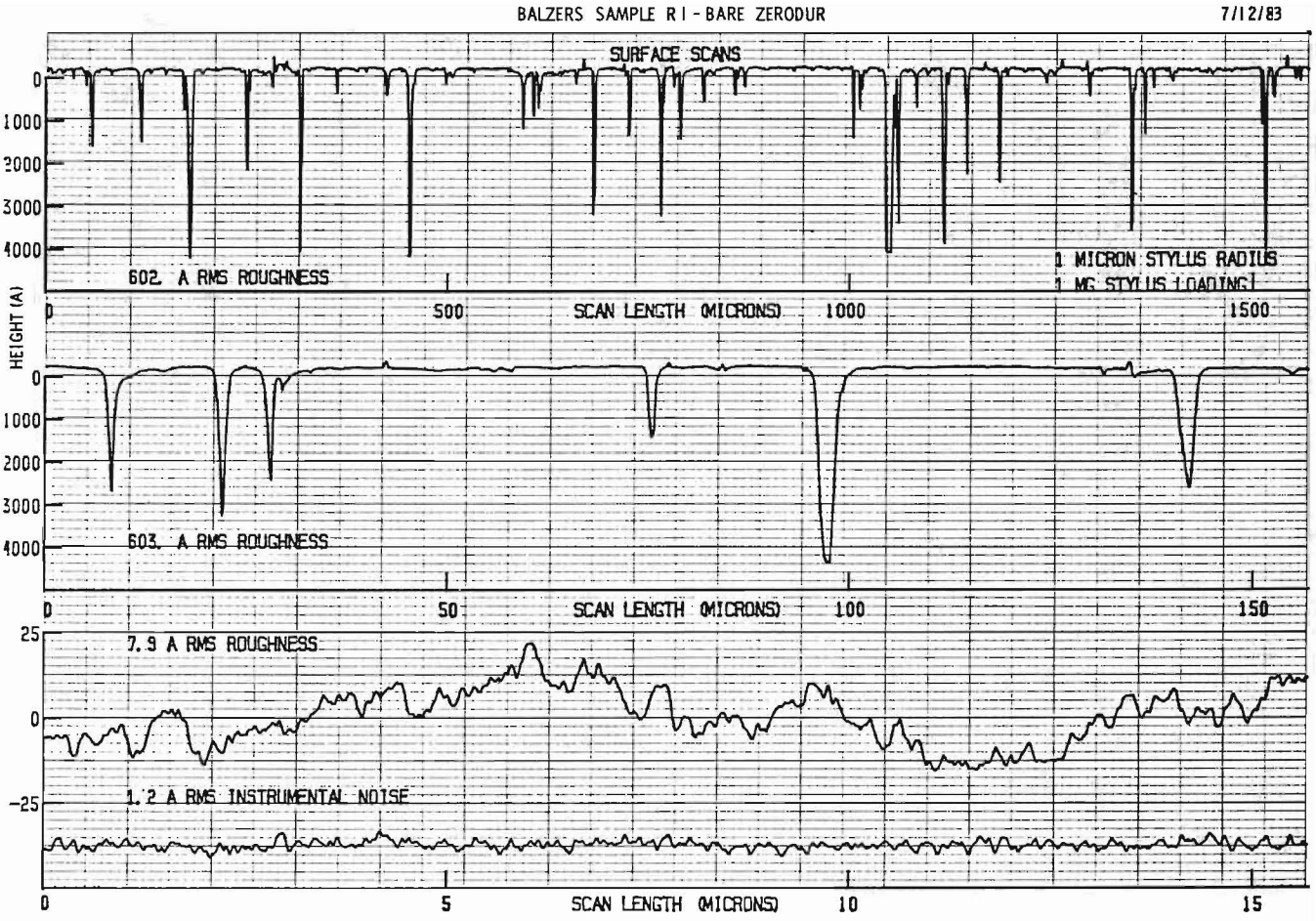


Figure 2. Talystep surface profiles of roughness standard R1, bare Zerodur portion.

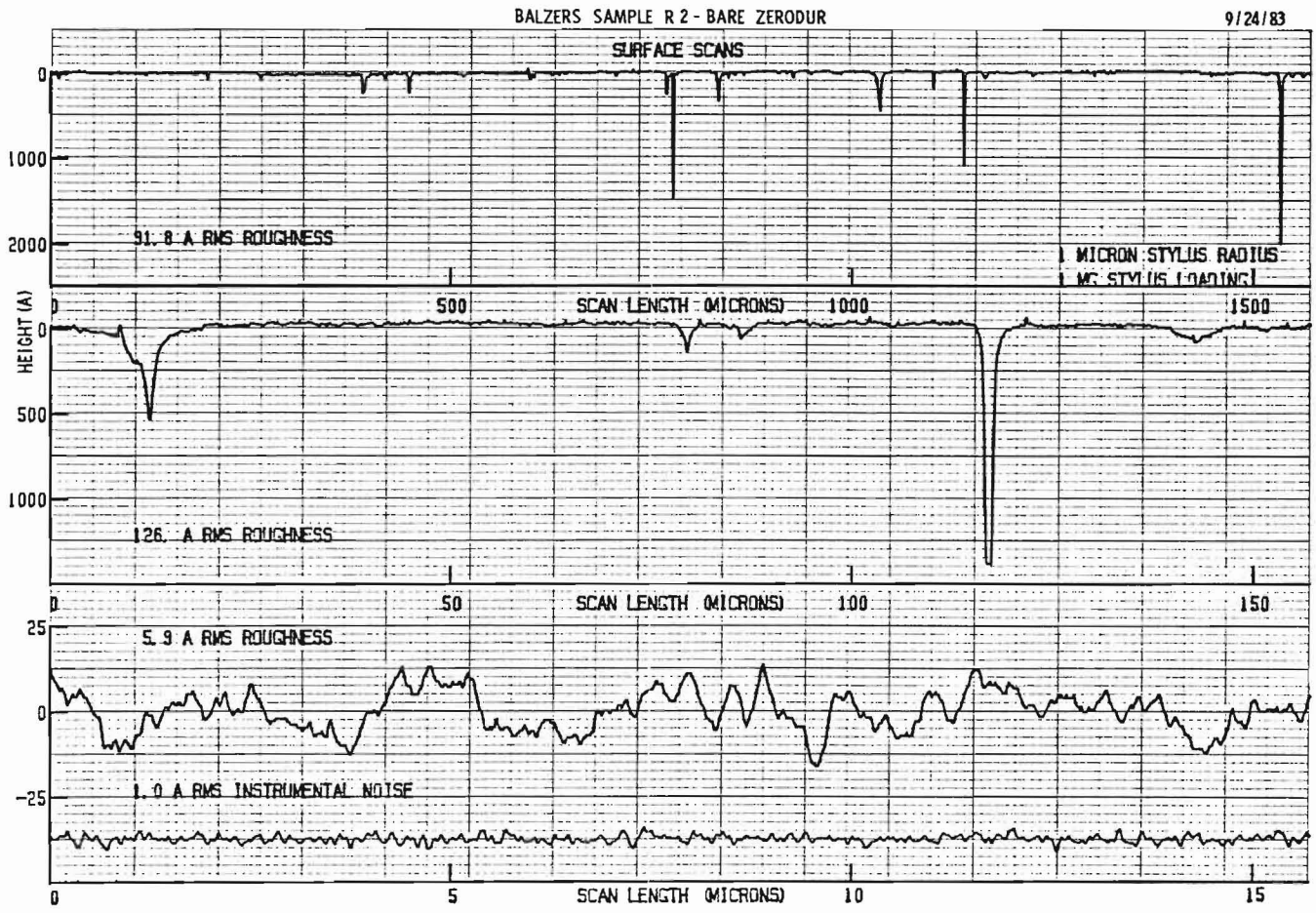


Figure 3. Talystep surface profiles of roughness standard R2, bare Zerodur portion.

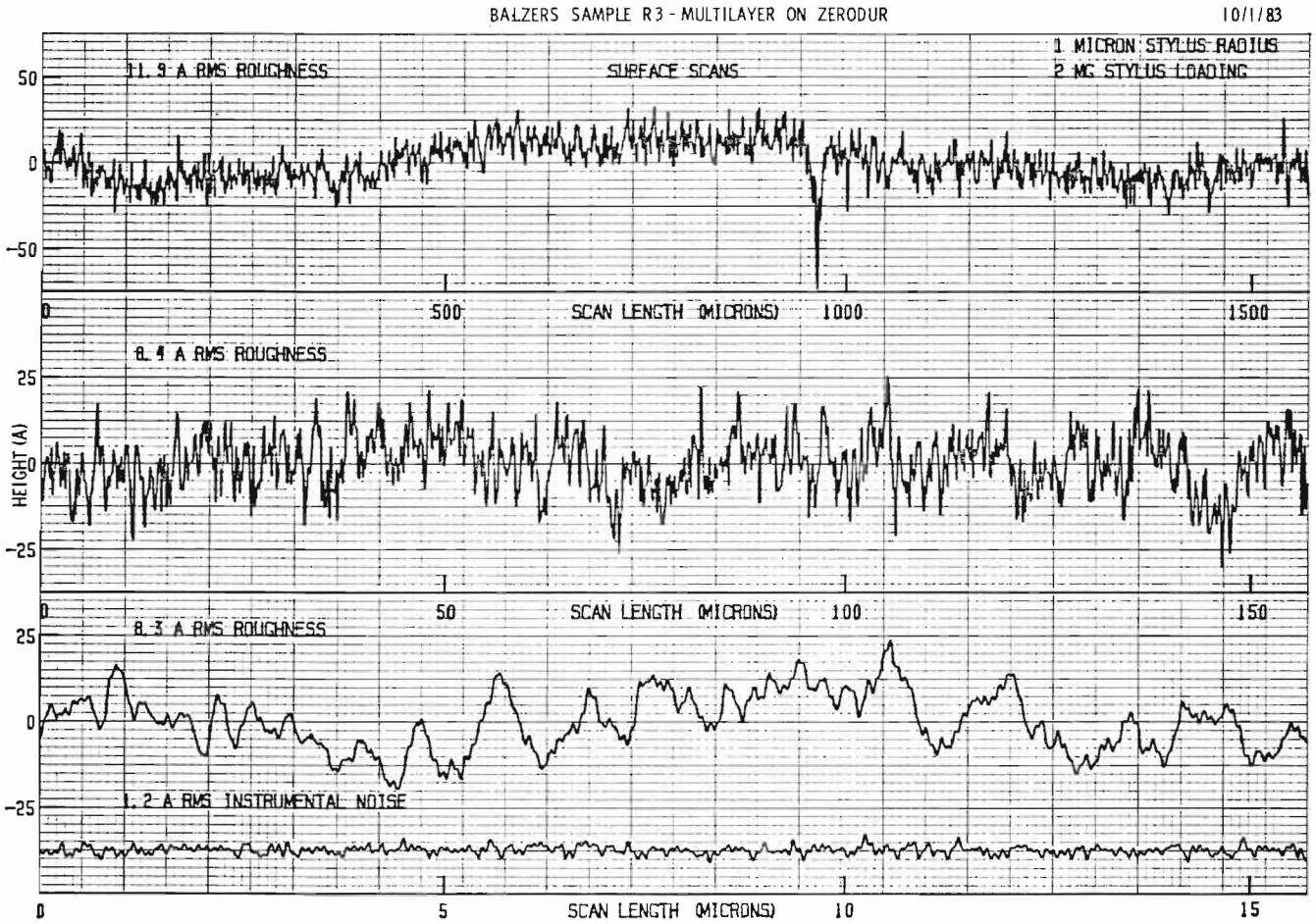


Figure 4. Talystep surface profiles of roughness standard R3, MLD film on Zerodur portion.

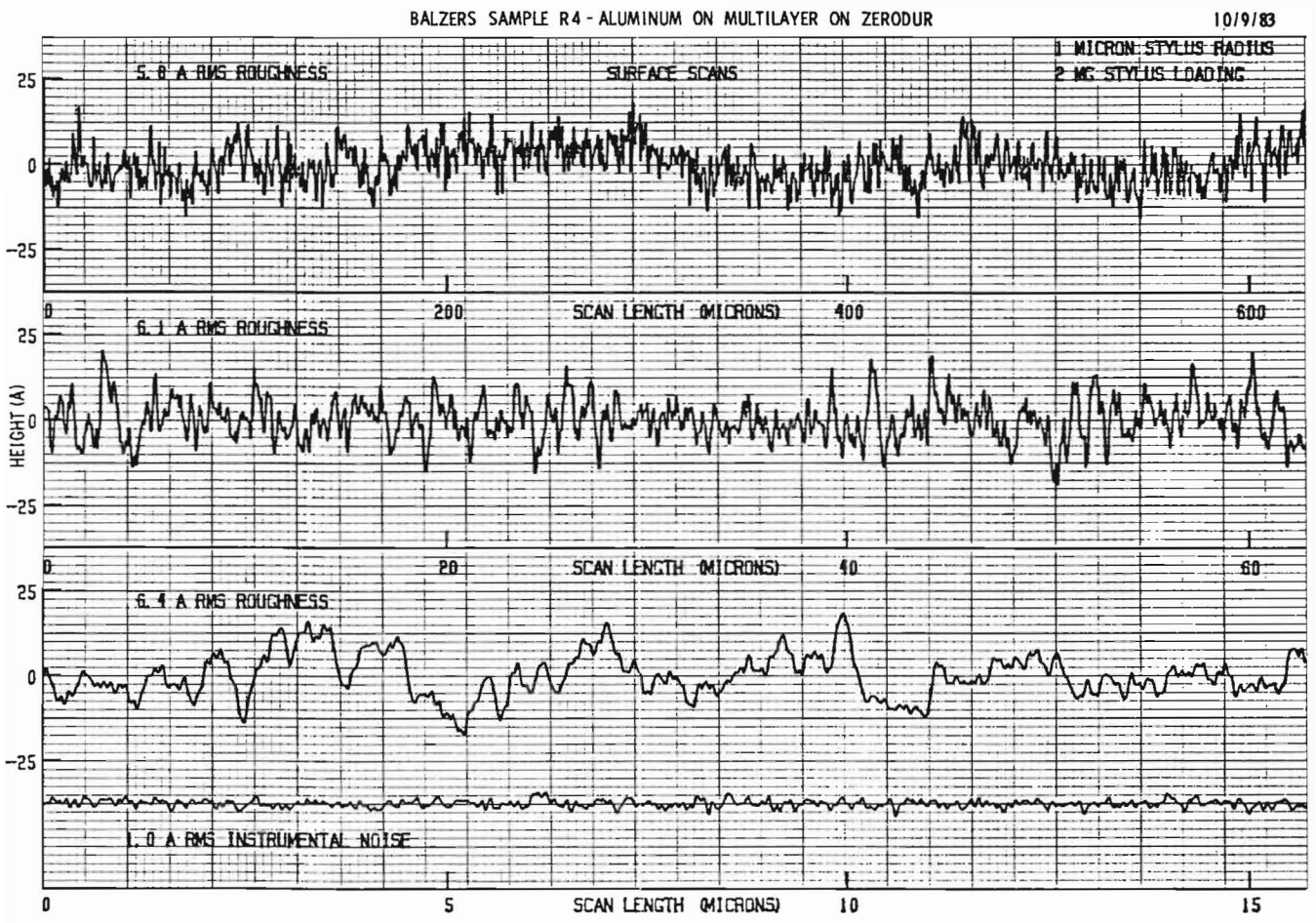


Figure 5. Talystep surface profiles of roughness standard R4, aluminum on MLD film on Zerodur portion.

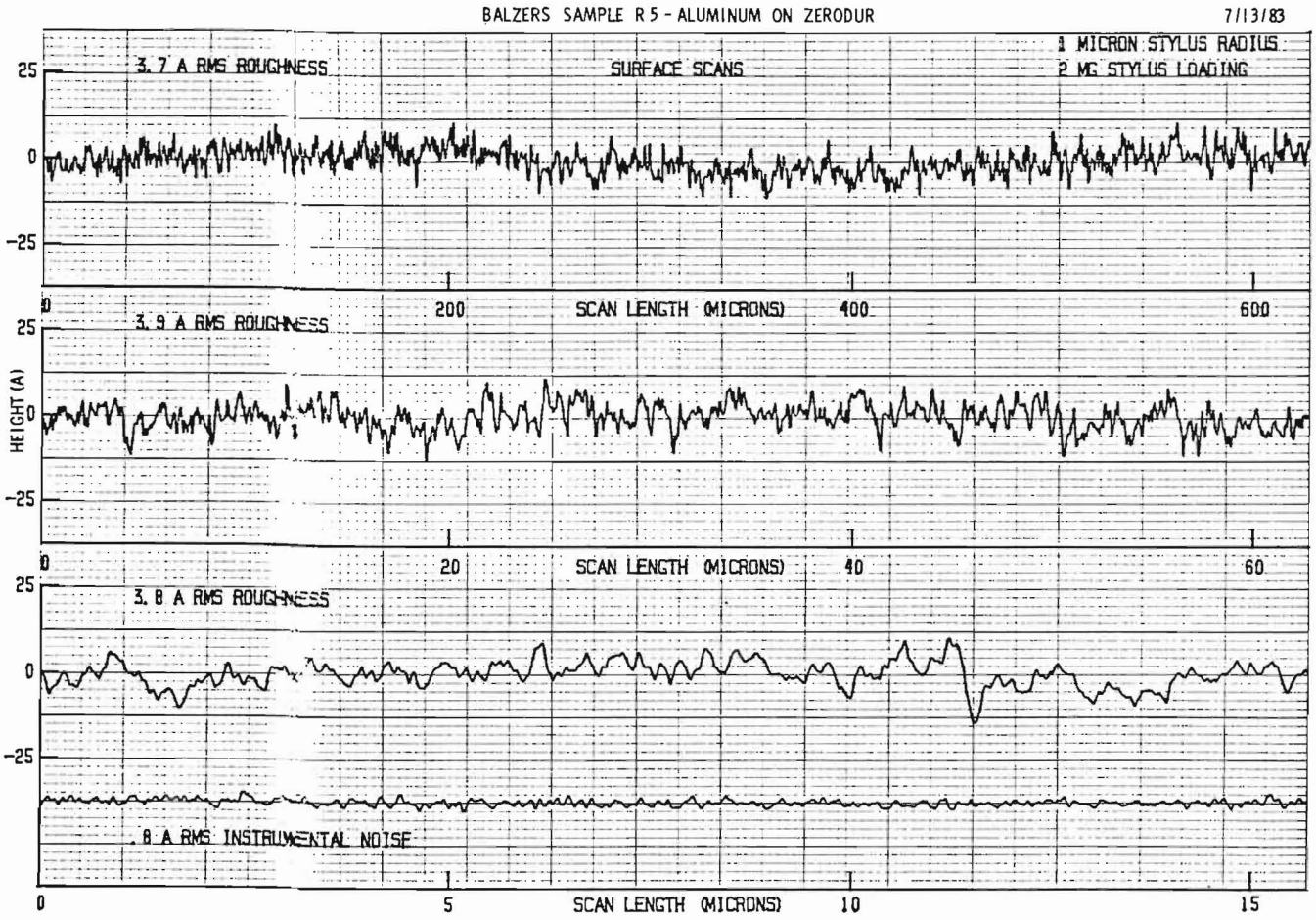
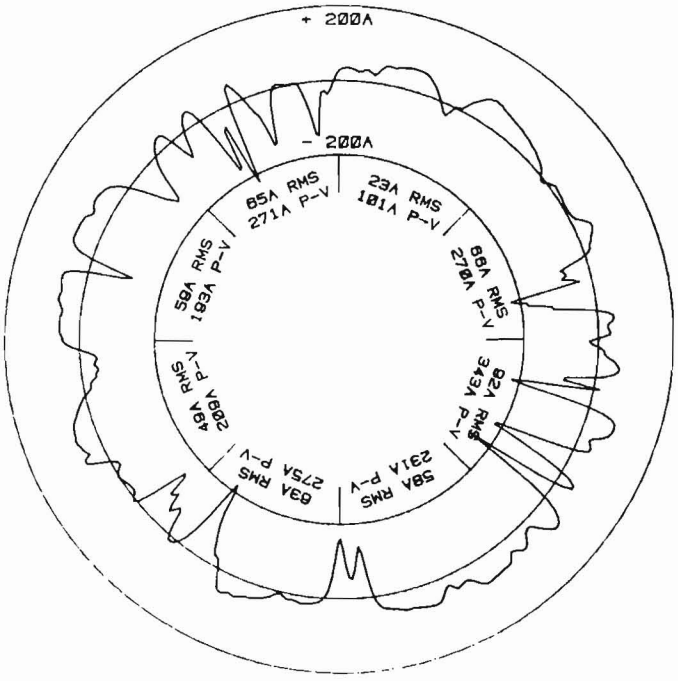


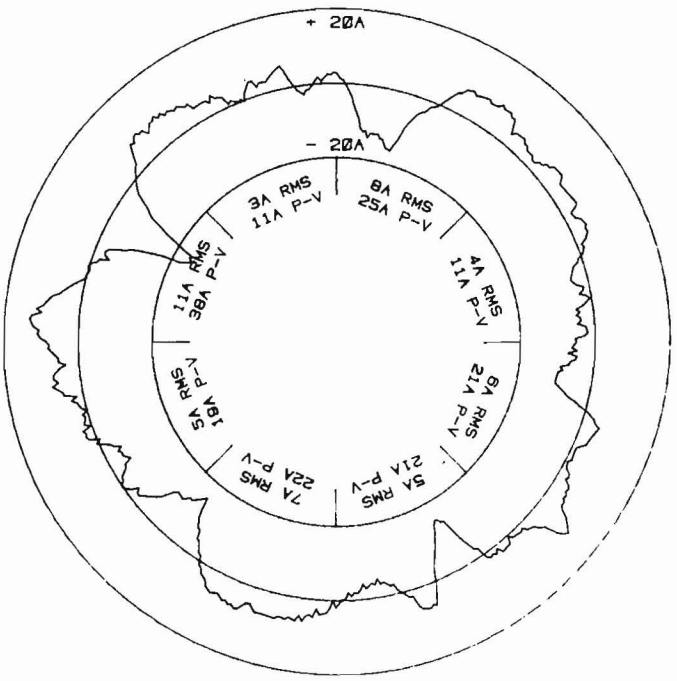
Figure 6. Talystep surface profiles of roughness standard R5, aluminum on Zerodur portion.



#R1 BARE ZERODUR
9/2/82 – 4:33 PM
CIRCLE DIAMETER 200 μm
CIRCLE CIRCUMFERENCE 628 μm

SURFACE PROFILE
65.7A RMS
343A P–V
42A ASTIG

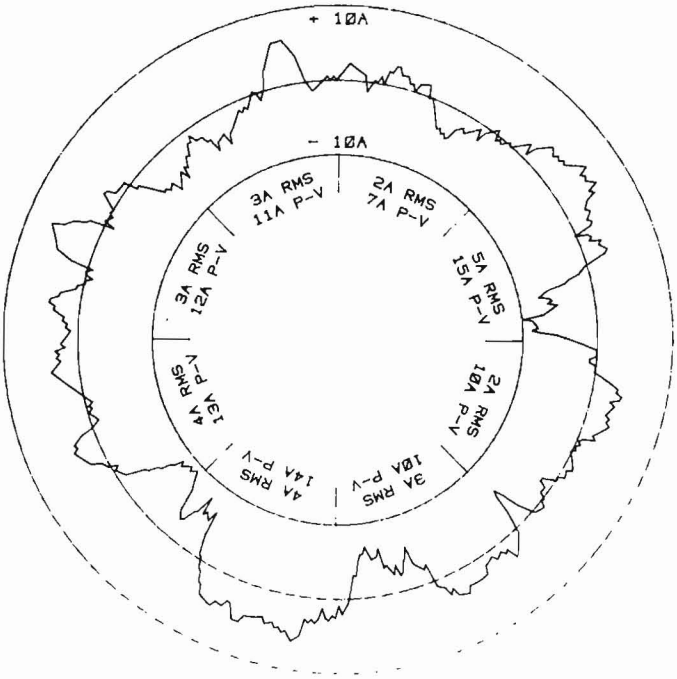
Figure 7. Livermore OHP surface profiles of roughness standard R1, bare Zerodur portion. The rms roughness, peak-to-valley roughness, and amount of astigmatism are also shown.



#R3 MULTILAYER
9/2/82 – 2:49 PM
CIRCLE DIAMETER 200 μm
CIRCLE CIRCUMFERENCE 628 μm

SURFACE PROFILE
6.8A RMS
38A P–V
4A ASTIG

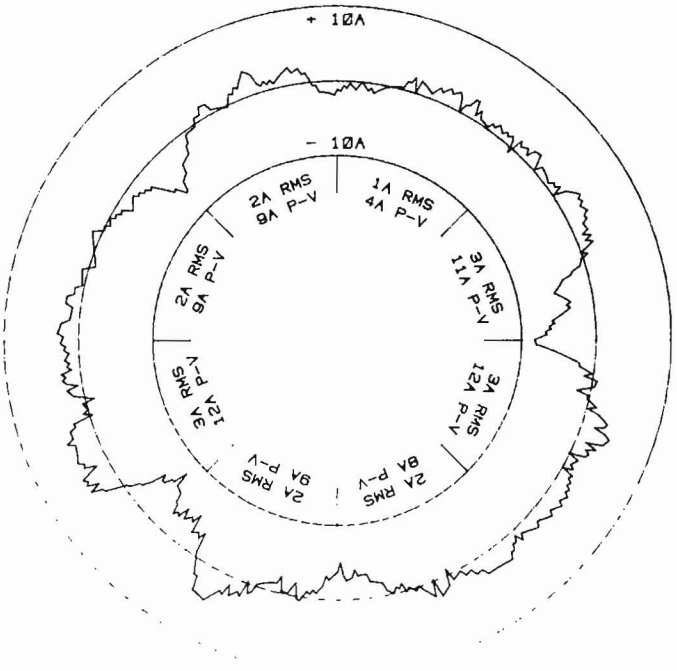
Figure 8. Livermore OHP surface profiles of roughness standard R3, MLD film on Zerodur portion.



#R4 ALUMINUM ON MULTILAYER
9/2/82 – 3:09 PM
CIRCLE DIAMETER 200 μm
CIRCLE CIRCUMFERENCE 628 μm

SURFACE PROFILE
3.5A RMS
16A P–V
5A ASTIG

Figure 9. Livermore OHP surface profiles of roughness standard R4, aluminum on MLD film on Zerodur portion.



#R5 ALUMINUM ON ZERODUR
9/2/82 – 3:27 PM
CIRCLE DIAMETER 200 μm
CIRCLE CIRCUMFERENCE 628 μm

SURFACE PROFILE
2.5A RMS
13A P–V
2A ASTIG

Figure 10. Livermore OHP surface profiles of roughness standard R5, aluminum on Zerodur portion.

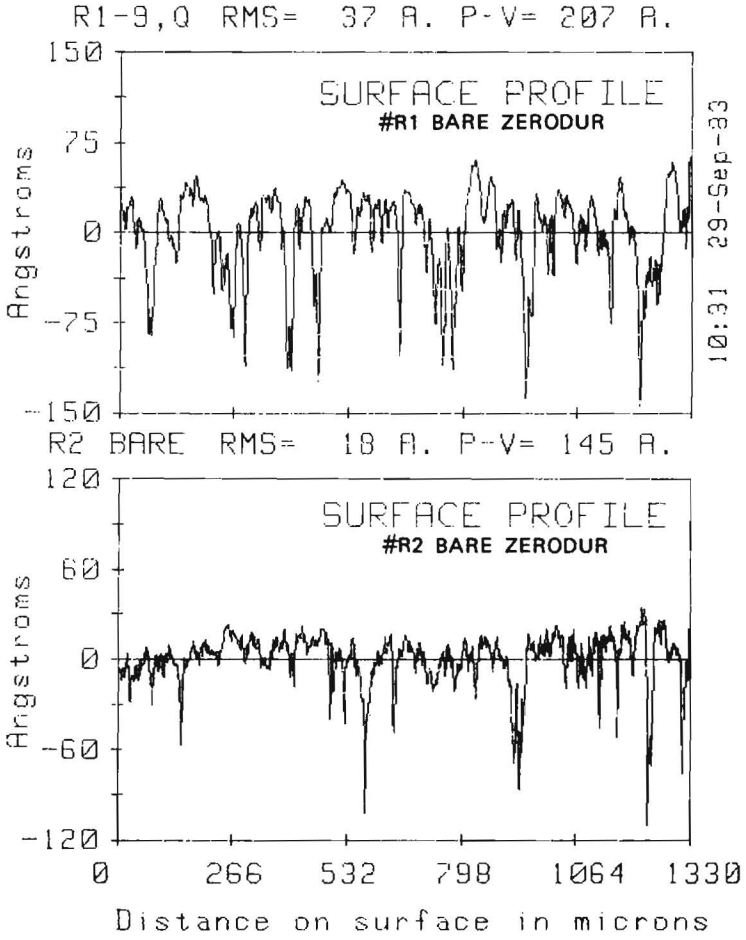


Figure. 11. NWC Wyko Mireau HI surface profiles of roughness standards R1 and R2, bare Zerodur portion. The rms roughness and peak-to-valley roughness values are shown.

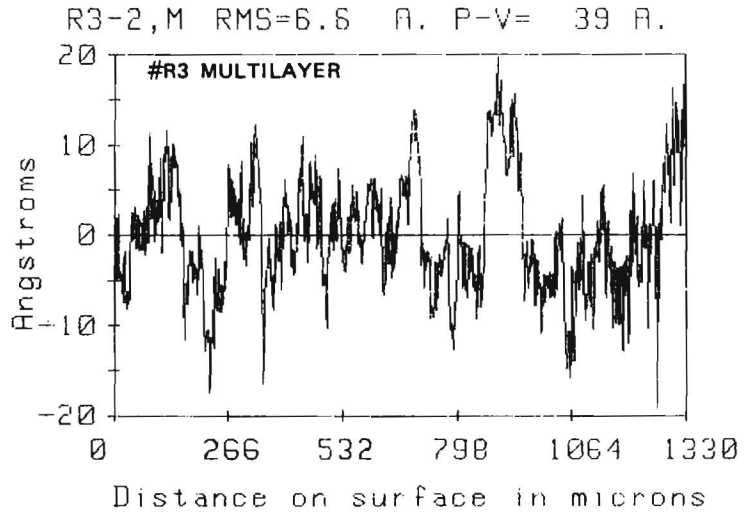


Figure 12. NWC Wyko Mireau HI surface profiles of roughness standard R3, MLD film on Zerodur portion.

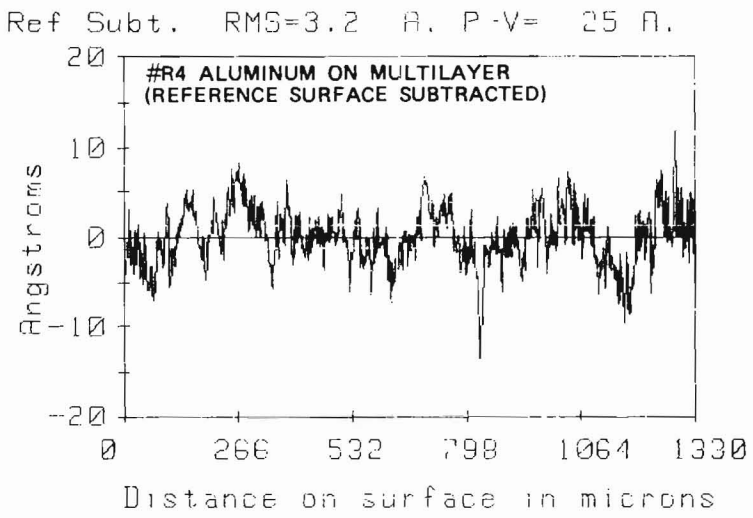


Figure 13. NWC Wyko Mireau HI surface profiles of roughness standard R4, aluminum on MLD film on Zerodur portion. The roughness on the reference surface has been subtracted.

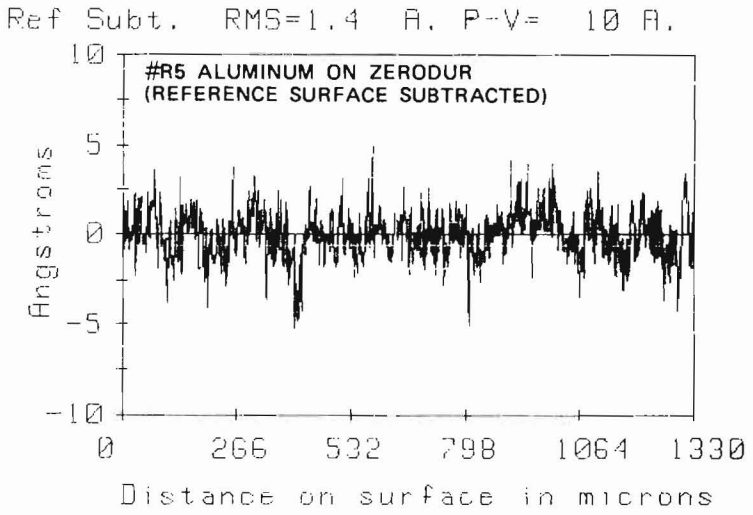


Figure 14. NWC Wyko Mireau HI surface profiles of roughness standard R5, aluminum on Zerodur portion. The roughness on the reference surface has been subtracted.

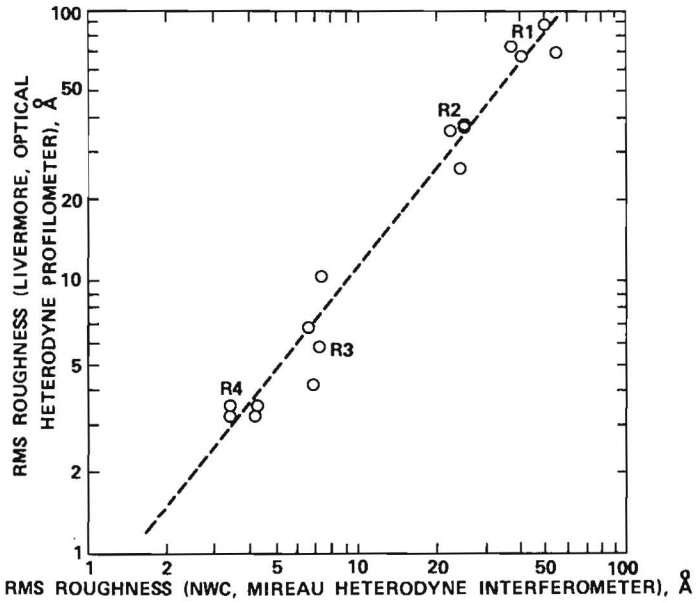


Figure 15. Comparison of the roughnesses for R1 to R4 as measured by the Livermore OHP and the NWC Wyko Mireau HI. Each point indicates one or more measurements on a given portion of the surface (bare, MLD-film coated, aluminum on MLD film, aluminum coated). The dashed line is an average drawn through the points.

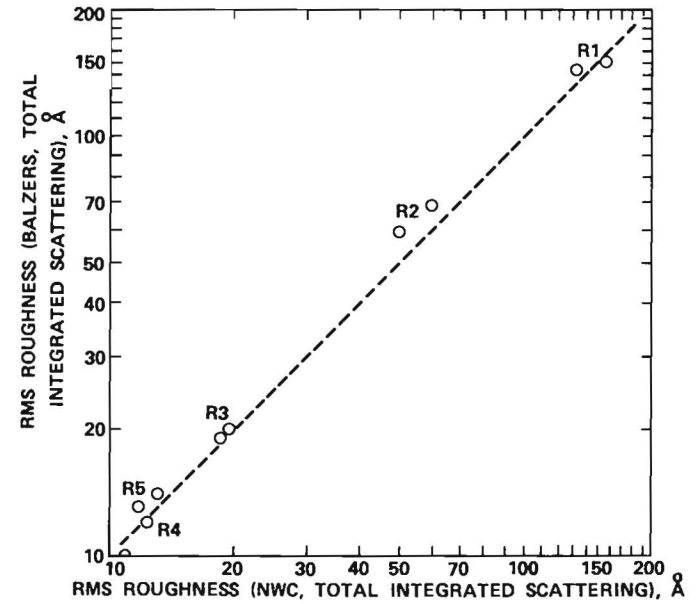


Figure 16. Comparison of the roughnesses derived from TIS measurements for R1 to R5 as measured at Balzers and at NWC. The dashed line is for equal roughnesses for each standard.

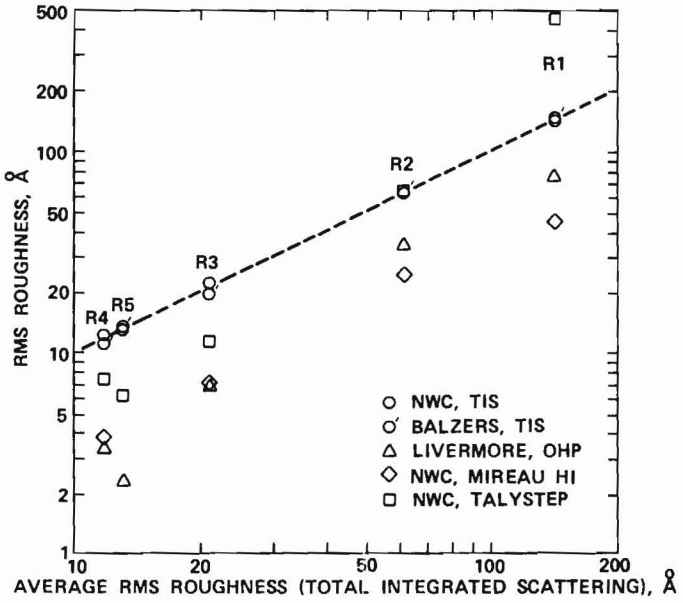


Figure 17. Summary of roughnesses for R1 to R5 measured using all techniques, plotted versus the average of NWC and Balzers TIS-derived roughnesses.

The Effects of Slope Error on the Imaging Quality of a Mirror as the Ratio of Surface Perturbation Depth to Wavelength Approaches Zero*

H. E. Bennett and D. K. Burge

Michelson Laboratory, Physics Division
Naval Weapons Center, China Lake, California 93555

Three parameters are needed to specify the quality of a polished mirror surface: (1) optical figure tolerance, (2) surface microroughness and scratch/dig specification, and (3) slope error. The slope error is a measure of surface ripple, i.e., long-range modulations or zones with wavelengths typically in the centimeter to tens-of-centimeters range. The increase in blur circle diameter and resulting decrease in resolution caused by slope error can normally be computed from geometrical optics, since the surface wavelength is much longer than the wavelength of incident radiation. However, as the depth of the surface perturbation becomes small compared to the optical wavelength (as may occur, for example, in going from the visible to the infrared), geometrical optics no longer applies and the effects of slope error are greatly reduced. A comparison of physical and geometrical optics calculations of the effect of slope error in this limiting case will be given.

Key words: optical testing; slope error; zones.

Introduction

The complete specification of mirror surface quality includes optical figure, slope error, and microroughness. The importance of optical figure in laser mirror applications is well understood. Figure errors cause wave front errors which can drastically reduce on-axis focused intensity, as seen in figure 1. Microroughness causes light to be scattered away from the specular direction. The angle to the specular direction at which light is scattered depends on the ratio of the distance between irregularities to the wavelength of light and is given by the grating equation. The angular dependence of scattered light as a function of wavelength is shown in figure 2. As the separation between irregularities becomes greater, the light is scattered into smaller and smaller angles from the specular direction. At normal incidence, the magnitude of light scattered at all angles is given by the expression $(4\pi\delta/\lambda)^2$, where δ is the rms deviation of the surface irregularities from the mean surface level and λ is the wavelength.

Slope error specifications are the least commonly used or well understood of the surface quality specifications. Slope errors, which commonly result from zones present in the mirror or from diamond turning, are related to light scattered at small angles to the specular direction and are often arrived at on the basis of geometrical optics. In this paper, it will be shown that when the depth of the irregularities is less than a wavelength, estimating the effect of slope error from geometrical optics leads to gross inaccuracies. Slope errors in this case are simply an extension of microirregularity scattering to very large separations between irregularities and are governed by physical, not geometrical, optics. As a result, a considerable relaxation in tolerance occurs, and slope errors which can be tolerated before mirror performance is significantly affected are much larger than would be anticipated from geometrical optics calculations.

Geometrical Optics Theory

Consider a spherical mirror with circular zones concentric with the optic axis. A cross section of this mirror is shown in figure 3. A source at a distance p from the mirror would be focused at a distance q were it not for the zones in the mirror. However, the zones cause the sagittal focus to move to q', a distance Δq from the zone-free focus. The blur circle diameter a at distance q is obtained from similar triangles:

*Work partially supported by Navy Independent Research funds.

$$a = \frac{d}{q}, \quad \Delta q \cong \frac{d}{q} \Delta q \quad , \tag{1}$$

where d is the width of the zone and $\Delta q \ll q$. From the lens equation,

$$\frac{1}{q} = \frac{2}{R} - \frac{1}{p} \quad , \tag{2}$$

where R is the radius of curvature of the mirror. Then

$$\Delta q = \frac{2q^2}{R^2} \Delta R \quad , \tag{3}$$

where ΔR is the change in radius of curvature of the mirror surface, i.e., the radius of curvature of the zone. The depth of the zone is related to its radius of curvature through the sagittal relation

$$h = \frac{d^2}{8R} \quad , \tag{4}$$

where h is the sagittal depth of the mirror. The depth of the zone Δh is then

$$\Delta h = \frac{d^2}{8R^2} \Delta R \quad . \tag{5}$$

Substituting eqs (5) and (3) into (1) gives the angular spread α of the blur circle to be

$$\alpha = \frac{a}{q} = \frac{16\Delta h}{d} \quad . \tag{6}$$

An alternate derivation* can be obtained from figure 4. Consider a single zone. The average slope of this zone is $\Delta h/(d/2)$. The maximum slope is twice the average slope, and the maximum beam deviation $\alpha/2$ from the no-zone conditions is then

$$\frac{\alpha}{2} = \frac{8\Delta h}{d} \quad , \tag{7}$$

which is equivalent to eq (6). Since the beam is deviated both above and below the no-zone direction, the total deviation of the light is α so that the blur circle diameter is αq.

---

*Proposed by Dr. D. L. Decker, Naval Weapons Center, China Lake, California.

It is convenient to relate the beam spread introduced by zones to that of the Airy disk, which is produced by pure diffraction of a perfect optical system. For a circular limiting aperture, the diffraction-limited angular beam spread is $\alpha_A = 1.22\lambda/D$, where D is the diameter of the exit pupil of the optical system. For a single mirror, D is then the mirror diameter.

Consider a 2-cm-diameter mirror having three concentric zones, each one-third wave in depth. From eq (6), the beam spread per unit mirror diameter is then $\alpha/D = 32\lambda/D$, about 26 times the diameter of the Airy disk. Figure 5(b) illustrates this case. The larger circle shows the blur circle diameter; the smaller one shows that from a perfect 2-cm-diameter mirror. The FRINGE optical analysis program, as adapted by Dr. James Wyant, Optical Sciences Center, University of Arizona, includes imaging predictions of geometrical optics and was used to ray trace this mirror and to calculate figure 5(a). The position of rays predicted to fall on the image plane if the pupil is uniformly irradiated with rays is shown by the symbols on figure 5(b). Nearly all of the ray positions predicted by this progam are seen to fall within the $32\lambda/D$ circle. They are more densely concentrated about the axis than about the periphery of that circle, but, plotted as a function of spot radius, the encircled energy rises almost linearly with spot radius as can be seen in figure 5(a).

Physical Optics Theory

The geometrical optics predictions are compared in figure 5 with those calculated from physical optics by taking the discrete Fourier transform of the wave front in the far field to obtain the point spread function (i.e., the blur circle). The program FRINGE, as modified by Wyant, was used for these calculations also. Physical optics predicts that 57% of the energy in this case will fall within the first Airy minimum. The geometrical optics calculation in this case is entirely inaccurate.

To explore this problem further, consider a torus with center at $\rho = 0$ in cyclindrical coordinates and with maximum height h. From the sagittal equation,

$$h = \frac{(a/2)^2}{2R} \quad , \tag{8}$$

where a is the chord of the toroidal segment and R is its radius of curvature. The equation of the torus is then

$$z = \frac{(\rho - c)^2}{2R} \quad , \tag{9}$$

where for the innermost zone, $c = a/2$; for the second zone, $c = 3a/2$; for the third zone, $c = 5a/2$; and so on. The slope of the torus is then

$$\frac{dz}{d\rho} = \frac{(\rho - c)}{R} \quad . \tag{10}$$

To keep the slopes of the torii constant as a decreases, R must decrease in proportion to a. From eq (8), the depth of the toroid must then decrease in proportion to its width to keep the slope constant. Given a fixed diameter, we may then create a series of samples, each with a different number of zones (torii) and with a decrease in their depth in the same proportion. Geometrical optics will predict that all these samples will have the same diameter blur circle, since their slopes are identical. However, from physical optics we would predict that when h, the zone depth, becomes less than the wavelength of light, the blur circle diameter will decrease until ultimately it is indistinguishable from the Airy disk. Samples with one and two zones of this type are shown in figure 6. Calculations were carried out for larger numbers of zones also. The results are shown in figure 7. Even if the zones are a wavelength in depth, the encircled energy is larger than that predicted by geometrical optics. As the zonal depth becomes smaller relative to a wavelength, the encircled energy plot approaches that for a zone-free surface λ/∞. If the depth of the zone is $\lambda/5$, for example, the encircled energy at the second Airy minimum, 2.23, is within 13% of the value 92% for a zone-free surface. Geometrical optics would in this case be in error by a factor greater than 6.

Conclusion

Geometrical optics can be reliably used for slope error calculations, provided the depth of zonal errors is large compared to the wavelength of light at which the mirror is to operate. If the zonal depth is comparable to or smaller than the wavelength, however, serious errors will result from this practice.

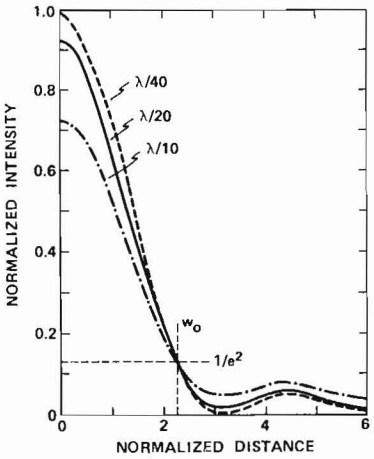


Figure 1. Intensity for various rms wave front aberrations. (After Barakat, R. Opt. Acta 18; 683; 1971.)

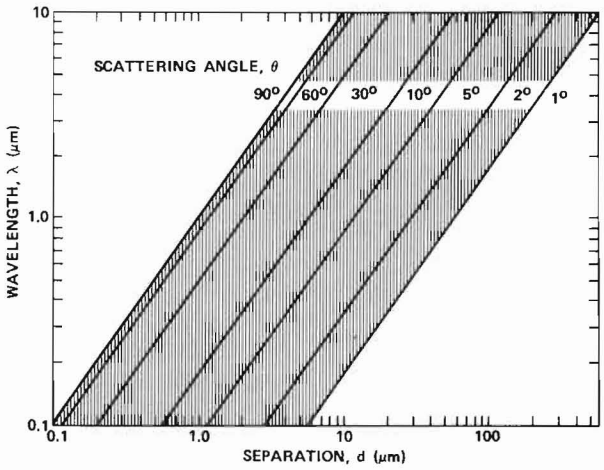


Figure 2. Angular dependence of scattered light as a function of separation of irregularities and of wavelength.

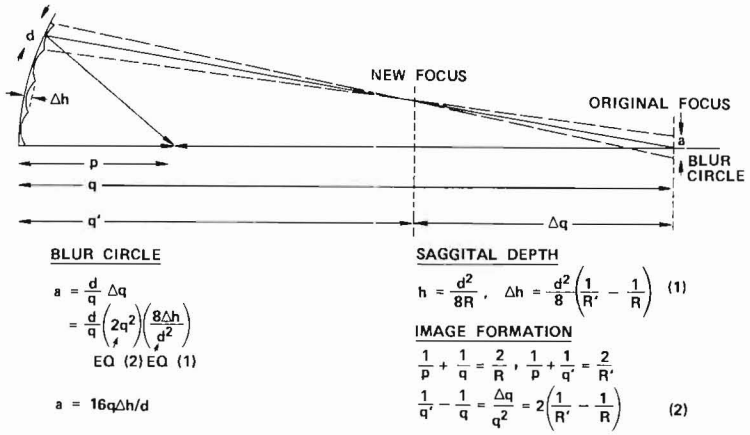
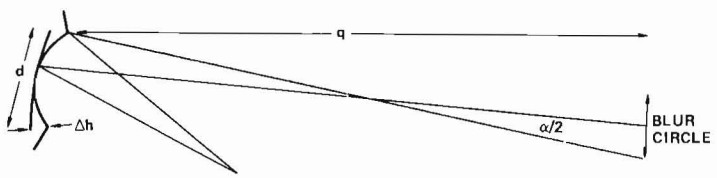


Figure 3. Effect of zones on the focus of a concave mirror.



AVERAGE SLOPE $\frac{\Delta h}{d/2}$

MAX SLOPE = 2 X AVERAGE SLOPE

BEAM DEVIATION $\alpha/2$ = 2 x MAX SLOPE

BLUR CIRCLE DIAMETER = $\frac{16q\Delta h}{d} = \alpha q$

Figure 4. Alternate derivation of effect of zones on the focus of a mirror. (After Decker, D. L., Naval Weapons Center.)

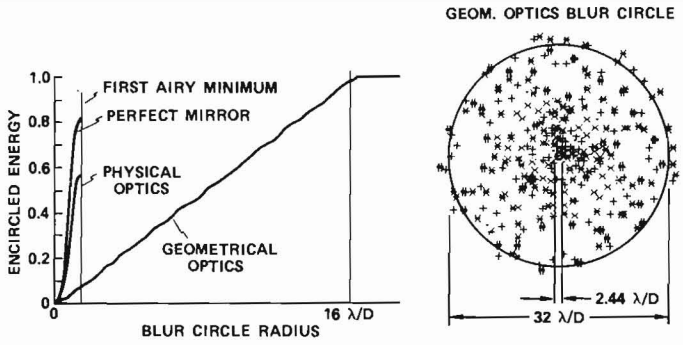


Figure 5. (a) Comparison of encircled energy as a function of blur circle radius predicted by geometrical and physical optics for a mirror with three concentric zones, 1/3 wave deep, 1/3 cm wide, and with a maximum slope of 4 waves/cm. (b) Geometrical optics blur circle calculated by ray tracing compared to size of central Airy spot as given by physical optics. Diffraction calculation shows 57% of energy is actually within first Airy minimum, 1.22 λ/D. If no zones were present, 81% of the energy would be within the first Airy minimum.

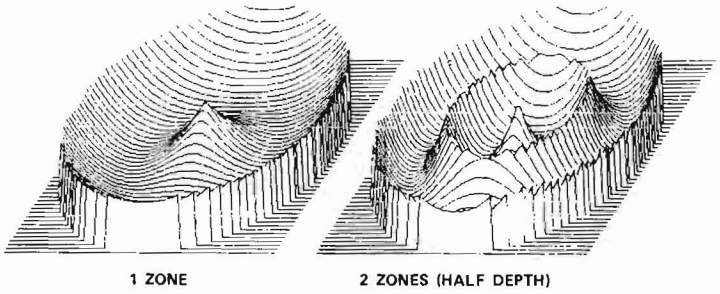


Figure 6. Computer-generated plots of one and two concentric zones as used in the calculations whose results are shown in figure 7. For constant slope error in the two cases, the zones in the 2-zone case are half the depth of the zone in the 1-zone case.

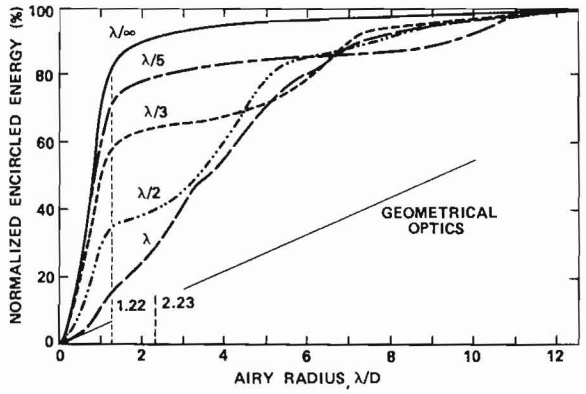


Figure 7. Encircled energy at focus as a function of radius calculated from physical optics for 1, 2, 3, and 5 zones having depths of 1, 1/2, 1/3, and 1/5 wavelength, respectively, and the geometrical optics prediction. The dashed vertical lines indicate the first and second Airy minimum.

Manuscript received 1-17-84/sar

1.06 Micron Laser Damage of Thin Film Optical Coatings - a Round Robin Experiment Involving Various Pulse Lengths and Beam Diameters

K. H. Guenther[a], T. W. Humpherys[b], J. Balmer[c], J. R. Bettis[b], E. Casparis[a], J. Ebert[d], M. Eichner[e], A. H. Guenther[f], E. Kiesel[d], R. Kuehnel[g], D. Milam[h], W. Ryseck[g], S. C. Seitel[i], A. Stewart[f], H. Weber[e], H. P. Weber[c], G. Wirtenson[h] and R. M. Wood[j]

A number of commercially available optical coatings, both antireflective and high reflective, have been tested for their laser induced damage threshold, involving a total of eight (8) different laboratories. The results obtained and the experimental methods used at these laboratories were discussed among the participants in this round robin at a minisymposium held at Balzers, Liechtenstein, December 9-10, 1982. A final report of the round robin and a summary of the conclusions drawn at that symposium are presented.

Key Words: Laser Induced Damage Thresholds; Laser Optics; Optical Coatings; and Standardization of Laser Damage Measurements

This paper is dedicated to Dr. A. Ross, former president of Balzers, on the occasion of his 70th birthday and his retirement.

[a] Quality Assurance Department, Balzers AG, FL-9496 Balzers, Principality of Liechtenstein

[b] European Office of Aerospace Research and Development, 223/231 Old Marylebone Road, London NW1 5TH, England

[c] Institute for Applied Physics, University of Berne, Sidlerstr. 5, CH-3012 Berne, Switzerland

[d] Institute for Quantum Optics, University of Hannover, Welfengarten 1, D-3000 Hannover, West Germany

[e] Physics Department, University of Kaiserslautern, Erwin-Schrödingerstr., D-6750 Kaiserslautern, West Germany

[f] Air Force Weapons Laboratory, United States Air Force, Kirtland AFB, NM 87117, U.S.A.

[g] SI FR Ort EO, Siemens AG, Bereich Funk und Radiosysteme, Hofmannstr. 51, P.O.B. 700074, D-7650 Munich, West Germany

[h] Lawrence Livermore National Laboratory, P.O. Box 5508, L-490, Livermore, CA 94550, U.S.A.

[i] Michelson Laboratory, Naval Weapons Center, China Lake, CA 93555, U.S.A.

[j] Hirst Research Centre, The General Electric Company, Ltd., East Lane, Wembley, Middlesex HA9 7PP, England

1. Introduction

Since the early days of laser physics and applications, thin film coatings have been performance and power density limiting elements in high power and high energy laser systems. Much work has been done in the past two decades in studying the phenomena, processes and causes connected with the laser induced damage of optical materials, surfaces and coatings. Many of the papers dealing with such topics have been collected in the Proceedings[1] of the Symposium on Laser Induced Damage in Optical Materials annually held at Boulder, Colorado. Despite the numerous publications, which mostly cover fundamental interactions, there seems to be a lack of a commonly accepted standard method on how to determine and report laser induced damage threshold (LIDT) values of thin film coatings. This is because of the highly individual approach of each laboratory testing LIDT's, and the specific nature of most of the experiments. Recently, some more comprehensive work has been published with a parametric study of laser induced damage of single layers of various materials used as optical thin films.[2]

For multilayer optical coatings, LIDT data have been obtained and published, particularly with respect to their application in laser fusion systems[3-6] under test conditions specific for that purpose. For commercial applications, however, only a few systematic investigations into the LIDT of coatings[7], production-run optical components[8], and fundamental limitations[9] have been reported for use at short wavelengths. There is still a lack of a standard method or procedure for obtaining reliable LIDT-values for commercial coatings which would be agreeable both to the vendor and the customer. One thing commonly agreed upon is that the LIDT-values depend on the test conditions, which, however, are seldom stated when specifying LIDT's of optical coatings. Usually oversimplified figures are indicated for energy or power density, and frequently the pulse duration (pulse length) is inadequately presented or completely missing. The purpose of the round robin experiment reported in this paper was to evaluate the experimental approaches as used at the various laboratories for their compatibility. Its objective was and still is to contribute to a desirable standardization in LIDT testing which, as a result of this test, seems to be possible.

2. Experimental Procedures

2.1. Layout of the Round Robin

Eight different laboratories were involved in the round robin. Some characteristic data of their experimental set-ups are summarized in table 1. The only one parameter common to all facilities was the laser wavelength which was 1064 nm for all tests. Four different multilayer coating designs were used, the samples being coated in three different batches each at the Balzers AG in Liechtenstein. Each sample was identified by a three digit code number. The first two digits indicate the type of coating, and the last identifies the laboratory conducting the laser damage investigations. The coatings employed in the test are listed in table 2, together with the design and the materials used, and the spectral specifications. In figure 1, typical reflectance curves of two of the AR-coatings as used in the experiment are shown. The two HR-coating systems employed were maximum reflectors designed for 1064 nm at 0° angle of incidence.

Table 1.

Summary of experimental conditions used at various laser laboratories

Laboratory	K'lautern	Hannover	LLNL	AFWL	Berne	Siemens	GEC	NWC
Sample set No.	**..0,..1**	**..2,..3**	**..4**	**..5**	**..6**	**..7**	**..8**	**..9**
Cleaning	blow dry air	blow dry N_2	Ethanol wipe	Ethanol wipe	blow dry N_2	blow dry N_2	blow dry N_2	blow dry N_2
Sample location	in F	in F	near F	in F	50 before F	in F	in F	in F
Focal length [mm]	150	50	4000 – 6000	1200	1000	50	100 and 300	165
Mode of operation $TEM_{m,n}$	0.0	∞,∞	0.0	0.0	0.0	multi	0.0	0.0
Polarization	circ.	lin.	lin.	lin.	lin.	lin.	lin.	lin.
Spot size d[μm], FW at $1/e^2$ intensity	470	210	4000	360	1100	340	150	40
Pulse length τ [ns], FWHM	10	12	1	5.9	$35 \cdot 10^{-3}$	20	15 and 25	13
Number of pulses per sample	20	20 – 40	⩾ 4	100	10	⩾ 10.000	500	30
Number of pulses per site	1	1	1	1	1	⩾ 10.000	1	1
Site selection	presel.	presel.	random	random circ.	presel.	random	random + presel.	random
Local separation [mm]	1 – 3	~2	5	~1	3	3 – 4	0.2	1
Assessement of damage	He-Ne-scattering	He-Ne-scattering, Nomarski micr.	visual micr. induced light	Nomarski micr.	He-Ne-scattering visual obser.	visual micr.	visual micr.	He-Ne-scattering
References	10	11, 12	13, 14	2, 9	15	16	17	18

Table 2.

Characterization of LIDT-Samples

Sample No.	Type of Coating (Balzers Prod. Name)	Design[x] and Layer Materials[xx]	Number of Layers	Spectral Specification
04. 05. 06	V-type AR coating (Laser-Transmax)	$A/k_1 L_1/k_2 H/2L_2/S$ $L_1 = MgF_2$ $L_2 = SiO_2$ H = Roma	3	$R \leqslant 0.1\%$ at 1.06 μm
10. 11. 12.	Laser-Mirror ("RS")	$A/2L/(HL)^{12}/H/S$ $L = SiO_2$ $H = Ta_2O_5$	26	$R \geqslant 99.7\%$ at 1.06 μm
16. 17. 18.	Laser-Mirror ("TS")	$A/2L/(HL)^{11}/H/S$ $L = SiO_2$ $H = TiO_2$	24	$R \geqslant 99.7\%$ at 1.06 μm
22. 23. 24.	Broad-Band AR-Coating VIS + AR (1.06 μm) (Duolin)	$A/LMH/^{xxx}S$ $L = MgF_2$ $M = Al_2O_3$ H = Roma	5	$R \leqslant 1.0\%$ 475 - 625 nm and 1060 nm

x) A = Ambient (Air, n = 1.0)
S = Substrate (BK7, n = 1.52)
L = Low-index, H = High-index, M = Medium-index — Layers of quarter-wave optical thickness (QWOT) at the design-wavelength (0° incidence)

xx) Roma = Balzers-proprietory coating material (oxide)

xxx) Proprietory Design

2.2. Sample Characterization

The substrates used were optical flats of 25.4 mm in diameter and 6 mm thick, made of Schott BK 7. The surfaces to be coated were superpolished in-house at Balzers AG. The surface roughness of the particular samples was not actually measured, however, from comparative roughness measurements of other substrates[19,20] which were prepared in the same manner, an rms roughness of about

6 Å was estimated. The surfaces to be coated were engraved with the sample number and ultrasonically cleaned before coating. The coating processes used with these samples were the same by intention as used with standard commercial products. After coating, the samples were packed into plastic containers and shipped to the laboratories without any preselection.

2.3. Experimental Set-Ups

Typical LIDT experimental set-ups include Nd-glass laser sources, beam handling and conditioning optics, beam diagnostics, and sample manipulating stages with assorted environmental conditioning or characterization features. Optical components such as mirrors, lenses, polarizers, attenuators, or apertures are used to condition and focus the beam. Pulse energies and beam temporal and spatial profiles are usually measured from a split-off portion of the beam, with the spatial data taken at an equivalent target plane. Samples are mounted on microprecision control stages for accurate adjustment and realignment. Two typical experimental arrangements are shown in figure 2. In situ optical microscopy or scattering measurements are sometimes part of the test chamber as portrayed in figures 2b and 3. The reader is kindly invited to refer to the cited publications annotated in table 1 for more experimental details.

2.4. Evaluation of Laser Induced Damage to Optical Coatings

One of the uncertain factors in determining laser damage thresholds is the variety of possibilities of how to define damage. This can range from minute changes in the morphology or the optical properties of the thin films, which are only detectable by Nomarski microscopy or auxiliary HeNe light scattering measurements respectively, to catastrophic damage creating plasma (flash), evaporation of coating material (erosion), and/or complete flaking (delamination) of the coatings, as presented in figure 4. In this experiment, no detection method was prescribed so that every participating team was free to use their usual method, which are also indicated in table 1. Auxiliary HeNe scattering accomplished similar to that at the Institute of Quantum Optics at Hannover[12], or as shown in figure 3, appears to be the most sensitive, as is further evident from figure 4.

Another problem connected with the general acceptance of laser damage test results is how the data is to be calculated and reported. Again, there are various possibilities: for instance, using Jcm^{-2}, $GWmm^{-2}$, or dB. During the symposium, the participants agreed that it was useful for comparison purposes to adopt an AFWL definition for a characteristic threshold energy, E_{th}, such that

$$\frac{E_{th}}{A} = \frac{1}{2} \cdot \frac{E_{max(ND)} + E_{min(D)}}{A}$$

where $E_{max(ND)}$ is the highest nondamaging energy and $E_{min(D)}$ is the minimum damage level in the thin film coating and A is the area of the incident beam on the coating taken at the $1/e^2$ points of the incident intensity which are easily determined from the 1/e points in amplitude. $E_{min(D)}$

is the critical value from the coating users' point of view since this "onset" of damage represents the level at which a flood-loaded sample will fail. $E_{max(ND)}$ is a useful number to the coating manufacturer and is more representative of the zero defect limit.

A corresponding spread is then defined as

$$S = \frac{E_{max(ND)} - E_{min(D)}}{E_{th}}$$

which is primarily defect dominated and is determined from a series of shots on the same coating sample. Examples of data reported in such a fashion are shown in figure 5. The vendor's goal is to produce coatings with spread values approaching zero. For the user, it is useful to know the minimum intensity at which damage occurs, which is

$$I_{min(D)} = E_{min(D)}/A/\tau$$

where τ is the temporal pulse duration measured to the half-power points (FWHM).

It is to be noted that the above definitions were employed for rapid intercomparison of results between laboratories and a number of limitations are therefore imposed. Among these are:

a. Beam spot size was taken at the $1/e^2$ intensity points. In most laser damage experiments, the beams are approximately Gaussian in profile, so the integrated energy distribution on the SAMPLE is mainly Gaussian. With deposition of total energy E into a Gaussian fluence distribution, the peak fluence is thereby given by

$$F_p = \frac{2E}{A}$$

which, for a pure Gaussian profile, is a factor of two larger than what is used herein and comes directly from using the 1/e radius as opposed to the decision to use the $1/e^2$ radius for comparisons in this study.

b. Variations between laboratories of the spatial distribution in the target plane were neglected for simplicity.

c. Computation of threshold fluence E_{th}/A uses only the two data points $E_{min(D)}$ and $E_{max(ND)}$ and does not include any statistical distribution of events across the damage/no-damage overlap region.

d. Variations in temporal pulse shapes between laboratories were assumed negligible and FWHM values were employed for intensity calculations.

Other types of data presentation typically used are shown in figures 6a and b.

3. Results

3.1. Raw Data

The results of the individual measurements abtained at the different facilities were converted at the symposium on the aforementioned basis into E_{min} and E_{max}. These data are collected in table 3 for the different types of coatings heading the columns, and the different facilities heading the rows in the order of the pulse lengths used. (Three individual samples per testing facility)

Table 3. LIDT Round Robin Damage Threshold Values

Coatings		RS		TS		LT		DN	
Facility		E_{min}	E_{max}	E_{min}	E_{max}	E_{min}	E_{max}	E_{min}	E_{max}
Berne		0.40	0.30	0.40	0.40	1.20	0.61	0.20	0.30
		0.40	0.30	0.40	0.30	0.41	0.19	0.30	0.30
		0.40	0.30	0.30	0.40	0.40	0.53	0.30	0.20
	Avg	0.40	0.30	0.37	0.37	0.71	0.34	0.27	0.27
LLNL		9.5	7.0	11.2	11.2	5.7	3.4	5.1	3.4
		11.2	9.5	11.2	9.5	5.7	4.7	5.1	3.4
		13.1	10.7	10.4	8.2	1.8	1.4	3.5	2.3
	Ave	11.3	9.1	10.9	9.6	4.4	3.2	4.6	3.0
AFWL		28.5	53.6	12.0	37.0	1.5	4.3	3.4	5.8
	Avg	28.5	53.6	12.0	37.0	1.5	4.3	3.4	5.8
K'lautern		71.5	82.0	81.4	90.8	15.4	19.8	19.8	23.7
		82.5	93.0	63.3	79.2	21.5	33.5	19.8	22.0
		88.0	96.3	69.9	89.6	24.2	34.7	14.3	18.2
	Avg	80.7	90.4	71.5	86.5	20.4	29.3	18.0	21.3
Hannover		53.5	65.3	36.4	42.4	8.2	10.0	4.4	7.3
		53.2	67.8	38.4	42.7	6.2	9.5	3.8	6.4
		58.0	62.0	29.4	33.6	9.5	10.6	5.8	9.4
	Avg	54.9	65.0	34.7	39.6	8.6	10.0	4.7	7.7
NWC		91.7	255.1	117.2	146.0	56.7	131.9	44.5	125.0
		153.3	253.1	112.2	161.3	23.5	52.4	50.6	153.6
		178.8	257.8	116.4	89.9	15.2	163.7	82.3	151.6
	Avg	141.3	255.3	115.3	132.4	31.8	116.0	59.1	143.4
GEC[a]		14.4	86.2	10.7	86.3	17.1	90.0	9.8	53.8
		15.1	86.2	11.7	86.3	13.8	90.0	14.3	86.2
		11.1	86.2	11.1	86.3	13.8	90.0	11.4	53.8
	Avg	13.5	86.2	11.2	86.3	15.1	90.0	11.8	64.6
Siemens		2.6	8.0	16.4	28.5	0.8	3.0	10.6	18.0
		2.6	7.8	26.6	37.5	1.0	2.6	21.6	37.5
		2.8	5.2	21.1	37.5	10.0	11.0	13.0	37.5
	Avg	2.7	7.0	21.4	34.5	3.9	5.5	15.1	31.0

[a] E_{min} data for 15 nsec pulses and E_{max} data for 25 nsec pulses

3.2. Graphic Representation

In order to obtain a better understanding of the results than is possible from the multitude of figures contained in the tables, and since there are two independent variables, pulse length τ and beam diameter d, which are thought to influence the dependent variables such as the laser damage threshold E_{th}, 3-D representations are utilized. Figures 7a-d show $E(\tau,d)$ for two AR and HR coatings. Damage thresholds are plotted versus both beam diameter and pulse width. Parallel projections of the threshold values on either axis allow one to view the pulse width or beam diameter dependence independently of the second parameter, but do not take its influence into account at all. A distinction has also been made between E_{min} and E_{max} which manifests itself as a color contrast.

3.3. Visual Assessment of Damage Sites

Having all the tested samples available for visual and microscopic inspection at the symposium, the participants agreed upon the characterization of the damage sites as given in table 4.

Table 4. Assessment of Laser Damage Sites for Various Test Conditions

Facility	τ(ns)	d(μm)	Form of Damage
Berne	$35 \cdot 10^{-3}$	1100	High density pits
LLNL	1.0	4000	Random pits
AFWL	5.9	360	Random pits
K'lautern	10	470	Flakes
Hannover	12	210	Flakes
NWC	13	40	Flakes, pits
GEC	15 or 25	150	Flakes
Siemens	20	340	Flakes

3.4. Micrographs of Damage

Two optical micrographs (Nomarski) each per facility and coating are shown in figures 8a-d for the Laser-Transmax, Duolin, and the two laser mirror coatings. The micrographs were taken from sites which show just noticeably visible damage, which means the damage threshold has beem moderately exceeded, and from heavily damaged spots.

4. Discussion

The results (raw data) of the round robin experiment were extensively discussed among the participants of the minisymposium in small working groups. The outcomes of these discussions are summarized in the following paragraphs.

4.1. Influence of Pulse Duration

If the laser damage thresholds, E_{min} and E_{max}, are plotted vs. the pulse duration τ on a double log scale, one can obtain straight lines (fig. 9a-d) for the various coatings, which yield the exponents b for the relation:

$$E_{th} = a_1 \cdot \tau^{b_1} \quad (1)$$

The coefficients a_1 and b_1 are listed in table 5 as A and B, respectively, together with the correlation coefficients R^2, the student's factor S and the statistical factor F. The B's are near the value of 0.5 for the expected square root dependency. However, thresholds measured at near 10 ns differed in some cases by more than a factor of 10, which leaves much indecision regarding the safe fluence at which these coatings could be used.

Table 5. Regression Analysis for $\log E = A + B \cdot \log \tau$

Coating	RS		TS		LT		DN	
Parameter	E_{min}	E_{max}	E_{min}	E_{max}	E_{min}	E_{max}	E_{min}	E_{max}
A	.785	.852	.746	.866	.455	.491	.414	.511
B	.634	.824	,708	,824	,417	.745	.639	.807
R^2	.497	.708	.752	.912	.373	.686	.733	.800
S	.582	.494	.370	.238	.492	.470	.353	.376
F	21.702	53.236	66.807	229.379	13.103	48.042	60.226	87.885

4.2. Influence of Beam Diameter

If the laser damage thresholds E_{min} and E_{max} are plotted vs. the beam diameter d on a double log scale, one can again obtain straight lines (fig. 10a-d), which fit the relation:

$$E_{th} = a_2 \cdot d^{-b_2} \quad (2)$$

The negative exponent indicates a trend that smaller beam diameters yield higher damage threshold values. This is because of the reduced probability of hitting a damage sensitive thin film defect. From some of the micrographs shown in figure 8, it can be clearly seen that laser induced damage is

dominated by coating and substrate surface defects. The parameters of the regression analysis are listed in table 6, again with the statistical parameters R^2, S, and F.

Table 6. Regression Analysis for log E = A + B · log d

Coating	RS		TS		LT		DN	
Facility	E_{min}	E_{max}	E_{min}	E_{max}	E_{min}	E_{max}	E_{min}	E_{max}
A	3.083	4.089	3.001	3.700	2.187	3.683	2.655	3.826
B	-0.743	-1.054	-0.708	-0.896	-0.575	-1.056	-0.719	-1.089
R^2	.275	.445	.302	.415	.285	.530	.373	.560
S	.698	.680	.622	.615	.526	.575	.538	.558
F	8.329	17.664	9.531	15.613	8.787	24.847	13.114	28.030

Results have recently been presented which deal with the problem of determining the minimum intensity sufficient to initiate damage at coating defects. Both S. Foltyn[21] and J. Porteus[22] have demonstrated that this onset intensity may be determined independently of spot size (although the experiment is less tedious with larger spots) and yield valuable information about the defect distribution itself. Figure 11 portrays such a method utilized by NWC in which an extrapolation method is used to determine the maximum damage threshold for which no damage will occur on a particular specimen. E_{th} or $I_{min(D)}$ represent the onset intensity only in the case that the spot size is larger than the mean defect separation which, according to another regression analysis and defect distribution evaluation performed[23] is the case of the coatings tested and is typical of most optical coatings. As coatings inprove, small spot measurements may not be practical in critical evaluations for large spot applications.

4.3. Determination of the Electric Field

Assuming that absorption of laser light by a plasma can be described by a Beer's law equation, Bettis et al[24] determined that

$$\nabla \cdot S^2 = \text{const} \qquad (3)$$

where τ is the pulse duration (FWHM) and S the Pointing Vector of the incident energy. Also,

$$\tau^{\frac{1}{2}} \cdot S = \text{const} \tag{4}$$

which means that

$$\tau^{\frac{1}{2}} \cdot \frac{E_{th}}{\tau} = \frac{E_{th}}{\tau^{\frac{1}{2}}} = \text{const} \tag{5}$$

If one assumes that it is the electrical field, E, which determines damage, then

$$\sqrt{E_{th}/\tau^{\frac{1}{2}}} = \text{const} \tag{6}$$

In table 7, the values calculated according to eq (6) from the E_{min} data are listed for four different coatings. The constancy is maintained to well within one order of magnitude.

Table 7. Comparison of LIDT Fields $(E_{Min}/\tau^{\frac{1}{2}})^{\frac{1}{2}}$

Pulse (nsec) / Coating	.035	1.0	5.9	10.0	12.0	13.0	15.0	20.0	Avg.
RS	1.46	3.36	3.43	5.05	3.98	6.26	1.87	0.78	3.27
TS	1.41	3.30	2.22	4.76	3.16	5.65	1.70	2.19	3.05
LT	1.95	2.10	0.79	2.54	1.58	2.97	1.97	0.93	1.85
DN	1.20	2.14	1.18	2.39	1.16	4.05	1.75	1.84	1.96

4.4. Spread

Spread as a function of pulse duration can exhibit a rather interesting behavior. For example, the IAP at the University of Berne and LLNL obtained negative spreads. This means that no overlap in energy densities occurs between the non-damage and the damage events.

The spread as a function of beam diameter shows a reverse behavior, i.e., it decreases as the beam diameter increases. This result is quite possible, since the probability of hitting a coating defect increases with larger beam diameters, which means that the LIDT's observed show less scatter in their values. However, it is not possible to fit the measured values with an analytic function with sufficient confidence.

5. Conclusions

From the manifold data, only the most interesting and promising relations could be evaluated to any extent. Other interrelations and test conditions which might be of interest, such as the reproducibility from coating batch to coating batch, the influence of aging, cleaning, and other test conditions which were different for the various laboratories were not investigated in full detail and are still to be elucidated from the vast amount of data.

However, the following conclusions which were tentatively drawn at the symposium can be further substantiated by the data evaluations presented in this paper:

5.1. Pulse Length

The pulse length (time) dependency, which was expected to be $\tau^{\frac{1}{2}}$, or at least τ^n with $n \simeq \frac{1}{2}$, is about in this range with n = 0.72 - 0.77 for the two HR and the multilayer AR coatings, and with n = 0.59 for the V-type AR coating. These values were obtained from a double log fit of the average damage threshold energy density E_{th} vs. τ with sufficiently high correlation coefficients of 0.62 to 0.88. A presentation of the regression analysis for this data is presented in Reference 23. The fact that there is less spread for shorter pulses means that damage is more deterministic rather than probabilistic, as is the case for longer pulses.

5.2. Spot Size

The spot size dependency was assumed to be proportional to d^{-m} with m somewhere in the range from 1 to 2. Indeed, linear regression analysis of both models yield about the same correlation coefficients and hence have the same adequacy. From the double log fit of E_{th} and d, we get regression coefficients m = 1.36 - 1.58, with slightly poorer correlation coefficients. These results mean that one cannot decide from the statistical point of view which exponent is preferred.

5.3. Minimum Threshold

The minimum detectable threshold is about the same for the same types of coatings (AR and HR) but clearly different between the different types. HR coatings are consistantly better than AR coatings which suffer from substrate surface defects even when superpolished and $\lambda/2$ barrier layers are employed.

5.4. N on 1

N on 1 experiments yield lower damage thresholds as compared to 1 on 1 experiments, depending on the level of conditioning. For the one N on 1 experiment included in this round robin, we observed roughly an order of magnitude lower minimum damage threshold intensities as compared with 1 on 1 experiments of the same pulse length.

5.5. Laser Modes

The influence of the mode of operation of the laser can be estimated from the results of the two facilities using TEM_{∞} as compared to those using TEM_{oo}. As can be expected, the damage intensities, $I(GW/cm^2)$, for the multimode operation are considerably lower than the single mode of comparable pulse duration. The latter yields higher damage threshold intensities, probably due to lower peak fields.

5.6. Electric Fields

The electric field, calculated as a value proportional to $\sqrt{E_i \cdot \tau^{\frac{1}{2}}}$, shows a remarkable agreement with the expected constancy. If one excludes the extreme values, the means for the different coatings are fairly close together, and the standard deviations are quite reasonable. Excluding the extremes might well be justified by the special test conditions at which they occur: the minima are either related to the picosecond experiment or to the N on 1 experiment. Both are likely to involve different interaction physics. The same is probably true for the experiment employing the smallest beam diameter, for which the maxima occur exclusively.

In conclusion, we can say that despite the extremely different testing conditions of the various experiments, it is possible to deduce some common relations and parameters. However, for the purpose of comparing LIDT data obtained at different facilities, it is highly desirable to have standardized test conditions. The majority of participants at the Leichtenstein minisymposium agreed on those proposed in table 8 as a first attempt to standardize LIDT experiments and reporting of the data.

Dr. A. P. Schwarzenbach of the Institute of Applied Physics, University of Berne and Mr. Roland Menningen of Balzers AG were of great help in the evaluation of the results. The further assistance of Mr. Menningen in preparing the 3-D graphs is greatly appreciated. The testing program and the Minisymposium were sponsored by the Thin Film Department of Balzers, and in part by the European Office of Aerospace Research and Development, and the United States Army Research, Development and Standardization Group under Contract Number DAJA45-83-M0043.

Table 8. Considerations for Standardization of LIDT - Testing of Optical Coatings

* Sample preparation and preconditioning
  - Cleaning: dry (oil-free) air or nitrogen blow to remove loosely residing particles, ethanol, methanol or isopropanol wipe (specify) to remove fingerprints and grease
  - Storage: use desiccator or dry air oven (at 100°C) for a minimum of 24 hours prior to testing
* Testing geometry:
  - Sample location: in focus of a convergent beam, focal length of focusing lens $L \geq 100$mm (if deviating, specify)
  - Angle of incidence: at coating design angle (if deviating, specify)
  - Separation of the testing sites on the sample surface: distance D between site centers: $D \geq 5xd$
  - Array of testing sites on the sample surface: regular (either a matrix, concentric circles or a spiral), in order to enable identification (no preselection)
* Laser pulse:
  - Mode of operation: TEM_{oo}
  - Polarization: linear, for oblique incidence both s and p
  - Spatial intensity distribution: Gaussian, or describe precisely when deviating
  - Spot diameter at the coating surface (or equivalent distance): full width (FW) at I_o/e^2, specify precisely when deviating
  - Pulse shape (time): Gaussian, or describe precisely when deviating
  - Pulse length (duration): full width at half maximum intensity (FWHM)
  - Number of pulses:
    - per site: preferably 1-on-1, if N-on-1, specify N and repetition frequency (rate)
    - per sample: depends on spot size d, $dxN_{sample} \geq 10000$ (d in μm)
  - Spot size: $d(1/e^2) \geq 300\mu m$ (at least larger than mean defect separation)
* Determination of LIDT
  - Definition of damage: set threshold for malfunction of the coating for the intended use (specify)
  - Detection of a damage event: specify use of
    - magnifier (power)
    - optical microscope (magnification)
    - auxiliary HeNe-laser light scattering (preferred)
  - Quantification of LIDT: utilize graphical presentation of damage probability distribution[22] or survival curve[21]. As a minimum, however, $E_{min(D)}[Jcm^{-2}]$ and/or $I_{min(D)}[GWcm^{-2}]$ should be specified.
* Documentation
  - Test conditions: document everything of the aforementioned items
  - Sample identification: mark appropriately in such a way that it is possible to relocate any site
  - Damage sites: it is useful to take micrographs at least of the minimum damage sites (just damaged)
  - Variations: note any deviations from the suggested procedures.

6. References

[1] The following Proceedings of the Boulder Laser Damage Symposium have been published:

A. J. Glass and A. H. Guenther, Eds, "Damage in Laser Glass", ASTM Spec. Tech. Publ. 469 ASTM Philadelphia, (1969).

A. J. Glass and A. H. Guenther, Eds, "Damage in Laser Materials", Natl. Bur. Stand. U.S. Spec Publ. 341 (1970).

A. J. Glass and A. H. Guenther, Eds, "Damage in Laser Materials: 1971", Natl. Bur. Stand. U.S. Spec. Publ. 356 (1971).

A. J. Glass and A. H. Guenther, Eds, "Laser Induced Damage of Optical Materials: 1972" Natl. Bur. Stand. U.S. Spec. Publ. 372 (1972).

A. J. Glass and A. H. Guenther, Eds, "Laser Induced Damage in Optical Materials: 1973" Natl. Bur. Stand. U.S. Spec. Publ. 387 (1973).

A. J. Glass and A. H. Guenther, Eds, "Laser Induced Damage in Optical Materials: 1974" Natl. Bur. Stand. U.S. Spec. Publ. 414 (1974).

A. J. Glass and A. H. Guenther, Eds, "Laser Induced Damage in Optical Materials: 1975" Natl. Bur. Stand. U.S. Spec. Publ. 435 (1975).

A. J. Glass and A. H. Guenther, Eds, "Laser Induced Damage in Optical Materials: 1976" Natl. Bur. Stand. U.S. Spec. Publ. 462 (1976).

A. J. Glass and A. H. Guenther, Eds, "Laser Induced Damage in Optical Materials: 1977" Natl. Bur. Stand. U.S. Spec. Publ. 509 (1977).

A. J. Glass and A. H. Guenther, Eds, "Laser Induced Damage in Optical Materials: 1978" Natl. Bur. Stand. U.S. Spec. Publ. 541 (1978).

H. E. Bennett, A. J. Glass, A. H. Guenther and B. E. Newmann, Eds, "Laser Induced Damage in Optical Materials: 1979" Natl. Bur. Stand. U.S. Spec. Publ. 568 (1980).

H. E. Bennett, A. J. Glass, A. H. Guenther and B. E. Newmann, Eds, "Laser Induced Damage in Optical Materials: 1980" Natl. Bur. Stand. U.S. Spec. Publ. 620 (1981).

H. E. Bennett, A. J. Glass, A. H. Guenther and B. E. Newmann, Eds, "Laser Induced Damage in Optical Materials: 1981" Natl. Bur. Stand. U.S. Spec. Publ. 638 (1983).

H. E. Bennett, A. J. Glass, A. H. Guenther and B. E. Newmann, Eds, "Laser Induced Damage in Optical Materials: 1982" Natl. Bur. Stand. U.S. Spec. Publ. 669 (1983).

Comprehensive review papers about these Symposia and their Proceedings have also been published:

A. J. Glass and A. H. Guenther, Appl. Opt., Vol. 12, p. 637, 1973; Vol. 13, p. 74, 1974; Vol. 14, p. 698, 1975; Vol. 15, p. 1510, 1976; Vol. 16, p. 1214, 1977; Vol. 17, p. 2386, 1978; Vol. 18, p. 2112, 1979.

H. Bennett, A. J. Glass, A. H. Guenther, and B. E. Newmann, Appl. Opt., Vol. 19, p. 2375, 1980; Vol. 20, p. 3003, 1981; Vol. 22, p. 3276, 1983.

[2] T. W. Walker, A. H. Guenther and P. Nielsen, "Pulsed Laser-Induced Damage to Thin-Film Optical Coatings - Part I: Experimental, Part II: Theory", IEEE J. Quant. Electron., Vol. QE-17, p. 2041, 1981.

[3] W. H. Lowdermilk, D. Milam and F. Rainer, "Optical Coatings for Laser Fusion Applications", Thin Solid Films, Vol. 73, p. 155, 1980.

[4] C. K. Carniglia, "Oxide Coatings for One Micrometer Laser Fusion Systems", Thin Solid Films, Vol. 77, p. 225, 1981.

[5] W. H. Lowdermilk, "Coatings for Laser Fusion" Optical Thin Films, Proc. of SPIE 325, p. 2, 1982.

[6] D. Milam, W. H. Lowdermilk, F. Rainer, J. E. Swain, C. K. Carniglia and T. Tuttle Hart, "Influence of Deposition Parameters on Laser-damage Threshold of Silica-tantala AR Coatings", Appl. Opt., Vol. 21, p. 3689, 1982.

[7] F. Rainer and T. F. Deaton, "Laser Damage Thresholds at Short Wavelengths", Appl. Opt., Vol. 21, p. 1722, 1982.

[8] T. F. Deaton, F. Rainer, D. Milam and W. L. Smith, "Survey of Damage Thresholds at 532 nm for Production-run Optical Components", Laser Induced Damage in Optical Materials: 1980, H. E. Bennett et el, Eds., NBS Spec. Publ. 620, p. 297, 1981.

[9] A. Stewart and A. H. Guenther, Laser Induced Damage in Optical Materials: 1982, H. E. Bennett et al, Eds, NBS Spec. Publ., to be published.

[10] M. Eichner and H. Weber, "Test Report of Laser Induced Damage", Manuscript, Dec 1982, to be published in Appl. Opt.

[11] H. Küster and J. Ebert, "Pyroelectric Measurement of Absorption in Oxide Layers and Correlation to Damage Threshold", Laser Induced Damage in Optical Materials: 1979, H. E. Bennett et al, Eds, NBS Spec. Publ. 568, p. 269, 1979.

[12] J. Ebert and E. Kiesel, "Measurement of Laser Induced Damage and Layer Temperature with Unstable Resonator Type Lasers", Manuscript, Dec 1982, to be published in Appl. Opt.

[13] D. Milam, J. B. Willis, F. Rainer, and G. R. Wirtenson, "Determination of Laser Damage Thresholds by Comparison with an Absolute Laser Damage Standard", Appl. Phys. Lett., Vol. 38, p. 402, 1981.

[14] D. Milam, "Measurement and Identification of Laser-Damage Thresholds in Thin Films", in Optical Coatings II, Proc. SPIE, Vol. 140, p. 52, 1978.

[15] J. E. Balmer, A. P. Schwarzenbach, and H. P. Weber, "Laser Damage Test on Balzers Thin Film Coatings", Manuscript, March 1983, to be published in Appl. Opt.

[16] N. Kühnel and W. Rysek, "Test Report of Laser Induced Damge of Balzers Thin Film Coatings", to be published in Appl. Opt.

[17] R. M. Wood, R. T. Taylor and R. L. Rouse, "Laser Damage in Optical-Materials at 1.06 microns", Optics and Laser Technology, p. 105, June 1975.

[18] S. C. Seitel, J. B. Franck, C. D. Marrs, and G. D. Williams, "Selective and Uniform Laser-induced Failure of Antireflection-coated $LiNbO_3$ Surfaces", IEEE J. Quantum Electron, Vol. QE-19, p. 475, 1983.

[19] K. H. Guenther and P. G. Wierer, "Surface Roughness Assessment of Ultrasmooth Laser Mirrors and Substrates", in Thin Film Technology, Proc. SPIE, Vol. 402, 1983 (in press).

[20] K. H. Guenther, P. G. Wierer, and J. M. Bennett, "Surface Roughness Assessment of Laser Mirrors and Substrates", to be submitted to Appl. Opt., 1984.

[21] S. R. Foltyn, "Spot-Size Effects in Laser Damage Testing", Fourteenth Annual Symposium on Optical Materials for High Power Lasers, Boulder, CO, Nov 1982.

[22] J. O. Porteus, "Determination of the Onset of Defect-Driven Pulsed Laser Damage in 2.7 Micron Optical Coatings", Fourteenth Annual Symposium on Optical Materials for High Power Lasers, Boulder, CO, Nov 1982.

[23] K. H. Guenther and R. Menningen, "1.06 μm Laser Damage of Optical Coatings: Regression Analysis of Round Robin Test Results", to be published in Appl. Opt.

[24] J. R. Bettis, R. A. House, and A. H. Guenther, "Spot Size and Pulse Duration Dependence of Laser Induced Damage", "Laser Induced Damage in Optical Materials: 1976, A. J. Glass and A. H. Guenther, Eds, NBS Spec. Publ. 462, p. 338, 1976.

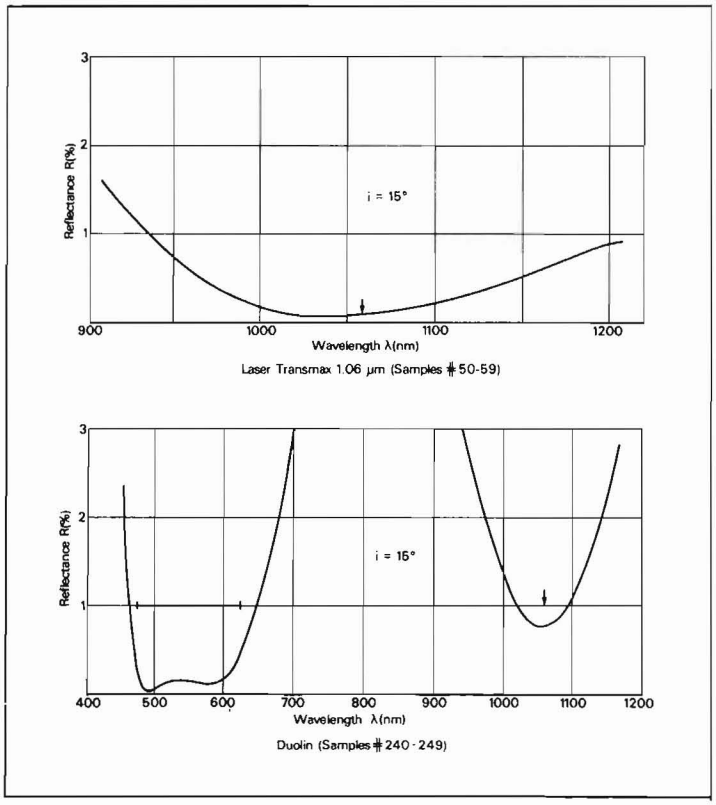


Figure 1. Typical AR-coatings used in the LIDT round robin experiment.

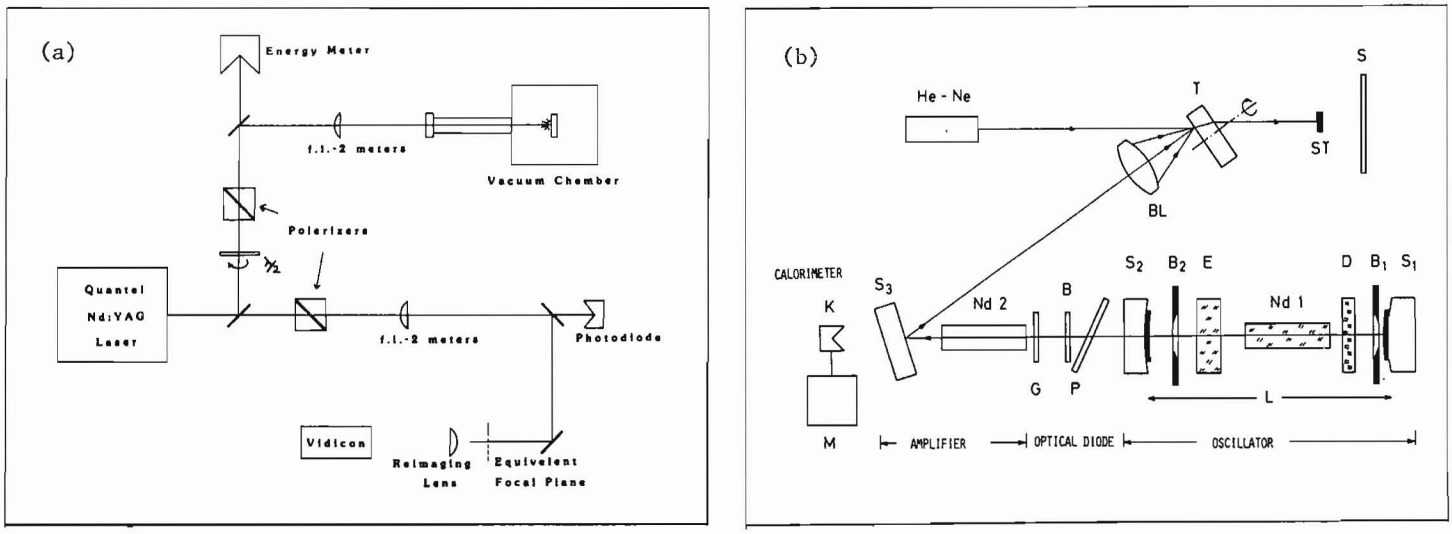
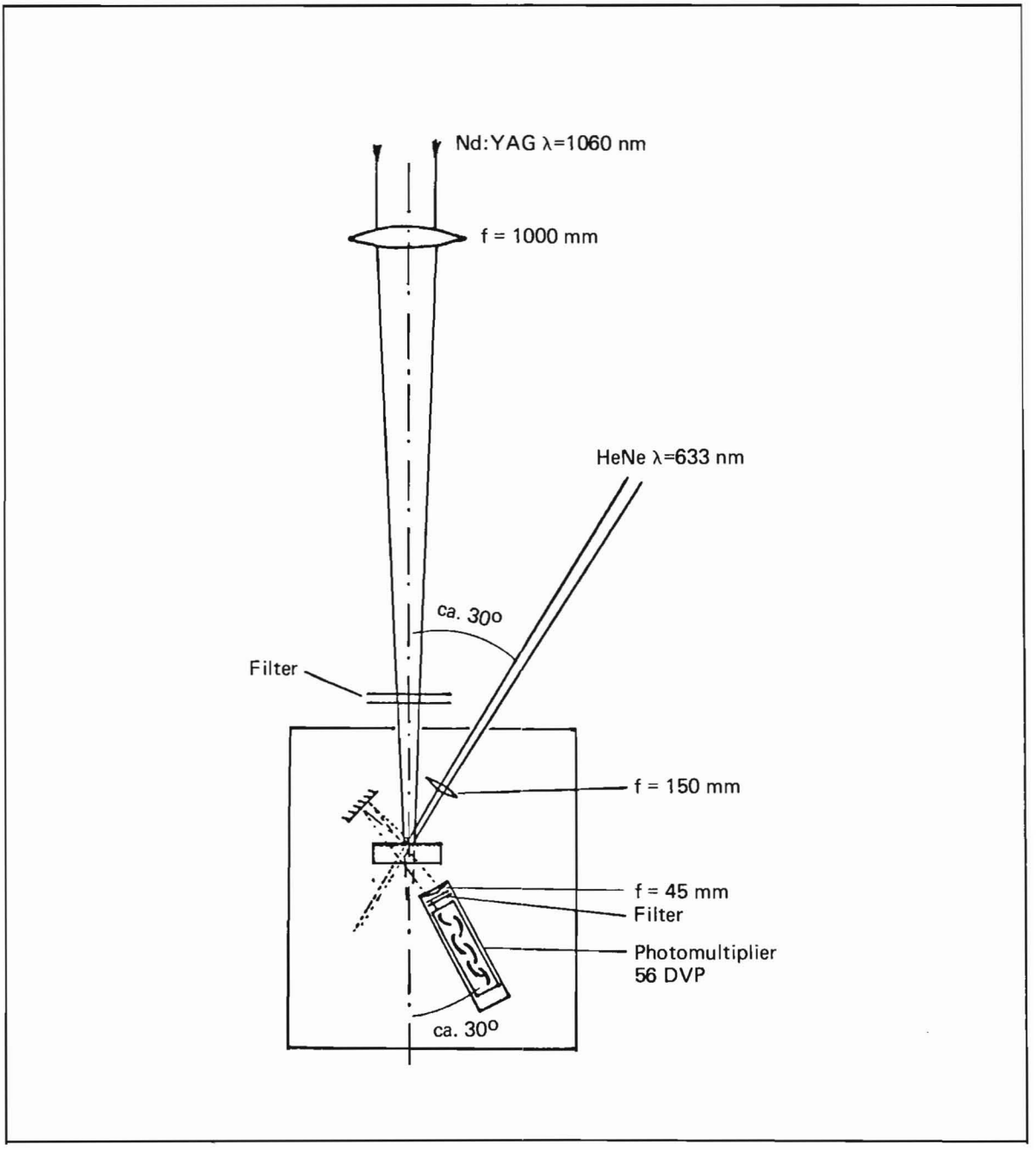


Figure 2. LIDT experimental set ups at (a) AFWL and (b) University of Kaiserslautern.



Laser induced damage to optical coatings:
Detection by auxiliary HeNe laser scattering
(Balmer, Schwarzenbach, Weber; Univ. of Berne)

Figure 3.

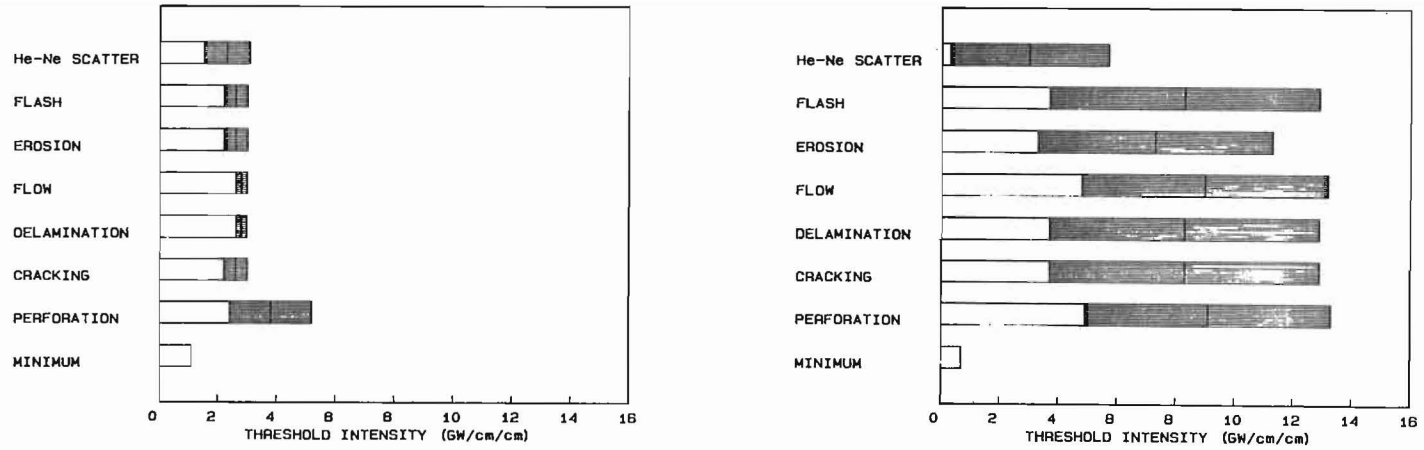


Figure 4. Multithreshold results for two Laser Transmax samples obtained at NWC (S. Seitel).

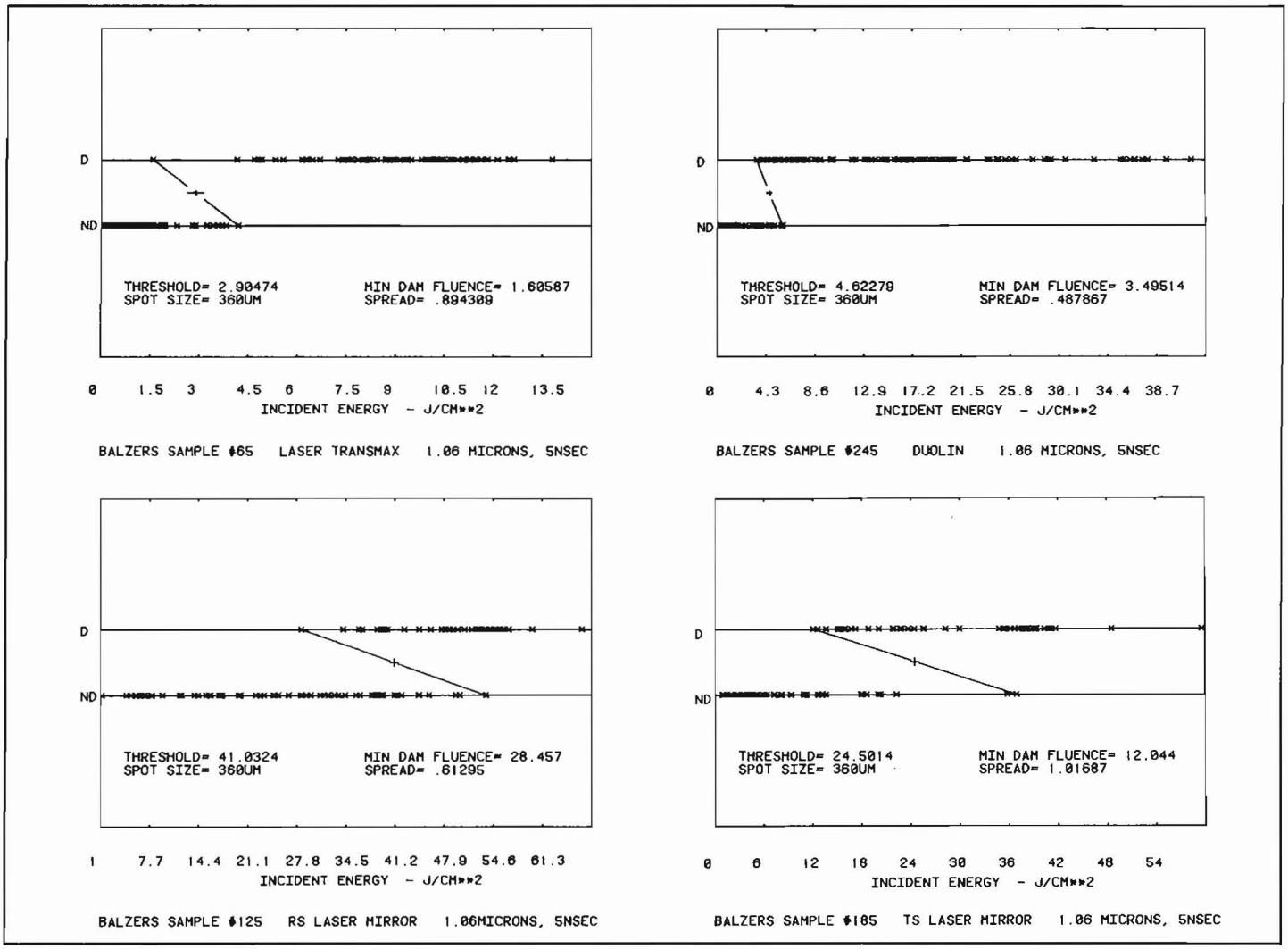


Figure 5. Representation of LIDT test data obtained at AFWL (A. Stewart and A. Guenther).

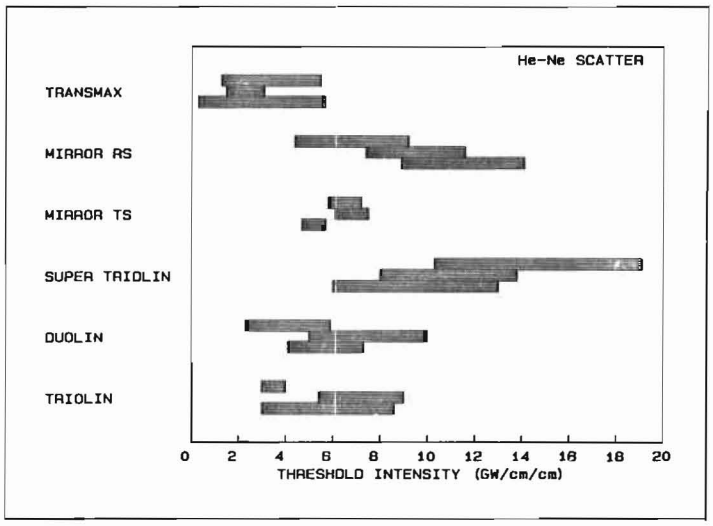


Figure 6a. LIDT test results obtained at NWC (S. Seitel): Uniform multithreshold results from visible scatter measurements.

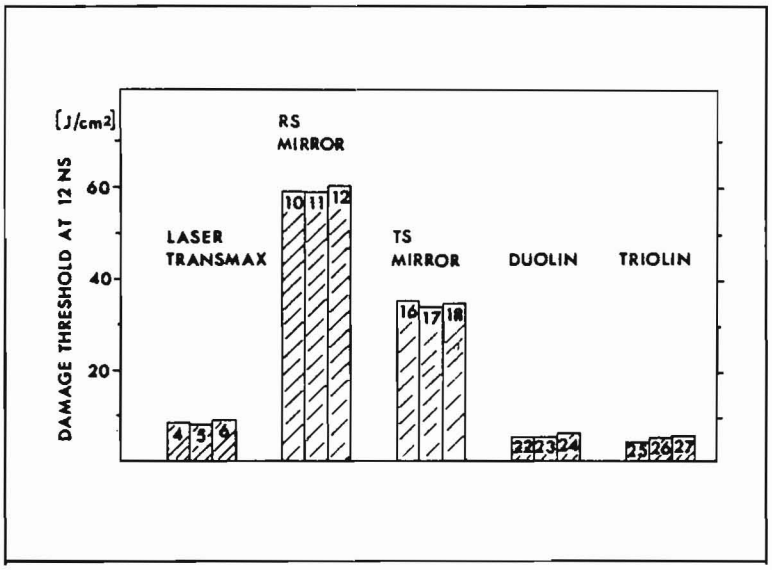
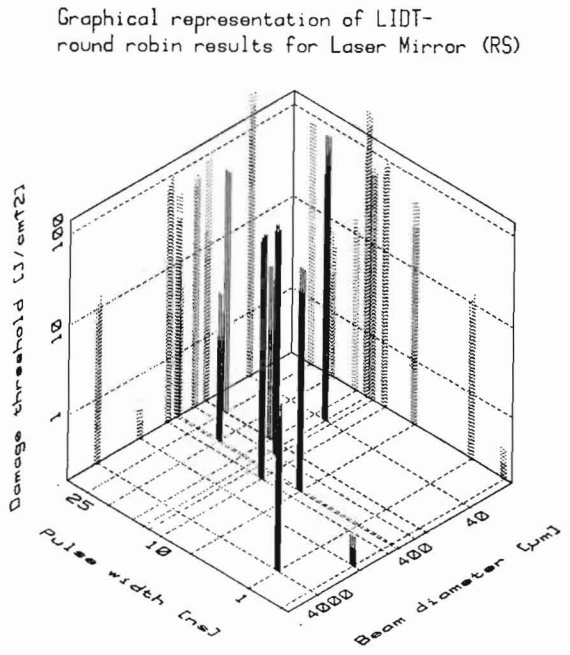
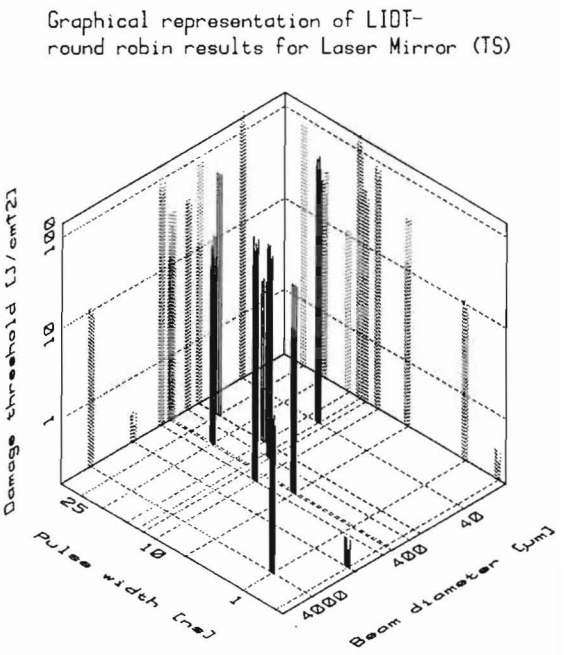


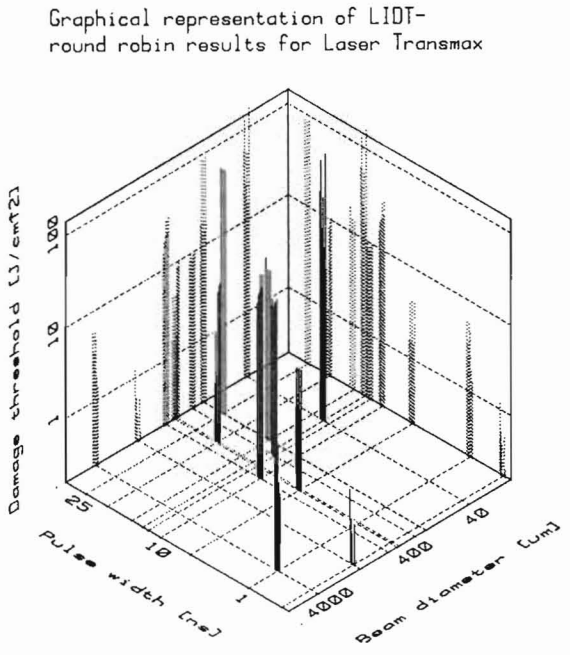
Figure 6b. LIDT test results obtained at the Institute of Quantum Optics, University of Hannover (Ebert and Kiesel).



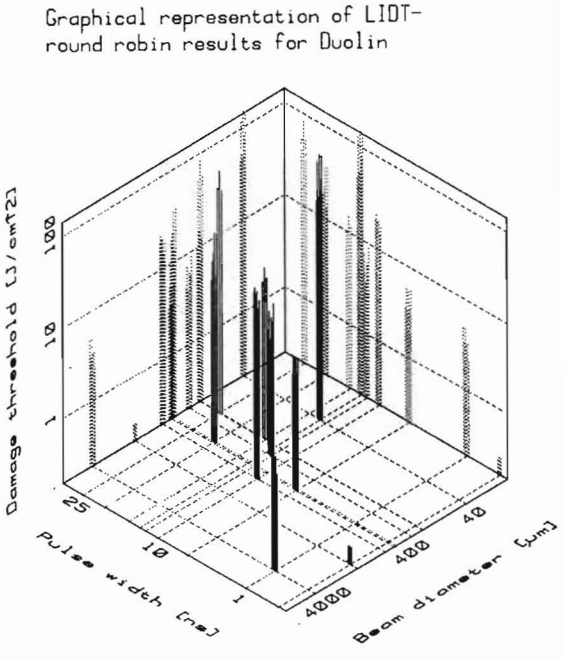
(a)



(b)

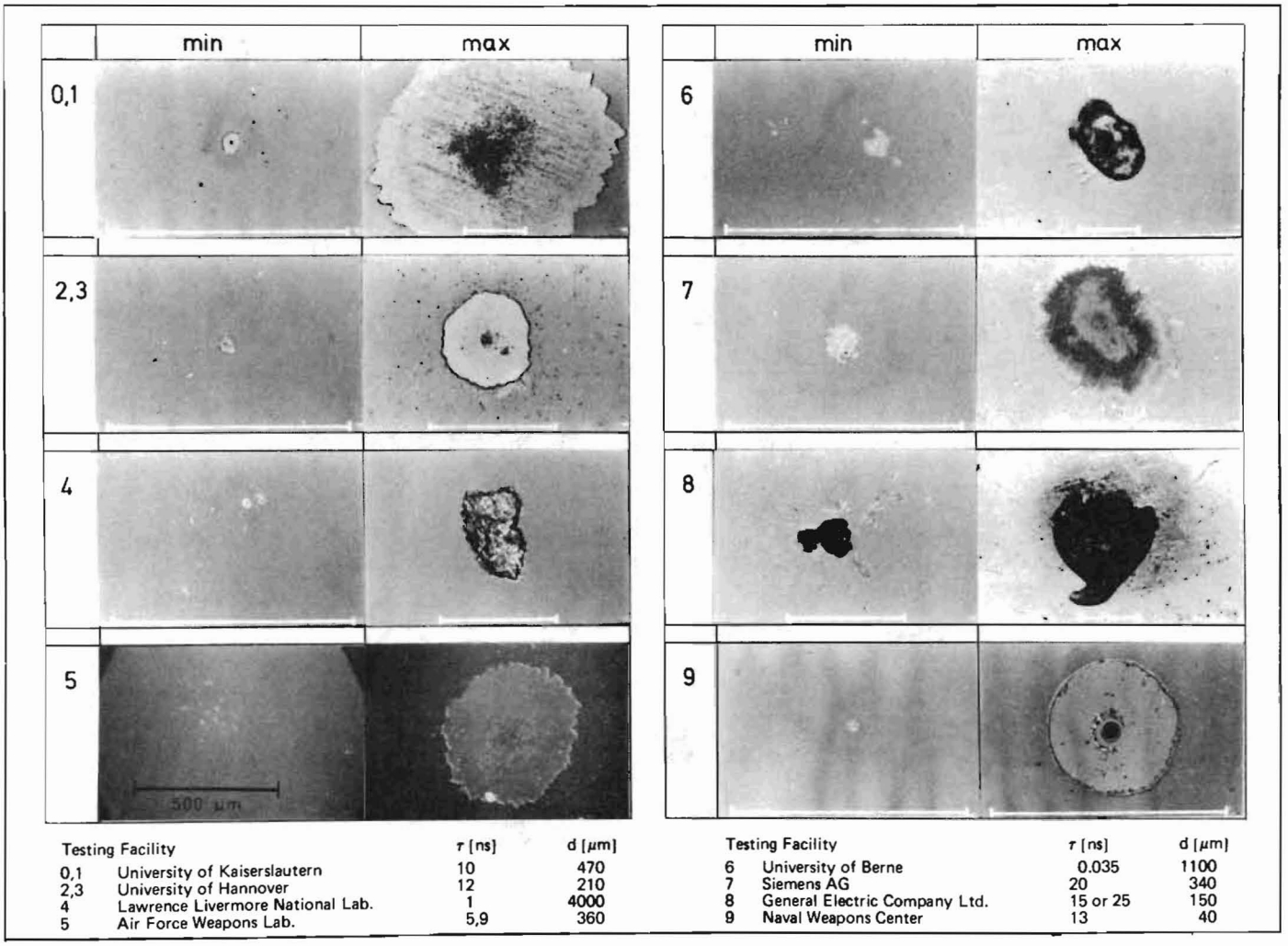


(c)



(d)

Figure 7. Graphical representation of LIDT round robin test results for (a) Laser Mirror (RS), (b) Laser Mirror (TS), Laser Transmax (LT), and (d) Duolin (DN).

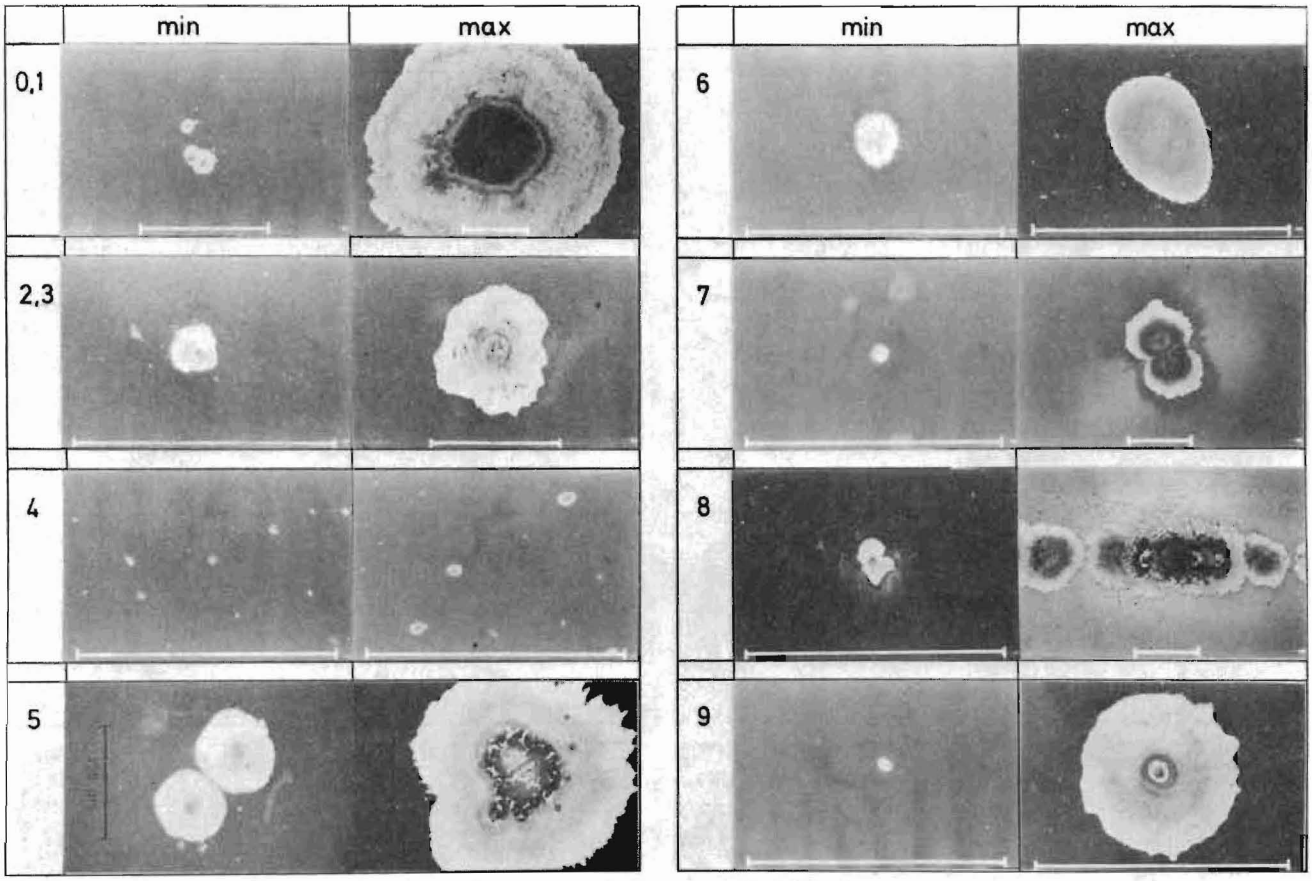


Testing Facility		τ [ns]	d [µm]
0,1	University of Kaiserslautern	10	470
2,3	University of Hannover	12	210
4	Lawrence Livermore National Lab.	1	4000
5	Air Force Weapons Lab.	5,9	360

Testing Facility		τ [ns]	d [µm]
6	University of Berne	0.035	1100
7	Siemens AG	20	340
8	General Electric Company Ltd.	15 or 25	150
9	Naval Weapons Center	13	40

Nomarski micrographs of 1.06 µm laser damage to an AR-coating (LT) just above damage threshold (min) and at heavily damaged sites (max). Scale bar = 500 µm if not otherwise stated.

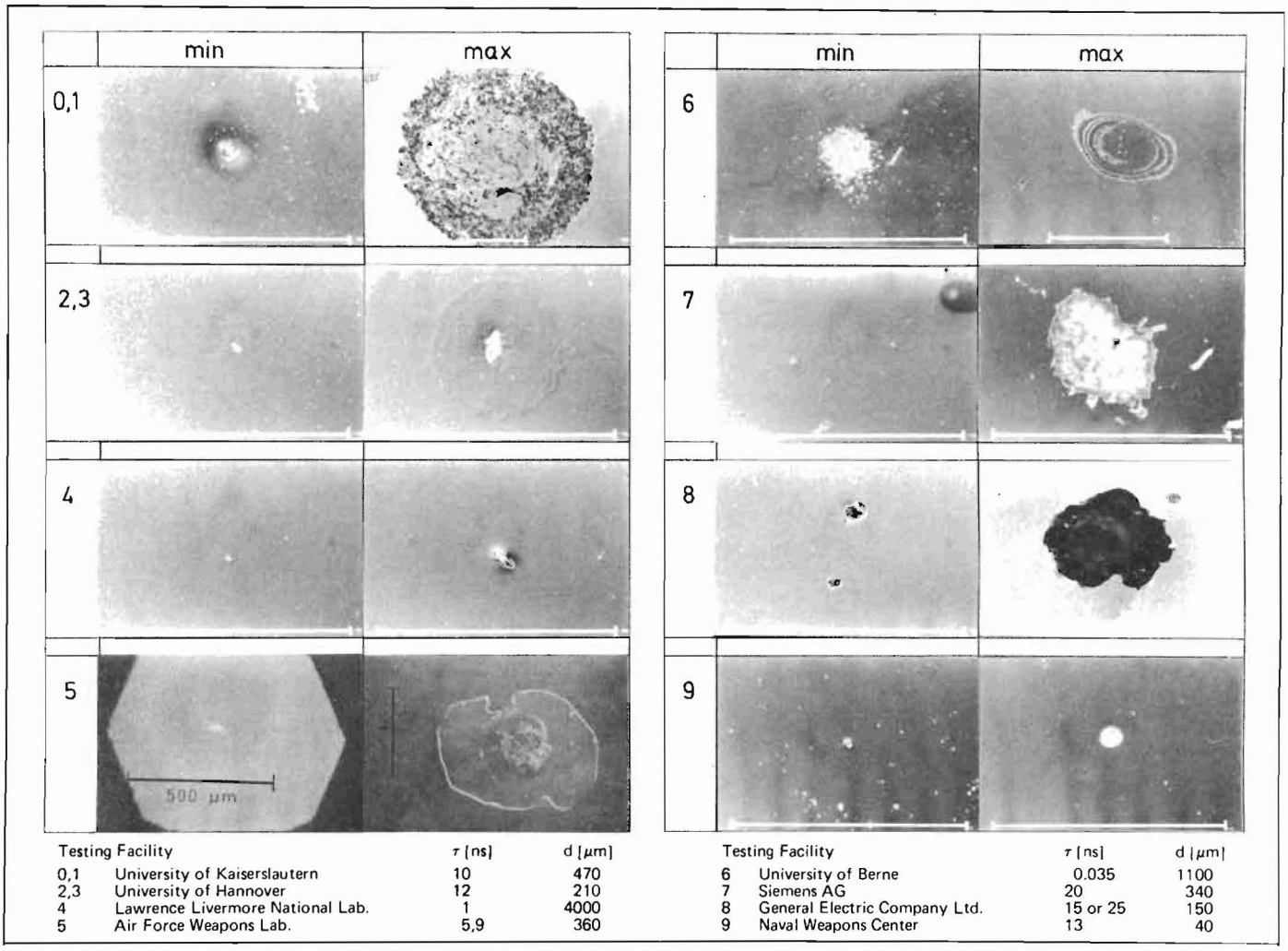
Figure 8a.



Testing Facility		τ [ns]	d [μm]
0,1	University of Kaiserslautern	10	470
2,3	University of Hannover	12	210
4	Lawrence Livermore National Lab.	1	4000
5	Air Force Weapons Lab.	5,9	360
6	University of Berne	0.035	1100
7	Siemens AG	20	340
8	General Electric Company Ltd.	15 or 25	150
9	Naval Weapons Center	13	40

Nomarski micrographs of 1.06 μm laser damage to an AR-coating (DN) just above damage threshold (min) and at heavily damaged sites (max). Scale bar = 500 μm if not otherwise stated.

Figure 8b.

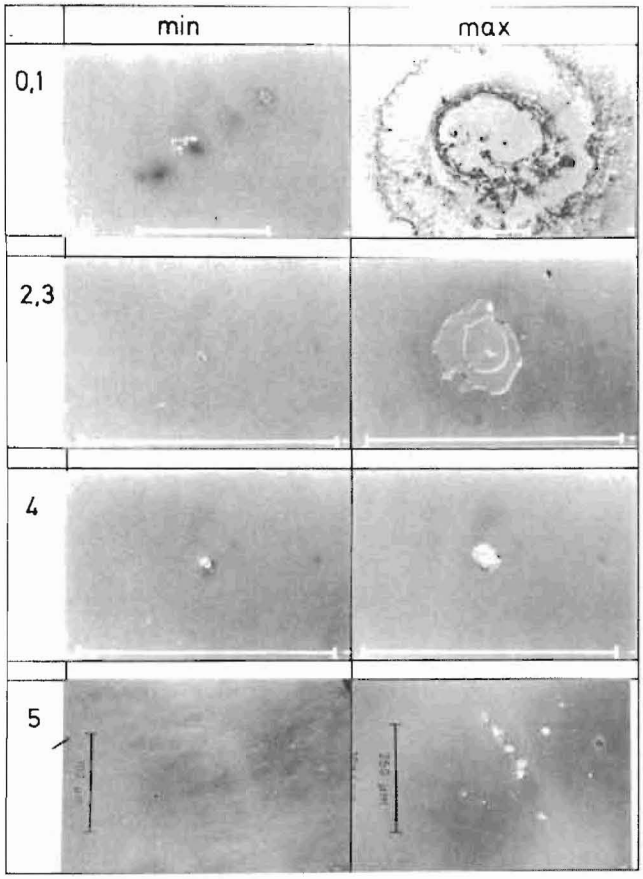


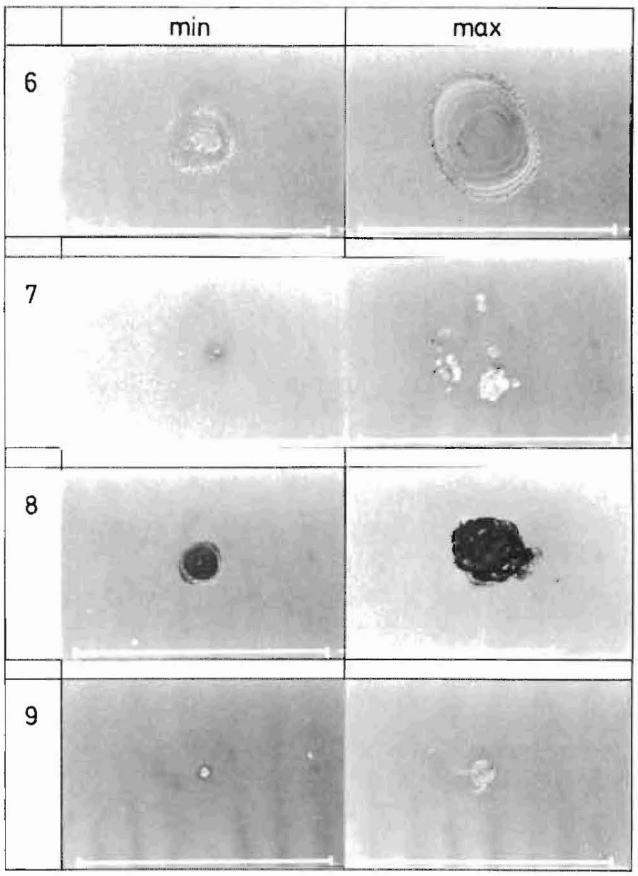
Testing Facility		τ [ns]	d [µm]
0,1	University of Kaiserslautern	10	470
2,3	University of Hannover	12	210
4	Lawrence Livermore National Lab.	1	4000
5	Air Force Weapons Lab.	5,9	360

Testing Facility		τ [ns]	d [µm]
6	University of Berne	0.035	1100
7	Siemens AG	20	340
8	General Electric Company Ltd.	15 or 25	150
9	Naval Weapons Center	13	40

Nomarski micrographs of 1.06 µm laser damage to a laser mirror (RS) just above damage threshold (min) and at heavily damaged sites (max). Scale bar = 500 µm if not otherwise stated.

Figure 8c.





Testing Facility		τ [ns]	d [μm]
0,1	University of Kaiserslautern	10	470
2,3	University of Hannover	12	210
4	Lawrence Livermore National Lab.	1	4000
5	Air Force Weapons Lab.	5,9	360

Testing Facility		τ [ns]	d [μm]
6	University of Berne	0.035	1100
7	Siemens AG	20	340
8	General Electric Company Ltd.	15 or 25	150
9	Naval Weapons Center	13	40

Nomarski micrographs of 1.06 μm laser damage to a laser mirror (TS) just above damage threshold (min) and at heavily damaged sites (max). Scale bar = 500 μm if not otherwise stated.

Figure 8d.

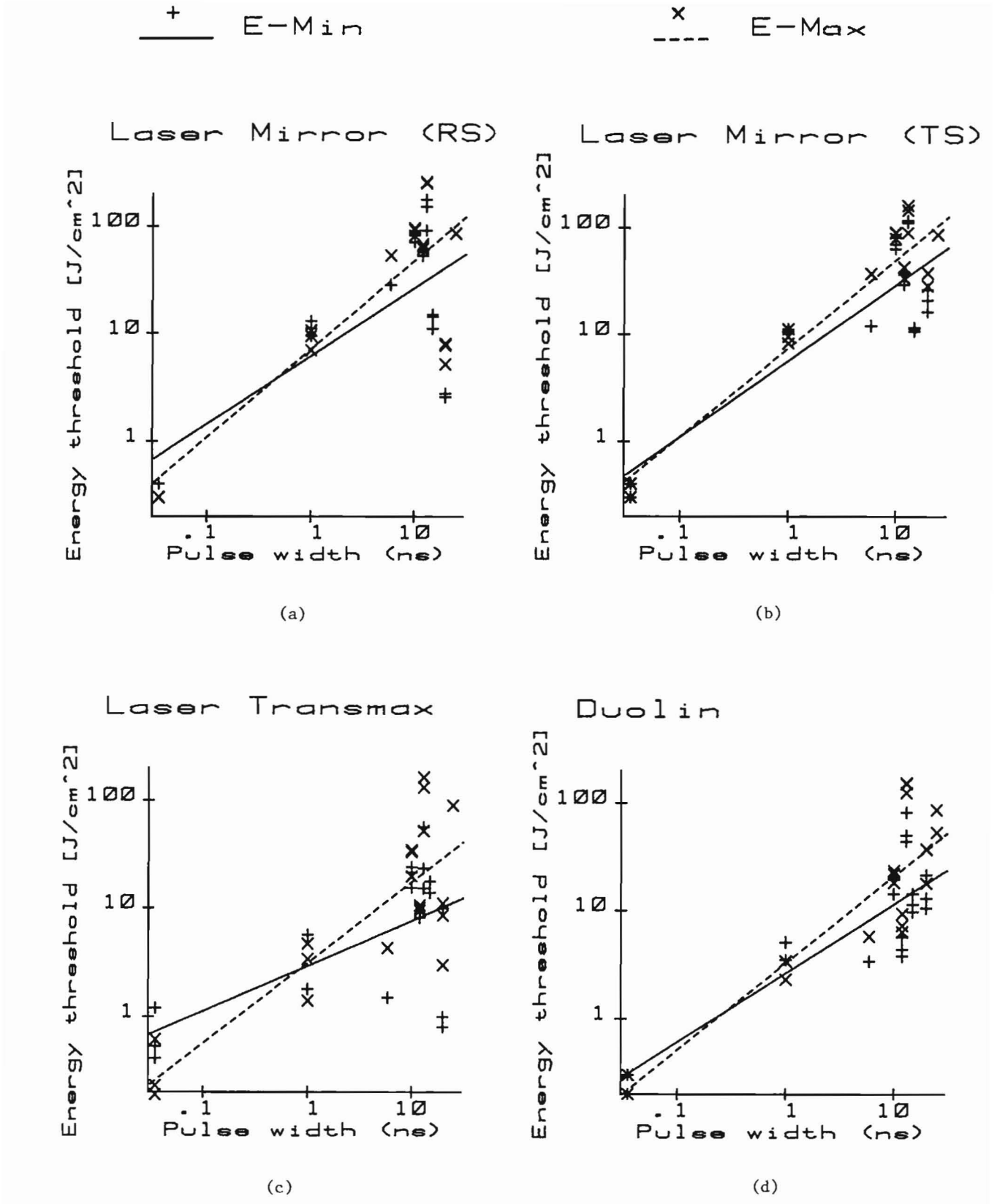


Figure 9. Damage thresholds vs. pulse width for (a) Laser Mirror (RS), (b) Laser Mirror (TS), (c) Laser Transmax (LT), and (d) Duolin (DN).

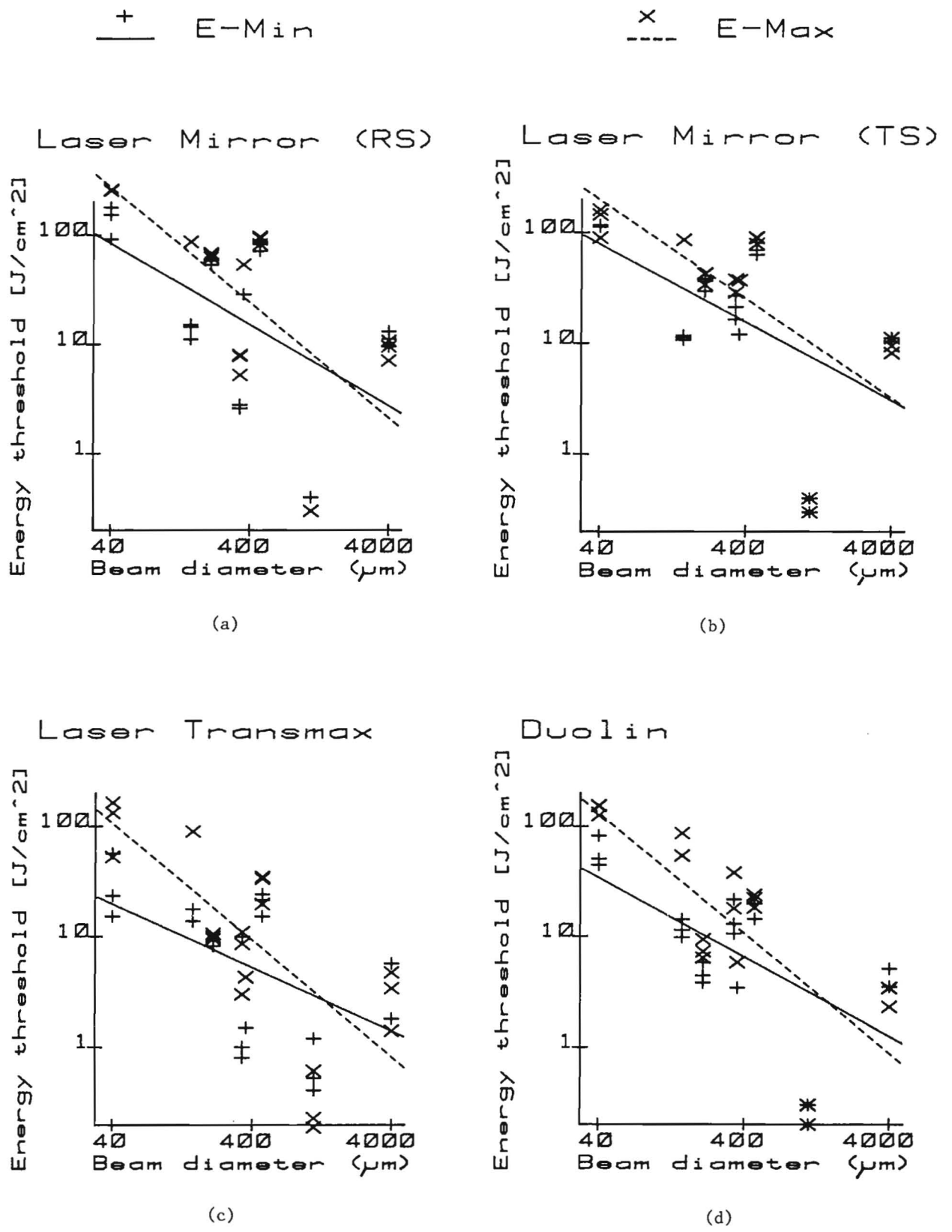


Figure 10. Damage thresholds vs. beam diameter for (a) Laser Mirror (RS), (b) Laser Mirror (TS), (c) Laser Transmax (LT), and (d) Duolin (DN).

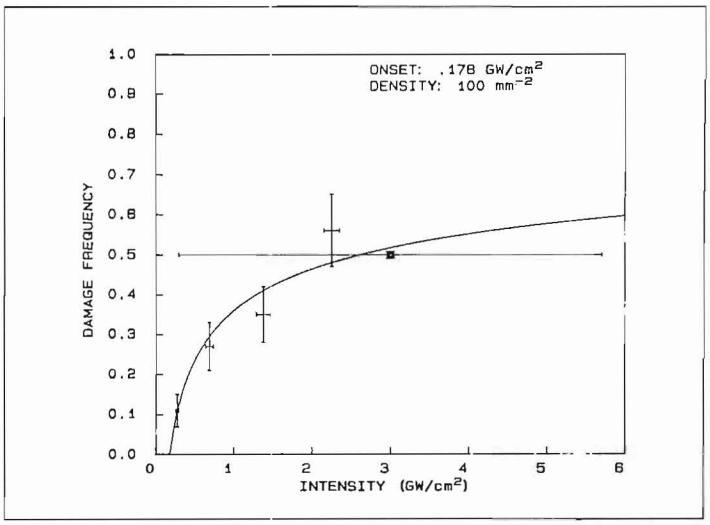


Figure 11. Determination of damage onset by extrapolation to zero failure rate as suggested by Porteus (Ref. 22). Data is on Laser Transmax sample at NWC (S. Seitel).

The reason for using photoelectric detection of light scattered from the damaged surface by a helium-neon laser as a means of damage detection was questioned. Its sensitivity was said to be far inferior to that of the logarithmic response of the eye. The speaker replied that a standardized means of damage detection which was not observed sensitive was needed, and, after extensive discussions, this method was agreed upon.

Manuscript received 3-22-84/sar

Measurements of the Dependence of Damage Thresholds on Laser Wavelength, Pulse Duration and Film Thickness*

F. Rainer, C. L. Vercimak and D. Milam

Lawrence Livermore National Laboratory
Livermore, CA 94550

C. K. Carniglia and T. Tuttle Hart

Optical Coating Laboratory, Inc.
Santa Rosa, CA 95403

Results of three experiments will be described. We used 351-nm and 355-nm pulses with durations of 0.6, 1, 5 and 9 ns to measure thresholds for a variety of anti-reflectance and high reflectance coatings. The functional form t^m, with t the pulse duration, was used to scale fluence thresholds measured at 0.6 ns to those measured at 9.0 ns. Values of the coefficient m ranged from 0.10 to 0.51. The average value was 0.30. In the second experiment, we measured thresholds at 1064 nm, 527 nm and 355 nm for single-frequency high reflectance ZrO_2/SiO_2 coatings. Coatings for all three frequencies were deposited simultaneously by use of masks in the coating chamber. Thresholds varied from 2-4 J/cm^2 at 355 nm to 7-10 J/cm^2 at 1064 nm. The third experiment measured thresholds at 355 nm for antireflection coatings made with layer thicknesses varying from greater than one wavelength to less than a quarterwavelength. A significant variation of threshold with coating thickness was not observed, but the median thresholds increased slightly as coating thickness increased.

Keywords: antireflective coatings; damage; laser-induced damage; optical coatings; pulse duration scaling; reflectors; thickness of coatings; wavelength scaling.

1. Introduction

Two purposes are served by measurement of the variation in laser-damage thresholds of thin-film coatings as a function of variations of the parameters of either the coating or the laser pulse. These measurements provide design data needed in fabrication of large lasers, and they assist the investigation of fundamental aspects of laser-induced damage. We have used 355-nm laser pulses to measure thresholds in coatings as a function of coating thickness and laser pulse duration, and have studied the spectral dependence of damage thresholds by measuring thresholds at wavelengths between 351 nm and 1064 nm. Results of these experiments were not accurately predicted by existing theory.

2. Experimental Procedure

Thresholds reported here were measured with beams that were 1-3 mm in diameter at the sample surface. The fluence at the most intense point in the beam was computed for each shot from measurements of the beam shape and pulse energies. Pulse durations ranged from 0.6-9 ns, and were specified with each set. Three different lasers were used in the experiments. Two of these were equipped with Nd:YAG oscillators and crystals of potassium dihydrogen phosphate (KDP) for harmonic conversion. These lasers provided pulses at 1064 nm, 532 nm and 355 nm. The third laser was similar, but was equipped with a Nd:YLF laser oscillator and provided pulses at wavelengths of 1053 nm, 527 nm and 351 nm. Although there is no reason to believe that the slight offset between the two sets of harmonic wavelengths is of significance in damage measurements, we will specify the exact wavelength used in each experiment.

Our experimental facilities and procedures for measuring damage thresholds have been described in detail elsewhere [1].

3. Experimental Results

3.1 Pulsewidth Scaling of Damage Thresholds

The purpose of these measurements was to begin generation of a data base that specifies safe operating fluences for 355-nm pulses with durations up to 10 ns. We used 351-nm pulses with durations of 1, 5 and 9 ns to test an assortment of AR and HR coatings that had previously been

*Work performed under the auspices of the U.S. Department of Energy by the Lawrence Livermore National Laboratory under contract W-7405-ENG-48.

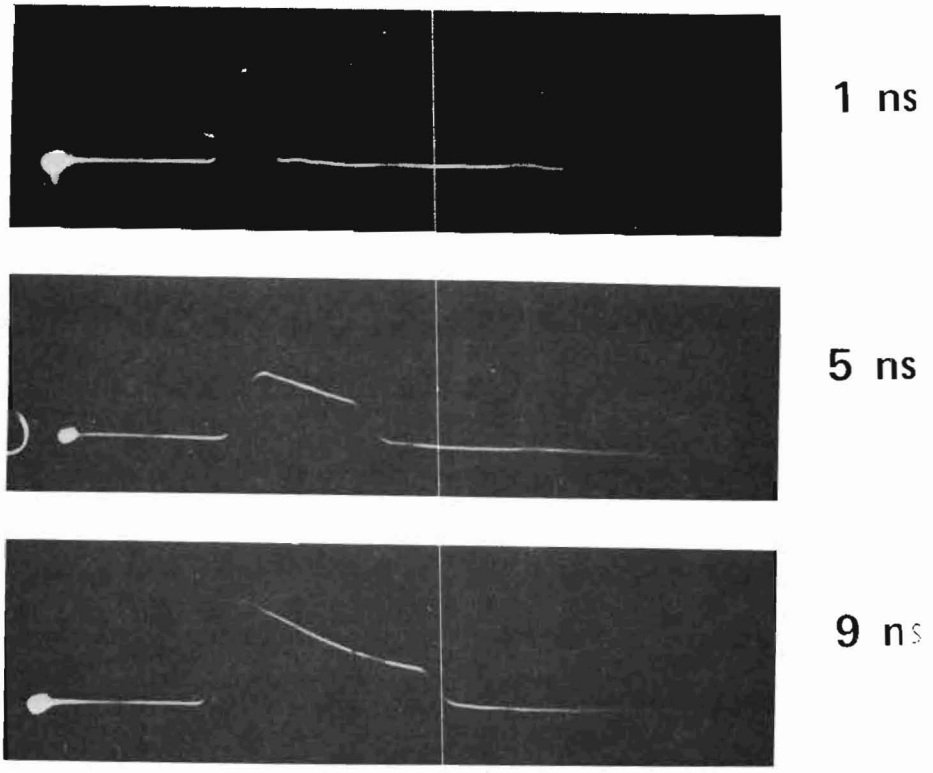


Figure 1. Temporal waveforms of 351-nm pulses.

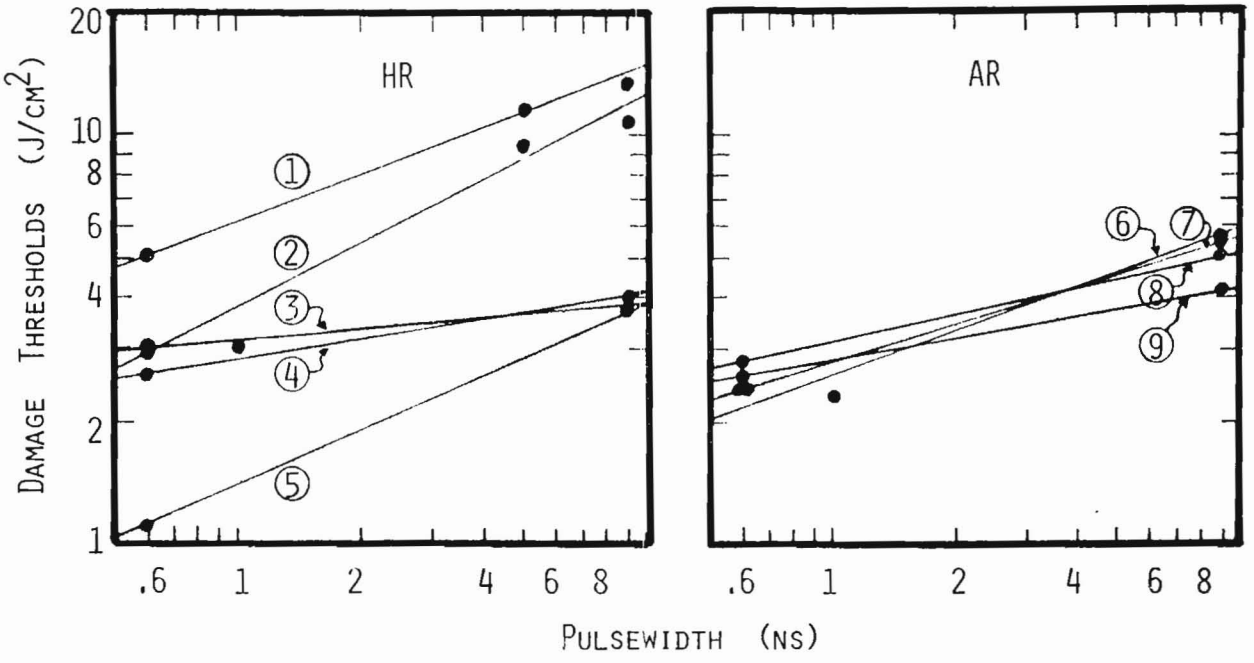


Figure 2. Laser damage scaling as a function of pulse duration for tests at 351-355 nm. Circled numbers refer to samples itemized in table 1.

tested with 0.6-ns, 355-nm pulses. Waveforms for the 351-nm pulses used in current tests are shown in figure 1. The pulses were all sliced from longer pulses by a Pockel's cell shutter, so prior to amplification the pulses had identical rise and fall times. After being amplified and harmonically converted, the 1-ns pulses had nearly Gaussian waveforms. The longer pulses were rectangular, but distorted by gain saturation in laser amplifiers and the nonlinear process of harmonic conversion. The waveforms shown are for high fluence pulses and represent the greatest distortion of pulse shapes.

Thresholds measured as a function of pulse duration are shown in figure 2. Circled numbers in figure 2 identify the sample associated with each set of data. The samples are described in table 1. We fitted the data in figure 2 to a simple power law which assumed that threshold T varied with pulse duration t according to $T=kt^m$. For five high reflectors, m ranged from 0.10 to 0.51 and averaged 0.32. For four antireflective coatings, m ranged from 0.19 to 0.35 and averaged 0.27.

Table 1. Pulsewidth Scaling of Laser Damage at 351-355 nm

#	Coating	Materials	Layers	OC/UC[a]	m[b]
1	HR	$Sc_2O_3/MgF_2/SiO_2$	21[c]	$\lambda/2$ MgF_2	0.37
2	"	ZrO_2/SiO_2	15	$\lambda/2$ SiO_2	0.51
3	"	ZrO_2/SiO_2	"	None	0.10
4	"	Ta_2O_5/SiO_2	"	"	0.17
5	"	HfO_2/SiO_2	"	"	0.46
6	AR	HfO_2/SiO_2	4[c]	$\lambda/2$ SiO_2	0.35
7	"	ZrO_2/SiO_2	"[c]	"	0.30
8	"	MgF_2/SiO_2	5[c]	"	0.22
9	"	Sc_2O_3/SiO_2	4[c]	λ SiO_2	0.19

a. OC ≡ overcoat on HR's; UC ≡ undercoat on AR's.
b. Temporal scaling coefficient: threshold $\propto t^m$.
c. Nonquarterwave-thick layers.

Values of m measured in other 355-nm damage experiments span the range $-0.05 \leq m \leq 0.74$, although most are between 0.3 and 0.4 [2] [3] [4]. These earlier tests were primarily for single-layer coatings, but the results are in general agreement with the results we have obtained in tests of multilayer coatings. However, the range of observed scaling factors is so large that the data provide little insight into the mechanism responsible for damage, and conversely, there is no readily apparent scaling rule that can be used to extrapolate thresholds. Therefore, it will be necessary to generate a data base at each pulse duration of interest until further progress is made in the understanding of pulse length scaling.

3.2 Wavelength Dependence of Damage Thresholds in HR Coatings

We tested three sets of zirconia/silica HR coatings. The coatings in the first, second and third sets had reflectance maxima centered at, respectively, 1064 nm,, 532 nm and 355 nm. Each coating consisted of 15 alterating high-index and low-index layers whose optical thicknesses were one-fourth the design wavelength. All coatings were deposited on BK-7 glass substrates and capped with a silica overcoat layer whose optical thickness was one-half the design wavelength. Coatings for all three wavelengths were deposited simultaneously by use of masking to allow deposition on some substrates of the thicker layers required for the longer wavelength coatings. Four coating runs were made, using substrate temperatures of 150C, 200C, 250C, and 300C.

In figure 3 we show histograms of thresholds of the HR coatings measured with 0.6-ns, 355-nm pulses, and with 1-ns pulses at both 527 nm and 1064 nm. The median thresholds at these three frequencies were, respectively, 2.5, 6.5 and 8.1 J/cm^2, although there was considerable scatter in 527-nm thresholds. Between the wavelengths of 355 nm and 527 nm, the median thresholds scale with wavelength λ as $\lambda^{2.4}$. From 527 nm to 1064 nm, the median thresholds scale as $\lambda^{0.3}$. Newnam and Gill reported that thresholds for single-layer coatings scaled as λ^4 between 266 nm and 355 nm [2]. Other studies [3] [4] [5] have shown that threshold usually decreases monotonically as wavelength decreases below 532 nm, and that the rate of decrease also increases as the wavelength approaches the uv bandedge of the coating material. There is some ambiguity in existing data as to whether 1064-nm thresholds are greater than 532-nm thresholds. Existing data are, therefore generally inconsistent with the theory of damage by avalanche ionization [6], and generally consistent with theories which assume that damage is caused by linear or nonlinear absorption [7].

Our tests of HR coatings also evaluated the dependence of damage threshold on the substrate temperature used during coating deposition. Thresholds as a function of substrate temperature are

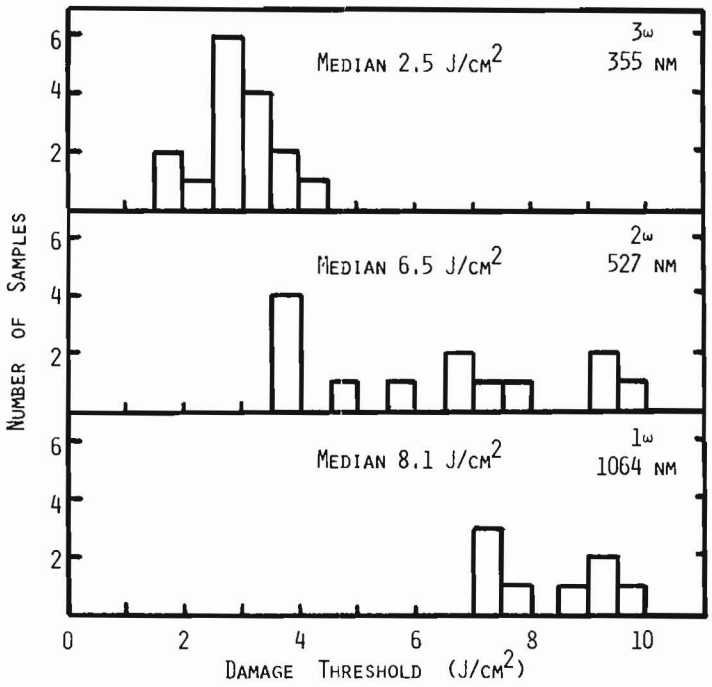


Figure 3. Laser damage thresholds of zirconia/silica HR coatings at three wavelengths. Tests were conducted with 0.6-1.0-ns pulses.

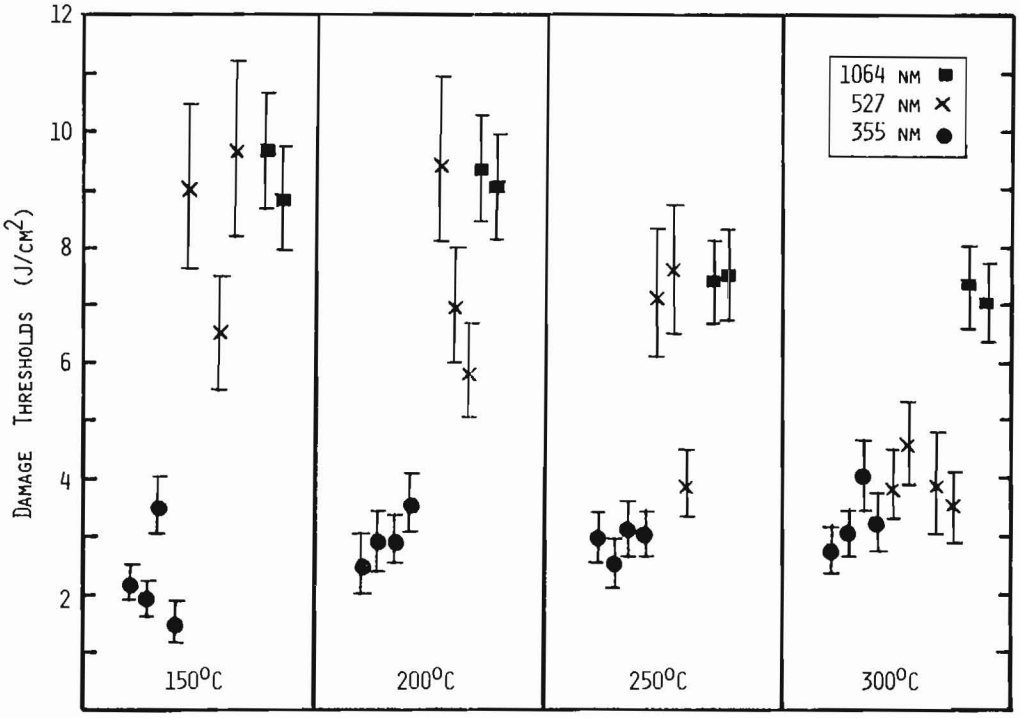


Figure 4. Wavelength and coating temperature dependence of laser damage thresholds for zirconia/silica HR coatings shown in figure 3. Tests were conducted with 0.6-1.0-ns pulses.

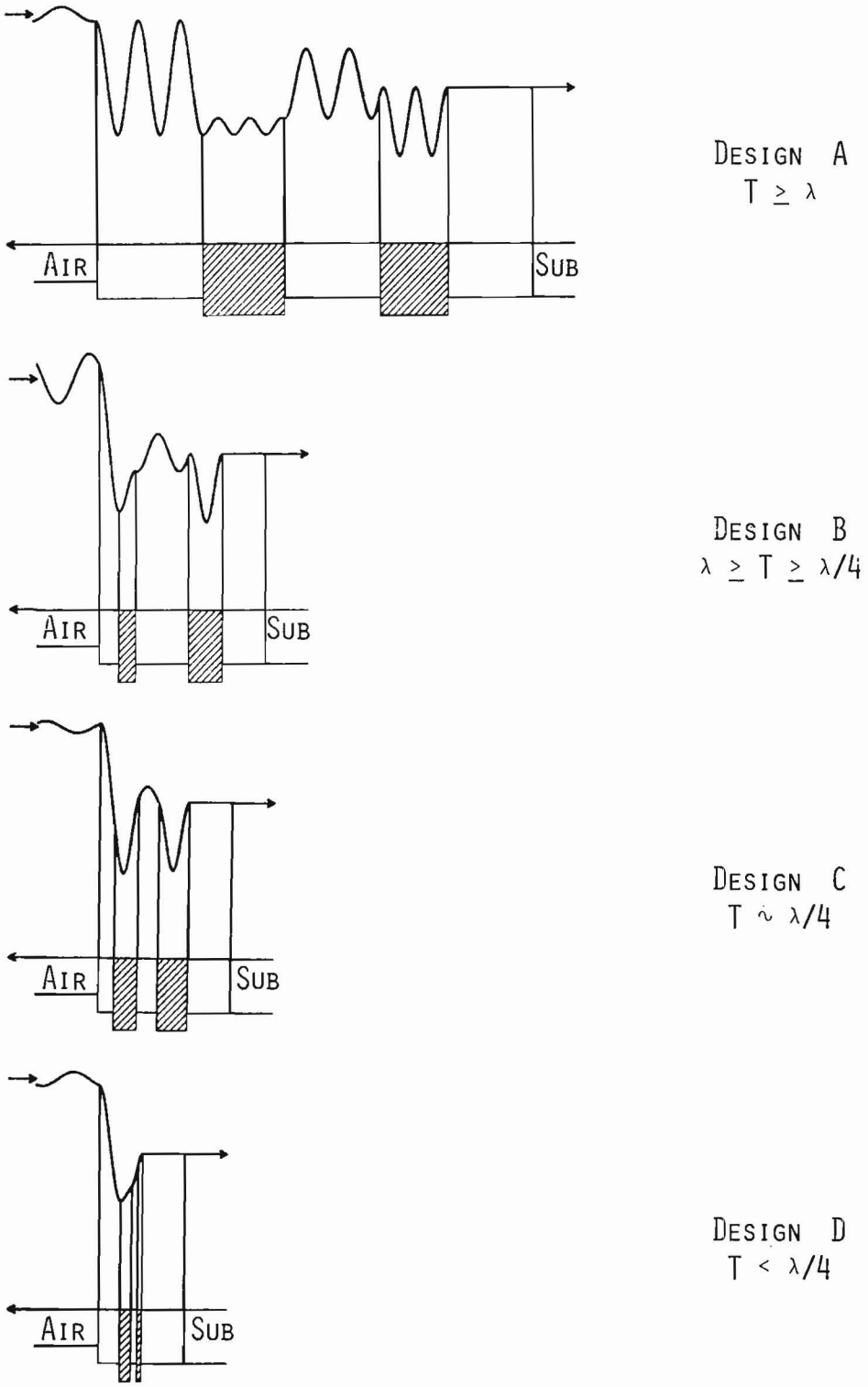


Figure 5. Standing wave intensity distributions in four-layer scandia/silica 355-nm AR coatings with a silica undercoat layer deposited on a silica substrate. The scandia layers are indicated by shading. The upper arrows indicate the intensity of the incident and transmitted fields. Each layer thickness is described by the design designation. The undercoat layer is fullwave thick in design A and halfwave thick in designs B, C and D.

shown in figure 4. On the average, coatings deposited at 150-250C had the highest thresholds at 1064 nm and 527 nm. This trend was previously observed in 1064-nm studies of antireflective coatings [8]. However, for 355-nm coatings, average thresholds were greatest for coatings deposited at 300C. Because there is significant scatter in the 527-nm data, and because these data are for coatings made in only a few coating runs, additional experimentation will be required to determine whether the trends in figure 4 are reproducible.

3.3 Damage Threshold Dependence on Film Layer Thickness

We studied the relationship between layer thickness in 355-nm four-layer scandia/silica AR coatings and thresholds of the coatings. Some layers in conventional 355-nm AR coatings are less than 40 nm in thickness, and we were concerned that such thin layers might be mechanically weak. Secondarily, the experiment provided an excellent evaluation of a recent theory which indicates that thresholds will increase as layer thickness decreases [7].

The coatings tested in this experiment are illustrated in figure 5. All of the coatings contained two scandia layers and two silica layers. In a given design, the thickness was different for each of the four layers. Among the four designs, optical thickness T for all layers in a given design satisfied the following conditions: A. $T \geq \lambda$, B. $\lambda \geq T \geq \lambda/4$, C. $T \sim \lambda/4$, and D. $T < \lambda/4$. Here, λ is 355 nm. Each coating was deposited over a silica undercoat layer which was a fullwave in optical thickness for design A and a halfwave in optical thickness for designs B, C and D.

The coatings were deposited by electron beam evaporation onto silica substrates that had been bowl-feed polished at OCLI. Two coating runs were made for each design, and three substrates were coated in each run.

Laser damage thresholds for these coatings are shown in figure 6. Filled circles indicate thresholds for coatings of each design that were made in the first deposition, and open circles are thresholds of coatings made in the second deposition. The median thresholds for the various designs, indicated by a horizontal bar, ranged from 2.4 to 3.1 J/cm^2. In determining the median for coatings of type B, we neglected data for coatings made in the second deposition. These coatings contained flaws that were visible as red flecks when these samples were backlighted with intense white light illumination. We believe the flaws resulted from improper cleaning of the substrates. However, whether or not these data are included, the study indicated there was little or no dependence of thresholds on layer thickness. If the three data are excluded, the remaining data show a slight trend toward higher thresholds for thicker coatings.

These data conflict with a theory recently published to explain laser damage that results from heating of impurities in films [7]. The theory considered the variation of particle absorptivity with particle size and indicated that small particles were less readily heated than were large particles, when all particles were small relative to the wavelength of the incident radiation. This, coupled with an assumption that maximum size of an inclusion was bounded by the thickness of coating layers, indicated that thresholds should increase as coating thickness decreases. For single-layer coatings, the measured scaling of thresholds with layer thickness agreed with predictions of the theory. Scaling of our data for four-layer AR coatings does not follow the theory.

The disagreement between the theory and data cannot be explained through consideration of internal standingwave intensity distributions in the coatings. The intensity distributions produced by irradiating coatings of each design with a 355-nm wave of unit intensity are shown in figure 5. The peak intensity at either the air interface or in the silica layers differs by only 10% among the four designs. At other interfaces and in the scandia layers, the peak intensity is the same in all designs. Adjusting measured thresholds to account for the small differences in internal intensities does not bring the data into accord with the theory.

Finally, we observed during these measurements a correlation between pit diameter and coating thickness which suggests that most damages were initiated deep within the coatings. Duthler showed that heating of an inclusion located near a surface produced a cone shaped pit whose outer diameter was proportional to the depth of the inclusion [9]. We observed that pit diameter scaled with total coating thickness; see Figure 7. We believe this indicates that most of the damages initiated near the interface between the inner scandia layer and the silica undercoat layer or at the substrate interface. This again seems to indicate that thresholds in these coatings were essentially independent of coating thickness; the inner scandia layer was one of the thickest layers in designs B and C and the thinnest layer in designs A and D.

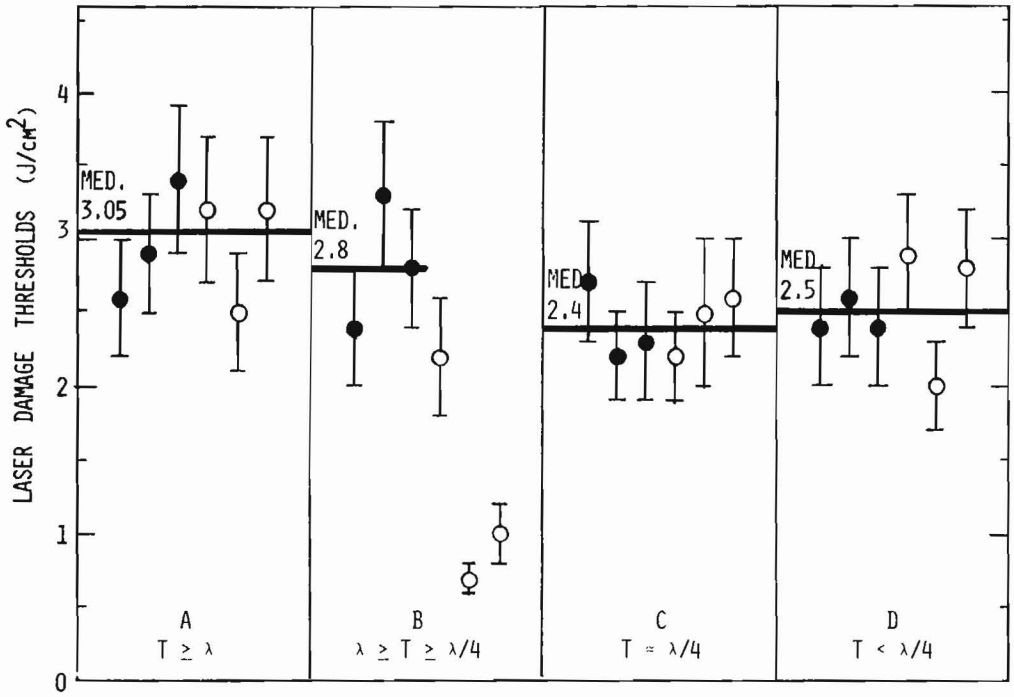


Figure 6. Laser damage threshold dependence on layer thickness T of individual layers in 355-nm scandia/silica AR coatings. Solid and open circles differentiate between samples fabricated in two separate coating deposition runs. Tests were conducted with 0.6-ns pulses.

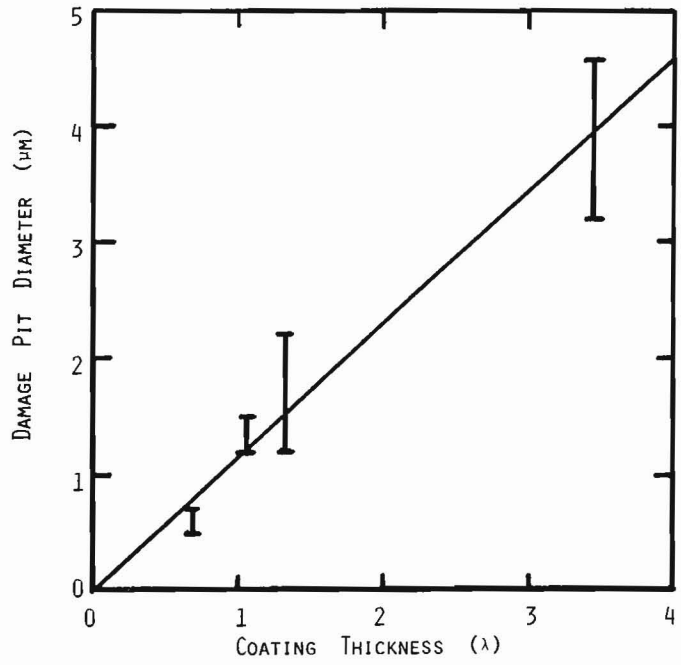


Figure 7. Damage pit diameter ranges of 355-nm scandia/silica AR coatings as a function of net coating thickness. Tests were conducted with 0.6-ns pulses.

4. Summary

We tested five HR and four AR coatings with 351-355-nm pulses having durations ranging from 0.6 to 9 ns. When the function t^m was fitted to the data, m ranged from 0.10 to 0.51 (0.32 average) in HR coatings and from 0.19 to 0.35 (0.27 average) for AR coatings.

Zirconia/silica HR coatings were tested with pulses having wavelengths of 1064 nm, 527 nm and 355 nm and pulse durations from 0.6-1.0 ns. Median thresholds observed at these three wavelengths were 8.1 J/cm^2, 6.5 J/cm^2 and 2.5 J/cm^2 respectively. In HR coatings for use at 1064 nm or 527 nm, thresholds of coatings deposited on substrates at 150-200C exceeded thresholds of coatings deposited at 250-300C. There was a slight reversal of this trend in 355-nm coatings.

In four-layer 355-nm scandia/silica AR coatings with total optical thicknesses ranging from 0.7 λ to 3.4 λ, thresholds were essentially independent of coating thickness. The diameter of damage pits in these coatings was proportional to coating thickness.

---

5. Acknowledgements

We appreciate capable assistance by M. C. Staggs who measured some thresholds reported here, and by S. E. Peluso who assisted in maintenance of the laser-damage facility.

6. References

[1] Rainer, F.; Deaton, T. F. Laser damage at short wavelengths. Applied Optics 21(10); 11722-1724; 1982 May 15.

[2] Newnam, B. E.; Gill, D. H. Ultraviolet damage resistance of laser coatings. Nat. Bur. Stand. (U.S.) Spec. Publ. 541; 1978 December. 190 p.

[3] Newnam, B. E.; Gill, D. H. Spectral dependence of damage resistance of refractory oxide optical coatings. Nat. Bur. Stand. (U.S.) Spec. Publ. 462; 1976 December. 292 p.

[4] Walker, T. W.; Guenther, A. H.; Nielsen, P. E. Pulsed laser-induced damage to thin-film optical coatings - Part 1: Experimental. IEEE J. Quant. Elect., QE-17 (10); 2041-2052; 1981 October.

[5] Foltyn, S. R.; Newnam, B. E. Multiple-shot laser damage thresholds of ultraviolet reflectors at 248 and 308 nm. Nat. Bur. Stand. (U.S.) Spec. Publ. 620; 1981 October. 265 p.

[6] Bloembergen, N.; Laser-induced breakdown in solids, IEEE J. Quant. Elect., QE-10; 375-386 1974 March.

[7] Walker, T. W.; Guenther, A. H.; Nielsen, P. Pulsed laser-induced damage in thin-film optical coatings - Part II: Theory. IEEE J. Quant. Elect., QE-17 (10); 2053-2065; 1981 October, and attached references.

[8] Milam, D.; Lowdermilk, W. H.; Rainer, F., Swain, J. E., Carniglia, C. K., Tuttle Hart, T. Influence of deposition parameters on laser-damage thresholds of silica-tantala AR coatings. Appl. Opt. 21 (20); 3689-3694; 1982 October.

[9] Duthler, C. J.; Sparks, M.; Extrinsic absorption in laser window materials. Nat. Bur. Stand. (U.S.) Spec. Publ. 414; 1974 December. 219 p.

Clarification of the coating design was requested. The speaker stated that each film had four layers and a beryl layer, which was a half-wave thick for the three thinner designs and one-wave thick for the thickest design. There was a variation in damage level with substrate temperature at which the film was prepared, even though the film design made the coatings independent of the E fields. A member of the audience suggested that an explanation of the variation with substrate temperature might be that, at lower temperatures, one gets a more amorphous but also less refined microstructure. Structural modifications can be obtained upon thermal heating, for example, with the laser beam. At higher substrate temperatures, there is a more refined microstructure which will not change any further upon heating but will result in lower damage thresholds.

Manuscript Received 12-30-83

A Fundamental Approach Towards Improved Optical Coatings

Keith L Lewis and James A Savage

Royal Signals and Radar Establishment
Malvern, Worcestershire, WR14 3PS, UK

The potential afforded by molecular beam epitaxy as a means of producing thin film materials in a highly controlled manner has been exploited using an ultra-high vacuum facility dedicated to the examination of all facets of thin-film technology as applied to optical coatings. The equipment allows deposition on ion-beam cleaned substrates either from molecular beams or by RF sputtering, and allows in situ characterisation by mass spectrometry, Auger Electron Spectroscopy and laser calorimetry. Application of the equipment is described with reference to the fabrication of ZnSe coatings. The composition of the residual atmosphere within the coating chamber is discussed with reference to the rate of adsorption of impurities onto the substrate whilst growth of the coating is underway. By ensuring the reduction of the partial pressures of water vapour and carbon monoxide to the low 10^{-10} mbar range, ZnSe films have been produced of up to 3 μm in thickness which have negligible values of absorptance at 10.6 μm. Such layers, although micro-polycrystalline, are mirror smooth and featureless, and of (111) orientation. Growth rates in excess of 1 μm/h are comparable with conventional coating techniques.

1. Introduction - The Case for a Fundamental Approach

The realisation of optical coatings with a high durability and low absorption has long been the goal of materials scientists and optical systems engineers alike. In general, progress in this area has been limited by the inability to carry out a systematic study of the fundamental materials issue involved. Despite this, significant advances have been made by the optimisation of various thin film fabrication techniques or by exploitation of alternative technology as for example typified by various surface modification techniques (leaching[1], ion implantation[2], etc). It is now clear however that a quantum leap in coating performance will not be realised unless a fundamental study is carried out of all the stages involved in coating fabrication.

A common factor in the failure of optical coatings under laser irradiation has been the lack of perfection and the relatively low purity of the coated material. Optical absorption levels are frequently too high and the refractive index uniformity of the thin film difficult to control. For example, in the case of ZnSe, despite the ability to grow bulk material by chemical vapour deposition with an absorption coefficient of 0.0005 cm^{-1} or less at 10.6 μm[3, 4], the effective absorption coefficient of the same material in thin film form is frequently in the range 5-20 cm^{-1} [5, 6].

Of equal importance to the need to improve the purity of the thin film structures, is the need to maintain stoichiometry of the material. This is particularly the case for binary semiconductor-type materials, where non stoichiometry can result in the generation of free charge carriers which interact strongly with radiation at long wavelengths. Indeed, Walsh and Bertke[8] have found that

significant variations in the zinc-selenium ratio of ZnSe can occur during RF sputtering. This parallels the results of O'Brien[6] which suggests that the Zn/Se ratio increases at higher deposition rates, resulting in higher infra-red absorption. High film absorption is often aggravated by the presence of further impurity species at the substrate/multilayer interfaces, which may also act as nucleation sites for the formation of pores or other undesirable morphological features. Pores and cracks are efficient absorbers of water and other impurities, many of which have significant optical absorption at 10.6 μm. Using an absorption coefficient of 10^3 cm^{-1} for liquid water Sparks[7] estimated that a fraction of 5×10^{-4} of pores filled with water were sufficient to give a surface absorptance of 10^{-4}. The impurities present at interfaces also contribute to the poor adhesion of thin film structures. The presence of these impurities can be avoided by effective surface cleaning techniques provided that care is taken to avoid readsorption prior to film deposition.

Extrinsic Stress in thin film coatings can arise from thermal expansion mismatch of the film relative to the substrate or as a consequence of the impurities present in the film. The former can be minimised by careful choice of the film/substrate combination. The latter, on the other hand, is generally of a compressive nature and can vary with thickness of the deposit: its reduction therefore implies the need to improve film purity.

Present-day thin film coatings are essentially of a polycrystalline morphology. In order to ensure a minimum surface energy, the surface of a polycrystalline layer must be irregular. This will of course affect the nucleation of any subsequent layers and will also result in significant scatter of transmitted radiation. In impure films, the grain boundaries act as sinks for impurities giving rise to refractive index inhomogeneities which further increase scatter levels. Surface texture can be reduced by producing oriented polycrystalline films, single crystal layers or amorphous layers. The choice ultimately depends on the film material and/or the film/ substrate combination.

In any vacuum deposition process, the degree of contamination of a surface by the residual environment of a coating chamber may be readily estimated using the Kinetic Theory of Gases from which the number of molecules of species i striking and adhering to the substrate per unit area is given by

$$R = \frac{s P_i}{\sqrt{2\pi m_i kT}} = \frac{2.67 \times 10^{22} \, s \, P_i \ (\text{m bar})}{\sqrt{m_i T}} \qquad \ldots (1)$$

where P_i is the partial pressure of i, m_i its molecular weight and s a sticking coefficient in the range 0 - 1, but frequently 0.1 for permanent gases. An ideal coating process would be configured so that this residual flux is negligible compared with the incident flux of material to be deposited. This can be achieved by increasing the incident flux (as in many high-rate sputtering techniques) or by decreasing the residual impurity flux by deposition under ultra-high vacuum conditions. In conventional evaporators, the base pressures achieved are of the order of 10^{-6} m bar and the dominant species present is H_2O due to outgassing of the coating chamber walls and substrate assembly. The partial pressure of H_2O is only slightly reduced by the incorporation of liquid nitrogen cooled cryopanelling since the rate-limiting process is desorption from the walls and not efficiency of pumping. Using equation (1) together with a sticking coefficient of 0.4 (see later), it is readily shown that a ZnSe surface would be covered with a monolayer of H_2O in 5 seconds. Since the

absorption coefficient of liquid water at 10.6 μm is approximately 10^3 cm^{-1}, only 10 Å H_2O is required with molecular bonding comparable to the liquid state to produce an absorptance of 10^{-4}. As such it suffices to say that any sample loaded into a conventional evaporator would be grossly contaminated with H_2O before deposition of any coating has commenced, giving rise to a high degree of interfacial absorption. Attempts at surface cleaning using ion beams are generally futile since the H_2O is rapidly readsorbed. The problem is not restricted to water - other molecular species (e.g. - CO_3, - SO_4, - SO_3, - CO_2, - CH_n) are commonly produced as a result of reactions during coating and give rise to significant absorption at 10.6 μm.

We have chosen to exploit the potential afforded by molecular beam epitaxy as a means of producing thin film materials in a highly controlled manner and have designed and constructed an ultra-high vacuum facility dedicated to the examination of all facets of thin film technology, as applied to high energy optical coatings. Application of the equipment is described with reference to the fabrication of ZnSe coatings which have already been identified as of potential for laser windows.

2. UHV Coating Facility

The ultra-high vacuum facility is shown in schematic form in figure (1). It is divided into three sections each separated by gate valves - a growth chamber, capable of a base pressure in the mid 10^{-11} m bar range, a sample preparation/measurement chamber (10^{-8} m bar) and loading chamber (10^{-8} m bar) which also contains a small RF sputtering source. The growth chamber is pumped by an array of five ion pumps giving a combined pumping speed of 200 ℓ sec^{-1}, supplemented by a liquid nitrogen cooled titanium sublimation pump. Three Knudsen sources each fitted with high purity graphite or boron nitride crucibles are arranged around the growth chamber so that their effusing beams converge at a common focal point. This arrangement allows the deposition of a wide range of materials including ternaries, or for example complex multilayers, simply by sequencing the opening of shutters in the beam paths. A molecular beam sampling mass spectrometer, situated within line of sight of the Knudsen sources allows examination of the effusing species. This, in conjunction with a quartz crystal monitor also allows in situ estimation of deposition rate. Optionally, direct monitoring of deposition rate is possible by virtue of the provisioning of ports suitable for optical reflectivity measurements. The substrate holder is configured to allow optical transmission measurements through the central portion of the sample. The holder is resistively heated and its temperature measured with a precision of $\pm$ 1°C by a platinum film thermometer.

Composition analysis of the deposited layer is effected by Auger Electron Spectrometry (AES) using an analyser situated within the deposition chamber. This is particularly useful for the growth of ternary materials where the composition of the product is critically dependant on the relative Knudsen cell temperatures. Since the analysis technique is only sensitive to the composition of the top atomic layer of the material, it can readily detect the presence of impurity species absorbed on the surface. In common with semiconductor processing, the technique is therefore used as an on-line monitor of surface cleanliness following sample preparation. Ion beam cleaning is carried out in the preparation chamber using 0-3 kV Ar^+ ions from a raster-scanning ion source. This assures uniform etching profiles.

The absorptance of the substrate is determined within the preparation chamber using adiabatic laser calorimetry by virtue of the unique sample holder configuration and provisioning of A/R coated ZnSe viewports at opposite ends of the chamber. The technique essentially follows that described

in a previous publication[9] including the use of electrical heating for calibration purposes. The ability to carry out the measurements within the high vacuum facility allows the unambiguous determination of the absorptance of the coatings. In fact, any increase in optical absorption on eventual exposure to air can be readily measured merely by admission of air into the preparation/ measurement chamber.

Substrates for coating are carefully cleaned with trichlorethane, followed by acetone before loading into the equipment. The loading chamber is then evacuated to a pressure of 5×10^{-7} m bar using a liquid nitrogen-trapped polyphyenyl ether diffusion pump before transfer of the sample in its holder to the preparation chamber.

Refractory materials (e.g. oxides, nitrides) can be deposited in the loading chamber using a small (2" diameter) RF plasma source. A separate UHV cryopump ensures the maintenance of the ultra-clean environment and provides the ability to cope with the high throughput of argon.

3. Analysis of Substrate Surface prior to deposition

The state of contamination of a typical ZnSe sample following loading into the equipment is shown by the AES trace of figure (2). The dominant impurity present is carbon, together with a significant amount of oxygen. Also notably present is a small amount of chlorine, presumably as a result of the cleaning in chlorinated solvent. The carbon and oxygen are presumably present as hydrocarbon, carboxylate ion species and water respectively since previous attenuated total reflectivity studies[4] suggested that these are the dominant molecular species most commonly found on ZnSe exposed to the atmosphere. These surface impurities are effectively removed by Ar^+ beam bombardment for 10 minutes at a density of approximately 200 $\mu A/cm^2$. This ion beam cleaning stage has been found to be important in ensuring effective adherence of subsequent coatings to the substrate. An experiment to demonstrate this was carried out using a GaAs substrate. A portion of the GaAs was ion beam cleaned and the entire substrate then subsequently coated with ZnSe at a deposition temperature of 50°C. A micrograph of a region of the sample encompassing the boundary between the cleaned and non-cleaned segments is shown in figure (3). This clearly shows delamination of the coating on the contaminated portion of the substrate. Delamination began immediately on exposure of the coated substrate to the atmosphere and was complete (on the uncleaned portion) within one or two minutes. This occurred despite an excellent lattice match between the film and substrate (ZnSe a_o = 5.667 Å GaAs a_o = 5.6534 Å).

4. Stoichiometry of ZnSe Source

The importance of stoichiometry has already been briefly discussed above in section 1. In order to ensure that the ZnSe source used in this work was free from undesirable effects, the dissociation constant for the evaporation process within the Knudsen oven was measured as a function of temperature. The actual source material used was a polycrystalline material which had been prepared[4] by chemical vapour deposition from mixtures of zinc vapour and hydrogen selenide, and was known from mass spectrographic and photoluminescence studies to be of extremely high purity. The material is known to evaporate congruently according to

$$ZnSe(s) \rightleftarrows Zn(v) + \tfrac{1}{2} Se_2(v)$$

and the relevant dissociation constant is given by

$$K_p = P_{Zn} \; P_{Se_2}^{\frac{1}{2}}$$

Since K_p is related to the enthalpy ΔH and entropy ΔS of dissociation by

$$\log K_p = \frac{-\Delta H}{RT} + \frac{\Delta S}{R}$$

the value of ΔH generated by measurements of P_{Zn} and P_{Se_2} within the effusing flux from the ZnSe may be used to demonstrate thermodynamic consistency. By measurement of the partial pressures using the mass spectrometer within line of sight of the source and plotting the results in the form $\log K_p$ against $1/T$, we have determined a value of ΔH of 83.8 K cal mol^{-1}. This value is in excellent agreement with published values[10, 11].

5. ZnSe Film Growth and Effect of Residual Coating Atmosphere on Impurity Absorption

Films of ZnSe were produced on glass, GaAs and ZnSe using the following typical deposition conditions.

ZnSe source temperature		950°C
Substrate temperature		175°C
Growth rate		1.2 μm/h
Residual partial pressures	H_2	8×10^{-9} m bar
	H_2O	2×10^{-10} m bar
	CO	2×10^{-10} m bar

The growth rate in excess of 1 μm/h is approximately an order of magnitude greater than rates used in typical semiconductor material growth by MBE and has been achieved merely by increase in source temperature. These rates are comparable with those achieved in conventional coating techniques.

The fluxes J_i of the coating species i arriving at the substrate are given by

$$J_i = \frac{P_i \; a}{\pi \; d^2 \; \sqrt{2\pi m_i kT}} \qquad \ldots (2)$$

where d is the distance of the surface (area a and temperature T) from the substrate. The impurity content of the coating is therefore given by

$$[C] = \frac{R}{\sum_{i=1}^{n} s_i \; J_i} \qquad \ldots (3)$$

where R is defined by equation (1).

We have assessed the importance of R by interrupting the coating process at an arbitrary stage and carrying out measurements of the rate of surface adsorption of different species using AES whilst monitoring the residual partial pressures by mass spectrometry. For example, when water vapour dominates the residual spectrum, even at a partial pressure of 4.5×10^{-9} m bar, saturation of the surface by oxygen occurs within 20 minutes as shown by figure (4). This is predicted by equation (1) using a value of s of 0.40. For a ZnSe growth rate of 2 μm/h (an impingement flux of 1.22×10^{15} molecules cm^{-2} sec^{-1}), the maximum concentration of H_2O adsorbed within a layer would be 0.05%. This formally results in a film absorption coefficient of 0.5 cm^{-1} at 10.6 μm assuming $\beta_{H_2O} = 10^3$ cm^{-1}. In general however, the partial pressure of H_2O in a UHV system is of the order of 10^{-10} m bar resulting in a maximum concentration of adsorbed H_2O in the ZnSe of only 10 ppm.

When the dominant residual species present in the coating plant are H_2 and CO, AES measurements show (figure 5) that only carbon is adsorbed on a clean ZnSe surface. Very little oxygen is detected which implies that under these conditions, the carboxylate ion[4] is not formed. Presumably the oxygen is being removed by reaction with the hydrogen present. For $P_{CO} = 5.3 \times 10^{-9}$ m bar, assuming a sticking coefficient of 0.1, coverage of the surface by CO is expected within 80 min. This is approximately equal to the time observed for the carbon AES signal to reach saturation. Measurements of the rate of carbon adsorption at lower CO partial pressures confirm that the surface coverage rates are substantially reduced (figure 6) and are only just detectable at $P_{CO} = 9 \times 10^{-10}$ m bar.

6. Assessment of ZnSe films

Films of ZnSe produced in this work on CVD ZnSe substrates have been assessed by laser calorimetry. Under the growth conditions listed in section 5 the following results were obtained.

Sample	Absorbance
ZnSe specimen, solvent cleaned, before coating	0.0019
Same specimen, following MBE deposition of ZnSe coating 1.7 μm thick	0.0018

Within the limits of experimental error, the two values are identical, signifying at the most a very low value of coating absorptance. This compares with an expected <u>increase</u> in absorptance of the order of 0.002 that would have occurred had the coating been produced by conventional techniques.

In each case, the coatings produced by MBE are mirror smooth and free from surface topography. The ZnSe coatings are always polycrystalline at growth temperatures near 200°C even on (100) oriented GaAs wafers. Comparison with the work of Smith and Pickhardt[12] and Yao and Maekawa[13] suggests that the growth temperatures used above are some 150°C too low to ensure a single crystal epitaxial product on GaAs, although Jones et al[14] report epitaxy on (100) GaAs at temperatures as low as 160-200°C. The essential difference in the technique of Jones et al is that they utilise RF sputtering in UHV rather than growth from thermal beams. In their case, the RF excited plasma may be contributing to surface diffusion processes during growth of the film, ensuring single crystal growth.

Although the ZnSe films produced in this work by MBE are polycrystalline, X-ray diffraction studies have shown that they are highly ordered and of (111) orientation. This is the case even when

the films are produced on glass substrates. It is believed that this highly oriented microstructure may be associated with the lack of surface topography of the films, and would be expected to result in low values of optical scatter. Together with their freedom from pores and inclusions, these low absorption ZnSe films have the potential of having a high failure threshold. It is arguable whether a single crystal film, with its freedom from impurity absorption at grain boundaries, would be less susceptiable to laser damage than polycrystalline material, since it is possible by UHV techniques to ensure that the grain boundaries are free from impurities. However, by virtue of the dangling bonds present, the grain boundaries may be effective as sinks for free charge carriers.

Copyright © Controller HMSO, London 1983.

7. References

[1] Schroeder, H. Proc. 10th Inst. Conf. on Glass, Kyoto 8-118 (1974).

[2] Townsend, P.D. Proc. SPIE International Conference, Geneva (1983).

[3] Raytran ZnSe: Raytheon Co., Waltham, Mass.

[4] Lewis, K.L. and Arthur, G.S. Proc. Boulder Laser Damage Symposium (1982).

[5] Walsh, D.A. and Detrio, J.A. Proc. Boulder Laser Damage Symposium 253 (1976).

[6] O'Brien, D.F. Proc. Boulder Laser Damage Symposium 276 (1977).

[7] Sparks, M. Proc. Boulder Laser Damage Symposium 203 (1976).

[8] Walsh, D.A. and Bertke, R.S. Proc. Boulder Laser Damage Symposium 271 (1977).

[9] Gibbs, R. and Lewis, K.L. J Phys E: Sci. Instrum. 11 304 (1978).

[10] Hall, K; Hill, J. and Lewis, K.L. Proc. 6th International Conf. on Chem. Vap Depn 36 (1977).

[11] Goldfinder, P. and Jeunehomme, M. Trans. Farad Soc. 59 2851 (1963).

[12] Smith, D.L. and Pickhardt, V.Y. J Appl. Phys 46 2366 (1975).

[13] Yao, T. and Maekawa, S. J. Crystal Growth 53 423 (1981).

[14] Jones, P.L.; Moore, D. and Cotton, D.R. J Crystal Growth 59 183 (1982).

The audience questioned whether MBE techniques could be scaled to produce thick coatings on large laser optics. The author replied that there does not appear to be a technical reason limiting MBE to small samples and coating thicknesses. Alternately, if one used MBE as a tool to improve more conventional coating processes, it would be less expensive than building a large MBE system.

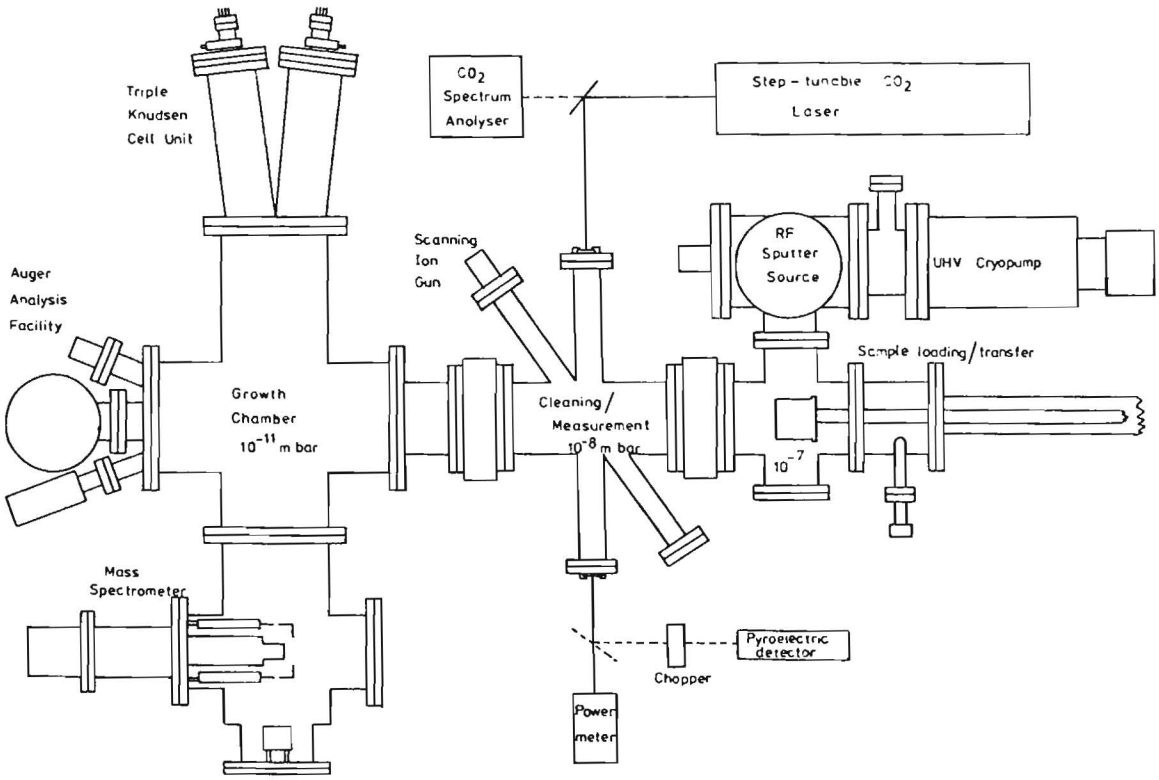


Figure (1) Schematic Diagram of Ultra High Vacuum Facility for Fundamental Research on Optical Coatings.

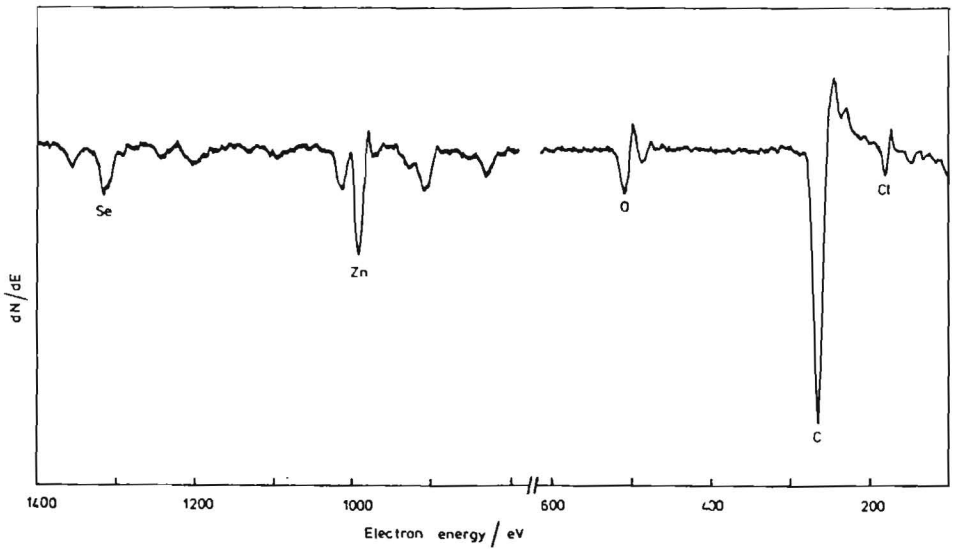


Figure (2) Auger Electron Spectrum of surface species on solvent-cleaned ZnSe. Very little change in the overall spectrum was detected even after the sample was left at 10^{-8} m bar for 15 hours.

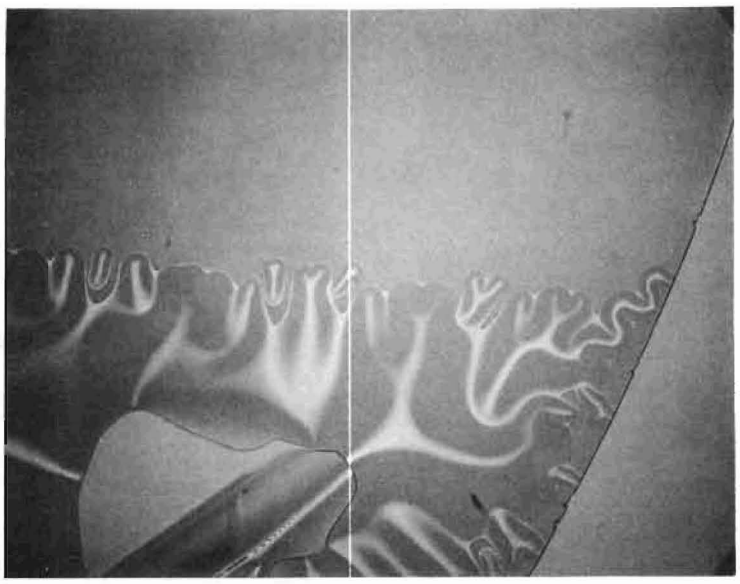


Figure (3) Micrograph of film of ZnSe on GaAs showing effect of delamination in lower region which was not cleaned by ion beam.

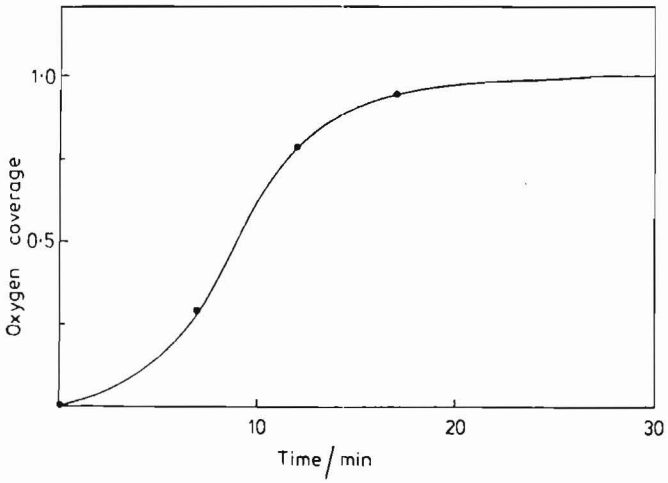


Figure (4) Increase in surface coverage of oxygen on pure ZnSe film on exposure to residual atmosphere with partial pressures P_{H_2} = 4.5×10^{-9} m bar, $P_{H_2} = 2.8 \times 10^{-9}$ m bar, $P_{CO} = 2.1 \times 10^{-9}$ m bar, $P_{CO_2} = 6.1 \times 10^{-10}$ m bar. No increase in carbon signal was detected.

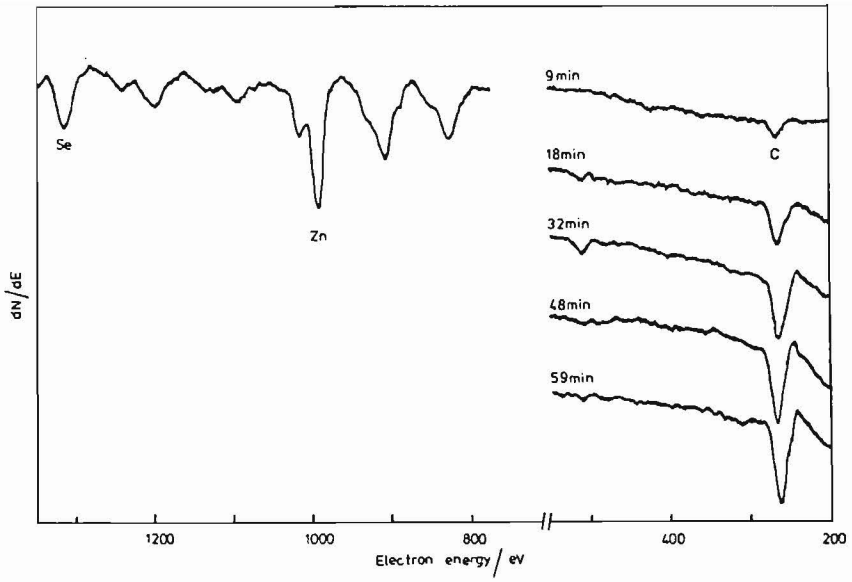


Figure (5) Variation in Auger Electron Spectrum of pure ZnSe film on exposure to residual atmosphere with partial pressures P_{H_2} = 1.3 x 10^{-8} m bar, P_{CO} = 5.3 x 10^{-9} m bar, P_{H_2O} = 7 x 10^{-10} m bar.

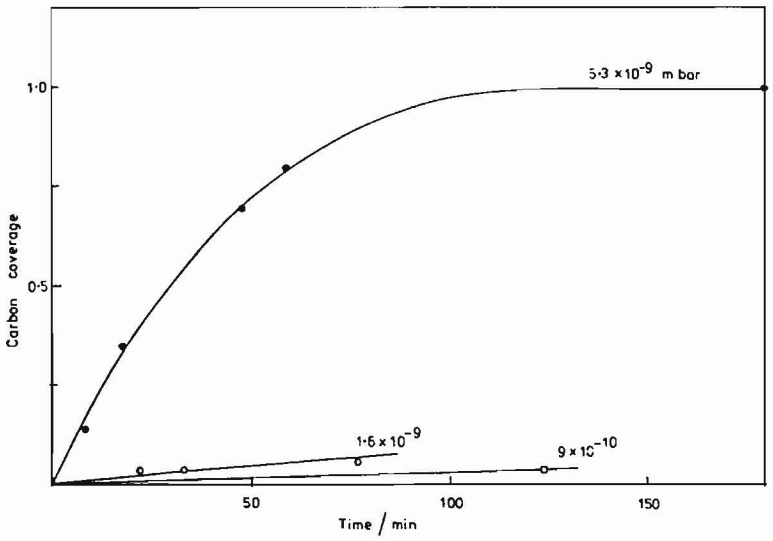


Figure (6) Comparison of rates of increase in surface coverage of carbon on pure ZnSe films on exposure to residual atmosphere containing different partial pressures of carbon monoxide.

RECEIVED 11-15-83

Development of RF-Sputtered Laser Coatings at Burleigh Northwest

David L. J. Lunt
Burleigh Northwest Optical, Inc.
Burleigh Park
Fishers, NY 14453

Complex dielectric coatings, with up to forty-three layers have been deposited using RF diode sputtering techniques. Deposition parameters have been established for ZrO_2, SiO_2 and Al_2O_3. Fabrication consistency has been high in both material properties and spectral response, and the coatings have shown useful damage, loss and environmental attributes, for laser applications, in the realms so far investigated.

Key Words: environmental stability; Excimer laser mirrors; infrared dichroics; monitoring accuracy; rf sputtering; thin film polarizers.

1. Introduction

We report here on preliminary results in the production of laser coatings by RF Sputtering. At Burleigh, we are concentrating on this form of deposition in an attempt to discover it's attributes and limitations in commercial applications. So far, three types of coatings have been investigated, and, in all cases, they show promise with respect to certain characteristics, and point to areas of further development.

Most of the previous work in this field[1,2,3] has been done with either single layers of material or small stacks of relatively simple structure with the aim of optimizing their laser damage resistance. The main emphasis of the present investigation is to look at the viability of the RF Sputtering process to deposit complex, large structures with specified spectral parameters and to look at the environmental stability of such structures.

2. Experimental

All depositions were performed in a modified, commercial sputtering chamber, arranged as an RF diode system (fig. 1). Power from a 3 KW, 13.56 MHz RF Generator can be directed to one of three, 8-inch targets via an impedance matching network. Substrates are supported, face up, on a water-cooled, indexing table such that the substrate/target distance can be varied between 2.5 & 4.0cm. The whole is supported on, and pumped by, a 6-inch diffusion pumped vacuum system incorporating a liquid nitrogen baffle and 'venetian blind' throttling valve.

Piezoelectric controlled gas inlet valves control the sputtering gas and reactive gas partial pressures, the former being in a feed-back loop with a capacitance manometer which monitors, and adjusts, the overall pressure in the chamber.

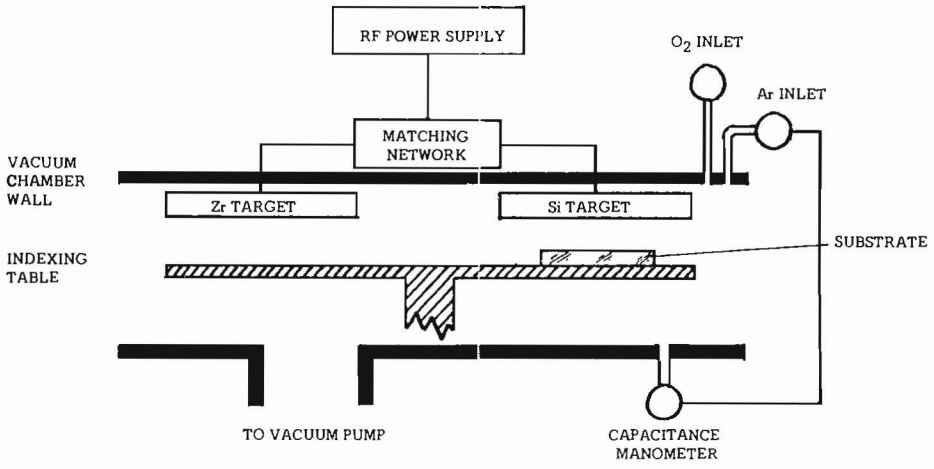


Figure 1. Schematic of RF Diode Sputtering System.

The mechanism of sputtering, in such a system has been described,[4,5] adequately, elsewhere and will not be repeated here.

In accordance with our present aim of looking at the design and structure of practical coatings for commercial applications, we have limited the number of materials used, so far, to three. The three target positions were installed with 8" x ¼", water-cooled targets of Si, Zr and Al. Each has an impurities level of $< 1.10^{-6}$. Similarly, we have limited the reactive gas to O_2, thus we have done all the investigation with the three oxides - ZrO_2, SiO_2 and Al_2O_3.

Overall, sputtering gas pressure has been maintained at 2.7Pa, a level deemed suitable, for present purposes, from previous reports.[1,2,3] Reactive gas partial pressure has been varied between 10% and 17.5%.

3. Material Constants

Prior to constructing coating stacks, an investigation was made of the refractive indices, dispersion and deposition rate of the three materials. These values are summarized in Table 1. There are some differences in these values compared to reports of previous work,[2,3] and these are merely noted here as they require further investigation. Significantly, the refractive index of the SiO_2 is very similar to that of bulk material. The refractive index of ZrO_2 is somewhat lower than previously reported,[1] and the deposition rates, in all cases, are also lower than in previous work. The deposition rates were calculated from the results of making single order (i.e. $\lambda/2$) filters of the appropriate material. For instance, for SiO_2, a coating was deposited consisting of:

HLLH

and for ZrO_2 the coating design was:

HLHLHHLHLH

where H represents $\lambda/4$ ZrO_2 and L represents $\lambda/4$ SiO_2. Both of these examples give transmission peaks sharp enough that measuring their wavelength position is very accurate.

Refractive index data was derived from measuring the reflectance of $\lambda/4$ layers deposited at various wavelengths. For this work, ZrO_2 and Al_2O_3 were deposited on fused silica substrates and SiO_2 on sapphire.

Table 1. Measured Characteristics of Reactively Sputtered Materials

MATERIAL	ZrO_2	SiO_2	Al_2O_3
DEP. RATE (@3W/cm^2)	9.35nm/min.	9.70nm/min.	6.60nm/min.
n @ 1064nm	2.00	1.45	-
n @ 550nm	2.03	1.46	-
n @ 350nm	2.10	1.475	1.63
n @ 308nm	2.15	1.48	1.65
n @ 249nm	2.25	1.50	1.75

4. Coating Design

Optimization of coating designs was performed on the Code $V^{(R)*}$ system. The coatings, so far investigated, were chosen from existing commercial requirements. The first example is a thin-film polarizer at Brewster's angle centered at 1064nm. In order to minimize the effects of environmentally induced spectral shifts, a primary consideration of the design exercise was to produce as wide a bandwidth as possible. In this instance, bandwidth refers to the spectral width over which the transmittance in 'P'-polarization is high and that in 'S'-polarization is low. The first design consisted of 43 layers made up of a 27 layer, $\lambda/4$ stack with "matching" layers of unequal thickness on either side to flatten the P-polarization transmission band. This example had a theoretical bandwidth of 45nm.

Results with this coating allowed us to embark on a second, improved polarizer. It was deemed advantageous to reduce the number of layers, if possible, in order to decrease total losses in the coating. Measurements of the environmental stability of the coatings and the reliability of deposition allowed this to be done by decreasing the required bandwidth and letting the computer program vary all the layers. The result was a 33 layer design with layer thicknesses all different and a theoretical bandwidth of 30nm.

The second coating example is an infrared dichroic. We had three similar requirements from customers. All three required high reflectance (> 99%) at 1064nm in 'P'-polarization. All required high transmittance in 'P'-polarization but in different wavelength regions. They were, respectively:

1300 - 1800nm
2200 - 3300nm
1500 - 4500nm

It was decided to attempt a design that would suffice for all three cases. This ultimately consisted of a 29 layer, all different thickness, stack of ZrO_2 and SiO_2 and had, theoretically, > 99.5% transmittance from 1230nm to 4500nm.

The third coating, for which we have only very preliminary results, presently, was a high reflecting, $\lambda/4$ stack for use with excimer lasers. This was done with both ZrO_2/SiO_2 and Al_2O_3/SiO_2 combinations with the stated aim of being able to use the resultant mirrors with the coating in contact with the laser gas.

5. Results

Adequate spectral characteristics were achieved from the first coating runs of both the thin-film polarizer and the infrared dichroic. Specifically, 'P' transmittance for the polarizer was 98% and 'S' transmittance < 0.5%, both measured at 1064nm. The bandwidth was 42nm. Reflectance measurements in 'P' polarization, indicated a total loss of ~ 0.7%. Eleven subsequent depositions also achieved a minimum of these specifications. The infrared dichroic had a measured 99.5% R at 1064nm and > 99% T from 1240nm to 4500nm. This coating has now been run seven times with similar results. These seven coatings were distributed between depositions on substrates of fused silica, calcium fluoride and sapphire.

The spectral shift versus humidity was determined for the polarizer by measuring the central wavelength after immersing the coating in distilled water for 72 hours and after subsequent baking for 24 hours, in vacuo. The resultant shifts of 1-2nm were probably within the measurement error of the equipment. This result indicated that it was not necessary to rely on excessive bandwidth in order to overcome the difficulties of environmental instability, and resulted in the second polarizer design. This again worked from the first deposition and is the solution presently in production. The measured losses in this coating appear to be < 0.4%. A typical angular scan, at 1064nm, of one of these polarizers is shown in figure 2.

The only result presently available for the excimer mirror sample, is a lifetime of 8.10^7 shots, for the ZrO_2/SiO_2 sample, in a commercial XeCl system, noted by one of our customers in a private communication. Investigations are presently being conducted along similar lines with Al_2O_3/SiO_2 stacks at 249nm as well as 308nm.

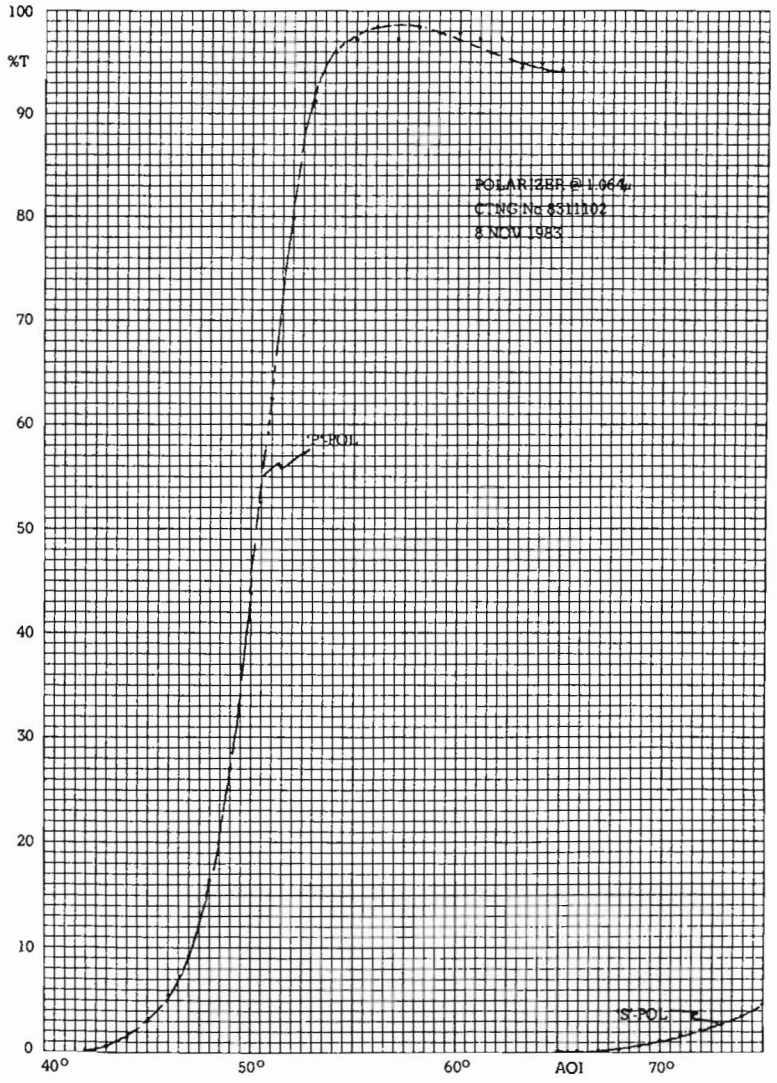


Figure 2. Angular Scan @ 1064nm of Thin Film Polarizer.

6. Conclusion

Current results indicate that coatings as deposited by RF Sputtering at Burleigh have significantly reduced the environmental instabilities caused by moisture which are a characteristic of evaporated coatings. It would also appear that the control presently excercised over the process parameters and the accuracy of monitoring is such as to allow complex coatings to be fabricated reliably and consistently. Previous work[3] has shown sputtered materials to have usefully higher laser damage thresholds, and this, together with the present work, indicates three criteria for assessing the potential of attempting a solution by sputtering. They are:

a) Requirement for higher damage threshold.
b) Requirement for high environmental stability.
c) The spectral characteristics requiring a highly complex design.

Thus far, our results have been commercially viable. However, further work is continuing in the use of other materials, reducing scattering and absorption losses and the production goal of fully automatic deposition.

7. References

[1] Pawlewicz, W. T., D. D. Hays, P. M. Martin; High Band Gap Oxide Optical Coatings for 0.25 - 1.06μm Fusion Lasers. Thin Solid Films, 73 (1980) 169-175.

[2] Pawlewicz, W. T., R. Busch; Reactively Sputtered Oxide Optical Coatings for Inertial Confinement Fusion Laser Components. Thin Solid Films, 63 (1979) 251-256.

[3] Pawlewicz, W. T., R. Busch, D. D. Hays, P. M. Martin, N. Laegreid; Reactively Sputtered Optical Coatings for use at 1064nm. Laser Induced Damage in Optical Materials. Nat. Bur. Stand. (U.S.) Spec. Publ. 508; 1979, 359-374 p.

[4] Hyman, P.; Ionic Bombardment Theory and Applications, J. J. Trillot, ed., Gordon & Breach, New York, 1964.

[5] Laegreid, N., G. K. Wehner; J. Appl. Phys., 32, (1961), 365-369.

* Code V(R) is a trademark of Optical Research Associates, Inc.

In response to the question, the speaker stated that they had not made direct measurements of the absorption coefficients of their evaporated layers, as distinct from absorption itself. They believed that much of the observed loss in transmission arose from scattered light rather than from absorption. Although evaporated zirconia is often homogeneous, they have not noticed any inhomogeneity in rf sputtered zirconia which is sufficient to affect the practical values of the multilayer coatings they have made. They have not studied the question in detail, however. They are producing coatings containing aluminum oxide and silicon dioxide which look quite promising in the ultraviolet from spectrophotometric tests of transmission and reflection. More careful absorption measurements are underway but no results yet. Varying the oxygen to argon rate from 17.5% to 10% oxygen increases the deposition rate by about 20%, but they did not notice any effect on the optical properties.

Manuscript received 3-21-84/sar

Comparison of Optical Coatings Deposited by Novel Physical and Chemical Techniques*

F. J. Wodarczyk, D. R. Strauss, and A. B. Harker

Rockwell International Science Center
P. O. Box 1085
Thousand Oaks, California 91360

We have undertaken a systematic study of various methods of depositing good quality thin films of optically interesting materials by different physical and chemical methods in an effort to identify promising techniques for producing low-absorbing, low-scatter, high damage-threshold coatings. The deposition methods studied include e-beam deposition in a UHV environment, sol-gel processes utilizing hot isostatic pressing (HIP) to densify the films, photochemical deposition using organometallic reagents entrained in inert or potentially reactive gas flows, and ion-beam deposition in a reactive environment. The deposited single-layer films were analyzed using various surface analysis techniques to provide information on film composition, stoichiometry, and impurity level.

Key words: AlN, hot isostatic pressing, organometallic reagents, photochemical deposition, reactive ion beam, sol-gel, surface analysis, TiO_2, ultrahigh vacuum.

1. Introduction

The extremely demanding environment of high-energy laser systems and the stringent requirements of laser gyro-based navigational systems have created a critical need to develop optical thin film coatings with properties more nearly approaching those of the bulk starting materials [1]. Undesirable properties exhibited by many present coatings include absorption due to impurities and defects, nonuniformity in chemical composition, thickness, and index of refraction, and high levels of stress between layers. These properties can lead to low damage thresholds and environmental instability in deposited coatings. The study of novel methods of thin film deposition reported here was undertaken to identify alternative techniques which show promise for circumventing some of these problems. The resultant coatings were analyzed using various surface analysis techniques including X-ray photoelectron spectroscopy (XPS), secondary ion mass spectroscopy (SIMS), and scanning Auger microscopy (SAM).

Several deposition techniques were used to deposit single-layer thin films of optically interesting materials. One material, TiO_2, was deposited using each technique and offers a basis for comparison. The methods studied were

1. conventional thermal evaporation using an electron beam source in a UHV deposition chamber;
2. sol-gel processing using hot isostatic pressing to help densify the films;
3. photochemical deposition using low pressures of organometallic reagents entrained in inert and reactive gas flows and irradiated with ultraviolet and visible lasers and lamps; and
4. ion-assisted deposition in a reactive environment.

Single layers of thin films were examined in order to simplify analysis and to be free of complications caused by additional interfaces, materials, and other sources of defects and absorption present in multilayer films.

*This work is supported in part by the Air Force Office of Scientific Research (AFSC) under Contract F49620-81-C-0074. The United States Government is authorized to reproduce and distribute reprints for governmental purposes notwithstanding any copyright notation hereon.

2. Electron Beam Evaporative Deposition Studies

Since many film properties, such as stoichiometry, purity, uniformity, and stress distribution, are inherently established by nucleation and interfacial effects, ultra-high vacuum (UHV) technology provides a means of depositing thin film coatings under conditions such that contamination of the film and interfaces by the chamber environment are minimized. We have designed and constructed a UHV thin film deposition chamber to study both conventional evaporative deposition as well as ion-beam assisted deposition methods.

The chamber consists of a stainless steel cylinder with multiple ports for the incorporation of various vacuum pumps, deposition sources, and monitoring and characterization instruments. A base pressure of less than 5×10^{-10} Torr is achieved after bakeout using a cryogenic pump on an 8" flange. A 330 l/s turbomolecular pump is used for initial high vacuum pumpout of the chamber or substrate load-lock as well as to maintain an operating pressure in the 10^{-4} Torr range during deposition when the system is operating with high gas flows. A Thermionics three-crucible electron beam thermal deposition source is mounted in the bottom of the chamber and shielded from the main deposition region by a cryopanel, which can be cooled with water or liquid nitrogen. A sample manipulator with micropositioners provides for both heating and cooling of the substrates as well as three-dimensional alignment, rotation, and tilt adjust. A sputter ion gun is directed at the sample and was used to clean the substrates prior to evaporative deposition. Windows allow access for an optical thickness monitor, ellipsometer, and laser beam irradiation of the substrate. A quartz crystal oscillator is used to monitor the thickness of the depositing films, and a residual gas analyzer monitors chamber gases at partial pressure as low as 10^{-13} Torr over a mass range 1 to 200 amu.

TiO_2 films were deposited on 1 in. diameter Pyrex or fused silica disks which were cleaned with dilute Alconox detergent, rinsed in deionized water, methanol, and ethanol, and then oven dried at 100°C. The TiO_2 starting material was Marz pure, and the O_2 was of research grade purity. Substrates were heated to 150°C by a ceramic element or an electron gun sample heater. The e-gun thermal source was degassed in vacuum at low power levels, and then depositions were carried out with a reactive O_2 background at pressures between 10^{-5} and 2×10^{-4} Torr. Deposition rates were on the order of 10 nm/min, and quarter- or half-wave optical thickness points were determined using the optical thickness monitor and an 800 nm narrowband filter before the detector.

The sample film absorption spectrum in the visible and near infrared was found to depend sensitively on O_2 background pressure, but optical absorption could usually be removed by heating in an oven. Figure 1 shows a visible spectrum of a TiO_2 coating that had been heated in air for 16 hours at 300-400°C. The upper spectrum (squares) is due to the pyrex substrate, while the points in circles trace the spectrum of the TiO_2 film after heating. From the match of the half- and full-wave points to the substrate transmittance, it can be seen that absorption is negligible to the accuracy of the measurement. The solid line is a numerical fit of the data which uses for the refractive index of TiO_2 a dispersion equation of the form

$$n^2 = A + \frac{B}{\lambda^2 - C} \qquad (1)$$

for wavelengths longer than 350 nm, below which TiO_2 absorption quickly dominates [2]. An observed shift in the half- and quarter-wave positions in the thin film spectrum after heating suggests a densification of the film, while XPS analysis shows that oven treatment caused the [O]/[Ti] ratio in the film to increase to the full stoichiometric value of 2. After oven treatment the film passed both adhesion and scratch tests, whereas similar films without oven heating failed. The likely explanation for the improved characteristics in oven treated films is that the films deposited under these conditions are porous and nonstoichiometric, but heating promotes further oxidation of the film, improving both the stoichiometry and film morphology. Scanning electron microscopy showed smooth surfaces, without the pinholes seen in some of the commercial films we have examined, although spitting by the evaporation source was evident from the 0.2-2 μm-sized particles in some films. X-ray diffraction measurements on several films revealed no TiO_2 diffraction patterns, indicating very small-grained crystals are deposited under the conditions used here.

Examination of the spectral fit in figure 1 shows reasonable agreement between experimental and calculated curves. Deviations are due mostly to the nonuniform film thickness. The numerical fit for this sample yielded A = 7.053, B = 0.1500, and C = 0.1135, while literature values [2] for rutile ordinary (extraordinary) rays are A = 5.913 (7.197), B = 0.2441 (0.3322), and C = 0.0803 (0.0843). These values give a refractive index at 633 nm of 2.76 for the fitted curve and 2.59 (2.89) for the literature ordinary (extraordinary) index.

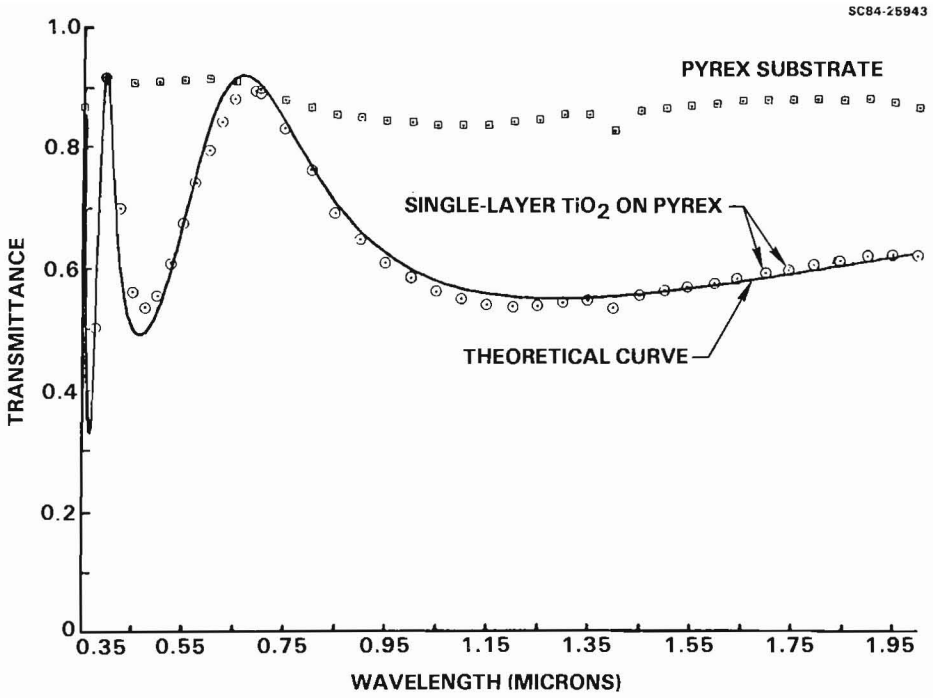


Figure 1. Visible spectrum of thermally-evaporated TiO_2 film (circles) and pyrex substrate (squares). The solid line is a numerical fit to the data using equation 1 for the TiO_2 dispersion and a constant index of 1.52 for the substrate.

3. Sol-Gel Deposition

Sol-gel processing is a wet-chemical technique which has recently been applied to the deposition of optical thin film coatings [3]. The fabrication of optical films through the use of sol-gel technology is attractive in that the process does not involve the complexities and equipment associated with conventional vacuum or UHV techniques. In this process a thin liquid film is hydrolyzed on a substrate, then rapidly fired to both oxidize and consolidate the film. The application solution is normally a dilute alcohol/water solution with an organometallic such as titanium n-propoxide. Amorphous films up to several hundred nm thick can be deposited by dipping, spinning, or spraying substrates with these solutions. Many favored optical materials can be deposited, such as TiO_2, Ta_2O_5, Al_2O_3, and SiO_2. An advantage of this technique is that the refractive index of the films can be changed by varying the sol-gel mix of the reagents and by introducing porosity.

The films produced in this manner have two major drawbacks for use in reflective coatings. First the rapid firing process can produce enclosed porosity. While porosity may be desirable for graded-index antireflection coatings, it is not useful in high reflection mirror coatings. Secondly, such porosity often serves as a site for the buildup of carbonyl impurities which act as absorption centers lowering the damage threshold of the film. This carbonyl impurity appears to arise from the metal alkoxide, not the solvent alcohol, judging from the similarity between XPS spectra of sol-gel films and photochemically produced films. This behavior was observed in making single layer sol-gel films of TiO_{1+x} on silicon and fused silica substrates.

To solve the problems of film porosity and residual hydrocarbon contamination, we embarked on a study to apply the Hot Isostatic Pressing (HIP) technique to sol-gel deposited coatings. In this method, the coatings are subjected to a high isostatic pressure of inert gas and high temperature for times on the order of hours. In our experiments, the Ar contained minute quantities of residual O_2 which was hoped would help oxidize the incorporated hydrocarbons. In initial experiments, OXCO Liquid Oxides (Oxitane Co., Akron, OH), proprietary alcoholic solutions of metal alkoxides, were used to form thin film coatings of TiO_2 on silicon and silica substrates. The substrates were dipped or spun in solutions with an equivalent oxide content of 3% TiO_2 under a He atmosphere, followed by vacuum-drying at 50°C. The coatings were then densified by rapid firing in air at temperatures from 400 to 600°C. Before HIP treatment the resulting films were approximately 5000 Å thick.

XPS and SIMS were used to analyze the coatings. Figure 2a shows the C 1s XPS spectrum taken on the surface of such a film before HIPping. The higher energy peak at 287 eV corresponds to a carbonyl carbon impurity in the film; the main line at 284.6 eV being that from adsorbed

adventitious carbon (CH_3-CH_x). Ion beam profiling showed this carbonyl impurity to be distributed throughout the film and to be present even after firing the films at 600°C for periods of 6 to 10 minutes. Longer or higher temperature firing of these films to remove the impurity leads to annealing and grain growth, inducing undesirable stress in the near amorphous films.

To observe if low temperature-high pressure hot isostatic pressing (HIP) would be beneficial, samples were HIPped at 600°C and 20,000 psi of Ar for periods up to one hour. As can be seen in figure 2b, this process indeed removed the deleterious carbonyl impurity while increasing the oxygen content of the film to $TiO_{1.7}$. The HIP treated films showed good hardness and adhesion to the substrates and no degradation in optical properties. Further work in applying this technique to multilayer coatings is being pursued.

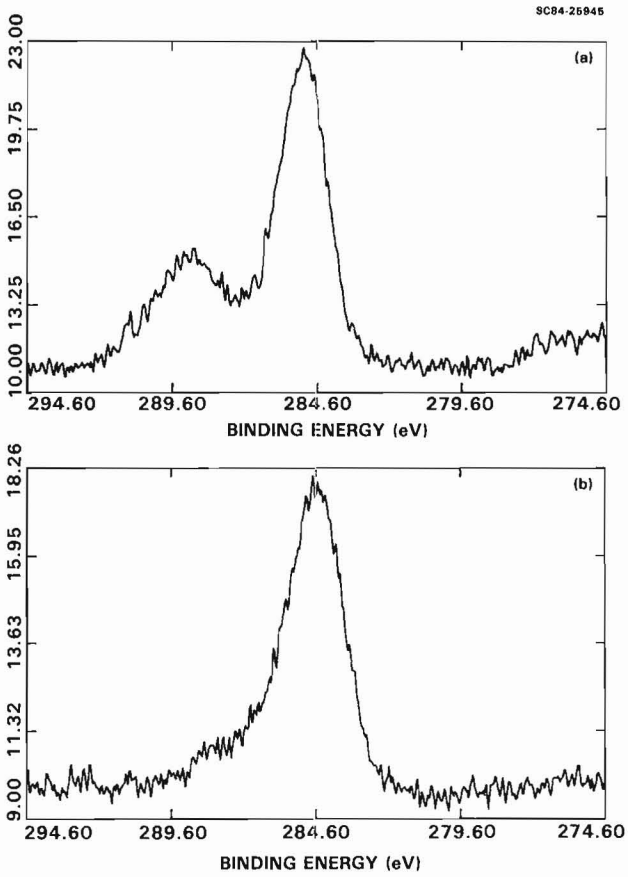


Figure 2. XPS C1s spectra from sol-gel TiO_2 coatings before and after hot isostatic pressing.

4. Photochemical Deposition

Chemical vapor deposition (CVD) is now routinely used for producing high purity semiconductor materials. Although good quality dielectric films have reportedly been made with CVD techniques [4], and there is a considerable literature on using photochemical methods of depositing thin films for various applications [5-11], these methods are not generally employed in optical coating fabrication. We therefore undertook a study to determine the feasibility of using photochemical techniques in producing optical-quality thin film coatings.

Photochemical methods share many advantages with CVD over evaporative techniques, such as allowing the deposition of refractory materials without using high source temperatures with their resulting contaminants. Photochemical methods also avoid some disadvantages of conventional CVD, such as high substrate temperature, which might aggravate problems due to thermal mismatch between film and substrate. Masking of a substrate is straightforward in a photochemical process, and thicknesses and mixture compositions can be well controlled using the excitation radiation intensity or reagent pressures.

Initial experiments were concerned with depositing films of Al_2O_3 by ultraviolet irradiation of flowing mixtures of trimethylaluminum (TMA) and an oxidizer (e.g., N_2O or O_2). Later experiments used the photodissociation of titanium (IV) isopropoxide, $Ti(OC_3H_7)_4$ to make TiO_2 films, analogous to the CVD reactions [12].

A variety of radiation sources were used in this work. Two excimer lasers offered high-power pulsed ultraviolet light: a Lambda Physik EMG 101 operating on the XeCl lines at 308 nm (70-100 mJ/10 ns pulse), and a Tachisto TAC-II operating on the KrF transition at 248 nm (10-20 mJ/10 ns pulse). A third laser, a Liconix 4050 He-Cd laser (8 mW at 326 nm), provided cw ultraviolet high intensity radiation. In addition, three high output power lamps were used to give more uniform, if somewhat less intense, cw radiation. These were an Oriel D_2 lamp (60 W), an Oriel Xe arc lamp (500 W), and a Carl Zeiss 200 W Hg lamp. In most experiments the output radiation was spatially filtered and focussed with lenses to obtain the most uniform beam profile.

The reagent organometallic compounds were obtained from Alpha Ventron. Since both compounds are water-sensitive, care was taken not to expose them to air. The TMA was subjected to freeze-pump-thaw cycles and vacuum distilled in a stainless steel vacuum line, while the titanium compound was used as supplied. Buffer gases (Ar, N_2, or He) were at least 99.99% pure.

The experiments were carried out in a stainless steel cell shown in figure 3. The cell was fitted with SiO_2 or CaF_2 windows mounted to allow irradiation either parallel or perpendicular to the substrate surface. The light input windows were purged with a flow of inert gas (Ar, He, or N_2) to prevent film deposition directly on them. Substrates were mounted either in the output port or in a copper holder in the cell which could be heated using ceramic-insulated hermetically sealed resistance heaters. Substrate temperatures were measured with Pt element resistance temperature detectors held against the substrate at two points. The cell was evacuated to the $\sim 10^{-3}$ Torr region using a trapped mechanical vacuum pump, and the entire vacuum system could be pumped to the 10^{-6} Torr range using a liquid nitrogen trapped oil diffusion pump. Pressures were measured a capacitance manometer.

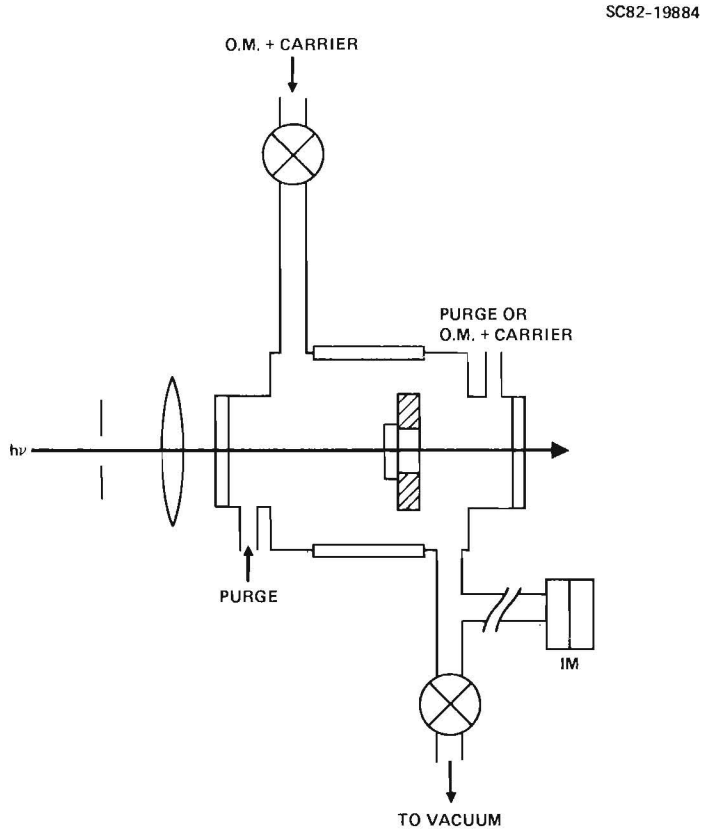


Figure 3. Schematic diagram of stainless steel photochemical deposition cell. Organometallic reagent (M.O.) entrained in low-pressure inert gas flows past the substrate mounted in the cell. Pressures are measured with inductance manometer (I.M.).

Initial experiments were conducted using a KrF laser to deposit Al_2O_3 films on room temperature CaF_2 substrates. The substrates were cleaned in vacuo with 100 pulses of focused KrF laser (15-20 mJ/pulse) and then a mixture of 7 Torr TMA and 40 Torr N_2) were added and irradiated with another 100 laser shots. Visual inspection of the substrates showed a clear rectangular deposit in the focused laser-irradiated area, which XPS analysis showed to be Al_2O_3. The XPS spectra show not only the usual adventitious C 1s signal at 284.6 eV, but also a C 1s peak at 289.3 eV. Ar+ sputtering of a subsequent sample showed this signal to be inherent in the film. This high energy peak is very likely due to a carbonyl, as in an ether or ester, and is strikingly like those found in the sol-gel films.

In the initial photochemical experiments to produce TiO_2 films from titanium isopropoxide, it was hoped that optical excitation might proceed by a sufficiently different pathway from CVD pyrolysis experiments so that no oxidizing ambient would be required in the reaction cell, simplifying the process. The vapor pressure of the isopropoxide at room temperature is estimated to be near 100 mTorr. The initial experiments were performed with the KrF laser at 248 nm, where the extinction coefficient is 2800 l/mole/cm [R13]. Flows of the order of 50 cc/min of isopropoxide entrained in He were pumped through the cell, while 100-200 pulses of 10 mJ each impinged on the room temperature quartz substrate. Smooth deposits with the profile of the laser spot were easily seen, but in addition there were lighter deposits outside the laser irradiation zone. The XeCl laser at 308 nm was also tried, and the resulting deposits, although optically inhomogeneous, were hard and very adherent.

XPS analysis showed that the film stoichiometry and mechanical properties were not as good as those of the e-beam evaporated films. Oven treatment of the photochemical films increased optical absorption in the films, in contrast to the thermally deposited films. The XPS data also show the presence of a Ti-containing organometallic component to the deposited film, a consequence of incomplete reaction.

Since the beam profile of our available pulsed lasers would not allow deposition of good optical quality films, high intensity ultraviolet lamps were used, which necessitated using longer irradiation times but yielded optically more acceptable coatings. A focused D_2 lamp ($\sim$ 30 W) was directed on a CaF_2 substrate for 15 hours in a cell with a total pressure of 10 Torr, mostly Ar. A film measured with a profiling stylus to have a thickness of $\sim$ 300 nm formed in the center, but in addition there was a thinner, lighter annular film. An 8 mW He-Cd laser at 326 nm, directed through a quartz light pipe to homogenize the output beam profile, similarly produced a film with a heavier, well-defined center where the laser hit and a light annular deposit around it. Light from the laser gas discharge, isolated by detuning the cavity mirrors to stop lasing, produced an even, homogeneous-appearing coating on the quartz substrate.

In an effort to determine the origin of the homogeneous-appearing annular film outside the irradiated zone, the standard gas mixture was flowed past the substrate for 3 days with no irradiation. The fragile thin flakes found on the substrate blew off easily and probably resulted from reaction with residual air or water contamination in the cell or flow system. When a Hg lamp was masked and directed parallel to a substrate surface, a light even film formed on the surface after 6 hours of flowing the Ti reagent in Ar. Thus it appears that at the reagent gas pressures used, the molecules which were dissociated some distance from the surface have time to diffuse to the substrate and deposit.

The effect of temperature on the film properties was also studied. It was found that substrate temperatures greater than 150°C caused film deposition over several hours, but that temperatures less than 110°C did not. However, substrates at 110°C which were irradiated with Xe or Hg lamps produced 0.3-0.5 μm thick deposits. These films were generally harder than most of the other photochemical films.

Some of the films produced by this technique were analyzed with an X-ray diffractometer, but no peaks were detected, indicating the absence of large crystalline grains. SEM photos with a resolution better than 100 nm similarly did not reveal large crystallites. XPS spectra were taken of representative films. Peak binding energies were found to be characteristic of Ti and O in the proper chemical environment for TiO_2, but the O/Ti ratios were less than 2. Examination of the spectrum in the C 1s region shows the same type of higher energy peak found in the TMA-produced photochemical deposits as well as in the sol-gel films, characteristic of a C bonded to an O, implying some organometallic incorporation in the Ti film.

Next, photolysis of the isopropoxide in the presence of oxidizer was attempted in order to improve the stoichiometry of the deposited films. The photolysis cell was prepared before each experiment by flowing dried N_2 or O_2 through the cell for several hours in order to purge the walls of H_2O. Early experiments used N_2 (4 Torr) as the carrier gas and N_2O (2 Torr) as the oxidant, while later experiments used O_2 as both carrier and oxidant gas at 10-20 Torr pressure. Reactions

were carried out with either Hg or Xe lamps and with substrate temperatures up to 120°C. XPS and SIMS spectra indicate that the best films result from photolysis of the isopropoxide in pure O_2 at pressures at or slightly above 10 Torr and with the substrate temperature about 120°C. They show little sign of the -CO- contamination exhibited by films made without oxidant.

5. Reactive-Ion Deposition

The secondary ion sputter deposition technique provides the experimentalist with direct control of primary beam energy, density, direction, and chemical composition [14]. Such independent control of deposition variables has led to the use of a dual-ion deposition technique in the production of ultra-high performance laser mirror coatings with reflectance better than 99.99% and scatter less than 1 ppm [15].

In this program a single 3 cm Kaufman ion source (Commonwealth Scientific) with a collimated beam was used to study the controlling process features. A single ion gun system was used in these initial experiments rather than the dual gun approach to simplify the experimental configuration. The primary ion beam (0-50 mA, 200-1500 V) passes through an electron neutralizer to minimize divergence and target charging. Typical operating conditions used a beam energy of 600-1000 V with an ion flux of 1 mA/cm^2. The secondary ions and atoms produced at the target are emitted with energies of 20 to 80 eV, producing film growth rates on the order of 40-50 Å/min.

The experimental arrangement is similar to that used by previous workers [16]. The ion beam is directed at a metal target 15 cm from the source with its normal 45 degrees to the beam direction. A substrate is mounted another 45 degrees from the target normal at a distance of 2-4 cm. A quartz crystal thickness monitor is positioned next to the substrate to follow the progress of the deposition. The chamber is continuously pumped, and flow rates for the gases used (99.995% N_2 with <1 ppm O_2 and 99.9995% Ar with <0.1 ppm O_2) are maintained between 0.5 and 5 sccm, using mass flow controllers. During deposition, the total chamber pressure reaches typically 10^{-4} Torr. No attempt was made to heat or cool either target or substrate. After several hours of operation the substrate temperature was measured to be less than 120°C.

Elemental metal targets were used for the deposition experiments because they are available in higher purity and exhibit larger sputter rates than dielectric targets. Substrate materials used were CaF_2, fused silica, and single crystal Si. Substrates were cleaned in detergent, rinsed in distilled water, cleaned again in ethanol, and dried in a 50°C oven, with final cleaning by ion beam sputtering in vacuum.

The deposited films were characterized by XPS and SIMS. Optical spectra were recorded on a Cary 14 UV-VIS-IR spectrometer, while refractive index data were gathered using an automated ellipsometer. Film thicknesses were measured using a Dektak II profiling stylus, and a scanning electron microscope was used to examine microscopic details of the coatings.

The initial materials deposited by the single ion gun technique were oxide coatings of Ti and Al. No O_2 was flowed through the Kaufman type ion source to prevent oxidation of the hot filament, so oxygen was provided by backfilling the chamber. Single layer films ~ 1000 Å thick on CaF_2 substrates were deposited at various O_2 partial pressures. The films showed adequate adhesion and hardness, but were optically absorbing. XPS analysis showed [O]/[Ti] and [O]/[Al] ratios in the films to be oxygen-deficient. At the highest O_2 partial pressure in the chamber, (5×10^{-5} Torr O_2/ 5×10^{-4} Torr Ar) the observed [O]/[Ti] value was only 1.6; similar results were observed with Al. The standard means of optimizing stoichiometry is to use low O_2 pressures in the Ar carrier gas through the primary Kaufman sources, and to use a second ion source to sputter the substrate surface with further oxygen ions and excited neutrals. These processes both require extensive optimization and introduce further complexity in the chemical and physical process. A second approach to improving the oxygen stoichiometry in these films would be the use of a FAB source, in which excited oxygen neutrals could be produced exclusively without a carrier gas and the problems associated with filament reactions in the Kaufman sources. Such experiments are currently beginning. Therefore, the reactive ion studies were shifted to the fabrication of AlN, since with Kaufman sources, the filaments last much longer with N_2 rather than O_2 as the reactive gas.

AlN was chosen for this study because it is a promising dielectric material for advanced coatings. It is transparent from 200 nm to above 14000 nm and has a refractive index near 2, making it a reasonable candidate for a high-index component. With its high melting point (>2200°C) and low chemical reactivity, AlN is an excellent material for situations requiring chemical and thermal stability, such as excimer laser coatings, where photochemical degradation of the films is a problem, or in ring-laser gyro mirrors, to avert damage to the coatings due to UV radiation from the laser cavity plasma. Optical thin films of AlN for electronic applications have been deposited previously by various techniques, including chemical vapor deposition [17-18], reactive evaporation [19-20], reactive RF sputtering [21-23], and reactive ion beam sputtering [24-26].

Initially a mixture of Ar and N_2 was used in the ion beam source directed at the pure Al foil target. The sputter rate decreased as the proportion of N_2 in the beam gas mixture increased, but the film stoichiometry and other properties were found to improve with increasing concentration of N_2. Therefore, for many experiments, pure N_2 was used as the sputtering gas, giving somewhat slower deposition rates but enhanced film properties. Films were deposited on both glass and silicon substrates. The ion gun was typically operated at 600 V with a beam current of 5 mA. Initial experiments used Ar as the ionizing gas with N_2 as backfill at 10^{-4} Torr, but XPS analysis of the resulting films showed mixed Al/AlN deposition. Using mixed N_2/Ar as the ionizing gas improved deposition to where the film showed no elemental Al and AlN deposition rates of 25 nm/hr. This agrees with work conducted by Harper, Cuomo and Hentzell [25] which has shown that stoichiometric AlN is formed when the N_2^+ and Al arrive at the substrate at a ratio N/Al>1.

Again, the physical properties (adhesion, hardness, abrasion resistance) were excellent. XPS analysis showed a [Al]/[N] ratio of 1.0 for films deposited with the higher N_2 concentrations in the flowing gas mixture, as found by other workers using plasma and ion sputter techniques [25]. The optical spectrum of the best samples showed no appreciable absorption in the visible region, and ellipsometry revealed a homogeneous nonabsorbing film with a refractive index of 2.05 at 633 nm, comparable to previously reported values, and a short wave length cutoff of 0.2 microns. The films resisted chemical etching in HF and in aqua regia, but could be etched in a mixture of HF and H_2O_2.

SEM analysis of the films showed them to have the roughened surface characteristic of ion deposition and showed an indication of oriented columnar growth with column widths of 200-500 nm. XPS analysis gave further indication that the film had some enclosed porosity in that oxygen was observed in the bulk of the film. Since oxygen in the deposition chamber is present at less than 10^{-9} Torr level and does not appear in pure Al films it is concluded that the AlN film adsorbed water into its structure upon exposure to air.

The excellent durability and optical properties of this film make it a candidate for further development and use of dual ion-beam assisted deposition is currently being pursued to remove the residual porosity from the films. It is expected that the problems with porosity in these AlN films will be eliminated with the use of a second ion or fast atom source irradiating the substrate directly. We are currently beginning such experiments with a view towards optimizing the deposited film for good optical and mechanical properties to apply toward UV-visible laser coatings.

6. Summary

Table 1 shows a comparison of the stoichiometry of representative TiO_2 films made in the experiments described here. In general, experience has shown that there is a direct correlation between the [O]/[Ti] ratio and film properties: the closer the ratio is to the stoichiometric value of 2.0, the better are the optical and mechanical characteristics of the films. Of all the techniques used in these experiments, only e-beam thermal evaporation yielded films with the proper stoichiometry, and then only after oven heating. However, TiO_2 is a difficult material to deposit, since Ti can form compounds with oxygen in several stable oxidation states. Furthermore, the stoichiometry of films deposited in these initial experiments improved steadily with our experience, and there is every expectation that each technique can be made to produce films with the proper chemical composition, and by implication, the proper physical properties. For example, work on photochemical deposition has shown that the incorporation of O_2 into the flowing gas mixtures greatly improves

Table 1. Some properties of the best TiO_2 films resulting from these studies.

		Mechanical Tests		
Sample	[O]/[Ti]	Adhesion	Hardness	Comments
TiO_2 Standard	2.0	--	--	Powder
E-beam evaporated	2.0	Pass	Pass	After oven treatment
Sol-gel	1.5	Pass	Pass	-CO- present
Sol-gel + HIP	1.7	Pass	Pass	-CO- reduced
Photochemical, no O_2	1.6	Pass	Fail	T ~ 100°C; -CO- present
Photochemical + O_2	1.8	Pass	Pass	T ~ 120°C; -CO- reduced
Reaction ion	1.6	Pass	Pass	Single ion beam

film properties. Optimization of pressures, flowrates, and other experimental conditions should result in good quality TiO_2 films. The dual-beam reactive ion method currently is used to produce TiO_2/SiO_2 films with extremely low absorption and good optical properties [15]. The second ion beam in dual ion experiments adds O to the film in a more reactive form and provides energy to the growing film at the surface, which improves the morphology of coating by removing voids and reducing crystallite formation. Similarly, refinements in the preparation and firing of the sol-gel coatings are also expected to bring these coatings up to good quality optical coating standards. Experiments on each of these techniques are continuing and are hoped to result in coatings with higher damage thresholds and better mechanical properties.

7. References

[1] Winsor, H. V. Requirements and speculations about Air Force and DoD needs for a systematic coating science and technology base. Optical thin films, Proc. SPIE 325: 12-20; 1982.

[2] DeVore, J.R. Refractive indices of rutile and sphalerite. J. Opt. Soc. Amer. 41: 416-419; 1951.

[3] Yoldas, B.E. Deposition and properties of optical oxide coatings from polymerized solutions. Appl. Opt. 21(16): 2960-2964; 1982.

[4] Tietjen, J.J. Chemical vapor deposition of electronic materials. Ann. Rev. Mater. Sci. 3: 317-326; 1973.

[5] Coombe, R.D.; Wodarczyk, F.J. UV laser-induced deposition of metal films. Appl. Phys. Lett. 37(9): 846-848; 1980.

[6] George, P.M.; Beauchamp, J.L., Deposition of metal films by the controlled decomposition of organometallic compounds on surfaces. Thin Solid Films 67: L25-L28; 1980.

[7] Allen, S.D. Laser chemical vapor deposition, a technique for selective area deposition. J. Appl. Phys. 52(11): 6501-6505; 1981.

[8] Ehrlich, D.J.; Osgood, Jr., R.M.; Deutsch, T.F. Photodeposition of metal films with ultraviolet laser light. J. Vac. Sci. Technol. 21(1): 23-32; 1982.

[9] Johnson, W.E.; Schlie, L.A. Photodeposition of Zn, Se, and ZnSe thin films. Appl. Phys. Lett. 40(9): 798-801; 1982.

[10] Solanki, R.; Boyer, P.K.; Collins, G.J. Low-temperature refractory metal film deposition. Appl. Phys. Lett. 41(11): 1048-1050; 1982.

[11] Chen, C.J.; Osgood, R.M. Surface-catalyzed photochemical reactions of physisorbed molecules. Appl. Phys. A31: 171-182; 1983.

[12] Yokozawa, M.; Iwasa, H.; Teramoto, I. Vapor deposition of TiO_2. Japan. J. Appl. Phys. 7: 96-97; 1968.

[13] Dijkgraaf, C.; Rousseau, J.P.G. Electronic transitions in $TiCl_4$, $TiCl_3OR$, $TiCl_2(OR)_2$, $TiCl(OR)_3$ and $Ti(OR)_4$ ($R = iC_3H_7$). Spectrochim. Acta 24A: 1213-1217; 1968.

[14] Harper, J.M.E.; Cuomo, J.J.; Kaufman, H.R. Technology and applications of broad-beam ion sources used in sputtering. Part II. Applications. J. Vac. Sci. Technol. 21(3): 737-756; 1982.

[15] Sanders, V. (Rockwell International Autonetics Marine Systems Division). Private communication.

[16] Weissmantel, C. Reactive film preparation. Thin Solid Films 32, 11-18, (1976).

[17] Chu, T.L.; Kelm, R.W. The preparation and properties of aluminum nitride films. J. Electrochem. Soc. 122(7): 995-1000; 1975.

[18] Zirinsky, S.; Irene, E.A. Selective studies of chemical vapor deposited aluminum nitride-silicon nitride mixture films. J. Electrochem. Soc. 125: 305-314; 1978.

[19] Winsztal, S.; Wnuk, B.; Mayewska-Minor, H.; Niemyski, T. Aluminum nitride thin films and their properties. Thin Solid Films 32: 251-254; 1976.

[20] Yamashita, H.; Fukai, K.; Misawa, S.; Yoshida, S. Optical properties of AlN epitaxial thin films in the vacuum ultraviolet region. J. Appl. Phys. 50: 896-898; 1979.

[21] Duchene, J. Radiofrequency reactive sputtering for deposition of aluminum nitride thin films. Thin Solid Films 8: 69-79; 1971.

[22] Noreika, A.J.; Francombe, M.H.; Zeitman, S.A. Dielectric properties of reactively sputtered films of aluminum nitride. J. Vac. Sci. Technol. 6: 194-197; 1969.

[23] McMahon, R.; Affinito, J.; Parsons, R.R. Voltage controlled reactive planar magnetron sputtering of AlN thin films. J. Vac. Sci. Technol. 20: 376-378; 1982.

[24] Weissmantel, C. Reactive film preparation. Thin Solid Films 32: 11-18; 1976.

[25] Harper, J.M.E.; Cuomo, J.J.; Hentzell, H.T.G. Quantitative ion beam process for the deposition of compound thin films. Appl. Phys. Lett. 43(6): 547-549; 1983.

[26] Birey, H.; Pak, S.-J.; Sites, J.R. Photoluminescence of gallium arsenide encapsulated with aluminum nitride and silicon nitride. Appl. Phys. Lett. 35(8): 623-625; 1979.

Optical Characterization of Low-Scatter, Plasma-Deposited Thin Films*

W. D. Partlow and W. J. Choyke
Westinghouse Research and Development Center
Pittsburgh, Pennsylvania 15235

and

Jean M. Bennett
Michelson Laboratory, Physics Division
Naval Weapons Center, China Lake, California 93555

and

Robert M. Silva
VTI, Inc.
4126 Linden Ave., Suite 102, Dayton, Ohio 45432

Plasma-deposited thin films, sometimes called plasma CVD or plasma-enhanced CVD, are deposited in a low pressure gas phase reaction that is controlled by a glow discharge plasma. Substrate temperatures of 200 - 300°C, low compared to conventional CVD processes, are typical for plasma-coating processes. This new coating method has wide possible applications in the optics area. In this paper we will describe studies that have been made to determine if the films are suitable for critical optical applications requiring highly uniform, low-scatter films that, for example, could be used as mirror coatings or as graded index antireflection coatings. We have evaluated the surface quality of SiO_2 and Si_3N_4 films approximately 1000 Å thick, plasma-deposited onto silicon and silicon carbide substrates. Evaluation techniques have included surface profiling using a Talystep instrument, Nomarski microscopy, and total integrated scattering. In all cases, comparisons have been made between the coated and uncoated substrates. The best Si_3N_4 films have been found to contour the very smooth surfaces onto which they were deposited, while the SiO_2 films added only a minimal additional roughness, of the order of 2.8 Å rms. Some problems have been encountered, however, with particulates contained in the films; techniques for minimizing these effects will be discussed.

Key words: optical scattering; silicon dioxide; silicon nitride; surface roughness; thin films.

Introduction

It is of interest to determine whether the new coating technique of plasma deposition, described in a companion paper in this conference [1][1], is capable of producing films suitable for critical optical applications that require highly uniform, low scatter films. In this paper we will describe studies made on films of two candidate materials, SiO_2 and Si_3N_4. Evaluation techniques have included surface profiling, Nomarski microscopy, and total integrated scattering (TIS). We will show that under the proper preparation conditions, excellent, smooth, low-scatter films of these materials can be produced.

Experimental Measurements

The films were deposited in a transverse flow plasma reactor [1] using directly coupled RF excitation to maintain the glow discharge plasma, as shown schematically in figure 1. The deposition parameters for the two types of films studied are presented in table 1. These parameters were selected to produce a low power density plasma to minimize volumetric reactions that can cause particulate formation; these same deposition conditions minimize reactant depletion which causes nonuniformity over the sample surface. Particulate formation in the gaseous phase was kept at

*Work supported by Navy Independent Research Funding.
[1]Figures in brackets indicate the literature references at the end of the paper.

negligible levels by heating the upper electrode as well as the lower electrode, and by repeatedly cleaning the reactor by plasma etching followed by acetone swabbing with lint-free cloth.

Two types of substrates were used for most of the experiments: silicon wafers and ultralow-scatter, polished, single crystal bulk silicon. The silicon wafers, 5.1 cm in diameter and 250-μm thick, were commercial semiconductor grade material of 22-30 Ω-cm resistivity that were obtained from Pensilco, Bradford, Pennsylvania. They were Czochralski-grown single crystals oriented <100> ± 1°. Both sides were polished to a "scratch-free" specification using a colloidal silica-based chemical/abrasive technique.

Bulk <111> single crystal substrates 38.6-mm diameter and 9.52-mm thick were polished to an ultralow-scatter finish using a proprietary chemical/abrasive technique developed by VTI. The substrates were polished in blocks of 18, and TIS measurements showed that the scattering from five samples from this block sent to the Naval Weapons Center was very similar. One polished 19.0-mm-diameter <111> single crystal silicon substrate was also used (from a block of 10).

A film was also coated on a 38.6-mm-diameter, 6.35-mm-thick, polished CVD (chemical vapor deposited) silicon carbide substrate. The silicon carbide had been polished to a low-scatter surface that, however, had a long range waviness component.

Nomarski microscopy [2,3] was used to inspect the bare and film-covered surfaces to determine that they were suitable for optical measurements, i.e., free of particulates, cleaning smudges, etc. (The bulk silicon substrates were shipped covered with a strippable film.) Surface profile measurements were made on the bare and film-covered substrates using a Talystep surface profiling instrument [4] that had a special 1-μm-radius diamond stylus; 1-2 mg loading was used in order not to damage the coatings. The profiles were digitized into 1000 data points per profile (selected lengths between 1.5 mm and 15 μm), and a linear least squares fit to all the data points gave a value for the mean surface level. Root mean square (rms) values of the deviations of the measured points from the straight line were the rms roughness values. The Optical Evaluation Facility [5,6] was used for measuring scattering into a hemisphere with the red krypton laser line (wavelength 6471 Å, beam diameter $\sim$ 1 mm) as a source. Measurements were made in a series of concentric circles at approximately 19 places on the sample.

In order to determine the uniformity of the refractive index and thickness of the films, ellipsometric measurements were made on a Rudolph Auto EL-2 ellipsometer (70° angle of incidence, He-Ne 6328 Å wavelength). Measurements were made at 9 points in a square grid, with 1.3-cm separation between points.

Results

Initial experiments were made on silicon wafers. The surface texture was barely observable in the Nomarski microscope, and no difference could be seen between the uncoated wafers and those coated with SiO_2, as shown in figure 2. Incidentally, it was found that the standard microelectronics "scrub and clean" cleaning procedure increased the surface roughness by a factor of between 2 and 10 over that of an as-received or chemically cleaned wafer. (The roughness for a 600-μm-long profile increased from about 10 Å rms to over 20 Å rms, while the very short range roughness for a 15-μm-long profile increased from about 0.6 Å rms to over 7 Å rms.)

Figures 3 and 4 show surface profiles for a 1925-Å-thick SiO_2 film on a silicon wafer and a similar uncoated wafer. By comparing the profiles in these two figures, it is seen that the SiO_2 film contained a few imbedded particulates (fig. 3, 600-μm-long scan) and had a microstructure that was slightly rougher than that of the bare substrate (figs. 3 and 4, 15-μm-long scans).

In order to determine the added roughness contributed by the SiO_2 film, one can use the approximate relation:

$$\delta_f = \sqrt{\delta_{fs}^2 - \delta_s^2} \quad , \tag{1}$$

where δ_f, δ_{fs}, and δ_s are the rms roughnesses of the film, the film-coated substrate, and the bare substrate, respectively. From the 15-μm-long scans in figures 3 and 4, the added film roughness was determined to be 2.8 Å rms. No added roughness could be detected for Si_3N_4 films on silicon wafers.

Ellipsometric measurements were made on films deposited on silicon wafers to determine refractive index (n) and film thickness (t) uniformity, with the following results at a wavelength of 6328 Å:

SiO_2:	$n = 1.717 \pm 0.009$	Si_3N_4:	$n = 1.868 \pm 0.001$
	$t = 1925 \pm 88$ Å ($\pm 4.6\%$)		$t = 992 \pm 23$ Å ($\pm 2.3\%$)

From our previous experience, the standard deviation of ~ 0.01 obtained for the refractive index of the SiO_2 film is typical of these coatings; the 0.001 value for the Si_3N_4 film is probably fortuitously low. The film thickness uniformity of $\pm 4.6\%$ for the SiO_2 and $\pm 2.3\%$ for the Si_3N_4 is excellent, making these films suitable for critical optical applications.

As can be seen in figures 3 and 4, silicon wafers are not the best optical substrates because of the ripple or surface waviness, which is particularly evident in the 600-μm-long scans, and can also be seen in the Nomarski micrographs of figure 2. For this reason, further experiments were performed on high-quality, low-scatter, polished optical substrates.

In the next experiment, an attempt was made to deposit a Si_3N_4 film on a very low-scatter silicon carbide substrate. Unfortunately, the film contained a large number of particulates; it was removed by repolishing the substrate. The surface finish on the repolished substrate was not as good as had been obtained originally, and the bare substrate was not reprofiled before depositing the second film. However, it appears that the Si_3N_4 film prepared using the parameters in table 1 did not increase the roughness of the substrate. The Nomarski micrograph of the film-coated silicon carbide surface shown in figure 5 is essentially featureless. (A slight mottling is barely detectable on the original photograph.)

After the deposition process was optimized, Si_3N_4 films were deposited on 38.6-mm-diameter and 19.0-mm-diameter ultralow-scatter, polished silicon substrates. The Nomarski micrograph of the film-covered surface (fig. 5) showed no detectable surface detail; none was evident on any of the unfilmed silicon surfaces. Figures 6 and 7 show surface profiles for an approximately 1000-Å-thick Si_3N_4 film on a 38.6-mm-diameter ultralow-scatter silicon substrate and for a comparable uncoated substrate. The differences between the roughnesses on the filmed and unfilmed substrates are not significant. Comparable profiles were measured on the 19.0-mm-diameter silicon substrate. It is seen that the microroughness of the Si_3N_4 film is less than the instrumental noise for the 15-μm-long profile, suggesting that much thicker films could be made before the added film roughness would become appreciable.

For many optical applications, scattering is the most important parameter since it can adversely affect system performance. Therefore, scattering into a hemisphere was measured relative to the incident beam intensity. The results are given in table 2 for the krypton λ 6471 Å red line. Since the film had two boundaries and since interference effects of the scattered light could occur within the film if the roughness on the two film surfaces was correlated, no attempt was made to obtain an effective rms roughness for the surface, or even a value for the TIS, which requires a knowledge of the total reflectance (specular plus diffuse) of the surface. The values in table 2 are not scaled by the reflectance of the surface; the film changes both the scattering level and the reflectance. For this reason, it is not fair to say that the film reduces the surface scattering. However, it is clear that scattering levels of filmed and unfilmed surfaces are not greatly different. The results for the Si_3N_4 film on the repolished silicon carbide substrate and the original bare silicon carbide surface are not directly comparable; the repolished surface is actually rougher than the original surface and, in addition, particulates in the film added to the scattering level. We can conclude from the results shown in table 2 that the scattering into a hemisphere measured relative to the incident beam intensity is not greatly different for film-covered and bare surfaces. Also, all the values are in the 10^{-5} range, comparable to the scattering level for a high quality silver film on a very smooth polished fused silica surface.

Conclusions

In conclusion, we have shown that it is possible to produce smooth, particulate-free, low-scatter films of Si_3N_4 and SiO_2 that have uniform thickness over diameters as large as 5.1 cm. The results reported here are initial attempts, and presumably even further improvements can be made. Thus we have shown that excellent optical properties can be obtained in these films, which can be deposited at relatively low substrate temperatures, and offer a high degree of selectability of composition for critical optical applications.

The authors would like to thank R. A. Madia at Westinghouse R and D Center, who assisted with the film preparation, and P. C. Archibald at the Naval Weapons Center, who made the scattering measurements.

References

[1] Partlow, W. D.; Heberlein, J. V. R. "Plasma deposited inorganic thin films for optical applications," this conference.

[2] Nomarski, G. M. "Differential microinterferometer with polarized waves," J. Phys. Radium 16; 9; 1955.

[3] Nomarski, G. M.; Weill, A. R. "Application à la métallographie des méthodes interférentielles à deux ondes polarisées," Rev. Metall. 52; 121; 1955.

[4] Bennett, J. M.; Dancy, J. H. "Stylus profiling instrument for measuring statistical properties of smooth optical surfaces," Appl. Opt. 20; 1785-1802; 1981.

[5] Bennett, H. E. "Scattering characteristics of optical materials," Opt. Engr. 17; 480-488; 1978.

[6] Archibald, P. C.; Bennett, H. E. "Scattering from infrared missile domes," Opt. Engr. 17; 647-651; 1978.

Table 1. Deposition parameters

Coating	Reactant gas ratios	Electrode temp., °C	Deposition rate, Å/min
SiO_2	SiH_4/N_2O:1/5.2	300	400
Si_3N_4	$SiH_4/NH_3/N_2$:1/18.5/8.6	300	100

Table 2. Hemispherical scattering measured relative to the incident beam intensity for plasma-deposited films and uncoated substrates (λ 6471 Å)

Si_3N_4 on silicon (0.75" diam)	$1.94 \pm 1.43 \times 10^{-5}$
silicon (0.75" diam)	$2.64 \pm 1.24 \times 10^{-5}$
Si_3N_4 on silicon (1.52" diam)	$2.63 \pm 1.16 \times 10^{-5}$
silicon (1.52" diam)	$2.76 \pm 3.45 \times 10^{-5}$
Si_3N_4 on silicon carbide (1.52" diam)[a]	$7.25 \pm 2.01 \times 10^{-5}$
silicon carbide (1.52" diam)	$2.59 \pm 0.33 \times 10^{-5}$
Silver on fused silica	$4.82 \pm 1.15 \times 10^{-5}$
Aluminum on Zerodur	$1.11 \pm 0.24 \times 10^{-4}$

[a]Repolished; rougher than original surface; particulates added to scattering level.

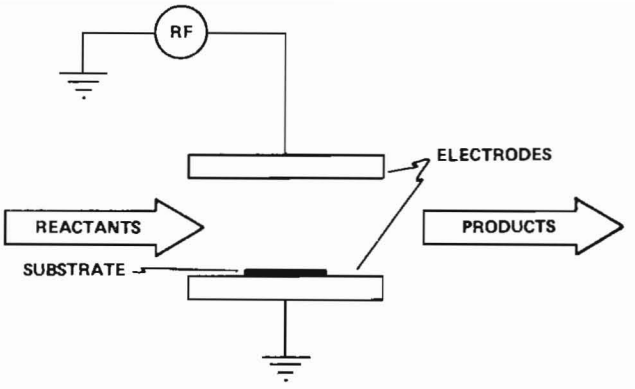


Figure 1. Schematic diagram of plasma reactor.

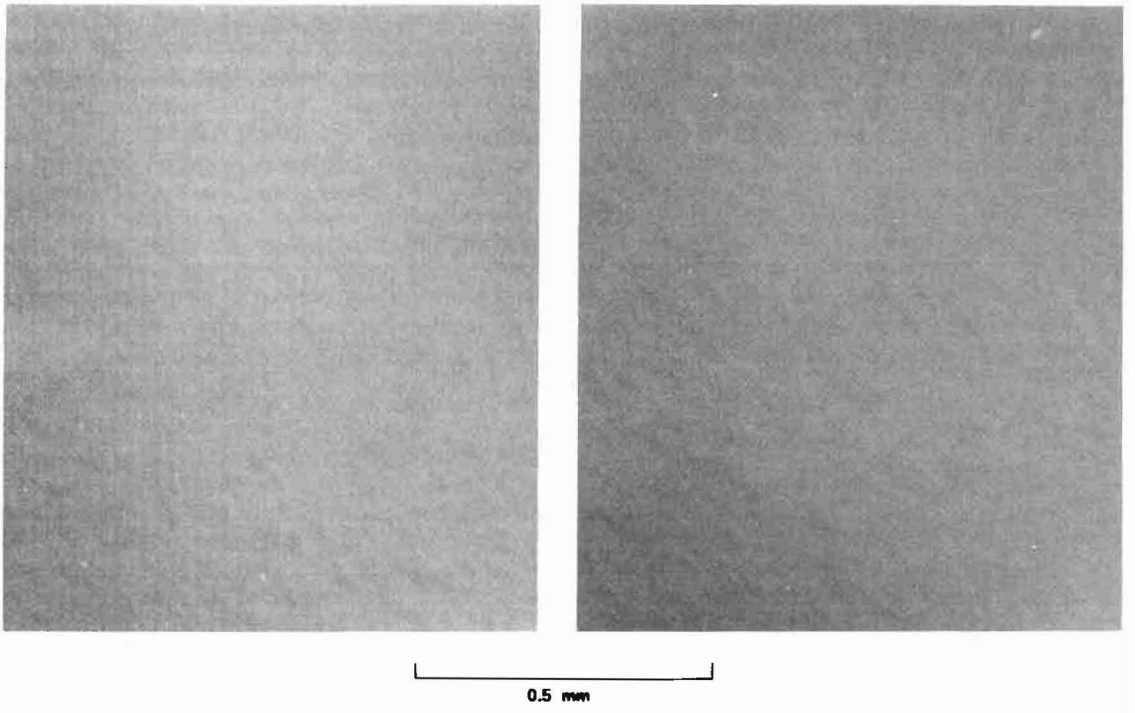


Figure 2. Nomarski micrographs of a plasma-deposited SiO_2 film on a silicon wafer and a bare silicon wafer.

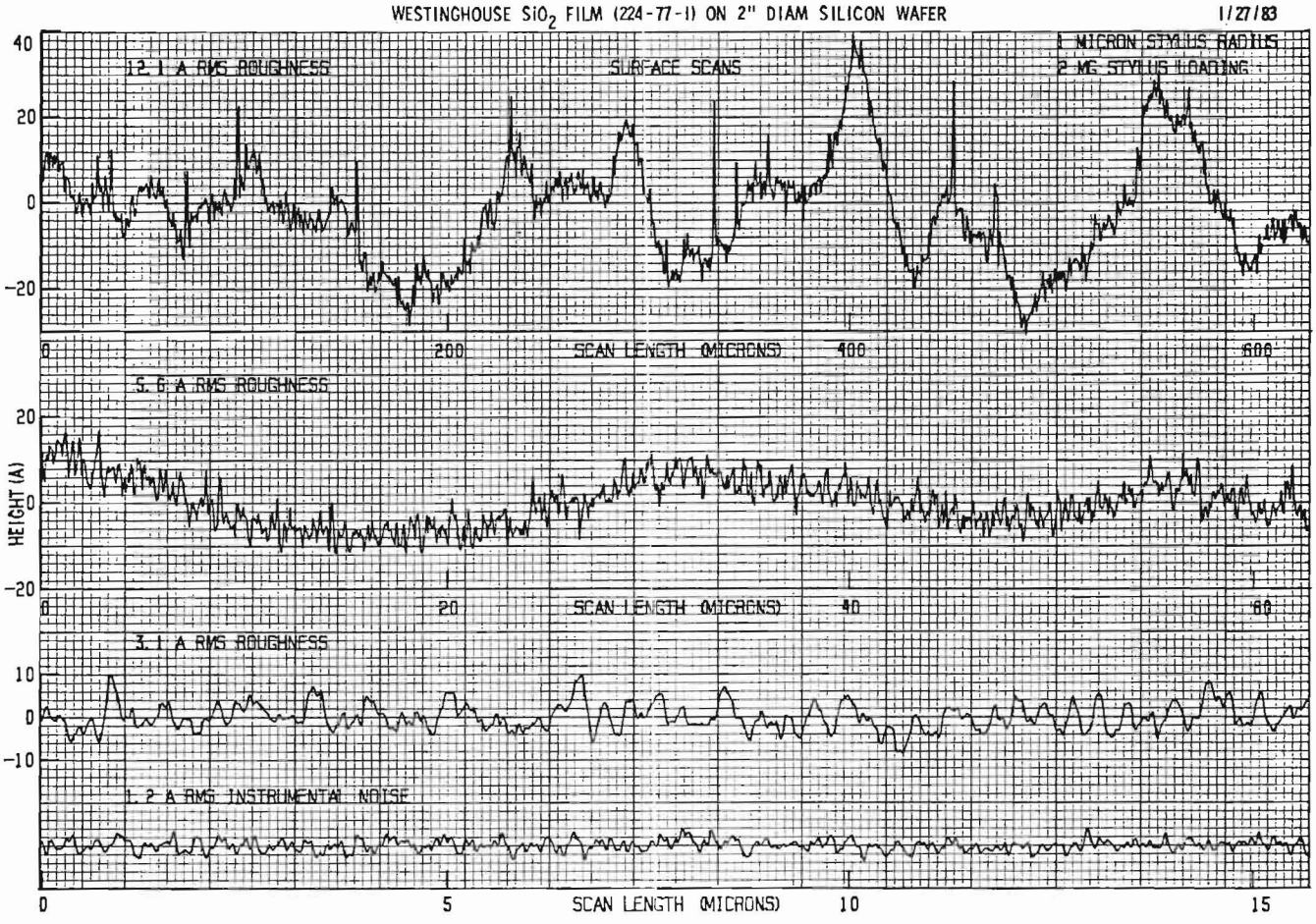


Figure 3. Talystep surface profiles of a plasma-deposited SiO_2 film on a silicon wafer.

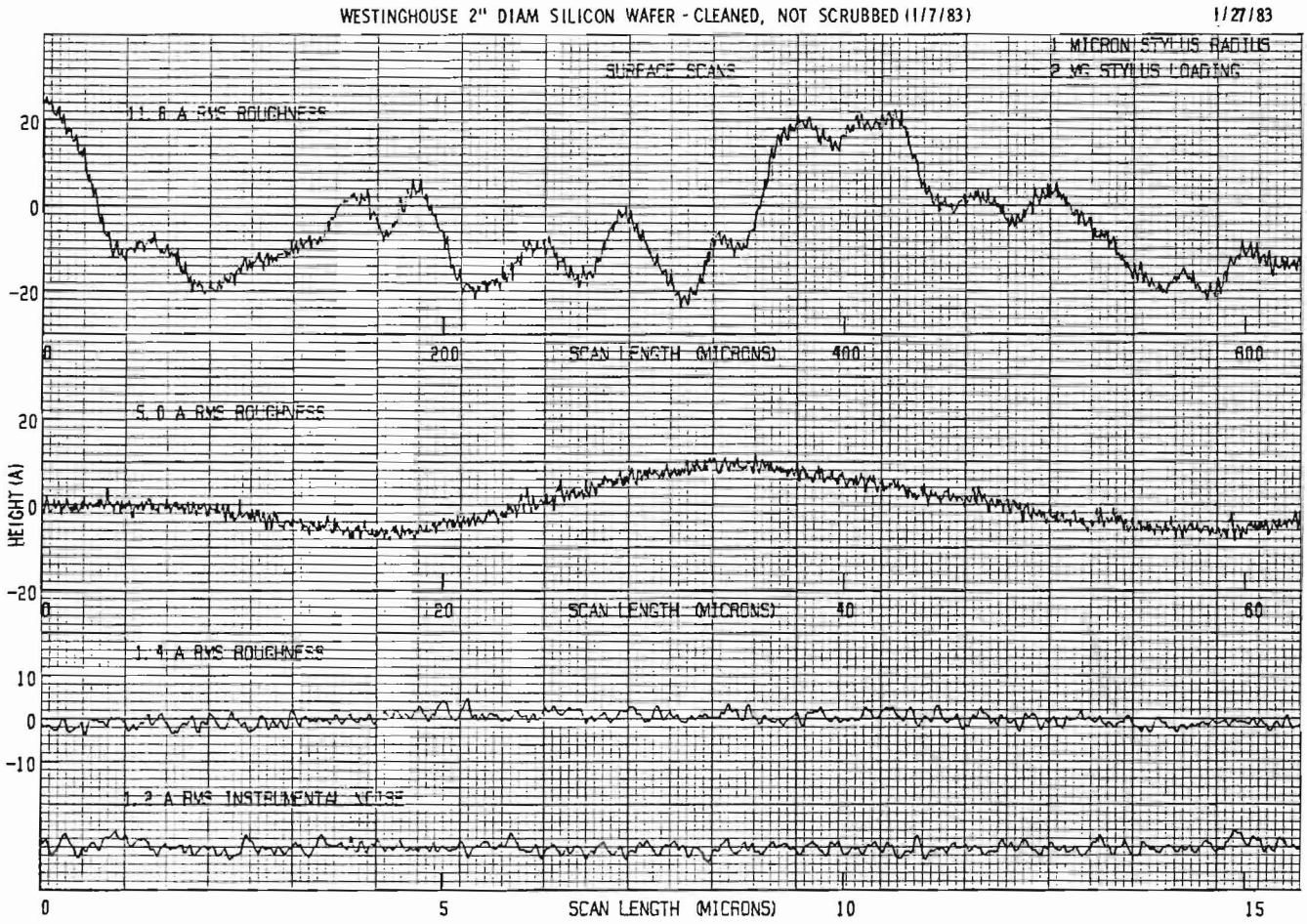


Figure 4. Talystep surface profiles of an uncoated silicon wafer.

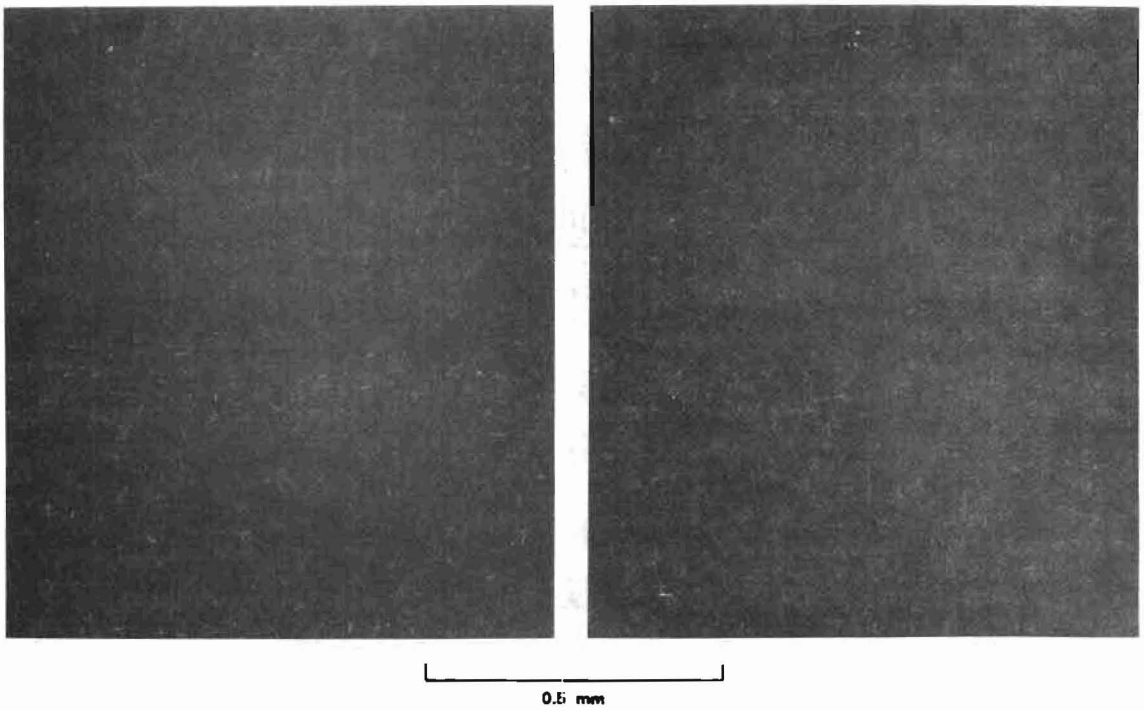


Figure 5. Nomarski micrographs of a plasma-deposited Si_3N_4 film on an ultralow scatter polished silicon substrate, and a similar film on a polished CVD silicon carbide substrate.

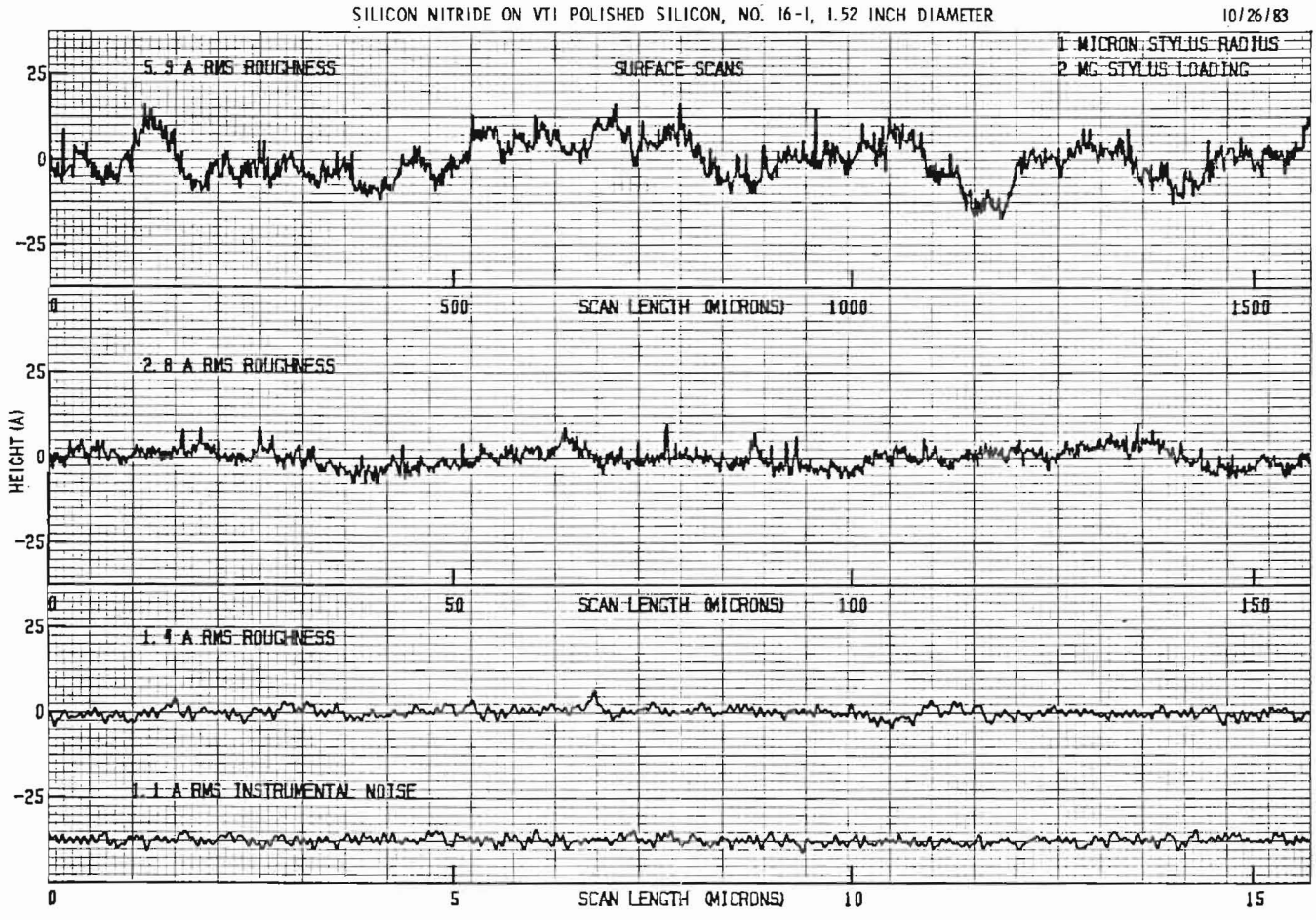


Figure 6. Talystep surface profiles of a plasma-deposited Si_3N_4 film on an ultralow scatter silicon substrate.

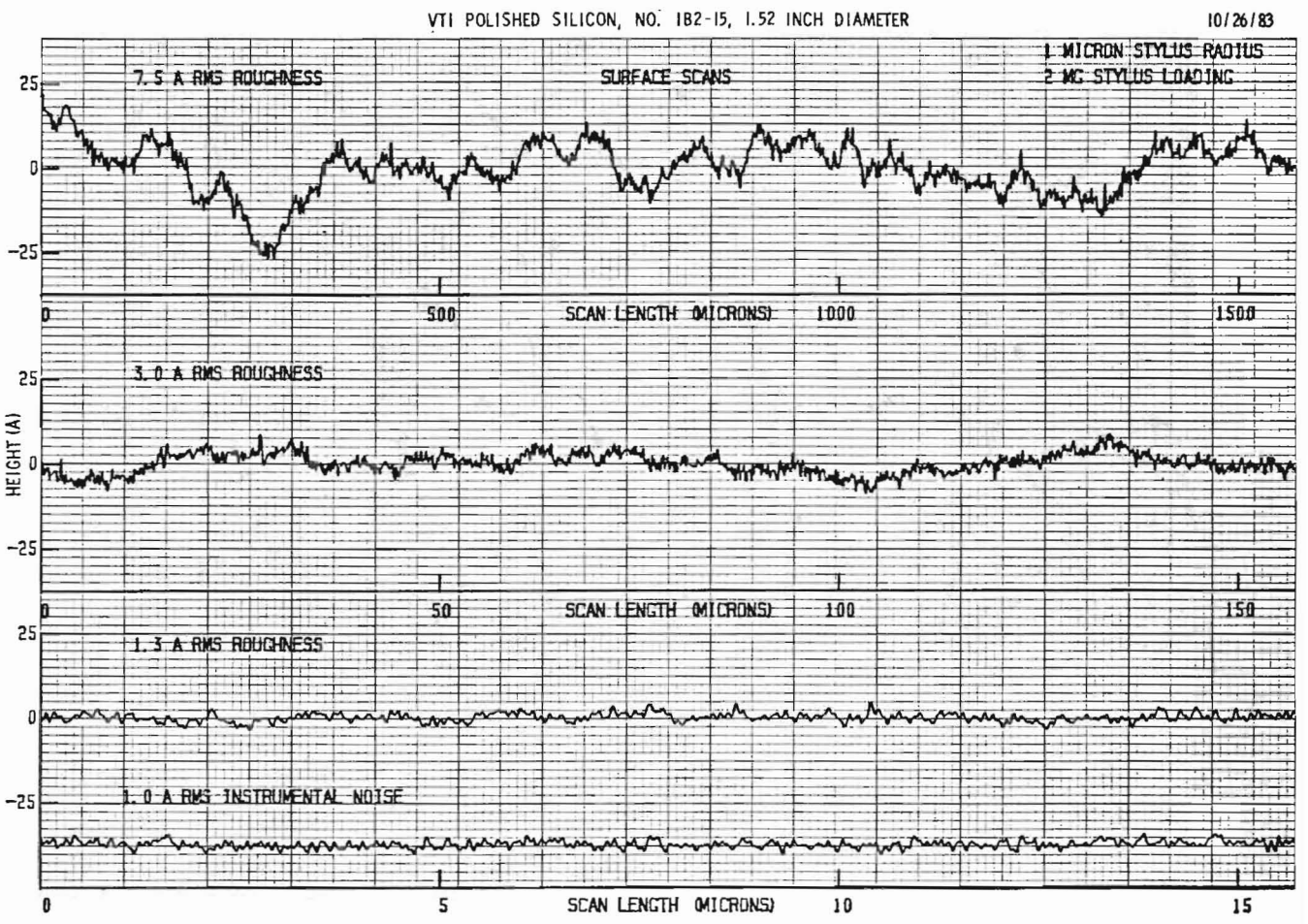


Figure 7. Talystep surface profiles of an uncoated ultralow scatter silicon substrate.

In response to a question, the speaker stated that the films were first deposited on silicon in order to do ellipsometry and then on soda lime glass. They were about 500 thick. Most of the photoreaction is believed to take place on the surface, according to experiments at Lincoln Laboratory. Volume reaction vs surface reaction is one of the questions remaining to be investigated at Westinghouse. The lasers used were mostly in the ultraviolet and included krypton fluoride (248 nm), xenon fluoride (350 nm), cadmium (356 nm), and various ultraviolet lamps. The yields appear to be similar at the different wavelengths although possibly slightly better for XeF.

RECEIVED: 11-15-83

Optical Properties of Ion-Beam Sputtered TiO_2 Films

H. Demiryont, D. B. Kerwin, and J. R. Sites

Physics Department, Colorado State University
Fort Collins, CO 80523

Ion-beam sputtered TiO_2 films were simultaneously deposited onto Corning 7059 and silicon substrates for ellipsometric and spectrophotometric investigation of optical parameters. Film thicknesses ranged from 5 to 500 nm, and spectrophotometer wavelengths from 400 to 2500 nm. Results from the two techniques agree well at the 632.8 nm wavelength used for ellipsometry.

At thicknesses above 100 nm and wavelengths above 1 μm, the TiO_2 refractive index was insensitive to changes in thickness or wavelength. It increased, as expected, at shorter visible wavelengths, and it decreased markedly for films below 100 nm in thickness. The index varied with the oxygen to argon ratio of the ion beam, showing a maximum value of 2.52 for 632.8 nm wavelength light. The extinction coefficient was too small for spectrophotometric measurement in the infrared; previous calorimetric measurements for half wave films at 1.06 μm showed absorption below 100 p/m. The extinction coefficient, however, increased in the visible, typically reaching values corresponding to a few tenths percent absorption at 0.4 μm.

Key words: optical coatings; ion beam; TiO_2; SiO_2; refractive index; ellipsometry.

1. Introduction

Titania, TiO_2, is one of the more common high refractive index materials used in optical coatings. When layered alternately with SiO_2, reflectivity in excess of 99.99% is possible. The optical properties of titania, however, are strongly dependent on fabrication procedures. Titania can be deposited by reactive e-beam evaporation of any of several oxides of titanium [1]. Such films are often porous and low in packing fraction. Martin et al [2] and Allen [3] have shown that ion bombardment of the growing film during deposition can increase both the packing fraction and the refractive index. The absorption of such films is strongly affected by the type of ions used and the ion to molecule arrival rate. Rf sputtered titania layers also vary considerably in their optical properties. The refractive index in this case shows a strong correlation with the structure and the size of the crystallites [4]. In this paper, the optical properties of ion-beam sputtered TiO_2 films will be discussed. These films are nearly amorphous, low in absorption, and relatively high in refractive index [5].

2. Fabrication

A titanium metal target was bombarded by a beam of argon and oxygen ions from a Kaufman-type ion source [6]. The ion energy was 1100 eV and the beam current density was 1.0 mA/cm^2. The argon and oxygen flow rates were adjusted so that the total chamber pressure was 8×10^{-5} torr. The ratio of oxygen to argon was varied, but most data was taken with a 1:1 mixture of ions. The resulting titania was simultaneously deposited onto silicon and Corning 7059 glass substrates at a rate of 20 Å/min. All deposition parameters, including growth rate and beam conditions, were continuously monitored and recorded with the aid of a small computer.

A series of titania films were deposited that ranged in thickness from 5 to 500 nm. In addition several thin (4 to 8 nm) films of SiO_2 were deposited using a fused silica target and a reduced oxygen to argon ratio. These films were used to calibrate the effect of native silicon oxides on the optical measurements.

3. Results

The transmission spectrum for each titania film on a glass substrate was measured with a Beckman spectrophotometer. A typical example for a relatively thick film (531 nm) is shown in figure 1. This film was deposited with argon and oxygen flow rates that led to equal partial pressures. The dashed lines labeled T^+ and T^- are the envelopes of the maximum and minimum transmissivity. The

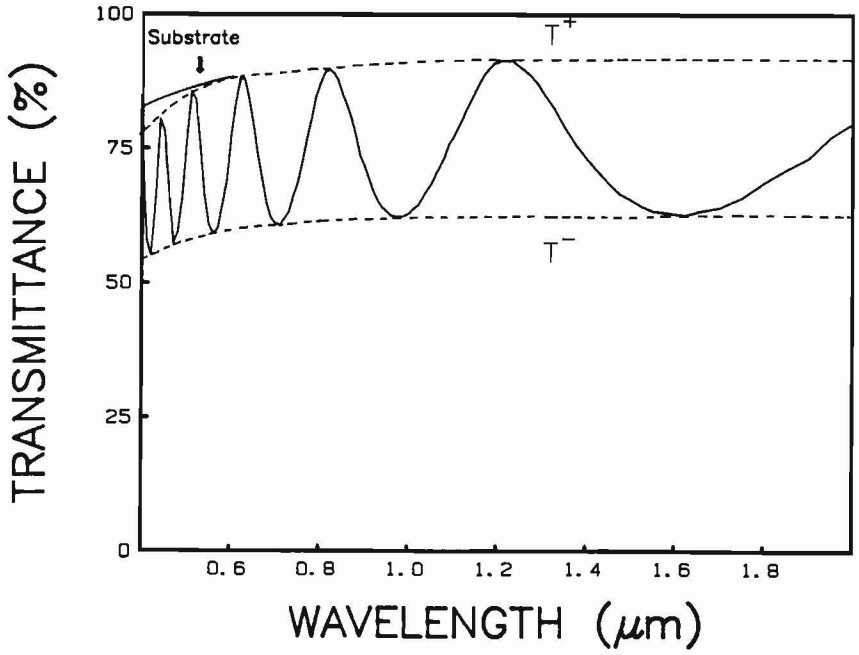


Figure 1. Transmission spectrum of 531 nm thick ion-beam sputter deposited titania film. T^+ and T^- are envelopes of maxima and minima.

substrate transmissivity is also shown in figure 1. On the scale used, it is indistinguishable from T^+, except at the lowest wavelengths, indicating the film absorption is relatively low. We will define

$$c(\lambda) = (1/T^-) - (1/T^+) \tag{1}$$

where T^+ and T^- are evaluated on the envelope at wavelength λ. The film index n_f is evaluated following reference [7]:

$$n_f(\lambda) = [n_s c(\lambda) + (n_s+1)^2/4]^{1/2} + [n_s c(\lambda) + (n_s-1)^2/4]^{1/2} \tag{2}$$

or equivalently from reference [8] as follows:

$$n_f(\lambda) = \{2n_s c(\lambda) + (1+n_s^2)/2 + [(2n_s c(\lambda) + (1+n_s^2)/2 - n_s^2]^{1/2}\}^{1/2} . \tag{3}$$

In both cases it is assumed that the absorption does not significantly affect the index determination. The Corning 7059 substrate index, n_s, is 1.51 and nearly dispersion-free over the region of interest.

The film thickness d_f can be calculated from the wavelengths of adjacent extrema, i and i+1, as follows:

$$d_f = 1/4[n_f(\lambda_i)/\lambda_i - n_f(\lambda_{i+1})/\lambda_{i+1}]^{-1} . \tag{4}$$

The extinction coefficient k is given by the following:

$$k_f(\lambda) = \frac{\lambda}{4\pi d_f} \ln \frac{u+(u^2-c^2+\sigma)^{1/2}}{2a} \tag{5}$$

where

$$u(\lambda) = 1/T^{-} + 1/T^{+} \tag{6}$$

$$\sigma = ((n_s^2-1)/4n_s)^2 \, (n_f-1/n_f)^2 \tag{7}$$

$$a = ((n_f+1)^3 \, (n_f+n_s^2)/8n_s n_f^2) \, . \tag{8}$$

The deduced values of n_f and k_f for several ion-beam sputtered films are shown in figure 2. As

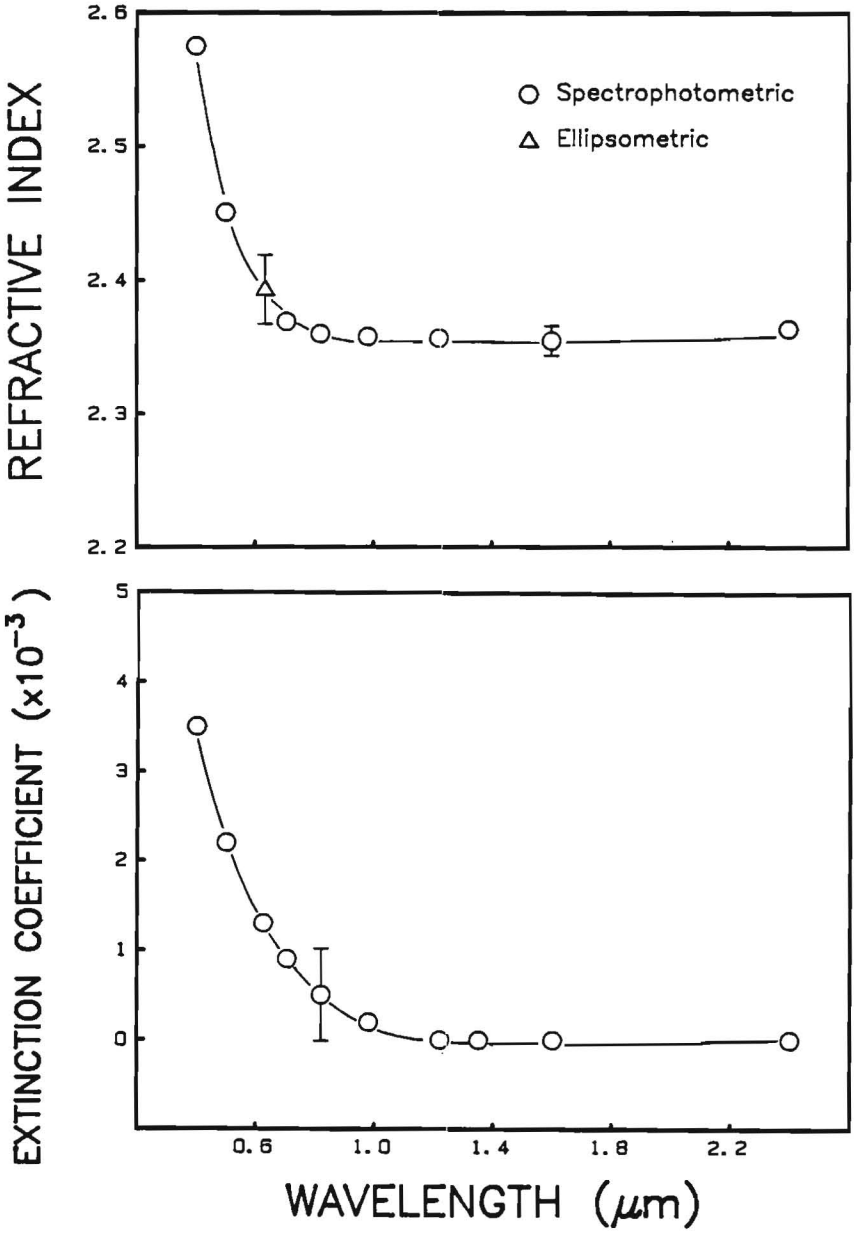


Figure 2. Wavelength dependence of titania refractive index and extinction coefficient. Triangular point is from ellipsometry; others from spectrophotometry.

expected the index vs. wavelength curve is flat and the extinction coefficient close to zero in the infrared. Moving into the visible, n_f increases and k_f becomes non-negligible, reaching a value of approximately 0.004 at 400 nm.

Ellipsometric measurements were made only at 632.8 nm, but the deduced values of n_f and d_f agreed well with the spectrophotometric values at this wavelength. Table 1 shows the comparison for three titania layers, and the triangular point on figure 2 shows the ellipsometric value, the error bar referring to the three films that varied slightly in index.

Table 1. Comparison of Ellipsometric and Spectrophotometric Data at 633 nm

Sample	Thickness		Refractive Index	
	Ellipsometer	Spectrophotometer	Ellipsometer	Spectrophotometer
30905H1	221.7 nm	221.2 nm	2.431	2.432
30909H1	306.0	305.6	2.337	2.380
30910H1	328.2	328.6	2.385	2.381

The refractive index of the ion-beam sputtered titania was found to vary with the ratio of oxygen to argon ions in the beam. This effect is shown in figure 3 where the total chamber pressure was held constant at 8×10^{-5} torr, but the fraction of oxygen was varied. At low oxygen pressures, as expected, the films were rich in titanium, had a metallic appearance, and gave large values of optical absorption.

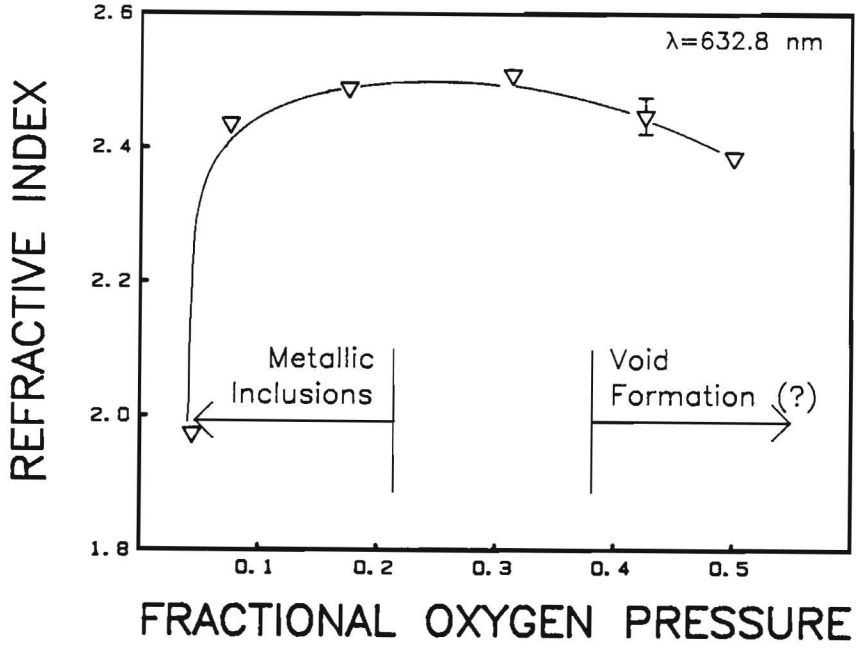


Figure 3. Dependence of refractive index in TiO_x films sputtered with varying oxygen to argon ion ratios. All films were in the 300 nm thickness range.

At oxygen levels above 30% the absorption was low, but at 40% and above the index of refraction dropped from its maximum value. The latter effect is tentatively attributed to a reduced atomic density of the films, but no direct evidence is currently available. The optimum ratio for high index and low absorption with the deposition system used appears to be around 35%.

The thickness dependence of the refractive index for ion-beam sputtered titania films is shown in figure 4. These films were sputtered with a 0.5 fractional oxygen pressure. All the data for films below 100 nm was ellipsometric. The thicker films, as discussed above, showed a close agreement between the two techniques. The thinner films shown in figure 4 have a marked decrease in refractive index. The curve in fact is very similar to reported data on refractive index vs. grain size for polycrystalline titania films [4].

We had some concern, however, that instrumental effects or analytical problems could have led to erroneous results in the thin film region. We therefore very carefully plotted the measured

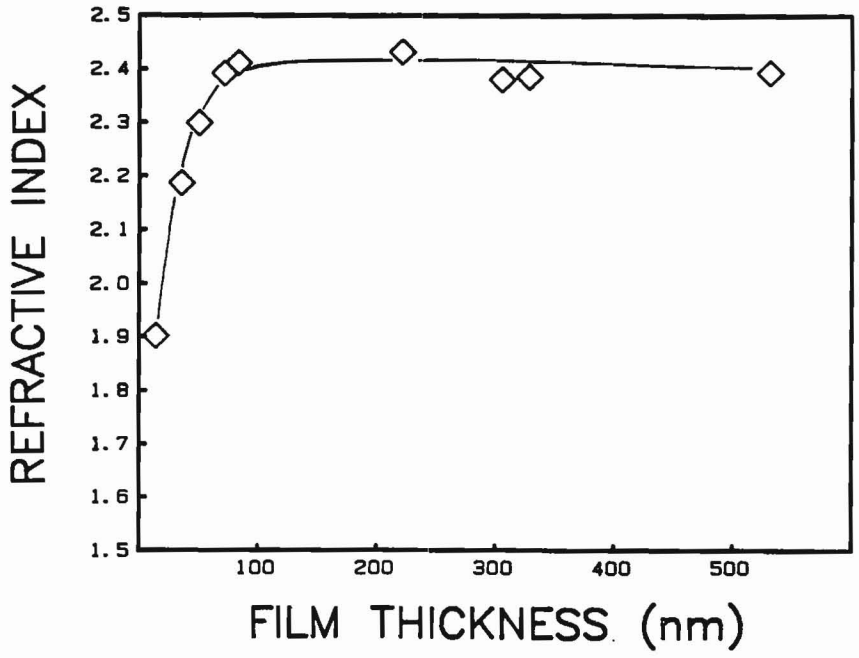


Figure 4. Thickness dependence of refractive index of titania films.

ellipsometric parameters against film thickness for both TiO_2 and SiO_2 films in the thin film limit as shown in figure 5. The thickness scale in this case was taken from the deposition time multiplied

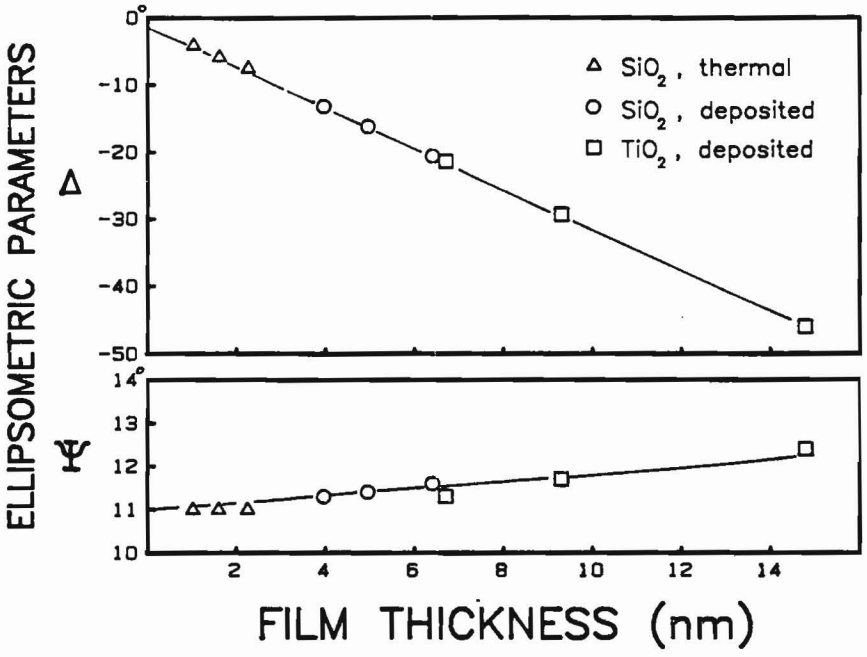


Figure 5. Ellipsometric angles, showing smooth extrapolation to zero thickness. Triangles are thermal SiO_2 on silicon, open circles sputtered SiO_2, and filled circles sputtered TiO_2.

by the previously determined deposition rate. That scale should be quite accurate and independent of the ellipsometric measurements. Both the TiO_2 and SiO_2 data appear smooth and approach a linear curve for the parameter Δ and a constant value for the parameter ψ in the thin film limit. The extrapolation to zero thickness yields the following:

$$\Delta_0 = -1.2° \qquad \psi_0 = 11.0° \tag{9}$$

which for the 70° angle of incidence used corresponds to a substrate complex refractive index of

$$n_s^* = 3.827 - 0.032i \qquad (10)$$

a value within the range of those attributed to silicon. Thus we conclude that the ellipsometric analysis is consistent and the decrease in index for the thin titania films in figure 4 is real.

4. Discussion

The refractive index of ion-beam sputter deposited titania films can be very high. Its magnitude, however, depends on the deposition conditions, especially the ratio of argon to oxygen in the ion beam. There is a problem, at least with the higher oxygen ratios, with a reduction of index in the thin film limit. This reduction likely indicates that voids are formed in the initial growth stages. Additional studies are planned to test whether the thickness effect can be eliminated with a lower oxygen ratio, and whether it is affected by pre-deposition etching, substrate bombardment, or deposition rate.

This work was supported in part by the Air Force Weapons Laboratory under Contract F29601-83-K-0079.

5. References

[1] Pulker, H. K.; Paesold, G.; Ritter, E. Refractive indices of TiO_2 films produced by reactive evaporation of various titanium-oxygen phases. Appl. Optics 15(12): 2986-2991; 1976 December.

[2] Martin, P. J.; Macleod, H. A.; Netterfield, R. P.; Pacey, C. G.; Sainty, W. G. Ion-beam-assisted deposition of thin films. Appl. Optics 22(1): 178-184; 1983 January.

[3] Allen, T. H. Ion assisted deposition of titania and silica films. Proc. International Ion Engr. Conf., Vol. II: 1305-1310; 1983 September.

[4] Pawlewicz, W. T.; Busch, R.; Hays, D. D.; Martin, P. M.; Laegreid, N. Reactively sputtered optical coatings for use at 1064 nm. NBS Special Publication 568: 359-375; 1979.

[5] Rossnagel, S. M.; Sites, J. R. X-ray photoelectron spectroscopy of ion-beam sputter deposited SiO_2, TiO_2, and Ta_2O_5. J. Vac. Sci. Technol. in press.

[6] Sites, J. R.; Gilstrap, P.; Rujkorakarn, R. Ion beam sputter deposition of optical coatings. Optical Engr. 22(4): 447-449; 1983 July/August.

[7] Ender, A.; Optical parameters of a weakly absorbing film on a non-absorbing substrate by spectrophotometric transmissivity. Ph.D. Thesis, Istanbul University, Turkey.

[8] Manifacier, J. C.; Gasiot, J.; Fillard, J. P. A simple method for the determination of the optical constants n,k and the thickness of a weakly absorbing thin film. J. Phys. E: Sci. Instrum. 9: 1002-1004; 1976.

Manuscript received 12-30-83/sar

IMPROVEMENT OF THE DAMAGE THRESHOLD OF HIGH REFLECTIVITY MULTIDIELECTRIC COATINGS 1.06 μM

B. GEENEN, A. MALHERBES, J. GUERAIN

Société MATRA, 94 Av. Victor HUGO
92502 RUEIL MALMAISON, FRANCE

D. BOISGARD, D. FRIART, F. GARAUDE

Commissariat à l'Energie Atomique
Centre d'Etudes de Limeil-Valenton
B.P. n° 27, 94190 Villeneuve-Saint-Georges, FRANCE

Development of new high power laser for laser-matter interaction in C.E.A. Limeil requires the realization of H.R. coatings with damage thresholds above 8 J/cm^2.

MATRA's laboratory "couches minces optiques" (thin optical layers) production commercial mirrors was around 3.5 J/cm^2 in 1982. In order to obtain better results we decided to improve the control of evaporation parameters such as :

- vacuum and regulation of oxygene pressure by means of a mass spectrometer
- better measurements of evaporation temperature and regulation of evaporation rate
- measurement and control of substrate temperature by pyrometric observation

and to automatize the process.

These different measurements and controls enable us to establish new processing operations giving better evaporation conditions.

The result was an increase of damage threshold from 3.5 J/cm^2 to 8 J/cm^2.

Key words : Damage threshold - Evaporation deposition - Mass spectrometer - Evaporation temperature, substrate temperature - TiO_2/SiO_2.

1. Analysis of residual gases in vacuum and control of oxygene

1.1. Analysis of residual gas in vacuum

Coupling a mass spectrometer to the evaporation chamber enables us to reach the optimum vacuum conditions by decreasing water vapor pressure and backscattering of hydrocarbon from the pumps.

1.2. Control of oxygene pressure

The mass spectrometer measures the pressure of the different gases in the evaporation chamber and drives the oxygene pressure, keeping it constant at the desired values throughout the different phases of evaporation.

It's then possible :

- to reproduce and change accurately those pressure conditions from one run to the other
- to make better correlation between damage threshold and evaporation conditions.

In all the evaporation described in this paper oxygene pressure was kept constant at 3.5×10^{-4} torr during the evaporation of TiO_2.

2. Measurement of evaporation temperature and regulation of deposition rate

TiO_2 and SiO_2 were used as high and low index materials for our H.R. mirrors.
We were very careful about TiO_2 evaporation.

2.1. Evaporation temperature of TiO_2

TiO_2 melt at 1800°C and at higher temperature the following reaction happens

$$2TiO_2 \rightleftharpoons Ti_2O_3 + \frac{1}{2} O_2$$

This reaction is reversible but most of the time TiO_2 dissociated and reoxygenation is difficult. In order to avoid dissociation and have a good deposition rate temperature should be kept at a reasonnable level. Temperature was measured at 2200°C by means of pyrometric observation.

2.2. Control and regulation of deposition rate

A 2200°C evaporation temperature of TiO_2 corresponds to a deposition rate of 3 Å/s which is measured with a piezo-electric quartz coupled to a system which makes an automatic feed-back control of the evaporation.

This has many advantages :

- regulation of deposition rate
- automatic stop at the required thickness
- no interruption between successive layers
- the reproducibility of our coatings is accurate enough to make a well defined parametric study.

Evaporation rates	TiO_2	3 Å/s
	SiO_2	10 Å/s.

3. Measurement of substrate temperature

Evaporation and substrate temperature have been measured at the same time with pyrometric observation.

Substrate temperature was choosen around 200°C, which seems to be a good value to obtain high damage threshold according to our experience and litterature

Substrate temperature is very sensitive to the optics dimensions and the pollution of the evaporation chambers walls ; it's important to measure this parameter accurately to reproduce it from one run to the other.

4. Damage threshold measurements

Our laser test facility is shown on figure 1. It was described last year in Boulder Damage Symposium. The main characteristics are :

- dimension of the spot around 2 mm ($1/e^2$)
- one shot every 10 s
- pulse duration 3 ns
- maximum delivered energy 300 mJ
- maximum delivered energy density 15 J/cm^2.

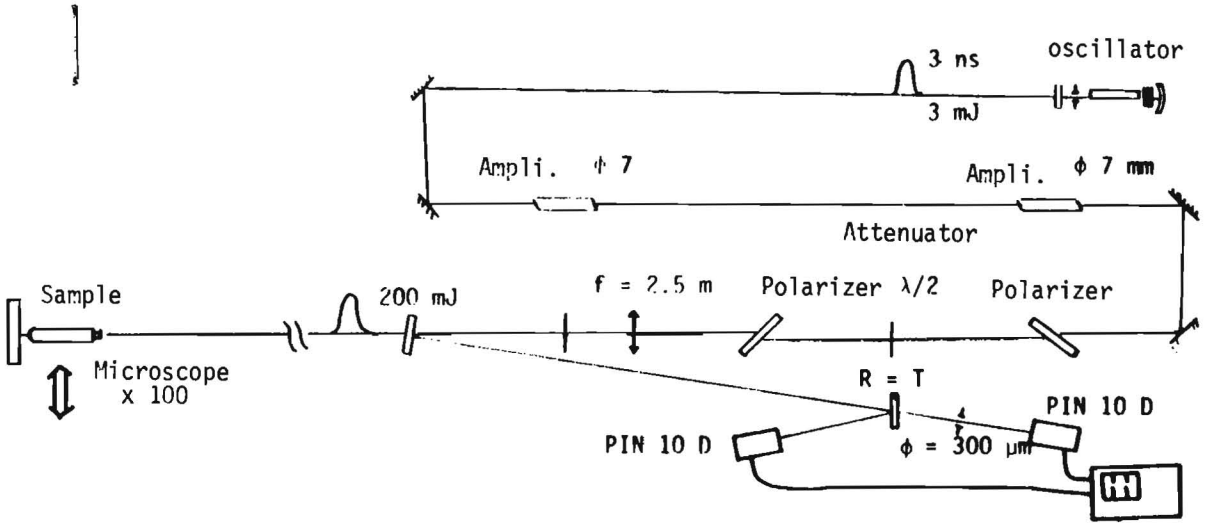


Figure 1 - Dage test facility at 1.06 µm in LIMEIL

Results of two sets of 4 different runs are reported on table 1 and 2.

5. Results

On table 1 all the improvements of the evaporation conditions are related to vacuum quality and a better regulation of oxygene pressure. TiO_2 evaporation is made with a focused e-beam.

On table 2 vacuum quality is slighty improved and TiO_2 evaporation occurs with an unfocused e-beam. On both tables results are around 8 J/cm^2.

NUMERO EVAPORATION	NUMERO ECHANTILLON	DIMENSIONS mm	SEUIL J/cm²	VALEUR MOYENNE J/cm²	VALEUR MOYENNE GLOBALE J/cm²
180/82/4	5	150	7.6	9.5	7.6
		200	11.5		
	9	200	9.4		
181/82/4	4	150	7.2	8	
		200	7.6		
	7	200	9.3		
183/82/4	12	150	6.2	7.9	
		200	12.1		
	17	200	5.3		
184/82/4	15	150	4.5	5.1	
		200	4.7		
	109	200	6		

Table 1 - Evaporation realized in December 82

NUMERO EVAPORATION	NUMERO ECHANTILLON	DIMENSIONS mm	SEUIL J/cm²	VALEUR MOYENNE J/cm²	VALEUR MOYENNE GLOBALE J/cm²
87/83/4	116	ϕ 200	6.5	7.5	8.3
	1	150 x 75	6.2		
		ϕ 50	5.2		
	2	150 x 75	9.1		
	11	160 x 55	10.5		
88/83/4	115	ϕ 200	5.5	7	
	4	150 x 75	5.8		
	3	" "	4.2		
	22	ϕ 50	12.6		
89/83/4	114	ϕ 200	12.0	8.76	
	6	150 x 75	8.3		
	5	150 x 75	6.9		
	13	" "	7.6		
	23	ϕ 50	7.7		
90/83/4	7	150 x 75	11.5	10.6	
	14	155 x 60	13.6		
	26	ϕ 200	6.7		

Table 2 - Evaporation realized in June 83

6. Discussion

Improvement of damage threshold seems to be influenced by the following parameters :

- vacuum quality
- accurate regulation of oxygene pressure
- evaporation temperature
- better control upon parameters reproducibility from one evaporation to the other.

Damage threshold versus residual gas pressures is summarized on table 3.

Tenue aux flux en J/cm² / Pression partielle en Torr	9.5	8	7.9	5.1	12
Méthane	10^{-7}	$1.7\ 10^{-7}$	1.10^{-7}	7.10^{-7}	$\leq 10^{-8}$
Vapeur d'eau	$1.8\ 10^{-6}$	$2.3\ 10^{-6}$	$1.7\ 10^{-6}$	2.10^{-6}	10^{-6}
Benzène	$3.4\ 10^{-9}$	$1.9\ 10^{-9}$	$< 10^{-9}$	$2.9\ 10^{-9}$	$< 10^{-9}$

Table 3 - Average damage threshold per run as a function of residual gas pressures

Damage threshold is very sensitive to backscattering of hydrocarbon (as far as the other residual gases are accurately controlled). Oils of the primary and secondary pumps were changed in order to obtain methane pressure as low as possible.

Water vapor pressure is more than 7 times lower than before these new processing operations were used.

7. Conclusion

The new processing operations resulting from measurements with a mass spectrometer increased the damage threshold H.R. mirrors from 3.5 to 8 J/cm².

The following parameters :

- oxygene pressure
- vacuum quality
- evaporation temperature and deposition rate
- substrate temperature.

are accurately known and controlled ; we are ready now to make significant parametric studies in the month to come.

RECEIVED: 12-30-83

Phase shift variations on HEL mirrors

Thomas A. Leonard and John S. Loomis
University of Dayton Research Institute
300 College Park
Dayton, Ohio 45469

An automated IR ellipsometer was used to measure the ellipsometric parameters, ψ and Δ, on multilayer mirrors at 3.80 μm. Spatial variations in differential phase shift, Δ, are modeled by thickness variations in the multilayer coating and variations in ψ are modeled by an absorption change.

Key words: infrared ellipsometry; phase shift; optical coating uniformity; FILM program

1. Introduction

Previous papers at this conference have discussed the use of differential phase shift variations as a sensitive measure of figure error caused by multilayer thickness variations [1,2,3]. In addition, variations in the reflectivity ratio can be modeled by absorption changes. It is essential to measure these variations at the wavelength of intended use because of the typically strong wavelength dependence exhibited by multilayer films. A rotating polarizer, infrared ellipsometer, was used to characterize three multilayer mirrors typical of damage-resistant HEL mirrors. The observed variations in phase shift and reflectivity ratio are compared to the expected thickness and absorption changes required to produce the variations.

2. Instrumentation

The ellipsometer configuration used for these measurements is shown in figure 1. It is based on a design described by Dignam at the University of Toronto [4] and developed further at the University of Dayton [5]. The rotating polarizer, PR, which is bracketed by the two stationary polarizers, P1 and P2, produces second and fourth harmonic modulation in the detected signal. The phase and amplitude of these two harmonics are determined by the azimuthal orientation of P1 and P2 and also by the ellipsometric parameters of the sample. The detector signal is digitized and Fourier transformed to extract the harmonic phase information, and the sample properties can be displayed directly.

Several ingredients are essential to successful operation of this type of ellipsometer.

a. The use of a computer simplifies data collection and subsequent model calculations considerably. The time required for multiple measurements is reduced from hours in a manual null ellipsometer to literally seconds, and as a result precision is improved enormously.

b. The polarizers are ion-beam-etched wire grids with a contrast ratio of 5,000 at 3.80 μm [6]. Their high contrast eliminates the need for accuracy-robbing, instrument-dependent corrections to the data. Their broad wavelength coverage allows the instrument to be tuned from 2.5 to 5 μm.

c. Accuracy approaching 0.01° and precision of 0.001° requires a very stable and "massive" mounting arrangement. Granite rails and heavy carriers provide the required stability.

d. The rotating polarizer assembly has gone through many design iterations to obtain suitable performance free of electrical noise and temperature rise. Both electrical noise and heat radiation can be phase locked to the rotating polarizer and can complicate the detector signal.

3. Parameters Measured

Changes in the polarization state of light as it reflects from a material are determined by the optical properties of the material, which are in turn related to fundamental material constants. There are just two basic changes that can occur with an electromagnetic wave as it reflects from an interface:

the phase (δ) of the wave oscillations can change, and the amplitude (r) of the wave can change. These changes are different for light which has its electric vector oscillating in the plane of incidence (p polarized component), and light for which the electric vector is perpendicular to the plane of incidence (s polarized component). An ellipsometer measures the result of these two changes and presents the measurement in terms of the ellipsometric parameters, Δ and ψ. The differential phase retardation, Δ and the amplitude ratio, tan ψ, are related to the complex reflection coefficients, r_p and r_s, (the Fresnel coefficients) in the following way:

$$\Delta = \delta_p - \delta_s, \qquad \tan \psi = \left| \frac{r_p}{r_s} \right| \tag{1}$$

where

$$r_p = \left| r_p \right| e^{j\delta_p}, \qquad r_s = \left| r_s \right| e^{j\delta_s} \quad . \tag{2}$$

The complex reflection coefficients are derived from electromagnetic propagation theory and contain fundamental material constants. Ellipsometric data are sometimes expressed as the ratio of the complex reflection coefficients

$$\rho = \frac{r_p}{r_s} = \tan \psi \, e^{j\Delta} \quad . \tag{3}$$

Calculation of the expected Δ and ψ for a complex multilayer coating is a fairly straightforward process which is part of most thin-film design programs. A thin-film design model with indices (λ dependent) and thickness for each layer results in a unique, easily calculated Δ and ψ for each ϕ_0 and λ. However, calculations in the reverse direction for more than two layers must be done on an iterative basis and do not necessarily lead to a unique set of indices and thicknesses. In principle, given unlimited accuracy in the ellipsometric data, multiple angle-of-incidence measurements can be used to uniquely define a multilayer coating. In practice, state-of-the-art accuracy requires that indices and thicknesses must be specified in the multilayer model for all but one layer.

4. Measurements on two samples from the same coating run

Figure 2 shows how the ellipsometric parameters vary across the aperture of a beam rotator witness sample (sample 81338-06) for a high-energy DF laser. There is considerable spatial averaging due to the 5-mm diameter probe beam, but the general trends are clear. The sample was rotated 90° about its normal and a second spatial scan was made. Regardless of spatial variations, the two scans should match at the center but they don't. Figure 3 clearly shows this azimuthal asymmetry or "birefringence" as the sample is rotated. This birefringence can be due to stress in the thin films, or it can be a direct result of asymmetries in the coating process.

A second beam rotator witness sample (sample 81338-09) was measured in the same way and the results are shown in figures 4 and 5. These samples were coated in the same coating run at different locations in the chamber. At first glance figures 2 and 4 show that this sample has less birefringence in ψ and more in Δ than does the first sample; however, the azimuthal variations show the same magnitude of fluctuations. In fact, the two azimuthal scans (figs. 3 and 5) can be overlaid exactly if they are shifted in phase by 150°. The starting point for the azimuthal scans is based on a tapped hole in the circumference of each substrate, but this may not correspond to any particular orientation in the coating chamber or to any preferential axis in the substrate material.

There is an offset of 0.6° in the absolute value of Δ between the two samples, but this does not seem to have affected the azimuthal scans. This Δ difference is probably a surface effect due to the past history of each sample or differences in the cleaning process before measurement. The samples were cleaned with acetone and lens tissue several times and then allowed to dry for 20 minutes before measurement. Phase shift typically changes by up to 10° on cleaning and then relaxes to a stable value in about 10 minutes. Both Δ and ψ measurements have been repeated (to $\pm$ 0.05°) on these samples up to two days later with no further cleaning.

5. Model calculations

The ellipsometric data presented here were compared to a multilayer model using the University of Dayton Research Institute FILM program developed by John Loomis. Indices were assumed for all materials at 3.80 μm and the layer thicknesses were also specified. The thickness of all layers was allowed to vary by the same percentage to fit Δ. The ψ variations were fit by varying absorption. This is the same approach suggested by Bennett and Burge [2].

Figure 6 shows the expected variation in Δ for a given percent change in the thickness of all layers. A one percent change in thickness should produce a -1.1° change in Δ. If the spatial fluctuations in Δ shown in figures 2 and 4 are indeed due to thickness variations, we see that they can be caused by a 2 percent variation. This is indeed a sensitive measure of thickness uniformity. Although the model assumes all layers vary by the same percentage, the outer-most layers will produce the greatest effect.

Figure 7 shows the expected variation in ψ for an increase in the absorption coefficient, β, for all of the layers. A β increase of 10 cm^{-1} which corresponds to an extinction coefficient increase of $3 \cdot 10^{-4}$ will change ψ by -0.1°. The actual absorption coefficients for each material are quite different so this modeling approach is not correct but it is perhaps indicative of changes expected. Changes in the outer-most layers will again have the greatest effect. If the spatial fluctuations in ψ shown in figures 2 and 4 are indeed due to absorption changes in the layers, they can be caused by a change of about 10 cm^{-1}. This would correspond to a reflectivity change of one percent on these samples.

6. Measurements on a third sample

Spacial variations in Δ and ψ for a third sample from a different HEL program are shown in figure 8. This sample has minimal birefringence and less Δ variation than the previous samples; however, ψ variations are greater. Graphs from the Bennett and Burge paper [2] can be used to estimate figure error or reflection changes for this mirror if desired; however, the main point is that these variations are quite different in shape then the first two samples.

7. Conclusions

We have demonstrated measurement of Δ and ψ variations to a precision of better than 0.01° at 3.8 μm. These variations are an extremely sensitive monitor of possible film thickness changes and absorption changes. There are obviously other causes for Δ and ψ variations, such as the birefringence demonstrated on two samples, but regardless of the causes, ellipsometry provides an excellent method of monitoring these effects.

8. Acknowledgments

The authors thank Captain M. Maclin of the Air Force Weapons Laboratory and Dr. H. Bennett of the Naval Weapons Center for furnishing samples for this study.

9. References

[1] Bennett, H. E., Burge, D. K., Multilayer thickness uniformities required to meet wave front error tolerances in laser mirrors. Bennett, H. E.; Glass; A. J.; Guenther, A. H.; Newnam, B. E., eds. Proceedings of the 12th annual symposium on optical materials for high power lasers; 1980 September 30-October 1; Boulder, Colorado. Nat. Bur. Stand. (U.S.) Spec. Publ. 620; 1983 October. 356-368.

[2] Bennett, H. E., Burge, D. K., Sensitive technique for measuring apparent optical figure error caused by coating nonuniformity, Presented at the 13th Annual Symposium on Optical materials for High Power Lasers, 17-18 November 1981, Boulder, Colorado.

[3] Guha, J. K., Scott, P. W., and Southwell, W. H., Effect of infrared coating nonuniformity on optical systems, Applied Optics, 19, (8), 1320, 1980 April.

[4] Stobie, R. W., B. Rao, and M. J. Dignam, Jour. Opt. Soc. of Amer. 65, 25, 1975 January.

[5] Leonard, T. A., Loomis, J. S., Harding, K. G., Scott, M., Design and construction of three infrared ellipsometers for thin film research, Optical Engineering, 21, (6), 971, 1982 November/December.

[6] Leonard, T. A., Infrared polarizer selection, SPIE Vol. 288, Los Alamos Conference on Optics (1981).

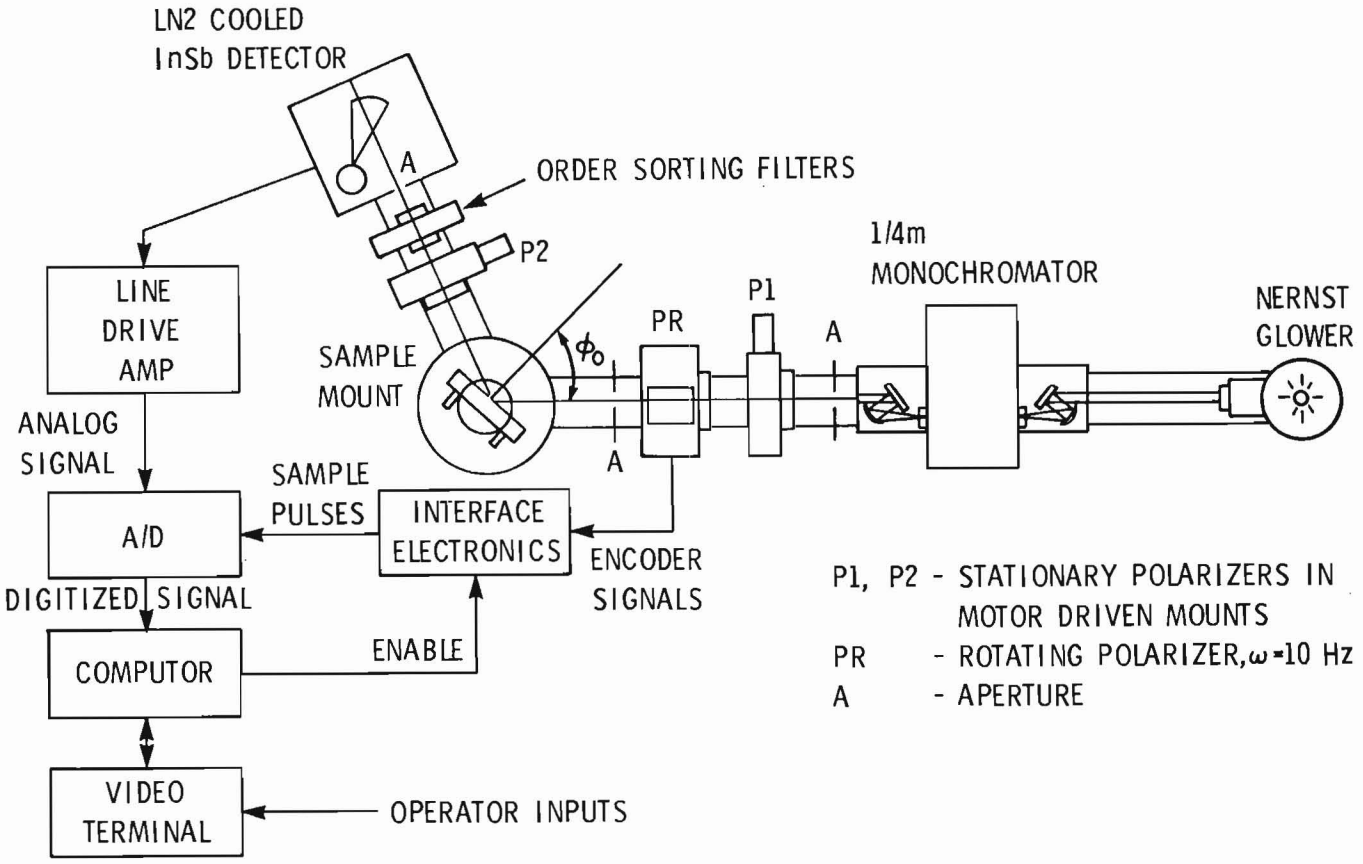


Figure 1. Schematic representation of the automated, infrared rotating polarizer ellipsometer at the University of Dayton. This instrument is tunable from 2.5 to 5 μm and can be used from 0.4 to 12 μm with simple changes in the light source, detector, and polarizers.

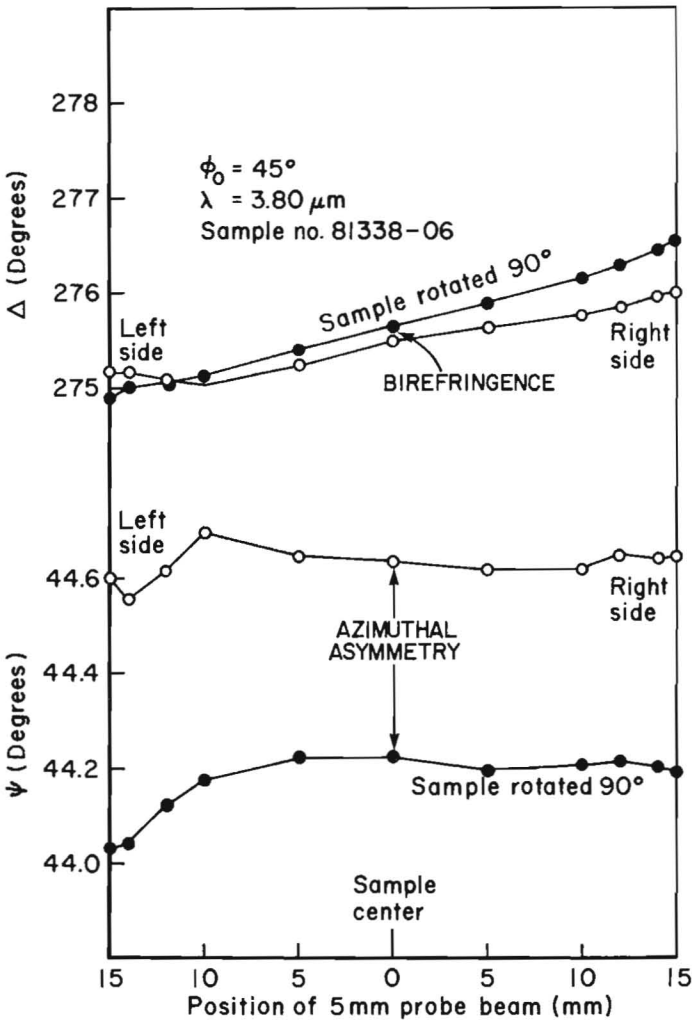


Figure 2. Spatial variations in Δ and ψ across the aperture of a high-reflectivity mirror. The sample was rotated 90° about a normal to its face to make the second orthogonal scan. This is an early beam rotator sample from the TAU program.

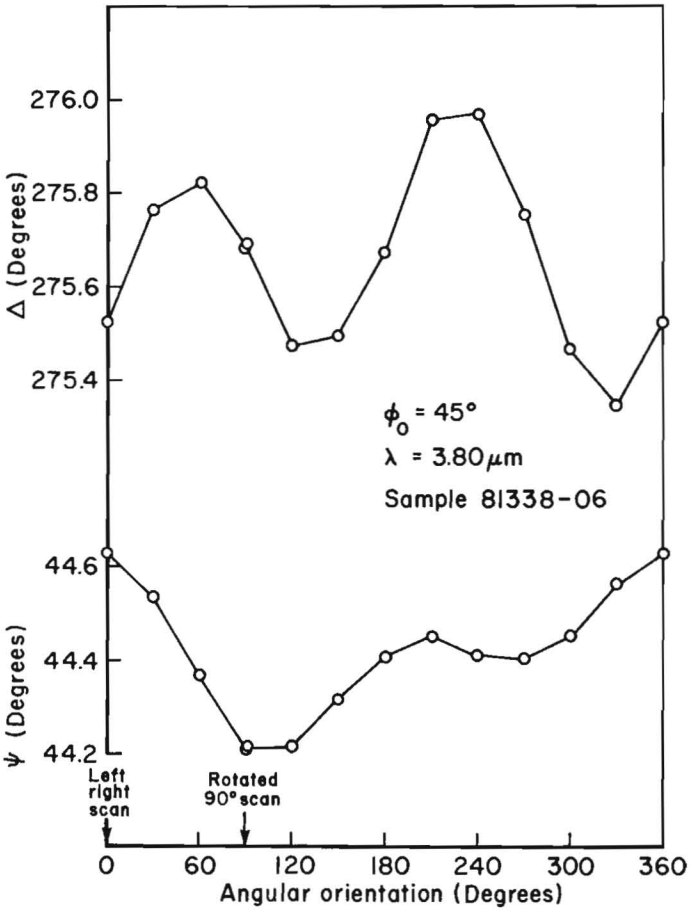


Figure 3. Azimuthal variations in Δ and ψ as the sample in figure 2 is rotated about a normal to its face.

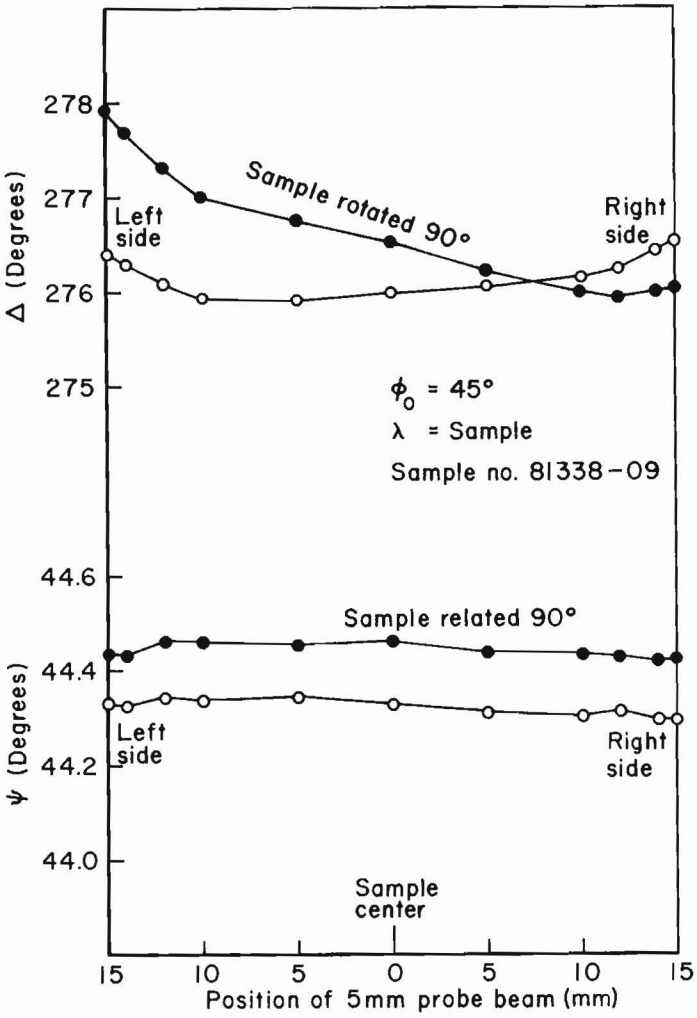


Figure 4. Spatial variations in Δ and ψ across the aperture of a second high reflectivity mirror similar to that in figure 2.

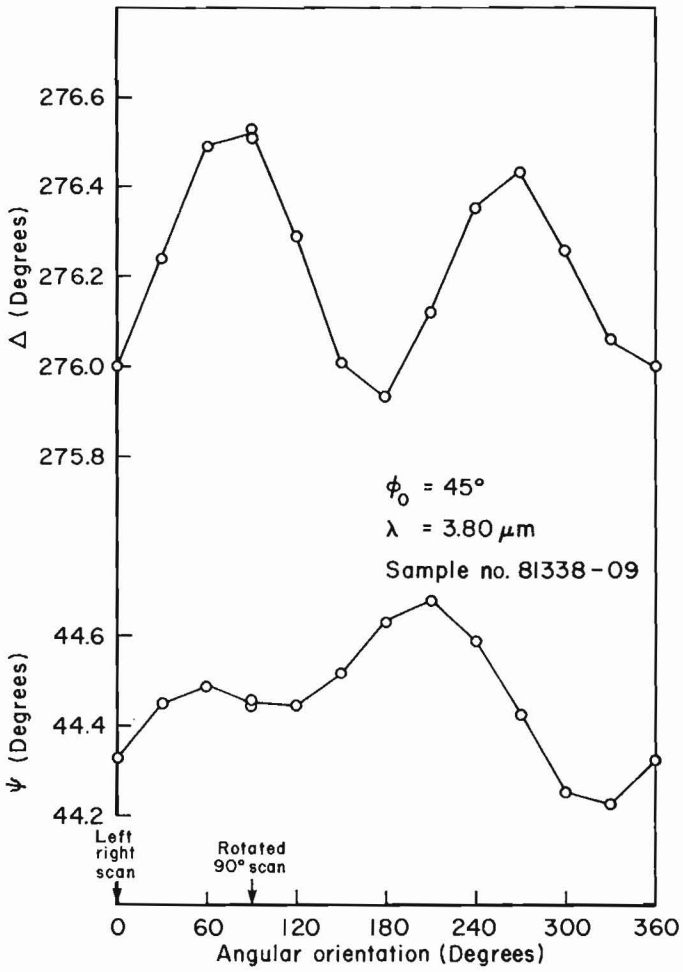


Figure 5. Azimuthal variations in Δ and ψ as the second sample is rotated about a normal to its face.

The comment was made that the rotational symmetry anomaly reported in this paper had also been observed at BTI and may be related to the way in which the metal substrate is prepared. It disappears in very well prepared substrates but is nearly always present. The orientation of the mirror in the system can thus affect the p and s reflectivities and phase shifts observed. The effect can in some cases be quite strong.

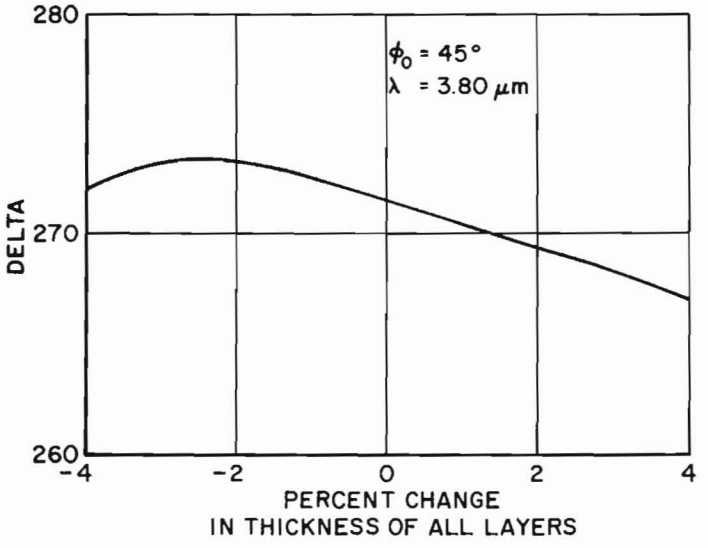


Figure 6. Variation in differential phase shift expected for a given thickness change in all layers as calculated with the FILM program. This multilayer coating can be described as $CeF_3(ThF_3ZnSe)^{11}Au$.

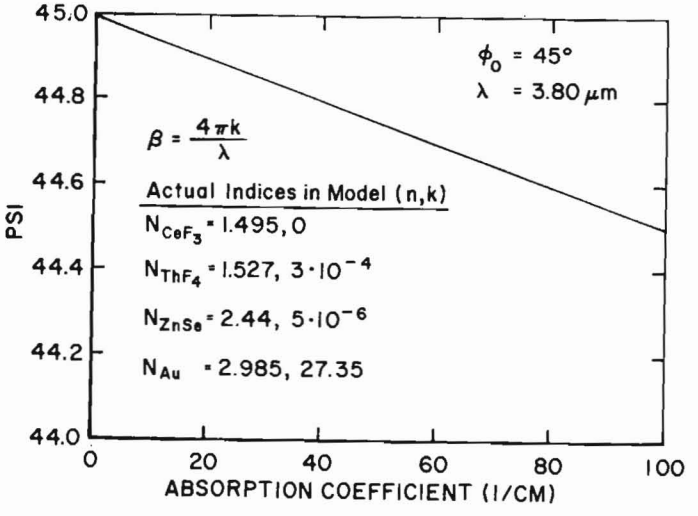


Figure 7. Variation in reflectivity ratio expected for an increase in absorption coefficient for all layers as calculated with the FILM program.

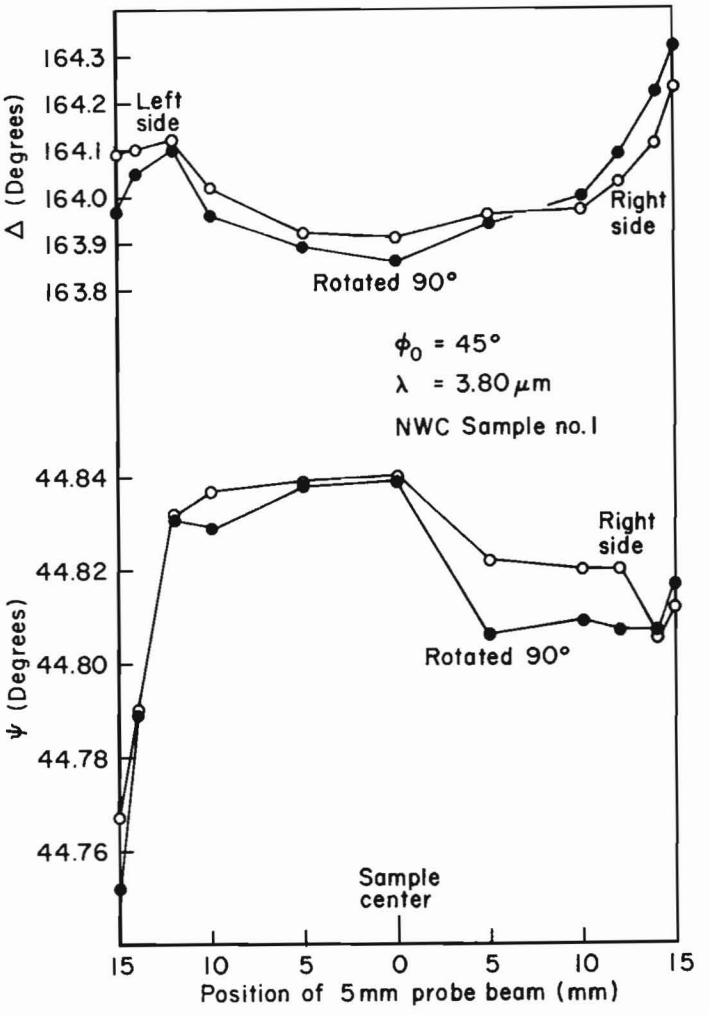


Figure 8. Spatial variations in Δ and ψ across the aperture of a witness sample mirror furnished by the Naval Weapons Center. The coating for this sample can be described as $(Z_nS/ThF_2)^4ZnS$ Ag centered at 3.8 μm with the innermost ThF_2/ZnS layer modified to correct for phase change at the Ag surface.

Manuscript received 1-26-84/sar

A Review of UV Coating Material Properties+

Marion L. Scott

R & D Associates, ATO 9377
Albuquerque, New Mexico 87119

Ultraviolet coating material properties are of considerable interest in coating analysis, coating fabrication, and UV laser system design. This review of the coating materials properties in the UV is intended to provide these interested parties with an up-to-date compendium of the relevant data available in this area. Examples of the material properties included are optical constants, physical constants, thermal constants, and laser damage thresholds.

Key Words: coating materials; properties; ultraviolet

1. Introduction

Ultraviolet coating materials are becoming more important as new laser sources are developed at these wavelengths. The coating material properties of most interest to a laser system designer are the optical properties and the damage threshold at the wavelengths of interest. However, other material properties may be necessary to model the behavior of these materials when they are subjected to heating, stress, abrasion, etc. In addition, material characteristics such as solubility, vapor pressure, hardness, and toxicity are important to coating fabrication personnel. Many of the parameters given in this review are the bulk material parameters because these are the only available values.

2. Materials

The coating materials covered in this review are limited to eleven fluorides and twelve oxides which all exhibit low loss spectral transmission in the ultraviolet. While other materials could have been included, the available data on these other materials did not warrant their inclusion in this compilation.

3. Physical Properties

Many applications of coating materials necessitate knowledge of the physical properties of the materials in order to assess performance limitations. The physical properties of the twenty materials surveyed are given in tables 1, 2, and 3. The values given in these tables for density, elastic and dielectric constants, and vapor pressure are bulk values and therefore these values should be used with some caution when applying them to thin films.

4. Thermal Properties

The thermal properties of these ultraviolet materials are given in table 4. Knowledge of these properties is important in modeling the thermal behavior of coatings made from these materials. The values given in the table are bulk values and therefore should be used with some caution when applying these values to thin films.

5. Parameters of Evaporated Films Compared to Bulk Values

Table 5 illustrates the kind of difficulty one might encounter when attempting to use bulk values for thin film parameters. Note particularly the large discrepancy in Young's modulus for magnesium fluoride and magnesium oxide as well as the change in sign for the coefficient of thermal expansion of thorium tetrafluoride. The author is grateful to Hal Bennett and his co-authors at NWC, China Lake for their permission to reprint this table from reference [3].

+ This work was sponsored by DARPA Contract F29601-82-C-0048.

6. Optical Properties

The optical properties of ultraviolet coating materials given in table 6 indicate that there is a diverse group of coating materials available for use in the ultraviolet spectrum. The spread in coating index of refraction (1.32-2.28) is suitable for most coating design requirements. The coating index of refraction is generally less than that of the bulk value due to the porous nature of thin films.

7. Laser Damage Threshold on Single λ/4 Layers

Single layer damage thresholds are given in table 7. These damage thresholds were reported in a previous Boulder conference [1] by Walker, et. al, or were published [2] by Gill and Newnam. This data shows clearly that laser damage thresholds for these materials increase with increasing wavelength and pulse width.

8. Laser Damage Threshold for Multilayer Coatings

Multilayer coating laser damage thresholds are given in table 8. These damage thresholds were measured by Steve Foltyn [10, 11, 12, 13] at the Los Alamos National Laboratory. Again, we see a clear trend of increasing damage thresholds with increasing wavelength. The data for a non-quarter wave design using Scandia/Magnesium Fluoride is shown to illustrate the improvement that can be achieved with manipulation of the internal standing wave field in the multilayer.

9. Laser Damage Thresholds for Bare UV Substrates

Substrate laser damage thresholds are given in table 9. These damage thresholds were also measured by Steve Foltyn [11] at the Los Alamos National Laboratory. The damage thresholds for bare substrates is seen to be significantly higher than coated substrates in most cases. Again the increase in threshold with an increase in wavelength can be noted.

10. Further Investigation Required

It is obvious from the omissions in the data tables given in this review that further measurements are required for these UV materials in all areas covered. In addition, the author would suggest that laser damage thresholds should be measured at longer pulse lengths in order to extend the validity of pulse length scaling rules established by these data.

11. References

1. T.W. Walker, et al. Pulsed Damage Threshold of Fluoride and Oxide Thin Films from 0.26 μm to 1.06 μm, NBS Special Publication 568, p. 405, July 1980.

2. D.H. Gill and B.E. Newman. Damage Resistance of UV Coatings, Laser Focus, p. 76, September 1979.

3. H.E. Bennett, et al. Ultraviolet Components for High-Energy Applications, NWC TP 6015, March 1978.

4. T. Lichtenstein, Handbook of Thin Film Materials, (University of Rochester), May 1979.

5. A.J. Moses. Optical Materials Properties, Handbook of Electronic Materials, Vol. 1, (IFI/Plenum, New York), 1971.

6. H.K. Pulker. Characterization of Optical Thin Films, Appl. Opt., Vol. 8, No. 12, June 1979.

7. J.F. Lynch, et al. Engineering Properties of Selected Ceramic Materials, (The American Ceramic Society, Inc., Columbus, Ohio), 1966.

8. Y.S. Youloukian and C.Y. Ho, eds. Thermophysical Properties of Matter, Vols. 2, 5 and 13, (Thermophysical Properties Research Center, Purdue University), 1970.

9. S.R. Foltyn and B.E. Newnam. Ultraviolet Damage Resistance of Dielectric Reflectors Under Multiple-shot Irradiation, IEEE JQE, Vol. QE17, #10, p. 2092, October 1981.

10. S.R. Foltyn. Ultraviolet Laser Damage Studies at Los Alamos, Los Alamos National Laboratory, Los Alamos, New Mexico, unpublished, January 1983.

11. S.R. Foltyn, Optical Coating Development and Excimer Laser Chemistry Studies, Los Alamos National Laboratory, Los Alamos, New Mexico, unpublished, March 1983.

12. S.R. Foltyn. Optical Coating Development and Excimer Laser Chemistry Studies, Los Alamos National Laboratory, Los Alamos, New Mexico, unpublished, June 1983.

13. S.R. Foltyn. Optical Coating Development, Los Alamos National Laboratory, Los Alamos, New Mexico, unpublished, August 1983.

Table 1. Physical properties I

	Density (g/cm^3)	Hardness	Packing Density	Stress	Structure	Vapor Pressure T(C°)	P(TORR)
NaF	2.6	Soft	•	•	Crystalline	1704°	760
LiF	2.64	Soft	•	Small tensile	Crystalline	1681°	760
CaF_2	3.2	Fairly Hard	0.57 @ 30°C	Low tensile	Crystalline	1400°	0.1
Na_3AlF_6	2.9	Soft	0.92 @ 190°C	Tensile	Crystalline	935°	0.1
AlF_3	2.9	Soft	0.64 @ 35°C	Low tensile	Amorphous	1537°	760
MgF_2	3.2	Hard	0.96 @ 300°C	5000 Kg/cm^2 tensile	Crystalline	1400°	0.01
ThF_4	6.3	Soft	•	1100 - 1500 Kg/cm Tensile	Amorphous	•	
LaF_3	6.0	Hard	0.80 @ 30°C	1000 Kg/cm^2 tensile	Crystalline	900°	10^{-4}
NdF_3	6.5	Hard	0.80 @ 30°C	•	Crystalline	900°	10^{-4}
CeF_3	6.2	Hard	0.80 @ 30°C	2300 Kg/cm^2 High tensile	Crystalline	900°	10^{-4}
PbF_2	8.2	Soft	0.91 @ 30°C	Compressive but tensile for thick	β PbF_2 Crystalline	1293°	760
SiO_2	2.2	Hard	0.98 @ 150°C	1570 Kg/cm^2 Compressive	Amorphous	2227°	760
Al_2O_3	3.98	Hard	1.0 @ 30°-300°	•	Amorphous	2977°	760
MgO	3.6	Hard	•	14000 Kg/cm^2 Compressive	Crystalline	1600°	10^{-4}
Gd_2O_3	7.64	Fairly Hard	•	•	•	•	
ThO_2	10.0	Hard	•	•	•	2100°	10^{-4}
Y_2O_3	4.8	Hard	•	•	Amorphous	•	
Sc_2O_3	•	Fairly Hard	•	•	Amorphous	•	
La_2O_3	6.5	Hard	•	•	Amorphous	2000°	10^{-4}
ZrO_2	5.6	Hard	0.82 @ 250°C	•	•	2200°	10^{-4}
HfO_2	•	Fairly Hard	•	3500 Kg/cm^2 tensile	•	•	
Ta_2O_5	8.2	Hard	•	•	Amorphous	1920°	10^{-4}
Sb_2O_3	5.2	•	•	•		1425°	760

Table 2. Physical properties II

	DURABILITY	SOLUBILITY	HYGROSCOPIC	TOXICITY
NaF	Removable with soft cloth rub	4.22g/100cc water, HF, slight alcohol	Yes	Poisonous
LiF	Removable with soft cloth rub	0.27g/100cc water, acids	Yes	Non-toxic
CaF_2	Removable with soft cloth rub	Ammonia salts, slight acids, hot H_2SO_2	Yes	Non-toxic
Na_3AlF_6	Removable with soft cloth rub	Slight cold water, decomposes in alkali	Moisture Sensitive	•
AlF_3	Not damaged by strong rub	0.56g/100cc cold water	No	Slightly toxic
MgF_2	Exceptionally abrasion resistant	0.0076g/100cc cold water HNO_3	No	•
ThF_4	•	Slight decomposes in dilute H_2SO_4 & HCl	•	•
LaF_3	•	Insoluble in water and acids	Resistant to humidity	•
NdF_3	•	Soluble in water	•	•
CeF_3	•	Insoluble in water and acids	Resistant to humidity	•
PbF_2	•	0.064g/100cc cold water, HNO_3	•	Poisonous
SiO_2	Very good abrasion resistance	Soluble in HF	No	Lung Fibrosis (dust)
Al_2O_3	Good abrasion resistance	Very soluble in alcohol, soluble in acids and alkali	No	Non-toxic
MgO	Forms hazy blue scattering film when used as an outer layer	0.0086g/100cc hot water, soluble in acids and ammonia salts	•	Non-toxic
Gd_2O_3	•	•	•	•
ThO_2	Exceptionally good abrasion resistance	Soluble in hot H_2SO_4	No	•
Y_2O_3	•	Soluble in dilute acids	Resistant to humidity	•
Sc_2O_3	•	Soluble in hot acids	•	•
La_2O_3	•	Decomposes in hot water, soluble in acids	Resistant to humidity	•
ZrO_2	Exceptionally good abrasion resistance	Soluble in HNO_3, hot concentrated HCl, and in HF and H_2SO_4	No	•
HfO_2	•	•	No	•
Ta_2O_5	Exceptionally good abrasion resistance	Soluble in HF	No	•
Sb_2O_3	•	Soluble in HCl and H_2SO_4 and in strong alkalies	No	Toxic

Table 3. Elastic and dielectric properties

	Young's Modulus (psi)	Shear Modulus (psi)	Bulk Modulus (psi)	Dielectric Constant
NaF	8.73×10^6	2.80×10^6	4.86×10^6	6.0
LiF	11×10^6	8×10^6	9×10^6	9.0
CaF_2	15×10^6	4.9×10^6	1.2×10^6	6.76
Na_3AlF_6	•	•	•	•
AlF_3	•	•	•	•
MgF_2	24.5×10^6	$\sim 9.42 \times 10^6$	$\sim 20.4 \times 10^6$	4.87
ThF_4	•	•	•	13
LaF_3	•	•	•	•
NdF_3	•	•	•	•
CeF_3	•	•	•	•
PbF_2	•	•	•	26.3
SiO_2	10.6×10^6	4.52×10^6	5.37×10^6	3.78
Al_2O_3	53×10^6	21.5×10^6	30×10^6	10.55
MgO	36.1×10^6	14.66×10^6	22.4×10^6	9.65
Gd_2O_3	18×10^6	•	•	•
ThO_2	34.9×10^6	13.66×10^6	25.9×10^6	10.6
Y_2O_3	16.6×10^6	•	•	5.0
Sc_2O_3	•	•	•	•
La_2O_3	•	•	•	•
ZrO_2	33×10^6	13.5×10^6	•	12.5
HfO_2	•	•	•	•
Ta_2O_5	•	•	•	•
Sb_2O_3	•	•	•	12.8

Table 4. Thermal properties

	Melt Temperature (C°)	Coefficient of Thermal Expansion (C°)	Thermal Conductivity (cal/cm/sec/C°)	Specific Heat (cal/C°/mole)	
					T(C°)
NaF	988	36×10^{-6}	5.05×10^{-2}	11.85	127^0
LiF	870	37×10^{-6}	2.7×10^{-2}	11.12	127^0
CaF_2	1360	24×10^{-6}	2.32×10^{-2}	17.65	127^0
Na_3AlF_6	1000	•	•	56.08	127^0
AlF_3	1100 (sublime)	•	•	20.62	127^0
MgF_2	1266	16×10^{-6}	3.5×10^{-2}	16.39	127^0
ThF_4	900	-2.5×10^{-6}	•	26.45	25^0
LaF_3	1750	4.6×10^{-6}	1.22×10^{-2}	•	
NdF_3	1410	•	•	•	
CeF_3	1460	•	•	22.65	127^0
PbF_2	855	10.8×10^{-6}	•	18.18	127^0
SiO_2	1710	0.5×10^{-6}	0.282×10^{-2}	12.98	127^0
Al_2O_3	2050	5.9×10^{-6}	10^{-5}	22.96	127^0
MgO	2800	10.5×10^{-6}	6×10^{-2}	10.17	127^0
Gd_2O_3	2329	6.6×10^{-6}	•	30.25	127^0
ThO_2	3350	7.24×10^{-6}	3.38×10^{-2}	16.10	127^0
Y_2O_3	2410	7.3×10^{-6}	3.19×10^{-2}	27.09	127^0
Sc_2O_3	•	6.6×10^{-6}	•	25.43	127^0
La_2O_3	2215	10.8×10^{-6}	•	28.04	127^0
ZrO_2	2700	4.2×10^{-6}	0.307×10^{-2}	15.26	127^0
HfO_2	2838	3.8×10^{-6}	0.39×10^{-2}	14.73	260^0
Ta_2O_5	1800	2.5×10^{-6}	•	35.26	127^0
Sb_2O_3	656	•	•	25.94	127^0

Table 5. Parameters of evaporated films compared to bulk values[+]

Material	Deposition temp.,	Film thickness, μm	Final av. stress, kg/cm	Expansion coef., $°C^{-1}$		Young's modulus, psi	
				Film[a]	Bulk[b]	Film[a]	Bulk[c]
SiO_2	230	0.48	-1500	0.70×10^{-6}	0.55×10^{-6}	3.1×10^{6}	10.6×10^{6}
ThF_4	200	1.40	1200	2.9×10^{-6}	-2.5×10^{-6}	2.0×10^{6}	...
MgF_2	230	1.00	2300	30×10^{-6}	13.7×10^{-6}	0.28×10^{6}	20×10^{6}
MgO	230	0.40	-14000	28×10^{-6}	10.5×10^{-6}	0.38×10^{6}	51×10^{6}
HfO_2	200	0.75	3500	1.4×10^{-6}	3.8×10^{-6}	11×10^{6}	...
ZrO_2	200	0.60	3200	1.1×10^{-6}	4.2×10^{-6}	17×10^{6}	33×10^{6}
TiO_2	150	0.55	2250	2.1×10^{-6}	$7\text{-}9 \times 10^{-6}$	13×10^{6}	...
LaF_3	250	0.85	1000	1.9×10^{-6}	4.6×10^{-6}	7.8×10^{6}	...

[a] Film values determined by Dr. A.M. Ledger of the Perkin-Elmer Corporation as part of this program.

[b] M. Sparks and C.J. Duthler. Theoretical Studies of High-Power Ultraviolet and Infrared Materials, 8th Technical Report, December 1976, DARPA Contract No. DAHC 15-73-C-0127, pp. 72-96.

[c] D.P. DeWitt. Handbook of the Optical, Thermal and Mechanical Properties of Six Polycrystalline Dielectric Materials, TPRC Report 19, December 1972. Thermophysical Properties Research Center, Purdue University, Lafayette, IN, 1972.

[+] Reprinted with permission from "Ultraviolet Components for High-Energy Applications," H.E. Bennett, et al., NWC TP 6015, March 1978.

Table 6. Optical properties

	Band Edge (μm)	Transparancy Range (μm)	Bulk Index of Refraction	Film Index of Refraction
NaF	.128	.2 - 11	1.32 - 1.33 (.55 - .40 μm)	1.29 - 1.30 (.55 μm)
LiF	.105	.11 - 7	1.39 - 1.40 (.55 - .40 μm)	1.3 (.55 μm)
CaF_2	.124	.15 - 12	1.43 - 1.44 (.55 - .40 μm)	1.23 - 1.46 (.55 μm)
Na_3AlF_6	•	.2 - 14	1.34 - 1.36	1.32 - 1.35 (.55 μm)
AlF_3	•	.2 - ?	1.38	1.23 - 1.38 (.55 μm)
MgF_2	.113	.11 - 4	1.38 - 1.39 (< 1 μm)	1.38 - 1.40 (.55 μm)
ThF_4	.250	.3 - 15	1.52 (< 1 μm)	1.5 (.55 μm)
LaF_3	.135	.25 - 2	1.60 - 1.61 (.55 - .40 μm)	1.55 - 1.65 [30° - 300°C] (.55 μm)
NdF_3	•	.25 - ?	1.60 (< 1 μm)	1.61 (.55 μm)
CeF_3	•	.3 - 5	1.62 (< 1 μm)	1.63 (.55 μm)
PbF_2	.185	.25 - 17	1.76	1.75 - 1.98 (.55 - .30 μm)
SiO_2	.159	.2 - 9	1.46 (< 1 μm)	1.45 - 1.46 (.55 μm)
Al_2O_3	.141	.2 - 7	1.77 - 1.78 (.55 - .40 μm)	1.54 - 1.63 [40° - 300°C] (.55 μm)
MgO	.175	.2 - 8	1.73 - 1.76 (.55 - .40 μm)	1.70 - 1.74 [50° - 300°C] (.55 μm)
Gd_2O_3	•	.32 - 15		1.8 (.55 μm)
ThO_2	.214	.3 - ?	2.2 (< 1 μm)	1.86 - 1.95 (.55 - .30 μm)
Y_2O_3	.200	.3 - 12	1.88 (< 1 μm)	1.87 - 1.89 (.55 - .33μm)
Sc_2O_3	•	.35 - 13	1.82 (< 1 μm)	1.84 - 1.88 (.55 μm)
La_2O_3	•	.3 - ?	1.87 (< 1 μm)	1.90 - 1.98 (.55 - .33 μm)
ZrO_2	.270	.34 - 12	2.15 (< 1 μm)	2.05 - 2.11 (.55 - .40 μm)
HfO_2	.240	.32 - 12		2.15
Ta_2O_5	•	.35 - 10	2.22 - 2.28 (.55 - .40 μm)	2.10 - 2.25 (.55 - .40 μm)
Sb_2O_3	•	.3 - ?	1.85 (< 1 μm)	2.04 - 2.29 (.546 - .366)

Table 7. Laser damage threshold on single λ/4 layers

	5ns 15 ns 1.06μm		5ns 15ns 0.53μm		5ns 15ns 0.353μm		5ns 15ns 0.265μm		22ns 0.266μm	27ns 0.355μm
NaF	•		•		•		•		10.8	>38
LiF	•		•		•		•		•	•
CaF_2	20.00	33.23	13.20	19.70	2.76	5.22	2.29	3.55	•	•
Na_3AlF_6	•		•		•		•		•	•
AlF_3	•		•		•		•		•	•
MgF_2	13.37	19.57	7.99	15.99	3.09	5.37	2.13	3.25	6.8	•
ThF_4	•	40.92	7.66	16.50	3.90	9.12	1.32	4.39	•	•
LaF_3	•		•		•		•		6.7	•
NdF_3	•		•		•		•		•	•
CeF_3	•		•		•		•		•	•
PbF_2	•		•		•		•		•	•
SiO_2	23.62	47.36	9.54	19.88	6.06	11.76	1.10	1.94	9.4 (λ/2)	•
Al_2O_3	13.15	20.14	7.33	13.39	2.79	6.07	2.21	2.02	2.6	5.9
MgO	14.95	15.01	8.87	16.25	2.86	3.91	1.31	2.34	•	•
Gd_2O_3	•		•		•		•		•	•
ThO_2	•		•		•		•		2.8	9.1
Y_2O_3	•		•		•		•		0.6	•
Sc_2O_3	•		•		•		•		•	•
La_2O_3	•		•		•		•		•	•
ZrO_2	10.08	9.53	6.78	6.23	1.89	2.27	0.54	•	1.5	7.1
HfO_2	8.52	13.16	5.08	9.20	3.47	4.32	0.77	1.42	1.3	•
Ta_2O_5	•		•		•		•		•	•
Sb_2O_2	•		•		•		•		•	•

Table 8. Laser damage threshold for multilayer coatings

	HR (.351 μm, 12 ns) (J/cm^2)	HR (.308 μm, 12 ns) (J/cm^2)	HR (.248 μm, 15 ns) (J/cm^2)	AR (.248 μm, 15 ns) (J/cm^2)	BEAMSPLITTER (.248 μm, 15 ns) (J/cm^2)
Al_2O_3/SiO_2	15.0	•	6.4	6.5	•
Al_2O_3/SiO_2	8.5	5.2	3.0	•	•
Sc_2O_3/MgF_2	6.9(10.6)*	5.4(6.8)*	2.9(4.2)*	4.2	2.3
Sc_2O_3/SiO_2	6.3	•	2.4	•	•
HfO_2/SiO_2	3.3	2.8	2.5	•	•
ZrO_2/SiO_2	3.0	•	•	•	•
Ta_2O_5/SiO_2	1.3	•	•	•	•
Y_2O_3/MgF_2	•	•	1.2	•	•
Y_2O_3/SiO_2	•	3.2	•	•	•
Al_2O_3/MgF_2	•	•	•	4.9	Crazed
ThF_4/MgF_2	•	•	•	6.0	•
ThF_4/Na_3AlF_6	•	2.8	3.3	•	•
LaF_3/MgF_2	•	•	•	4.0	•

* Value in parenthesis is for non-quarter wave design.

LASER DAMAGE THRESHOLDS FOR BARE SUBSTRATES

	.248 μm (15 ns) (J/cm^2)	.351 μm (12 ns) (J/cm^2)
Fused Silica		
Dynasil 1000	6.9	21.1
Suprasil 2	7.7	21.8
Suprasil 2	9.0	30
Sapphire	1.3	•
CaF_2	3.3	18.3
LiF	4-6	•
MgF_2	17.4	20.2

Recent Damage Results for Antireflection Coatings at 355 nm

T. Tuttle Hart and C. K. Carniglia

Optical Coating Laboratory, Inc.
2789 Northpoint Parkway, Santa Rosa, CA 95407-7397

and

F. Rainer and M. C. Staggs*

Lawrence Livermore National Laboratory
University of California
P.O. Box 5508, L-470, Livermore, CA 94550

High-index and low-index thin-film antireflection (AR) coatings for use at 355 nm have been tested to determine their resistance to laser damage. All coatings consisted of dielectric materials which were vacuum deposited onto bowl-feed polished Suprasil II by evaporation. Laser damage studies were made by irradiating several sites on each sample with a 0.6 ns, 355 nm laser pulse. Each site was irradiated by only one pulse.

High-index coatings were made with both a high-index material and a low-index material. The high-index materials chosen for this study were scandia (Sc_2O_3), hafnia (HfO_2), and zirconia (ZrO_2), while the low-index materials were silica (SiO_2) and magnesium fluoride (MgF_2). All coatings had four non-quarterwave thick layers plus a halfwave-thick undercoat (barrier layer) of the low-index material. Average damage threshold values for four samples of each type ranged from 2.4 J/sq. cm to 3.1 J/sq. cm. Coatings made from scandia/magnesium fluoride had the highest damage thresholds.

Low-index coatings contained only low-index materials. The low-index materials chosen for this study were samarium fluoride (SmF_3), lanthanum fluoride (LaF_3) thorium fluoride (ThF_4), silica, magnesium fluoride, and lithium fluoride (LiF). AR coatings containing three to six quarterwave-thick layers plus a halfwave-thick barrier layer were made from nine combinations of these six materials. Average damage threshold values for four to six samples of each type ranged from < 1.0 J/sq. cm to 2.8 J/sq. cm. Coatings made from samarium fluoride/magnesium fluoride had the highest damage thresholds.

One set of four scandia/silica coatings was measured at both 355 nm and 248 nm. Damage thresholds at 248 nm for these parts were determined using 20 ns laser pulses. The average threshold was 4.2 J/sq. cm.

Keywords: antireflection coating; barrier layer; electric field; laser damage; optical coating.

*Work performed under the auspices of the U.S. Department of Energy by Lawrence Livermore National Laboratory under Contract #7405-ENG-48.

1. Introduction

AR coatings on transmitting optics reduce the reflection losses in a laser system. AR coatings with good resistance to laser damage are, therefore, essential if high output energy is to be obtained from a laser.

The purpose of this study was to determine which dielectric materials would yield AR coatings with the highest laser damage thresholds at 355 nm, the third harmonic wavelength of Nd:YAG. Fifteen different AR coatings of two basic types were studied: high-index/low-index coatings with conventional four-layer non-quarterwave designs, and low-index/low-index coatings with three- to six-layer quarterwave designs. The high-index materials (scandia, zirconia, and hafnia) were chosen because they are UV transparent and commonly used in the industry. The low-index materials (lithium fluoride, magnesium fluoride, silica, thorium fluoride, lanthanum fluoride, and samarium fluoride) were chosen because they had high damage thresholds when tested as single layers at 248 nm (KrF laser) by Lawrence Livermore National Laboratory [1].

2. Samples

All coating consisted of dielectric materials which were vacuum deposited onto bowl-feed polished Suprasil II substrates by evaporation. Only bowl-feed polished substrates [2] were used for this study because coatings on this type of substrate historically have higher damage thresholds than similar coatings on conventionally-polished substrates [3].

Because it has been successful in increasing the damage thresholds of AR coatings in other studies at 1064 nm [4,5] and 248 nm [6,7], a halfwave-thick barrier layer was deposited between the substrate and the first layer of the AR coating for all coatings in this study. This barrier layer affects neither the electric-field distribution in the coating nor the spectral performance of the coating, but apparently provides better mechanical and/or chemical properties at the substrate/film interface.

Halfwave-thick overcoat layers have been shown to increase the damage thresholds of high reflector coatings [5,6,7], presumably by increasing the mechanical strength of the film. Although no high reflector coatings were made in this study, one AR coating design contained a halfwave silica overcoat because the material combination (silica/lithium fluoride) lent itself well to this experiment.

Conventional AR coatings are made from a combination of a high-index material and a low-index material. A two-layer design provides a low reflectance value at the design wavelength, but the spectral width of this reflectance minimum is narrow, and the spectral positioning of the minimum is very sensitive to coating errors. A four-layer design provides a broad minimum in reflectance and allows a much larger production tolerance. In fact, if a four-layer design is optimized with an emphasis on spectral width, a reflectance minimum wide enough to encompass two wavelengths of interest (in this case 248 nm and 355 nm) may be obtained. One such coating was made for this study and will be reported on later in this paper.

All high-index/low-index coatings contained four non-quarterwave thick layers plus a halfwave-thick barrier layer of the low-index material used in the design. Each material combination required a slightly different design. The spectral performance and E-field distribution for a typical high-index AR are shown in figure 1. Four material combinations were tested: scandia/magnesium fluoride, scandia/silica, hafnia/silica, and zirconia/silica. Two samples of each material combination were coated per run. Additionally, scandia/silica AR's of a different design were coated and had three samples per run. Each run was repeated as a check of run-to-run variation. All coatings were designed to be AR's at 355 nm; however, one of the scandia/silica designs was also an AR at 248 nm. This set of four parts was, therefore, damage tested at both wavelengths. The spectral performance and E-field distribution at 248 nm for these dual-wavelength coatings can be seen in figure 2.

Low-index AR coatings were made with two low-index materials. Since low-index materials have higher laser damage thresholds than high-index materials [8,9], it was hoped that AR's made only of low-index materials would have damage thresholds that exceeded those of conventional high-index/low-index films. The indices of refraction for the six materials used in these low-index coatings ranged from 1.35 to 1.62.

Taking into account that some difference in refractive index is necessary to achieve low reflectance, nine low-index material combinations were chosen. Two samples of each material combination were coated per run, except for the cases of samarium fluoride/magnesium fluoride and samarium fluoride/silica, which had three samples per run. Each run was repeated as a check of run-to-run variation.

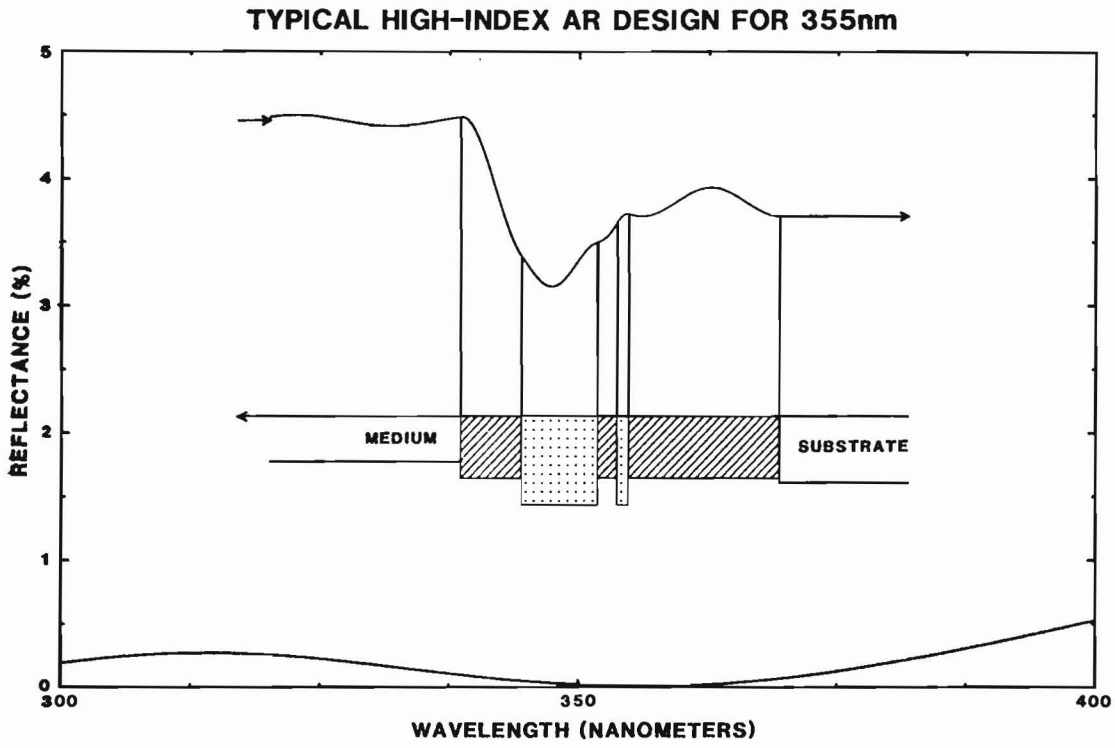


Figure 1. Spectral performance and E-field distribution (at 355 nm) for a typical high-index AR.

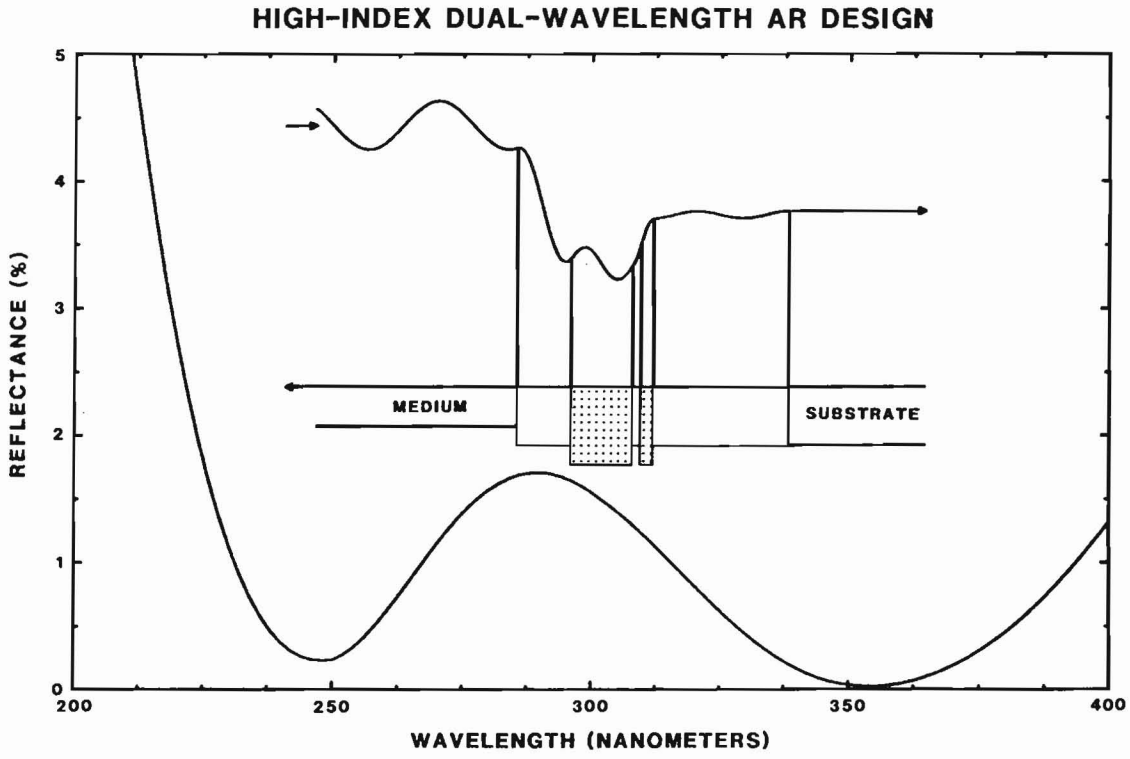


Figure 2. Spectral performance and E-field distribution (at 248 nm) for a high-index dual-wavelength AR.

Designs for these coatings contained three to six quarterwave-thick layers plus a halfwave-thick barrier layer of silica, with the exception of the samarium fluoride/magnesium fluoride design, which had a magnesium fluoride barrier layer. The number of layers in each design was determined by the difference in indices of the two coating materials. In general, the smaller the difference in index, the more layers required to achieve low reflectance. The spectral performance and E-field distribution for a typical low-index AR are shown in figure 3. Note that the reflectance minima for these low-index AR coatings were narrow compared to those for four-layer high-index/low-index coatings.

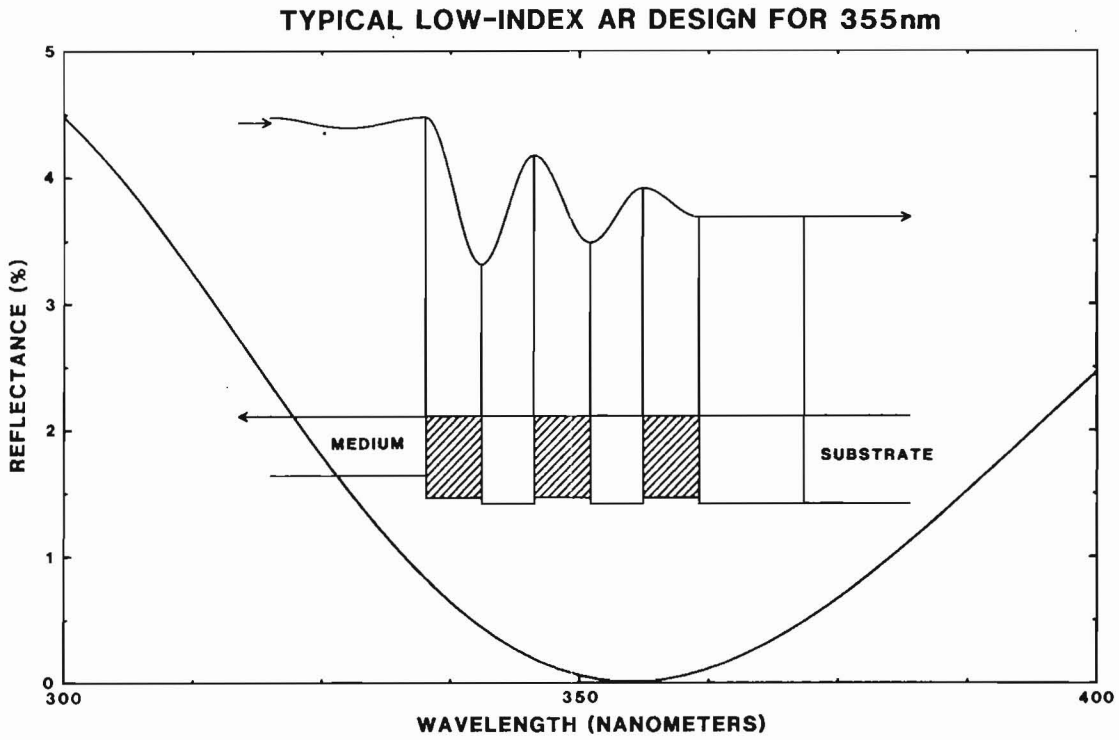


Figure 3. Spectral performance and E-field distribution (at 355 nm) for a typical low-index AR.

3. Damage Testing

Laser damage testing was done at Lawrence Livermore National Laboratory using a 1064 nm Nd:YAG laser which had been frequency tripled to give 0.6 ns, 355 nm laser pulses. The laser beam was focused to give a beam with a diameter of approximately 2.0 mm at the sample surface. The beam profile and pulse energy were recorded for each shot.

The laser damage threshold of each sample was determined by irradiating several different sites on the sample with one laser pulse per site. Each site was inspected immediately prior to and after irradiation with an optical microscope employing Nomarski differential interference contrast. Damage was defined to be any visible change to the site caused by the laser pulse. The threshold of a sample was that value halfway between the lowest fluence which caused damage and the highest fluence which did not.

The thresholds at 248 nm were determined using 20 ns pulses from a 248 nm KrF laser. At the sample surface, the laser beam was 1.5 mm in diameter with an intensity spike 100 μm in diameter.

4. Data and Discussion

The results of the laser damage studies at 355 nm are summarized in figures 4 and 5 and in table 1. In both figure 4 and figure 5, the vertical axis represents the damage threshold in J/sq. cm. The same vertical scale is used for both figures. The horizontal axis serves to identify the coatings whose thresholds appear directly above. Coatings are grouped by material combination and/or design and each darkened circle represents the damage threshold of one sample. The error bar for each sample represents the range between the lowest fluence which caused damage and the highest fluence which did not. Vertical lines separate the groups (types) of coatings. The average damage

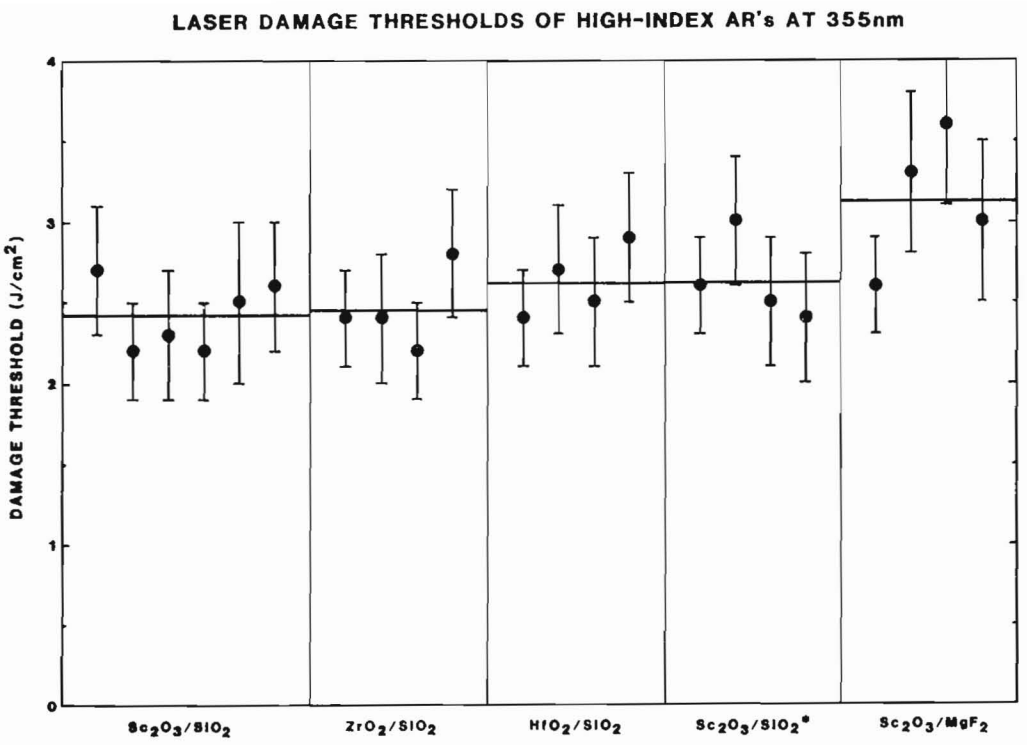


Figure 4. Laser damage thresholds of high-index AR's. Each darkened circle represents the damage threshold of one sample. The error bar for each sample represents the range between the lowest fluence which caused damage and the highest fluence which did not. The average damage threshold for each type of coating is indicated by a horizontal bar. The coatings are arranged in order of increasing average threshold. *Dual-wavelength AR.

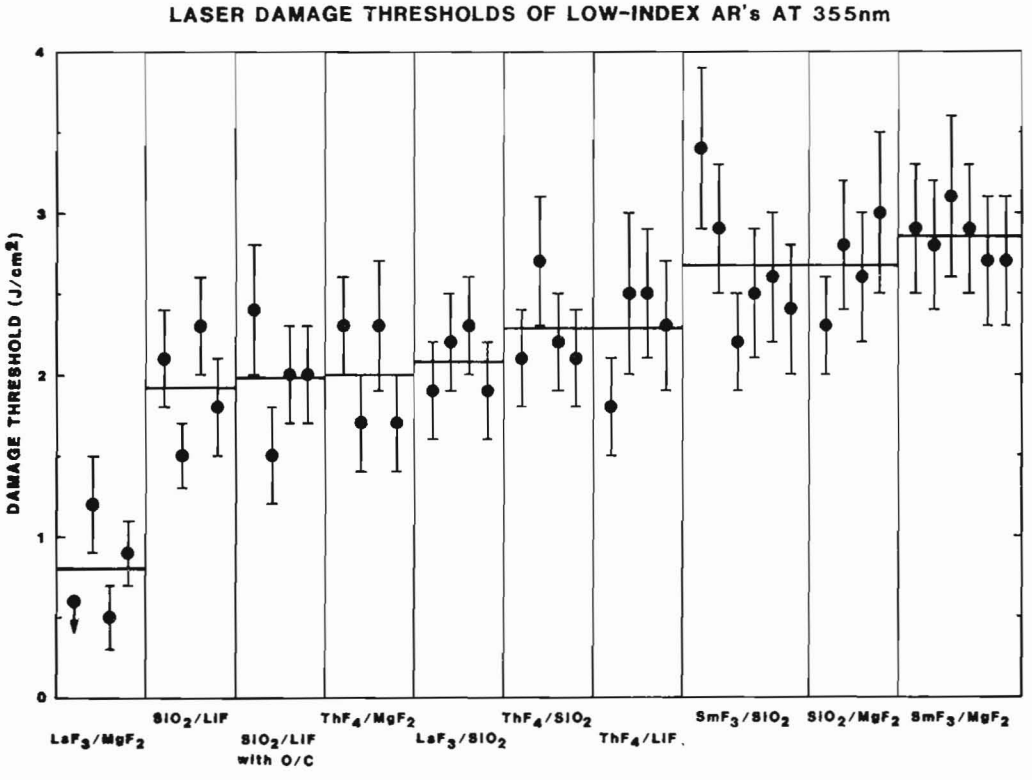


Figure 5. Laser damage thresholds of low-index AR's. Refer to caption for figure 4.

threshold for each type of coating is shown in table 1 and is indicated by a horizontal bar in figures 4 and 5.

Table 1. Table of Laser Damage Thresholds

Material Combination	Coating Type†	Average Threshold (J/cm^2)
Sc_2O_3/MgF_2	High-index	3.1
SmF_3/MgF_2	Low-index	2.8
SmF_3/SiO_2	Low-index	2.7
SiO_2/MgF_2	Low-index	2.7
Sc_2O_3/SiO_2*	High-index	2.6
HfO_2/SiO_2	High-index	2.6
ZrO_2/SiO_2	High-index	2.4
Sc_2O_3/SiO_2	High-index	2.4
ThF_4/LiF	Low-index	2.3
ThF_4/SiO_2	Low-index	2.3
LaF_3/SiO_2	Low-index	2.1
ThF_4/MgF_2	Low-index	2.0
SiO_2/LiF + O/C	Low-index	2.0
SiO_2/LiF	Low-index	1.9
LaF_3/MgF_2	Low-index	<1.0

†See description of high- and low-index coatings in Section 2.

*Dual-wavelength design.

As seen in figure 4, the average damage thresholds for the high-index coatings were essentially the same (2.4 - 2.6 J/sq. cm), except for the scandia/magnesium fluoride coatings. The scandia/magnesium fluoride coatings had an average threshold of 3.1 J/sq. cm, and one of these parts had a threshold of 3.6 J/sq. cm. This average threshold value is approximately 20% higher than the average threshold values for the other high-index coatings.

As seen in figure 5, the average damage thresholds for the low-index coatings (with the exception of lanthanum fluoride/magnesium fluoride) were fairly evenly distributed over a range of values of 1.9 - 2.8 J/sq. cm. The coatings made from samarium fluoride/magnesium fluoride had the highest average thresholds (2.8 J/sq. cm). The highest damage threshold for a single low-index AR sample was 3.4 J/sq. cm for a samarium fluoride/silica coating. The addition of a halfwave silica overcoat to the silica/lithium fluoride coating did not increase its damage threshold to any significant degree.

The range of thresholds at 248 nm for the four scandia/silica dual-wavelength AR's was 3.0 J/sq. cm to 4.8 J/sq. cm. The average damage thresholds of previously-studied, single-wavelength, 248 nm scandia AR's had a range of 4.0 to 6.1 J/sq. cm [7]. Thus, the dual-wavelength AR's were comparable in performance to the single-wavelength AR's. At 355 nm, these coatings had an average damage threshold of 2.6 J/sq. cm, while the scandia-silica coatings of the single-wavelength design had an average threshold of 2.4 J/sq. cm.

5. Conclusions

The highest average laser damage thresholds for 355 nm AR coatings in this study were achieved with coatings made from scandia/magnesium fluoride and samarium fluoride/magnesium fluoride. Coatings made with only low-index materials had thresholds comparable to those made with conventional high-index/low-index material combinations, even though the thresholds of low-index materials exceeded those of high-index materials when tested as single layers. The AR's which had magnesium fluoride as the low-index material and as the barrier layer had the highest thresholds for both high-index coatings and low-index coatings. This indicates that AR coatings containing magnesium fluoride as the low-index material should be studied further.

The authors wish to acknowledge the work of Bill Klapp in preparing the coatings for this study.

6. References

[1] Rainer, F.; Lowdermilk, W. H.; Milam, D.; Carniglia, C. K.; Tuttle Hart, T.; Lichtenstein, T.L.; Materials for optical coatings in the UV, to be published in the report of the 1982 Boulder Conference.

[2] Dietz, R. W.; Bennett, J. M.; Bowl feed technique for producing supersmooth optical surfaces. Appl. Opt. 5(5): 881-882; 1966 May.

[3] Lowdermilk, W. H.; Milam, D.; Rainer, F.; Damage to coatings and surfaces by 1.06 μm pulses. Nat. Bur. Stand. (U.S.) Spec. Publ. 568; 391-398; 1979.

[4] Apfel, J. H.; Enemark, E. A.; Milam, D.; Smith, W. L.; Weber, M. J.; The effects of barrier layers and surface smoothness of 150-ps, 1.064 μm laser damage of AR coatings on glass. Nat. Bur. Stand. (U.S.) Spec. Publ. 509; 255-259; 1977.

[5] Carniglia, C. K.; Oxide coatings for one micrometer laser fusion systems. Thin Solid Films 77: 225-238; 1981.

[6] Tuttle Hart, T.; Lichtenstein, Terri L.; Carniglia, C. K.; Effects of undercoats and overcoats on damage thresholds of 248 nm coatings. Nat. Bur. Stand. (U.S.) Spec. Publ. 638; 344-349; 1981.

[7] Rainer, F.; Lowdermilk, W. H.; Milam, D.; Tuttle Hart, T.; Lichtenstein, T. L.; Carniglia, C. K.; Scandium oxide coatings for high-power UV laser applications. Appl. Opt. 21(20): 3685-3688; 1982 October 15.

[8] Bettis, Jerry R.; Guenther, Arthur H.; The refractive index dependence of pulsed laser induced damage. Nat. Bur. Stand. (U.S.) Spec. Publ. 414; 214-217; 1974.

[9] Newnam, Brian E.; Gill, Dennis H.; Ultraviolet damage resistance of laser coatings. Nat. Bur. Stand. (U.S.) Spec. Publ. 541; 190-201; 1978.

Manuscript received 7-2-84/sar

Recent Damage Results on High Reflector Coatings at 355 nm

C. K. Carniglia and T. Tuttle Hart

Optical Coating Laboratory, Inc.
2789 Northpoint Parkway
Santa Rosa, CA 95407-7397

F. Rainer and M. C. Staggs*

Lawrence Livermore National Laboratory
University of California
P.O. Box 5508, L-470
Livermore, CA 94550

Several studies of damage induced by 0.6 ns, 355 nm laser pulses have been carried out on thin-film reflectors. The reflectors consisted of dielectric materials vacuum-deposited onto BK7 substrate by evaporation. Each part was damage tested on several sites using one laser shot per site.

Quarterwave stacks of various material combinations were used to make a series of reflectors. Four to six parts were tested for each of four materials combinations. The average damage thresholds obtained for these coatings were 3.5 J/sq. cm for scandia/magnesium fluoride, 3.0 J/sq. cm for zirconia/silica, 2.4 J/sq. cm for tantala/silica and 1 J/sq. cm for hafnia/silica. Interestingly, there was no improvement in those reflectors to which a halfwave silica overcoat was added. This is contrary to previous results at 1064 nm and 248 nm.

A series of zirconia/silica reflectors was made using coating temperatures ranging from 150°C to 300°C. The thresholds were slightly improved by coating at higher temperatures.

Coatings made of zirconia/silica with outer quarterwave layers of samarium fluoride and either silica or magnesium fluoride were also tested. Thresholds for these coatings ranged from 1.7 to 2.8 J/sq. cm and were slightly lower than the thresholds of the zirconia/silica stacks alone.

Scandia/magnesium fluoride coatings with non-quarterwave designs have been shown to be effective in raising the damage threshold of high reflectors at 248 nm. Such designs reduce the electric field intensity in the outer scandia layers. The damage thresholds of several non-quarterwave designs were compared. The highest threshold, 5.1 J/sq. cm, was achieved by reducing the electric field in the two outer scandia layers.

Key words: damage; electric field; high energy laser; laser damage; reflectors; thin film.

1. Introduction

One of the continuing challenges facing the high energy laser field is the development of optical coatings that can withstand high laser fluences. This paper reports the results of research efforts to improve the laser damage resistance of high reflector (HR) coatings of the type that would be used in a 355 nm laser system. The research was a joint effort between Optical Coating Laboratory, Inc. (OCLI) and Lawrence Livermore National Laboratory (LLNL).

---

*Work performed under the auspices of the U.S. Department of Energy by Lawrence Livermore National Laboratory under Contract No. W-7405-ENG-48.

The coatings were made at OCLI in a 1.2 meter box coating machine. All materials were deposited by evaporation using an electron gun source. The substrate for all coatings was BK7, which had been polished by Zygo Corporation using a continuous feed polishing technique.

The damage testing was done by LLNL using a frequency tripled Nd-glass laser. The 355 nm, 0.6 ns laser pulses were focused to give a beam with a 1 mm diameter at the coating surface. Each test site was irradiated with one laser pulse and the presence of damage was determined visually using Nomarski microscopy. The accuracy of the damage threshold determination was ± 10% for each part.

We have looked at the effects of coating materials, coating designs, and process parameters on laser damage thresholds. Several of the ideas reported here have been motivated by previous successes with 20 ns pulses at 248 nm (KrF laser) [1-4], and 1 ns pulses at 1064 nm (Nd-glass) [5,6]. The next five sections discuss the results of our studies of coating materials, silica overcoats, coating temperatures, an alternate high-index material for the outer layers, and effects of electric field distribution within the coatings.

2. Coating Materials

A standard HR coating consists of alternate layers of two materials having different indices of refraction. Each layer has an optical thickness of one quarter of the laser wavelength and the outermost quarterwave layer must be of the high-index material. For this study, four high-index and two low-index materials were incorporated into the HR coatings tested. These six materials are listed in table 1, together with their refractive indices and approximate UV cutoff wavelengths.

Table 1. Coating Materials for 355 nm HR's

		Refractive Index	UV Cutoff Wavelength (nm)
Ta_2O_5	(tantala)	2.27	297
ZrO_2	(zirconia)	2.07	230
HfO_2	(hafnia)	2.04	225
Sc_2O_3	(scandia)	1.97	215
SiO_2	(silica)	1.48	<200
MgF_2	(magnesium fluoride)	1.39	<200

Tantala, zirconia, and hafnia were combined with silica in standard 15-quarterwave layer HR designs. Scandia was combined with both silica and magnesium fluoride in a quarterwave design that had demonstrated a high damage threshold at 248 nm [2,3]. The design incorporated five scandia/magnesium fluoride pairs on top of five scandia/silica pairs. In addition, a halfwave protective layer of magnesium fluoride was added to the top of this quarterwave stack. The complete design is given in table 4 in section 6.

Six HR's containing scandia and four HR's of each of the other material combinations were tested. The damage thresholds are given in figure 1. The circles represent the damage thresholds of individual HR's, and the error bars indicate the uncertainty in the thresholds. The line through each set of data represents the average threshold for those data. The scandia/magnesium fluoride/silica HR's averaged 3.5 joules/ sq. cm, which was the highest average threshold of the group. The 3.0 joules/sq. cm average for zirconia/silica HR's was also quite high. However, the 1.0 joules/sq. cm

average for the hafnia/silica coatings was quite low. Based on UV cutoff wavelength (lower) and refractive index (lower) one might have expected the HR's containing the hafnia to have higher thresholds than those containing zirconia and tantala.

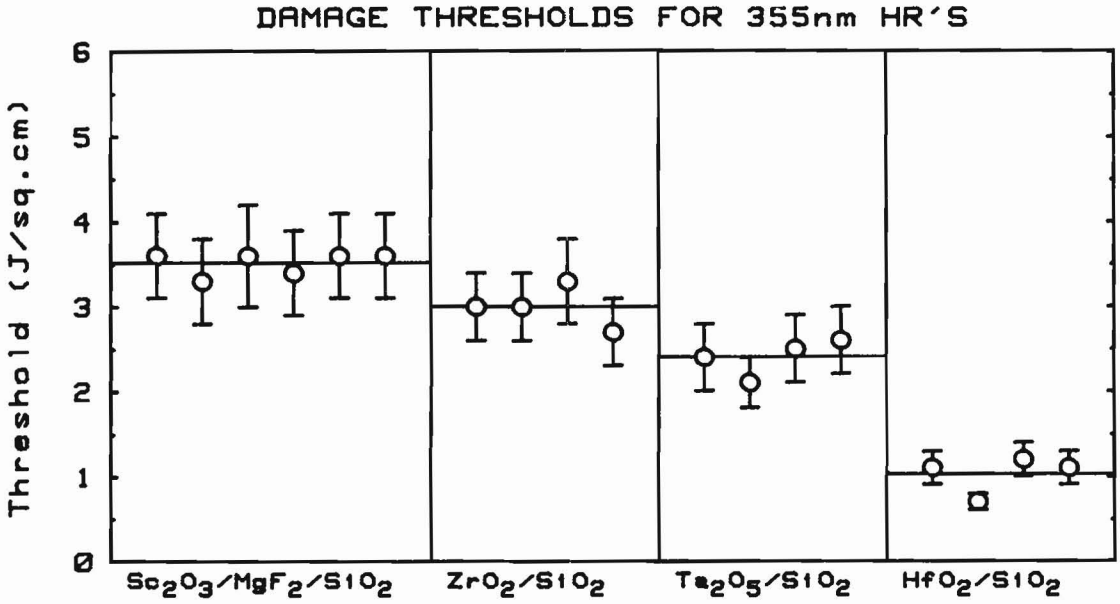


Figure 1. Laser damage thresholds of 355 nm HR's. Each circle represents the damage threshold of one sample. The error bar for each sample represents the range between the lowest fluence which caused damage and the highest fluence which did not. The average damage threshold for each type of coating is indicated by a horizontal bar. The coatings are arranged in order of decreasing average threshold.

The success of the scandia design might be due, in part, to either the presence of magnesium fluoride instead of silica in the outer layers, or to the magnesium fluoride overcoat. Because of the high cost of scandia compared to zirconia, it is important to determine whether the higher thresholds of the scandia HR's are due to properties inherent to scandia, or whether they are due to the silica or magnesium fluoride. A zirconia/magnesium fluoride/silica HR with a design similar to the scandia HR should, therefore, be tested.

3. Halfwave Silica Overcoat

A design trick which has proven useful at other laser wavelengths is the addition of a halfwave silica overcoat to the quarterwave stack. This layer, which affects neither the reflectance of the stack nor the electric field distribution within the stack, has produced significant improvements in damage thresholds. For example, at 1064 nm, the halfwave silica overcoat increased the damage threshold of titania/silica HR's by a factor of 1.6 [5,6]. The factor of two improvement observed for 248 nm scandia/magnesium fluoride/silica HR's was even more dramatic [1,2].

We investigated the effectiveness of halfwave silica overcoats for the zirconia, hafnia, and tantala HR's reported on in section 2. In each coating run, four HR's were coated - two with and two without the overcoat. This was accomplished by first coating all four parts with the HR combination. Next, two of the parts were covered using a movable mask and the overcoat was applied to the remaining two parts. Two runs were made using each combination of coating materials, resulting in four parts of each type.

The effect of the halfwave silica overcoat was a 20% decrease in the average thresholds of the zirconia/silica and tantala/silica HR's. Thus, the overcoat was detrimental to the performance of these HR's. The average threshold of the hafnia/silica HR's was unchanged by the overcoat, but it was so low to start with (1 joule/sq. cm), that the overcoat would not be expected to have much of an effect. These results indicate that the damage threshold of silica may be a limiting factor at 355 nm. This was unexpected since silica works well at 248 nm [1,2].

4. Substrate Temperature

One of the parameters affecting the properties of optical coatings is the temperature of the substrate during the coating process. Higher temperatures generally lead to coatings with larger grain size and lower damage threshold. Lower coating temperatures have been helpful in increasing the damage thresholds of tantala/silica antireflection coatings at 1064 nm [7]. Zirconia/silica HR's were used to study the effects of temperature on damage thresholds. This material combination was chosen because the threshold of the zirconia HR's is relatively high (see fig. 1) and because zirconia is a common coating material and is relatively inexpensive compared to scandia. Therefore, any improvement in threshold would be beneficial.

The zirconia/silica HR's were coated using four substrate temperatures: 150°C, 200°C, 250°C, and 300°C. Four parts were coated at each temperature in two separate runs of two parts each. The average damage thresholds are summarized in table 2. The HR's made at the three higher temperatures had essentially the same average threshold of about 3 joules/sq. cm. The lowest coating temperature produced a slightly lower threshold. Thus, we conclude that for coating temperatures over 200°C, the threshold of zirconia/silica HR's is unaffected by temperature.

Table 2. Average Damage Thresholds for Zirconia/Silica HR's

Coating Temperature	Threshold J/cm^2
300°C	3.2
250°C	2.9
200°C	3.0
150°C	2.3

5. Samarium Fluoride Outer Layers

Samarium fluoride is a material with an intermediate refractive index value of 1.63 at 355 nm. Damage results on antireflection coatings at 355 nm indicate that samarium fluoride has a damage threshold comparable to scandium oxide [8]. To test samarium fluoride as the high-index layer of an HR would require a large number of layers. An alternate approach to testing samarium fluoride in an HR configuration is to incorporate it into a small number of the outermost layers of a standard HR. The basic HR would then provide high reflectivity, but the samarium fluoride would experience the largest electric fields and thus be the major factor in determining the damage threshold of the coating.

The basic reflector used for this test was a zirconia/silica HR with 15 layers. Six such HR's were coated in a single run. Then, with the help of movable masks, two pairs of samarium fluoride/silica layers were added to two of the parts and four pairs to two other parts. Finally, a halfwave silica overcoat was added to all six HR's. A similar coating run was made using magnesium fluoride as the low index material in the outer pairs (but still using silica for the halfwave overcoat). The damage results for these twelve parts (two of each type) are presented in table 3. These data

indicate that the samarium fluoride outer pairs were detrimental to the damage threshold of the base stack. The thresholds for the outer pairs containing magnesium fluoride were somewhat better than those containing silica. In either case, the samarium fluoride outer layers failed to improve the threshold of the basic HR's.

Table 3. Zirconia/Silica HR's with Samarium Fluoride Outer Pairs

	Average Damage Thresholds (J/cm^2)	
Number of Pairs	SmF_3/MgF_2	SmF_3/SiO_2
0	3.0	2.8
2	2.5	1.85
4	2.4	1.9

6. Suppressed Electric Fields

It is possible to modify the thicknesses of the outer layers of an HR to reduce or suppress the electric field in the high-index material. Because high-index materials are generally more damage prone than low-index materials, reducing the electric field in the high-index layers is expected to increase the damage threshold of the HR [9,10]. This approach has proven successful for scandium oxide/magnesium fluoride/silica HR's at 248 nm [3] and also at 308 nm [11],

Four different HR designs were tested. They are listed in table 4. The basic HR consisted of five pairs of scandia/silica followed by five pairs of scandia/magnesium fluoride. The use of silica in the first five pairs helped to reduce the overall stress in the coating. If only magnesium fluoride is used for the low index layers, the stress becomes quite tensile and crazing of the coating may occur. Damage results for the basic HR have already been reported in section 2. The design labeled "one pair suppressed" has a thinner outer scandia layer and a thicker magnesium fluoride layer beneath it. The thicknesses have been chosen so that the peak electric field in this scandia layer is reduced to the same level as in the next lower scandia layer [10]. A similar approach was used to suppress the field in the outer two scandia/magnesium fluoride pairs. To provide an additional test, the reverse approach was used in the design labeled "one pair suppressed (MgF_2)" in table 4. Here the thickness of the magnesium fluoride layer was reduced and the thickness of the outer scandia layer increased until the peak field in the modified magnesium fluoride layer was equal to the peak field in the next lower layer. Note that all four designs ended with a half-wave magnesium fluoride overcoat.

Table 4. Suppressed Electric Field Designs

1. Basic HR	sub/$(HL)^5(HL')^5H$ L'L'/air
2. One Pair Suppressed	sub/$(HL)^5(HL')^4H$ 1.5L' 0.6H L'L'/air
3. Two Pairs Suppressed	sub/$(HL)^5(HL')^3H$ 1.5L' 0.6H 1.6L' 0.5H L'L'/air
4. One Pair Suppressed (MgF_2)	sub/$(HL)^5(HL')^4H$ 0.5L' 1.4H L'L'/air
Quarterwave layers at 355:	H = Sc_2O_3, L = SiO_2, L' = MgF_2

Six parts of each design were tested - three parts from each of two coating runs. The results are shown in figure 2. The best thresholds were observed for the HR's with two modified pairs of layers. The average threshold for the six parts was 4.9 joules/sq. cm, a 40% increase over the standard HR containing only quarterwave layers. The results for the design which suppressed the electric field in the outer magnesium fluoride layer are somewhat scattered, but the average is lower than the standard design.

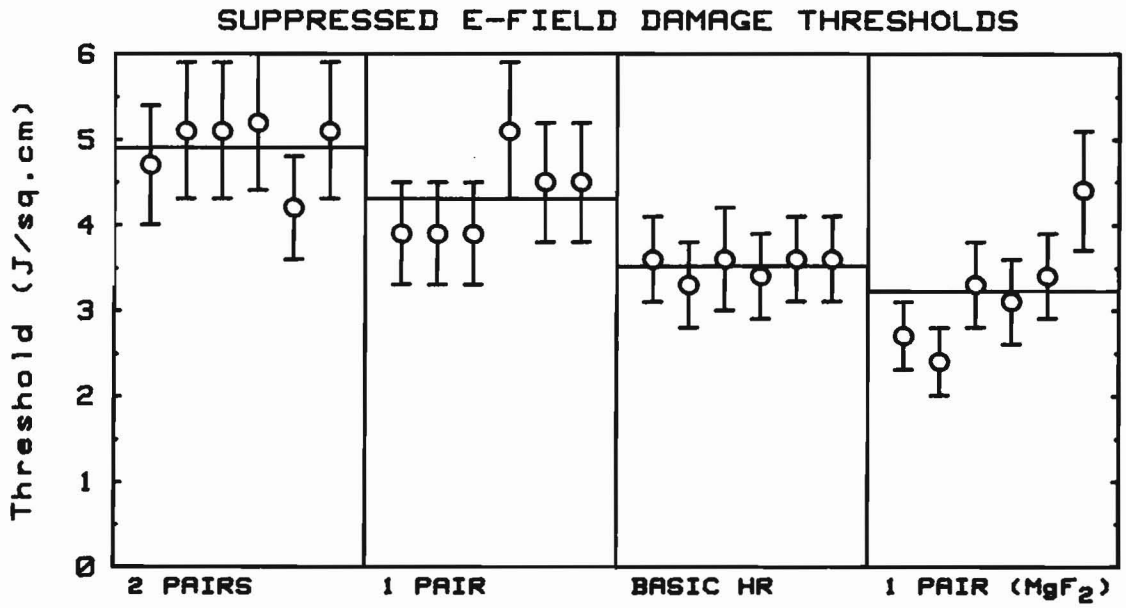


Figure 2. Laser damage thresholds for the suppressed electric field HR designs in table 4. Refer to caption for figure 1.

7. Conclusions

HR's incorporating scandium oxide have demonstrated the highest damage thresholds at 355 nm. These high thresholds can be further enhanced by suppressing the electric fields in the outer scandia layers. There is some indication that magnesium fluoride is a more damage-resistant low-index material than silica at 355 nm. This needs to be tested further.

The authors wish to acknowledge the work of Bill Klapp in preparing the coatings for this study.

8. References

[1] Rainer, F.; Lowdermilk, W. H.; Milam, D.; Tuttle Hart, T.; Lichtenstein, T. L.; Carniglia, C. K. Scandium oxide coatings for high-power UV laser applications. Appl. Opt. 21(20): 3685-3688; 1982 October 15.

[2] Tuttle Hart, T.; Lichtenstein, T. L.; Carniglia, C. K.; Rainer, F. Effects of undercoats and overcoats on damage thresholds of 248 nm coatings. Nat. Bur. Stand. (U.S.) Spec. Publ. 638; 1981. 344-349.

[3] Newnam, B. E.; Foltyn, S. R.; Jolin, L. J.; Carniglia, C. K. Multiple-shot ultraviolet laser damage resistance of nonquarterwave reflector designs for 248 nm. Nat. Bur. Stand. (U.S.) Spec. Publ. 638; 1981. 363-379.

[4] Rainer, F.; Lowdermilk, W. H.; Milam, D.; Carniglia, C. K.; Tuttle Hart, T.; Lichtenstein, T. L. Damage thresholds of thin film materials and high reflectors at 248 nm. Nat. Bur. Stand. (U.S.) Spec. Publ. 669; 1982. 274-281.

[5] Carniglia, C. K. Oxide coatings for one micrometer laser fusion systems. Thin Solid Films 77(3): 225-238; 1981 March 6.

[6] Carniglia, C. K.; Apfel, J. H.; Allen, T. H.; Tuttle, T. A.; Lowdermilk, W. H.; Milam, D.; Rainer, F. Recent damage results on silica/titania reflectors at 1 micron. Nat. Bur. Stand. (U.S.) Spec. Publ. 568; 1979. 377-390.

[7] Milam, D.; Lowdermilk, W. H.; Rainer, F.; Swain, J. E.; Carniglia, C. K.; Tuttle Hart, T. Influence of deposition parameters on laser-damage threshold of silica-tantala AR coatings. Appl. Opt. 21(20): 3689-3694; 1982 October 15.

[8] Tuttle Hart, T.; Carniglia, C. K.; Rainer, F.; Staggs, M. C. Recent damage results for antireflection coatings at 355 nm. Nat. Bur. Stand. (U.S.) Spec. Publ.; 1983 (To be published).

[9] Newnam, B. E.; Gill, D. H. Laser damage resistance and standing-wave fields in dielectric coatings. J. Opt. Soc. Am. 66(2): 166A; 1976 February.

[10] Apfel, J. H. Optical coating design with reduced electric field intensity. Appl. Opt. 16(7): 1880-1885; 1977 July.

[11] Foltyn, S. R.; Jolin, L. J.; Newnam, B. E. Progress in ultraviolet damage testing at Los Alamos. Nat. Bur. Stand. (U.S.) Spec. Publ. 669; 1982. 266-273.

The comment was made that it is gratifying to see that the all-fluoride combination samarium fluoride-magnesium fluoride seems to work well. In another paper in this conference, their performance will be shown to bear up very well compared to the oxides, and they are very good in excimer laser systems in regard to insensitivity to chemical attack.

Manuscript received 5-24-84 /sar

Alumina/Silica Multilayer Coatings for Excimer Lasers*

S. R. Foltyn and L. J. Jolin

Los Alamos National Laboratory
Los Alamos, NM 87545

The coating parameter that most strongly influences optical damage resistance is the choice of materials used to produce a component. During the course of testing of hundreds of ultraviolet reflectors involving 12 different material combinations, multilayer stacks of Al_2O_3/SiO_2 have demonstrated a superior ability to resist laser-induced damage. Further, damage thresholds for these coatings are at least twice as high as for reflectors composed of other materials: In particular, thresholds of 6 J/cm^2 at 248 nm (15 ns) and 12 J/cm^2 at 351 nm (12 ns) have been measured. Comparative results are presented for a variety of materials at both wavelengths as are preliminary results for alumina-based antireflective coatings.

Key words: Al_2O_3; coating materials; excimer optics; laser-induced damage; multilayer dielectric reflectors; ultraviolet reflectors.

1. Introduction

In this work we report on an extensive survey of materials and vendors for multilayer dielectric reflectors at excimer wavelengths. As a result of this study we provide a ranking of material combinations for ultraviolet reflectors with alumina/silica demonstrating the best performance. In an attempt to explain this ranking, two theoretical models are invoked. Although based upon distinctly different physical phenomena, both demonstrate how Al_2O_3 could be more damage resistant than other common materials and, interestingly, both models predict even better performance for BeO.

2. Test Conditions

Laser pulse lengths at 248 and 351 nm were 15 and 12 ns FWHM, respectively, and the pulse repetition frequency was 35 pps. Both sets of results were generated with a nominally 0.5 mm mean spot diameter; however, a spotsize-independent method of measuring the damage threshold [1] was employed. Briefly, damage threshold was defined as the zero-percent intercept of a damage probability curve, or alternately, as the highest fluence at which damage could not be produced. Damage consisted of physical disruption of the coating which generally began within the first few shots and which frequently evolved, during successive shots, from micron-size pits to a complete failure of the irradiated area. Finally, all testing was of the n-on-m variety wherein m sites were tested at each fluence (m=10) and each nondamaging site was irradiated for n shots (n=140).

3. Results and Discussion

In figure 1 are summarized test data for both 248 nm and 351 nm reflectors with each point representing a single coating run. Excepting the aluminum reflectors, which are shown for purposes of comparison, the coating designs were all of the type

$$S\ H(LH)^nLL$$

*This research was performed under the auspices of the U.S. Department of Energy and the Defense Advanced Research Projects Agency.

where S is a fused silica substrate, H and L are quarterwave layers of the high- and low-index materials, and n is the number of layer pairs deposited in order to achieve high reflectance. Some general comments on these results are summarized below.

- Thresholds for various material combinations range over nearly two orders of magnitude and, while it is probable that some rearrangement will occur in material rankings as testing continues, only Al_2O_3/SiO_2 has demonstrated 248-nm performance at levels in excess of 4 J/cm^2.

- Assuming, as discussed in a later section, that the high-index material controls damage resistance of a material pair, a question is raised regarding the poor performance of alumina with either NaF or Na_3AlF_6, especially when both were produced by vendors who had been successful with alumina/silica. In the case of the former, the reason is almost certainly related to the fogged condition of the reflectors as delivered. In the alumina/cryolite, however, no problem was indicated by physical appearance or optical performance of the coatings. It was later found that the vendor had used a different coating chamber than that used for alumina/silica depositions, but in the absence of any additional details, no conclusion can be drawn.

- Implicit in figure 1 is a factor-of-two increase in 351-nm thresholds over those for the same materials at 248 nm. Assuming a power-law wavelength dependence, this translates to a threshold scaling of λ^2.

- The reflectors of figure 1 were provided by over fifteen vendors. Alumina/silica samples were purchased from seven vendors; of these seven, four have delivered parts with thresholds over 4 J/cm^2 at 248 nm, and/or over 8 J/cm^2 at 351 nm. These vendors* are:

  Airtron Optical and Magnetic Components
  Broomer Research Corporation
  Coherent Optics Division
  Spectra Physics, Inc. - Optics Division

- Examination of figure 1 reveals, qualitatively, an inverse relationship between threshold and index of refraction of the high-index component. A practical consequence of this is that, for damage-resistant components, system designers will be constrained to use materials with a low index ratio. The result is shown (fig. 2) in spectral transmittance curves for reflectors of Sc_2O_3/SiO_2 and Al_2O_3/SiO_2. The sample using scandia (n=1.90) achieves a good broadband reflectance with only 23 layers, while the alumina (n=1.65) version requires 49 layers—resulting in the narrow band—to achieve a somewhat lower reflectance.

Although the emphasis thus far has been on reflectors, some preliminary results have been obtained for antireflection coatings as well. Table 1 contains a summary of these results showing that, for an appropriate design, AR thresholds can be as high as for reflectors composed of the same materials.

Table 1. Alumina-Based Antireflection Coatings

Design[a]	Threshold (J/cm^2) 248 nm, 15 ns
S HL	3.4
S LLHL	6.0
S L'L'HL	5.1
S L'L'HL'	4.9

[a] S = substrate (Suprasil 2), H = Al_2O_3, L = SiO_2, L' = MgF_2. All designs had R < (0.5%).

*This list is not the result of a comprehensive vendor's survey, nor does it constitute an endorsement by the University of California, the Los Alamos National Laboratory, or the authors.

4. Modeling the Results

Empirical studies such as the one previously described frequently lose their significance without a suitable physical argument to explain the results. It is fortunate that, in this case, two models exist which potentially offer such an explanation. Unfortunately, at this point neither theory nor experiment is sufficiently mature to allow a conclusion about which model, if either, is correct.

4.1. Damage as an Avalanche Breakdown Process

The first of these two models was presented at the Boulder Damage Symposium in 1975 [2]. It is an avalanche breakdown argument which concludes that the first electrons in the avalanche process are liberated when the local rms electric field in the coating reaches a value proportional to the quantity N/n^2-1, where N is the atomic number density and n is the index of refraction of the material being damaged. It was soon realized, however, that when the proportionality constants are included—the complete expression for the threshold electric field is

$$\frac{N}{n^2-1}\,\frac{q_e}{\varepsilon_o}\,x_{cr}\,\sqrt{10^{-5}}$$

where x_{cr} is the critical electron displacement of about 2 Å—the result is a threshold prediction which is highly optimistic. For the present results, the prediction is optimistic by two orders of magnitude in fluence theshold, or by a factor of ten in terms of field strength. Nevertheless, by ignoring for now the magnitude discrepancy and simply considering the proportionality, very good agreement is found between the material ranking predicted by N/n^2-1 and that observed experimentally (fig. 3).

At this point, a digression is necessary to discuss the assumptions that were made in the construction of figure 3.

- Damage occurs in the high-index component of a multilayer. This follows from the generally accepted argument that high-index materials are more readily damaged than materials with a low index.

- Only the performance envelope of figure 1 is used in the plot of figure 3. This assumes that the envelope represents optimum performance for each material and in addition allows that less damage resistant coatings can be made from any material.

- The factor needed to account for magnitude differences between theory and experiment is approximately the same for all materials tested. This implies that the data in figure 3 should lie on a straight line and that only the slope of the line is in question.

- The linear regression fit in figure 3 uses the origin and all points except three. ZrO_2 and PbF_2 were excluded from the fit because both damaged in a non-normal mode that was indicative of a uniform absorption process—not surprising for these materials at 248 nm. BeO was also excluded but for a different reason: It is assumed that the single coating run evaluated here was not representative of optimized BeO. More on BeO appears at the end of this section.

Returning to the subject of the predicted magnitude of the threshold electric field: We postulate that electric field enhancement at cracks or voids in the coating is responsible for the factor-of-ten discrepancy. It is well known that coatings possess a columnar structure and it is not unreasonable to expect that within this structure exist localized geometric imperfections of an appropriate size. Calculations of electric field enhancement at defects of an appropriate size are available [3], although the enhancement magnitude is far lower than a factor of ten. This subject will be revisited in a future paper.

As mentioned previously, it appears that BeO in figure 3 is not performing as expected. If this is the case continued development work should lead to 248-nm thresholds of about 10 J/cm^2 for reflectors based on BeO. Work is currently underway to test this hypothesis.

4.2. Damage as a Thermal Process

Another model has recently been proposed [4] in which, instead of being geometric features, the defects are strongly absorbing spherical inclusions (later versions of this model generalize the

inclusion shape). The theory predicts that damage occurs when the inclusion/host system reaches some critical temperature and that this temperature is related to the ability of the host to conduct heat away from the defect site. Numerically, the damage threshold fluence should be proportional (for constant pulselength) to $(\rho C_p K)^{1/2}$, where the quantitites represent the density, specific heat, and thermal conductivity, respectively of the host material.

Figure 4 is a plot of various oxide damage thresholds versus the thermal properties of the materials in bulk form. Absolute threshold predictions are not possible due to a general lack of thermal properties of thin films, and because the critical temperature is unknown. As a result of these uncertainties, the credibility of figure 4 is in question. It is shown here because, as measured, good performance is indicated for alumina, and because a completely different physical model has again predicted even better performance for BeO. If the fitted line is correct, 248 nm thresholds in excess of 15 J/cm^2 could be expected for BeO-based reflectors.

It should be noted in closing that preliminary evidence exists [5] which indicates that BeO is more damage resistant than Al_2O_3 in the ultraviolet.

5. Conclusions

We have presented the results of a large survey of vendors and materials for ultraviolet reflectors. We find that Al_2O_3/SiO_2 is the most damage resistant material combination, but that, based upon either of two theoretical models, BeO may prove to be a superior high-index material.

6. References

[1] Foltyn, S. R. Spotsize Effects in Laser Damage Testing. Nat. Bur. Stand. (U.S.) Spec. Publ. 669; 1982, 368 p.

[2] Bettis, J. R.; House, R. A.; Guenther, A. H.; Austin, R. The Importance of Refractive Index, Number Density, and Surface Roughness in the Laser-Induced Damage of Thin Films and Bare Surfaces. Nat. Bur. Stand (U.S.) Spec. Publ. 435; 1975. 289 p.

[3] Bloembergen, N. Role of Cracks, Pores, and Absorbing Inclusions on Laser-Induced Damage Threshold at Surfaces of Transparent Dielectrics. Appl. Opt. 12(4):661-664; 1973 April.

[4] Lange, M. R.; McIver, J. K.; Guenther, A. H.; Walker, T. W. Pulsed Laser Induced Damage of an Optical Material with a Spherical Inclusion: Influence of the Thermal Properties of the Materials. Nat. Bur. Stand. (U.S.) Spec. Publ. 669; 1982. 380 p.

[5] Ebert, J. Activated Reactive Evaporation. Seddon, R. I., ed. Proceedings of Optical Thin Films meeting; 1982 January 26-27; Los Angeles, California. SPIE Vol. 325; 1982. 29-38.

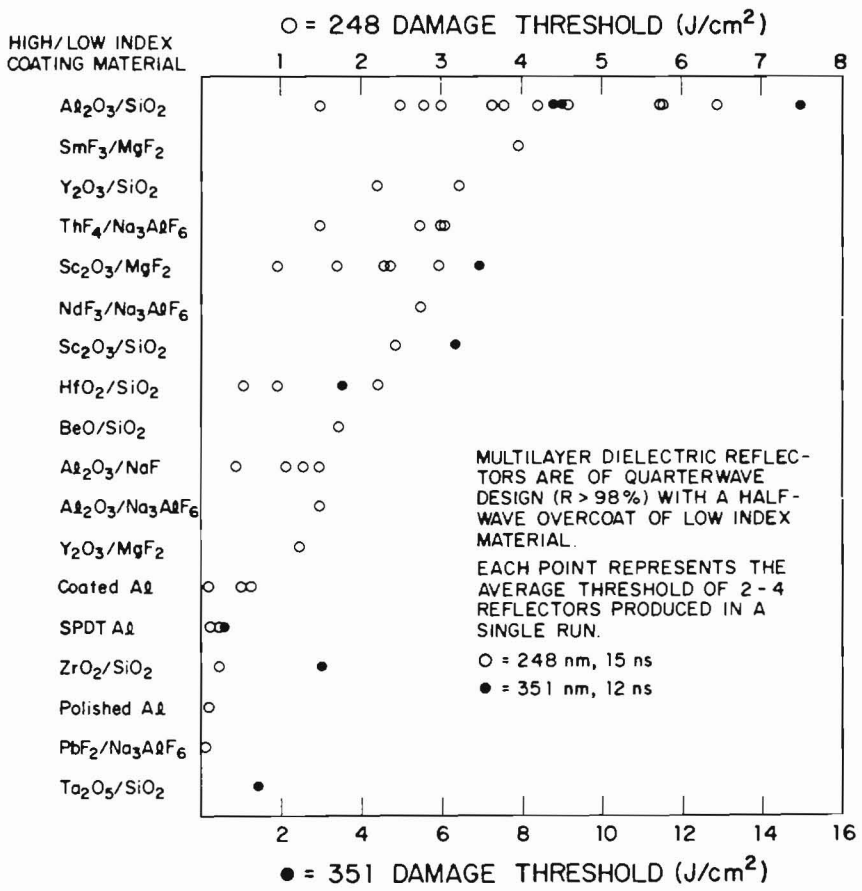


Figure 1. Damage thresholds for various reflector material combinations. Each point represents the average threshold for a single coating run. Dielectric reflectors were of all-quarterwave design with a halfwave overcoat.

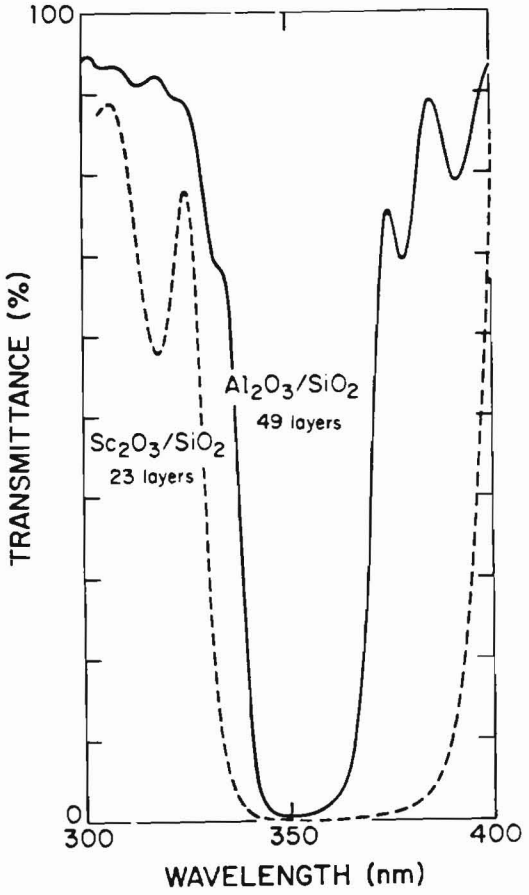


Figure 2. Spectral transmittance curves for two 351 nm reflectors. Although alumina/silica offers the highest damage resistance, it suffers from a low index ratio and a corresponding narrow bandwidth.

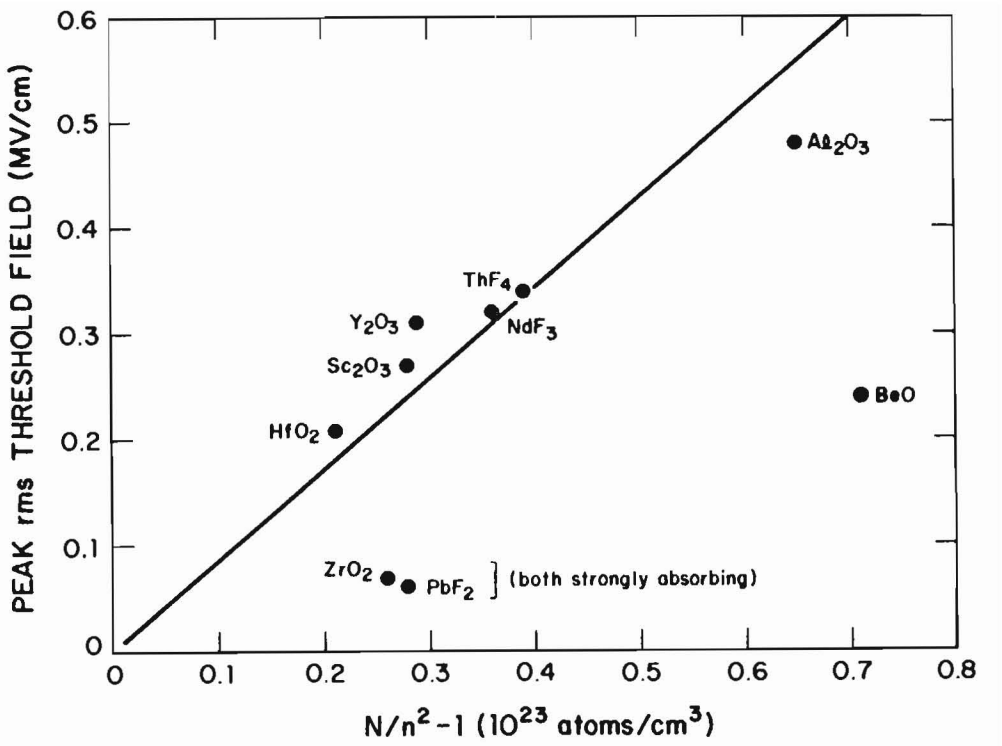


Figure 3. Measured threshold electric fields at 248 nm, 15 ns plotted against N/n^2-1 after reference [2]. While ZrO_2 and PbF_2 absorb strongly at this wavelength, it is postulated that BeO could approach the fitted line with continued optimization.

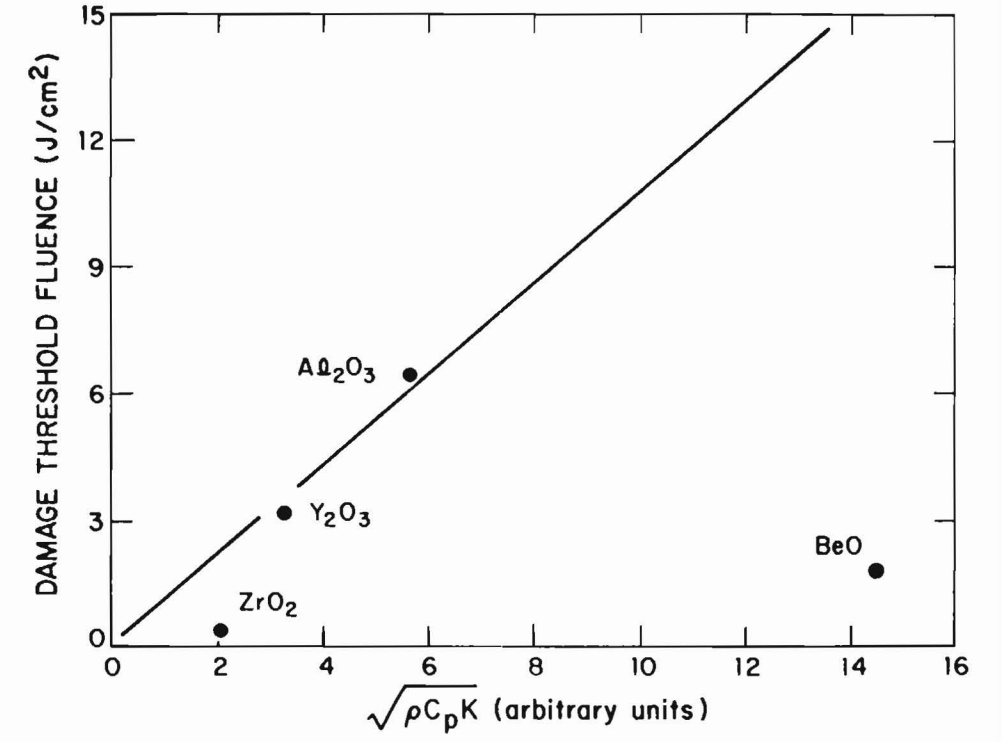


Figure 4. Measured thresholds plotted against ($\rho C_p K$) after reference [4]. Although lacking thermal data for thin films, this analysis also predicts very high damage resistance for BeO.

Photothermal Deflection Microscopy of HR and AR Coatings+

W.C. Mundy, J.E.L. Ermshar, P.D. Hanson and R.S. Hughes

Department of Physics and Computer Science
Pacific Union College
Angwin, CA 94508

Last year at this syposium we reported on the initial results of photothermal deflection microsocopy (PDM) studies of single layer dielectric thin films [1]. The high spatial resolution, low-level absorption capabilities of PDM were demonstrated in the form of two-dimensional absorption contour maps of such films.

In this paper we report on PDM measurements of a number of HR and AR coatings provided by Lawrence Livermore Laboratory and the Naval Weapons Center. The absorption data obtained from these measurements provide the first phase of absorption/damage correlation studies and as these absorption measurements were recently completed, no correlation data are yet available.

Resolution improvements, measurement methodology and a number of absorption contour maps are presented. Two interesting observations yet to be explained are described and some future experiments are suggested.

Key words: defect location; optical absorption; photothermal deflection; surface defects; thin films.

1. Introduction

The physical phenomena responsible for the photothermal deflection effect have been reviewed earlier [1]. Meanwhile it has come to our attention that the radiant energy which is converted to thermal energy may cause local thermal expansion (surface buckling) [2] as well as variations in the index of refraction of the medium and/or the atmosphere adjacent to the sample surface [3]. In any event, the probe beam is deflected indicating absorption at or near the sample surface. Investigation of the nature of the deflection can yield information as to whether the deflection is caused primarily by surface or volume absorption [2]. This paper simply reports further application of photothermal deflection microscopy (PDM) to locate defects in HR and AR coatings on high energy laser optical elements, refinements in the system, and some interesting characteristics of some of the samples.

2. Experimental Arrangement

An optical schematic of the PDM system is presented in figure 1. While the basic arrangement is the same as that reported last year, the focal lengths of both the pump beam and probe beam focusing lenses were changed from 120 mm and 75 mm to 50 mm and 25 mm respectively. This change resulted in a fifty percent reduction in detector output signal and increased the resolution so that absorption sites exhibiting full-width, half-maximum (FWHM) diameters of 8 μm were observed, about half that of the minimum FWHM previously obtained.

3. Sample Discussion

Since last year's symposium at Boulder we have performed PDM measurements on a variety of uncoated substrates and thin film coatings. Eleven samples have been studies under contract, six for the Naval Weapons Ceneter (NWC) and five for Lawrence Livermore Laboratory (LLL). Also, Optical Coating Laboratory, Inc. has provided samples to help quantify absorption data.

+Supported in part by the Lawrence Livermore Laboratory and the Naval Weapons Center.

Of the eleven optical components studied under contract, seven were high reflectance and three were anti-reflective in nature and one was a super polished silica substrate. It is not the intent of this paper to present the details on either the samples or the PDM results as this will be done in the correlation papers to follow. We wish, however, to convey the capabilities of PDM, a sampling of PDM results and some of the trends observed to date.

4. Measurement Methodology

Prior to mounting the optical element under investigation, fiducial marks are scribed on opposing edges of the coated surface. After sample mounting, the coordinates of each mark are recorded when the focused pump beam is centered on the mark. Thus, when the sample is remounted, the new coordinates of the fiducial marks are compared to the earlier ones and simple geometric considerations, which can be readily programmed, allow for any rotation or translation between the two mountings.

The samples are thoroughly cleaned a minimum of three times using lens tissue and methanol immediately before mounting. When an absorption signal is obtained, the site is again carefully cleaned and rescanned to insure the validity of the signal. (On occasion the signal disappears after this second cleaning process.)

The study of a sample is initiated by making "area" scans of about 1 mm x 2 mm with the sample being translated in 12 μm steps. Absorption sites that appear in these area scans are then scanned "locally" in 4 μm steps covering an area of about 80 μm x 160 μm centered on the site of interest. Pictorial representations of the sample including fiducial marks and areas scanned are an important part of the data recording and tracking process. Figures 2 and 3 are representations of the same sample drawn to the scales of 4.5/1 and 22.5/1 respectively. The number of each scan in the order of which it was performed is indicated in figure 3.

The PDM signal must be maximized for each sample and the relative positions of the focused pump and probe beams on the sample surface play an important role in the signal maximizing process. Data on the nature of the signal (level and response curve) as a function of pump and probe beam displacement are presented in the following section.

5. Results

Figure 4 shows a number of absorption sites detected while performing area scan number 14 of figure 3. The local scan of the uppermost absorption site, i.e., scan number 24 of figure 3, is presented in figure 5. Keep in mind that each pixel in the local scans corresponds to a 4 μm x 4 μm sample area. This absoption site is composed of two overlapping absorbers with their centers separated by approximately 20 μm.

A close approximation of the size of an absorber (FWHM) can be obtained from a knowledge of the uniform background signal level and the signal level corresponding to each color break point. Using these data for the two overlapping absorber shown in figure 6, FWHM diameters of 18-20 μm (upper) and 20 μm (lower) were obtained.

As one would expect, absorption site densities have been found to vary dramatically from sample to sample, from 17 sites in only 0.00435 sq. in. (ZrO_2/SiO_2 HR) to zero sites in 0.045 sq. in. (Ta_2O_5/SiO_2 AR). Also, absorption site sizes varied from 8 μm (current resolution limit) to of the order of 100 μm. The level of the uniform background absorption signal also varied significantly from sample to sample and that of AR coatings was generally lower than that of HR coatings.

An interesting phenomenon was observed on a half-wave coating of TiO_2 provided by OCLI. When the pump beam was kept fixed at one location for a period of time, the absorption at that location increased, doubling in about two minutes. Subsequent to turning the pump beam off for a period of time, a scan across the site indicated that the absorption had decreased. Figure 7 shows a scan across four sites each of which had been exposed to the pump beam for two minutes at about forty minute intervals. The scan was made immediately after the fourth exposure. The plot of signal versus time in figure 8

indicates a linear dependence and that the background signal level should return to its unaffected value in about six hours. Making sure that the power density on the film was held constant in each case, this experiment was repeated using the seven highest gain argon-ion laser lines. This effect was found to be independent of the argon-ion laser wavelength.

The reverse effect, i.e., a decrease in the absorption signal with pump beam exposure, was observed in a ZrO_2/SiO_2 HR coating. Further studies have not yet been made on this sample.

For most coatings studied the signal was maximized when the pump and probe beams were adjacent to each other at the surface. This would be expected if there was either a "buckling" of the surface or a bubble of heated air centered at the pump beam. The signal typically dropped to zero when the beams were coincident and the phase of the signal shifted 180 degrees when the relative locations of the pump and probe beams were swapped, which is consistant with either the buckling or the bubble effect. In addition, when the detector was translated across the probe beam, the resulting intensity versus detector position curve resembled that of the derivative of a Gaussian. However, the signal from one sample, a HfO_2/SiO_2 HR, was maximized when the pump and probe beams were coincident. Figure 9 shows the signal strength plotted as a function of probe beam detector position for this sample. These data are shown for four relative positions of the pump and probe beams ranging from separated to coincident. Increasing separation of the beam centers was accompanied by not only a decrease in signal strength, but also a change in the shape of the response curve. In all cases other than coincident, an unsymmetrical response curve was observed. For the case of coincident beams, the response curve indicates that the intensity of the probe beam rather than the angle of reflection was being modulated. We refer to this effect as intensity modulation in contrast to the normally observed deflection modulation. The unique characteristics of this coating responsible for this behavior are unknown.

6. Future Work

As damage site diameters of the order of 1 μm are routinely observed in large spot, short pulse damage testing, it is planned to improve the resolution of Pacific Union College's PDM system (currently approximately 8 μm). It is anticipated that changes in both hardware and software should provide for a resolution close to 1 μm.

We are currently studying the pump beam exposure-induced change in absorption reported above and the relaxation times associated with these absorption changes.

A study of the intensity modulation effect reported above may lead to an explanation of the responsible mechanism.

A better understanding of the nature of the deflection signal (with regard to phase, deflection amplitude, and chopping frequency dependence) could possibly lead to a separation of surface and bulk absorptions.

A collaborative effort will continue with OCLI in an effort to obtain a calibration of the system and on some of the above projects.

The authors are indebted to C.K. Carniglia of Optical Coating Laboratory, Inc. for helpful discussions, cooperative experimentation and sample design and fabrication.

7. References

[1] Mundy, W.C., Hughes, R.S., Carniglia, C.K., Photothermal Deflection Microscopy of Dielectric Thin Films. Presented at the Fourteenth Annual Symposium on Optical Materials for High Powers Lasers, Boulder, CO., 1982.

[2] Olmstead, M.A. and Amer, N.M., A New Probe of the Optical Properties of Surfaces. J. Vac. Sci. Technol. 1(3): 751-755; 1983.

[3] Mundy, W.C., Hughes, R.S., Carniglia, C.K., Photothermal Deflection Microscopy of Dielectric Thin Films. Appl. Phys. Lett. Accepted for publication Dec. 1983.

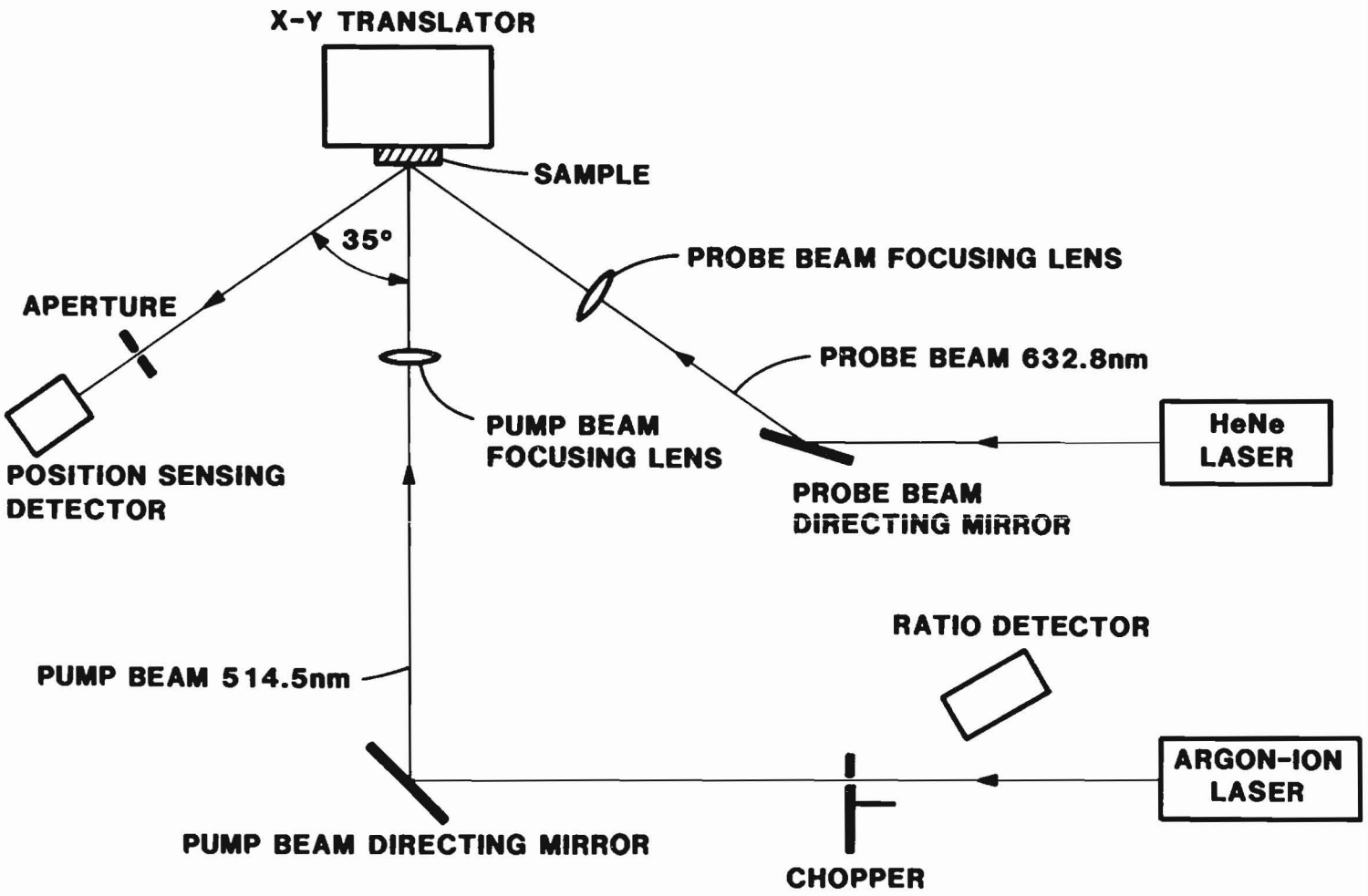


Figure 1. Optical schematic of the photothermal deflection microscopy system.

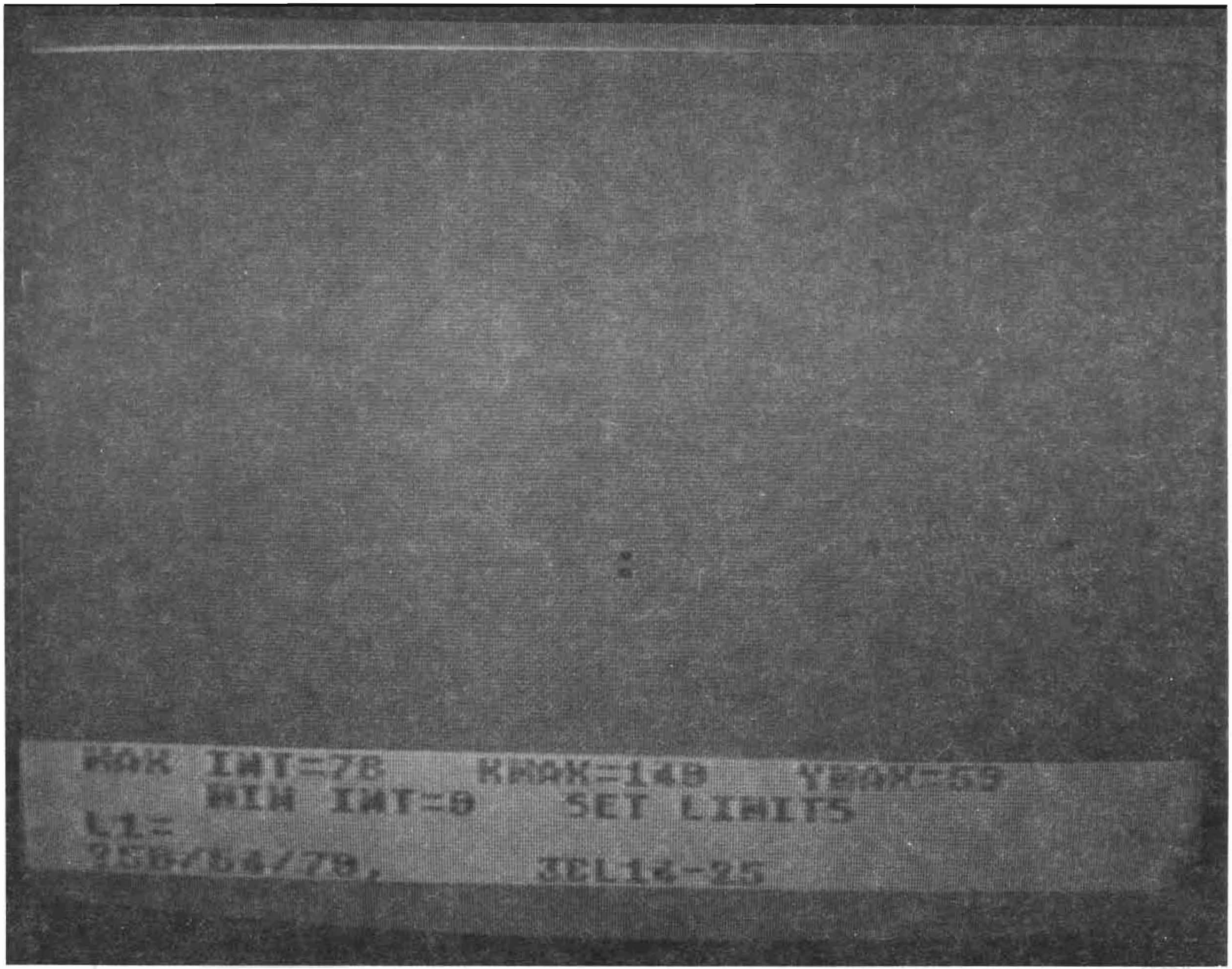


Figure 4. 1 mm x 2 mm area scan of NWC sample number 3. (Scan number 14 of figure 3.)

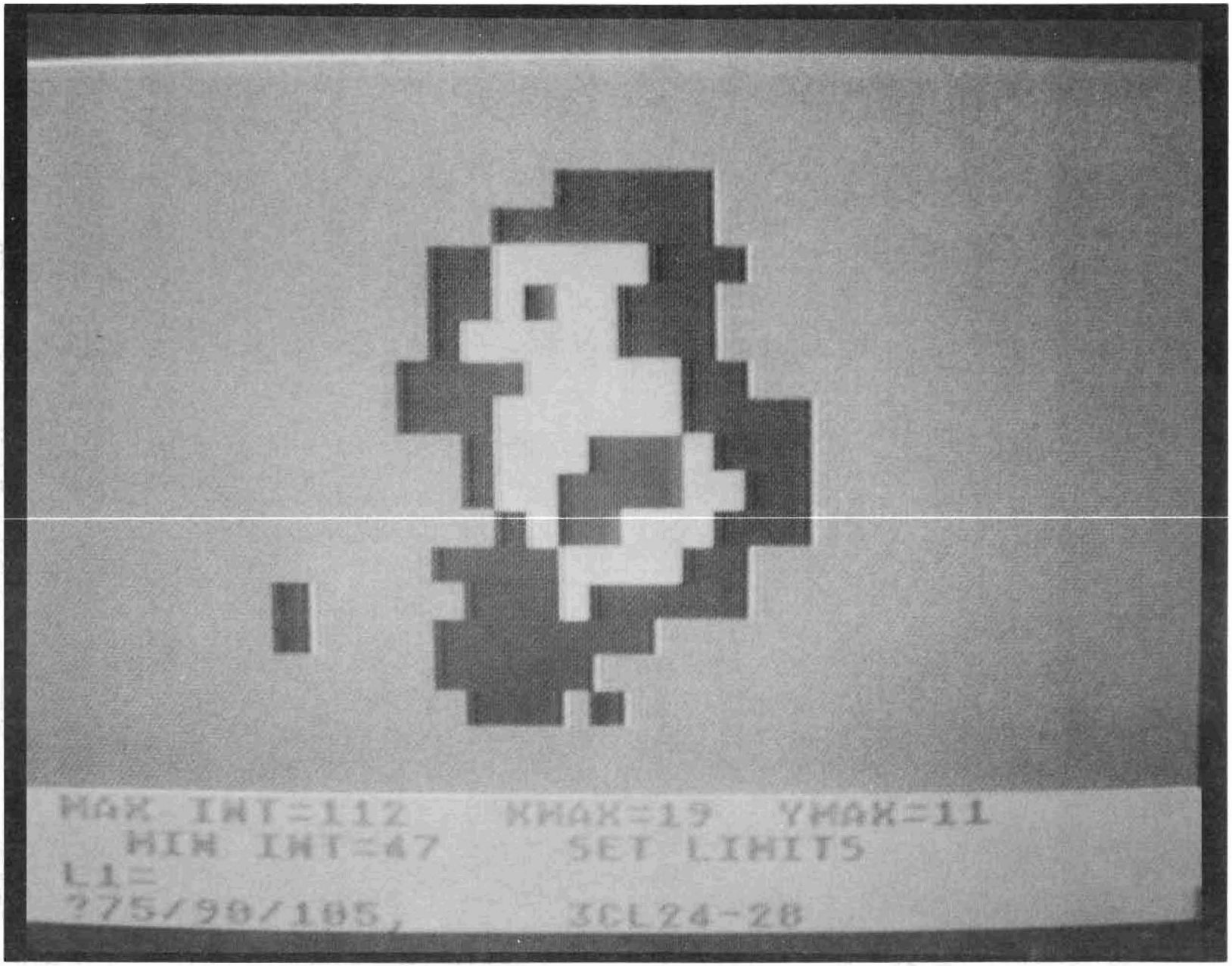


Figure 5. 80 μm x 160 μm local scan of NWC sample number 3. (Scan number 14 of figure 3 and uppermost absorption site of figure 4.)

Figure 6. Two resolved overlapping absorption sites having FWHM diameters of 18-20 μm (upper) and 20 μm (lower).

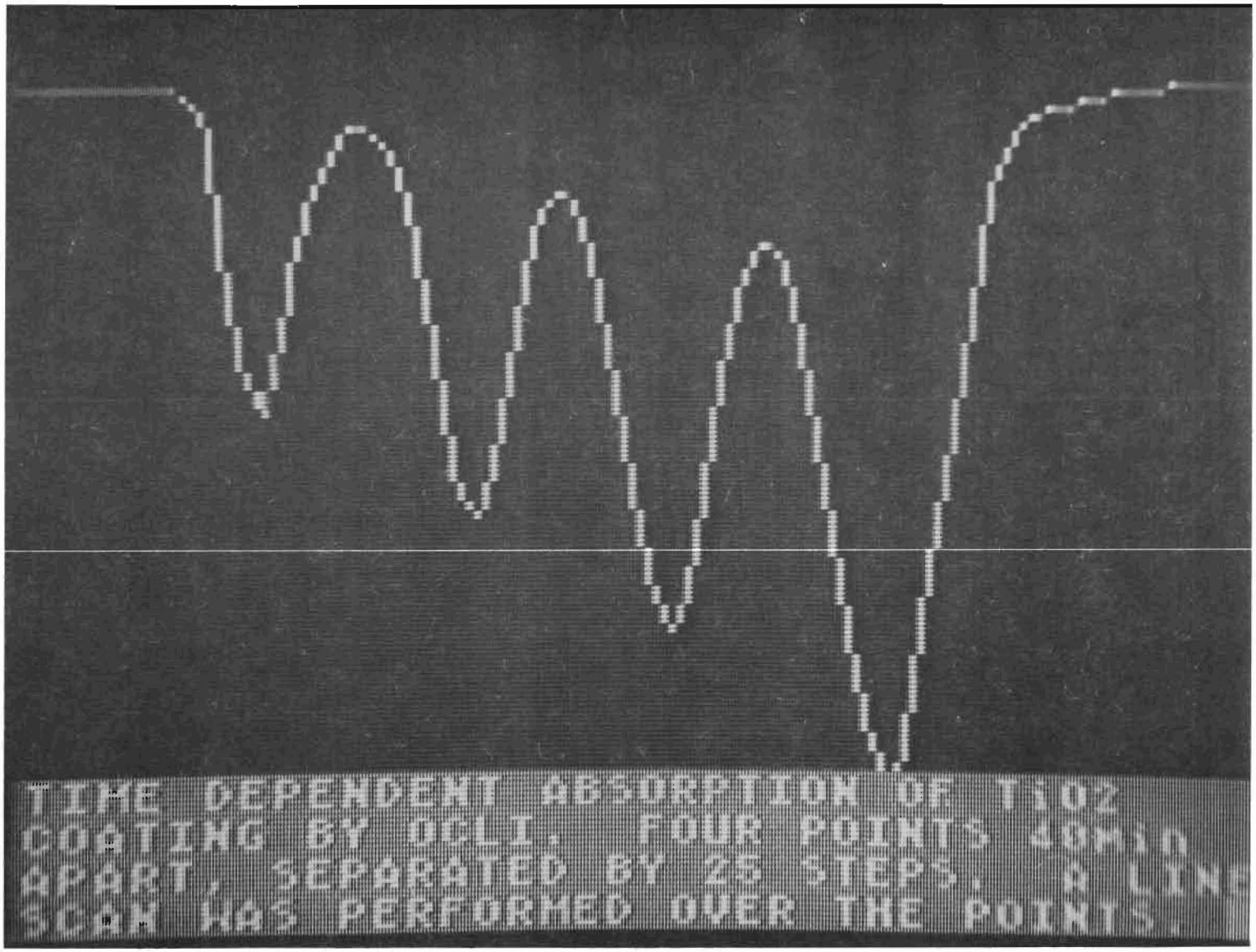


Figure 7. Line scan of four absorption sites induced by pump beam in a half-wave coating of TiO_2. Sites were irradiated, from left to right, for 2 minutes each at 40 minute intervals. Scan was made immediately after rightmost site was produced.

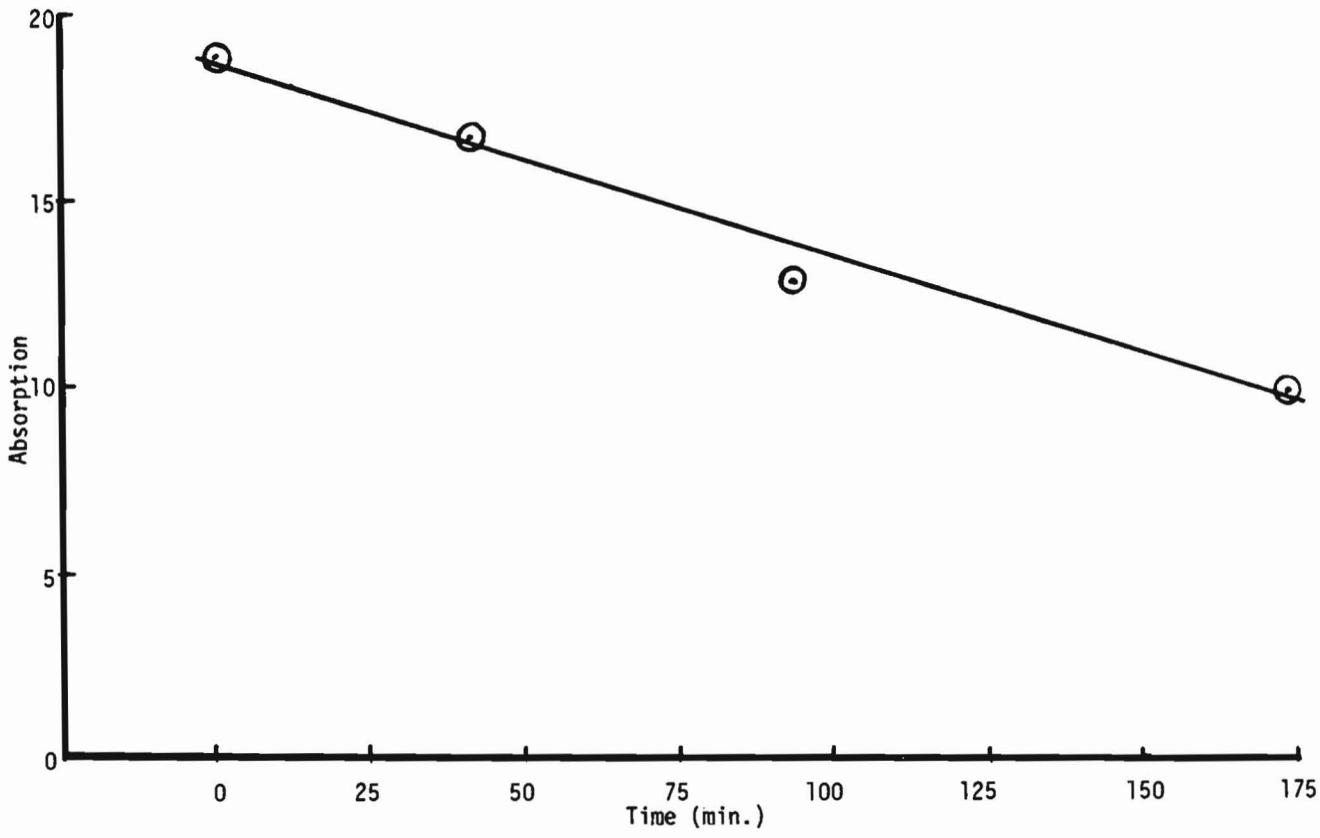


Figure 8. Signal intensity versus time following exposure plot produced form line scan in figure 7.

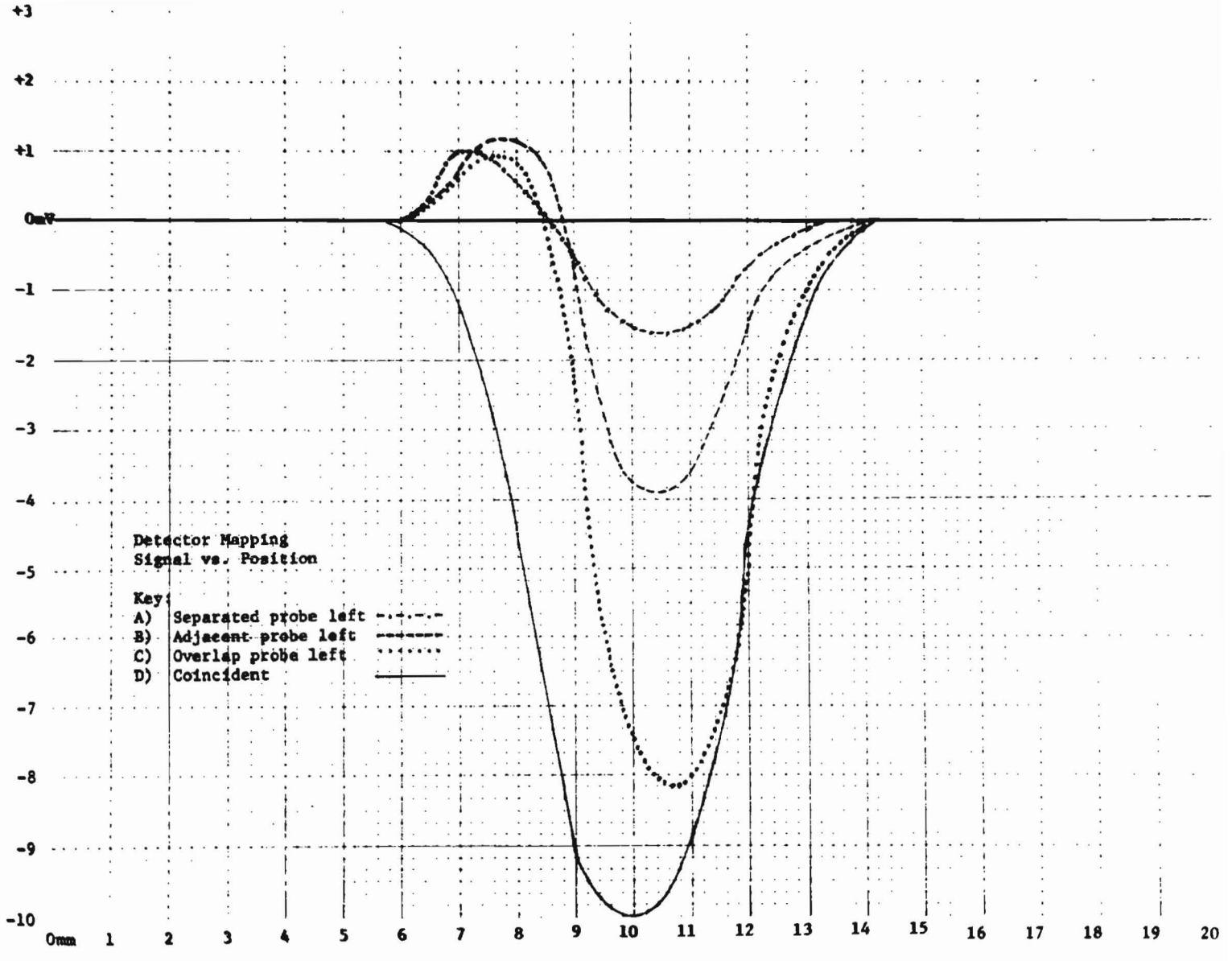


Figure 9. Plots of signal intensity versus probe beam's lateral position for four relative positions of the pump and probe beam's centers.

Manuscript received 3-22-84/sar

Laser Damage in Porous-Silica Antireflection Films*

W. H. Lowdermilk, J. G. Wilder, N. J. Brown,
C. A. Gunderson, D. Milam, F. Rainer, and M. C. Staggs

Lawrence Livermore National Laboratory
Livermore, CA 94550

We used 355-nm, 0.6-ns pulses to measure laser-damage thresholds of porous-silica antireflection coatings deposited from a polymer solution onto fused silica substrates. For 118 coatings with optical thickness of 500-600 nm, the median threshold was less than 2 J/cm^2, and thresholds were not systematically dependent on either the level of filtration of the coating solution or the procedure used to clean the substrates. For coatings 87-90 nm in optical thickness, thresholds were as large as 9 J/cm^2, which is the threshold of the bare polished surfaces of the fused silica substrates. The data suggests that carbon residues from the coating solution are responsible for damage in the thicker coatings.

Keywords: porous silica antireflection coatings; uv laser damage; polymer silica.

1. Introduction

Antireflection coatings on fused silica lenses and windows in the output stages of the NOVA laser may be subjected to beam fluences as large as 5 J/cm^2 delivered in 1.0-ns, 351-nm pulses.[1] A major effort to develop damage-resistant antireflection (AR) coatings for NOVA is being made through a contract with the Westinghouse Research and Development Center in Pittsburgh. The contract will provide evaluation of porous silica coatings deposited from a polymer solution derived from ethyl silicate. Study of this coating process has been broken into three major segments: (1) research at Westinghouse to define a usable coating solution and to demonstrate fabrication of solution-deposited broadband antireflective coatings, (2) transfer of the coating technology to a clean room environment at Livermore to allow final development of a damage-resistant coating, and (3) fabrication of an apparatus for coating large (1-m diameter) optical components. Here we review laser-damage studies associated with the first two phases of the work.

2. Evaluation of Porous Coatings 500-600 nm in Thickness

Westinghouse personnel have demonstrated broadband antireflectivity in coatings with thickness of 500-600 nm, and provided coatings with thresholds of 2-4 J/cm^2 (0.6 ns, 355 nm, 1-mm diameter beam).[2] The laser-damage pits in these coatings suggested that the damage was caused by heating of dirt particles deposited from the solution, or by heating of contaminants that were either in or on the substrate surface. Because cleanliness seemed important, the research coating apparatus at Livermore was installed in a class-100 clean room. Initial emphasis at Livermore was given to filtering the coating solutions, cleaning the substrates, and to studies of contamination that might be introduced while the coatings were being baked or etched.

We found that the constituents of the polymerized solution, ethyl alcohol, nitric acid, water and ethyl silicate, could individually be filtered to 0.02 μm. Polymerized solutions could readily be filtered to 0.1 μm, and with some difficulty could be filtered to 0.02 μm.

To address the concern that contaminants on substrate surfaces might be incorporated into coatings, we evaluated several procedures for substrate cleaning. In a typical cleansing, the substrate was soaked in mild acids or bases, scrubbed with rotary brushes while immersed in a solution of water and surfactant, rinsed with ethyl alcohol, and then spun dry. Various acids, bases and degreasing agents were tried, including mixtures of HF acid and water which completely removed the polished surface. In study of a given cleaning procedure, coatings were deposited on some substrates which had been subjected to the entire procedure, and on some substrates which had been subjected to various permutations or subgroups of the steps in the procedure. As a control, some substrates were cleaned only by drag-wiping them with tissue wetted with ethanol or acetone.

*Work performed under the auspices of the U.S. Department of Energy by the Lawrence Livermore National Laboratory under contract W-7405-ENG-48.

We also varied the conditions under which the coatings were deposited and cured. The wet coating layers were initially dried in the ambient air of the clean room. Later, a cover was installed over the coating station so the coatings could be dried in filtered nitrogen. The coatings were baked in various ovens, some of which were lined with fused silica and could be filled with a flowing mixture of selected gases. We evaluated coatings baked in oxygen, and in mixtures of oxygen and nitrogen.

During this study of deposition parameters, the coating thickness was maintained at about 500 nm, which, with proper index gradation, is adequate to provide antireflectance between 350 and 1000 nm. The laser-damage thresholds of many of the test coatings were measured with 0.6-ns, 355-nm pulses focused to a diameter of about 1 mm at the sample surface. For 38 coatings made at Livermore from carefully filtered solutions, on substrates cleaned by several procedures, the median threshold was 1.2 J/cm^2. For 89 coatings made at Westinghouse under less stringent control of cleanliness, the median threshold was 2.1 J/cm^2. Only two coatings had thresholds greater than our goal, 5 J/cm^2. Histograms of damage thresholds are shown in Figs. 1 and 2. We are reasonably certain that some of the least of these thresholds resulted from use of improperly filtered solutions or non-optimum deposition parameters that were included in some parameter studies. Further, we have since determined that the bare-surface threshold of some substrates provided by one vendor is less than 5 J/cm^2. However, many of the coatings were deposited under supposedly optimum conditions on substrates whose median bare-surface threshold is 9 J/cm^2. Therefore, we concluded that the thresholds were being limited by an intrinsic characteristic of the coatings, thought to be carbon residue from the coating solution.

3. Sources of Carbon in Porous Silica Coatings

There are two potential sources of carbon in silica films made by the Westinghouse process. The coating solution contains polymer silica molecules that are produced in a two-step process. Ethyl silicate is stirred into a mixture of ethyl alcohol, water and nitric acid, producing the following reactions:

$$SiX_4 + H_2O \rightarrow X_3SiOH + HX,$$
$$X_3SiOH + SiX_4 \rightarrow X_3Si\text{-}O\text{-}SiX_3 + HX,$$
$$X_3S\text{-}O\text{-}SiX_3 + H_2O \rightarrow X_3Si\text{-}O\text{-}SiX_2OH + HX,$$
$$X_3Si\text{-}O\text{-}SiX_2OH + SiX_4 \rightarrow X_3Si\text{-}O\text{-}SiX_2\text{-}O\text{-}SiX_3 + HX,$$
etc.,

where -X represents $-OCH_2CH_3$. In the second and fourth steps, polymerization may also proceed through reaction of hydrolyzed ethyl silicate molecules;

$$X_3SiOH + X_3SiOH \rightarrow X_3Si\text{-}O\text{-}SiX_3 + H_2O.$$

4. Elimination of Carbon from Porous Coatings

The carbon contained in ethyl side groups and in the ethanol solvent is a necessary constituent of the coating solution. Ethyl side groups could be eliminated by additional hydrolysis, but excess hydrolysis of a solution produces a rigid gel and excess hydrolysis during drying of a wet layer produces a dense coating. Therefore, carbon must be present to retain fluidity in the solution and porosity in the coatings. However, because the coating layers were only 500 nm in thickness, we initially believed that the solvent would be eliminated by evaporation and that ethyl side groups would decompose during the post-deposition bake at 400-500°C. Our failure to control coating thresholds by manipulation of variables such as substrate cleanliness suggested that carbon was being retained.

We are evaluating two general procedures for improving carbon elimination; (1) addition to the solution or wet coating of a chemical agent which attacks the carbon, and (2) thinning the coatings to ease carbon removal.

The additive first evaluated was water. While excess water promotes densification of wet coating layers, we thought it might be possible to maintain porosity by adding water to coatings which had been thoroughly dried. We applied air saturated with water vapor to coatings which had first been thoroughly dried in dry N_2 at room temperature, and to coatings which had been baked for 30 minutes in dry nitrogen at 130°C. In all instances except one, additional hydrolysis produced dense coatings whose refractive indices were only slightly less than that of fused silica. Etching simply removed such coatings without significantly altering their porosity. The exception was a single sample that was dried at 130°C in dry nitrogen and then held in steam at 130°C for an hour. The coatings on this sample remained somewhat porous and after etching provided partial antireflectivity (two-surface transmission > 97% at 355 nm). While hydrolysis deserves additional study and may be useful in making fully dense coatings, it seems unlikely that hydrolysis is a usable technique for eliminating carbon from porous coatings.

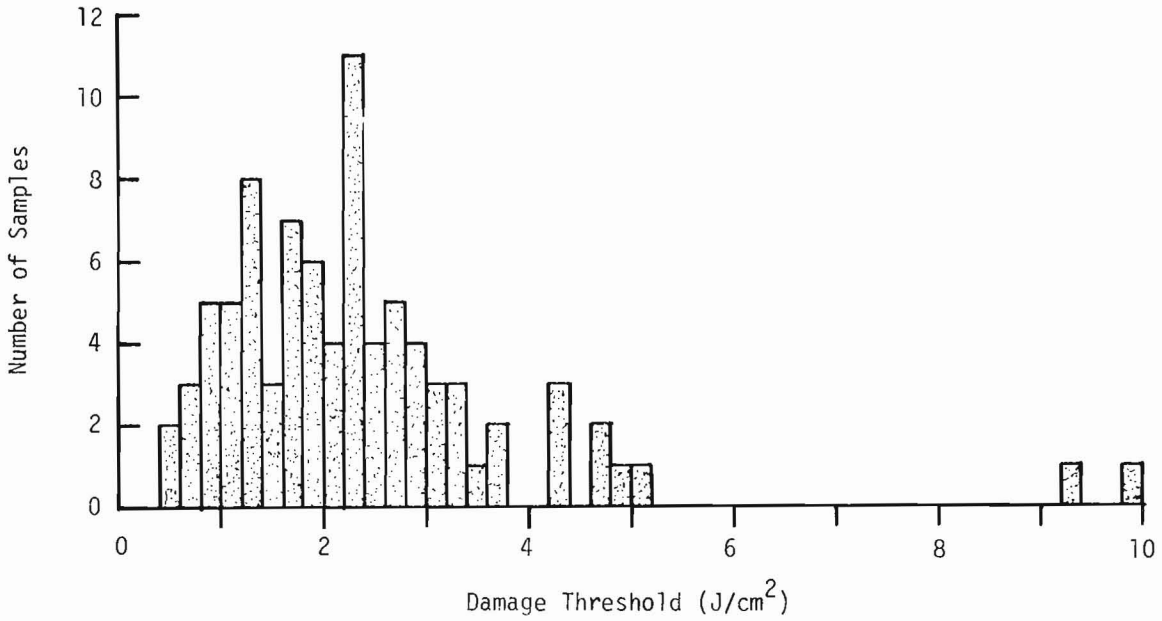


Figure 1. Laser-damage thresholds (0.6-ns, 355-nm) of porous silica coatings made at Westinghouse Research and Development Center. The median threshold was 2.1 J/cm^2. Coatings with thresholds of 5.2 J/cm^2 or less were 500-600 nm in optical thickness. The two coatings with thresholds > 9 J/cm^2 were < 200 nm in thickness.

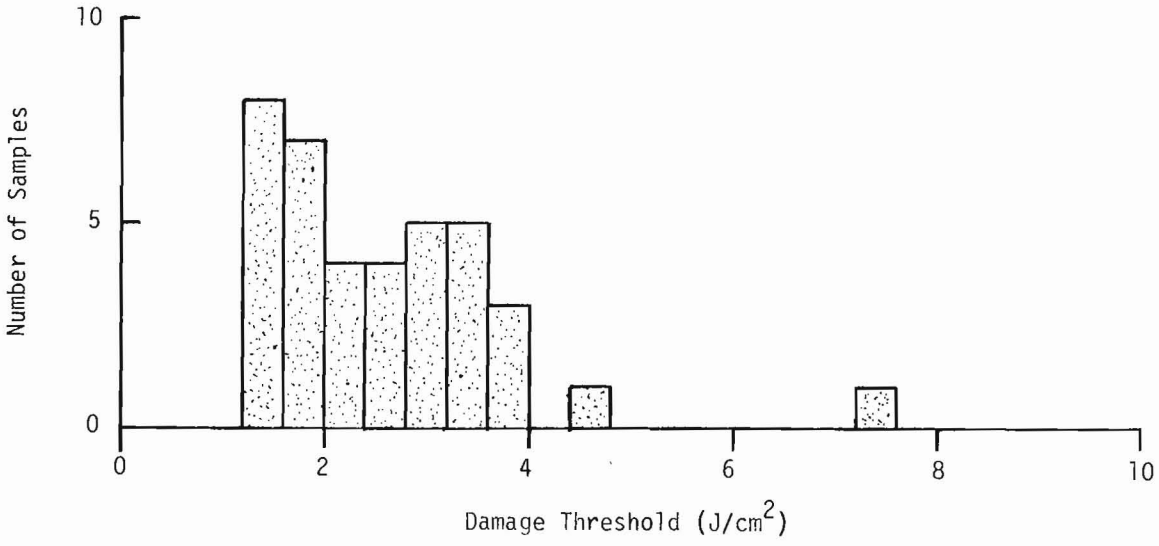


Figure 2. Laser-damage thresholds (0.6-ns, 355-nm) of porous-silica antireflection coatings 500-600 nm in optical thickness. The coatings were fabricated at Livermore.

We have also attempted to incorporate oxidizing agents directly into the coating solution. For example, ammonium nitrate is slightly soluble in ethanol, and would decompose into ammonia and nitric acid during the baking of the coating. The nitric acid would be locally available to assist in oxidization of hydrocarbons. However, we have not yet managed to fabricate damage resistant coatings by use of oxidizers.

The most successful technique yet found for aiding carbon elimination is to thin the coatings. We modified the coating process to produce coatings with optical thickness of 80-90 nm. Details of this modified process are given in an appendix. Study of thin coatings produced two results. First, thresholds of some thin coatings were as large as 9 J/cm^2 which is the threshold of the bare polished surface of the substrate, see Fig. 3. Further, the thresholds were rather insensitive to the cleanliness of the process. Large thresholds were obtained using solutions filtered only to 0.2 μm deposited on substrates cleaned only by drag-wiping with tissue wetted with alcohol. This confirms our belief that carbon entrapment limited thresholds of the thicker (500 nm) coatings that we initially studied.

Secondly, we found that the refractive index of the thinner layers was homogeneous rather than graded. Fig. 4 is a transmission spectrum of a fused silica window with thin silica coatings on both surfaces. The spectrum can be closely modeled by assuming that the layers are homogeneous films 69 nm in thickness with refractive index n = 1.28. The only indication of index gradation is that the transmission in the near infrared slightly exceeded the transmission computed for homogeneous layers.

The thinned layers will meet the immediate requirements of NOVA for damage resistant 351-nm antireflection coatings. Thicker coatings will be required to obtain broadband antireflectivity. Current research involves determining the maximum thickness that can be deposited in a single layer without trapping carbon, evaluation of thick coatings made by stacking multiple thin coatings, and studies of additional procedures for making carbon-free thicker coatings.

5. Summary

Porous silica coatings were produced by a sol-gel technology using polymer silica coating solutions. Porous layers ∿ 500 nm in thickness provided broadband antireflectivity. The median damage thresholds of such coatings made at Westinghouse and at Livermore were, respectively, 2.1 and 1.2 J/cm^2 (0.6 ns, 355 nm). The damage threshold was relatively insensitive to the cleanliness of the coating process, and seemed to be limited by an intrinsic characteristic of the coating.

Porous layers with optical thicknesses of 80-90 nm were antireflective at 351 nm, and had thresholds as large as 9 J/cm^2, confirming our belief that thresholds in thicker coatings were limited by trapped carbon residues.

We have not yet identified a reproducible process for producing damage-resistant films (thresholds > 5 J/cm^2) that are antireflective over the whole spectrum from 351 to 1053 nm.

6. Appendix. Procedure Used to Make Thin Porous Silica Coating

Small quantities of solution used for coating 5-cm diameter test substrates were made by adding 208 g of ethyl silicate to a mixture containing 127 g of ethanol, 38.7 g of water and 0.25 g of 70% concentration nitric acid. The molar ratio of water to ethyl silicate was 2.15:1. The solution was stirred for 4 hours at the reflux temperature of ethanol, cooled to room temperature, and diluted by addition of 382 g of ethanol to reduce the silica content to about 8%. Coatings were deposited by withdrawing a substrate vertically from the solution at the rate of 4 cm/min. The wet coatings were thoroughly dried in dry nitrogen and then baked 4 hours at 400 to 500 C in flowing oxygen. After the coated substrates cooled, they were etched 4 min. in a 0.00002 molar solution of hydrofluoric acid, rinsed in water, then in ethanol, and allowed to dry in air.

Although this process produced useful coatings, it may not be optimized and its development is continuing. For example, the coating thickness is controlled by the silica content and viscosity of the polymer solution, the withdrawal rate of the substrate, the drying rate of the wet layer, and by partial sintering of the porous layer which occurs at temperatures above 450°C. The optimum procedure for stabilizing and controlling coating thickness has not been determined.

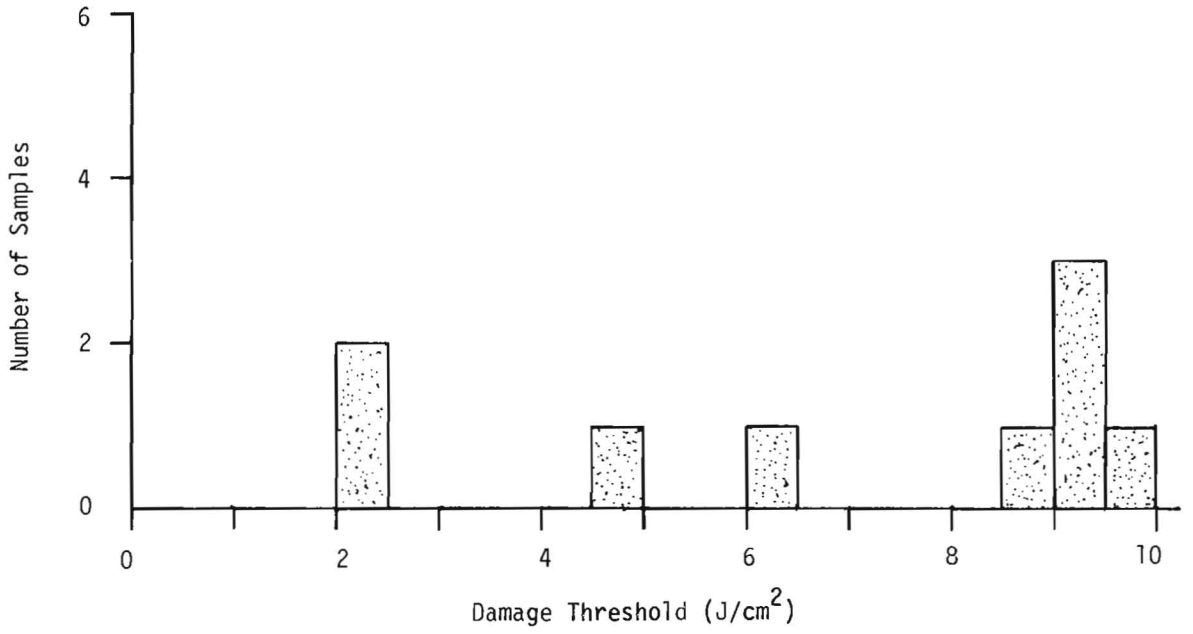


Figure 3. Laser-damage thresholds (0.6-ns, 355-nm) of porous silica antireflection coatings 80-90 nm in optical thickness. The coatings were fabricated at Livermore.

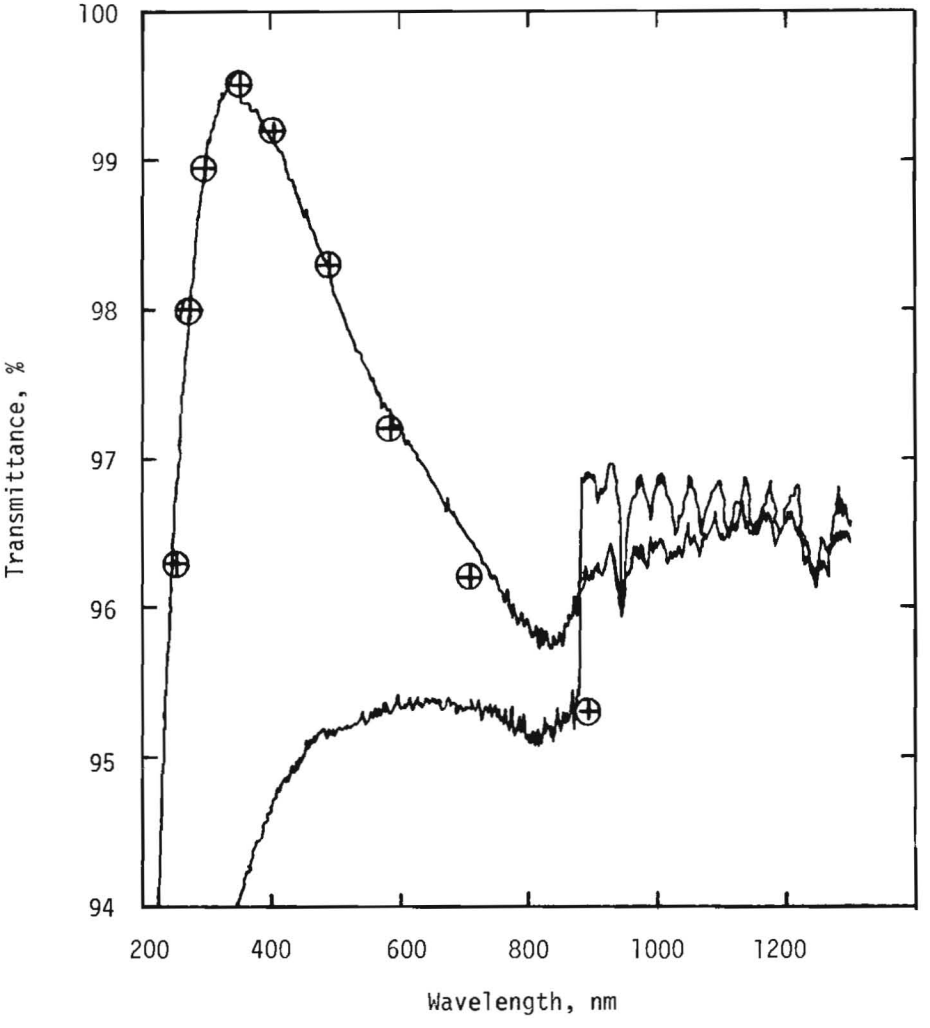


Figure 4. Two-surface transmittance spectrum of a fused silica window with porous silica antireflection coatings. The lower curve is transmittance measured after completion of coating deposition but prior to etching. Circled data were computed by assuming the coatings were homogeneous layers with physical thickness of 69 nm and refractive index η=1.28. Abrupt steps at 900 nm are an artifact caused by detector changes in the spectrometer.

7. Acknowledgements

The authors are grateful to I. M. Thomas for extensive discussions of the chemistry of the sol-gel coating process. Giles Peterson wrote the computer code used to calculate transmission spectra for the porous silica coatings, and provided the theoretical fit to the spectrum in Fig. 4.

8. References

[1] W. W. Simmons and R. O. Godwin, Nova Laser Fusion Facility: Design and Assembly Overview, J. Nuclear Technology/Fusion, Vol. 4, pp. 8, July 1983.

[2] B. E. Yoldas, D. P. Partlow and H. D. Smith, "Polymer Oxide Antireflection coating for Fused Silica", elsewhere in these proceedings.

The question was raised as to whether a low film damage threshold might not simply be the result of a low damage threshold substrate. The speaker replied that if the substrate had a low damage threshold, it would not support the high film threshold trying to be obtained. In the data he showed, however, all films were on Zygo-polished fused silica, which they have tested enough over the years to be confident that the substrate thresholds will run over 8 J/cm^2.

Another questioner pointed out that if one of the big lenses was damaged by a laser, a promising outcome of this coating technique was the possibility of being re-treated without loss of a very expensive optic. The speaker stated that although they do no yet have specific data on that point for fused silica, it is probably possible. For BK-7, a lot of careful work has been done with the neutral solution process, and in that case one can recoat the optic up to 10 times without damaging its figure.

Manuscript received 5-14-84/sar

Defect Damage Precursors in Visible-Wavelength Mirrors*

C. D. Marrs and J. O. Porteus

Michelson Laboratory, Physics Division
Naval Weapons Center, China Lake, California 93555

J. R. Palmer

Comarco, Incorporated
1201 N. China Lake Blvd., Ridgecrest, California 93555

Video monitoring of pulsed visible-wavelength mirror damage has led to observation of illuminated defects as a precursor to observable microscopic damage. The blue-green illuminating radiation is produced in individual 0.5 μs pulses by a tunable flashlamp-pumped dye laser. The laser light is focused on multilayer dielectric or metal surfaces in an ≃ 0.5 mm ($D - 1/e^2$) spot with a reproducible, flat-top spatial profile. An area slightly larger than the focal spot is viewed with a close-focusing Questar telescope equipped with a highly sensitive video camera. Typically, at nondamaging energy densities, defect sites within the focal spot area appear to be brightly illuminated at the laser wavelength. In dielectric mirrors, the illumination pattern depends on the laser wavelength, suggesting a sensitivity to defect position with respect to the standing wave field. At higher energy densities, laser damage originates only at certain defect sites, while other areas fail to damage even after many laser pulses. This paper presents results of an experimental characterization of the described phenomena.

Key words: dielectric mirrors; laser damage; nondestructive test; visible mirrors.

Introduction

The resistance of optical coatings to pulsed laser-induced damage is limited by certain types of defects introduced during substrate preparation and coating fabrication [1].[1] These defects adversely influence the local optical and thermal properties so as to initiate laser-induced damage well below the intensity required to damage the host material. An understanding of critical defect characteristics and their relationship to damage initiation is important for development of optical coatings that can operate at their intrinsic limits. This understanding has been severely limited by the inability to detect these defects nondestructively.

Recently, video microscopy of pulsed visible-wavelength laser damage on multilayer dielectric mirrors has revealed a defect illumination (DI) effect that offers a means of nondestructive defect detection. Typically, the effect appears as a pattern of several intense highly localized images in the laser irradiated area. These images tend to persist for some time after the larger image of background laser light has vanished. Correlation in position with damage initiation sites appearing at higher laser intensities indicates that the point-like images are in fact defects. This paper describes qualitative characteristics of DI as observed with the video microscopy system (VIMS) and provides a tentative physical interpretation based on these observations.

Experimental Procedure

The test facility (fig. 1) has been described in detail in the literature [2]. The laser source specifications are given in table 1. The VIMS is composed of a Questar Model QM1 close-focusing telescope coupled to a color video camera and broadcast-quality video recording system. Two different color video cameras were used because of their differing image retention time (lag) and light level sensitivity. The lag was determined for each by viewing submillisecond strobe pulses through a pinhole. Pinholes of 390 and 50 μm were used to approximate the laser-illuminated area and the DI image size, respectively. The results given in table 2 show a marked dependence of lag on image size for the Saticon camera, which was used for most of the DI observations.

*Work supported by Defense Advanced Research Projects Agency and Navy Independent Research Funds.
[1]Numbers in brackets indicate the literature references at the end of the paper.

The test specimens were four multilayer dielectric mirrors and two diamond-turned (DT) metals (see table 3). Of the former, three were broadband mirrors designated BBM#1, BBM#2, and LDM (low defect mirror). The fourth was an edge mirror (EM), which is highly reflective at only one of the laser wavelengths used. The DT metals were of 2024 Al and oxygen-free high-conductivity Cu.

Results and Discussion

Four DI characteristics evaluated within the limitations of the VIMS were (1) intensity decay time, (2) wavelength (apparent color) compared to the laser light, (3) intensity dependence on laser wavelength, and (4) polarization. Using the charged coupled device (CCD) camera, the DI decay time was observed to be no longer than the 16.7 ms field display time of the recording system.

As the wavelength is changed between 476 and 515 nm, the DI light maintains the same color as the laser light. This result argues more strongly for scattering than for defect luminescence as the defect illumination mechanism. The wavelength modulation of p-polarized DI intensity is demonstrated in figures 2(a) and 2(b). These patterns were obtained from the same area of BBM#1 at 515 and 476 nm, respectively. Differences in intensity are especially apparent in the circled areas. At least two defects visible at 476 nm cannot be seen at 515 nm. Observe that the reflectance of this mirror is essentially the same at both wavelengths (see table 3). On another mirror, denoted EM, the same experiment yielded similar results. Yet this mirror was designed to be reflective at only 476 nm (see Table 3). The variation in intensity is shown in figures 3(a) and 3(b); specifically notice the circled areas. Possible explanations are (1) modulated differences in the standing-wave intensity at different defect depths in the multilayer coating and (2) differences in scattered intensity, which would depend strongly on the wavelength relative to defect size [3]. To determine if any laser modification of the samples was occurring and to check the reproducibility of the patterns, the wavelength was varied from one to the other several times. The DI patterns were quite reproducible, and no detectable modification was observed at the energy densities used.

The polarization of the DI light relative to the p-polarized laser light was evaluated with a polarizer placed in front of the VIMS. Figures 4(a) through 4(c) show the polarization characteristics from BBM#1 at 515 nm. Comparison of these DI patterns viewed under the indicated polarization shows a substantial s-component even though illuminated with p-polarized laser light. Similar observations were made on BBM#2 and EM. These results contrast to those observed from the DT metals, where virtually no s-polarized DI light was detected (see figs. 5(a) through 5(c) and 6(a) through 6(c) for results on DT Al and DT Cu, respectively). It was found that the DI pattern on the metals did not vary after rotation of the DT marks from perpendicular to parallel with the polarized laser light. The same observations were found when the wavelength was changed to 476 nm. For dielectric mirrors, the depolarization of the laser light could arise from a large defect size relative to the wavelength (Mie scattering) or an anisotropic polarizability of the individual defects [3]. On the metals, an isotropic polarizability of the defects and small defect size relative to the wavelength would support the observed results.

The progression from DI to laser-induced damage as the laser intensity is increased is shown in figures 7(a) through 7(e). The mirror is BBM#2 irradiated at 515 nm and viewed with p-polarization. Starting at a level sufficient to observe the DI pattern, the energy density was increased $\sim 20\%$ on successive laser pulses until damage occurred. Figure 7(a) shows the undamaged surface before laser irradiation, illuminated with a tungsten lamp. Comparison of DI with a nondamaging [fig. 7(b)] and subsequent damaging [fig. 7(c)] pulse of roughly 200% higher intensity shows damage initiated at the laser-illuminated defect enclosed by the solid circle. This damage is shown under tungsten illumination in figure 7(d). The defect enclosed by the dashed circle in figures 7(b) and 7(c) damage on a later pulse, as seen by tungsten illuminated in figure 7(e). Many similar test sequences have shown that damage occurs only at defects indicated by DI. Although such defects are usually visible on the first laser pulse, occasionally they do not appear until after several nondamaging pulses of increasing intensity. Not all DI-indicated defects produce damage; for those that do, we have not been able to determine any peculiar polarization or intensity characteristics. Experience with one mirror, LDM, which has a damage threshold roughly seven times higher than the others, suggests some general correlation of damage with apparent defect size. This particular mirror produced no large defect images (see fig. 8) but showed an unusually large number of small images and had a correspondingly high measured scatter (see table 3).

Conclusions

Defect illumination (DI) characteristics obtained with the video microscopy system (VIMS) are consistent with scattering from defects that interact strongly with laser radiation by virtue of their size and location in a multilayer dielectric coating. The persistence of DI after the laser pulse, which greatly enhances defect visibility, is explained by the peculiar lag characteristics of video cameras. Defect-initiated laser damage requires the same strong defect interaction that produces DI but may involve additional defect characteristics not revealed by DI. Determination of such

characteristics will require more definitive analytical methods such as scanning electron microscopy, Auger microscopy, and laser-induced desorption [4], in conjunction with DI and laser damage measurements.

References

[1] Donovan, T. M., Naval Weapons Center, private communication.

[2] Marrs, C. D.; Faith, W. N.; Dancy, J. H.; Porteus, J. O. "Pulsed laser-induced damage of metals at 492 nm," Appl. Opt. 21; 4063-4066; 1982.

[3] van de Hulst, H. C. Light scattering by small particles. New York; Wiley; 1957.

[4] Allen, S. D.; Porteus, J. O.; Faith, W. N. "Infrared laser-induced desorption of H_2O and hydrocarbons from optical surfaces," Appl. Phys. Lett. 41; 416-418; 1982.

Table 1. Laser source specifications

Laser	pulsed dye laser
Dye/solvent	LD490/MeOH
Tuning range	460 to 530 nm
Pulse width	0.5 μs
Lens[a]	280 mm
Spatial profile	FW at $1/e^2$ 420 μm Flat top to ±5% over 240 μm
Polarization	p

[a]Effective focal length.

Table 2. Light levels and lag characteristics of cameras

Camera	Minimum luminescence (lux)	Lag (No. of fields)[a] 390 μm image	Lag (No. of fields)[a] 50 μm image
Three-tube Saticon	150	3	> 10
CCD, solid-state	500	≤ 1	< 1

[a]Field display time is 16.7 ms.

Table 3. Sample characteristics

	Reflectance (515 nm)	Reflectance (497 nm)	Reflectance (476 nm)	Absorptance (497 nm)	Total integrated scattering (497 nm)
Dielectric mirrors					
BBM#1	0.995	0.995	0.992	4×10^{-4}	2×10^{-3}
BBM#2	0.995	0.995	0.995	---	5×10^{-4}
EM	0.269	0.984	0.994	8×10^{-4}	6×10^{-4}
LDM	0.991	0.987	0.946	---	4×10^{-3}
Metal mirrors					
Al, DT[a]		0.918			
Cu, DT		0.466			

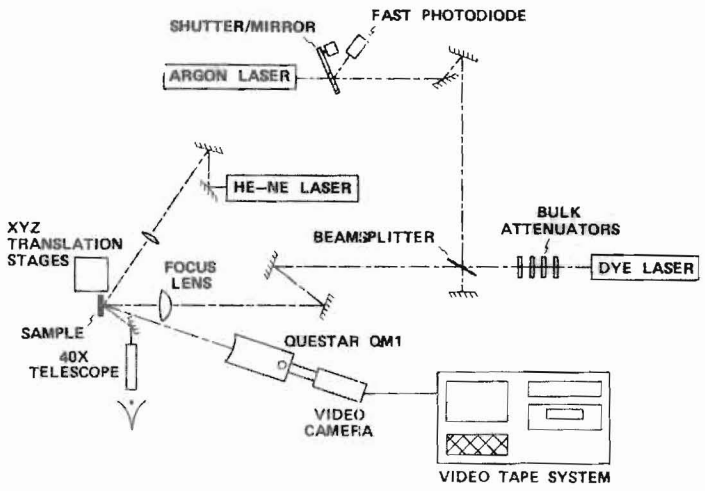
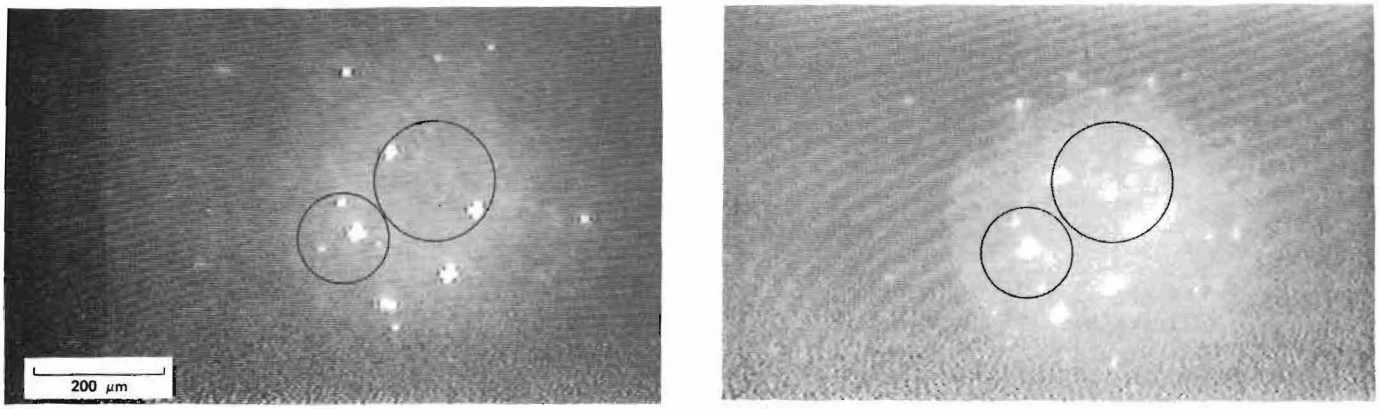
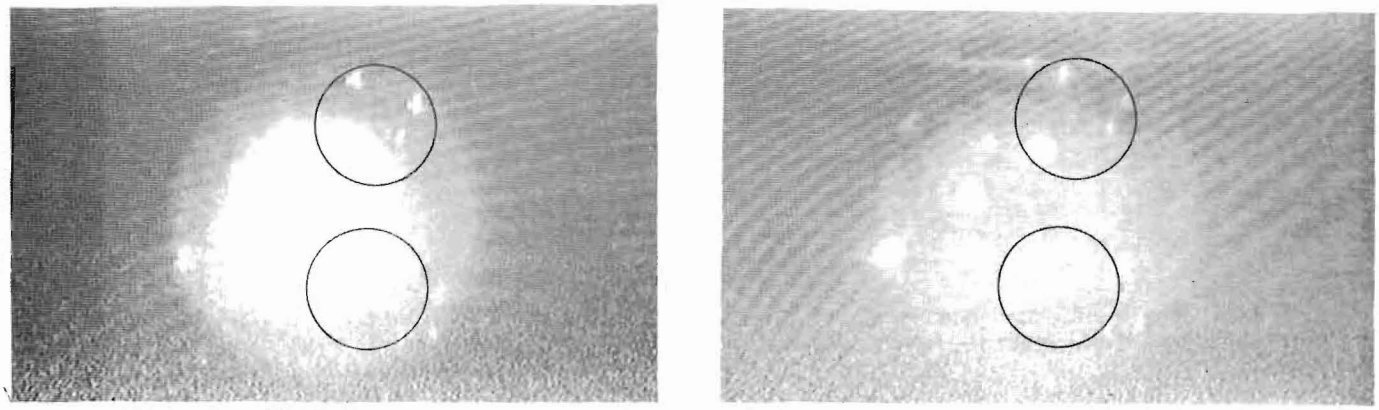


Figure 1. Test facility and VIMS.



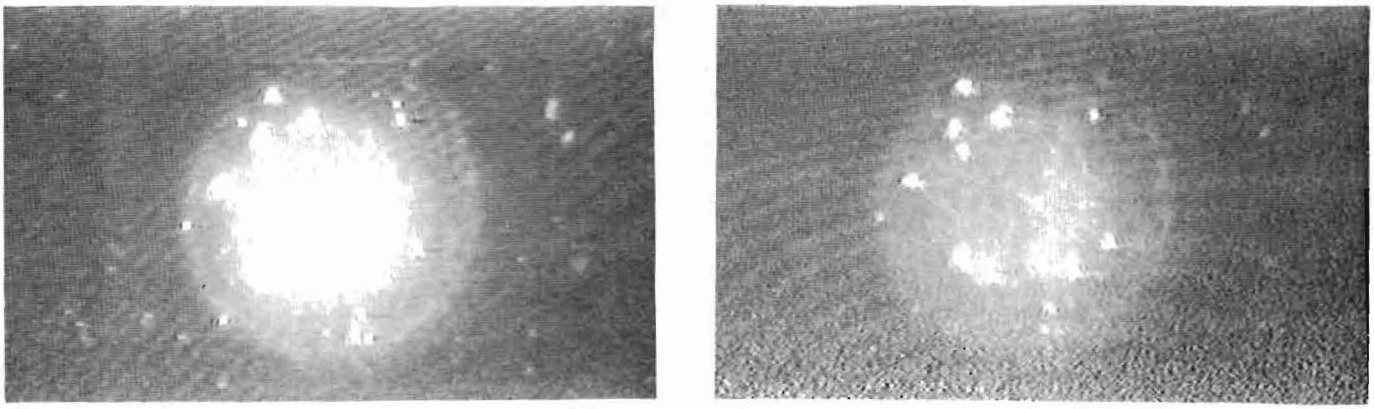
(a) (b)

Figure 2. Wavelength modulation of p-polarized DI intensity from BBM#1 at (a) 515 nm and (b) 476 nm.

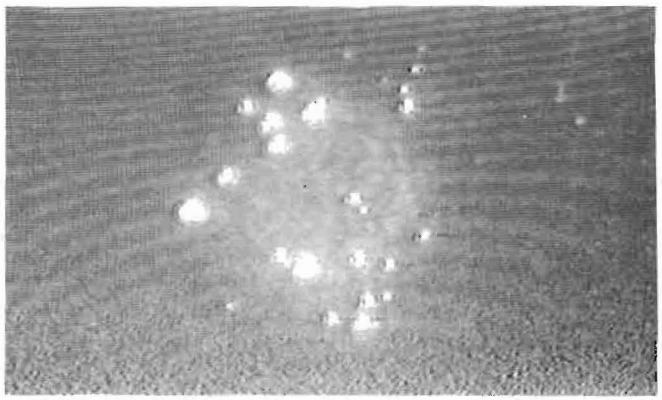


(a) (b)

Figure 3. Wavelength modulation of p-polarized DI intensity from EM at (a) 515 nm and (b) 476 nm.

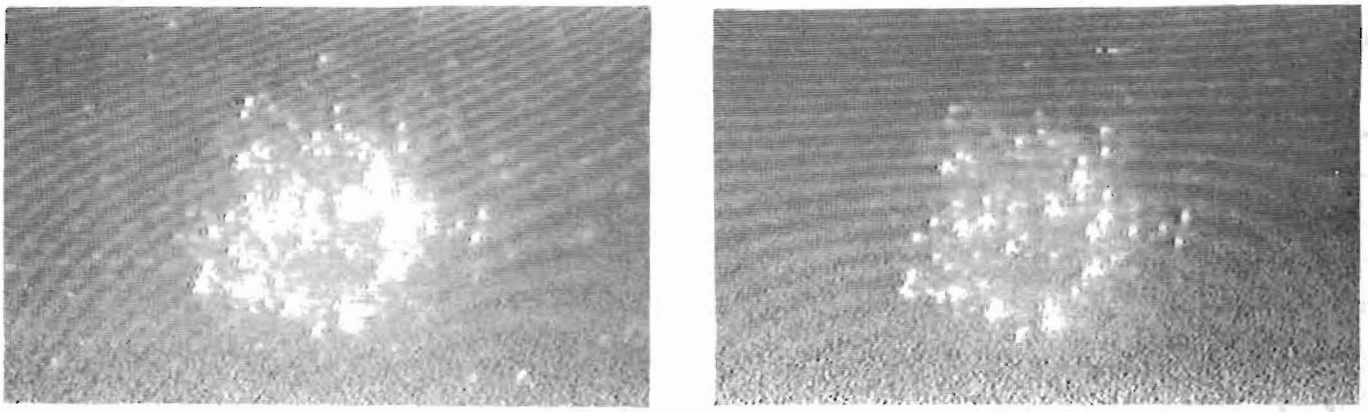


(a) (b)



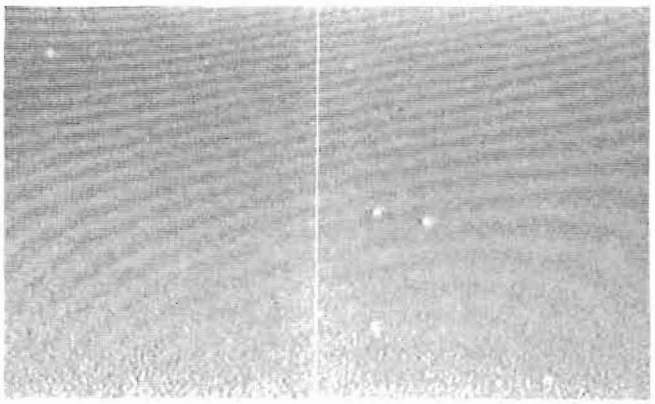
(c)

Figure 4. Polarization dependence of DI intensity from BBM#1 at 515 nm viewed with (a) unpolarized, (b) p-polarized, and (c) s-polarized light.



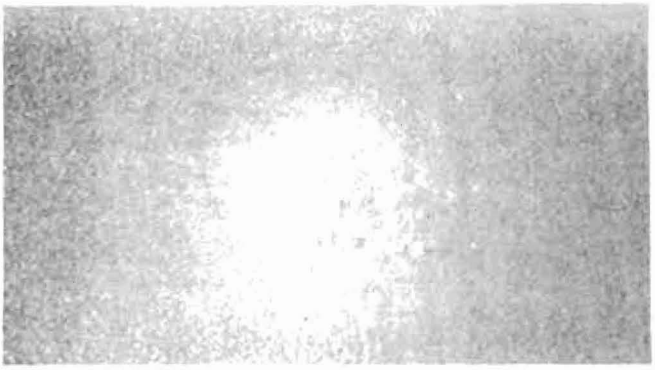
(a) (b)

Figure 5. Polarization dependence of DI intensity from DT Al at 515 nm viewed with (a) unpolarized and (b) p-polarized light.

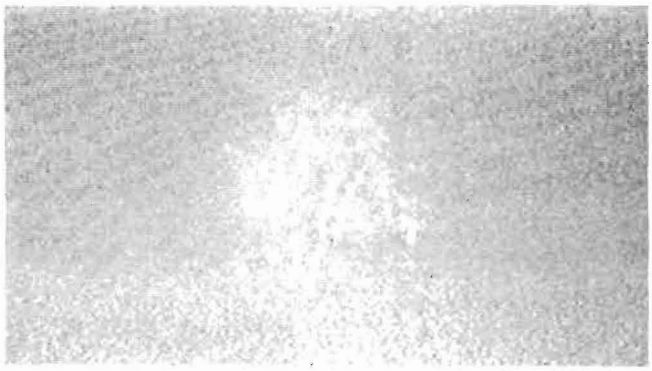


(c)

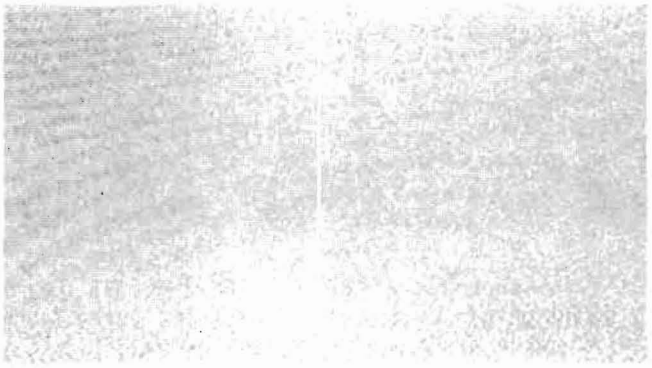
Figure 5 (Contd.). Polarization dependence of DI intensity from DT Al at 515 nm viewed with (c) s-polarized light.



(a)

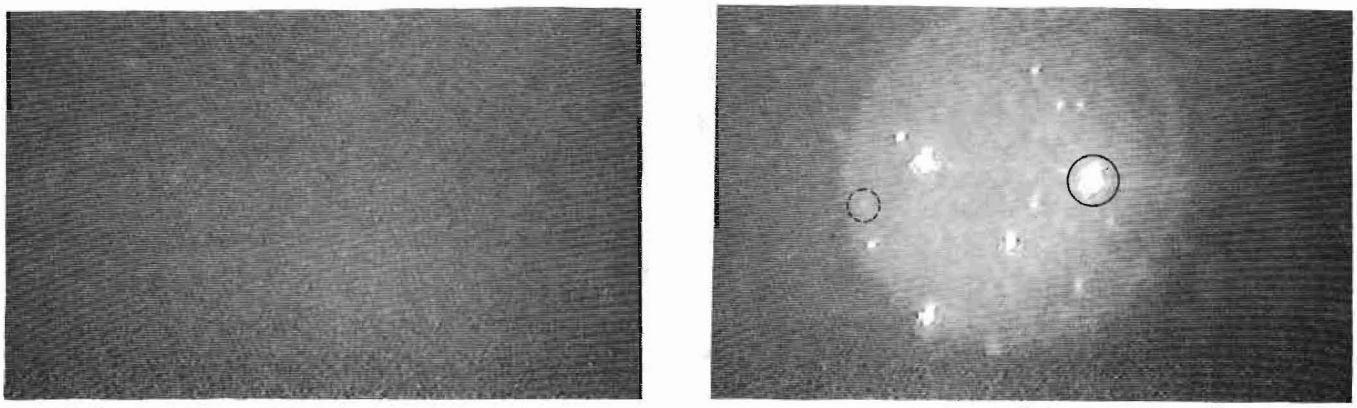


(b)



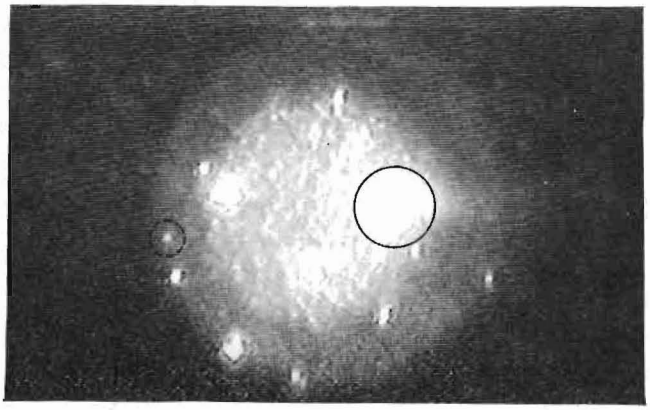
(c)

Figure 6. Polarization dependence of DI intensity from DT Cu at 515 nm viewed with (a) unpolarized, (b) p-polarized, and (c) s-polarized light.

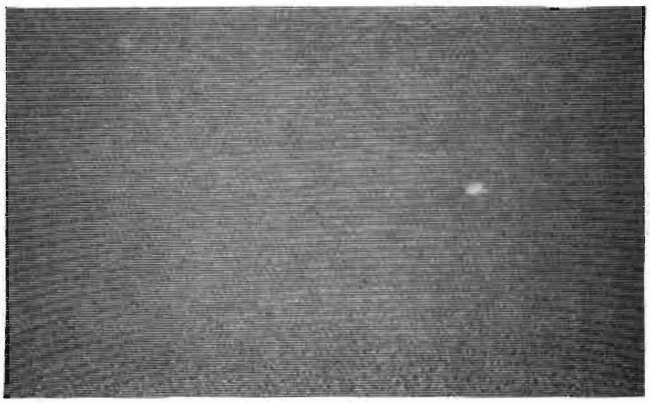


(a)

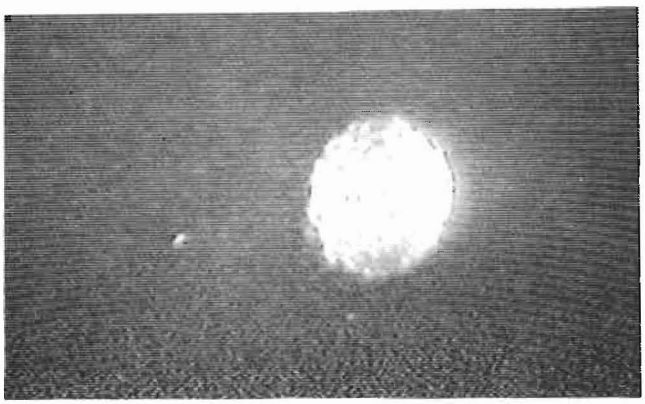
(b)



(c)



(d)



(e)

Figure 7. Progression from DI to laser-induced damage on BB#2 at 515 nm viewed with p-polarization: (a) surface, no damage, (b) nondamaging laser pulse, (c) laser pulse producing observable damage shown in (d), and (e) damage produced after another laser pulse.

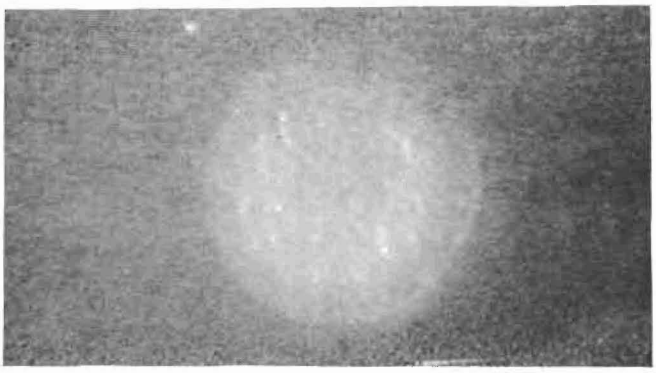


Figure 8. DI intensity from LDM at 497 nm.

Characterization of Micron-Sized, Optical Coating Defects by Photothermal Deflection Microscopy

J. A. Abate [1], A.W. Schmid, M. J. Guardalben, D. J. Smith [2], and S. D. Jacobs

Laboratory for Laser Energetics, University of Rochester, 250 East River Road, Rochester, New York 14623

Information about the localized absorbing defects in optical thin films is required for a better understanding of laser-induced damage. Photothermal deflection microscopy offers a nondestructive optical diagnostic which can yield spatially resolved absorption data on simple and multiple-layer AR and HR dielectric coatings. This paper describes the computer-controlled apparatus used to generate absorption maps of dielectric thin films and an experiment in which a partial correlation between localized absorption sites and damage caused by nanosecond laser irradiation at 351 nm is established.

An absolute calibration of absorption for our measurement technique is presented here. Micron-sized absorbtive defects of Cu were introduced into our coatings to provide a means of calibration. Also presented here are some preliminary data on the modification of the absorption signatures measured by photo-thermal deflection as a function of the location of the defect within the coating layers.

Key Words: coating defects; laser damage; photothermal deflection

Presently the most successful theory [3,4] describing the damage of optical thin films by high power laser radiation attributes the damage process to isolated microscopic impurities, or defects, in the deposited coating. In this theory, the impurity absorbs the incident radiation causing the local temperature to rise, eventually producing melting, vaporization, or fracture of the material surrounding the impurity.

This impurity model can explain many of the observed scaling effects seen in thin film damage studies. The observed decrease in damage threshold with decreasing wavelength can be attributed to the increase in Mie absorption with decreasing particle size, and the well-known result that Mie scattering is strongest for particles whose size is comparable to the incident light wavelength. The observation that the damage threshold increases with thinner films can be explained by the exclusion of larger, easier to damage, impurities as the physical thickness of the film is reduced. The observation of very high damage thresholds for small incident laser spot sizes is consistent with damage being caused by localized impurities: when the spot size is small compared to the mean distance between impurities, it is possible to avoid these weaker areas and measure higher thresholds. In addition, it has been shown for oxide and fluoride films that the dependence of damage and thermal properties on laser pulse width is consistent with the impurity model. [3]

Very little is known, however, concerning the exact nature or density of these damage-causing impurities. It has been determined from damage morphology [5-7] that the impurities must be small in size, typically several microns or less in diameter. One of the objectives of this work has been to see if a direct connection exists between the localized absorption properties of a thin film and the appearance of damage in a thin film.

Apparatus

Several attempts have been made to use photothermal effects to investigate surface and subsurface structure in solids and in thin films. [8-13] Photothermal imaging has developed into a very powerful non-destructive testing technique. All previous methods have lacked sufficient spatial resolution to detect submicron-sized objects of interest to laser-damage studies. Some defects have been seen in thin films, [9-12] but their size, typically 20 microns or larger, is not consistent with the experimental observation of micron-size pits in damage coatings at threshold.

The apparatus we have used to locate micron-size absorbing impurities in dielectric thin films is shown schematically in figure 1. It relies on the photothermal deflection [13] of a probe laser to measure the absorption of energy from the pump laser in a localized area. The pump beam consists of temporally modulated light (800 Hz) from an argon-ion laser (351 nm or 514 nm) focused to a spot by a 60X microscope objective. The sample of interest is kinematically mounted on a computer-controlled X-Y translation stage, which has a minimum step size of 0.4 μm. A HeNe laser probe beam is reflected off the sample surface at a shallow angle (fig. 2).

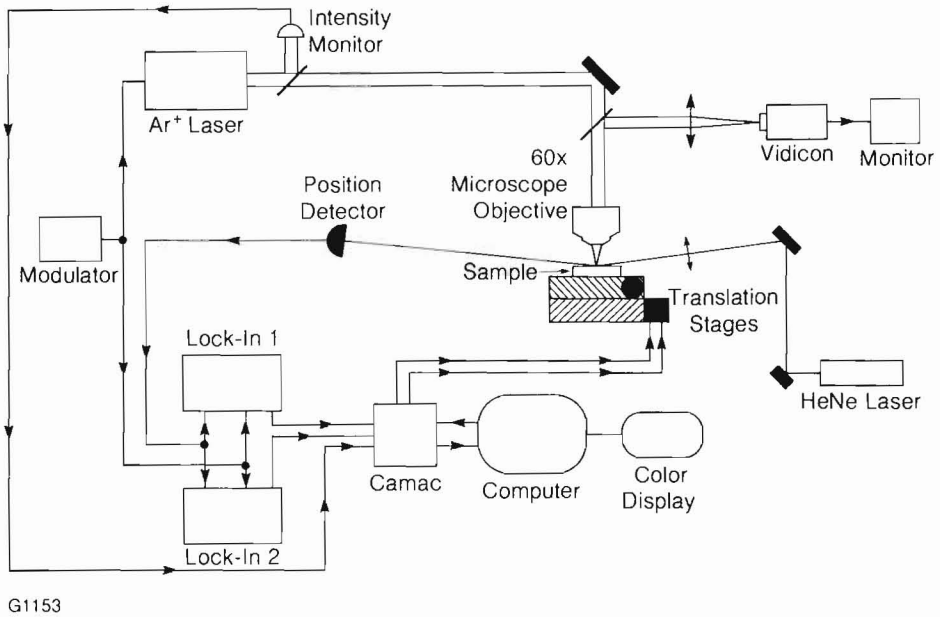


Figure 1 Block diagram of the photothermal deflection apparatus.

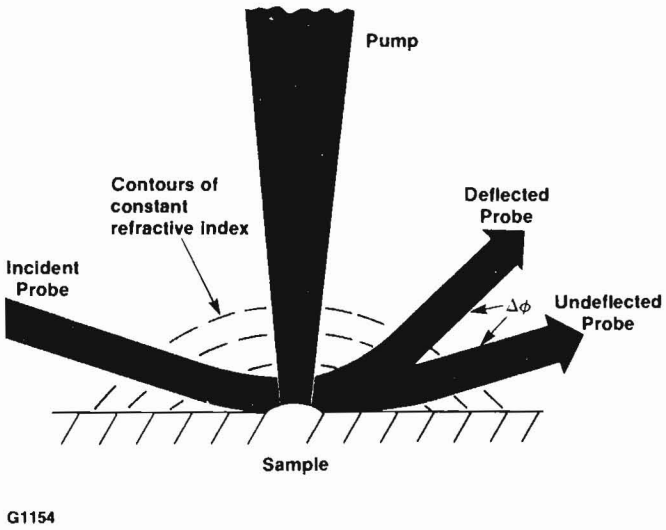


Figure 2 Photothermal-Deflection mapping of defects in a thin film sample. Pump laser energy is absorbed by a defect with two consequences: (i) the surrounding air is heated, leading to a refractive index gradient; and (ii) thermal expansion in the absorption region causes a "bump" to form on the sample surface.

The probe beam is focused to a spot size of 75 μm surrounding the pump beam focus. The probe center intersects the sample surface slightly displaced from the pump beam. This particular geometry was first used by Olmstead et al. [14] and was pointed out to us by Mundy et al. [12] The probe beam is deflected off the "bump" caused by the local heating and resulting thermal expansion of the substrate.

The modulated displacement of the probe laser is measured by a position sensor (United Detector Technologies SC-25) connected to a set of lock-in amplifiers arranged in quadrature to measure both the amplitude and phase of the position signal. A DEC 11/23 computer controls the position of the sample and reads the output of the lock-in amplifiers. False color absorption maps of the coatings of interest are produced on a Chromatics color graphics display.

In order to demonstrate a connection between absorptive impurities and damage, we have made absorption maps of several coatings and then exposed these coatings to high intensity laser light on

the LLE UV damage-testing facility. [15] Photomicrographs and absorption maps of sample coatings were taken both before and following the damage test. Typical examples are shown in figures 3 and 4. The pump beam's wavelength was 351 nm and its spot size was 1.0 ± 0.2 microns. The pump power was 100 mwatts. The coating sample was raster scanned with a step size of 0.8 microns. In many cases the absorption map before damage showed small areas of high absorption that were not visible in the darkfield photomicrographs (See fig. 3). When the coating shown in figure 3 was exposed to a laser irradiance approximately 20% above its single shot damage threshold, several localized areas on the coating were afterwards seen to have damaged (photomicrograph of fig. 4a).

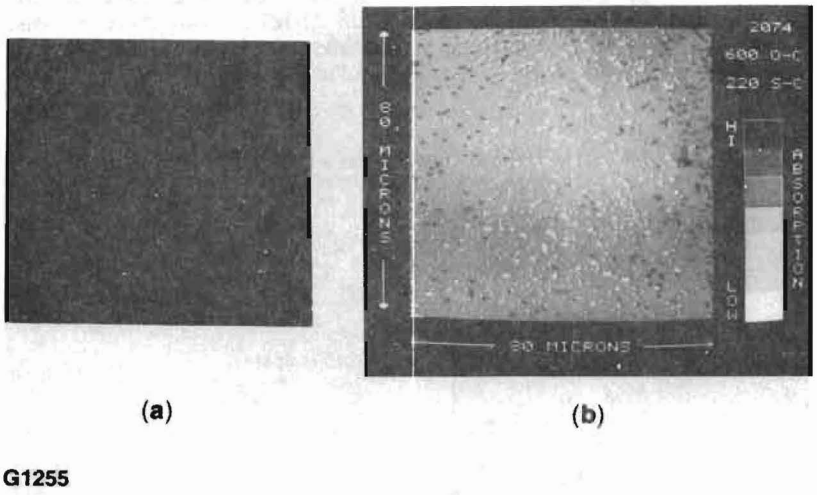


Figure 3 (a) Photomicrograph and (b) absorption map of Ta_2O_5-SiO_2 351-nm HR coating before damage test.

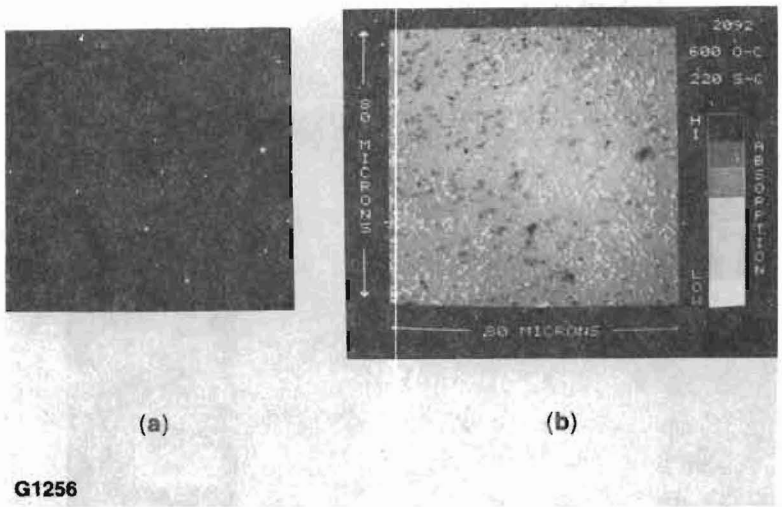


Figure 4 (a) Photomicrograph and (b) absorption map of Ta_2O_5-SiO_2 351-nm HR coating after damage test.

In addition, the absorption map of the same area (fig. 4b) shows clearly increased absorption in the region which showed a defect in figure 3b. There are also several areas which show damage in figure 4a but no strong absorption signature in figure 3b. In these cases, it is uncertain whether our sensitivity is insufficient to detect the damage-causing impurities, or whether other mechanisms besides linear absorption are acting to initiate some of the damage. Attempts are being made to increase the sensitivity of our apparatus to further explore this question.

Absorption Calibration

In order to relate the photo-thermal deflection signal measured on our apparatus to the absorption coefficient of the material causing the deflection, we deposited small "islands" of a known material, of a known size and thickness on a fused quartz substrate. The material chosen was Cu and the islands were created by coating through a laser drilled mask. The geometry for the calibration is shown in figure 5. It consisted of a 4 x 4 array of one micron spots and a set of 4 ten micron spots on the perimeter to aid in locating the array. The pump laser was operated at 514.5 nm with a power of 2 mwatts and had a spot size of 2.0 ± 0.2 microns. The thickness of the coating was determined by standard laser ratiometer absorption techniques in an area of the coating adjacent to the masked area and using tabulated values for the absorption coefficient of Cu. The coating uniformity over the mask was quite good. The Cu coatings used were typically 480Å thick. The mask's small holes were measured using an SEM and were found to vary from 0.5 to 1.5 microns in diameter. A scan of the Cu islands is shown in figure 6 along with a calibrated gray scale indicating the product of absorption coefficient and thickness.

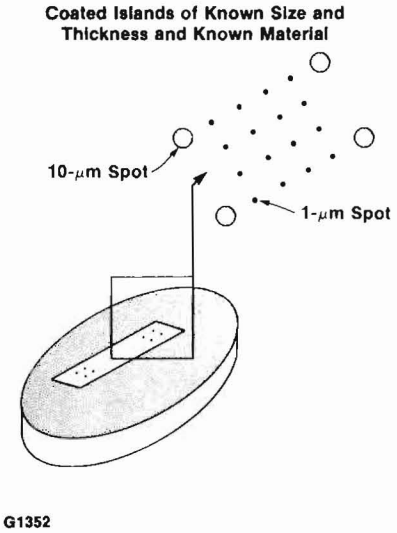


Figure 5 Geometry used in absorption calibration.

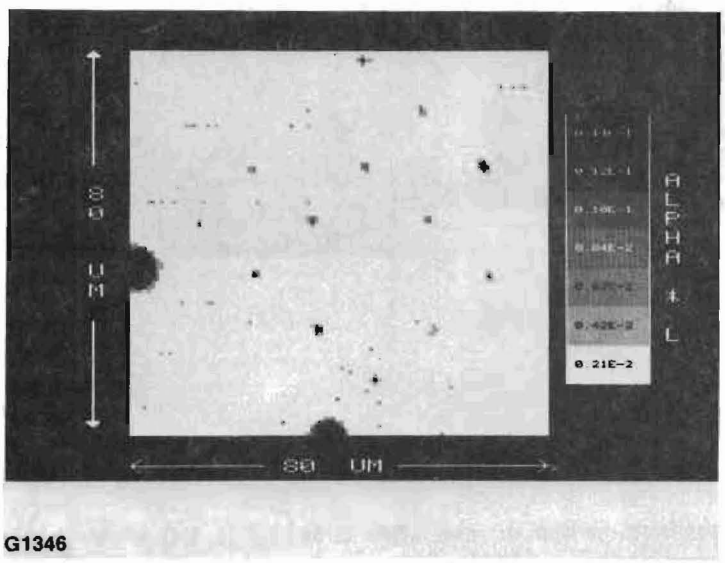


Figure 6 Calibrated absorption map of 1 micron and 10 micron diameter copper islands.

When the cross-sectional area of the absorbing volume becomes smaller than that of the pump beam, only a portion of the incident energy is transformed into heat and into resulting thermal and acoustic waves. The ultimate detectivity in this case will depend not only on the absorption coefficient and the thickness of the inclusion, but also on the ratio of the cross-sections of the pump beam and the

absorbing region, the distance between the inclusion and the coating surface interface, and the thermal properties of the material in which the inclusion is embedded. It should be clear that the pump-beam spot size must be kept as small as possible in order to detect the absorbing inclusions in thin films with maximum sensitivity.

If the defect is larger than the pump beam spot size then the photothermal deflection method is capable, as we have shown here, of giving a quantitative result for the absorption coefficient-thickness product. If the detailed intensity profile of the pump beam were known in the plane of the absorbing defect, it would be possible to deconvolute a scan like that shown in figure 7 to obtain absolute absorption information. For the cases of interest for dielectric coating defects, spatial resolution of the pump beam's profile would have to be better than 0.1 micron, which would be difficult.

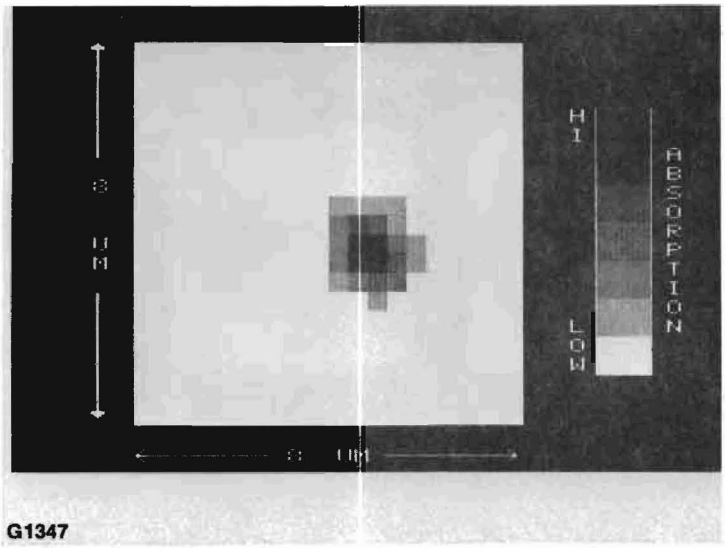


Figure 7 Absorption map of 1 micron Cu island on the surface of a fused silica substrate.

Defect Signatures

The same masking geometry was used to investigate the effect of the position of a known defect placed within the coating's thickness. The reproducibility of our apparatus is demonstrated in figure 8. A single Cu island on the surface of a fused quartz substrate was scanned (2326 in fig. 8) and then removed from the photothermal deflection apparatus and sent through a typical coating run thermal cycle. The sample was then scanned again (2328 in fig. 8) several days later. With this as a reference we investigated the effect of overcoating the Cu island with different thicknesses of a transparent material.

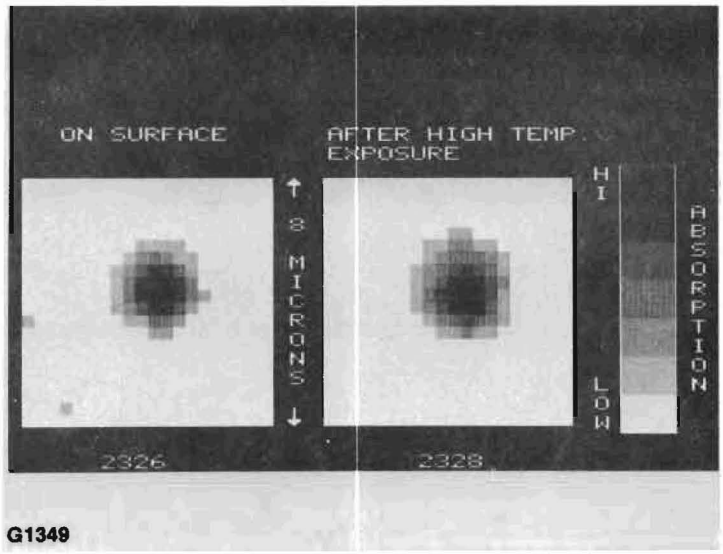


Figure 8 Absorption maps of the same 1 micron Cu island before and after thermal cycling of the substrate.

Figure 9 shows that there was very little effect when the 48 nm thick Cu island was overcoated with 200 nm of MgF_2. The strength of the photo-thermal signals was the same, within our reproducibility (see fig. 8). We next overcoated the same island with an additional one micron of SiO_2 and as is seen in figure 10, the signal increased slightly even though the absorbing material was now buried below more than one micron of material. There was an even more dramatic change in the photo-deflection phase map in this case. Figure 11 shows the phase relationship between the photothermal-deflection signal and that of the pump beam. The area affected by the pumping beam seems to be somewhat larger when buried inside the SiO_2. Much more data, with materials of varing thermal properties, are needed before the current models [16] for this effect can be tested. We are, however, encouraged that this method of detection holds the promise of more information on the nature and location of absorbing defects in thin films.

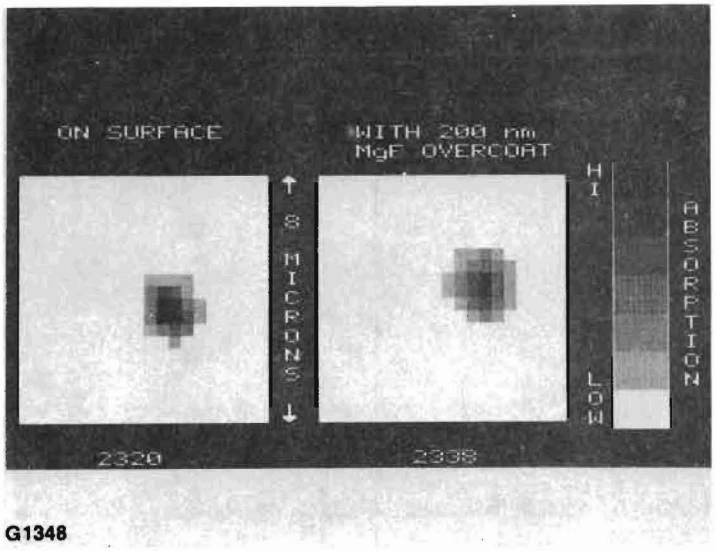


Figure 9 Absorption maps of 1 micron Cu island before and after overcoating with 200 nm of MgF_2.

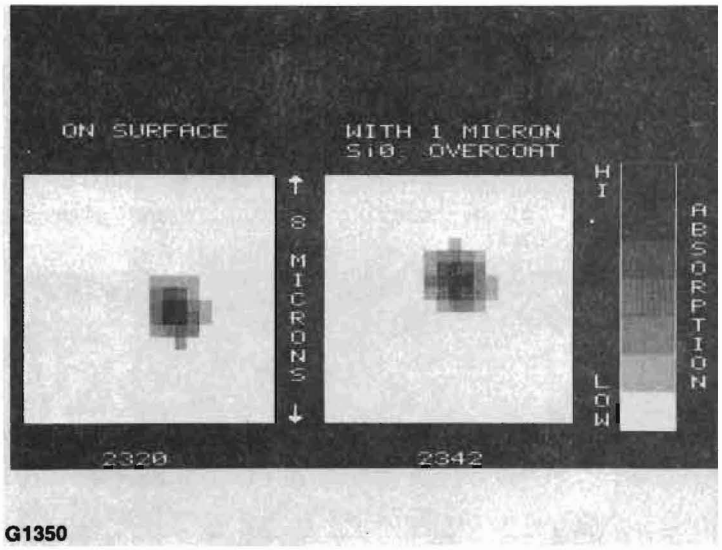


Figure 10 Absorption maps of 1 micron Cu island before and after overcoating with an additional 1 micron of SiO_2.

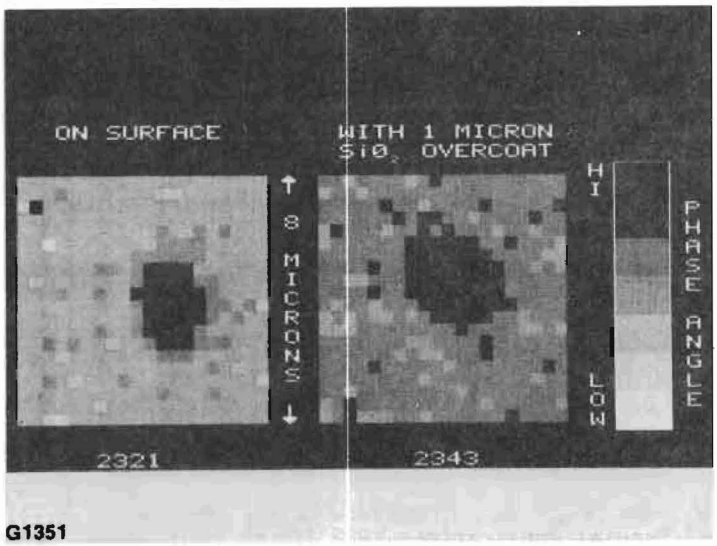


Figure 11 Phase maps of 1 micron Cu island before and after overcoating with additional 1 micron of SiO_2.

Conclusion

We have taken a first step towards understanding the role of absorptive inclusions in the damage process of thin films. We have demonstrated that photothermal deflection microscopy can detect submicron absorbing impurities in optical coatings. We have also demonstrated a method that allows for the absolute calibration of the photo-thermal deflection technique for a particular apparatus when the absorbing defect is larger than the pump beam spot size. We have also described some of the limitations of the technique when the absorbing inclusions are smaller than the pump beam spot size.

Acknowledgement

This work was partially supported by the U.S. Department of Energy Inertial Fusion Project under contract number DE-AC08-80DP40124 and by the Laser Fusion Feasibility Project to the Laboratory for Laser Energetics which has the following sponsors: General Electric Company, Northeast Utilities, New York State Energy Research and Development Authority, The Standard Oil Company (Ohio), The University of Rochester, and Empire State Electric Energy Research Corporation. Such support does not imply endorsement of the content by any of the above parties.

References

1 The Standard Oil Co. (Ohio), on assignment at the Laboratory for Laser Energetics; present address - Kodak Research Laboratory, Rochester, New York.

2 The Center for Advanced Optical Technology, Institute of Optics, University of Rochester.

3 WALKER, T.W., GUENTHER, A.H. and NIELSEN, P.E., IEEE J. Quant. Elect. 17, 2053 (1981).

4 See references 21-48 in (3).

5 LOWDERMILK, W.H., MILAM, D., RAINER, F., in "Laser Induced Damage in Optical Materials", H.E. Bennett, A.J. Glass and A.H. Guenther, and B.E. Newnam, Eds., Washington, D.C., US, GPO, NBS Special Publ. 568, 391 (1979).

6 CARNIGLIA, C.K., APFEL, J.H., ALLEN, T.H., TUTTLE, T.A., LOWDERMILK, W.H., MILAM, D., AND RAINER, F., in "Laser Induced Damage in Optical Materials", H.E. Bennett, A.J. Glass, A.H. Guenther, B.E. Newnam, Eds., Washington, D.C., US, GPO, NBS Special Publ. 568, 377 (1979).

7 WALKER, T.W., GUENTHER, A.H., AND NIELSEN, P.E., IEEE, J. Quant. Elect. 17, 2041 (1981).

8 WONG, Y.H., THOMAS, R.L., HAWKINS, G.F., Appl. Phys. Lett. 32, 538 (1978).

9 FREESE, R.P. AND TEEGARDEN, K.J., in "Laser Induced Damage in Optical Materials", H.E. Bennett, A.J. Glass, A.H. Guenther, B.E. Newnam, Eds., Washington, DC, US, GPO, NBS Special Publ. 568, 313 (1979).

10 ATLAS, D.S., M.S. Thesis, Institute of Optics, University of Rochester, 1981.

11 ABATE, J.A., JACOBS, S.D., PISKOROWSKI, W.S., AND POTTENGER, T.P., CLEO, 1982 Conference, Phonix, Arizona, 1982.

12 MUNDY, W.C., HUGHES, R.S., AND CARNIGLIA, C.K. in "Laser Induced Damage in Optical Materials", H.F. Bennett, A.H. Guenther, D. Milam, B. Newnam, Eds., to be published 1982.

13 BOCCARA, A.C., FOURNIER, D., AND BADOZ, J., Appl. Phys. Lett. 36, 130 (1980).

14 OLMSTEAD, M., AMER, N.M., FOURNIER, D., AND BOCCARA, A. C., Appl. Phys. 32, 141 (1983).

15 ABATE, J.A., ROIDES, R., JACOBS, S.D., PISKOROWSKI, W., AND CHIPP, T., in "Laser Induced Damage in Optical Materials", NBS Special Publication, 1982 (to be published).

16 OPSAL, J. AND ROSENCWAIG, J. Appl. Phys. 53(6), June 1982.

32. Abate et al.

The speaker stated that they have gone to a grazing incidence technique rather than a skimming technique over the surface because they find it far more sensitive (about an order-of-magnitude increase in signal). It is not the refractive index change of air above the sample that they are measuring but actually a thermal expansion of the material. Since possible scattered light from the surface would not be modulated temporally, the phase-sensitive detection system will not see scattering. They find that for a good coating, they do not see any permanent change in the coating at power levels of 100 mW in a 1- m spot (10 MW/cm^2). They thus typically scan at this power level. Some coatings do damage, and they have to reduce this level in that case. They chose this technique rather than scanning with an electron beam (the so-called thermal wavelength processing) because the optical technique is nondestructive. The e-beam technique gives higher spatial resolution but is a destructive test.

Manuscript received 1-23-84/sar

EXPERIMENTAL OBSERVATION AND COMPUTER SIMULATION OF THE MICROSTRUCTURE OF VAPOR DEPOSITED THIN FILMS

K. H. Guenther

Balzers AG
FL-9496 Balzers, Liechtenstein

The microstructure of thin films applied by conventional physical vapor deposition for use as optical coatings is columnar for most of the materials commonly used. This has been established for about a decade through numerous experimental observations employing microfractographical replication for use with high resolution transmission electron microscopes. Scanning electron microscopes are more useful investigating coating defects, the most remarkable of these defects being known as nodules. From fundamental considerations of nucleation and growth of thin films, the origin of both columns and nodules, and the dependence of their appearance on the deposition conditions, are discussed in some detail. A simple 2-D simulation model assuming very limited surface mobility of adatoms or admolecules shows striking similarities to peculiar properties of both columnar and nodular growth seen in actual investigations. Conclusions are drawn as to how the two types of microstructures described influence general thin film properties, but in particular as to how they influence possible laser damage mechanisms.

This paper is of a tutorial nature, although most of the results presented are from the author's own work, some of them having been published previously.

Key words: computer simulation; electron microscopy; microstructure; optical coatings; physical vapor deposition (PVD); thin films

1. Introduction

1.1. Coating Techniques for High Energy Laser Components

Thin films for optical applications have been produced for many years. The main method is thermal evaporation of coating materials from either a boat or an e-beam source in a high vacuum environment. This simplest of physical vapor deposition (PVD) processes is most likely still the standard industrial technique used to produce high quality optical coatings. Some novel deposition methods have been recently developed and applied to produce high energy laser (HEL) coatings [1]. Frequently, the coatings obtained by these novel methods are claimed to have superior properties as compared to conventional ones in terms of optical and environmental stability, and hopefully also in terms of improved laser damage thresholds. These properties are critical for any film and they are strongly dependent on its microstructure [2,3]. In order to understand the origin of thin film microstructure and how it is influenced by the deposition parameters, we should restrict our investigations to films prepared by a straightforward, well characterized process, which is the aforementioned thermal evaporation PVD.

1.2. Nucleation and Growth of Thin Films

Papers on numerous fundamental experiments, employing well defined substrates (vacuum cleaved crystals or mica), deposits (noble metals) and deposition conditions (point sources, molecular beams, ultra high vacuum environment) have been published [4]. The results of those experiments show that the impinging particles (adatoms, admolecules) have a specific surface mobility, which can range from zero on up.

One parameter determining the surface mobility is the ratio of the substrate surface temperature to the bulk melting point of the coating material. If this ratio is low, which is the case for most of the oxides commonly used in optical coatings for example, the surface mobility is also low. This means that the incoming vapor particles may stick where they arrive first. In contrast, low melting point metals have a rather high surface mobility, which allows the adatoms or admolecules to travel across the surface after condensation to energetically preferred sites, where they nucleate. Surface mobility increases as the substrate temperature increases, even during the thermal post-treatment after deposition.

Surface mobility (or surface self diffusion) is, of course, also dependent on the nature of the momentary surface i.e. whether the adspecies undergo heterogeneous or homogeneous condensation. Usually, low surface mobility is connected with three dimensional island growth, whereas high surface mobility means that the growth of the film takes place in a more or less two dimensional manner, completing a monolayer before the second layer begins to form (layer growth). In the case of gold deposited on single crystal sodium chloride, for instance, three dimensional island growth with subsequent coalescence of the growing clusters has been observed for the heterogeneous nucleation phase. Once the film becomes continuous, homogeneous condensation causes further growth to be by layers, indicating increased surface mobility of the adatoms as compared to the initial stages of heterogeneous condensation with preferred nucleation at lattice sites [5].

The mobility of condensed vapor particles is also influenced by the presence or absence of simultaneously impinging particles, either vapor atoms/molecules or residual gas atoms/molecules. One has to bear in mind that at technical vacuum conditions of about 10^{-5} mbar background pressure, the flux of residual gas particles impinging onto a surface is of the same order of magnitude as the intentionally deposited vapor flux. If either flux is increased, for instance by raising the evaporation rate or enhancing the O_2 partial pressure as used for reactive processes, the individual adatom or admolecule is literally "frozen" onto the site where it initially arrived. This yiels the same results as a comparable lowering of the substrate temperature, namely a highly disordered film microstructure which becomes eventually amorphous when the surface mobility is sufficiently lowered.

2. Experimental Techniques for Microstructural Investigations

2.1. Morphological Characterization

The fundamental size of thin film microstructure, both in the condensation and nucleation stage of growth, and in the final film is of molecular order, no matter how thick the final film is. Hence, we need high resolution imaging techniques in order to be able to see these microstructures. The technique of choice is electron microscopy [6]. Modern transmission electron microscopes (TEM) offer a superior resolution of 0.1-0.2 nm as compared to scanning electron microscopes (SEM) for which the best values are given as 3-4 nm.

Since it is very difficult and cumbersome, although not impossible, to prepare thin film cross-sections for direct observation in the TEM [7], powerful replication techniques have been developed [8,9]. The cleaved fracture edge of a thin film on its substrate is preshadowed with a refractory metal (Pt, Ta, W) at a shadowing angle of about 10-30° both to the surface of the film and to the fracture edge. We routinely use a mixture of platinum and carbon (Pt/C), which is coevaporated by means of a thin Pt-wire on a sharpened carbon rod burning in an arc. The resolution of this shadowing technique is about 5 nm at best. Mixtures of tantalum and tungsten (Ta/W) have been found to give even higher resolution because the shadowing particles are smaller [10], but they are more difficult to evaporate (they need a point-source such as an electron beam evaporator), and the shadowing films are less stable chemically than Pt/C-films.

After preshadowing, pure carbon support films are deposited on the specimen. In case of cleaved thin film cross sections which exhibit a 90° sharp edge between the surface of the film and its fractured profile, it is advisable to use two different evaporation directions for the supporting film, inclining to the surface and to the fracture at about 10°. Then, the shadowing together with the supporting films are stripped from the specimen by inserting it slowly and at a slightly oblique angle into diluted hydrofluoric acid, which dissolves the original specimen, leaving a clean, electron transparent carbon replica on which the specimen's topographical features are imprinted. Obviously, the investigation of the replica can only supply topographical information, and no chemical analysis such as by X-ray fluorescence can be made from the replica. Transmission electron micrographs were taken with a Siemens Elmiskop 1A electron microscope.

The big advantage of the SEM is its capability for direct observation of the specimen surface which also allows X-ray fluorescence analysis. Although the nominal best resolution values of SEMS are about equal or even better than the approximately 5 nm of the Pt/C-shadowed replicas for the TEM, the SEM gives inferior pictures at high magnifications. This is particularly true for dielectric thin films which must be coated with a conductive film in order to prevent charging. However, the SEM is very useful for the investigating rather macroscopic coating defects such as pinholes, spatters, or nodules. SEMs used in this work were a Cambridge Stereoscan S-600, a Jeol JSM 35, and an Amray AMR 1600, equipped with a Balzers-Pfeiffer turbomolecular pump.

2.2. Crystallographical Analysis

There are a variety of methods available. Of the more conventional ones, electron diffraction, both in transmission and in reflection, are well known and equally well understood from a theoretical point of view. High energy electron diffraction (HEED) can be easily performed in a TEM with appropriate diffraction stages and attachments. Depending on the primary electron energy, the information depth for reflection HEED is about ten nanometers, which is also the maximum specimen thickness for transmission HEED. In contrast, low energy electron diffraction (LEED) is very sensitive to surface adsorbates and is thus preferentially employed for studying the interaction of mono- and submonolayers on single crystal surfaces, rather than the microcrystallinity of thin films.

X-ray diffraction is perhaps the most common method for investigating the structure and microstructure of solids. Its application for thin films is somewhat limited, however, because of the large penetration depth of the X-rays, which also contains contributions from the bulk substrate. This limitation can be overcome by comparative studies of identical substrates, some uncoated and some coated with the thin film to be studied. For the X-ray analyses of dielectric multilayer coatings referred to later, a Philips PW 1050 powder X-ray diffractometer with a graphite monochromator was employ. Cu K_α radiation was used (wavelength 0.154 nm).

More recent methods are Raman spectroscopy and Extended X-ray Absorption Fine Structure (EXAFS) measurements which have been used, for example, in the microstructural characterization of Ge thin films on glass and on silicon substrates [11].

3. Computer Simulation of Thin Film Microstructures

3.1. 2-D Model

Perhaps the earliest and meanwhile most frequently cited attempts to simulate columnar thin film microstructure are those of Dirks and Leamy [12]. Their 2-D simulation model assumes hard disks serially impinging onto a perfectly flat surface at a fixed oblique angle. Further, the disks are assumed to stick where they arrive (either on the substrate surface or on another, already deposited disk) or to roll into the nearest saddle position formed by previously deposited disks. These assumptions represent the behaviour of real deposits having very low or no surface mobility at all, which is equivalent to a high activation energy. It should be noted that the simulations by Dirks and Leamy used a pure kinematical cardboard model which was also used in the animated film by the same authors shown after this talk [13].

Since the activation energy is positively correlated with the melting point of the bulk material, refractory oxides (as used for optical interference films) are perfect candidates for the aforementioned simulation model of thin film microstructure assuming low surface mobility. Hence, we are making use of this model by implementing it in a personal computer program, rather than repeating the mechanistical animation of Dirks and Leamy.

3.2 Hardware

Two different personal computer systems were used. The one was an ITT 2020 (modified Apple II) with 48kB RAM and a monitor with 192x360 pixels (full graphic screen). For hard copies of the screen pictures, a Tectronix Video Hard Copy Unit 4632 was used. The second system consisted of a Commodore 3032 (32kB RAM) used with a Tectronix 4662 Plotter. Whereas the "molecules" or "atoms" are shown as dots in the first system, they appear as circles in the second computer output.

4. Experimental Results

4.1. Cross-section Electron Micrographs of Dielectric Thin Films

4.1.1. Columnar microstructure

The microstructure most frequently observed in electron microscopical investigations of fractured (cleaved) thin film optical coatings is that of columns, which are thought to be densly packed, enclosing voids which are columnar as well. Important to note is that the voids are hypothetical, as they have never been pictured, neither by direct observation nor by transmission electron microscopy using replicas - because of their size which is below the resolution of both methods.

The microstructure depends strongly on the deposition conditions [14], as shown in figure 1. The columns increase in diameter with the substrate temperature (fig. 2a) and also with the film thickness (fig. 2b). The first function is easily explainable by an increase in the surface mobility of both the vapor admolecules and impurity admolecules, allowing the first to pack more densely and the second to segrate more easily at the forming grain boundaries. The film thickness dependency of the column (grain) diameter is not as easily explainable. Since a growing column or grain certainly does not know how tall it should become, it also cannot know how large it would get in diameter. A possible explanation would be that the columns consist of, for instance fibrous, subunits which bunch together more and more as the film thickness increases. Indeed, such fibrous substructures were found for TiO_2 single layers of intentionally exaggerated thickness (fig. 3), which were not dissolved completely by the hydrofluoric acid etch routinely used with the replica preparation of the specimen. A similar observation was made with likewise chemically etched Ge films by Messier [15].

4.1.2. Nodular thin film defects

Nodular defects [16] - or nodules in short - are defined as isolated structures protruding from the average thin film surface in a dome-like manner when observed with a high resolution optical microscope (Nomarski), or with the SEM, from the undisturbed surface. Scratching the thin film coating (which may be a multilayer) or cleaving it together with its substrate, reveals that the nodules most often originate either at small asperities at the substrate surface (fig. 4a), or at tiny coating material spatters incorporated in the growing film (fig. 4b).

Nodules are shaped like inverted cones, either parabolic or linear, increasing their diameter considerably with the distance above the tip of the inverted cone. However, the protrusion of the distortion has always been found constant along the axis of a nodule, and is the same for the outermost dome and the nucleus of the defect. This feature can be seen particularly well in multilayer stacks on which a smooth cross-sectional fracture has been made either by cleaving or by metallographical polishing (fig. 5). From such micrographs, one can see that the individual layer sequence is maintained within the multilayer stack, giving evidence that nodules are growth defects and not massive spatter particles or empty bubbles, as sometimes assumed.

In fact, although a nodule is nothing else than the reproduction of an individual minute particulate or an asperity, and is thus essentially of the same chemical composition as the undisturbed film, nodules tend to behave like independent particles incorporated into the film. For instance, they separate frequently as a whole from the surrounding, undisturbed film, popping out and leaving a hole behind (fig. 6a). This may be caused by external forces such as cleaning or wiping after the film has been completed, or even during the deposition process because of intrinsic mechanical stresses. The latter case can be assumed if secondary nodular growth occurs inside a hole presumably previously occupied by a nodule (fig. 6b).

An interesting case of nodular growth has been observed with Ta_2O_5/SiO_2 multilayer stacks. It was dependent on the residual oxygen pressure during evaporation of the Ta_2O_5 layers. At higher oxygen pressures, the multilayer coatings exhibited a very high density of nodules. The density decreased dramatically as the oxygen pressure was lowered (fig. 7). This case of nodular growth without apparent roots in terms of surface asperities or spatter particles will be discussed later in more detail.

4.2. 2-D Simulated Thin Film Growth Structures

The aforementioned computer simulation model with its random serial deposition of hard discs which stick immediately where they arrive (either on the substrate or on predeposited discs), shows various patterns depending on the border conditions assumed in each case.

4.2.1. Undisturbed growth, fixed substrate, normal incidence, constant particle flux

A chain-like network results with its general orientation perpendicular to the substrate. Rather large voids occur, which correspond to a very porous structure in real thin films (fig. 8a).

4.2.2. Undisturbed growth, fixed substrate, oblique incidence, constant particle flux

The mean orientation of the chains is such that they incline towards the angle of particle incidence. If there are no obstacles in the trajectories of the particles, the resulting chain inclines exactly in the direction from which the particles came. However, if the particles already deposited shadow the trajectories of the incoming particles, the resulting mean orientation angle of the chains to the substrate normal becomes smaller than the angle of incidence (fig. 8b). In fact, the inclination angle of the chain can be determined according to the tangent rule, which was found empirically by Nieuwenhuizen and Haanstra [17]. More densely packed chains are observed, which resemble the experimentally found columnar microstructure, if one allows for slight relaxation of the deposited particles. This means that the impinging discs can move into the nearest saddle or triangle position formed by those discs already deposited [12].

4.2.3. Undisturbed growth, rotating substrate, oblique incidence, random variations of particle flux

A more realistic simulation of the actual situation inside a coating chamber was carried out, i.e. assuming substrates mounted atop a rotating cage, vapor sources located off the rotation axis, fluctuating vapor rate. The rate was varied by multiplying a mean value with a random number created by the random number generator of the particular computer. The substrate motion above the vapor sources was taken into account by including a sinusoidal temporal change of the angle of particle incidence between two (exaggerated) maxima. If the extreme angles of particle incidence are equal but on opposite sides of the substrate surface normal, the mean orientation of the resulting simulated microstructure is perpendicular to the substrate surface, which agrees with the experimental findings. Strikingly, under these conditions the same branching, fibrous substructure of columns can be seen in the model (fig. 8c) as are seen in the TEM replica micrograph of the thick TiO_2 layer (fig. 3).

4.2.4 Growth distortions (other conditions as in 4.2.3.)

We arbitrarily introduced a single non-uniformity - for instance a 2x8 disc array simulating a surface asperity on the base line (fig. 8d), or a 7-disc densely packed hexagonal array formed during the simulated growth (fig. 8e) which represents a microspatter (or a molecular cluster formed in the vapor phase). The resulting 2-D patterns resemble in a very striking manner the shapes of nodules seen in cross-sectional SEM micrographs. Just as in the micrographs, the protrusion height of the nodular growth defect remained constant throughout the film, being equal to the size of the triggering distortion. Void formation at the edge of the nodule, as distinctly seen in the simulation, has also been found in fractured cross-sections of thick single layers (fig. 4b) as well as in polished crosssections of multilayers [14].

4.3. X-ray Diffraction Analysis of Crystallographical Microstructure Modifications

A TiO_2/SiO_2 multilayer system, designed as a broadband mirror for the visible, was manufactured by vacuum deposition onto glass substrates at a nominal substrate temperatur of about 250°C (measured with an infrared radiation thermometer). An X-ray diffraction analysis of the coatings, without further post treatment, revealed that only a very small amount of the TiO_2 was crystalline and the rest seemed to be amorphous. After post-deposition annealing at 250°C for 2 hours in a hot air oven, the microstructure changed to a predominantly polycrystalline one, which was identified as Anatas (fig. 9). Of course, these structural changes cracked the films, presumably because of volume changes or intrinsic stress generation.

5. Discussion

5.1. Columnar Microstructure

The thin films formed by the dielectric materials commonly used for optical coatings (refractory oxides, magnesium fluoride, zinc sulfide, etc.) almost always exhibit columnar microstructure when they are vapor-deposited under standard high vacuum conditions. One definite exception is SiO_2, which has always been found to form structureless, amorphous glass-like films. This may be due to the glass-forming properties of SiO_2, but also to its relatively lower melting point as compared to other oxides. From the positive correlation between surface (activation) energy and the melting point of the bulk thin film material already mentioned, we can conclude that condensed SiO_2 molecules have higher surface mobility and hence they can relax more easily, which leads to the formation of the glass-like films.

Magnesium fluoride has an even lower melting point than SiO_2, meaning it could be a candidate for structureless films, but in fact it also forms columnar microstructures in its thin films. In this case, the reason is the high binding energy which causes MgF_2 to evaporate in undissociated molecular form [18]. The comparably larger molecules have a reduced surface mobility.

For zinc sulfide, seemingly contradictory observations have been made. Lissberger and Pearson [19] found ZnS to form structureless films like SiO_2, whereas our own electron micrographs always showed a columnar thin film microstructure for ZnS. The only apparent difference between the two experiments was the residual background pressure in the vacuum chambers. Whereas our films were deposited under standard high vacuum conditions of about 1.10^{-5} mbar, Lissberger and Pearson deposited their ZnS films under better vacuum conditions of about 1.10^{-7} mbar background pressure. The pronounced influence of the vacuum conditions can even be seen from the micrographs of ZnS/-MgF_2 multilayer stacks (fig. 10). The very first ZnS layer, deposited onto the substrate, reveals a very weak microstructure, tending towards the amorphous form as shown by Lissberger and Pearson. However, the second ZnS layer on top of the first MgF_2 layer, already exhibits the familiar columnar microstructure. A possible explanation would be the increase in the background pressure during the course of the deposition caused by desorption from the chamber walls, stops, feedthroughs, etc., in the vicinity of the heated evaporation source, due to the temperature rise.

From other investigations it is known that the incorporation of impurities into the growing film leads to an increased formation and stabilization of grain boundaries. The impurities segregate at these boundaries preventing the grains from growing together even when annealed at higher temperatures. The impurities may be excessive sulphur originating from the dissociation of ZnS [18] or hydrocarbon molecules from oil diffusion pumps [20], but also nitrogen, oxygen or water vapor. For reactive metals such as aluminium, chemisorption of oxygen along the edges of growing grains limits the mobility of atoms between grains, leading to the formation of pronounced columns [21].

For the limit case of no surface mobility of the adspecies, there is a major discrepancy between the experimentally observed and the computer simulated microstructures in the case of fixed substrates. One gets loose packing of particles and high ratio of voids in the computer simulation (fig. 8a), properties not found in real thin films. At oblique angles of particle incidence the computer simulated columns incline according to the experimentally deduced tangent rule (fig. 8b). Hence the simulation agrees fairly well with the experiment in this respect. However, although the inclined simulated columns become somewhat thicker than those at normal incidence, the packing density still does not agree very well with the experimental findings. The situation improves drastically for the simulation of film growth on rotating substrates. The voids are apparently filled more easily by the varying angles of particle incidence, which leads eventually to the branching, fibrous substructures in the computer simulation (fig. 8c). These have been found in at least one case of a real thin film (fig. 3).

It should be emphasized again that the computer simulation model used in this investigation is a purely kinematical one, not taking into account surface or particle energies or potentials, nor attractive forces, binding energies, crystallographical orientations etc. Hence, the influence of substrate temperature, and effects of charging, diffusion, or crystallization cannot be considered. Nevertheless, the striking similarity of the basic microstructural patterns of real thin films and computer simulated thin films indicates that the low or absence of surface mobility assumed for the limit case model may apply [22].

5.2. Nodular Thin Film Defects

From experimental observations, three different reasons for the formation of nodules have been found so far:

(1) Surface asperities on the original substrate which may originate from general surface roughness due to insufficient polishing, from polishing residues such as disintegrated agglomerates of polishing grains, or from insufficient cleaning or dried-on cleaning agent residues. This list is by no means complete and can be extended to include dust grains, fibres etc. We know from practical experience that badly treated substrate surfaces are more prone to the formation of nodular defects [23] than well-treated ones which are commonly called "superpolished".

(2) Coating material spatters which are incorporated into the growing single or multilayer thin film coating. This seems to happen particularly with high rate evaporation sources such as e-beam guns and magnetrons, but of course has been also observed with conventional thermal (boat) evaporation. Coating materials may behave very differently in this respect, and avoiding spatters is a matter of technical experience.

(3) Excessive oxygen flux impinging on the growing thin film surface during evaporation simultaneously with the deliberately deposited material. This has been observed for aluminium films by Barna et al. [21], who describe this effect as whiskers growth, and for the aforementioned Ta_2O_5/SiO_2 multilayer systems. In the latter case, the phenomenon can be thought to be caused by the deposition of molecular clusters which form in the initial vapor phase under high partial oxygen pressure. However, as there is no experimental evidence for this assumed cluster formation, other mechanisms may also be the cause.

For coatings in HEL applications, nodules can be assumed to trigger laser induced damage. Even if a nodule originates from a very tiny surface asperity, and thus does not contain any foreign and in particular absorbing material, it will heat up much more than the surrounding undisturbed film if it is actually separated from it by a small gap. (This gap can sometimes actually be seen in electron micrographs). In fact, Donovan [24] has experimental evidence that nodules indeed act as preferred laser induced damage sites. Whether or not thermal isolation is the real cause has not been decided as yet. Another possibility would be a focussing effect of the microlens shaped nodule on the triggering asperity or (perhaps absorbing) spatter particle. Murphy has treated the micro-optical properties of nodules in infrared coatings in some detail [25].

Admittedly, the computer simulation results of growth distortions may be of limited value because they were obtained with only a 2-D model and, moreover, are limited to a film thickness of a few molecular layers. Thus the value of direct comparisons with real growth distortions of much larger size is questionable. However, if one considers the simulation patterns as representing the very initial stages of defect growth, which can be assumed to proceed in the same manner until the film reaches real dimensions, the simulation of growth distortions gives essential clues:

(1) One major reason for the appearance of nodular growth seems to be low or no surface mobility of the admolecules or adatoms, as assumed in the limit case simulation model. Low surface mobility may have several reasons, such as a low ratio of substrate temperature to the melting point of the coating material. If this is below approx. 0.25 to 0.30, a nodular-like growth structure appears in the three temperature zone model of thin film growth according to Movchan and Demchishin [26]. Other reasons for low surface mobility may be high deposition rate or high residual pressure (partial or total), as discussed earlier.

(2) Nodular-like growth patterns are observed even with minute distortions such as the 7-particle array shown in the simulation results. This would give a plausible explanation of the influence of the oxygen partial pressure observed experimentally, if cluster formation in the vapor phase is assumed.

(3) The simulation confirms experimentally observed properties of nodules, such as their separation from the surrounding undisturbed film by pronounced void formation, maintainance of the individual layer sequence, and constant replication of the triggering distortions height throughout the film, generated by the purely kinematical growth model.

5.3 Crystallographic Microstructure

Although not included in the 2-D computer simulation model, crystallographic orientation certainly plays also a role in the formation of columnar microstructure [21] and hillocks [27]. If individual columns are faceted single crystals, the presence of such facets may further enhance the self-shadowing effect. Just as for columnar growth, a certain surface mobility of the incident atoms or molecules is also a prerequisite for microcrystalline growth. As can be seen from Fig. 1, at low substrate temperatures a highly disordered morphological and consequently an almost amorphous microstructure results. In the same micrograph, pronounced columnar microstructure of the TiO_2 films in the multilayer deposited at elevated substrate temperatures can also be seen. This indicates that these films may be polycrystalline. These assumptions are backed by the X-ray diffraction analyses of TiO_2/SiO_2 multilayers shown in Figure 9. Whereas the original multilayer deposited at a nominal substrate temperature of 250°C reveals only a few crystalline phases, these phases increase considerably after a thermal post-treatment in air for 2 hours at nominally the same temperature. This example shows that crystallographic modifications can occur at relatively low temperatures some time after deposition. If we keep in mind that the optical interference coatings are heated to 600°C and more in laser damage events [28], we can imagine that their crystalline microstructure is dramatically changed, which may eventually cause the coating to fail. (Quasi-)amorphous coatings may be preferrable from the basic consideration that they contain fewer inhomogeneities than columnar (and polycrystalline) ones, thus leading to higher laser damage thresholds when deposited at lower substrate temperatures [29]. However, it has been shown that the laser damage thresholds of low temperature coatings scatter more widely about their (higher) mean value than the thresholds of coatings deposited at higher (conventional) substrate temperatures [30]. This observation can also be explained by sudden modifications of the microcrystalline structure which can happen at elevated temperatures, caused by impurities in the film absorbing heat in the intense laser beam. Microstructural modifications are more likely to happen in amorphous than in already polycrystalline films.

6. Conclusions

The morphological microstructure of conventional PVD coatings has been evaluated experimentally by means of high resolution microscopy and microfractography. More detailed knowledge of the observed microstructures has been gained by using a simple, 2-D simulation model. This leads to the following conclusions and recommendations for the fabrication of low-defect optical coatings, suitable for HEL applications:

(1) The surface of the substrate to be coated should be as smooth as possible, and free of any particular asperties.

(2) For conventional PVD, the coating process must be adjusted so that neither material spatters ejected from the vapor source, nor molecular clusters above a critical size (which remains to be determined) reach the surface to be coated.

(3) The deposition rate must not be too high, otherwise relaxation processes of the particles already deposited may be inhibited, and perhaps also allowing clusters to form in the vapor phase.

(4) The residual background pressure should be as low as possible, and the vacuum, in particular, should be free of hydrocarbon contamination.

(5) Novel deposition processes which supply more energy to the deposited atoms or molecules promise better film properties, because these particles would have higher surface mobility and form more bulk-like, defect-free thin films because of higher relaxation.

The crystallographic microstructure of thin films seems to be closely connected to the morphological one, in that at a low substrate temperature to melting point ratio (quasi-) amorphous films are formed by high disorder. If this disorder becomes ordered because additional energy is supplied to the film either during or after deposition (for instance by heating it), the microstructure becomes polycrystalline. At a sufficiently high surface energy during deposition such as that supplied by an ion beam or a plasma, even a bulk-like thin film microstructure may be obtained.

SiO_2, as the material which always forms really amorphous thin films, may be an exception to the dielectrics commonly used for optical coatings, in that it has a lower melting point compared

to the other refractory oxides and hence a higher substrate temperature to melting point ratio under standard conditions. This leads to enhanced surface mobility of the incident molecules which in turn tends to eliminate column formation [22]. In addition, SiO_2 has inherent glass-forming properties not found with the other oxides.

The author would like to thank colleague researchers working in the same field, amongst them A.G. Dirks and H.A. Macleod, for fruitful discussions. The computer simulation model was programmed by H. Leonhard of the Institute of Physical Chemistry at the University of Innsbruck, Austria. E. Casparis-Hauser and A. Peuker, who were both with the author's department when the experimental work was done, assisted in scanning electron microscopy and the preparation of transmission electron microscopy specimens, respectively. The author is also indepted to A. Preisinger, Institute of Mineralogy, Crystallography and Structural Chemistry of the Technical University Vienna, for the X-ray diffraction analyses and to R. Abermann, Institute of Physical Chemistry, University of Innsbruck, for the permission to use their electron microscope. The help of Ms. K. O'Day with the style of the English manuscript is gratefully acknowledged. Special thanks is due to Major T.W. Humpherys of the EOARD/AFOSR in London for the encouragement to contribute this paper to the 15th Boulder Laser Damage Symposium, and for providing substantial travel support by arranging a window-on-science-visit to the United States. Finally, the permission of the management of the Balzers AG to contribute and to publish this paper is appreciated.

7. References

[1] See, for instance, the contributions to this conference by Lewis, K. L.; Savage, J. A.: A fundamental approach towards improved optical coatings (molecular beam epitaxy); Lunt, D.: Developments in RF sputtered laser coatings; Partlow, W. D.; Heberlein, J. V. R.: Plasma deposited inorganic thin films for optical applications; Wodarczyk, F. J.; Strauss, D. R.; Harker, A. B.: Comparison of optical coatings deposited by novel physical and chemical techniques, in Laser Induced Damage In Optical Materials: 1983, Bennett, H. E.; Guenther, A. H.; Milam, D.; Newnam, B. E., eds.; Nat. Bur. Stand. (U.S.) Spec. Publ.

[2] Ritter, E.,Appl. Opt. 15; 2318; 1976

[3] Macleod, H. A.,Proc. SPIE 325; 21; 1982

[4] For a concise review, see for instance Vook, R. W., Proc. SPIE 346; 2; 1982

[5] Koch, F. A.; Horng, D. T.; Vook, R. W., J. Vac. Sci. Techn. 9; 511; 1972

[6] Guenther, K. H.; Pulker, H. K., Appl. Opt. 15; 2992; 1976

[7] Bach, H.; Schröder, H., Z. Physik 224; 122; 1969

[8] Pearson, J. M., Thin Solid Films 6; 349; 1970

[9] Pulker, H. K.; Guenther, K. H., Vakuum-Technik 21; 201; 1972

[10] Abermann, R.; Bachmann, L., Naturwiss. 56; 324; 1969

[11] Evangelisti, F.; Garozzo, M.; Conte, G., J. Appl. Phys. 53; 7390; 1982

[12] Dirks, A. G.; Leamy, H. J., Thin Solid Films 47; 219; 1977

[13] A copy of the film "thin film microstructure" by A. G. Dirks and H. J. Leamy can be purchased from Philips Research Laboratories, Eindhoven, The Netherlands.

[14] Guenther, K. H., Proc. SPIE 346; 9; 1982

[15] Messier, E., cited in [3]

[16] Guenther, K. H., Appl. Opt. 20; 1034; 1981

[17] Nieuwenhuizen, J. H.; Haanstra, H. B., Philips Techn. Rev. 27; 87; 1966

[18] Pulker, H. K.; Jung, E., Thin Solid Films 4; 219; 1969

[19] Lissberger, P. H.; Pearson, J. M., Thin Solid Films 34; 349; 1976

[20] Müller; H.; Heinevetter, U.; Kaiser, N.; Gloede, C., Kristall/Technik 12; 695, 1977

[21] Barna, P. B.; Reicha, F. M.; Barcza, G.; Gosztola, L; Koltai, F., Vacuum 33; 25; 1983

[22] Leamy, H. J.; Gilmer, G. H.; Dirks, A. G., The microstructure of vapor deposited thin films, chapter 4 in Current Topics in Material Science, Vol. 6. E. Kaldis, ed. New York, Amsterdam: North Holland Publ. Comp.; 1980. 311-344.

[23] Guenther, K. H., Thin Solid Films 77; 239; 1981

[24] Donovan, T., Naval Weapons Center, China Lake, CA.: pers. comm.; 1983

[25] Murphy, J., Proc. SPIE 246; 64; 1980

[26] Movchan, B. A.; Demchishin, A. V., Fiz. Met. Metalloved 28; 653; 1969

[27] Reicha, F. M.; Barna, P. B., Acta Phys. Acad. Sci. Hung. 49; 237; 1980

[28] Küster, H.; Ebert, J., in Laser Induced Damage In Optical Materials: 1979, Bennett, H.E.; Glass, A. J.; Guenther, A. H.; Newnam, B. E., eds; Nat. Bur. Stand. (U.S.) Spec. Publ. 568; 1980. 269

[29] Milam, D.; Rainer, F.; Lowdermilk, W. H.; Swain, J.; Carniglia, C. K.; Tuttle Hart, T., in Laser Induced Damage In Optical Materials: 1981, Bennett, H. E.; Guenther, A. H.; Milam, D.; Newnam B. E., eds; Nat. Bur. Stand. (U.S.), Spec. Publ. 638; 1983. 446

[30] Rainer F.; Vercimak, C. L.; Milam, D.; Carniglia, C. K.; Tuttle Hart, T., in Laser Induced Damage In Optical Materials: 1983, Bennett, H. E.; Guenther, A. H.; Milam, D.; Newnam B. E., eds; Nat. Bur. Stand. (U.S.), Spec. Publ. xxx, 1984. xxx

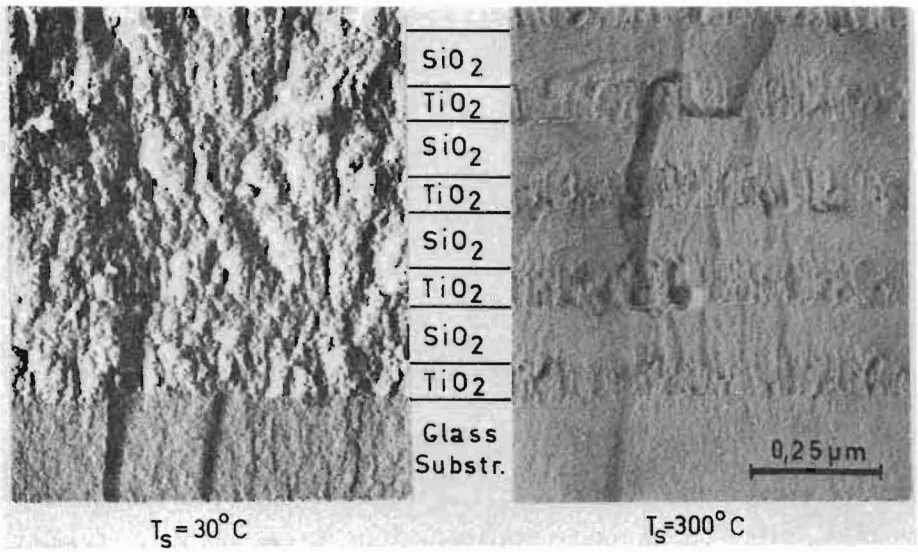
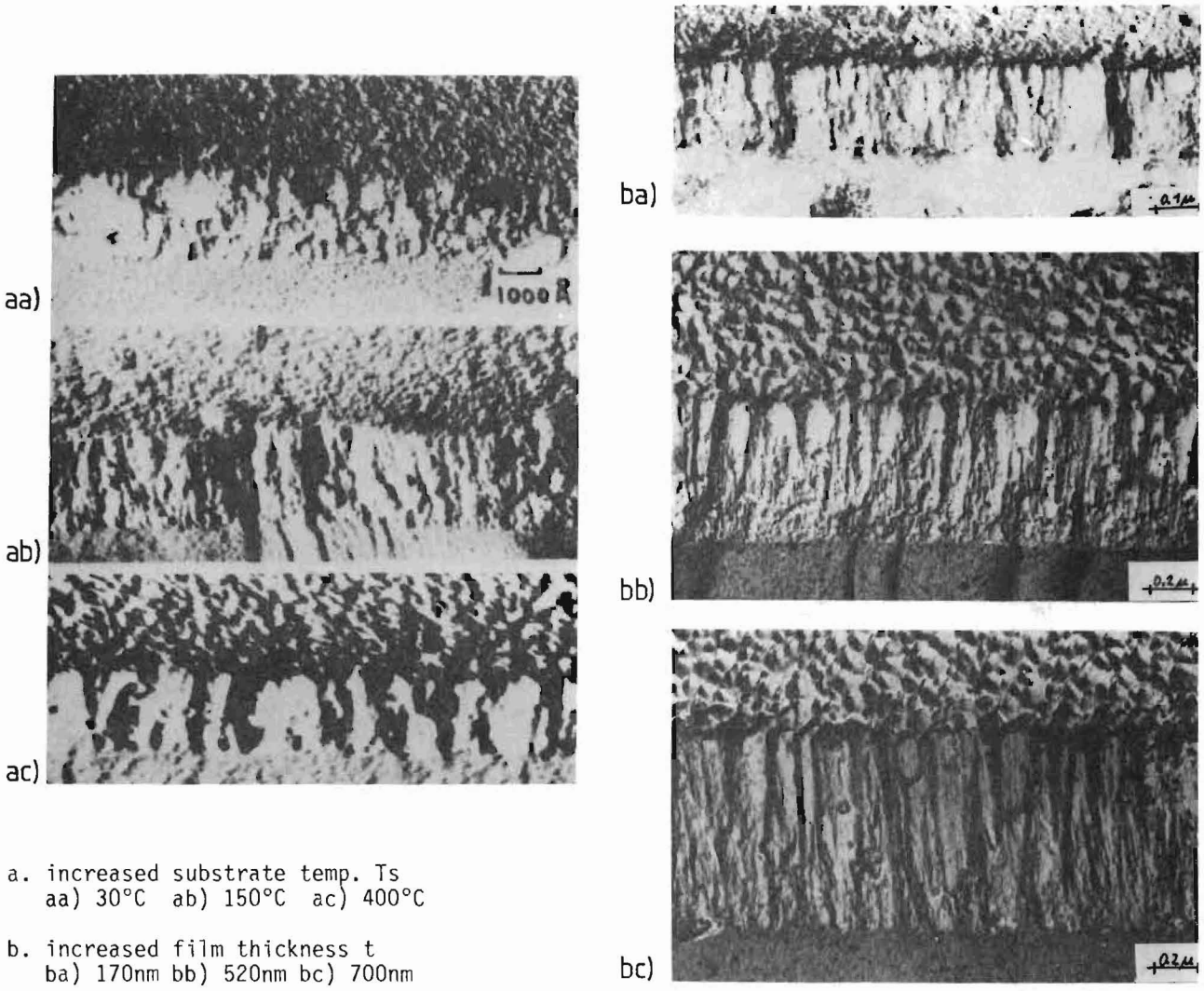


Figure 1. Cross-section of TiO_2/SiO_2 multilayers vapor-deposited at different substrate temperatures T_s (transmission electron micrographs of Pt/C replica)



a. increased substrate temp. Ts
aa) 30°C ab) 150°C ac) 400°C

b. increased film thickness t
ba) 170nm bb) 520nm bc) 700nm

Figure 2. Cross-section of single TiO_2 layers with columnar microstructure

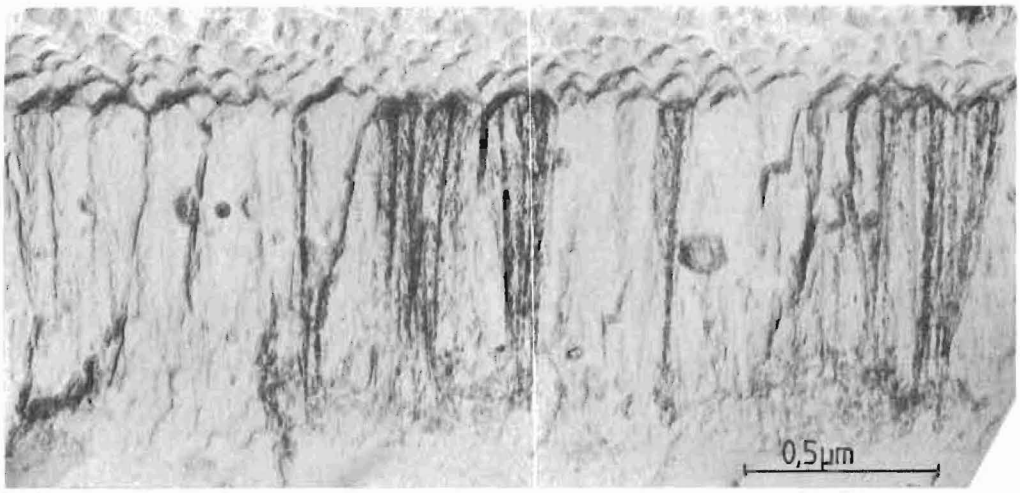


Figure 3. Fibrous substructures in TiO_2 thin films, disclosed by incomplete dissolution of actual film substance remaining on the carbon replica.

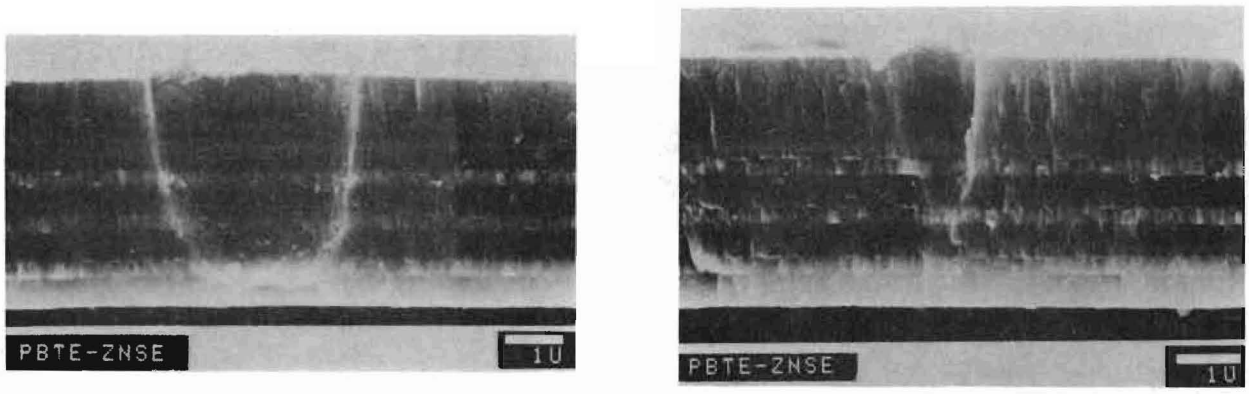


Figure 4. Scanning electron micrographs disclosing the origin of nodules
a. substrate surface asperities b. coating material spatters

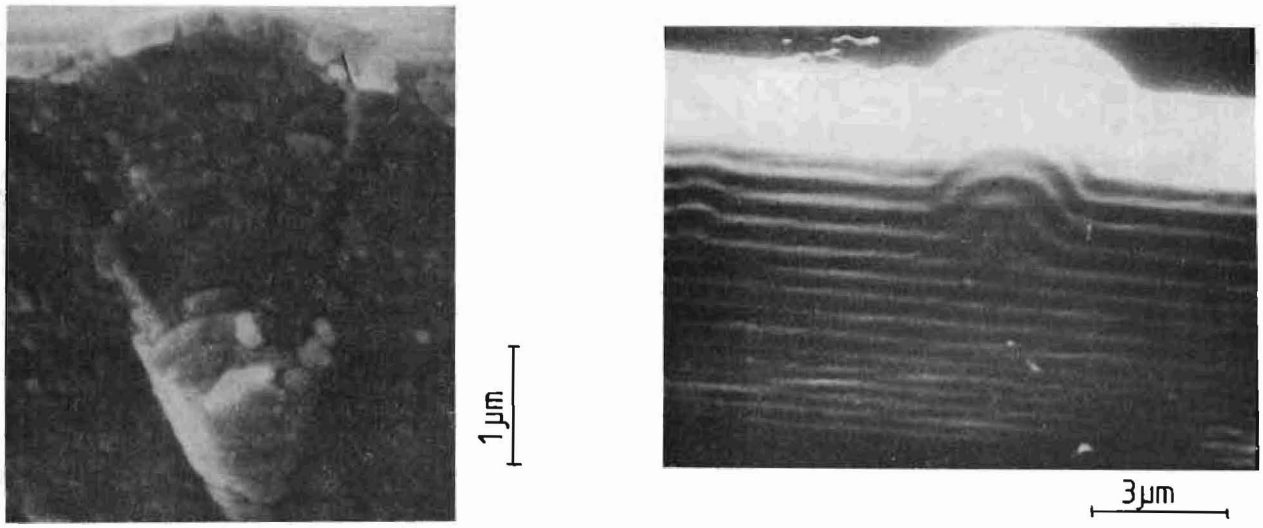


Figure 5. Cross-sections of nodules in multilayer stacks showing that the layer sequence is maintianed inside the nodules (SEM-micrographs)
a. cleaved specimen b. polished cross-section

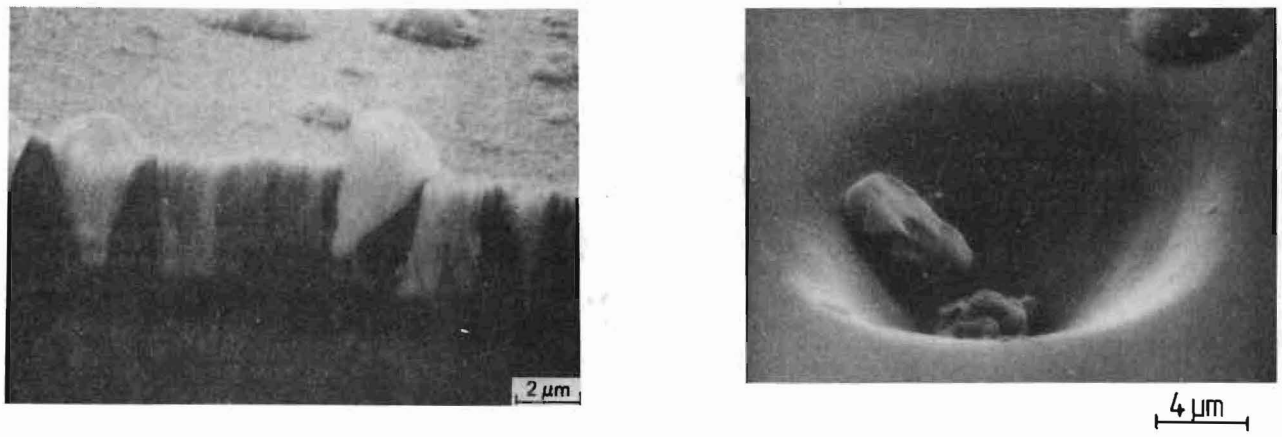
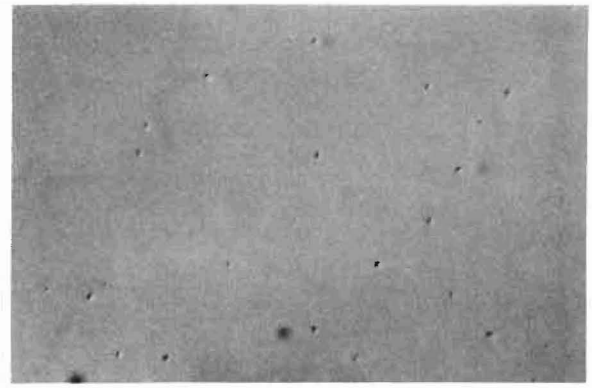
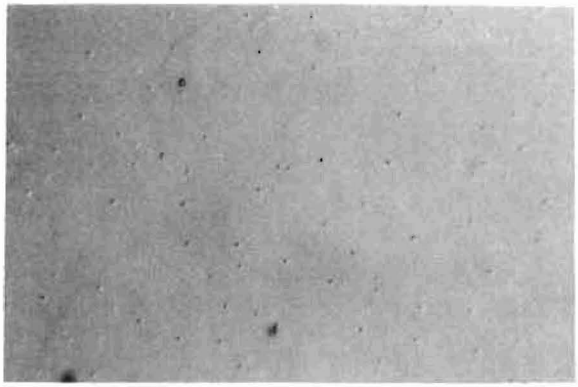


Figure 6. Holes in optical coatings caused by separating nodules (SEM-micrographs)
a. nodule popping out as a whole b. secondary nodule growth in a hole



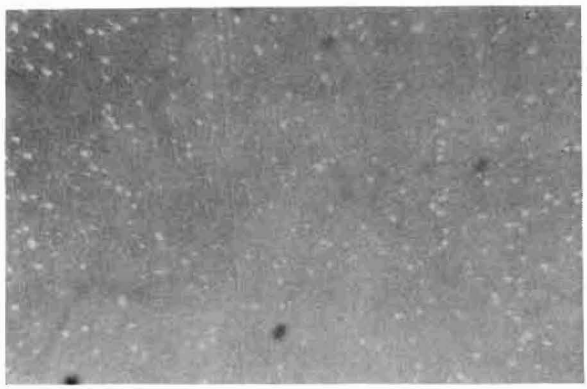
$p(O_2) = 0{,}9 \cdot 10^{-4}$ mbar

100 µm



$p(O_2) = 1{,}2 \cdot 10^{-4}$ mbar

100 µm



$p(O_2) = 1{,}5 \cdot 10^{-4}$ mbar

100 µm

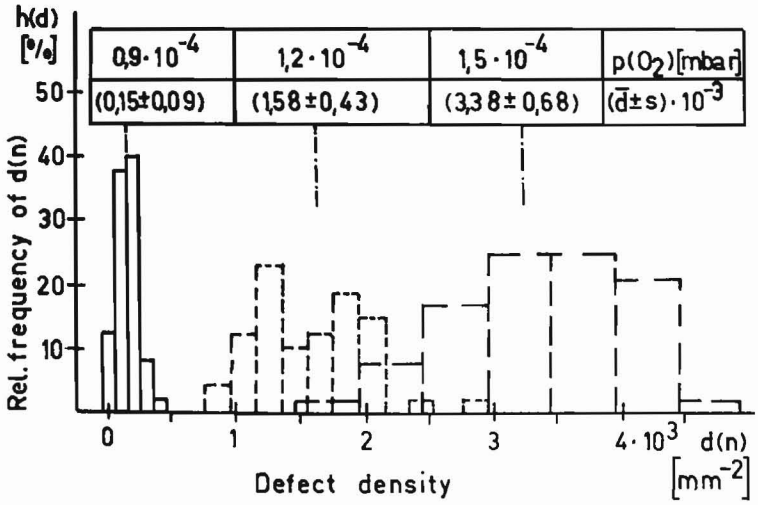
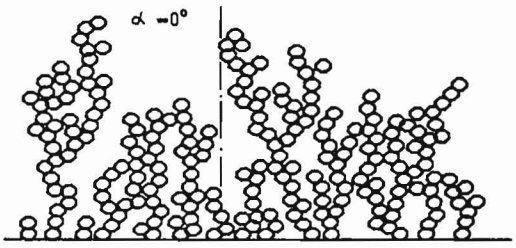
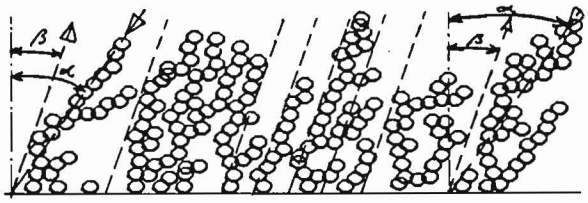


Figure 7. Nodular growth in a Ta_2O_5/SiO_2 multilayer as a function of the residual oxygen pressure:
a.-c. optical micrographs of coatings deposited at $p(O_2) = 0.9; 1.2; 1.5 \times 10^{-4}$ mbar
d. nodule density vs. $p(O_2)$

a)



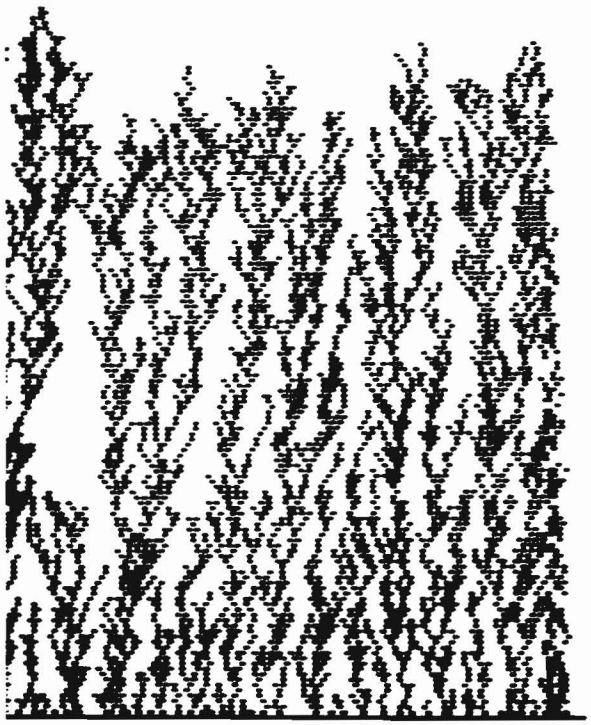
b)

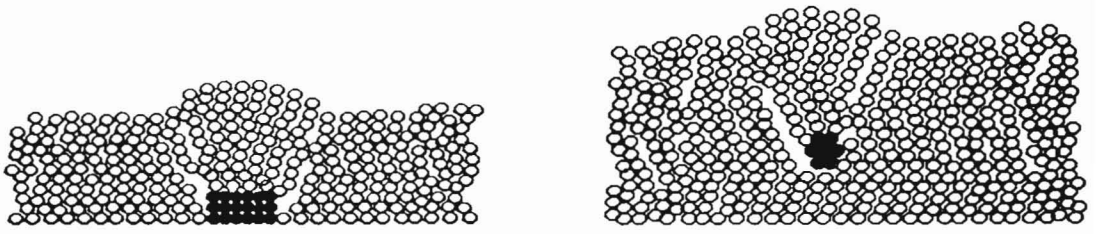


$\tan(\alpha) = 2 \tan(\beta)$

Figure 8. 2-D simulated thin film growth structure

c)





d) e)

Figure 8. 2-D simulated thin film growth structure (see text)

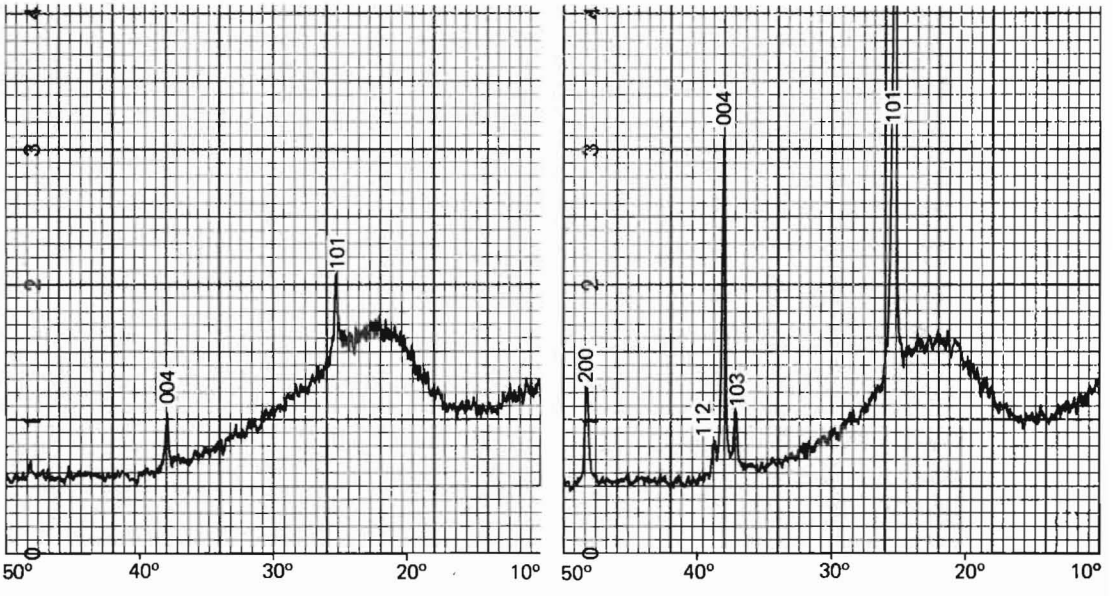


Figure 9. X-ray diffraction analysis of TiO_2 as contained in a TiO_2/SiO_2 multilayer
a. as deposited (T_s=250°C) b. after annealing at 250°C for 2

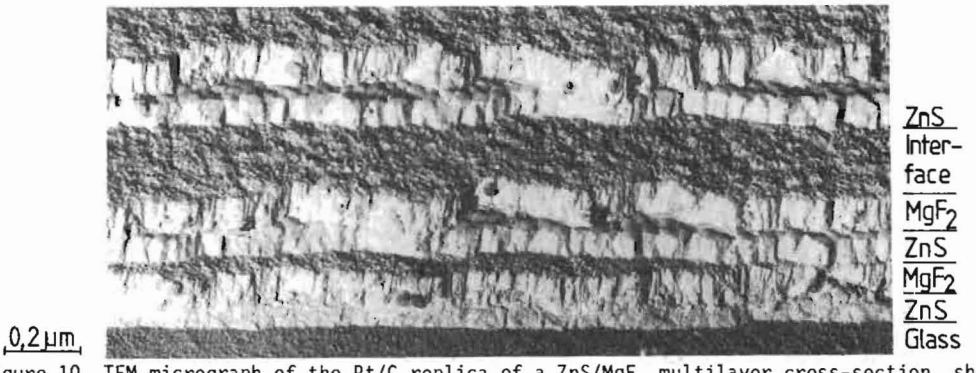


Figure 10. TEM-micrograph of the Pt/C-replica of a ZnS/MgF_2 multilayer cross-section, showing nearly amorphous microstructure for the ZnS layer next to the substrate, whereas the further ZnS layers exhibit a columnar microstructure.

In response to a question, the author pointed out that there is recent evidence in the literature that, when nodules are present, laser damage occurs primarily at sites where nodules occur. Nodules form from nucleation sites, which are not necessarily caused by phenomena such as particles of molten material being ejected from a boat and striking the substrate. The nucleation sites may be formed as part of the same process by which columnar structure in films is formed. For example, the speaker has done coating runs with silica microlayers at different oxygen partial pressures and found a good correlation between nodule formation and the partial pressure of oxygen. The model proposed is that if there are too many oxygen molecules arriving simultaneously with the coating material, it will cause very small localized clusters to form on the substrate surface. The ultimate conclusion is that columnar structure is basically the same as nodule formation but on an order-of-magnitude-lower scale. If one can arrange to have very high surface mobility, for example, by supplying additional energy to the substrate surface, one should get rid of columnar microsturcture and inhibit nodule formation.

A Wide Spectrum Antireflective Coating For Silica Optics And Its Damage Resistance At 350 nm

B. E. Yoldas and D. P. Partlow
Westinghouse Research and Development Center
Pittsburgh, Pennsylvania 15235

and

H. D. Smith
Westinghouse Hanford
Richland, Washington 99352

A wide-spectrum antireflective coating has been developed for fused-silica optics. This coating provides antireflectivity down to ~300 nm on fused silica, increasing its transmission to better than 99%. The coating is a single-layer graded-index film applied from special polymer-oxide solutions. The graded index results from nonscattering porosity and tailoring of the pore morphology. Unlike state-of-the-art techniques, however, the method does not involve phase-separated glasses, not does it require etching for the creation of porosity. The damage thresholds of coated fused silica optics at 350 nm initially varied from less than 1 J/cm^2 to 9 J/cm^2. The main causes of this large variation in the damage threshold were investigated and determined to be substrate polishing, substrate surface cleaning, and coating solution chemistry and processing which, under certain conditions, leads to carbon formation during the heat treatment of the coating.

Key words: Antireflective coating; coating for silica optics; graded index coating; laser damage threshold; laser-induced damage; polymer oxide coating; silica film; thin film.

1. Introduction

Operation at the first (1ω) and second (2ω) harmonics of the Nd glass laser, 1.05 μm and 0.53 μm, respectively, presents no outstanding problem for optical systems, since glasses with excellent transmission at these wavelengths are available, and methods of forming antireflective (AR) surfaces on these glasses are well known. Operation at the third harmonic, 0.35 μm (3ω), however, requires lenses and windows of fused silica, since other available glasses absorb light at these short wavelengths [1]. Previously available methods for forming AR surfaces depend on the presence of separated glass phases, and thus cannot be applied to fused silica [2-5]. But operation of the laser system without an AR coating on the fused silica lenses causes substantial energy loss, since there are numerous lenses and windows in series. For this reason, Lawrence Livermore National Laboratories (LLNL) subcontracted a project to Westinghouse to develop a coating for fused silica lenses providing AR properties over the first three harmonics, with an additional requirement that the AR coating be laser damage resistant at 0.35 μm.

If a homogeneous single-layer film, antireflective at the 350 nm wavelength, were to be formed on fused silica, this layer would have to have an index of refraction of 1.215 (the square root of the substrate index), and a thickness of 72 nm ($t_c = \lambda/4\ n_c$). This low index requirement makes it practically impossible to design a dense single layer AR film on SiO_2. However such low indices can be attained by introduction of ~60% non-scattering porosity.

The porosity and index of refraction in this type of material are related by [6]

$$(n_p)^2 = (n^2-1)\ (1-P) + 1 \qquad (1)$$

where n_p and n are the indices of the porous and non-porous materials and P is the volume fraction of non-scattering porosity. The requirement that the coating be non-absorbing at 350 nm limits the coating material to a few oxides, e.g., SiO_2, Al_2O_3, La_2O_3, ThO_2, HfO_2. All of these oxides except SiO_2 have a rather high index of refraction, thus requiring substantial porosity, e.g., over 80%, to lower their index to the level needed for a suitable AR coating on silica lenses. This limits the composition to SiO_2 for all practical purposes.

Still, a porous coating whose refractive index is the square root of that of the substrate and whose thickness is tuned to suppress reflection at a particular wavelength will not do so across the entire spectrum. Broad-band antireflection may, however, be accomplished using a coating whose refractive index closely matches that of the substrate at the contact interface, but gradually decreases outward, ideally approaching the index of the surrounding atmosphere. The effectiveness of such coatings is much less sensitive to thickness variations.

Introduction of graded porosity in a glass surface layer may be accomplished in various ways. Such porous layers have been formed by chemical leaching of a phase separated glass or by neutral solution processing but, again, the glass compositions required are highly absorbing at 350 nm [2-5]. Deposition of optical oxide films from metal-organic compounds is also known [7-9]. This method has the advantage that the coating is essentially independent of substrate composition. Furthermore, these films can be made to include rather high porosities, and the pore morphology can subsequently be graded. This paper describes the formation of such a graded-index, wide-spectrum AR coating of SiO_2 for silica lenses, and includes results of an initial investigation on the laser damage resistance of coated silica optics.

2. Formation of Antireflective Coating on SiO_2

The SiO_2 film is deposited from a polymer solution produced by controlled hydrolysis of silicon ethoxide, $Si(OC_2H_5)_4$, in ethanol, $C_2H_5(OH)$, with HNO_3 as a reaction catalyst. Depending on the method chosen for film deposition, the solution may vary from ~15 to 16 wt. % equivalent SiO_2, and the water of hydrolysis may vary from ~2.0 to 2.2 moles per mole ethoxide. The details of solution preparation and resulting polymerization are presented elsewhere [10]; control of these processes is necessary to ensure wetting of the SiO_2 substrate and attainment of a specific pore morphology, while avoiding densification of the film during heat treatment. It has been shown that such properties of oxide polymers can be significantly altered through substructure modification by controlled processing of precursor solutions [11,12].

Deposition of the coating from a solution can be done either by a spinning or by an immersion and draining process. Spin application was used in the early development of the AR coating, where the substrates were 5 cm diameter quartz discs. In this method, cleaned substrates were vacuum mounted on a variable speed chuck, the solution was deposited on the top surface, and the substrate was spun at a rate of 2500-5000 rpm (fig. 1).

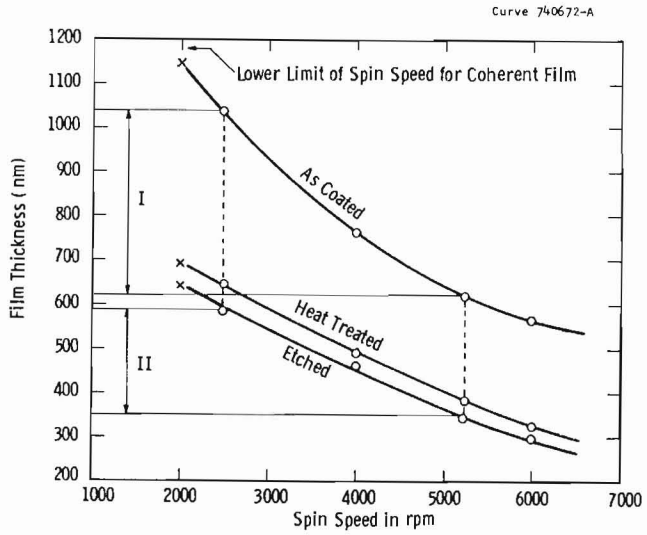


Figure 1. Film thickness decreases as spin application speed is increased and is further reduced during heat treatment and etching. Area I designates the unfired film thickness range which, after firing and etching, translates to Area II. Only films falling within Area II show acceptable AR characteristics.

The transition from spin-coating to drain coating proved to be more than just a mechanical one; it required fundamental changes in the chemistry of the polymer solution as well as in the heat treatment of the coating.

The thickness of the film applied from a solution depends on two groups of factors: those related to the solution and those related to the processing. In drain coating, the thickness, t, of the film can be represented by the equation:

$$t = \frac{2\ V_s\ n}{d \cdot g}^{1/2} \qquad (2)$$

where V_s is the pull or drain rate, n is solution viscosity, d is the density of film and g is the gravitational constant. It must be noted that this equation is for undried films and, in our case, a drying factor must also be introduced. Wet films, even at optical thicknesses, are observed to run and drain when coated on vertical surfaces. A fast evaporation freezes the films and results in deposition of thicker coatings.

Figure 1 shows coating thickness as a function of application rate in the spin coating of 5 cm diameter quartz discs. Initial unfired coating thicknesses varying from approximately 500 nm to 1100 nm were obtained. Under these conditions, films thicker than 1000-1100 nm tend to craze upon heat treatment and are not acceptable. On the other hand, films thinner than ~600 nm become too thin after heat treatment to produce good antireflectivity in the desired spectral range.

Figure 2 shows coating thickness as a function of pull or drain rate in the drain coating process. (Note that the drain coating solution differs from the spin coating solution). As shown, in this case, polymer orientation is such that the coating starts to show crazing at 700 nm. It must also be mentioned that the thickness dependence on drain rate, shown in figure 2, will change somewhat with drying conditions.

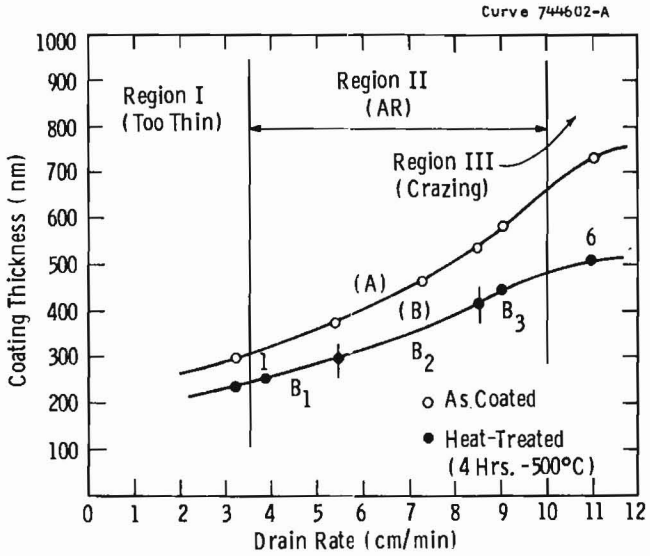


Figure 2. Thickness of a SiO_2 coating deposited on optically polished fused silica as a function of application rate using the drain coating technique. (A) is for unfired films, and (B) is for heat-treated films. Only films within region II show acceptable AR characteristics.

Ability to deposit very uniform thickness films by drain coating was demonstrated by interferometer and profilometer measurements of such films. If the substrate is not totally immersed in solution, a thinner coating is deposited on the upper 0.5-1.0 cm before the coating thickness stabilizes at withdrawal rates of 5-10 cm/min.

The applied film dries to a porous polymer layer having a general composition of $SiO_{2-(x+y/2)}(OH)_y(OR)_x$. OH and OR groups constitute ~25% of the total weight and are bound at the terminating ends of the polymer molecules, whose main skeleton is similar to SiO_2 glass. OH groups make up ~20% of the total polymer weight, while (OR) groups contribute perhaps 2-4%. Heat treatment is performed first to reduce the deposited coating to a pure organic-free oxide layer, SiO_2, and second to modify the original pore size. Temperatures of 450-500°C are required for the pyrolysis reaction.

Through complete pyrolysis of the material, a porous SiO_2 film is formed. The porosity is continuous, that is, interconnected, and open, with a configuration somewhat similar to closely spaced worm holes. The percent porosity and pore size depend to a degree on the preparation method, but the pyrolyzed material is normally about 55% porous with pore diameters of 2-3 nm. Grading of this porosity to a depth of one quarter of the longest wavelength is accompanied by enlargement of the

surface pores which is sufficient to cause the pores to join, leading to scattering at the shorter wavelengths, e.g., 350 nm. For this reason the initial pore size must be reduced below a critical size without causing pore closure (Fig. 3).

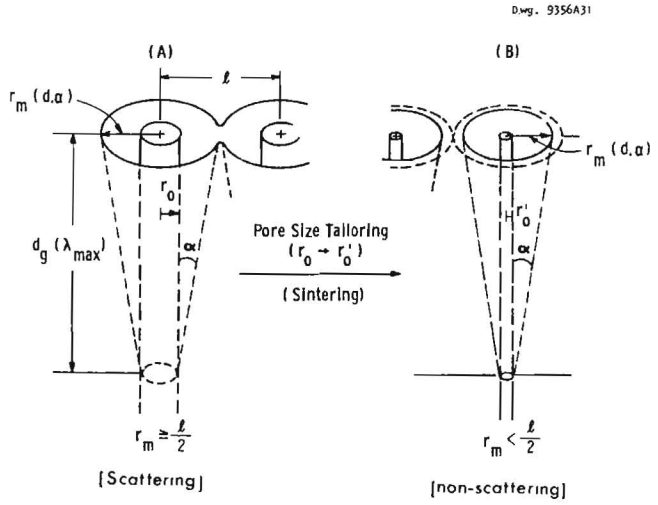


Figure 3. Gradation of the initial pores (shown Schematically as cylinders) by etching to a depth d_g may cause surface pore enlargement that results in joining of pores (A). This is prevented by shrinking the initial pore diameter r_0 to r_0' by a heat treatment before grading (B).

The heat-treatment designed for the spin-applied coating, i.e., 585°C for 16 hours, results in a 37-40% thickness shrinkage which corresponds to a reduction of approximately 70% in the pore diameter, reducing the original pore size to less than 1 nm (perhaps as low as 0.6 - 0.7 nm). Only such a small initial pore size appears to be suitable for index grading without causing scattering at the 350 nm wavelength. The effect of this heat treatment on the index of refraction of the coating at various stages is treated in detail elsewhere [13]. In the case of drain coating, the heat treatment of the coating to produce a suitable pore size and matrix is significantly different. A 4-hour treatment at 485-500°C has been found to be sufficient.

Figures 1 and 2 also show the effect of such a heat treatment on the thickness of the film deposited by spin and drain coating techniques. One noteworthy feature is that the shrinkages caused by the heat treatment of drain coated films is much smaller than for spin coated ones (~23% vs 40%, for example). Also, crazing of the film occurs at a lower thickness than for the spin coating (~700 nm vs ~1000 nm). This phenomenon is thought to be due to deposition of the denser films with drain coating by more efficient polymer orientation and alignment.

The subject of graded films and the mathematical treatment of the optical response that might be expected from such films have been addressed in the literature [3, 15-18]. A schematic representation of such a graded film is shown in figure 4.

In the initial stages of this project, there was no difficulty in producing an antireflective coating with less than 0.5% reflectivity over the entire 350 nm to 1100 nm spectral range. However, transmission curves of the same films showed precipitous drops in the transmission toward the UV, so that the transmission was often as low as 70-80% at 350 nm. This problem of scattering was addressed by first shrinking the pore size through heat treatment and second by formulating an etchant that creates a gradation in pore size one-quarter wavelength deep without enlarging any of the pores to a size they join and scatter. When proper porosity grading was done, spin applied coatings (and that particular solution) tended to produce transmission curves which sloped down toward the UV. Although readings close to 100% were not unusual between 1100 and 800 nm, the transmission gradually dropped to about ~98% around 300 nm. On the other hand, the coating deposited by draining often showed an increasing transmission toward the UV. It is also possible to produce flattened curves where the transmission stays over 99.5% through the entire 800 to 350 nm region (See figure 5).

3. Laser Damage Investigations At 3ω

Laser-induced damage to AR coatings is often the limiting factor in operation of high power lasers [1-19]. The mechanisms which cause laser damage in optical materials are numerous and have

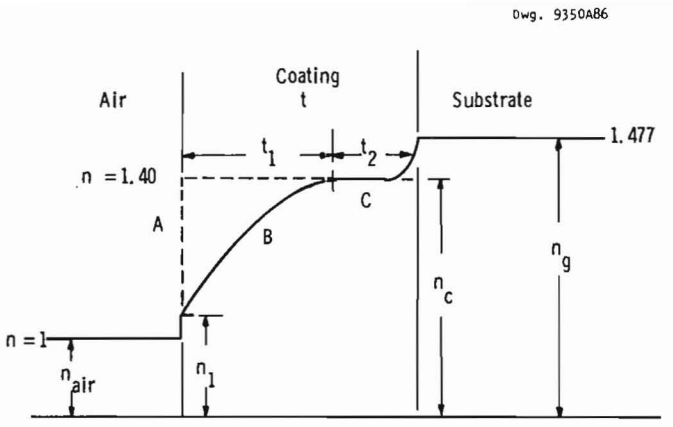


Figure 4. Schematic representation of a graded index film on fused silica at 350 nm.

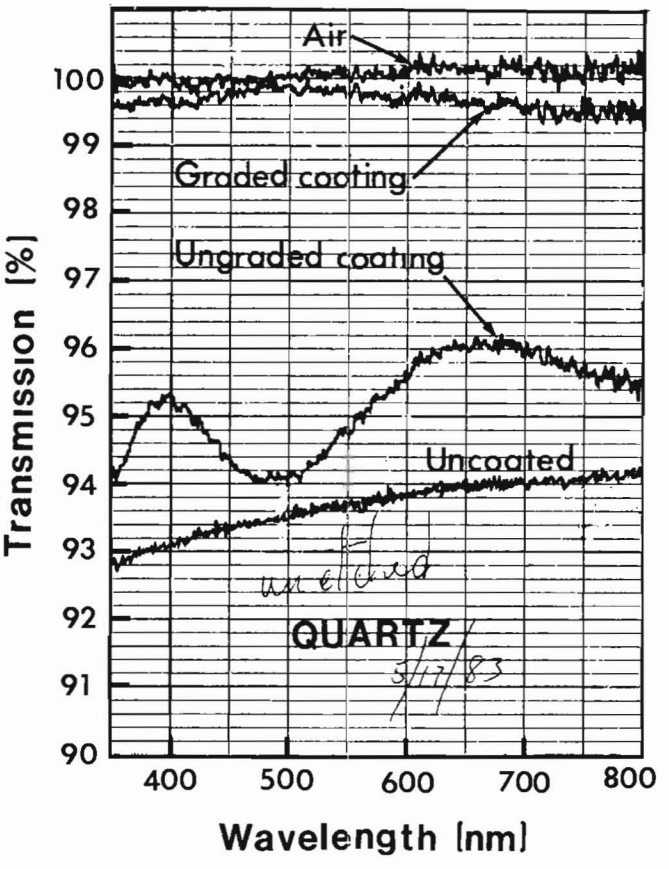


Figure 5. Spectral transmission curves for a drain-coated fused silica substrate, before and after gradation of the pores. Note that there is no deterioration in ultraviolet transmission of the graded coating curve. Reference curves for silica and for air are also included.

been reviewed by other authors [20-25]. These causes are generally divided into two categories. The first is intrinsic non-linear processes which are determined by the nature of the material. This category was not of particular concern to us since SiO_2 has a sufficiently high intrinsic damage threshold for the intended purpose. The second category of laser damage is caused by included particulates as well as chemical variations and inhomogenieties which lead to localized absorption; this determines the actual practical irradiation level. This second category of laser damage

essentially governed the threshold values in this work and therefore was a prime subject of investigation.

In this work the damage measurements were done exclusively at 3ω (350 nm). The coatings were applied to 5 cm diameter optically polished fused silica discs provided by LLNL using both spin and drain coating application methods. The damage measurements were done at LLNL under the supervision of Dave Milam. In excess of one hundred samples were treated [26]. Damaged sites were later examined by optical microscopy as well as SEM.

In the early part of the work, a great emphasis was placed on filtration of the coating solution, since it was thought that inclusion of particulates in the solution was the main cause of laser damage. However, it soon became apparent that this was not a dominating factor, although it may have been a contributing factor. First, some highly damage resistant coatings were produced without solution filtration, and second, the density of the damage sites appeared to far exceed what one might reasonably expect from a population of particulate inclusions. Furthermore, when a group of substrates was coated in succession with the same solution and heat treated together, they exhibited entirely different damage behavior.

Optical observation of laser damage sites revealed a very significant piece of data: that almost all laser damage sites were originating from the same depth, which corresponded to the coating thickness. This indicated that the substrate surface or the substrate/coating interface was playing a very significant if not a dominating role in laser damage. Based on this observation various substrate surface cleaning methods were investigated. These included both chemical and mechanical techniques.

The first group of samples showing encouraging damage thresholds had been made from substrates which were cleaned using an automated scrubbing technique used in the semiconductor processing industry. The thresholds of this group ranged from 3.5 to 5 J/cm^2 (see table 1). However, further experiments showed that scrubbing of the substrate surfaces in no way guaranteed a reproducibly high damage threshold. Large numbers of samples were prepared to test the effect of variations in substrate cleaning, coating deposition method, heat treatment, etching, etc. It became clear that laser damage in these samples was being induced by a number of factors, and their effects overlapped.

Table 1. Laser Damage Thresholds of Spin Coated Samples* At 351 nm With A 0.6 ns Pulse

(W) Sample No.	SiO_2 Disk No.(#)	L.L. Test	Damage Threshold (†) (J/cm^2)
142-1	3372	L-180	3.3 ± 0.5
142-2	3368	L-181	4.3 ± 0.6
142-3	3378	L-182	5.0 ± 0.7
142-4	3391	L-183	4.6 ± 0.7
142-5	3411	L-184	<2
142-6	3415	Not Tested	Not Tested
142-7	3416	L-185	4.3 ± 0.6

(†) As observed by Nomarski Microscopy.

(*) Spin coated on in-house polished 5 cm silica discs at 4000 rpm (142-1 at 300 rpm), fired at 585°C for 16 hrs in a O_2/N_2 atmosphere, and porosity graded.

(#) These discs had originally been polished and numbered by Zygo but were re-polished by Westinghouse before these samples were coated.

The mulciplicity of the sources of laser damage is also indicated by Figures 6 and 7. Figure 7 shows that the activation energy for the origination of new damage sites was strongly sample-dependent. The reason for this may be related either to the size of the absorption sites [20], or to differences in the nature of the absorption sites. Indeed there are several distinctly different types of damage morphology indicated by visual observations of hundreds of damage sites. Four types of damage morphology often encountered in these samples are also shown in figure 7.

The presence of cracks or crazing in the coating also did not appear to cause laser damage. Cracks in these coatings are generally caused by one of two mechanisms. One occurs when the deposited coating is too thick, e.g., thicker than 500 - 600 nm. We have never observed any laser damage

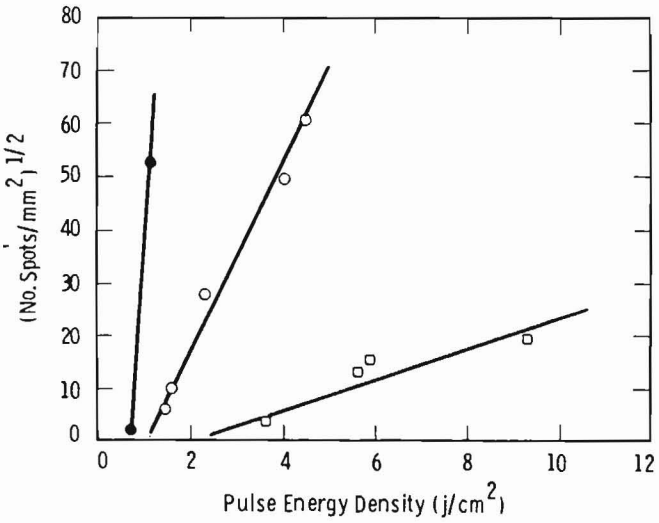


Figure 6. Number of laser damage pits vs pulse energy density.

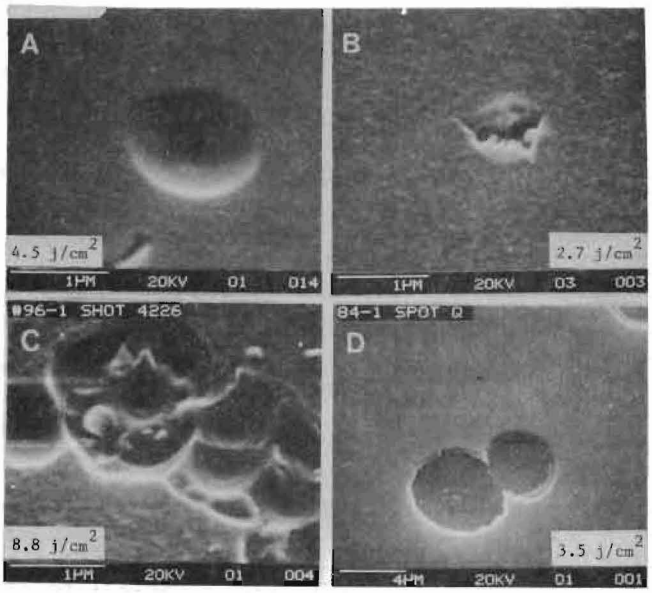


Figure 7. Scanning electron micrographs of some typical laser damage morphologies observed in SiO_2 polymer oxide coatings.

associated with this type of crazing. The other happens when an included contaminating particle generates a crack; we observed no laser damage sites associated with this type of crack either.

On the other hand, scratches on the substrate caused during polishing may be very detrimental. For example, a sample exhibiting a very high laser damage threshold, i.e., 8.8 J/cm^2, contained a thin streak of intense damage running across the laser-irradiated spot, as shown in figure 8. Further examination revealed that the damage streak coincided with a linear feature on the fused silica which happened to cross the irradiated area. Basically, the feature looked like a polishing defect such as an incompletely removed scratch, which extended some distance beyond the boundaries of the irradiated area in both directions. Such a defect might trap polishing compounds which would be extremely difficult if not impossible to remove by normal cleaning techniques. With certain configurations, such features could exhibit damage by "self-focusing" at very high power.

Fused silica surfaces are susceptible to impregnation by submicron size polishing compound particles during the polishing process. These particles may either get wedged into very small reatures on the surface (e.g., 1-2 nm), or may be partially embedded in the incompletely hydrolyzed gel-like skin of the polished SiO_2 surface. Some fusion or diffusion may also occur. It has been shown that such particles cannot be removed by jets of liquid or gas or by routine cleaning techniques; even further polishing may do nothing more than drive these particles toward the interior of the substrate. This type of absorbing site on the substrate surface may not show apparent damage unless it is covered by a coating. Only the blowout of the coating may make the interaction of the site with the laser visible. The effect of polishing on the damage threshold has been noted by Rainer, Milam, Lowdermilk and others [27,28]. They found that both fused silica and BK-7 glass showed significantly higher laser damage threshold values when the polishing was done by the "bowl-feed" method than by conventional polishing. The importance of polishing is confirmed in table 2 where samples made using Zygo-polished substrates had damage thresholds of 3 to 9 J/cm^2, while the Unertl-polished substrates which were coated in the same batch damaged at 1.9 J/cm^2 or below.

Another important factor involved in laser damage is the formation of carbonaceous clusters in the coating during pyrolysis. The possibility of such an occurrence was clearly known, since the precursor solution contains alkyl groups. However, efforts to analyze for carbon content of these films by ESCA were frustrated by the thinness of coating and the low level of carbon. Finally, an exploratory investigation of the coating material obtained in bulk form through the gelling of the precursor coating solution revealed some very significant results, and these studies are ongoing. Thus far it has been shown that thinner coatings as well as longer aging of the polymer coating solution tend to alleviate the problem of carbon formation.

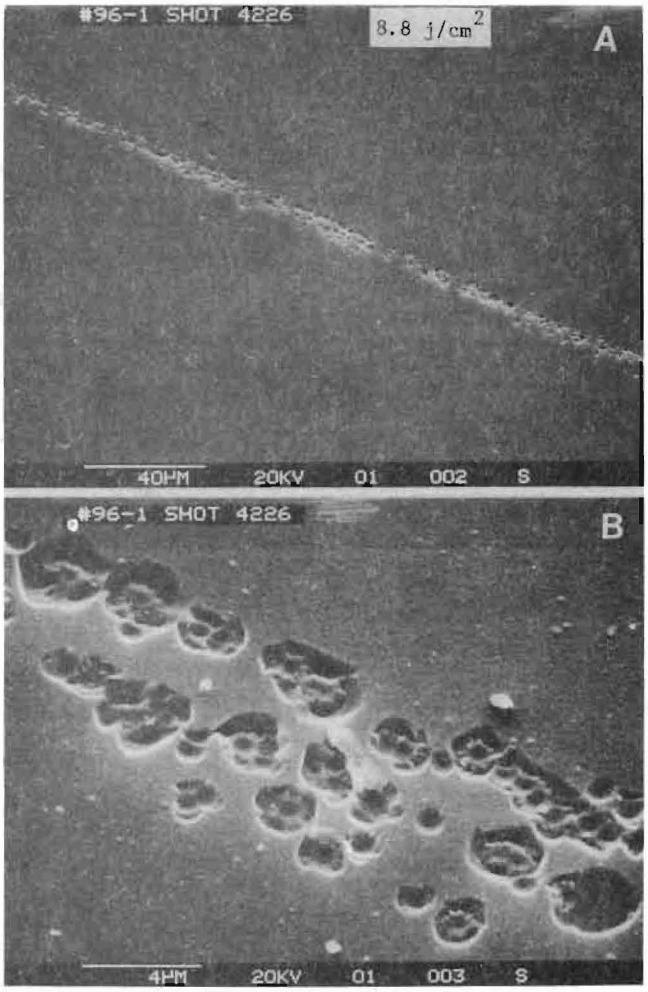


Figure 8. Scanning electron micrograph of a linear array of damage sites in the SiO_2 coating coinciding with a polishing defect in the underlying substrate (A). Enlargement of these damage pits (B).

Table 2. Effect of Silica Substrate And Its Polishing On The Laser Damage Threshold At 350 nm

Sample	Polish	Substrate	Damage Threshold[a] (J/cm^2)
3629	Zygo	Suprasil	3.3
3621	Zygo	Suprasil	>9.06
3622	Zygo	Suprasil	3.3
3630	Zygo	Suprasil	3.0
86	Unertl	Corning 7940	1.7
79	Unertl	Corning 7940	1.7
36	Unertl	Corning 7940	1.9
29	Unertl	Corning 7940	0.8
3626	Westinghouse	Suprasil	3.1
85	Westinghouse	Corning 7940	2.8

All substrates were cleaned similarly, including scrubbing.

[a]Tested at Lawrence Livermore National Labs by Dave Milam.

4. Conclusion

A wide spectrum antireflective coating for SiO_2 optics covering the first, second, and third harmonics of the Nd glass laser has been developed. This porosity-graded SiO_2 coating has been deposited from polymer solutions on fused silica substrates, and laser damage thresholds as high as 9 J/cm^2 at 350 nm with 0.6 ns pulses have been measured at LLNL.

The sources of laser damage in this system appear to fall into three major areas:

- o Substrate preparation; i.e., polishing, cleaning, handling.
- o Coating solution chemistry and processing; i.e., carbon formation.
- o External or environment-induced effects; i.e., inclusion of contaminants, etc.

The work done on this project was funded by Lawrence Livermore National Laboratories. The laser damage measurements were done at Lawrence Livermore National Labs under the supervision of Dr. David Milam. Authors also thank M. C. Staggs, F. Rainer and other Lawrence Livermore Personnel for their valuable contributions.

5. References

[1] W. H. Lowdermilk and D. Milam, Appl. Phys. Lett. 36 (11), 891 (1980).

[2] S. P. Mukherjee and W. H. Lowdermilk, J. Non-Cryst. Solids 48, 177 (1982).

[3] A. Smakula, Glastech. Ber. 19 (12), 377 (1941).

[4] K. B. Blodgett, Phys. Rev. 55, 391 (1939).

[5] M. J. Minot, J. Opt. Soc. Am. 66, 515 (1976).

[6] B. E. Yoldas, Appl. Opt., 19 (9), (1980).

[7] H. Schroeder, in Physics of Thin Films 5, 87, G. Hass and R. Thun, editors, Academic Press, New York (1969).

[8] B. E. Yoldas and T. W. O'Keefe, Appl. Opt. 18, 3133 (1979).

[9] B. E. Yoldas, Ibid 21 (16), 296 (1982).

[10] B. E. Yoldas and D. P. Partlow, manuscript in preparation.

[11] B. E. Yoldas, J. Non-Cryst. Solids 51, 105 (982).

[12] Idem, J. Am. Ceram. Soc. 65, 388 (1982).

[13] B. E. Yoldas and D. P. Partlow, accepted for publication in Appl. Opt., February, 1984.

[14] T. H. Elmer and F. W. Martin, Am. Ceram. Soc. Bull. 58 (11), 1092 (1979).

[15] H. Shhroter, Ann. Physik. 39, 55 (1941).

[16] R. Jacopsson, in Progress in Optics V, 249, E. Wolf, editor, North-Holland, Amsterdam (1966).

[17] M. Born and E. Wolf, Principles of Optics, 55, Pergamon Press, New York (1975).

[18] S. F. Monaco, J. Opt. Soc. Am. 51 (3), 280 (1961).

[19] L. M. Cook and K.-H. Mader, Laser Focus, 73, March, 1983.

[20] M. Bass, SPIE 76, 15 (1976).

[21] N. Bloembergen, Appl. Opt. 12, 661 (1973).

[22] M. J. Soileau, J. P. Porteus, P. A. Temple, and M. Bass, presented at the Fifth Laser Window Conference, Las Vegas, Nevada, Dec, 1975.

[23] D. W. Fradin, "Laser Induced Damage in Solids," Ph.D. Thesis, Harvard University, March, 1973.

[24] R. W. Hopper and D. R. Uhlmann, J. Appl. Phys. 41, 4023 (1970).

[25] J. J. O'Dwyer, The Theory of Dielectric Breakdown in Solids, Oxford University Press, London (1964).

[26] W. H. Lowdermilk, D. Milam, and J. G. Wilder, presented at the Fifteenth Annual Boulder Damage Symposium, Boulder, CO, Nov. 15, 1983.

[27] D. Milam, W. H. Lowdermilk, F. Rainer, J. E. Swain, C. K. Carniglia, and T. Tuttle Hart, Appl. Opt. 21 (20), 3689 (1982).

[28] F. Rainer, W. H. Lowdermilk, D. Milam, T. Tuttle Hart, T. L. Lichtenstein, and C. K. Carniglia, Ibid, 3685 (1982).

It was pointed out that heat treatment in a low-pressure oxygen plasma as a way to oxidize material is similar to old glow discharge cleaning.

PLASMA DEPOSITED INORGANIC THIN FILMS FOR OPTICAL APPLICATIONS

W. D. Partlow and J.V.R. Heberlein

Westinghouse Research and Development Center
Pittsburgh, PA 15235

Plasma deposited thin films, widely used in semiconductor processing, have begun to be used in optical applications such as anti-reflective coatings and optical waveguides. Amorphous films of refractory materials such as SiO_2, SiC, and Si_3N_4 have been applied with high optical perfection on substrates at 200-300°C with this process. Control of index of refraction has been achieved by selecting appropriate deposition parameters.

We describe the plasma deposition process and the properties of these coatings. We present applications and discuss how these coatings may be applied to more demanding optical applications in the future such as graded index films, rugate coatings, and vacuum UV reflecting films. We see that hydrogen inclusion in the films is a factor that must be controlled, and we propose methods to accomplish this.

Key words: optical; thin films; plasma; deposition; inorganic.

Introduction

Plasma film deposition has been used as a low temperature deposition process for a number of years. However, its applications have been restricted primarily to semiconductor processing. In this contribution, we want to describe what is known about the process and examine what properties of the process would make it attractive for other applications, particularly as optical coatings. We describe the physics and chemistry of the deposition process, properties of the films, and we review the types of films that have been produced with the process. The second section describes the established applications, and in the last section we discuss the potential of the plasma process for new applications and the research efforts needed to exploit the full potential of this deposition process.

1. Description of Current Technology

Amorphous thin films of inorganic materials may be deposited with high optical perfection on substrates at typically 200-300°C in a glow discharge plasma operated at about 1 torr pressure. This modified CVD process accomplishes the reaction with high energy electrons from the plasma instead of thermal activation as in conventional pyrolytic CVD processes, producing fundamentally different types of films. Figure 1 shows schematically an example of how plasma silicon carbide is produced from silane and methane reactants via radicals formed in the plasma and combining on the surface. [1] Plasmas generated with DC to RF sources have been used with a variety of excitation coupling schemes. [2] Two examples are shown in figure 2. Substrates may be exposed to or shielded from direct contact with the plasma. A photograph of a reactor with direct coupling is shown in figure 3. The reactions of the adsorbed radicals on the substrate surface proceed under strong non-equilibrium conditions and under the influence of bombardment of both charged and neutral particles from the plasma.

These conditions result in film properties that can depart widely from the properties of the corresponding equilibrium bulk material. However, variation of reacting gas composition, plasma excitation, gas flow kinetics, and substrate temperature and bias allows control of the film composition and properties over a rather wide range.

The films have in general smooth and glassy morphologies which are usually associated with higher deposition temperatures, [3] and non-equilibrium compositions can be "frozen" into the films. For example, SiO_x films may be formed with $0 \leq X \leq 2$. [4] The films usually are in compressive stress, are non-porous, [5] and contain reactant species such as hydrogen. [6] They have good adherence to many metal, glass and crystalline substrates, including Al, Au, Ag, Fe, SiO_2, Al_2O_3, Si, SiC, and $LiNbO_3$.

Deposition rates of 100 Å/min. to 500 Å/min. are typical for these coatings, and most reported applications have used film thicknesses of 2 μm or less. Poor adherence has been observed for films thicker than several μm due to the compressive stresses obtained at low deposition temperatures of 200-300°C. These stresses can be reduced with higher substrate temperatures. At temperatures of 600-700°C, the plasma serves as a mechanism assisting the pyrolitic CVD, increasing deposition rates and increasing the "effective" deposition temperature with ion bombardment. Epitaxial layers have been grown with plasma assisted CVD at these temperatures. [7]

Several of the properties of plasma deposited films make them very attractive for optical applications. Visibly clear films are obtained for wide band gap materials such as silicon oxide and nitride, although band gaps have been reported to be lower in the plasma thin films than in the bulk materials. [8] Band gaps and refractive indices can be adjusted by controlling film composition. The reported refractive index values of the films range from 1.4 for low density SiO_2 to 3.8 for a-Si, and specific values between those extremes are obtained either by varying the stoichiometry of a binary film such as SiO_x, by using mixtures such as SiO_xN_y, or by varying the film density.

Excellent film quality and uniformity have been observed in a comprehensive characterization study of plasma thin films. [9] The best silicon nitride films were found to introduce less than 1 Å rms roughness to smooth substrates, and a SiO_2 film added only a minimal amount of 2.8 Å rms. Correspondingly low optical scattering was observed for these samples. Thickness uniformity of 2 to 5% and refractive index uniformity of about 0.5% have been obtained on 5 cm discs.

Plasma deposited thin films can be applied with a high degree of conformality, so that micron size surface features such as steps and grooves are covered with high uniformity, as shown in figure 4.

Table 1 lists a number of thin films that have been produced by plasma deposition. [2,10] The most widely used films are silicon compounds generated using silane chemistry, and require only readily available bottled gas reactants. Vapors containing cations other than silicon can be obtained at sufficiently high vapor pressures, for example, as halides, but relatively few types of films using this approach have been reported.

2. Existing and Emerging Applications

Most applications that have reached commercial status are in semiconductor processing. [6,10] Plasma deposited silicon oxide serves as an excellent transfer layer for tri-level resist pattern deposition schemes because of its uniformity and excellent etching properties. Plasma silicon nitride is used as a dielectric insulation layer in IC devices, and as a diffusion barrier because of its non-porous nature. Its high hydrogenation makes it a good passivation layer for silicon surfaces. Both the oxide and nitride are useful as encapsulation and protective coatings in various semiconductor device applications. Doped plasma deposited amorphous silicon has been used for both p and n junction layers. [11] It has been considered as an approach for producing low cost solar cells. [12]

Considerably less use has been made of plasma deposited films in optical applications. Among the applications in the literature are a four layer broadband antireflective coating produced with off-stoichiometry silicon nitride, [13] and a low loss silicon nitride optical waveguide. [14] We have also produced selected refractive index single layer AR coatings for several applications with silicon rich silicon nitride.

3. Future Applications and Research Needs

We are presently developing silicon carbide thin films as high normal incidence reflectors of 10-20 eV UV radiation, and for high hardness coating applications. It is necessary to control the band structure of this material to duplicate the high VUV reflecting properties of pyrolytic CVD silicon carbide. [15] Reduction of hydrogen inclusion and control of stoichiometry is required, and use of halide reactants or other alternatives to conventional silane chemistry may be necessary.

There are many properties of plasma deposited thin films that make them appear to be promising as coatings for high power laser optics. Their high optical quality has been demonstrated, [9,14] although as yet laser damage tests for these coatings have not been reported. The selectability of the refractive index of these films make them attractive for multilayer dielectric coatings, and since the film properties can be continuously varied during deposition, rugate and other graded index coatings may be obtained with the plasma process.

Other promising future applications exist in the field of integrated optics, where low loss waveguides with specially tailored properties are needed for temperature sensitive devices, and

where the conformal property of these films will be useful for coating grooves and shaped surface features.

Besides the research necessary for controlling the band structure and gas atom inclusions in plasma deposited thin films, we see a need to obtain and characterize coatings with a large variety of materials. We anticipate further increases in the range of refractive index, and optical transparency for a wider range of wavelengths. Also, compatibility between the films and a larger variety of substrates can be achieved with different types of films. Ultimately, an understanding of the deposition process has to be obtained using sophisticated diagnostics and modelling, both of the gas and solid phases. Theoretical modelling of the plasma composition and of the band structure of the films would be useful. Desorption spectroscopy of adsorbed species is needed to understand the fundamental deposition processes. [16]

4. Summary

Plasma deposition is a promising technique for highly demanding optical applications. In particular, extremely smooth surfaces have been obtained with films deposited at relatively low substrate temperatures of approximately 300°C. Also, the selectability of the refractive index over a wide range (1.4 to 3.8), and the waveguiding capabilities of the plasma deposited thin films have been demonstrated. In order to fully exploit the potential of plasma deposited thin films for optical applications, research is needed on the effect of gas atom inclusions on the band gap, and on the use of a larger variety of materials, as well as studies of the fundamental surface deposition processes.

5. Acknowledgements

The authors wish to acknowledge R. A. Madia who has been instrumental in developing and operating the plasma thin film laboratory at Westinghouse R&D Center, and to C. S. Liu for helpful discussions and collaborations. We also wish to thank M. W. Cresswell for the micrograph figure 4.

6. References

[1] Y. Catherine, G. Turban, and B. Grolleau, Thin Solid Films 76, 23 (1981).

[2] J. R. Hollahan and R. S. Rosler, Thin Film Processes, Ed. by John L. Vossen and Werner Kern, p. 335, Academic Press, New York, 1978.

[3] Wayne L. Johnson, Solid State Technology, p. 191 (April 1983).

[4] Alan R. Reinberg, J. Electronic Matls. 8 No.3, 345 (1979).

[5] Evert P.G.T. van de Ven, Solid State Technology, p. 167 (April 1981).

[6] A. C. Adams, Solid State Technology, p. 135 (April 1983).

[7] S. Suzuki and T. Itoh, J. Appl. Phys. 54 No.3, 1466 (1983).

[8] Myron J. Rand and David R. Wonsidler, J. Electrochem. Soc. 125, 99 (1978).

[9] W. D. Partlow, W. J. Choyke, Jean M. Bennett, and Robert M. Silva, "Optical Characterization of Low Scatter, Plasma Deposited, Thin Films," This Conference.

[10] Myron J. Rand, J. Vac. Sci. Tech. 16 (2), 420 (1979).

[11] W. E. Spear and P. G. Lecomber, Philos. Mag. 33, 935 (1976).

[12] D. E. Carlson and C. R. Wronski, Appl. Phys. Lett. 28, 671 (1976).

[13] C. C. Johnson and T. Wydeven, Solar Energy 31, 355 (1983).

[14] S. Sriram, W. D. Partlow, and C. S. Liu, Applied Optics 22 (23), 3664 (1983).

[15] Victor Rehn and W. J. Choyke, Nuclear Instruments and Methods 177, 173 (1980).

[16] J. T. Yates, Jr., in Methods of Experimental Physics, Ed. by R. L. Dark (in press).

Table 1. Plasma Deposited Inorganic Thin Films

Commercial:	
	Silicon Oxide
	Silicon Nitride
	Amorphous Silicon
Well Developed:	
	Non-stoichiometric Silicon Oxide, Nitride
	Mixed Silicon Oxide-Nitride
	Silicon Carbide
	Amorphous Germanium
Reported:	
	Aluminum Oxide, Nitride
	Germanium Oxide, Carbide
	Boron Nitride
	Phosphorous Nitride
	Arsenic
	Titanium Oxide
	Other Oxides (B, Sn, Fe, Ta, Mixed)

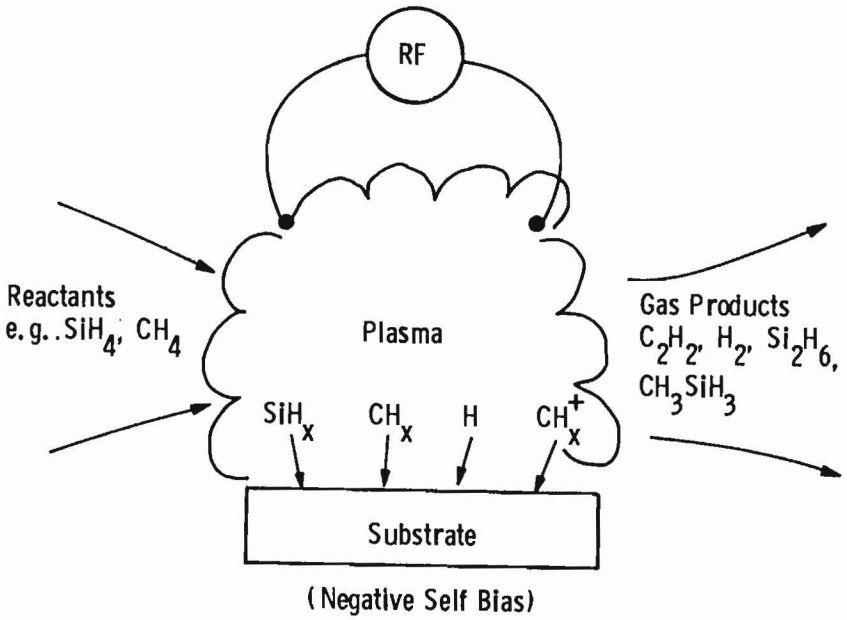


Figure 1. Schematic representation of the important processes in the plasma deposition of silicon carbide.

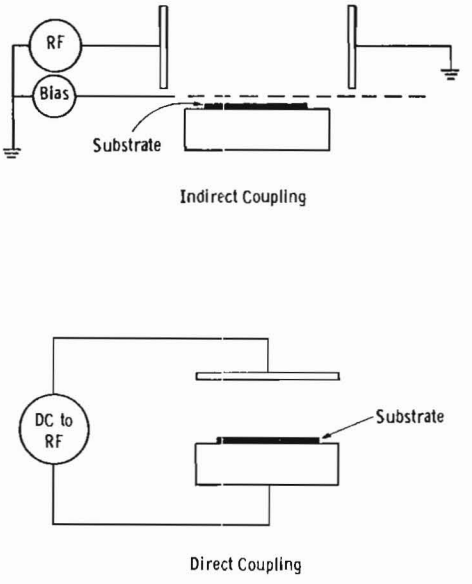


Figure 2. Two types of excitation coupling schemes used in plasma deposition.

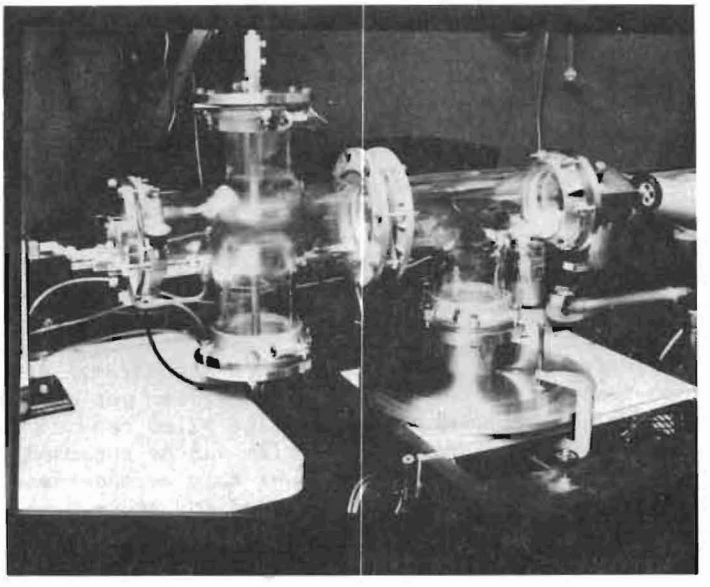


Figure 3. Research plasma deposition reactor.

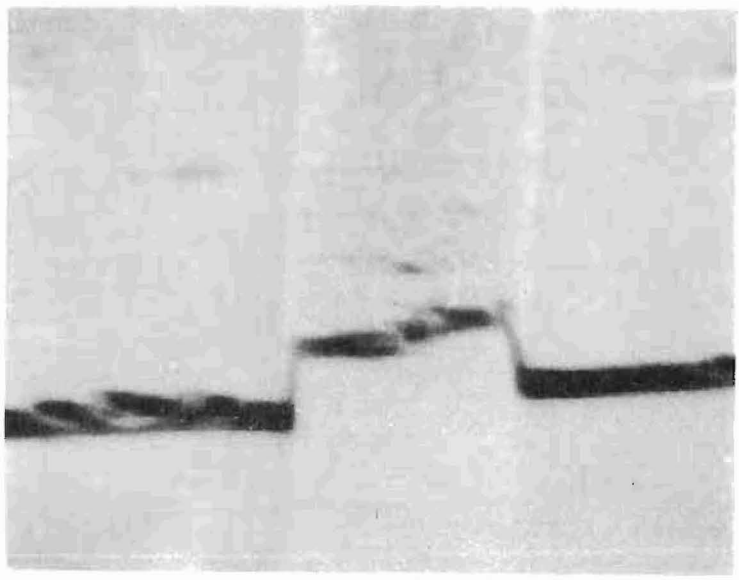


Figure 4 Micrograph of a 4000 Å layer of plasma deposited SiO_2 conformally covering a two micron size surface feature.

In response to a question, the speaker stated that they had not made any detailed measurements of absorption on the films they produced. (Very low absorption coefficients can be achieved, however. 1 dB/cm, which is equivalent to a 10^{-3} cm^{-1} absorption coefficient, has been achieved in a silicon nitride film.) The films show good transmission at a wavelength of 6328 ', are generally clear since they are silicon-rich, but begin to yellow as the band gap moves. The refractive index can be selected over a very broad range of values and can be tuned to three decimal places. The temperature of the deposition process is typically 200 to 300°C, which is significantly lower than pyrolytic CVD. The plasma replaces the pyrolytic reaction mechanism, lowering the temperature. Even the room-temperature components in the system get coated, but the film stresses increase as the temperature becomes lower and the films tend to pop off. By learning how to control the ion bombardment, this problem can be attacked and the deposition temperature probably can be pushed even lower than we have used so far for good films. In addition to oxides, the technique has been used for at least one phosphide, but no sulfides so far. What is needed is to find compounds having a vapor pressur of 1 torr or more at room temperature or to put the entire reactor in an oven.

Manuscript received 1-10-84/sar

Laser-Induced Emission and Laser Damage of Optical Components

D. B. Nichols, D. J. Morris, M. P. Bailey, and R. B. Hall

Boeing Aerospace Company
Seattle, WA 98124

The role of point defects in the failure of high-power laser optical components has been the subject of many analytical and experimental studies. We describe a related surface effect, newly observed, which is visible-wavelength emission from component surfaces undergoing exposure to infrared laser radiation at levels far below the visible damage threshold. This effect has been observed on a variety of optical components, including coated reflectors and uncoated window materials. In large-spot tests, the total emission amplitude exhibits strong time dependence. Spatial imaging shows distinct point sources of the visible emission, some of which recur during multiple-shot tests. Spatial correlations between (a) microscopic surface defects visible before damage, (b) emission points due to laser irradiation, and (c) damage points due to high-power laser irradiation, have been studied using spatial mapping techniques with indexing uncertainties of $\sim 25\,\mu$m. For dielectric coatings, a strong correlation is observed between the recurrent visible emission points, and pulsed laser damage points.

Key words: damage precursors; high-power laser optics; infrared lasers; laser damage; microscopic surface mapping; multilayer dielectric films; optical components; point defects; pulsed DF chemical lasers; surface diagnostics; visible-wavelength emission.

1. Introduction

In the initial stages of large-spot pulsed laser damage, failure is often observed as a pattern of scattered craters on an optical-component surface. This behavior is usually attributed to point defects which have a lower damage threshold than the surrounding areas. The effects of such discrete centers of damage can be evident even after catastrophic damage of a dielectric-coated element (see figure 1 of reference [1][1]).

2. Laser-induced Emission

In work designed to clarify the mechanisms of defect damage, we have observed visible-wavelength emission from the surfaces of several types of optical components during exposure to non-damaging infrared laser pulses. In one configuration, an evaporated-aluminum mirror was exposed to a 4 μsec FWHM DF laser pulse at a fluence below 1 J/cm^2. Light collected from a large solid angle ($\sim\pi$ steradians) was directed to a photomultiplier tube. The resulting signal, figure 1, showed strong time dependence. The dotted curve is the waveform of the incident laser pulse. Several tests showed that this radiation, induced by the incident DF laser pulse, lay in the visible wavelength region. The phototube spectral response (S-11) peaks at 440 nm, and is down two orders of magnitude at 310 nm and 660 nm. Visible flashlamp radiation from the pulsed DF laser was excluded from the target room by 13 mm of silicon, and the visible radiation from the target did not correspond to flashlamp radiation either in time or in pulse shape.

Under similar conditions a CaF_2 sample also exhibited strongly time-dependent visible emissions, as shown in figure 2. The solid curve is for exposure to high, but non-damaging, fluence. The dashed curve, with a large change of scale, shows the response when the incident DF pulse fluence is reduced by a factor of more than 300. This illustrates the fact that visible-wavelength emission can be observed on a variety of materials, and can occur far below damage threshold.

The time structure of these total-sample surface emissions indicated that several individual points, with distinct temporal waveforms, could be contributing to the total signal. Component surfaces were therefore

[1] Numbers in brackets indicate the literature references at the end of this paper.

optically imaged in order to spatially resolve the emission, and visible emission during laser exposure was recorded on film. The film had a long-wavelength cutoff of 650 nm.

Distinct points of emission were observed. As an example, a diamond-turned copper sample was repeatedly irradiated with the DF pulse of figure 1, at a fluence near 5 J/cm^2, far below the damage threshold. In six successive laser exposures, some 40 emitting points were observed. A number of those recurred on successive shots. A small subset of these points showed emission on every shot.

3. Damage Correlation

Correlation between emission points and damage points was investigated using the pulsed chemical laser beam of the PHOCL-10 device [2]. Figures 3 and 4 give the beam characteristics. The DF laser pulse had a 4.7 μs full-width at half-maximum, and produced the spatial profile of figure 4 at the focal plane of a 50.8 cm focal-length final mirror. The effective e^{-2} diameter was 0.7 cm.

Figures 5-8 are photographs of the surface of a reflector, dielectric-enhanced for λ = 3.6 - 4.2 μm. The sample was a ThF_4/ZnS coating on a molybdenum substrate. Fiducial marks in the lower left and upper right corners are separated by about 1 cm. Figure 5 shows the sample surface before any laser exposure, illuminated by a microscope light ("illuminated" hereafter), and photographed at 10X. Figure 6 shows the same area observed in a darkened target room, during exposure to an 8 J/cm^2 pulse. The fiducial marks are separately illuminated to provide spatial indexing. Several emitting points are visible. Figure 7 is an illuminated micrograph of this area after the exposure of figure 6. Figure 7 is nearly identical to figure 5, demonstrating that the laser shot of figure 6 did not produce microdamage points, which would be readily visible in figure 7 down to diameters of 10 μm.

Figure 8 is a similar illuminated photograph showing the initial microdamage pattern which occurred at higher, damaging, fluences. A spatially indexed comparison of figures 6 and 8 shows that, of the eight prominent emission points of figure 6, six correspond exactly (i.e., to within 30 μm in both X and Y coordinates) with damage points. Thus six of the some 29 damage points of figure 8 were "predicted" by the non-damaging "interrogation" shot of figure 6.

Figure 9 gives results for fifteen such interrogation shots. The lower plot gives the exposure schedule, and the upper plot indicates the occurrence of laser-induced emission points. The emission data of Run Number 6 of figure 9 is the example used for figure 6. For purposes of tabulating results, a circular boundary was drawn around the final cluster of damage points in figure 8; figure 9 refers to the area inside that boundary.

In figure 9, each emitting point is designated by an index number, in order to show which points exhibited emission more than once, and to determine possible patterns of recurrence. Those which later became damage points are marked with an "x." It is apparent, first, that the probability of observing emission is higher for laser runs which have a significant fluence increment over previous runs; a step upward in laser energy enhances emission, while emission diminishes during repeated runs at constant fluence.

Secondly, it can be seen that emission points which did not go on to damage (observed in Runs 9 and 12) were precisely those points which did not recur on successive shots of higher fluence. This is related to a useful rule, which we have not yet seen violated: Every emission point which recurs becomes a damage point.

A closely connected question is the relationship between damage points and the usual anomalies or points visible under a microscope before any laser exposure. Historically this relationship has been shown to be weak and of little use. This was also observed in the present work. Within the final damage circle, (figure 8) fourteen points were visible in the illuminated pretest micrograph of figure 5. Eight of those became damage points, and the total number of damage points was 29. In other cases, such pretest illuminated micrographs were unable to indicate any of the final damage points, while infrared-induced emission successfully predicted several of the damage points.

4. Summary

Characteristics observed to date for pulsed-laser-induced emission may be summarized as follows:

(1) Visible wavelength emission may occur during the exposure of an optical component to pulsed infrared laser radiation.

(2) The emission is not specific to one exposure wavelength, although the discussion in this report is restricted to the wavelengths of pulsed DF lasers.

(3) The emission is observed on a variety of optical components, including coated reflectors and uncoated window materials.

(4) The emission can occur at incident fluence levels far below the visible damage threshold of the optical component.

(5) The emission from an extended sample surface exhibits significant temporal structure (on a microsecond scale in the present work).

(6) The emission from an extended sample surface can be spatially resolved into discrete contributions which appear as point sources of visible light.

(7) In multiple-exposure measurements, emitting points on a component surface can be identified as recurrent or non-recurrent.

(8) Initial tests on dielectric-enhanced reflectors have shown a strong correlation between (a) recurrent, non-damaging, laser-induced emission points, and (b) subsequent laser-induced damage points.

This method does not designate all the points which will fail, but it shows promise of reliably indicating, in a non-destructive predamage diagnostic, a subset of points which will certainly fail. Successful application of such a diagnostic would clearly be important both for studies directed to understanding point-defect damage mechanisms, and for improving damage thresholds through modification of fabrication techniques, guided by predamage analysis of points which can be expected to fail.

This work was supported by Boeing IR&D funds, and by the U. S. Army Missile Command through Contract DAAH01-81-D-A019 with M. K. Associates, Inc.

5. References

[1] Nichols, D. B., Hall, R. B., and House, R. A., Large-spot DF laser damage of dielectric-enhanced mirrors, NBS Spec. Publ. 509, 325 (1978).

[2] Nichols, D. B., Hall, R. B., and McClure, J. D., Photoinitiated $F_2 + H_2/D_2$ chain-reaction laser with high electrical efficiency, J. Appl. Phys. 47, 4026 (1976).

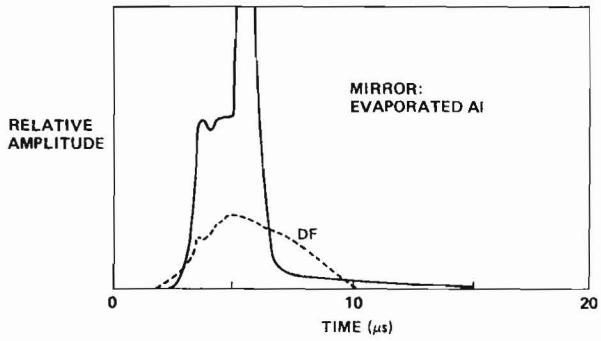


Figure 1. Light emission (solid curve) due to exposure of an evaporated aluminum mirror to a DF laser pulse (dotted curve). Peak fluence is 0.6 J/cm^2, and spot size (effective e^{-2}) is 0.5 cm diameter.

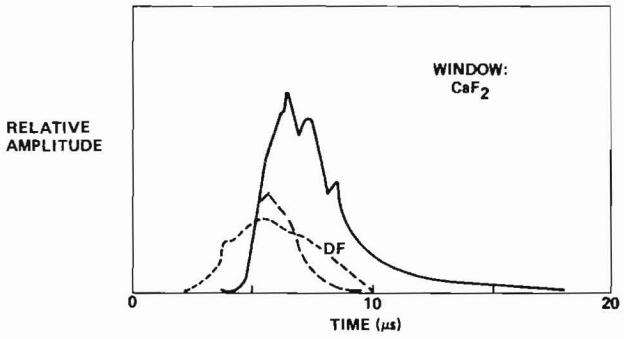


Figure 2. Relation of light emission to an incident DF pulse (dotted curve) for non-damaging exposures of widely different energies. The solid curve is for incident fluence e_o. The dashed curve, plotted with a large change of scale, is for incident fluence of $e_o/350$.

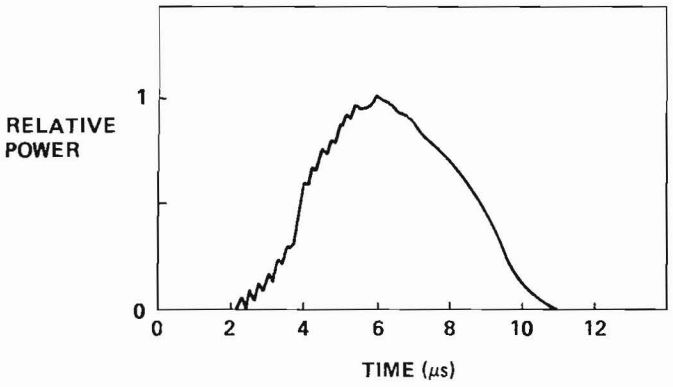


Figure 3. Temporal waveform of the DF pulsed chemical laser.

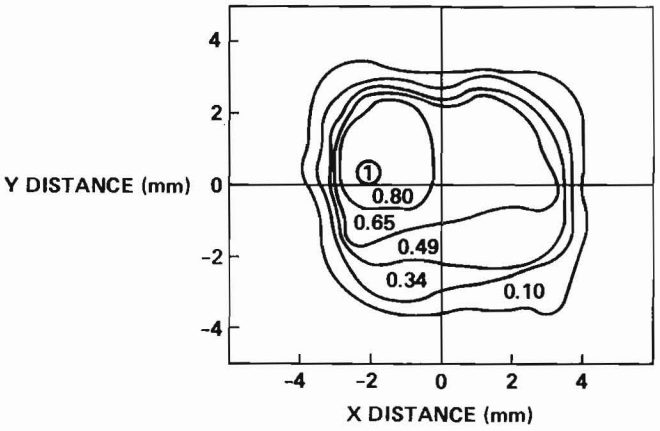


Figure 4. Far-field spatial profile of the DF laser. The effective e^{-2} diameter is 0.7 cm.

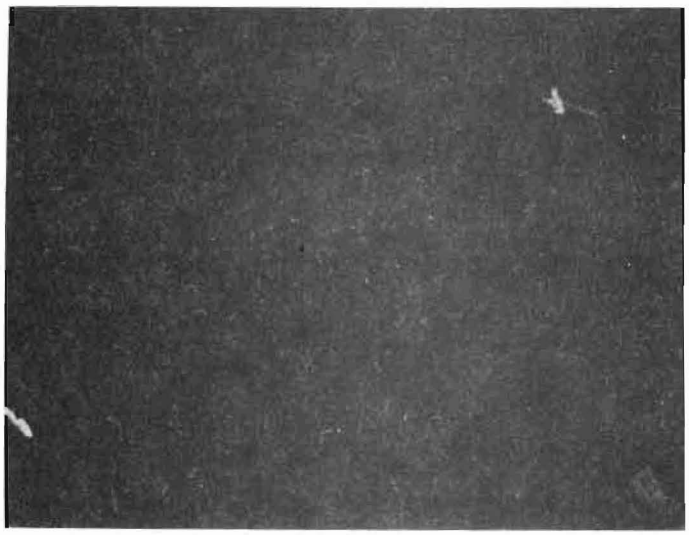


Figure 5. Illuminated micrograph of a ThF_4/ZnS Sample (G24) before laser exposure. Fiducial marks in two corners are separated by about 1 cm.

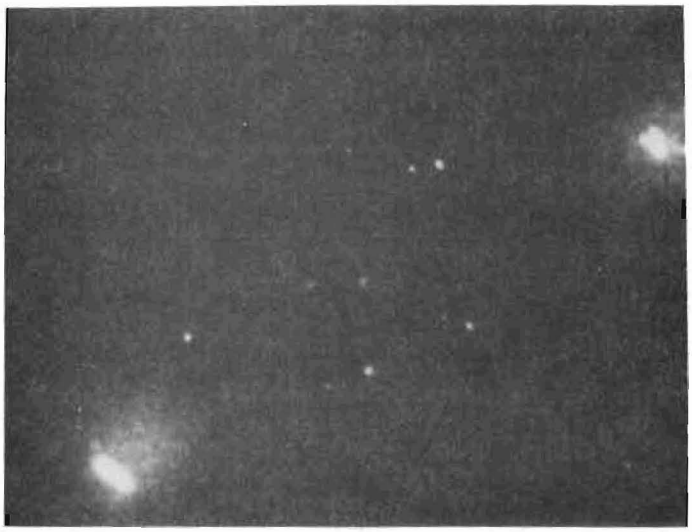


Figure 6. Surface area of figure 5 as observed during exposure to an 8 J/cm^2 DF laser pulse. Several emitting points are visible. The two fiducial marks are separately illuminated.

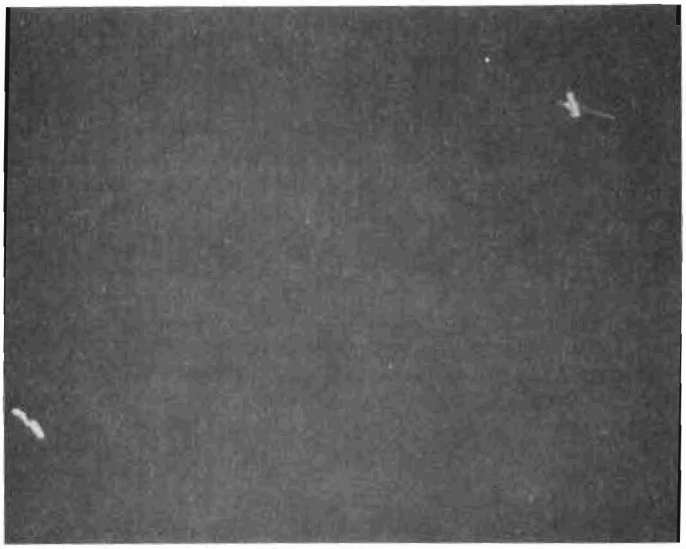


Figure 7. A repeat of figure 5, taken after the laser exposure of figure 6.

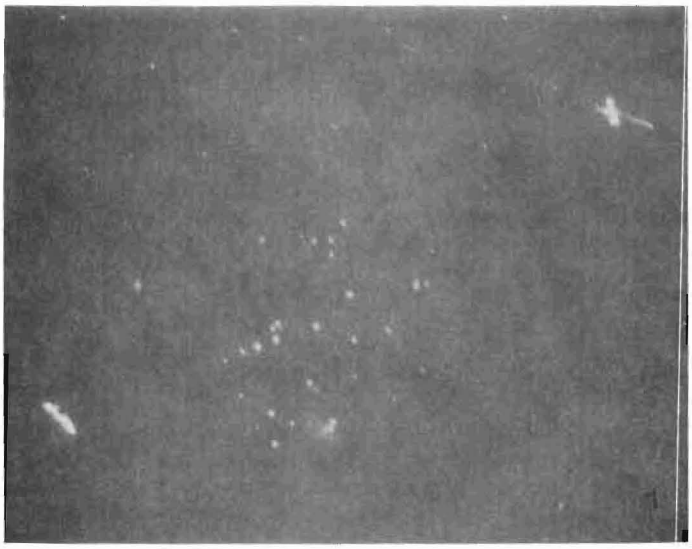


Figure 8. Surface area of figure 5 after exposure to damaging fluences, exhibiting microdamage pattern.

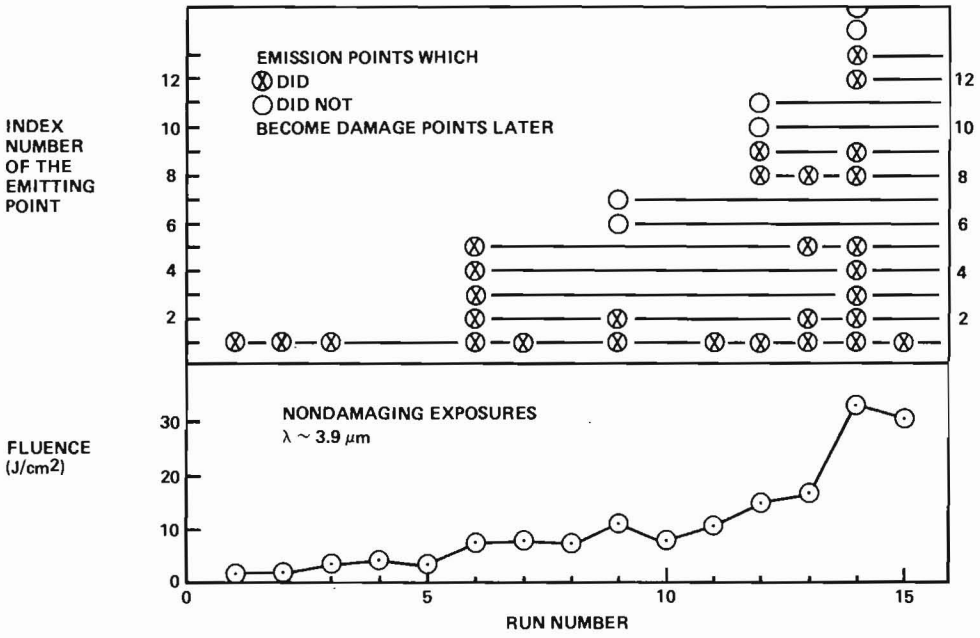


Figure 9. Exposure record and point emission for Sample G24. Only 2 of 15 non-correlating emission points (open circles) are plotted for Run No. 14.

Charge Emission and Related Precursor Events Associated with Laser Damage

Michael F. Becker,[a] Fred E. Domann,[b]
Alan F. Stewart, and Arthur H. Guenther

Air Force Weapons Laboratory
Kirtland Air Force Base, NM 87117

Charge emission and surface photoconductivity were used to investigate possible precursors to laser damage, including surface cleaning and hardening. Experiments were conducted with a 1.06 micron ND:YAG laser with 5 nsec pulses. A wide range of samples were investigated, including diamond-turned copper mirrors, silicon wafers, and half-wave dielectric films of ThF_4, Al_2O_3, and Ta_2O_5 on fused silica.

Charge emission at 1/10 of the single pulse damage threshold was observed for the copper mirrors. Declining emission for successive pulses was characteristic of surface cleaning. Emitted charge quantities increased monotonically with fluence prior to damage, but the charge emission was noisy with site-to-site variations. For silicon, damage was simultaneous with charge emission for both 1-on-1 and N-on-1 tests. The damage morphologies for the two cases were distinctly different. Nonlinear absorption measurements were conducted on silicon for fluences below the single pulse damage threshold.

The two oxide dielectric films had gold electrodes evaporated on them leaving gaps of 0.75 to 2.0 mm for measuring surface conduction. Charge was collected from this configuration at 1/20 of the single pulse threshold. The charge quantity was very noisy and apparently uncorrelated with fluence. Surface hardening was observed for the ThF_4 film and it did not emit until damage was initiated.

Key words: charge emission; photoconductivity; diamond turned copper; silicon; thorium fluoride; tantalum oxide; aluminum oxide; surface cleaning; surface hardening; thin films.

1. Introduction

In this work, charge emission and surface photoconductivity were used to investigate possible precursors to laser damage, including predamage effects, surface cleaning and hardening, and damage signatures. Experiments were conducted with a 1.06 micron Nd:YAG laser with 5 nsec pulses. A wide range of samples were investigated, including diamond-turned copper mirrors, silicon wafers, and dielectric films on fused silica.

Our objective was to investigate the relation between charge evolution processes such as emission and photoconductivity, and laser induced damage or precursor events to laser damage such as laser surface cleaning. In that this work is of a survey nature and was conducted mainly during the course of a summer, it tends to suggest more questions and promising lines of investigation than it does answers.

Laser induced cleaning of alkali halide surfaces was observed by Allen et al [1] using 2.8 μm and 3.7 μm laser radiation. Although they monitored neutral particle emission, it is reasonable to assume that a fraction of the desorbed species will be ionized, especially at the shorter laser wavelength of 1.06 μm. Laser induced emission of both ions and neutral atoms was reported by Schmid et al [2] for several alkali halide materials. Such emission was observed at energy fluences below the single shot damage threshold, at a laser wavelength of 694 nm.

There are a wealth of similar observations of laser induced charged and neutral particle emission from semiconductors such as CdS [3-4], CdSe [5], and silicon [6-7, 11-12]. In the case of silicon,

---

[a] SCEEE Fellow, permanent address: University of Texas at Austin, Electrical Engineering Department, Austin, TX 78712

[b] SCEEF Fellow, permanent address: University of Wisconsin-Platteville, Department of Physics, Platteville, WI 53818

some controversy has been generated in the relation of laser induced melting to the process of annealing ion implantation damage. In addition, the emission from silicon has been ascribed to thermal emission, while the emission of alkali halide species is believed to be multi-quantum, rather than thermal, in nature. Emission from silicon has been observed only accompanied by damage, and can be used as a reliable indicator of damage [11-12]. The suggestions of this previous work are that charge emission is useful in the study of pre-damage surface cleaning, for those materials which emit prior to damage; and in the study of multi-pulse damage statistics, for those which do not emit prior to damage.

An additional aspect of this work is an attempt to extend the experiments on bulk photoconductivity induced during damage by Yasojima, et al [8], and Sharma and Rieckhoff [9], to the area of thin film coatings. Experiments will be described in which a substrate-electrode configuration is designed and the various photoconduction paths for this configuration are analyzed.

2. Experimental

2.1 Laser System

The laser system used in these experiments was a Quantel Nd:YAG laser with one amplifier module. The output pulses at 1.06 μm were 5.1 ± .1 nsec long as determined by a fast vacuum photodiode. The passively Q-switched pulses were single longitudinal and axial mode. After amplification, the laser pulses passed through an attenuator consisting of a rotating half wave plate and a polarizer. At the sample location, the beam was brought to a focus by a 2 m focal length lens. The focal plane of the lens was scanned with a narrow (<50 μm) slit to determine the beam spot size. The $1/e^2$ radius was 180 μm. In addition, the beam profile was reasonably Gaussian. The laser energy in the focal plane was determined using a reference energy meter sampling a split off portion of the incident beam. It was calibrated using a second meter placed behind the focal plane. Using this data, which is acquired for every shot, the fluence (energy/area), and the intensity (power/area) for each shot is determined.

2.2 Samples

A wide variety of samples were used in these experiments. Single crystal <1,1,1> silicon wafers 1 mm thick and polished on both sides represented semiconducting materials. In fact, 1.06 μm represents band edge optical excitation for silicon. Metals were represented by diamond turned OFHC copper mirrors. Several thin film coatings were tested representing fluorides and oxides. One sample of a quarter wave of thorium fluoride film on fused silica was tested. A set of samples from OCLI, each consisting of a half wave layer of tantalum oxide or aluminum oxide on a fused silica substrate, were tested. One sample of each coating type was tested without modification while one of each had surface electrodes deposited for photoconductivity experiments.

The photoconductivity samples are shown in fugure 1. Evaporated chrome-gold electrodes 100 nm thick are placed on top of the dielectric film. When a bias is applied and if appreciable photoconductivity exists, the charge flow to the electrodes can be measured. The stainless steel evaporation mask was designed with recessed areas so that minimal area of the dielectric film is actually contacted by the mask. (fig. 1a.) The array of electrodes, shown in figure 1b, has various electrode gap widths ranging from .8mm to 2.0 mm. At typical bias voltages of 800 to 1500 V, this gives tangential electric fields in the dielectric films from 5×10^4 to 2×10^6 V/m.

All the samples were cleaned in an automated photoresist spinner using acetone, deionized water, and dry nitrogen without their surfaces being touched by any solid materials.

2.3 Diagnostics

The principal diagnostics used in these experiments are Nomarski microscopy, collection of emitted charge using a biased charge collection electrode, and collection of photoconduction charge on thin dielectric films using the evaporated electrode structure described previously. All the samples and charge collection diagnostics were placed in a vacuum chamber pumped by a cryopump to about 10^{-6} torr. The samples were held on a 3-axis remotely controlled stage.

The microscopic observations were conducted on a matching, manually controlled stage, so that each irradiation site could be inspected for possible damage. Damage was defined as any discernable change in the surface at up to 400x magnification. The smallest damage features observed were pits on the order of one micron in size.

Emitted charge was collected by a biased wire placed 2 cm above the sample and only slightly off the beam axis. The bias potential was +1500 V which was found to be sufficient to collect all emitted negative charge. Emission current versus bias voltage was found to saturate several hundred volts below

this value. The negative charge pulses were amplified by a charge sensitive amplifier (Amptek A-203 and A-206) which had a sensitivity of 1.75×10^{-13} V/Coul. In practice, the ultimate sensitivity was limited by interference from local electromagnetic sources to about 10^{-15} Coulomb with a dynamic range of two orders of magnitude. The signal from the charge amplifier was processed and stored by a Tektronics transient recorder and mini-computer.

The photoconductivity samples were used with the same charge amplifier and data acquisition system as described above. The samples with electrodes were placed in a Macor ceramic holder as pictured in figure 1b. Gold plated relay contacts made contact with the gold electrodes to supply the bias potential and collect the charge signals. It should be pointed out that only the dominant conduction signal can be observed with this configuration, and that three potential conduction paths exist: through the vacuum above the sample, through the thin film, and transverse to the film and in the substrate or substrate-film interface. In the presence of large charge emission, the first of these paths will dominate. Photoconductivity in the solids can only be studied when there is no charge emission.

3. Silicon

Silicon was investigated with the main objective to extend previous studies of the damage morphology and charge emission of silicon for picosecond laser pulses [10-12] to the nanosecond pulse regime. For 60 psec pulses, no charge emission was observed unless there was also surface damage of the silicon in both the 1-on-1 and N-on-1 damage regimes. The threshold for N-on-1 damage was found to depend inversely on the number of pulses, and the damage morphology changed distinctly between the 1-on-1 and N-on-1 regimes. All of these effects were found to repeat for 5 nsec pulses.

In these experiments with 5 nsec pulses, the threshold for single pulse damage was 1.6 J/cm^2. For six pulses, the threshold was 1.1 J/cm^2, in agreement with the expected behavior. In addition, the absolute magnitude of these threshold fluences is very nearly identical for 60 psec and our 5 nsec pulses. Typical damage morphologies for these experiments are shown in figure 2. Figures 2a and 2b show single pulse damage near the threshold fluence and above the threshold fluence respectively. Both show generally smooth, melt-like features. Near threshold, ripples can be observed with a spacing equal to the free space wavelength as predicted by Sipe, et al [13]. Figure 2c shows N-on-1 damage morphology for N=6. In this case, the groove structure is somewhat more developed than in similar tests at other sites. The resulting chains of pits, spaced by the free space wavelength normal to the optical electric field, are identical to those observed by Becker, et al [10-12] for multi-pulse damage with picosecond pulses. This change from smooth to pit morphology is believed to represent a change from a uniformly melted surface (starting from heterogeneously nucleated sites) in 1-on-1 damage to only heterogeneous melt sites in N-on-1 damage.

Large charge emission, which saturated the detection electronics, was found to accompany those shots in which damage was observed; and no detectable charge emission was observed for the undamaged sites. In addition, in picosecond pulse N-on-1 experiments, the onset of damage was found to correlate with the onset of charge emission. This finding was not explicitly verified in the study; however, in our N-on-1 experiments, damage was always found to accompany one or more charge emission events and never found when no emission occurred.

The nonlinear absorption of the silicon sample (1 mm thick) was measured for fluences below the single shot damage threshold. The experiment was conducted in exactly the same way as the damage experiments except the sample was not in vacuum and a second energy probe was placed behind the sample. The data is shown in figure 3. There is a large increase in absorption versus increasing fluence. This is in qualitative agreement with the expected increase due to the excitation of free carriers and their subsequent optical absorption. The small signal intercept is in agreement with accepted values for the reflectivity and absorption coefficient for high resistivity silicon.

4. Diamond Turned Copper

Diamond turned copper mirrors showed very different charge emission behavior from silicon. For single pulse experiments, two thresholds were observed, one for damage and another for charge emission at less than one-tenth the damaging fluence. The data for one sample is shown in figure 4. The damage threshold is at 2.1 J/cm^2 while the threshold for charge emission is at .12 J/cm^2.

When N-on-1 experiments were conducted, behavior resembling charge emission associated with the surface cleaning of the sample was observed. A set of experiments with sets of six nearly equal energy pulses on the same site was conducted to explore the cleaning behavior. These results are also shown in figure 4 with data represented by the "6"s. At fluences not too far above the threshold for charge emission, the emission fell to zero before the sixth pulse. The emission would not resume at this site unless the laser fluence was raised. At higher fluences, the charge emission would not terminate after

six pulses. This type of behavior resembles that observed by Allen, et al [1] for the desorption of water from CaF_2 by 2.8 μm laser radiation. That is, the flux of desorbed molecules or ions is limited by the density of foreign particles on the surface, and cleaning can be achieved with a finite number of pulses. Just below the single pulse damage threshold, damage was observed after six pulses (although it is not known at which pulse the damage was initiated). Little data was taken at this fluence, but the behavior indicates that the N-on-1 threshold is lower than the 1-on-1 pulse threshold as predicted by Lee, et al [14].

For fluences just above the threshold for charge emission, the charge amplifier did not saturate, and the amount of charge emitted could be studied as a function of fluence. That result is shown in figure 5. The emission shows a noisy but monotonic increase as a function of fluence. Because of the scatter in the data, there is no way to discriminate between a power law dependence and an inverse negative exponential dependence. Theoretically, the former dependence is associated with multi-photon processes and the latter is associated with thermal emission over an energy barrier.

Nomarski micrographs of single pulse damage sites on copper are shown in figure 6 at fluences just above threshold and well above threshold. Again, the expected optical wavelength spaced ripples are clearly seen in figure 6b. Small melt pits are seen at lower fluences. Because the damage threshold for this mirror is not near the best for diamond turned copper mirrors, the pit damage may be associated with local imperfections.

5. Dielectric Thin Films

Both fluoride and oxide dielectric films were tested. Surprisingly, the thorium fluoride film showed charge emission very different from both oxide films. It behaved like silicon and did not emit until damage occurred, while the oxide films resembled copper in that the emission or photoconductivity initiated at fluences well below the 1-on-1 damage threshold.

5.1 Thorium Fluoride

The thorium fluoride film was tested for damage threshold and accompanying charge emission. As mentioned above, this film did not show any measurable charge emission when damage did not occur, and always gave emission when damage was observed. The data is shown in figure 7 and indicates identical 1-on-1 damage and charge emission thresholds of 10.4 J/cm^2.

A second major difference in the thorium fluoride film was that it showed an increase rather than a decrease in threshold for repeated pulses at the same site. This hardening effect is illustrated in figure 7 by the horizontal bars. Each bar represents a site which was irradiated by a sequence of pulses of monotonically increasing fluence. The initial fluence is at the left end of the bar and the final damaging fluence is at the right end of the bar. The total number of shots is shown on the bar, and these shots are roughly equally spaced in fluence between the highest and lowest values. The hardening effect raised the damage threshold from 1.5 to 2 times. Although this effect is no doubt dependent on the exact sequence of processing pulses, this dependence was not explored in further detail. The damage morphology did not yield any additional information. Dielectric film damage morphologies will be discussed briefly later.

5.2 Oxides

Most of the experimental work and all the charge measurements with the oxide coatings were done on the samples prepared with photoconductivity electrodes. Both the tantalum oxide and the aluminum oxide coatings showed lower thresholds for charge collection than damage. Based on the fact that the photoconductivity time waveforms were identical to the charge emission waveforms and the fact that the charge signal decreased when the samples were tested in air, we conclude that the photoconductivity signal is primarily due to charge emission. Subsequent reference to "charge emission" for these samples is referring to data collected by the surface electrodes. They are clearly capable of collecting all the emitted negative charge when biased above 1200 volts. The fact that these films showed apparent cleaning effects at low fluences lends further credibility to the assertion that only emitted charge is being observed and that any true photocurrent is much too small to be observed.

The emission and damage threshold behavior for the two oxide coatings is shown in figures 8 and 9. Both show charge emission thresholds 10 to 20 times lower than the 1-on-1 damage thresholds. The N-on-1 damage behavior of these samples was not studied.

The matching non-electroded films were tested for 1-on-1 damage threshold to compare with the electroded samples. The non-electroded tantalum oxide film was found to have a slightly lower damage threshold than the electroded sample, 10 versus 18 J/cm^2. On the other hand, the bare aluminum oxide

sample had a much larger damage threshold than the electroded sample. The plain sample threshold was greater than 50 J/cm^2, and difficult to measure with the experimental configuration used, versus 8 J/cm^2 for the electroded sample.

Every effort was made during the electrode evaporation to avoid contamination of the film between the electrodes. The evaporation mask was etched such that it only contacted the film near the edge of the electrode. There is, however, a precedent for a metallic electrode affecting the electronic properties of a substrate up to one millimeter away in the transverse direction. Such an effect has been observed using photoemission techniques [15]. In addition, high migration rates for metal ions have recently been measured in oxide films [16]. It is possible that there were subtle effects due to the electrodes on the photoconductivity samples.

Data was taken on the quantity of emitted charge versus laser fluence with the electroded samples. Unlike the copper mirror, no trend could be observed. The extreme site-to-site fluctuations coupled with the somewhat limited dynamic range of the charge amplifier frustrated attempts to observe any systematic dependence of the emission on fluence.

The damage morphology of the dielectric films is generally uninformative. Holes in the films as small as several microns were observed. Typical micrographs are shown in figure 10. It is perhaps intriguing that each damage hole shows a central feature, regardless of the film composition.

6. Conclusions

We conclude that charge emission is a useful diagnostic in the study of laser damage. The charge emission behavior of different optical materials falls into two distinct groups: emission coincides with damage, and emission precedes damage at roughly one-tenth of the damaging fluence.

Of the samples observed in this study, single crystal silicon and thorium fluoride thin films fall into the first category. This makes charge emission a useful tool in N-on-1 damage experiments in which charge emission reveals the first pulse at which damage occurs, and experiments may be designed to stop at this point. Other observations on the damage of silicon showed the same behavior for 5 nsec pulses as had previously been observed for 60 psec pulses. These observations include the inverse dependence of threshold on number of pulses incident on the same site, and differing damage morphologies for 1-on-1 and N-on-1 damage.

Whereas in silicon the damage threshold decreases with increasing numbers of pulses, thorium fluoride films hardened with repeated laser shots and the damaging fluence increased by 1.5 to 2 times. The oxide dielectric films were not examined for this behavior.

In the second group of materials, charge emission prior to damage seems to be at least in part associated with laser cleaning of the sample surface. Diamond turned copper and the oxide thin films showed this behavior; with copper being studied more extensively. The charge emitted from copper with the first laser pulse increased monotonically with fluence. After repeated pulses, the charge emission would disappear until the laser energy was increased. Copper also showed evidence of having an inverse dependence of threshold on the number of pulses.

Dielectric film samples with surface electrodes to measure photoconductivity effects showed conduction due solely to charge emission and conduction in the vacuum above the film. The process of adding electrodes to the samples had an unpredictable effect on the damage threshold.

For this second group of samples, charge emission seems to be a simple way of studying laser surface cleaning prior to damage. With more dynamic range in the charge detection electronics it may be possible to differentiate between cleaning events and damaging events.

Research sponsored by the Air Force Office of Scientific Research/AFSC, United States Air Force, under Contract F49620-82-C-0035. The United States Government is authorized to reproduce and distribute reprints for governmental purposes notwithstanding any copyright notation hereon.

M. F. Becker also acknowledges the support of the DoD Joint Services Electronics Program at the University of Texas through AFOSR contract F49620-82-C-0033.

7. References

[1] Allen, Susan D.; Porteus, J. O.; Faith, W. N. Infrared laser-induced desorption of H_2O and hydrocarbons from optical surfaces. Appl. Phys. Lett. 41(5): 416-418; 1982 September 1.

[2] Schmid, Ansgar; Bräunlich, Peter; Rol, Pieter K. Multiphoton-induced directional emission of halogen atoms from alkali halides. Phys. Rev. Lett. 35(20): 1382-1385; 1975 November 17.

[3] Namiki, A.; Watabe, K.; Fukano, H.; Nishigaki, S.; Noda, T. Behavior of positive ions ejected from laser-irradiated CdS. J. Appl. Phys. 54(6): 3443-3447; 1982 June.

[4] Namiki, A.; Watabe, K.; Fukano, H.; Nishigaki, S.; Noda, T. Ejection of atoms and molecules from highly excited CdS. Sur. Sci. 128: L242-L248; 1983.

[5] Aleksandrov, I. N.; Bykova, T. T. Laser-induced ion emission from cadmium selenide. Sov. Phys. Tech. Phys. 25(6): 727-729; 1980 June.

[6] Lui, J. M.; Yen, R.; Kurz, H.; Bloembergen, N. Phase transformation on and charged particle emission from a silicon crystal surface, induced by picosecond laser pulses. Appl. Phys. Lett. 39(9): 755-757; 1981 November 1.

[7] Van Vechten, J. A. Comment on "phase transformation on and charged particle emission from a Si crystal surface induced by ps laser pulses." J. Appl. Phys. 53(12): 9202-9203; 1982 December.

[8] Yasojima, Yoshiyuki; Ohmori, Yutaka; Okumura, Norio; Inuishi Yoskio. Optical dielectric breakdown of alkali-halide crystals by Q-switched lasers. Jap. J. Appl. Phys. 14(6): 815-823; 1975 June.

[9] Sharma, Bhim S.; Rieckhoff, Klaus E. Laser-induced photoconductivity in silicate glasses by multiphoton excitation, a precursor of dielectric breakdown and mechanical damage. Can. J. of Phys. 45: 3781-3791; 1967.

[10] Becker, M. F.; Walser, R. M.; Jhee, Y. K.; Sheng, D. Y. Picosecond laser damage mechanisms at semiconductor surfaces. SPIE 322 Picosecond Lasers and Applications; Bellingham, WA: Society of Photo-Optical Instrumentation Engineers: 93-98; 1982.

[11] Becker, M. F.; Jhee, Y-K.; Bordelon, M.; Walser, R. M. Charged particle exoemission from silicon during multi-pulse laser induced damage. Fourteenth Annual Symposium: Optical Materials for High Power Lasers, Nat. Bur. Stand. Special Publ.; 1982.

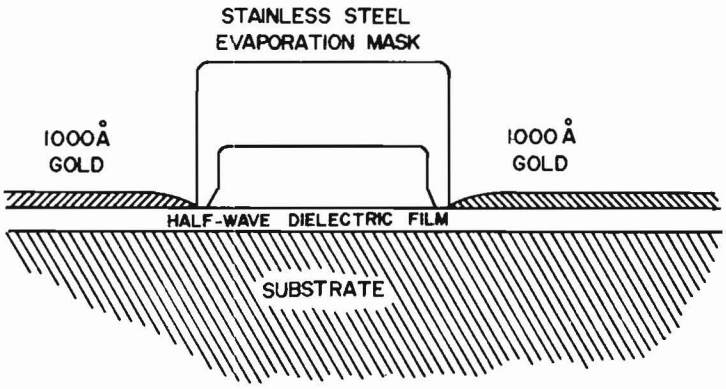
[12] Becker, M. F.; Jhee, Y-K.; Bordelon, M.; Walser, R. M. Observations of an incubation period for multi-pulse laser induced damage. Proceedings of the Conference on Lasers and Electro-Optics, CLEO '83, Optical Soc. of Am.; Washington, DC; 1983.

[13] Sipe, J. E.; Young, J. F.; Preston, J. S.; van Driel, H. M. Laser induced periodic surface structure. Phys. Rev. B. 27, 1141; 1983.

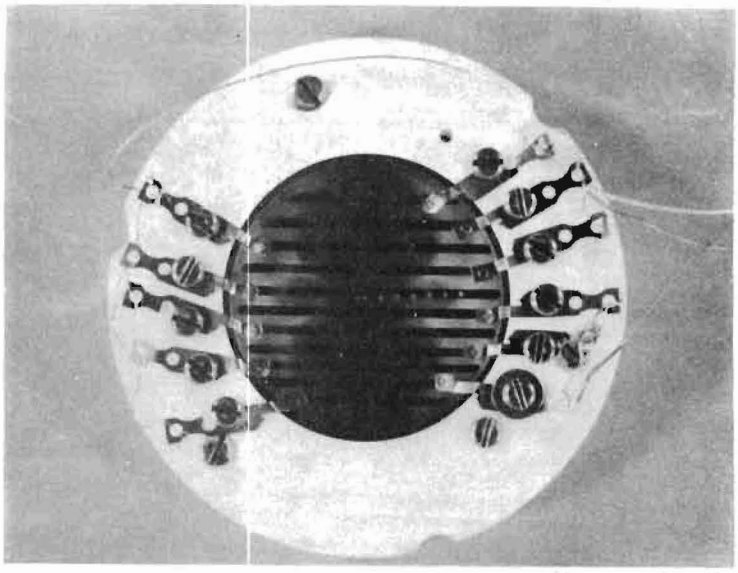
[14] Lee, C. S.; Koumvakalis; Bass, M. A theoretical model for multiple-pulse laser-induced damage to metal mirrors. J. Appl. Phys. 54(10): 5727-5731; 1983 October.

[15] Wooten, F.; Spicer, W. E. Surface effects, band bending, and photoemission in semiconducting films of Cs_3Sb. Sur. Sci. 1: 367-377; 1964.

[16] McBrayer, J. D.; Swanson, R. M.; Sigmon, T. W. Observation of rapid field aided migration of silver in metal-oxide-semiconductor structures. Appl. Phys. Lett. 43, 653; 1983.

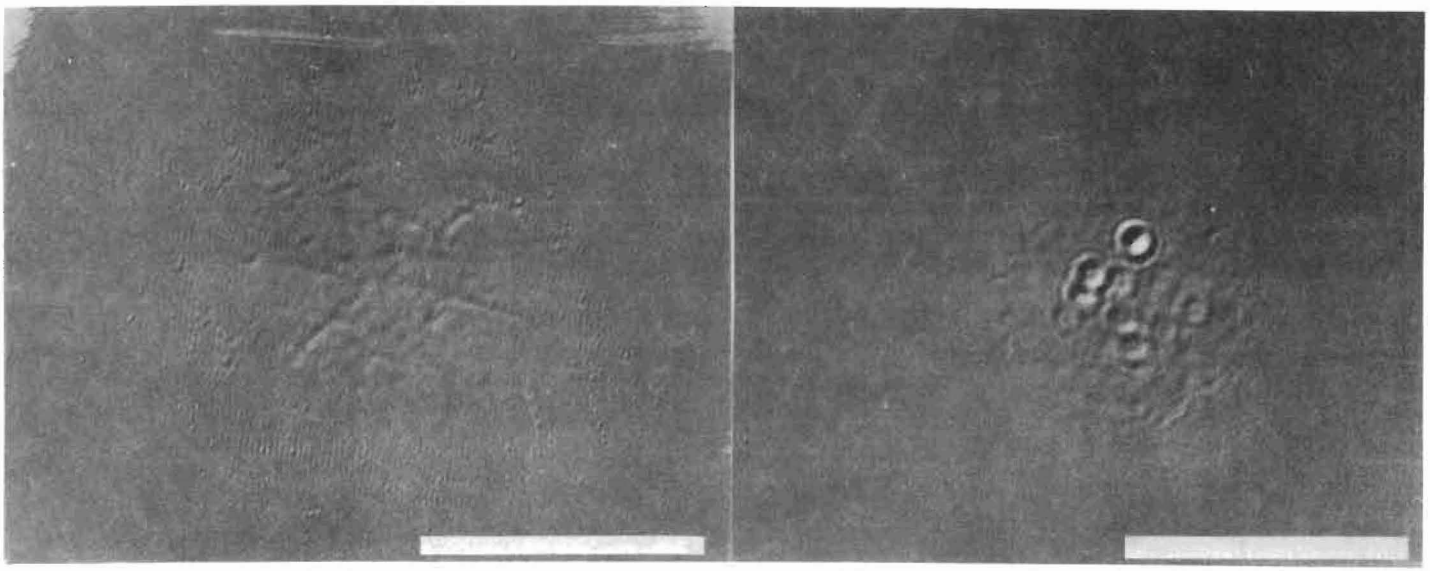


a. Cross section of sample showing contacted evaporation mask.



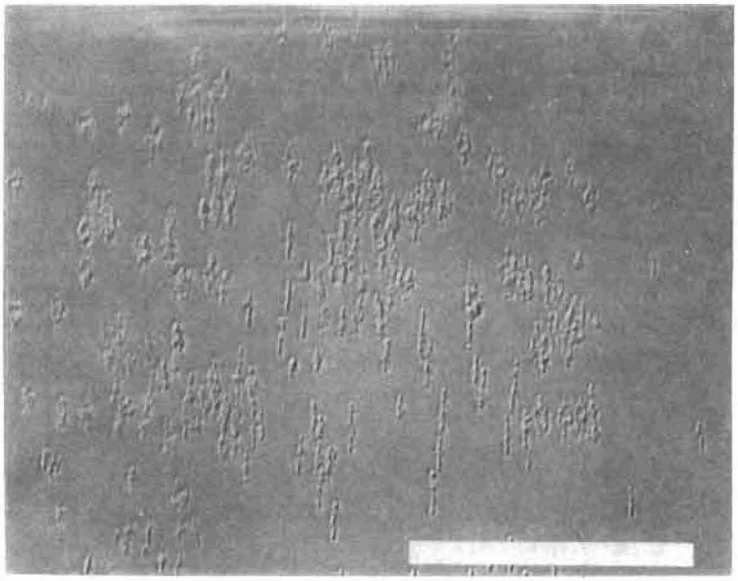
b. Photograph of a sample mounted in a Macor holder with electrodes. Reference laser damage spots are visible on the center electrode.

Figure 1: Photoconductivity samples.



a. Single 1.82 J/cm^2, pulse, near threshold. Bar is 50 μm.

b. Single 2.62 J/cm^2 pulse. Bar is 100 μm.



c. Six pulses, 1.12 J/cm^2 average fluence, charge emission occurred for the last three pulses. Bar is 50 μm.

Figure 2: Nomarski micrographs of damage morphologies on <1,1,1> silicon.

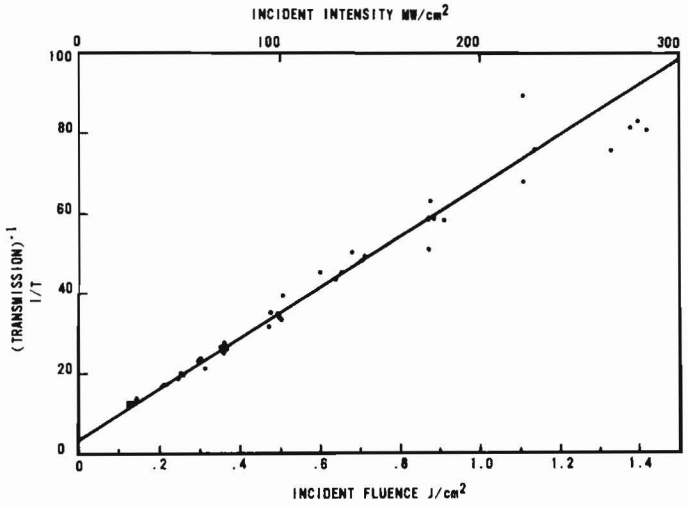


Figure 3: Nonlinear transmission of <1,1,1> silicon.

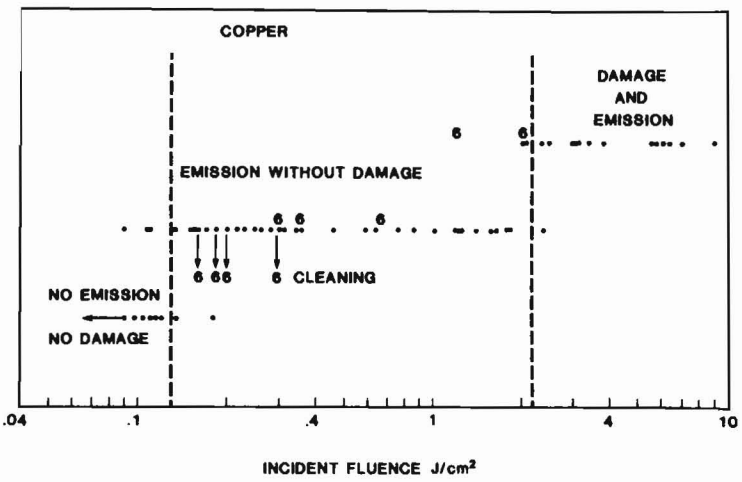


Figure 4: Damage and charge emission statistics for diamond turned OFHC copper mirror. The dots represent single shot events. The sixes represent the results of 6 pulses at the average fluence indicated. Their interpretation is discussed in the text.

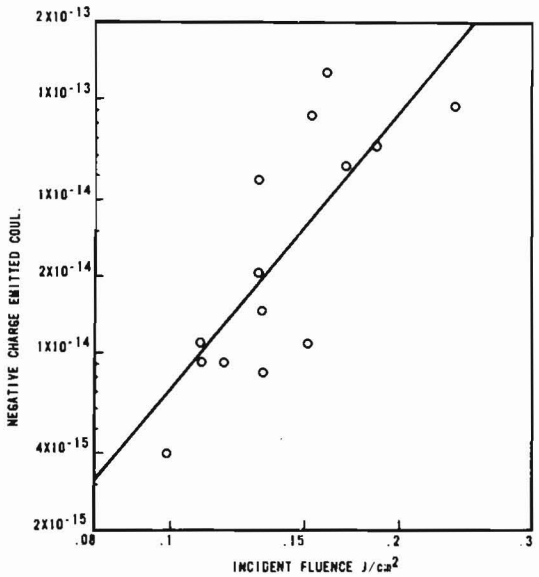
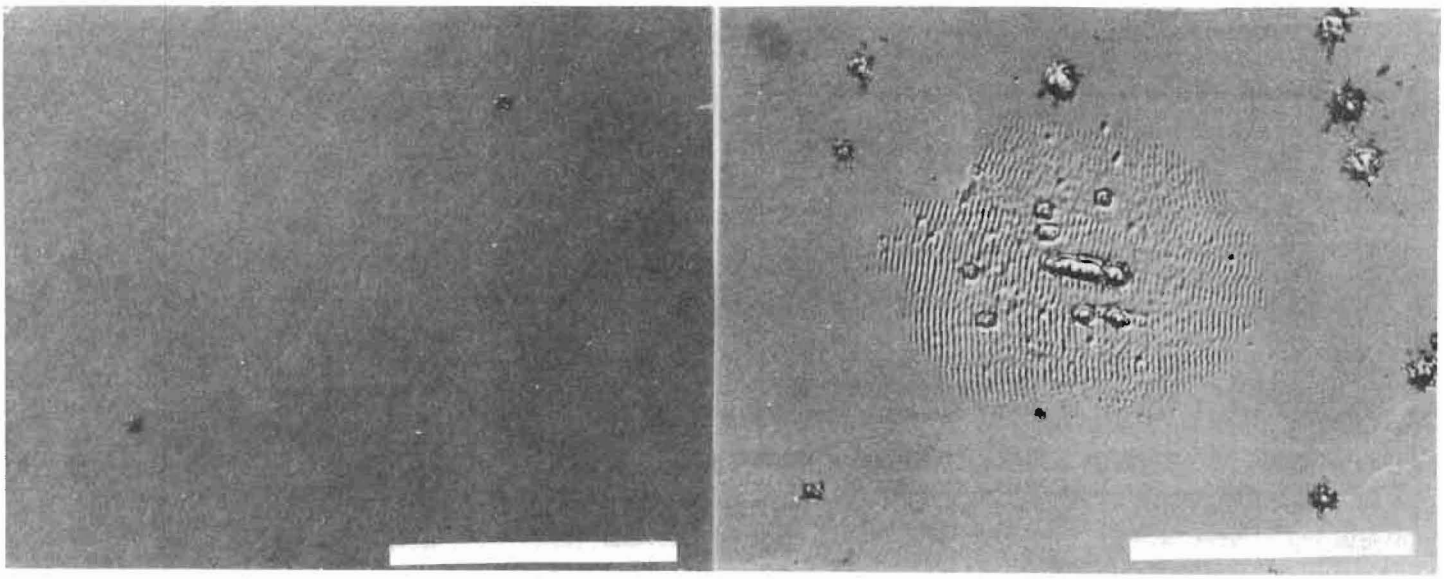


Figure 5: Negative charge emission versus laser fluence for diamond turned copper mirror. Fluence is near the 1-on-1 threshold for charge emission.



a. Single 3.13 J/cm^2 pulse, near threshold, two small damage pits are visible.

b. Single 6.08 J/cm^2 pulse.

Figure 6: Nomarski micrographs of damage morphologies on the diamond turned copper mirror. Bars are 50 μm.

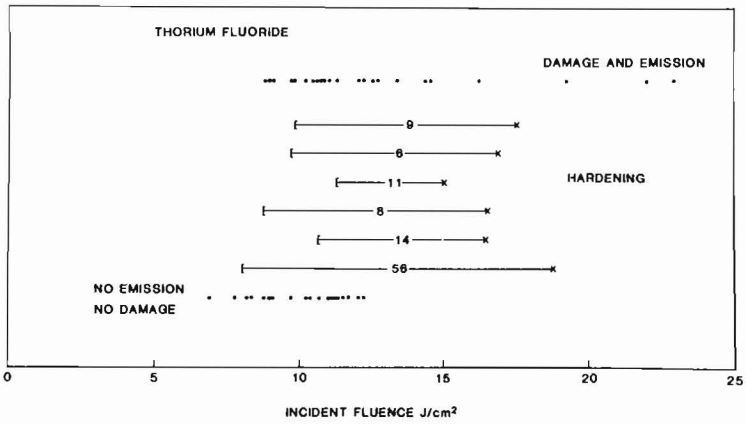


Figure 7: Damage and charge emission statistics for a quarter wave thorium floride coating on fused silica. The dots represent single pulse events while the bracketed lines indicate sequences of pulses of increasing of energy and are discussed in the text.

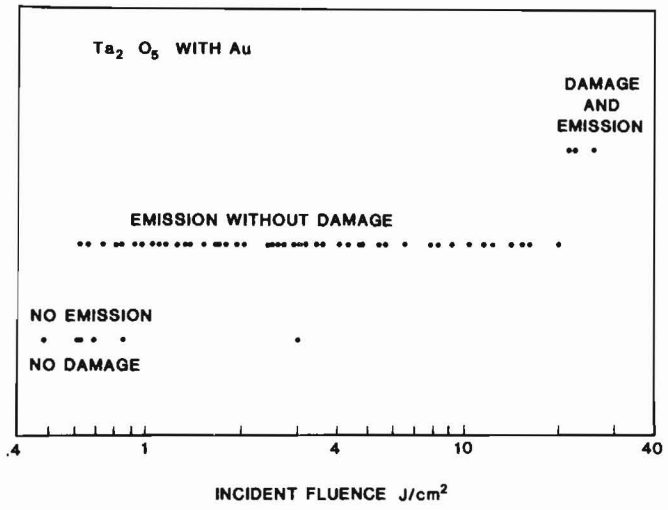


Figure 8: Damage and charge emission statistics for a half wave tantalum oxide film on fused silica with gold photoconductivity electrodes. All points represent single pulse events.

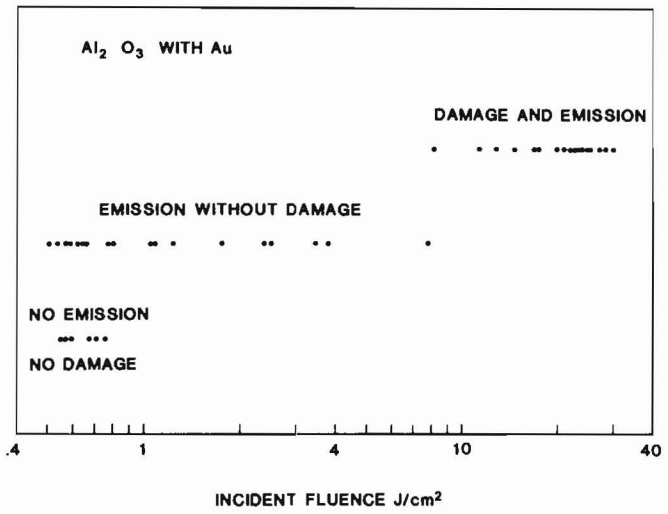
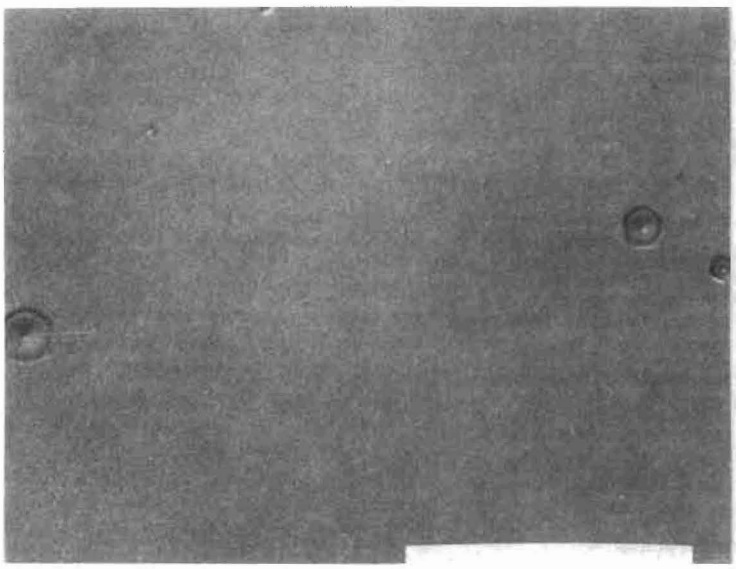
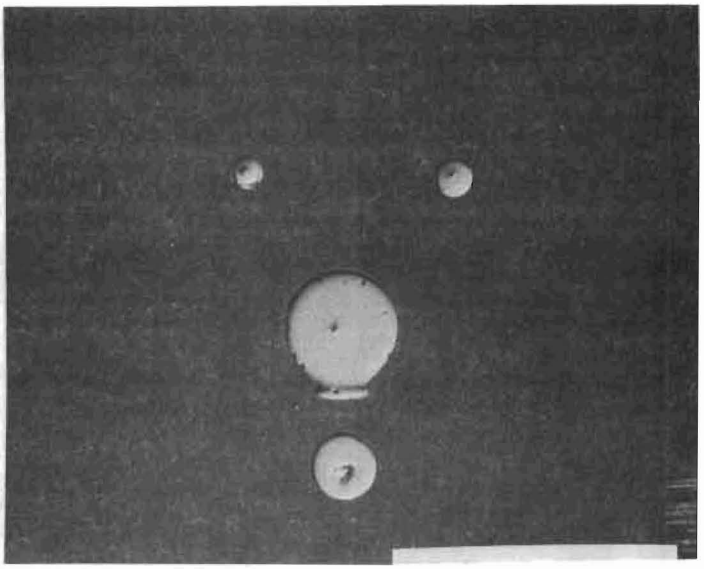


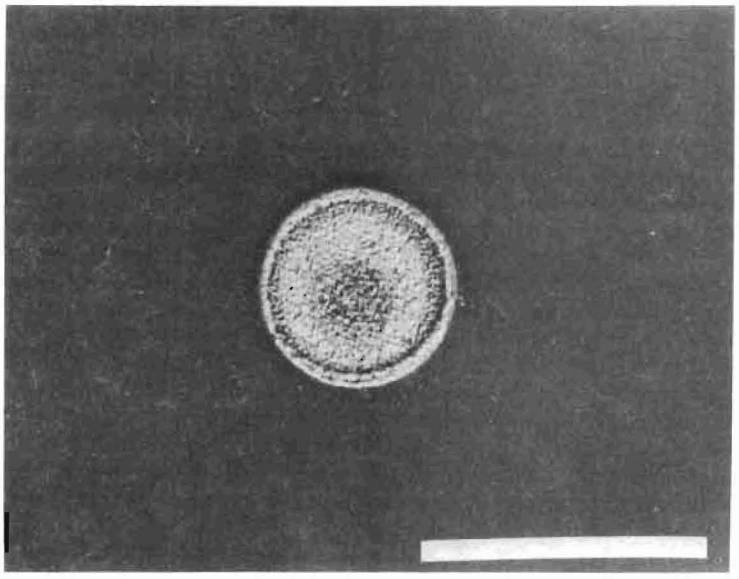
Figure 9: Damage and charge emission statistics for a half wave aluminum oxide film on fused silica with gold photoconductivity electrodes. All points represent single pulse events.



a. Single 14.5 J/cm^2 pulse on the quarter wave thorium fluoride coating. Bar is 50 μm.



b. Single 22.5 J/cm^2 pulse on the half wave tantalum oxide coating with electrodes. Bar is 100 μm.



c. Single 23.3 J/cm^2 pulse on the half wave aluminum oxide coating with electrodes. Bar is 50 μm.

Figure 10: Nomarski micrographs of damage morphologies for the dielectric film samples.

It was suggested that the 3-orders-of-magnitude difference reported in the paper may have resulted from a combination of two-photon absorption and, for the longer pulses, free-carrier absorption arising from the few two-photon-generated carriers. A way to get around this problem is to look for two-photon absorption at very low fluences and then look at varying pulse widths to obtain the free-carrier parameter. A paper describing such an approach for II-VI compounds was given by M. J. Soileau and others at this conference two years ago. The speaker said they had taken some preliminary data using low intensity nanosecond pulses which seemd to show the same larger number found for the other data, but they had used only two pulse lengths. He felt the questioner could very well be correct. However, in response to another question, he pointed out that the observed effect could not be explained in terms of thermally generated free-carrier absorption from uniformly heated silicon even though the wavelength, 1)m, is within the band edge. The heating is 100 to 200°C at most. If nonuniform heating occurred, as suggested by the microscopic evidence, hot spots could appear which melt and potentially influence the nonlinear absorption. With a nanosecond pulse one gets more heating than from a picosecond pulse.

A suggestion was made that the emission observed may have been related to the desorption mechanisms reported by Allen and Porteus. The speaker replied that only for copper was there enough data to relate to the Allen-Porteus experiment. The little data available on the dielectrics suggest that fluroides do not emit and that oxides do. This determination should be followed up to see if the above is a general characteristic of these classes of materials.

In response to another question, he replied that there were too many parameters in the experiment to extract meaningful activation energies. They also were unable to measure the uncoated substrate threshold, which was fused silica.

Manuscript received 2-4-85/sar

Predamage Threshold Electron Emission From Insulator and Semiconductor Surfaces

W. J. Siekhaus, J. H. Kinney, D. Milam
Lawrence Livermore National Laboratory
Livermore, California 94550

Predamage electron emission shows a dependence on fluence, bandgap and wavelength consistent with multiphoton excitation across the bandgap and inconsistent with avalanche ionization and thermionic emission models. The electron emission scales with pulselength as $\tau^{-1/2}$.

Key words: GeO_2, laser damage, multiphoton excitation, predamage electron emission, pulselength scaling, SiO_2, ZnS

1. Introduction

Optically transparent materials exposed to laser irradiation of sufficient intensity suffer irreversible damage, thereby limiting the performance of most high power laser systems. The damage threshold in the bulk depends on its impurity concentration. The threshold for optical surfaces is usually lower, as much as an order of magnitude or more, and is highly dependent on surface preparation. The physical phenomena involved in damage are presently not well understood. [1]

Damage at bare surfaces appears to result from electron avalanche-ionization and subsequent absorption by the created plasma. One has to postulate that the electron avalanche ionization creates a conduction band electron density of $N > 10^{17}$ el/cm^3 in the surface region for damage to occur. [2] Alyassini and Parks [3] estimated from changes in the reflected intensity of a probe beam that 10^{18} el/cm^3 are present in the conduction band at the surface when damage occurs.

In this study we measure the emission of these electrons from surfaces of insulators and semiconductors as a function of laser intensity, wavelength and pulse duration.

The long range objective is to use photoelectron emission as a tool to predict surface damage thresholds and to determine the effect of surface structures and surface composition on damage thresholds.

Laser induced charged particle emission from insulator surfaces has been studied before [see ref. 4 and references therein], but found to be irreproducible. It is our contention that the irreproducibility is a consequence of irreproducible surface conditions created by performing the experiments in vacua with pressures great than 10^{-6} torr.

2. Experimental Procedure

We used equipment and techniques developed at LLNL for rapid and reliable laser-damage threshold measurements. [5] The laser has a wavelength of 1064 nm and a pulse-width variable from 1 ns to 40 ns. Frequency doubling and tripling equipment has been used. Laser pulse energy is measured by calorimeters developed at LLNL. The peak fluence is measured in two ways: (1) A silicon-vidicon system [6] electronically records pulse intensity and computer analysis determined peak fluence within several minutes after exposure. (2) The pulse also exposes a photographic plate, which is later developed, densitometered and analyzed to obtain peak fluence. Agreement between these two measurements in now ± 10%.

The target is held inside a insulated Faraday cup suspended on a precision manipulator in a UHV vacuum system (Figure 1). The openings in a Faraday cup are slits 1/2 inch wide and 1 inch high. The beam diameters is approximately 3 mm. The diameter of the inner Faraday cup is 4 inches. In the experiments reported here no voltage is applied between the target and the Faraday cage. The emitted charge is measured with a Digital Keithley Autoranging Coulombmeter (Model 616). During the laser pulse the ion pump and the ion gauge are switched off to reduce the background of charged particles in the chamber held at pressures lower than 10^{-7} Pa by a Helium Cryopump. An experiment begins by exposing the target to several laser pulses with a fluence 1/4 to 1/2 of the damage threshold until reproducible electron emission is measured. These "surface cleaning" pulses are associated with measurable bursts in the pressure of the vacuum chamber, indicating that laser stimulated desorption of contaminants from the target surface occurs. Re-contamination of the surface thereafter is small since the laser fires approximately every 3 minutes, and only a small fraction of a monolayer would readsorb from the vacuum environment at 10^{-7} Pa during 3 minutes. All measurements are performed on the same precleaned spot unless the

damage threshold is accidentally exceeded. A new spot is then cleaned. The new spot yields the same results, within experimental errors. The data shown in the next section are usually from a number of different sites.

3. Results

1.) Electron emission as a function of Laser Fluence (Pulse length = 1 ns). Figure 2 shows electron emission as a function of fluence for ZnS and SiO_2 for $h\nu$ = 1.16 eV. The slope of the best fit lines is indicated. Figure 3 gives electron emission as a function of laser fluence for $h\nu$ = 3.5 eV for W, ZnS, GeO_2 and SiO_2. Table I summarized the observed functional dependence of electron emission as a function of fluence for two wavelengths and a number of different materials.

2.) Electron emission as a function of pulselength. Figures 4 and 5 depict the electron emission from CdTe as a function of laser fluence for $h\nu$ = 1.16 eV at pulselengths of 1 ns, 9 ns and 40 ns. In Figure 5 the fluences at different pulselengths are scaled according to (pulse length)$^{1/2}$, e.g., the electron emission observed for fluence I is plotted as fluence I/(pulse-length)$^{1/2}$. Figure 6 documents for $h\nu$ = 1.16 eV the electron emission as a function of fluence from ZnS for 1 ns and 20 ns pulselength. In Figure 7 we have plotted for $h\nu$ = 1.16 eV the electron emission from NaCl as a function of fluence for 1 ns and 40 ns pulselength. In Figure 8 the results for 40 ns pulselength have been plotted at a flux scaled by $40^{-1/2}$.

4. Summary

The results of laser induced electron from surfaces emission allow the following conclusions:

1) The electron emission shows a functional variation with fluence up to the damage threshold consistent with a model that assumes that electron emission into the vacuum is controlled by multiphoton excitation across the bandgap (see table 1). The dependence on bandgap and wavelength are inconsistent with a model assuming thermionic electron emission.

2) There is no evidence of an avalanche process as one approaches the threshold for optically visible damage.

3) The electron emission scales with pulselengths for materials with narrow and wide bandgaps as $\tau^{-1/2}$, when τ is the pulselength.

5. Conclusion

Pre-damage electron emission is a reproducible measure of the approach of a surface to the damage threshold. The spatial variation of electron emission will be used in the future to determine which local impurities or local structural variations lead to damage.

6 References

[1] W. L. Smith, "Laser-Induced Breakdown in Optical Materials," Optical Engineering 17, 489 (1978), A. J. Glass, A. H. Guenther, Eds., NBS Special Publication 509.

[2] S. Brawer, "Phenomenological Theory of Laser Induced Damage in Insulators," Phys. Rev. B20, 3422, (1979).

[3] N. Alyassini and J. H. Parks, J. Appl. Phys. 48, 629 (1977).

[4] V. P. Krutyakova and V. N. Smitnov, Sov. Phys. Tech. Phys. 24 (9) Sept. 1979.

[5] D. Milam, "Measurement and Identification of Laser Damage Thresholds in Thin Films," Proceeding of the Society of Photo-Optical Instrumentation Engineers, Vol. 140, Optical Coatings II (1978).

[6] W. L. Smith, A. J. DeGroot, and M. T. Weber, "Silicon Vidicon Systems for Measuring Laser Intensity Profiles," Appl. Opt. 17, 3938 (1978).

Work performed under the auspices of the U. S. Department of Energy by the Lawrence Livermore National Laboratory under contract number W-7405-ENG-48.

EXPERIMENTAL EQUIPMENT

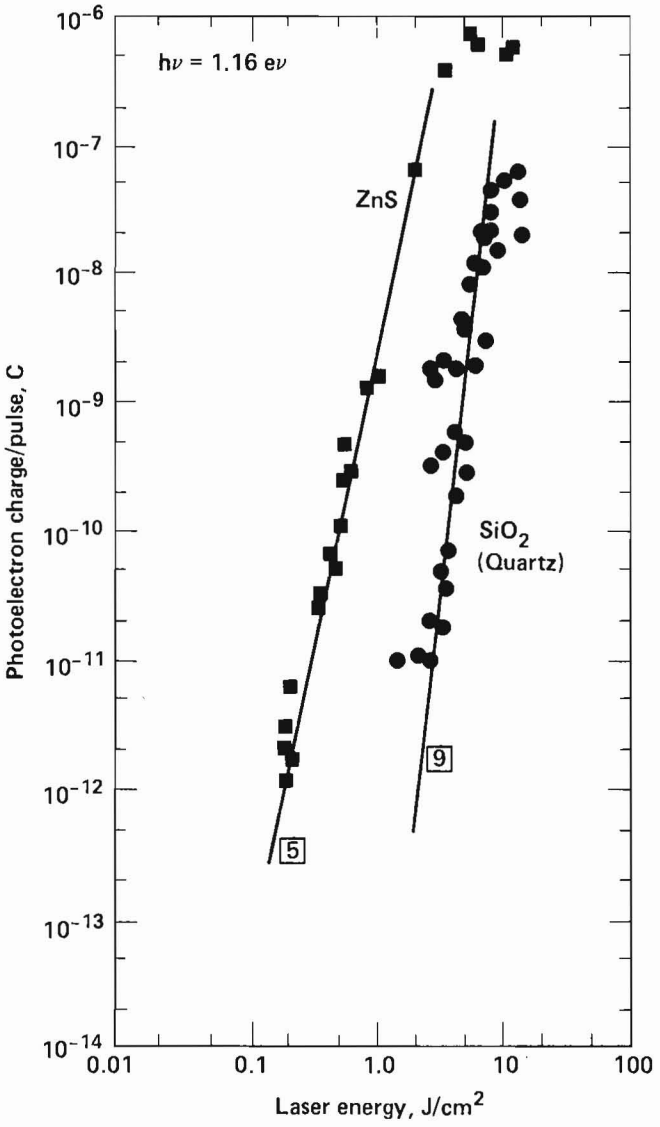


Figure 2. Electron emission as a function of fluence. hν = 1.16 eV

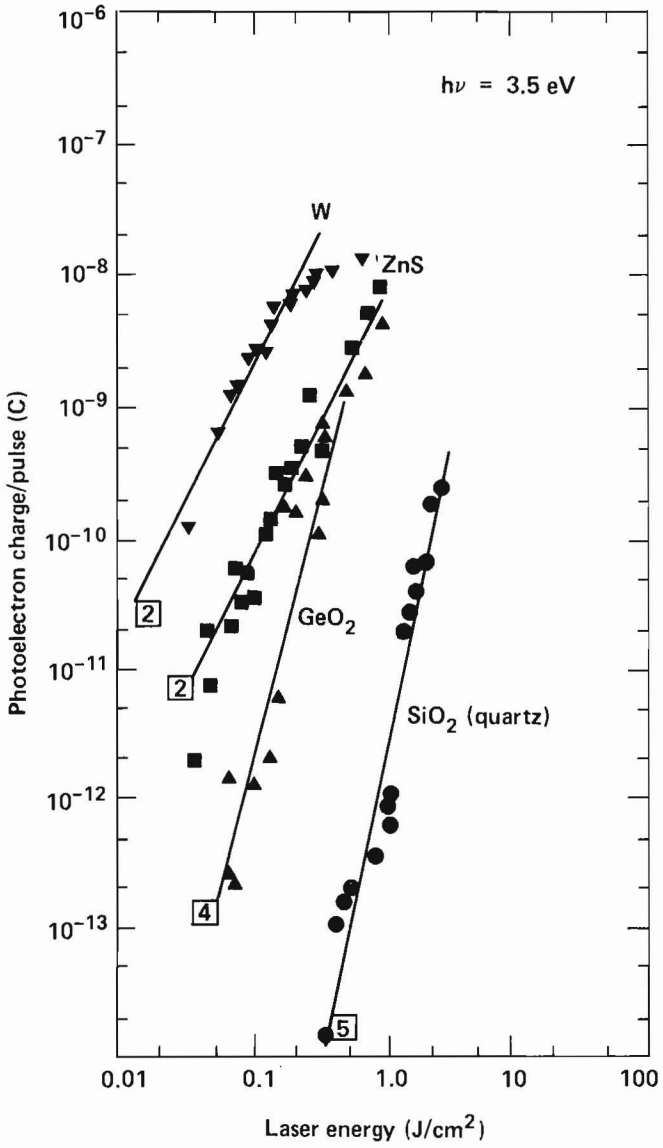


Figure 3. Electron emission as a function of fluence. hν = 3.5 eV

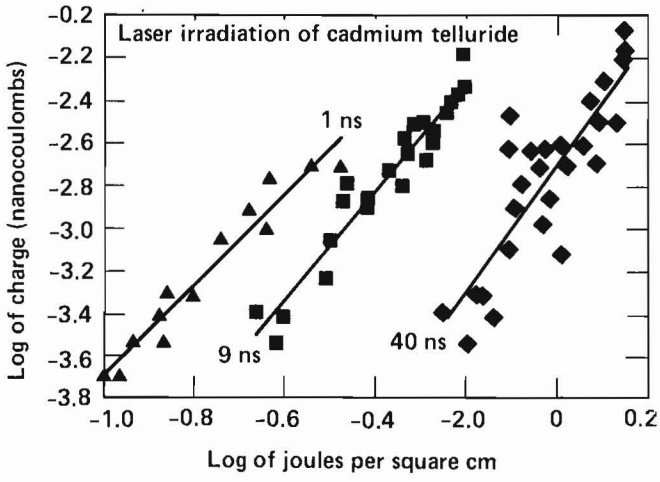


Figure 4. Electron emission from CdTe as a function of fluence. Pulse length 1 ns, 9 ns, 40 ns

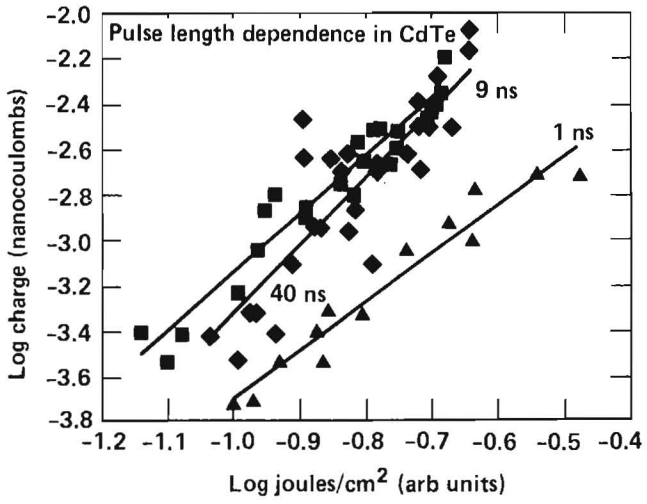


Figure 5. Electron emission from CdTe as a function of fluence. Pulse length 1 ns, 9 ns, 40 ns. The abscissa is scaled by (pulse length)$^{-1/2}$ for each pulse length.

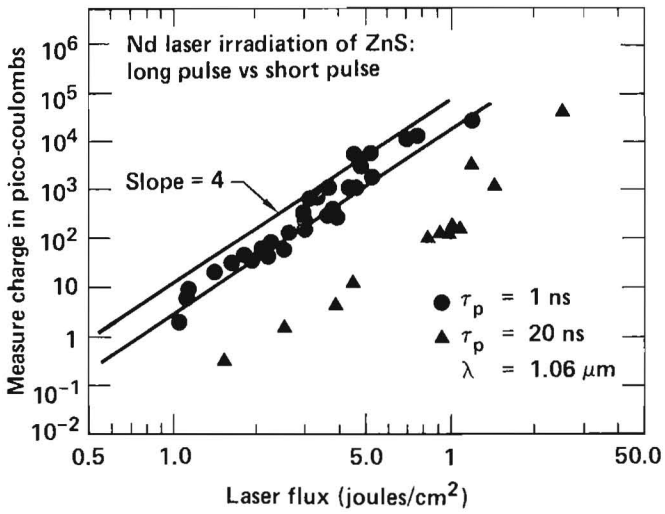


Figure 6. Electron emission from ZnS as a function of fluence. Pulse length 1 ns and 40 ns.

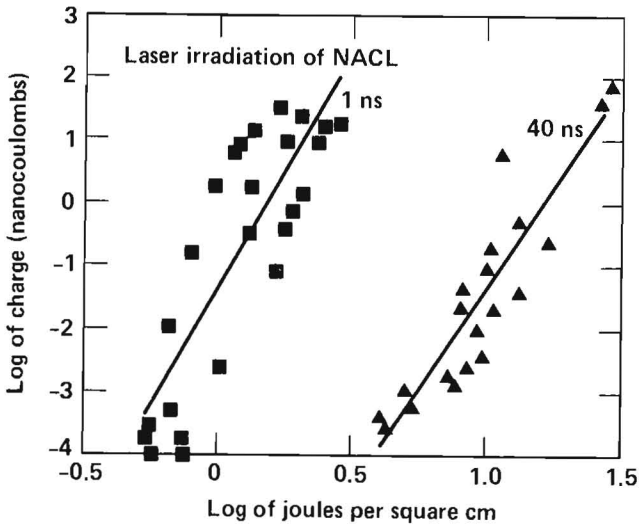


Figure 7. Electron emission from NaCl as a function of fluence. Pulse length 1 ns and 40 ns.

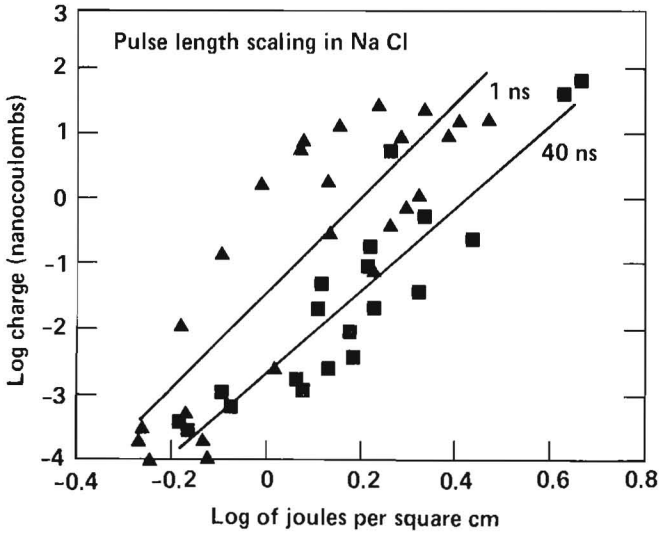


Figure 8. Electron emission from NaCl as a function of fluence. Pulse length 1 ns and 40 ns. The abscissa is scaled by (pulse length)$^{-1/2}$ for the 40 ns pulse length experiments.

Table 1

Material	E_{gap} (eV)	E_{work} (eV)	E_{γ}	$N^*_{predicted}$	$N^*_{observed}$
CdTe	1.5	6.0	1.16	2	2
NaCl	8.75	4.2	1.16	8	8-9
SiO_2	8-8.4	5.0	1.16 3.5	7-8 3	9 5
ZnS	3.88	5.5	1.16 3.5	4 2	4-5 2

*Predicted slope from a simple, multiphoton model: $(E) = AI^N$

A member of the audience agreed with the speaker that a very good vacuum is needed for emission experiments but pointed out that one cannot assume a negative electron is emitted. It may be a negative ion, as was demonstrated by Schmidt of the University of Rochester in 1975 for emission from sodium chloride. Also, charge emission from semiconductor surfaces cannot be compared with those from dielectrics. The differences relate to point defects production; one cannot draw charges out of a sodium chloride surface without seriously affecting the surrounding lattice. In this case, entirely different effects than electron emission can be seen. The speaker agreed that the matter should be considered further.

Another member of the audience reiterated that semiconductors and insulators are different, pointing out that in observations on silicon surfaces they saw equal amounts of positive and negative charge, which appear to obey a multi-photon curve but can also be fit to a thermal emission curve. The morphology and microscopy verify that there were hot, molten areas on the surface.

Manuscript received 1-9-84/sar

Laser Induced Damage of a Thin Film With an Absorbing Inclusion: Thermal Considerations of Substrates and Absorption Profiles

Michael R. Lange and John K. McIver

Institute for Modern Optics
University of New Mexico
Albuquerque, New Mexico 87131

and

Arthur H. Guenther

Air Force Weapons Laboratory
Kirtland Air Force Base, New Mexico 87115

A study of pulsed laser induced damage to thin films is conducted within the context of the impurity-dominated damage model in which the thin film component of the model is emphasized. In this case, a cylindrical impurity is embedded in a single thin film layer between a free surface and a substrate. The effect of the substrate is studied by varying its thermal properties with respect to those of the thin film. The nonuniform distribution of radiation in the film is incorporated into the model by assuming that the absorption is proportional to the standing wave intensity pattern of the field. These results are compared to the results found in previous studies of impurities embedded in infinite mediums.

Key Words: cylindrical inclusions, laser induced damage; standing waves; substrates; thermal properties; thin films.

1. Introduction

Recent studies have given credence to the general absorbing impurity model of pulsed laser induced damage in optical thin films [1,2]. One gross feature in these models that has received inadequate treatment is the thin film aspect of the problem. The incident laser pulse has been assumed sufficiently short such that no significant effect could be produced by the thin film aspect of the problem including the effect of an underlying substrate. The model has conveniently treated the interaction as having taken place in an infinite medium of specified material properties.

The work presented herein, is a study of a cylindrical impurity embedded in a single layer thin film with an underlying substrate whose thermal character ranges from non-conducting to highly conducting. The reason for choosing a cylindrical impurity is three fold; cylindrical or columnar-like impurities in thin films can occur [3,4]; the effect of the substrate is maximized (providing an upper bound) by having a large area in contact with it (as opposed to a point contact such as with a sphere), and finally because it affords a mathematical simplicity through the matching of boundary conditions.

In addition, absorption profiles are investigated in the film by allowing the absorption to be proportional to the local intensities. It is assumed that standing wave intensity distributions occur in the film.

As a result of the analysis it is concluded that the geometry of a thin film along with the shape of the particle is not significant as long as the volume to cross section ratio of the impurity is the same as that of a sphere; that a substrate with a high thermal conductivity can have a significant effect as a thermal sink for thin films and long pulses; and that the absorption distribution can be an important consideration for high intensity short pulse irradiations.

The terms "thin films, short pulses ..., etc." are those that are thin, short, etc. with respect to the scale of diffusivities in (cm^2/s) of the materials involved.

2. Model

Aspects of the basic model are shown in figure 1. A cylindrical impurity of radius 'a' is embedded in a thin film, thickness ℓ, with different thermal properties. The diameter of the inclusion is assumed to be much smaller than the spot size of the laser illuminating the sample so that the impurity sees a uniform intensity in the radial direction. The film and inclusion are in "perfect" thermal contact with an underlying substrate. The thermal conductivity K(J/cm-s-K) and thermal diffusivity D(cm^2/s) are labled by a subscript i, h, s refering to the inclusion, film (host) and substrate respectively. The thermal properties of the system along with the absorption cross section are taken to be independent of temperature. The inclusion is the only part of the system that absorbs incident radiation. Furthermore, the absorption cross section is taken to be equal to the geometric cross section (πa^2) of the cylindrical inclusion. As was the case for the previously studied spherical model, damage is assumed to occur when the surface of the impurity reaches some critical material dependent temperature T_c.

Exact solutions are found for the extreme cases of a non-conducting substrate and an infinitely conducting substrate with either uniform or standing wave absorption distributions. These are derived through a combination of integral (spatial) transform and Laplace (temporal) transform technique. An approximate solution is also found for the important realistic case of a finite valued thermally conducting substrate. All of these cases are compared with numerical finite element analysis for consistency.

From the exact solutions of the diffusion equation one finds a temperature field as a function of the incident intensity. This is inverted to solve for the incident intensity times pulse length E(J/cm^2) at which damage ensues.

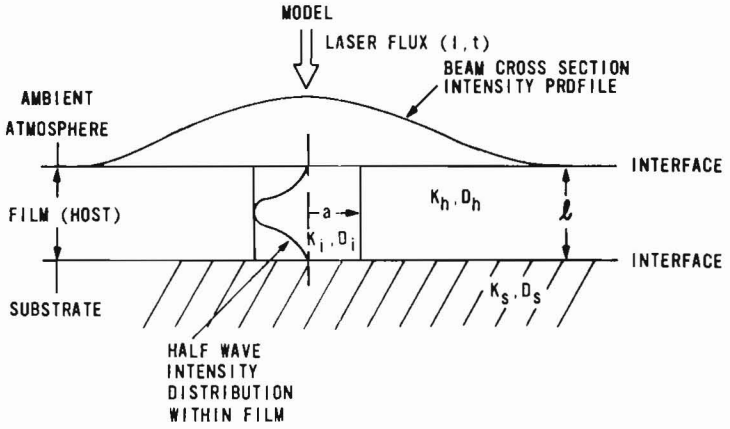


Figure 1. A description of the general model is shown here. There is a cylindrical impurity of radius "a" embedded in a thin film of thickness (interfaced with a substrate. The thermal properties of the impurity, host and substrate and subscripted with i, h, and s, respectively. The diameter of the inclusion is assumed to be much smaller than the spot size of the laser illuminating the sample. Radiation is absorbed in the inclusion and the diffusion equation governs the temperature field that results.

3. Results

Once the solutions for the damage threshold in (J/cm^2) for a given pulse length are known, the thin film character and substrate effects in extreme limiting cases are determined. In order to isolate the substrate effects from radial diffusion the limit as $a \to \infty$ is taken. Expressions for the damage threshold scaling are found to be:

$$E \propto \frac{T_c t K_i}{\frac{2D_i t}{\ell} + \frac{\ell}{4\pi^2}\left(1 - \mathrm{Exp}\left[-\left(\frac{2\pi}{\ell}\right)^2 D_i t\right]\right)} \tag{1}$$

and furthermore as $t \to 0$

$$E \propto \frac{T_c \ell K_i}{D_i} \tag{2}$$

For the long pulse limit, that is $t >> \ell^2/(4D_i\pi^2)$ we find

$$E \propto \frac{T_c t K_i}{\frac{2D_i t}{\ell} + \frac{\ell}{4\pi^2}} \tag{3}$$

By comparison, for a substrate which is infinitely conducting for which $t \to 0$,

$$E \propto \frac{T_c \ell K_i}{D_i} \tag{4}$$

And finally, for the long pulse limit with an infinitely conducting substrate, $t >> 4\ell^2/(9D_i\pi^2)$,

$$E \propto \frac{T_c t K_i}{\ell} \tag{5}$$

The important scaling trends of the damage threshold are: the linear dependence upon temperature T_c, the linear dependence upon the thickness of the film ℓ for very shortpulse lengths ($t \to 0$) the inverse thickness dependence for long pulses with an infinitely conducting substrate and the various pulse length dependences (e.g. none as $t \to 0$ and linear in t for long pulse with infinitely conducting substrates). Some of these dependences begin to appear in figure 2 for the range of pulse lengths plotted. For example we begin to see an inverted thickness dependence for long pulses and a highly conducting substrate.

It should be noted that these scalings are in extreme limits and are not intended to be useful design relations. For example, no host dependence appears because of the limit ($a \to \infty$). These relations are intended to give insight into the effects or lack of effects of thin film/substrate system parameters.

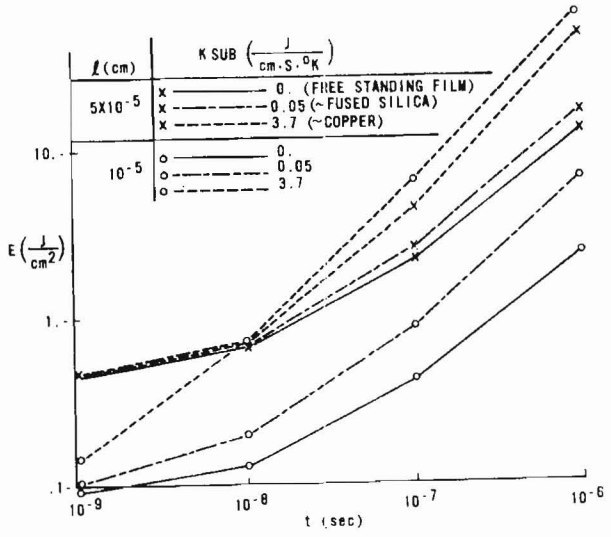


Figure 2. The plot shown here is damage threshold "E" v.s. pulse length for two different film thicknesses and three different substrate conductivities.

The general thermal parameter dependences of the problem due to radial heat diffusion is determined by insulating the substrate and varying the host film and impurity thermal conductivities. As with previous spherical impurity studies [5], the damage threshold increases with increasing host thermal conductivity. Also, damage threshold is essentually insensitive to the thermal conductivity of the inclusion.

A more interesting exercise is to set $\ell \doteq (4/3)a$ so that the length of the inclusion varies as the radius of the inclusion. What this does is to force the volume to be proportional to a^3 and the cross section to be proportional to a^2. When this is done a minimum value of the damage threshold is found (i.e. a radius which damages easiest) and scaling laws for host conductivity and pulse length are found much like to ones predicted for spherical impurity particles [5]. The end result of this analysis is that the details of geometry are not that important to the thermal aspects of the problem as long as the volume of the impurity is proportional to some mean radius cubed and the absorption cross section is proportional to some mean radius squared. So, if the impurities are irregularly shaped particles, as is probably the case, then the thermal scaling laws derived from an ideal geometry model should still apply.

The final aspect of the problem studied has the effect of the intensity distribution within the film. It is easily seen from figure 3 that high intensity I(J/cm -s) short pulses can lead to very high temperature gradients. If the intensity is high enough (I_3 in fig. 3) with a $\sin^2$ half wave, and the pulse length short enough, very high temperatures can be reached in the center of the film while the boundaries remain nearly at their initial value. In this case a substrate will have very little effect regardless of how highly conducting it may be.

Again, the descriptors short, long, ect. refer to a comparison with scales determined by the diffusivities D involved. For example: the diffusion length $\delta = \sqrt{D_i t}$ for I_3 is approximately 1/40 the thickness of the film. At this depth into the film the temperature is still quite small. Thus, this rough measure of the range of effect of one point upon another indicates that the boundary temperature will not be effected significantly. On the other hand if we decrease the thickness of the film by a factor of ten with the same pulse length, δ is approximately 1/4 of the film thickness. Refering to figure 4 we see a significant effect on the temperature profile of substrates with various conductivities.

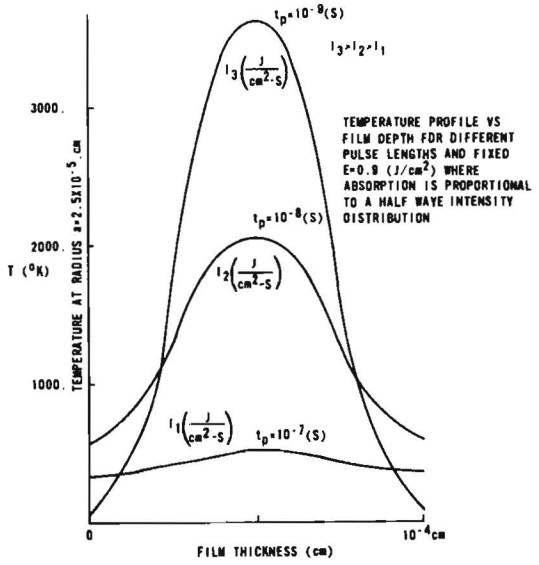


Figure 3. This is a plot of temperature v.s. film depth when the absorbed energy is proportional to a standing wave. Three different Intensities are shown. The same total energy is deposited for all three (i.e. It = Constant).

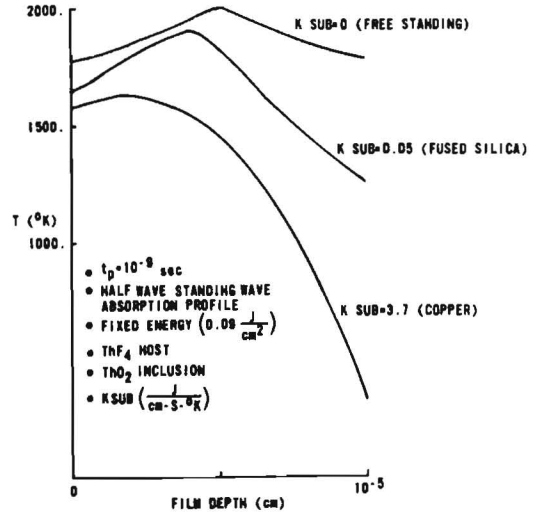


Figure 4. This is a plot of temperature v.s. film depth when the absorbed energy is proportional to a standing wave. The effect of three different substrate thermal conductivities are plotted.

If, instead of a half wave intensity distribution, we have a wave such that the maximum intensity is at the interface with the film and substrate, there would be a considerable effect for good conducting substrates at much smaller δ parameters.

4. Conclusion

To understand the significance of the various effects addressed in this paper, the important aspects of damage mechanisms must be determined. For example: in figure 4, for the parameters given, the maximum temperature attained can be decreased by adding higher conducting substrates. So, if a critical temperature maximum in the impurity or at the impurity surface is the criterion for damage, the damage threshold has been increased. However, the temperature gradient has been increased significantly. So, if mechanical stress due to a temperature gradient in the impurity is the dominant factor, the damage threshold may have been decreased by using a substrate with higher conductivity. It should also be noted that a substrate of higher conductivity decreases the gradient with in the substrate.

For high intensity and short pulses the substrate may not play any significant role. This situation could occur if the absorption is proportional to a standing half wave or if isolated absorption occurs within the film. For optical frequencies and standard thin film materials the absorber cannot be too isolated. Both experimental and theoretical evidence [2] indicates that impurity dominated damage occurs for particles on the order of the film thickness. However, a spherical particle with a diameter equal to the film thickness is only in point contact with a substrate and therefore somewhat isolated. It should be safe to assume that if the diffusion length $\delta << \ell$, the film thickness, and substrate can not play a significant role. With the recent trends towards repetitively pulsed lasers, though, this would not be the case.

Some of the effects mentioned above, such as intensity distributions due to various fractional wave length films, film thickness variation for fixed half wave, or other standing wave patterns and pulse length dependence may be observed in the experimental data of Walker et al. [1]. This model is too simple to claim, an unambiguous or even an adequate explanation. It merely indicates that these considerations should be kept in mind.

In Walker's data [1] the dependence upon film thickness is clear. If for example only half wave films are compared, then as the film thickness decreases so does the damage threshold. This may be crudely thought of as the effect of depositing some amount of energy in a smaller region.

On the other hand, as the film decreases in thickness for a fixed wave length, the damage threshold increases. This process both changes the distribution of the standing wave and decreases the region that is absorbing. All evidence tends to indicate that if the impurity can be restricted to a size that is small with respect to the wavelength, the damage threshold increases. As mentioned previously, this could also be due in part to the fact that for a particle that is small compared to the wavelength, the absorption is probably uniform and does not have large thermal gradients as shown in figure 3.

Perhaps the more important conclusion of this work is that the specific details of the shape of the impurity are not important to the thermal diffusion aspect of the problem. This applies as long as the volume, and therefore the heat containment, scales as some mean radius cubed, and the absorption cross section (a strongly absorbing impurity [2],) scales as that radius squared.

5. References

[1] T. W. Walker, A. H. Guenther and P. E. Nielsen, "Pulsed Laser-Induced Damage to Thin-Film Optical Coatings", IEEE J. Quant. Electron. 17 (10); 1981 October.

[2] M. R. Lange, J. K. McIver and A. H. Guenther, "Laser Damange Threshold Predictions Based on the Effects of Thermal and Optical Properties Employing a Spherical Impurity Model", NBS Spec. Pub. (This Edition); 1983.

[3] Karl Guenther, "Nodular Defects in Dielectric Multilayers and Thick Single Layers, Appl. Opt. 20 (6); 1034-1038; 1981.

[4] H. Angus McLeon, "Microstructure of Optical Thin Films", SPIE 325; 21-28; 1982.

[5] M. R. Lange, J. K. McIver and A. H. Guenther, "Pulsed Laser Induced Damage of an Optical Material With a Spherical Inclusions: Influence of the Thermal Properties of the Materials", Eds., H. E. Bennett, A. H. Guenther, D. Milam, B. E. Newnam; NBS Spec. Pub. 669; 380-386; 1982.

Manuscript received 1-9-84/sar

Laser Damage Threshold Predictions Based on the Effects of Thermal and Optical Properties Employing a Spherical Impurity Model

Michael R. Lange and John K. McIver

Institute for Modern Optics
University of New Mexico
Albuquerque, New Mexico 87131

and

Arthur H. Guenther

Air Force Weapons Laboratory
Kirtland Air Force Base, New Mexico 87115

The influence of the thermal and optical properties of thin films on the damage threshold for pulsed laser induced damage is studied via the spherical impurity damage model. A previous study employing the geometric cross section of the impurity as the absorption cross section of the incident laser predicted several scaling laws. Those scaling laws gave the damage threshold as a function of the laser pulse parameters along with the thermal properties of the thin film and impurity. That model neglected the effect of the optical properties of the thin film and impurity and the wave nature of the incident laser. These are incorporated in the present study by utilization of Mie scattering theory resulting in somewhat modified scaling laws. The absorption cross section results from Mie theory are presented and discussed along with a comparison of the scaling laws with each other and with experimental data. No simple scaling laws for the optical properties are apparent and, as such, a numerical study of these are conducted and the trends suggested by the analysis are compared with experimental observation.

Keywords: absorption cross section; laser induced damage; Mie theory; spherical inclusions; thermal properties.

1. Introduction

The damage of an optical thin film by short-pulse laser irradiation can be considered as due to a combination of three physical processes. These are the absorption of radiant energy, the heating of the impurities and adjacent film, and the thermo-mechanical response of the film/substrate system. Of course, these processes do not occur independently. All take place during and to some extent after the laser pulse. The complete process of absorption depends strongly not only upon the optical properties, but as well on the temperature and state of the materials involved. Yet, because the purpose of many damage studies is to determine the physical process whose onset guarantees or at least precedes material damage, investigation of isolated mechanism can be of great assistance in unraveling the role of material and design variables in the overall intricate interaction/response scenario.

The three most frequently proposed models that are used to describe the damage mechanisms of thin films are avalanche ionization [1], multiphoton ionization [2] and enhanced absorption by impurities embedded in the thin film [3-5], as well as a combination of two or more of them [6]. Because of gross uncertainties in the many parameters that are employed in these theories, none can be relied upon to make an accurate prediction of absolute damage thresholds. For example, multiphoton and avalanche ionization depend strongly on the band structure of the material; whereas the impurity model requires the knowledge of the size, type, shape, and distribution of the inclusions. These difficulties require that the comparison of these models with experiments be on the basis of their ability to predict the variation of the damage threshold with easily controlled and measurable experimental and material parameters.

In this paper, the emphasis will be on the impurity model since it seems to be the most widely accepted at this time [7,8]. A study of the influence of the thermal and optical properties of the host and impurity on the damage threshold is thus most suitable. In what is to follow, an analysis of the heat conduction problem is formulated and solved exactly in terms of an integral for the case

of a small absorbing sphere embedded in a dielectric matrix. Since the size of the inclusion is generally limited by the thickness of the optical thin film (usually less than one wavelength in optical thickness), Mie scattering is used as the origin for the absorption cross section. Results of the numerical studies of the solution are then presented. Finally, an analytical expression for the damage threshold is derived that is valid when the product of the thermal diffusivity and laser pulse duration is large in comparison to the square of the radius of the impurity. The latter part of this work compares the damage threshold predicted by this model with available experimental data. The article ends with a summary of the sensitivity of the damage threshold to the thermal and optical properties of the inclusion and host. Some of the limitations of the proposed model are also presented.

2. Theory

The model most frequently employed in the study of impurity-dominated damage starts with a spherical, absorbing particle embedded in a generally nonabsorbing host [9]. Damage is assumed to occur when the surface of the impurity reaches a designated critical temperature. In reality, the damage threshold may not be sensitive to the absolute temperature since the rate of change of temperature with respect to time is extremely large. What is important is that whatever temperature is chosen be material dependent (e.g.. its melting point).

The temperature (T) as a function of position (r) from the center of the impurity and time (t) is determined by the equation:

$$\frac{1}{D_i}\frac{\partial T_i}{\partial t} = \frac{1}{r^2}\frac{\partial}{\partial r}\left(r^2\frac{\partial T_i}{\partial r}\right) + \frac{A}{K_i} \qquad 0 \leqslant r < a \tag{1}$$

$$\frac{1}{D_h}\frac{\partial T_h}{\partial t} = \frac{1}{r^2}\frac{\partial}{\partial r}\left(r^2\frac{\partial T_h}{\partial r}\right) \qquad r > a \tag{2}$$

$$T_i(r) = T_h(r) = 0 \qquad t = 0 \tag{3}$$

where D and K are respectively the thermal diffusivity in cm^2/s and thermal conductivity in $J/(cm\text{-}s\text{-}K)$, the subscripts i and h refer to the inclusion and the host, A is the source term in $J/(cm^3 s)$, and "a" is the radius of the impurity in cm. From the equations, it is evident that absorption occurs solely in the impurity. The source term can be rewritten in terms of the incident laser intensity (I in W/cm^2) and the absorption cross section (Q in cm^2) as:

$$A = \frac{3QI}{4\pi a^3} \qquad 0 < t < t_\ell$$

$$A = 0 \qquad t > t_\ell \tag{4}$$

where t_ℓ is the duration of the laser pulse.

Because there is no experimental data to assess the degree of thermal contact between the host and inclusion (i.e., the heat transfer coefficient), ideal boundary conditions are assumed: i.e.,

$$T_i = T_h$$

$$k_i \frac{dT_i}{dr} = k_h \frac{dT_h}{dr} \quad \text{at} \quad r = a \tag{5}$$

The exact solution to eq (1-3) with boundary condition (5) was obtained by Goldenberg and Tranter [10]. Their result is:

$$T = \frac{3QI}{4\pi k_i a}\left\{\frac{1}{3}\frac{k_i}{k_h} + \frac{1}{6}\left(1 - \frac{r^2}{a^2}\right) - \frac{2ab}{r\pi}\int_0^\infty e^{\frac{-y^2 t}{\gamma}} \frac{(\sin y - y\cos y)\sin(r\frac{y}{a})\,dy}{y^2[(c\sin y - y\cos y)^2 + b^2y^2\sin^2 y]}\right\} \tag{6}$$

where use has been made of eq (4). The constants in the expression are:

$$\gamma = \frac{a^2}{D_i}, \quad c = 1 - \frac{k_h}{k_i}, \quad \text{and} \quad b = (k_h/k_i)(D_i/D_h)^{1/2}$$

This solution was based upon the assumption that the absorption cross section along with the thermal constants are independent of T.

Because an optical thin film layer is typically an optical wavelength or less in thickness, the radius of an inclusion will in most cases be a half-wave-length or less. For these sized particles, the adsorption cross section is derivable from Mie scattering theory [11,12] which depends on the complex index of refraction $\tilde{n}_i$ and the radius of the inclusion as well as the nondimensional size parameter

$$q \equiv 2\pi a/\lambda_h \tag{7}$$

where

$$\lambda_h = \lambda_0/n_h \tag{8}$$

is the wavelength of the radiation in the host. Here, λ_0 is the wavelength of the radiation in free space and n_h is the real part of the index of refraction of the host. Inasmuch as $n_h > 1$, the optical properties of the host influence the absorption of radiation through the wavelength eq (8) seen by the inclusion and therefore through the size parameter eq (7).

Using eq (6) and the well known expression for Mie scattering [11,12], the incident laser intensity I that must be applied for a time t_ℓ in order to raise a point at r to a temperature T can

be determined. If T is chosen as the critical temperature T_c at which damage first occurs, then I is the damage threshold for the point at r. In the remainder of this discussion, our attention will be confined to a shell at r = a. Likewise, in keeping with common usage, damage threshold will from now on refer to the quantity It ≡ E in J/cm^2, realizing one should always specify the temporal aspect of the incident radiation.

3. Results

Because of the complexity of the expression for the Mie absorption cross section and the fact that no analytical expression is known to exist for the integral in eq (6), numerical methods must be used to evaluate the damage threshold. In table 1, the numerical values of the parameters that were used in this study are presented. They are chosen so as to correspond approximately to the realistic case of a ThO_2 impurity buried in a ThF_4 host.

Table 1. Quantities employed in the analysis of a ThO_2, impurity (subscript i) embedded in a ThF_4 host (subscript h).

Thermal Properties		Reference
K_h	0.1 (J/cm-s-K)	(19)
K_i	0.142 (J/cm-s-K)	(22)
D_h	0.05 (cm /s)	(19)
D_i	0.0594 (cm /s)	(22)
Optical Properties		
n_h	1.6	(17)
$\tilde{n}_i$	1.9 - .005i	(17)
Laser		
t_ℓ	10^{-8} (s)	
λ_0	10^{-4} (cm)	
Damage Condition		
T_c	2000 K	

Figures 1, 2, and 3 show the sensitivity of the damage threshold to the laser pulse width, the thermal conductivity of the host, and the thermal conductivity of the impurity for different film thicknesses. In these cases, the minimum damage threshold has been chosen to correspond to the thickness of the films. This is because Mie theory, with optical properties corresponding to assumed impurities, places the minimum damage threshold generally outside of the film thickness. These plots exhibit some interesting trends. For example, as "a" decreases, figures 1 and 2 show that as $a \to 0$, $\alpha \to 1$ for

$$E\alpha(K_h t_\ell)^\alpha \tag{9}$$

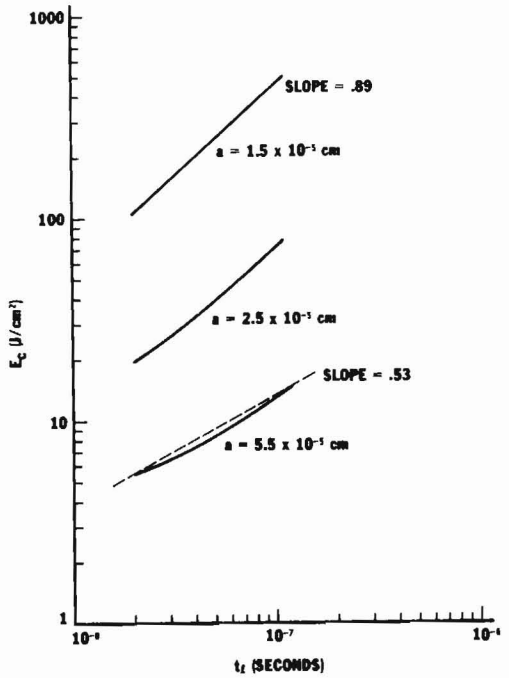


Figure 1. Damage threshold as a function of pulse duration for different sized inclusions. The values of the parameters associated with impurity/host combinations are listed in table 1.

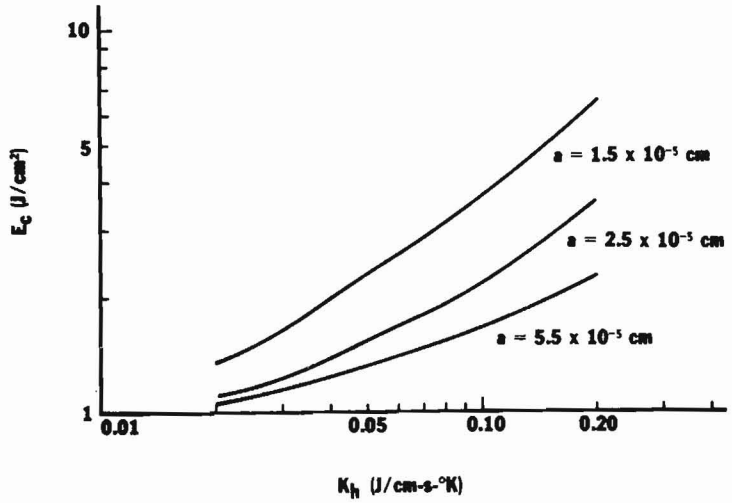


Figure 2. Damage threshold as a function of host conductivity for various radii of the impurity. The ratios of the conductivity to the diffusivity is held constant ($K_h/D_h = 2$).

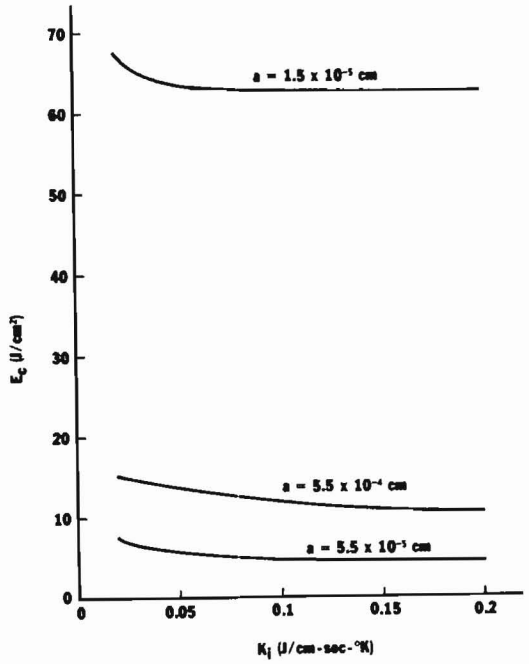


Figure 3. Damage threshold as a function of impurity conductivity for various impurity radii. the ratio of the conductivity to the diffusivity is held constant ($K_i/D_i = 2.39$).

This can also be concluded through an expansion of eq (6). When $t_\ell/\gamma = (D_i t_\ell/a^2) > 1$, the integral in eq (6) is dominated by the exponential quantity. To a good approximation, the remainder of the integrand can then be replaced by its value at $y = 0$. Using these approximations. Equation (6) at $r = a$ reduces to

$$E_C = It_\ell = \frac{4\pi T_C}{Q} \frac{aK_h t_\ell}{1 - \frac{a}{(\pi D_h t_\ell)^{\frac{1}{2}}}} \tag{10}$$

Furthermore, as $a \to 0$,

$$E \to \frac{4\pi T_C}{Q} aK_h t_\ell \ , \tag{11}$$

thus reflecting the trend indicated in figures 1 and 2. Note also that in this limit the damage threshold becomes insensitive to impurity properties. On the other hand, when $a^2 > D_i t_\ell$, the scaling for K_h and t_ℓ is no longer a simple power law. Here the effect of the impurity properties also becomes more apparent, as can be seen in figure 3. This is shown both by increasing "a" or by decreasing $D_i = (K_i/\rho_i C_\rho)$, where C_ρ is the heat capacity in J/g-K of the impurity at constant pressure and ρ is the density in g/cm^3.

Although the steps leading to eq (10) are independent of the absorption cross section, whether or not this expression can be identified with the measured damage threshold of the system depends on

Q. If Q is given by the Mie absorption cross section, using the initially assumed values of optical properties, then as noted above the damage threshold is determined by the film thickness; and eq (9) gives the correct expression. If, on the other hand, $Q \alpha a^2\pi$, then the diameter of the inclusion that is most easily damaged is less than the film thickness [13]. The damage is now determined by the size of this critical particle rather than the film thickness (see reference 13 for details). A comparison between the predictions of the two absorption models is given in table 2.

Table 2. Variation of damage threshold with impurity size "a" when $a^2 \leq D_i t_\ell$.

Q	a		Thermal Properties		Laser Pulse Duration
	Minimum Threshold	Region	Host	Inclusion	
Q_{Mie} Weakly absorbing	a = L/2	$a \to 0$	$E \propto (Kt_\ell)^1$	No Dependence	t_ℓ
		$a^2 \tilde{\propto} D_i t_\ell$	No simple Power Law	Weak Dependence	No simple Power Law
$Q_{Mie} \propto \pi a^2$ (Ref. 13)	$a \ni dE/da \doteq 0$	$a^2/D_i t_\ell \to 0$	$E \propto (K_h)^{1/2}$	No Dependence	$(t_\ell)^{1/2}$
		$a^2 \tilde{\propto} D_i t_\ell$	$E \tilde{\propto} (K_h)^{1/2}$	Weak Dependence	$(t_\ell)^{1/2}$

If the optical properties are not those necessarily of the assumed impurity or they are changed by some process such as non-linear absorption, Mie theory is still applicable. Particles describing a minimum damage threshold can have diameters generally less than the film thickness. That is to say, Mie theory can produce absorption cross sections $Q \tilde{\propto} \pi a^2$.

By considering some mechanism that increases the imaginary part of the index of refraction $Im(\tilde{n})$ (e.g. Non-linear absorption) it is found that there is an $Im(\tilde{n})$ which provides a maximum absorption. In other words $Im(\tilde{n})$ may increase to some finite value which maximizes the absorption. The fact that there is a value of $Im(\tilde{n})$ that maximizes the absorption can be understood by considering the limits of $Im(\tilde{n})$ in going to zero so that no volumetric absorption occurs and $Im(\tilde{n})$ in going to infinity where the incident field is totally reflected, and again, no absorption occurs.

This maximum absorption cross section can be clearly demonstrated by referring to figure (4). For moderate $Re\{\tilde{n}\}$ of standard thin films, numerical studies exhibit trends as given in figure (4). For small $Im(\tilde{n}) \equiv n'$ ($n' << 1$), the absorption cross section oscillates about the sloped dashed line. As n' increases up to about 1.75 the initial sloping portion of the curve (region 1) increases in slope and the oscillations damp out. The curve peaks at a size parameter "q" of about $\pi/5$. Following this peak $Q/\pi a^2$ decreases and starts to asymptoptically approach $Q = \pi a^2$ in a manner such that $Q \tilde{-} a^2$. The beginning of this a region is generally at $q \simeq 1$. As n' increases further, the absorption cross section decreases along lines of constant "q" as if multiplied by subsequently smaller multiplicative factors. To see how this affects the scaling, refer to figures (5) and (6).

Figure (5) is a typical damage threshold v.s. impurity radius plot. The locus of points which gives the radius of particles most easily damaged is determined for an assumed $Q = \pi a^2$ and follows a path of $a_{min} \propto \sqrt{K t_\ell}$. Along the path (dashed line) damage threshold $E \propto \sqrt{K_h t_\ell}$. On either side of this locus of points "E" scales as $(K_h t_\ell)^\gamma$ where γ is not in general a constant power. In the limit of $a >> a_{min}$, $\gamma \to 0$ and as $a \to 0$, $\gamma \to 1$. Figure (6) demonstrates how the scaling is effected by the absorption cross section as determined by Mie theory. The family of curves given by $Q = \pi a^2$ may be shifted into region A or B on figure (5) when $Q = \pi a^2$ is replaced by $Q = Q_{MIE}$. This shift (or q-pulling) is driven by Q_{MIE} giving a higher absorption, therefore a lower damage threshold, for either a higher or lower generalized size parameter. For example: higher absorption occurs for lesser generalized size parameters when the a_{min} locus, given by $Q = \pi a^2$, falls in region 2 of figure (4). Note that when the locus falls into region 3, there is essentially no pulling and $Q_{MIE} \tilde{-} \pi a^2$ results. This regains the $\sqrt{K t_\ell}$ dependence of $Q = \pi a^2$ when using Mie theory for Q.

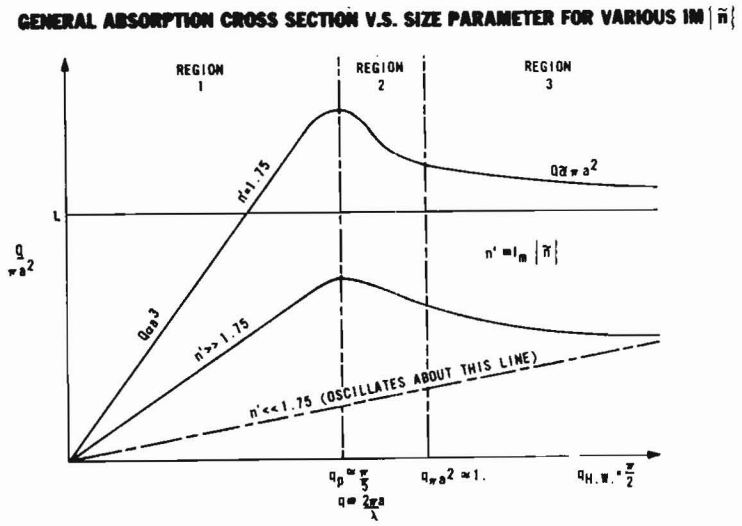


Figure 4. General absorption cross section v.s. size parameter for various Im$\{\tilde{n}\}$.

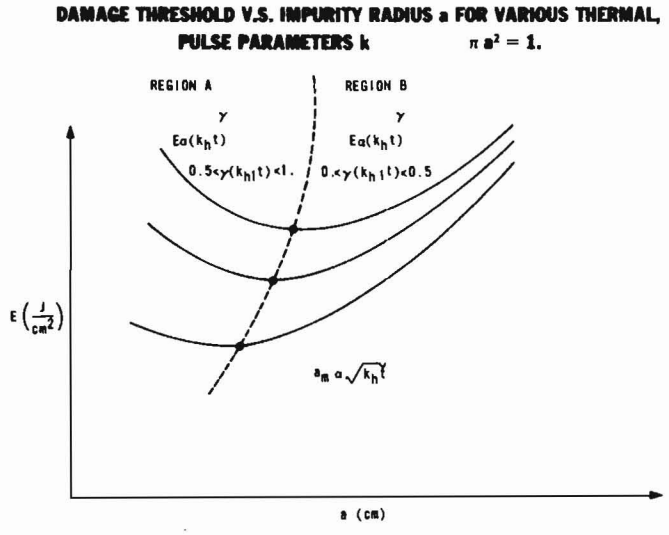


Figure 5. Damage threshold v.s. impurity radius a for various thermal, pulse parameters $K_h t_\ell$ with $Q/\pi a^2 = 1$.

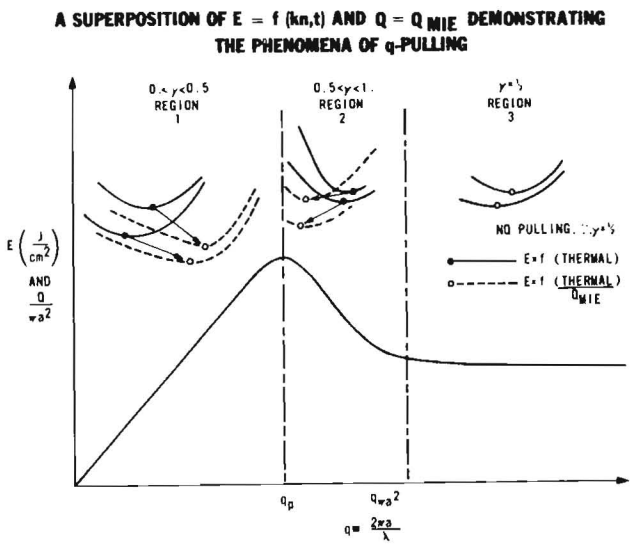


Figure 6. A superposition of $E = f(K_h, t)$ and $Q = Q_{MIE}$ demonstrating the phenomena of q-pulling.

4. Experimental Comparison

Many experimental observations can be explained by this model. From figure (4) of the absorption cross section versus the generalized size parameter, the wavelength dependence is quite clear since varying the wavelength merely shifts the q-axis by a multiplicative factor (since $q \equiv (2\pi a/\lambda)$. Though the wavelength dependence is readily evident, it is not simple. It varies differently depending upon whether a is in region one, two or three. It, as well, depends upon n'.

If n' is $\lesssim 1$. Region 1 blends into region 3 without any region 2(i.e. no peak occurs) and Q approaches πa^2 asymptoptical from beneath. In this case as λ decreases absorption always increases (since $(1/\lambda) \propto q$) and thus the damage threshold decreases. If n' $\simeq$ 1.75 the damage threshold can increase or decrease with wavelength depending upon the region into which a_{min} falls (note maximum figure 4). Additionally, if n' << 1.75 the damage threshold can increase or decrease with wavelength as well since many peaks can occur due to multipole resonances. It should be mentioned here that though resonances can lead to many very sharp peaks, damage threshold should not radically change over a small wavelength region due to the fact that a distribution of particle sizes is highly probable [14].

The data plotted in figure (7), with constants from table 3, shows a clear square root of K_h and t_ℓ dependence. This indicates that $Q_{MIE} \simeq \pi a^2$ (region 3 of fig. (6)) as indicated in eq (12) and shown in reference [13]. Since the two sets of data plotted are at different wavelengths, this indicates no wavelength dependence. This is as it should be since $Q \simeq \pi a^2$. However, some other data [5] at shorter pulse lengths (5 and 15 nsec) shows a very strong wavelength dependence. Since the locus of points $a_{min} \propto \sqrt{t_\ell}$ for $Q = \pi a^2$ a shorter pulselength can move a_{min} and therefore q_{min} into region 1 or 2 (see fig. (6)) from region 3. In region 1 or 2 one would expect a strong wavelength dependence. Numerical studies indicate that an index of refraction can be chosen that places these regions where just such a behavior could occur. Further study is necessary for more quantitative results.

The dependence of the damage threshold on the thermal properties of the host is more difficult to confirm unambiguously from the available experimental data. For instance, the damage thresholds for different materials under identical conditions cannot be discussed as a function of the thermal conductivities of the materials alone since the temperature at which a sample damages is also material dependent, likewise structural factors such as stress [17], adhesion, etc. are material

Table 3. Thermophysical properties of materials commonly used in optical thin film coatings.

Material	Index	K (J/cm-s-K)	C_ρ (J/g-K)	ρ (g/cm^3)	$T_{(melting)}$ (K)
Al_2O_3	1.72	0.346[20]	0.774[21]	4[25]	2325[21]
HfO_2	2.25	~0.017*[20]	0.168[20]	8.68[20]	3137[20]
LaF	1.59	0.0508[22]	0.462[23]	5.94[23]	1763[19]
LiF	1.37	~0.017*[20]	1.61[21]	2.635[20]	1121[21]
MgF_2	1.43	0.116	0.394	3.1766[20]	1536[21]
MgO	1.83	0.6[22](crys)	0.92[21]	3.77[20]	3098[21]
SiO_2	1.44	0.14[25]	0.737[20]	2.32[20]	1696[21]
ThF_4	1.59	0.1[19]	0.359[22]	6.32[20]	1380[20]
ThO_2	1.90	0.142[22]	0.234[22]	10[20]	3540[20]
Y_2O_3	2.10	0.0246*	0.451[22]	5.01[20]	2683[22]
ZrO_2	2.25	0.011[22] 0.0166[20]	0.46[21]	5.7[20]	2950[21]

*Extrapolated

dependent and affect the damage threshold. Therefore, any change in the composition of a sample changes several parameters at once; i.e., there is an as yet unknown interdependency. We are then faced with the problem of solving eq (5) numerically on a case-by-case basis or else finding a relevant asymptotic expression. An example of the latter approach is given in eqs (10), (11) and (12). If we assume strongly absorbing particles so that $Q_{MIE} \simeq \pi a^2$ then

$$E \propto 16\, T_C(\rho_h C_{\rho h} K_h t_\ell)^{\frac{1}{2}} \tag{12}$$

As mentioned previously this scaling agrees remarkably well with the data form Lawrence Livermore National Laboratories [18] and the data of Bettis, et al. [15] in figure (7).

The data of Walker, et al. [5] does not scale according to this relation. The power scaling of this data varies from $\gamma = 0$ to 1 for $(K_h t_\ell)^\gamma$. As noted if a_{min} falls between region 1 and 2 as indicated in figure (6) this is as would be expected. Further study is obviously dictated for more quantitative results.

5. Conclusion

In the work reported herein, the effect of the thermal and optical properties of the inclusion and host on the pulsed laser induced damage threshold of optical thin film was investigated. The major result of this work is that the size of the inclusion and its optical properties govern the absorption of radiation, whereas the thermal properties of the host are most important in the establishment of the damage threshold. In general, the damage threshold given in J/cm^2 has been found to increase as the duration of the laser pulse increases, as the thermal conductivity of the host increases, or as the imaginary part of the index of refraction of the impurity decreases (below a certain point). Furthermore, the damage threshold is relatively insensitive to the thermal properties of the impurity.

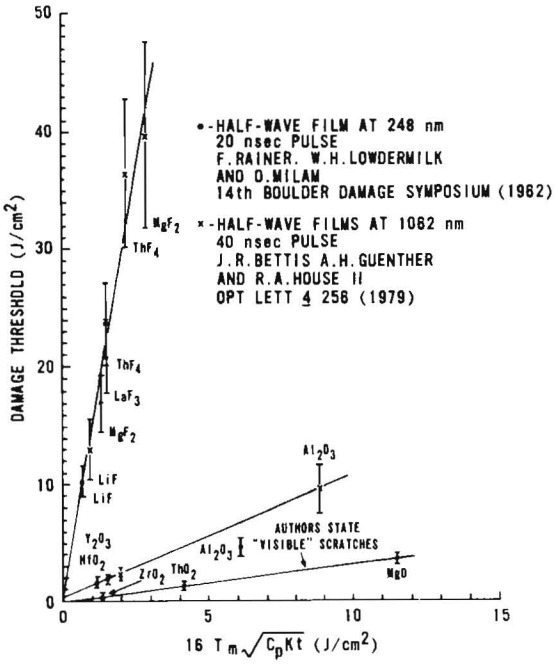


Figure 7. Comparison between the measured damage threshold and that calculated from the inclusion-dominated model. Damage threshold from two different experiments are used; dots are data from reference [18] with t_ℓ = 40 ns and λ = 0.248 μm, and x's are data from reference [15] with t_ℓ = 20 ns and λ = 1.06 μm. The values from reference [15] had been corrected for surface roughness. The thermophysical properties used to evaluate the calculated damage threshold for different materials are listed in table 2.

The way in which the damage threshold scales with the thermal properties of the host is in general a complicated function. Within certain limited ranges of pulse lengths and particle sizes ($D_i t_\ell \geq a^2$ approximate scaling laws can be derived. In this case, if the absorption cross section is determined by Mie theory with weakly absorbing particles or even strongly absorbing for $a^2 << Dt_\ell$ and $a \geq \lambda/4$ the damage threshold varies linearly as the thermal conductivity of the host and the laser pulse duration. If, on the other hand, the cross section is determined by the area intercepting the radiation (πa^2) which can occur for strongly absorbing particles with $a^2 \leq Dt_\ell$, $a \geq \lambda/4$, then the damage threshold varies as the square root of the laser pulse duration and thermal conductivity of the host [13]. Data is available that fits both scaling laws in the appropriate limits.

The situation regarding the influence of optical properties is a complicated one. Behavior is best understood by study of the absorption cross section. This seems to explain the trends in much of the data studied. The largest uncertainty at present is the imaginary part of the index of refraction. The data tends to indicate that it is larger than that of any of the previously assumed impurities. This could be due in part to non-linear absorption. Indices of refraction can be chosen that explain the behavior of the data, but this is as yet without any solid justification.

6. References

[1] E. M. Ephstein, Sov. Phys. Solid State 11, 2213 (1970.

[2] L. V. Keldysh, Sov. Phys., JETP 20, L307 (L965).

[3] M. Sparks and C. J. Duthler, Appl. Phys. 44,3038 (1973).

[4] S. L. Anisimov and B. I. Makshantsev, Sov. Phys., Solid State 14, 743 (1973).

[5] T. W. Walker, A. H. Guenther, and P. Nielsen, IEEE J. Quant. Electron. QE-17, 2053 (1981).

[6] A. Vaidyanathan, T. W. Walker, and A. H. Guenther, Phys. Rev. B 20, 3526 (1979).

[7] T. W. Walker, A. H. Guenther, and P. E. Nielsen, IEEE J. Quant. Electron. QE-17, 2041 (1981).

[8] D. Milam, R. A. Bradbury, and M. Bass, Appl. Phys. Lett. 23, 654 (1973).

[9] C. J. Duthler and M. J. Sparks, Laser Induced Damage in Optical Materials, Eds. A. J. Glass and A. H. Guenther (U.S. Govt. Printing Office, Washington, D.C., 1974), NBS Special Publ. 414, p. 219.

[10] H. Goldenberg and C. J. Tranter, Brit. J. Appl. Phys. 2, 296-298 (1952).

[11] H. C. Van de Hulst, Light Scattering by Small Particles, (Wiley, New York, 1957).

[12] M. Born and E. Wolf, Principles of Optics, 5th Ed. (Pergamon, New York, 1975).

[13] M. R. Lange, J. K. McIver, A. H. Guenther, and T. W. Walker, Laser Induced Damage In Optical Materials, Eds., H. E. Bennett, A. H. Guenther, D. Milam, and B. E. Newnam (U. S. Govt. Printing Office, Washington, D.C., 1982), NBS Special Publication 669, p. 380-386.

[14] V. V. Aretem'ev, A. M. Bonch-Bruevich, I. E. Morichev, N. L. Ivanova, and A. G. Vinogradskii, Sov. Phys. Tech. 22, 106 (1977).

[15] J. R. Bettis, A. H. Guenther, and P. A. House III, Opt. Lett. 4, 256 (1979).

[16] See for example articles in the Proceedings of the Boulder Damage Symposium.

[17] R. R. Austin, R. C. Michaud, A. H. Guenther, J. M. Putman, and R. Harniman, Laser Induced Damage in Optical Materials, Eds. A. J. Glass and A. H. Guenther (U.S. Govt. Printing Office, Washington, D.C., 1972), NBS Special Publication 372, p. 135.

[18] F. Rainer, W. H. Lowdermilk, D. Milan, C. K. Carniglia, and T. L. Lichtenstein, Laser Induced Damage In Optical Materials, Eds., H. E. Bennett, A. H. Guenther, D. Milam, and B. E. Newnam (U. S. Govt. Printing Office, Washington, D.C., 1982), NBS Special Publication 669, p. 274-281.

[19] M. Sparks and C. J. Duthler, Theoretical Studies of High-Power Ultraviolet and Infrared Materials, Eighth Technical Report, ARPA Contract No. DAHC-15-73-C-0127 (unpublished).

[20] Handbook of Thermophysical Properties of Solid Materials, A. Goldsmith, T. E. Watemann and H. J. Hirschhorn (MacMilian Company, New York, 1961).

[21] JANAF Thermochemical Tables, 2nd Eds. (U.S. Govt. Printing Office, Washington, D.C., 1971), NSRDS-NBS 37.

[22] Thermophysical Properties of Matter, Y. S. Touloukian, Dir. (Plenum Press, New York, 1970).

[23] W. G. Lyon, D. W. Osborn, H. E. Flowtown, F. Grandjean, W. N. Hubbard, and G. K. Johnson, J. Chem. Phys. 69, 167 (1978).

[24] V. Ya. Chekhovskoi, G. I. Stavrovskii, A. I. Pustil'nik, T. S. Sedykh, and A. B. Ivanov, Heat Transfer, Sov. Research. No. 2, 68 (1973).

[25] Handbook of Tables for Applied Engineering Science, second Ed., Ed. R. C. Weast (C.R.C. Press, Cleveland, 1973).

It was suggested that at some long pulse length the model would break down in terms of the square root dependence. As a rule of thumb a value of 100 ns was suggested as a reasonable cutoff.

"ANALYTICAL MODEL FOR EVALUATING TRANSIENT, STEADY-STATE, COATING DAMAGE THRESHOLD, OPTICAL DISTORTION, AND AXIAL GRADIENT FOR EXTERNALLY COOLED LASER MIRRORS."

James R. Palmer

Weapons Support Division
COMARCO, Inc.
1417 N. Norma Street, Ridgecrest, California 93555
Weapons System Effectiveness Contract N60530-83-D-0024
for the
Naval Weapons Center, China Lake, California 93555

There are a number of requirements in high energy laser systems to provide optical elements that are not integrally cooled. However, there are many instances where a cooling gas, such as helium or nitrogen, may be used to cool the front and back surfaces in order to reduce optical distortion.

In order to evaluate the response of an optic to this type of cooling, first order analytical techniques have been generated to determine transient and steady-state temperature distributions through a fully irradiated optic, an irradiated spot on a large optic, and a toroidal shaped beam (i.e., hole in the beam), on a large optical element.

Cooling temperatures and damage relationships coupled with optical path differences of the flowing gas are treated for evaluation. Optical distortion of the element due to radial and axial temperature gradients are treated for both transient and steady-state conditions and for various gas flow dynamics.

Key words: cooled laser mirrors; mirror distortion; transient gradients; coating damage.

INTRODUCTION

It is not uncommon, in high energy laser systems, to minimize the cost of optical components by using uncooled polished, or diamond turned, metal mirrors. Very often these mirrors are used in non-critical areas of the optical train. Even so, an effort is undertaken to minimize the amount of optical distortion that these mirrors introduce in the optical path. A large component to the distortion is generated by the thermal gradient that is manifested in the mirror.

Ideally, then, one would want to reduce the distortion, resulting from the thermal gradient, to the greatest extent possible. One technique for reducing the axial thermal gradient is to pass an inert gas across the surfaces of the optic to remove the heat. This technique lends more to optics that are not in a vacuum environment. It may, however, be valuable in those situations where the inert gas may be used simply to remove dust particles or moisture from optics that will be subjected to a vacuum after the cleaning process.

In other situations, one may wish to cool the metal optics to a particular temperature, i.e., back to ambient, after a laser run. This may permit the system to be operated with more cycles than if the optics cooled down due to free convection and radiation.

The purpose of this paper, then, is to provide a first order analytical technique for evaluating velocities, film coefficients, and gradient distributions for a fully irradiated optic, an irradiated spot on a large optic, and a toroidal shaped beam mode on a large optical element. These techniques will permit the analyst to determine, in a reasonably quick fashion, whether the optic will respond the way that it is required. This technique does not purport to provide the detailed information that may ultimately be required and which is more suitable to a detailed numerical analysis technique.

---

*Numbers in brackets indicate the literature references at the end of the paper.

Symbols used in this paper are given below. Metric values.

A_1 = Irradiated area of optic, cm^2

a = -0.5d, cm

b = Radius from center of optic for radius of toroid ring, cm

c = Specific heat, J/Kg - °C

d = Orifice diameter, cm

D = Modulus of Rigidity, N · M = $\frac{Et^3}{12(1 - \mu_o{}^2)}$

E = Young's Modulus, N/M^2

$\mathscr{F}_o$ = Absorbed flux density, W/cm^2

GR_H = Grashof Number, dimensionless

h_c = Heat transfer film coefficient, W/cm^2 - °C

I_o = Modified zero order Bessel Function, dimensionless

K = Thermal conductivity, W/cm - °C

L_o = t = Thickness of optic (face-plate), cm

M = Bending moment, N · M/M

N_t = Index of refraction of gaseous medium, dimensionless

N_o = Index of refraction of gaseous medium at 273.15°K

P = $[\pi(D)R'(\hat{Q})2]$, N

P_o = Absolute pressure, mm Hg

$\hat{Q}$ = Apparent load, N/M^2

R = Radius of optic, cm

R_1 = b

R_o = Free radius generated by axial gradient, m

R' = Half-width of toroidal ring, cm

R_e = $\frac{VL\rho}{\mu}$ = Reynold's Number, dimensionless

r = Radius at which velocity is 1/2 $\bar{U}_z$, cm

r_o = Radius at which velocity = 0

$\bar{T}$ = Average temperature through the laminar boundary layer, °K

T_o = Surface temperature of optic, °C

T_∞ = Temperature of flowing gas, far removed from optical surface, °C

T = Temperature in the boundary layer at (X,Y) coordinate, °C

T_1 = T_o

T_2 = Backsurface surface temperature of optic, °C

U_s = Cross flow velocity, m/sec^E

$\bar{U}_z$ = Average axial velocity, m/sec

U_R = Velocity at radius (r), m/sec

U_p = Velocity in the orifice, m/sec

U_∞ = Average gas velocity outside the boundary layer, m/sec

V_x = Velocity of the gas in the boundary layer at (X,Y) coordinate, m/sec

X = Distance along flow path from origin, m

Y = Distance removed from origin normal to flow path, m

α = Thermal diffusivity, cm^2/s

α_o = Coefficient of thermal expansion, $°C^{-1.0}$

μ = Viscosity, Kg/cm - s

μ_o = Paesion's Ratio, dimensionless

υ = μ/ρ

ρ = Density, Kg/cm^3

τ = Run time, sec

β = Coefficient of expansion of cooling median, $°K^{-1.0}$

ϵ_m = Eddy viscosity, Kg/cm - s

ζ_2 = Eddy diffusion, cm^2/s

δ = Boundary layer thickness, m

$$\text{erf}(x) = \frac{2}{\sqrt{\pi}}\int_0^x e^{-\xi^2}\, d\xi$$

$$\text{erfc}(x) = [1 - \text{erf}(x)]$$

$$\text{ierfc}(x) = \frac{1}{\sqrt{\pi}} e^{-x^2} - \frac{2x}{\sqrt{\pi}}\int_x^\infty e^{-\xi^2}\, d\xi$$

The first set of circumstances that must be addressed are the conditions of the flowing gas after the gas exits from a bounded, Navier-Stokes, relationship into an unbounded environment where the gas is free to expand, virtually without restraint. What will the velocity profile look like some distance away from the exit? What will be the velocity some distance away from the exit both on axis and radially distributed? These questions must be answered in order to provide an average velocity for computing the heat transfer film coefficients and the average thickness of the boundary layer so that the optical path distortion may be calculated.

The velocity distribution in a round free jet has been studied by a number of investigators. Hintz [1] describes the classical theories of Boussinesq, Prandtl, and Reichardt. For the problem under consideration, however, the simpler theory based on the use of eddy viscosity will be used. [2] [3]

For the case of a jet emptying into an unbounded plenum with eddy viscosity (ϵ_m) independent of axial length (z), and dependent on eddy diffusion (ζ_2) only:

The mass balance equation is:

$$\frac{\partial}{\partial_z}(U_s + \bar{U}_z) + \frac{1}{R}\frac{\partial}{\partial_R}(R\,\bar{U}_R) = 0 \tag{1}$$

The similarity relationships are:

$$U_z = U_p\left(\frac{z+a}{d}\right)^p f(\zeta_2) \tag{2}$$

$$U_R = U_p\left(\frac{z+a}{d}\right)^r g(\zeta_2) \tag{3}$$

$$-\overline{U_R U_z} = U_p^2\left(\frac{z+a}{d}\right)^s h(\zeta_2) \tag{4}$$

Substitution of the similarity relationships into Eq. 1 yields:

$$\rho f(\zeta_2) - q\,\zeta_2\frac{df}{d\zeta_2} + \frac{1}{\zeta_2}\frac{d}{d\zeta_2}[\zeta_2\, g(\zeta_2)] = 0 \tag{5}$$

Which is independent of (z) when p, q, and r satisfy:

$$p + q - r = 1.0$$

The momentum balance equation for the (z) axial direction, applying the boundary-layer approximations, will be:

$$(U_s + U_z) \frac{\partial \bar{U}_z}{\partial_z} + \bar{U}_R \frac{\partial \bar{U}_z}{\partial R} = \frac{1}{R} \frac{\partial}{\partial R} R \left(-\overline{U_R U_z}\right) \tag{6}$$

For the case of ($U_s = 0$), i.e., no cross flow of the fluid in the unbounded plenum, Eq. 6 becomes:

$$-\left(f^2 + \zeta_2 f \frac{df}{d\zeta_2}\right) + g \frac{df}{d\zeta_2} = \frac{1}{\zeta_2} \frac{d}{d\zeta_2} (\zeta_2 h) \tag{7}$$

For $p = -1$ and $q = 1$, Eq. 5 becomes:

$$\frac{d}{d\zeta_2} (\zeta_2 f) = \frac{1}{\zeta_2} \frac{d}{d\zeta_2} (\zeta_2 g) \tag{8}$$

With integration,

$$\zeta_2 g = \zeta_2^2 f - \int_0^{\zeta_2} d\zeta_2 \zeta_2 f \tag{9}$$

Setting $\int_0^{\zeta_2} d\zeta_2 \zeta_2 f = F(\zeta_2)$

where

$$f = \frac{1}{\zeta_2} \frac{dF}{d\zeta^2} \text{ and } g = \frac{dF}{d\zeta_2} - \frac{1}{\zeta_2} F$$

So that Eq. 8 becomes:

$$-\frac{d}{d\zeta_2} \left| \frac{F}{\zeta_2} \frac{dF}{d\zeta_2} \right| = \frac{d}{d\zeta_2} (\zeta_2 h) \tag{10}$$

Integration provides:

$$\zeta_2 h = -\frac{F}{\zeta_2}\frac{dF}{d\zeta_2} = -f\int_0^{\zeta_2} d\zeta_2\,\zeta_2 f \tag{11}$$

In accordance with the boundary assumptions,

$$\epsilon_m = \frac{-\overline{U_R U_z}}{\partial U_z/\partial R} = \text{constant} \tag{12}$$

$$\therefore \epsilon_m = 0.0116\, U_p d$$

from Eq. 9 and Eq. 11

$$-F\frac{dF}{d\zeta_2} = \frac{\epsilon_m f(0)}{U_{z_{max}}(z+a)}\zeta_2^2\frac{d}{d\zeta_2}\left(\frac{1}{\zeta_2}\frac{dF}{d\zeta_2}\right) \tag{13}$$

Which integrates to:

$$\frac{\epsilon_m f(0)}{U_{z_{max}}(z+A)}(\zeta_2\frac{dF}{d\zeta_2} - 2F) = \frac{1}{2}F^2 \tag{14}$$

The constant of integration is zero because $\zeta_2 = 0$ and $F(\zeta_2)$ must also be zero

Then;

$$F(\zeta_2) = \frac{2C\zeta_2^2}{1 + \left|U_{z_{max}}(z+A)/2\epsilon_m f(0)\right| C\zeta_2} \tag{15}$$

So that:

$$f(\zeta_2) = \frac{1}{\zeta_2}\frac{dF}{d\zeta_2} = \frac{4C}{\left\{1 + C\left[U_{z_{max}}(z+a)/2\epsilon_m f(0)\right]\zeta_2^2\right\}^2} \tag{16}$$

The constant (C) follows for the condition of $\zeta_2 = 0$; So that, $C = 1/4\, f(0)$

Which provides:

$$\frac{\bar{U}_z}{\bar{U}_{z_{max}}} = \left[1 + \frac{U_{z_{max}}(z+a)}{8\epsilon_m}\zeta_2^2\right]^{-2.0} \tag{17}$$

$$\overline{U}_{z_{max}} = \left[\frac{z + a}{d}\right]^{-(2/3)} (Up) \tag{18}$$

For a constant value of (ϵ_m) across the main part of the jet with a subsequent velocity distribution, the shear-stress distribution is found from:

$$\frac{\tau_{Rz}}{\rho U_{z_{max}}} = \frac{1}{2}\zeta_2 \left[1 + \frac{U_{z_{max}} (z + a)}{8 \epsilon_m} \zeta_2^2\right]^{-3.0} \tag{19}$$

The shear stress has a maximum value at:

$$(\zeta_2)_{optimum} = \left[\frac{8 \epsilon_m}{5 U_{max} (z + a)}\right]^{0.5} \tag{20}$$

And the shear stress at half $U_{z_{max}}$ is found from:

$$(\zeta_2)_{1/2} = \left[\frac{8 (\sqrt{2} - 1.0) \epsilon_m}{U_{z_{max}} (z + a)}\right]^{0.5} \tag{21}$$

Knowing the value of $(\zeta_2)_{1/2}$ the radius for this value is found from:

$$r = (\zeta_2)_{1/2} (z + a) \tag{22}$$

Consequently, knowing that the velocity distribution follows the Gaussian error integral, then,

$$r_o = (\zeta_2)_{1/2} (z + a) 3.0 (.441)^{-1.0} \tag{23}$$

where

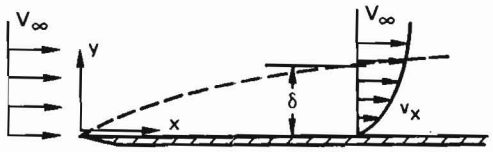
$U_z = 0$

There will often be a concern, relative to an optical path difference that may develop, for the amount of temperature gradient that will result in the flowing gas boundary layer. The laminar boundary layer thickness and velocity profiles are copiously reported by the investigators. [3] [4] [5] [6] [7]

The approximate integral mtehod provides a velocity distribution as:

$$\frac{v_x}{v_\infty} = \frac{3}{2}\left[\frac{Y}{4.64\left(\frac{v_x}{v_\infty}\right)^{0.5}}\right] - \frac{1}{2}\left[\frac{Y}{4.64\left(\frac{v_x}{v_\infty}\right)^{0.5}}\right]^3 \quad [7] \tag{24}$$

For $0 \leq Y \leq \delta_{(x)}$



HYDRODYNAMIC BOUNDARY LAYER ON FLAT PLATE

The boundary layer thickness, as a function of distance (x) is found from:

$$\delta_{(x)} = 4.64\left[\frac{v_x}{v_\infty}\right]^{0.5} \quad [7] \tag{25}$$

Equations 24 and 25 require a steady, fully developed flow as boundary conditions.

Under steady-state conditions, the temperature gradient will follow the velocity gradient, i.e.,

$$\frac{T-T_\infty}{T_0-T_\infty} = \frac{3}{2}\left[\frac{Y}{4.64\left(\frac{v_x}{v_\infty}\right)^{0.5}}\right] - \frac{1}{2}\left[\frac{Y}{4.64\left(\frac{v_x}{v_\infty}\right)^{0.5}}\right]^3 \tag{26}$$

Figure (1.0) provides an illustration of how an optic may be provided with a cooling gas. The cooling jets are placed around the periphery of the optic. Knowing the diameter of the optic, one may determine the maximum axial distance of flow, average velocity, average Reynold's number, average boundary thickness, average velocity, and average temperature profile through the gas boundary layer.

The change in the index of refraction for a gaseous median is found from:

$$\eta_T = 1 + \left[\left(\frac{\eta_0 - 1}{1+\beta T}\right)\left(\frac{P}{760}\right)\right] \quad [8] \tag{27}$$

The average heat transfer film coefficient will be found from:

For gases with $P_R \geqslant 0.5$ and $R_{e_x} < 5(10^5)$

$$h_c = \left(\frac{k}{R}\right)\left[0.332\ R_{e_x}^{0.5}\ Pr^{1/3}\right] \quad [9] \tag{28}$$

For gases with $P_R \geqslant 0.5$ and $R_{e_x} > 5(10^5)$

$$h_c = \left(\frac{k}{R}\right)\left[0.0296\ R_{e_x}^{0.8}\ Pr^{0.6}\right] \quad [9] \tag{29}$$

Knowing the average film coefficient across the optic, the steady-state and transient temperature of the optic may be evaluated.

For a fully irradiated optic—steady-state conditions—back surface uncooled

$$\Sigma Q = \bar{h}_c A_1 [T_1 - T_\infty] + \frac{KA_1}{L_o}(T_1 - T_2) \tag{30}$$

$$\Sigma Q = \bar{h}_c A_1 [T_1 - T_\infty] + \frac{T_2 - T_\infty\,(K)}{(\alpha\tau)^{0.5}\ 2\ \text{ierfc}\left[\frac{L_o}{2(\alpha\tau)^{0.5}}\right]} A_1 \tag{31}$$

For a known run time (τ), the two equations are solved simultaneously for T_1 and T_2, so that:

$$\Sigma Q + \bar{h}_c A_1 T_\infty = h_c A_1 T_1 + \frac{KA_1}{L_o} (T_1) - \frac{KA_1}{L_o} (T_2) \tag{32}$$

$$\Sigma Q + \bar{h}_c A_1 T_\infty + \left[(\alpha\tau)^{0.5} \; 2 \; \text{ierfc}\left(\frac{L_o}{2(\alpha\tau)^{0.5}}\right) A_1 \right]^{-1.0} T_\infty \; K = \bar{h}_c A_1 T_1 + \left[(\alpha\tau)^{0.5} \; 2 \; \text{ierfc}\left(\frac{L_o}{2(\alpha\tau)^{0.5}}\right) A_1 \right]^{-1.0} \times K \times T_2 \tag{33}$$

$$\bar{h}_c A_1 = A_o \tag{34}$$

$$\frac{KA_1}{L_o} = B_o \tag{35}$$

$$\left[(\alpha\tau)^{0.5} \; 2 \; \text{ierfc}\left(\frac{L_o}{2(\alpha\tau)^{0.5}}\right) A_1 \right]^{-1.0} K = C_o \tag{36}$$

Then Eq. 32 and Eq. 33 reduce to:

$$\Sigma Q + A_o T_\infty = A_o T_1 + B_o T_1 - B_o T_2 \tag{37}$$

$$\Sigma Q + C_o T_\infty = A_o T_1 + C_o T_2 \tag{38}$$

The next step is to check for the amount of time necessary to achieve steady-state on the first surface.

So that

$$T_1 - T_\infty = \frac{2 \mathcal{F}_o (\alpha\tau_o)^{0.5}}{K} \left\{ \frac{1}{\sqrt{\pi}} e^{-x^2} 2x \int_x^\infty e^{-\xi^2} d\xi \right\} \quad [10] [11] [12] \tag{39}$$

Then, time to achieve steady-state temperature will be:

$$\tau_o = \left| \frac{T_1 - T_\infty \; (K)}{\mathcal{F}_o (\alpha)^{0.5} \; (1.1284)} \right|^2 (3600) \quad \text{seconds /hr} \tag{40}$$

If $\tau \sim \tau_o$ then the ambient temperature (T_∞) of the cooling medium should be reduced; or, the velocity of the cooling medium should be increased.

The thermal bowing due to the axial gradient if found from

$$m = \frac{\alpha_\theta (T_1 - T_2)(1 + \mu_\theta) D}{t} \quad [13] \tag{41}$$

Apparent load is found from

$$\hat{Q} = \frac{m\,(16)}{(1 + \mu_\theta) R^2} \quad [12]\,[13] \tag{42}$$

and, deflection of a circular plate, clamped at the edges, is found from:

$$\Delta = \frac{\hat{Q} R^4}{64D} \quad [12]\,[13] \tag{43}$$

Deflection of a circular plate, simply supported at the edges,

$$R_o = \frac{t}{\alpha_\theta (T_1 - T_2)} \quad [12]\,[13] \tag{44}$$

$$\hat{Q}_o = \frac{8D\,(1 + \mu_\theta)}{R_o (R^2)} \quad [12]\,[13] \tag{45}$$

and

$$\Delta = \frac{\hat{Q}_o R^4}{64D} + \frac{\hat{Q}_o R^4}{16D\,(1 + \mu_\theta)} \quad 13] \tag{46}$$

For a circular plate supported at edge at 3 points, 120° apart, the load uniformly distributed, the deflection at the center is found from:

$$\Delta = \frac{0.0362\pi\, \hat{Q}_o 2^4}{D} \quad [13] \tag{47}$$

For those cases and conditions where it is desired to cool the optic back to the original ambient conditions, after a laser run, the final temperature may be found from:

For an initial constant temperature differential (V), the temperature change with time is found from:

$$v = h \int_o^\infty \phi\,(x + \eta, t)\, e^{-h\eta_\eta} = \frac{2Vh}{\sqrt{\pi}} \int_o^\infty e^{-h\eta} \left[\int_o^{(x+\eta)/2\sqrt{\alpha\eta}} e^{-\mu^2}\, d\mu \right] d\eta \quad [10] \tag{48}$$

$$v = \frac{2V}{\sqrt{\pi}} \int_0^{x/2\sqrt{\alpha\tau}} e^{-\mu^2}\, d\mu + \frac{V}{(\pi\alpha\tau)^{0.5}}\, e^{hx + h^2\alpha\tau} \int_0^{\infty} e^{-(x+\eta+2h\alpha\tau)^2/4\alpha\tau}\, d\eta \qquad [15] \qquad (49)$$

In the second integral set:

$$x + \eta + 2h\alpha\tau = 2\sqrt{\alpha\tau}\,\mu$$

Then:

$$v = \frac{2V}{\sqrt{\pi}} \int_0^{x/2(\alpha\tau)^{0.5}} e^{-\mu^2}\, d\mu + \frac{2V}{\sqrt{\pi}}\, e^{hx + h^2\alpha\tau} \left[\int_0^{\infty} e^{-\mu^2}\, d\mu - \int_0^{(x+2h\alpha\tau)/2(\alpha\tau)^{0.5}} e^{-\mu}\, d\mu \right] \qquad [10] \qquad (50)$$

which will give:

$$\frac{v}{V} = \frac{2}{\sqrt{\pi}} \int_0^{x} e^{-\xi^2} d\xi + \left\{ e^{(hx + h^2\alpha\tau)} \left[\frac{2}{\sqrt{\pi}} \int_x^{\infty} e^{-\xi^2} d\xi \right] \right\} \qquad [10] \qquad (51)$$

where

$$T_1 - T_0 = V = \frac{\mathcal{F}_0\,(\alpha\tau)^{0.5}}{K}\ 1.1284 \text{ for a fully irradiated optic} \qquad [10] \qquad (52)$$

For the irradiated first surface only, set x = z = 0, then

$$\frac{v}{V} = e^{h^2\alpha\tau}\, \mathrm{erfc}\left[h\,(\alpha\tau)^{0.5}\right] \qquad [10] \qquad (53)$$

There are systems which use a repetitive pulsed laser rather than single pulse or continuous wave. For this type of system, the temperature of the optic, i.e., temperature gradient will continue to change with each duty cycle of the laser until quasi thermal equilibrium is achieved.

The temperature rise for each pulse will be found from Eq. 52. So that:

$$\Delta T_o = \frac{\mathcal{F}_o(\alpha\tau_1)^{0.5}}{K}\ 1.1284$$

The temperature dimunition for each portion of the off cycle is found from Eq. 51.

$$\frac{\Delta T_1}{\Delta T_0} = \mathrm{erf}\left[\frac{x}{2(\alpha\tau_2)^{0.5}}\right] + \left[e^{(h\,x + h^2\alpha\tau_2)}\ \mathrm{erfc}\left\{\frac{x}{2(\alpha\tau_2)^{0.5}} + h(\alpha\tau_2)^{0.5}\right\}\right]$$

where

τ_1 = "on" cycle time

τ_2 = "off" cycle time

Then: For one complete duty cycle

$$\Delta T_1 = \frac{\mathcal{F}_o(\alpha\tau_1)^{0.5}}{K} \; 1.1284 \left\{ \operatorname{erf}\left[\frac{x}{2(\alpha\tau)^{0.5}}\right] + e^{(h\,x + h^2\alpha\tau_2)} \operatorname{erfc}\left\{\frac{x}{2(\alpha\tau_2)^{0.5}} + h\,(\alpha\tau_2)^{0.5}\right\}\right\} \tag{54}$$

So that, for (N) number of cycles

$$\Delta T_{(N)} = \left[\Delta T_1 (Y')^N + \Delta T_1 (Y')^{N-1} + \Delta T_1 (Y')^{N-2} + \ldots \Delta T_1 (Y')^{N=1}\right] \tag{55}$$

where

Y' = Eq. 51

For no cooling except heat sinking to the back of the optic, the value of (h) is found from:

$$h = \frac{1}{L_o}$$

L_o = Thickness of the optic

If the optics are in a vacuum, the temperature will continue to rise until an equilibrium between the optic and the surroundings can be achieved through radiation.

That is, when

$$Q_{in} = \bar{h}_R A_1 (T_1 - T_s) = Q_{out} \qquad [14] [15] [16]$$

Where

$$\bar{h}_R = \frac{1.0}{\left(\frac{1}{\varepsilon_1} - 1\right) + \frac{A_1}{A_2}\left(\frac{1}{\varepsilon_2} - 1\right) + \frac{1}{F_{1-2}}} \left[\frac{0.172\left|\left(\frac{T_1'}{100}\right)^4 \left(\frac{T_2'}{100}\right)^4\right|}{T_1' - T_2'}\right] \qquad [14] [15] [16] \tag{56}$$

If the optic is not in a vacuum, the temperature will continue to rise until equilibrium between the optic and the surrounding environment can be achieved through free-convection.

That is, when:

$$Q_{in} = \bar{h}_c A_1 (T_1 - T_\infty) = Q_{out}$$

Where:

$$\bar{h}_c = .508 \left[\frac{P_R}{0.952 + P_R} GR_D P_R \right]^{0.25} \quad \text{FOR } GR_D < 10^{10} \quad \text{Assuming vertical optic} \qquad [9] [16] \qquad (57)$$

or

$$\bar{h}_c = 0.024 \left[\frac{P_R^{1.17}}{1 + 0.494 P_R^{2/3}} GR_D \right]^{2/5} \quad \text{for } GR_D > 10^{10} \quad \text{Assuming Vertical Optic} \qquad [9] [16] \qquad (58)$$

where

$$P_R = \text{Prandtl Number } \frac{C \mu}{K}$$

$$GR_D = \left[\frac{g \beta \rho^2 \Delta T D^3}{\mu^2} \right]$$

For a cooled laser mirror the ramp temperature will continue to rise to the point of steady-state and will have a saw-tooth structure for each pulse thereafter. So that;

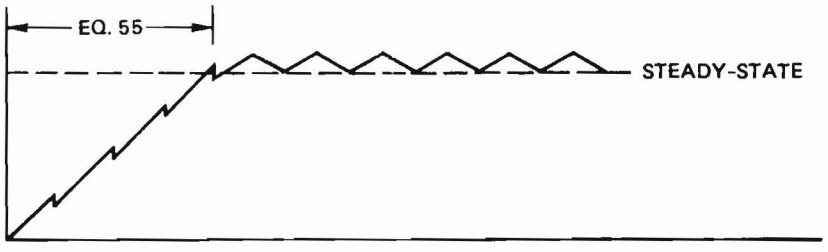
$$\Sigma Q = \bar{h}_c (A_1) (T_2 - T_\infty) + \frac{KA_1}{z} (T_1 - T_2) \qquad (59)$$

$$\Sigma Q = \bar{h}_c (A_1) (T_2 - T_\infty) + \frac{(T_1 - T_\infty) K}{(A_1) (\alpha \tau_1)^{0.5} 1.1284 \left\{ \text{erf} \left[\frac{z}{2(\alpha \tau_2)^{0.5}} \right] + \exp \left(h z + h^2 \alpha \tau_2 \right) \times \text{erfc} \left[\frac{z}{2(\alpha \tau_2)^{0.5}} + h (\alpha \tau_2) \right] \right\}} \qquad (60)$$

where

τ_1 = pulse width "on" cycle
τ_2 = pulse width "on" cycle + "off" cycle
z = face plate thickness of laser mirror

In order to determine the value of (T_1) for the pulse "on" cycle, substitute τ_1 for τ_2 in the second expression of Eq. 60.



There are a number of cases whre the optic is not fully irradiated. This condition results from a large optical element irradiated with a laser spot size substantially smaller than the diameter of the element.

The temperature distribution for this condition, with gas flowing over the front surface is found from:

$$\frac{R_l}{2(\alpha\tau)^{0.5}} < 3.0, \text{ then, the following analysis applies} \qquad [12]$$

Temperature distribution for actively cooling the optic, follows:

$$\Sigma Q = h_c \pi R_l^2 \left[T_1 - T_\infty\right] + \frac{K\pi R_l^2}{L_o}\left(T_1 - T_2\right) \qquad (61)$$

$$\Sigma Q = h_c \pi R_l^2 \left[T_1 - T_\infty\right] + \frac{\left(T_2 - T_\infty\right) K}{\left\{2\,\text{ierfc}\left[\frac{L_o}{2(\alpha\tau)^{0.5}}\right] - 2\,\text{ierfc}\left[\frac{(L_o^2 + R_l^2)^{0.5}}{2(\alpha\tau)^{0.5}}\right]\right\}\pi R_l^2\,(\alpha\tau)^{0.5}} \qquad (62)$$

Equations 61 and 62 are solved in similar fashions as Eq. 32 through Eq. 38.

So that:

$$A_o = h_c \pi R^2 \qquad (63)$$

$$B_o = \frac{K\pi R^2}{L_o} \qquad (64)$$

$$C_o = \frac{K}{\left\{2\,\text{ierfc}\left[\frac{L_o}{2(\alpha\tau)0.5}\right] - 2\,\text{ierfc}\left[\frac{(L_o{}^2 + R_1{}^2)^{0.5}}{2(\alpha\tau)0.5}\right]\right\}\pi R_1{}^2\,(\alpha\tau)0.5} \qquad (65)$$

Then:

$$\Sigma Q = A_o T_1 - A_o T_\infty + B_o T_1 - B_o T_2 \qquad (66)$$

$$\Sigma Q = A_o T_1 - A_o T_\infty + C_o T_2 - C_o T_\infty \qquad (67)$$

Which will provide;

$$\Sigma Q + A_o T_\infty = A_o T_1 + B_o T_1 - B_o T_2 \qquad (68)$$

$$\Sigma Q + A_o T_\infty + C_o T_\infty = A_o T_1 + C_o T_2 \qquad (69)$$

A major difference, however, is to be found in the evaluation of the distortion. Because the gradient is localized in the center of the optic, the deflection will appear to be resisted by a fully clamped geometry, so that

$$m = \frac{\alpha_o (T_1 - T_2) + (1 + \mu_o) D}{L_o} \tag{70}$$

$$\hat{Q} = \frac{m(16)}{(1 + \mu_o) R_1^2} \tag{71}$$

where

R_1 = radius of the beam

The deflection of the optic, assuming simply supported conditions, is a combination of the center deflection and edge deflection in order to accommodate the slopes of the two. For a circular optic concentrically loaded over a circle of radius (R_1), the deflection is found from:

$$\Delta = \frac{P}{16\pi D} \left[\frac{3 + \mu_o}{1 + \mu_o} R^2 + R_1^2 \ln \frac{R_1}{R} - \frac{7 + 3\mu_o}{4(1 + \mu_o^2)} R^2 \right] \quad [13] \tag{72}$$

It is not uncommon for a beam to be toroidal in geometry. In this case, the beam will appear as a ring on the optical element.

For this case, the temperature rise, as a function of run time, follows the equation of

$$\Delta T_{R(F)} = \frac{Q\tau}{8(\pi\alpha\tau)^{1.5} \rho c_p} \exp\left[- \frac{R_1^2 + R'^2}{4\alpha\tau} \right] I_o \left[\frac{R_1 R'}{2\alpha\tau} \right] \quad [10] \tag{73}$$

The temperature rise for the back surface is found from:

$$\Delta T_{R(B)} = \frac{Q\tau}{8(\pi\alpha\tau)^{1.5} \rho c_p} \exp\left[- \frac{R_1^2 + R'^2 + L_o^2}{4\alpha\tau} \right] I_o \left[\frac{R_1 R'}{2\alpha\tau} \right] \tag{74}$$

Temperature distribution for actively cooling the optic, follows:

$$\Sigma Q = h_c \text{Å} [T_1 - T_\infty] + \frac{K\text{Å}}{L_o} (T_1 - T_2) \tag{75}$$

$$\Sigma Q = h_c \text{Å} [T_1 - T_\infty] + \frac{(T_2 - T_\infty) 8 (\pi\alpha\tau)^{1.5} \rho c_p}{\tau \left[\exp\left(- \frac{R_1^2 + R'^2 + L_o^2}{4\alpha\tau} \right) I_o \left[\frac{R' R_1}{2\alpha\tau} \right] \right]} \tag{76}$$

where

Å = area of the irradiated toroid

Again, Eq. 75 and 76 must be solved simultaneously.

The deflection for this type of geometry, on a simply supported round optic, is found from:

$$\Delta = \frac{P}{8\pi D}\left[2b^2 \ln\frac{b}{R} + (R^2 - b^2)\frac{(3+\mu_g)R^2 - (1-\mu_g)b^2}{2(1+\mu_g)R^2}\right] \tag{77}$$

where

$R_1 = b$ = radius from center of optic to radius of toroid ring

Care must be taken when using Eq. 73 and Eq. 74. For materials with very low thermal diffusivities, the two equations "blow-up".

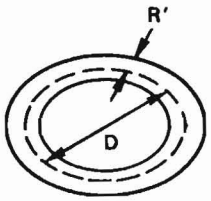
The suitability of these two equations may be evaluated using the following expressions:

Maximum ΔT over a rectangle is evaluated from:

$$\Delta T_{max} = \frac{2\mathcal{F}_o}{K\pi}\left\{a\left[\ln\left(L + (L^2 + a^2)^{0.5} - \ln a\right)\right] + L\left[\ln\left(a + (a^2 + L^2)^{0.5} - \ln L\right)\right]\right\} \quad [10] \tag{78}$$

where

$a = R'$ = half-width of the ring
$L = \pi D$
D = median diameter of the toroid



The time to achieve the maximum ΔT is found from:

$$\tau = \left[\frac{K\Delta T\pi^{0.5}}{2\mathcal{F}_o(\alpha)^{0.5}}\right]^2 \tag{79}$$

Determine the value of (Z_o)

$$Z_o = \frac{K\Delta T_{max}\pi^{0.5}}{2\mathcal{F}_o(\alpha\tau_1)^{0.5}} \tag{80}$$

where

τ_1 = actual run time

$Y_o = \dfrac{1.0}{Z_o}$ if $Y_o > 1.0$, Eq. 73 and Eq. 74 are applicable;
if $Y_o < 1.0$, Eq. 78 is applicable

If $Y_o < 1.0$, the actual temperature rise for τ_1 is found from:

$$\Delta T_o = \Delta T_{max} \ (Y_o) \tag{81}$$

CONCLUSION

The basic techniques for evaluating an optical element with gas cooling have been presented. Obviously, not all of the possible conditions and techniques can be presented in a single paper. However, those techniques which have been presented, while not totally comprehensive, are at least representative of the more common problems associated with non-integrally cooled optics. Using these first order analytical tools will allow the analyst to obtain a "ballpark" value of what may be anticipated for a given set of conditions to be employed. Once the analyst has determined the general amount of gradient and cooling for a given optic, or system of optics, there may be a requirement to know in very great detail the precise amount of distortion and cooling. If precise information is required, a detailed numerical analysis may be in order.

REFERENCES

1. Hintz, J. O. *Turbulence*. 2nd ed., New York; McGraw-Hill; 1975.

2. Bird, B. R.; Stewart, W. E.; Lightfoot, E. N. *Transport Phenomena*. New York; John Wiley and Sons; 1960.

3. Schlichting, H. *Boundary Layer Theory*. 6th ed., New York; McGraw-Hill; 1968.

4. Eckert, E. R. G. *Heat and Mass Transfer*. 2nd ed., New York; McGraw-Hill; 1959.

5. Kays, W. M. *Convective Heat and Mass Transfer*. New York; McGraw-Hill; 1966.

6. Rohsenow, W. M.; Choi, H. Y. *Heat, Mass, and Momentum Transfer*. Englewood Cliffs; Prentice-Hall; 1961.

7. Cebeci, T.; Bradshaw, P. *Momentum Transfer in Boundary Layers*. New York; McGraw-Hill; 1977.

8. Gray, D. E., ed. *American Institute of Physics Handbook*. 3rd ed., New York; McGraw-Hill; 1972.

9. Edwards, D. K.; Denny, V. E.; Mills, A. F. *Transfer Processes*. 2nd ed., New York; McGraw-Hill; 1979.

10. Carslaw, H. S.; Jaeger, J. C. *Conduction of Heat in Solids*. 2nd ed., London; Oxford University Press; 1959.

11. Palmer, J. R.; Bennett, H. E. *Laser Induced Damage to Optical Materials*. NBS (U.S.) Spec. Pub. 638, September 1983; pp. 493-509.

12. Palmer, J. R. *Optical Engineering*. 22(4); July/August 1983; pp. 435-446.

13. Temoshenko, S.; Woinowsky-Krieger, S. *Theory of Plates and Shells*. 2nd ed., New York; McGraw-Hill; 1959.

14. Hottel, H. C.; Sarofin, A. F. *Radiative Transfer*. New York; McGraw-Hill; 1967.

15. Siegel, R.; Howell, J. R. *Thermal Radiation Heat Transfer*. 2nd ed., New York; McGraw-Hill; 1981.

16. Kreith, F. *Principles of Heat Transfer*. 2nd ed., Scranton; International Textbook Co.; 1966.

"A COMPREHENSIVE ANALYTICAL THEORY FOR UNIFYING PULSED AND CONTINUOUS WAVE LASER DAMAGE ON METAL MIRRORS, ENCOMPASSING THE RELATIONSHIP OF SMALL SPOT TO LARGE SPOT SIZE DAMAGE ON METAL MIRRORS."

James R. Palmer

Weapons Support Division
COMARCO, Inc.
1417 N. Norma Street, Ridgecrest, California 93555
Weapons System Effectiveness Contract N60530-83-D-0024
for the
Naval Weapons Center, China Lake, California 93555

A theoretical model has been developed which provides for evaluating both pulse and continuous wave laser damage on metal mirrors. The model technique employs the three-dimensional Palmer-Bannett model as a base. Using the fullwidth, half-band temporal profile for the pulse time constant and the thermal diffusivity of copper as a baseline, the time constant is corrected for other materials by the ratio of thermal diffusivities.

Basically, the theoretical concept rests on the premise that neither the Drude theory nor the Jakob-Kelvin theory are completely correct for short-pulsed (i.e., less than a microsecond) time constants. The heat sink below the first few angstroms acts as a dampening coefficient. The metal does not appear to be able to respond to the very short time constants and, as a consequence, the temperature versus reflectivity does not hold in straight-forward fashion. As the time constants extend into the microsecond regime, and longer, the relationships of temperature versus reflectivity become more representative.

Melt and Slip thresholds for copper, silver and gold have been presented previously [1]. The data have been generated for wavelengths of 1.06 μm, 2.7 μm, 3.8 μm, and 10.6 μm. Varying spot-sizes and different pulse widths were used. The theoretical model has been applied against this datum with excellent results ranging from 99.8% to 82% agreement.

Based on the relationship suggested by the three-dimensional Palmer-Bennett model and the unifying theory suggested, spot size dependence may be determined for given metal diamond turned mirror substrates.

The basis for damage, selected for the theory, is the point where slip phenomena occurs in the metal surface. This selection is more than arbitrary. Slip phenomena becomes the first indication that there is a permanent disruption to the optical surface. Further, slip and melt would seem to be the most thermally dependent manifestations of disruption.

Key words: pulsed lasers; continuous wave lasers; diamond turned metal mirrors, slip band damage; melt threshold.

*Numbers in brackets indicate the literature references at the end of the paper.

INTRODUCTION

Both the Drude Model and the Jakob-Kelvin Model relate absorptance, reflectivity, and emissivity to the conductivity of the metal. However, in both cases, the model depends on an adiabatic condition for the respective metal. For the conditions of a pulsed, or continuous wave laser, the adiabatic condition may not exist. A non-linear gradient develops between the irradiated surface and a depth into the optic where the temperature rise is 0. This axial depth for a pulsed laser will be on the order of of several microns, depending on spot size, optical material, and pulse width. The axial depth for a continuous wave laser will be of the order of several hundred microns, and again depending on the spot size, optical material, and run time.

The free electron theory of Drude is generally represented, for metals, as a number of free electrons moving in spaces between the atoms. He assumed that the motion of these electrons can be treated as though they were molecules of an ideal gas as pictured by the kinetic theory [2]. The electrical conductivity, from the Drude theory, is expressed as,

$$C = \frac{Ne^2\lambda\upsilon}{6RT} \qquad [2] \qquad (1)$$

where:

- n = electrons per unit volume
- e = electronic charge
- v = electron velocity
- λ = vt
- t = time between collisions
- R = gas constant
- T = absolute temperature

This expression for dc electrical conductivity has been metamorphased to.

$$\rho = \frac{M\Gamma}{Ne^2} \qquad [3] \qquad (2)$$

and for frequencies in the range $\Gamma \ll \omega < \omega p$, the optical absorption, according to the Drude theory is,

$$\alpha_p = \frac{\rho\omega p}{2\pi} \qquad [3]\,[4] \qquad (3)$$

where:

- ρ = resistance, ohm-cm
- Γ = electron relaxation frequency, rad/sec
- ωp = plasma frequency, rad/sec
- m = electron mass

The model used in the NWC prediction, for temperature dependent absorption, is,

$$\alpha_{(T)} = \alpha_p + \alpha_{f(T)} - \alpha_{f(T_o)} \qquad [5] \qquad (4)$$

where:

α_o = total absorptance at room temperature

$\alpha_f(T) - \alpha_f(T_o)$ = free electron contribution in excess of free electron absorption $\alpha_f(T_o)$ at room temperature T_o

$$\alpha_{f_{(T)}} = a\omega\left\{\left[1+\left(\frac{b\rho}{\omega}\right)\right]^{0.5} - 1.0\right\}^{0.5}$$

where:

ω = angular frequency of radiation

a = $3.948\ (10^{-17})f^{3/2}$ (sec)

b = $4.545\ (10^{14})f^{-3}$ ($\mu\Omega$ - cm - s)$^{-1.0}$

f = free electron sphere radius

ρ = resistance, $\mu\Omega$ - cm

The Jakob-Kelvin Model begins with Planck's theoretical expression for the intensity of monochromatic, upolarized radiation, normal to the radiating surface. So that,

$$\eta_{b,\lambda} = 2c^2h\,\frac{\lambda^{-5.0}}{e^{ch/k\lambda T}-1.0} = \frac{2c_1\,\lambda^{-5.0}}{e^{c_2/\lambda T}-1.0} \qquad [6] \qquad (5)$$

where:

c = velocity of light

h = Planck's quantum constant

k = Boltzmann's constant

c_1 = first constant of Planck's Law

c_2 = second constant of Planck's Law

The coefficient of refraction for waves entering a metal is found from:

$$n = c\ [k_e \mu_m \tau_c]^{0.5} \qquad (6)$$

where:

c = velocity of light

k_e = electrical conductivity, sec/cm^2

μ_m = magnetic permeability, dimensionless

τ_c = period of electromagnetic wave

The reflectivity for normal incidence of radiation (ϕ = 0)

$$\rho_{m,\lambda,0} = 1 - \frac{2}{n} \qquad (7)$$

and emissivity is found from

$$\epsilon_{m,\lambda,0} = \frac{2}{n} \qquad (8)$$

Assuming $\mu_m = 1.0$ for metals for air and vacuum, $R_e = \frac{1}{k_e}$, and λ/c with λ in centimeters;

$$\epsilon_{m,\lambda,0} = 1 - \epsilon_{m,\lambda,0} = 1 - \frac{2}{\sqrt{30}}\left[\frac{R_e}{\lambda}\right]^{0.5} \tag{9}$$

From Kirshoff's law, emissivity perpendicular to the surface is found from:

$$\epsilon_{m,\lambda,0} = \frac{\eta_{m,\lambda,0}}{\eta_{b,\lambda}} \tag{10}$$

From Aschkinass; [7]

$$\eta_{m,\lambda,0} = 0.74\sqrt{R_e}\; c_1 \frac{\lambda^{-5.5}}{e^{c_2/\lambda T} - 1.0} \tag{11}$$

where:

$$R_e = R_{e273}\left[\frac{T}{273}\right] \tag{12}$$

R_{e273} = electrical resistivity of the metal ot 0°C = 273°K
T = temperature of interest - °K

Then:

$$\frac{\eta_{m,\lambda,0}}{\eta_{b,\lambda}} = .0221\left[\frac{R_e}{\lambda}\right]^{0.5} \tag{13}$$

Schmidt and Eckert replaced Eq. 7 and Eq. 8 [7] with

$$\rho_{m,\lambda,0} = \frac{2n^2 - 2n + 1}{2n^2 + 2n + 1} \tag{14}$$

$$= 1 - \frac{2}{n} + \frac{2}{n^2} - \frac{1}{n^3} + \frac{1}{2n^5} - \frac{1}{2n^6} \cdots$$

So that, instead of Eq. 9

$$\rho_{m,\lambda,0} = \frac{60\,\lambda/R_e - 2\,[30\,\lambda/R_e]^{0.5} + 1.0}{60\,\lambda/R_e + 2\,[30\,\lambda/R_e]^{0.5} + 1.0} \tag{15}$$

$$= 1 - \frac{2}{30}\left[\frac{R_e}{\lambda}\right]^{0.5} + \frac{2}{30}\left(\frac{R_e}{\lambda}\right) + \cdots$$

The approximate formula is then,

$$\rho_{m,\lambda,0} = 1 - \epsilon_{m,\lambda,0} = 1.0 - 0.365\left[\frac{R_e}{\lambda}\right]^{0.5} + 0.0464\left[\frac{R_e}{\lambda}\right] \tag{16}$$

Because the two models require an adiabatic boundary condition, we would argue that neither is a complete description of the change in reflectivity for an optical element with a substantial heat sink immediately below the irradiated surface.

The Palmer-Bennett Model requires a time averaged absorbed flux density [9] [10] [11] [12]. For short pulse conditions, into the microsecond regime, the optical material cannot respond thermally to the incident radiation. As a consequence, the material, several microns below the surface, is not aware of the surface phenomena. The heat sink below the immediate surface would appear to dampen the electron activity on the surface. The temperature distribution is not linear. It follows a curve as shown in Figure 1.0.

A more representative change in the reflectivity would seem to follow:

$$\rho_\lambda = \rho_{o,\lambda} \exp\ (-k \cdot 0.5 \cdot \tau) \tag{17}$$

where:

$$k = \frac{1}{\tau} \ln\left|\frac{\rho_{D,\lambda}}{\rho_J}\right| \tag{18}$$

$$\rho_0 = \rho_{D,\lambda} - \frac{\left|\rho_{D,\lambda} - \rho_{J,\lambda}\right|}{\Sigma\Delta_T}\ (T_1 - T_x) \tag{19}$$

$$\Sigma\Delta_T = T_{amb} - T_{melt} \tag{20}$$

$$T_x = [T_{amb} + T_{melt}]\ 2^{-1.0} \tag{21}$$

where:

τ = full-width half-band of pulse.
$\rho_{D,\lambda}$ = diamond turned measured reflectivity at ambient temperature and wave length.
$\rho_{J,\lambda}$ = Jakob-Kelvin reflectivity at ambient temperature and wave length.

The Palmer-Bennett Model requires a time averaged pulse width. This requirement may be accommodated by using the ratio of thermal diffusivities for the various materials at ambient temperature. Because of the substantial data base regarding copper, all other materials are related to the thermal diffusivity of copper.

The ability of a heat sink to absorb more, or less, of the pulse, then, is modified as follows:

$$\lambda = \frac{\alpha_x}{\alpha_{Cu}}\ (\tau) \tag{22}$$

where:

τ = full-width half-band of the actual pulse

α_{Cu} = thermal diffusivity of copper, $\frac{K}{\rho c_p}$

α_x = thermal diffusivity of compared, material (x) $\frac{K_x}{\rho_x c_{p_x}}$

For example:

The thermal diffusivity of copper = 1.14 cm^2/sec
The thermal diffusivity of gold = 1.21 cm^2/sec [13]

If the full-width half-band is 0.5 μsec then, the pulse time of absorptance for the gold would be:

$$\tau_{gold} = \frac{1.21}{1.14} (0.5\ \mu sec)$$

$$\tau_{gold} = 0.53\ \mu sec$$

Because the gold can diffuse the absorbed flux density faster than the copper, the gold must absorb more of the pulse to achieve the same temperature at the surface.

This mathematical technique was applied against the calculated and measured melt thresholds of diamond turned copper, silver, and gold at 1.06 μm, 2.7 μm, 3.8 μm, and 10.6 μm [1] [5].

	Spot dia.
The full-width half-band for 10.6 μm (Cu) was 2.0 μsec	238.0 μm
The full-width half-band for 3.8 μm (Cu) was 0.40 μsec	63.2 μm
The full-width half-band for 2.7 μm (Cu) was 0.50 μsec	53.4 μm
The full-width half-band for 1.06 μm (Cu) was 0.009 μsec	52.4 μm

The relationship between the predicted values for melt, using the foregoing model, and the actual measurements is shown in Figure 2.0. The slip thresholds for these materials becomes the first plastic-permanent disruption of the optical surface. Based upon the average melt to slip ratios for the various wavelengths, the slip temperature for copper is ≅732°C. For gold the slip temperature is ≅637°C, and, for silver, the slip temperature is ≅336°C.

Then, the basic expression follows:

Basic Palmer-Bennett expression for temperature increase of surface

$$\Delta_T = \frac{2 I_o (1 - \rho\lambda) (\alpha_x \tau_x)^{0.5}}{K_x} \left\{ \frac{1}{\sqrt{\pi}} e^{-x^2} - \frac{2x}{\sqrt{\pi}} \int_x^{\infty} e^{-\xi_d^2} \right\} \tag{23}$$

For $\frac{R}{2\sqrt{\alpha_x \tau_x}} \geqslant 3.0$ Eq. 23 becomes

$$\Delta_T = \frac{I_o (1 - \rho_\lambda) (\alpha_x \tau_x)^{0.5}}{K_x} 1.1284 \tag{24}$$

For $\frac{R}{2\sqrt{\alpha_x \tau_x}} \geq 3.0$, the axial thermal diffusion depth is found from:

$$Z = 6(\alpha_x \tau_x)^{0.5} \tag{25}$$

For $\frac{R}{2\sqrt{\alpha_x \tau_x}} < 3.0$, the axial thermal diffusion depth is found from:

$$Z = 6(\alpha\tau)^{0.5} - 2R \tag{26}$$

and the temperature increase is found from:

$$\Delta_T = \frac{2I_o(1-\rho_\lambda)(\alpha_x\tau_x)^{0.5}}{K_x}\left\{\left[\frac{1}{\sqrt{\pi}}e^{-x^2} - \frac{2x}{\sqrt{\pi}}\int_x^\infty e^{-\xi^2}d\xi\right] - \left[\frac{1}{\sqrt{\pi}}e^{-Y^2} - \frac{2Y}{\sqrt{\pi}}\int_Y^\infty e^{-\xi^2}d\xi\right]\right\} \tag{27}$$

which reduces to:

$$\Delta_T = \frac{I_o(1-\rho_\lambda)(\alpha_x\tau_x)^{0.5}}{K_x}\left\{2\,\text{ierfc}\left[\frac{z}{2(\alpha_x\tau_x)^{0.5}}\right] - 2\,\text{ierfc}\left[\frac{(z^2+R^2)^{0.5}}{2(\alpha_x\tau_x)^{0.5}}\right]\right\} \tag{28}$$

It becomes apparent that spot size dependence is a function of laser beam diameter, optical element thermal properties, and pulsed or continuous wave run time.

So that when $\frac{R}{2\sqrt{\alpha_x\tau_x}} \geq 3.0$ there will be no radial diffusion and Eq. 24 may be used. However, when $\frac{R}{2\sqrt{\alpha_x\tau_x}} < 3.0$ then Eq. 28 must be used. The use of Eq. 28 indicates spot size dependence. However, the same expression accommodates this dependence. One may argue, then, that the larger the laser beam diameter, or the smaller the square root of the product of thermal diffusivity and irradiance time, the less dependent is the spot size.

Figure 2.0 shows the relationship of the model prediction as the measured experimental results. There are two columns which show the predicted fluence to melt using Eq. 24 and Eq. 28. Additionally, the model was compared to the experimental work of S. J. Thomas, et. al. [14]. This experiment was conducted on the LASL.L-9 Gigawatt Test Facility. A Gaussian beam at 10.6 μm and 1.7 ns pulse width is produced by this machine. The $1/e^2$ spot radius was 1 mm. Single point diamond turned copper mirrors were subjected to one-on-one shots at twenty-five (25) different sites in both vacuum and in air. The average damage (melt) threshold of both air and vacuum was 14.6 J/cm^2. The authors suggest, "On the average mirror 8.5 ±1.0 J/cm^2 is a safe level, corresponding to 71 ±12% of the single-shot threshold."

Using Eq. 24 and allowing the temperature to raise 1911°F from an ambient of 70°F, then;

$$\Delta_T = \frac{I_o(1-\rho\tau)(\alpha\tau)^{0.5}}{K}(1.1284)$$

will yield

$$\frac{1911(224)}{\left[(1-0.99)\left(\frac{4.42 \times 1.7(10^{-9})}{3600}\right)^{0.5} 1.1284\right]} = 2.6258(10^3)\ \frac{BTU}{HR - FT^2}$$

$$= 8.2281(9)\ W/cm^2$$

$$= 14.08\ J/cm^2$$

As stated before, the average slip threshold for copper should be on the order of 732°C (1349°F).

Slip threshold should be $\left[\frac{1349}{(1911 + 70)}\right]$ (14.08) = 9.6 J/cm^2.

The suggestion by S. J. Thomas, et. al., is that a single point diamond turned copper mirror should not witness a fluence greater than 8.5 ±1.0 J/cm^2 to maintain a safe level below slip threshold which comports to the calculation above.

CONCLUSION

The free electron Drude Model and the Jakob-Kelvin Model satisfy the steady-state condition for temperature dependent reflectivity. However, they do not appear to satisfy the conditions for fast transient response. The free electron thermal equilibrium relaxation time is on the order of 10^{-14} seconds. This is obviously a shorter time, by orders of magnitude, when compared to the pulse width [15]. However, the thermodynamic response of a free electron metal, i.e., good conductor, at 1 μm of depth is on the order of 1 (10^{-6}) second for copper, aluminum, gold, and 0.5 (10^{-6}) second for silver. Based upon the thermodynamic response, as a function of thermal diffusivity, the presented model permits evaluation of both pulsed and continuous wave laser response of diamond turned metal mirrors, to a first order approximation, in the infrared wavelength regime.

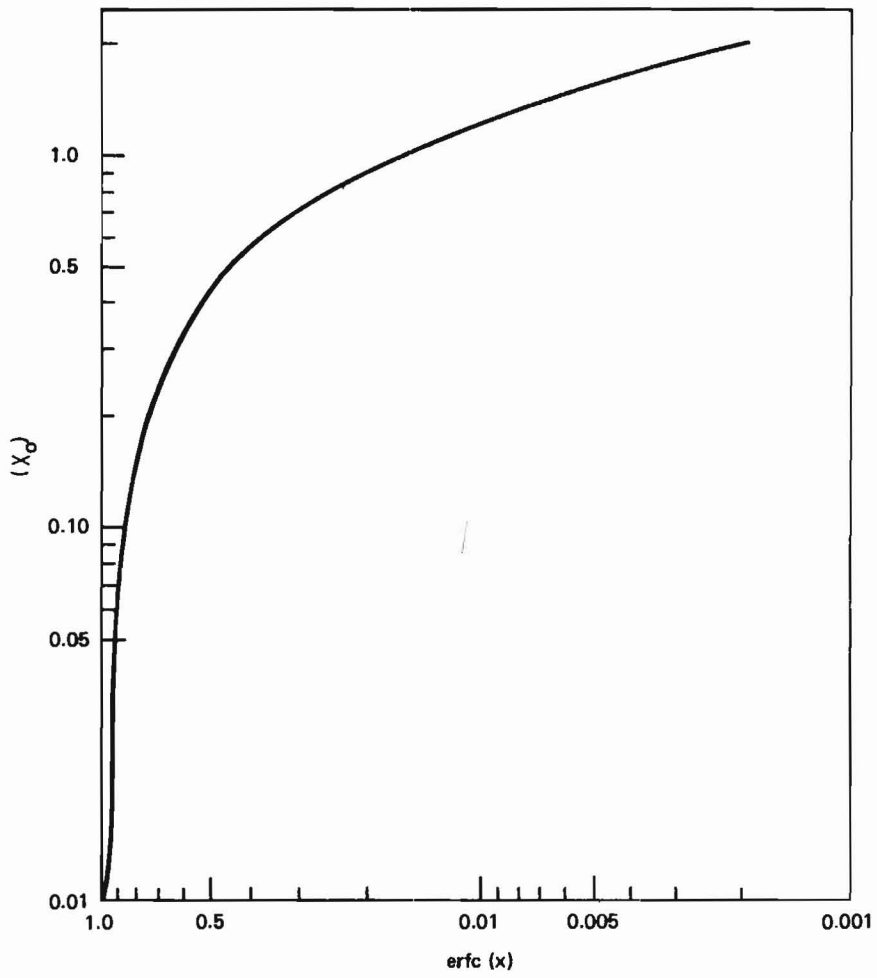


Figure 1.0

J/cm² NWC MEAS. FLUENCE	J/cm² NWC PRED. FLUENCE	J/cm² PALMER-BENNETT PRED. FLUENCE	MEAS./PRED AGREEMENT		SURFACE TEMP RISE		SPOT SIZE		WAVELENGTH	$\rho\lambda$	SPOT SIZE (μ)
			NWC	PALMER-BENNETT	EQ 24°F	EQ 28°F	YES	NO			
Cu 476	415	482.8	0.872	1.014	1980.8	1981		X	10.6	0.99	238
Ag 373	349	377.7	0.936	1.013	1760.6	1760.6		X		0.99	
Au 275	256	283	0.931	1.029	1944.9	1945		X		0.987	
Cu 176	245	186.2	1.392	1.058	1979.4	1981		X	3.8	0.988	63.2
Ag 237	224	236.5	0.945	0.998	1780.8	1760.6		X		0.991	
Au 120	161	120	1.342	0.000	1945.1	1945		X		0.9861	
Cu 194	234	189.6	1.206	0.977	1991	1981		X	2.7	0.9872	53.4
Ag 201	224	238	1.114	1.184	1848	1760.6	X			0.99	
Au 123	161	113.5	1.303	0.923	1959	1945		X		0.9832	
Cu 9.0	14.7	9.36	1.63	1.04	1981	1981		X	1.06	0.9654	52.4
Ag 10.5	13.9	11.2	1.32	1.07	1760.6	1760.6		X		0.9724	
Au 5.6	7.5	6.08	1.34	1.09	1945	1945		X		0.9582	

FLT TEMP:

Cu = 1981°F = 1083°C
Ag = 1760°F = 960°C
Au = 1945°F = 1063°C

Figure 2.0

REFERENCES

1. Porteus, J.; Decker, D.; Faith, W.; Grandjean, D.; Seitel, S.; Soileau, M. *Pulsed Laser-Induced Melting of Precision Diamond-Machined Cu, Ag, and Au at Infrared Wavelengths*. IEEE J. Quantum Electronics; October 1981.

2. Hune-Rothery, W. *The Metalic State*. Oxford, England; Oxford Press; 1931.

3. Kittel, C. *Introduction to Solid State Physics*. 4th ed.; New York, NY; John Wiley and Sons; 1971.

4. Sparks, M.; Loh, E. *Temperature Dependence of Absorptance in Laser Damage of Metallic Mirrors: I Melting*. J. Opt. Soc. Am.; 1979.

5. Porteus, J.; Decker, D.; Seitel, S.; Soileau, M. *Dependence of Metal Mirror Damage Threshold on Wavelength, Material, Pulse Length, and Preparation Method*. Bennett, H. E.; Glass, A. J.; Guenther, A. H.; Newnam, B. E.; ed.; Nat. Bur. Std. (U.S.) Spec. Pub. 620; 1981; pp. 201-215.

6. Jakob, M. *Heat Transfer*. Vol. 1; New York, NY; John Wiley and Sons; 1953.

7. Aschkinass, E. *Annalen d. Physik*. Berlin, Germany; (17) 1905.

8. Schmidt, E.; Eckert, E. *Forscheeng a.d. Geb. d Ingenieurwes*. Berlin, Germany; (6) 1935.

9. Bennet, H. E. *Insevsitivity of the Catastrophic Damage Threshold of Laser Optics to Dust and Other Defects*. Bennett, H. E.; Glass, A. J.; Guenther, A. H.; Newnam, B. E.; ed.; Boulder, CO; Nat. Bur. Std. (U.S.) Spec. Pub. 620; October 1981.

10. Palmer, J. R.; Bennett, H. E. *Relationship Between Coating Defects and the Limiting Flux Density a Cooled Laser Mirror Can Withstand*. Bennett, H. E.; Glass, A. J.; Guenther, A. H.; Newnam, B. E.; ed.; Boulder, CO; Nat. Bur. Std. (U.S.) Spec. Pub. 638; September 1983.

11. Palmer, J. R. "First Order Analytical Technique for Evaluating Heat Transfer, Coolant Channel Thermal and Pressure Ripple, Bending, Burnout, and Coating Damage on Single and Multiple Layer Laser Mirror Cooled Heat Exchanges." Presented at the 14th Annual Symposium on Optical Materials for High Energy Lasers; Boulder, CO; 16-17 November 1982.

12. Palmer, J. R. "Continuous Wave Laser Damage on Optical Components." *Optical Engineering*. Vol. 22; No. 4; July/August 1983.

13. Barnes, W. P. "Optical Materials - Reflective." in *Applied Optics and Optical Engineering*. Vol. VII; Shannon, R. R.; Wyant, J. C.; ed.; New York, NY; Academic Press; 1979.

14. Thomas, S. J.; Phipps, C. R.; Harrison, R. F. *Optical Damage Limitations for Copper Mirrors Used in CO_2-ICF Laser Systems*. Bennett, H. E.; Glass, A. J.; Guenther, A. H.; Newnam, B. E.; ed.; Boulder, CO; Nat. Bur. Std. (U.S.) Spec. Pub. 620; October 1981.

15. Decker, D. L.; Hodgkin, V.A. *Wavelength and Temperature Dependence of the Absolute Reflectance of Metals at Visible and Infrared Wavelengths*. Bennett, H. E.; Glass, A. J.; Guenther, A. H.; Newnam, B. E.; ed.; Boulder, CO; Nat. Bur. Std. (U.S.) Spec. Pub. 620; October 1981.

The speaker agreed with a questioner that it was not clear whether the model presented would apply to dielectrics. He suggested that the Drude model used might not apply to pulsed laser damage to metals if equilibrium conditions were not established. This conclusion was questioned by members of the audience.

Manuscript received 5-24-84/sar

Catastrophic versus Microscopic Damage: Applicability of Laboratory Measurements to Real Systems*

S. R. Foltyn and L. J. Jolin

Los Alamos National Laboratory
Los Alamos, NM 87545

At ultraviolet wavelengths, damage to both coatings and bare surfaces is dominated by the presence of discrete localized defects. During multiple-shot irradiation, the overwhelming majority of these defects are damaged by the first or first few shots. Initially, damage morphology is that of a crater of approximately 10 μm in diameter; however, upon continued irradiation, one of two events can occur: either the crater grows to catastrophic dimensions or it remains unchanged. In the latter case, the damage is only observable under a microscope, it may be indistinguishable from cosmetic defects present before irradiation, and it is likely that any related degradation in optical performance is unmeasurable.

In view of the generally accepted definition of laser damage (i.e., any visible change in the surface), it is important to consider the implications for real systems. These are discussed in the context of ultraviolet test results for both coatings and surfaces.

Key words: catastrophic damage; damage morphology; laser-induced damage; microscopic damage; multiple-shot irradiation.

1. Introduction

The subject of catastrophic versus microscopic damage is not new to these proceedings [1]. In this paper we offer results of a preliminary investigation in which it was found that a rigid definition of damage may be unrealistic, may unfairly constrain the design of practical systems, and may mislead investigators attempting to optimize a production process. A major question remains, however, regarding the actual optical degradation associated with microscopic damage. A possible solution is the establishment of an objective damage criterion.

2. Catastrophic versus Microscopic Damage: Definitions and Discussion

2.1. Catastrophic Damage

Figure 1. is a micrograph of catastrophic damage on a 351-nm reflector.[1] On the first shot, a few barely visible pits were formed. On succeeding shots these pits grew, merged, and became the 1-mm-wide footprint that is shown. Although variable, this particular damage site has grown to the 25% intensity contour of the elliptical test spot—clearly a catastrophic failure. The peak fluence in this test was slightly over threshold and damage at the edge of the footprint has occurred at a fluence well below the threshold level.

This form of catastrophic damage, pitting followed by growth, is observed primarily in multilayer dielectric reflectors—over 90% of the uv reflectors tested at Los Alamos have damaged in this mode. Another form of catastrophic damage is illustrated in figure 2. In this case, usually observed at fluence levels well above threshold on AR's and bare surfaces, a dense collection of pits has formed but no growth is observed during continued irradiation. In that a significant fraction of the irradiated area has been disturbed, it is certain that an actual component thus damaged would be rendered useless, hence the designation—albeit subjective—catastrophic. To quantify the degree of

*This research was performed under the auspices of the U. S. Department of Energy and the Defense Advanced Research Projects Agency.

[1]Test conditions for all present results are: λ=351 nm, τ=12 ns, and prf=35 pulses/sec. Testing was n-on-m where, at each test fluence, ten sites were irradiated for 140 shots or more.

damage would require a measurement of optical degradation[2] such as a change in reflectance or scatter. In a practical sense, damage may eventually be evaluated on the basis of comparing such measurements to system requirements rather than on the basis of visual observations.

2.2 Microscopic Damage

Figure 3. illustrates the morphology of microscopic damage. The two damage pits (circled to distinguish them from surrounding cosmetic defects) were produced in a 351-nm AR coating irradiated at slightly above the damage threshold. At much higher fluence values, these pits would evolve into catastrophic damage, but at an intermediate level, no further change was observed during irradiation for 10^4 shots. This behavior is typical of most but not all uv AR coatings tested at Los Alamos.

Features of microscopic damage are summarized below.

- Small pits, usually less than 20-μm diameter.
- Indistinguishable from cosmetic defects (pinholes, dust) at 100X magnification.
- Low surface density—fewer than 10 mm^{-2}.
- No growth under continued irradiation except at very high fluence levels.
- Observed primarily on bare surfaces and antireflection coatings.

3. Damage Morphology

The morphology of a precursor to catastropic damage is shown in figure 4. at various SEM magnifications. The frame in the upper left shows the pits as seen in the test facility viewing system. The 49-layer coating has been removed down to the substrate and a commonly observed crater in the fused silica substrate is visible. The author of reference [1] finds size to be a critical parameter for damage growth related to absorbing defects under cw irradiation; we suggest that electric field enhancement at the broken edges of the coating is a possible growth mechanism here.

The absence of these rough edges in a microscopic damage site is shown in figure 5. A cosmetic defect appears in the frame at lower right to demonstrate the similarity between the two, and also to illustrate that, by careful observation, damage sites <u>are</u> distinguishable from pinholes by virtue of the discoloration that surrounds them.

4. Test Results and Discussion

Figure 6. is the result of separating catastrophic from microscopic damage events on uncoated CaF_2 at 351 nm. The curves are normalized to the catastrophic damage threshold. As fluence was gradually increased, microscopic damage was first observed at about 30% of the catastrophic threshold. The shallow slope of the probablity curve, and the resulting high level of statistical noise, indicate a relatively low density of defects responsible for microscopic damage. At the catastrophic threshold, a transition occurs to a higher density of defects that are now responsible for damage accompanied by growth. Whether this is a result of the presence of two different types of defect, or simply a different response at higher fluence levels by a single class of defect is, at this point, unknown.

Figures 7. and 8. are curves generated in a similar manner, but now the emphasis is on the optimization of deposition rates for antireflection coatings. The results are summarized in table 1.

---

[2]There are preliminary indications [2] that the energy loss associated with a damage pit is far greater than would be expected from simple consideration of the amount of visibly damaged surface area.

Table 1. Influence of Deposition Rate upon Damage Thresholds

Deposition Rate	Microscopic Threshold	Catastrophic Threshold
2Å/sec	4.7 J/cm^2	5.9 J/cm^2
7Å/sec	3.9 J/cm^2	8.7 J/cm^2

[a] Al_2O_3/SiO_2; 4-layer AR's at 351 nm; R=0.3%.

As can be seen, if microscopic damage proves to be optically detrimental, slightly better performance is available at the lower deposition rate. Alternately, if only concerned about catastrophic damage, the higher deposition rate offers better performance. Admittedly, these considerations ignore other factors such as durability or optical performance that may also vary with deposition rate: The point, however, is that depending on the type of damage being considered, completely different results are obtained in the attempt to optimize this coating parameter.

5. Conclusions

We have examined two different types of laser-induced damage behavior. One type is nongrowing, possibly harmless, and is primarily observed on uncoated surfaces and antireflection coatings. The other type involves growth to catastrophic dimensions with continued irradiation, and is generally seen on reflectors. The significance of microscopic damage remains to be determined; it clearly will always have a place in coating research, but may eventually be neglected in the design of real systems.

6. References

[1] Bennett, H. E. Insensitivity of the Catastrophic Damage Threshold of Laser Optics to Dust and Other Surface Defects. Nat. Bur. Stand. (U.S.) Spec. Publ. 620; 1980. 256 p.

[2] Marrs, D., Naval Weapons Center (private communication).



Figure 1. Catastrophic damage in a 351 nm reflector. At slightly over threshold, the initially small damage sites grew with continued irradiation to the 25% intensity contour of the beam.

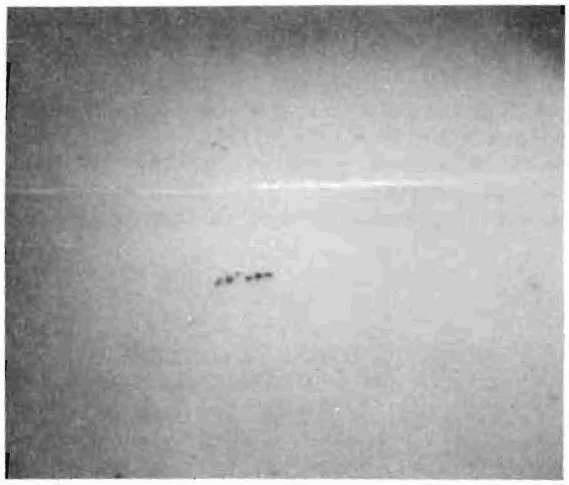


Figure 2. This type of catastrophic damage is stable under continued irradiation, but, due to the size and density of pits, optical performance has been degraded.

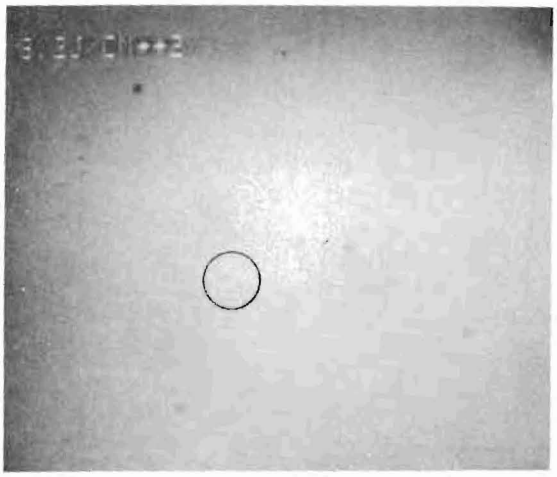
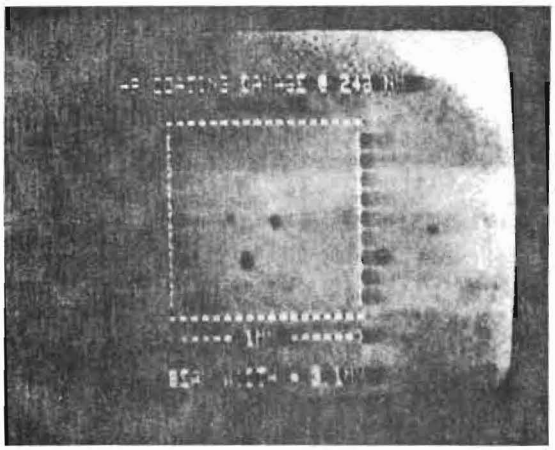


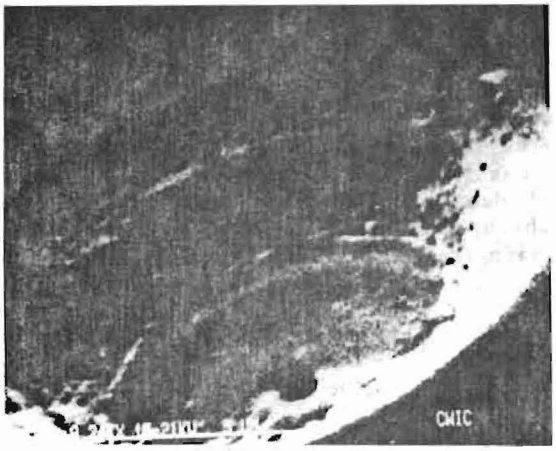
Figure 3. The microscopic damage (circled) is nearly indistinguishable from cosmetic defects. At fluence levels well above threshold, these sites did not grow for 10^4 shots. The effect upon optical performance is unknown.



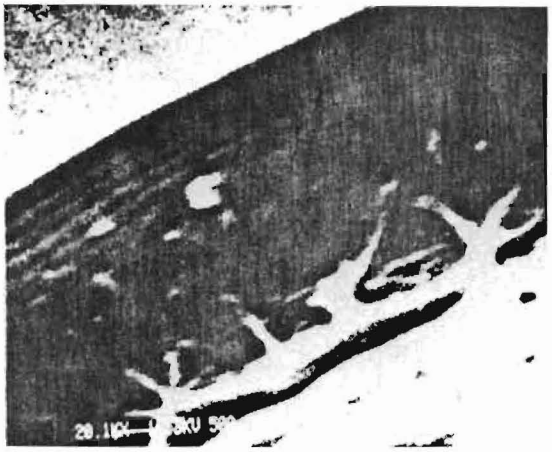
MICROSCOPE/VIDEO at ~ 100 x



SEM at ~ 1200 x

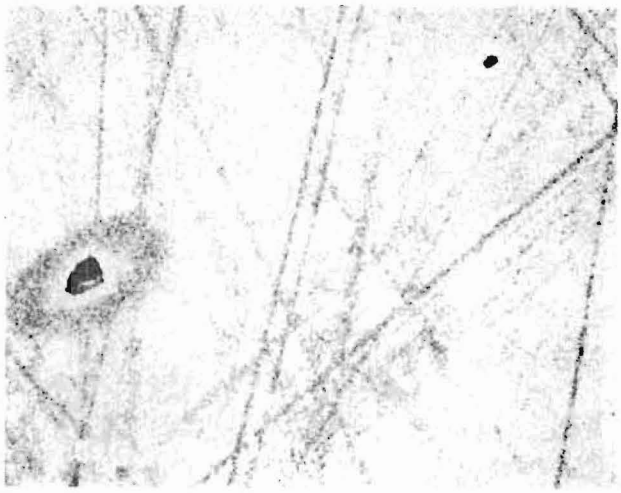


SEM at ~ 9000 x



SEM at ~ 20 000 x

Figure 4. Precursors to catastrophic damage in a 49-layer reflector. One possible growth mechanism is electric field enhancement at the broken edges of the coating.





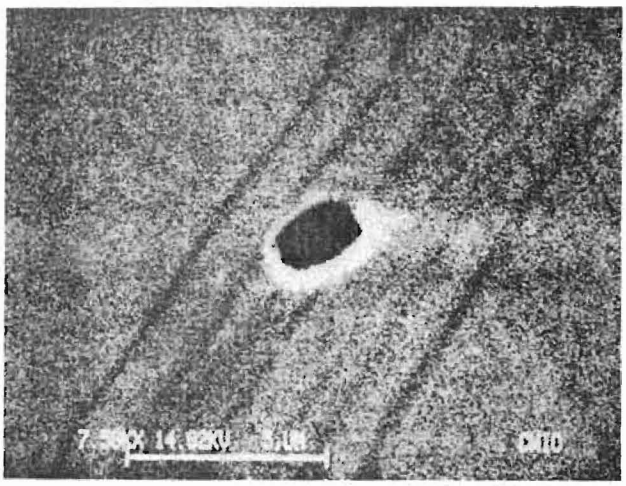


Figure 5. Microscopic damage in a 351 nm AR. The top frame (SEM at 1500X) shows a damage pit and surrounding discoloration at left center and a cosmetic defect at upper right. The cosmetic defect was undisturbed at the fluence which produced damage. The damage site and the defect, which appears to be a 1-μm pinhole, are shown again (center and bottom, respectively) at 7500X.

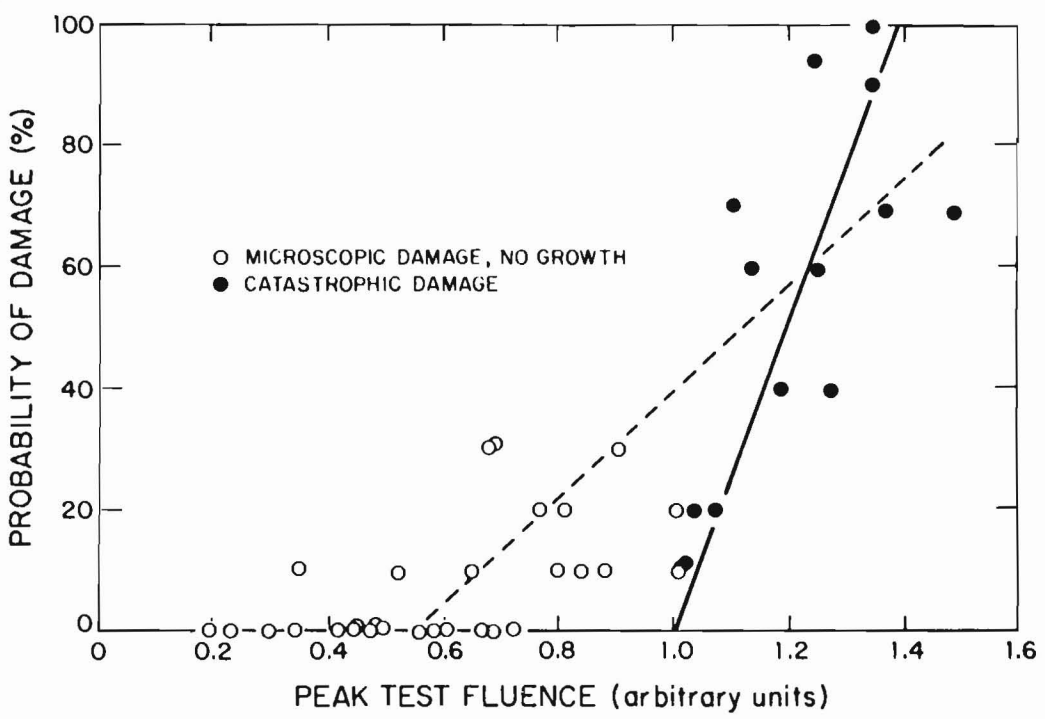


Figure 6. Damage probability curves for uncoated CaF_2 at 351 nm. Two distinct curves result from separating catastrophic and microscopic damage.

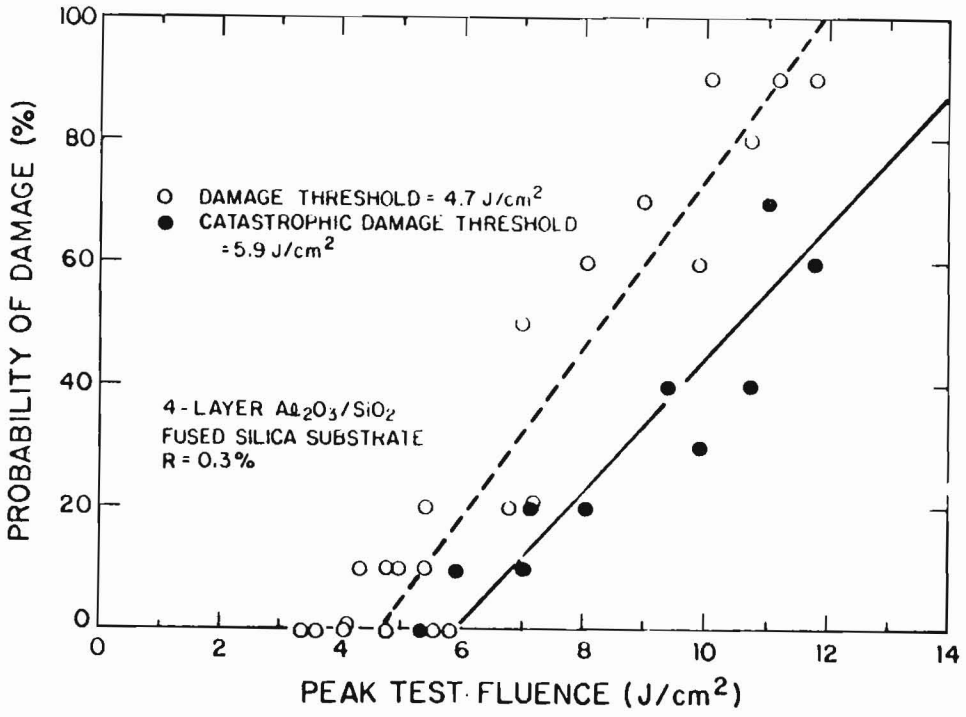


Figure 7. Damage curves for an antireflection coating produced at a slow deposition rate.

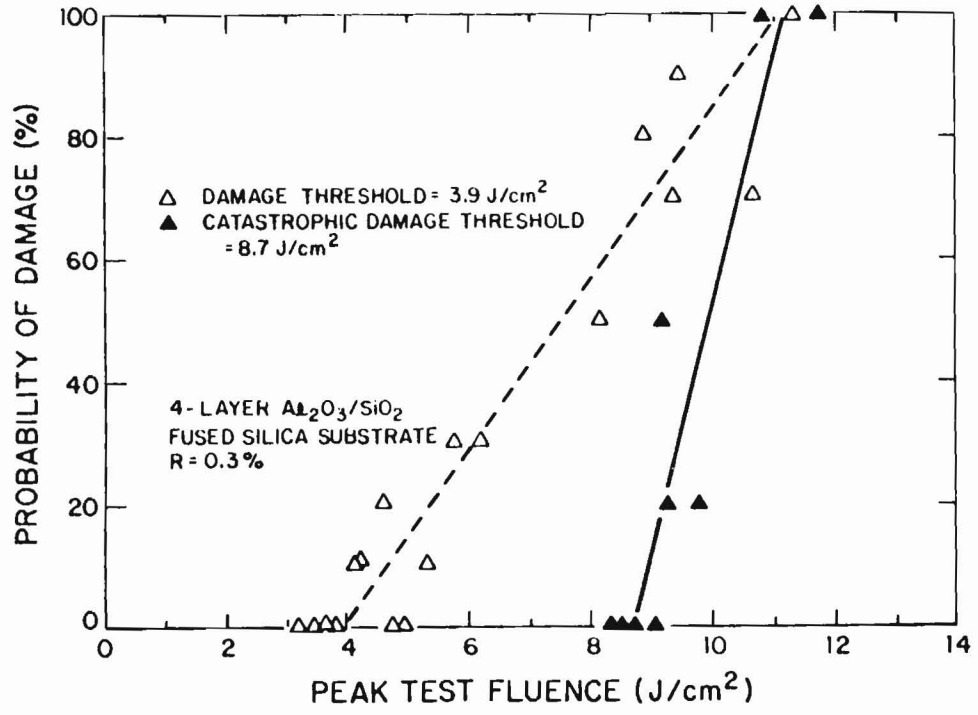


Figure 8. Damage curves for an antireflection coating produced at a higher deposition rate than that of figure 7. While the slower rate gives a higher microscopic threshold, a higher catastrophic threshold results from a higher deposition rate.

It was suggested that to determine if a damage site is stationary or not as defined in the theory presented, it would be necessary to perform n-on-1 tests, not merely the more common 1-on-1 tests. The speaker agreed and pointed out that it may be necessary for the optical designer to determine the life of the optics in terms of number of shots and the level of scattering that can be tolerated.

In response to another question, the speaker stated that he had not worked out a thermal analysis of irradiance-level-spot-size-growth for pulsed irradiation similar to that reported by Dr. H. E. Bennett for cw irradiation. Such a relation apparently exists, based on the qualitative information on spot sizes in the AR coating and reflector, and he felt it should be explored. Experimentally, when pits which form in the wings of the laser spot are moved into a higher fluence area, they do not grow in most cases. The density of microscopic damage sites is probably very nearly equal to the number of cosmetic defects that were present before irradiation. Also, experimentally, the damage sites in high reflectance multilayer coatings tend to grow, whereas those in antireflective coatings do not. There is no obvious explanation for this effect at present.

Manuscript received 3-13-84/sar

Toward Improved Accuracy in Limited-Scale Pulsed Laser Damage Testing Via the "Onset Method"*

S. C. Seitel and J. O. Porteus

Michelson Laboratory, Physics Division
Naval Weapons Center, China Lake, California 93555

A recently reported method for determining the defect damage onset (minimum intensity for defect initiated damage) in optical surfaces offers certain advantages over more conventional methods. First of all, the onset is a more reliable and useful indication of operational performance than conventionally measured thresholds, which may depend strongly on the size of the tested area. Secondly, measurement of damage frequency vs intensity provides valuable information on defect densities. This permits more effective use of a limited test area and provides a basis for defect classification. Effective limited-scale testing is becoming increasingly important as larger optical surfaces and reduced defect densities are made possible by improved coating technology.

In this paper, the onset method is mainly applied to 1.06 μm coatings, tested with a 40 μm ($D-1/e^2$) Gaussian focal spot and 2.7 μm coatings, tested with a 67 μm spot. Comparisons are made between onsets and conventionally measured thresholds, including a demonstration of convergence with large-spot thresholds from other laboratories. Examples of damage frequency distributions indicating the presence of more than one class of defect will also be shown. Finally, the onset model is extended to include flat-topped spatial profiles, and possible advantages over Gaussian profiles are noted.

Key words: defect-initiated laser damage; onset method; thin film coatings.

Introduction

Laser damage data often are expressed in terms of the intensity at which the probability of failure on a single shot is 50%. This conventional damage threshold by definition represents the mean of a distribution which may extend to much lower levels of test irradiation [1].[1] This is especially important when the damage process is initiated at isolated defects whose mean separation is comparable to the diameter of the irradiated area. Recent results suggest it often is more appropriate to evaluate damage susceptibility in terms of the onset of this distribution. Foltyn [2] has reported evidence that the conventional damage threshold definition is inherently dependent upon the diameter of the illuminated area, concluding that the damage threshold should be defined as that intensity at which the probability of failure first departs from zero, i.e., the maximum nondamaging intensity, which is not spot-size dependent. Porteus [3] has reported similar findings and further has concluded that, by appropriate modeling of the defect distribution functions, it is possible to extract most probable values for this "onset" intensity from rather scattered failure-frequency data.

In this paper, the earlier work [3] in onset extraction is extended and applied to visible, near IR, and IR multilayer coatings. A brief review of the onset method is given and a solution developed for the special case of a Gaussian intensity distribution in the irradiated spot. An explicit spot-size scaling rule results, independent of the defect ensemble. Different models for the defect ensemble functions are used to fit experimental curves, and the necessity of assuming a nondegenerate model for some coatings is demonstrated. An example of a coating with two well-defined defect types contributing to failure is shown. Finally, the model is "extended" to the mathematically simpler case of a "top-hat" spatial profile, and the potential advantages over a Gaussian intensity distribuiton are noted.

*Work supported by Navy Independent Research Funding.
[1] Numbers in brackets indicate the literature references at the end of the paper.

Onset Model Review and Spot-Size Scaling

A detailed theoretical development of the onset model and its associated data analysis algorithms is given in ref. [4]. Only the principal conclusions and implications are reviewed in this section. In the case of pulsed, laser-induced failure of optical surfaces and thin films containing isolated defect sites, an appropriate expression for the probability of failure on a single shot is

$$P = 1 - \exp\left[-\int_A dA \int_0^{I(x,y)} f(I_d)dI_d\right] \quad . \tag{1}$$

An important assumption made in the derivation of this expression is that each individual defect has a uniquely defined failure intensity I_d. Of course, different defects may fail at different levels, and thus the ensemble function $f(I_d)$ represents the number of defects per unit area which will fail between I_d and $I_d + dI_d$. Here $I(x,y)$ may be interpreted either as the temporal peak intensity or the fluence at a point x,y on the surface, as appropriate. The spatial integration is taken over the area A of the irradiated spot.

Specification of the spatial intensity distribution $I(x,y)$ permits development of a spot-size scaling relationship, without requiring detailed knowledge of the defect ensemble. A Gaussian profile may be expressed in polar coordinates as

$$I = I_a \exp(-r^2/w^2) \quad , \tag{2}$$

where I_a is the axial intensity and w is the natural Gaussian radius, or half-width at 1/e. Combining eqs (1) and (2) and differentiating on I_a yields

$$\frac{1}{1-P}\frac{dP}{dI_a} = 2\pi \int_0^{\infty} f\left[I_a \exp(-r^2/w^2)\right] r \exp(-r^2/w^2)dr \tag{3}$$

$$= \pi w^2 \frac{1}{I_a}\int_0^{I_a} f(I')dI' \quad .$$

Reintegrating on I_a,

$$P(I_a) = 1 - \exp\left\{-\pi w^2 \int_0^{I_a} \left[\frac{1}{I}\int_0^{I} f(I')dI'\right]dI\right\} \quad . \tag{4}$$

The significance of this last expression is that the integrals are independent of the spot radius w. The nominal irradiated area (πw^2) appears only as a simple scale factor multiplying them.

It is possible to invert the damage probability expression and obtain a formal solution for the damage ensemble:

$$f(I_a) = \frac{1}{\pi w^2 (1-P)} \left[\frac{dP}{dI_a} + \frac{I_a}{1-P}\left(\frac{dP}{dI_a}\right)^2 + I_a \frac{d^2P}{dI_a^2}\right] \quad . \tag{5}$$

In principle, an experimental measurement of damage frequency as a function of applied intensity should reveal the appropriate damage ensemble directly. To accomplish this, the data would have to be sufficiently well behaved to permit extraction of both the first and second derivatives. In practice, it is seldom possible to obtain failure frequency data of the required precision. A useful alternate approach is to postulate a simple trial model for the damage ensemble, calculate the corresponding damage probability curve, and see how well it reproduces the experimental data.

Defect Ensembles and Experimental Examples

The simplest model for the defect ensemble is obtained by assuming that all defects do fail at exactly the same intensity I_o. In this degenerate case, the ensemble function f(I') in eq (4) takes the mathematical form of a delta function about I_o, normalized to the areal density of defects N:

$$f(I') = N\delta(I' - I_o) \quad . \tag{6}$$

The resultant probability of failure $P(I_a)$ is given by

$$P(I_a) = 1 - \left(\frac{I_a}{I_o}\right)^{-\pi w^2 N} \quad . \tag{7}$$

This last expression essentially is identical to that derived in ref. [2] for a single layer. Equations (6) and (7) are plotted in figure 1. Although the solid and dashed curves reach a 50% damage frequency (or conventional threshold) at different intensities, they have the same onset. The parameter separating these curves is the product of the Gaussian spot area and the defect density. Thus, the smaller the irradiated spot or the lower the defect density, the higher the conventional threshold, in agreement with experimental experience. The negative curvature of the damage probability near onset is characteristic of this degenerate onset model and beam profile combination. Physically, the increase of failure probability with applied intensity occurs only because the area irradiated at greater than the damage level I_o increases, thus encompassing more defects.

An example of damage frequency data which is described well by the degenerate model is shown in figure 2. This 1.06 μm multilayer narrow-band antireflection coating is a commercial product [5] which was damage tested at the Naval Weapons Center (NWC) as part of the round-robin experiment reported by Guenther [6]. Column 1 of table 1 contains pertinent measurement parameters. Of particular interest is the nominal Gaussian spot radius of 14 μm, which corresponds to a diameter at $1/e^2$ of approximately 40 μm. In current laser-damage practice, this is a very small spot.

A typical data point was obtained by exposing many sites on the surface to single pulses at a fixed intensity and noting the percentage which failed. The procedure was then repeated at other intensities, to develop the overall experimental trend shown. The number of sites exposed at a given intensity was not fixed, in contrast to the procedure of ref. [2], but rather was determined by monitoring the standard error in the damage frequency as the data were acquired [4]. The solid curve represents the least-squares fit to the theoretical model, assuming a degenerate defect ensemble. More complicated ensembles, as described below, also were considered in analyzing this coating, but

the degenerate assumption yielded the least mean square deviation. The onset fluence extracted by this procedure was 2.5 ± 1.0 J/cm^2.

The density of defects, also obtained as a fit parameter, was approximately 4×10^4 cm^{-2}. This corresponds to a mean defect spacing of about 50 μm, which is larger than the irradiated spot size. Thus there should be a significant discrepancy between the conventional threshold and the onset. The most probable value for the threshold fluence was determined by standard techniques [7] to be 51 ± 43 J/cm^2. The large uncertainty is another consequence of the fact that the defect spacing is not small compared to the spot size. For this sample, tested with this spot size, the ratio of threshold to onset is approximately 20.

Seven other laboratories also evaluated examples of this coating as part of the round-robin experiment [6]. Since the range of spot sizes employed varied two orders of magnitude, it should be possible to test the spot-size predictions of the onset model. Unfortunately, the experimental parameters other than spot size also varied greatly, which makes interpretation of the round-robin results difficult. Three laboratories used experimental parameters (except spot size) sufficiently similar to NWC's to make a rough comparison of results possible. That is, the temporal pulse duration (FWHM) was between 1 and 20 ns, the sites exposed were randomly selected, only one exposure was made per site, and the analysis was based on a "go/no-go" decision whether damage occurred at a particular site. Table 2 lists these laboratories, ordered by decreasing spot size, together with the number of examples of this coating tested, and the mean thresholds reported. Also shown is the onset value for the sample of figure 2. Clearly, it is this onset, rather than the small-spot threshold measured at NWC, which agrees better with the large-spot thresholds from the other laboratories.

The important point is not the detailed quantitative comparison, which is rendered doubtful at best by remaining uncompensated differences in experimental parameters and procedures between the four selected laboratories. Rather, the significant observation illustrated here is that the onset approach does yield failure levels which are independent of spot size and which agree with conventional thresholds obtained with spot sizes much greater than the mean defect spacing. This allows testing with smaller, less expensive sources, a desirable option as coatings continue to improve.

Not all samples can be fitted so conveniently with the degenerate model. For some, it is necessary to use a more flexible model, which assumes that the defect damage levels are distributed across intensity. A simple power-law model for the ensemble function f(I') provides sufficient flexibility to fit all of the data obtained at NWC to date:

$$f(I') = C(I' - I_o)^p \quad ; \quad I' > I_o \tag{8}$$

$$= 0 \quad ; \quad I' < I_o \ .$$

Here the power p is an arbitrary real number, and the multiplying constant C is determined from the cumulative normalization relation

$$\int_{I_o}^{I_n} f(I')dI' = N(I_n) \quad , \tag{9}$$

where $N(I_n)$ is the density of defects contributing to failure when the local intensity has any arbitrary value I_n.

Typically, negative, nonintegral powers are required to fit the coatings tested at NWC. Figure 3 shows examples of such defect ensembles. The simplest case, p=0, is shown at the upper left. Below

onset, the number per unit intensity interval of defects which will fail is zero, while above onset, it is a constant. As the power becomes more negative, the distribution of defect failure levels becomes less uniform and tends to peak about the onset intensity. In the limit as p approaches -1, the ensemble becomes degenerate in nature, as indicated at lower right. While the degenerate (p=-1) and the "uniform" (p=0) cases, which have easily visualized physical interpretations, serve as bounds on the ensemble in the analyses reported here, p is not restricted to this range by physical considerations. Positive powers may be appropriate for other coatings.

Figure 4 contains the failure probability curve corresponding to the uniform ensemble. As in the degenerate case, the onset is independent of spot size and defect density, while the threshold is not. The shape of the curve differs, however. Near the onset, the curvature is positive, not negative. This occurs because the continuum of failure levels in the ensemble function requires that the density of damaged sites increase with intensity, as well as the area irradiated above onset.

An example of a coating which requires a nondegenerate ensemble is shown in figure 5. This 2.7 μm multilayer mirror was tested at its design wavelength using a 67-μm-diameter spot. Experimental parameters are contained in column 2 of table 1. The dashed line represents the least squares fit obtained with the degenerate ensemble and predicts an onset, in arbitrary units, of one. The solid line results from a more general least squares analysis in which the power, p=-0.3, was extracted as a fit parameter. The improvement in fit is obvious. It is significant that the onset predicted in this case is lower than the degenerate case prediction by approximately a factor of two.

An example of a coating which is almost, but not quite, degenerate in character is shown in figure 6. This multilayer broad-band antireflection coating also is a commercial product [8] which was tested as part of the round-robin experiment. Because of the large uncertainties in the measured failure rates, it is difficult to argue that the solid (power-law) curve is superior to the dashed (degenerate) curve. An additional data point, taken at approximately 8 J/cm^2, would resolve the question. Again, the onset predicted from the best-fit model, p=-0.75, is lower by about a factor of two than the degenerate case prediction. The density of defects contributing to failure when the damage frequency is 10% is 2×10^4 cm^{-2}, corresponding to a mean separation of approximately 70 μm.

Figure 7 contains an example of a coating which is more uniform in character. This 2.7-μm multilayer mirror was tested at its design wavelength, using the 67-μm-diameter spot. Once again, the degenerate prediction is higher than the p=-0.25 best-fit prediction by about a factor of two.

A final example is shown in figure 8. Again, this is a 2.7-μm mirror tested with a 67-μm-diameter spot. At about 2.5 times the onset fluence, the experimental data break sharply upward, as if a second damage process, different in character (i.e., with a different defect ensemble) and with a higher onset, were suddenly contributing. A modification of the onset analysis procedure was required to fit this coating. The three lowest-fluence points were treated separately first; the best fit was p=-0.65. The fitted function then was subtracted from the data, and the remaining experimental points analyzed. For this second component, the degenerate ensemble yielded the lowest mean square deviation. The sum of these two components agrees with the raw data reasonably well. The lower component is apparent only when the failure frequency is 10% or less. Thus, for some samples at least, it is necessary to acquire data at very low damage frequencies to avoid serious overestimation of the onset.

Extension to "Top-Hat" Spatial Profile

Gaussian spatial profiles commonly are employed in laser damage testing, since the TEM_{oo} spatial mode is reasonably easy to obtain from the test source, can be characterized accurately, and has desirable propagation properties. However, this introduces a complication into the onset analysis, in that the sample area illuminated with more than the onset intensity is a function of the axial intensity. If the irradiated area were held constant, then the variation of failure rate with intensity would depend only on the form of the defect ensemble itself, and the analysis would be simplified. This can be achieved if the spatial profile in the target plane is a "top-hat"; that is, if the intensity is constant out to the beam radius, and zero beyond.

Equation (5) is the formal solution for the damage ensemble in the case of a Gaussian beam profile. The corresponding formula in the top-hat case is [4]

$$f(I_a) = \frac{1}{\pi w^2 (1-P)} \left[\frac{dP}{dI_a}\right] \quad . \tag{10}$$

Since the second derivative of the damage probability curve does not appear in this expression, the prospects for recovering the form of the damage ensemble directly from the experimental data are improved.

In figure 9, the calculated damage probability curves for the Gaussian and top-hat spatial profiles are compared on the right. The curves are normalized to equal total powers at equal axial intensities, and the degenerate defect ensemble, shown on the left, was assumed. At the onset, the damage probability rises discontinuously from zero in both cases, but for the top-hat profile, it is a true step function with height proportional to the product of the irradiated area and the defect density. The slope is not dependent upon either spot size or defect density, in contrast to the Gaussian case. The corresponding top-hat experimental data should rise sharply also. Thus, less precision in the determination of the experimental failure rates would be required for an accurate extrapolation to the onset.

Similar results are obtained with distributed defect ensembles. In figure 10, the uniform ensemble, p=0, was assumed. Here the top-hat damage probability curve does exhibit some curvature, since not all the defects in the irradiated area fail at the same level. But the slope still is steeper than in the Gaussian case, making extraction of the onset from the corresponding experimental data easier.

Conclusions

The onset intensity for defect damage is a more reliable and useful indication of the operational performance of a coating than the conventional threshold, which depends strongly on the size of the tested area. Experimental failure frequency curves may be analyzed, using simple physical models for the defect ensemble, and information about the density of defect sites, as well as the onset itself, may be extracted. This method allows more effective use of limited test area, a fact which is becoming increasingly important as larger optical surfaces and reduced defect densities are made possible by improved coating technology.

The 1.06 μm coatings analyzed to date appear to be degenerate in character, in that a defect ensemble sharply peaked about the onset intensity most closely reproduces the data. A logical interpretation is that one or, at most, a limited number of closely related defect types contribute to failure. In contrast, distributed defect ensembles are more appropriate to the 2.7 μm coatings studied, which may indicate that several different defect types are present. The complex failure frequency curve for one 2.7 μm example strongly suggests that the defect types are grouped in two broad classes, possibly corresponding to different damage processes. An alternate explanation, namely that the two components originate from similar defects at different depths in the dielectric stack, seems less likely in view of their different ensembles.

The true degenerate ensemble emerged unambiguously as the appropriate choice only for the narrow-band antireflection coating tested at 1.06 μm. In all other cases, a distributed ensemble provided a better least squares fit. Assumption of the degenerate ensemble where not appropriate led to an underestimate of the onset intensity by about a factor of two. Good damage frequency statistics near the onset are required for definitive characterization of the defect ensemble.

Finally, the onset model suggests that failure frequency data obtained with a top-hat spatial profile in the target plane will rise from onset more steeply than their Gaussian counterparts. Less precision in the experimental data is required for accurate extrapolation to the onset, and it may be possible to recover the form of the damage ensemble directly.

References

[1] Seitel, S. C.; Franck, J. B.; Marrs, C. D.; Williams, G. D. "Selective and uniform laser-induced failure of antireflection-coated $LiNbO_3$ surfaces," IEEE J. Quantum Electron. QE-19; 475-479; 1983.

[2] Foltyn, S. R. "Spot size effects in laser damage testing," Fourteenth annual symposium on optical materials for high power lasers, 1982 November 15-17; Boulder, CO. (Proceedings in process.)

[3] Porteus, J. O. "Determination of the onset of defect-driven pulsed laser damage in 2.7 μm optical coatings," High power laser optical components meeting, 1982 November 18-19; Boulder, CO. (Proceedings in process.)

[4] Porteus, J. O.; Seitel, S. C. "Absolute onset of optical surface damage using distributed defect ensembles" (to be published).

[5] Laser Transmax antireflection coating, Balzers Ltd., Balzers, Principality of Liechtenstein.

[6] Guenther, K. H.; et al. "1.06 micron laser damage of thin film optical coatings — a round robin experiment involving various pulse lengths and beam diameters" (elsewhere in these proceedings).

[7] Seitel, S. C.; Porteus, J. O. "1.06 μm laser damage round-robin testing with 13 ns pulse duration and 40 μm spot size" (to be published).

[8] Super-Triolin, broad-band (0.43 - 1.06 μm) antireflection coating, Balzers Ltd., Balzers, Principality of Liechtenstein.

[9] Porteus, J. O.; et al. "Pulsed laser-induced melting of precision diamond-machined Cu, Ag, and Au at IR wavelengths," IEEE J. Quantum Electron. QE-17; 2078-2085; 1981.

Table 1. Experimental parameters

Test wavelength	1.06 μm	2.7 μm
Sample preparation	dry N_2 blow	dry N_2 blow
Test geometry	In focus of convergent beam	
Lens focal length	165 mm	126 mm
Spot diameter at $1/e^2$	40 μm	67 μm
Angle of incidence	3 deg	5 deg
Test site array	rectangular	rectangular
Test site separation	0.5 mm	0.5 mm
Pulses per site	1	1
Pulses per sample	variable[a]	variable[a]
Laser source	Nd:YAG	Nd:YAG
Polarization	linear	linear
Transverse mode	TEM_{00}	LOUR[b]
Spatial profile	near Gaussian[c]	near Gaussian[d]
Temporal profile	near Gaussian[c]	gain-switched[d]
Pulse duration	13 ns	100 ns
Damage definition	scatter change	visible change
Detection method	aux He-Ne beam	20X microscope

Notes:

[a] Determined during experiment; see text.
[b] Lowest order unstable resonator.
[c] See ref. [7].
[d] See ref. [9].

Table 2. Damage threshold comparison[a]

Laboratory	Spot size (μm)	No. of samples	Mean threshold (J/cm^2)
Naval Weapons Center	40	3	48 ± 9[b]
Air Force Weapons Laboratory	360	1	2.9
University of Kaiserslautern	470	6	20 ± 4
Lawrence Livermore National Laboratory	4000	3	3.7 ± 1.9
Onset fluence		1	2.5

Notes:

[a] Round-robin data; see ref. [6].
[b] Round-robin data corrected for non-Gaussian spatial and temporal profiles; see ref. [7].

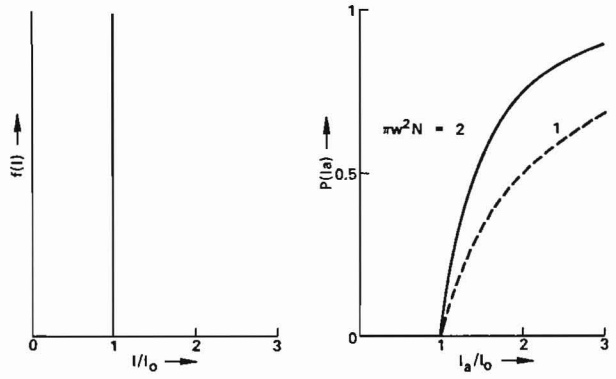


Figure 1. Degenerate defect ensemble (left) and corresponding damage probability curve (right).

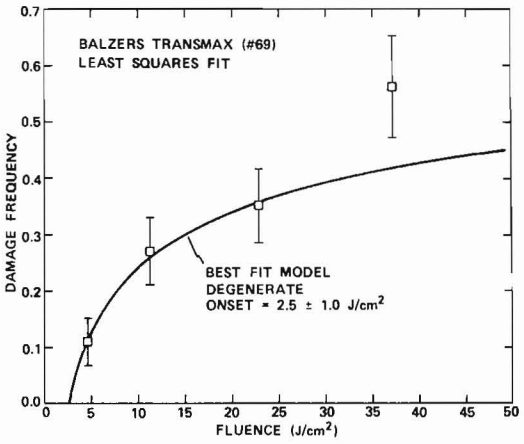


Figure 2. Damage frequency versus axial fluence for 1.06 μm narrow-band anti-reflection coating on BK-7 glass substrate. The solid curve is the least-squares fit, assuming the degenerate ensemble.

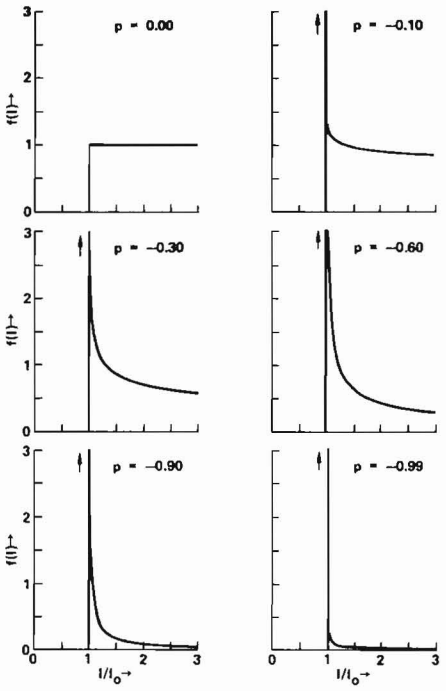


Figure 3. Examples of power-law ensembles for $-1 < p \leq 0$. The power-law ensemble approaches the degenerate ensemble as $p \to -1$.

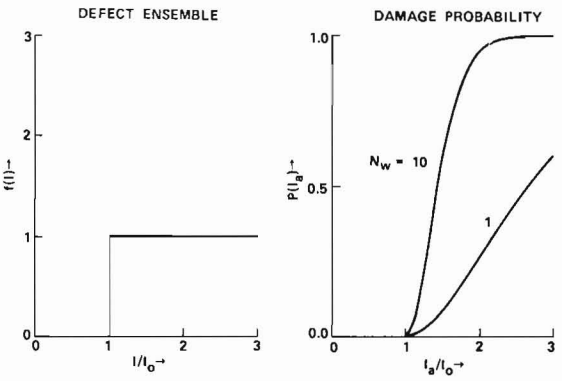


Figure 4. Uniform (p = 0) power-law defect ensemble (left) and corresponding damage probability curve (right).

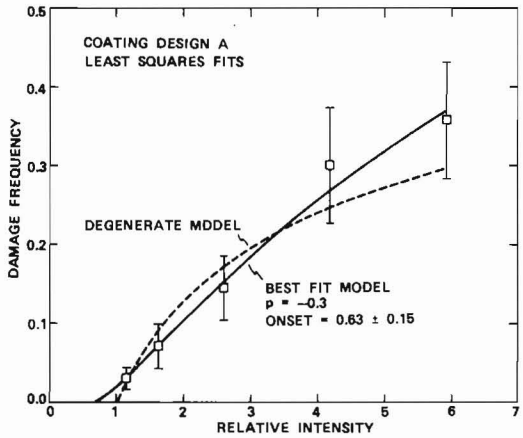


Figure 5. Damage frequency versus axial fluence (arbitrary units) for an experimental 2.7 μm high-reflectance multilayer coating. The best-fit power-law ensemble (solid curve) predicts a lower onset than the degenerate case ensemble (dashed curve).

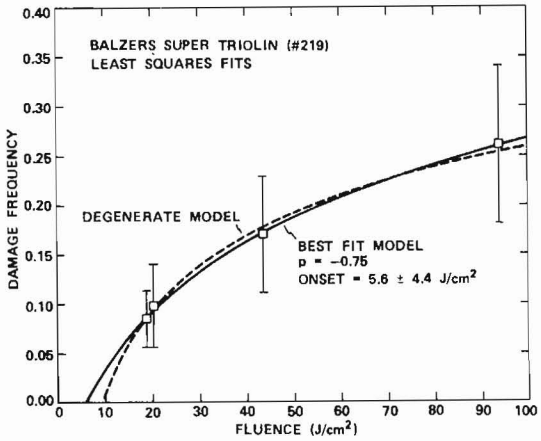


Figure 6. Damage frequency versus axial fluence for broad-band visible/1.06 μm antireflection coating on BK-7 glass substrate. The best-fit ensemble (solid curve) is nearly degenerate but predicts a lower onset.

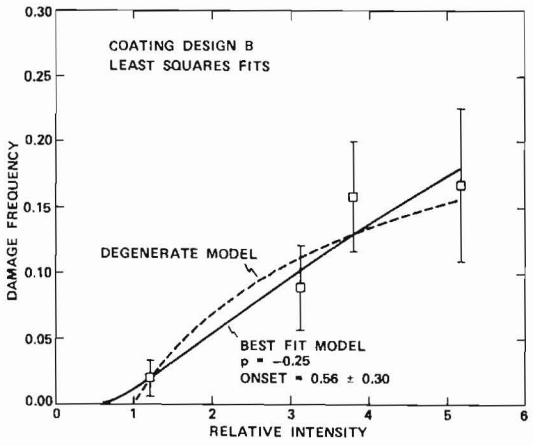


Figure 7. Damage frequency versus axial fluence (arbitrary units) for an experimental 2.7 μm high-reflectance multilayer coating. The best-fit ensemble (solid curve) is nearly uniform.

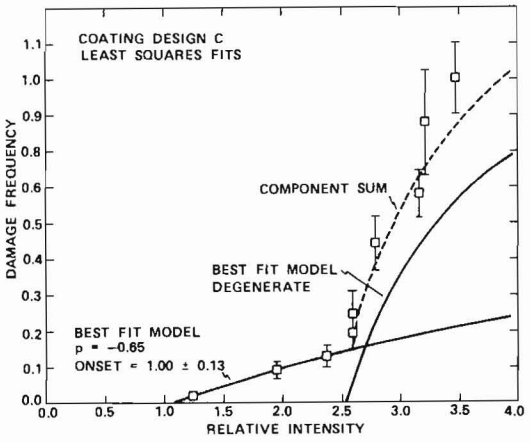


Figure 8. Damage frequency versus axial fluence (arbitrary units) for an experimental 2.7 μm high-reflectance multilayer coating. The dashed curve is the sum of two separately computed components (solid curves) which assume different defect ensembles.

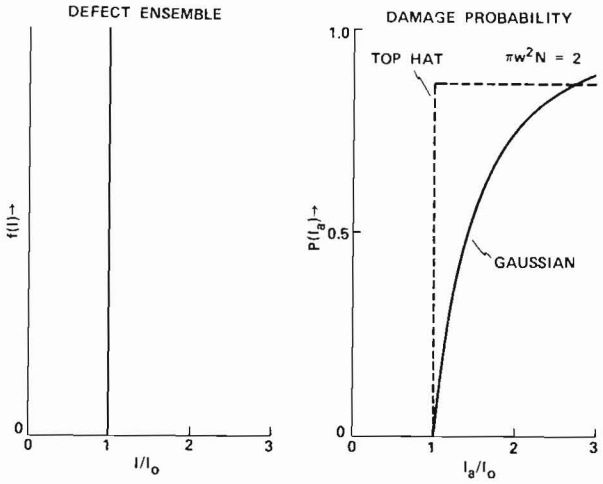


Figure 9. Degenerate defect ensemble (left) and corresponding damage probability curves (right) for Gaussian beam profile (solid curve) and top-hat beam profile (dashed curve). The curves are normalized to equal total powers at equal axial intensities.

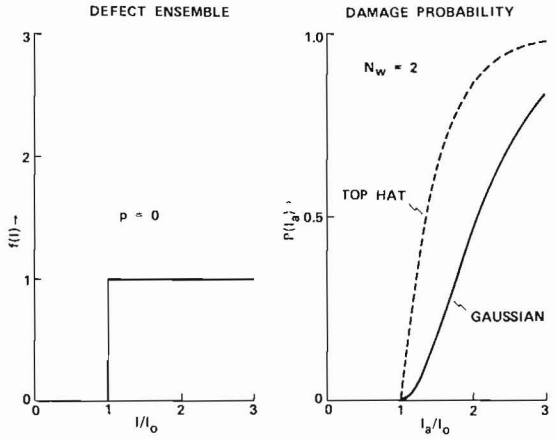


Figure 10. Uniform (p = 0) defect ensemble (left) and corresponding damage probability curves (right) for Gaussian beam profile (solid curve) and top-hat beam profile (dashed curve). The curves are normalized to equal total powers at equal axial intensities. Here $N_w = \pi w^2 N(2I_o)$.

It was pointed out that defect ensembles were addressed in the earlier Boulder Symposium, particularly the 1973-74 symposium. Although they were not treated in the same way, articles by Dr. DeShazer, Picard, and Milam in that period furnished a good background for the present work. It was also pointed out that as coatings get better there may not be enough defects to generate good statistics and one must test the whole part.

Manuscript received 3-21-84/sar

The Effects of Self-Focusing on Laser-Induced Breakdown

William E. Williams, M. J. Soileau, and Eric W. Van Stryland

Center for Applied Quantum Electronics
Department of Physics
North Texas State University
Denton, Texas 76203

The polarization dependence of laser-induced breakdown and beam distortions in the transmitted time integrated spatial profile were used to determine the effects of self focusing on picosecond breakdown threshold measurements in fused silica and NaCl. The results at 1.06 and 0.53 μm laser wavelength indicate that, for focused geometries, no significant self-focusing occurs in these materials until the beam power approaches P_2, the second critical power for self-focusing.

Key words: critical powers; fused quartz; laser damage; NaCl; picosecond pulses; self focusing; 0.53 μm; 1.06 μm.

1. Introduction

Early in the history of studies of laser-induced damage effects, self-focusing was recognized as one of the major contributors to catastrophic, irreversible changes in material properties [1]. Over the years many studies, both theoretical and experimental, have been conducted in attempts to account for self-focusing effects in bulk damage experiments. However, due to the complexity of the problem, agreement between theory and experiment have been mixed. While accurate, direct measurements of the nonlinear index of refraction, n_2, have been made using interferometry [2,3,4], the power for which significant changes occur in the linear propagation of focused Gaussian beams through nonlinear materials is not well established experimentally. In this paper we will present data which indicates that, for picosecond damage experiments, the important power for focused geometries is the so-called second critical power, P_2 [5]. This conclusion is based upon measurements of the polarization dependence of the breakdown powers and measurements of beam distortions in the transmitted, time-integrated spatial profile made with an optical multichannel analyzer. The results for two materials, one sample each of NaCl and fused quartz, will be presented in the paper. Breakdown data for these two samples has been presented in an earlier work for conditions in which self-focusing effects were not important [6,7].

2. Experiment

The laser system used in this study and in previous studies of picosecond laser-induced damage was a mode-lock, Nd:YAG oscillator-amplifier system producing 40 psec (FWHM) pulses at 1.06 μm. With the aid of a frequency doubler, 30 psec pusles at 0.53 μm were also produced. The system produces single pulses of measured Gaussian spatial profile. Essential details as to shot-to-shot pulse-width monitoring, pulsewidth characterization, energy monitoring, and spatial profile measurement are described in references 6,7,8,9.

As in earlier measurements, the pulse is focused into the bulk of the sample using various "best formed" lenses designed for minimum spherical aberration. The polarization (either linear or circular) incident on the sample was changed by adding a quarter-wave plate before the focusing lens. Transmission through the sample was monitored using a calibrated peak-and-hold detector, or, in the case of beam distortion measurements, using a vidicon tube operated in a region of linear response.

3. Theory

A large volume of work has been devoted to the study of self-focusing effects in solids [1]. In all cases the theories developed to describe the process indicate that self-focusing is dependent on the power of the laser beam in the material. Two critical powers of importance are often cited in the literature for Gaussian beams. The first of these, P_1, is as follows [5]:

$$P_1 = \frac{c\lambda^2}{32\pi^2 n_2} \tag{1}$$

where c is the speed of light in vacuum, λ is the laser wavelength and n_2 is the nonlinear index of refraction. Note that P_1 is inversely proportional to n_2. Many theories based on the constant shape approximation have assumed that a catastrophic collapse of the beam will occur in the material when the beam power approaches P_1. This idea was first suggested by Zverev et. al. [10] and later used extensively by other workers in reducing damage data [11,12,13]. However, exact solutions of the nonlinear wave equation made by Marburger [5] have shown that even for focused geometries, significant deviations from normal linear propagation do not occur until the beam power exceeds P_1 and a catastrophic collapse of the beam within the depth of focus does not occur until the beam power exceeds the second critical power P_2. P_2 is defined as (for Gaussian beams)

$$P_2 = 3.77\ P_1 \tag{2}$$

The factor of 3.77 comes from numerical solutions of the nonlinear wave equation [5].

Up to this point the theories make no mention of the mechanisms producing the nonlinear index. The only assumption made is that an index change is produced such that

$$\Delta n = n_2 \langle E \rangle^2 \tag{3}$$

where Δn is the change in index and E is the electric field. An alternative way of expressing the index change which has come into more common use recently is

$$\Delta n = \gamma I \tag{4}$$

where I is the irradiance and γ is a nonlinear index coefficient. γ and n_2 are related by a constant [2].

$$n_2\ (\text{esu}) = \left(\frac{cn_o}{40\pi}\right)\gamma(m^2/w) \tag{5}$$

where c is the speed of light in vacuum (m/sec) and n_o is the linear index of refraction. Many mechanisms can give rise to self-focusing effects in solids. For nanosecond and longer pulse durations, electrostriction, thermal self-focusing, and the electronic Kerr effect can all contribute to a catastrophic self focus. For picosecond pulse durations the dominant mechanism is believed to be the electronic Kerr effect. Thus the use of short pulses presents us with the advantage that we need only consider the fast nonlinearity in our data analysis. A second, and very important advantage is that the electronic Kerr effect is polarization dependent. This polarization dependence presents one with an easy way of determining whether or not self-focusing effects are present in damage measurements.

Early papers in the literature have shown that the nonlinear refractive index for isotropic materials (such as fused quartz) and linearly polarized light is given by [14,15]

$$n_2\ (\text{L.P.}) = \frac{12\pi}{n_o}\chi^{(3)}_{1111} \tag{6}$$

where n_o is the linear index of refraction and $\chi^{(3)}_{1111}$ is a third order nonlinear susceptibility tensor element. If the incident field is circularly polarized then

$$n_2\ (C.P.) = \frac{24\pi}{n_o}\,\chi^{(3)}_{1122} \tag{7}$$

However, a symmetry relation exists for isotropic materials such that

$$\chi^{(3)}_{1111} = 2\chi^{(3)}_{1122} + \chi^{(3)}_{1221} \tag{8}$$

Measured values for these tensor elements indicate that for fused quartz $\chi^{(3)}_{1122}$ is approximately equal to $\chi^{(3)}_{1221}$ [15]. Thus we can express equation (7) in terms of the same $\chi^{(3)}$ tensor element as equation (6) giving

$$n_2\ (C.P.) = \frac{8\pi}{n_o}\,\chi^{(3)}_{1111} \tag{9}$$

Thus we see that the ratio of n_2 for circular polarization to n_2 for linear polarization is 2/3. This implies that the ratio of the critical powers for self-focusing for the two cases is 1.5.

Let us now extend this idea to cubic materials such as NaCl. For a beam linearly polarized along a 100 axis the expression for n_2 is the same as eq. (6), i.e.,

$$n_2\ (L.P., 100) = \frac{12\pi}{n_o}\,\chi^{(3)}_{1111} \tag{10}$$

For circularly polarized light with the plane of polarization perpendicular to a 100 axis, n_2 is given by [2]

$$n_2\ (CP, 100) = \frac{6\pi}{n_o}\left[\chi^{(3)}_{1111} + 2\chi^{(3)}_{1122} - \chi^{(3)}_{1221}\right] \tag{11}$$

and for a beam circularly polarized in a plane perpendicular to a 111 axis we have

$$n_2\ (CP, 111) = \frac{4\pi}{n_o}\left[\chi^{(3)}_{1111} + 4\chi^{(3)}_{1221} - \chi^{(3)}_{1221}\right] \tag{12}$$

Using measured values of the various $\chi^{(3)}$ tensor elements taken from the literature for NaCl [16,17] we find that the mean value for the ratio of the critical powers is 1.41, nearly the same as the isotropic case. Depending on the propagation direction this ratio can vary from 1.37 to 1.46 for NaCl. If we extend this concept to measurements of bulk optical breakdown and if self focusing dominates the breakdown process, then, in both the isotropic and cubic cases, the ratio of the breakdown powers for the two polarization states should be equal to the ratio of the critical powers.

The polarization dependence of self-focusing has already been well established experimentally. For example, Moran et. al. [14] measured n_2 for various laser glasses using time resolved interferometry and found that n_2 (L.P.) $\cong$ 1.5 n_2 (C.P.). Feldman et. al. [18] measured the breakdown powers as a function of polarization for fused quartz and other glasses using nanosecond pulse durations at 1.06 μm. The additional contributions from electrostriction and thermal effects complicated the interpretation of his data. However, he used the observed polarization dependence in an attempt to separate the various contributions to n_2 and was the first to point out that the presence or absence of self-focusing in breakdown measurements could be determined by measuring the breakdown threshold power as a function of polarization. We use this concept in our own measurements to

determine the contribution of self-focusing. In the next section we will present data which shows the onset of self-focusing in a sample of fused quartz and NaCl.

4. Results

Figure 1 is a plot of the ratio of the breakdown power for circular polarization to the breakdown power for linear polarization as a function of the focal spot radius in air. The material is fused quartz, the laser wavelength is 0.53 μm, and the pulse duration is 30 psec (FWHM). Three regions of interest are clearly evident. For small focal radii and small breakdown powers the ratio, $P_{B\text{circular}}/P_{B\text{linear}}$, is approximately unity, indicating the lack of electronic self-focusing. For focal radii greater than 23 μm and large breakdown powers the ratio has saturated to the theoretical value of 1.5 indicating the dominance of self-focusing in this region. The transition regime shows the data increasing from unity to the theoretical maximum. The data clearly shows the onset of electronic self-focusing in fused quartz.

Now, rather than looking at the ratio of the critical powers as we did in Figure 2 let us examine the behavior of the breakdown powers directly for the same sample and wavelength. In Figure 2 we have plotted the breakdown power in megawatts as a function of the focal spot radius in air for the fused quartz sample. The triangles represent the breakdown powers for linear polarization, the circles are the breakdown powers for circular polarization. The horizontal dotted line represents the P_2 critical power for linear polarization calculated from measured n_2 values of this sample. The measurements of n_2, which involve beam distortions in the transmitted, time integrated spatial profile, are described more fully in reference 19, also in these proceedings. As can be seen, the breakdown power for linear polarization increases with increasing focal radius, then saturates at P_2 for longer focal radii as long as the sample thickness is less than or equal to the Rayleigh range. In the region where the breakdown power becomes constant, the polarization ratio saturates to 1.5. Similar results are seen for fused quartz at 1.06 μm. Both of these trends indicate that self-focusing dominates the breakdown process when the breakdown power approaches P_2.

In the next few paragraphs we extend this technique to study self-focusing effects in NaCl. We will first examine the behavior of the polarization ratio. Figure 3 is a plot of the ratio, $P_{B\text{circular}}/P_{B\text{linear}}$, as a function of the focal spot radius in air for NaCl. The laser wavelength is 0.53 μm and the pulsewidth is 30 psec. As in the case of fused quartz we see three regions of interest in Figure 3. For small focal radii and small breakdown powers the ratio is approximately unity indicating the lack of electronic self-focusing. For large focal radii and large breakdown powers the ratio saturates near the mean theoretical maximum of 1.41 indicated by the dotted line. In this region self-focusing dominates the breakdown process. The transition regime shows the ratio increasing from unity to the theoretical maximum.

Let us now examine the dependence of the breakdown powers directly rather than the ratio of the breakdown powers for the same NaCl sample. Figure 4 is a plot of the breakdown power in megawatts as a function of the focal spot radius in air. The triangles are the breakdown powers for linear polarization, the circles represent the breakdown powers for circular polarization. The horizontal dotted line represents the P_2 critical power for linear polarization calculated from measured n_2 values of this sample. As in the case of fused quartz the breakdown power for linear polarization increases with increasing focal radius then saturates to P_2 for larger focal radii. In the region where the breakdown powers become constant the ratio of the breakdown powers saturates near the theoretical maximum. Similar results are seen for this sample at 1.06 μm. We will discuss some of those measurements and their significance in the next paragraph. Thus, as for the case of fused quartz the data shown in figures 3 and 4 show that self-focusing dominates the breakdown process when the breakdown power approaches P_2.

At this point we remind the reader of the definition of the critical power for self focusing. P_2 is the least power for which a catastrophic collapse will occur for both focused and unfocused geometries [5]. The point of maximum on axis intensity does not occur at the beam waist, it occurs "downstream" of the beam waist at a distance comparable to the Rayleigh range in the material for $P = P_2$. If the sample thickness is thinner than the Rayleigh range then insufficient nonlinear material exists for self-focusing to cause a catastrophic collapse of the beam to occur in the material at P_2. For damage dominated by self-focusing this means that the material will not fail until the beam power exceeds P_2. This type of behavior can be seen in the data presented in Figure 5. Here we have plotted the breakdown power in megawatts as a function of the focal spot radius in air for the NaCl sample. The laser wavelength is 1.06 μm and the pulsewidth is 42 psec (FWHM). The horizontal dotted line represents the P_2 critical power calculated from measured n_2 values of this sample. The vertical dashed line divides the data for which the sample thickness is less than the Rayleigh range (region to the left) from that in which the sample is thick compared to the Rayleigh range (region to the right). Let us first examine only the triangular data points which are for a sample thickness of 2 inches. If we examine the data for the "optically thick" (region to the left) case we see that the breakdown power increases with increasing focal radius then appears to be saturating to P_2 for larger

focal radii up to the Rayleigh range. However, when the sample becomes "optically thin" i.e., short compared to the depth of focus (region to the right) the breakdown power continues to increase. If we now rotate the sample so that the beam propagates through 1 inch of material instead of 2 inches, a dramatic increase in the breakdown power is observed. This is seen by examining the data points for the 150 μm spot size. The triangular point is for a sample thickness of 2 inches, the point represented by the X is for 1 inch of material. No other parameters have been changed. To show that the change in the breakdown power was not due to an orientational effect a similar test was performed for a case where the sample was thick compared to the Rayleigh range for 1 inch of material. No change in the breakdown power was observed when the sample was rotated. This simple test clearly shows the effects of self-focusing in the breakdown measurements. In all cases bulk damage data is presented even though the rear surface often damaged prior to the bulk.

A separate method of detecting self-focusing in solids involves measurements of beam distortions in the transmitted, time-integrated far field spatial profile made with an optical multichannel analyzer [19]. The results for fused quartz at 1.06 μm are shown in Figure 6. The solid trace is a cross sectional slice through the center of the 1.06 μm beam after transmission through the sample for an input power of 0.8 MW. The dotted line is a Gaussian fit to the profile. The modulation on the experimental trace is due to interference fringes from a 1.06 μm spike filter placed after the sample and does not represent a real modulation of the beam in the sample. Measurements for smaller focal geometries, i.e., tighter focusing, indicate that no measurable distortions exist for input powers up to and beyond 0.8 MW. If we now increase the beam power to 4.0 MW, weak beam distortions appear as seen by the dashed curve in Figure 6. Energy is being diffracted into the wings of the beam due to the index nonlinearity. The sample damaged near the P_2 critical power of 6.5 MW for this focal geometry. Similar results were seen for the NaCl sample in that no measurable distortion of the beam existed until the beam power approached P_2 for the material.

5. Conclusion

In summary we have shown that the critical power of importance for focused geometries and Gaussian input beams is the second critical power P_2. We base this conclusion upon measurements of the polarization dependence of picosecond laser-induced breakdown and upon measurements of beam distortions in the transmitted, time-integrated spatial profile. A simple extension of the beam distortion measurements allowed us to measure the nonlinear refractive index, n_2, in these materials. The method, which is described in greater detail in these proceedings, is simple, it measures n_2 near the damage threshold, and it is independent of damage threshold measurements [19]. The significance of this work should be emphasized. Much of the early experimental work on self-focusing used the scaling law proposed by Zverev et. al. [10] to correct the data for self-focusing. In that work the critical power of importance was assumed to be P_1. Spot size dependences of the laser-induced damage thresholds were assumed to be merely a reflection of the effect of self-focusing since the breakdown powers were in most cases a fair fraction of P_1 [7,20]. However, since both self-focusing theory predicts and this work confirms that the critical power is in fact P_2 and not P_1 then the spot size dependences are due to other mechanisms in the material; possibly due to the contribution of defects to the laser-induced damage thresholds. Work which used the method of Zverev et. al. needs to be reexamined.

This work was sponsored by the Office of Naval Research; the National Science Foundation, Grant #ECS-8310625; and the North Texas State University Faculty Research Fund.

6. References

[1] For a representative sampling of the literature of this period see the proceedings of the symposium on Laser-Induced Damage in Optical Materials, National Bureau of Standards (U.S.) Special Publications #341 (1970), #356 (1971), #372 (1972), #387 (1973), #414 (1974), #435 (1975), #462 (1976), as well as the rest of the symposia series.

[2] M. J. Weber, D. Milam, and W. L. Smith, Opt. Eng., Vol. 17, #5, 463, 1978.

[3] K. J. Witte, M. Galanti, and R. Volk, Opt. Commun., Vol. 34, 278, 1980.

[4] Michael J. Moran, Chiao-Yao She, and Robert L. Carmen, IEEE Jour. Quant. Elec., QE-11, #6, 259, 1975.

[5] J. H. Marburger, Progress in Quantum Electronics, edited by J. H. Sanders and S. Stenhold (Pergamon, Oxford, 1975), Vol. 4, Part 1, pp. 35-110.

[6] M. J. Soileau, William E. Williams, Eric W. Van Stryland, Thomas F. Boggess, and Arthur L. Smirl, to be published in the proceedings of the 1982 Conference on Laser-Induced Damage in Optical Materials, Boulder, Colorado.

[7] M. J. Soileau, William E. Williams, Eric W. Van Stryland, Thomas F. Boggess and Arthur L. Smirl, Opt. Eng., Vol. 22, #4, 424, 1983.

[8] E. W. Van Stryland, M. J. Soileau, Arthur L. Smirl, and William E. Williams, Phys. Rev. B 23, 2144, 1981.

[9] William E. Williams, M. J. Soileau, and Eric W. Van Stryland, Appl. Phys. Lett., Vol. 43, #15, 352, 1983.

[10] G. M. Zverev and V. A. Pashkov, Sov. Phys. JETP, Vol. 30, #4, 616, 1970.

[11] D. W. Fradin, IEEE Jour. Quant. Elec. QE-9, 954, 1973.

[12] W. Lee Smith, J. H. Bechtel, and N. Bloembergen, Phys. Rev. B, Vol. 12, 706 (1975).

[13] W. Lee Smith, J. H. Bechtel, and N. Bloembergen, Phys. Rev. B, Vol. 15, 4039 (1977).

[14] R. W. Hellwarth, Progress in Quantum Electronics, Vol. 5, pp. 1-68, Pergamon Press, NY, 1977.

[15] Adelbert Owyoung, IEEE Jour. Quant. Elec. QE-9, 1064, 1973.

[16] P. D. Maker and R. W. Terhune, Phys. Rev., Vol. 137, #3A, 801, 1965.

[17] W. K. Burns and N. Bloembergen, Phys. Rev. B, Vol. 4, #10, 3437, 1972.

[18] Albert Feldman, Deane Horowitz, and Roy M. Waxler, IEEE Jour. Quant. Elec., QE-9, 1054, 1973.

[19] William E. Williams, M. J. Soileau, and Eric W. Van Stryland, to be published in the proceedings of the 1983 Conference on Laser-Induced Damage in Optical Materials, Boulder, Colorado.

[20] Larry D. Merkle, Michael Bass, and Randall T. Swimm, Opt. Eng., Vol. 22, #4, 405, 1983.

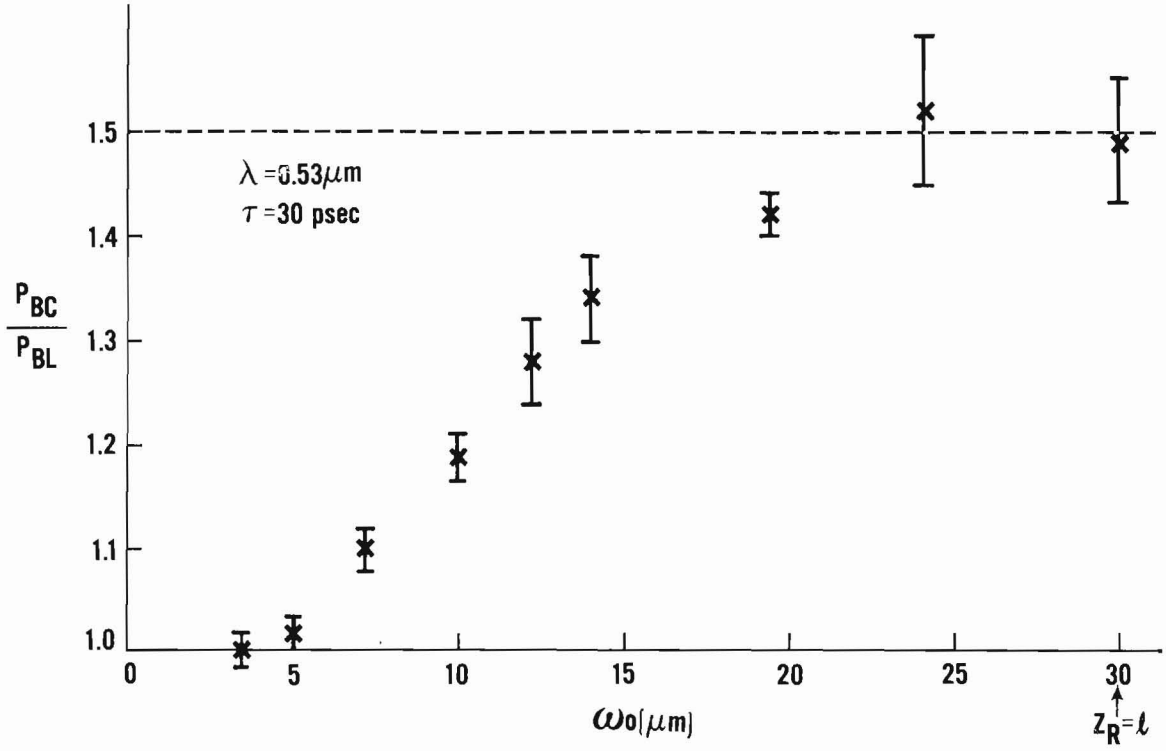


Figure 1. $P_{Bcircular}/P_{Blinear}$ as a function of the focal spot radius in air for fused quartz (sample #79-FQ-7940-1). The laser wavelength is 0.53 μm and the pulsewidth is 30 psec (FWHM). The horizontal dotted line represents the theoretical maximum for the ratio in the case where the electronic Kerr effect is the dominant mechanism leading to self-focusing.

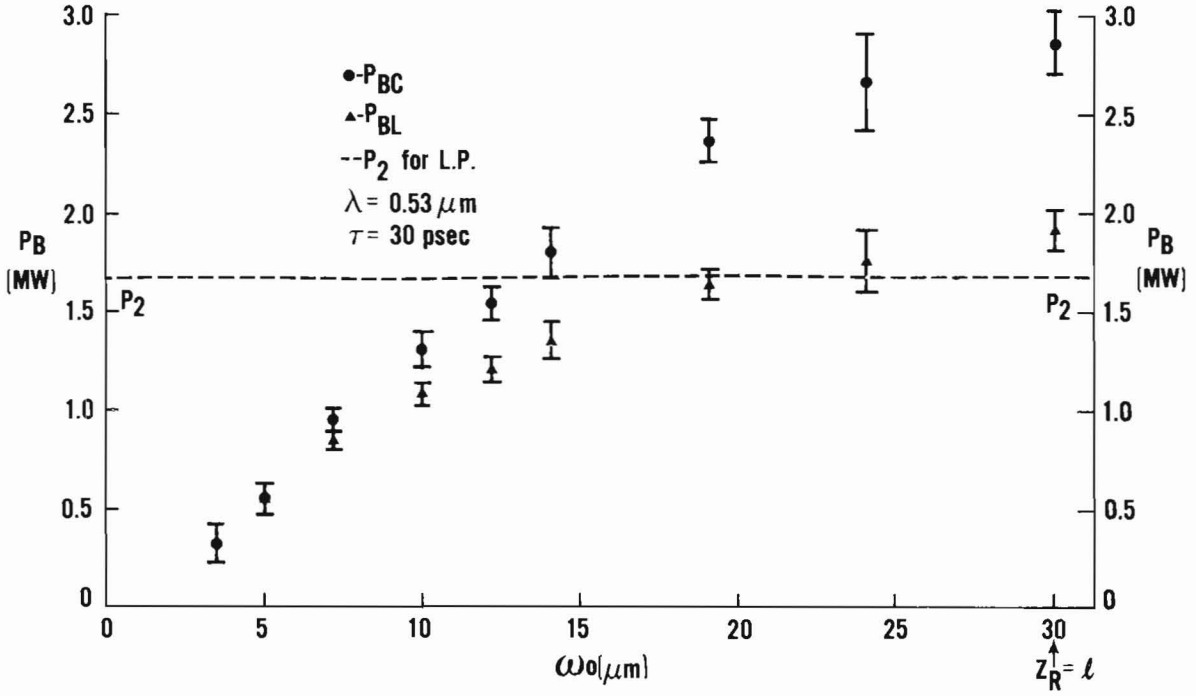


Figure 2. P_B as a function of the focal spot radius in air for fused quartz (sample #79-FQ-7940-1). The laser wavelength is 0.53 μm and the pulsewidth is 30 psec (FWHM). The triangles represent the breakdown powers for linear polarization, the circles are the breakdown powers for circular polarization. The horizontal dotted line represents the P_2 critical power calculated from the measured n_2 value of this sample.

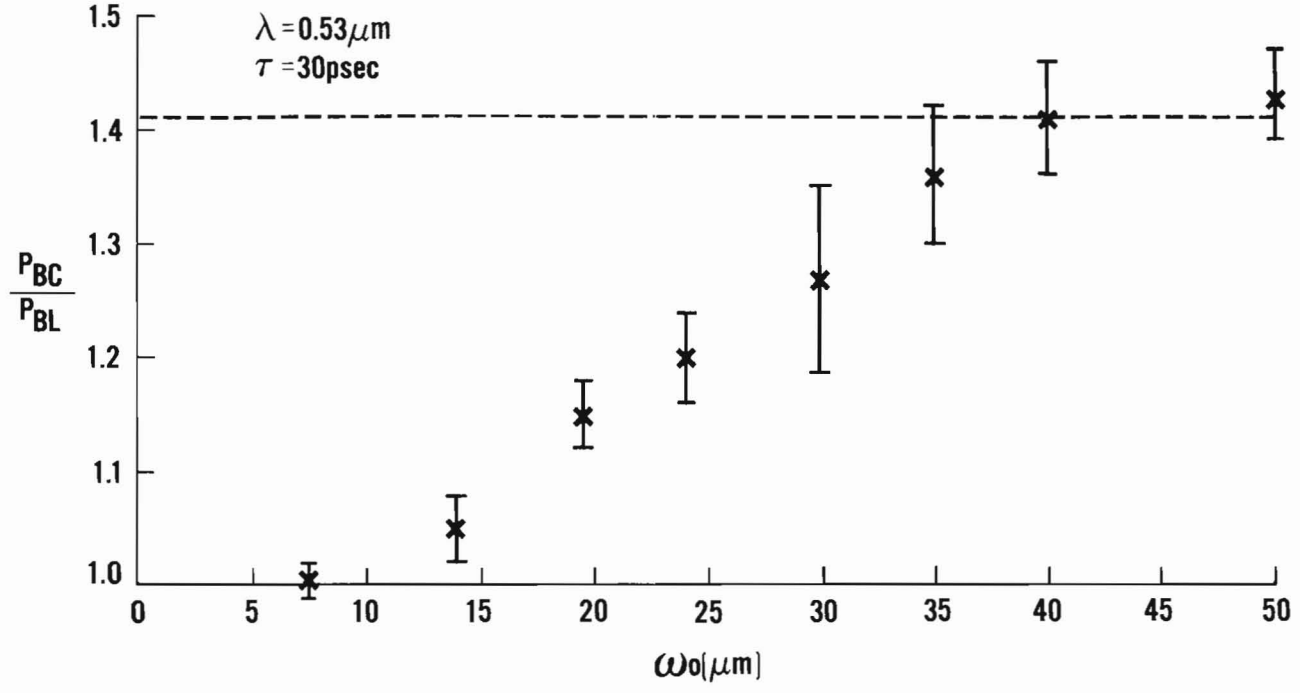


Figure 3. $P_{B\text{circular}}/P_{B\text{linear}}$ as a function of the focal spot radius in air for NaCl (sample #82-NC-1). The laser wavelength is 0.53 μm and the pulsewidth is 30 psec (FWHM). The horizontal dotted line represents the mean theoretical maximum for the ratio in the case where the electronic Kerr effect is the dominant mechanism leading to self-focusing.

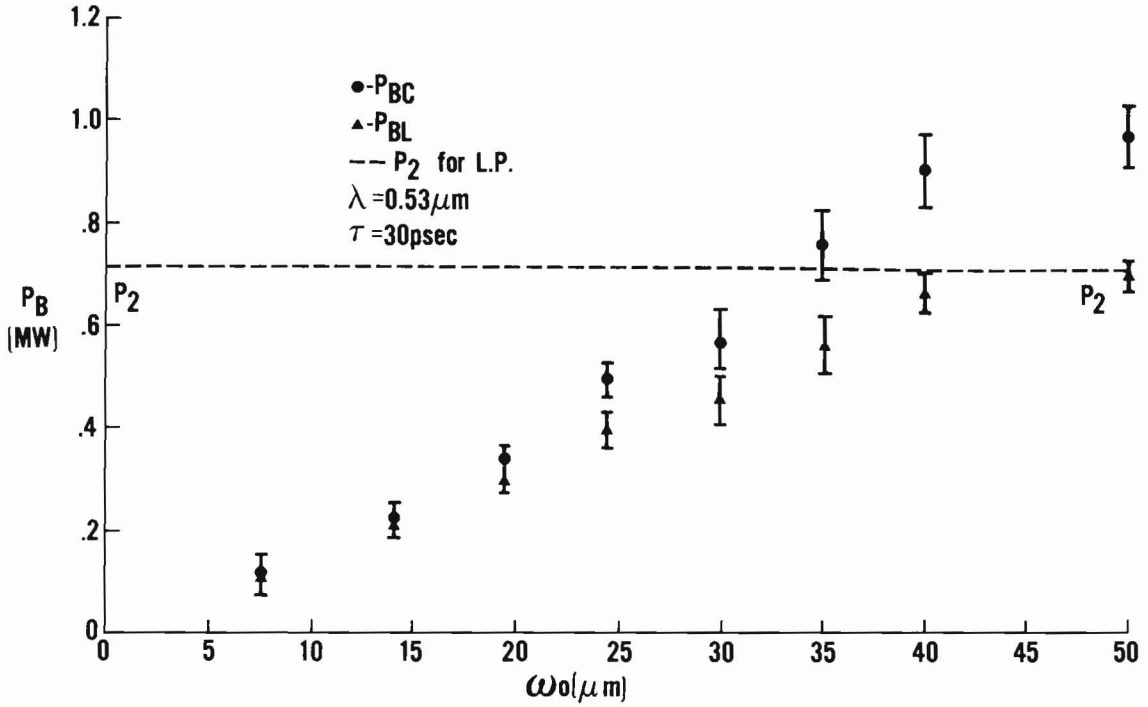


Figure 4. P_B as a function of the focal spot radius in air for NaCl (sample #82-NC-1). The laser wavelength is 0.53 μm and the pulsewidth is 30 psec (FWHM). The triangles represent the breakdown powers for linear polarization, the circles are the breakdown powers for circular polarization. The horizontal dotted line represents the P_2 critical power calculated from the measured n_2 value of this sample.

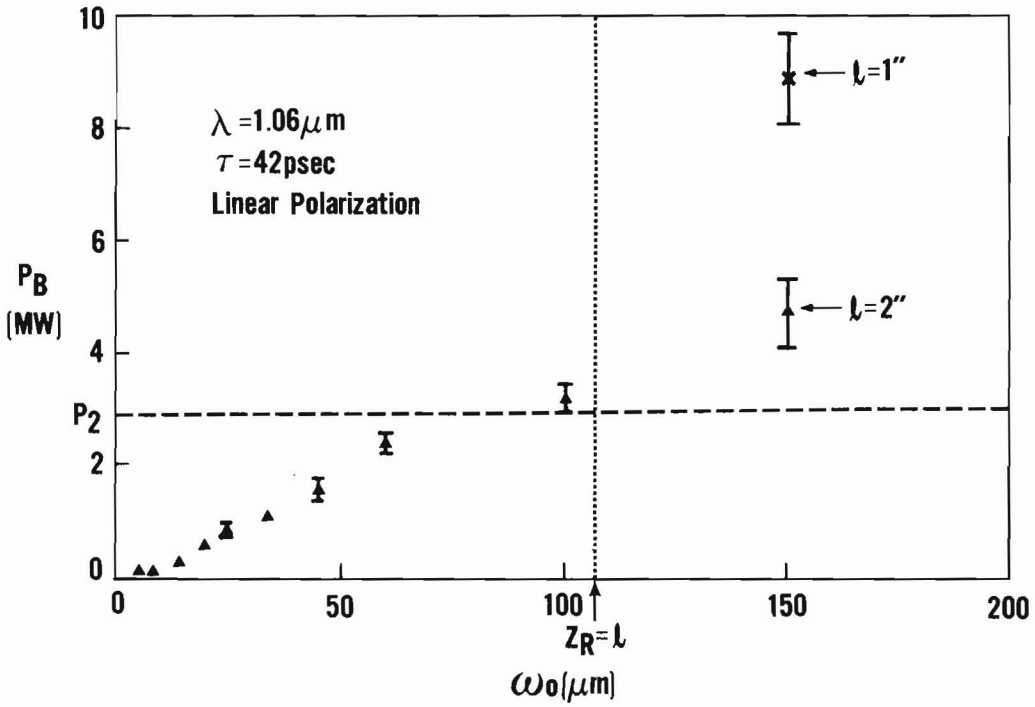


Figure 5. P_B as a function of the focal spot radius in air for NaCl (sample #82-NC-1). The laser wavelength is 1.06 μm and the pulsewidth is 42 psec (FWHM). All the data points are breakdown powers for linear polarization. The horizontal dotted line represents the P_2 critical power calculated from the measured n_2 values of this sample. The vertical dotted line represents the focal radius for which the sample thickness (2 inches) equals the Rayleigh range in the material. The two data points for the 150 μm spot size represent the breakdown powers for two different thicknesses of the same sample.

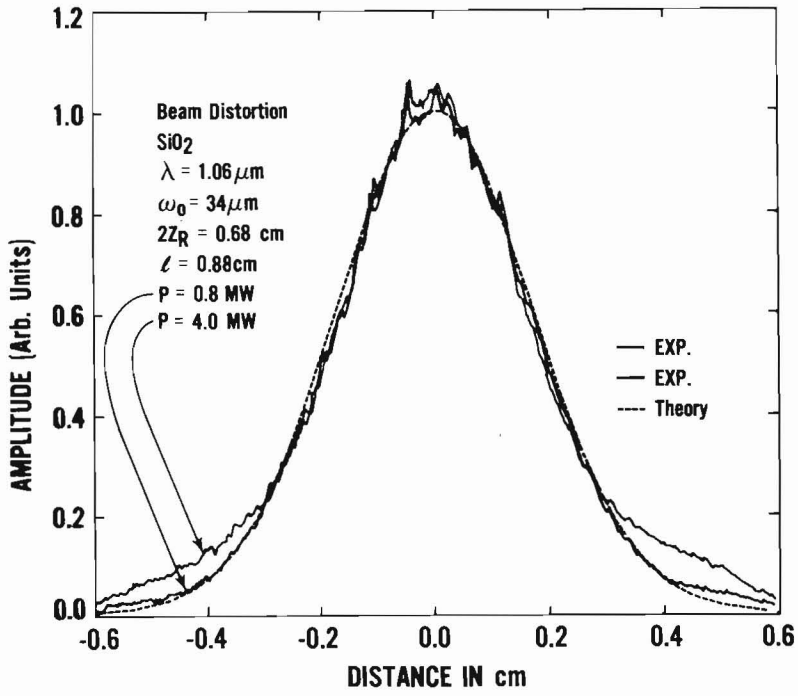


Figure 6. Beam distortion measurements. This is a plot of the far field profile of the 1.06 μm beam after propagation through the fused quartz sample. The two solid lines represent experimental traces for different input powers. The dotted trace is a theoretical Gaussian fit of the lower power experimental trace. The P_2 critical power for this sample and this wavelength is 6.5 MW.

Simple Direct Measurements of n_2

William E. Williams, M. J. Soileau, and E. W. Van Stryland

Center for Applied Quantum Electronics
Department of Physics
North Texas State University
Denton, Texas 76203

A simple direct method for measurements of n_2 is described. The method involves measurements of beam distortions in the transmitted, time-integrated spatial profile using an optical multichannel analyzer. A model is described which allows extraction of n_2 from fits of experiment to computer generated theoretical spatial profiles. The results for picosecond pulses at 1.06 μm and 0.53 μm are presented for three materials: fused quartz, NaCl, and CS_2. Little dispersion in n_2 is seen for each material over the wavelength range studied.

Key words: beam distortions; CS_2; fused quartz; NaCl; n_2; picosecond pulses; 0.53 μm; 1.06 μm.

1. Introduction

In this paper a technique is described which allows the determination of the nonlinear refractive index, n_2 in highly transparent materials. The technique involves measurements of beam distortions in the transmitted, time integrated, far field spatial profile using an optical multichannel analyzer (OMA). A model is presented in which a Gaussian shaped phase transparency is created at the beam waist in an optically thin material (sample thickness < Rayleigh range). The transparency produces a phase retardation which is reflected in the far field transmitted energy distribution. Comparison of experiment to computer generated theoretical curves allows the amount of phase retardation at the waist to be measured. n_2 can then be determined using the measured values of the phase retardation, the sample thickness, and the peak-on-axis irradiance. The n_2 values thus obtained for CS_2, NaCl, and fused quartz compare favorably with previous results which used interferometric techniques [1,2].

2. Experiment

The experimental apparatus is shown schematically in figure 1. The laser source for this study was a microprocessor-controlled, passively mode-locked, Nd-YAG system operated at 1.06 μm. A single pulse of measured Gaussian spatial profile was switched out of the resulting mode-locked train and amplified. The temporal pulsewidth was 40 psec (FWHM). Shot-to-shot variation in both energy and pulsewidth were monitored by the methods described in reference 3. Attenuation of the energy in the pulse was achieved using a half-wave plate, polarizer combination which produced no measurable aberrations on the focused beam. Two wavelengths were used separately in this study, the fundamental wavelength of 1.064 μm and the second harmonic (0.532 μm). Generation of 30 picosecond pulses at 0.53 μm was achieved using a temperature tuned CD*A crystal. Characterization of the 0.53 μm pulses is described in greater detail in reference 4.

A single element 450 mm focal length lens was used to focus the beam. This lens is of "best form" design, i.e., designed for minimum spherical aberration. The focal geometry was chosen so that the Rayleigh range of the focused beam in the material was greater than the sample thickness. In this manner for the powers used, the nonlinear index, n_2, distorts only the phase of the beam while it is inside the material. All changes in the spatial propagation of the beam occur after the sample [5]. The transmitted spatial profile was monitored in the far field using a vidicon tube operated in a region of linear response. The vidicon tube was interfaced with a microprocessor-controlled optical multichannel analyser (OMA) [6]. This system allows shot-to-shot monitoring of the fluctuation in the far field energy distribution. Since the vidicon detector looks at the time-integrated spatial profile any absorption of the beam could lead to erroneous results. Transmission measurements made with a calibrated peak-and-hold detector indicate that less than a 10% reduction in the transmitted energy occurs in the materials studied at the damage threshold and no measurable change in transmission occurs below the damage threshold. All data presented in this paper was taken at irradiance levels below the threshold for damage.

3. Theory

As mentioned earlier, if we place the material in a focal condition in which the sample thickness is smaller than the Rayleigh range the nonlinear index, n_2, will distort only the phase of the beam while it is inside the material. This will hold true even for powers on the order of or greater than the critical power for self focusing as long as the material thickness is less than the self focusing length [5]. This phase distortion will lead to a spatial distortion of the far field energy distribution, which we measure. The model by which we numerically fit the spatial distortion in the far field to the phase retardation in the material was first described by Weaire et. al. [7] in studies of self-defocusing in InSb. The essential details are given in the next few paragraphs.

A Gaussian shaped phase transparency, T(r), is created at the waist of the focused beam. The field incident on the transparency is given by

$$E_1(r) = A \text{ Gaus } (\frac{r}{b}) \tag{1}$$

where we have used the notation of Gaskill [8] to express the radial component of $E_1(r)$, i.e.,

$$\text{Gaus } (\frac{r}{b}) = \exp [-\pi(\frac{r}{b})^2] \tag{2}$$

where b is $\sqrt{\pi}$ times the HW $1/e^2$ M in irradiance. T(r), the phase transparency, is given by

$$T(r) = \exp [2\pi i \phi \text{ Gaus } (\frac{r}{b})] \tag{3}$$

where ϕ gives the strength of the phase retardation at r=0, i.e., ϕ is the phase retardation at the peak of the beam relative to the wings. The field after the transparency, $E_2(r)$ is simply the product of $E_1(r)$ and T(r), i.e.,

$$E_2(r) = A \text{ Gaus } (\frac{r}{b}) \exp [2\pi i \phi \text{ Gaus } (\frac{r}{b})] \tag{4}$$

By expanding the exponential term in T(r) we can rewrite this product as a sum of Gaussians of differing widths

$$E_2(r) = A \sum_{j=0}^{\infty} \frac{(2\pi i \phi)^j}{j!} \text{ Gaus } (\frac{r}{w_j}) \tag{5}$$

where

$$w_j^2 = \frac{b^2}{2j + 1} \tag{6}$$

The problem now reduces to propagating each of the Gaussians to the far field and summing the result. Thus the field $E_3(r)$ at some distance z (near or far field) from the phase transparency is given by

$$E_3(r) = \sum_{j=0}^{\infty} A_j \text{ Gaus } (\frac{r}{d_j}) \text{ q } (r; \frac{1}{\lambda R_j}) \frac{(2\pi i \phi)^j}{j!} \tag{7}$$

where

$$q\left(r;\frac{1}{\lambda R_j}\right) = \exp\left(\frac{i\pi r^2}{\lambda R_j}\right)$$

$$d_j = \frac{\lambda z}{w_j}\sqrt{1+\left(\frac{w_j^2}{\lambda z}\right)^2}$$

$$A_j = A\left(\frac{w_j}{d_j}\right)\exp\left(kz + \Phi_j\right) \tag{8}$$

$$R_j = z\left[1+\left(\frac{w_j^2}{\lambda z}\right)^2\right]$$

$$\Phi_j = \tan^{-1}\left(\frac{-\lambda z}{w_j^2}\right)$$

Again we have used the notation of Gaskill [8] to propagate each of the Gaussian beams. Finally, since detectors respond to irradiance rather than the field we square the result for $E_3(r)$

$$I_3(r) = \left|E_3(r)\right|^2 \tag{9}$$

We now use the expression for $I_3(r)$ to numerically model the propagation of a Gaussian beam through a phase transparency.

In figure 2 we present the results of such numerical computations. The curves in the figure represent cross-sectional slices of the spatial profile along r through the point of maximum on axis irradiance. These profiles are analagous to the beam scans obtained experimentally with the OMA system. Parameters such as wavelength, focal spot radius, and distance from the beam waist used to produce the curves are shown within the figure. The solid line is the result for an initially Gaussian beam at the waist with no phase retardation. If we now apply a peak-on-axis phase retardation of $\lambda/2$ we get the result shown in the figure by the broken line (— — —) which overlaps the undistorted case near the peak. The intensity maxima in each curve have been normalized to unity. In comparing the case shown by the dashed line to the undistorted case shown by the solid line we see that energy has clearly been diffracted into the wings of the beam.

Let us now remind the reader that up to this point the model previously described assumes that the phase transparency has already been created in the material when the pulse encounters it. The case described in the previous paragraph is what would be seen if we could time-resolve the signal from the vidicon detector and examine the spatial profile for the given phase retardation at the peak of the temporal pulse. Since the phase transparency is created by the laser pulse, and our detector looks at the time-integrated spatial profile, we must take these effects into account.

We first assume that the mechanism producing the phase transparency in the material responds instantaneously to the field. We then modify equation 7 to take into account the temporal dependence, i.e.,

$$E_3'(r,t) = \sum_{j=0}^{\infty} A_j\ \text{Gaus}\left(\frac{r}{d_j}\right)\ \text{Gaus}\left(\frac{t}{t_p}\right)\ q\left(r;\frac{1}{\lambda R_j}\right)\ \frac{(2\pi i\phi')^j}{j!} \tag{10}$$

where

$$\phi' = \phi \, \text{Gaus} \left(\frac{t}{t_p}\right) \tag{11}$$

The fluence distribution measured by the vidicon detector is then given by

$$I_3'(r) = \int_{-\infty}^{\infty} E_3'(r,t) \, E_3'^{*}(r,t) \, dt \tag{12}$$

Thus the final time integrated irradiance distribution [after normalization, i.e., plot $I_3'(r)/I_3'(0)$] is shown in figure 2 by the dotted line (---------) for the same peak phase retardation as the time resolved case.

As can be seen in figure 2 the effect is reduced but still easily detectable. The assumption that the mechanism producing the phase transparency responds instantaneously to the field should be valid for both SiO_2 and NaCl for our pulse durations (> 30 psec). In both cases, the dominant mechanism producing the phase transparency is the electronic Kerr effect. The same should hold for CS_2 where molecular reorientation (2.1 psec response time) [9] dominates the self-focusing process. For materials where the mechanism producing n_2 does not respond to the field on a time scale short compared to the optical pulse width the material response function must be included in the time integral.

Let us now examine, theoretically, what happens to the beam profile as the peak phase retardation is increased. In figure 3 we examine the far field transmitted beam profile as a function of phase retardation for the same input parameters as figure 2. Again the cases shown are the time-integrated response. Significant deviations start to appear on the beam profile for a peak phase retardation of 0.3λ. As we increase the peak phase retardation, more and more energy is diffracted into the wings of the beam.

By comparing these theoretical curves to those obtained experimentally with the OMA system we can measure the phase retardation produced by a given material as a function of the input irradiance. The change in index in the material can be determined by

$$\Delta n = \frac{\phi\lambda}{2\pi l} \tag{12}$$

where l is the sample thickness. Since we measure the irradiance rather than the field it is convenient to define Δn as

$$\Delta n = \gamma I \tag{13}$$

where I is the peak on axis irradiance and γ is a nonlinear index coefficient. The alternative definition commonly used is

$$\Delta n = n_2 \langle E \rangle^2 \tag{14}$$

where E is the electric field and n_2 is the nonlinear index of refraction. By measuring both Δn and I we can calculate the nonlinear index coefficient, γ. γ is related to n_2 by a constant [2].

$$n_2 \ (\text{esu}) = \left(\frac{cn_o}{40\pi}\right)\gamma \ (m^2/W)$$

where c is the speed of light in vacuum (m/sec) and n_0 is the linear index of refraction.

4. Results

Figure 4 is a single shot trace of the far field, 1.06 μm beam profile after transmission through a NaCl sample. The sample thickness is approximately 1/2 the Rayleigh range. Other experimental parameters are shown within the figure. The inset in figure 4 shows the transmitted beam profile for the same input parameters as the main figure, but low input irradiance. If we increase the peak-on-axis irradiance by a factor of 10 we get the results shown in the main figure by the solid line. The dotted line is an excellent fit of the theory to experiment for a peak phase retardation of 0.50λ. From the phase retardation, sample thickness, and the peak-on-axis irradiance we obtain a value for n_2 in NaCl of 1.3×10^{-13} esu for 40 psec pulses at 1.06 μm.

Figure 5 is an expansion of the inset figure shown in figure 4. The solid line represents a single shot trace through the center of the beam for low input irradiance. The dotted line is a theoretical fit of the data for no phase retardation. Thus the beam in the far field is clearly Gaussian and the beam width at this position closely matches the calculated linear optics beam width.

Experimental data for CS_2 and SiO_2 are shown in figures 6 and 7 respectively. In figure 6 we examine the far field beam profile after transmission through CS_2 for 40 psec pulses at 1.06 μm. Here the sample thickness is approximately 1/4 the Rayleigh range. As before, the inset shows the transmitted beam profile for low input irradiance. The excellent fit of theory (dotted line) to experiment (solid line) gives $n_2 = 150 \times 10^{-13}$ esu. In figure 7 we examine the experimental results for fused quartz for 30 psec pulses at 0.53 μm. The sample thickness is 1/2 the Rayleigh range. From the data we obtain an n_2 value of 0.6×10^{-13} esu.

In Table I we summarize the results of n_2 measurements in all three materials at 1.06 μm and 0.53 μm. The error bars shown for n_2 in our work are the relative errors obtained from at least ten separate measurements for each sample at each wavelength. The phase retardations used in the measurements varied from 0.3 to 0.6λ. The absolute errors for our measurements are estimated to be ±20%. The results for CS_2 are in excellent agreement with the results of Witte, et al. [1], using 700 psec pulses at 1.32 μm. The error bars shown for their work are the absolute errors. The measurement method was time integrated interferometry. In addition, the results for NaCl are in excellent agreement with the work of Weber, et. al. [2], using 100 psec pulses at 1.06 μm. The method of measurement was time resolved interferometry with the absolute errors for their work shown in the table. The differences between our results and those of Weber, et al. [2] for SiO_2 will be discussed in the conclusion. In all three materials, little or no dispersion in n_2 was seen for the two wavelengths at which measurements were made.

5. Conclusion

In this paper a technique for measuring n_2 in highly transparent materials was presented. The method involved measuring beam distortions in the transmitted, time-integrated, far field beam profile with an optical multichannel analyzer. Comparison of experiment to computer generated theoretical curves allowed the amount of phase retardation at focus to be measured. n_2 was then calculated using this and other known constants. The technique is simple, it measures n_2 near the damage threshold, and it is independent of damage threshold measurements.

The results of n_2 measurements in CS_2 and NaCl are in excellent agreement with the results obtained by other workers using interferometric techniques [1,2]. The results for fused quartz also compare favorably to previous results but agreement is not as good as for the other two materials. While the differences may simply be a reflection of the absolute errors, the possibility exists that the differences are real. In comparing our results in fused quartz with Weber, et al. [2], one must note that the irradiance values in our work are at least a factor of 10 higher than those in the previous work. Other mechanisms may be coming into play at these irradiance levels which reduce the value of n_2 in this material. Further evidence for this is seen in recent work reported by Smith, et al. [10], at the 1983 Cleo meeting held in Baltimore, Maryland, in May. In that work, an n_2 value of 0.6×10^{-13} esu was reported for fused quartz at a laser wavelength of 351 nm. The measurement technique was very similar to our own in that distortions in the transmitted beam profile were measured near damage and compared to numerical simulations using n_2 as an adjustable parameter. Such a reduction in n_2 would have favorable implications in many areas of high energy laser research.

The authors would like to thank Dr. Thomas F. Boggess for his efforts in developing the numerical code which made this work possible. This work was sponsored by the Office of Naval Research, the National Science Foundation and the North Texas State University Faculty Research Fund.

6. References

[1] K. J. Witte, M. Galanti and R. Volk, Opt. Commun., Vol. 34, pp. 278-282, 1980.

[2] M. J. Weber, D. Milam, and W. L. Smith, Opt. Eng., Vol. 17, #5, pp. 463-469, 1978.

[3] E. W. Van Stryland, M. J. Soileau, Arthur L. Smirl, and W. E. Williams, Phys. Rev. B, 23, 2144 (1981).

[4] M. J. Soileau, William E. Williams, Eric W. Van Stryland, Thomas F. Boggess, and Arthur L. Smirl, Opt. Eng., Vol. 22, pp. 424-430, 1983.

[5] J. H. Marburger, Progress in Quantum Electronics, J. H. Sanders and S. Stenholm, eds., New York: Pergamon, 1977, pp. 35-110.

[6] E G & G Princeton Applied Research OMA 2 System. Includes model 1252E IR enhanced vidicon detector, model 1216 detector controller and model 1215 console with full memory. Address - P.O. Box 2565, Princeton, New Jersey 08540.

[7] D. Weaire, B. S. Wherrett, D. A. B. Miller, and S. D. Smith, Opt. Lett., Vol. 4, #10, pp. 331-333, 1979.

[8] J. D. Gaskill, "Linear Systems, Fourier Transforms, and Optics," John Wiley and Sons, New York, pp. 420-443, 1978.

[9] J. Reintjes, R. V. Carman, and F. Shinizu, Phys. Rev., Vol. A8, pp. 1486-1503, 1973.

[10] W. L. Smith, W. E. Warren, C. L. Vereimak, and W. T. White, "Nonlinear Refractive Index at 351 nm by Direct Measurement and Modeling of Small Scale Self Focusing," Third Annual Conference on Lasers and Electro-Optics, Baltimore, Maryland, May 17-20, 1983.

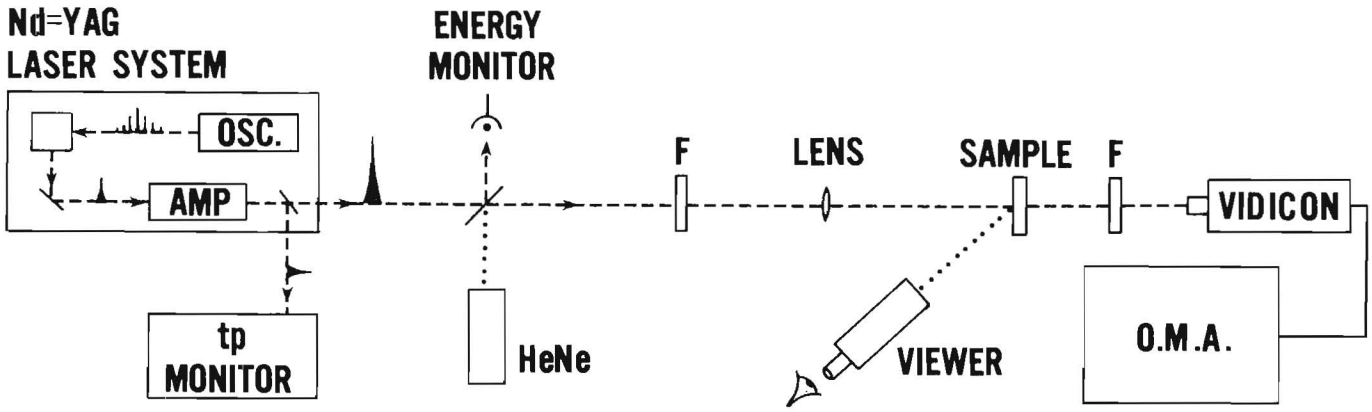


Figure 1. Experiment.

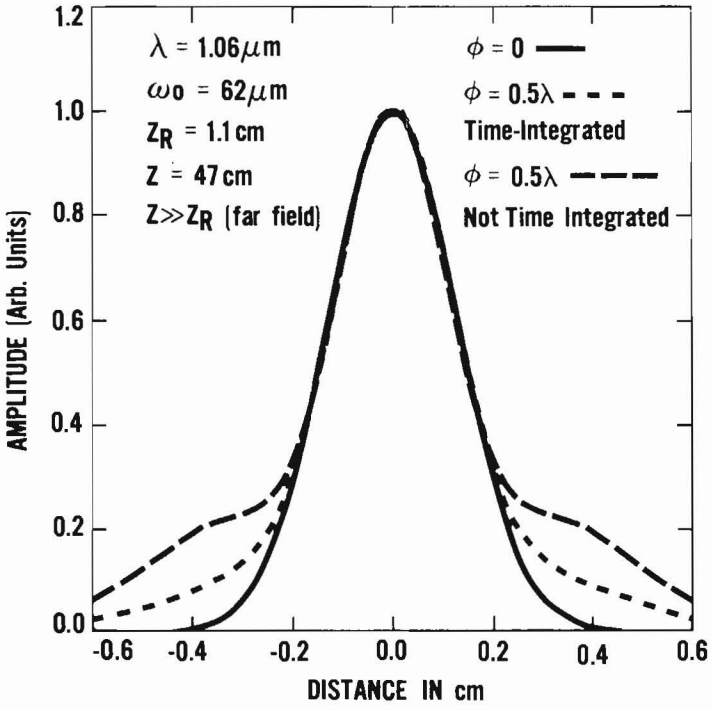


Figure 2. Theoretical far field beam profiles after transmission through a Gaussian phase transparency. λ is the laser wavelength, ω_0 is the HW $1/e^2$ M in irradiance, Z_R is the Rayleigh range, and z is the distance from the beam waist. The solid curve is the result for no phase retardation (ϕ=0). The dashed curve (— — —) is the result for a peak phase retardation of $\lambda/2$ and no time integration. The dotted curve (---------) is the result for the same phase retardation as the dashed curve with the time integration included in the theory. All curves are plots of $I_3(r)/I_3(0)$.

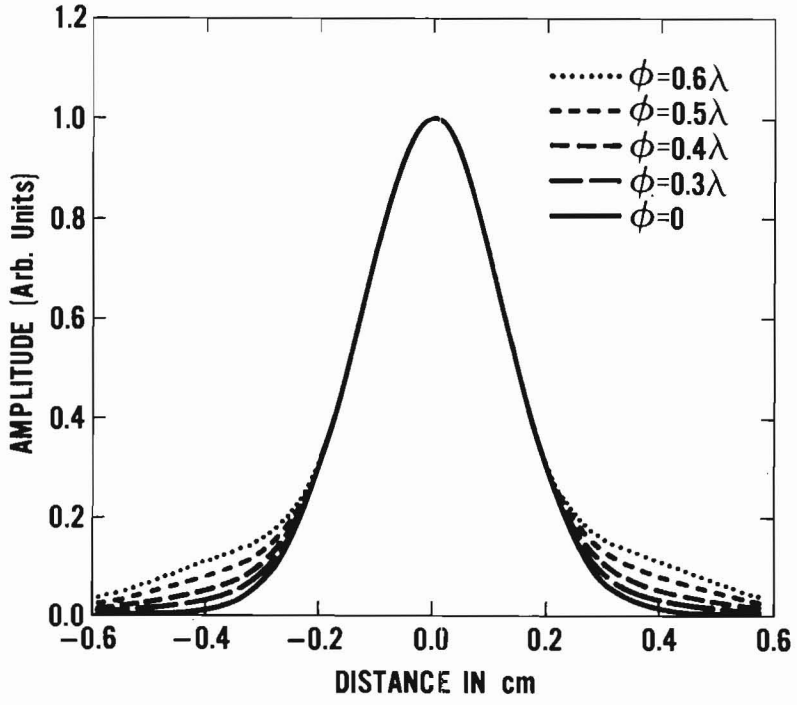


Figure 3. Theoretical far field beam profiles as a function of phase retardation. The same input parameters (λ, ω_0, z) shown in figure 2 are used to produce these profiles. For comparison we have plotted $I_3(r)/I_3(0)$ in each case.

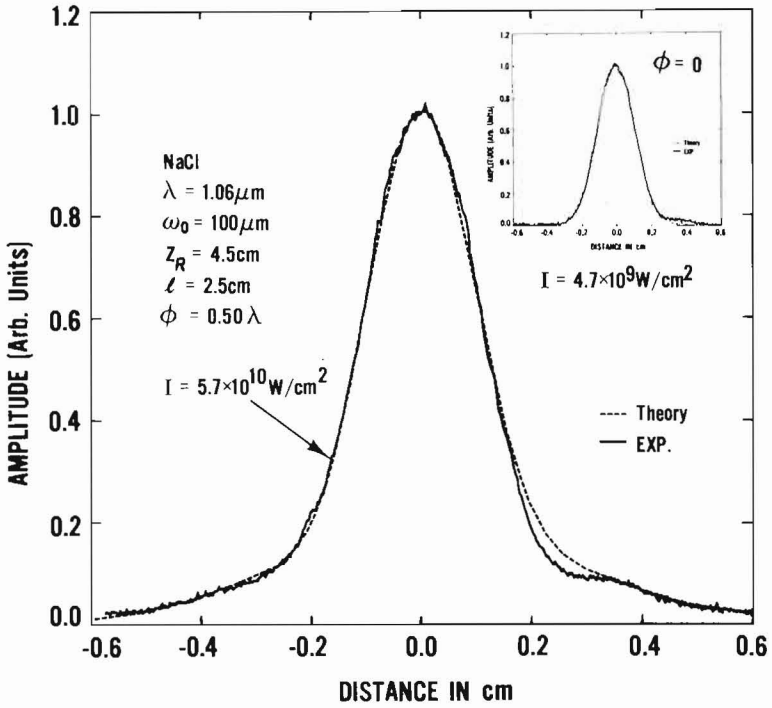


Figure 4. Far field beam profile after transmission through NaCl. The inset shows the beam profile for the same input parameters as the main figure, but low input irradiance. The inset is enlarged in figure 5. If we increase the peak-on-axis irradiance a factor of 10 we get the results shown by the solid line in the main figure. The dotted line is an excellent fit of the theory to experiment for a peak phase retardation of $\lambda/2$. From the phase retardation, sample thickness, and the peak-on-axis irradiance we obtain $n_2 = 1.3 \times 10^{-13}$ (esu) for 40 psec pulses at 1.06 μm. The input power for the high irradiance case is 8.0 MW.

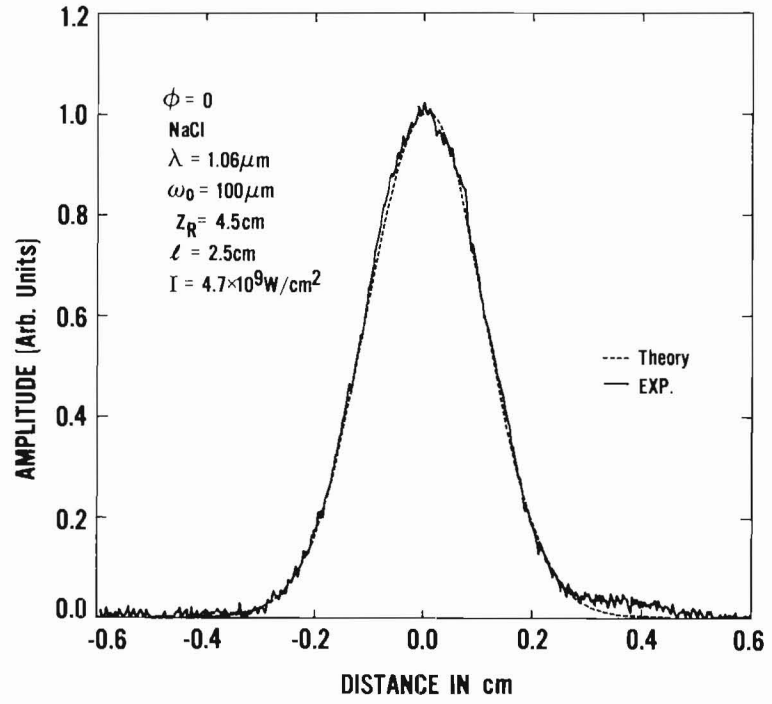


Figure 5. Far field beam profile after transmission through NaCl. The case shown by the solid line is for low input irradiance. The dotted line is a theoretical fit for no phase retardation. The beam is clearly Gaussian and the beam width closely matches the calculated linear optics beam width. The input power is 0.7 MW.

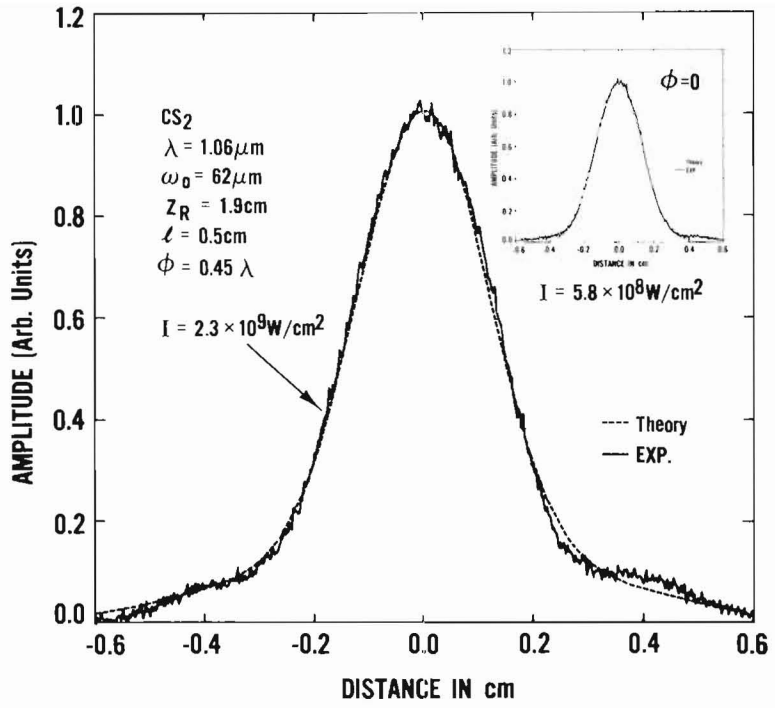


Figure 6. Far field beam profile after transmission through CS_2. The inset shows the low irradiance fit. The excellent fit of theory to experiment for the case of high input irradiance gives $n_2 = 1.3 \times 10^{-11}$ esu for 40 psec pulses at 1.06 μm. The input power is 140 kW for the high irradiance case.

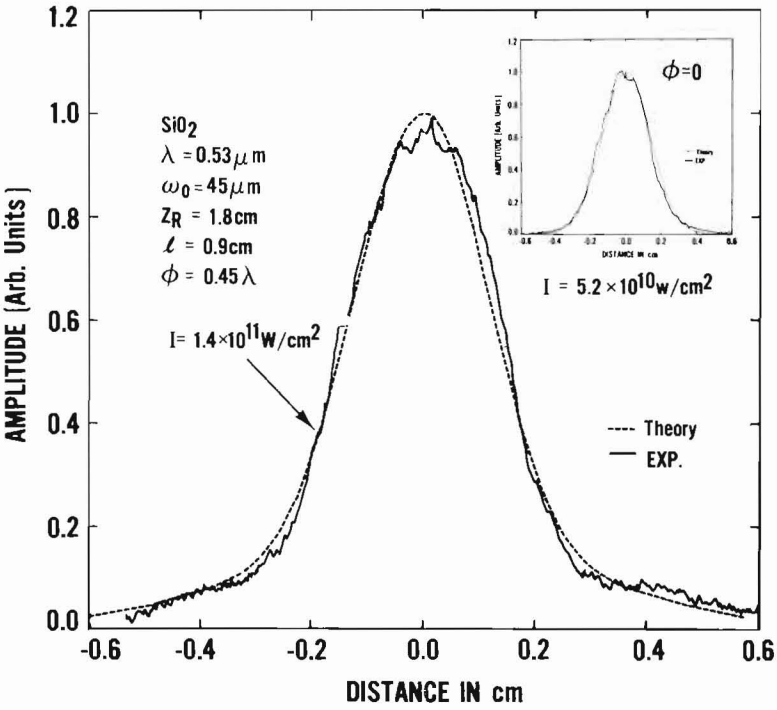


Figure 7. Far field beam profile after transmission through fused quartz. The inset shows the results for low input irradiance. The excellent fit of theory to experiment gives $n_2 = 0.6 \times 10^{-13}$ esu for 30 psec pulses at 0.53 μm. The input power is 4.0 MW for the high irradiance case.

n_2 MEASUREMENTS IN LIQUIDS AND SOLIDS

Material	Wavelength (μm)	n_2 ($\times 10^{-13}$ esu) This Work	n_2 ($\times 10^{-13}$ esu) Others Workers
CS_2	1.06	128 ± 10	125 ± 30[a]
	0.53	123 ± 10	
NaCl	1.06	1.37 ± 0.15	1.22 ± 0.21[b]
	0.53	1.38 ± 0.13	
SiO_2	1.06	0.62 ± 0.03	0.95 ± 0.10[b]
	0.53	0.60 ± 0.04	

(a) K.J. Witte, M. Galanti, and R. Volk, Opt. Commun., Vol. 34, pp 278-282, 1980; Time Integrated Interferometry at 1.32 μm.

(b) M.J. Weber, D. Milam, and W.L. Smith, Opt. Eng., Vol. 17, #5, pp 463-469, 1978; Time Resolved Interferometry at 1.06 μm.

Table I. n_2 measurements in CS_2 (reagent grade), NaCl (Harshaw laser grade) and fused quartz (Corning 7940) at laser wavelengths of 1.06 μm and 0.53 μm. The error bars shown for our work are the relative errors obtained from at least ten separate measurements for each sample at each wavelength. The absolute errors for our work are estimated to be ± 20%. The error bars shown for the results of other workers are the absolute errors.

Manuscript received 2-2-84/sar

Refractive Index of Ternary and Quaternary Compound Semiconductors Below the Funadmental Absorption Edge: Linear and Nonlinear Effects

B. Jensen and A. Torabi

Dept. of Physics
Boston University
Boston, Mass. 02215

The index of refraction n is calculated as a function of frequency and mole fraction x for the following compounds: $Hg_{1-x}Cd_xTe$, $Al_xGa_{1-x}As$, and $In_{1-x}Ga_xAs_yP_{1-y}$ lattice matched to InP. Lattice matching of $In_{1-x}Ga_xAs_yP_{1-y}$ to InP requires that $x = 0.466\ y$. The theoretical result for the refractive index is obtained from a quantum mechanical calculation of the dielectric constant of a compound semiconductor. It is given in terms of the basic material parameters of band gap energy, effective electron mass m_n, effective heavy hole mass m_p, spin orbit splitting energy, lattice constant, and carrier concentration n_e or p for n-type or p-type materials, respectively. If these quantities are known as functions of mole fraction x, there are no adjustable parameters involved. A negative change in the refractive index near the fundamental absorption edge is predicted on passing radiation through a crystal if the change in carrier concentration of the initially unoccupied conduction band is assumed proportional to internal intensity I. Comparison of theory with experimental data is given.

Key words: Optical constants; optical materials; refractive index; semiconductors.

1. Introduction

The refractive index of a ternary or quaternary compound semiconductor is an important parameter in the guiding, coupling, and modulation of radiation for applications in integrated optics. The spectral region of interest is the region near but below the fundamental absorption edge, and lies in the infrared for the majority of materials we consider. Experimental data on the spectral dependence of refractive indices are available for a number of compounds [1] - [5]. However there have been few theoretical analyses of the subject. The usual Kramers Kronig analysis requires a knowledge of the complete spectrum of the imaginary part of the complex dielectric constant in order to calculate the real part of the dielectric constant at a single frequency. Use of this method leads ultimately to the introduction of parameters whose relation to experimentally available material parameters such as band gap energy, effective mass, and carrier concentration, can be vague.

2. Theory

We give an expression for the real part of the refractive index n which is derived from a calculation of the complex dielectric constant using the quantum density matrix equation of motion [6] - [10] and the band structure and electronic wave functions of the Kane theory [11]. This enables the calculation of n as a function of frequency, mole fraction, and the following experimentally available parameters only, with no adjustable constants.

G = band gap energy

m_n = electron effective mass at the band edge

m_p = heavy hole effective mass at the band edge

Δ = spin orbit splitting energy (1)

a = lattice constant

n_e = free electron concentration (for n-type materials)

p = free hole concentration (for p-type materials)

The above quantities are functions of temperature, and hence the refractive index is a function of temperature.

The real part of the refractive index is given as a function of frequency and carrier concentration, or z and y_F, near the fundamental absorption edge by [7], [8]

$$n(z,y_F) = [1 + 2C_o((y_B-y_F) - z(\tan^{-1}(y_B/z) - \tan^{-1}(y_F/z)))]^{\frac{1}{2}} \quad (2)$$

where

$z = (1 - (\hbar w/G))^{\frac{1}{2}}$, $\hbar w$ - photon energy

$C_o = C_o(G, m_n, m_p, \Delta)$

$y_F = y_F(G, m_n, n_e)$ for n-type materials (3)

$y_F = y_F(G, m_n, m_p, p)$ for p-type materials

$y_F = 0$ for pure materials with $n_e = p = 0$

Also

$$y_B = \frac{n^2(0,0) - 1}{2C_o} = m(a_o - a) \quad (4)$$

where n(0,0) is the refractive index of a pure material at the fundamental absorption edge (z = 0) and a is the lattice constant.

$$m = \begin{cases} 3.04 \pm 0.08 & \text{Å}^{-1}, \text{ III-V compounds} \\ 0.346 \pm 0.020 & \text{Å}^{-1}, \text{ II-VI compounds} \\ -5.128 \pm 1.210 & \text{Å}^{-1}, \text{ IV-VI compounds} \end{cases} \quad (5)$$

$$a_o = \begin{cases} 7.49 \pm 0.04 & \text{Å}, \text{ III-V compounds} \\ 17.37 \pm 0.88 & \text{Å}, \text{ II-VI compounds} \\ 5.238 \pm 0.236 & \text{Å}, \text{ IV-VI compounds} \end{cases} \quad (6)$$

The numerical values in eqs (5) and (6) are given for T = 300 K^{O}. The quantities C_o and y_B are constants for a given compound which depend on lattice constant and on the band structure parameters of the Kane theory. The carrier concentration dependence occurs through y_F. Frequency dependence occurs through z. Specifically,

$$C_o = (w_v^2 / w_g^2)\,(3/2)\,\eta$$

$$\eta = \begin{cases} 2/3, & \Delta/G << 1, \quad \text{small spin orbit splitting limit} \\ 3/2, & \Delta/G >> 1, \quad \text{large spin orbit splitting limit} \end{cases}$$

$$w_g = G/\hbar = \text{angular frequency at the band edge}$$

$$w_v^2 = 4\pi e^2 N_v^* / m_n \quad (\sec^{-2})$$

$$N_v^* = N_v (m_r/m_n)^{3/2}$$

$$N_v = (4/3)(2/\pi^2 \lambda\!\!\!^{-}_c^3) \tag{7}$$

$$\lambda\!\!\!^{-}_c = \hbar/m_n \alpha_o c = \text{cm}$$

$$\alpha_o = (G/2m_n c^2)^{1/2}$$

$$m_r = m_n m_p/(m_n + m_p) = \text{reduced mass}$$

$$y_F = 2(n_e/N_v)^{1/3} \quad , \text{ n-type materials}$$

$$y_F = \lambda\!\!\!^{-}_r k_h \quad , \text{ p-type materials}$$

$$\begin{cases} \lambda\!\!\!^{-}_r = (m_n/m_r)^{1/2}\, \lambda\!\!\!^{-}_c/2 \\ k_h = (3\pi^2 p)^{1/3} \end{cases}$$

$$y_F = 0 \quad , \text{ pure materials}$$

Therefore, if G, m_n, m_p, Δ, a, and n_e or p are known, there are no adjustable parameters, and the refractive index is uniquely determined.

For a ternary compound, such as $Hg_{1-x}Cd_xTe$, one now requires G, m_n, and m_p as functions of mole fraction x. Various expressions are given in the literature. We use

$\underline{Hg_{1-x}Cd_xTe}$:

$$\begin{aligned} G\ (eV) &= 6.006\times10^{-4}T(1 - 1.89x) + 1.948x - 0.337 \\ m_n/m &= 0.11x + 0.029(1-x) \\ m_p/m &= 0.35x + 0.3(1-x) \end{aligned} \tag{8}$$

where T is the temperature in ^{o}K [12],[13]. The small spin orbit splitting limit applies for $x \gtrsim 0.6$. For $x < 0.6$, η is treated as an adjustable parameter in a comparison of theory and experiment. This results in a value for η of (0.687 ± 0.014) at T = 300 ^{o}K and (0.7686 ± 0.073) at T = 250 ^{o}K, as opposed to the small spin orbit splitting limit value of 0.667.

$Al_xGa_{1-x}As$:

$$\begin{aligned} G\ (eV) &= 1.435 + 1.209x + 0.386\ x^2 \quad [14] \\ m_n/m &= 0.067 + 0.083\ x \quad [15] \\ m_p/p &= 0.48 + 0.81\ x \quad [15] \end{aligned} \tag{9}$$

The above numerical coefficients are for T = 300°K, and the small spin orbit splitting limit applies.

$In_{1-x}Ga_xAs_yP_{1-y}$: $(x = 0.466y)$

$$\begin{aligned} G\ (eV) &= 1.35 - 0.72y + 0.12y^2 \quad [16] \\ m_n &= xym_n\ (GaAs) + x(1-y)m_n\ (GaP) + y(1-x)m_n(InAs) + (1-x)(1-y)m_n(InP) \\ m_p &= xym_p\ (GaAs) + x(1-y)m_p(GaP) + y(1-x)m_p(InAs) + (1-x)(1-y)m_p(InP) \end{aligned} \tag{10}$$

The following values of m_n and m_p for the various compounds, and the small spin orbit splitting limit, are used.

Sample	m_n/m	m_p/m
GaAs	0.07	0.5
GaP	0.13	0.8
InP	0.07	0.4
InAs	0.028	0.33

Using available experimental results for the lattice constant, [16] - [18], the spectral dependence of the refractive index can be calculated for the various compounds as a function of frequency, mole fraction, and carrier concentration. Results are given, and comparison with experimental data discussed, in Section 3.

The nonlinear intensity dependent refractive index can be calculated using the theory presented above and the following model. In the steady state solution of the rate equation, [19] the carrier concentration n_e is proportional to the internal applied field intensity I as follows.

$$n_e = KI \tag{11}$$

where

$$K = \alpha\tau_L/nw \tag{12}$$

In (12), τ_L is the carrier lifetime, and α the interband absorption coefficient for $\hbar w < G$. It therefore must correspond to an indirect absorption process, such as photon assisted absorption or multiphoton absorption. As we are interested in applications involving integrated optics, at relatively low intensities, we consider α to be intensity independent and use experimental measurements for this quantity. The concentration dependence of the refractive index occurs through

$$y_F = 2(n_e/N_v)^{1/3} \tag{13}$$

and results from a band filling model [7]. We now examine the change in $n(z,y_F)$ which occurs on passing radiation of intensity I and angular frequency w, (where $\hbar w < G$) through a pure crystal in which the carrier concentration of the initially unoccupied conduction band, and hence the initial y_F, is zero. The initial index of refraction at the frequency corresponding to z is

$$n(z,0) = (1 + 2C_0 y_B(1-(z/y_B)\tan^{-1}(y_B/z)))^{\frac{1}{2}} \tag{14}$$

For arbitrary values of y_F/z such that $z < 1$, one can write the final index of refraction from eq (2) as

$$n(z,y_F) = n(z,0) + \Delta n \tag{15}$$

$$\Delta n \cong -(C_0 y_F/n(z,0))(1-(z/y_F)\tan^{-1}(y_F/z)) \tag{16}$$

where terms of order y_F/y_B and z/y_B have been neglected. This is permissible for y_F and z sufficiently small, as y_B ranges from around 3 to 6 while y_F and z are small compared with unity. The inverse tangent can be expanded in two limits as

$$\tan^{-1}(y_F/z) \cong \begin{cases} (y_F/z) - (1/3)(y_F/z)^3 & , (y_F/z) \ll 1 \\ (\pi/2) - (z/y_F) + (1/3)(z/y_F)^3 & , (y_F/z) \gg 1 \end{cases} \tag{17}$$

One finds the following limiting forms from (16).

$$\begin{aligned} n(z,y_F) &= n(z,0) + \Delta n \\ \Delta n &= -(C_0/3z^2 n(z,0))\, y_F^3 \quad , (y_F/z) \ll 1 \end{aligned} \tag{18}$$

In the opposite limit, one has

$$\begin{aligned} n(z,y_F) &= n(z,0) + \Delta n \\ \Delta n &\cong -(C_0/y_F/n(z,0))(1 - (\pi/2)(z/y_F) + (z/y_F)^2) \cong -(C_0/n(0,0))\, y_F \quad , (z/y_F) \ll 1 \end{aligned} \tag{19}$$

To proceed further, one must specify the form of τ_L eq (12). We consider two cases

Case 1: Concentration independent carrier lifetime:

$$\tau_L = \tau_o = \text{constant} \tag{20}$$

$$K = \alpha\tau_o/\hbar w = K_o$$

$$n_e = K_o I = (\alpha\tau_o/\hbar w) I$$

$$y_F = 2(n_e/N_v)^{1/3} = 2(K_o/N_v)^{1/3} I^{1/3}$$

$$\Delta n = -(8C_oK_o/3z^2N_vn(z,0)) I = n_2 I \qquad (y_F/z) << 1$$

$$\Delta n = \frac{-(2C_o(K_o/N_v)^{1/3})}{n(0,0)} I^{1/3} = n_3 I^{1/3} \quad , \qquad (z/y_F) << 1$$

For Case 2, in which the carrier lifetime is independent of carrier concentration, and for a fixed nonzero value of z, the chance in the refractive index is linear in I for low intensities such that $(y_F/z) << 1$, and goes as $I^{1/3}$ for high intensities such that $(z/y_F) << 1$.

Case 2: Concentration dependent carrier lifetime:

$$\tau_L = T_o/n_e^2 = \tau_o n_o^2/n_e^2 \quad , \quad T_o = \text{constant} = \text{sec/cm}^6 = \tau_o n_o^2 \tag{21}$$

$$K = \alpha T_o/(\hbar w)\, n_e^2 = K_o (n_o/n_e)^2$$

$$n_e = KI = (\alpha T_o/\hbar w)(1/n_e^2) I$$

$$n_e = (\alpha T_o/\hbar w)^{1/3} I^{1/3}$$

$$y_F = 2(n_e/N_v)^{1/3}$$

In this case, Δn goes as $y_F^3 \alpha n_e \alpha I^{1/3}$ for $(y_F/z) << 1$, and as $y_F \alpha n_e^{1/3} \alpha I^{1/9}$ for $(z/y_F) << 1$. In either case, there is a tendency for the dependence of Δn on intensity to saturate as carrier concentration is increased. The limits $\Delta n \alpha I$ and $\Delta n \alpha I^{1/3}$ have been observed in InSb and in $Hg_{0.79}Cd_{0.21}Te$, respectively [20],[21].

In the above, we have considered a pure crystal where the initial carrier concentration, and hence the inital y_F, is zero. In this case, the change in intensity ΔI is approximately equal to I. In general, the change in refractive index Δn for a given change in intensity ΔI is

$$\Delta n = \frac{\partial n(z,y_F)}{\partial y_F} \delta y_F = \frac{dn}{dI} \Delta I \tag{22}$$

$$\delta y_F = (y_F/3)(\delta n_e/n_e)$$

$$\frac{\partial n}{\partial y_F} = -(C_o/n(z,y_F))\,(y_F^2/(y_F^2 + z^2))$$

If $n_e = K_o I$, where K_o as given in (20) is constant,

$$\frac{dn}{dI} = -(8C_oK_o/3N_v n(z,y_F))\,(1/(y_F^2 + z^2)) \qquad (23)$$

and one obtains the previous result in the limit that $y_F/z \to 0$ and $\Delta I = I$. In this case, the change in refractive index is linearly dependent on I and $dn/dI = n_2$ is not a function of intensity at low intensities, while at high intensities, a nonlinear regime is attained in which dn/dI becomes dependent on I. One can calculate this effect for a given material if α and τ_L can be measured or calculated. The absorption coefficient has been measured in the case of InSb, and τ_L is known approximately. Hence numerical results can be obtained and compared with experiment.

3. Comparison with Experimental Results

$Hg_{1-x}Cd_xTe$:

Figure 1 shows the refractive index of $Hg_{1-x}Cd_xTe$ as a function of photon energy and different mole fractions x. The numerical values given in tables 1 and 2 have been used in calculating the theoretical results which are listed in table 3. The sample is assumed to be n-type with a carrier concentration $n_e = 1.0\times10^{17}$ cm^{-3}. The reduction of the refractive index as one increases x, which is mainly due to the increase of band gap energy G with x, is noticeable. The same effect has been observed in the compound $Al_xGa_{1-x}As$ as one increases the Al mole fraction at frequencies just below the fundamental absorption edge [2]. The theoretical refractive index at $T = 300^oK$ and at $T = 250^oK$ is shown in figure 2, and compared with experimental results [1] for $Hg_{0.795}Cd_{0.205}Te$. The decrease of the refractive index with temperature is due to the fact that band gap energy is an increasing function of temperature for this value of x, while C_o is a decreasing function of G. At $T = 300^oK$, for $Hg_{0.795}Cd_{0.205}Te$, the values of the material parameters are G = 0.18 eV, a = 6.465 Å, $m_n/m = 0.046$ and $m_p/m = 0.31$. Since the experimental value of n_e was unknown, and the small spin orbit splitting limit does not hold for $x < 0.6$, the comparison of theory and experiment assumed n_e and η as adjustable parameters. This resulted in a value of $n_e = (1.30 \pm 0.13)\times10^{18}$ cm^{-3} and $\eta = (0.687 \pm 0.014)$ as opposed to the small spin orbit splitting limit of $\eta = 0.667$. A similar treatment at $T = 250^oK$ yielded $\eta = (0.7686 \pm 0.073)$ and $n_e = (2.06 \pm 0.67)\times10^{18}$ cm^{-3} with G = 0.16eV. Further discussion is given in Reference [10].

$Al_xGa_{1-x}As$:

Theoretical results have been calculated here for the ternary compound $Al_xGa_{1-x}As$ for $0 \le x \le 0.3$ using the values of the experimental parameters at 300^oK given in eq (9). In making an effort to compare theory and experiment, one encounters difficulty due to variation in the reported values of the band gap energy as a function of x. One also finds variation in reported values of the electron and especially the heavy hole effective mass, and often there are no

experimental values of electron or hole density for samples on which measurements are made. We have therefore calculated theoretical results over the range of available reported values for G, m_n, and m_p [8]. The example we present here is a typical result. As materials technology improves, and more reliable values for material parameters become available, it will be possible to predict the refractive index more precisely. As experimental results, we use the values for the refractive index reported by Casey et al, as well as we can determine these from the data given there. All calculations have been made on the assumption that the electron density is 10^{16} cm^{-3}, although one might expect that the free carrier concentration would vary as x is varied for a given level of doping. The lattice constant varies only slightly as x is varied, and hence y_B is slowly varying, ranging from 5.55 at x = 0 to 5.44 for x = 0.2. Results are shown in figure 4. Agreement is best at smaller x. There is an uncertainty in x of ± 0.02, and the best fit at higher x is obtained on choosing the smallest value for x consistent with the uncertainty involved. For example, one obtains a better fit of the curve marked x = 0.29 to the experimental data on taking x = 0.27 instead, which is still within limits of the uncertainty in x. The usual trend toward a smaller refractive index for a material with a larger band gap energy is observed, and it is seen that one can vary n continuously through a range of values by choosing x appropriately for a fixed frequency. This is the property which is useful for guiding radiation for applications in integrated optics.

$In_{1-x}Ga_xAs_yP_{1-y}$:

The quaternary material $In_{1-x}Ga_xAs_yP_{1-y}$ has generated much interest recently because it can be grown epitaxially on InP without lattice mismatch over the composition range $0 \leq y \leq 1.0$ provided x = 0.466y. We give the theoretical calculation of the refractive index of $In_{1-x}Ga_xAs_yP_{1-y}$ as a function of frequency and mole fraction y (where x = 0.466y) using the material parameters given in eq (10) for T = 300°K. The numerical values of G(eV), C_o, a(Å), and y_B as a function of y are listed in table 4. Results are shown in figure 4 as a function of photon energy and y increments of 0.2. We have assumed the sample to be intrinsic, with no carrier concentration, which implies that y_F is zero. The decrease in refractive index with an increase in band gap energy at a fixed frequency is again noted. Theoretical (solid line) and experimental (open circle) values of refractive index versus wavelength are shown in figure 5 for the case of y = 1.0 and x = 0.425. The experimental results are taken from Reference [4]. The fit of data to the theoretical refractive index gives the carrier concentration to be $n_e = (1.26 \pm 0.60)x10^{17}$ cm^{-3}.

The Nonlinear Refractive Index:

To compare theory and experimental results for the nonlinear change in the refractive index we have calculated Δn and -dn/dI as a function of photon energy for InSb at T = 77°K. The experimental results of Miller et al have been used [20]. Table 5 lists the experimental parameters which enable one to calculate the refractive index change Δn. It also gives the calculated value of Δn as a function of the photon energy. To calculate -dn/dI, which in the limit of low intensity I or small y_F/z becomes $n_2 = \Delta n/I$, one needs to know both the absorption coefficient α (cm^{-1}) and the recombination time τ_L. Miller et al [20] have measured the absorption coefficient over a range of frequencies which includes the fundamental absorption edge. Such a measurement includes the contribution of direct absorption above the fundamental absorption edge and the contribution of free carrier absorption below the absorption edge. Free carrier absorption involves

the absorption of a photon accompanied by scattering of an electron between initial and final states which lie in the conduction band, and hence does not contribute to a filling of the conduction band [22]. In the calculation of Δn, where n_e is given by (11) and (12), we are only interested in the contribution to α which results in a filling of the conduction band for frequencies below the fundamental absorption edge. This contribution is expected to be only a fraction of the measured absorption coefficient, which includes extraneous processes.

Figure 6 shows the experimental [20] value of -dn/dI as a function of photon energy along with the theoretical value calculated using the measured α, which we expect to be an upper limit on the correct value. Numerical values are given in table 6. The fit of theory with the experimental results estimates the recombination time τ_L to be (16.27 ± 1.09)ns. The reported value of the recombination time ranges from 200 ns to 800 ns [23]. Miller uses 400 ns for the recombination time in his calculations. As one can see from (12), use of an absorption coefficient that is too large would be expected to result in prediction of a recombination time that is too small, as α and τ_L appear as a product. The problem could be investigated by calculating theoretically the contribution of free carrier absorption for frequencies below the fundamental absorption edge, and subtracting the result from the measured absorption coefficient [24]. Regardless of the fact that the theoretical calculations have been performed using values of α and τ_L that are expected to be too large and too small, respectively, the resultant value for K in eq (12) is thought to be of the right order of magnitude, as there is qualitiative agreement between theoretical and experimental results in figure 6.

In conclusion, we have summarized the calculation of the linear index of refraction as a function of frequency and mole fraction x for ternary and quaternary compound semiconductors with the band structure of the Kane theory, and have discussed the calculation of the nonlinear effect for the binary compound InSb. Theoretical and available experimental results are compared in all cases.

4. Acknowledgement

This research was supported by the U.S. Department of Energy under Contract DE-AC02-79ER10444.

5. References

[1] E. Finkman, Y. Nemirovsky, J. Appl. Phys. 50, 4356 (1979).

[2] H.C. Casey, D.D. Sell, M.B. Panish, Appl. Phys. Lett. 24, 63 (1974).

[3] J. Stone, M.S. Whalen, Appl. Phys. Lett. 41, 1140 (1982).

[4] P. Chandra, L.A. Colden, K.E. Strege, Electron. Lett. 17, 6 (1981).

[5] D.D. Sell, H.C. Casey, Jr., K.W. Wecht, J. Appl. Phys. 45, 2650 (1974).

[6] B. Jensen, IEEE J. Quantum Electron. QE-18, 1361 (1982).

[7] B. Jensen, A. Torabi, IEEE J. Quantum Electron. QE-19, 448 (1983).

[8] B. Jensen, A. Toarbi, IEEE J. Quantum Electron. QE-19, 887 (1983).

[9] B. Jensen, A. Toarbi, J. Appl. Phys. 54, 3623 (1983).

[10] B. Jensen, A. Torabi, J. Appl. Phys. 54, 5945 (1983).

[11] E.O. Kane, J. Phys. Chem. Solids 1, 249 (1957).

[12] J. Calas, J. Allgre, C. Fau, Phys. Status Solidi B 107, 275 (1981).

[13] G.L. Hansen, J.L. Schmit, T.N. Casselman, J. Appl. Phys. 53, 7099 (1982).

[14] J.C. Dyment, Y.C. Cheng, A.J. SpringThorpe, J. Appl. Phys. 46, 1739 (1975).

[15] H.C. Casey, Jr., J. Appl. Phys. 49, 3684 (1978).

[16] R.E. Nahory, N.A. Pollack, W.D. Johnson, Jr., R.L. Barns, Appl. Phys. Lett. 33, 659, (1978).

[17] M. Neuberger, II-VI Ternary Compound Data Tables (Hughes Aricraft Co.,Culver City, California 1972).

[18] N. Neuberger, Cadmium Telluride and the Cadmium Telluride Mercury System (Hughes Aircraft Co., Culver City, California 1967).

[19] R.K. Jain, M.B. Klein, Appl. Phys. Lett. 35, 454 (1979).

[20] D.A.B. Miller, C.T. Seaton, M.E. Price, S.D. Smith, Phys. Rev. Letters 47, 197 (1981).

[21] J.R. Hill, G. Parry, A. Miller, Optics Commun. 43, 151 (1982).

[22] B. Jensen, Ann. Phys. 80, 284 (1973).

[23] R.G. Van Welzeni, J.P. Zeeuwn, Solid State Electron. 21, 1591 (1978).

[24] B. Jensen, A. Torabi, Proceedings of SPIE-The International Society for Optical Engineering, May 1984. (To be published.)

Table 1. The values of lattice constants $a(\mathring{A})$ and y_B as a function of x for $Hg_{1-x}Cd_xTe$.

x	$a(\mathring{A})$	y_B
0.35	6.464	3.7765
0.50	6.469	3.7748
0.65	6.473	3.7734
0.75	6.475	3.7727
0.85	6.477	3.7720

Table 2. Values of G, y_F, and C_o for $Hg_{1-x}Cd_xTe$ using the band gap of Reference [12].

x	G(eV)	y_F	C_o
0.35	0.4057	0.368	1.825
0.50	0.6469	0.264	1.526
0.65	0.8880	0.208	1.358
0.75	1.0487	0.183	1.279
0.85	1.2095	0.163	1.215

Table 3. The theoretical value of the refractive index n as a function of photon energy and cadmium mole fraction x for $Hg_{1-x}Cd_xTe$ calculated using the parameters listed in tables 1 and 2.

$\hbar\omega$ (eV)	n	n	n	n	n
0.10	3.232	2.960	2.801	2.724	2.661
0.20	3.329	3.010	2.834	2.751	2.683
0.30	3.459	3.067	2.870	2.779	2.707
0.40	3.649	3.134	2.910	2.810	2.731
0.50	...	3.217	2.953	2.843	2.758
0.60	...	3.334	3.005	2.880	2.787
0.70	...	...	3.066	2.922	2.819
0.80	...	...	3.148	2.972	2.855
0.90	...	...	...	3.033	2.896
1.00	...	...	...	3.120	2.944
1.10	...	...	...	...	3.007
1.20	...	...	...	...	3.109
x	0.35	0.50	0.65	0.75	0.85

Table 4. The numerical values of G(eV), $a(\mathring{A})$, and y_B as a function of y for $In_{1-x}Ga_xAs_yP_{1-y}$ with x = 0.466y.

y	G(eV)	$a(\mathring{A})$	C_o	y_B
0.0	1.350	5.86960	1.113	4.9246
0.1	1.279	5.86910	1.143	4.9261
0.2	1.211	5.86872	1.171	4.9273
0.3	1.145	5.86847	1.199	4.9280
0.4	1.081	5.86834	1.224	4.9284
0.5	1.020	5.86832	1.247	4.9285
0.6	0.961	5.86843	1.270	4.9282
0.7	0.905	5.86866	1.289	4.9275
0.8	0.851	5.86901	1.306	4.9264
0.9	0.799	5.86949	1.320	4.9249
1.0	0.750	5.87008	1.330	4.9231

Table 5. Theoretical values of refractive index change Δn for InSb at $77^{\circ}K$.

$G(eV) = 0.227$ eV	$n_e = 4 \times 10^{14} (cm^{-3})$
$m_n = 0.0133\ m_o$	$C_o = 3.047$
$m_p = 0.18\ m_o$	$y_B = 3.0634$
$\eta = 3/2$	$y_F = 0.162$

$\Delta n \times 10^2$	$\hbar w$(eV)
1.52	0.215
1.63	0.216
1.75	0.217
1.88	0.218
2.05	0.219
2.25	0.220
2.48	0.221
2.79	0.222
3.18	0.223
3.73	0.224
4.52	0.225
5.88	0.226

Table 6. Theoretical values of -dn/dI as a function of photon energy for InSb at 77°K. The measured absorption coefficients of Reference [20] have been used.

$-dn/dI \times 10^3$	$\hbar\omega$(eV)
0.84	0.217
1.07	0.218
1.29	0.219
1.53	0.220
1.75	0.221
2.08	0.222
2.60	0.223
3.22	0.224
5.60	0.225
8.16	0.226

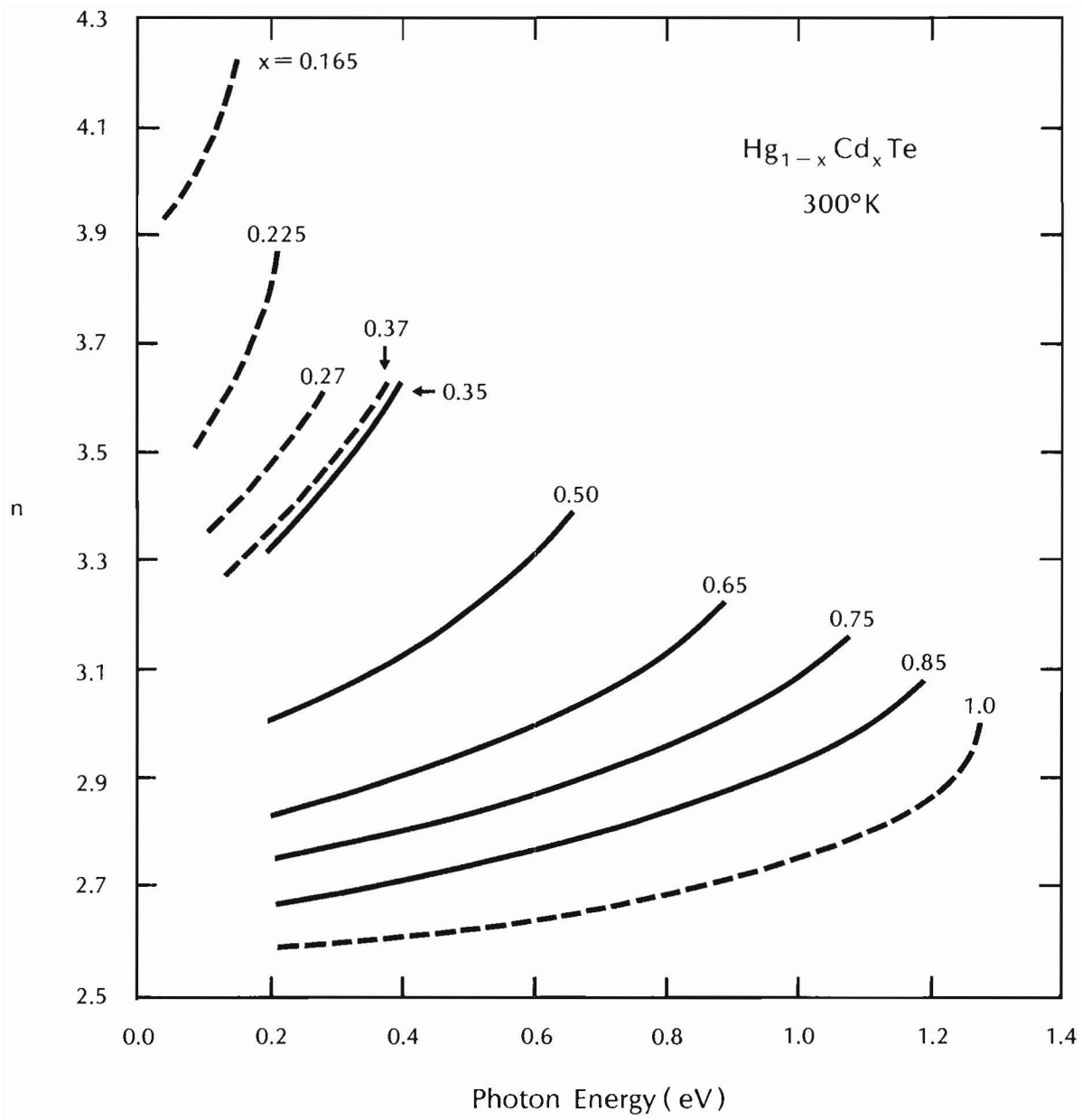


Figure 1: Theoretical refractive index n (solid lines) and experimental refractive index (dashed lines) for the compound $Hg_{1-x}Cd_xTe$ as a function of photon energy (eV) and mole fraction x.

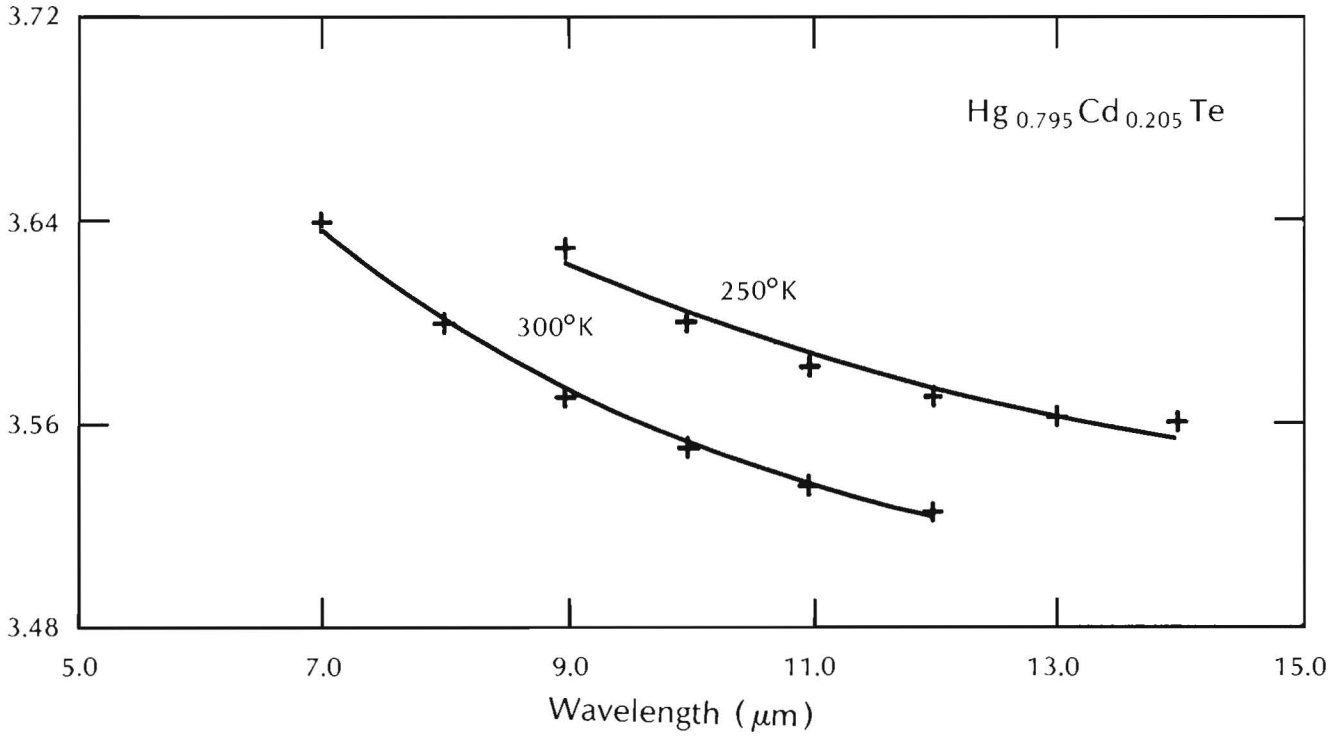


Figure 2: The temperature dependence of the theoretical refractive index (solid lines) and the experimental refractive index (dashed lines).

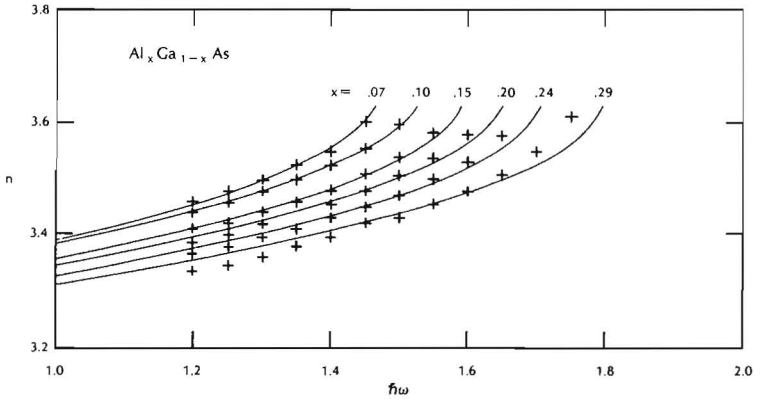


Figure 3: Theoretical (————) and experimental (+++++++++) values of the refractive index of $Al_xGa_{1-x}As$ versus photon energy. A carrier concentration $n_e = 10^{16}$ cm-3 has been assumed in the theoretical calculation. There is an uncertainty in x of ± 0.02, and the best fit at higher x is obtained on choosing the smallest value for x consistent with the uncertainty involved.

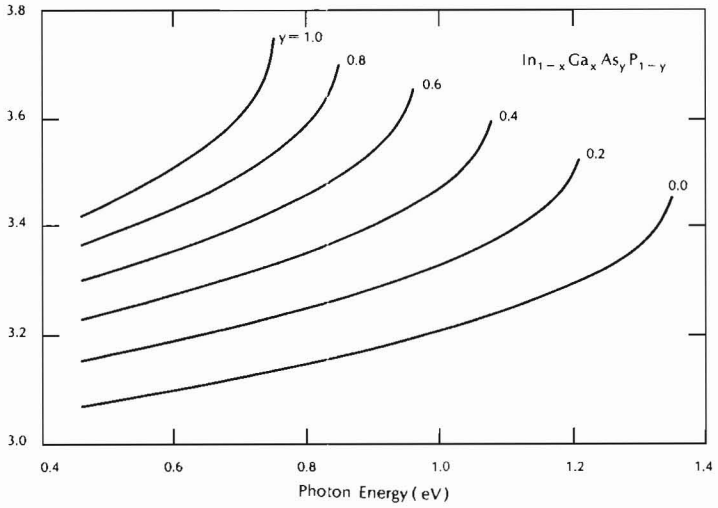


Figure 4: Theoretical values of the refractive index n for the quaternary compound $In_{1-x}Ga_xAs_yP_{1-y}$ as a function of photon energy (eV) and y increments of 0.2. Lattice matching requires x = 0.466y. We assume the sample to be intrinsic, with no carrier concentration.

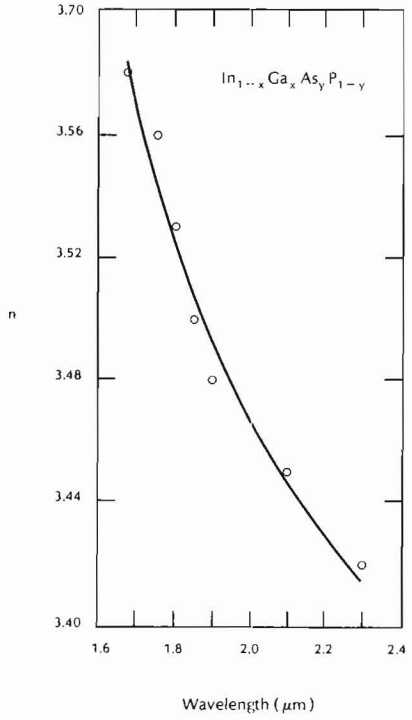


Figure 5: Theoretical (solid line) and experimental (open circle) [4] values of the refractive index of $In_{1-x}Ga_xAs_yP_{1-y}$ versus wavelength (μm).

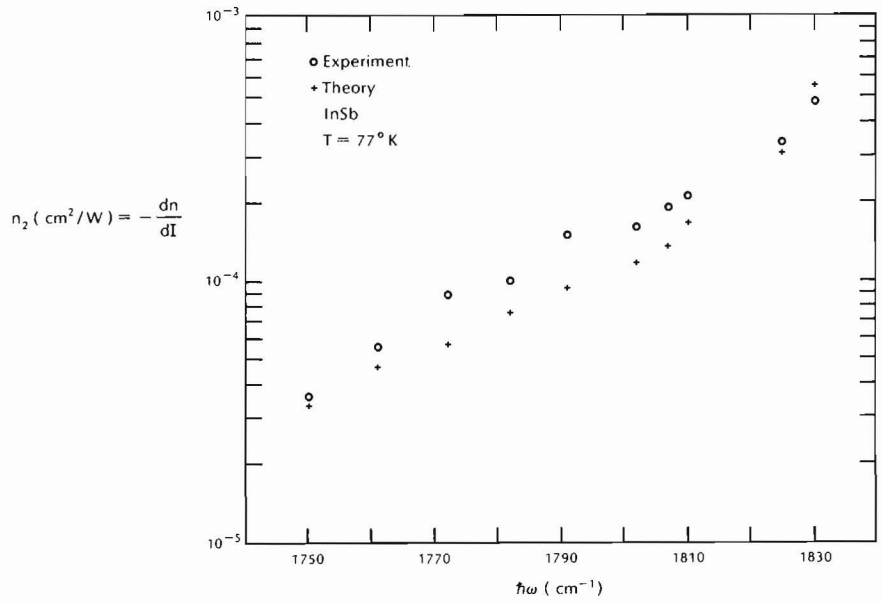


Figure 6: Experimental [20] and theoretical values of -dn/dI calculated as a function of photon energy.

Applicability of the theory to very wide bandgap materials was questioned. The speaker believed it should apply. It was also pointed out that no contribution from core levels was assumed in the theory. The speaker agreed but had not developed an estimate of how important this contribution might be.

Boulder Damage Symposium
1983 Attendees

Joseph A. Abate
Sohio-LLE
University of Rochester
250 E. River Road
Rochester, NY 14623
716-275-5181

M. A. Acharekar
ILS
3404 N. OBT
Orlando, FL 32804
305-295-4010

Albert Alexander
USAF
FJSRL/NH
USAF Academy
Colorado Springs, CO 80840
303-422-3125

Sherwin Amimoto, MS-753
Aerospace Corp.
Box 92957
Los Angeles, CA 90009
213-648-7660

Joe Apfel
Optical Coating Laboratory, Inc.
2789 Northpoint Parkway
Santa Rosa, CA 95401
707-525-7010

Walter B. Atkinson
Riverside Research Institute
1701 N. Fort Myer Drive
Arlington, VA 22209
703-522-2310

William P. Barnes, Jr.
Itek Optical Systems
10 Maguire Road
Lexington, MA 02173-3199
617-276-2246

Michael Bass
Center for Laser Studies
University of Southern California
University Park DRB 17
Los Angeles, CA 90089-1112
213-743-7994

William T. Beauchamp
Optical Coating Laboratory, Inc.
2789 Northpoint Parkway
Santa Rosa, CA 95401
707-525-7649

Michael F. Becker
University of Texas
Electrical Engineering Dept.
Austin, TX 78712
512-471-3628

B. Bendow
BDM Corp.
1801 Randolph S.E.
Albuquerque, NM 87106
505-848-5129

Harold E. Bennett
Naval Weapons Center
Code 38101 Michelson Laboratory
China Lake, CA 93555
619-939-2869

Jean M. Bennett
Naval Weapons Center
Code 38101 Michelson Laboratory
China Lake, CA 93555
619-939-2869

James H. Bentley
Commander: USAM/COM
DRSMI-RHS (Bentley)
Redstone Arsenal, AL 35898
205-876-8181

Vahram W. Biricik
Northrop Res. & Technology Center
One Research Park
Palos Verdes Peninsula, CA 90274
213-377-4811

Norman L. Boling
Optical Coating Lab, Inc.
Dept. 272-5
2789 Northpoint Parkway
Santa Rosa, CA 95401
707-525-7645

Dennis Burge
Naval Weapons Center
Code 3816
China Lake, CA 93555
619-939-3832

Charles Carniglia
Optical Coating Laboratory, Inc.
2789 Northpoint Parkway
Santa Rosa, CA 95401
707-525-7010

Jack P. Chambers
Two-Six Incorporated
934 Sarver Rd.
Sarver, PA 16056
352-4455, ext. 266

Charles Cockrum
Laser Power Optics
11211 Sorrento Valley Rd.
San Diego, CA 92121
619-455-0751

Barry Cole
Honeywell
10701 Lyndale Ave. South
Bloomington, MN 55420
612-887-4497

Joseph F. Connolly
CVD Incorporated
35 Industrial Parkway
Woburn, MA 01801
617-933-9243

Verne R. Costich

Ed Danielewicz
Laser Power Optics Corp.
11211 Sorrento Valley Rd.
San Diego, CA 92121
619-455-0751

Terrence F. Deaton
Frank J. Seiler Research Laboratory
United States Air Force Academy
Colorado Springs, CO 80840
303-472-3502

Donald Decker
Naval Weapons Center
Code 3816
China Lake, CA 93555
619-939-3247

Hulya Demiryont
Colorado State University
Physics Dept.
Fort Collins, CO 80523
303-491-5850

John A. Detrio
University of Dayton
Research Institute
300 College Park
Dayton, OH 45469
513-229-3527

Fred Domann
Univ. of Wisconsin--Platteville
Dept. of Physics
Platteville, WI 53818
608-342-1657

T. M. Donovan
Naval Weapons Center Code 3818
China Lake, CA 93555
619-939-3852

John A. Dye
United Technologies Research Center
Optics & Applied Technology Lab
P.O. Drawer 4181
West Palm Beach, FL 33402
305-840-1577

A. M. Easton
Ferranti PLC
Dunsinane Ave.
Dundee, Scotland
0382-89311

John Eggleston
Mathematical Sciences Northwest, Inc.
2755 Northup Way
Bellevue, WA 98004
206-827-0460

Osama El-Bayoumi
USAF
RADC/ESM
Hanscom AFB, MA 01731
617-861-5832

Ed Enemark
Optical Coating Laboratory, Inc.
2789 Northpoint Parkway
Santa Rosa, CA 95401
707-525-7010

Dennis G. Fischer
Coherent, Inc.
2301 Lindbergh St.
Auburn, CA 95603
916-823-9550

Diane M. Fischer
USAF
AFWL/ARAO
Kirtland AFB, NM 87117
505-844-0226

Steven E. Fischer
Rockwell/Rocketdyne
P.O. Box 5670
Kirtland AFB, NM 87108
505-846-6175/255-9483

Stephen R. Foltyn
Los Alamos National Laboratory
CHM-5, MS J566
Los Alamos, NM 87545
505-667-1123

Daniel Friart
Commissariat A L/Energie Atomique
Centre D'Etudes de Limeil
Boite Postale 27
94190 Villeneuve St. Georges
France
569 96-60

George Gardopee
Perkin-Elmer Corp.
MS/955
Electro-Optical Div.
100 Wooster Heights Rd.
Danbury, CT 06810
203-797-6171

George A. Graves
University of Dayton
KL 162
300 College Park
Dayton, OH 45469
513-229-4343

Jeffrey W. Griffin
Pacific Northwest Laboratory
P.O. Box 999
Richland, WA 99352
509-375-2081

Mark J. Guardalben
University of Rochester
Laboratory for Laser Energetics
250 East River Road
Rochester, NY 14623
716-275-3418

A. H. Guenther
AFWL/CA
Kirtland AFB, NM 87117

Karl H. Guenther
Balzers AG
Liechtenstein

K. D. Hachfeld
Laser Inc.
Picker Rd.
Box 537
Sturbridge, MA 01566
617-347-7314

Steven Hadley
CVI Laser
P.O. Box 11308
Albuquerque, NM 87192
505-296-9541

Bill Hansen
Optical Coating Lab., Inc.
2789 Northpoint Parkway
Santa Rosa, CA 95401
707-525-7042

Bill Herrmann, Jr.
Opti-Electronic Corp.
11744 Pagemill Rd.
Dallas, TX 75243
214-349-0190

Robert N. Hindy
Rockwell International-
Rocketdyne Div.
6633 Canoga Ave.
Canoga Park, CA 91304
213-700-4851

Lowell M. Hobrock
Hughes Aircraft Company
P.O. Box 902
Bldg. E1-MF102
El Segundo, CA 90245
213-645-9606

Samuel J. Holmes
Northrop Res. & Technology Center
One Research Park
Palos Verdes Peninsula, CA 90274
213-377-4811

Alan K. Hopkins
AFWAL/Materials Lab
W-PAFB, OH 45433
513-255-6652/6671

Long-Sheng Hsu
Colorado State University
Physics Department
Fort Collins, CO
303-491-5524

Marshall Huberman
TRW Space & Technology Group
One Space Park
01/1060
Redondo Beach, CA 90278
213-535-5375

R. S. Hughes
Dept. of Physics & Computer Science
Pacific Union College
Angwin, CA 94508
707-965-7269

Thomas W. Humpherys
U.S. Air Force
EOARD Box 14
FPO NY 09510
UK/409 4318

Hugh H. Hurt
Naval Weapons Center
Code 3816
China Lake, CA 93555
619-939-3049

John P. Jackson
Kawan Sciences
1500 Garden of the Gods Rd.
Colorado Springs, CO 80933
303-599-1961

Stephen D. Jacobs
University of Rochester
250 East River Road
Rochester, NY 14623
716-275-5101

B. Jensen
Dept. of Physics
Boston University
Boston, MA 02215
617-353-2610/2600

Jerry Johnston
Optical Coating Laboratory, Inc.
2789 Northpoint Parkway
Santa Rosa, CA 95401
707-525-7148

Kenneth Jungling
University of New Mexico
Albuquerque, NM 87131
505-277-3317

John A. Kardach
USAF AFIT/EN
Box 4215
Wright-Patterson AFB, OH 45433
255-7270/5533

T. Kardos
Broomer Research Labs.
3 Beech St.
Islip, NY 11751
516-277-0500

C. Klein
Aerospace Corp.
M4-980
P.O. Box 92957
Los Angeles, CA 90009
213-648-6226

Walter L. Knecht
AFWAL/MLPO
Wright Patterson AFB, OH 45433
513-255-4474

Barry Koepke
Honeywell Inc.
Ceramics Center
5121 Winnetka Ave. N.
New Hope, MN 55428
612-536-3145

William A. Koldewyn
Scientech, Inc.
5649 Arapahoe
Boulder, CO 80303
303-444-1361

H. Kuester
Schott Glaswerke, Mainz
Dept Applikation Phys. Opt.
Mainze, West Germany

David S. Kyser
Naval Weapons Center Code 3818
China Lake, CA 93555
619-939-2690

Michael R. Lange
Institute for Modern Optics
University of New Mexico
Albuquerque, NM 87131

Thomas A. Leonard
Univ. of Dayton Research Inst.
300 College Park KL-464
Dayton, OH 45469
513-229-3724

Keith L. Lewis
Royal Signals & Radar Establishment
St. Andrews Rd.
Malvern
Worcestershire WR14 3 PS
United Kingdom
06845 2733, ext. 3062/2003

Jacques F. Linder
Hughes Aircraft Co.
21000 E. El Segundo Blvd.
El Segundo, CA 90274
213-616-6182

Carmina Londono
Avco Everett Research
Laboratory, Inc.
2385 Revere Beach Parkway
Everett, MA 02149
617-381-4225

Ben A. Loving
Hughes Aircraft Company
2000 E. El Segundo Blvd.
Attn: Bldg #1/MS C175
El Segundo, CA 90245
213-616-3369

W. H. Lowdermilk
LLNL
POB 4508 M/S L490
Livermore, CA 94550
415-422-5498

Bo Ljung
Singer-Kearfott Div.
1225 McBride Ave.
Little Falls, NJ 07474
201-785-2761

David Lunt
Burleigh Northwest Optical Inc.
Burleigh Park
Fishers, NY 14453

Michael Lunt
Technical Optics Ltd.
Second Ave.
Onchan, Isle of Man
British Isles
44624 4443

Myron T. Maclin
USAF
AFWL/ARAO
Kirtland AFB, NM 87117
505-844-1776

Taaro Mandre
TRW Space & Technology Group
One Space Park
01/1251
Redondo Beach, CA 90278
213-536-4878

Frane Marcelja
Corion Corporation
73 Jeffrey Ave.
Holliston, MA 01746
617-429-5065

Armen Mardiguian
US Air Force Academy
Dept. of Physics
Colorado Springs, CO 80840
303-472-4619

Charles L. Marquardt
Code 6551
Naval Research Laboratory
Washington, DC 20375
202-767-4871

C. Denton Marrs
Naval Weapons Center
Code 3817
China Lake, CA 93555
619-939-2470

Diane J. Martin
USAF
AFWL/ARAO
Kirtland AFB, NM 87117
505-844-0721

James W. Mayo III
USAF
AFWL/ARAO
Kirtland AFB, NM 87117
505-844-0721

Fred McClung
Hughes Aircraft Company
2650 Yale Blvd, S.E.
Albuquerque, NM 87106
505-242-9818

Robert A. McGee
LLNL
7000 East Ave.
Livermore, CA 94550
415-422-8381

Michael McGuirk
Perkin-Elmer
MS 420
Main Ave.
Norwalk, CT 06856
203-834-4921

John K. McIver
University of New Mexico
Dept. Physics & Astronomy
Albuquerque, NM 87131
505-277-6713

Jim McNally
USAF
9608 Avenida de la Luna NE
Albuquerque, NM 87111
505-822-8143

J. R. McNeil
University of New Mexico
Electrical Engineering Dept.
Albuquerque, NM 87131
505-277-5502

Larry D. Merkle
University of Arkansas
Physics Dept.
Fayetteville, AR 72701
501-575-6571

David Milam
Lawrence Livermore National Laboratory
P.O. Box 5508, L-490
Livermore, CA 94550
415-422-5499

Robert E. Miller
Hughes Aircraft Co.
Electro-Optical & Data Systems
E1, M/S D160
P.O. Box 902
El Segundo, CA 90245
213-616-6232

Shashanka S. Mitra
Dept. of Electrical Engineering
University of Rhode Island
Kingston, RI 02881

N. Kent Moncur
KMS Fusion, Inc.
3621 South State Road
P.O. Box 1567
Ann Arbor, MI 48106
313-769-8500

Dennis Morelli
Optical Coating Laboratory, Inc.
2789 Northpoint Parkway
Santa Rosa, CA 95401
707-525-7010

Patricia L. Morse
USAF
AFWL/ARAO
Kirtland AFB, NM 87117
505-844-0226

Bill W. Mullins
Dept. of Physics
USAF Academy
Colorado Springs, CO 80840
303-472-4158

George Nado
Texas Instruments
Box 226015, M/S 3196
Dallas, TX 75266
214-995-6412

Brian E. Newnam
Los Alamos National Laboratory
MS-J564
Los Alamos, NM 87545
505-667-7979/7102

Davis B. Nichols
Boeing Aerospace Company
Mail Stop 8H-18
P.O. Box 3999
Seattle, WA 98124
206-773-8938

Robert M. O'Connell
Univ. of Missouri - Columbia
Electrical Engineering Dept.
Columbia, MO 65201
314-882-8373

James R. Palmer
COMCARO
1417 North Norma
Ridgecrest, CA 93555
619-446-4511

Deborah Partlow
Westinghouse R&D Center
1310 Beulah Rd.
Pittsburgh, PA 15235
412-256-1836

W. D. Partlow
Westinghouse R&D Center
1310 Beulah Rd.
Pittsburgh, PA 15235
412-256-1632

David Payne
Particle Measuring Systems
1855 S. 57th Court
Boulder, CO 80301
303-443-7100

W. K. Pendleton
Air Force Weapons Lab.
Office of Chief Scientist
Kirtland AFB, NM 87117
505-844-9856

Adrei Petelin
Fusion Systems
12140 Park Lawn Drive
Rockville, MD
301-881-5400

Robert Poirier
M/S 420
The Perkin-Elmer Corp.
77 Danbury Rd.
Wilton, CT 06897
203-834-4934

James O. Porteus
Naval Weapons Center
Code 3816
China Lake, CA 93555
619-939-3827

Kopel Rabinovitch
Electro Optics Industries, Ltd.
P.O. Box 1165
Rehovot 76110
Israel

Frank Rainer
Lawrence Livermore Nat'l. Lab.
P.O. Box 5508, L-490
Livermore, CA 94550
415-422-4376

John H. L. Ranson
Pilkington P. E.
Glascoed Road
St. Asaph
Clwyd Wales
United Kingdom
0745-583301

Herman Reedy
Two-Six Incorporated
Saxonburg Blvd.
Saxonburg, PA 16056
412-352-1504

Stanley J. Refermat
Eastman Kodak Company
901 Elmgrove Road
Rochester, NY 14650
716-724-5426

Aloyce Rholl
Honeywell Systems & Research Center
2600 Ridgeway Pkwy
Minneapolis, MN 55440
612-378-4519

Andrew Romberger
Frank J. Seiler Res. Lab.
USAF Academy
FJSRL/NH
USAF Academy, CO 80840
303-472-3122

J. Earl Rudisill
Laser Power Optics
11211 Sorrento Valley Rd.
San Diego, CA 92121
619-455-0751

Roger L. Rypma
Boeing Military Airplane Co.
220 Wynn Dr.
Mail Stop JW-51
Huntsville, AL 35805
205-532-8379

Ted T. Saito
E. J. Seiler Res. Lab.
FJSRL/CC
USAF Academy, CO 80840
303-472-3120

Paul Schall
M2/321
Aerospace Corp.
P.O. Box 920957
Los Angeles, CA 90009
213-648-7502

Ansgar Schmid
Laboratory for Laser Energetics
Univ. of Rochester
250 East River Road
Rochester, NY 14623
716-275-3541

Elliot R. Schulman
United Technologies Research Center
Silver Lane
East Hartford, CT 06108
203-727-7179

Marion L. Scott
R&D Associates
ATO 9377
Albuquerque, NM
505-844-8446

Ronald M. Sega
Univ. of Colorado at
Colorado Springs
Dept. of Elect. Engineering
Colorado Springs, CO 80933-7150
303-593-3510

S. C. Seitel
U.S. Naval Weapons Center
Code 3817
China Lake, CA 93555
619-939-3049

Alan A. Shaffer
Dept. of Chemistry
USAF Academy
Colorado Springs, CO 80840
303-472-3240

C. Y. She
Physics Dept.
Colorado State Univ.
Fort Collins, CO 80523
303-491-6261

Jeffrey B. Shellan
W. J. Schafer
22222 Sherman Way #205
Canoga Park, CA 91303
213-704-1455

Keith R. Shillito
USAF
AFWL/ARAO
Kirtland AFB, NM 87117
505-844-1776

Ken Siegenthaler
F. J. Seiler Research Lab.
FJSRL/NA
USAFA, CO 80840
303-472-3122

Wilbert Siekhause
Lawrence Livermore National Lab.
P.O. Box 8081 MS-L311
Livermore, CA 94550

Robert M. Silva
VTI, Inc.
4126 Linden Ave., Suite 102
Dayton, OH 45432
513-254-6201

Meyer Silver
TRW
One Space Park
Redondo Beach, CA 90278
213-535-8252

Robert A. Simms
Litton Industries
1215 So Sz St.
Tempe, AZ 85281

James R. Sites
Physics Dept.
Colorado State University
Fort Collins, CO 80523
303-491-5850

Philip Slobodsky
Electro Optics Industries, Ltd.
P.O. Box 1165
Rehovot 76110
Israel

M. J. Smith
Avco Everett Research Lab.
2385 Revere Beach Parkway
Everett, MA 02149
617-381-4697

Bob Soales
CVI Laser
200 Dorado Pl. SE
Albuquerque, NM 87109
505-296-9541

M. J. Soileau
Center for Appl. Quantum Elect.
North Texas State University
P.O. Box 5368
Denton, TX 76203
817-565-3263

William H. Southwell
Rockwell Science Center
1049 Camino Dos Rios
Thousand Oaks, CA 91360
805-498-4545

Mike C. Staggs
Lawrence Livermore National Lab.
P.O. Box 5508, L-490
Livermore, CA 94550

Dennis W. Stevens
General Dynamics
Convair Div.
P.O. Box 85357
San Diego, CA 92138
619-573-4376

Alan F. Stewart
AFWL/ARAO
Kirtland AFB, NM 87117
505-844-7368

Charter Stinespring
Aerodyne Research Inc.
45 Manning Rd.
Billerica, MA 01821
617-663-9500

W. Kent Stowell
USAF
AFWAL/AADO-2
Wright-Patterson AFB, OH 45433
513-255-5147

Charles L. Strecker
AFWAL/MLPJ
Wright-Patterson AFB, OH 45433
513-255-3228

Orven F. Swenson
USAFA/DFP
USAF Academy
Colorado Springs, CO 80840
303-472-2601
AV259-2601

G. Bruce Taggart
BDM Corp.
7915 Jones Branch Dr.
McLain, VA 22102
703-821-4263

Raymond L. Taylor
CVD Incorporated
35 Industrial Parkway
Woburn, MA 01801
617-933-9243

Paul A. Temple
Naval Weapons Center Code 3816
China Lake, CA 93555
619-939-3247

Bruce A. Tirri
Perkin-Elmer Corporation
Optical Operations Div.
77 Danbury Rd.
Wilton, CT 008
203-834-4794

Scott J. Thomas
Los Alamos Nat'l. Lab.
P.O. Box 1663, MS J566
Los Alamos, NM 87545
505-667-6952

Gerald Titmuss
British Aerospace
Dynamics Group
Filton
Bristol BS10 GLP
United Kingdom
0272-693831, ext. 1012

John F. Turner
USAF
AFWL/ARAO
Kirtland AFB, NM 87117
505-844-1776

Trudy Tuttle Hart
Optical Coating Lab., Inc.
2789 Northpoint Parkway
Santa Rosa, CA 95401
707-525-7192

Christopher John Varney
British Aerospace PLC
Dynamics Group
EOC 267 Filton
Bristol, Avon
United Kingdom
0272-693831, ext. 1012/1014

Charmaine Vercimak
Lawrence Livermore National Lab.
P.O. Box 5508, L-490
Livermore, CA 94550

Marc von Gunten
Spectra-Physics, Inc.
Optics Div.
1250 West Middlefield Rd.
Mountain View, CA 94042-7303
415-961-2550, ext. 3008

Thomas W. Walker
USAF
AFWL/ARAO
Kirtland AFB, NM 87117
505-844-0721

Anetta J. Weber
USAF
AFWL/ARAO
Kirtland AFB, NM 87117
505-844-0721

John J. Wharton
USAF AFIT/ENP
Wright-Patterson AFB, OH 45430
513-255-4498

John Wilder
Bendix Field Engineering Corp.
Lawrence Livermore National Lab.
P.O. Box 5508-L-486
Livermore, CA 94550
415-423-3855

William E. Williams
Center for Applied Quantum Electronics
North Texas State University
P.O. Box 5368
Denton, TX 76203
817-565-3263

C. B. Willingham
Raytheon Company
Research Div.
131 Spring St.
Lexington, MA 02173
617-863-3062

G. Richard Wirtenson
Lawrence Livermore National Lab.
P.O. Box 808, L-491
Livermore, CA 94550
FTS 532-1332

Francis J. Wodarczyk
Rockwell International Science Center
1049 Camino Dos Rios
Thousand Oaks, CA 91360
805-498-4545

R. M. Wood
G.E.C. pls
G.E.C. Research Lab.
East Lane
Wembley
Middlesex
United Kingdom
01-904-1262, ext. 205

Frank Woodberry
Rocketdyne Div.
Rockwell International
6633 Canoga Ave., FA42
Canoga Park, CA 91304
213-700-4931

Guy T. Worth
Rockwell International/
Rocketdyne Div.
Albuquerque Optical Support Office
P.O. Box 5670
Kirtland AFB, NM 87185
505-846-2431

Bulent E. Yoldas
Westinghouse R & D Center
1310 Beulah Road
Pittsburgh, PA 15235
012-256-3269

☆U.S. GOVERNMENT PRINTING OFFICE: 1986-491-070/20319

NBS-114A (REV. 2-80)

U.S. DEPT. OF COMM. BIBLIOGRAPHIC DATA SHEET (See instructions)	1. PUBLICATION OR REPORT NO. NBS/SP-688	2. Performing Organ. Report No.	3. Publication Date November 1985

4. TITLE AND SUBTITLE

Laser Induced Damage in Optical Materials: 1983

5. AUTHOR(S) Editors: Harold E. Bennett (NWC), Arthur H. Guenther (AFWL), David Milam (LLNL), and Brian E. Newnam (LANL)

6. PERFORMING ORGANIZATION *(If joint or other than NBS, see instructions)*

NATIONAL BUREAU OF STANDARDS
U.S. DEPARTMENT OF COMMERCE
GAITHERSBURG, MD 20899

7. Contract/Grant No.

8. Type of Report & Period Covered

Final

9. SPONSORING ORGANIZATION NAME AND COMPLETE ADDRESS *(Street, City, State, ZIP)*

National Bureau of Standards
American Society for Testing and Materials
Office of Naval Research
Department of Energy
Defense Advanced Research Project Agency
Air Force Office of Scientific Research

10. SUPPLEMENTARY NOTES

Library of Congress Catalog Card Number 85-600630

☐ Document describes a computer program; SF-185, FIPS Software Summary, is attached.

11. ABSTRACT *(A 200-word or less factual summary of most significant information. If document includes a significant bibliography or literature survey, mention it here)*

The Fifteenth Annual Symposium on Optical Materials for High Power Lasers (Boulder Damage Symposium) was held at the National Bureau of Standards in Boulder, Colorado, Nov. 14-16, 1983. The Symposium was held under the auspices of ASTM Committee F-1, Subcommittee on Laser Standards, with the joint sponsorship of NBS, The Defense Advanced Research Project Agency, the Department of Energy, the Office of Naval Research, and the Air Force Office of Scientific Research. Approximately 200 scientists attended the Symposium, including representatives of the United Kingdom, France, Israel and West Germany. The Symposium was divided into sessions concerning Materials and Measurements, Mirrors and Surfaces, Thin Films, and finally Fundamental Mechanisms. As in previous years, the emphasis of the papers presented at the Symposium was directed toward new frontiers and new developments. Particular emphasis was given to materials for high power apparatus. The wavelength range of prime interest was from 0.6 μm to the uv region. Highlights included surface characterization, thin film-substrate boundaries, and advances in fundamental laser-matter threshold interactions and mechanisms. The scaling of damage thresholds with pulse duration, focal area, and wavelength was discussed in detail. Harold E. Bennett of the Naval Weapons Center, Arthur H. Guenther of the Air Force Weapons Laboratory, David Milam of the Lawrence Livermore National Laboratory, and Brian E. Newnam of the Los Alamos National Laboratory were co-chairmen of the Symposium.

12. KEY WORDS *(Six to twelve entries; alphabetical order; capitalize only proper names; and separate key words by semicolons)*

laser damage; laser interaction; optical components; optical fabrication; optical materials and properties; thin film coatings.

13. AVAILABILITY

☒ Unlimited

☐ For Official Distribution. Do Not Release to NTIS

☒ Order From Superintendent of Documents, U.S. Government Printing Office, Washington, D.C. 20402.

☐ Order From National Technical Information Service (NTIS), Springfield, VA. 22161

14. NO. OF PRINTED PAGES

581

15. Price